

NODYCON Conference Proceedings Series

Walter Lacarbonara
Balakumar Balachandran
Michael J. Leamy · Jun Ma
J. A. Tenreiro Machado
Gabor Stepan *Editors*


Advances in Nonlinear Dynamics

Proceedings of the Second International
Nonlinear Dynamics Conference
(NODYCON 2021), Volume 1

 Springer

NODYCON Conference Proceedings Series

Series Editor

Walter Lacarbonara , Sapienza University of Rome, Rome, Italy

The NODYCON Conference Proceedings Series presents early findings and case studies from a wide range of fundamental and applied work across multidisciplinary fields that encompass Nonlinear Dynamics. Series volumes follow the principle tracks or focus topics featured in the biennial International Nonlinear Dynamics Conference. Volumes in the series feature both well-established streams of research as well as novel areas and emerging fields of investigation.

More information about this series at <https://link.springer.com/bookseries/16666>

Walter Lacarbonara • Balakumar Balachandran
Michael J. Leamy • Jun Ma • J. A. Tenreiro Machado
Gabor Stepan
Editors


Advances in Nonlinear Dynamics


Proceedings of the Second International
Nonlinear Dynamics Conference
(NODYCON 2021), Volume 1


 Springer


Editors


Walter Lacarbonara 
Department of Structural
and Geotechnical Engineering
Sapienza University of Rome
Rome, Italy

Michael J. Leamy 
Department of Mechanical Engineering
Georgia Institute of Technology
Atlanta, GA, USA

J. A. Tenreiro Machado 
ISEP-Institute of Engineering
Polytechnic of Porto
Porto, Portugal

Balakumar Balachandran 
Department of Mechanical Engineering
University of Maryland
College Park, MD, USA

Jun Ma 
Department of Physics
Lanzhou University of Technology
Lanzhou, Gansu, China

Gabor Stepan 
Department of Applied Mechanics
Budapest University of Technology and
Economics
Budapest, Hungary

ISSN 2730-7689

ISSN 2730-7697 (electronic)

NODYCON Conference Proceedings Series

ISBN 978-3-030-81161-7

ISBN 978-3-030-81162-4 (eBook)

<https://doi.org/10.1007/978-3-030-81162-4>

© The Editor(s) (if applicable) and The Author(s), under exclusive license to Springer Nature Switzerland AG 2022

This work is subject to copyright. All rights are solely and exclusively licensed by the Publisher, whether the whole or part of the material is concerned, specifically the rights of translation, reprinting, reuse of illustrations, recitation, broadcasting, reproduction on microfilms or in any other physical way, and transmission or information storage and retrieval, electronic adaptation, computer software, or by similar or dissimilar methodology now known or hereafter developed.

The use of general descriptive names, registered names, trademarks, service marks, etc. in this publication does not imply, even in the absence of a specific statement, that such names are exempt from the relevant protective laws and regulations and therefore free for general use.

The publisher, the authors and the editors are safe to assume that the advice and information in this book are believed to be true and accurate at the date of publication. Neither the publisher nor the authors or the editors give a warranty, expressed or implied, with respect to the material contained herein or for any errors or omissions that may have been made. The publisher remains neutral with regard to jurisdictional claims in published maps and institutional affiliations.

This Springer imprint is published by the registered company Springer Nature Switzerland AG
The registered company address is: Gewerbestrasse 11, 6330 Cham, Switzerland

Preface

This volume is part of three volumes collecting the *Proceedings of the Second International Nonlinear Dynamics Conference (NODYCON 2021)* held as a virtual (online) conference, February 16–19, 2021. NODYCON was launched in 2019 to foster the tradition of the conference series originally established by Prof. Ali H. Nayfeh in 1986 at Virginia Tech, Blacksburg, VA, USA, as the Nonlinear Vibrations, Stability and Dynamics of Structures Conference. With the passing in 2017 of Prof. Nayfeh, NODYCON 2019 was organized as a collective tribute to Prof. Nayfeh. NODYCON 2019 received an extraordinary response from the community with 408 abstracts (out of 450 submissions) presented by nearly 400 participants from 68 countries.

After the successful launch of NODYCON, NODYCON 2021, originally planned to be held in Rome, was hosted as a virtual (online) conference given the uncertainties related to the COVID-19 world crisis. The online conference was creatively designed to help corroborate and cement the sense of cohesiveness and liveliness of the NODYCON community. The NODYCON 2021 online conference featured 16 keynotes and mini-keynotes of broad interest, a panel, two workshops, and 442 oral presentations covering recent advances in the rich spectrum of topics covered by *Nonlinear Dynamics*, including new frontiers and challenges. The Special Session and Panel entitled “*Complex dynamics of COVID-19: modeling, prediction and control*” offered important outlooks into the nonlinear dynamic evolution and prediction of the global disease spreading across different scales by using a variety of analysis tools and modeling approaches.

For NODYCON 2021, the Organizing Committee received 478 abstracts and, after rigorous review cycles, 442 one-page abstracts were accepted and published in the [Conference Book of Abstracts](#).

The diverse topics covered by the papers were clustered along the following four major themes to organize the technical sessions:

- A. Concepts and methods in nonlinear dynamics
- B. Nonlinear dynamics of mechanical and structural systems
- C. Nonlinear dynamics and control
- D. Recent trends in nonlinear dynamics

The authors of a selection of approximately 60 papers were invited to publish in the Special Issue of *Nonlinear Dynamics* entitled “NODYCON 2021 Second International Nonlinear Dynamics Conference.” At the same time, about 200 full papers were submitted to *Advances in Nonlinear Dynamics – Proceedings of the Second International Nonlinear Dynamics Conference (NODYCON 2021)* within the newly established *NODYCON Conference Proceedings Series*. One hundred and eighty-one papers were accepted. These papers have been collected into three volumes, which are listed below together with a sub-topical organization.

Volume 1: Nonlinear Dynamics of Structures, Systems, and Devices

- A. Fluid-structure interaction
- B. Mechanical systems and structures
- C. Computational nonlinear dynamics
- D. Analytical techniques
- E. Bifurcation and dynamic instability
- F. Rotating systems
- G. Modal interactions and energy transfer
- H. Nonsmooth systems

Volume 2: Nonlinear Dynamics and Control

- A. Nonlinear vibration control
- B. Control of nonlinear systems and synchronization
- C. Experimental dynamics
- D. System identification and SHM
- E. Multibody dynamics

Volume 3: New Trends in Nonlinear Dynamics

- A. Complex dynamics of COVID-19: modeling, prediction and control
- B. Nonlinear phenomena in bio- and eco-systems
- C. Energy harvesting
- D. MEMS/NEMS
- E. Multifunctional structures, materials and metamaterials
- F. Nonlinear waves
- G. Chaotic systems, stochasticity and uncertainty

I wish to acknowledge the work and dedication of the co-editors of the NODYCON 2021 Proceedings: Prof. Bala Balachandran (University of Maryland, College Park, USA), Prof. Michael J. Leamy (Georgia Institute of Technology, USA), Prof. Jun Ma (Lanzhou University of Technology, China), Prof. Jose Antonio Tenreiro Machado (Instituto Superior de Engenharia do Porto, Portugal), and Prof. Gabor Stepan (Budapest University of Technology and Economics, Hungary).

The success of the fully online conference NODYCON 2021 is due to the efforts, talent, energy, and enthusiasm of all researchers in the field of nonlinear dynamics who wrote, submitted, and presented their papers in a very lively way. Special praise is also deserved for the reviewers who invested significant time in reading, examining, and assessing multiple papers, thus ensuring a high standard of quality for this conference proceedings.

NODYCON 2021 Chair

Walter Lacarbonara, Rome, Italy
May 2021

Preface for Volume 1: Nonlinear Dynamics of Structures, Systems and Devices

Volume 1 of the NODYCON 2021 Proceedings is composed of 77 chapters, which are spread across the following groupings: i) fluid-structure interactions (12 papers), ii) mechanical systems and structures (16 papers), iii) computational nonlinear dynamics (13 papers), iv) analytical techniques (12 papers), v) bifurcation and dynamic instability (10 papers), vi) rotating systems (4 papers), vii) modal interactions and energy transfer (3 papers), and viii) nonsmooth systems (7 papers). Due to the cross-cutting nature of the topics, the editors acknowledge that a paper placed in one grouping could have easily been placed in another grouping as well. As one reads through these 77 contributions, one will note the use of a wide range of experimental, analytical, and numerical techniques for study of the nonlinear dynamics of a wealth of systems across different length and time scales.

In the area of nonlinear dynamics concerning fluid-structure interactions, the reader will find efforts concerning fluid flow in pipes, arteries, and relief valves (X. Wang *et al.*; H. Carpenter *et al.*; R. Orsino *et al.*; and W. Song *et al.*); on flow past heat exchangers, and dynamics due to wind loads, concerning flutter, and wake and vortex-induced vibrations (S.R. Rajidi *et al.*; K.H. Lee *et al.*; J. Viba *et al.*; R. Mondal *et al.*; M. Hollm *et al.*; L.S. Madi *et al.*); and concerning strong viscosity and damping (A. Mukhopadhyay *et al.*; A. Nuriev and A. Kamalutdinov).

In the area of mechanical systems and structures, the reader will find treatments of beams, plates, caps, arches, and shells (G. Iarriccio and F. Pellicano *et al.*; J.K.A. Pereira *et al.*; M. Shitikova and A. Krusser; X. Haoran and H. Yuda; U. Eroğlu and G. Ruta; D. Addressi *et al.*; and P. Di Re *et al.*); applications such as cranes, cable car systems, gyroscopes, and spacecraft (M. Metelski *et al.* (2 papers); C.A. Fonseca *et al.*; I. Gebrel *et al.*; A. Doroshin; B. Ma *et al.*); and normal forms, perpetual manifolds, and sensitivity analysis (A. Nasir *et al.*; F. Georgiades; Z. Cao *et al.*).

In the area of computational nonlinear dynamics, the reader will find studies concerning data-driven methods and analytical methods for fatigue crack and failure (M. Farid; S. Guth and T. Sapsis); reduced-order models (N.N. Balaji and M.R.W. Brake; Y. Shen *et al.*; K. Vlachas *et al.*); continuation methods (C. Marry *et al.*; and M. Blyth *et al.*); statistical analyses (C. Argáez *et al.*); global connections and Wendland functions (B.-W. Qin *et al.*; C. Argáez *et al.*); functionally graded

shells (L. Kurpa *et al.*); structural optimization (S. Dou); and incremental harmonic balance (S. Dou).

In the area of analytical techniques, the reader will find a diversity of efforts concerning the van der Pol, Helmholtz, self, and Duffing oscillators (F. Afzali *et al.*; E. Gourdon *et al.*; P. Udalov *et al.*; A. Dhar and I.R.P. Krishna); hybrid analytical-numerical, expansion, and symbolic methods (M.-H. Tien and K. D'Souza; A. Belyakov and A. Seyranian; P. Gomes *et al.*); supersymmetry (E. Howard *et al.*); stability analysis (L.F. Vesa *et al.*); generic canard explosions (B.-W. Qin *et al.*); non-rectification of heat (S. Carillo *et al.*); and exact solutions to polynomial semi-definite problems (L. Menini *et al.*).

In the area of bifurcation and dynamic stability, the reader will find a range of topics concerning rolling pendulum systems (K. Hedrih); fiber-reinforced polymer systems and the Ziegler column (J. C. Coaquira *et al.*; G. Franzini and C. Mazzili); rotor systems (X. Zhang *et al.*); characterization of resonances (M. Volvert and G. Kerschen); cell mapping for global attractors (X. Wang *et al.*); Neimark-Sacker bifurcation (E. Added and H. Gritli); degenerate bifurcation (A. Algaba *et al.*); stability boundaries (E. Freire *et al.*); and systems subjected to quasi-periodic excitations (K. Prabith and I.R.P. Krishna).

In the area of rotating systems, the reader will find studies on precise balancing technology (S. Zhao *et al.*); backward whirling (T. Alzarooni and M.A. AL-Shudeifat); stochastic resonances (E. Kremer); and internal resonances (B. Zhang *et al.*).

In the area of modal interactions and energy transfers, the reader will find studies concerning systems with internal resonances (G. Gobat *et al.*; A. Muralidharan and S.F. Ali) and beam impact dynamics (Y. Georgiou).

In the area of nonsmooth systems, the reader will find studies related to multi-degree-of-freedom oscillators (W. Dai and J. Yang); systems with dry friction (D. Lyu *et al.*); piecewise linear systems (H. Zhang *et al.*); nonlinear oscillators with compliant contacts (P. Kumar *et al.*); an aeroelastic system (D. Tripathi *et al.*); and stability analysis of switched systems (A. Platonov; Y. Zhou and Z. Wang).

In conclusion, this volume represents a multifaceted cross-section of recent advances in fluid-structure interactions, mechanical systems and structures, computational nonlinear dynamics, analytical techniques, bifurcation and dynamic instability, rotating systems, modal interactions and energy transfers, and nonsmooth systems. We hope that readers will benefit from the rich work portrayed here on nonlinear dynamics of structures, systems, and devices and that this work will spur and inspire new ideas and future contributions.

Co-editors of the NODYCON 2021 Proceedings

Bala Balachandran, College Park, MD, USA

Walter Lacarbonara, Rome, Italy

Michael J. Leamy, Atlanta, GA, USA

Jun Ma, Lanzhou, China

J. A. Tenreiro Machado, Porto, Portugal

Gabor Stepan, Budapest, Hungary

May 2021

Contents

Part I Fluid-Structure Interaction

Nonlinear Dynamics of Cross-flow Heat Exchanger Tube Conveying Fluid	3
Rajidi Shashidhar Reddy, Abhay Gupta, and Satyajit Panda	
Approximate Model of Flat Ribbon Vibrations in the Wind	15
Janis Viba, Grigory Panovko, Alexander Gousskov, and Martins Irbe	
Wall Shear Stress for an Aorta with Aneurysms Via Computational Fluid Dynamics	27
Xiaochen Wang, Mergen H. Ghayesh, Andrei Kotousov, Anthony C. Zander, and Peter J. Psaltis	
Effect of Nonlinear Blood Viscosity on LDL Transport and Fluid-Structure Interaction Biomechanics of a Multi-stenosis Left Circumflex Coronary Artery	39
Harry J. Carpenter, Mergen H. Ghayesh, Anthony C. Zander, and Peter J. Psaltis	
Reduced-Order Modelling of Flutter Oscillations Using Normal Forms and Scientific Machine Learning	49
K. H. Lee, D. A. W. Barton, and L. Renson	
Synchronization Study on Vortex-Induced Vibrations Using Wake Oscillator Model	65
Rik Mondal, Chandan Bose, and Sirshendu Mondal	
Effects of Strong Viscosity with Variable Fluid Properties on Falling Film Instability	75
Anandamoy Mukhopadhyay, Souradip Chattopadhyay, and Amlan K. Barua	

Nonlinear Hydrodynamic Damping of Elastic Vibrations of Beams Near a Plane Boundary 87
 Artem Nuriev and Airat Kamalutdinov

Hydrodynamic Forces Acting on Cylindrical Piles Subjected to Wind-Forced Random Nonlinear Water Waves 95
 Marten Hollm, Leo Dostal, and Robert Seifried

A 3D Nonlinear Reduced-Order Model of a Cantilevered Aspirating Pipe Under VIV 107
 Renato Maia Matarazzo Orsino, Celso Pupo Pesce, Fernando Geremias Toni, Wagner Antonio Defensor Filho, and Guilherme Rosa Franzini

3D Reduced-Order Model for an Orthotropic Stiffened Piezoelectric Cantilevered Flexible Cylinder Under VIV 119
 Leticia S. Madi, Guilherme J. Vernizzi, Celso P. Pesce, Wagner A. Defensor Fo., and Guilherme R. Franzini

Dynamics of the Fluid-Structure Coupling Model of a Direct-Acting Relief Valve 131
 Wen Song, Maolin Liao, Yanli Xin, Xiaoyong Wang, Ke Fan, and Yongdong Li

Part II Mechanical Systems and Structures

Nonlinear Dynamics of Spherical Caps..... 143
 Giovanni Iariccio and Francesco Pellicano

Exploring the Dynamics of Viscously Damped Nonlinear Oscillators via Damped Backbone Curves: A Normal Form Approach ... 155
 Ayman Nasir, Neil Sims, and David J. Wagg

Influence of Circumferential Discontinuity of an Elastic Foundation on the Nonlinear Dynamics of Cylindrical Shells with Functionally Graded Material 167
 Jonathas K. A. Pereira, Renata M. Soares, Frederico M. A. Silva, and Paulo B. Gonçalves

The Effect of Boundary Conditions on Nonlinear Vibrations of Plates on a Viscoelastic Base via the Fractional Calculus Standard Linear Solid Model 179
 Marina V. Shitikova and Anastasiya I. Krusser

Augmented Perpetual Manifolds, a Corollary: Dynamics of Natural Mechanical Systems with Eliminated Internal Forces 189
 Fotios Georgiades

Application of RFEM to Modelling Dynamics of Lattice-boom Offshore Cranes 201
 Marek Metelski, Iwona Adamiec-Wójcik, Łukasz Drag, and Stanisław Wojciech

Dynamic Models of Cranes Applied to Offshore Wind Farm Service..... 213
 Marek Metelski, Łukasz Drag, and Stanisław Wojciech

Axisymmetric Nonlinear Free Vibration of a Conductive Annular Plate Under Toroidal Magnetic Field 225
 Xu Haoran and Hu Yuda

Modelling and Analysis of Vibrations on an Aerial Cable Car System with Moving Mass..... 237
 Cesar Augusto Fonseca, Guilherme Rodrigues Sampaio, Geraldo F. de S. Rebouças, Marcelo Pereira, and Americo Cunha Jr.

Influence of Model Nonlinearities on the Dynamics of Ring-Type Gyroscopes 247
 Ibrahim F. Gebrel, Ligang Wang, and Samuel F. Asokanthan

Gravitational Dampers for Unloading Angular Momentum of Nanosatellites 257
 Anton V. Doroshin

Studies on the Liquid Sloshing and Rigid-Liquid-Flexible Coupling Dynamics of Spacecraft 267
 Bole Ma, Baozeng Yue, Yong Tang, and Jiarui Yu

Direct Sensitivity Analysis of Dynamic Responses for Nonlinear Structure 281
 Zhifu Cao, Qingguo Fei, Dong Jiang, Rakesh K. Kapania, Hui Jin, and Rui Zhu

Perturbations for Non-Local Elastic Vibration of Circular Arches 291
 Ugurcan Eroglu and Giuseppe Ruta

Two-Scale Curved Beam Model for Dynamic Analysis of Masonry Arches 303
 Daniela Addessi, Paolo Di Re, Cristina Gatta, and Mariacarla Nocera

Enriched Vlasov Beam Model for Nonlinear Dynamic Analysis of Thin-Walled Structures 315
 Paolo Di Re, Daniela Addessi, and Cristina Gatta

Part III Computational Nonlinear Dynamics

Nonlinear Modal Analysis Through the Generalization of the Eigenvalue Problem: Applications for Dissipative Dynamics 329
 Nidish Narayanaa Balaji and Matthew R. W. Brake

Continuation-Based Design of Self-Contacting Soft Robotic Manipulators	341
Christopher Marry, Harry Dankowicz, and Girish Krishnan	
Bayesian Local Surrogate Models for the Control-Based Continuation of Multiple-Timescale Systems	351
Mark Blyth, Lucia Marucci, and Ludovic Renson	
Predicting the Type of Nonlinearity of Shallow Spherical Shells: Comparison of Direct Normal Form with Modal Derivatives	361
Yichang Shen, Nassim Kesmia, Cyril Touzé, Alessandra Vizzaccaro, Loïc Salles, and Olivier Thomas	
Parametric Model Order Reduction for Localized Nonlinear Feature Inclusion	373
Konstantinos Vlachas, Konstantinos Tatsis, Konstantinos Agathos, Adam R. Brink, Dane Quinn, and Eleni Chatzi	
Nonlinear Vibration of Functionally Graded Shallow Shells Resting on Elastic Foundations	385
Lidiya Kurpa, Tetyana Shmatko, and Jan Awrejcewicz	
High-Order Approximation of Global Connections in Planar Systems with the Nonlinear Time Transformation Method	395
Bo-Wei Qin, Kwok-Wai Chung, Antonio Algaba, and Alejandro J. Rodríguez-Luis	
Analytic Methods for Estimating the Effects of Stochastic Intermittent Loading on Fatigue-Crack Nucleation	407
Stephen Guth and Themistoklis Sapsis	
Data-Driven Method for Real-Time Prediction of Fatigue Failure Under Stochastic Loading	421
Maor Farid	
An Improved Formulation for Structural Optimization of Nonlinear Dynamic Response	433
Suguang Dou	
An Improved Tensorial Implementation of the Incremental Harmonic Balance Method for Frequency-Domain Stability Analysis	443
Suguang Dou	
Statistical Analysis of an Iterative Algorithm Class for Dynamical Systems	453
Carlos Argáez, Peter Giesl, and Sigurdur Freyr Hafstein	
WendlandXool: Simplified C++ Code to Compute Wendland Functions ..	465
Carlos Argáez, Peter Giesl, and Sigurdur Freyr Hafstein	

Part IV Analytical Techniques

Resonances of a Forced van der Pol Equation with Parametric Damping 477
 Fatemeh Afzali, Ehsan Kharazmi, and Brian F. Feeny

Analysis of General Piecewise-Linear Non-Smooth Systems Using a Hybrid Analytical-Numeric Computational Method 489
 Meng-Hsuan Tien and Kiran D’Souza

Analytical Approximation of Forced Oscillations of Nonlinear Helmholtz Resonator by Homotopy Analysis Method 503
 Emmanuel Gourdon, Alireza Ture Savadkoochi, and Claude-Henri Lamarque

Nonlinear Aspects of One-dimensional Supersymmetry 515
 Eric Howard, Iftekher S. Chowdhury, Ian Nagle

Global Stability Analysis of An Unemployment Model with Two Distributed Time Delays 525
 Loredana Flavia Vesa, Eva Kaslik, and Mihaela Neamțu

Estimating Generic Canard Explosions via Efficient Symbolic Computation 537
 Bo-Wei Qin, Kwok-Wai Chung, Antonio Algaba, and Alejandro J. Rodríguez-Luis

A Study of the Self-Oscillating Regime in the Problem of an Atomic Force Microscope in the Contact Mode 549
 Pavel Udalov, Ivan Popov, and Alexey Lukin

Non-Rectification of Heat in Graded Si-Ge Alloys 563
 S. Carillo, M. G. Naso, E. Vuk, and F. Zullo

Expansion of Evolution Matrix and Lyapunov Exponents with Respect to Parameters 575
 Anton O. Belyakov and Alexander P. Seyranian

Classification of a Family of Lorenz Knots with Reducible Symbolic Sequences 585
 P. Gomes, N. Franco, and L. Silva

An Algorithm to Determine the Exact Solution to Polynomial Semi-Definite Problems: Application to Structural Optimization 597
 Laura Menini, Corrado Possieri, and Antonio Tornambe

Semi-Analytical Approaches for Solving Duffing Oscillator with Multi-Frequency Excitation 609
 Aalokeparno Dhar, I. R. Praveen Krishna

Part V Bifurcation and Dynamic Instability

Bifurcation and Triggers of Coupled Singularities in the Dynamics of Generalized Rolling Pendulums..... 625
 Katica R. (Stevanović) Hedrih

Parametric Instability and Bifurcation of Thin-Walled Axially Compressed Long FRP Columns..... 637
 Julio C. Coaquira, Daniel C. T. Cardoso, Paulo B. Gonçalves, and Diego Orlando

Analysis of Nonlinear Behaviors in Active Magnetic Bearing-Rotor System 649
 Xiaoshen Zhang, Zhe Sun, Wolfgang Seemann, Lei Zhao, Zhao Jingjing, and Zhengang Shi

Characterizing Fundamental, Superharmonic, and Subharmonic Resonances Using Phase Resonance Nonlinear Modes 661
 Martin Volvert and Gaëtan Kerschen

An Adaptive Sub-Cells Interpolation Method to Enhance Computational Efficiency for Global Attractors of Nonlinear Dynamical Systems..... 673
 Xi Wang, Jun Jiang, and Ling Hong

Birth of the Neimark–Sacker Bifurcation for the Passive Compass-Gait Walker 683
 Essia Added and Hassène Gritli

A Degenerate Double-Zero Bifurcation in a Normal form of Lorenz’s Equations 699
 Antonio Algaba, M. Cinta Domínguez-Moreno, Manuel Merino, Alejandro J. Rodríguez-Luis

Numerical Studies on the Nonlinear Dynamics of the Ziegler Column under Pulsating Follower Force 711
 Guilherme Rosa Franzini and Carlos Eduardo Nigro Mazilli

Hidden Regularity of Stability Boundaries in Two-step Hill’s Equations 723
 Emilio Freire, Manuel Ordóñez, Enrique Ponce

Bifurcation Studies of a Nonlinear Mechanical System Subjected to Multi-Frequency-Quasi-Periodic Excitations..... 735
 K. Prabith and I. R. Praveen Krishna

Part VI Rotating Systems

A Novel Balancing Method of the Rotor System Using Load Identification and FIR Filter-Based Force Estimation Technique 749
 Shibo Zhao, Xingmin Ren, Kuan Lu, Yongfeng Yang, Lihui Li, and Chao Fu

Post-Resonance Backward Whirl Analysis of Accelerating Cracked Overhung Rotor System Using Fatigue Crack Model..... 761
 Tariq Alzarooni and Mohammad A. AL-Shudeifat

Stochastic Resonances and Antiresonances in Rotating Mechanisms..... 771
 Eugen Kremer

Internal Resonances of a Rotating Pre-deformed Blade Under a Harmonic Gas Pressure 783
 Bo Zhang, Hu Ding, and Li-Qun Chen

Part VII Modal Interactions and Energy Transfer

Investigation of Quasi-Periodic Solutions in Nonlinear Oscillators Featuring Internal Resonance 797
 Giorgio Gobat, Attilio Frangi, Cyril Touzé, Louis Guillot, and Bruno Cochelin

Theoretical Investigations on an Internally Resonant Piezoelectric Energy Harvester 807
 Aravindan Muralidharan and Shaikh Faruque Ali

On Learning the Impact Dynamics of a Physical Beam Structure Coupled to a Multi-Stable Continuum..... 817
 Ioannis T. Georgiou

Part VIII Non-smooth Systems

Vibration Analysis of a Multi-DOF Impact Oscillator with Multiple Motion Constraints..... 831
 Wei Dai and Jian Yang

Design of NARX Model for Dry Friction System of the Three-Piece Bogie..... 841
 Dali Lyu, Qichang Zhang, and Shuying Hao

A Generalized Solution Scheme Using an Implicit Time Integrator for Piecewise Linear and Nonlinear Systems..... 853
 Huimin Zhang, Runsen Zhang, Andrea Zaroni, and Pierangelo Masarati

Dynamics of Discontinuous Nonlinear Oscillators with Compliant Contacts Subjected to Combined Harmonic and Random Loadings 865
 Pankaj Kumar, S. Narayanan, and Sayan Gupta

Response Analysis of Coupled Non-Smooth Nonlinear Aeroelastic System Subjected to Stochastic Input Fluctuations 877
Dheeraj Tripathi, Sai Vishal, Chandan Bose, and J Venkatramani

Stability Analysis for a Class of Non-Stationary Impulsive Switched Systems..... 887
Alexey Platonov

State-Dependent Switching Law for Stabilization to a Switched Time-Delay System with Two Unstable Subsystems 899
Yusheng Zhou and Zaihua Wang

Index..... 913

Part I
Fluid-Structure Interaction

Nonlinear Dynamics of Cross-flow Heat Exchanger Tube Conveying Fluid



Rajidi Shashidhar Reddy, Abhay Gupta, and Satyajit Panda

1 Introduction

The flow-induced vibration (FIV) is regarded as major problem in the heat exchangers (HE) of power plants, petroleum refineries, chemical plants, nuclear reactors, etc. A typical cross-flow HE transfers the heat between an internal fluid flowing through the tubes and an external fluid flowing across the tubes. The high flow velocities from the requirement of maximum and efficient heat transfer rate cause different kinds of instabilities in the slender flexible HE tubes leading to tube-to-support and tube-to-tube impact vibrations in HE array that induces the fretting failure of tubes affecting production, economy and human safety. Thus, a large amount of research had been conducted to study FIV of the tubes due to external [1, 2] and internal flows [3].

The external cross-flow mainly causes fluidelastic instability (FEI) in the tube beyond a critical flow velocity inducing the flutter of tubes [4]. A good number of theoretical and experimental works have been conducted in the literature to understand the mechanism of FEI and to develop an accurate model [5, 6] to analyse the same. These studies revealed that at low mass damping parameters, FEI arises through negative fluid damping [6] from the tube to surrounding fluid interaction. Whereas for the high mass damping parameters, FEI appears through the fluidelastic-stiffness-type mechanism from tube to neighbouring tubes and fluid interaction. Consequently, it was showed that at low mass damping parameters, one flexible tube in an array of rigid tubes undergoes FEI at an approximately same flow velocity as an array of flexible tubes [6] and valid mainly for the rotated triangular and in-line square array geometries [7, 8]. Hence, many works have been conducted

R. S. Reddy (✉) · A. Gupta · S. Panda
Indian Institute of Technology Guwahati, Guwahati, Assam, India
e-mail: rsreddy@iitg.ac.in

on the dynamics of a single flexible tube in an array of rigid tubes [4, 8–15] to study the effect of geometrical nonlinearity [14], axial loading [9, 14], tube-support impact [3, 9, 15], wear and fatigue, etc.

Apart from the studies of FEI due to external flow, there exists a substantial literature on the FIV of the tubes conveying fluid. The steady internal flow mainly causes divergence in the tube with supported ends and flutter in the cantilever tube [3]. In most of the engineering applications, the fluid flow in a tube becomes pulsatile due to the bends, valves, change of cross-sections, pumps, etc. in the piping networks. This pulsatile flow mainly causes parametric resonance/instability [16] such as primary, secondary, combinatory resonances resulting in the oscillatory motion of the tube. In all of these resonances, the principal primary parametric resonance is the most critical one and appears at the pulsatile flow excitation frequency of twice the natural frequency of the tube [16]. A significant amount of literature is available on the study of parametric instability regions and the corresponding nonlinear dynamics of the tube conveying pulsatile flow [3, 17, 18].

According to the knowledge of authors, in most of the theoretical and experimental studies related to the instability of the heat exchanger tubes, the effect of internal flow is omitted. A recent experimental study [19] considering the cross-flow turbulence excitation and internal steady flow revealed a rise in amplitude of vibration of the tube due to the increased mass of the system. Thus, it may be important for the design of HE array to consider the effect of internal flow as the dynamics may significantly vary due to the presence of aforesaid kinds of instability. Therefore, the authors are intended to study the effect of internal steady/pulsatile flow of the fluid on the nonlinear dynamics of heat exchanger tube under FEI and the same is presented in the following sections.

2 System Model and Governing Equation of Motion

A schematic diagram of fluid conveying heat exchanger tube of an inline square array subjected to an external cross-flow is shown in Fig. 1. The pinned supports are considered at the ends of the tubes. According to Euler-Bernoulli beam theory and plug-flow model, the governing differential equation of motion of tube conveying pulsatile flow while considering the geometric stretching nonlinearity due to its transverse deflection ($w(x, t)$) can be given as [16, 20, 21],

$$\begin{aligned} & (m_f + m_p) \ddot{w} + E^* I \dot{w}'''' + 2m_f U \dot{w}' + EI w'''' + \left[m_f U^2 + m_f \dot{U} (L - x) \right. \\ & \left. - (EA/2L) \int_0^L (w')^2 dx - (E^* A/L) \int_0^L w' \dot{w}' dx \right] w'' = F_{\text{ext}}, \\ & m_f = (\pi/4) \rho_f D_i^2, \quad m_p = \rho_p A, \quad A = (\pi/4) (D_o^2 - D_i^2), \quad I = (\pi/64) (D_o^4 - D_i^4) \end{aligned} \quad (1)$$

where ρ_f and ρ_p are densities of internal fluid and tube, respectively; F_{ext} is external transverse distributed force per unit length; U is pulsatile flow velocity of the

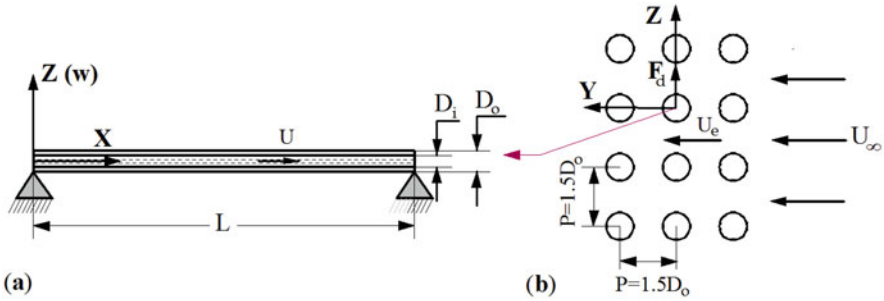


Fig. 1 Schematic diagram of (a) a simply supported flexible fluid conveying tube at the midst of (b) three-row in-line square array under cross-flow with a pitch to diameter ratio 1.5

internal fluid ($U = U_f(1 + \lambda \cos \omega t)$), where λ and ω are pulsatile velocity-amplitude and frequency respectively; D_o , D_i , and L are the outer diameter, inner diameter, length of the tube, respectively; E and E^* are Young's modulus and viscous dissipation parameter of the material of the tube, respectively.

The cross-flow is modelled with a quasi-steady model [4, 7, 9, 13, 15] that most realistically models the cross-flow over tube array based on the concept of time delay (Δt) between tube motion and fluid dynamic forces generated from its motion. It mainly uses four experimentally derived parameters accounting for the flow effects in the practical system such as drag (C_D) and lift (C_L) coefficients, time-delay parameter (μ) and added mass coefficient of external fluid (C_{ma}). Considering an external flow with low mass damping parameter (<300), the dynamic coupling of the tube with the motion of neighbouring tubes may be neglected [2]. Accordingly, the cross-flow induces a dynamic transverse distributed force on the tube (F_{ext} , Eq. (1)) that can be written [4] as,

$$F_{ext}(w, \dot{w}, \ddot{w}) = -m_e \ddot{w} - B \dot{w} + C w(x, t - \Delta t),$$

$$m_e = \frac{\pi}{4} \rho_e D_o^2 C_{ma}, \quad B = \frac{1}{2} \rho_e U_e D_o C_D, \quad C = \frac{1}{2} \rho_e U_e^2 D_o \frac{\partial C_L}{\partial w}, \quad \Delta t = \mu \frac{D_o}{U_e} \quad (2)$$

where U_e is the gap flow velocity of external fluid; ρ_e is the density of external fluid; Therefore, the nonlinear governing equation of motion of the tube conveying steady/pulsatile flow and subjected to an external cross-flow in an array can be obtained by substituting the Eq. (2) in Eq. (1) [22] as

$$(m_f + m_p + m_e) \ddot{w} + B \dot{w} - C w(x, t - \Delta t) + E^* I \dot{w}'''' + 2m_f U \dot{w}' + EI w'''' + \left[m_f U^2 + m_f \dot{U} (L - x) - (EA/2L) \int_0^L (w')^2 dx - (E^* A/L) \int_0^L w' \dot{w}' dx \right] w'' = 0 \quad (3)$$

For expressing the governing equation of motion (Eq. (3)) in the dimensionless form, the following dimensionless quantities are introduced:

$$\eta = \frac{w}{D_o}, \quad \xi = \frac{x}{L}, \quad \tau = \Omega_1 t, \quad \Omega_1 = \lambda_1^2 \sqrt{\frac{EI}{m_p L^4}}, \quad \Omega = \frac{\omega}{\Omega_1}, \quad \tilde{m} = \frac{m_p}{\rho_f D_o^2}, \quad u_e = \frac{2\pi U_e}{D_o \Omega_1},$$

$$k_c = \frac{AD_o^2}{2I\lambda_1^4}, \quad v = \left(\frac{m_f}{EI}\right)^{1/2} UL, \quad \beta_e = \frac{m_e}{m_p + m_e}, \quad \beta_f = \frac{m_f}{m_p + m_f}, \quad \alpha = \frac{\lambda_1^2 E^*}{L^2} \left(\frac{I}{E m_p}\right)^{1/2}$$
(4)

In Eq. (4), λ_1 is the dimensionless eigenvalue corresponding to the first mode of a pinned-pinned beam (i.e. $\lambda_1 = \pi$). Introducing these dimensionless quantities of Eq. (4) in Eq. (3), the dimensionless governing equation of motion can be obtained as,

$$M_1 \ddot{\eta} + C_1 \dot{\eta} + \left[K_1 v^2 + C_2 \dot{v} (1 - \xi) - k_c \int_0^1 (\eta')^2 d\xi - 2 k_c \alpha \int_0^1 \eta' \dot{\eta}' d\xi \right] \eta''$$

$$+ K_1 \eta'' + K_1 \alpha \eta'''' + 2C_2 v \dot{\eta}' - K_2 \eta (\xi, \tau - T) = 0,$$

$$M_1 = 1 + \frac{\beta_e}{1 - \beta_e} + \frac{\beta_f}{1 - \beta_f}, \quad K_1 = \frac{1}{\lambda_1^4}, \quad K_2 = \frac{u_e^2}{8\pi^2 \tilde{m}} \frac{\partial C_L}{\partial \eta}, \quad C_1 = \frac{u_e C_D}{4\pi \tilde{m}},$$

$$m_1 = \sqrt{\frac{\beta_f}{1 - \beta_f}}, \quad C_2 = \frac{m_1}{\lambda_1^2}, \quad T = \mu \frac{2\pi}{u_e}$$
(5)

The above dimensionless governing equation (Eq. (5)) is discretized using the analytical Galerkin method, where the transverse displacement is expressed in terms of eigenbasis functions (ϕ_i) and generalized coordinates (q_i) as,

$$\eta (\xi, \tau) = \sum_{i=1}^N \phi_i (\xi) q_i (\tau), \quad \phi_i = \sqrt{2} \sin (i\pi \xi)$$
(6)

Therefore, by substituting Eq. (6) into Eq. (5) and integrating within the limits of $\xi = 0$ and 1, the discretized form of the governing equation of motion can be obtained as

$$\mathbf{M} \ddot{\mathbf{q}} + \mathbf{G} \dot{\mathbf{q}} + \mathbf{K} \mathbf{q} + \mathbf{K}_\tau \mathbf{q} (\tau - T) + k_c \left(\mathbf{q}^T \mathbf{C} \mathbf{q} \right) \mathbf{C} \mathbf{q} + 2 k_c \alpha \left(\mathbf{q}^T \mathbf{C} \dot{\mathbf{q}} \right) \mathbf{C} \mathbf{q} = \mathbf{0},$$

$$\mathbf{G} = C_1 \mathbf{I} + 2C_2 v \mathbf{B} + K_1 \alpha \mathbf{A}, \quad \mathbf{K} = \left(K_1 v^2 + C_2 \dot{v} \right) \mathbf{C} - C_2 \dot{v} \mathbf{D} + K_1 \mathbf{A}, \quad \mathbf{K}_\tau = -\mathbf{K}_2 \mathbf{I}$$
(7)

where the analytical forms of the matrices \mathbf{A} , \mathbf{B} , \mathbf{C} , \mathbf{D} are given in Ref. [21]. The above set of simultaneous delay temporal differential equations (Eq. 7) are solved in MATLAB using the built-in solver 'dde23'. The solver utilizes the adaptive Runge-Kutta explicit time integration method. For the evaluation of results, the number of basis functions $N = 4$ is decided by conducting a convergence study on the evaluation of dynamic response. Whereas, an initial condition, $q_1 = 0.001$, $q_i = 0$ ($i \neq 1$), $\dot{\mathbf{q}} = \mathbf{0}$ is used for the time integration.

3 Results and Discussion

In this section, the numerical results are presented to investigate the nonlinear dynamics of a heat exchanger tube conveying steady/pulsatile flow and subjected to an external cross-flow. The geometrical parameters of the tube D_o , D_i , L are taken as 27 mm, 24 mm, 2 m, respectively. The material properties of the tube (steel) are taken as $E = 200$ GPa, $\rho_p = 7800$ kg/m³, $E^*/E = 8 \times 10^{-5}$. The internal and external fluid is considered as water with density $\rho_f = 1000$ kg/m³. The geometrical and material properties are taken such that the mass damping parameter is less than 300 [6] so that the modelling for the dynamics of a tube in a flexible heat exchanger array is valid. The Reynolds number of cross-flow (6067 (0.2 m/s)-30,337 (1 m/s)) is also considered to be very high so that the assumption of constant fluid force coefficients is valid [6, 11]. Considering the in-line square array with a pitch to diameter ratio 1.5, the experimental parameters are taken as $C_D = 0.26$, $\partial C_L/\partial \eta = -8.1$, $\mu = 1$ and $C_{ma} = 1.2$ [4, 6]. The natural frequency of the tube can be obtained as $\Omega = 1$ (112.8 rad/s) ($\beta_e = \beta_f = 0$), 0.76 ($\beta_f = 0$, $\beta_e = 0.423$), 0.82 ($\beta_f = 0.325$, $\beta_e = 0$), 0.67 ($\beta_f = 0.325$, $\beta_e = 0.423$). Reduced velocity and Reynolds number of the internal flow for $U_f = 5$ m/s can be obtained as 11.6 and 134,230, respectively.

In order to verify the present formulation and in-house code, bifurcation diagrams for the amplitude of flutter of HE tube under cross-flow as well as the amplitude of parametric resonant vibration of tube conveying pulsatile flow are evaluated and shown in Fig. 2. For this purpose, Eq. (7) is solved in the time domain keeping the appropriate terms related to the corresponding flows. The good agreement between the present results and the similar results available in the literature verifies the account of the influence of internal and external flows on the HE tube.

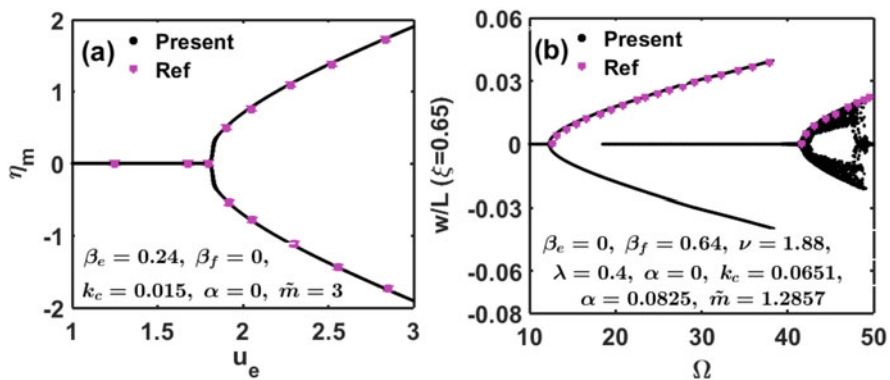


Fig. 2 Validation of bifurcations diagrams of (a) flutter amplitude of HE tube under cross-flow with Ref. [9], (b) parametric resonant amplitude of tube conveying pulsatile flow with Ref. [22]

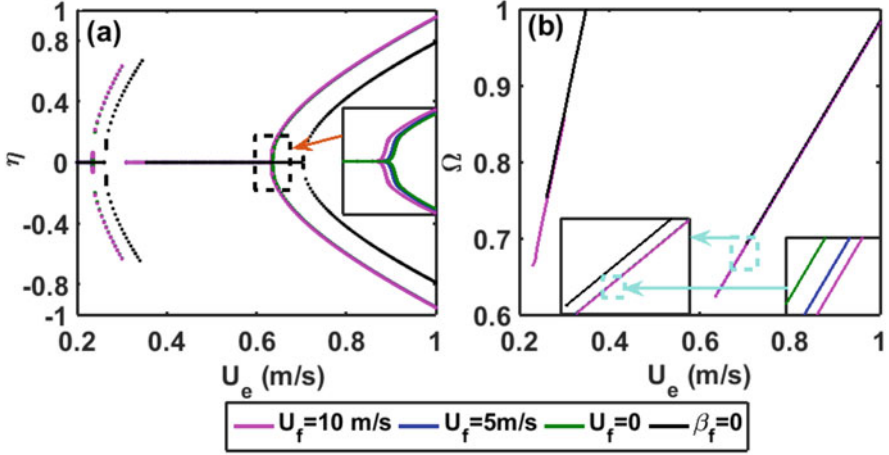


Fig. 3 (a) Bifurcation diagram for the oscillation of HE tube conveying steady flow ($\lambda = 0$) with respect to cross-flow velocity, (b) corresponding variation of frequency of oscillation

3.1 Effect of Internal Steady Flow on the Dynamics of Cross-flow HE Tube

In order to study the effect of internal steady flow ($\lambda = 0$), the bifurcation diagrams with respect to cross-flow velocity are evaluated (Fig. 3a) for the cases of only external flow ($\beta_f = 0$) and with different internal flow velocities. The corresponding flutter frequencies are depicted in Fig. 3b. The comparison of bifurcations diagrams for $\beta_f = 0$ and $U_f = 0$ clearly shows that the mass of internal fluid enhances the amplitude of periodic oscillations and reduces the critical cross-flow velocity (0.7029 m/s (C) to 0.6342 m/s (D), Fig. 3a) with a slight reduction of the oscillation frequencies. These phenomena mainly occur due to an increase in the inertia of the system because of an increase in effective mass owing to the internal fluid. However, the effect of flow velocity on the dynamics or aforesaid parameters can be seen as negligible. It may be due to a very less increase of compressive stress in the tube due to centrifugal force ($m_f U_f^2$) of internal flow.

3.2 Effect of Internal Pulsatile Flow on the Dynamics of Cross-flow HE Tube

Figure 4a–c shows the bifurcation diagrams with respect to cross-flow velocity at different pulsatile flow excitation frequencies of $\Omega = 1.2, 1.5$ and 1.8 ($\lambda = 0.4, U_f = 5$ m/s), respectively. It can be seen that quasiperiodic oscillations appear while the periodic oscillations appear in a small range of cross-flow velocities. However,

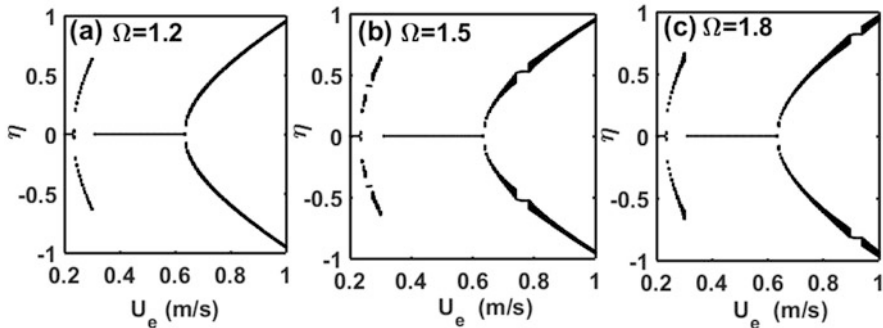


Fig. 4 Bifurcation diagrams with respect to cross-flow velocity at different pulsatile flow ($U_f = 5$ m/s, $\lambda = 0.4$) excitation frequencies of (a) $\Omega = 1.2$, (b) $\Omega = 1.5$ and (c) $\Omega = 1.8$

the cross-flow velocity range of periodic oscillations gradually shifts to the higher velocities with increasing the pulsatile flow excitation frequency. The reason may be realized from Figs. 4 and 3b, since these velocity ranges can be seen around a cross-flow velocity where the pulsatile flow excitation frequency becomes twice of the corresponding flutter frequencies (Fig. 3b). Thus, the periodic response occurs due to the parametric resonance with respect to flutter frequency while the quasi-periodic oscillations may be due to the multi-frequency excitation on the tube from the pulsatile flow as well as FEI.

For further illustration of these phenomena, the bifurcation diagrams with respect to pulsatile flow excitation frequency are shown in Fig. 5 for different cross-flow velocities along with the case of only internal flow ($\beta_e = 0$). Figure 5a shows the periodic oscillations due to the principal primary parametric resonance that appears at an excitation frequency equal to twice of the natural frequency of tube conveying steady flow ($U_f = 5$ m/s, $\lambda = 0$). With an increase in the cross-flow velocity, the parametric resonance first disappears (0.2 m/s, Fig. 5b) and then appears beyond the critical cross-flow velocity (0.635, 0.65 m/s, Fig. 5c–d) at the frequency of twice of the corresponding flutter frequencies for steady internal flow ($\Omega = 0.624, 0.639$).

To understand the characteristics of quasiperiodic response, the time histories, phase plots and frequency spectrums are studied and presented at various pulsatile flow excitation frequencies ($U_e = 0.65$ m/s, $U_f = 5$ m/s, $\lambda = 0.4$) in Fig. 6a–h. First of all, for the confirmation of quasiperiodic nature of the response, Lyapunov exponents are evaluated for the delay differential system corresponding to the parameters of Fig. 5d and the variation of first three exponents is shown in Fig. 6i. The appearance of the first two vanishing exponents dictates the existence of 2-torus quasiperiodic response, while only one vanishing exponent dictates the existence of periodic response. Figure 6c and f clearly shows the period-2 oscillations at a pulsatile flow excitation frequency equal to the twice of flutter frequency (Fig. 3b). The two sets of Figs. 6a, d, g and 6b, e, h show the quasiperiodic response at $U_e = 1.15$ and 1.25 respectively. The frequency spectrums clearly show that the flutter frequency appears as carrier frequency along with the sideband frequencies. Near

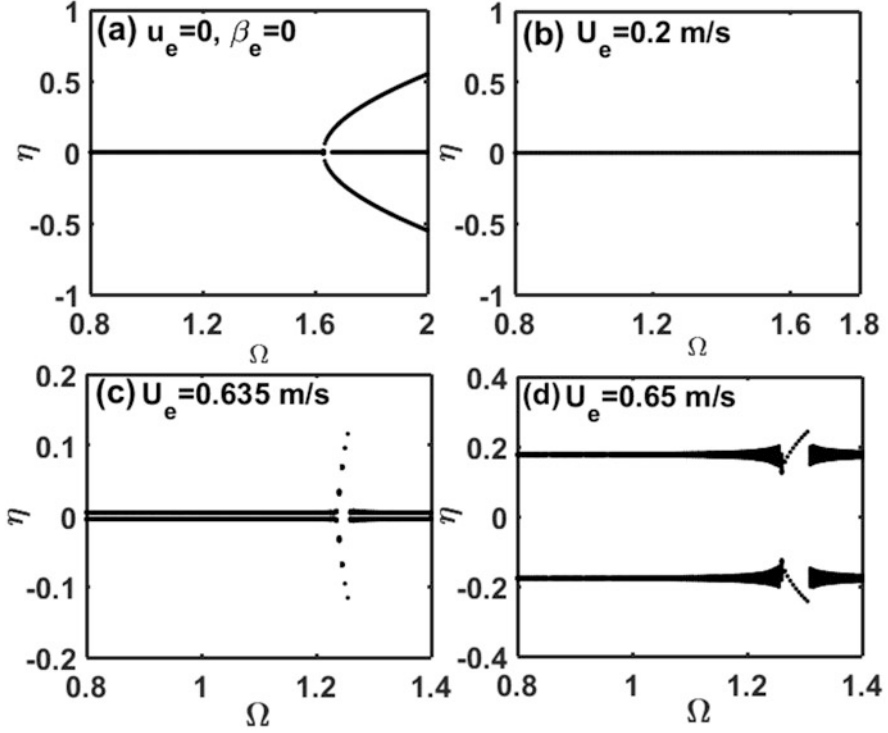


Fig. 5 Bifurcation diagrams with respect to pulsatile flow ($U_f = 5$ m/s, $\lambda = 0.4$) excitation frequency at different cross-flow velocities (a) $U_e = 0$, $\beta_e = 0$, (b) $U_e = 0.2$ m/s, (c) $U_e = 0.635$ m/s, (d) $U_e = 0.65$ m/s

the pulsatile flow excitation frequency equal to the twice of flutter frequency, the sideband frequencies gradually converge towards the carrier frequency and result in parametric resonance with period-2 oscillations.

From Fig. 5, it is observed that parametric resonance due to pulsatile flow disappears at subcritical cross-flow velocities where FEI does not appear. In order to understand the mechanism behind this behaviour, parametric instability regions are plotted in Fig. 7a for increasing cross-flow velocity from subcritical to supercritical values. It can be observed that the parametric instability regions gradually reduce and shift to higher pulsatile flow velocity-amplitudes with increasing cross-flow velocity up to certain velocity and then increases. Thus, the appearance of parametric instability can be seen ($\lambda < 0.5$) around the cross-flow velocities corresponding to FEI. It may be due to the induced damping from the time delay effect because it causes fluid forces to act in the same direction as well as opposite to the direction of motion of the tube. Generally, the out-of-phase component may introduce the damping in the system. Thus, the variation of in-phase ($K_2 \cos T$) and out-of-phase ($K_2 \sin T$) components of the fluid forces (Eq. (7)) is illustrated in Fig. 7b. Similar to

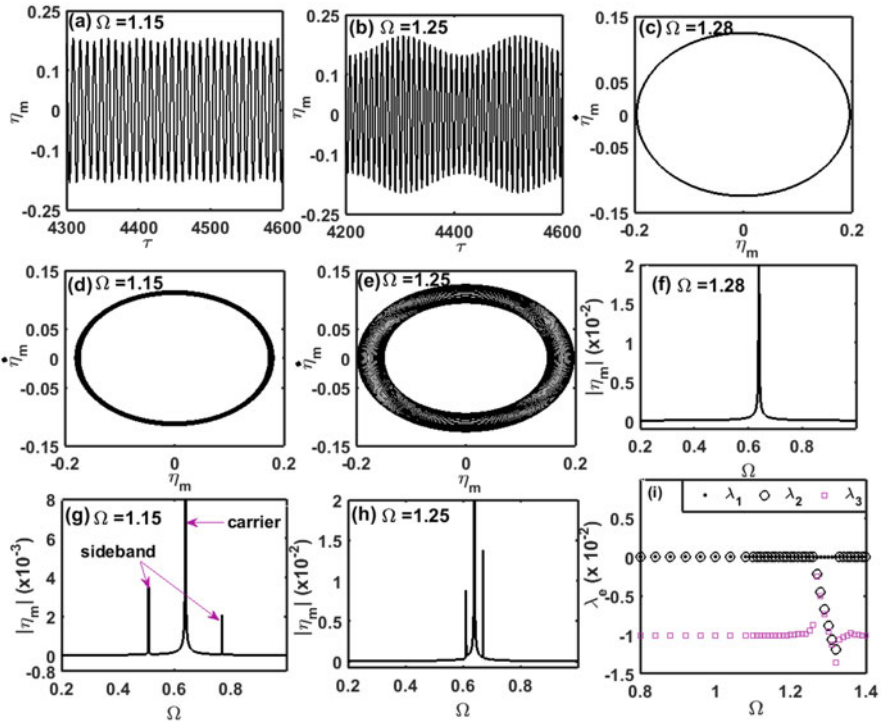


Fig. 6 Steady-state responses of HE tube ($U_f = 5$ m/s, $\lambda = 0.4$, $U_e = 0.65$ m/s): time histories at (a) $\Omega = 1.15$, (b) $\Omega = 1.25$; phase plots at (c) $\Omega = 1.28$, (d) $\Omega = 1.15$, (e) $\Omega = 1.25$, frequency spectrums at (f) $\Omega = 1.28$, (g) $\Omega = 1.15$, (h) $\Omega = 1.25$, and (i) variation of Lyapunov exponents corresponding to Fig. 4(d)

the effect on parametric instability regions, it can be observed from Fig. 7b that the out-of-phase component of fluid force increases far from the cross-flow velocities corresponding to FEI. Thus, the time delay effect may be the main reason behind the disappearance of parametric instability. Therefore, the parametric instability due to the internal pulsatile flow can be eliminated by maintaining cross-flow velocity in its subcritical range.

4 Conclusions

In this work, the nonlinear dynamics of slender heat exchanger tube of an in-line square array conveying steady/pulsatile flow and subjected to the external cross-flow is studied. The tube is modelled using Euler-Bernoulli beam theory while the plug-flow and quasi-steady models are utilized to model the internal and external flows, respectively. Following the derivation of governing delay differential equation of

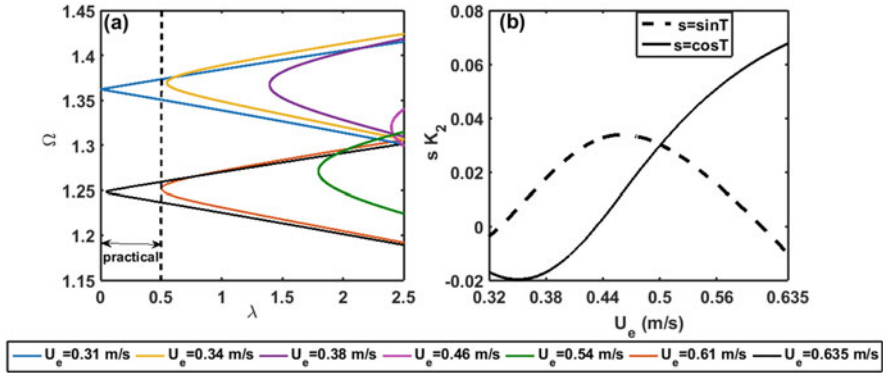


Fig. 7 Variation of (a) parametric instability regions ($U_f = 5$ m/s) with cross-flow velocity, (b) in-phase and out-of-phase components of fluid dynamic forces on the HE tube

motion, it is solved through Galerkin discretization and Runge-Kutta method time integration method. The parametric instability regions are evaluated using Bolotin's method.

The investigation on the effect of internal steady flow revealed an increase in the amplitude of periodic oscillations of the flutter of the tube but the reduction of critical cross-flow velocity and flutter frequency. Whereas these variants are very low for an increase in internal flow velocity. However, for the supercritical cross-flow velocities, the internal flow pulsation along with FEI induces 2-torus quasiperiodic oscillations instead of periodic oscillations while exhibiting an insignificant change in the oscillation amplitude. Here, the flutter frequency appears as its carrier frequency. Near the pulsation frequency equal to twice the flutter frequency, the side-band frequencies gradually converge towards the carrier frequency and result in parametric resonance with period-2 oscillations. Whereas for the subcritical cross-flow velocities, the damping phenomenon due to the time delay effect is shown to eliminate the parametric instability. This study may provide new insights into the design of heat exchangers for estimating the effect on fretting-wear due to the qualitative and quantitative changes in the response. This effect of internal flow may qualitatively remain the same even for practical heat exchangers.

References

1. R.A. Ibrahim, Mechanics of pipes conveying fluids—Part II: Applications and Fluidelastic problems. *J. Press. Vessel. Technol.* **133**, 24001-1–24001–30 (2011)
2. D.S. Weaver, A review of cross-flow induced vibrations in heat exchanger tube arrays. *J. Fluids Struct.* **2**, 73–93 (1988)
3. M.P. Paidoussis, *Fluid–Structure Interactions: Slender Structures and Axial Flow*, vol 1 (Academic Press, London, 2014)

4. M.P. Paidoussis, G.X. Li, Cross-flow-induced chaotic vibrations of heat-exchanger tubes impacting on loose supports. *J. Sound Vib.* **152**, 305–326 (1992)
5. S. Kaneko, T. Nakamura, F. Inada, M. Kato, K. Ishihara, T. Nishihara, N.W. Mureithi, M.A. Langthje, *Flow-Induced Vibrations: Classifications and Lessons from Practical Experiences: Second Edition* (Butterworth-Heinemann, 2013)
6. S.J. Price, M.P. Paidoussis, A single-flexible-cylinder analysis for the fluidelastic instability of an array of flexible cylinders in cross-flow. *J. Fluids Eng.* **108**, 193 (1986)
7. S.J. Price, B. Mark, M.P. Paidoussis, An experimental stability analysis of a single flexible cylinder positioned in an array of rigid cylinders and subject to cross-flow. *J. Press. Vessel Technol.* **108**, 62–72 (1986)
8. A. Khalifa, D. Weaver, S. Ziada, A single flexible tube in a rigid array as a model for fluidelastic instability in tube bundles. *J. Fluids Struct.* **34**, 14–32 (2012)
9. A. Sadath, V. Vinu, C.P. Vyasarayani, Vibrations of a simply supported cross flow heat exchanger tube with axial load and loose supports. *J. Comput. Nonlinear Dyn.* **12**, 051001 (2017)
10. M. Hassan, A. Mohany, Fluidelastic instability modeling of loosely supported multispan u-tubes in nuclear steam generators. *J. Press. Vessel Technol. Trans. ASME.* **135**, 11306 (2013)
11. T. Sawadogo, N. Mureithi, Fluidelastic instability study in a rotated triangular tube array subject to two-phase cross-flow. Part I: Fluid force measurements and time delay extraction. *J. Fluids Struct.* **49**, 1–15 (2014)
12. J. Lai, L. Sun, P. Li, Flow-induced instability and nonlinear dynamics of a tube array considering the effect of a clearance gap. *Nucl. Eng. Technol.* **51**, 1650–1657 (2019)
13. N.W. Mureithi, M.P. Paidoussis, S.J. Price, The post-hopf-bifurcation response of a loosely supported cylinder in an array subjected to cross-flow. Part II: Theoretical model and comparison with experiments. *J. Fluids Struct.* **8**, 853–876 (1994)
14. L. Wang, H.L. Dai, Y.Y. Han, Cross-flow-induced instability and nonlinear dynamics of cylinder arrays with consideration of initial axial load. *Nonlinear Dyn.* **67**, 1043–1051 (2012)
15. T. Jiang, P. Li, J. Ma, T. Tan, Nonlinear dynamics of a cantilevered tube with clearance constraint subject to two-phase cross-flow. *J. Sound Vib.* **459**, 114857 (2019)
16. M.P. Paidoussis, N.T. Issid, Experiments on parametric resonance of pipes containing pulsatile flow. *J. Appl. Mech.* **43**, 198–202 (1976)
17. M.P. Paidoussis, C. Sundararajan, Parametric and combination resonances of a pipe conveying pulsating fluid. *J. Appl. Mech.* **42**, 780–784 (1975)
18. A. Czerwiński, J. Łuczko, Parametric vibrations of flexible hoses excited by a pulsating fluid flow, Part II: Experimental research. *J. Fluids Struct.* **55**, 174–190 (2015)
19. K. Shahab, N. Luqman, Experimental study on cross-flow induced vibrations in heat exchanger. *China Ocean Eng.* **31**, 91–97 (2017)
20. L. Wang, A further study on the non-linear dynamics of simply supported pipes conveying pulsating fluid. *Int. J. Non. Linear. Mech.* **44**, 115–121 (2009)
21. R.S. Reddy, S. Panda, G. Natarajan, Nonlinear dynamics of functionally graded pipes conveying hot fluid. *Nonlinear Dyn.* **99**, 1989–2010 (2020)
22. J.D. Jin, Z.Y. Song, Parametric resonances of supported pipes conveying pulsating fluid. *J. Fluids Struct.* **20**, 763–783 (2005)

Approximate Model of Flat Ribbon Vibrations in the Wind



Janis Viba , Grigory Panovko , Alexander Gousov , and Martins Irbe 

1 Introduction

One of the most complex objects in the calculations of nonlinear dynamics in nature, technology and everyday life is the model of a straight flat ribbon (belt, tape and strip) (Fig. 1). The object under study consists of a flat ribbon 1, the ends of which are statically stretched in the direction of the z -axis with a force \bar{T} on the supports 2 ($Oxyz$ – a fixed coordinate system with origin in the centre of the ribbon). An additional flat element 3 is attached to the centre of the ribbon. Such a ribbon is subjected to an airflow 4 at a constant velocity \bar{V} . The direction of flow is parallel to the x -axis and directed in the plane of the original position of the ribbon. Typically, such a circuit can operate in addition to the acting gravitational forces on the oscillation-absorbing or suggestive forces generated by the limiting or electromagnetic elements.

Without stopping at the problems of mathematical simplification of the interaction between this infinite degree of airflow (∞ DOF) and solids (6DOF), we note that the 3DOF system will be further analysed. In this system, generalized coordinates are two centre C translational motions (parallel to the x and y axes) and rotational motion at an angle φ around the axis parallel to the z axis (Fig. 1b).

J. Viba · M. Irbe (✉)
Riga Technical University, Riga, Latvia
e-mail: martins.irbe@rtu.lv

G. Panovko
Mechanical Engineering Research Institute of Russian Academy of Sciences, Moscow, Russia

A. Gousov
Mechanical Engineering Research Institute of Russian Academy of Sciences, Moscow, Russia
Bauman Moscow State Technical University, Moscow, Russia

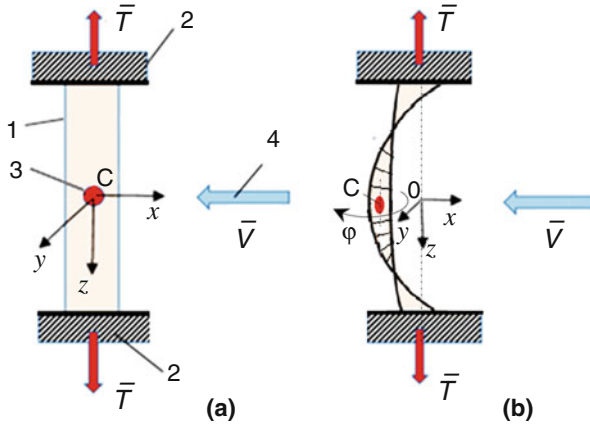


Fig. 1 Model of straight flat ribbon in the initial (a) and deformed (b) states

Long-term scientific research has shown theoretically and experimentally that placing the ribbon parallel to the wind flow causes flow-induced forced oscillations. Scientific research has adopted such a fluctuation system as a “flutter”. In addition, these interactions and stationary, sometimes irregular oscillations can be used to generate energy in a micro generator [1–7]. In this case, the system becomes more complicated, because the magnetic element of the electrodynamic generator must be attached to the ribbon.

For example, experimental studies for the change of the angle of attack (turning angle φ , 1DOF) are given in [1]. In this work, experimental apparatus is developed to study the effects of parameters such as wind speed, position and size of the magnets, pre-applied tension of the membrane, angle of attack of the membrane, and the direction of the generator on the output power and frequency of the wind belt. The experimental tests are carried out in a subsonic wind tunnel. Research is useful for the analysis of similar devices and for testing new theories in practice, for example, it is found out how the frequency of flutter movement depends on the flow rate in a given range.

A semi-empirical nonlinear aerodynamic model of a piezoelectric power generation device is proposed in [2]. It shows how to determine the parameters of an empirical model with a wind tunnel test. Of course, such an approach is justified by improving the given design or optimizing the parameters.

A new fundamental (non-empirical) method for approximating flutter motion in two-dimensional (2DOF) space has been developed in [3]. In this work, the Galerkin method is used to approximate the time-space model [4]. The obtained two-second order differential equations are numerically modelled. As a result, it is shown how this method can determine the boundary cycles of nonlinear dynamics and their bifurcations.

In addition, there are many other significant studies on the use of different ribbons and sensors with different properties to generate energy from flow by flapping and bending body motion [8–27].

Taking into account the previously analysed works, the following conclusions can be drawn:

1. So far, the interaction and motion of ribbon and airflow have not been fully studied even in the simplest case of cross-flow.
2. It is necessary to supplement the existing methods and develop new methods that would allow to analyse and optimize the movement of the ribbon-type system at the given criterion and constraints.
3. In parallel with the development of analytical methods, experimental studies must be carried out in wind tunnels or in nature.

2 Approximate Model

The approximate model includes a thin symmetrical rectangular plate 5 fixed to the base 6 by four stretched elastic bands 1–4 (Fig. 2). The characteristic geometrical parameters of the system are the distance between the elastic bands $2a$ and their length L , the width of the plate B and the height H (Fig. 2b). The plate has mass m and moment of inertia J_z with respect to the central z -axis, respectively. The simplified model assumes that the z -axis is vertical and thus the tensile forces of the elastic elements compensate the gravitational interaction. In the analysis of the model, the forces of two main interactions must be determined: the forces from the airflow with velocity V parallel to x axis and the forces in the elastic elements.

The model assumes that the elastic bands are stretched evenly and the initial motion conditions of the system are such that the plate moves parallel to the plane

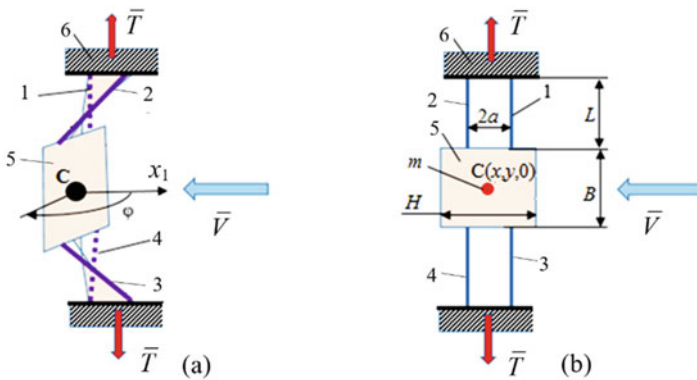


Fig. 2 Approximate model in the xyz space (a) and geometrical parameters of the system (b)

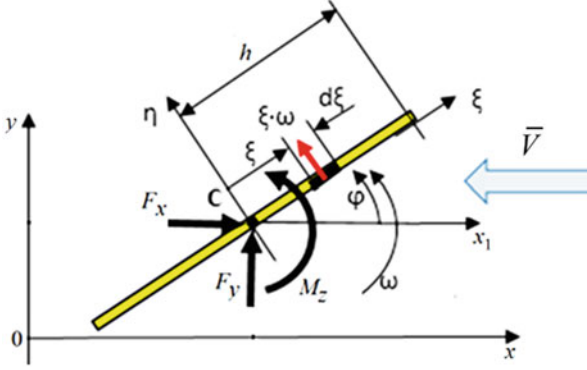


Fig. 3 Components of forces and moments in interaction with air flow

Oxy (Fig. 3). For further calculations, the moving axes $\xi C\eta$, which move together with the plate, were selected (Fig. 3).

The differential equations of motion of the simplified model as a three-degree of freedom system are as follows (Fig. 3):

$$m\ddot{x} = F_x; \quad m\ddot{y} = F_y; \quad J_c\ddot{\varphi} = M_z. \quad (1)$$

Here

$$\begin{aligned} F_{(x,y)} &= P_{e(x,y)} + P_{f(x,y)} + R_{(x,y)}; \\ M_z &= M_z(P_{e(x,y)}) + M_z(P_{f(x,y)}) + M_z(R_{(x,y)}), \end{aligned} \quad (2)$$

where m is a reduced mass; J_c is a reduced moment of inertia of the system against the z axis at the centre of mass C ; \ddot{x} , \ddot{y} , $\ddot{\varphi}$ are the second derivatives of the corresponding generalized coordinates x , y and φ at time t ; F_x , F_y and M_z are the projection of the forces acting on the system on the x , y axes and the sum of the force's moments around the central z axis; $P_{e(x,y)}$ are the components of elastic band's forces; $P_{f(x,y)}$ are the components of flow interaction's forces; $R_{(x,y)}$ are the components of damping forces, including energy generator interactions; $M_z(P_{e(x,y)}, P_{f(x,y)}, R_{(x,y)})$ are the moments of the above-described components. It is recommended to choose the main parameters of the proposed 3DOF model (for mass, moment of inertia, stiffness, etc.) by classical mechanics reduction problems.

It should be noted that in a given model, forces $R_{(x,y)}$ and moment $M_z(R_{(x,y)})$ could be of a different nature, for example, as energy generator interactions. They can be expressed as linear or nonlinear functions of generalized velocities. It will be used here in numerical modelling as next form:

$$R_{(x,y)} = \begin{Bmatrix} -b_1\dot{x} \\ -b_2\dot{y} \end{Bmatrix}; \quad M_z(R_{(x,y)}) = -b_3\dot{\varphi},$$

where b_1 , b_2 and b_3 are the constants.

For further clarity, other forces $P_{e(x,y)}$, $P_{f(x,y)}$ and moments $M_z(P_{e(x,y)})$, $M_z(P_{f(x,y)})$ are discussed in separate sections.

2.1 Airflow Interaction Forces

When determining the air interaction, the flow velocity V , parallel to the x -axis and the fact that the additional plate moves in a flat motion with the coordinates x , y and φ , must be taken into account. The theory of solving such a problem is developed in works [28, 29]. According to this theory, the principle of superposition is applied, dividing the interaction into two zones: the pressure zone and the suction zone [28]. For the determination of forces in a flat plate in the pressure zone, the projection of the absolute velocity of each point of local interaction to normal must first be found [29]. For this purpose, the vector relative rotation velocity $\xi \cdot \omega$ must be added to the local points, where ξ is a local coordinate along ξ axis, but ω is an angular velocity of plate (Fig. 4). The resulting velocity must then be projected onto the area normally and the force must be found as a function of this square of that projection. Accordingly, the interaction of the suction zone is observed by the proportionality coefficient from the interaction of the suction zone [28, 29]. The following is a closer look at this force determination procedure. According to the given 3DOF model of motion, the expression of the relative velocity of a local point in vector form is as follows (Fig. 4):

$$V_{\xi,\eta} = \left\{ \begin{array}{l} -(V + \dot{x}) \cos(\varphi) - \dot{y} \sin(\varphi) \\ (V + \dot{x}) \sin(\varphi) - \dot{y} \cos(\varphi) - \xi \omega \end{array} \right\} \cdot \left\{ \begin{array}{l} i \\ j \end{array} \right\}, \quad (3)$$

where i, j are the unit vectors for the moving coordinate axes; \dot{x} , \dot{y} and ω are the first derivatives of the respective coordinates x , y and φ at time t .

Using expression (3) we can find the normal components of the flow interaction N_f and the moment M_f as follows [28, 29]:

$$N_f = (1 + C) B \rho \left[\int_{-h}^h [(V + \dot{x}) \sin(\varphi) - \dot{y} \cos(\varphi) - \xi \omega]^2 \right] \cdot \varepsilon \cdot d\xi, \quad (4)$$

$$M_z(P_{f(x,y)}) = (1 + C) B \rho \left[\int_{-h}^h [(V + \dot{x}) \sin(\varphi) - \dot{y} \cos(\varphi) - \xi \omega]^2 \right] \cdot \xi \cdot \varepsilon \cdot d\xi. \quad (5)$$

Here

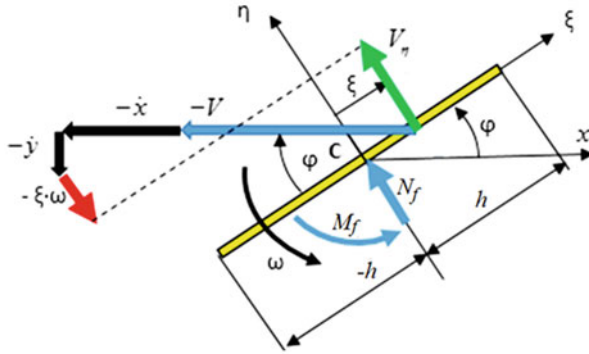


Fig. 4 Components of the relative velocity of a local point and velocity projection V_n on a normal direction

$$\varepsilon = \text{sign} [(V + \dot{x}) \sin(\varphi) - \dot{y} \cos(\varphi) - \xi \omega], \quad (6)$$

where $(1 + C)$ is a constant that describes the Drag coefficient of an object shape, for example, $C = 0,5$ [28]; B is a width of the plate; ρ is an air density; h is a half of plate height [28, 29].

Accordingly, the projections of the flow interaction forces to be placed in Eq. (2) are (7):

$$P_{f(x)} = -N_f \sin(\varphi); \quad P_{f(y)} = N_f \cos(\varphi). \quad (7)$$

Without stopping at the problems of space-time integration of expressions (2), (4), (5), and (6), we note that in numerical calculations it is possible to divide the height $2a$ of the plate into smaller areas where the value of ε can be controlled with sufficient accuracy.

2.2 Forces in the Elastic Elements

The values of the tensile forces $P_{e(1,3)}$ and $P_{e(2,4)}$ in elements 1–4 of the accepted model (see Fig. 3) in the linear case are as follows:

$$P_{e(1,3)} = c(D_{0(1,3)} - L + D_0); \quad P_{e(2,4)} = c(D_{0(2,4)} - L + D_0). \quad (8)$$

Here

$$D_{0(1,3)} = \sqrt{L^2 + [x - a(1 - \cos(\varphi))]^2 + [y + a \sin(\varphi)]^2};$$

$$D_{0(2,4)} = \sqrt{L^2 + [x + a(1 - \cos(\varphi))]^2 + [y - a \sin(\varphi)]^2};$$

where c is the stiffness, $D_{0(1,2,3,4)}$ is the elements 1–4 lengths in the given time, and D_0 is the initial tension length. The distances L, a are given in Fig. 2.

Using the expression (7) the forces $P_{e(x,y)}$ projection and moments $M(P_{e(x,y)})$ can be found in the following form:

$$\begin{aligned} P_{e(x)} &= -2c \left(P_{e(1,3)} \frac{x-a(1-\cos(\varphi))}{D_{0(1,3)}} - P_{e(2,4)} \frac{x+a(1-\cos(\varphi))}{D_{0(2,4)}} \right); \\ P_{e(y)} &= -2c \left(P_{e(1,3)} \frac{y+a \sin(\varphi)}{D_{0(1,3)}} - P_{e(2,4)} \frac{y-a \sin(\varphi)}{D_{0(2,4)}} \right); \end{aligned} \tag{9}$$

$$\begin{aligned} M(P_{e(x,y)}) &= 2c \left[P_{e(1,3)} \frac{x-a(1-\cos(\varphi))}{D_{0(1,3)}} - P_{e(2,4)} \frac{x+a(1-\cos(\varphi))}{D_{0(2,4)}} \right] a \sin(\varphi) \\ &+ 2c \left[-P_{e(1,3)} \frac{y+a \sin(\varphi)}{D_{0(1,3)}} + P_{e(2,4)} \frac{y-a \sin(\varphi)}{D_{0(2,4)}} \right] a \cos(\varphi). \end{aligned} \tag{10}$$

As before, the expressions (9) and (10) must be placed in the differential equations (2), which must then be integrated with a computer.

2.3 Results of Numerical Calculations

When analysing the numerically obtained three differential equations (1), it is necessary to understand the scope of the problem, which includes a system of nonlinear dynamics with about ten parameters (they are $C, B, D, L, V_0, c, J_z, b_1, b_2, b_3$). In addition, the result will depend on the movement of six initial conditions. Therefore, we show here only some of the modelling examples given in Figs. 5, 6, 7, and 8.

Numerical modelling was performed in the SI system at the following parameters: $V = 10; C = 0,5; B = 0,1; D = 1 \cdot 10^{-4}; L = 0,075; c = 50 \cdot 10^3; J_z = 2 \cdot 10^{-4}; m = 0,04; h = 0,02; a = 0,01; b_1 = 7; b_2 = 5; b_3 = 1 \cdot 10^{-4}$.

The results of numerical modelling show that the oscillations of the centre of mass or the flattening of the plate occur at a very high frequency (Fig. 8). This can be explained by the fact that the ribbon has a small mass at a given tensile strength.

Fig. 5 Centre of mass motion in phase plane x, \dot{x}

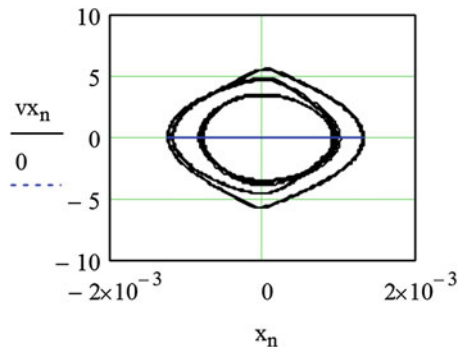


Fig. 6 Centre of mass motion in phase plane y, \dot{y}

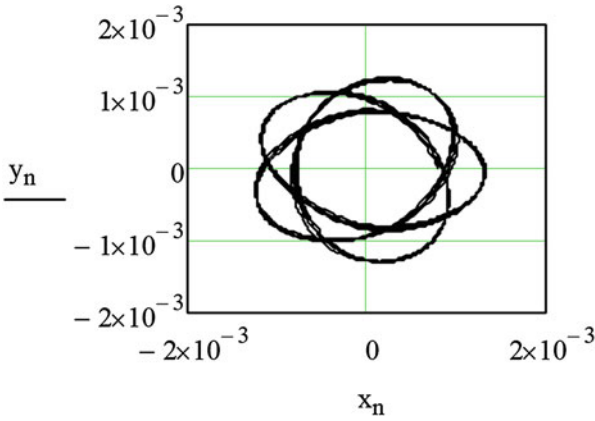
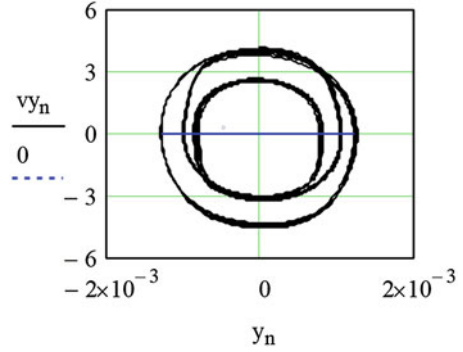
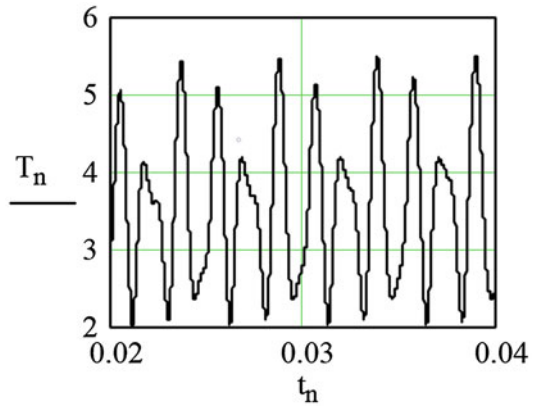


Fig. 7 Centre of mass motion in vertical plane x, y

Fig. 8 Total tensile strength T of the elastic elements, depending on the time



In addition, it should be noted that in this model in the future all aspects of the theory of nonlinear dynamics will be observed: bifurcations; strange attractors; rare modes; local and global stability calculations and others.

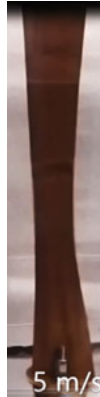


Fig. 9 Sample in a wind tunnel at a velocity V of 5 m/s

2.4 Results of Experimental Investigation

Small experiments were performed in the next Armfield wind tunnel: (Fan: downstream of the working section of airspeed between 0 and 26 m/s). Balance: Lift ≈ 7.0 N, Drag ≈ 2.5 N. Working section: 304 mm wide, 304 mm high, 457 mm long [30]. Three-dimensional tensile force sensor was used as the main vibration measuring instrument. The 3-axial force sensor ME K3D120, nominal force 500 N, accuracy class: 0.5% is used. It is connected with GSV 4USB 4-channel measurement amplifier. Sampling frequencies up to 500 Hz [31]. To illustrate the experiment, a photo and analysis of the average tensile strength T of the device are given in system SI in Figs. 9 and 10.

The experiment was performed at the following flow rates: $V = 5; 7; 9$; A ribbon with a length of 0.25 m, width 0.04 m and thickness 0.001 m was chosen, which roughly corresponded to the computer-modelling example in Fig. 8. The results obtained by the force sensor were processed digitally. The average values of the obtained ribbon tension force are shown in Fig. 10. Additional experimental results in the interpolation range $5 < V < 11$ m/s were approximated by the step function $T = 0,056 \cdot V^{1,798} + 0,506$ (Fig. 10). In addition, the result of the experiment and an example of computer modelling results at a speed of 10 m/s are analysed (Figs. 5, 6, 7, 8, and 10).

The reliability of the experiment and the theory can be described as follows:

- (a) the error of the mean deviations of the approximation curve is 4.17%;
- (b) of the approximation curve ($V = 10$ m/s) the error of the experimental deviation at this point is 7.28%;
- (c) theoretical and experimental error ($V = 10$ m/s) is 5.81%.

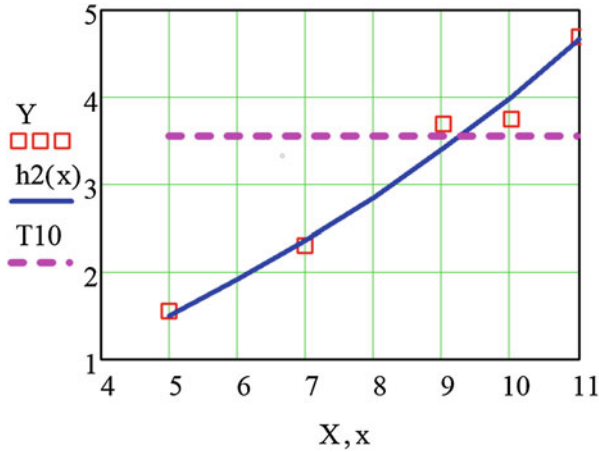


Fig. 10 Total average tensile strength T of the elastic ribbon depending on the flow velocity V : X , x – velocity; Y – experiment; $h_2(x)$ – approximation by step function; T_{10} – computer modelling results with $V = 10$ m/s (see Fig. 8)

3 Conclusions

1. A three-dimensional analytical model has been developed, which allows analysing, synthesizing and optimizing the interaction and motion of the ribbon and wind flow.
2. The main advantage of the model is that it significantly reduces the workload of solving space-time tasks by reducing the movement of a continuous environment and a flexible ribbon object to 3DOF.
3. The approximate analytical method can be applied in the analysis of vibrations of existing objects as well as in the synthesis of new mechatronic systems with application in energy extraction from airflow.
4. Subsequent numerical and experimental studies should determine how to select the main parameters of the 3DOF system, using, for example, the Galerkin method or others [4].

Acknowledgements This research is funded by the Russian Science Foundation, project No. 18-19-00708 and supported by Riga Technical University's Doctoral Grant program.

References

1. V.D. Quy, N. van Sy, D.T. Hung, V.Q. Huy, Wind tunnel and initial field tests of a micro generator powered by fluid-induced flutter. *Energy Sustain. Dev.* **33**, 75–83 (2016)
2. M. Bryant, E. Garcia, Modelling and testing of a novel aeroelastic flutter energy harvester. *J. Vib. Acoust* **133**(1), 011010 (2011)

3. A. Afanaseva, A. Gousskov, G. Panovko, Nonlinear dynamics of a thin narrow ribbon in an airflow. *Vibroeng. Proc.* **32**, 105–110 (2020)
4. Galerkin, B.G.: Rods and Plates, Series Occurring in Various Questions Concerning the Elastic Equilibrium of Rods and Plates, *Vestnik Inzhenerov i Tekhnikov*, (Engineers and Technologists Bulletin), vol. 19, pp. 897–908 (1915), (in Russian), (English Translation: 63–18925, Clearinghouse Fed. Sci. Tech. Info. (1963)
5. S. Li, J. Yuan, H. Lipson, Ambient wind energy harvesting using cross-flow fluttering. *J. Appl. Phys.* **109**(2), 026104 (2011)
6. J. Sirohi, R. Mahadik, Harvesting wind energy using a galloping piezoelectric beam. *J. Vib. Acoust.* **134**(1), 011009 (2009)
7. L. Tang, M. Paidoussis, J. Jiang, Cantilevered flexible plates in axial flow: Energy transfer and the concept of flutter-mill. *J. Sound Vib.* **326**(1–2), 263–276 (2009)
8. S. Wang et al., Flow-driven triboelectric generator for directly powering a wireless sensor node. *Adv. Mater.* **27**, 240–248 (2015)
9. X. Wang, S. Wang, Y. Yang, Z.L. Wang, Hybridized electromagnetic–triboelectric nanogenerator for scavenging air-flow energy to sustainably power temperature sensors. *ACS Nano* **9**, 4553–4562 (2015)
10. CE: J. Bae, J. Lee, S. Kim, J. Ha, B.S. Lee, Y. Park, C. Choong, J.B. Kim, Z.L. Wang, H.Y. Kim, J.J. Park, U.I. Chung, Flutter-driven triboelectrification for harvesting wind energy. *Nat. Commun.* **5**, 4929 (2014). PMID: 25247474. <https://doi.org/10.1038/ncomms5929>
11. H. Guo et al., Airflow-induced triboelectric nanogenerator as a self-powered sensor for detecting humidity and airflow rate. *ACS Appl. Mater. Interfaces* **6**, 17184–17189 (2014)
12. Y. Yang et al., Triboelectric nanogenerator for harvesting wind energy and as self-powered wind vector sensor system. *ACS Nano* **7**, 9461–9468 (2013)
13. M.J. Shelley, J. Zhang, Flapping and bending bodies interacting with fluid flows. *Annu. Rev. Fluid Mech.* **43**, 449–465 (2011)
14. L.-Q. Chen, H. Ding, Two nonlinear models of a transversely vibrating string. *Arch. Appl. Mech.* **78**, 321–328 (2008)
15. K. Taira, T. Colonius, Three-dimensional flows around low-aspect-ratio flat-plate wings at low Reynolds numbers. *J. Fluid Mech.* **623**, 187–207 (2009)
16. S. Lee et al., Super-flexible nanogenerator for energy harvesting from gentle wind and as an active deformation sensor. *Adv. Funct. Mater.* **23**, 2445–2449 (2013)
17. O. Doaré, S. Michelin, Piezoelectric coupling in energy-harvesting fluttering flexible plates: Linear stability analysis and conversion efficiency. *J. Fluid. Struct.* **27**, 1357–1375 (2011)
18. F. Fei, J.D. Mai, W.J. Li, A wind-flutter energy converter for powering wireless sensors. *Sensor. Actuat. A Phys.* **173**, 163–171 (2012)
19. J. Peng, S.G. Chen, Flow-oscillating structure interactions and the applications to propulsion and energy harvest. *Appl. Phys. Res.* **4**, 1–14 (2012)
20. R. Zhang et al., Nanogenerator as an active sensor for vortex capture and ambient wind-velocity detection. *Energy Environ. Sci.* **5**, 8528–8533 (2012)
21. S. Niu et al., Theory of sliding-mode triboelectric nanogenerators. *Adv. Mater.* **25**, 6184–6192 (2013)
22. L. Lin et al., Segmentally structured disk triboelectric nanogenerator for harvesting rotational mechanical energy. *Nano Lett.* **13**, 2916–2923 (2013)
23. G. Cheng, Z.-H. Lin, L. Lin, Z. Du, Z.L. Wang, Pulsed nanogenerator with huge instantaneous output power density. *ACS Nano* **7**, 7383–7391 (2013)
24. Y. Wang, Y. Yang, Z.L. Wang, Triboelectric nanogenerators as flexible power sources. *J. Flex Electron* **1**, 10 (2017)
25. S. Lee et al., Super-flexible nanogenerator for energy harvesting from gentle wind and as an active deformation sensor. *Adv. Funct. Mater.* **23**, 2445–2449 (2013)
26. Y. Xie et al., Rotary triboelectric nanogenerator based on a hybridized mechanism for harvesting wind energy. *ACS Nano* **7**, 7119–7125 (2013)
27. R.K. Jauman, M.K. Parmar, P.S. Gurubelli, Added mass and aeroelastic stability of a flexible plate interacting with mean flow in a confined channel. *J. Appl. Mech.* **81**(4), 041006. (9 pages).

Paper No: JAM-13-1214 (2014)

28. I. Tipans, J. Viba, M. Irbe, S.K. Vutukuru, Analysis of non-stationary flow interaction with simple form objects. *Agron. Res.* **17**(1), 1227–1234 (2019)
29. S. Koundinya, S.K. Vutukuru, I. Tipans, I. Viba, I. Martins, Form optimization and interaction analysis of plane symmetry prism in air. *Eng. Rural Dev.* **19**, 739–746 (2020)
30. <https://scientificservices.eu/item/subsonic-wind-tunnel/16>
31. <https://www.me-systeme.de/shop/en/sensors/force-sensors/k3d/k3d120/k3d120-50n9>

Wall Shear Stress for an Aorta with Aneurysms Via Computational Fluid Dynamics



Xiaochen Wang , Mergen H. Ghayesh , Andrei Kotousov , Anthony C. Zander , and Peter J. Psaltis 

1 Introduction

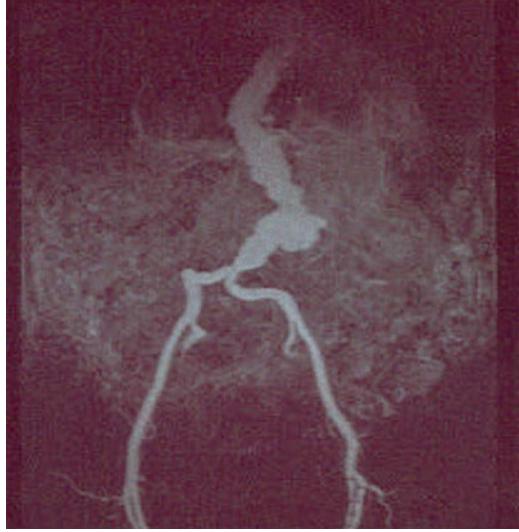
Cardiovascular diseases are considered as one of the most significant causes of death, representing nearly 31% of global annual death in 2019 [1]. Aortic aneurysms are identified as the most common aortic diseases diagnosed with high risks. Aortic aneurysm, as an abnormal condition related to aorta dilation, can lead to fatal consequences such as aortic rupture, which is considered unpredictable and generally unrecoverable [2]. Ruptures related to aortic aneurysms are usually associated with the weak regions of the aortic wall under high shear stress, and the initial estimation of the aneurysm condition is thus critical for rupture prediction in both research and medical practice fields [3]. The mortality of abdominal aortic aneurysm (AAA) is relatively high, with 15% for an AAA with dissection or rupture [4]. Figure 1 shows a gadolinium-enhanced MRI image of an abdominal aortic aneurysm. Clinical standards to diagnose the presence of an aortic aneurysm are based on whether the maximum diameter of an AAA exceeds 5.5 cm [5]. However, a number of studies stated that nearly 24% of AAAs with a smaller maximum aortic diameter (<5.5 cm) were ruptured [6]. Limitations of using only AAA maximum diameter as the only indicator to predict the rupture risk are highlighted in many studies [7]. Therefore, a better and comprehensive rupture predictor is necessary for the diagnosis of weak regions and prevention of rupture.

X. Wang · M. H. Ghayesh (✉) · A. Kotousov · A. C. Zander
School of Mechanical Engineering, University of Adelaide, Adelaide, South Australia, Australia
e-mail: mergen.ghayesh@adelaide.edu.au

P. J. Psaltis
Vascular Research Centre, Heart Health Theme, South Australian Health & Medical Research Institute (SAHMRI), Adelaide, South Australia, Australia

Department of Medicine, University of Adelaide, Adelaide, South Australia, Australia

Fig. 1 MRI of an abdominal aortic aneurysm showing tortuous aorta and iliac arteries [8]



An AAA brings lower wall mechanical resistance and hence changes to local blood pressure; a rupture in an AAA is commonly found at where the arterial wall experiences high flow-induced wall stresses [9]. Further, such shear stress can cause degradation of elastin. Also, the presence of thrombus can be observed in most of AAA walls with different composition and mechanical behaviour; all these factors would increase the wall stress [6, 9]. It has been proved that aortic expansion could lead to a low wall shear stress load, generally less than 0.4 Pa as well as intraluminal thrombus (ILT) accumulation [7]. The flow-induced damage or rupture in the blood vessel is caused due to the high shear stress or high pressure-distribution working on endothelial cells in the artery wall by blood flow. In accordance with the law of Laplace, there is also a positive correlation between the artery diameter and pressure on the inner surface of an aortic wall [10].

A computational fluid dynamics (CFD) analysis allows examinations on wall shear stress numerically to investigate nonlinear dynamics and changes in the mechanical properties of the aortic wall caused by aortic aneurysms [11]. This technique has also been employed in some other vascular diseases, including peripheral artery diseases and coronary artery diseases [12]. To establish a specific model with indicators to reveal the risk of rupture associated with an AAA, several different biomechanical parameters need to be taken into consideration, such as pulsatile blood flow, the non-Newtonian fluid, and shapes and sizes of different aneurysms, which eventually lead to the determination of shear stress distributions. Evidence showed that structural-only model without fluids underestimates the peak wall stress by 30.2% [6]. Joly et al. [9] conducted a rigid wall hypothesis validation by observing lumen segmentation in different time of the cardiac cycle, i.e., systole and diastole. The movement surface variation for patients with an AAA is 0.96%, while for a healthy patient, it is 4.41% maximum; it was concluded that a rigid wall assumption is valid for an AAA study due to the changes in arterial wall properties.

In this study, the flow-induced wall shear stress and pressure distribution inside a simplified patient-specific aorta model are obtained based on a CFD simulation. Models are developed by incorporating the following parameters: non-Newtonian blood flow, a pulsatile blood flow velocity and size and shape of aneurysm. This study aims to predict the internal pressure and wall shear stress together with physiological parameters. A model of healthy descending aorta was also built to compare the impact of the aneurysm. For all the numerical results presented in this chapter, a mesh convergence has been examined to ensure reliable and accurate results.

2 Methodology

2.1 Geometry

The geometry of virtual realistic three-dimensional models was obtained and constructed using geometrical parameters of an AAA from patient-specific geometry profile generalised by Soudah et al. [4]. Simplification retains major parameters used for describing this patient-specific model, including aneurysm length, the maximum diameter of the aneurysm, AAA proximal neck diameter, normal abdominal aorta diameter, the actual length of the AAA centreline, tortuosity index and asymmetry of the aneurysm. For a healthy aorta as a controlled case, the maximum diameter is assumed to be equal to the proximal neck diameter. Figure 2 shows the geometry of the diseased and healthy abdominal aortas under anterior view.

2.2 Boundary Conditions

The blood velocity profile used in this simulation is based on patient-specific data obtained from PC-MRI 3D blood flow velocities [13]. Based on the experimental data for the mean velocity across the descending aorta lumen within a cardiac cycle from literature, Fig. 3 is plotted based on 20 divisions using a Fourier series [13]. From the profile, it can be visualised that four stages are presented in one cardiac cycle: systolic acceleration (0.1 s), systolic peak (0.18 s), systolic deceleration (0.3 s) and diastole (0.85 s).

Another boundary condition applied is the outlet pressure; the average pressure in the AAA outlet section is around 13.332 kPa, according to patient-specific outlet pressures adopted from Refs. [4, 14].

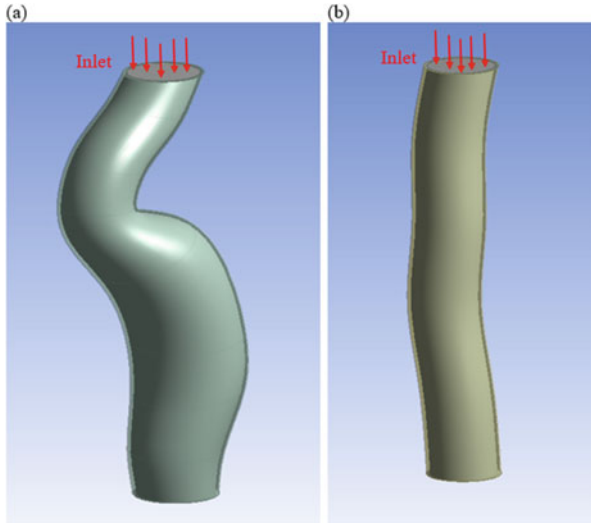


Fig. 2 Schematics of an abdominal aorta: (a) aneurysmal aorta with maximum diameter < 5.5 cm; (b) a healthy aorta with uniform aortic diameter

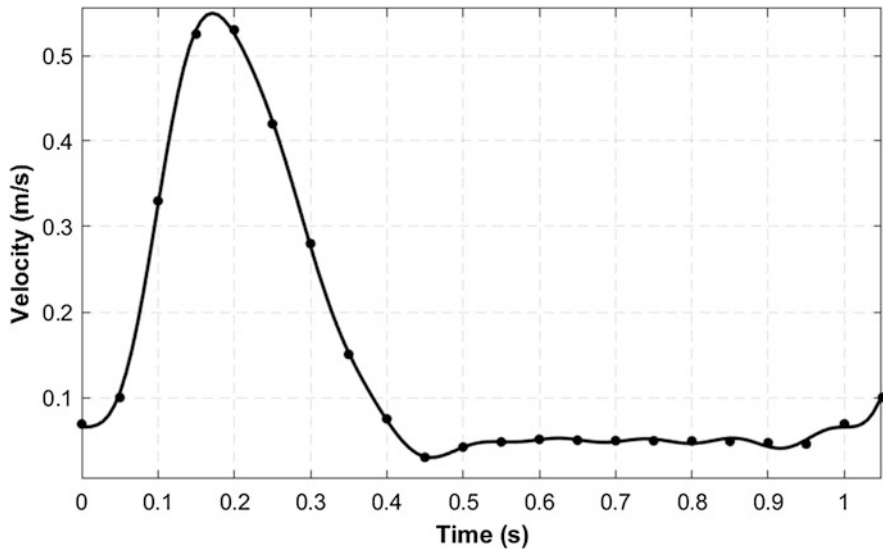


Fig. 3 Pulsatile blood flow velocity

2.3 Non-Newtonian Blood Flow Simulation

The main functions of blood flow in aorta include delivering oxygen and nutrient to the whole body. Blood flow also undertakes resistance due to the architecture of

the vascular system and behaviour of blood cells and plasma. From a macroscopic perspective, blood shows complex fluid viscosity as a non-Newtonian fluid. Several studies have reported that there are differences in wall shear stress distribution of artery when using Newtonian and non-Newtonian fluid models [15]. In this work, incompressible non-Newtonian flow is considered, and the non-Newtonian model follows Quemada model. From the literature, Quemada model was initially developed by Quemada [16, 17], and can be expressed with two major variables via

$$\mu_{\text{eff}} = \mu_p \left(1 - \alpha \frac{k(\gamma, \alpha)}{2} \right)^{-2} \quad (1)$$

$$k(\gamma, \alpha) = \frac{k_0(\alpha) + k_\infty \sqrt{\gamma/\gamma_c(\alpha)}}{1 + \sqrt{\gamma/\gamma_c(\alpha)}} \quad (2)$$

$$k_0 = e^{3.874 - 1041\alpha + 13.8\alpha^2 - 6.378\alpha^3} \quad (3)$$

$$k_\infty = e^{1.3435 - 2.803\alpha + 2.711\alpha^2 - 0.6479\alpha^3} \quad (4)$$

$$\gamma_c(\alpha) = e^{-6.1508 + 27.923\alpha - 25.6\alpha^2 + 3.679\alpha^3} \quad (5)$$

where $\alpha = 0.45$, $\mu_p = 1.32 \times 10^{-3}$ Pa•s, γ represents the magnitude of the shear stress tensor $\gamma_{ij} = (\partial u_i/\partial x_j + \partial u_j/\partial x_i)$ [18].

Application of the Quemada model includes taking into account the shear-thinning behaviour of the blood and accounts for the decrease in viscosity under shear strain. The Quemada model has been evaluated as a well-fitted model that describes the viscosity in blood rheology [18].

Governing equations for blood motions in the aorta follow the conservation of momentum and mass based on the Navier-Stokes equations for incompressible and non-Newtonian flow from Eqs. (6) and (7), solved by FLUENT (ANSYS Academic Research 2020R1) [4, 15, 18].

$$\rho_f \Delta \cdot \mathbf{v} = 0 \quad (6)$$

$$\rho_f \frac{\partial \mathbf{v}}{\partial t} + \rho_f \left((\mathbf{v} - \dot{\mathbf{d}}_f) \bullet \nabla \right) \mathbf{v} = \nabla \bullet \boldsymbol{\tau}_f + \mathbf{f}_f^B \quad (7)$$

where ρ_f is the density of the fluid, \mathbf{v} is the velocity vector, $\dot{\mathbf{d}}_f$ is the velocity vector for moving coordinates, $\boldsymbol{\tau}_f$ is the fluid stress tensor, and \mathbf{f}_f^B represents the body forces per unit volume.

3 Results and Discussion

An aortic rupture could occur mainly due to the following reasons: material property failure of the intima layer on the aneurysm or changes in blood flow caused by geometry variation associated with aneurysm [19]. In order to compare the effect of aneurysm shape and blood pulsation, an index – to analyse the wall condition and risk of rupture or dissection – is developed, which considers the aneurysmal shape, wall shear stress velocity profiles and pressure distribution. Conclusions can be drawn from the stress concentration investigation as maximum wall shear stress occurs when pulsation reaches its late systolic states, and the stress concentration changes significantly with the size of aneurysms.

3.1 Velocity Profiles

The results for velocity streamline at late systole within a cardiac cycle are significantly different. As seen in Fig. 4, for an aneurysmal aorta, a rapid decrease in the velocity in late systole stage causes blood recirculation at the aneurysm sac. This phenomenon contributes to the deposition of platelets and would cause changes

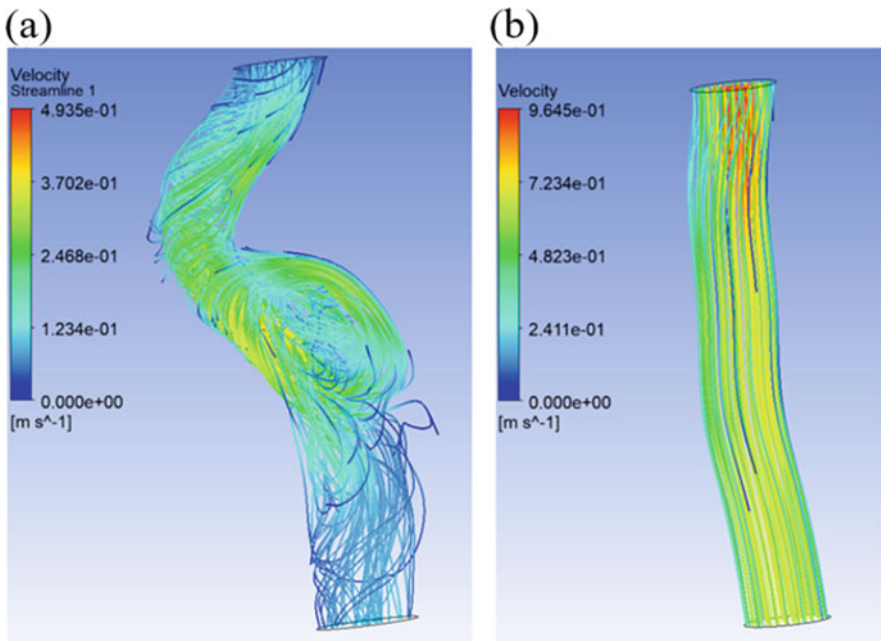


Fig. 4 The velocity distribution at late systole for (a) aneurysmal aorta and (b) healthy aorta

in the material properties of the aortic wall. The two models analysed in this study indicate that with higher tortuosity, irregular flow can be observed in diseased aorta compared with the controlled case. Two types of irregular flow can be noticed: a helix flow (in AAA neck) and a recirculation (in AAA sac). Blood recirculation is one of the major causes of ILT formation as they stimulate endothelium loss and platelet aggregation, and thus reduce the wall stiffness and cause possible rupture or dissections.

3.2 Pressure Distributions

Imbalanced flow deformation is due to the irregular shape of the aorta and the pulsatile inlet boundary condition. Thus, the imbalance flow also causes the flow recirculation in the aneurysmal sac, which would potentially accelerate the dilation and contribute to aortic dissection [4]. The enlarged sac in an aneurysmal aorta promotes the flow recirculation, and from the results of velocity profiles, the formation of vortex flow starts from late systole, and notable pressure drop would occur from the AAA sac as a result of energy losses due to helix flow and recirculation. With the flow acceleration and deceleration, there is a corresponding positive and negative pressure difference from inlet to outlet. Therefore, the dynamic vortices are developed during the deceleration period when the pressure gradient reverses. However, from Fig. 5, the maximum pressure and its variation with the

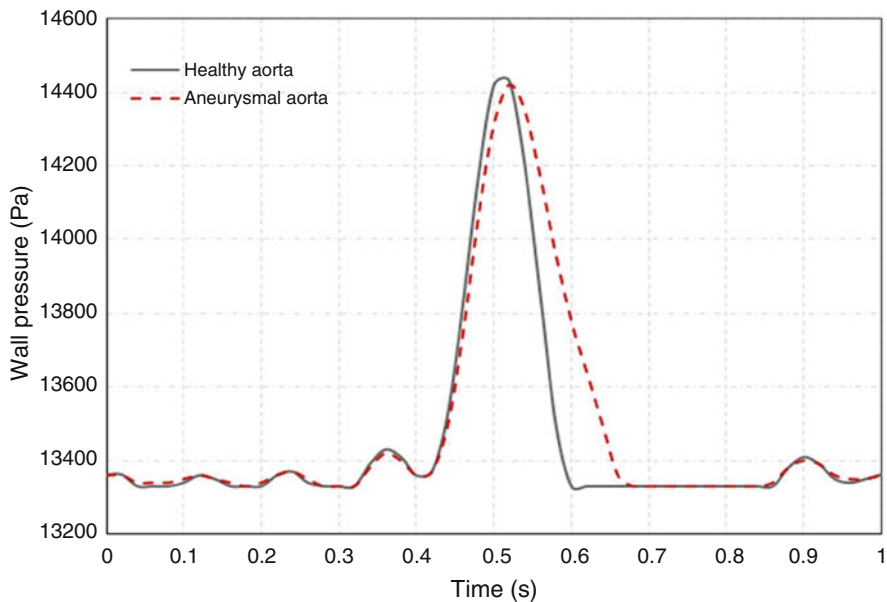


Fig. 5 Wall pressure change with time for two models of healthy and aneurysmal abdominal aortas

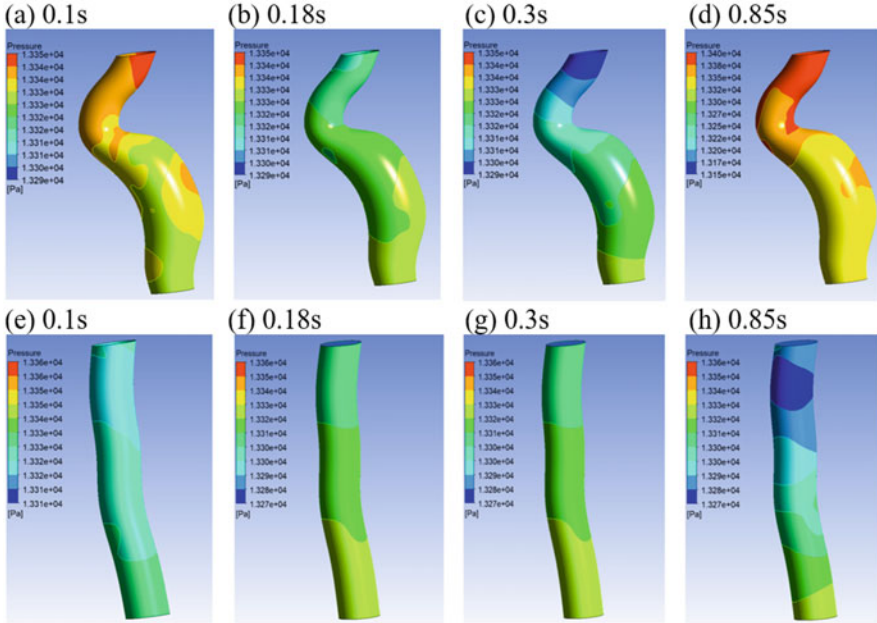


Fig. 6 Pressure distribution for aneurysmal aorta at: (a) $t = 0.1$ s; (b) $t = 0.18$ s; (c) $t = 0.3$ s; (d) $t = 0.85$ s; pressure distribution for healthy aorta at: (e) $t = 0.1$ s; (f) $t = 0.18$ s; (g) $t = 0.3$ s; (h) $t = 0.85$ s

blood pulsation do not show a significant difference. A conclusion can be drawn that the presence of the AAA makes the pressure difference during each cardiac cycle reverse and causes blood recirculation. Figure 6 visualises the pressure contours of two models at different stages, from which it can be concluded that for the aneurysmal aorta, the pressure reaches its maximum at the inlet regions in diastole, and in systole, the maximum pressure altered to the outlet region. Meanwhile, the healthy aorta always has higher pressure close to the outlet than inlet.

3.3 Wall Shear Stress

Abrupt changes in wall shear stresses are generally associated with sudden atherosclerosis in aorta geometry or narrowing in the vessel lumen [19]. The flow-induced maximum wall shear stresses for the two models are displayed in Fig. 7, from which it can be observed that the maximum wall shear stress occurs at late systole for both the models. The maximum value for the aneurysmal aorta is 16.8 Pa, while for the healthy aorta, it is 5.565 Pa. As seen in Fig. 8, the tortuosity and growing aneurysm change the stress distribution and hence lead to the initiation of rupture for sufficiently large wall shear stresses.

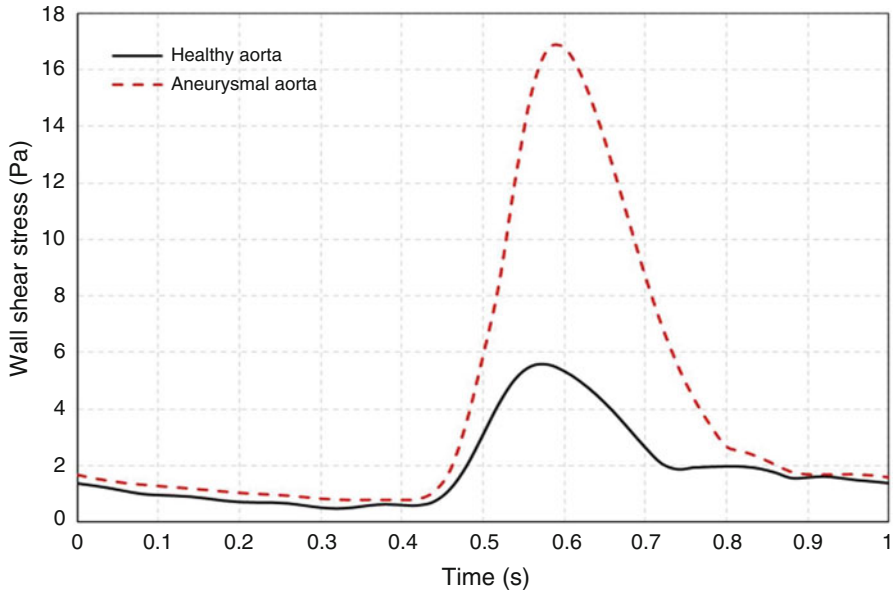


Fig. 7 Wall shear stress change in time for two models: healthy and aneurysmal abdominal aortas

The CFD models discussed in this chapter were proposed and validated with those available in the literature for simpler models. Under the same lumen geometry index, the wall internal pressure contour and the velocity across the lumen of this study have a similar maximum value patterns as those in the literature. As a summary of results, the velocity flow distribution has higher values during systole, but helicity and recirculation appear during diastole. Evidence has shown that due to the dynamic effect of the flow recirculation, the lumen wall would experience a reversed pressure gradient in each cardiac cycle, which would influence the wall stiffness. The aneurysm neck appears to have a higher risk for rupture due to the high concentration of flow-induced wall shear stress.

4 Conclusions

The study discussed in this chapter investigated the wall shear stress and pressure associated with hemodynamics in patient-specific AAA and healthy aortas under pulsatile non-Newtonian flow conditions. For both the healthy and diseased aortas, the influences of geometry and hemodynamics were examined. The following conclusions can be drawn from the results: (1) flow recirculation present in aneurysm sac region would potentially lead to the initiation of ILT; (2) tortuosity of the AAA increases the chance of potential rupture even when maximum aortic diameter is small; (3) the maximum wall shear stress occurs at the aneurysm neck;

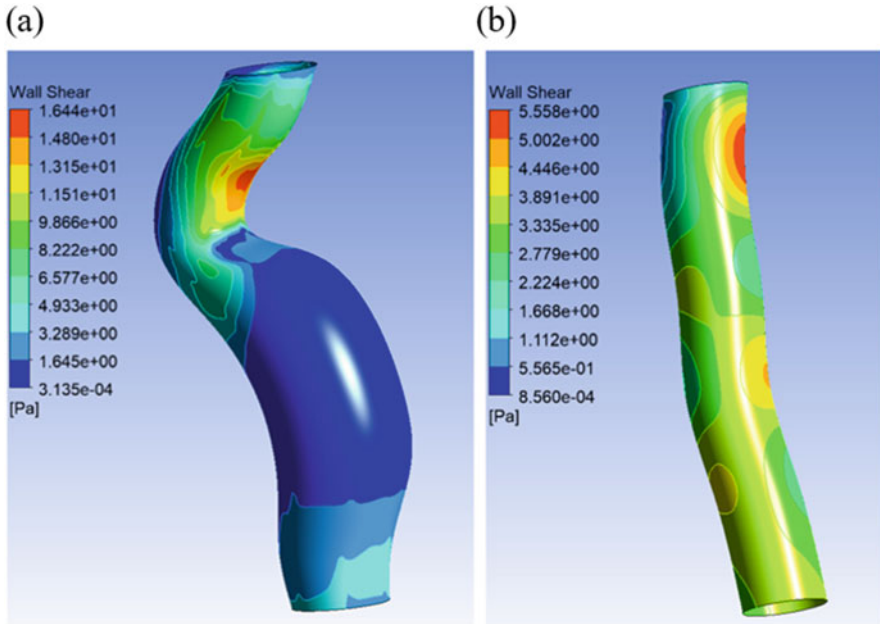


Fig. 8 Wall shear stress distribution at $t = 0.58$ s for (a) the aneurysmal aorta and (b) the healthy aorta

(4) pressure gradients are significantly different for an aneurysmal aorta when compared to the healthy one. From these findings, the importance of changing the clinical diagnosis and prevention is highlighted as tortuosity would be more critical than the aneurysm size in rupture prediction. It is essential to include more specific clinical data to improve the model accuracy in the future study. In addition, this study does not consider the interaction between the blood flow and the hyperelastic walls. Although it has been proved that it is reasonable to use a CFD analysis due to the stiffer aortic wall in the aneurysm sac caused by the decrease in elastic fibres and collagen fibres, certainly a fluid-structure interaction can describe the flow-induced dynamics of blood vessel more accurately.





References

1. World Health Organisation. Cardiovascular diseases (CVDs) (2017)
2. M. Bäck et al., Biomechanical factors in the biology of aortic wall and aortic valve diseases. *Cardiovasc. Res.* **99**(2), 232–241 (2013)
3. M.J. Salameh, E.V. Ratchford, Aortic dissection. *Vasc. Med.* **21**(3), 276–280 (2016)
4. E. Soudah et al., CFD modelling of abdominal aortic aneurysm on hemodynamic loads using a realistic geometry with CT. *Comput. Math. Methods Med.* **2013**, 472564 (2013)

5. E.K. Shang et al., Local wall thickness in finite element models improves prediction of abdominal aortic aneurysm growth. *J. Vasc. Surg.* **61**(1), 217–223 (2015)
6. S. Lin et al., Fluid-structure interaction in abdominal aortic aneurysm: Effect of modeling techniques. *Biomed. Res. Int.* **2017**, 7023078 (2017)
7. A. Forneris et al., A novel combined fluid dynamic and strain analysis approach identified abdominal aortic aneurysm rupture. *J. Vasc. Surg. Cases Innov. Tech.* **6**(2), 172–176 (2020)
8. N. Sakalihasan, R. Limet, O. Defawe, Abdominal aortic aneurysm. *Lancet* **365**(9470), 1577–1589 (2005)
9. F. Joly et al., Flow stagnation volume and abdominal aortic aneurysm growth: Insights from patient-specific computational flow dynamics of Lagrangian-coherent structures. *Comput. Biol. Med.* **92**, 98–109 (2018)
10. J.-B. Choi et al., Pressure distribution and wall shear stress in stenosis and abdominal aortic aneurysm by computational fluid dynamics modeling (CFD). *Korean J. Chem. Eng.* **31**(3), 402–411 (2014)
11. G. Martufi et al., Is there a role for biomechanical engineering in helping to elucidate the risk profile of the thoracic aorta? *Ann. Thorac. Surg.* **101**(1), 390–398 (2016)
12. M.C. Whitlock, W.G. Hundley, Noninvasive imaging of flow and vascular function in disease of the aorta. *JACC Cardiovasc. Imaging* **8**(9), 1094–1106 (2015)
13. T.A. Hope et al., Comparison of flow patterns in ascending aortic aneurysms and volunteers using four-dimensional magnetic resonance velocity mapping. *J. Magn. Reson. Imaging* **26**(6), 1471–1479 (2007)
14. J. Chen, X.-Y. Lu, Numerical investigation of the non-Newtonian pulsatile blood flow in a bifurcation model with a non-planar branch. *J. Biomech.* **39**(5), 818–832 (2006)
15. B.M. Johnston et al., Non-Newtonian blood flow in human right coronary arteries: Transient simulations. *J. Biomech.* **39**(6), 1116–1128 (2006)
16. D. Quemada, Rheology of concentrated disperse systems and minimum energy dissipation principle: I. Viscosity-concentration relationship. *Rheologica Acta* **16**(1), 82–94 (1977)
17. D. Quemada, Rheology of concentrated disperse systems II. A model for non-newtonian shear viscosity in steady flows. *Rheol. Acta* **17**(6), 632–642 (1978)
18. S. Pirola et al., On the choice of outlet boundary conditions for patient-specific analysis of aortic flow using computational fluid dynamics. *J. Biomech.* **60**, 15–21 (2017)
19. P. Crosetto et al., Fluid–structure interaction simulation of aortic blood flow. *Comput. Fluids* **43**(1), 46–57 (2011)

Effect of Nonlinear Blood Viscosity on LDL Transport and Fluid-Structure Interaction Biomechanics of a Multi-stenosis Left Circumflex Coronary Artery



Harry J. Carpenter , Mergen H. Ghayesh , Anthony C. Zander , and Peter J. Psaltis 

1 Introduction

Low-density-lipoproteins (LDL) are widely associated with cardiovascular disease and the initiation and progression of atherosclerosis. Their accumulation at the artery wall, coupled with dysfunction of the endothelial cells that constitute the innermost layer of the artery [1], leads to the formation of atherosclerotic plaques. With growth over time, these plaques narrow the lumen, often leading to heart attack. Heart attack and cardiovascular disease are now seen as one of the largest economic burdens on society [2]. While medical technologies are advancing rapidly, they cannot yet assess the highly nonlinear interactions in the coronary vasculature, hence, cannot provide predictions on disease progression. The biomechanical analysis of the coronary system using fluid-structure interaction (FSI) techniques shows significant promise to address this gap and sheds light on the mechanisms leading to cardiovascular disease and heart attack.

Literature to date has predominately focused on computational fluid dynamics (CFD) techniques to investigate fluid dynamics/blood haemodynamics in the coronary vasculature [2]. Often blood viscosity is simplified to being Newtonian [3] despite its complex micro-constituents resulting in non-Newtonian properties.

H. J. Carpenter (✉) · M. H. Ghayesh · A. C. Zander
School of Mechanical Engineering, University of Adelaide, Adelaide, South Australia, Australia
e-mail: harry.carpenter@adelaide.edu.au; mergen.ghayesh@adelaide.edu.au

P. J. Psaltis
Vascular Research Centre, Lifelong Health Theme, South Australian Health and Medical Research Institute (SAHMRI), Adelaide, South Australia, Australia

Adelaide Medical School, University of Adelaide, Adelaide, South Australia, Australia

Department of Cardiology, Central Adelaide Local Health Network, Adelaide, South Australia, Australia

Several investigations assume that fluid strain rates exceed the range where non-Newtonian fluid characteristics result in meaningful changes in outcomes, an assumption that yields reasonable results in many CFD applications [4]; however, for accurate assessment of artery biomechanics non-Newtonian power law models best describe realistic patient properties and result in significant alterations in WSS [5]. Accurate WSS assessment is critical due to its influence on LDL transport in the vasculature [6], with LDL concentration seen as a better predictor of plaque progression than WSS alone. While CFD-based models exhibited an inverse relationship between LDL concentration and WSS, fluid-structure interaction (FSI) techniques were shown to alter both WSS and LDL concentration [7] and could more accurately capture effects such as heart dynamics [8]. FSI-based models also show potential to link artery wall mechanics and particle transport [9], allowing for analysis of LDL infiltration from the fluid into the intima layer at regions of high particulate concentration [10]. However, these investigations are yet to include or quantify the effect of changes in non-Newtonian fluid viscosity.

The innovation in this paper is the investigation and quantification of the impact that varying nonlinear blood viscosity within physiological ranges has on LDL transport in a realistic FSI model of the left circumflex coronary artery. Included in the model are hyperelastic, viscoelastic and multi-layered arterial walls, three-dimensional motion, two lipid-rich plaques, pulsatile blood velocity/pressure, non-Newtonian blood flow and discrete phase particle transport. It is the first time that the relationship between nonlinear viscosity changes, driven by physiological haematocrit variability, and LDL transport has been investigated, which could provide important outcomes for clinicians and present best practice fluid characteristics for coronary biomechanical modelling.

2 In vivo-based Model

Invasive angiography from a healthy male aged 24 with no angiographically evident atherosclerosis was used as the basis for the model. Heart rate was 43 bpm (cardiac cycle of 1.4 s). The three-dimensional centreline was constructed by choosing two image planes with angle greater than 30 degrees between them [11]. End-diastole images were chosen from each plane and processed in MATLAB (version 2018b, Mathworks, Natick, MA, US) by manually picking points along the artery edges. The centreline was generated by taking the midpoint of orthogonal projections running between each edge line which was then imported into Autodesk[®] Inventor LT[™] (Autodesk, Inc. 2019). Each two-dimensional centreline was projected normally from its respective plane, with the intersection of the two projections giving the three-dimensional vessel centreline. Cross-sections were assumed circular, spaced at one-millimetre intervals along the centreline with diameters taken as the average of the two respective angiographic images. Future work could include more advanced methods to extract the complex artery cross section geometry [12]. Proximal and distal sections of the artery are shown in Fig. 1a. Intima and Adventitia

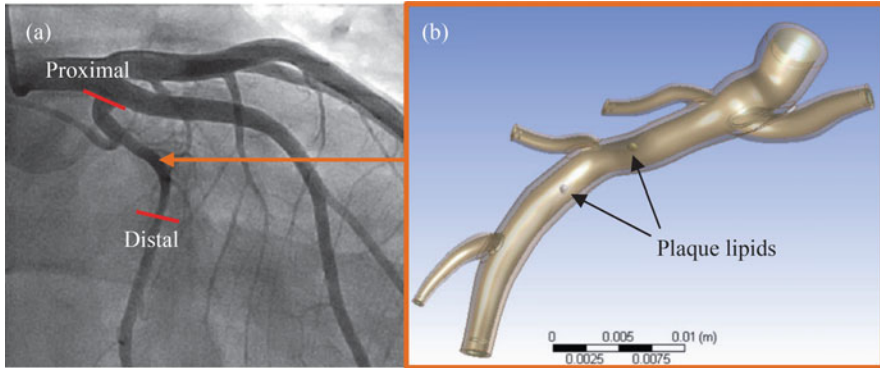


Fig. 1 (a) Angiography of the left vascular tree with proximal and distal locations of the left circumflex artery to be analysed and (b) the reconstructed three-dimensional model

thicknesses were 5.75% and 16.3% of the lumen diameter [13], respectively. Two plaques were placed on opposing sides of the artery at known high-risk areas (low WSS regions on the inside of bends) shown in Fig. 1b.

3 Computational Approach

The FSI model was analysed using ANSYS® (version 19.0, ANSYS Inc., Cannonsburg, PA, US) with two-way coupling between the fluid and structural domains and two-way coupling between the continuous fluid and discrete phases. Artery hyperelastic properties were defined using the five-parameter Mooney-Rivlin model [5] with coefficients obtained by curve fitting to longitudinal tensile test data for the intima and adventitia [13] assuming isotropic, nearly incompressible material. Viscoelastic effects using Prony shear relaxation [8] were defined with coefficients used from the work in Ref. [5] which were fitted to experimental data. The Horn-Schunk optical flow method was utilized through MATLAB's computer vision toolbox, with velocity vectors of the lumen boundary averaged across four consecutive pixels to minimize noise, then converted to meters per second, divided into equally spaced points along the two-dimensional curve and projected normal to the plane. The midpoint of the minimum distance between projections was taken as the three-dimensional temporal and spatial location. The result was applied as transient displacement boundary conditions (Fig. 2) to the inlet and outlets.

Fluid boundary conditions, $F(t)$, were set based on [14], with pulsatile, fully developed inlet velocity and out of phase transient pressure outlets, which were matched to patient-specific data, described by an eleven-term Fourier series

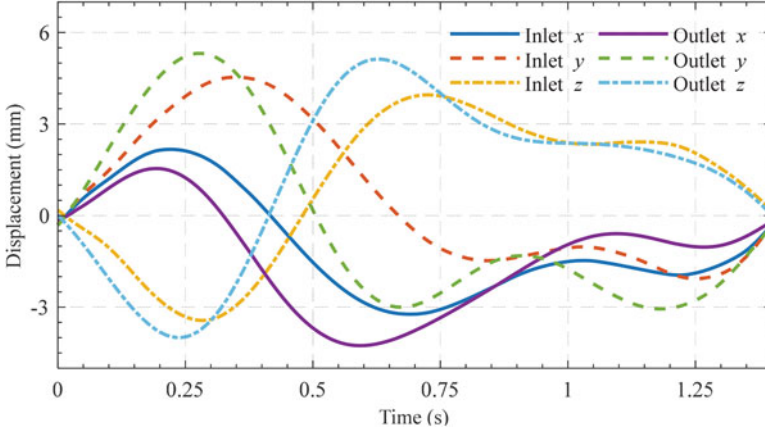


Fig. 2 Transient displacement applied to the inlet and outlets of the model

Table 1 Fourier series coefficients for inlet velocity (m/s) and outlet pressures (Pa)

	a_1	a_2	a_3	a_4	a_5	a_6	a_7	a_8	a_9	a_{10}	a_{11}
Inlet ($\times 10^{-3}$)	113	44.6	15.3	25.0	21.2	-3.04	-4.00	2.09	-8.15	-6.76	0.024
Outlet	1948	291	-525	-202	218	140	0.869	6.15	-4.20	-44.3	-18.8
	b_1	b_2	b_3	b_4	b_5	b_6	b_7	b_8	b_9	b_{10}	b_{11}
Inlet ($\times 10^{-3}$)	5.01	-16.7	-6.05	1.68	-19.2	-17.2	-1.66	-3.91	-5.65	5.27	2.50
Outlet	-750	-1232	-383	324	185	-60.8	-39.4	6.58	-27.2	-8.10	11.8

$$F(t) = a_0 + \sum_{n=1}^{11} a_n \cos\left(\frac{2\pi}{1.4}nt\right) + b_n \sin\left(\frac{2\pi}{1.4}nt\right), \quad (1)$$

with a_0 equal to 0.154 and 1.01×10^4 for inlet and outlet, respectively, and coefficients a_{0-11} and b_{1-11} as outlined in Table 1.

Fluid viscosity was set according to the nonlinear Power law non-Newtonian model [4].

$$\mu = \mu_0(\dot{\gamma})^{n-1}, \quad (2)$$

where μ_0 and n are the zero-strain viscosity and power law index, respectively. For haematocrit of 40% $\mu_0 = 0.0147$, $n = 0.6155$; for 60% $\mu_0 = 0.0472$ and $n = 0.5036$ based on curve fitting of data from [15]. Fluid strain rate is represented by $\dot{\gamma}$.

The discrete phase model approach was used to incorporate LDL particle transport in the fluid in ANSYS Fluent. Here, the particle force balance in the arbitrary x direction with the Stokes-Cunningham drag law applied for submicron, spherical particles [16] is described by

$$\frac{du_p}{dt} = \frac{18\mu}{d_p^2 \rho_p C_c} (u - u_p) + \frac{g_x (\rho_p - \rho)}{\rho_p} + F_x, \quad (3)$$

where u and u_p are the fluid and particle velocities respectively, ρ and ρ_p are the fluid and particle densities respectively, μ is the fluid viscosity, d_p is the particle diameter, g_x is the gravitational force in the x direction, C_c is the Cunningham correction factor and F_x is a force term which includes the effect of rotating reference frame, pressure gradient forces and stochastic tracking forces where the turbulent dispersion of the particles is predicted using instantaneous velocity of the fluid. While LDL particles are not perfectly spherical, in this preliminary investigation we make this assumption for simplicity. The LDL particle diameter was defined based on the Rosin-Rammler diameter distribution to capture size variation from $1.8\text{--}2.5 \times 10^{-8}$ m [17] with a distribution parameter of 3.5. Due to the small particle size, Brownian motion is considered as well as discrete random walk for turbulent dispersion. Average particle inlet flow rate was 1.64×10^{-18} kg/s [7] for a particle density of 1031 kg/m^3 [18]; particle inlet velocity matched the fluid inlet velocity and fluid density was set to 1050 kg/m^3 [4]. Wall boundary conditions were set as reflective conditions and a mean wall roughness of 5×10^{-5} m was assumed. The simulation was run over two-time steps (2×1.4 s cardiac phases). A time step of 0.007 s was used with up to 30 system coupling iterations, 26 structural iterations and 100 fluid iterations per timestep with a further 3000 discrete particle phase steps per time step. Structural mesh varied from 0.1 to 0.25 mm and the fluid domain was discretized with 0.15 mm mesh and a boundary layer thickness to 0.05 mm.

4 Results and Discussion

Results were analysed at local WSS minima proximal to Plaque 1 and distal to Plaque 2. All results presented are analysed from the second cardiac cycle to ensure convergence. With the accumulation of LDL at the wall of the artery seen as a major contributor to atherosclerosis initiation and progression as well as a potential factor in endothelial permeability [19], we assessed LDL mass concentration, as a measure of accumulation, as a risk factor. Curves along the lumen-wall interface (Curves 1 and 2) were used to analyse WSS, LDL concentration and von Mises stress during the systole (contraction) and diastole (rest) cycles and are outlined in Fig. 3. Transient results for proximal and distal local minima are shown in Fig. 4. Increased viscosity (60% haematocrit) sees a 46% increase in WSS and a more significant 126% increase in LDL concentration. Distal to Plaque 2 turbulent eddies begin to alter the profile of LDL accumulation, with comparable peak concentration but a significant increase of 330% seen by the highlighted secondary peak, shown in Fig. 4b, emphasizing the highly nonlinear nature of the interactions. Steep

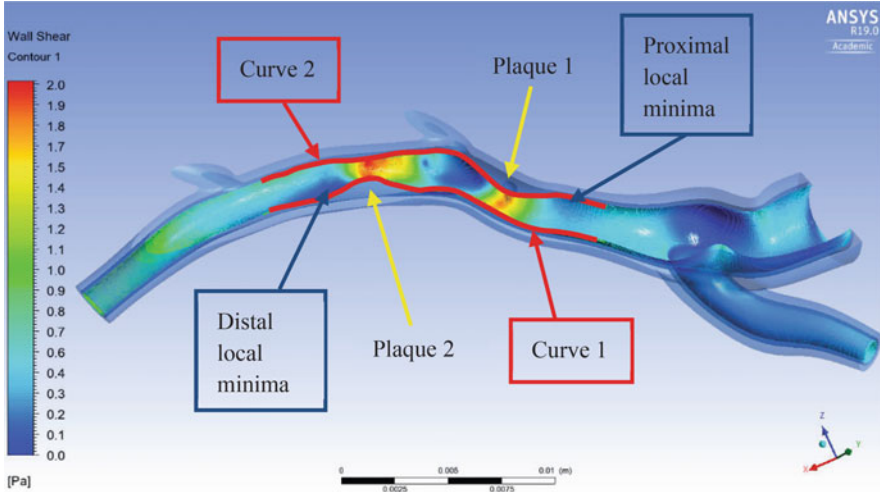


Fig. 3 WSS distribution at $t = 1.6$ s (0.2 s into second cardiac cycle at end diastole). Maxima occur at the stenosis throat with local minima at plaque shoulders. Transient WSS and LDL concentration are assessed at the highlighted local minima proximal to Plaque 1 and distal to Plaque 2

WSS gradients show a significant clearing effect with dramatic decreases in LDL concentration for both viscosity profiles (40% and 60% haematocrit). Mean LDL concentration is increased by 29% and 38% at the proximal and distal locations respectively when viscosity increases. These locations also see a decrease in the oscillatory shear index (OSI) and slight increases in time-averaged wall shear stress (TAWSS). At end systole Curves 1 and 2 show comparable WSS results with peaks across the plaque locations, as seen in Fig. 5. This highlights how Newtonian fluid assumptions may hold in higher WSS/strain rate environments that are exacerbated by the rigid wall assumptions of CFD techniques. Nonlinear fluid viscosity, however, results in significant alteration of LDL concentration, with a 308% increase for 60% haematocrit at the region distal to Plaque 2, shown in Fig. 5a; Curve 2 in Fig. 5b sees less significant changes. End diastole results in a significant alteration in both WSS and LDL concentration. Figure 6a shows a 35% increase in wall shear stress with increased viscosity/haematocrit; however, a 74% decrease in LDL concentration at regions distal to both plaque sites is seen; mean LDL concentration along Curve 1 is decreased by 28% for the 60% haematocrit model. Both curves show a decrease in OSI and a slight increase in TAWSS with increased viscosity, with no significant changes in their distribution. Conversely, at the location proximal to Plaque 2 a 309% increase in peak LDL concentration results for increased viscosity, shown in Fig. 6b. The von Mises stress showed no significant changes due to blood viscosity. As von Mises stress could play a role in endothelial dysfunction, regions with both increased von Mises stress

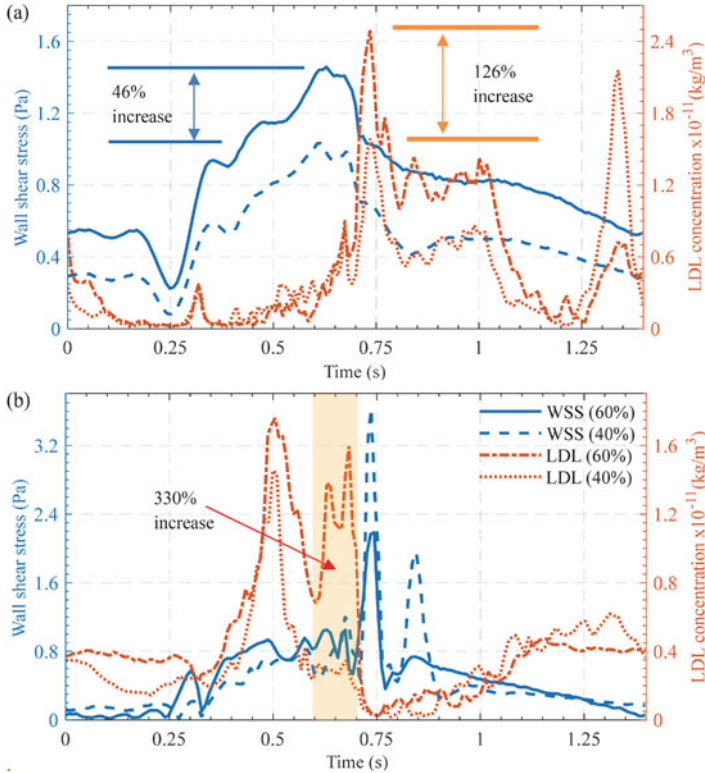


Fig. 4 Relationship between transient wall shear stress and LDL mass concentration when nonlinear fluid viscosity is varied (based on haematocrit increasing from 40% to 60%) at locations proximal to Plaque 1 (a) and distal to Plaque 2 (b). Results highlight the sensitivity of low wall shear stress regions to fluid viscosity changes with the impacts resulting in considerable variation in LDL mass concentration. The legend shown in (b) applies to both sub-figures

and increased LDL particle concentration could present an opportunity for plaque progression. This occurs distal to Plaque 2, suggesting this as a possible site for disease progression.

5 Conclusions

The effects of varying non-Newtonian fluid properties (depending on blood micro-constituents) on LDL transport have been investigated in a realistic FSI model of the left circumflex coronary artery. Critically, it is the first time that the interaction between LDL concentration and nonlinear blood viscosity variation within physiological ranges (based on haematocrit percentage) is investigated. Results show

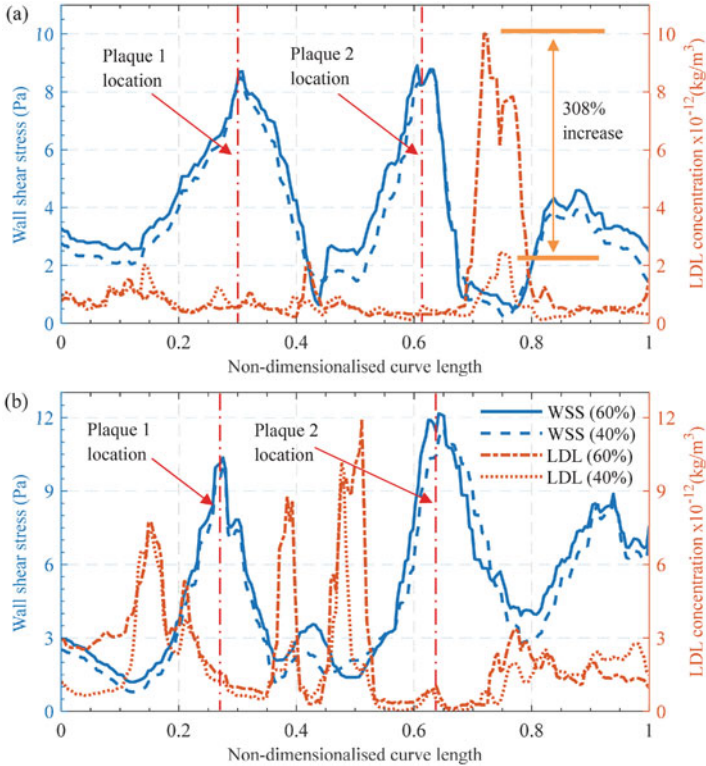


Fig. 5 Comparison of WSS and LDL concentration at end systole cycle ($t = 0.7$ s in second cardiac cycle) along Curve 1 (a) and Curve 2 (b) for haematocrit values of 40% and 60%. WSS peaks across plaque locations while LDL concentration peaks at plaque shoulders where WSS is lowest. The legend shown in (b) applies to both sub-figures and Curve 1 and 2 are described in Fig. 3

increased viscosity leads to increases in the minimum WSS and a mean increase in LDL concentration at both proximal and distal locations. Interestingly, at end diastole, lower viscosity results in a significant increase in LDL concentration along one side of the artery wall, highlighting the inherent nonlinearity in the interaction. The alignment of von Mises stress at the intima wall with peak LDL concentration suggests a potential disease progression site, although this is highly dependent on blood viscosity. This highlights the importance of both accurate nonlinear fluid properties and LDL transport in fluid-structure interaction biomechanical modelling of the coronary vasculature when investigating potential disease progression.

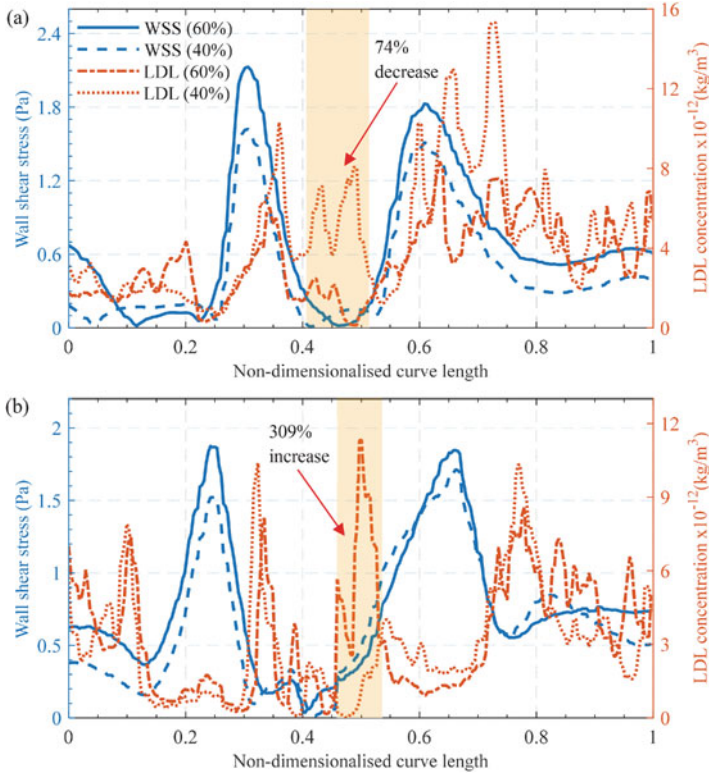


Fig. 6 Comparison of WSS and LDL concentration at end diastole cycle ($t = 0.2$ s in second cardiac cycle) along Curve 1 (a) and Curve 2 (b) for haematocrit values of 40% and 60%. The legend shown in (a) applies to both sub-figures and Curve 1 and 2 are described in Fig. 3

References

1. S. Fernando, C.A. Bursill, S.J. Nicholls, P.J. Psaltis, Pathophysiology of atherosclerosis, in *Mechanisms of Vascular Disease: A Textbook for Vascular Specialists*, ed. by R. Fitridge, (Springer International Publishing, 2020), pp. 19–45
2. H.J. Carpenter, A. Gholipour, M.H. Ghayesh, A.C. Zander, P.J. Psaltis, A review on the biomechanics of coronary arteries. *Int. J. Eng. Sci.* **147**, 103201 (2020)
3. M. Kachanov, B. Abedian, On the isotropic and anisotropic viscosity of suspensions containing particles of diverse shapes and orientations. *Int. J. Eng. Sci.* **94**, 71–85 (2015)
4. B.M. Johnston, P.R. Johnston, S. Corney, D. Kilpatrick, Non-Newtonian blood flow in human right coronary arteries: Transient simulations. *J. Biomech.* **39**(6), 1116–1128 (2006)
5. A. Gholipour, M.H. Ghayesh, A. Zander, R. Mahajan, Three-dimensional biomechanics of coronary arteries. *Int. J. Eng. Sci.* **130**, 93–114 (2018)
6. J.V. Soulis, D.K. Fytanidis, V.C. Papaioannou, G.D. Giannoglou, Wall shear stress on LDL accumulation in human RCAs. *Med. Eng. Phys.* **32**(8), 867–877 (2010)
7. S. Chung, K. Vafai, Effect of the fluid–structure interactions on low-density lipoprotein transport within a multi-layered arterial wall. *J. Biomech.* **45**, 371–381 (2012)

8. H. Carpenter, A. Gholipour, M. Ghayesh, A.C. Zander, P. Psaltis, In vivo based fluid-structure interaction biomechanics of the left anterior descending coronary artery. *J. Biomech. Eng.* **143**(8), 081001 (2021)
9. M. Roustaei, M.R. Nikmaneshi, B. Firoozabadi, Simulation of Low-Density Lipoprotein (LDL) permeation into multilayer coronary arterial wall: Interactive effects of wall shear stress and fluid-structure interaction in hypertension. *J. Biomech.* **67**, 114–122 (2018)
10. N. Koshiba, J. Ando, X. Chen, T. Hisada, Multiphysics simulation of blood flow and LDL transport in a porohyperelastic arterial Wall model. *J. Biomech. Eng.* **129**(3), 374–385 (2006)
11. M. Sharzehee, Y. Chang, J.-P. Song, H.-C. Han, Hemodynamic effects of myocardial bridging in patients with hypertrophic cardiomyopathy. *Am. J. Phys. Heart Circ. Phys.* **317**(6), H1282–H1291 (2019)
12. F. Galassi, M. Alkhalil, R. Lee, P. Martindale, R.K. Kharbanda, K.M. Channon, et al., 3D reconstruction of coronary arteries from 2D angiographic projections using non-uniform rational basis splines (NURBS) for accurate modelling of coronary stenoses. *PLoS One* **13**(1), e0190650 (2018)
13. G.A. Holzzapfel, G. Sommer, C.T. Gasser, P. Regitnig, Determination of layer-specific mechanical properties of human coronary arteries with nonatherosclerotic intimal thickening and related constitutive modeling. *Am. J. Phys. Heart Circ. Phys.* **289**(5), 2048–2058 (2005)
14. J.S. Tran, D.E. Schiavazzi, A.B. Ramachandra, A.M. Kahn, A.L. Marsden, Automated tuning for parameter identification and uncertainty quantification in multi-scale coronary simulations. *Comput. Fluids* **142**, 128–138 (2017)
15. P.W. Rand, E. Lacombe, H.E. Hunt, W.H. Austin, Viscosity of normal human blood under normothermic and hypothermic conditions. *J. Appl. Physiol.* **19**(1), 117–122 (1964)
16. H.P. Zhu, Z.Y. Zhou, R.Y. Yang, A.B. Yu, Discrete particle simulation of particulate systems: Theoretical developments. *Chem. Eng. Sci.* **62**(13), 3378–3396 (2007)
17. K. El Harchaoui, W.A. van der Steeg, E.S.G. Stroes, J.A. Kuivenhoven, J.D. Otvos, N.J. Wareham, B.A. Hutten, J.J.P. Kastelein, K.-T. Khaw, S.M. Boekholdt, Value of low-density lipoprotein particle number and size as predictors of coronary artery disease in apparently healthy men and women. *J. Am. Coll. Cardiol.* **49**(5), 547–553 (2007)
18. S. Eisenberg, D.W. Bilheimer, R.I. Levy, F.T. Lindgren, On the metabolic conversion of human plasma very low-density lipoprotein to low density lipoprotein. *Biochim. Biophys. Acta* **326**(3), 361–377 (1973)
19. A.I. Sakellarios, M.I. Papafaklis, P. Siogkas, L.S. Athanasiou, T.P. Exarchos, K. Stefanou, C.V. Bourantas, K.K. Naka, L.K. Michalis, O. Parodi, Patient-specific computational modeling of subendothelial LDL accumulation in a stenosed right coronary artery: Effect of hemodynamic and biological factors. *Am. J. Phys. Heart Circ. Phys.* **304**(11), H1455–H1470 (2013)

Reduced-Order Modelling of Flutter Oscillations Using Normal Forms and Scientific Machine Learning



K. H. Lee, D. A. W. Barton, and L. Renson

1 Introduction

Over the last decade, machine learning approaches have opened up many new opportunities for exploiting data. However, in the context of physical engineered systems machine learning is often constrained by burdensome data requirements and a lack of interpretability. In recent years there has been a push towards combining physics-based models (usually differential-equation-based models) with machine-learned models in an attempt to incorporate expert knowledge to reduce data requirements and simultaneously increase the interpretability of the models. Recent examples include physics-informed neural networks (PINNs) [1, 2], where differential-equation models are incorporated into the cost function used for learning the neural network; neural differential equations [3, 4], which use a neural network on the right-hand side of the differential equation; and universal differential equations [5], which use arbitrary machine-learned models as sub-components of a differential-equation model. Each of these approaches has had some success in their respective fields but application to nonlinear differential-equation models that undergo qualitative changes of behaviour (bifurcations) is very limited.

As such, in this chapter we focus on a combined differential-equation/machine learning approach to produce an accurate model of the nonlinear dynamic behaviour of a physical engineered system; specifically we focus on an aerofoil undergoing aero-elastic flutter oscillations caused by a Hopf bifurcation.

K. H. Lee (✉) · D. A. W. Barton

Department of Engineering Mathematics, University of Bristol, Bristol, UK
e-mail: jz18526@bristol.ac.uk; david.barton@bristol.ac.uk

L. Renson

Department of Mechanical Engineering, Imperial College London, London, UK
e-mail: l.renson@imperial.ac.uk

The underpinning idea is to start with a normal-form-like model of the bifurcation phenomena of interest and then attempt to learn a coordinate transformation from the normal-form model to the physical coordinate system. We illustrate this idea using a 6-dimensional aero-elastic flutter model as the ground truth and learn a coordinate transform to a (modified) 2-dimensional Hopf bifurcation normal form. The ultimate aim is to use this approach on a physical wind-tunnel-based experiment; the underlying assumption is that we are able to reveal the fundamental bifurcation structure of a physical experiment using techniques such as control-based continuation [6, 7] to create a simple phenomenological model that recreates the bifurcation structure.

We begin by outlining a particular variant of control-based continuation that can be used on autonomous self-excited systems in order to extract the bifurcation structure from the physical experiment. Subsequently, in Sect. 3, we detail the architecture of the hybrid differential-equation/machine-learned model used to learn the bifurcation structure revealed by control-based continuation. The specific application area is presented in Sect. 4 along with the details of the data-driven model in this context in Sect. 5. Results of the methodology and conclusions are provided in Sect. 6 and Sect. 7, respectively.

2 Bifurcation Structure of an Experiment

Control-based continuation (CBC) [6–10] is a scheme to reveal the bifurcation structure of an uncontrolled physical nonlinear experiment via controlled experiments. In CBC, a root-finding problem is constructed such that, when a root is found by iteratively refining the control target, the output of the controlled experiment corresponds to a steady state (either an equilibrium or a limit cycle) of the uncontrolled system. Hence, the control scheme is rendered non-invasive. Previously, CBC has only been applied to periodically forced systems. Here, we will show how CBC can be applied to self-excited systems undergoing a Hopf bifurcation.

The key benefit of CBC is that it provides information about the unstable long-time dynamics; this is particularly important at bifurcation points where the dynamics are often organised by the unstable orbits. A common example is a subcritical Hopf bifurcation where unstable orbits separate the stable equilibrium from areas that spiral outwards, often to a large amplitude limit cycle oscillation. As such, when constructing mathematical models, information about the unstable orbits is invaluable.

Previous studies with CBC have relied on periodic forcing to avoid practical issues around the synchronisation of the control target with the intrinsic dynamics of the experiment. Without periodic forcing, small errors in estimating the frequency of oscillation cause phase drift between the periodic control target (generated by the control system) and the response of the experiment. Consequently, when considering a Hopf bifurcation of an autonomous system alternative approaches are

required. Here we make use of phase-plane CBC (PP-CBC), a geometric approach to controlling the response of the experiment.

To explain the methodology of PP-CBC, we first assume that the dynamical system under the experiment is governed by a parameter-dependent autonomous ODE as

$$\dot{\mathbf{z}} = \mathbf{F}(\mathbf{z}, \mu), \quad (1)$$

where $\mathbf{F}(\mathbf{z}, \mu) : \mathbb{R}^N \times \mathbb{R} \rightarrow \mathbb{R}^N$ is the parameter-dependent vector field, $\mathbf{z} \in \mathbb{R}^N$ is the vector of the state variables, and μ is the bifurcation parameter. Furthermore, we assume that this ODE exhibits periodic solutions that emerge from a Hopf bifurcation for some value of μ .

A required feature of the limit cycles is that the measured response generates a closed curve on some physically measurable two-dimensional plane; PP-CBC uses a coordinate system within this plane to define the error between the control target and the measured orbit. Let the corresponding coordinates be defined as $z_1 = \pi_1 \circ \mathbf{z}$, $z_2 = \pi_2 \circ \mathbf{z}$, where π_1 and π_2 are appropriate projections. Furthermore, define the instantaneous amplitude and phase angle on the (z_1, z_2) plane as

$$R = \sqrt{z_1^2 + z_2^2}, \quad \text{and} \quad \phi = \tan^{-1} \left(\frac{z_2}{z_1} \right).$$

We assume that R is a 2π -periodic function of ϕ . As such, R can be expressed as a Fourier series. Similarly, the control target can be defined by its Fourier coefficients. Thus, the mathematical model of the controlled experiment takes the form

$$\dot{\mathbf{z}} = \mathbf{F}(\mathbf{z}, \mu) + \mathbf{c}(z_1, z_2, \hat{\mathbf{C}}), \quad (2)$$

where the $\hat{\mathbf{C}} \in \mathbb{R}^{2n_h+1} = (\hat{a}_0, \dots, \hat{a}_{n_h}, \hat{b}_1, \dots, \hat{b}_{n_h})$ is the control target defined by its (truncated) Fourier coefficients. Finally, the feedback control force \mathbf{c} is chosen to be

$$\mathbf{c}(z_1, z_2, \hat{\mathbf{C}}) = \left(K_1(z_1 - \hat{R} \cos(\phi)) + K_2(z_2 - \hat{R} \sin(\phi)) \right) \mathbf{e}_c, \quad (3)$$

where the instantaneous amplitude of the control target is given by

$$\hat{R} = \hat{\mathbf{C}} \cdot [1, \cos(\phi), \dots, \cos(n_h\phi), \sin(\phi), \dots, \sin(n_h\phi)]^T, \quad (4)$$

$\mathbf{e}_c \in \mathbb{R}^N$ is the direction vector of the control force as determined by the physical constraints on the experiment, and (K_1, K_2) are the control gains. Although the control target varies periodically, there is no explicit dependence on time. Instead, the dependence on the instantaneous phase allows us to avoid synchronisation problems.

The main goal of PP-CBC is to determine $\hat{\mathbf{C}}$ such that $\|\mathbf{c}(z_1, z_2, \hat{\mathbf{C}})\| < \epsilon$, i.e., approximately non-invasive control for sufficiently small ϵ . In this case, the control target $\hat{\mathbf{C}}$ approximates a solution of the uncontrolled system (1) with the accuracy of approximation given by ϵ . This goal is formulated as a root-finding problem.

As previously mentioned, we assume the existence of limit cycles of (2) and discretise the instantaneous amplitude using a Fourier projection such that $\Phi(R) : C_p([0, 2\pi], \mathbb{R}) \rightarrow \mathbb{R}^{2n_h+1} = (a_0, \dots, a_{n_h}, b_1, \dots, b_{n_h})$, where

$$a_0 = \frac{1}{2\pi} \int_0^{2\pi} R d\phi, \quad (5a)$$

$$a_n = \frac{1}{\pi} \int_0^{2\pi} R \cos(n\phi) d\phi \quad \text{for } n = 1, 2, \dots, n_h, \quad (5b)$$

$$b_n = \frac{1}{\pi} \int_0^{2\pi} R \sin(n\phi) d\phi \quad \text{for } n = 1, 2, \dots, n_h. \quad (5c)$$

Finally, we arrive at a discretized zero problem $\Phi(R) - \hat{\mathbf{C}} = 0$, which can be solved using standard root-finding methods to achieve non-invasive control. This zero problem is the difference between the measured limit cycle and the desired limit cycle as defined by the control target vector $\hat{\mathbf{C}}$ (see Fig. 1 for a visualisation of the concept).

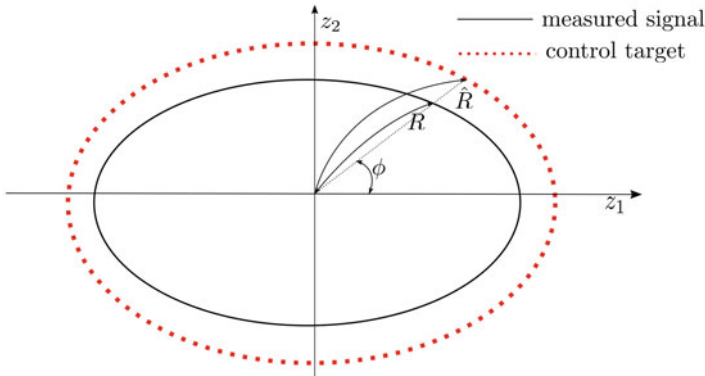


Fig. 1 Geometric illustration of the phase-plane CBC. The control force is determined by the difference between the instantaneous amplitudes of the control target and the measured response at the measured instantaneous phase

3 Structure of the Data-Driven Model

The goal of this chapter is to construct accurate data-driven models of a nonlinear system by incorporating prior knowledge of the bifurcations that occur. Here, the prior knowledge is encoded as a normal form of the bifurcation and a mapping from the normal-form coordinates to the physical coordinates is learnt from data.

Assume that the vector field (1) has an equilibrium at the origin that undergoes a Hopf bifurcation at $\mu = \mu_0$. From centre manifold theory, we know that (1) has a two-dimensional centre manifold [11] parametrized by μ near $(\mathbf{z} = 0, \mu = \mu_0)$. Furthermore, we assume that we can measure the limit cycles that reside on the attracting centre manifold [11] via PP-CBC as described above.

The linearisation of \mathbf{F} at $(\mathbf{z} = \mathbf{0}, \mu = \mu_0)$, that is $D\mathbf{F}(\mathbf{0}, \mu_0)$, has a 2-dimensional centre subspace E^c with purely imaginary eigenvalues and a $N - 2$ -dimensional hyperbolic subspace E^h in our setting. Therefore, there exists a parameter-dependent centre manifold W_μ^c as a graph $\mathbf{y} = \mathbf{h}(\mathbf{x}, \mu - \mu_0)$ [11]

$$W_\mu^c = \{(\mathbf{x}, \mathbf{y}) \mid \mathbf{y} = \mathbf{h}(\mathbf{x}, \mu - \mu_0)\}, \quad (6)$$

where $\mathbf{x} = (x_1, x_2) \in E^c$, and $\mathbf{y} \in E^h$. Note that $x_1 \pm x_2i$ corresponds to the eigenvector of purely imaginary eigenvalue of $D\mathbf{F}(\mathbf{0}, \mu_0)$.

The dynamics on the centre manifold can be expressed as

$$\begin{aligned} \dot{x}_1 &= -\omega x_2 + f_1(x_1, x_2, \mu - \mu_0) \\ \dot{x}_2 &= \omega x_1 + f_2(x_1, x_2, \mu - \mu_0), \end{aligned} \quad (7)$$

where the (f_1, f_2) is the projection of the nonlinear part of the vector field $\mathbf{F}(\mathbf{z}, \mu)$ to $\mathbf{x} \in E^c$ and $\pm i\omega$ are eigenvalues corresponding to E^c at $\mu = \mu_0$.

In general, we consider the two-dimensional parameter-dependent ODE

$$\frac{d\mathbf{u}}{dt} = \mathbf{g}(\mathbf{u}, \nu), \quad (8)$$

where $\mathbf{g}(\mathbf{u}, \nu) : \mathbb{R}^2 \times \mathbb{R} \rightarrow \mathbb{R}^2$ is topologically equivalent to the dynamics on the attracting centre manifold given by (7). As a result of topological equivalence, there exists a homeomorphism $\mathbf{U}(\mathbf{u}, \nu) : \mathbb{R}^2 \times \mathbb{R} \rightarrow \mathbb{R}^2 \times \mathbb{R}$ between the coordinates of (8) and the physical coordinates of (2), defined in a neighbourhood of $(\mathbf{u}, \nu) = (0, 0)$ (see Fig. 2).

The underlying premise of this chapter is that it is possible to efficiently learn the coordinate transform \mathbf{U} from experimental data, given an appropriate choice of \mathbf{g} . For our purposes the Universal Approximation property [12, 13] of deep neural networks provides an appropriate model structure learning the transform.

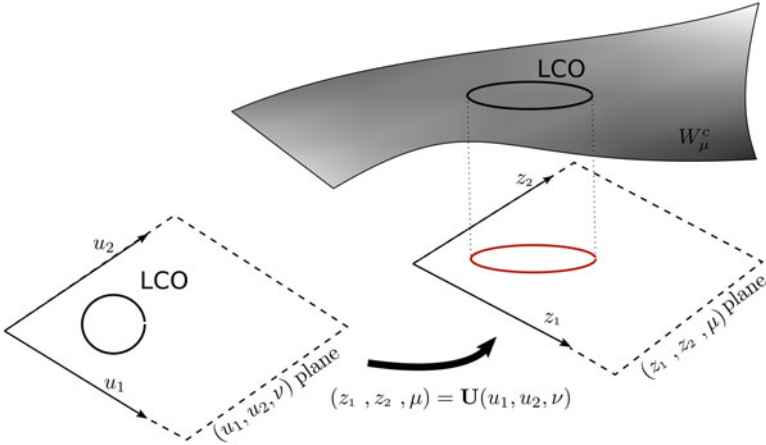


Fig. 2 Geometric illustration of the coordinate transformation U from the underlying model in (\mathbf{u}, ν) to the physical coordinates (\mathbf{z}, μ)

4 A Model of Aero-Elastic Flutter

To illustrate this data-driven approach, we consider a mathematical model of an aerofoil undergoing aero-elastic flutter oscillations as given by Abdelkefi et al. [14]. This model provides the ground truth in place of a physical experiment for which the ground truth is unknown. The model is 6- dimensional and takes the form

$$\mathbf{M}\ddot{\mathbf{z}} + \mathbf{D}\dot{\mathbf{z}} + \mathbf{K}\mathbf{z} + \mathbf{N}(\alpha) = 0, \quad (9)$$

where $\mathbf{z} = [h, \alpha, w]^T$ comprises heave h , pitch angle α , and an aerodynamic variable for the unsteady flow w ; \mathbf{M} , \mathbf{D} , and \mathbf{K} are mass, damping, and stiffness matrices, respectively. The bifurcation parameter is the airspeed and is contained within the \mathbf{D} and \mathbf{K} matrices. For the full specification of the matrices and parameter values, see the appendix. The nonlinearity is purely a function of the pitch angle α and is given by

$$\mathbf{N}(\alpha) = [0, k_{\alpha 2}\alpha^2 + k_{\alpha 3}\alpha^3, 0]^T. \quad (10)$$

For appropriate parameter values, the model undergoes a subcritical Hopf bifurcation followed by a saddle-node bifurcation of limit cycles as the airspeed is varied. Julia code to simulate orbits of model is available in [15].

To mimic the experimental procedures used, we add control for use with PP-CBC to (9). Control forces are applied via an additional force in the heave direction as follows:

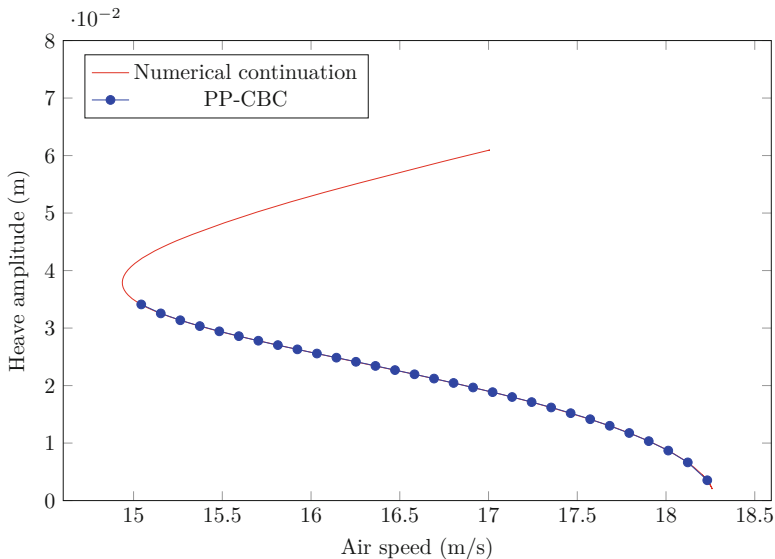


Fig. 3 Comparison of the bifurcation diagram of (9) and (11) demonstrating that PP-CBC provides a good approximation to the uncontrolled dynamics

$$\mathbf{M}\ddot{\mathbf{z}} + \mathbf{D}\dot{\mathbf{z}} + \mathbf{K}\mathbf{z} + \mathbf{N}(\alpha) = \left(K_1(h - \hat{R} \cos \phi) + K_2(\alpha - \hat{R} \sin \phi) \right) \mathbf{e}_c, \quad (11)$$

where, in this case, $\mathbf{e}_c = [1, 0, 0]^T$. The phase angle ϕ is given by $\phi = \tan^{-1}(\alpha/h)$, and for the discretisation of the control target, the Fourier series was truncated at ten terms ($n_h = 10$).

In order to verify that PP-CBC, as would be used in a physical experiment, provides a good approximation to the true dynamics of the underlying system, we compute the bifurcation diagram of both (9) and (11) using our own numerical continuation codes (available to download from [15]). The results of the computation are shown in Fig. 3; there is no visible difference between the two bifurcation diagrams. (The bifurcation diagram for the stable part is not reproduced for PP-CBC since it could be reproduced by open-loop experiments.) Comparisons at the level of individual (unstable) periodic orbits are shown in Fig. 4; there is good agreement between the orbits of (9) and (11); moreover, it can be seen that the control forces act to stabilise the system as intended, as shown by the Floquet multipliers of the orbit.

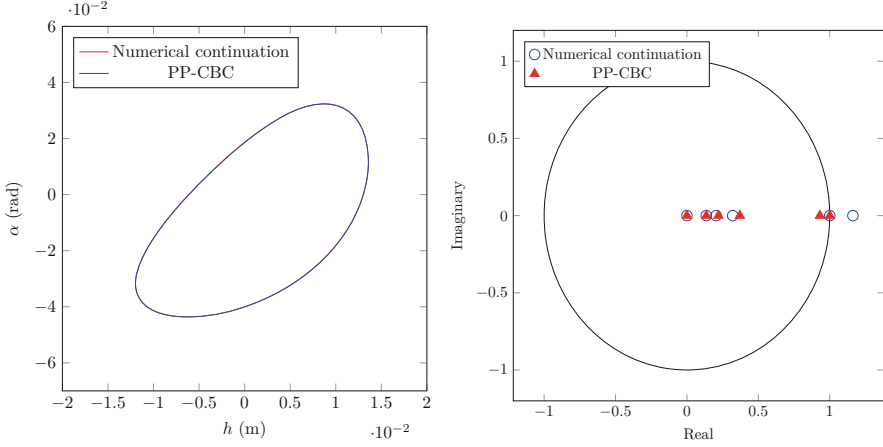


Fig. 4 A comparison of the unstable limit cycles of (9) and (11) at an airspeed of 16 ms^{-1} . The left-hand panel shows a phase-plane projection of the limit cycles in the (h, α) plane. The right-hand panel shows the Floquet multipliers of the two limit cycles; as desired, the control scheme stabilises the unstable limit cycle

5 Constructing the Data-Driven Model

The underlying assumption of this chapter is that PP-CBC is able to reveal the bifurcation structure of an underlying physical experiment (see, for example, Fig. 3). To this end, as a starting point for a data-driven model of (9), we choose the Hopf bifurcation normal form modified to create a saddle-node bifurcation in the branch of limit cycle oscillations:

$$\begin{aligned} \dot{u}_1 &= \nu u_1 - \Omega u_2 + a_2 u_1 (u_1^2 + u_2^2) - u_1 (u_1^2 + u_2^2)^2 \\ \dot{u}_2 &= \nu u_2 + \Omega u_1 + a_2 u_2 (u_1^2 + u_2^2) - u_2 (u_1^2 + u_2^2)^2, \end{aligned} \quad (12)$$

where Ω is the phase speed, a_2 is a positive constant that determines the position of the bifurcation and its criticality, and ν is the bifurcation parameter. The bifurcation structure of (12) can be seen more clearly when transformed to polar coordinates to give

$$\dot{r} = \nu r + a_2 r^3 - r^5 \quad (13a)$$

$$\dot{\theta} = \Omega. \quad (13b)$$

Since (13a) is decoupled from (13b), plotting the fixed points of (13a) shows the Hopf bifurcation followed by a saddle-node bifurcation.

The next step is to incorporate the data-driven aspect of the model by defining the transformation between the coordinate system of (12) and (9). To improve the convergence of the optimiser used as part of the machine learning, we split the transformation into two components:

$$\mathbf{U}(\mathbf{u}, \nu) = \begin{bmatrix} T_1(\mathbf{u}, \nu) + \text{NN}_{\theta_1}(\mathbf{u}, \nu) \\ \nu + \mu_0 \end{bmatrix}, \quad (14)$$

where $T_1(\mathbf{u}, \nu) : \mathbb{R}^2 \times \mathbb{R} \rightarrow \mathbb{R}^2$ is a simple transformation that has the form

$$T_1(\mathbf{u}, \nu) = \|\mathbf{u}\| \cdot [\gamma_1, \gamma_2]^T + \begin{bmatrix} \gamma_3 & \gamma_4 \\ \gamma_5 & \gamma_6 \end{bmatrix} \mathbf{u}^T, \quad (15)$$

which is a combination of linear transformation and a function that gives a shift proportional to the amplitude of the response in (\mathbf{u}, ν) coordinates with unknown parameters $\gamma_1, \dots, \gamma_6$. The neural network $\text{NN}_{\theta_1} : \mathbb{R}^2 \times \mathbb{R} \rightarrow \mathbb{R}^2$ consists of three input nodes, two hidden layers each with 21 neurons, and two output nodes.

All nodes use tanh as the activation function. In the initial stage of training, NN_{θ_1} is set to zero and T_1 is optimised with a fixed value of $a_2 = 3.65$ and $\mu_0 = 18.3$ (estimated from a crude visual match). In the second and final stage of training, NN_{θ_1} , a_2 , and μ_0 are allowed to vary in addition to T_1 . While in principle T_1 is an unnecessary addition to \mathbf{U} since the neural network is sufficient to approximate the transformation, it was found that this staged optimisation approach converges much more reliably than using the neural network alone.

The cost function for training is defined by the sum of the Euclidean distances between the actual response and the learnt response in Fourier space. For the flutter model there are coexisting limit cycle oscillations (LCOs) with different stabilities bounded in parameter values by those of the Hopf bifurcation and the saddle-node bifurcation (see Fig. 3), and so we split the LCOs into two sets, one unstable and one stable. For training data, we take m_s time-series measurements of the instantaneous amplitude from the upper-stable branch of LCOs labelled R_i^s where $i = 1, 2, \dots, m_s$ along with m_u measurements from the lower-unstable branch labelled R_i^u where $i = 1, 2, \dots, m_u$. Corresponding solutions are calculated from the data-driven model at the same bifurcation parameter values for both the stable and unstable branches, labelled \bar{R}_i^s and \bar{R}_i^u , respectively. The final cost function is

$$\mathcal{E}_{\mathbf{U}} = \sum_{i=1}^{m_s} \|\Phi(\bar{R}_i^s) - \Phi(R_i^s)\| + \sum_{i=1}^{m_u} \|\Phi(\bar{R}_i^u) - \Phi(R_i^u)\|, \quad (16)$$

where Φ is Fourier projection (5).

While (12) is a good approximation to the dynamics close to the Hopf bifurcation, away from the Hopf bifurcation the phase speed Ω (frequency of oscillation) varies. As such, to better capture the behaviour, we allow the phase speed to vary and treat it as a second function to learn, as given by

$$\Omega(\mathbf{u}, \nu) = \omega_0 + \text{NN}_{\theta_2}(\mathbf{u}, \nu), \quad (17)$$

where ω_0 is a constant and $\text{NN}_{\theta_2}(\mathbf{u}, \nu)$ is a neural network with three input nodes, two hidden layers each with 31 nodes, and a single output node. All nodes use the tanh activation function. Since the original cost function (16) is invariant with respect to the phase speed (by construction), this second function can be optimised after the initial training is complete.

Take $d_i^s(t)$ to be the time-series measurements in physical coordinates of an LCO on the upper-stable branch, with $d_i^u(t)$ being corresponding measurements on the lower-unstable branch. The cost function used to train Ω is thus

$$\mathcal{E}_{\Omega} = \sum_{i=1}^{m_s} \sum_j \|\mathbf{U}(\mathbf{u}_i^s(t_j), \mu_i^s) - \mathbf{d}_i^s(t_j)\| + \sum_{i=1}^{m_u} \sum_j \|\mathbf{U}(\mathbf{u}_i^u(t_j), \mu_i^u) - \mathbf{d}_i^u(t_j)\|, \quad (18)$$

where u_i^s and u_i^u are time-series measurements calculated from the data-driven model.

6 Results

To train the data-driven model, we used 10 samples of stable LCOs and 2 samples of unstable LCOs taken from (9), as marked in Fig. 5.

The optimisation routines were implemented in Julia using the Flux.jl [16] deep learning package and stochastic gradient descent. Time series of the differential equations were calculated with the DifferentialEquations.jl [17] and DiffEqFlux.jl [5] packages, making use of pullbacks to enable the computation of derivatives of the cost functions.

As shown in Fig. 5, the solution branches of the normal-form-based model (12) and the underlying flutter mode (9) match well. This is particularly remarkable when considering the simplicity of the normal-form-based model (12) and the relatively sparse training dataset provided.

Figure 6 shows a comparison of the phase portraits of individual LCOs close to the training points, one stable and one unstable. As expected due to the proximity to the training data, the phase portraits show good agreement. Moreover, the phase portraits show that the learnt transformation is non-trivial since the phase portraits are clearly not circular as would be expected from the Hopf bifurcation normal form used.

Away from the training points, there is a larger discrepancy between the phase portraits as shown in Fig. 7; however, the discrepancy is still relatively small. This provides confidence in the method since the model appears to interpolate well.

Finally, Fig. 8 shows time series of two LCOs. While there are slight discrepancies at high amplitude, it can be seen that the learnt phase speed allows the time series to be matched well.

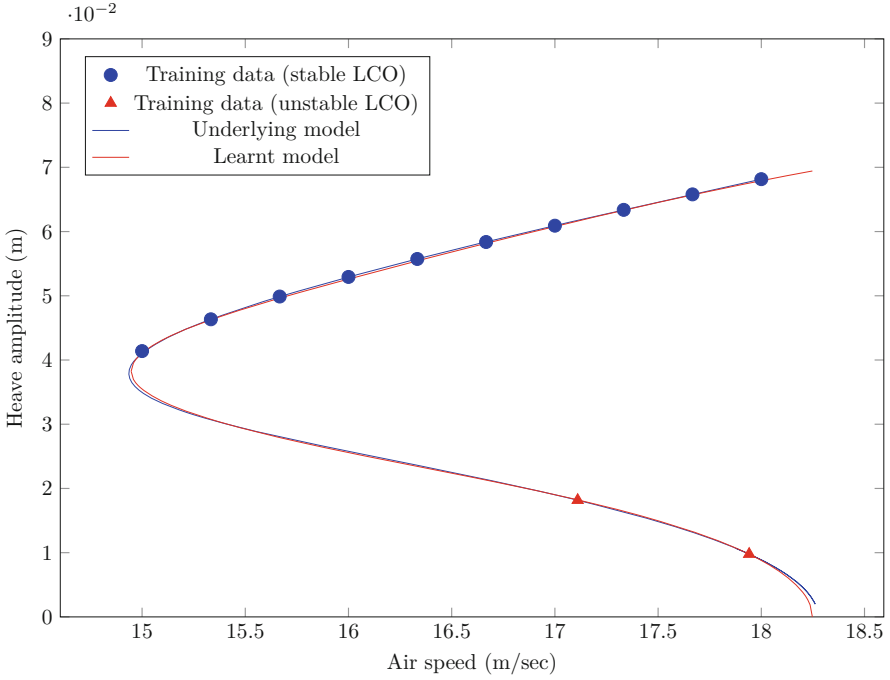


Fig. 5 A bifurcation diagram showing a comparison between the results of the hybrid differential-equation/machine-learned model and the underlying ground truth (9). Training data used for machine learning is shown by the markers on the bifurcation curve. There is good agreement between the two models even away from the training points

7 Conclusions

This chapter has proposed a hybrid machine learning/differential-equation approach to the modelling of nonlinear experiments exhibiting different regimes of qualitative behaviour separated by bifurcations. We have shown that the required knowledge of the bifurcation structure can be extracted from a physical experiment by use of phase-plane control-based continuation. This knowledge is then used to generate a normal-form-like model that qualitatively matches the bifurcation structure of the underlying experiment. Measured data is then used with machine learning algorithms to construct a coordinate transformation between the normal-form-like model and the physical coordinate system.

We have shown that this approach is an effective way to generate an accurate nonlinear model based on limited data. In this chapter, the behaviour of a 6-dimensional aero-elastic flutter model is reproduced using only 12 measured limit cycle oscillations. Overall, this combination of knowledge of the physical system and machine learning appears to be very versatile and opens up a wide range of possibilities for future modelling work on nonlinear physical systems

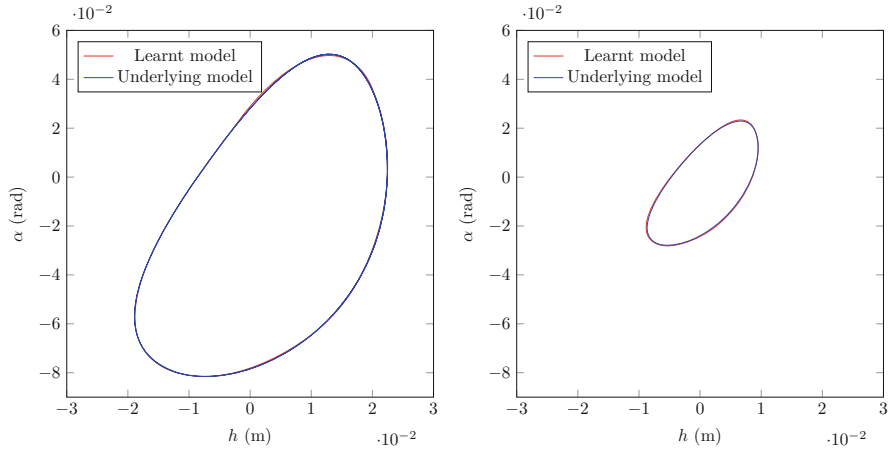


Fig. 6 Comparison of the phase portraits of the hybrid model and the underlying ground truth (9). The limit cycles shown are calculated at an air speed of 15.0 ms^{-1} (left panel; stable oscillation) and 17.1 ms^{-1} (right panel; unstable oscillation). These points are close to the training data points and, as such, show very good agreement

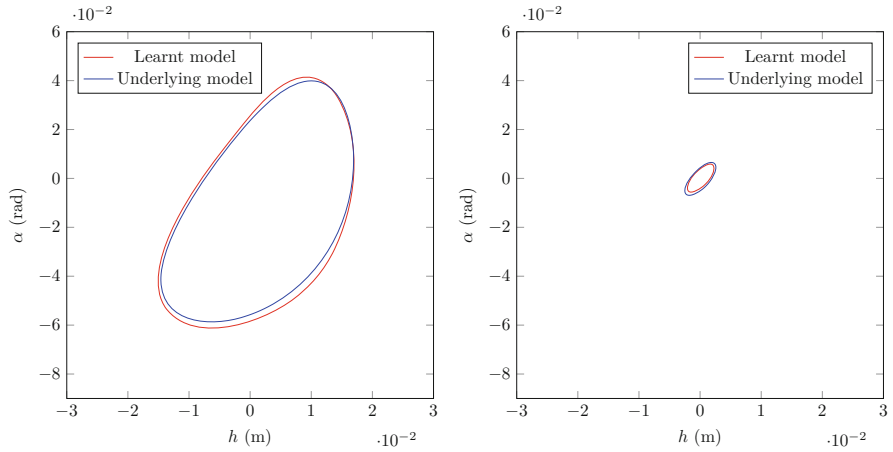


Fig. 7 Comparison of the phase portraits of the hybrid model and the underlying ground truth (9) away from the training points. The limit cycles shown are calculated at an air speed of 15.4 ms^{-1} (left panel; unstable oscillation) and 18.13 ms^{-1} (right panel; unstable oscillation). Despite being away from the training points, there is still good agreement

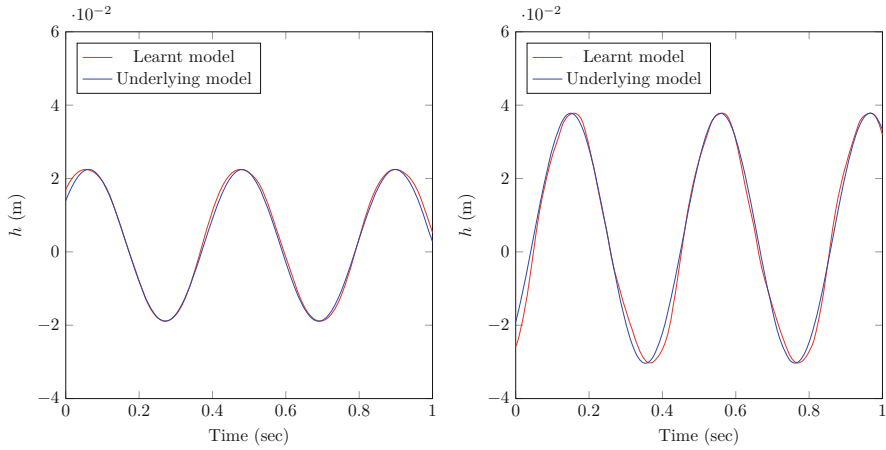


Fig. 8 Comparison of the time-series response in the heave variable. The left-hand panel shows the response at an air speed of 15.0 ms^{-1} and the right-hand panel shows the response at an air speed of 18.0 ms^{-1}

where experimental data is available, even where the underlying physics is poorly understood (e.g., synthetic biology) or ill defined (e.g., macroscopic behaviour of people in crowds).

Acknowledgments K.H.L. was supported by a PhD Scholarship from the University of Bristol, D.A.W.B. was supported by the EPSRC (EP/K032738/1), and L.R. was supported by the Royal Academy of Engineering (RF1516/15/11).

Appendix: Parameters of Aero-Elastic Flutter Model

The model matrices of (9), as derived in [14], are given by

$$\mathbf{M} = \begin{bmatrix} m_T + \pi\rho b^2 & mx_\alpha b - a\pi\rho b^3 & 0 \\ mx_\alpha b - a\pi\rho b^3 & I_\alpha + \pi(1/8 + a^2)\rho b^4 & 0 \\ 0 & 0 & 1 \end{bmatrix}, \quad (\text{A.1a})$$

$$\mathbf{D} = \begin{bmatrix} c_h + \pi\rho bU & (1 + (1/2 - a))\pi b^2 U & 2\pi U^2 b(c_1 c_2 + c_3 c_4) \\ -\pi(a + 1/2)\rho b^2 & c_\alpha + (1/4 - a^2)\pi\rho b^3 U & -2\pi\rho b^2 U^2(a + 1/2)(c_1 c_2 + c_3 c_4) \\ -1/b & a - 1/2 & (c_2 + c_4)U/b \end{bmatrix}, \quad (\text{A.1b})$$

$$\mathbf{K} = \begin{bmatrix} k_h & \pi\rho bU^2 & 2\pi U^3 c_2 c_4(c_1 + c_3) \\ 0 & k_\alpha - \pi(1/2 + a)\rho b^2 U^2 & -2\pi\rho bU^3(a + 1/2)(c_2 c_4(c_1 + c_3)) \\ 0 & -U/b & c_2 c_4 U^2 / b^2 \end{bmatrix}. \quad (\text{A.1c})$$

Table A.1 Parameters values of the aero-elastic flutter model (9)

Parameter	Value	Parameter	Value
b	0.15	I_α	0.1726
a	-0.5	x_α	0.24
ρ	1.204	c_α	0.5628
k_h	3529.4	c_h	15.4430
m_w	5.3	c_0	1
m_T	16.9	c_1	0.1650
k_α	54.11	c_2	0.0455
$k_{\alpha 2}$	751.6	c_3	0.335
$k_{\alpha 3}$	5006	c_4	0.3

The parameter values used are given in Table A.1.

References

1. M. Raissi, P. Perdikaris, G.E. Karniadakis, Physics-informed neural networks: a deep learning framework for solving forward and inverse problems involving nonlinear partial differential equations. *J. Comput. Phys.* **378**, 686–707 (2019)
2. X. Jia, J. Willard, A. Karpatne, J.S. Read, J.A. Zwart, M. Steinbach, V. Kumar, Physics-guided machine learning for scientific discovery: an application in simulating lake temperature profiles (2020)
3. R.T.Q. Chen, Y. Rubanova, J. Bettencourt, D.K. Duvenaud, Neural ordinary differential equations, in *Advances in Neural Information Processing Systems* (2018), pp. 6571–6583
4. Y. Hu, S. Boker, M. Neale, K.L. Klump, Coupled latent differential equation with moderators: Simulation and application. *Psychol. Methods* **19**(1), 56 (2014)
5. C. Rackauckas, Y. Ma, J. Martensen, C. Warner, K. Zubov, R. Supekar, D. Skinner, A. Ramadhan, Universal differential equations for scientific machine learning (2020). arXiv preprint arXiv:2001.04385
6. D.A.W. Barton, J. Sieber, Systematic experimental exploration of bifurcations with noninvasive control. *Phys. Rev. E* **87**(5), 052916 (2013)
7. J. Sieber, B. Krauskopf, Control based bifurcation analysis for experiments. *Nonlinear Dyn.* **51**(3), 365–377 (2008)
8. L. Renson, A.D. Shaw, D.A.W. Barton, S.A. Neild, Application of control-based continuation to a nonlinear structure with harmonically coupled modes. *Mech. Syst. Signal Process.* **120**, 449–464 (2019)
9. L. Renson, A. Gonzalez-Buelga, D.A.W. Barton, S.A. Neild, Robust identification of backbone curves using control-based continuation. *J. Sound Vib.* **367**, 145–158 (2016)

10. D.A.W. Barton, Control-based continuation: Bifurcation and stability analysis for physical experiments. *Mech. Syst. Signal Process.* **84**, 54–64 (2017)
11. J. Carr, *Applications of Centre Manifold Theory*, vol. 35 (Springer, Berlin, 2012)
12. H. Lin, S. Jegelka, ResNet with one-neuron hidden layers is a universal approximator, in *Advances in Neural Information Processing Systems* (2018), pp. 6169–6178
13. D.A. Winkler, T.C. Le, Performance of deep and shallow neural networks, the universal approximation theorem, activity cliffs, and QSAR. *Mol. Inf.* **36**(1–2), 1600118 (2017)
14. A. Abdelkefi, R. Vasconcellos, A.H. Nayfeh, M.R. Hajj, An analytical and experimental investigation into limit-cycle oscillations of an aeroelastic system. *Nonlinear Dyn.* **71**(1–2), 159–173 (2013)
15. K.H. Lee, A numerical simulation of an ML model of flutter (2020). https://github.com/Kyoungyunlee/MLflutter_numerical. Accessed September 2020
16. M. Innes, Flux: Elegant machine learning with Julia. *J. Open Source Softw.* **3**(25), 602 (2018)
17. C. Rackauckas, Q. Nie, DifferentialEquations.jl—a performant and feature-rich ecosystem for solving differential equations in Julia. *J. Open Res. Softw.* **5**(1) (2017)

Synchronization Study on Vortex-Induced Vibrations Using Wake Oscillator Model



Rik Mondal, Chandan Bose, and Sirshendu Mondal

1 Introduction

Vortex-induced vibration (VIV) occurs when the shed vortices behind a bluff body exert oscillatory forces on the flexible structure. The structural vibration thus produced, in turn, affects the vortex-shedding pattern, giving rise to two-way-coupled interactions. VIV can limit the life expectancy of materials through fatigue damage and may even lead to catastrophic failures in the engineering systems, such as chimneys, suspended cables for bridges, power transmission lines, marine risers, towing cables to name a few. On the other hand, VIV has recently been successfully exploited to extract the flow energy for renewable energy harvesting. It has direct applications in many industrial and engineering systems and therefore has been a subject of extensive experimental and numerical investigations in the recent past [1, 2].

VIV is characterized by the phenomenon of synchronization or lock-in. For low flow speeds, the vortex-shedding frequency remains the same as that of a fixed cylinder, particular to the Strouhal number. On the contrary, as the flow speed is increased, the shedding frequency no longer obeys the Strouhal relationship and synchronizes with the oscillation frequency of the cylinder. To that end, large body motions are observed as the structure exhibits near-resonance dynamics when the vortex-shedding and body oscillation frequencies coalesce into a single frequency close to its natural frequency, marking the onset of the lock-in regime [1]. This synchronization or lock-in phenomenon is dependent on several factors, among

R. Mondal (✉) · S. Mondal

Department of Mechanical Engineering, National Institute of Technology Durgapur, Durgapur, India

C. Bose

Department of Aerospace and Mechanical Engineering, University of Liège, Liège, Belgium

which the Reynolds number, the material damping and structural stiffness, the mass ratio and associated added mass effect are worth mentioning [2]. Navrose and Mittal [3] have revealed the mechanism of synchronization and lock-in during VIV of a transversely oscillating cylinder through linear stability analysis.

To avoid the prohibitive computational cost of high-fidelity CFD simulations, phenomenological low-order models of VIV for a one degree-of-freedom (Dof) structures, considering a wake or fluid oscillator has been established to be very much effective in capturing the essential dynamics of VIV [4]. The classical VDP model is considered to be the base skeleton of the family of wake oscillator models used to estimate the aerodynamic loads for predicting cross-flow VIV [5]. In this modelling framework, the forcing term in the wake oscillator model is considered to be proportional to structural acceleration, ensuring that both the wake motion (or aerodynamic lift force) and structural motion drive each other. Furthermore, a number of modifications have been implemented on this simplistic model over the years to capture the underlying physics better and have a better validation with the experimental results [6–8]. The weakly non-linear VDP oscillator results in steady periodic response but may also give rise to chaotic response when the non-linearity is strong [9].

While a majority of the existing studies in the literature have investigated the VIV phenomenon by coupling a linear structure with the wake oscillator model, there is a lack of understanding on the effect of structural non-linearity on the synchronization behaviour. Note that the presence of structural non-linearity can significantly alter the coupled fluid-elastic interactions. Hence, there is a need to investigate the synchronization characteristics of VIV with a non-linear structural oscillator in comparison to a linear one. Additionally, although the synchronization limits have been identified through a number of studies, the synchronization route is not clearly established from the dynamical systems point of view. The present study takes up this analysis by considering a cubic non-linearity in the structure coupled with a weakly non-linear VDP oscillator. A detailed response analysis is carried out from the purview of synchronization theory.

The remainder of this chapter is organized in the following sections. The mathematical modelling is depicted in Sect. 2. Section 3 describes the synchronization measures adopted in this chapter to characterize the coupled VIV response. The primary findings of this chapter for a linear and a non-linear structural model and the accompanied discussion are presented in Sect. 4. Finally, this chapter ends with the summary of salient findings in Sect. 5.

2 Mathematical Model

In this chapter, we adopt a simplistic low-order model of transverse VIV, where the single DoF structure is described by a linear ($\alpha = 0$) as well as non-linear ($\alpha \neq 0$) oscillator (Eq. 1), and a classical VDP oscillator (Eq. 2) is selected for capturing the wake dynamics. For the sake of simplicity, a linear coupling is considered similar

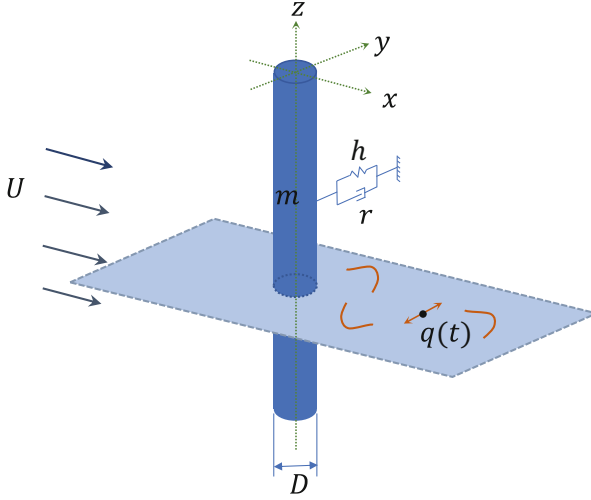


Fig. 1 Schematic for 2-D vortex-induced vibration in a fluid-elastic system comprising of coupled structure and wake oscillators. h and r are the representative of stiffness and damping coefficient of the elastic structure

to the model described in [5]. Although a number of modified wake oscillator models [6–8] are available, we stick to the canonical VDP model to constrict our focus solely on the synchronization behaviour. Figure 1 shows the schematic of the cylindrical structure of mass m and diameter D exhibiting cross-flow (y -direction) oscillations under steady uniform inflow with free stream velocity, U .

$$\ddot{y} + (2\zeta\delta + \frac{\gamma}{\mu})\dot{y} + \delta^2 y + \alpha y^3 = s; \quad (1)$$

$$\ddot{q} + \epsilon(q^2 - 1)\dot{q} + q = f. \quad (2)$$

Here, $y(t)$ is the structural displacement and $q(t)$ is the wake parameter. The coupling between structure and wake is modelled through s and f . s captures the effect of vortices on the structure as $s = Mq$, and f models the effect of structural motion on the wake as $f = A\dot{y}$ (velocity coupling) and $f = A\ddot{y}$ (acceleration coupling). The parameters and their values are given as follows. Here, ζ is the structure reduced damping (0.0052), δ is the reduced angular frequency of the structure ($1/0.2U_r$, where U_r is the reduced flow velocity), γ is a stall parameter (0.8), μ is the dimensionless mass ratio (1.1938), M is the mass number (0.0419), A is the coupling strength (12), and ϵ is the non-linearity parameter in VDP oscillator (0.3). The details of the model and the values of all model parameters can be found in [5]. Following [10], a cubic non-linearity is added to the structure oscillator with non-linearity coefficient α .

The governing equations of this VIV system (Eqs. 1 and 2) are numerically integrated using a Runge–Kutta method-based solver ODE45, available in MATLAB. Removing the initial transients, the time series of the structure ($y(t)$) and the wake ($q(t)$) variables are analysed to evaluate various synchronization measures, described in Sect. 3, in order to obtain amplitude, phase, and frequency of oscillations.

3 Synchronization Measures

Synchronization is a fundamental non-linear phenomenon for two or more interactive oscillators, wherein the time periods of the oscillators match due to coupled interactions. In this regard, coupling strength between these oscillators is a crucial parameter that determines the state of synchronization. The occurrence of synchronization is usually examined by studying the locking of phase (or frequency) of the signals [11]. In this chapter, the phase of a signal is estimated following Hilbert-transform-based analytic signal approach [12].

An analytic signal is a complex quantity, denoted by $\zeta(t)$, whose real part is the original signal, $y(t)$, and imaginary part is the Hilbert transform of it, $y_H(t) = 1/\pi$ P.V. $\int_{-\infty}^{\infty} (y(\tau)/(t - \tau))d\tau$, where P.V. is the Cauchy principle value of the integral. Thus, an analytic signal is defined as $\zeta(t) = y(t) + iy_H(t) = A(t)e^{i\phi(t)}$, where $\phi(t)$ and $A(t)$ represent the instantaneous phase and the instantaneous amplitude of the signal, respectively. The synchronization of coupled oscillators is investigated by studying the relative phase and is calculated as $\Delta\phi_{i,j}(t) = |\phi_j(t) - \phi_i(t)|$.

In this chapter, we quantify the degree of synchronization between structure and wake oscillators using the phase-locking value (PLV) and relative mean frequency ($\Delta\omega$). PLV is defined as, $PLV = N^{-1} \sum_{i=1}^N e^{i\Delta\phi(t)}$, and computes the mean variability of instantaneous relative phases [13]. This measure approaches 1 for a perfectly synchronized state and becomes close to 0 for a perfectly desynchronized state of oscillations. On the other hand, the frequency entrainment is analysed by calculating relative mean frequency that is defined as $\Delta\omega = |\langle\omega_i(t)\rangle_t - \langle\omega_j(t)\rangle_t| = |\langle\frac{d\phi_i(t)}{dt}\rangle_t - \langle\frac{d\phi_j(t)}{dt}\rangle_t|$.

Note that the notion of synchronization is applicable to the interaction between two self-sustained oscillators. In the present model, the structure oscillator, in isolation, does not behave like a self-sustained one. Therefore, we only use the synchronization measures to analyse the phase and frequency relations between structure and wake oscillators.

4 Results and Discussions

The synchronization results are presented by comparing and contrasting the cases considering the structure oscillator to be linear ($\alpha = 0$ in Eq. 1) and non-linear ($\alpha \neq 0$ in Eq. 1). We have investigated the synchronization behaviour for a range of positive as well as negative α values; however, we present the results only for two representative cases at $\alpha = 100$ and $\alpha = -100$ as we did not observe any change in the dynamics for in-between positive and negative values.

4.1 Linear Structure Oscillator

The numerical solver is first validated by plotting the variation in structural oscillation amplitude (Y_0) as a function of reduced flow velocity (U_r) considering both velocity and acceleration coupling with the same calculated analytically by Facchinetti et al. [5] (Fig. 2). We further compare with the experimental results of Govardhan and Williamson [14]. The numerical results are found to closely follow the trend of analytical results (Fig. 2). The difference in numerical values between analytical and numerical solutions can be attributed to the approximation involved in the analytical formulations.

As observed in Fig. 2 and also has been concluded by Facchinetti et al. [5], although this simplistic model is not capable of capturing the correct experimental amplitude, the sustained lock-in behaviour is correctly obtained through the acceleration coupling in contrast to the velocity coupling. Therefore, we

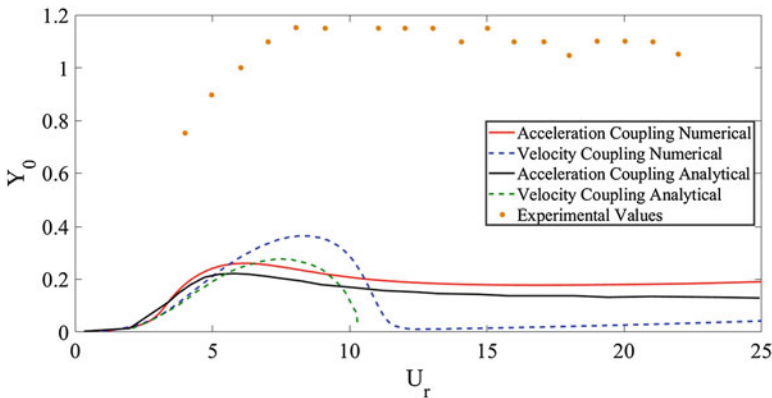


Fig. 2 The change in amplitude of structure oscillation (Y_0) with the variation of reduced flow velocity (U_r). Numerical solutions are plotted with analytical results of [5] for both velocity and acceleration coupling, together with the experimental results of [14]

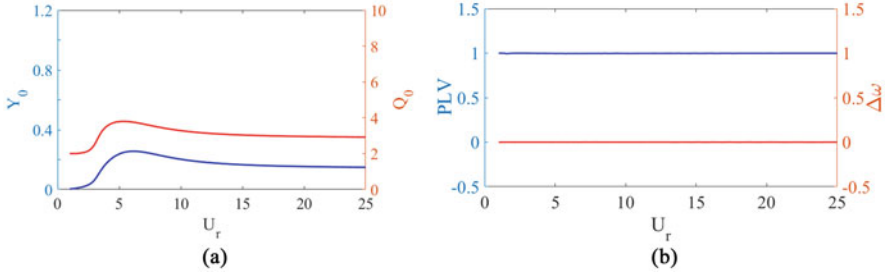


Fig. 3 (a) Amplitude of structural and wake oscillation as a function of reduced flow velocity (U_r). (b) Variation in phase-locking value and relative mean frequency between structure and wake oscillator with flow velocity

consider only acceleration coupling in the rest of this chapter. Next, we present the synchronization feature between structure and wake oscillator as U_r is varied.

Towards that, the oscillation amplitudes of the structure and the wake are presented in Fig. 3a. We observe that large-amplitude oscillation persists for high reduced velocities, which is representative of persistent lock-in [5]. The phase and frequency synchronization between structure and wake oscillations is then analysed by evaluating PLV and relative-mean-coupled frequency ($\Delta\omega$), respectively. These are plotted as a function of U_r in Fig. 3b. It is observed that two oscillators remain phase- and frequency-locked throughout the range of flow speed as inferred from the values of PLV close to 1 and $\Delta\omega$ close to 0. Next, the case with non-linear structure oscillator is investigated.

4.2 Non-Linear Structure Oscillator

In this section, we discuss the coupled dynamics of structure and wake oscillators, considering a cubic non-linearity in structural stiffness. With this modification, the structure can be described by a Duffing oscillator. To study the effect of non-linearity, we choose the non-linearity coefficient of the Duffing oscillator (Eq. 1), α to be +100 and -100, following [10]. The bifurcation diagram of the peaks of structural oscillation as a function of U_r is shown in Fig. 4.

The sharp increase in the peak values around $U_r = 5$ shows the lock-in zone and associated amplification of structural oscillations for both $\alpha = 100$ (Fig. 4a) and $\alpha = -100$ (Fig. 4b). A single peak value is obtained for most of the U_r range considered, indicating the presence of a steady limit cycle oscillation (LCO). However, interestingly, we find three distinct peaks, indicating period-3 oscillation in the structural response for $U_r = 1.57$ – 1.77 , shown as insets in Fig. 4. Furthermore, a slight amplification in the structural oscillation is noticed around $U_r = 1.68$. This change in the dynamical behaviour is also reflected in the synchronization feature between the structure and wake oscillations, which will

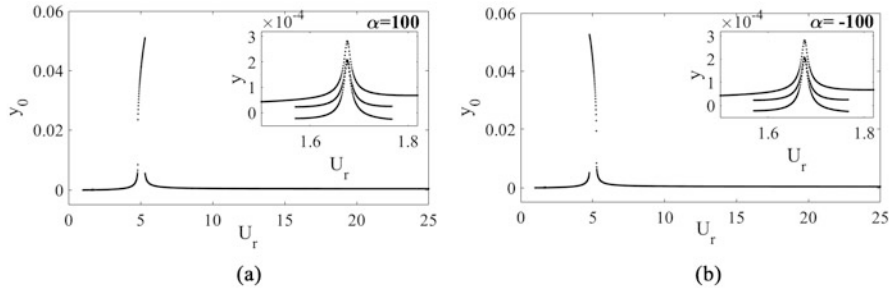


Fig. 4 Bifurcation diagrams of the peaks of structural oscillation as a function of reduced flow velocity (U_r). The zoomed period-3 oscillations observed around $U_r = 1.68$ are depicted as insets. (a) $\alpha = 100$. (b) $\alpha = -100$

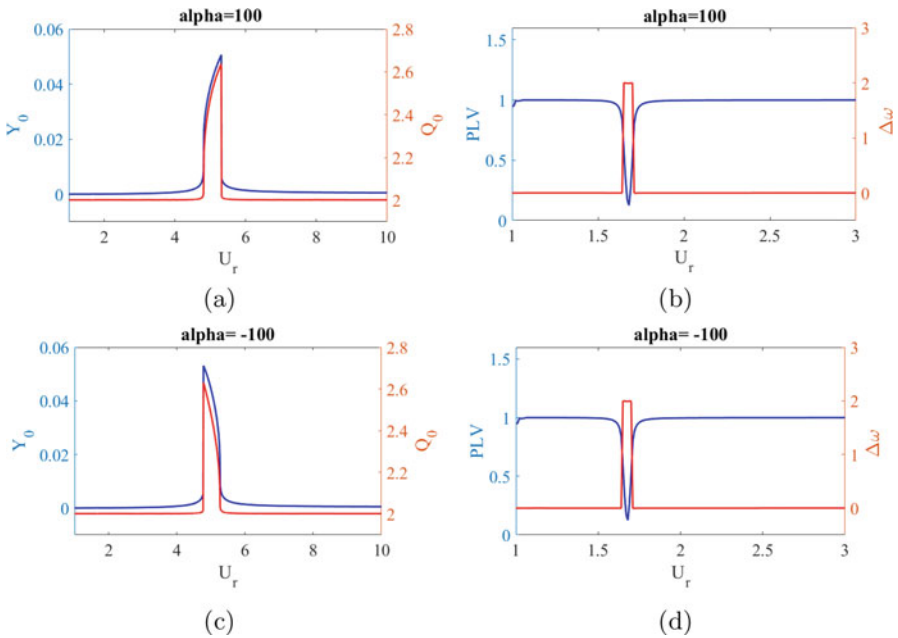


Fig. 5 Amplitude response with respect to reduced flow velocity is shown for $\alpha = 100$ (a) and $\alpha = -100$ (c). Variation in PLV and relative mean frequency ($\Delta\omega$) with U_r is shown for $\alpha = 100$ (b) and $\alpha = -100$ (d)

be presented in the following. However, studying the emergence of such dynamics with given coupled oscillators system is beyond the scope of the present study and the authors are presently working towards this.

Studying synchronization between a non-linear structural oscillator and a non-linear wake oscillator can be insightful for the practical situation. Towards that, amplitude of the structural and wake oscillators are first plotted against reduced flow velocity (U_r) for the non-linearity parameter $\alpha = 100$ (Fig. 5a) and $\alpha = -100$

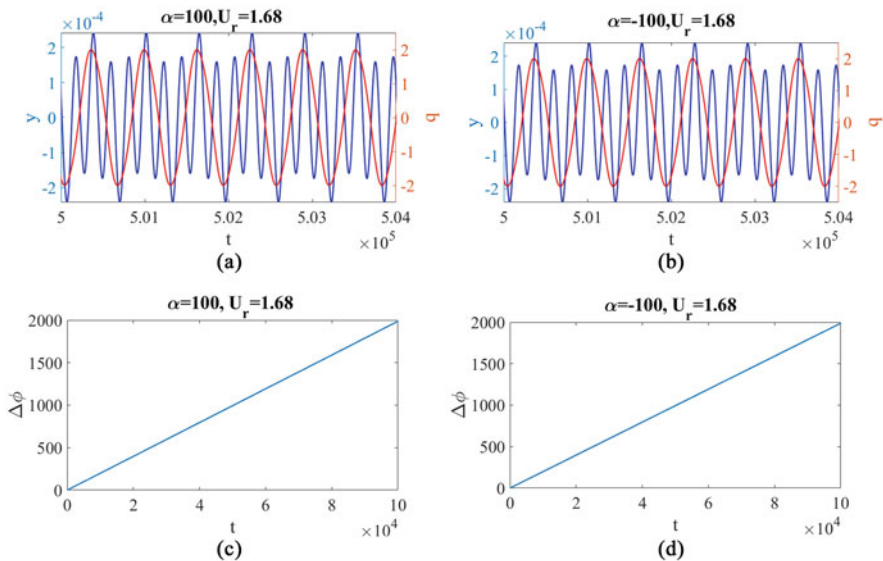


Fig. 6 Overlapped time series of structure (y) and wake (q) oscillations for (a) $\alpha = 100$ and (b) $\alpha = -100$. Corresponding relative phase dynamics is shown in (c) and (d), respectively

(Fig. 5c). The amplitude response with a non-linear structure oscillator is found to have a bounded lock-in regime in contrast to the persistent lock-in as observed for the linear structure oscillator. The present results show a close agreement with those reported by Vigneshvar et al. [10]. However, analysing the coupled dynamics brings out an interesting phenomenon.

Similar to the previous case, the measures, PLV and $\Delta\omega$, are plotted as a function of U_r for $\alpha = 100$ and $\alpha = -100$ in Fig. 5b, d, respectively. PLV is found to be 1 for all values of U_r (including the lock-in regime) except a small regime around $U_r = 1.68$. The low values of PLV observed around $U_r = 1.68$ imply phase-asynchronous behaviour between structure and wake oscillators. The difference in mean frequencies is also observed as expected, indicating the absence of frequency locking. In this range of U_r values, period-3 oscillations are observed for structure oscillator (Fig. 4) that gives rise to the mismatch of time scales between structure and wake oscillation. For a better understanding of the coupled interaction, we next analyse the dynamics of structure and wake oscillations and the relative phase dynamics.

Overlapped time series for structure (y) and wake (q) oscillations are shown for $\alpha = 100$ (Fig. 6a) and $\alpha = -100$ (Fig. 6b). Period-3 oscillations are apparent in structure dynamics (in blue), whereas wake continues to oscillate with a single period (in red) irrespective of hardening or softening non-linearity. Such a disparity leads to a difference in their mean frequencies (observed in Fig. 5b and d). This difference in their mean frequency is also manifested in relative phase dynamics ($\Delta\phi(t)$) that are shown for $\alpha = 100$ (Fig. 6c) and $\alpha = -100$ (Fig. 6d). The

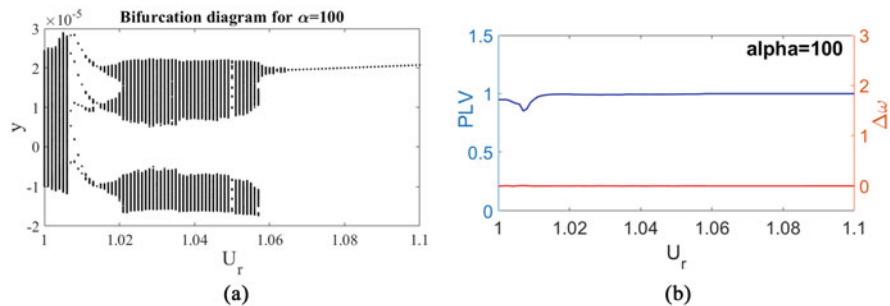


Fig. 7 (a) Peaks of structural oscillations are plotted against low value of flow speed. (b) Corresponding PLV and relative mean frequency are shown

relative phase is observed to grow monotonically with time, known as phase drifting [11]. This implies the absence of phase locking or phase synchronization between structure and wake oscillator at $U_r = 1.68$ for both cubic hardening and softening non-linearity. Such an asynchronous regime is observed only with non-linear structure oscillator. The authors are currently working on why there is a difference in dynamical and synchronization behaviour at $U_r = 1.68$.

We further notice an interesting dynamical transition for low values of flow velocity ($U_r < 1.1$) as depicted in Fig. 7. This shows multiple peaks for short range U_r . Although the dynamical transition appears to be very rich (Fig. 7a), we find frequency entrainment for all values of U_r and phase locking for major part of U_r values. However, this needs a thorough investigation and will be taken as future scope of this chapter.

5 Conclusions

This chapter focuses on the coupled interaction between the structure and wake oscillators, usually considered for modelling VIV. The wake dynamics is modelled as a classical VDP oscillator, whereas the structural motion is modelled with a linear as well as a non-linear Duffing oscillator. The coupled dynamics between these oscillators are studied by invoking synchronization theory. To that end, phase and frequency locking is characterized by evaluating PLV and relative mean frequency. The coupled system with linear structure oscillator exhibits phase and frequency locking throughout the range of flow speed considered. The fact that the phase locking outside the lock-in regime does not follow the experimental observation might be a model artifact and therefore needs to be addressed in future. On the other hand, the system with non-linear structure oscillator exhibits asynchronous behaviour prior to lock-in regime. Further, at low flow speed, the coupled system is observed to apparently show a very rich dynamics with a detour from the completely phase-synchronized behaviour. However, a detailed investigation on the dynamics

and synchronization of such a simplistic model with non-linear structural oscillator needs to be carried out and the authors are currently working on it.

References

1. C.H.K. Williamson, R. Govardhan, Vortex-induced vibrations. *Ann. Rev. Fluid Mech.* **36**, 413–455 (2004)
2. R.D. Gabbai, H. Benaroya, An overview of modeling and experiments of vortex-induced vibration of circular cylinders. *J. Sound Vib.* **282**(3–5), 575–616 (2005)
3. Navrose, S. Mittal, Lock-in in vortex-induced vibration. *J. Fluid Mech.* **794**, 565–594 (2016)
4. R.E.D. Bishop, A.Y. Hassan, The lift and drag forces on a circular cylinder oscillating in a flowing fluid. *Proc. R. Soc. Lond. Ser. A. Math. Phys. Sci.* **277**(1368), 51–75 (1964)
5. M.L. Facchinetti, E. De Langre, F. Biolley, Coupling of structure and wake oscillators in vortex-induced vibrations. *J. Fluids Struct.* **19**(2), 123–140 (2004)
6. R.H.M. Ogink, A.V. Metrikine, A wake oscillator with frequency dependent coupling for the modeling of vortex-induced vibration. *J. Sound Vib.* **329**(26), 5452–5473 (2010)
7. Y. Qu, A.V. Metrikine, A single Van der Pol wake oscillator model for coupled cross-flow and in-line vortex-induced vibrations. *Ocean Eng.* **196**, 106732 (2020)
8. P.A. Opinel, N. Srinil, Application of wake oscillators to two-dimensional vortex-induced vibrations of circular cylinders in oscillatory flows. *J. Fluids Struct.* **96**, 103040 (2020)
9. H. Fotsin, S. Bowong, Adaptive control and synchronization of chaotic systems consisting of Van der Pol oscillators coupled to linear oscillators. *Chaos, Solitons Fractals* **27**(3), 822–835 (2006)
10. V. Vigneshvar, S.R. Vishwanth, S. Venkateshwaran, B. Balaram, A comparative study of wake oscillator models for flow induced vibrations. *AIP Conf. Proc.* **2134**(1), 080006 (2019)
11. A. Pikovsky, J. Kurths, M. Rosenblum, J. Kurths, *Synchronization: A Universal Concept in Nonlinear Sciences*, vol. 12 (Cambridge University Press, Cambridge, 2003)
12. M.G. Rosenblum, A.S. Pikovsky, J. Kurths, Phase synchronization of chaotic oscillators. *Phys. Rev. Lett.* **76**(11), 1804 (1996)
13. S. Aydore, D. Pantazis, R.M. Leahy, A note on the phase locking value and its properties. *Neuroimage* **74**, 231–244 (2013)
14. R. Govardhan, C.H.K. Williamson, Modes of vortex formation and frequency response of a freely vibrating cylinder. *J. Fluid Mech.* **420**, 85–130 (2000)

Effects of Strong Viscosity with Variable Fluid Properties on Falling Film Instability



Anandamoy Mukhopadhyay, Souradip Chattopadhyay, and Amlan K. Barua

1 Introduction

The effect of thermophysical properties with temperature variation for a thin film flow along an inclined plane is a challenging problem due to its complicated formulation. To avoid this complexity most of the researchers consider the thermophysical properties, such as viscosity, density, thermal conductivity, surface tension, etc. as constants for non-isothermal flow. Using the long-wave expansion method, Goussis and Kelly [1] first studied the effects of viscosity variation on the stability of a non-isothermal thin liquid film flow along an inclined plane. To obtain relatively simple analytical results, they assumed the variation of the viscosity to be exponential with the temperature that is an approximation to the Arrhenius-type relation. They found that heating destabilizes the flow, whereas cooling stabilizes it. Since the Arrhenius-type viscosity variation is based on physical grounds, therefore Goussis and Kelly [2] further studied the above-stated problem considering the Arrhenius model as well as by exponential model using the Orr–Sommerfeld equation. They compared the results obtained by both the models and found qualitatively the same results stated earlier.

Hwang and Weng [3] investigated the linear as well as weakly nonlinear stability analysis of thin liquid film flow along a heated (cooled) rigid inclined plane considering the viscosity variation of the Arrhenius model with the temperature. Both the stability analysis again confirms that heating destabilizes the flow and cooling stabilizes it, as obtained by Goussis and Kelly [2].

A. Mukhopadhyay (✉)

Department of Mathematics, Vivekananda Mahavidyalaya (The University of Burdwan), West Bengal, India

S. Chattopadhyay · A. K. Barua

Department of Mathematics, Indian Institute of Technology Dharwad, Karnataka, India
e-mail: 183111001@iitdh.ac.in; abarua@iitdh.ac.in

Using the viscous scales and long-wave theory Reisfeld and Bankoff [4] derived an evolution equation of a heated liquid thin film flow, considering the dynamic viscosity as the linear function of temperature. They derived a relation between the physical time variable for the temperature-dependent viscosity with that of the time scale for constant viscosity when the Biot number is very small/very large. They found that for large Biot numbers, due to variable viscosity, the rupture time of the thin liquid film decreases relative to that of constant viscosity.

Pascal et al. [5] presented an analytical study of the interfacial instability of a thin film flow along a uniformly heated inclined plane. To show the effect of variation of different thermophysical properties, they assumed the linear variation of density, dynamical viscosity, thermal conductivity, and specific heat along with the temperature variation of surface tension. Later, D'Alessio et al. [6] studied the effects of linear variation of different thermophysical quantities except for the specific heat, on gravity-driven thin film flow along a uniformly heated incline. In both these studies, only linear stability analysis was performed.

Mukhopadhyay and Chattopadhyay [7] proposed an analytical model of a thin, Newtonian film flowing down a uniformly heated inclined plane, considering a linear variation of various thermophysical properties. They performed both linear as well as weakly nonlinear stability analysis and captured the effect of different thermophysical properties on different stable/unstable zones.

In this study, we take all fluid properties including mass density, viscosity, surface tension and thermal diffusivity to be temperature dependent. We assume that the density, surface tension and thermal diffusivity vary linearly whereas the viscosity varies exponentially with small variation of temperature. The exponential variation of viscosity is physically more viable than its linear variation with temperature. We aim to figure out the effects of strong (exponential variation) and weak (linear variation) viscosity on the instability phenomena of the flow dynamics.

2 Physical Model and Formulation

We consider the two-dimensional laminar flow of a viscous, incompressible, Newtonian, thin liquid film along an impermeable inclined plane of inclination γ with the horizon that is uniformly heated from below with the temperature $T = T_W > T_\infty$ where T_∞ is the ambient air temperature above the fluid layer (see Fig. 1). We choose x, z -axes along the stream-wise and cross-stream direction of the flow, respectively. The density (ρ), surface tension (σ), thermal diffusivity (κ), and dynamical viscosity (μ) are temperature-dependent fluid properties. We assume that ρ, σ , and κ are varying linearly [7] with a small variation of temperature $\Delta T = (T_W - T_\infty) (> 0)$, whereas μ varies exponentially as

$$\begin{aligned} \rho &= \rho_\infty [1 - K_\rho (T - T_\infty) / \Delta T], & \sigma &= \sigma_\infty [1 - K_\sigma (T - T_\infty) / \Delta T], \\ \kappa &= \kappa_\infty [1 + K_\kappa (T - T_\infty) / \Delta T], & \mu &= \mu_\infty \exp[-K_\mu (T - T_\infty) / \Delta T], \end{aligned} \quad (1)$$

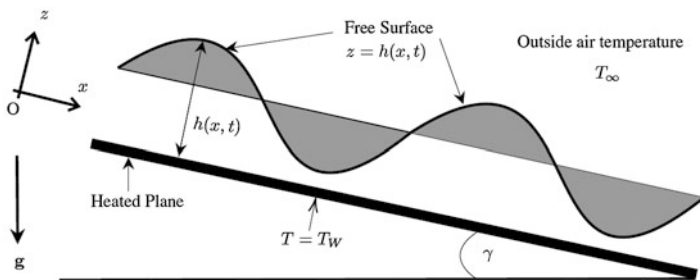


Fig. 1 The flow configuration

where ρ_∞ , σ_∞ , κ_∞ and μ_∞ are the values of ρ , σ , κ , and μ at the reference temperature $T = T_\infty$. Also $K_\rho = 1/\rho_\infty (-d\rho/dT)_{T=T_\infty} \Delta T$, $K_\sigma = 1/\sigma_\infty (-d\sigma/dT)_{T=T_\infty} \Delta T$, $K_\kappa = 1/\kappa_\infty (d\kappa/dT)_{T=T_\infty} \Delta T$ and $K_\mu = 1/\mu_\infty (-d\mu/dT)_{T=T_\infty} \Delta T$ are the parameters measuring the rate of change with respect to temperature.

Using (1), the governing equations (5)–(8) and the boundary conditions (9)–(14) of the problem formulated by Mukhopadhyay and Chattopadhyay [7] are made dimensionless by using viscous-gravity length scale $l_{v_\infty} = (v_\infty^2/(g \sin \gamma))^{1/3}$ and time scale $t_{v_\infty} = (v_\infty/(g \sin \gamma)^2)^{1/3}$ as

$$(x, z) = \bar{h}_N (x^*, z^*), h = \bar{h}_N h^*, t = (t_{v_\infty} l_{v_\infty} / \bar{h}_N) t^*, p = p_\infty + \rho_\infty (l_{v_\infty} \bar{h}_N / t_{v_\infty}^2) p^*,$$

$$(u, w) = \left(\bar{h}_N^2 / (t_{v_\infty} l_{v_\infty}) \right) (u^*, w^*), T = T_\infty + T^* \Delta T,$$

where \bar{h}_N is the uniform film thickness of the basic flow and $v_\infty = \mu_\infty / \rho_\infty$ is the kinematic viscosity at $T = T_\infty$.

In terms of these dimensionless variables, the equations of motion, energy, wall boundary conditions, and free-surface boundary conditions of [7] reduce to the following non-dimensional form after removing the star decoration as:

(i) Governing equations $[(x, z, t) \in \mathbb{R} \times (0, h) \times [0, \infty)]$:

$$u_x + w_z = 0, \quad (2)$$

$$3Re(u_t + uu_x + ww_z) = -p_x + (1 - K_\rho T) - K_\mu \exp(-K_\mu T) (u_x T_x + u_z T_z) \\ + \exp(-K_\mu T) (u_{xx} + u_{zz}), \quad (3)$$

$$3Re(w_t + uw_x + ww_z) = -p_z - \cot \gamma (1 - K_\rho T) + \exp(-K_\mu T) (w_{xx} + w_{zz})$$

$$-K_\mu \exp(-K_\mu T) (w_x T_x + w_z T_z), \quad (4)$$

$$3RePr (T_t + uT_x + wT_z) = K_\kappa (T_x^2 + T_z^2) + (1 + K_\kappa T) (T_{xx} + T_{zz}). \quad (5)$$

(ii) Boundary conditions on $z = 0$:

$$u = w = 0 \quad \text{and} \quad T = 1. \quad (6)$$

(iii) Boundary conditions on the free surface $z = h(x, t)$:

$$\exp(-K_\mu T) [(u_z + w_x) G - 2(u_x - w_z) h_x] + MF (T_x + h_x T_z) = 0, \quad (7)$$

$$p = 2 \exp(-K_\mu T) [u_x h_x^2 - (u_z + w_x) h_x + w_z] F^{-2} - (We - MT) h_{xx} F^{-3}, \quad (8)$$

$$w = h_t + u h_x, \quad (9)$$

$$(1 + K_\kappa T) (T_z - T_x h_x) + BFT = 0, \quad (10)$$

where $Re = g \sin \gamma \bar{h}_N^3 / (3\nu_\infty^2)$, $Pr = \nu_\infty / \kappa_\infty$, $We = \sigma_\infty / (\rho_\infty g \bar{h}_N^2 \sin \gamma)$, $M = (-d\sigma/dT)_{T=T_\infty} \Delta T / (\rho_\infty g \bar{h}_N^2 \sin \gamma)$, $B = k_g \bar{h}_N / k_T$ are the Reynolds number, Prandtl number, Weber number, film Marangoni number, and free-surface Biot number, respectively. Here we introduce $G = (1 - h_x^2)$ and $F = (1 + h_x^2)^{1/2}$. If we set K_ρ , K_μ , K_σ , and K_κ to 0, the above set of Eqs. (2)–(10) completely matches with the study of Kalliadasis et al. [8].

3 Long-Wave Expansion

To perform long-wave expansion of the governing equations and associated boundary conditions, we introduce a small parameter $\epsilon (\ll 1)$ through the transformations $(\partial_t, \partial_x) \rightarrow \epsilon (\partial_t, \partial_x)$ and $w \rightarrow \epsilon w$ followed by an asymptotic series expansion of all pertinent variables in powers of ϵ as

$$u = u_0 + \epsilon u_1 + \dots, \quad w = w_0 + \epsilon w_1 + \dots, \quad p = p_0 + \epsilon p_1 + \dots, \quad T = T_0 + \epsilon T_1 + \dots. \quad (11)$$

We assume that Re , Pr are of $O(1)$, M is of $O(1/\epsilon)$, We is of $O(1/\epsilon^2)$, and B is of $O(\epsilon^2)$ for our further investigation.

Substituting (11) into the re-scaled governing equations as well as boundary conditions and collecting the coefficients of like powers of ϵ , the zeroth- and first-order equations are obtained and the corresponding solutions are determined. Following Mukhopadhyay and Chattopadhyay [7], we obtain the evolution equation in terms of $h(x, t)$ as

$$h_t + A(h)h_x + \epsilon \left[B(h)h_x + \epsilon^2 C(h)h_{xxx} \right]_x + O(\epsilon^2) = 0, \quad (12)$$

where

$$\begin{aligned} A(h) &= (1 - K_\rho) \{ \exp(K_\mu) - \epsilon \exp(2K_\mu) \} h^2, \\ B(h) &= (2/5) Re (1 - K_\rho)^2 \exp(3K_\mu) h^6 - (1/3) \cot \gamma (1 - K_\rho) \exp(K_\mu) h^3, \\ C(h) &= (1/3) We (1 - K_\sigma) \exp(K_\mu) h^3. \end{aligned}$$

4 Stability Analysis

To study the growth of the disturbance with respect to the basic flow, the dimensionless film thickness in the perturbed state may be written as $h(x, t) = 1 + \eta(x, t)$, where $\eta(x, t) \ll 1$ represents the perturbation at any instant. We eliminate the dependency of Eq. (12) on ϵ by the transformations $(t, x) = \epsilon(\tilde{t}, \tilde{x})$. Applying these transformations with the perturbed film thickness, Eq. (12), after dropping the tilde sign and retaining the terms up to the order $O(\eta^3)$, reduces to the following form:

$$\begin{aligned} \eta_t + A\eta_x + B\eta_{xx} + C\eta_{xxxx} + A'\eta\eta_x + B'(\eta\eta_{xx} + \eta_x^2) + C'(\eta\eta_{xxx} + \eta_x\eta_{xxx}) + \frac{1}{2}A''\eta^2\eta_x \\ + B''\left(\frac{1}{2}\eta^2\eta_{xx} + \eta\eta_x^2\right) + C''\left(\frac{1}{2}\eta^2\eta_{xxx} + \eta\eta_x\eta_{xxx}\right) + O(\eta^4) = 0, \end{aligned} \quad (13)$$

where A, B, C and their corresponding derivatives are evaluated at $h = 1$.

To discuss the linear stability analysis, we consider only the linearized part of Eq. (13). To study the linear response for a sinusoidal perturbation of the film we assume the infinitesimal perturbation as

$$\eta = \xi \exp[i(kx - \omega t)] + \text{c.c.}, \quad (14)$$

where $\xi \ll 1$ is the amplitude of the disturbance, k is the wavenumber, and $\omega = \omega_r + i\omega_i$ is the complex frequency where ω_r, ω_i are the real and complex parts, respectively, and c.c. represents complex conjugate of the term preceding it.

Substituting (14) in the linearized part of (13) and then separating the real, imaginary parts, we obtain $\omega_r = Ak$ and $\omega_i = Bk^2 - Ck^4$. We observe that the

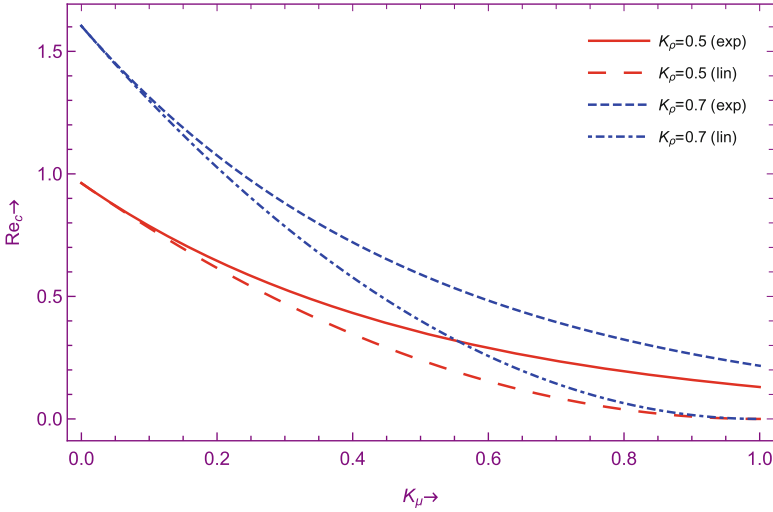


Fig. 2 Variation of critical Reynolds number (Re_c) with the variation of K_μ for different K_ρ with the fixed inclination $\gamma = \pi/3$

linear phase speed $c_r = \omega_r/k = A$, i.e., independent of k that implies that the wave is non-dispersive. The disturbance is asymptotically stable or unstable according to $\omega_i < 0$ or $\omega_i > 0$. Also, the neutral stability condition $\omega_i = 0$ gives two branches of the neutral curves $k = 0$, $k = \sqrt{B/C}$, and the flow instability takes place in between them.

The minimum Re at which instability sets in is known as the critical Reynolds number (Re_c) and is obtained as

$$Re_c = \frac{5 \exp(-2K_\mu)}{6(1 - K_\rho)} \cot \gamma. \quad (15)$$

If we consider $K_\mu \in (0, 1)$ to be small, then $\exp(-2K_\mu) \approx (1 - K_\mu)^2$ and therefore Re_c obtained by (15) exactly matches with Re_c obtained by Mukhopadhyay and Chattopadhyay [7]. Further, for isothermal case with constant viscosity and density ($K_\mu = 0 = K_\rho$), Eq. (15) reduces to $(5/6) \cot \gamma$ as obtained by Benjamin [9] and Yih [10]. Moreover, Re_c in (15) is independent of K_σ and K_κ .

Expanding $\exp(-2K_\mu)$ in Taylor series, it is easy to show that for $K_\mu \in (0, 1)$, $\exp(-2K_\mu)$ is always greater than $(1 - K_\mu)^2$. This implies that for a fixed K_ρ , Re_c in (15) is always greater than that of its corresponding value obtained by Mukhopadhyay and Chattopadhyay [7]. Therefore, flow is more stable when the variation of viscosity is exponential in comparison to its linear variation $\forall K_\mu \in (0, 1)$. Figure 2 demonstrates the variation of Re_c with a variation of $K_\mu \in [0, 1)$, and it confirms the previous claim. Moreover, for both the cases (exponential and linear variation), it interprets that as K_μ increases, Re_c decreases, i.e., linear stable

zone decreases. Physically, as $K_\mu (> 0)$ increases, the dynamic viscosity decreases, and therefore, the Reynolds number, which is the ratio of inertial and viscous forces, increases. As the inertia force increases, it leads to the destabilization of the flow system. On the other hand for a fixed K_μ as $K_\rho (> 0)$ increases, Re_c increases for exponential as well as the linear variation of viscosity. Physically as K_ρ increases, the density of the liquid decreases; therefore, the mass flow rate decreases, which leads to the stabilization of the flow system.

The linear theory fails to capture the flow behaviour accurately as the amplitude of the perturbation grows to a finite value. Therefore, it is necessary to perform weakly nonlinear stability analysis in the vicinity of the upper branch of the neutral curve within a thin band of width $\zeta \ll 1$. Following [7, 11–13], we obtain complex Ginzburg–Landau equation for filtered waves as

$$\frac{\partial \xi}{\partial t_2} - \zeta^{-2} \omega_i \xi + (J_2 + i J_4) |\xi|^2 \xi = 0, \quad (16)$$

where the expressions of J_2, J_4 are

$$J_2 = \frac{1}{2} \left(-B''k^2 + C''k^4 \right) + \frac{(A')^2 k^2 - 2(B'k^2 - 7C'k^4)(B'k^2 - C'k^4)}{16Ck^4 - 4Bk^2},$$

$$J_4 = \frac{1}{2} A''k + \frac{A'k(B'k^2 - 7C'k^4) + 2A'k(B'k^2 - C'k^4)}{16Ck^4 - 4Bk^2}.$$

Further, the threshold amplitude and the nonlinear wave speed are obtained by $\sqrt{\omega_i/J_2}$ and $Nc_r = c_r + c_i (J_4/J_2)$, where $c_i = \omega_i/k$. The variation of J_2 and ω_i with the variation of K_μ is portrayed in Fig. 3 for a fixed $k = 0.045$. Analysing the nature of Fig. 3, we found that the subcritical unstable ($\omega_i < 0, J_2 < 0$), unconditional stable ($\omega_i < 0, J_2 > 0$), supercritical stable ($\omega_i > 0, J_2 > 0$), and explosive zones ($\omega_i > 0, J_2 < 0$) are possible with the variation of K_μ . Similarly, for a fixed wavenumber and properly chosen parameters, it is observed that all the above stability zones may exist with the variation of K_ρ and K_σ [7]. Thus, K_μ, K_ρ , and K_σ control the stability criteria of the flow dynamics.

5 Numerical Simulation

To capture the flow dynamics over a large period of time, we numerically solve (12) in the spatial interval $[-\pi/k, \pi/k]$ by considering the initial free surface as

$$h(x, 0) = 1 - 0.1 \cos(kx). \quad (17)$$

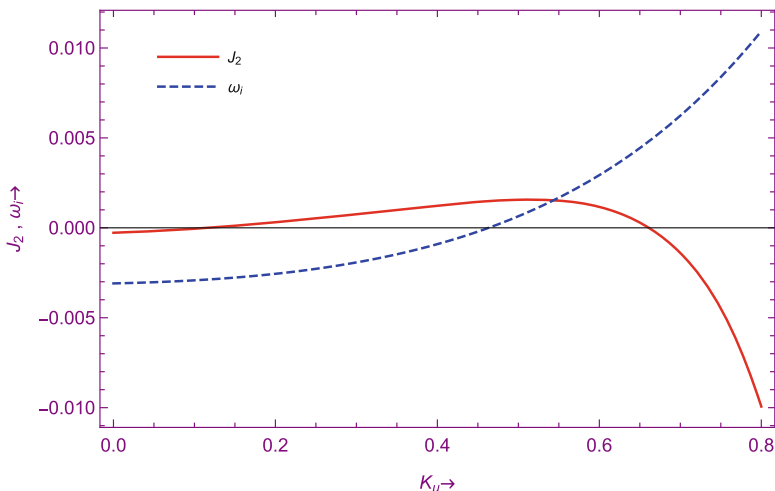


Fig. 3 Variation of J_2 and ω_i with the variation of K_μ for fixed values of $k = 0.045$, $K_\rho = 0.5$, $K_\sigma = 0.1$, $Re = 10$, $We = 4000$, $\epsilon = 0.1$, and $\gamma = \pi/3$

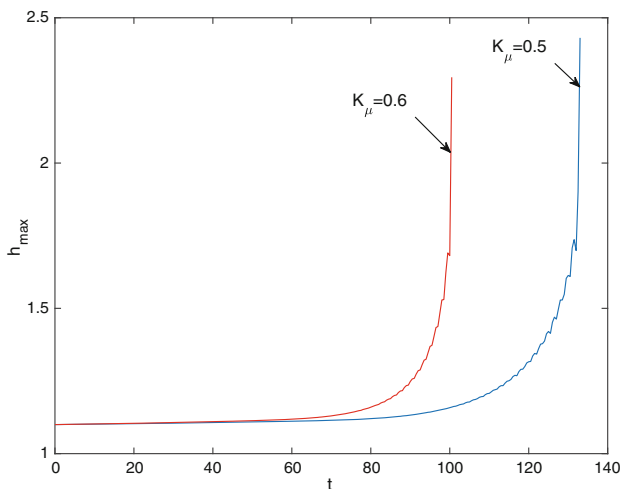


Fig. 4 Maximum amplitude (exponential variation of viscosity) of the wave for fixed values of $K_\rho = 0.5$, $K_\sigma = 0.1$, $k = 0.045$, $Re = 10$, $We = 4000$, $\epsilon = 0.1$, and $\gamma = \pi/3$

We apply the Crank–Nicolson scheme and choose $\Delta t = 0.01$, the number of node points $N = 100$ in space and stopping criteria for the iteration in the Newton–Raphson method, $tol=10^{-6}$.

The evolution of maximum (h_{max}) and minimum (h_{min}) thickness is presented in Figs. 4 and 5 for different K_μ and for a fixed value of other parameters when the viscosity variation is exponential. Figure 4 shows that for fixed K_μ as the time t

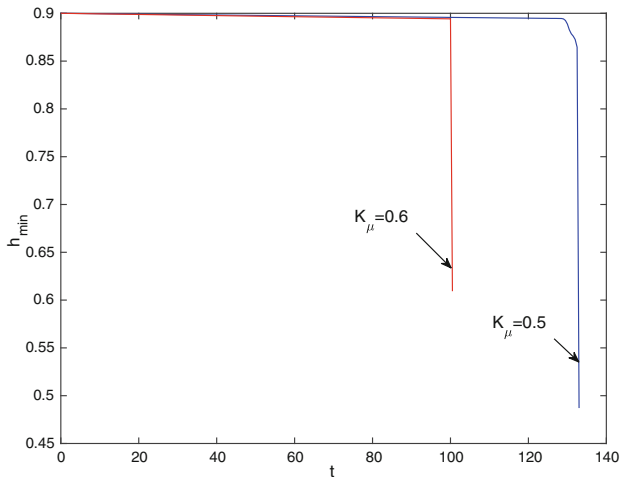


Fig. 5 Minimum amplitude (exponential variation of viscosity) of the wave for fixed values of $K_\rho = 0.5$, $K_\sigma = 0.1$, $k = 0.045$, $Re = 10$, $We = 4000$, $\epsilon = 0.1$, and $\gamma = \pi/3$

increases, h_{\max} and h_{\min} do not saturate to the basic state and further drift away from the basic state. Careful observation of Figs. 4 and 5 interprets that as K_μ increases, the drift for both h_{\max} and h_{\min} occurs within a short period of time. The numerical simulation points out the destabilizing behaviour of increment of K_μ as already found in linear as well as weakly nonlinear studies.

Figures 6 and 7 show the time behaviour of the maximum h_{\max} and minimum thickness h_{\min} for different K_μ and for a fixed value of other parameters when the viscosity variation is linear. We can easily observe that for the linear variation of viscosity, both h_{\max} and h_{\min} drift away from the basic state in a shorter time as compared to the cases for exponential variation of viscosity (Figs. 4 and 5). The numerical simulations confirm the results found based on linear and weakly nonlinear stability analysis.

6 Conclusions

We investigate the stability and dynamics of a thin film down a uniformly heated impermeable inclined plane. The fluid properties such as density, surface tension, and thermal diffusivity vary linearly, whereas the dynamical viscosity varies exponentially with the small variation of the temperature. The main purpose of the present investigation is to compare the instability phenomena by accounting the exponential (strong viscosity) and linear (weak viscosity) variation of viscosity. Both analytical and numerical methods have been utilized to better understand how the complicated interplay between heating and variable fluid properties affects the stability of the flow. The normal mode approach of the linear study establishes that the flow is more stable for exponential variation of viscosity rather than linear. The

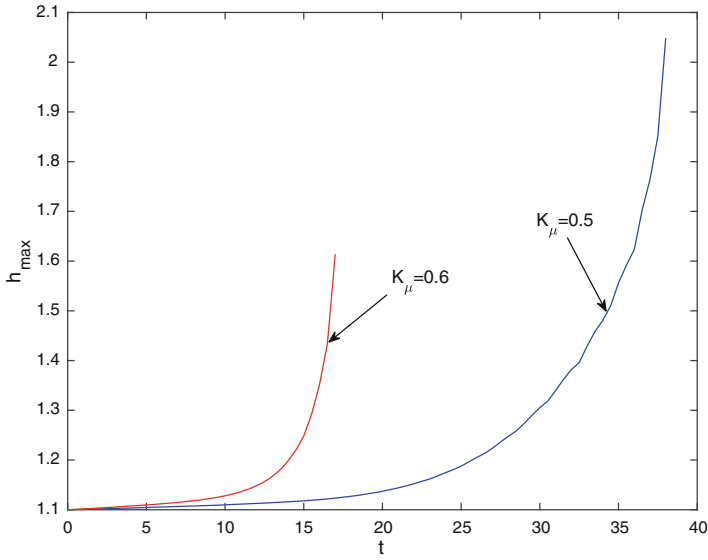


Fig. 6 Maximum amplitude (linear variation of viscosity [7]) of the wave for fixed values of $K_\rho = 0.5$, $K_\sigma = 0.1$, $k = 0.045$, $Re = 10$, $We = 4000$, $\epsilon = 0.1$, and $\gamma = \pi/3$

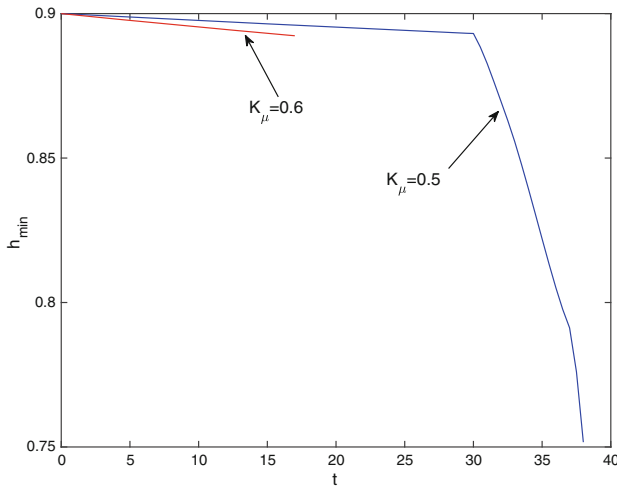


Fig. 7 Minimum amplitude (linear variation of viscosity [7]) of the wave for fixed values of $K_\rho = 0.5$, $K_\sigma = 0.1$, $k = 0.045$, $Re = 10$, $We = 4000$, $\epsilon = 0.1$, and $\gamma = \pi/3$

numerical simulation successfully captures the evolution of the free-surface flow and confirms the results of the linear and weakly nonlinear studies.

Acknowledgments AKB acknowledges the partial support of the Science and Engineering Research Board (SERB), Department of Science and Technology, Government of India for this work through the Startup Research Grant SRG/2019/001233.

References

1. D.A. Goussis, R.E. Kelly, Effects of viscosity variation on the stability of film flow down heated or cooled inclined surfaces: long-wave length analysis. *Phys. Fluids* **28**, 3207–3214 (1985). <https://doi.org/10.1063/1.865368>
2. D.A. Goussis, R.E. Kelly, Effects of viscosity variation on the stability of a liquid film flow down heated or cooled inclined surfaces: finite wave length analysis. *Phys. Fluids* **30**(4), 974–982 (1987). <https://doi.org/10.1063/1.866284>
3. C.C. Hwang, C.I. Weng, Non-linear stability analysis of film flow down a heated or cooled inclined plane with viscosity variation. *Int. J. Heat Mass Transf.* **31**(9), 1775–1784 (1988). [https://doi.org/10.1016/0017-9310\(88\)90192-5](https://doi.org/10.1016/0017-9310(88)90192-5)
4. B. Reisfeld, S.G. Bankoff, Nonlinear stability of a heated thin liquid film with variable viscosity. *Phys. Fluids* **2**(11), 2066–2067 (1990). <https://doi.org/10.1063/1.857790>
5. J.P. Pascal, N. Gonputh, S.J.D. D'Alessio, Long-wave instability of flow with temperature dependent fluid properties down a heated incline. *Int. J. Eng. Sci.* **70**, 73–90 (2013). <https://doi.org/10.1016/j.ijengsci.2013.05.003>
6. S.J.D. D'Alessio, C.J.M.P. Seth, J.P. Pascal, The effects of variable fluid properties on thin film stability. *Phys. Fluids* **26**(12), 122105–122115 (2014). <https://doi.org/10.1063/1.4904095>
7. A. Mukhopadhyay, S. Chattopadhyay, Long wave instability of thin film flowing down an inclined plane with linear variation of thermophysical properties for very small Biot number. *Int. J. Non-linear Mech.* **100**, 20–29 (2018). <https://doi.org/10.1016/j.ijnonlinmec.2018.01.005>
8. S. Kalliadasis, C. Ruyer-Quil, B. Scheid, M.G. Velarde, *Falling Liquid Films* (Springer, Berlin, 2012). <https://doi.org/10.1007/978-1-84882-367-9f>
9. T.B. Benjamin, Wave formation in laminar flow down an inclined plane. *J. Fluid Mech.* **2**(6), 554–573 (1957). <https://doi.org/10.1017/S0022112057000373>
10. C.S. Yih, Stability of liquid flow down an inclined plane. *Phys. Fluids* **6**(3), 321–334 (1963). <https://doi.org/10.1063/1.1706737>
11. A. Mukhopadhyay, A. Mukhopadhyay, Nonlinear stability of viscous film flowing down an inclined plane with linear temperature variation. *J. Phys. D Appl. Phys.* **40**, 5683–5690 (2007). <https://doi.org/10.1088/0022-3727/40/18/025>
12. A. Mukhopadhyay, A. Mukhopadhyay, Stability of conducting viscous film flowing down an inclined plane with linear temperature variation in the presence of a uniform normal electric field. *Int. J. Heat Mass Transf.* **52**, 709–715 (2009). <https://doi.org/10.1016/j.ijheatmasstransfer.2008.06.043>
13. A. Mukhopadhyay, S. Chattopadhyay, A.K. Barua, Stability of thin liquid film flowing down a rotating horizontal or inclined plane by momentum-integral method. *Eur. J. Mech. B/Fluids* **75**, 58–70 (2019). <https://doi.org/10.1016/j.euromechflu.2018.12.002>

Nonlinear Hydrodynamic Damping of Elastic Vibrations of Beams Near a Plane Boundary



Artem Nuriev and Airat Kamalutdinov

1 Introduction

Studies of aero-hydrodynamic effects acting on elongated small beam structures undergoing elastic vibrations have been actively developed in the last two decades in connection with the emergence of a number of innovative technological solutions based on piezoelectric bending actuators. Due to their energy efficiency and mobility, piezoelectric actuators are being successfully introduced in the field of robotics, as a part of propulsion systems of autonomous underwater and aircraft vehicles, as cooling systems and energy harvesters in microelectronics, as pump systems in microfluidic devices, etc.

Most of the modern studies of vibrations of long elastic beams in a fluid are based on a simplified quasi-two-dimensional model of interaction (see, e.g. [1–8]). In the case of vibrations in unbounded fluid the hydrodynamic forces in each cross-section can be represented (as for the case of oscillations of a rigid cylindrical body) as functions of two main parameters: the dimensionless vibration frequency β and the dimensionless local oscillation amplitude of the cross-section KC_{loc}

$$KC_{loc}(z) = 2\pi \frac{U_{loc}(z)}{b\omega} = 2\pi \frac{A_{loc}(z)}{b}, \quad \beta = \frac{b^2\omega}{2\pi v}. \quad (1)$$

A. Nuriev (✉)

Kazan Federal University, Department of Aerohydrodynamics, Kazan, Tatarstan, Russia

e-mail: nuriev_an@mail.ru

<https://kpfu.ru/Artem.Nuriev>

A. Kamalutdinov

Kazan National Research Technical University named after A. N. Tupolev, Department of Structural Strength, Kazan, Russia

Here $U_{\text{loc}}(z) = A_{\text{loc}}(z)\omega$ and $A_{\text{loc}}(z)$ are the velocity oscillation amplitude and the oscillation amplitude of the cross-section $z = \text{const}$, respectively, b is the width of the beam, ω is the angular frequency, and ν is the fluid viscosity. For the case of vibrations of the beam near the solid boundary, it is also necessary to take into account the gap distance s between the plane boundary and the beam. Usually as the third governing dimensionless parameter of the flow problem the gap-to-width ratio σ is chosen (see, e.g. [9, 10]):

$$\sigma = s/b. \quad (2)$$

In fact, the limits of applicability of the quasi-two-dimensional hypothesis are only partially investigated. Three-dimensional studies of vibrations of long beams in unbounded fluid were carried out in [11, 12]. Their results show that in the range of small vibration amplitudes $\text{KC}_{\text{loc}}(l) < 0.3$ (where l is the length of the beam), a quasi-two-dimensional flow can be observed around the beams with a relative length $L = l/b \geq 3$. In the range of moderate and large amplitudes $2 < \text{KC}_{\text{loc}}(l) < 6$, the flow around the beam can be considered as quasi-two-dimensional for $L \geq 10$. For the case of vibrations of beams near a plane boundary, there are very few detailed studies of three-dimensional flows (see, e.g. [13]). Almost all of them consider vibrations of very short beams, the flows around which are essentially three-dimensional.

In this chapter, we carry out a three-dimensional numerical simulation of the flow around long beams vibrating near a plane boundary in order to study the structure of hydrodynamic forces and the ability of a quasi-two-dimensional model to predict them.

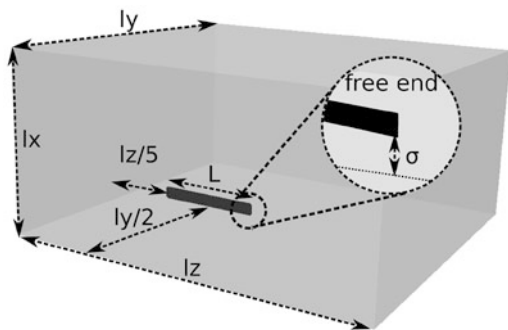
2 Problem Statement

Let us conduct a study of the hydrodynamic forces acting on infinitely thin long cantilever beams with a length l and a width b ($l \gg b$) that perform flexural vibrations in the first natural mode in an incompressible viscous fluid near a plane boundary. Consider the case when the bending plane is parallel to the plane boundary (the gap distance between the plane boundary and the beam is constant and equal to s). Normalizing the time, spatial coordinates, velocity, and pressure on bU_L^{-1} , b , U_L , $U_L^2\rho$, respectively, where $U_L = U_{\text{loc}}(L)$ is the velocity of the free end of the beam, we write the Navier–Stokes system of equations to describe the fluid motion

$$\frac{\partial \mathbf{U}}{\partial t} + \mathbf{U} \cdot \nabla \mathbf{U} = -\nabla p + \frac{1}{\text{KC}\beta} \nabla^2 \mathbf{U}, \quad (3)$$

$$\nabla \cdot \mathbf{U} = 0.$$

Fig. 1 The configuration of the computational domain



Here p is the dimensionless pressure, $\mathbf{U} = (u_x, u_y, u_z)$ is the dimensionless velocity, $L = l/b$ is the dimensionless length of the beam, and $KC = KC_{loc}(L)$ is the dimensionless amplitude of oscillation of the free end of the beam. The dimensionless oscillation amplitude of the cross-section KC_{loc} , the dimensionless frequency β , and the gap-to-width ratio σ are determined by the formulas (1), (2).

Numerical modeling of fluid flow around the beam is carried out in a rectangular parallelepiped with dimensions (l_x, l_y, l_z) . The configuration of the computational domain is shown in Fig. 1.

To describe the motion of a beam in a fluid, we use the classical Euler–Bernoulli theory, according to which at an arbitrary time the position of any point of the beam in the dimensionless variables is defined by the following formula:

$$w(\xi, t) = \frac{KC}{2\pi} W(\xi) \sin\left(\frac{2\pi}{KC}t\right), \quad \xi = z/L, \quad 0 \leq \xi \leq 1, \quad (4)$$

where W ($W(1) = 1$) is the oscillation profile that is determined as

$$W(\xi) = -\frac{1}{2} \left(\cos(k\xi) - \cosh(k\xi) + \frac{\sin k - \sinh k}{\cos k + \cosh k} (\sin(k\xi) - \sinh(k\xi)) \right), \quad (5)$$

$$\cos k \cosh k = -1. \quad (6)$$

We consider the vibrations of the beam in the first natural mode, so we find $k = 1.875$ as the smallest positive root of the characteristic equation (6).

In the dimensionless formulation, the hydrodynamic forces acting on the surface element S of the beam can be calculated as

$$\mathbf{F} = \left(\int_S p \mathbf{n} ds - \int_S \mathcal{G} \cdot \mathbf{n} ds \right),$$

where \mathbf{n} is the unit normal vector to S and \mathcal{G} is a viscous stress tensor.

3 Numerical Model

The numerical solution of the resulting problem was carried out on the basis of the OpenFOAM package. A description of the numerical scheme can be found in the work [12].

4 Results

Consider the results of three-dimensional numerical simulations obtained for infinitely thin beams with a relative length $L = 20$, focusing on the distribution of the F_y force component along the beam (that is inline with velocity of vibrations), in the following range of parameters: $1 \leq KC \leq 6$, $200 \leq \beta \leq 430$, $\sigma \geq 0.5$.

We use the Morison expansion [14] for the analysis of the inline force F_y :

$$F_y(z) = C_M \frac{\pi^2}{2KC} W(z/L) \sin\left(\frac{2\pi}{KC}t\right) - C_D \frac{W(z/L)^2}{2} \left| \cos\left(\frac{2\pi}{KC}t\right) \right| \cos\left(\frac{2\pi}{KC}t\right).$$

The first term in this expansion is proportional to the acceleration. It describes the added mass force that affects the change of the frequency of vibrations (see, e.g. [6]). The second term is proportional to the square of the velocity. It defines the drag force that is responsible for the hydrodynamic damping of the beam vibrations. The added mass coefficient C_M and the drag coefficient C_D are calculated on each oscillation period $T = KC$ using the integration:

$$C_M = \frac{4}{\pi^2 W} \int_{t_0}^{T+t_0} F_y \sin\left(\frac{2\pi}{KC}t\right) dt, \quad C_D = -\frac{3\pi}{2TW^2} \int_{t_0}^{T+t_0} F_y \cos\left(\frac{2\pi}{KC}t\right) dt.$$

In Fig. 2, added mass and drag coefficients (C_M , C_D) are shown as functions of KC_{loc} for the case of a large distance from the screen (hereinafter referred to as $\sigma = \infty$). In the considered parameter range, the value of the coefficient C_M is almost completely determined by KC_{loc} as the quasi-two-dimensional model states. The presence of three-dimensional effects can be seen only near the free end of the beam for the high values of KC . In the middle part of the beam, the obtained values of C_M are in good agreement with numerical estimates of C_M for the pure plane flows [15] and with the experimental measurements of C_M [16].

The drag coefficient C_D depends not only on the local parameters of the oscillation of the cross-section, but also on the global amplitude KC . When $KC \leq 1$ (see the results for $KC = 1$, $\beta = 200$ in Fig. 2), one can see the best match between the C_D values obtained in two-dimensional and three-dimensional calculations. As KC get larger, the drag coefficient values start to increase near the fixed end of the beam (for small KC_{loc} values). At the same time, in the middle part of the beam, the hydrodynamics for all values of KC remains close to two-dimensional one. The

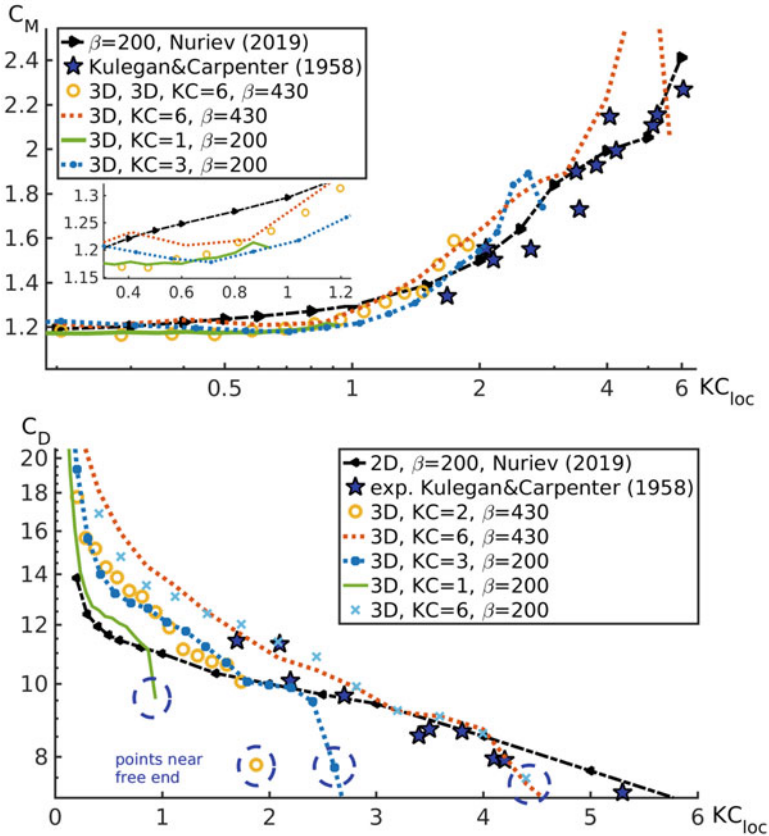


Fig. 2 The dependence of C_M and C_D on KC_{loc} for $\sigma = \infty$

values of the local drag coefficient C_D in this part of the beam agree well with the data for the plate. In the vicinity of the free end of the beam, the value of C_D rapidly decreases in all calculations.

As the beam approaches the plane boundary, the $C_D(KC_{loc})$ dependencies change significantly. In Fig. 3 the results of two-dimensional and three-dimensional calculations for the cases $\sigma = 1, 0.5$ are shown. As you can see, the role of three-dimensional effects near solid boundaries is largely enhanced. The data of the two-dimensional modeling predict an almost proportional increase of C_D by 25% in the range $0.2 < KC \leq 2$ for $\sigma = 0.5$. The results of the three-dimensional modeling indicate a much more significant increase of C_D in the region of small values of the local amplitude (more than 50% at $KC_{loc} = 0.2$ for $\sigma = 0.5$ compared to $\sigma = \infty$). At the same time, in a fairly wide zone near the free end, the values of C_D become lower than the data obtained in two-dimensional modeling. This suggests that near the plane boundary, the results of two-dimensional modeling can be used to obtain

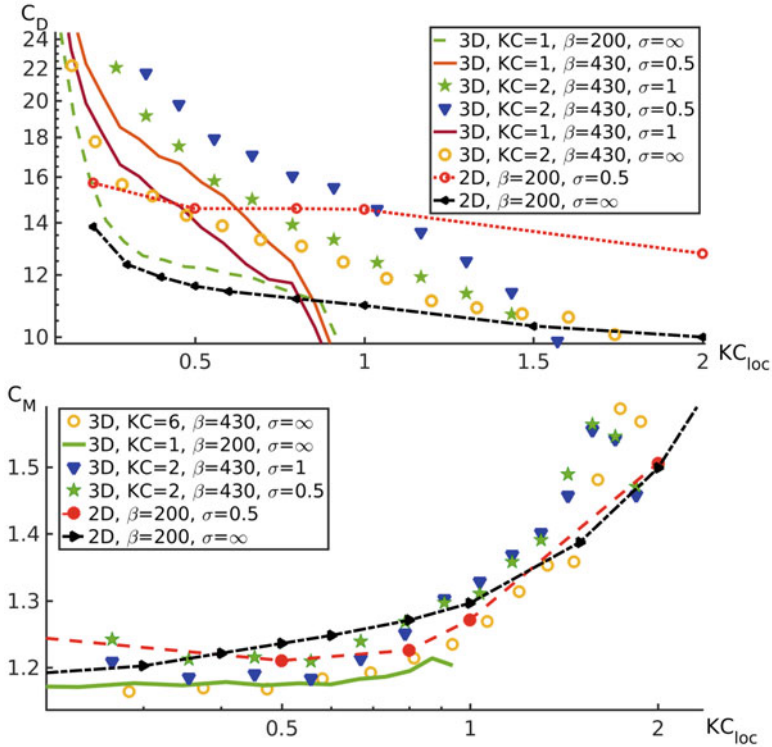


Fig. 3 The dependence of C_D and C_M on KC_{loc} for different values of σ

only a first-order approximation for the hydrodynamic damping force acting on the beam.

In contrast to the drag force, the added mass force in the considered range of parameters slightly changes with decreasing distance to the plane boundary (see Fig. 3). The dependences for C_M obtained in the framework of two-dimensional and three-dimensional models for $\sigma = 0.5, 1$ are in good agreement with similar dependences for the added mass coefficient in an unbounded fluid. Three-dimensional effects have a visible influence on C_M only in the vicinity of the free end of the beam.

5 Conclusions

In this chapter, a study of the hydrodynamic effects acting on long beams that perform flexural vibrations in a viscous incompressible fluid was carried out. The analysis of the dependences of the drag force and the added mass force on the

vibration amplitude and distance from the boundary was made. According to the results of the study, the following key results were obtained:

1. For the long beams, located far from the plane boundary, the values of C_D and C_M in the middle part of the beam are close to the quasi-two-dimensional estimates. The values of C_M for long beams and plates on average differ by no more than 6%. In the middle part of long beams, the values of the drag coefficient differ from the values of C_D for the plates by no more than 9%.
2. The values of the coefficient C_D begin to change significantly as the gap-to-width ratio decreases to $\sigma \leq 1$. The results of three-dimensional modeling indicate a significant increase of the values of C_D , especially in the region of small values of the local amplitude of oscillations KC_{loc} . The enhancement of the role of three-dimensional effects in the vicinity of the plane boundary significantly reduces the accuracy of quasi-two-dimensional models for estimating C_D . In contrast to the drag force, the added mass force in the considered range of parameters ($\sigma \geq 0.5$) slightly changes with decreasing gap distance to the plane boundary. The dependences for C_M obtained in the framework of two-dimensional and three-dimensional models for $\sigma = 0.5, 1$ are in good agreement.

Acknowledgement The reported study was supported by RFBR, research project No. 19-38-60023.

References

1. M. Aureli, M. Porfiri, Low frequency and large amplitude oscillations of cantilevers in viscous fluids. *Appl. Phys. Lett.* **96**, 164102 (2010). <https://doi.org/10.1063/1.3405720>
2. C.N. Phan, M. Aureli, M. Porfiri, Finite amplitude vibrations of cantilevers of rectangular cross sections in viscous fluids. *J. Fluids Struct.* **40**, 52–69 (2013). <https://doi.org/10.1016/j.jfluidstructs.2013.03.013>
3. R.A. Bidkar, M. Kimber, A. Raman, A.K. Bajaj, S.V. Garimella, Nonlinear aerodynamic damping of sharp-edged flexible beams oscillating at low Keulegan-Carpenter numbers. *J. Fluid Mech.* **634**, 269–289 (2009). <https://doi.org/10.1017/s0022112009007228>
4. A.G. Egorov, A.M. Kamalutdinov, A.N. Nuriev, V.N. Paimushin, Theoretical-experimental method for determining the parameters of damping based on the study of damped flexural vibrations of test specimens 2. Aerodynamic component of damping. *Mech. Comp. Mater.* **50**, 267–278 (2014). <https://doi.org/10.1007/s11029-014-9413-3>
5. A.G. Egorov, A.M. Kamalutdinov, A.N. Nuriev, V.N. Paimushin, Experimental determination of damping of plate vibrations in a viscous fluid. *Doklady Phys.* **62**, 257–261 (2017). <https://doi.org/10.1134/S1028335817050068>
6. A.G. Egorov, A.M. Kamalutdinov, A.N. Nuriev, Evaluation of aerodynamic forces acting on oscillating cantilever beams based on the study of the damped flexural vibration of aluminium test samples. *J. Sound Vib.* **421**, 334–347 (2018). <https://doi.org/10.1016/j.jsv.2018.02.006>
7. A.L. Facci, M. Porfiri, Nonlinear hydrodynamic damping of sharp-edged cantilevers in viscous fluids undergoing multi-harmonic base excitation. *J. Appl. Phys.* **112**, 124908 (2012). <https://doi.org/10.1063/1.4769307>

8. J.E. Sader, Frequency response of cantilever beams immersed in viscous fluids with applications to the atomic force microscope. *J. Appl. Phys.* **84**, 64 (1998). <https://doi.org/10.1063/1.368002>
9. C. Xiong, L. Cheng, F. Tong, H. An, Oscillatory flow regimes for a circular cylinder near a plane boundary. *J. Fluid Mech.* **844**, 127–161 (2018). <https://doi.org/10.1017/jfm.2018.164>
10. H. Xiu, R.B. Davis, R.C. Romeo, Edge clearance effects on the added mass and damping of beams submerged in viscous fluids. *J. Fluids Struct.* **83**, 194–217 (2018). <https://doi.org/10.1016/j.jfluidstructs.2018.08.016>
11. A.L. Facci, M. Porfiri Analysis of three-dimensional effects in oscillating cantilevers immersed in viscous fluids. *J. Fluids Struct.* **38**, 205–222 (2013). <https://doi.org/10.1016/j.jfluidstructs.2012.11.006>
12. A. Nuriev, A. Kamalutdinov, O. Zaitseva, Hydrodynamics around long vibrating beams. *J. Fluids Struct.* **101**, 103203 (2021). <https://doi.org/10.1016/j.jfluidstructs.2020.103203>
13. M.H. Oh, J. Seo, Y.-H. Kim, M. Choi, Endwall effects on 3D flow around a piezoelectric fan. *Eur. J. Mech. B/Fluids* **75**, 339–351 (2019). <https://doi.org/10.1016/j.euromechflu.2018.10.021>
14. J.R. Morison, J.W. Johnson, S.A. Schaaf, The force exerted by surface waves on piles. *J. Pet. Tech.* **2**, 149–154 (1950). <https://doi.org/10.2118/950149-g>
15. A.N. Nuriev, A.M. Kamalutdinov, A.G. Egorov, A numerical investigation of fluid flows induced by the oscillations of thin plates and evaluation of the associated hydrodynamic forces. *J. Fluid Mech.* **874**, 1057–1095 (2019). <https://doi.org/10.1017/jfm.2019.477>
16. G.H. Keulegan, L.H. Carpenter, Forces on cylinders and plates in an oscillating fluid. *J. Res. Nat. Bur. Stand.* **60**, 423–440 (1958). <https://doi.org/10.6028/jres.060.043>

Hydrodynamic Forces Acting on Cylindrical Piles Subjected to Wind-Forced Random Nonlinear Water Waves



Marten Hollm, Leo Dostal, and Robert Seifried

1 Introduction

Extreme water waves pose a huge risk for ships, offshore structures, and all persons present. In order to make these mechanical structures resistant against upcoming waves, it is necessary to know which hydrodynamic forces are acting on them. For a pile, these forces can be computed by the equation of Morison [1] if the underlying sea state is known.

For the study of water waves in the presence of random wind, Dias et al. [2] have shown that it is sufficient to consider the Euler equations of fluid dynamics instead of the Navier–Stokes equations. But since these equations are costly to solve numerically, Zakharov [3] has shown that weakly nonlinear solutions of the Euler equations can be reduced to solutions of the nonlinear Schrödinger equation (NLS). After Zakharov has presented his results without the presence of wind, Leblanc [4] has extended this by a constant unidirectional wind forcing. In order to model the wind conditions more realistically, Dostal et al. [5] have studied the behavior of such solutions in the presence of random wind forcing. They have concluded that these solutions can exist in deep water even in the presence of random wind.

A closer look at the sea surface reveals the irregularity of ocean waves. Therefore, Fischer et al. [6] have considered the influence of an irregular sea on the solitary solution of the NLS. A result of this analysis is that such a disturbance does not destroy the solitary structure of the solutions. Although solitary waves can exist in the environment of random wind and irregular waves, it is not clear how the trajectories of water particles and the corresponding hydrodynamic forces acting on

M. Hollm (✉) · L. Dostal · R. Seifried

Institute of Mechanics and Ocean Engineering, Hamburg University of Technology, Hamburg, Germany

e-mail: marten.hollm@tuhh.de; dostal@tuhh.de; robert.seifried@tuhh.de

<https://www.tuhh.de/alt/mum/home.html>

mechanical structures are changed by these processes. In order to calculate them, the velocity potential corresponding to the water waves has to be calculated. Carter et al. [7] have theoretically presented how the velocity potential corresponding to a solution of the NLS can be computed for the case of regular waves without forcing. In this chapter, the effects of random wind and irregular seas on water trajectories and hydrodynamic forces acting on a cylindrical pile are studied using the results of Carter et al. [7] and the equation of Morison [1].

This chapter is structured as follows: In Sect. 2, the NLS for nonlinear dissipative waves in deep water excited by random wind is introduced, the modeling of random wind is shortly described, and the solitary solution disturbed by random waves is presented. Furthermore, it is summarized how water particle trajectories and the hydrodynamic forces acting on a cylindrical pile can be calculated. Based on this, Sect. 3 presents results for the solitary solution, which is either excited by random wind or disturbed by irregular seas. Finally, this chapter ends with a conclusion in Sect. 4.

2 Construction of the Velocity Potential

In order to compute the velocity potential and the hydrodynamic forces acting on mechanical structures, it is necessary to review the derivation of the NLS. Thereby, random wind is considered.

2.1 Approximation of the Euler Equations

Deep water waves under the action of wind and dissipation in a sea of constant depth $z = -h$ are considered. Thereby, the surface elevation at time t and space x is given by $z = \eta = \eta(x, t)$. Here, x denotes the horizontal and z the vertical axis. Furthermore, it is assumed that the still water level is located at $z = 0$ and that the waves do not break such that $\eta(x, t)$ is uniquely defined everywhere. Under the assumption of an irrotational velocity field with velocity potential $\phi = \phi(x, z, t)$ and a wind-induced pressure $P_a(x, t)$ at the free surface, the Euler equations of fluid dynamics become [2]

$$\phi_{xx} + \phi_{zz} = 0, \quad \text{for } -h \leq z \leq \eta(x, t), \quad (1)$$

$$\eta_t + \phi_x \eta_x - \phi_z = 2\nu \eta_{xx}, \quad \text{for } z = \eta(x, t), \quad (2)$$

$$\phi_t + \frac{1}{2}(\nabla\phi)^2 + g\eta = -\frac{P_a}{\rho_w} - 2\nu\phi_{zz}, \quad \text{for } z = \eta(x, t), \quad (3)$$

$$\phi_z = 0, \quad \text{for } z = -h, . \quad (4)$$

Thereby, ∇ denotes the nabla operator in space, g the acceleration due to gravity, ρ_w the constant density of water, and μ the water kinematic viscosity, which includes all dissipative effects.

Since the boundary conditions are formulated at the unknown surface elevation $\eta(x, t)$, the computation of solutions takes a considerable computational effort. In order to reduce this effort, the method of multiple scales is used, cf. [8]. Following [9], the scalings

$$\xi := \varepsilon(x - c_g t), \quad \tau := \varepsilon^2 t, \quad c_g := \frac{g}{2\omega} (\tanh kh + kh(1 - \tanh^2 kh)) \quad (5)$$

are introduced, whereby ε denotes the wave steepness, c_g the group velocity, ω the wave frequency, and k the wave number of the corresponding carrier wave. Then, η and ϕ are expanded in series of the form

$$\eta(x, t) = \sum_{n=1}^{\infty} \varepsilon^n \sum_{m=-n}^n \eta^{n,m}(\xi, \tau) E^m, \quad \phi(x, z, t) = \sum_{n=1}^{\infty} \varepsilon^n \sum_{m=-n}^n \phi^{n,m}(\xi, z, \tau) E^m, \quad (6)$$

where

$$\eta^{(n,-m)} = \bar{\eta}^{(n,m)}, \quad \phi^{(n,-m)} = \bar{\phi}^{(n,m)}, \quad E := \exp(i(kx - \omega t)). \quad (7)$$

Thereby, a bar denotes the complex conjugate.

In a similar way, the wind-induced pressure field P_a evaluated at $z = 0$ is expanded. Assuming an order of $\mathcal{O}(\varepsilon^3)$, P_a is expanded as

$$P_a(x, t) = \sum_{n=1}^{\infty} \varepsilon^{n-1} \sum_{m=-n}^n p^{n,m}(\xi, \tau) E^m. \quad (8)$$

Next, the series (6) and (8) are substituted into the Euler equations (1–4). Considering all terms up to order $\mathcal{O}(\varepsilon^3)$ and $h \rightarrow \infty$, i.e. deep water, the wind-forced NLS can be derived from the Euler equations [5] as

$$i\psi_\tau - \frac{\omega}{8k^2} \psi_{\xi\xi} - \frac{1}{2} \omega k^2 |\psi|^2 \psi = -i \frac{p^{1,1}}{2\rho_w} - 2i\nu k^2 \psi. \quad (9)$$

Thereby, $p^{1,1}$ denotes the first-order term of Eq. (8). The solutions of the NLS yield the wave envelope, from which the corresponding wave elevation η can be computed by

$$\eta(x, t) = \varepsilon \psi(\xi(x, t), \tau(x, t)) \exp(i(kx - \omega t)) + c.c., \quad (10)$$

where *c.c.* denotes the complex conjugate of the previous term.

2.2 Modeling of Random Wind

In order to model the stochastic wind in a realistic way, we follow the procedure of Dostal et al. [5], who have used the Miles mechanism [10, 11]. This has proven to be a simple, but versatile model for wind-induced wave growth [12]. Following Dostal et al. and using only the wind pressure component in phase with the wave slope, $p^{1,1}$ can be simplified for a logarithmic velocity profile in the boundary layer to

$$p^{1,1}(\xi, \tau) = -\frac{\omega^2}{2g} \rho_a \beta \left(\frac{u_*(\xi, \tau)}{\kappa} \right)^2 \psi(\xi, \tau), \quad (11)$$

whereby ρ_a is the density of air, β is a coefficient as explained below, u_* is the friction velocity, and κ is the Karman constant. Assuming a given wind velocity $U(\xi, z, \tau)$ at height z , the corresponding friction velocity $u_*(\xi, \tau)$ can be iteratively computed by

$$U(\xi, z, \tau) = \frac{u_*(\xi, \tau)}{\kappa} \ln \left(\frac{z}{z_0} \right). \quad (12)$$

Here, the roughness length z_0 is given by $z_0 = \alpha_{ch} u_*^2 / g$ with the Charnock's constant $\alpha_{ch} \approx 0.01875$. Following Dostal et al. [5], a realistic stochastic time-dependent wind $U(z, \tau)$ can be computed by a CARMA(2,1)-process. Thereby, typical wind velocity spectra in the surface boundary layer are approximated, which were measured by Van der Hoven [13]. This approach allows wind fluctuations in the range of seconds and minutes as well as wind gusts to be represented by this process.

After computing u_* as a stochastic process, $p^{1,1}$ is a stochastic process as well. Substituting Eq. (11) into the NLS (9) leads to

$$i \psi_\tau - \frac{\omega}{8k^2} \psi_{\xi\xi} - \frac{1}{2} \omega k^2 |\psi|^2 \psi = i \zeta \psi, \quad (13)$$

whereby

$$\zeta(\xi, \tau) = \frac{k\omega}{2g} \frac{\rho_a}{\rho_w} \beta \left(\frac{u_*(\xi, \tau)}{\kappa} \right)^2 - 2\nu k^2 \quad (14)$$

is the difference between stochastic wind excitation and constant dissipative effects. Thereby, the only unknown parameter is β . Conte and Miles [14] have computed β as a function of $\kappa c / u_*$, where c is the phase velocity of the wave. In all further calculations, the dimensionless roughness length $\kappa^2 g z_0 / u_* = 0.003$ is chosen.

2.3 Choice of the Initial Condition

In order to compute numerical solutions of the forced NLS (13), an initial condition has to be chosen. Thereby, the stationary soliton solution of the unperturbed NLS, which is given by Eq. (13) with $\zeta = 0$, is considered. This solution has an amplitude constant in time and is given for an arbitrary constant a_0 by

$$\psi = a_0 \operatorname{sech}(\sqrt{2} a_0 k^2 x) \exp\left(-i \frac{1}{4} |a_0 k|^2 \omega t\right). \quad (15)$$

In order to model the sea surface more realistically, an irregular sea surface is added to the initial condition. Thereby, random long-crested sea waves are modeled by the superposition of harmonic waves with wave frequencies ω and wave numbers $k(\omega)$. The corresponding wave amplitudes A depend on the underlying sea state given by the corresponding one-sided spectral density $S(\omega)$. According to [6], the irregular sea elevation $Z(x, t)$ can then be calculated by

$$Z(x, t) = \int_0^\infty \cos(\omega t - k(\omega)x + \varepsilon(\omega)) \sqrt{2S(\omega)} d\omega, \quad (16)$$

whereby the integral is not a Riemann integral but a summation rule over the frequencies ω . With that, a disturbed initial condition based on the analytical solution $\psi(\xi, \tau)$ is given by Fischer et al. [6]

$$\tilde{\psi}_0(\xi) = \left(1 + \frac{Z(\xi, 0)}{|\psi(\xi, 0)|}\right) \psi(\xi, 0). \quad (17)$$

Figure 1 illustrates the effect of a random sea state onto a soliton solution of wave frequency $\omega = 1$ rad/s using Eq. (17).

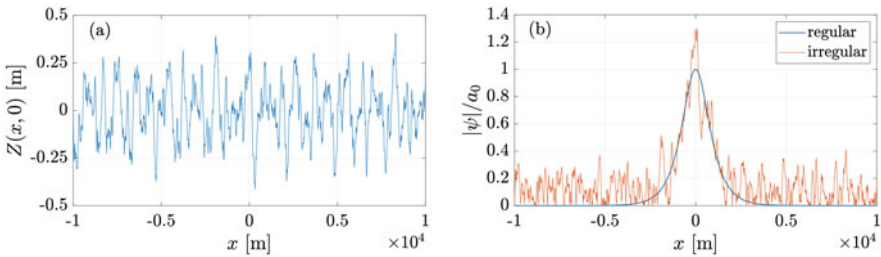


Fig. 1 (a) General random sea state using a Pierson–Moskowitz spectrum [15] with significant wave height $H_s = 0.6$ m and modal frequency $\omega_m = 0.25$ rad/s. (b) Soliton solution with wave frequency $\omega = 1$ rad/s at time $t = 0$ s with and without the irregular disturbance illustrated in (a)

2.4 Hydrodynamic Forces Acting on a Cylindrical Pile

After solving the wind-forced NLS using the relaxation pseudo-spectral scheme, which is presented in [5], the corresponding wave surface can be computed by Eq. (10). Moreover, it is possible to compute the wave kinematics, particle trajectories, and hydrodynamic forces acting on submerged mechanical structures. In order to do this, the velocities and accelerations of the water particles can be determined by differentiation of the corresponding velocity potential. Using the method of multiple scales, Carter et al. [7] have shown that the velocity potential can be reconstructed in a similar way as the free surface profile and have given the corresponding results for the NLS equation. Please note that compared to our case the complex conjugate of the NLS (13) is used by Carter et al. [7]. In order to compute the potential of the NLS (13) itself, the approach of Carter et al. has to be adjusted, whereby the complex conjugated equations (24a-27g) from [7] have to be used. The resulting velocity potential is given by

$$\phi(x, z, t) = \left\{ -\frac{i\varepsilon\omega}{k}\hat{\psi} + \frac{\varepsilon^2\omega}{2k^2}\hat{\psi}_X + \varepsilon^3 \left(\frac{ik\omega}{2}|\hat{\psi}|^2\hat{\psi} + \frac{3i\omega}{8k^3}\hat{\psi}_{XX} \right) \right\} E + \mathcal{O}(\varepsilon^4) + c.c., \quad (18)$$

whereby $\hat{\psi} = \psi(X - iZ, T)$, $X = \varepsilon x$, $Z = \varepsilon z$, $T = \varepsilon^2 t$, $E = \exp(kz + i(kx - \omega t))$ and *c.c.* denotes the complex conjugate. Since ψ is unknown at location $X - iZ$, $\hat{\psi}$ is also unknown and has to be determined by solving

$$\hat{\psi}_Z = -i\hat{\psi}_X, \quad (19)$$

$$\hat{\psi} = \psi \quad \text{at } Z = 0. \quad (20)$$

After computing the velocity potential ϕ , the velocity u in x -direction, v in z -direction, and acceleration a in x -direction can be computed by

$$u(x, z, t) = \frac{\partial\phi}{\partial x}(x, z, t), \quad v(x, z, t) = \frac{\partial\phi}{\partial z}(x, z, t), \quad a(u, z, t) = \frac{\partial u}{\partial t}(x, z, t). \quad (21)$$

With that, the trajectory $(x(t), z(t))$ of a water particle is described by

$$\frac{dx}{dt} = u(x(t), z(t), t), \quad \frac{dz}{dt} = v(x(t), z(t), t). \quad (22)$$

In order to compute the horizontal hydrodynamic force dF_x acting on a part dz of a vertical pile with diameter D , the equation of Morison [1] is used:

$$dF_x = C_m \rho_w \frac{\pi D^2}{4} dz a + C_d \frac{\rho_w}{2} D dz |u| u. \quad (23)$$

An integration of dF_x over the wetted part of the cylinder leads to the resulting hydrodynamic force. Thereby, C_m is the inertia and C_d is the drag coefficient. In

all the following simulations, a cylindrical pile with diameter $D = 6$ m in a water depth of $H = 30$ m is used. Following the suggestion of Sarpkaya [16], the inertia and drag coefficient in Eq. (23) are chosen as $C_m = 1.8$ and $C_d = 0.64$, respectively.

3 Numerical Results

In this section, the effects of random wind and a disturbed initial sea surface on a solitary solution are considered. For these cases, the corresponding particle trajectories and Morison forces are compared.

3.1 The Influence of Random Wind

First of all, the soliton solution excited by random wind is considered. The pile is placed in such a way that it is reached by the solitary wave after a long simulation time. Figure 2 shows the soliton solution with and without the presence of a random wind excitation with a mean velocity $V_m = 50$ km/h at a constant height $z = 50$ m. As was also presented by Dostal et al. [5], the zero water level gets disturbed and the envelope amplitude is slightly growing in time. But although the solution gets steeper and higher, the solitary structure of the soliton is not destroyed by random wind fluctuations.

The influence of the random wind on the particle trajectories is shown in Fig. 3. Thereby, particles starting at $x = 0$ m and at heights from $z = 0$ m to $z = -10$ m are considered with and without a stochastic wind excitation. Similar results for the case without wind excitation are shown by Carter et al. [7], who have used an analytical formulation. It is shown that the wind have a huge influence on the system. Higher waves lead to a higher displacement in vertical direction, and the

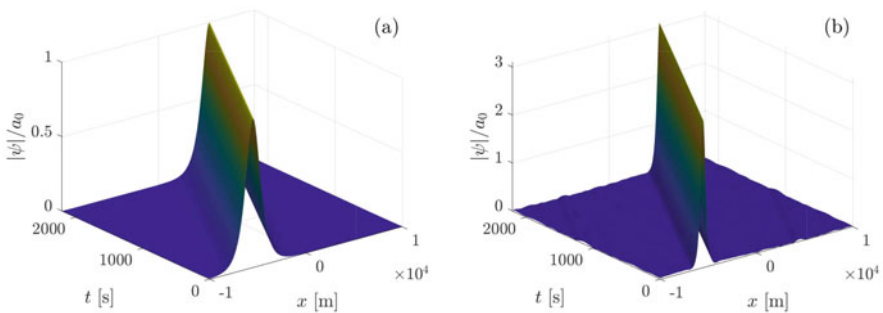


Fig. 2 Temporal evolution of a solitary solution without (a) and with (b) the presence of random wind

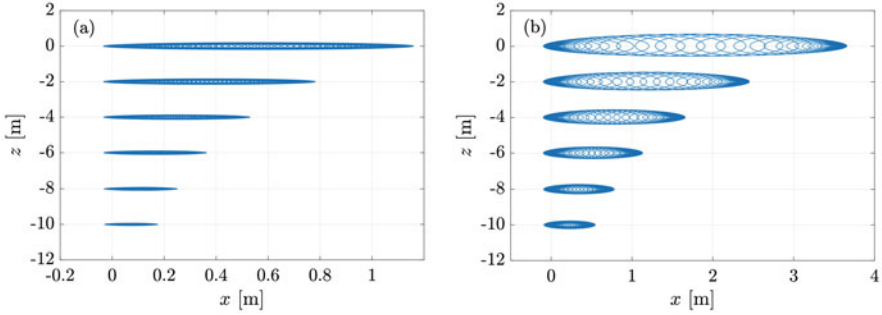


Fig. 3 The paths of six particles at different heights in the time interval $t \in [0\text{ s}, 2200\text{ s}]$ during the propagation of a solitary wave without (a) and with (b) the presence of random wind

horizontal Lagrangian drift, i.e. the difference between the end and start positions of the different particles in horizontal direction, grows up. Due to this larger drift, a growing Morison force is expected.

In order to show the effect of the wind at the pile, the Morison force (23) is integrated from the wave surface $\eta(x, t)$ to the ground, which is assumed at depth $z = -30\text{ m}$. The sea surface and the corresponding Morison force F_x at $x = 0\text{ m}$ with and without the presence of wind are presented in Fig. 4a, b. It is shown that the forces are acting in a shorter period of time, but with an amplitude multiplied by the factor about three. In order to show the effect of the wind in more detail, Fig. 4c presents the sea surface and forces for a short time period. It is shown that the water waves and the corresponding forces are time shifted. This results from the fact that the force depends on the acceleration and velocity of the water particles. In addition to this, it can again be seen that a stochastic wind process leads to different wave heights and forces.

3.2 The Influence of an Irregular Sea Surface

Next, a solitary solution disturbed by a random sea surface is considered. Thereby, the disturbance and initial condition shown in Fig. 1 are used. The corresponding temporal development of the disturbed soliton is shown in Fig. 5. Although the constant wave envelope, which is characteristic for the soliton, is replaced by an oscillating behavior, the structure of the solitary solution is preserved.

Figure 6 shows that the disturbance has a huge impact at the trajectory of a particle starting at $(0, 0)$. Although the end position of the water particle is in both cases nearly the same, the temporal evolution of the trajectory is different. In order to show the effect on the hydrodynamic forces acting on a cylindrical pile, Fig. 7 illustrates the wave heights and forces for the regular as well as for the irregular sea state. It can be seen that the maximal height of the waves and forces stays in the

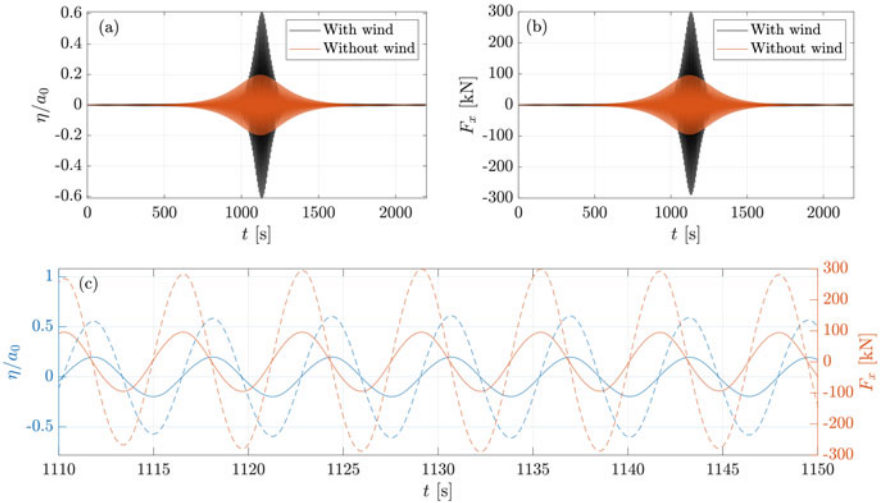


Fig. 4 (a) Sea surface at $x = 0$ m and (b) the corresponding Morison force acting on a cylindrical pile. A closer look at the sea surface with (dash) and without a stochastic wind (solid) is presented in (c)

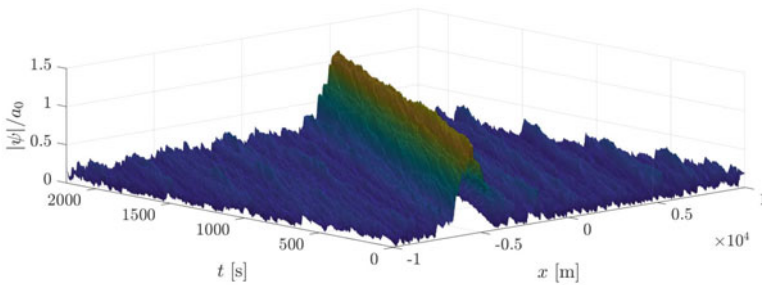


Fig. 5 Temporal evolution of a solitary solution in an irregular sea state

same order of magnitude, but the temporal evolution is different as well. Therefore, an irregular sea state has less effect on the maximal force amplitude, but it has an effect on the temporal behavior.

4 Conclusions

A novel approach to examine the hydrodynamic forces acting on a cylindrical pile is developed, which is based on the paths of fluid particles underneath of solutions to the NLS. The foundation is the theory of Carter et al. [7]. Looking at the solitary wave solutions of the NLS, the influence of a stochastic wind excitation and of

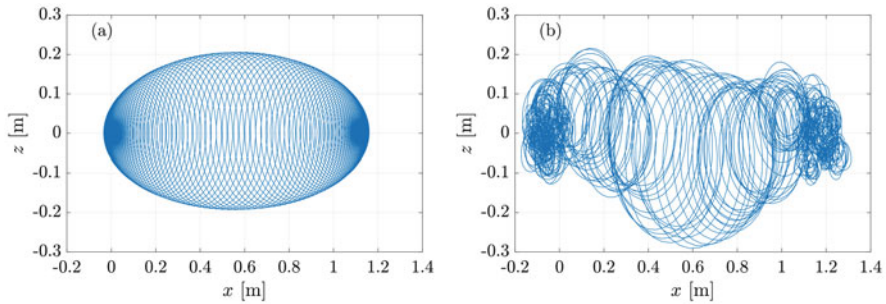


Fig. 6 The paths of a water particle starting at position $(0, 0)$ in the time interval $t \in [0 \text{ s}, 2200 \text{ s}]$ during the propagation of a solitary wave without **(a)** and with **(b)** an initial disturbance

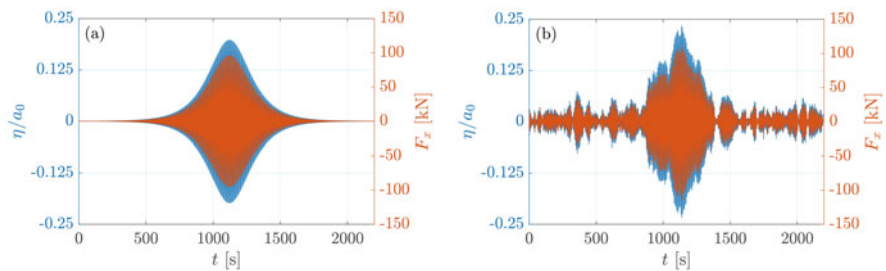


Fig. 7 Sea surface and corresponding force on pile at $x = 0 \text{ m}$ without **(a)** and with **(b)** an irregular disturbance of the sea

an irregular sea state on the water particles and hydrodynamic forces is studied. It is shown that a random wind increases the wave heights in such a way that the water particles are moving over a larger horizontal distance. This leads to a higher maximal force acting on the pile. On the other hand, a disturbance due to an irregular sea disturbs the temporal behavior of the excitation force and particle paths. Thereby, an increase of the maximal force could not be observed. Therefore, it can be concluded that these two processes have a considerable influence on the water waves and their resulting forces acting on mechanical structures.

References

1. J.R. Morison, J.W. Johnson, S.A. Schaaf, The force exerted by surface waves on piles. *J. Pet. Technol.* **2**(5), 49–154 (1950)
2. F. Dias, A.I. Dyachenko, V.E. Zakharov, Theory of weakly damped free-surface flows: a new formulation based on potential flow solutions. *Phys. Lett. A* **372**(8), 1297–1302 (2008)
3. V.E. Zakharov, Stability of periodic waves of finite amplitude on the surface of a deep fluid. *J. Appl. Mech. Tech. Phys.* **9**(2), 190–194 (1968)

4. S. Leblanc, Amplification of nonlinear surface waves by wind. *Phys. Fluids* **19**(10), 101705 (2007)
5. L. Dostal, M. Hollm, E. Kreuzer, Study on the behavior of weakly nonlinear water waves in the presence of random wind forcing. *Nonlinear Dyn.* **99**(3), 2319–2338 (2020)
6. H. Fischer, M. Hollm, L. Dostal, Soliton Collision in Random Seas. arXiv preprint arXiv:2007.12642 (2020)
7. J.D. Carter, C.W. Curtis, H. Kalisch, Particle trajectories in nonlinear Schrödinger models. *Water Waves* **2**(1), 31–57 (2020)
8. A.H. Nayfeh, *Perturbation Methods* (Wiley, New York, 1973)
9. A. Davey, K. Stewardson, On three-dimensional packets of surface waves. *Proc. R. Soc. Lond. A* **338**, 101–110 (1974)
10. J.W. Miles, On the generation of surface waves by shear flows. *J. Fluid Mech* **3**(2), 185–204 (1957)
11. J.W. Miles, On the generation of surface waves by shear flows. Part 2. *J. Fluid Mech* **6**(4), 568–582 (1959)
12. T.S. Hristov, S.D. Miller, C.A. Friehe, Dynamical coupling of wind and ocean waves through wave-induced air flow. *Nature* **422**, 55–58 (2003)
13. I. Van der Hoven, Power spectrum of horizontal wind speed in the frequency range from 0.0007 to 900 cycles per hour. *J. Meteorol.* **14**(2), 160–164 (1957)
14. S.D. Conte, J.W. Miles, On the numerical integration of the Orr-Sommerfeld equation. *J. Soc. Ind. Appl. Math.* **7**(4), 361–366 (1959)
15. W.J. Pierson, L. Moskowitz, A proposed spectral form for fully developed wind seas based on the similarity theory of S.A. Kitaigorodskii. *J. Geophys. Res.* **69**(24), 5181–5190 (1964)
16. T. Sarpkaya, *Vortex shedding and resistance in harmonic flow about smooth and rough circular cylinders at high Reynolds numbers* (Naval Postgraduate School Monterey CA, 1976)

A 3D Nonlinear Reduced-Order Model of a Cantilevered Aspirating Pipe Under VIV



Renato Maia Matarazzo Orsino, Celso Pupo Pesce, Fernando Geremias Toni, Wagner Antonio Defensor Filho, and Guilherme Rosa Franzini

1 Introduction

The dynamics of cantilevered aspirating pipes has been the focus of thorough investigations along the last 60 years, as testimonies to the treatise by Païdoussis [1]. Many have been the efforts to deal with instability issues, either through theoretical or experimental approaches. In fact, after [2] and [3], it has been shown that a weak instability may arise at very low internal flow speeds, due to three-dimensional effects at the aspirating pipe entrance [4]. Such a phenomenon has also been analyzed and discussed from the experimental and numerical points of view by Kuiper and Metrikine [5, 6].

On the other hand, vortex-induced vibration (VIV) of flexible vertical cantilevered rods has been intensively studied for the last three decades; see earlier works by, e.g., [7] and [8]. Recently, applications in offshore engineering, as sea water intake risers [9], raised the practical importance of assessing the dynamics of long cantilevered pipes under concomitant actions of internal and external flow.

This chapter aims at presenting a 3D ROM for an archetypical problem. A previous work by Orsino et al. [10] presented a 3D ROM of a cantilevered flexible cylinder conveying fluid under VIV. Nevertheless, that paper was restricted to the “discharging pipe case.” In this chapter, the same rationale is followed in order to address “aspirating pipes.” The generalized extended Hamilton principle for non-material volumes is applied [11], under the usual plug flow hypotheses. The effect of the aspirating flow at the entrance considers a modified version of [4] model. Non-conservative generalized forces due to vortex shedding are simply considered with a wake-oscillator model scheme, inspired by the work of [12].

R. M. M. Orsino · C. P. Pesce (✉) · F. G. Toni · W. A. D. Filho · G. R. Franzini
Offshore Mechanics Laboratory, Escola Politécnica, University of São Paulo, São Paulo, Brazil
e-mail: reorsino@usp.br; ceppesce@usp.br; fernando.toni@usp.br; wadfilho@usp.br;
gfranzini@usp.br

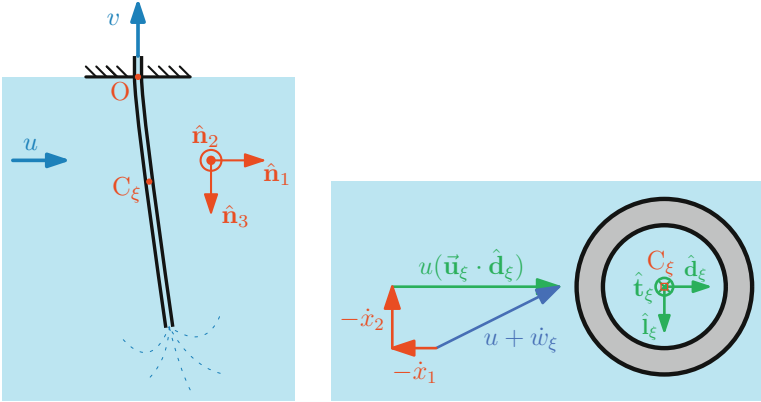


Fig. 1 Schematic representation of a submerged cantilevered flexible pipe aspirating fluid (left) and detail of a cross-section of this pipe (right)

The reduced-order model is set by using the Modular Modeling Methodology (MMM), introduced by Orsino [13, 14], for lumped systems and extended further to distributed ones [15, 16]. The 3D ROM is herein constructed for a long Euler–Bernoulli linear elastic beam, allowed to undergo large displacements. The whole formulation is given in dimensionless variables. An eigenvalue (root loci) analysis at the trivial equilibrium position is carried out to guide choosing the simulation scenarios. Numerical simulations illustrate the model response and the effects on VIV, around the onset of instability at low internal velocities, by varying an integral parameter related to the flow profile at the aspirating inlet.

2 Modeling

Consider a slender cylindrical flexible pipe, mounted vertically as a cantilever and immersed in an infinite and open homogeneous fluid medium (Fig. 1). Assume that, far from the pipe, the external flow is steady and horizontal. The pipe, in turn, aspirates fluid at a constant rate. For further simplification of the analysis, the pipe is considered homogeneous and inextensible, behaving like an Euler–Bernoulli linear elastic beam. Small strains are implied, though large displacements are allowed to occur. Moreover, the internal flow along the pipe, apart from the inlet sector (whose length is negligible when compared to the total length), is modeled as a plug flow.

In order to express the model in non-dimensional form, denoted by l the total length of the pipe, by EI its bending stiffness, and by m_a the total mass of fluid displaced in the external medium in the presence of the pipe. Adopt m_a , l and $\sqrt{m_a l^3 / EI}$ as the respective scales for mass, length, and time.

Denote by ξ the non-dimensional arc-length coordinate measured along the center line of the pipe from the fixed top end (outlet section) at $\xi = 0$ to the free end

(inlet section) at $\xi = 1$. The center O of the outlet section is adopted as the origin of a coordinate system $\mathbf{N} = (\mathbf{O}, \hat{\mathbf{n}}_1, \hat{\mathbf{n}}_2, \hat{\mathbf{n}}_3)$ fixed to an inertial reference frame. The unit vector $\hat{\mathbf{n}}_3$ is vertical and points downward. Denote by C_ξ the center of the cross-section located at ξ , and let $\vec{\mathbf{r}}$ be the non-dimensional position vector from O to C_ξ . Partial derivatives of $\vec{\mathbf{r}}$ with respect to the non-dimensional arc-length coordinate ξ and to the non-dimensional time τ are indicated by $\vec{\mathbf{r}}'$ and $\dot{\vec{\mathbf{r}}}$, respectively. Notice that due to the inextensibility hypothesis, $\vec{\mathbf{r}}'$ must always be a unit vector tangent to the center line.

Also, let $u\vec{\mathbf{u}}_\xi$ be the non-dimensional free-stream velocity at the depth of C_ξ , with $u > 0$ being a constant parameter chosen as a representative of the non-dimensional magnitude of the external flow, and $\vec{\mathbf{u}}_\xi$ being a horizontal vector that may vary with depth that represents the shape of this free-stream profile. Thus, define a cross-section-fixed coordinate system $\mathbf{S}_\xi = (C_\xi, \hat{\mathbf{d}}_\xi, \hat{\mathbf{l}}_\xi, \hat{\mathbf{t}}_\xi)$, with the unit vector $\hat{\mathbf{t}}_\xi = \vec{\mathbf{r}}'$ being the local tangent to the center line (i.e., orthogonal to the corresponding cross-section) and $\hat{\mathbf{l}}_\xi$ being orthogonal to $\vec{\mathbf{u}}_\xi$. The acceleration of C_ξ can be either represented in terms of its components \ddot{r}_k ($k = 1, 2, 3$) in \mathbf{N} or by its components \ddot{x}_k ($k = 1, 2, 3$) in \mathbf{S}_k , the same being valid for the decomposition of the virtual displacements $\delta\vec{\mathbf{r}}$:

$$\ddot{\vec{\mathbf{r}}} = \ddot{r}_1\hat{\mathbf{n}}_1 + \ddot{r}_2\hat{\mathbf{n}}_2 + \ddot{r}_3\hat{\mathbf{n}}_3 = \ddot{x}_1\hat{\mathbf{d}}_\xi + \ddot{x}_2\hat{\mathbf{l}}_\xi + \ddot{x}_3\hat{\mathbf{t}}_\xi \quad (1)$$

$$\delta\vec{\mathbf{r}} = \delta r_1\hat{\mathbf{n}}_1 + \delta r_2\hat{\mathbf{n}}_2 + \delta r_3\hat{\mathbf{n}}_3 = \delta x_1\hat{\mathbf{d}}_\xi + \delta x_2\hat{\mathbf{l}}_\xi + \delta x_3\hat{\mathbf{t}}_\xi. \quad (2)$$

Let μ_p and μ_i be the linear mass densities of the pipe itself and of the fluid inside the pipe, respectively. Since the plug flow hypothesis is considered, the non-dimensional relative velocity of the flow internal to the pipe with respect to the center line can be expressed as $-v\vec{\mathbf{r}}'$, v being a constant parameter. Also, let $\gamma = gl^2m_a/EI$ be the non-dimensional acceleration of gravity. Since the effects of gravity (weight and buoyancy) and flexural rigidity of the pipe can be included in potential energy parcels, the Lagrangian of the system can be computed by the following expression:

$$L = \frac{1}{2} \int_0^1 \left[\mu_p |\dot{\vec{\mathbf{r}}}|^2 + \mu_i |\dot{\vec{\mathbf{r}}} - v\vec{\mathbf{r}}'|^2 + 2\gamma(\mu_p + \mu_i - 1)\vec{\mathbf{r}} \cdot \hat{\mathbf{n}}_3 - \vec{\mathbf{r}}'' \cdot \vec{\mathbf{r}}'' \right] d\xi. \quad (3)$$

Structural damping effects, added mass, lift and drag effects due to the pipe interaction with external flow and inertial effects due to the flux of momentum in the inlet section of the pipe are included as the following virtual work parcels:

$$\begin{aligned} \delta W = & - \int_0^1 \beta \dot{\vec{\mathbf{r}}} \cdot \delta\vec{\mathbf{r}} d\xi - \int_0^1 \ddot{\vec{\mathbf{r}}} \cdot (\mu_{a,1}\hat{\mathbf{d}}_\xi\hat{\mathbf{d}}_\xi + \mu_{a,2}\hat{\mathbf{l}}_\xi\hat{\mathbf{l}}_\xi + \mu_{a,3}\hat{\mathbf{t}}_\xi\hat{\mathbf{t}}_\xi) \cdot \delta\vec{\mathbf{r}} d\xi \\ & + \int_0^1 \frac{2u^2}{\pi d_e} (\dot{c}_1\hat{\mathbf{d}}_\xi + \dot{c}_2\hat{\mathbf{l}}_\xi) \cdot \delta\vec{\mathbf{r}} d\xi + \left[\mu_i v (\dot{\vec{\mathbf{r}}} - \chi v\vec{\mathbf{r}}') \cdot \delta\vec{\mathbf{r}} \right]_{\xi=1}. \end{aligned} \quad (4)$$

In these expressions, β is a non-dimensional constant of proportional damping, d_e is the non-dimensional external diameter of the pipe, and χ is an empirical parameter related to the geometry of the internal flow velocity profile close to the inlet section. The definition of χ is discussed later in Sect. 2.2. Also, considering the axisymmetry of the pipe, the linear added mass density dyadic is expressed simply as $(\mu_{a,1}\hat{\mathbf{d}}_\xi\hat{\mathbf{d}}_\xi + \mu_{a,2}\hat{\mathbf{1}}_\xi\hat{\mathbf{1}}_\xi + \mu_{a,3}\hat{\mathbf{t}}_\xi\hat{\mathbf{t}}_\xi)$. Moreover, \hat{c}_k ($k = 1, 2$) represent the generalized hydrodynamic force coefficients expressed in the cross-section-fixed coordinate system \mathbf{S}_ξ .

Denoting by \mathbf{R}_ξ the rotation matrix between the coordinate systems \mathbf{S}_ξ and \mathbf{N} , the following identities must be satisfied so that the formulation presented in Eqs. (3) and (4) leads to equations of motion that are compatible with the modeling assumptions and motion constraints of the system:

$$\bar{\mathbf{r}}' = \hat{\mathbf{t}}_\xi, \quad \hat{\mathbf{1}}_\xi \cdot \bar{\mathbf{u}}_\xi = 0 \text{ and } (\ddot{r}_1, \ddot{r}_2, \ddot{r}_3)^\top = \mathbf{R}_\xi(\ddot{x}_1, \ddot{x}_2, \ddot{x}_3)^\top. \quad (5)$$

The hydrodynamic force coefficients, on the other hand, can be computed according to a usual phenomenological model defined by the following equations (see also Fig. 1):

$$(u + \dot{w}_\xi)^2 = ((u\bar{\mathbf{u}}_\xi - \dot{\bar{\mathbf{r}}}) \cdot \hat{\mathbf{d}}_\xi)^2 + (\dot{\bar{\mathbf{r}}} \cdot \hat{\mathbf{1}}_\xi)^2 \quad (6)$$

$$\dot{c}_1 = \frac{u + \dot{w}_\xi}{u^2} \left[\bar{C}_D^0(u\bar{\mathbf{u}}_\xi - \dot{\bar{\mathbf{r}}}) \cdot \hat{\mathbf{d}}_\xi + \frac{q_\xi}{\hat{q}} \hat{C}_L^0 \dot{\bar{\mathbf{r}}} \cdot \hat{\mathbf{1}}_\xi \right] \quad (7)$$

$$\dot{c}_2 = \frac{u + \dot{w}_\xi}{u^2} \left[\frac{q_\xi}{\hat{q}} \hat{C}_L^0(u\bar{\mathbf{u}}_\xi - \dot{\bar{\mathbf{r}}}) \cdot \hat{\mathbf{d}}_\xi - \bar{C}_D^0 \dot{\bar{\mathbf{r}}} \cdot \hat{\mathbf{1}}_\xi \right]. \quad (8)$$

Following the conventions adopted in the phenomenological model proposed by [12] for a rigid cylinder under single-dof VIV, \bar{C}_D^0 corresponds to the mean drag coefficient, \hat{C}_L^0 to the amplitude of the lift coefficient of a stationary rigid cylinder and $\hat{q} = 2$. The wake variables q_ξ , in turn, are defined locally, at each cross-section of the pipe, according to the following forced van der Pol oscillator, whose parameters are herein identical to the ones adopted in [12], despite the fact that we treat a flexible pipe:

$$\ddot{q}_\xi + \varepsilon\omega_s(q_\xi^2 - 1)\dot{q}_\xi + \omega_s^2 q_\xi = \frac{A}{d_e} \ddot{\bar{\mathbf{r}}} \cdot \hat{\mathbf{1}}_\xi. \quad (9)$$

Particularly, the non-dimensional vortex shedding frequency is computed by the expression $\omega_s = 2\pi uSt/d_e$. The values of ε and A , on the other hand, are adjusted according to the VIV response regime, which is identified by the value of the reduced velocity $U_m^* = 2\pi u/(\omega_m d_e)$. In this expression, ω_m stands for the m -th mode natural frequency of the pipe, considering free oscillations in water around the static equilibrium configuration of the pipe when $u = 0$.

It should be noticed that just one wake oscillator has been adopted at each section, in the cross-wise instantaneous direction of the relative external flow. Differently, in the 3D ROM model by Orsino et al. [10], two wake oscillators were adopted, one cross-wise and the other in-line with the relative external flow, inspired by the model adopted in [17], for a 2-dof rigid cylinder under VIV. In those cases, the in-line oscillator is set in dual resonance with the cross-wise one.

Moreover, as shown experimentally [7], for low values of specific mass, here computed as $(\mu_p + \mu_\perp)$, flexible pipes, as well as rigid rods with 2-dof, present cross-wise VIV amplitude curves, as a function of reduced velocities, with initial, upper, and super-upper response branches [18, 19]. The lock-in peak appears at larger reduced velocities when compared to the single-dof rigid cylinder case. This means that further work is surely needed on adjusting the present modeling scheme for flexible pipes.

Proceeding, in order to derive a reduced-order model for this system, the following discretization scheme can be introduced in the formulation presented in Eqs. (3) and (4): $r_k = \xi \delta_{k3} + \tilde{\mathbf{r}}_k^\top(\xi) \mathbf{r}_k(\tau)$, $x_k = \tilde{\mathbf{x}}_k^\top(\xi) \mathbf{x}_k(\tau)$ and $c_k = \tilde{\mathbf{C}}_D^0 \delta_{k1} + \tilde{\mathbf{c}}_k^\top(\xi) \mathbf{c}_k(\tau)$, with δ_{kl} representing the Kronecker delta. In such case, $\mathbf{r}_k(\tau)$ is a n -vector of generalized coordinates, while $\mathbf{x}_k(\tau)$ and $\mathbf{c}_k(\tau)$ are n -vectors of quasi-coordinates. On the other hand, $\tilde{\mathbf{r}}_k(\xi)$, $\tilde{\mathbf{x}}_k(\xi)$, and $\tilde{\mathbf{c}}_k(\xi)$ are the n -vectors of projection functions that identically satisfy the boundary conditions of the problem.

From now on, consider that $\tilde{\mathbf{u}}_\xi = \hat{\mathbf{n}}_1$, i.e., the free-stream profile of the external flow is uni-directional along the length of the pipe, and assume that $\tilde{\mathbf{r}}_k(\xi) = \tilde{\mathbf{x}}_k(\xi) = \tilde{\mathbf{c}}_k(\xi) = \tilde{\mathbf{h}}(\xi)$ with $\tilde{\mathbf{h}}(\xi)$ representing the n -vector of normalized mode shapes¹ of a cantilevered Euler–Bernoulli beam.

2.1 Relaxed Model and Constraint Enforcement Strategy

Defining $\mathbf{G}_{ij} = \int_0^1 \tilde{\mathbf{h}}^{(i)}(\xi) \otimes \tilde{\mathbf{h}}^{(j)}(\xi) d\xi$, $\mathbf{g}_i = \int_0^1 \tilde{\mathbf{h}}^{(i)}(\xi) d\xi$ and $\mathbf{E}_{ij} = \tilde{\mathbf{h}}^{(1)}(1) \otimes \tilde{\mathbf{h}}^{(j)}(1)$, the equations of motion that follows from the formulation presented in Eqs. (3) and (4) when the constraints in Eqs. (5)–(8) are neglected, which correspond to the “relaxed model” in the scope of the Modular Modeling Methodology (MMM), can be expressed as $\tilde{\mathbf{r}}_k = \mathbf{0}$ and $\tilde{\mathbf{x}}_k = \mathbf{0}$ ($k = 1, 2, 3$), with:

$$\begin{aligned} \bar{\mathbf{r}}_k &= (\mu_p + \mu_\perp) \mathbf{G}_{00} \ddot{\mathbf{r}}_k + [\mu_\perp v (\mathbf{G}_{10} - \mathbf{G}_{01} - \mathbf{E}_{00}) + \beta \mathbf{G}_{00}] \dot{\mathbf{r}}_k \\ &\quad + \left[\mathbf{G}_{22} - \mu_\perp v^2 (\mathbf{G}_{11} - \chi \mathbf{E}_{01}) \right] \mathbf{r}_k - \delta_{k3} \left[\gamma (\mu_p + \mu_\perp - 1) - (\chi - 1) \mu_\perp v^2 \right] \mathbf{g}_0 \end{aligned} \quad (10)$$

$$\bar{\mathbf{x}}_k = \mu_{a,k} \mathbf{G}_{00} \ddot{\mathbf{x}}_k - \frac{2u^2}{\pi d_e} \left(\mathbf{G}_{00} \mathbf{c}_k + \delta_{k1} \tilde{\mathbf{C}}_D^0 \mathbf{g}_0 \right). \quad (11)$$

¹ Therefore, in this case, \mathbf{G}_{00} is a $n \times n$ identity matrix.

In order to obtain a consistent reduced-order model from this formulation using the MMM, it is necessary to enforce the constraints described by Eqs. (5)–(8). However, since each variable among the r_k , x_k , and c_k is expressed in the ROM as a function of n generalized coordinates, it is only possible to ensure the enforcement of these constraint equations at n cross-sections along the pipe, for instance, at $\xi = 1/n, 2/n, \dots, 1$. Thus, the generalized coordinates vector \mathbf{q} adopted in this model must be composed by the n -vectors $\mathbf{r}_k(\tau)$, $\mathbf{x}_k(\tau)$, and $\mathbf{c}_k(\tau)$ ($k = 1, 2, 3$) as well as by the variables adopted for parameterizing \mathbf{R}_ξ (Rodrigues parameters, in the present case), w_ξ , and q_ξ ($\xi = 1/n, 2/n, \dots, 1$).

Therefore, writing down the “relaxed model” in the matrix form $\mathbf{M}(\tau, \mathbf{q})\ddot{\mathbf{q}} = \mathbf{f}(\tau, \mathbf{q}, \dot{\mathbf{q}})$ and the constraint equations in the form $\mathbf{A}(\tau, \mathbf{q}, \dot{\mathbf{q}})\ddot{\mathbf{q}} = \mathbf{b}(\tau, \mathbf{q}, \dot{\mathbf{q}})$, and considering a matrix \mathbf{S} defining a linear operator *onto* $\ker(\mathbf{A})$, the reduced-order model of this system can be expressed in the form [14]:

$$\begin{bmatrix} \mathbf{S}^T \mathbf{M} \\ \mathbf{A} \end{bmatrix} \ddot{\mathbf{q}} = \begin{bmatrix} \mathbf{S}^T \mathbf{f} \\ \mathbf{b} \end{bmatrix}. \quad (12)$$

2.2 On the Modeling of the Aspiration of Fluid

Denote by $\vec{\mathbf{p}}$ the position vector of a fluid particle inside the pipe. Assume that, at each cross-section ($0 \leq \xi \leq 1$), $(\dot{\vec{\mathbf{p}}} - \dot{\vec{\mathbf{r}}})|_\xi = \vec{\mathbf{v}}_\xi(\tau, \mathbf{q})$ is a function of time and of the configuration of the system only. Indeed, such an assumption is an extension of the plug flow hypothesis already considered for $0 \leq \xi < 1 - \delta$ ($\delta \ll 1$), in which $(\dot{\vec{\mathbf{p}}} - \dot{\vec{\mathbf{r}}})|_\xi = -v\hat{\mathbf{t}}_\xi$.

According to the generalized Hamilton’s principle for non-material volumes [11], the virtual work associated with the flux of mass through the inlet (S_1) and outlet (S_0) sections of the pipe, due to the aspiration of fluid, can be expressed as the sum of the following terms:

$$\delta W_m = \iint_{S_1} \frac{1}{2} \rho (\dot{\vec{\mathbf{p}}} \cdot \dot{\vec{\mathbf{p}}}) (\delta \vec{\mathbf{p}} - \delta \vec{\mathbf{r}}) \cdot \hat{\mathbf{t}}_1 \, dS - \iint_{S_1} \rho (\dot{\vec{\mathbf{p}}} \cdot \delta \vec{\mathbf{p}}) (\dot{\vec{\mathbf{p}}} - \dot{\vec{\mathbf{r}}}) \cdot \hat{\mathbf{t}}_1 \, dS. \quad (13)$$

Indeed, since the outlet section of the pipe is clamped (i.e., $\delta \vec{\mathbf{p}} = \delta \vec{\mathbf{r}} = \vec{\mathbf{0}}$), only the influx of mass, at the inlet section, gives a non-zero contribution to this virtual work. The first integral in Eq. (13) is also zero since $(\delta \vec{\mathbf{p}} - \delta \vec{\mathbf{r}})|_{\xi=1} = \vec{\mathbf{v}}_1 d\tau \Rightarrow (\delta \vec{\mathbf{p}} - \delta \vec{\mathbf{r}})|_{\xi=1} = \vec{\mathbf{0}}$. Thus,

$$\delta W_m = - \left[\iint_{S_1} \rho (\vec{\mathbf{v}}_1 \cdot \hat{\mathbf{t}}_1) (\dot{\vec{\mathbf{r}}} + \vec{\mathbf{v}}_1) \, dS \right] \cdot \delta \vec{\mathbf{r}}. \quad (14)$$

Due to continuity, since the plug flow hypothesis is assumed for $0 \leq \xi < 1 - \delta$ ($\delta \ll 1$), $\iint_{S_1} \rho (\vec{\mathbf{v}}_1 \cdot \hat{\mathbf{t}}_1) \, dS = -\mu_{\pm} v$. Finally, imposing an extra hypothesis that

the internal flow has an axisymmetric profile at each cross-section of the pipe (see Fig. 2), it can be stated that Eq. (14) is equivalent to the last term in Eq. (4) provided that the non-dimensional parameter χ is defined as follows:

$$\chi = \frac{1}{\mu_{\perp} v^2} \left| \iint_{S_1} \rho (\vec{v}_1 \cdot \hat{\mathbf{t}}_1)^2 \, dS \right|. \quad (15)$$

A CFD analysis was performed in STAR-CCM [20], in which a stationary hollow cylindrical pipe aspirates incompressible fluid from the external medium at a constant rate. According to the velocity profile obtained from this simulation, the values of χ were computed not only at the inlet section itself, but also at some other cross-sections within the inlet sector, as presented in Fig. 2. It is noticeable that close to the inlet section the value of χ goes up to 1.35. Thus, in the analyses presented in the following sections, two values of χ are adopted: 1, which corresponds to a localized plug flow approximation, and 1.35.

3 Stability Analysis

In this section, the stability of the trivial equilibrium configuration, in which the pipe remains vertical in the absence of free stream in the external medium ($u = 0$), is analyzed. Root-loci diagrams obtained from the linearized reduced-order model reveal how the eigenvalues of the system vary with the internal flow velocity v .

Particularly, adopting the values presented in Table 1 for the non-dimensional parameters of the model and setting the number of projection functions adopted in the derivation of the ROM to be $n = 5$, the corresponding root-loci diagrams for $\chi = 1$ and $\chi = 1.35$ are the ones presented in Fig. 2. In these diagrams, the absolute value of the imaginary parts of the eigenvalues λ , which correspond to the oscillation frequencies of each of the $n = 5$ modes of the model, is displayed in the vertical axis. The associated real parts of these eigenvalues, in turn, are represented by a temperature map color scale, in which the cold colors correspond to stability ($\text{Re}(\lambda) < 0$), while the hot ones indicate an unstable response of the system at that internal flow velocity.

Table 1 Values adopted for non-dimensional parameters of the model in the numerical analyses

Pipe				Wake-oscillator model [12]			
Par.	Value	Par.	Value	Par.	Value	Par.	Value
d_e	0.02	μ_{\perp}	0.48	\tilde{C}_D^0	1.1856	$A(U_2^* < 6.5)$	4
β	1.0	$\mu_{a,1}$	1.0	\hat{C}_L^0	0.3842	$A(U_2^* > 6.5)$	12
γ	1.0	$\mu_{a,2}$	1.0	\hat{q}	2	$\epsilon(U_2^* < 6.5)$	0.05
μ_D	1.92	$\mu_{a,3}$	0.01	St	0.1932	$\epsilon(U_2^* > 6.5)$	0.7

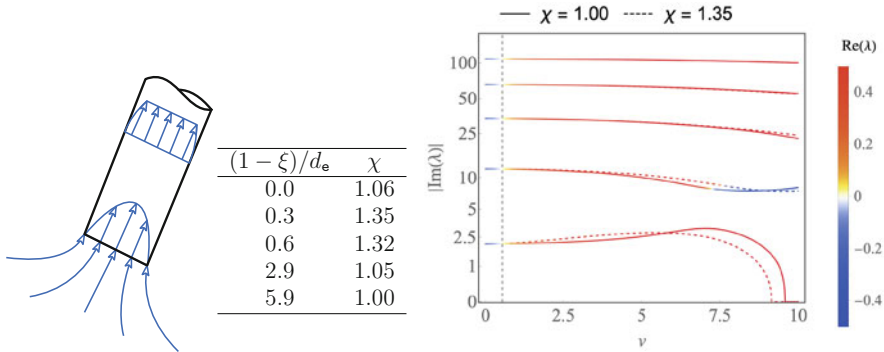


Fig. 2 Left: schematic representation of an axisymmetric velocity profile close to the inlet section of the pipe and estimation of χ along the inlet sector of a stationary hollow cylindrical pipe according to the CFD analysis developed by Rosetti [20]. Right: root loci ($|\text{Im}(\lambda)|$) vs. v , with $\text{Re}(\lambda)$ represented by the color scale) of the linearized model of the cantilevered pipe aspirating fluid for two different values of χ

It is remarkable that the vertical equilibrium configuration of the system is stable only for low values of v . The pipe does not exhibit an unstable response at very low velocities for any rate of aspiration due to the presence of structural damping. Indeed, the critical value $v \approx 0.52$ above which instability arises is predominantly a function of β , being almost insensitive to the factor χ that, as observed, does not affect significantly the root-loci diagrams either.

Notice also that the second mode becomes stable again at high velocities ($v \approx 7.4$, $\chi = 1$; $v \approx 7.5$, $\chi = 1.35$). Around the new transition of the second mode to stability, the imaginary part of the first eigenvalue attains a maximum, followed by a steeped decreasing trend, down to a bifurcation point at zero.

4 VIV Response Analysis

Still considering the reduced-order model with $n = 5$ and the parameters shown in Table 1, the response of the system under VIV can be assessed by performing numerical simulations. First, the following velocities of internal flow are chosen: (i) $v = 0$, which corresponds to the absence of internal flow in which case the single fluid–structure interaction phenomenon would be vortex-induced vibrations; (ii) $v = 0.50$, slightly below the critical value of v , corresponding to a stable vertical equilibrium configuration; and (iii) $v = 0.54$, slightly above the aforementioned critical value. Particularly for $v = 0.54$ the dynamic response is investigated by considering both $\chi = 1$ and $\chi = 1.35$, which leads to the four scenarios of internal flow illustrated in Fig. 3.

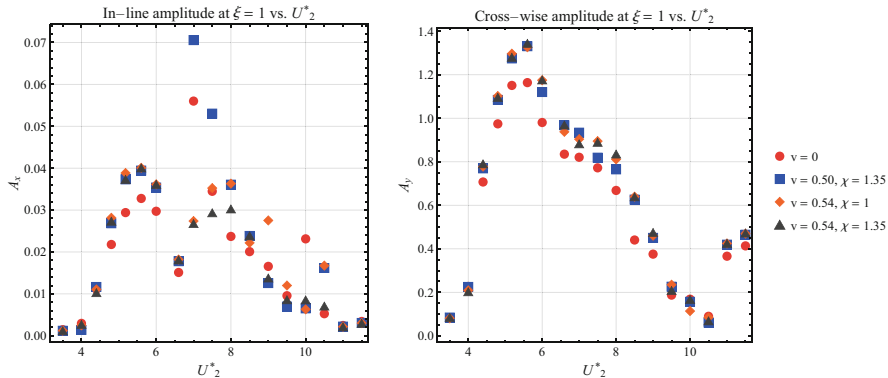


Fig. 3 In-line and cross-wise amplitudes of the oscillations of the center of the inlet section of the pipe as a function of U_2^* for all the analyzed scenarios

For each scenario, 18 numerical simulations were performed, varying the external flow free-stream speeds over a range in which the respective second mode of vibration (check the values of ω_2 in Fig. 2) is fully excitable ($3.5 \leq U_2^* \leq 11.5$).

Denote by x and y the oscillating parts of the steady-state responses of the coordinates $r_1(\tau, \xi)$ and $r_2(\tau, \xi)$, normalized per unit of external diameter of the pipe. Figure 3 exhibits the amplitudes of x and y that are referred, respectively, as in-line (A_x) and cross-wise (A_y) amplitudes, as a function of U_2^* for each of the four scenarios of internal flow considered. It is noticeable that when compared to the scenario $v = 0$ the cross-wise amplitudes increase in the presence of internal flow both in the upper and lower branches. Comparing the scenarios defined close to the critical value $v \approx 0.52$, however, it can be stated that A_y responses are almost insensitive to the internal flow velocity v and to the factor χ , even though some sensitivity to these parameters is observed in the A_x responses. It should be observed that the in-line amplitudes seem to be underestimated by the model, particularly when the $v = 0$ scenario is compared with 2-dof VIV experiments found in the literature, e.g., [18]. Another remarkable characteristic of the responses observed in Fig. 3 is the increase of A_y for $U_2^* \geq 10.5$. Since $\omega_3/\omega_2 \approx 2.8$, this interval corresponds to $U_3^* > 3.7$, which indicates that the observed phenomenon corresponds to an excitation of third mode responses.

Figure 4, in turn, focuses on detailing the dynamic response in the scenario $v = 0.54$ and $\chi = 1.35$ in the 2nd mode lock-in peak simulation $U_2^* = 1/St = 5.18$, exhibiting the steady-state y vs. x trajectories and the associate cross-wise vs. in-line force coefficients plots (i.e., \hat{c}_2 vs. \hat{c}_1) for 5 selected cross-sections along the pipe. In this simulation, it is noticeable the dual resonance between the in-line and cross-wise responses, both in the shape of the trajectories and in the relation between the force coefficients, which is induced mathematically by the phenomenological model adopted, Eqs. (6)–(9). The synchronicity indicates the resonant response of the second mode of the system, as expected.

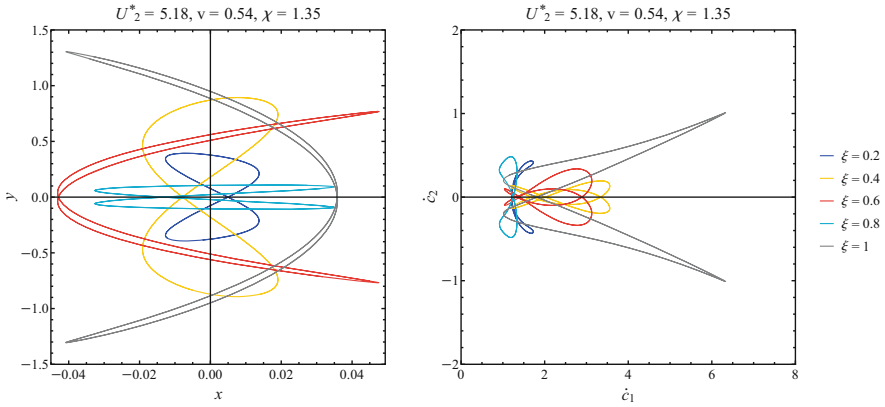


Fig. 4 Steady-state trajectories of centers and \dot{c}_2 vs. \dot{c}_1 plots for 5 cross-sections along the pipe for a 2nd mode lock-in peak simulation scenario with $v = 0.54$ and $\chi = 1.35$

5 Conclusions

This chapter introduced a 3D nonlinear reduced-order model for a pipe aspirating fluid under the concomitant effect of vortex-induced vibrations by following the Modular Modeling Methodology approach [13, 14]. By the use of the extended Hamilton principle for non-material volumes [11], a model for the aspiration procedure was proposed. Interactions of the pipe with the external flow were modeled according to a phenomenological model available in the literature for the VIV response of a rigid cylinder. After a stability analysis of the system and a study of VIV responses in properly selected scenarios, it can be preliminarily stated that for internal flow velocities below a critical value and even slightly above, the dynamics of this system is dominated by the interaction with the external flow, being much less sensible to the parameters associated to the fluid aspiration. Certainly, further studies on this problem should concentrate first on adjusting the phenomenological VIV model scheme to flexible cylinders. Experimental results must then be used, both (i) under pure VIV, with 2-dof rigid cylinders, as those by Jauvtis and Williamson [18], Franzini et al. [21] and with cantilevered flexible cylinders, as those by Pesce and Fajarra [7] and (ii) from new specific experiments with aspirating pipes under VIV.

Acknowledgments The authors gratefully acknowledge Shell Brasil for sponsoring this research work and ANP (Brazil's National Oil, Natural Gas, and Biofuels Agency) for the strategic support provided through the R&D levy regulation. The authors are also grateful to Dr. Guilherme F. Rosetti for the CFD analysis that led to an estimation of the non-dimensional χ . This study was financed in part by the Coordenação de Aperfeiçoamento de Pessoal de Nível Superior—Brasil (CAPES)—Finance Code 001. C. Pesce and G. Franzini acknowledge CNPq research grants n. 308230/2018-3 and 305945/2020-3, respectively.

References

1. M.P. Paidoussis, *Fluid-Structure Interactions: Slender Structures and Axial Flow*, vol. 1 (Academic Press, London, 2014)
2. M.P. Paidoussis, Aspirating pipes do not flutter at infinitesimally small flow. *J. Fluids Struct.* **19**, 419–425 (1999)
3. M.P. Paidoussis, C. Semler, M. Wadham-Gagnon, A reappraisal of why aspirating pipe do not flutter at infinitesimal flow. *J. Fluids Struct.* **20**, 147–156 (2005)
4. D.B. Giacobbi, S. Rinaldi, C. Semler, M.P. Paidoussis, The dynamics of a cantilevered pipe aspirating fluid studied by experimental, numerical and analytical methods. *J. Fluids Struct.* **30**, 73–96 (2012)
5. G.L. Kuiper, A.V. Metrikine, A new time-domain drag description and its influence on the dynamic behaviour of a cantilever pipe conveying fluid. *J. Fluids Struct.* **23**, 429–445 (2007)
6. G.L. Kuiper, A.V. Metrikine, Experimental investigation of dynamic stability of a cantilever pipe aspirating fluid. *J. Fluids Struct.* **24**, 541–558 (2008)
7. C.P. Pesce, A.L.C. Fujarra, Vortex-induced vibrations and jump phenomenon: Experiments with a clamped flexible cylinder in water. *Int. J. Offshore Polar Eng.* **10**, 26–33 (2000)
8. A.L.C. Fujarra, C.P. Pesce, F. Flemming, C.H.K. Williamson, Vortex-induced vibration of a flexible cantilever. *J. Fluids Struct.* **15**, 651–658 (2001)
9. S. Xiang, P. Cao, J. He, S. Kibbee, S. Bian, Water intake riser model test and numerical calibration, *Proc. the ASME 2015 34th International Conference on Ocean, Offshore and Arctic Engineering, OMAE 2015, St John's, Canada, May 31–June 5* (2015)
10. R.M.M. Orsino, C.P. Pesce, G.R. Franzini, A 3D non-linear reduced order model for a cantilevered pipe conveying fluid under VIV, in *Proc. 9th International Symposium on Fluid-Structure Interactions, Flow-Sound Interactions, Flow-Induced Vibration & Noise, FIV 2018, Toronto, Canada, July 8–11* (2018)
11. L. Casetta, C.P. Pesce, The generalized Hamilton's principle for a non-material volume. *Acta Mech.* **224**(4), 919–924 (2013)
12. R.H.M. Ogink, A.V. Metrikine, A wake oscillator with frequency dependent coupling for the modeling of vortex-induced vibration. *J. Sound Vib.* **329**(26), 5452–5473 (2010)
13. R.M.M. Orsino, A contribution on modeling methodologies for multibody systems. Ph.D. Thesis, Universidade de São Paulo (2016)
14. R.M.M. Orsino, Recursive modular modelling methodology for lumped-parameter dynamic systems. *Proc. R. Soc. A: Math. Phys. Eng. Sci.* **473**, 2204 (2017)
15. R.M.M. Orsino, C.P. Pesce, Reduced order modeling of a cantilevered pipe conveying fluid applying a modular methodology. *Int. J. Non-Linear Mech.* **103**, 1–11 (2018)
16. R.M.M. Orsino, C.P. Pesce, G.R. Franzini, Cantilevered pipe ejecting fluid under VIV. *J. Braz. Soc. Mech. Sci. Eng.* **40**(11), 542 (2018)
17. G.R. Franzini, L.O. Bunzel, A numerical investigation on piezoelectric energy harvesting from vortex-induced vibrations with one and two degrees of freedom. *J. Fluids Struct.* **77**, 196–212 (2018)
18. N. Jauvtis, C. Williamson, The effect of two degrees of freedom on vortex-induced vibration at low mass and damping. *J. Fluid Mech.* **509**, 23–62 (2007)
19. C.P. Pesce, A.L.C. Fujarra, The 'super-upper branch' VIV response of flexible cylinders, in *4th Conference on Bluff Body Wakes and Vortex-Induced Vibrations, BBVIV4, Santorini, Greece, June 21–24*. (2005)
20. G.F. Rosetti, CFD analysis performed by STAR-CCM+. Private communication (2019)
21. G.R. Franzini, R.T. Gonçalves, J.R. Meneghini, A.L.C. Fujarra, One and two degrees-of-freedom vortex-induced vibration experiments with yawed cylinders. *J. Fluids Struct.* **42**, 401–420 (2013)
22. G. Hamel, *Theoretische Mechanik* (Springer, Berlin, 1949)

3D Reduced-Order Model for an Orthotropic Stiffened Piezoelectric Cantilevered Flexible Cylinder Under VIV



Leticia S. Madi, Guilherme J. Vernizzi, Celso P. Pesce, Wagner A. Defensor Fo., and Guilherme R. Franzini

1 Introduction

Vortex-induced vibration (VIV) is a nonlinear resonant fluid–structure interaction phenomenon due to the synchronization of vortex shedding frequency with one of the natural frequencies of the structure. In engineering projects, VIV is usually studied as a problem to be mitigated, as it is a factor of great impact in fatigue analysis. Nevertheless, this phenomenon may be approached from a different perspective, within the context of energy harvesting. In this case, the objective is a controlled amplification of the response, to be used for obtaining electric energy. As an example, [1] present the concept of VIVACE (Vortex-Induced Vibration Aquatic Clean Energy), a device based on a series of cylinders in tandem arrangement that uses electromagnetic transducers to convert structural kinetic energy into electricity.

Many of the classical studies of VIV phenomena concern rigid cylinders mounted on an elastic base. However, from the low-power-energy-harvesting perspective, the phenomenon on flexible cylinders with orthotropic bending stiffness may be considered an interesting endeavor, since VIV leads to self-excited and self-limited oscillations and, in this particular case, higher amplitudes are maintained for a broad band of frequencies. First observed in [2] and later confirmed in [3], experiments with flexible cylinders with larger stiffness in the in-line direction compared to the cross-flow ones showed a new branch of response, called by the authors high-speed mode. This new branch observed is stable and extends, with high-frequency response, to large incoming flow velocities. The in-line and cross-wise amplitudes obtained in this study for the first two bending vibration modes of a cantilever of frequency ratio 4:1 are shown in Fig. 1, represented by their dominant intrinsic

L. S. Madi (✉) · G. J. Vernizzi · C. P. Pesce · W. A. Defensor Fo. · G. R. Franzini
University of São Paulo, Escola Politécnica, Offshore Mechanics Laboratory, São Paulo, Brazil
e-mail: leticia.madi@usp.br; guilherme.jorge.lopes@usp.br; ceppesce@usp.br; wadfilho@usp.br
<http://lmo.poli.usp.br>

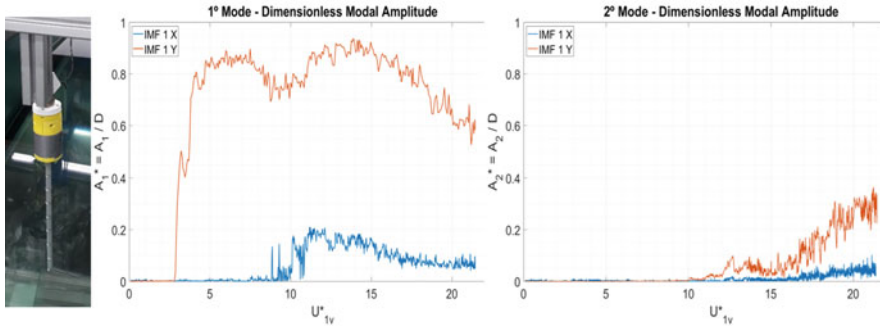


Fig. 1 Modal VIV response branches for orthotropic stiffened flexible cantilevered cylinder: experimental set-up, in-line and cross-wise modal amplitudes as functions of reduced velocity (adapted from [3])

mode function (IMF); see [4] for the definition of an IMF within the empirical mode decomposition and [5] for their application in VIV analysis. This phenomenon has been thought to be primarily caused by twisting–bending coupling, triggered by VIV.

Concerning energy conversion, piezoelectric energy harvesting is a useful solution for reduced power demanded by electronic devices. Experimental and numerical studies on piezoelectric flexible cantilevered beams are found in [6, 7] and [8].

As a theoretical approach, this chapter derives a reduced-order model for studying a cantilevered piezoelectric harvester with orthotropic bending stiffness under VIV. The equations of motion coupling mechanical and electrical subsystems, as well as the wake-oscillator model for the fluid–structure interaction, are addressed in Sect. 2. Numerical simulations at chosen scenarios illustrate the problem in Sect. 3.

2 Mathematical Model

The system modelled in this chapter is represented in Fig. 2. The harvester is composed of a cantilevered flexible polymeric cylinder molded over a flat bar constituted by a metallic substrate between two piezoelectric material layers connected in series to an electrical resistance.

For the mathematical modelling, the Bernoulli–Euler’s cantilever model is taken. A fixed frame XYZ with origin at the clamped end of the beam is adopted, with X parallel to the incident flow direction, Y parallel to the cross-wise direction, and Z aligned with the beam axis. The displacements in each of these directions are U , V , and W , respectively (see Fig. 2). The extended Hamilton’s principle for dissipative systems then reads

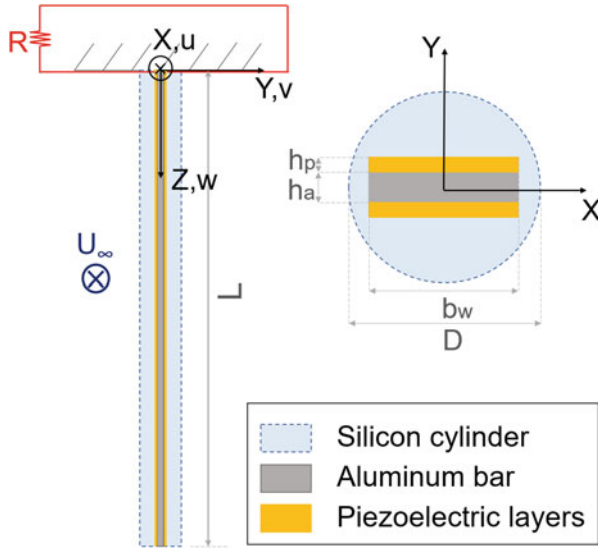


Fig. 2 Schematic representation of the energy harvesting system

$$\int_{t_1}^{t_2} [\delta\mathcal{T} - \delta\mathcal{V} + (\delta\mathcal{W}_{nc} + \delta\mathcal{W}_{i,e})] dt = 0. \quad (1)$$

Being μ the mass per unit length, J_p the mass moment of inertia around Z , and θ the twist angle, the variation of the kinetic energy is given as

$$\int_{t_1}^{t_2} \delta\mathcal{T} dt = - \int_{t_1}^{t_2} \int_0^L [\mu (\ddot{u}\delta u + \ddot{v}\delta v + \ddot{w}\delta w) + J_p \ddot{\theta}\delta\theta] dZ dt. \quad (2)$$

The potential energy \mathcal{V} can be divided into a portion due to external potential fields, a portion due to strain energy, and a portion corresponding to the electric field in the piezoelectric layers, namely $\mathcal{V} = \mathcal{V}_f + \mathcal{V}_k + \mathcal{V}_e$. Since the external conservative forces are weight and buoyance, it follows that:

$$\delta\mathcal{V}_f = - \int_0^L \gamma \delta w dZ, \quad (3)$$

with γ being the immersed weight per unit length. Following, the variation of the strain energy, considering a linear-elastic and piezoelectric behavior for the materials, is written as

$$\delta\mathcal{V}_k = \int_0^L \iint_A [E \varepsilon_{zz} \delta \varepsilon_{zz} + G (\gamma_{xz} \delta \gamma_{xz} + \gamma_{yz} \delta \gamma_{yz})] dA dZ, \quad (4)$$

with ε_{zz} being the axial strain, while γ_{xz} and γ_{yz} are the distortions in the cross-section plane. In turn, E and G are the Young and Shear moduli, respectively. Since the cross-sections are composed of different materials, the area integrals must be carried out for each element. In order to proceed with a formulation that takes into account axial extensibility, torsion, and bending in both transversal directions, the relations presented in [9] for the axial strain and the distortions are used for each element of the cross-section. These relations are correct up to second order, leading to a model correct up to nonlinearities of third order. Substituting those relations and adding up terms from different elements of the cross-sections lead to

$$\begin{aligned} \delta\mathcal{V}_k = & \int_0^L \left[EA \left(w' + \frac{(u')^2}{2} + \frac{(v')^2}{2} \right) + \frac{EI_p}{2} (\theta')^2 \right] [\delta w' + u' \delta u' + v' \delta v'] dZ \\ & + \int_0^L \left[EI_p \left(w' + \frac{(u')^2}{2} + \frac{(v')^2}{2} \right) \theta' + \frac{EI_4}{2} (\theta')^3 \right] \delta \theta' dZ \\ & + \int_0^L EI_X v'' \delta v'' + EI_Y u'' \delta u'' + GI_p \theta' \delta \theta' dZ. \end{aligned} \quad (5)$$

The stiffness products are taken in the whole cross-section, which requires the contribution of each element to be added up. The area moment of inertia around axis X and Y are I_X and I_Y , respectively, while $I_p = I_X + I_Y$ is the polar moment of inertia, I_t is the torsional moment of inertia, and I_4 is an area integral given by

$$I_4 = \iint_A (X^2 + Y^2)^2 dA. \quad (6)$$

Now, for the electric component of the deformation in the bimorphic piezoelectric layers, following [8], the variation of the piezoelectric potential energy is given by

$$\delta\mathcal{V}_e = - \int_0^L \left(\frac{e_{31}}{2h_p} M_X \bar{V} \delta v'' + \frac{e_{31}}{2h_p} M_X v'' \delta \bar{V} \right) dZ. \quad (7)$$

Only the coupling between the displacements v and the voltage \bar{V} appears since the static moment of each piezoelectric layer with respect to the Y axis is zero. Equation (7) already added up both piezoelectric layers. The absolute value of the static moment of each piezoelectric layer is M_X , h_p is the thickness of each layer, and e_{31} is the constant of piezoelectric coupling. Finally, completing the conservative terms, the variation of the generated electric energy is given as [8]:

$$\delta\mathcal{W}_{i,e} = \int_0^L \left(\frac{e_{31}}{2h_p} M_X \bar{V} \delta v'' + \frac{e_{31}}{2h_p} M_X v'' \delta \bar{V} + \frac{\bar{E}A_p}{2h_p^2} \bar{V} \delta \bar{V} \right) dZ. \quad (8)$$

To close the mathematical model, the variation of the work of non-conservative forces is given as

$$\delta \mathcal{W}_{nc} = \int_0^L \left[(f_u - c_u \dot{u}) \delta u + (f_v - c_v \dot{v}) \delta v \right] dZ + Q \delta \bar{V}, \quad (9)$$

with Q being the electric charge output of the electrical system, c_u and c_v are the linear structural damping coefficients in the X and Y directions, respectively, while f_u and f_v are the hydrodynamic forces in those same directions. Collecting all variational terms in the extended Hamilton's principle (Eq. 1), developing the appropriate algebraic operations, and deriving the equation of the electric charge with respect to time, one obtains the following system of nonlinear partial differential equations of motion:

$$\mu \ddot{w} - EA (w'' + u' u'' + v' v'') - EI_p \theta' \theta'' - \gamma = 0; \quad (10)$$

$$\mu \ddot{u} + c_u \dot{u} + EI_Y u'''' - \left[EA u' \left(w' + \frac{(u')^2}{2} + \frac{(v')^2}{2} \right) + \frac{EI_p}{2} u' (\theta')^2 \right]' = f_u; \quad (11)$$

$$\mu \ddot{v} + c_v \dot{v} + EI_X v'''' - \left[EA v' \left(w' + \frac{(u')^2}{2} + \frac{(v')^2}{2} \right) + \frac{EI_p}{2} v' (\theta')^2 \right]' - \frac{e_{31} M_X \bar{V}''}{h_p} = f_v; \quad (12)$$

$$J_p \ddot{\theta} - GI_t \theta'' - \left[EI_p \theta' \left(w' + \frac{(u')^2}{2} + \frac{(v')^2}{2} \right) + \frac{EI_4}{2} (\theta')^3 \right]' = 0; \quad (13)$$

$$\int_0^L \frac{e_{31}}{h_p} M_X \dot{v}'' dZ + \frac{\bar{E} A_p L}{2 h_p^2} \dot{\bar{V}} + \frac{\bar{V}}{R} = 0. \quad (14)$$

To complete the set of equations of motion, the hydrodynamic forces are adapted from the model presented in [10]. Here, the wake variable q is taken as a continuous variable that may vary with Z . The hydrodynamic forces are then written as

$$\begin{aligned} f_u = & -\mu_a \ddot{u} - \frac{1}{2} \left(\frac{q C_L}{2} \right) \rho D \dot{v} \sqrt{(U_\infty - \dot{u})^2 + \dot{v}^2} \\ & + \frac{1}{2} C_D \rho D (U_\infty - \dot{u}) \sqrt{(U_\infty - \dot{u})^2 + \dot{v}^2} \\ & + \frac{1}{2} \alpha \left(\frac{q C_L}{2} \right)^2 \rho D (U_\infty - \dot{u}) \sqrt{(U_\infty - \dot{u})^2} \end{aligned} \quad (15)$$

$$f_v = -\mu_a \ddot{v} + \frac{1}{2} \left(\frac{q C_L}{2} \right) \rho D (U_\infty - \dot{u}) \sqrt{(U_\infty - \dot{u})^2 + \dot{v}^2} - \frac{1}{2} C_D \rho D \dot{v} \sqrt{(U_\infty - \dot{u})^2 + \dot{v}^2}. \quad (16)$$

The coefficients C_L and C_D are the amplitude of oscillation of the lift coefficient for a stationary cylinder and the mean drag coefficient for a stationary cylinder, respectively. In turn, μ_a is the potential added mass for the cross-section and α is a coefficient related to the drag amplification during VIV. The wake variable follows the forced van der Pol equation:

$$\ddot{q} + \varepsilon_v \omega_s (q^2 - 1) \dot{q} + \omega_s^2 q - \frac{\kappa}{D} \ddot{u} q = \frac{A_v}{D} \ddot{v}, \quad (17)$$

with ω_s being the vortex shedding frequency, while ε_v and A_v are, respectively, a van der Pol equation parameter and a coupling coefficient, both determined experimentally [10]. In order to numerically integrate the mathematical model, a Galerkin projection is made on the systems defined by Eqs. (11)–(14) and Eq. (17). For the trial functions, the first three modes of vibration of the cantilever beam are taken for the transversal displacements together with one mode for the axial displacement and one for the angle of twist. For the wake variable, the three modal shapes for transversal vibrations are also adopted as projection functions. Due to the presence of the square root dependency on the velocity of each cross-section in the hydrodynamic forces, the reduced-order model does not show up a closed mathematical expression. This leads the projection for those terms to be made at every time step of a numerical simulation.

Aiming at concluding the description of the mathematical modelling, a discussion is needed on the adopted wake-oscillator model. The model was taken from [10], where the parameters ε_v and A_v are dependent on the reduced velocity that is related to the incident flow, as $U_r = U/f_n D$, being f_n the natural frequency corresponding to the transversal oscillations of a rigid cylinder mounted on an linear-elastic 2-dof system. Herein, an *ad hoc* assumption is made to extend this dependency to the case of a flexible cylinder, by taking f_n as the natural frequency related to vibration modes dominated by transversal oscillations. It is assumed that these parameters are independent for each component of q obtained after the Galerkin projection, being taken as $\varepsilon_{v,i}$ and $A_{v,i}$, with i being the mode number of the component, ranging from one to three in the present work. With those assumptions, and using a Heaviside function to represent that the electric tension output occurs only at the clamped end as in [8], after some cumbersome algebraic work, the equations for the reduced-order model are

$$m^w \ddot{w}_1 + \beta^w w_1 + \sum_{k=1}^3 \sum_{l=1}^3 \beta_{k,l}^{uu} u_k u_l + \sum_{k=1}^3 \sum_{l=1}^3 \beta_{k,l}^{vv} v_k v_l + \beta^{\phi\phi} \phi_1^2 = 0; \quad (18)$$

$$\begin{aligned}
m_i^u \ddot{u}_i + c_i^u \dot{u}_i + \sum_{l=1}^3 \beta_{i,l}^u u_l + \sum_{l=1}^3 \beta_{i,l}^{uw} u_l w_l + \sum_{j=1}^3 \sum_{k=1}^3 \sum_{l=1}^3 \beta_{i,j,k,l}^{uuu} u_j u_k u_l \\
+ \sum_{j=1}^3 \sum_{k=1}^3 \sum_{l=1}^3 \beta_{i,j,k,l}^{uvv} u_j v_k v_l + \sum_{l=1}^3 \beta_{i,l}^{u\phi\phi} u_l \phi_1^2 = f_i^u;
\end{aligned} \tag{19}$$

$$\begin{aligned}
m_i^v \ddot{v}_i + c_i^v \dot{v}_i + \sum_{l=1}^3 \beta_{i,l}^v v_l + \sum_{l=1}^3 \beta_{i,l}^{vw} v_l w_l + \sum_{j=1}^3 \sum_{k=1}^3 \sum_{l=1}^3 \beta_{i,j,k,l}^{vuu} v_j u_k u_l \\
+ \sum_{j=1}^3 \sum_{k=1}^3 \sum_{l=1}^3 \beta_{i,j,k,l}^{vvv} v_j v_k v_l + \sum_{l=1}^3 \beta_{i,l}^{v\phi\phi} v_l \phi_1^2 + d_i \bar{V} = f_i^v;
\end{aligned} \tag{20}$$

$$m^\phi \ddot{\phi}_1 + \beta^\phi \phi_1 + \beta^{w\phi} w_1 \phi_1 + \beta^{\phi\phi\phi} \phi_1^3 + \sum_{k=1}^3 \sum_{l=1}^3 \beta_{k,l}^{uu\phi} u_k u_l \phi_1 + \sum_{k=1}^3 \sum_{l=1}^3 \beta_{k,l}^{vv\phi} v_k v_l \phi_1 = 0; \tag{21}$$

$$\ddot{q}_i + \epsilon_{v,i} \left[\sum_{j=1}^3 \sum_{k=1}^3 \sum_{l=1}^3 Q^{i,j,k,l} q_j q_k \dot{q}_l \right] - \epsilon_{v,i} St U_r \dot{q}_i + (St U_r)^2 q_i = A_{v,i} \ddot{v}_i; \tag{22}$$

$$\dot{\bar{V}} + \eta \bar{V} + \sum_{l=1}^3 \zeta_l \dot{v}_l = 0, \tag{23}$$

with u_i , v_i , and w_i being the degrees of freedom relative to the projections of u , v , and w , respectively. The index i refers to each of the three modal components adopted for displacements u and v . The twist is ϕ , S_t is the Strouhal number, and $U_r = U_\infty/f_{y1}D$ is the reduced velocity according to the frequency of the first natural mode in the Y direction.

3 Results and Discussion

A case study is presented aiming at illustrating simulations based on the proposed mathematical model. An aluminum flat bar of dimensions $10 \text{ mm} \times 40 \text{ mm}$ gives the structure with a frequency ratio close to 4:1 between in-line and cross-wise directions. The structural and electric parameters considered are presented in Table 1, where the index a refers to the aluminum bar, s to the silicon cylinder, and p to the piezoelectric material. In order to analyze the response including the three transverse modes in the Galerkin projection, reduced velocities up to 75 were

Table 1 Simulation parameters

Parameter	Value	Parameter	Value	Parameter	Value
L	1500 mm	E_a	70 GPa	ν_s	0.33
D	45 mm	E_s	15 MPa	ν_a	0.39
b_w	4 mm	E_p	60.6 GPa	ν_p	0.33
h_a	1 mm	ρ_s	2710 kg/m ³	e_{31}	16.6 C/m ²
h_p	0.3 mm	ρ_a	1100 kg/m ³	ϵ_{33}	25.5 nF
		ρ_p	7500 kg/m ³	R	10 k Ω

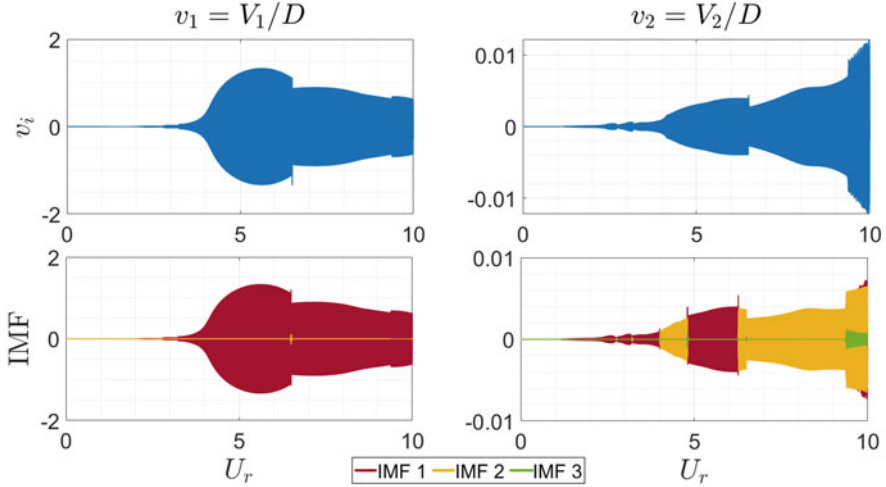


Fig. 3 Cross-wise modal displacements and respective IMF, normalized with respect to the cylinder diameter, as a function of reduced velocity based on the first transversal mode natural frequency in still water. Reduced velocity linearly increasing with time at a rate $U_r = \alpha t$, $\alpha = 0.01$

considered. Practical design aspects such as intensity of incoming flow velocity and the structure strength were not considered in the present simulations.

Equations (18)–(23) were numerically integrated under two different conditions: (i) steady states obtained from a step-by-step increase in reduced velocity; (ii) continuously increasing or decreasing the reduced velocity linearly with time. In case (ii), a very slow increasing (or decreasing) rate is applied, at a time scale much longer than the typical shedding periods, such that the ratio between them lies in the interval $195 < \text{ratio} < 3500$, being always of order 100 or larger. Hilbert–Huang analyses were undertaken for the in-line and cross-wise displacements time series; [3–5]. An empirical mode decomposition (EMD) algorithm is applied to each of the modal time series, obtaining their respective intrinsic mode functions (IMF) as exemplified in Fig. 3. A Hilbert transform is then calculated for these IMF, obtaining the instantaneous amplitude modulation and response frequency of the system.

Typical response amplitudes were calculated from the peak of the obtained spectra, which are dominated by a single frequency value at each time instant. The sum of the modal responses is presented in Fig. 4. Results for the simulation run with linearly increasing velocities are represented in blue and for decreasing velocities in red. Markers (*) are steady-state amplitude responses obtained from series simulated at those respective reduced velocities.

As seen in Fig. 4, the transverse amplitudes exhibit three locked-in responses, corresponding to the transverse natural frequencies of the structure. A hysteresis loop, a phenomenon commonly present in experimental VIV studies, can be identified as jumps between coexisting modes, where dynamic bifurcations show up clearly. Such a jump phenomenon is clearly depicted in the interval $55 < U_r < 75$, where the transversal modes 2 and 3 coexist. As for the in-line response, a first peak of amplitude is observed at reduced velocities around $U_r = 5.5$, along with the transverse lock-in peak. The first in-line mode lock-in is also observed at higher reduced velocities, close to $U_r = 15$.

When compared to the results presented in Fig. 1, the model herein developed shows good qualitative results for typical VIV response. However, the high-energy response branch, clearly observed in the experimental campaigns [2, 3], was not captured by the proposed mathematical model. In addition, amplitudes in longitudinal direction are considerably smaller than the ones obtained experimentally. As a matter of fact, the high-speed (energy) response branch was thought to be caused by the structure dynamics, through the twisting–bending coupling. As this coupling has been taken into account, with twisting terms considered up to third order, it appears that, so far, the fluid–structure interaction phenomenon has not been modelled properly, at least not sufficiently well. Further investigation is surely needed regarding the nature and the modelling of this intriguing fluid–structure interaction phenomenon.

Even not capturing the high-speed (energy) response branch and assuming the present reduced-order model as valid, an estimate for the electric power harvested from the system was carried out. The results are presented in Fig. 5.

The power generated increases at a very strong rate with the vibration frequency of the system, varying from very low values (of order of a few mW) at small reduced velocities, close to the first mode lock-in peak, to low ones (of order of 1W) harvested at higher modes of vibration.

4 Concluding Remarks

A 3D mathematical model was proposed for the representation of a flexible piezoelectric energy harvester under VIV, coupling structural, electrical, and hydrodynamics effects. The structural part of the model derived in this chapter is robust including, besides bending, axial displacements and torsion. For the fluid–structure interactions, represented by a wake-oscillator model, qualitative VIV aspects were recovered, including hysteresis loops at reduced velocity ranges where

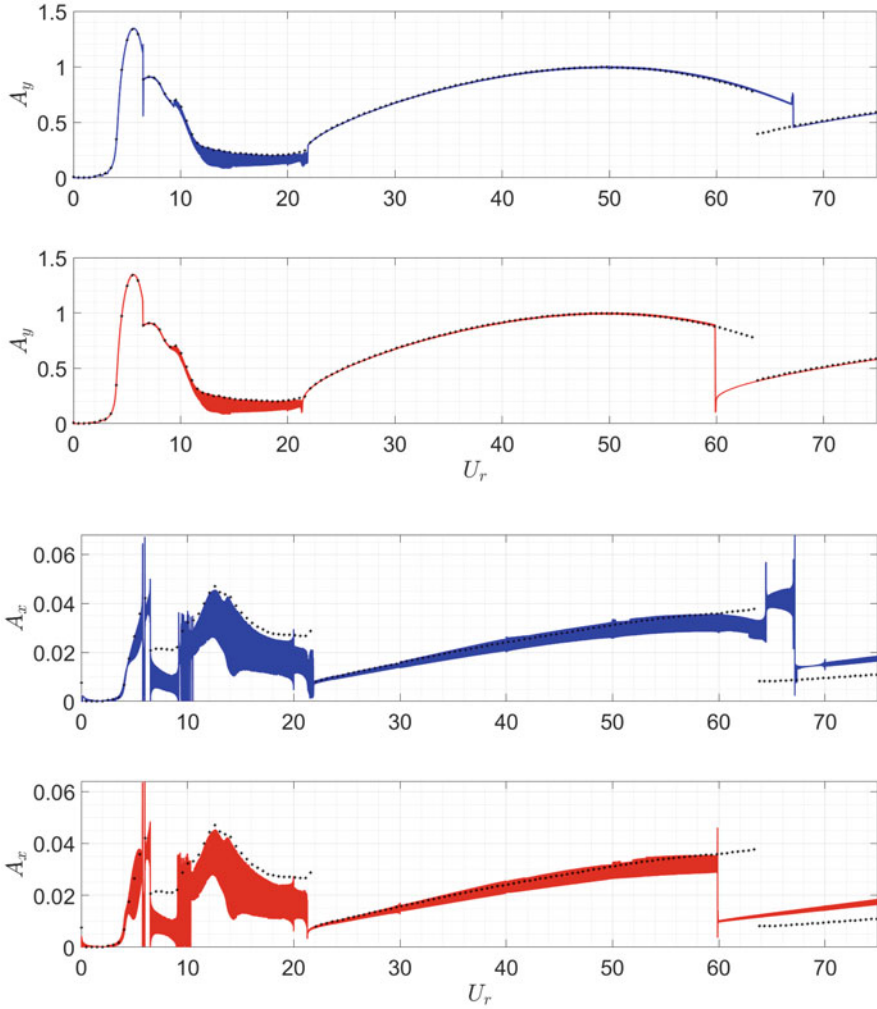


Fig. 4 Cross-wise and in-line amplitudes, normalized with respect to the cylinder diameter, as a function of reduced velocity based on the first transversal mode natural frequency in still water. Continuous line: varying current speed slowly; in blue: increasing velocity; in red: decreasing velocity. Modal amplitudes are determined by taking the Hilbert transform of the dominant IMF, within a EMD scheme [3, 4]. Dots represent amplitudes measured after a steady-state response is attained

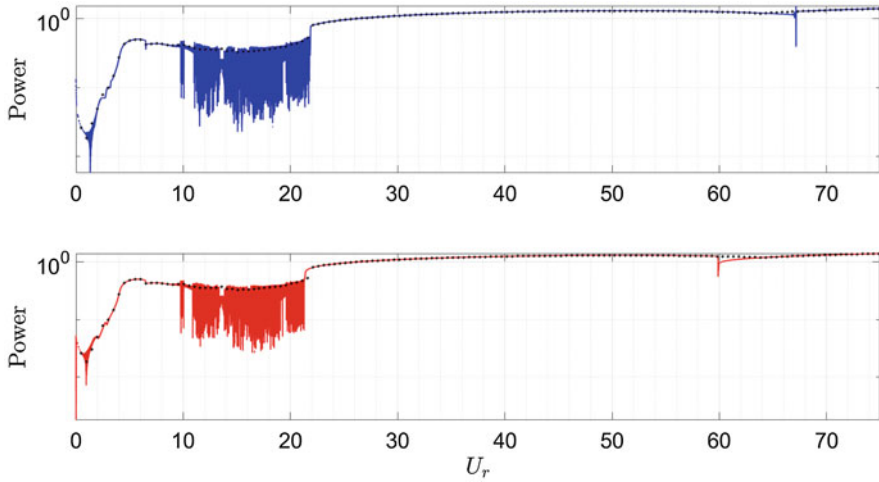


Fig. 5 Electric power harvested. Measure given in Watts. See Fig. 4 caption, for explanation on lines and dots

vibration modes switching occurs. However, the high-energy branch experimentally observed has not been captured by the present model yet. Therefore, the forms of the equations of the phenomenological model, alongside the calibration of its parameters, are objects of further work. In turn, as expected, the electric power harvested is highly dependent on the frequency of the system. Considering the results obtained by this model, the system presents a potential for energy harvesting, in different scales, at lower and higher modes, with distinct applications for each case. An experimental campaign on this subject is planned to be carried out in the near future.

Acknowledgments L. Madi and W. Defensor Fo acknowledge their PhD scholarships, supported by the CAPES social demand, through the Graduate Program in Naval and Ocean Engineering (PPGEN). G. Vernizzi acknowledges the São Paulo Research Foundation (FAPESP), for the PhD scholarship 2016/25457-1. C.P. Pesce acknowledges the CNPq Research Grant 308230/2018-3 and the Technological Research Institute of São Paulo State (IPT) for partial support given to L. Madi through its Young Talent Program.

References

1. M.M. Bernitsas, K. Raghavan, Y. Ben-Simos, E.M.H. Garcia, VIVACE (vortex induced vibration aquatic clean energy): a new concept in generation of clean and renewable energy from fluid flow, in *Proceedings of OMAE2006—International Conference on Offshore Mechanics and Arctic Engineering* (2006)
2. A. Fujarra, C.P. Pesce, F. Flemming, C. Williamson, Vortex-induced vibration of a flexible cantilever. *J. Fluids Struct.* **15**, 651–658 (2001)

3. W.A. Defensor Fo., C.P. Pesce, G.R. Franzini, An experimental investigation on vortex-induced vibrations of cantilevered flexible cylinders with orthotropic bending stiffness, in *Proceedings of 9th International Symposium on Fluid-Structure Interactions, Flow-Sound Interactions, Flow-Induced Vibration and Noise*, Toronto, 2018
4. N.E. Huang et al., The empirical mode decomposition and the Hilbert spectrum for non-linear and non-stationary time series analysis. *Proc. R. Soc. Lond. A* **454**, 903–995 (1998)
5. C.P. Pesce, A.L.C. Fajarra, L.K. Kubota, The Hilbert-Huang spectral analysis method applied to VIV, in *Proceedings of 25th International Conference on Offshore Mechanics and Arctic Engineering*, Hamburg, 2006
6. Tanaka, H., “Generalized basic equations for bending motions of piezoelectric bars formulated from Hamilton’s principle”, *The Journal of the Acoustical Society of America*, 95(4):1768–1772, (1994).
7. A. Abdelkefi, F. Najar, A.H. Nayfeh, S. Ben Ayed, An energy harvester using piezoelectric cantilever beams undergoing coupled bending–torsion vibrations. *Smart Mater. Struct.* **20**(11), 115007 (2011)
8. A. Erturk, D.J. Inman, *Piezoelectric Energy Harvesting* (Wiley, London, 2011)
9. M.R.M. Crespo Da Silva, Non-linear flexural-flexural-torsional-extensional dynamics of beams—I. Formulation. *Int. J. Solids Struct.* **24**(12), 1225–1234 (1988). [https://doi.org/10.1016/0020-7683\(88\)90087-X](https://doi.org/10.1016/0020-7683(88)90087-X)
10. Y. Qu, A.V. Metrikine, A single van der Pol wake oscillator model for coupled cross-flow and in-line vortex-induced vibrations. *Ocean Eng.* **196**, 106732 (2020)

Dynamics of the Fluid-Structure Coupling Model of a Direct-Acting Relief Valve



Wen Song, Maolin Liao, Yanli Xin, Xiaoyong Wang, Ke Fan, and Yongdong Li

1 Introduction

Direct-acting relief valve is widely applied for pressure adjustment in fuel pump [1–3]; however, as the pressure fluctuation at the relief valve due to the influences of external environment, the valve element can lose its stability via Hopf bifurcation [4, 5], and which can further enter into chaos via grazing bifurcation due to the axial impact between the valve element and valve seat [6–8]. In addition, when the fuel flows through the valve element in a narrow space with high speed, the vortex-shedding behind the valve element can excite its vibration in the vertical direction [9, 10], which further triggers its vertical impact with the valve seat. Therefore, a 2-DOF fluid-structure coupling dynamic model is proposed in the present work, to investigate the correlation between the vibration condition of valve and the sudden jump of pressure of the pump observed in experiments.

2 Mathematical Modelling

In this section, a 2-DOF mathematical model about the fluid-structure coupling system of a direct-acting relief valve is developed. Primarily, the physical model is simplified from the schematical of the direct-acting relief valve; based on which,

W. Song · Y. Li

China Shipbuilding Industry Corporation 705 Research Institute, Xi'an, China

M. Liao (✉) · Y. Xin · X. Wang · K. Fan

School of Mechanical Engineering, University of Science and Technology, Beijing, China

e-mail: liaomaolin@ustb.edu.cn

the dynamic model is developed and its corresponding nondimensionalization is conducted.

2.1 Physical Model

Based on the schematic of the direct-acting relief valve shown in Fig. 1a, the physical model can be simplified [6, 7] as shown in Fig. 1b, in which, two Kelvin-Voigt models ($c_1 - k_1$, $c_2 - k_2$) are utilized to describe the vibrations of the valve element (m) in both the axial and vertical directions. The axial vibration originates from the interaction between the force of the fluid pressure difference at the valve port (F_{out}) and the force (F_{back}) acting on the back pressure rod. While the vertical vibration of the valve element is determined by both the inlet pressure force (F_{in}) and the lifting force caused by the vortex shedding in vortex-induced vibration (VIV). In addition, x and y are used to represent the displacements of the valve element in the axial and vertical directions, respectively.

2.2 Dynamic Model of Relief Valve

In order to develop the dynamic model of the relief valve, both a nonlinear fluid differential pressure model at valve port [6–8] and a nonlinear wake oscillator model are used [9, 10]; meanwhile, the contact nonlinearity between the valve element and valve seat is also taken into consideration [11–13]. Therefore, a compact form of the dynamic model of the direct-acting relief valve system can be described as

$$\begin{cases} \dot{x} = v \\ \dot{v} = -\frac{c_1}{m}v - \frac{k_1}{m}(x + x_0) - \frac{\rho_w g h \pi r_b^2}{m} + \frac{p}{m} \pi r_z^2 \\ \dot{y} = u \\ \dot{u} = -\frac{c_2 + c_f}{m + m_f}u - \frac{k_2}{m + m_f}y - \frac{P_{\text{in}} \cdot 2r_b \cdot (x + x_1) \cdot C_d}{m + m_f} + \frac{1}{2} \frac{\rho_o V_{\text{valve}}^2 \pi r_o^2 x_1 \cdot C_l}{m + m_f} \\ \dot{p} = \frac{E}{V} \left(Q_P - A(x, y) \cdot C_d \cdot \sqrt{\frac{2}{\rho_o} p} \right) \\ \dot{q} = w \\ \dot{w} = f_s - c_3 \Omega_f (q^2 - 1) w - \Omega_f^2 q \end{cases} \quad (1)$$

Moreover, a detailed introduction about all the parameters and their corresponding values for this relief valve system is listed in Table 1 in Sect. 3.

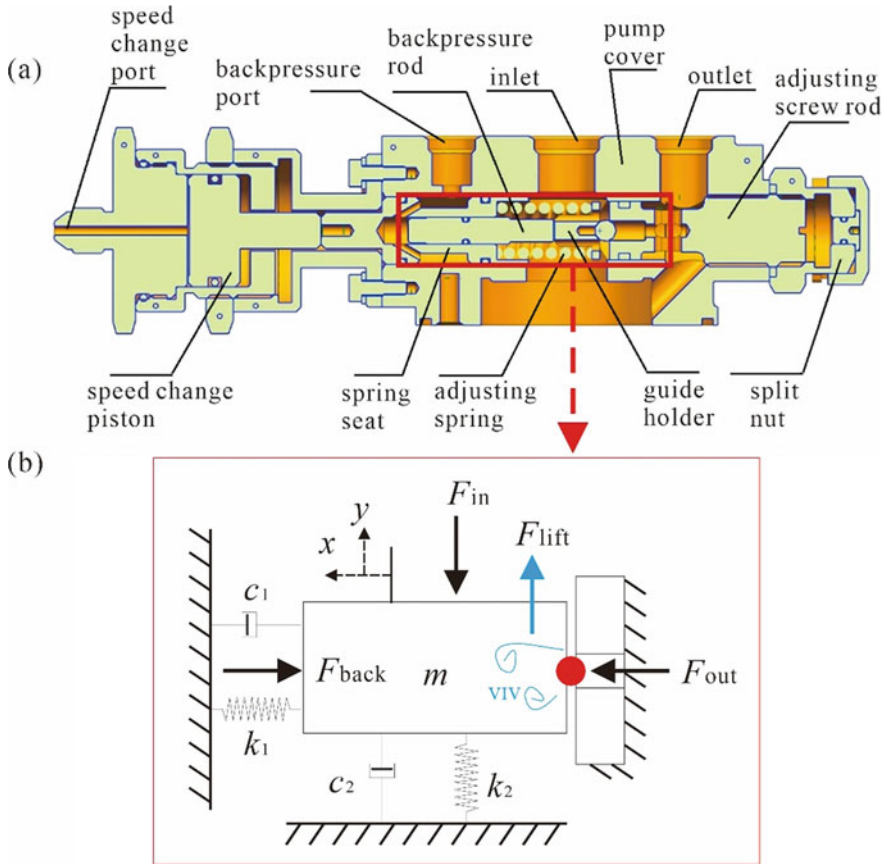


Fig. 1 Schematic of the direct-acting relief valve (a) and its corresponding 2-DOF physical model (b)

2.3 Nondimensionalization of Dynamic Model

Before the numerical simulation, the developed dynamic model is further nondimensionalized to obtain the dimensionless equations. Firstly, three basic reference parameters of the studied system are defined, including the natural frequency Ω_0 , the reference time t_r , and the reference displacement x_r as

$$\Omega_0 = \sqrt{\frac{k_1}{m}}, \quad t_r = \sqrt{\frac{m}{k_1}}, \quad x_r = \frac{\pi r_b^2 p_o}{k_1} \tag{2}$$

where p_o is the atmospheric intensity of pressure. Based on the above three basic reference parameters, eight dimensionless variables can be obtained as

Table 1 List of system parameters

Parameters	Signs	Units	Values
Rod body's total mass	m	kg	$13.7e-3$
Oriented seat's spring stiffness	k_1	N/m	$1.266e5$
Spring precompression	x_o	m	$2.227e-3$
Overflow amount	Q_p	m^3/s	$7.67e-5$
Density of water	ρ_w	kg/m^3	1000
Density of fuel	ρ_o	kg/m^3	1232
Pump inlet pressure	p_{in}	Pa	$0.4e6 \sim 0.8e6$
Pump outlet pressure	p_{out}	Pa	$10e6$
Radius of back-pressure ejector pins	r_b	m	$3.0e-3$
Radius of ball valve	r_o	m	$2.3812e-3$
Radius of valve seat channel	r_z	m	$2.2e-3$
Radius of pump inlet	x_1	m	$8e-3$
Atmospheric pressure	p_o	Pa	$1e5$
Washer's damping	c_1	$N \cdot s/m$	30
Vertical vibration damping of the rod string	c_2	$N \cdot s/m$	30
Fluid damping	c_3	1	0.9
Vertical stiffness of the rod string	k_2	N/m	$1e6$
Fluid compression modulus	E	Pa	$5e9$
Pore throat's fluid volume	V	m^3	$1.1404e-7$
Fluid resistance coefficient	C_d	1	1.0
Fluid lift coefficient	C_l	1	0.2
Added mass coefficients	C_m	1	1.0
Strouhal number	S_t	1	$0.15 \sim 0.2$
Restitution coefficient of impact	r	1	$0.2 \sim 0.4$

$$\begin{cases} \tau = \frac{t}{t_r}, & y_1 = \frac{x}{x_r}, & y_2 = \frac{t_r}{x_r} v, & y_3 = \frac{y}{x_r} \\ y_4 = \frac{t_r}{x_r} u, & y_5 = \frac{p}{p_o}, & y_6 = q, & y_7 = t_r w \end{cases} \quad (3)$$

Therefore, the dynamic model of the direct-acting relief valve system can be transformed into the dimensionless equations as

$$\begin{cases} y_1' = y_2 \\ y_2' = -\xi_1 y_2 - (y_1 + \delta_0) - \eta + \lambda y_5 \\ y_3' = y_4 \\ y_4' = -\xi_2 y_4 - \kappa y_3 - \zeta (y_1 + \delta_1) + \gamma y_6 \\ y_5' = q - \beta \sqrt{y_5} \\ y_6' = y_7 \\ y_7' = -\xi_3 (y_6^2 - 1) y_7 - \alpha y_6 + 12 y_{acc} \end{cases} \quad (4)$$

where y_{acc} is the nondimensional acceleration of valve element in the vertical direction, and $12y_{\text{acc}}$ is generally applied to describes the influence of the structure on the vortex-induced vibration [10, 11].

Moreover, in order to obtain the simplified form of Eq. 4, 14 new dimensionless parameters, such as damping ratio, spring precompression ratio, system stiffness ratio, dimensionless depth, and dimensionless pump displacement, are defined as

$$\left\{ \begin{array}{l} \xi_1 = \frac{c_1}{\sqrt{k_1 m}}, \quad \xi_2 = \frac{c_2 + c_f}{\sqrt{m + m_f}} \cdot t_r, \quad \xi_3 = c_3 \Omega_f \cdot t_r \\ \delta_0 = \frac{x_o}{x_r}, \quad \delta_1 = \frac{x_1}{x_r}, \quad \eta = \frac{\rho_w g}{p_o} \cdot h \\ \lambda = \frac{r_z^2}{r_b^2}, \quad \kappa = \frac{k_2}{m + m_f} \cdot t_r^2, \quad \zeta = \frac{2r_b p_{\text{in}}}{k_1} \\ q = \frac{E Q_p \sqrt{\frac{m}{k_1}}}{V p_o}, \quad \alpha = \Omega_f^2 \cdot t_r^2, \quad \mu = \frac{m + m_f}{\rho_o \pi r_z^2 x_1} \\ \beta = \frac{E}{V} \cdot C_d A(x, y) \sqrt{\frac{2m}{\rho_o k_1 p_o}} \\ \gamma = \frac{C_f}{4\pi^2 S_i^2 \mu} \cdot \frac{r_z^2}{x_r x_1} \cdot \Omega_f^2 \cdot t_r^2 \end{array} \right. \quad (5)$$

In summary, a complete dynamic model about the fluid-structure coupling system of the direct-acting relief valve has been developed.

3 Comparison of Experiments and Numerical Simulations

Based on the developed mathematical model in Sect. 2, the numerical simulation of the studied system about the relief valve can be carried out, and thus the comparison between the numerical simulation and the experimental measurements. For this purpose, the actual parameters of an experimental device are used as the system parameters for numerical simulations, see Table 1.

3.1 Condition One: 0.8 MPa Inlet Pressure

Primarily, the 0.8 MPa inlet pressure was considered since the unstable vibration of the relief valve was explored experimentally in such condition, see Fig. 2a. Figure 2a shows the variations of the pump inlet pressure, outlet pressure, and back pressure from top to bottom. Moreover, the back pressure is determined by the hydraulic pressure; hence the water depth can be calculated according to the back pressure, and the corresponding result is depicted as the green curve in the third subplot of Fig. 2a. During the experimental test, the torpedo was gradually sunk to the water depth of 300 m, and then slowly lifted to the water surface. It can be seen from Fig. 2a that an obvious pressure step appears at 20 s, whose corresponding water depth is around 100 m where the back pressure rod was in contact with the guide holder. From then on, the vibration condition of the relief valve can be simulated

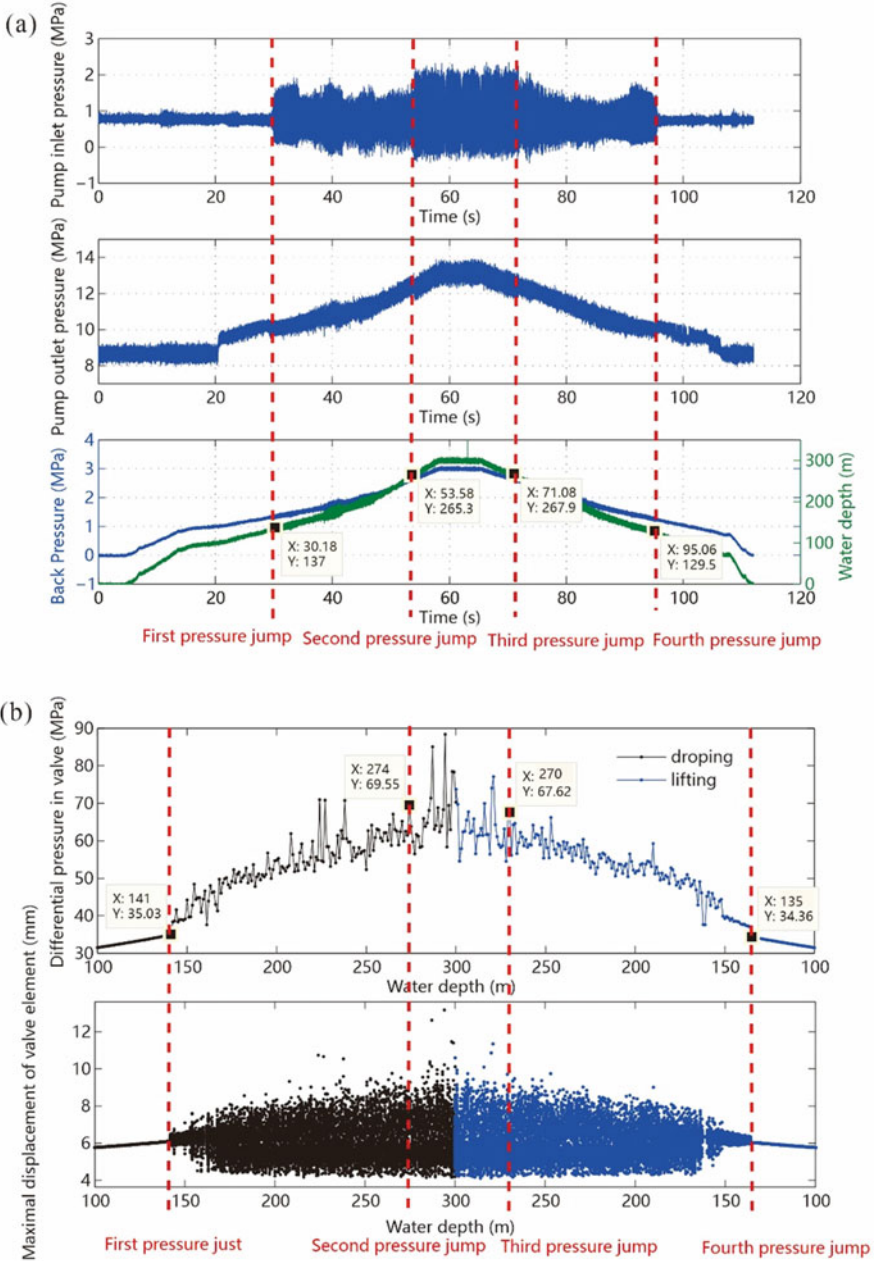


Fig. 2 Experimental signal (a) and numerical simulation (b) for the case with inlet pressure 0.8 MPa

by the developed mathematical model, since the valve element (m) simplified in the physical model consists of both the back pressure rod and the guide holder, see Fig. 1. Therefore, the range of the water depth for the numerical simulation was set as [100 m, 300 m] with the depth interval 1 m, and the obtained result is shown in Fig. 2b. Specifically, the differential pressure at the valve port reflects the correlation between the inlet pressure and the outlet pressure, which is basically consistent with the trend of the outlet pressure measured during the experimental tests, since the outlet pressure is much greater than the inlet pressure. In addition, due to the narrow flow area at valve port, its differential pressure is larger than the pressure measured in both the pump outlet and the pump inlet.

In addition, it is found from Fig. 2 that the relief valve is unstable which experienced two sudden jumps of pressure during either the dropping process or the lifting process. Specifically, during the process of dropping the relief valve from 100 m to 300 m, the experimental signals showed the first sudden jump of pressure at 137 m where an obvious pressure pulse can be observed. With the further increase of the water depth, the experimental signals showed another sudden jump of pressure at 265.3 m, whose inlet pressure was further magnified. Similarly, during the process of lifting the relief valve from 300 m to 100 m, two sudden jumps of pressure appeared at 267.9 m and 129.5 m, respectively. When compared with the numerical simulations with the corresponding experimental measurements, the same phenomenon can be observed. Specifically, during the dropping process, the water depths of the two pressure jumps appeared at 141 m and 274 m, respectively. While in the lifting process, the water depths for the two pressure jumps appeared at 270 m and 135 m, respectively. Figure 3 displays three typical vibration conditions of the valve element obtained by numerical simulation; they represent the vibration conditions of the valve element in the three depth regions divided by two pressure jumps.

Furthermore, according to the error calculation, comparing with the experimental measurements, the errors of the predicted depths for the four pressure jumps by the numerical simulations are limited in 5%, which demonstrates the correctness and accuracy of the developed mathematical model effectively.

3.2 Condition Two: 0.4 MPa Inlet Pressure

For this studied relief valve, the sudden jumps of pressure appeared in the case with 0.8 MPa inlet pressure brings negative influences on the system stability; hence, the main purpose of this study is to eliminate these pressure jumps. Comparing with the modification of structure parameters, the control of the pump inlet pressure is the most convenient way during the practical operation. According to the massive numerical simulation, 0.4 MPa inlet pressure was explored as the ideal parameter, and its corresponding experimental test was also verified by the numerical result, see Fig. 4. There is only one pressure step which has appeared at the water depth of 59.56 m. This is the position where the back pressure rod was in contact with

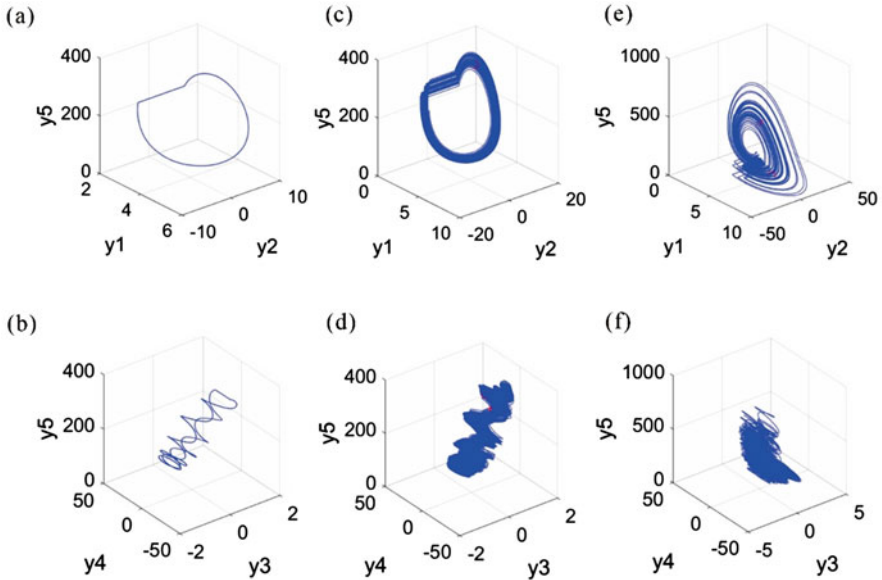


Fig. 3 2-D and 3-D phase portraits of the valve element in both the axial and vertical directions at the water depths (a) 100 m axial vibration, (b) 100 m vertical vibration, (c) 150 m axial vibration, (d) 150 m vertical vibration, (e) 300 m axial vibration, (f) 300 m vertical vibration, respectively

the guide holder. Except that, no other pressure jump was observed, namely, the relief valve maintained stable condition during both the dropping and lifting process, and this is the expected working condition of the relief valve. Hence, according to the developed mathematical model, the optimized parameters can be explored to maintain the stability of the system during its varied working condition, which can be further applied for the design and optimization of the structure and control parameters for this or similar systems.

4 Concluding Remarks

In this present work, a 2-DOF dynamic model was developed to simulate the fluid-structure system of a direct-acting relief valve. When compared with the experimental measurements, the prediction errors of the water depths for sudden jumps of pressure from the numerical simulation were less than 5%. Therefore, the results of numerical simulation were in good accordance with the experimental measurements, which verified the correctness and accuracy of the developed mathematical model.

In order to eliminate the pressure jumps explored during experimental tests, the pump inlet pressure was adjusted, when it was decreased from 0.8 MPa to 0.4 MPa,

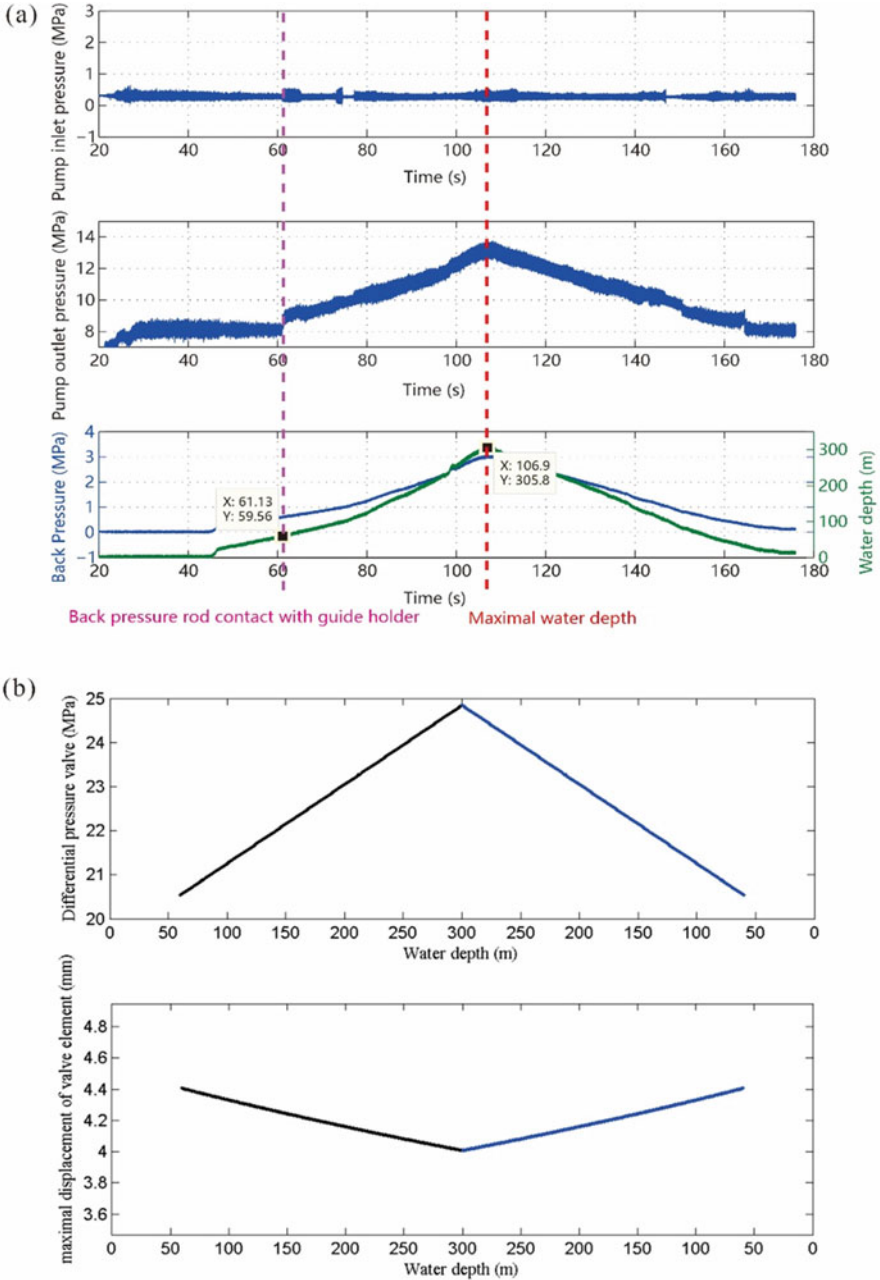


Fig. 4 Experimental signal (a) and numerical simulation (b) for the case with inlet pressure of 0.4 MPa

the pressure jumps that ever appeared during the dropping and lifting process were removed totally, which further verified the proposed mathematical model in the paper. Moreover, for the future work, this model can be applied for the design and optimization of both the structure parameters and the control parameters for this or similar dynamic systems.

References

1. Bukowski J V, Goble W M, Gross R E, et al. Analysis of spring operated pressure relief valve proof test data: Findings and implications. *Process. Saf. Prog.*, 37(4):467–477 (2018)
2. K. Hyunjun, K. Sanghyun, et al., Optimization of operation parameters for direct spring loaded pressure relief valve in a pipeline system. *J. Press. Vessel. Technol.* **140**(5), 051603 (2018)
3. J. Lei, J. Tao, C. Liu, et al., Flow model and dynamic characteristics of a direct spring loaded poppet relief valve. *Proc. Inst. Mech. Eng. C J. Mech. Eng. Sci.* **232**(9), 1657–1664 (2018)
4. C. Bolin, A. Engeda, Analysis of flow-induced instability in a redesigned steam control valve. *Appl. Therm. Eng.* **83**, 40–47 (2015)
5. S. Wu, C. Li, Y. Deng, Stability analysis of a direct-operated seawater hydraulic relief valve under deep sea. *Math. Probl. Eng.*, 5676317 (2017)
6. C.J. Hős, A.R. Champneys, K. Paul, et al., Dynamic behavior of direct spring loaded pressure relief valves: III valves in liquid service. *J. Loss Prev. Process Ind.* **43**, 1–9 (2016)
7. C. Hős, A.R. Champneys, Grazing bifurcations and chatter in a pressure relief valve model. *Physica D* **241**(22), 2068–2076 (2012)
8. R.D. Eyres, P.T. Piiroinen, A.R. Champneys, et al., Grazing bifurcations and chaos in the dynamics of a hydraulic damper with relief valves. *SIAM J. Appl. Dyn. Syst.* **4**(4), 1075–1106 (2005)
9. A. Beune, J. Kuerten, M. Van Heumen, CFD analysis with fluid-structure interaction of opening high-pressure safety valves. *Comput. Fluid* **64**, 108–116 (2012)
10. L. Lin, G. Ling, Y. Wu, Nonlinear fluid damping in structure-wake oscillators in modeling vortex-induced vibrations. *J. Hydrodyn.* **21**(1), 1–11 (2009)
11. M.L. Facchinetti, E.D. Langre, F. Biolley, Coupling of structure and wake oscillators in vortex-induced vibrations. *J. Fluids Struct.* **19**(2), 123–140 (2004)
12. M. Liao, J. Ing, M. Sayah, et al., Dynamic method of stiffness identification in impacting systems for percussive drilling applications. *Mech. Syst. Signal Process.* **80**, 224–244 (2016)
13. M. Liao, J. Ing, J. Paez Chavez, et al., Bifurcation techniques for stiffness identification of an impact oscillator. *Commun. Nonlinear Sci. Numer. Simul.* **41**, 19–31 (2016)

Part II
Mechanical Systems and Structures

Nonlinear Dynamics of Spherical Caps



Giovanni Iarriccio  and Francesco Pellicano 

1 Introduction

The present study is focused on nonlinear vibrations of spherical thin-walled caps, which are a kind of structure widely used in engineering: pressure vessels, aerospace and aeronautical components, civil structures like roofs.

Most of the previous theoretical studies on this topic were focused on axisymmetric vibrations [1, 2], which neglect the possible onset of non-symmetric vibrations due to the activation of asymmetric modes via nonlinear interactions.

This study aims to extend the recent analysis presented in Ref. [3], where a new method is proposed to analyze axisymmetric and asymmetric vibrations of thin-walled shallow spherical caps under the action of uniform static and fluctuating pressure; the objective is investigating possible nonlinear modal interactions that can lead to the activation of asymmetric modes.

In order to develop the method, the Novozhilov's thin shell theory is considered [4], such theory allows an accurate kinematic modeling in the case of moderately large displacements. To analyze the nonlinear PDE set arising from the Novozhilov theory, a meshless discretization approach is considered: the three displacement fields are expanded through a double series: in the meridional direction Legendre polynomials are considered in order to respect boundary conditions, in the circumferential direction a Fourier series is used due to the periodicity. The nonlinear reduced-order model is analyzed by means of path-following techniques and direct time integration has been carried out as well; these numerical techniques allow to investigate the dynamic scenario in detail. Results reveal that the axisymmetric oscillations lose stability close to the resonance, the instability of axisymmetric

G. Iarriccio · F. Pellicano (✉)

Department of Engineering "Enzo Ferrari", Centre InterMech MoRe, University of Modena and Reggio Emilia, Modena, Italy

e-mail: francesco.pellicano@unimore.it

vibration gives rise to the onset of asymmetric vibration of the spherical cup, even though the pressure field is uniform.

2 Novozhilov’s Nonlinear Shell Theory

Consider a partially spherical cap-like structure having radius R , circular base radius a , cap height s , half-opening angle φ_b , and thickness h , see Fig. 1. $(O; \varphi, \vartheta)$ is a curvilinear coordinate system, where the origin O is located at the apex of the cap, (φ, ϑ) are the meridional and circumferential coordinates, respectively. The three displacement fields describe the motion of the generic point P , which lies on the middle surface: $u(\varphi, \vartheta, t)$ in the meridional direction, $v(\varphi, \vartheta, t)$ in the circumferential direction and $w(\varphi, \vartheta, t)$ in the radial direction; t is the time variable.

The Novozhilov’s nonlinear shell theory is based on Love’s first approximations [5] where the small displacements assumption is relaxed: (i) the shell is thin $h \ll R$, (ii) strains are small, (iii) transverse normal stresses are small, and (iv) normal to the undeformed middle surface remain normal after deformation, and no thickness stretching is present.

The Lamé parameters for the undeformed middle surface of a shallow spherical cap are $A_1 = R$, and $A_2 \cong R \cdot \varphi_b \cdot \eta$, where $\eta = \varphi/\varphi_b$ is a non-dimensional meridional coordinate.

The strain components at an arbitrary point of the shell $\hat{\varepsilon}_\eta, \hat{\varepsilon}_\vartheta$, and $\hat{\gamma}_{\eta\vartheta}$ are

$$\hat{\varepsilon}_\eta = \varepsilon_\eta + z \cdot k_\eta, \quad \hat{\varepsilon}_\vartheta = \varepsilon_\vartheta + z \cdot k_\vartheta, \quad \hat{\gamma}_{\eta\vartheta} = \gamma_{\eta\vartheta} + z \cdot k_{\eta\vartheta}. \tag{1}$$

$\varepsilon_\eta, \varepsilon_\vartheta$, and $\gamma_{\eta\vartheta}$ are the middle surface strain and k_η, k_ϑ , and $k_{\eta\vartheta}$ are the changes in curvature and torsion of the middle surface [6]. By using the Novozhilov’s shell theory [3, 4], $\varepsilon_\eta, \varepsilon_\vartheta, \gamma_{\eta\vartheta}, k_\eta, k_\vartheta$, and $k_{\eta\vartheta}$ can be expressed as follows:

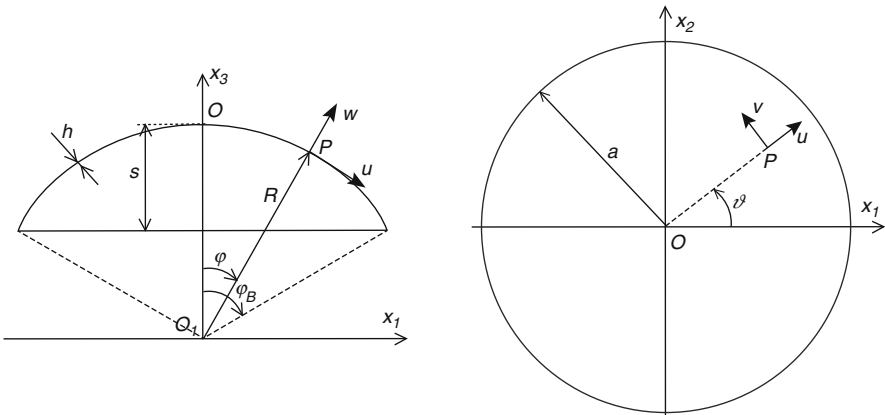


Fig. 1 Shallow spherical cap: cross section (left) and top view (right)

$$\varepsilon_\eta = e_{11} + \frac{w_0}{R} \cdot e_{11} + \frac{1}{A_1} \frac{\partial w_0}{\varphi_B \partial \eta} \cdot e_{13} + \frac{1}{2} \left(e_{11}^2 + e_{12}^2 + e_{13}^2 \right), \quad (2.a)$$

$$\varepsilon_\vartheta = e_{22} + \frac{w_0}{R} \cdot e_{22} + \frac{1}{A_2} \frac{\partial w_0}{\partial \vartheta} \cdot e_{23} + \frac{1}{2} \left(e_{22}^2 + e_{21}^2 + e_{23}^2 \right), \quad (2.b)$$

$$\begin{aligned} \gamma_{\eta\vartheta} = e_{12} + e_{21} + \frac{w_0}{R} (e_{12} + e_{21}) + \frac{1}{A_1} \frac{\partial w_0}{\varphi_B \partial \eta} \cdot e_{23} + \frac{1}{A_2} \frac{\partial w_0}{\partial \vartheta} \cdot e_{13} + e_{11} \cdot e_{21} + \\ e_{22} \cdot e_{12} + e_{13} \cdot e_{23}, \end{aligned} \quad (2.c)$$

$$k_\eta = -\frac{1}{A_1} \frac{\partial e_{13}}{\varphi_B \partial \eta} + \frac{e_{11} + e_{22}}{R}, \quad (2.d)$$

$$k_\vartheta = -\frac{1}{A_1 A_2} \frac{\partial A_2}{\varphi_B \partial \eta} e_{13} - \frac{1}{A_2} \frac{\partial e_{23}}{\partial \vartheta} + \frac{e_{11} + e_{22}}{R}, \quad (2.e)$$

$$k_{\eta\vartheta} = -\frac{1}{A_2} \frac{\partial e_{13}}{\partial \vartheta} - \frac{1}{A_1} \frac{\partial e_{23}}{\varphi_B \partial \eta} + \frac{1}{A_1 A_2} \frac{\partial A_2}{\varphi_B \partial \eta} e_{23}. \quad (2.f)$$

where e_{11} , e_{12} , e_{13} , e_{21} , e_{22} , and e_{23} are

$$e_{11} = \frac{1}{A_1} \frac{\partial u}{\varphi_B \partial \eta} + \frac{w}{R}, \quad (3.a)$$

$$e_{12} = \frac{1}{A_2} \frac{\partial u}{\partial \vartheta} - \frac{1}{A_1 A_2} \frac{\partial A_2}{\varphi_B \partial \eta} v, \quad (3.b)$$

$$e_{13} = -\frac{u}{R} + \frac{1}{A_1} \frac{\partial w}{\varphi_B \partial \eta}, \quad (3.c)$$

$$e_{21} = \frac{1}{A_1} \frac{\partial v}{\varphi_B \partial \eta}, \quad (3.d)$$

$$e_{22} = \frac{1}{A_1 A_2} \frac{\partial A_2}{\varphi_B \partial \eta} u + \frac{1}{A_2} \frac{\partial v}{\partial \vartheta} + \frac{w}{R}, \quad (3.e)$$

$$e_{23} = -\frac{v}{R} + \frac{1}{A_2} \frac{\partial w}{\partial \vartheta}. \quad (3.f)$$

In case of thin shells, the nonlinear terms in the changes in curvature and torsion can be neglected [7].

The elastic strain energy U_S of a thin shallow spherical cap, under the hypotheses of plane stress, homogeneous and isotropic material, is given by [6]

$$U_S = \frac{1}{2} \frac{Eh}{1-\nu^2} \int_{\eta_0}^1 \int_0^{2\pi} \left(\varepsilon_\eta^2 + \varepsilon_\vartheta^2 + 2\nu\varepsilon_\eta\varepsilon_\vartheta + \frac{1-\nu}{2} \gamma_{\eta\vartheta}^2 \right) A_1 A_2 \varphi_B d\vartheta d\eta + \\ + \frac{1}{2} \frac{Eh^3}{12(1-\nu^2)} \int_{\eta_0}^1 \int_0^{2\pi} \left(k_\eta^2 + k_\vartheta^2 + 2\nu k_\eta k_\vartheta + \frac{1-\nu}{2} k_{\eta\vartheta}^2 \right) A_1 A_2 \varphi_B d\vartheta d\eta, \quad (4)$$

where E and ν are the Young's modulus and the Poisson's ratio, respectively; membrane and bending energies are uncoupled due to thinness approximation.

The kinetic energy T_S of a thin shallow spherical cap, neglecting the rotary inertia, is given by

$$T_S = \frac{1}{2} \rho_S h \int_{\eta_0}^1 \int_0^{2\pi} \left(\dot{u}^2 + \dot{v}^2 + \dot{w}^2 \right) A_1 A_2 \varphi_B d\vartheta d\eta, \quad (5)$$

where ρ_S is the mass density of the shell material, the time derivatives are denoted by the overdots.

To avoid the singularity in the origin of the meridional coordinate, a small conical hole at the apex of the spherical cap is considered. Following the results given in Ref. [8], the hole has a half-nondimensional opening angle $\eta_0 = 0.00125$.

3 Displacement Fields Expansion and Reduced-order Model

The first step of the approach consists in analyzing the linearized equations in order to obtain an approximation of the eigenfunctions. Under the hypothesis of synchronous motion, i.e., the same time-law $f(t)$ is assumed for all the displacement fields, the generic mode of vibration can be written as:

$$u(\eta, \vartheta, t) = U(\eta, \vartheta) f(t), \quad v(\eta, \vartheta, t) = V(\eta, \vartheta) f(t), \\ w(\eta, \vartheta, t) = W(\eta, \vartheta) f(t). \quad (6)$$

The eigenfunctions $U(\eta, \vartheta)$, $V(\eta, \vartheta)$, and $W(\eta, \vartheta)$ are expanded by using the following expression:

$$U(\eta, \vartheta) = \sum_{m=0}^{M_u} \sum_{n=0}^N \tilde{U}_{m,n} P_m^*(\eta) \cos(n\vartheta), \quad (7.a)$$

$$V(\eta, \vartheta) = \sum_{m=1}^{M_v} \tilde{V}_{m,0} P_m^*(\eta) + \sum_{m=0}^{M_v} \sum_{n=1}^N \tilde{V}_{m,n} P_m^*(\eta) \sin(n\vartheta), \tag{7.b}$$

$$W(\eta, \vartheta) = \sum_{m=0}^{M_w} \sum_{n=0}^{N_w} \tilde{W}_{m,n} P_m^*(\eta) \cos(n\vartheta). \tag{7.c}$$

$P_m^*(\eta)$ is the m -th Legendre polynomial (of the first kind) shifted in $\eta \in [0, 1]$, m and n are the numbers of meridional half-waves and circumferential waves, respectively [3].

Clamped boundary conditions are applied on the circular planform edge of the spherical cap:

$$u = v = w = \frac{\partial w}{\partial \eta} = 0 \quad \text{for } \eta = 1. \tag{8}$$

Since the Rayleigh-Ritz method requires that the trial functions respect at least the geometric boundary conditions, no stress-free boundary conditions have been imposed at $\eta = \eta_0$ [9]. Equations (8) are imposed to the series (7.a, 7.b, and 7.c), this leads to the following linear algebraic system, valid for any $\vartheta \in [0, 2\pi]$ and $n \in [0, N]$

$$\begin{aligned} \sum_{m=0}^{M_u} \tilde{U}_{m,n} P_m^*(\eta) = 0, \quad \sum_{m=0}^{M_v} \tilde{V}_{m,n} P_m^*(\eta) = 0, \\ \sum_{m=0}^{M_w} \tilde{W}_{m,n} P_m^*(\eta) = 0, \quad \sum_{m=0}^{M_w} \tilde{W}_{m,n} \frac{\partial}{\partial \eta} P_m^*(\eta) = 0. \end{aligned} \quad \text{for } \eta=1 \tag{9}$$

The system (9) can be solved analytically in terms of $(\tilde{U}_{0,n}, \tilde{V}_{0,n}, \tilde{W}_{0,n}, \tilde{W}_{1,n})$, $(\tilde{U}_{0,n}, \tilde{V}_{0,n}, \tilde{W}_{0,n}, \tilde{W}_{1,n})$ which can be expressed in terms of the remaining unknown coefficients. After the imposition of the boundary conditions, the number of degrees of freedom (dofs) of the discretized system N_{\max} is equal to

$$N_{\max} = (M_u + M_v + M_w + 3 - b)(N + 1), \tag{10}$$

where b is the number of boundary conditions to be respected ($b = 4$ for a clamped spherical cap).

The Lagrangian variables $(\tilde{U}_{m,n}, \tilde{V}_{m,n}, \tilde{W}_{m,n})$ are reordered in a vector $\tilde{\mathbf{q}}$, see Ref. [10]; imposing the stationarity of the Rayleigh’s quotient, and using Eqs. (4) and (5), it is possible to obtain the secular equation for the spherical cap

$$\left(-\omega^2 \mathbf{M} + \mathbf{K}\right) \tilde{\mathbf{q}} = \mathbf{0}, \quad (11)$$

where ω is the circular frequency, and $\tilde{\mathbf{q}}$ is the eigenvector.

The i -th solution of (11), $\left(\omega^{(i)}, \tilde{\mathbf{q}}^{(i)}\right)$, is used in (7) in order to get the approximation of the i -th eigenfunction of the linearized operator.

In the nonlinear analysis, the full expression of (2.a-f) are considered, the hypothesis of synchronous motion is relaxed, and the displacement fields re-expanded as follows

$$u(\eta, \vartheta, t) = \sum_i^{M_{u,1}} \sum_j^{N_u} \left[U_{i,j}^{(d)}(\eta, \vartheta) f_{u,i,j}^{(d)}(t) + U_{i,j}^{(c)}(\eta, \vartheta) f_{u,i,j}^{(c)}(t) \right], \quad (12.a)$$

$$v(\eta, \vartheta, t) = \sum_i^{M_{v,1}} \sum_j^{N_v} \left[V_{i,j}^{(d)}(\eta, \vartheta) f_{v,i,j}^{(d)}(t) + V_{i,j}^{(c)}(\eta, \vartheta) f_{v,i,j}^{(c)}(t) \right], \quad (12.b)$$

$$w(\eta, \vartheta, t) = \sum_j^{M_{w,1}} \sum_n^{N_w} \left[W_{i,j}^{(d)}(\eta, \vartheta) f_{w,i,j}^{(d)}(t) + W_{i,j}^{(c)}(\eta, \vartheta) f_{w,i,j}^{(c)}(t) \right]. \quad (12.c)$$

where superscripts d and c indicate the two conjugate modes, the subscripts i and j are related to the number of meridional half-waves and circumferential waves, respectively, and $f_{u,i,j}^{(d)}(t)$, $f_{u,i,j}^{(c)}(t)$, $f_{v,i,j}^{(d)}(t)$, $f_{v,i,j}^{(c)}(t)$, $f_{w,i,j}^{(d)}(t)$, and $f_{w,i,j}^{(c)}(t)$ are the unknown generalized coordinates. A proper selection of the integers $M_{u,1}$, $M_{v,1}$, $M_{w,1}$, N_u , N_v , and N_w allows reliable results to be obtained with a reduced dimension of the nonlinear problem.

The unknown generalized coordinates are ordered into a vector $\mathbf{q}(t)$ and the equations of motion are derived through the Lagrange's equations

$$\frac{d}{dt} \left(\frac{\partial T_S}{\partial \dot{q}_j} \right) + \frac{\partial U_S}{\partial q_j} = \frac{\partial W_p}{\partial q_j}, \quad \text{for } j = 1, 2, \dots, N_{\text{dofs}}. \quad (13)$$

The expression of the j -th generalized force due to a hydrostatic external pressure $p(t)$ [11] leads to

$$\frac{\partial W_p}{\partial q_j} \simeq \int_{\eta_0}^1 \int_0^{2\pi} p(t) \left[-\frac{\partial u}{\partial q_j} e_{13} - \frac{\partial v}{\partial q_j} e_{23} + \frac{\partial w}{\partial q_j} (1 + e_{11} + e_{22}) \right] A_1 A_2 \varphi_B d\vartheta d\eta, \quad (14)$$

Considering a harmonic pressure with a static component and introducing a damping matrix into the system, the Eq. (13) can be written in state-space form

$$\begin{cases} \dot{\mathbf{q}} = \mathbf{y} \\ \dot{\mathbf{y}} = \mathbf{M}^{-1} (-\mathbf{C}\mathbf{y} - \mathbf{K}_{\text{NL}}\mathbf{q} + \mathbf{p}_s + \mathbf{p}_d \cos(\Omega t)) \end{cases} \quad (15)$$

$\mathbf{M}^{-1}\mathbf{C}$ is a diagonal damping matrix of elements $2 \zeta_j \omega_j$, ζ_j , and ω_j are the modal damping ratio and the natural frequency of the j -th generalized coordinate, respectively. The system (15) is suitable for direct numerical integration in time as well as for bifurcation analysis of the periodic solutions using a continuation software.

In the following, the equations of motion have been reduced to a nondimensional form using the dimensionless variables $\hat{\mathbf{q}} = \mathbf{q}/h$, and $\tau = \omega_0 t$, where ω_0 is a suitable circular frequency of a reference mode of vibration; the static and dynamic pressure amplitudes, p_s and p_d , respectively, have been normalized with respect to the Zoelly’s critical buckling pressure p_{cr} of an isotropic and homogeneous complete spherical shell [12]

$$p_{\text{cr}} = \frac{2 E}{\sqrt{3(1-\nu^2)}} \left(\frac{h}{R}\right)^2 \quad (16)$$

4 Numerical Results for Harmonic Pressure

A shallow spherical cap made of steel and rigidly clamped on the boundary is considered for numerical analysis. In Table 1, the geometric dimensions and material properties of the case study are listed. Same data are assumed in Ref. [3].

For spherical caps with such slenderness $\lambda = 6$, the buckling mode with $n = 2$ circumferential waves has a relevant role [13] thus, the modes with $n = 2$ (and multiples) are considered into the nonlinear reduced order model. As done in Ref. [3], a 38 dofs model (considering conjugate asymmetric modes) is used for studying the nonlinear dynamic behavior of the cap under a harmonic pressure, see Table 2. The natural frequency of the first axisymmetric modes, $\omega_{1,0}$ is the reference frequency $\omega_{1,0}$ for time nondimensionalization, and a modal damping factor $\zeta = 0.012 \zeta_j = 0.012$ are assumed for every mode.

The software AUTO [14] is used to investigate the stability and bifurcation of periodic solutions of the ODE system (15).

Figure 2a shows the amplitude-frequency diagram of the cap under a harmonic pressure; $\max(f_{w,1,0}/h)$ states for the maximum amplitude of $f_{w,1,0}$ within the period, normalized to the shell thickness h . A softening behavior is shown, the

Table 1 Dimensions and material properties of the structure

R	h/R	a	s	φ_b	E	ρ_s
0.8 m	1/300	0.152 m	0.0147 m	11.0°	200 GPa	7800 $\frac{\text{kg}}{\text{m}^3}$

Table 2 Displacement fields expansion terms in (12.a, 12.b, and 12.c)

$m \backslash n$	1	2	3	4	5	6
0	w, u	w, u	w, u	w, u	w, u	w, u
2	w, v, u	w, v, u	w, v, u	–	–	–
4	v	v	v	v	–	–

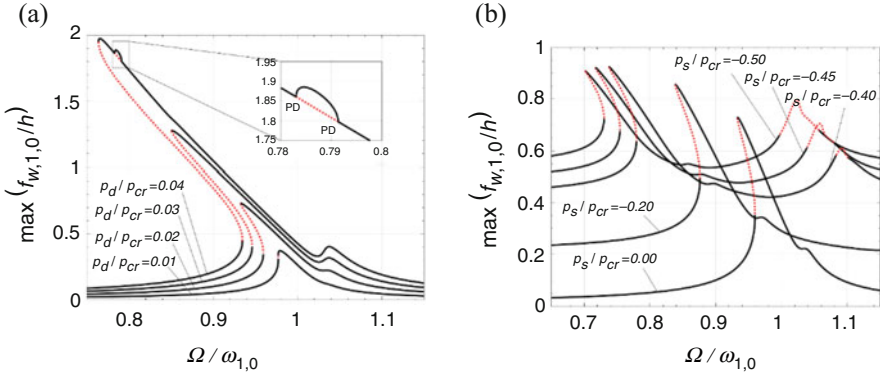


Fig. 2 Amplitude-frequency diagrams: (a) softening behavior in absence of static pressure, (b) effect of an increasing static pressure for a fixed dynamic pressure amplitude [3]

response is purely axisymmetric. For $p_d/p_{cr} = 0.04$, period doubling bifurcations (PD) occur at $\Omega/\omega_{1,0} = 0.78$, and $\Omega/\omega_{1,0} = 0.79$.

Assuming a fixed dynamic pressure amplitude $p_d/p_{cr} = 0.02$, in Fig. 2b the effects of a negative static pressure p_s are shown. As p_s decreases, the resonance peaks move to lower frequencies; the resonance peaks at $\Omega/\omega_{1,0} > 1$, which are visible only for $p_s/p_{cr} < -0.4$ in the investigated frequency range, are due to the axisymmetric cap mode with two meridional half-waves ($m = 2$).

An in-depth analysis is carried out for the case with $p_s/p_{cr} = -0.4$ and $p_d/p_{cr} = 0.02$, see Fig. 3a, b: within the unstable frequency range $\Omega/\omega_{1,0} \in [1.083, 1.102]$, following the period doubling bifurcations (PD), the cap response is characterized by the activation of conjugate asymmetric modes, and several bifurcations and multiple cusp points can be observed.

This complex behavior should deserve a specific analysis of possible chaotic response, as suggested in Ref. [15] for a similar dynamic scenario. Using the numerical integrator RADAU5 [16], the time response is numerically computed by assuming the following parameters: the sampling frequency is 40 times the forcing frequency, 40 frequency steps with an amplitude $\omega/\Omega = 0.01$, 300 periods of excitation, and for cutting out the transient, only the last 100 periods of excitation are retained in the post-processing analysis. For the sake of brevity, only results obtained for a downward forcing frequency variation are reported here.

Focusing the analysis on the asymmetric generalized coordinate $f_{w,1,2}^{(d)}$, the bifurcation diagram of the Poincaré section is shown, see Fig. 4a. A period doubling bifurcation occurs at $\omega/\Omega = 1.101$, and the response of the cap ceases to be

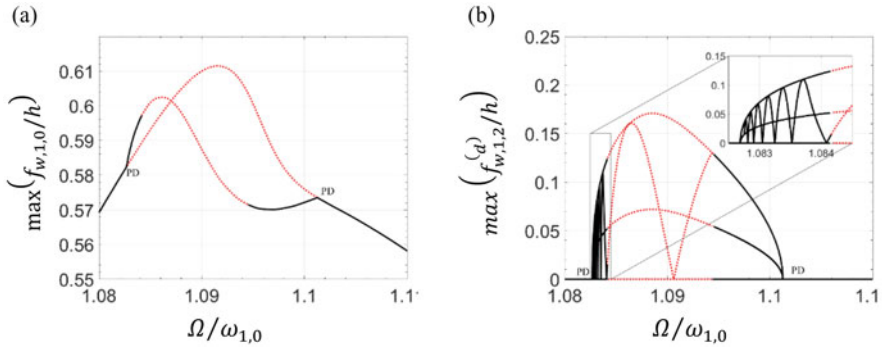


Fig. 3 Detailed views of the period doubling path following: (a) axisymmetric generalized coordinate, (b) asymmetric generalized coordinate [3]

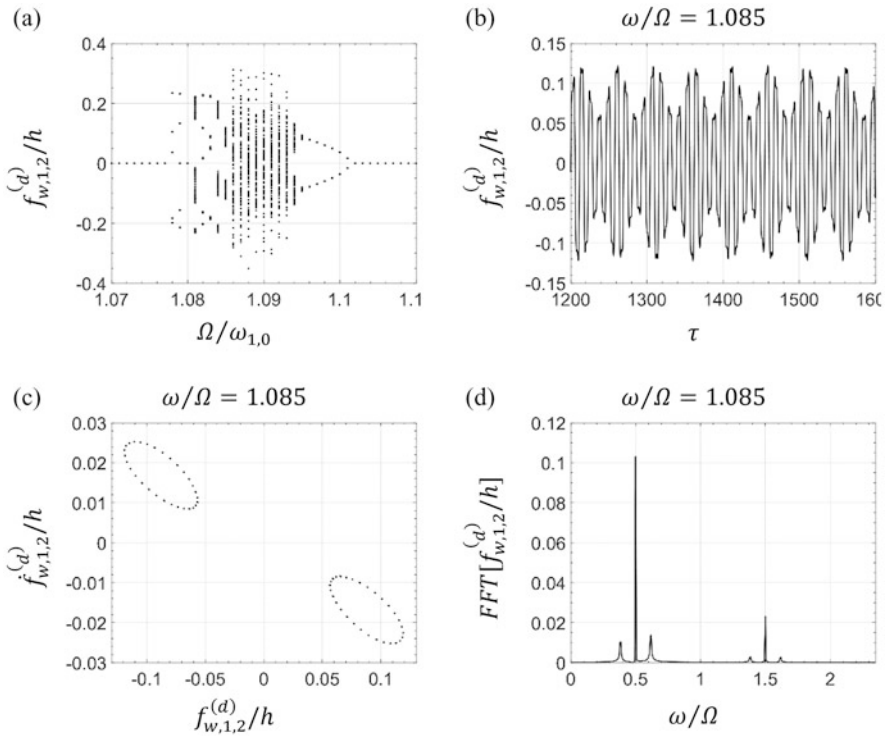


Fig. 4 Direct time integration of the equations of motion: (a) bifurcation diagram of the Poincaré section, (b) time history, (c) Poincaré map, (d) Fourier spectrum

axisymmetric. In the interval $\omega/\Omega \in [1.085, 1.095]$ chaotic vibrations take place; at $\omega/\Omega = 1.085$ the response becomes quasi-periodic until $\omega/\Omega = 1.077$, where the shell vibration becomes periodic and axisymmetric.

As an example, for $\omega/\Omega = 1.085$, the time history, the Poincaré map and also the Fourier spectrum are shown in Fig. 4b–d: the Poincaré map shows two circles, and the Fourier spectrum has few well-pronounced peaks, where the main harmonic component has $\omega/\Omega = 0.5$, with side-bands at $\omega/\Omega = 0.39$ and $\omega/\Omega = 0.62$. It is possible to confirm that, in this case, the spherical cap shows a periodic vibration with period 2.

5 Conclusions

In this paper, a numerical investigation into nonlinear dynamics of shallow spherical caps under external pressure is presented. A nonlinear model of the spherical cap, based on Novozhilov's nonlinear shell theory, is developed.

The main result of this work consists in finding the activation of asymmetric states in the cap response under symmetric pressure distribution: near the resonances, the cap vibrations lose stability and turn out to be chaotic, with non-negligible asymmetric motion. It means that a reduced-order model, which takes into account only axisymmetric modes, would fail to predict the large-amplitude dynamic behavior of the cap when subjected to a harmonic uniform pressure.

Future analyses will investigate the sensitivity of nonlinear vibrations of the cap to geometric imperfections, possible mode interactions due to internal resonances, and to fully validate the numerical results, experimental tests should be carried out.

References

1. H.A. Evensen, R.M. Evan-Iwanowski, Dynamic response and stability of shallow spherical shells subject to time-dependent loading. *AIAA J.* **5**(5), 969–976 (1967)
2. P.L. Grossman, B. Koplík, Y.Y. Yu, Nonlinear vibrations of shallow spherical shells. *J. Appl. Mech.* **36**(3), 451–458 (1969)
3. G. Iarriccio, F. Pellicano, Nonlinear dynamics and stability of shallow spherical caps under pressure loading. *ASME J. Comput. Nonlinear Dynam.* **16**(2), 021006 (2021)
4. V.V. Novozhilov, *Foundations of the Nonlinear Theory of Elasticity* (Graylock Press, Rochester, 1953) (now available from Dover, NY, USA)
5. A.E.H. Love, The small free vibrations and deformations of a thin elastic shell. *Philos. Trans. R. Soc. London A* **179**(491–546) (1888)
6. A.W. Leissa, *Vibration of Shells, NASA SP-288* (Government Printing Office, Washington, DC, 1973) (now available from The Acoustical Society of America)
7. M. Amabili, Non-linear vibrations of doubly curved shallow shells. *Int. J. Non-Linear Mech.* **40**(5), 683–710 (2005)
8. V.C.M. De Souza, J.G.A. Croll, An energy analysis of the free vibrations of isotropic spherical shells. *J. Sound Vib.* **73**(3), 379–404 (1980)
9. M. Strozzi, F. Pellicano, Nonlinear vibrations of functionally graded cylindrical shells. *Thin-Walled Struct.* **67**, 63–77 (2013)
10. F. Pellicano, Vibrations of circular cylindrical shells: Theory and experiments. *J. Sound Vib.* **303**(1–2), 154–170 (2007)

11. M. Amabili, I.D. Breslavsky, Displacement dependent pressure load for finite deflection of doubly-curved thick shells and plates. *Int. J. Non-Linear Mech.* **77**, 265–273 (2015)
12. R. Zoelly, Ueber ein knickungsproblem an der kugelschale. PdD Thesis, ETH Zurich (1915)
13. N. Huang, Unsymmetrical buckling of thin shallow spherical shells. *J. Appl. Mech.* **31**(3), 447–457 (1964)
14. E.J. Doedel, A.R. Champneys, T.F. Fairgrieve, Y.A. Kuznetsov, B. Sandstede, X. Wang, *AUTO 97: Continuation and Bifurcation Software for Ordinary Differential Equations (with HomCont)* (Concordia University, Montreal, 1997)
15. P.B. Gonçalves, Jump phenomenon, bifurcations, and chaos in a pressure loaded spherical cap under harmonic excitation. *Appl. Mech. Rev.* **46**(11S), S279–S288 (1993)
16. G. Wanner, E. Hairer, *Solving Ordinary Differential Equations II* (Springer, Berlin Heidelberg, 1996)

Exploring the Dynamics of Viscously Damped Nonlinear Oscillators via Damped Backbone Curves: A Normal Form Approach



Ayman Nasir, Neil Sims, and David J. Wagg

1 Introduction

Nonlinear oscillators are widely used for modelling real-life engineering applications, including various types of single-degree-of-freedom (SDOF) and multi-degree-of-freedom (MDOF) oscillators. For instance, single-mode approximations of some structural elements such as cables and beams are typical examples of nonlinear SDOF systems, while MDOF systems involve innumerable applications according to the nature and complexity of the system being considered. One important aspect of such nonlinear oscillator systems is the inclusion of viscous damping and how it can affect the dynamical behaviour. Thus, in this chapter, an approximate analytical technique for computing the damped backbone curves resulting from the inclusion of viscous damping is presented.

The backbone curve concept has been used extensively in nonlinear dynamics—see for example [1] and references therein for early examples. There are several definitions of backbone curves in the literature—see for example the discussion in [2]. In our interpretation, a backbone curve can be considered to be a submanifold of an underlying invariant manifold representing periodic solutions (in the vicinity of an equilibrium point) of the nonlinear oscillator under consideration. More specifically, the backbone curves considered in this chapter will be defined as curves that join all the points of maximum displacement amplitude of the underlying periodic solutions as a function of the response frequency (defined below) of the oscillator.

Backbone curves have been studied extensively for undamped nonlinear oscillator systems, and we follow established convention by calling these conservative

A. Nasir (✉) · N. Sims · D. J. Wagg
University of Sheffield, Sheffield, UK
e-mail: amnasir1@sheffield.ac.uk; n.sims@sheffield.ac.uk; david.wagg@sheffield.ac.uk

backbone curves—a recent application can be found in [3]. Several authors have considered the more difficult problem of computing backbone curves for nonlinear oscillators with damping. For example, Touzé et al. [4, 5] proposed a method using a real normal form (see [6] for the definition of real normal form), Krack [7] proposed a method based on the addition of fictitious forces, and Breunung and Haller [2] present a method using spectral submanifolds. Non-conservative nonlinear oscillators have also been studied in terms of nonlinear normal modes following the work of Shaw and Pierre [8]. For instance, Jiang et. al. [9] introduced a Galerkin-based technique where damping and forcing are included in the nonlinear oscillator under consideration.

In this chapter, an approximate analytical methodology is used to compute the damped backbone curves of SDOF nonlinear oscillators, which along with numerical continuation techniques can be used to characterise the frequency response functions of the nonlinear oscillator under consideration. There are two motivations for introducing this new method. First, the method we present here is considerably simpler to apply than some of the methods cited above. Second, the method is related to previous techniques that to date have not been used in the context of damped backbone curves. Specifically, the work of Burton [10] and the Wentzel, Kramers and Brillouin (WKB) transformation [11] both of which are described in further detail below.

Furthermore, the normal form method used here is implemented symbolically using Maple software and thus in principle can be generalised to include any order of the polynomial nonlinear terms. Two examples will be shown to demonstrate the application of the technique to nonlinear oscillators and to obtain the associated damped backbone curves.

2 Formulation

To start, we consider the example of a damped nonlinear oscillator of the form

$$\ddot{x} + 2\zeta\omega_n\dot{x} + \omega_n^2x + \varepsilon f(x) = 0, \quad (1)$$

where $\omega_n = \sqrt{k/m}$ is the linear natural frequency, $\zeta = c/2m\omega_n$ is the damping ratio, ε is a small parameter, and $f(x)$ is a nonlinear function of x . Here, m is the mass in kg, k is the linear stiffness in N/m, and c is the viscous damping coefficient in kg/s. For linear differential equations with viscous damping, using the Wentzel, Kramers and Brillouin (WKB) transformation, [12–14], one can remove the damping term as will be discussed later on. This method of transformation is also called the “method of reduction of order” [11] or the “normal form” [15].

The method in the form presented here is a variation on the WKB method, where an assumed solution is selected such that when substituted into Eq. (1) the transformed equation of motion does not contain a damping term. Hence, the assumed solution has the form

$$x = q(t)e^{-\zeta\omega_n t}. \quad (2)$$

Then for the linear case, when $\varepsilon = 0$, substituting (2) into (1) gives

$$\ddot{q} + \omega_d^2 q = 0, \quad (3)$$

where $\omega_d = \omega_n \sqrt{1 - \zeta^2}$ is the damped natural frequency. Eq. (3) is a linearised version of Eq. (1) that has been transformed into what appears to be an undamped (conservative) oscillator with a damped natural frequency, ω_d . Eq. (3) has solutions that are an infinite family of periodic solutions that depend on the initial conditions, $q(0)$ and $\dot{q}(0)$. For the nonlinear case, when $\varepsilon \neq 0$, this family of periodic solutions will correspond to the *damped nonlinear normal mode(s)* with associated *damped backbone curve(s)*.

3 The Cubic Nonlinearity Case

Considering the case when $\varepsilon \neq 0$, and $f(x) = \alpha x^3$ (the Duffing oscillator), then substituting Eq. (2) into Eq. (1) leads to

$$\ddot{q} + \omega_d^2 q + \varepsilon e^{-3\zeta\omega_n t} \alpha q^3 = 0, \quad (4)$$

so that now a time-dependent exponential function appears as part of the nonlinear term. Dealing with this type of equation presents obvious difficulties, those to be discussed in detail later. But first, we consider a method designed to overcome the difficulties for a more general class of nonlinear oscillators.

3.1 Burton's Method

In the work of Burton, [10], the approximation $\omega^2(t)x = \omega_n^2 x + \varepsilon f(x)$ is made, so that the general expression for the nonlinear oscillator, Eq. (1), becomes

$$\ddot{x} + 2\zeta\omega_n \dot{x} + \omega^2(t)x = 0, \quad (5)$$

where $\omega(t)$ is a time-varying "frequency" function. Using the transformation where $x = q(t)e^{-\zeta\omega_n t}$ substituted into Eq. (5), we now obtain

$$\ddot{q} + \hat{\omega}_d(t)^2 q = 0, \quad (6)$$

where $\hat{\omega}_d(t)^2 = \omega^2 - \zeta^2\omega_n^2$ is a time-varying approximation to the damped natural frequency of the system (similar results were obtained by Kourdis and Vakakis [16]).

Note also that in the case $\omega(t)$ is periodic, then Eq. (6) is a form of the widely studied Hill equation, [17].

3.2 Finding Approximate Solutions to Eq. (6)

Using a similar approach to [10, 16], we now assume a trial solution of $q = u_p + u_m$ where

$$u_p = \frac{U(t)}{2} e^{i\psi(t)} \quad \text{and} \quad u_m = \frac{U(t)}{2} e^{-i\psi(t)}, \quad (7)$$

where $U(t)$ is a time-dependent amplitude, and $\psi(t)$ is a time-dependent phase. The following relationships are assumed to hold for $\psi(t)$

$$\frac{d}{dt} \psi(t) = \omega_r(t) \quad \text{and} \quad \psi(0) = \psi_0, \quad (8)$$

where $\omega_r(t)$ is the time-dependent response frequency and ψ_0 is the phase lag (assumed to not be a function of time). Using those definitions, we have

$$q = U(t) \left(\frac{e^{i\psi(t)} + e^{-i\psi(t)}}{2} \right).$$

Substituting into Eq. (6) and equating the coefficients of the exponential terms give

$$\begin{aligned} \ddot{U} + i\dot{\omega}_r U + 2i\omega_r \dot{U} + (\omega_d(t)^2 - \omega_r^2)U &= 0, \\ \ddot{U} - i\dot{\omega}_r U - 2i\omega_r \dot{U} + (\omega_d(t)^2 - \omega_r^2)U &= 0, \end{aligned} \quad (9)$$

which are complex conjugate expressions. We can now compare the coefficients of the real and imaginary parts of either of the equations in Eq. (9) to get

$$\begin{aligned} \text{Re: } \ddot{U} + (\hat{\omega}_d^2 - \omega_r^2)U &= 0, \\ \text{Im: } \frac{\dot{\omega}_r}{2\omega_r} + \frac{\dot{U}}{U} &= 0. \end{aligned} \quad (10)$$

The second equation in Eq. (10) can be solved in the following way:

$$\int_0^t -\frac{\dot{\omega}_r}{2\omega_r} dt = \int_0^t \frac{\dot{U}}{U} dt \rightsquigarrow \omega_r(t)^{-\frac{1}{2}} \omega_r(0)^{\frac{1}{2}} = \frac{U(t)}{U(0)} \rightsquigarrow U(t) = U(0) \left(\frac{\omega_r(0)}{\omega_r(t)} \right)^{\frac{1}{2}}, \quad (11)$$

which gives the relationship between the time-dependent amplitude and the time-dependent frequency. As a result, the complete solution can be written as

$$x = e^{-\zeta\omega_n t} X(0) \left(\frac{\omega_r(0)}{\omega_r(t)} \right)^{\frac{1}{2}} \cos \psi(t), \quad (12)$$

where $X(0) = Q(0) = U(0)$ is the initial amplitude of displacement at time $t = 0$ (assuming for now that $\psi_0 = 0$). From Eq. (12), the amplitude decay of the solution can be defined as

$$\frac{x}{X(0)} = e^{-\zeta\omega_n t} \left(\frac{\omega_r(0)}{\omega_r(t)} \right)^{\frac{1}{2}} \rightsquigarrow t = \frac{1}{\zeta\omega_n} \ln \left[\frac{X(0)}{x} \left(\frac{\omega_r(0)}{\omega_r(t)} \right)^{\frac{1}{2}} \right], \quad (13)$$

which can be used to get an expression for the time-dependent amplitude decay of the oscillator. We note that the first equation of Eq. (10) is a conservative oscillator equation with frequency $\sqrt{\hat{\omega}_d^2 - \omega_r^2}$. To find a solution for this and Eq. (13), we need more specific detail on the exact form of $\omega(t)$. Generally, this type of Hill equation is approximated using a Fourier type expansion, but it depends on the specific properties of the frequency function. We will continue by first looking at Burton's method of solutions for the Duffing oscillator [10].

3.3 *Burton's Solution for the Duffing Oscillator*

To continue, Burton's method then computes the response frequency by studying the original problem Eq. (1) but without damping ($\zeta = 0$) and with $f(x)$ defined. Using harmonic balance, or a normal form method (see, for example, [3]) applied to the Duffing oscillator (i.e., $f(x) = \alpha x^3$), the following backbone curve relationship is obtained up to ε^1 accuracy

$$\omega_r(t) = \sqrt{\omega_n^2 + \varepsilon \frac{3\alpha}{4} U(t)^2} \quad \text{and} \quad \omega_r(0) = \sqrt{\omega_n^2 + \varepsilon \frac{3\alpha}{4} U(0)^2}.$$

These expressions give frequency approximations and can be used in Eq. (13) to give amplitude approximations.

3.4 *An Approximation for Small Damping*

If the viscous damping is sufficiently small, then an assumption that $2\zeta\omega_n = \hat{\varepsilon}$ can be assumed, where $\hat{\varepsilon} \ll 1$ and the nonlinear parameter α can be rescaled such that $\hat{\varepsilon}\hat{\alpha} = \varepsilon\alpha$. Then, we can rewrite the oscillator equation of motion as

$$\ddot{x} + \hat{\varepsilon}\dot{x} + \omega_n^2 x + \hat{\varepsilon}f(x) = 0, \quad (14)$$

or for the example of the Duffing oscillator

$$\ddot{x} + \hat{\varepsilon}\dot{x} + \omega_n^2 x + \hat{\varepsilon}\hat{\alpha}x^3 = 0, \quad (15)$$

then, by applying the WKB approach using $x = q(t)e^{-\frac{\hat{\varepsilon}}{2}t}$, we get

$$\ddot{q} + \omega_d^2 q + \hat{\varepsilon}e^{-\hat{\varepsilon}t}\hat{\alpha}q^3 = 0. \quad (16)$$

Now, by applying an approximation of the exponential function $e^{-\hat{\varepsilon}t} = 1 - \hat{\varepsilon}t + \dots \mathcal{O}(\hat{\varepsilon}^2 t^2)$, one should obtain

$$\ddot{q} + \omega_d^2 q + \hat{\varepsilon}(1 - \hat{\varepsilon}t)\hat{\alpha}q^3 = 0 \rightsquigarrow \ddot{q} + \omega_d^2 q + \hat{\varepsilon}\hat{\alpha}q^3 + \dots \mathcal{O}(\hat{\varepsilon}^2) = 0. \quad (17)$$

Finally, by applying a normal form transformation (or harmonic balance method) to Eq. (17), we obtain an approximate frequency–amplitude relationship, or the damped backbone curve of this oscillator [18].

$$\omega_r \approx \sqrt{\omega_d^2 + \varepsilon \frac{3\alpha}{4} U^2}, \quad (18)$$

where the rescaling has been removed, and since a steady-state solution is desired, ω_r and U are both assumed to be time independent. A numerical example is shown in Fig. 1, where the damped backbone curves (given by Eq. (18)) are plotted along with the undamped (conservative) backbone curves, which is governed by the same expression as Eq. (18) but with ω_d replaced by ω_n on the right-hand side.

In order to study the effect of changing the nonlinear coefficient, α , for the Duffing oscillator, in both hardening and softening cases, Fig. 2 has been generated for the case when $\omega_n = 1$ rad/s and $\zeta = 0.1$ and a range of both negative and positive α values. The damped backbone curves are computed using the proposed approximate technique, while the forced-damped frequency response curves are found using numerical continuation (COCO toolbox in Matlab). From Fig. 2, it is clear that, for each value of the nonlinear coefficient, the damped backbone curves follow the curvature of the resonant peak defined by the forced-damped frequency response curves, and the two lines cross close to the peak of each forced-damped frequency response curve. This level of matching occurs, despite the truncation at order ε^2 , and demonstrates the potential usefulness of this simple and direct method in order to obtain an approximation to the damped backbone curve.

In order to investigate the effect of varying the damping ratio on the overall results of this method, Fig. 3 shows the frequency–amplitude response for the damped Duffing oscillator when ζ is varied. The numerical values chosen for this graph are $\varepsilon\alpha = 0.4$, $\omega_n = 1$ rad/s. From this figure, it is noticed that the damped backbone curves start from the damped natural frequency, ω_d on the horizontal axis, and for each value of ζ , the damped backbone curves and the forced-damped

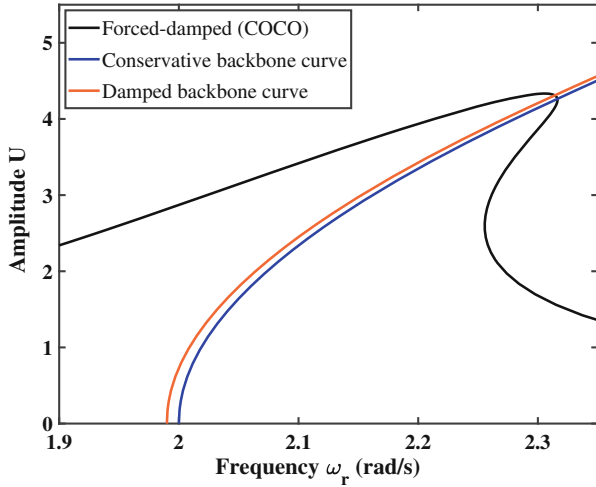


Fig. 1 Conservative (undamped) and damped backbone curves when $\varepsilon\alpha = 0.4$, $\omega_n = 2$ rad/s, and $\zeta = 0.1$. The damped backbone curve can be compared to the forced-damped frequency response curves (denoted “Forced-damped (COCO)” in the legend) and computed using COCO, this forced-damped frequency response shows both stable and unstable parts as a single solid line

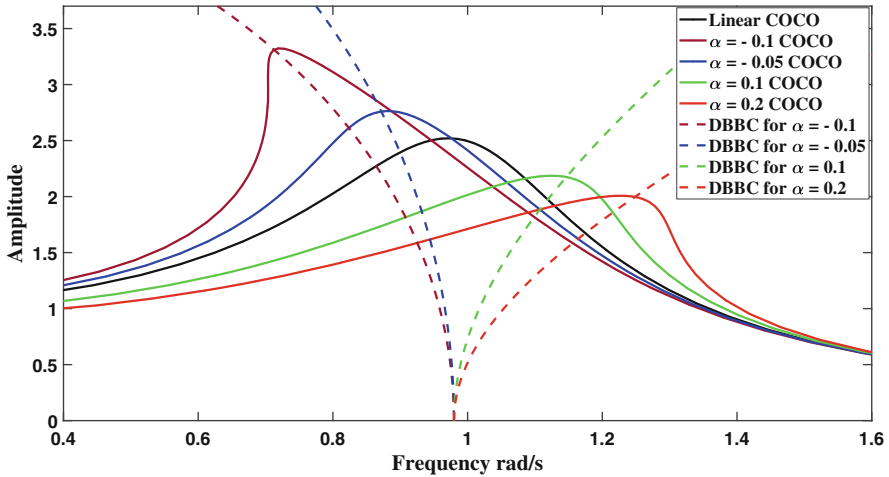


Fig. 2 Damped backbone curves (denoted DBBC in the legend) for different values of α , when $\varepsilon = 1$, $\omega_n = 1$ rad/s, and $\zeta = 0.1$ compared to the forced-damped frequency response curves (denoted COCO in the legend). The linear forced-damped frequency response curve (denoted “Linear COCO” in the legend) is plotted for comparison. Note that because ζ and ω_n are the constants the damped backbone curves all start from the same point on the frequency axis

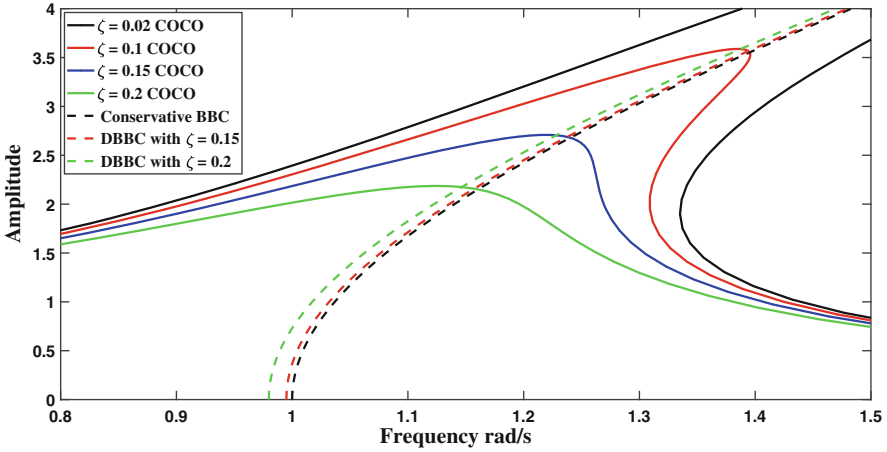


Fig. 3 Damped backbone curves (denoted DBBC in the legend) for different values of ζ , when $\varepsilon\alpha = 0.4$ and $\omega_n = 1$ rad/s, compared to the forced-damped frequency response curves (denoted COCO in the legend). The conservative backbone curve with $\zeta = 0$ (denoted “conservative BBC” in the legend) is shown for comparison. The forced-damped frequency response curves represent both stable and unstable parts of the solution

frequency response curves intersect at a similar position to the results shown in the previous two figures.

4 Analysis of SDOF Systems with Polynomial Type Nonlinearities

Considering a SDOF nonlinear oscillator with polynomial nonlinear stiffness term and small viscous damping, then the EOM can be studied using the normal form method (Sect. 2). The general form for this SDOF oscillator is

$$\ddot{x} + \varepsilon\dot{x} + \omega_n^2 x + \varepsilon f(x) = 0, \quad (19)$$

where the nonlinear vector $f(x)$ contains all the polynomial nonlinear stiffness terms. Using a normal form method (or any other appropriate method such as harmonic balance), it is possible to find the conservative backbone curve, computed in this case to ε^1 accuracy (and in principle, for any degree of the polynomial nonlinearity). As shown above, the approximate expressions for the damped backbone obtained in this way replaces the natural frequency, ω_n , with the damped natural frequency, ω_d . This approximation of the damped backbone curve is restricted to weak nonlinearities and small damping; however, compared to other techniques, the simplicity of this technique has the potential to be useful for some non-conservative

systems. It is noteworthy that ε^1 normal form analysis in this chapter is able to precisely detect the effect of odd nonlinear terms appearing in the equations of motion, while for even nonlinearities, the analysis needs to be extended to include ε^2 .

4.1 Example: Cubic–Quintic Oscillator with Viscous Damping

The problem of a cubic–quintic viscously damped SDOF oscillator is now considered. In the literature, the conservative case of this oscillator has been studied by a number of authors, e.g., [1, 19, 20]. The equation of motion for the damped-unforced cubic–quintic nonlinear oscillator can be written as

$$\ddot{x} + \varepsilon \dot{x} + \omega_n^2 x + \varepsilon \alpha_1 x^3 + \varepsilon \alpha_2 x^5 = 0, \tag{20}$$

where $\varepsilon \approx 2\zeta\omega_n$ and the coefficients of the nonlinear terms are assumed to be relatively small. In order to visually illustrate the damping effect for this system, Eq. (12) can be used to generate the phase portrait for this oscillator for any given initial condition. For example, Fig. 4 shows the phase portrait for the cubic–quintic oscillator for various values of ζ at the following initial conditions $x(0) = 0.2$ m and $\dot{x}(0) = 0.0$ m/s. Now ε^1 normal form analysis can be applied to Eq. (20) in order to find the damped backbone curve of this oscillator, [21], which gives

$$\omega_r = \sqrt{\omega_d^2 + \varepsilon \frac{3\alpha_1}{4} U^2 + \varepsilon \frac{5\alpha_2}{8} U^4}. \tag{21}$$

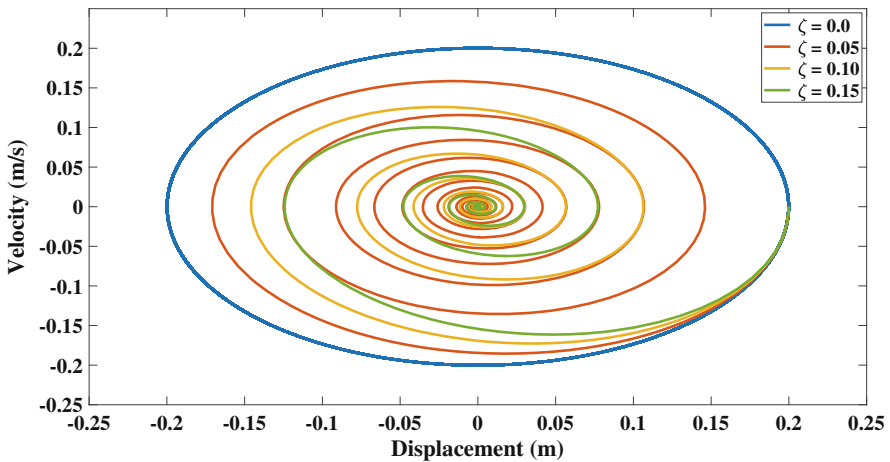


Fig. 4 Phase portrait for the damped cubic–quintic when $\varepsilon\alpha = 0.1$, $\omega_n = 2$ rad/s, and different values of ζ

Accordingly, Eq. (21) can be directly used to obtain the damped backbone curves for this oscillator for small damping.

5 Conclusions

The problem of viscously damped nonlinear oscillators with geometric polynomial stiffness nonlinearities has been discussed in this chapter. The proposed technique is related to the WKB and Burton methods, in combination with a normal form method. Approximate damped backbone curves were analytically computed and compared to the numerically computed forced-damped frequency response curves. In comparison to conservative backbone curves, damped backbone curves should be more closely related to the numerically computed forced-damped frequency response curves.

Furthermore, when the damping is relatively small, the proposed technique can be used to analyse oscillators with multiple polynomial nonlinearities, and straightforward approximations to the damped backbone curves are obtained in the form of explicit expression truncated to ε^1 order. While the proposed technique can be directly implemented for many engineering applications, some restrictions need to be realised. The technique is relatively simple to apply, but less sophisticated than some other proposed methods. Furthermore, at present, it is limited to use in small damping cases, and for ε^1 accuracy. Moreover, the technique still needs to be extended to study MDOF systems.

Acknowledgement A. Nasir is fully funded by AlZaytoonah University of Jordan to obtain his PhD at the University of Sheffield.





References

1. A.H. Nayfeh, D.T. Mook, *Nonlinear Oscillations* (Wiley, New York, 1995)
2. T. Breunung, G. Haller, Explicit backbone curves from spectral submanifolds of forced-damped nonlinear mechanical systems. *Proc. R. Soc. A* **474**, 20180083 (2018)
3. A. Elliott, A. Cammarano, S. Neild, T. Hill, D. Wagg, Using frequency detuning to compare analytical approximations for forced responses. *Nonlinear Dyn.* **98**(4), 2795–2809 (2019)
4. C. Touzé, O. Thomas, A. Chaigne, Hardening/softening behaviour in non-linear oscillations of structural systems using non-linear normal modes. *J. Sound Vib.* **273**, 77–101 (2004)
5. C. Touzé, M. Amabili, Nonlinear normal modes for damped geometrically nonlinear systems: application to reduced-order modelling of harmonically forced structures. *J. Sound Vib.* **298**, 958–981 (2006)
6. C.-H. Lamarque, C. Touzé, O. Thomas, An upper bound for validity limits of asymptotic analytical approaches based on normal form theory. *Nonlinear Dyn.* **70**(3), 1931–1949 (2012)
7. M. Krack, Nonlinear modal analysis of nonconservative systems: extension of the periodic motion concept. *Comput. Struct.* **154**, 59–71 (2015)
8. S.W. Shaw, C. Pierre, Normal modes for non-linear vibratory systems. *J. Sound Vib.* **164**, 85–124 (1993)

9. D. Jiang, C. Pierre, S. Shaw, Nonlinear normal modes for vibratory systems under harmonic excitation. *J. Sound Vib.* **288**(4–5), 791–812 (2005)
10. T. Burton, On the amplitude decay of strongly non-linear damped oscillators. *J. Sound Vib.* **87**(4), 535–541 (1983)
11. A.C. King, J. Billingham, S.R. Otto, *Differential Equations* (Cambridge University Press, Cambridge, 2003)
12. G. Wentzel, Eine verallgemeinerung der quantenbedingungen für die zwecke der wellenmechanik. *Z. Phys.* **38**(6–7), 518–529 (1926)
13. L. Brillouin, La mécanique ondulatoire de schrödinger; une méthode générale de résolution par approximations successives. *Compt. Rend. Hebd. Seances Acad. Sci.* **183**, 24–26 (1926)
14. H.A. Kramers, Wellenmechanik und halbzahlige quantisierung. *Z. Phys.* **39**(10–11), 828–840 (1926)
15. G. Stephenson, P.M. Radmore, *Advanced Mathematical Methods for Engineering and Science Students* (Cambridge University Press, Cambridge, 1990)
16. P.D. Kourdis, A.F. Vakakis, Some results on the dynamics of the linear parametric oscillator with general time-varying frequency. *Appl. Math Comput.* **183**(2), 1235–1248 (2006)
17. L. Brillouin, A practical method for solving Hill's equation. *Q. Appl. Math.* **6**(2), 167–178 (1948)
18. D.J. Wagg, S.A. Neild, *Nonlinear Vibration with Control*, 2nd edn. (Springer, Berlin, 2015)
19. M. Sulemen, Q. Wu, Comparative solution of nonlinear quintic cubic oscillator using modified homotopy method. *Adv. Math. Phys.* **2015**, 932905 (2015)
20. M. Razzak, An analytical approximate technique for solving cubic-quintic Duffing oscillator. *Alexandria Eng. J.* **55**, 2959–2965 (2016)
21. S.A. Neild, D.J. Wagg, Applying the method of normal forms to second-order nonlinear vibration problems. *Proc. R. Soc. Lond. A* **467**, 1141–1163 (2128)

Influence of Circumferential Discontinuity of an Elastic Foundation on the Nonlinear Dynamics of Cylindrical Shells with Functionally Graded Material



Jonathas K. A. Pereira , Renata M. Soares , Frederico M. A. Silva ,
and Paulo B. Gonçalves 

1 Introduction

Cylindrical shells resting on an elastic foundation are common structures in several engineering fields. In many applications, discontinuities of the elastic foundation along its circumferential direction are observed. However, the nonlinear dynamic behavior of cylindrical shells with a discontinuous elastic foundation is seldom treated in the literature. The majority of the works focus on the analysis of problems with elastic foundation surrounding the entire shell surface. Amabili and Dalpiaz [1] performed a linear analysis of cylindrical shells resting on an elastic foundation with circumferential discontinuity. The displacement field is expanded in the Fourier series with the analyses focusing on the convergence of the solution and comparisons with a finite element model. Tj et al. [2, 3] developed parametric studies to demonstrate the influence of the elastic foundation contact area on the linear vibrations of the cylindrical shell. Considering the nonlinear behavior of the cylindrical shell, Nejad and Bideleh [4] studied the vibrations of cylindrical shells on an elastic foundation considering the discontinuous elastic base on the circumferential direction and subjected to a lateral loading. Recently, Rodrigues [5] and Silva et al. [6] analyzed the nonlinear vibrations considering the discontinuity in the longitudinal direction of the cylindrical shell, contrasting the discontinuous elastic case with the elastic base across the entire shell. Then, based on a previous work [6], a consistent transversal displacement field that contains the main modal coupling to describe the nonlinear behavior of FG cylindrical shell resting in the

J. K. A. Pereira · R. M. Soares · F. M. A. Silva (✉)
Federal University of Goiás, Av. Universitária, Goiás, Brazil
e-mail: jonathaskennedy@yahoo.com.br; renatasoares@ufg.br; silvafma@ufg.br

P. B. Gonçalves
Pontifical Catholic University, Rio de Janeiro, Brazil
e-mail: paulo@puc-rio.br

circumferential discontinuous elastic base is here proposed and the parametric analysis clarifies the influence of the discontinuous foundation on the nonlinear shell vibrations.

2 Theoretical Formulation

Consider a perfect cylindrical shell with radius R and thickness h , where $h \ll R$, length L . Figure 1a shows the cylindrical shell geometry, the x , θ , and z coordinate system and the associated displacements in the axial (u), circumferential (v), and transversal (w) directions, respectively. The cylindrical shell is composed of a functionally graded (FG) material, whose properties vary along the thickness, obeying Hooke's law. The physical parameters E , ρ , and ν are described, assuming a sandwich distribution, by:

$$P = (P_A - P_C) V_A(z) + P_C, \text{ with } V_A(z) = \left(1 - \frac{4z^2}{h^2}\right)^{2N+1} \quad (1)$$

where P_A and P_C are the properties of materials A and C , respectively, $V_A(z)$ is the sandwich gradation equation, and N is the gradation exponent of the material.

The cylindrical shell is resting on a discontinuous elastic foundation in the circumferential direction, delimited by the angles θ_E and θ_D , as shown in Fig. 1b, where the origin of the circumferential coordinate axis is also shown. The cylindrical shell is submitted to a time-dependent lateral pressure given by

$$P(t) = P_L W_\theta \sin\left(\frac{m\pi x}{L}\right) \cos(\omega_1 t) \quad (2)$$

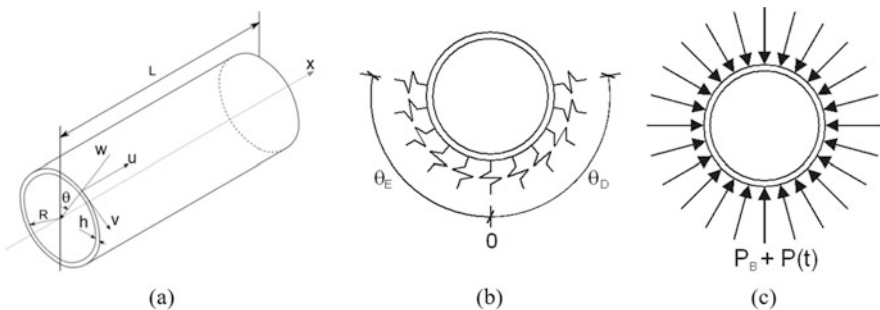


Fig. 1 Shell characteristics: (a) geometry, (b) discontinuous foundation in the circumferential direction, and (c) harmonic lateral pressure

where P_L is the forcing magnitude, W_θ is a function that determines the distribution of the load in the circumferential direction, m is the number of half-waves in the longitudinal direction, ω_1 is the excitation frequency, and t is the time.

The nonlinear equations of motion based on Donnell shallow theory are given by:

$$\begin{aligned}
 -N_{x,x} - \frac{1}{R}N_{x\theta,\theta} &= 0, & -\frac{1}{R}N_{\theta,\theta} - N_{x\theta,x} &= 0, \\
 \rho_1\ddot{w} - M_{x,xx} - \frac{2}{R}M_{x\theta,x\theta} - \frac{1}{R^2}M_{\theta\theta,\theta\theta} + \frac{N_\theta}{R} + (N_x\beta_{x0} + N_{x\theta}\beta_{\theta0})_{,x} & & (3) \\
 + \frac{1}{R}(N_{x\theta}\beta_{x0} + N_\theta\beta_{\theta0})_{,\theta} - P_B - P &= -2\eta_1\rho_1\omega_0\dot{w} - \eta_2C_{11}\nabla^4\dot{w}.
 \end{aligned}$$

where $N_x, N_\theta, N_{x\theta}$ are membrane stresses and $M_x, M_\theta, M_{x\theta}$ are bending and torsional moments, ∇^4 the bi-harmonic operator in cylindrical coordinates, η_1 is the viscous damping parameter, η_2 the material damping, ω_0 the natural frequency, and ρ_1 the average density of the material.

The membrane and flexural stress are given by:

$$\begin{Bmatrix} N_x \\ N_\theta \\ N_{x\theta} \\ M_x \\ M_\theta \\ M_{x\theta} \end{Bmatrix} = \begin{bmatrix} A_{11} & A_{12} & 0 & B_{11} & B_{12} & 0 \\ A_{12} & A_{11} & 0 & B_{12} & B_{11} & 0 \\ 0 & 0 & A_{66} & 0 & 0 & B_{66} \\ B_{11} & B_{12} & 0 & C_{11} & C_{12} & 0 \\ B_{12} & B_{11} & 0 & C_{12} & C_{11} & 0 \\ 0 & 0 & B_{66} & 0 & 0 & C_{66} \end{bmatrix} \begin{Bmatrix} \varepsilon_{x0} \\ \varepsilon_{\theta0} \\ \gamma_{x\theta0} \\ \kappa_{x0} \\ \kappa_{\theta0} \\ \kappa_{x\theta0} \end{Bmatrix} \tag{4}$$

where the extensional, coupling, and bending stiffnesses of the FG material are given, respectively ($i, j = 1, 2, 6$):

$$(A_{ij}, B_{ij}, C_{ij}) = \int_{-h/2}^{+h/2} Q_{ij}(1, z, z^2) dz, \quad \text{with } Q_{11} = \frac{E}{1-\nu^2}, \quad Q_{12} = \frac{E\nu}{1-\nu^2}, \quad Q_{66} = \frac{E}{2(1-\nu)} \tag{5}$$

and $\varepsilon_{x0}, \varepsilon_{\theta0}, \gamma_{x\theta0}, \kappa_{x0}, \kappa_{\theta0}$, and $\kappa_{x\theta0}$ are defined as:

$$\begin{aligned}
 [\varepsilon_{x0}, \varepsilon_{\theta0}, \gamma_{x\theta0}] &= \left[u_{,x} + \frac{1}{2}w_{,x}^2, \frac{1}{R}(v_{,\theta} + w) + \frac{w_{,\theta}^2}{2R^2}, \frac{1}{R}u_{,\theta} + v_{,x} + \frac{w_{,x}w_{,\theta}}{R} \right] \\
 [\beta_{x0}, \beta_{\theta0}, \kappa_{x0}, \kappa_{\theta0}, \kappa_{x\theta0}] &= \left[-w_{,x}, -\frac{w_{,\theta}}{R}, w_{,xx}, -\frac{w_{,\theta\theta}}{R^2}, -\frac{2w_{,x\theta}}{R} \right]
 \end{aligned} \tag{6}$$

The elastic foundation reaction, considering the Winkler model, is given by:

$$P_B = -K_W w [H(\theta - \theta_E) - H(\theta - \theta_D)] \tag{7}$$

where K_W is the foundation stiffness and H is the Heaviside function.

3 Reduced-order Model of the Shell Considering Discontinuous Boundary in the Circumferential Direction

To obtain the reduced-order model and following numerical results, consider a simply supported perfect cylindrical shell with radius $R = 0.6$ m, length $L = 0.6$ m, thickness $h = 0.003$ m, and $\theta_D = -\theta_E = 22.5^\circ$. The FG shell is composed of the following materials: steel (material A) and a ceramic (material C), whose properties are: $E_A = 205.1 \times 10^9$ N/m², $\rho_A = 8900$ kg/m³, $\nu_A = 0.31$, $E_C = 322.3 \times 10^9$ N/m², $\rho_C = 2370$ kg/m³, and $\nu_C = 0.24$.

As shown by Amabili and Dalpiaz [1], to ensure the convergence of the solution considering the elastic base circumferential discontinuity, a large number of terms in the Fourier series of the transversal displacement is necessary. However, in a nonlinear dynamic scenario, this consideration demands a lot of computational effort. So, from a perturbation procedure [6], a reduced-order model to describe the nonlinear dynamic behavior of the FG cylindrical shell is derived. To achieve this purpose, the ABAQUS[®] FEM software is used to model the problem and the resulting displacement field is expanded in a Fourier series.

For the quantification of the participation of each term in the modal expansion, the Parseval theorem is employed, assuming that the velocity field is analogous to the transversal displacement. Then, the relation of the kinetic energy of shell and the terms of Fourier series is given by:

$$\int_L \int_h \int_{2\pi R} \rho \dot{f}(\theta)^2 d\theta dz dx = \frac{\omega_0^2}{2\pi} \int_L \int_h \int_{\omega} \rho F(i\omega)^2 d\omega dz dx \quad (8)$$

where ω_0 is the natural frequency of the shell and $F(i\omega)$ is the amplitude of the frequency obtained by the Fourier transform.

Figure 2 shows that the main cosine and sine modes of the Fourier series are similar in magnitude [1], where $K_W = K_{nW} A_{11} / R^2$. However, for intermediary terms, the magnitudes of the “cosine modes” and “sine modes” are different, with the “cosine modes” higher than those of the “sine modes”. The slow decrease of the modal amplitudes justifies the large number of terms necessary to obtain the convergence of displacement field in [1]. These results are independent of the stiffness of the elastic base.

Here, a perturbation method is adopted to derive a consistent reduced-order nonlinear model of displacement field. Figure 3 shows the behavior of accumulated kinetic energy, where it is observed that in the region $7 < \omega < 9$ represents 80% and 85% total kinetic energy of, respectively, the cosine series and sine series. Thus, the seed solution for the perturbation method [6] is given by:

$$w_0 = \sum_{i=8,9} \overline{W}_{i,1}^C(\tau) \cos(i\theta) \sin(q\xi) + \sum_{i=8,9} \overline{W}_{i,1}^S(\tau) \sin(i\theta) \sin(q\xi) \quad (9)$$

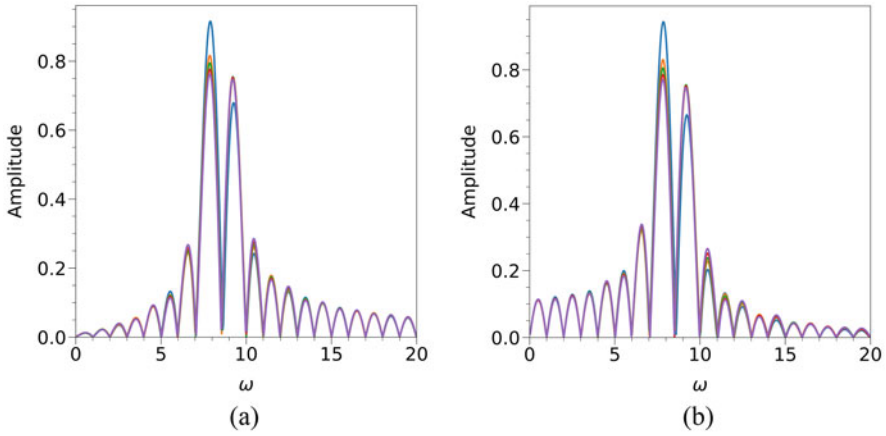


Fig. 2 Frequency spectrum of the cylindrical shell for different K_{nW} values. (a) “Cosine mode” and (b) “Sine mode”. — $K_{nW} = 0.003$, — $K_{nW} = 0.015$, — $K_{nW} = 0.03$, — $K_{nW} = 0.06$ and — $K_{nW} = 0.12$

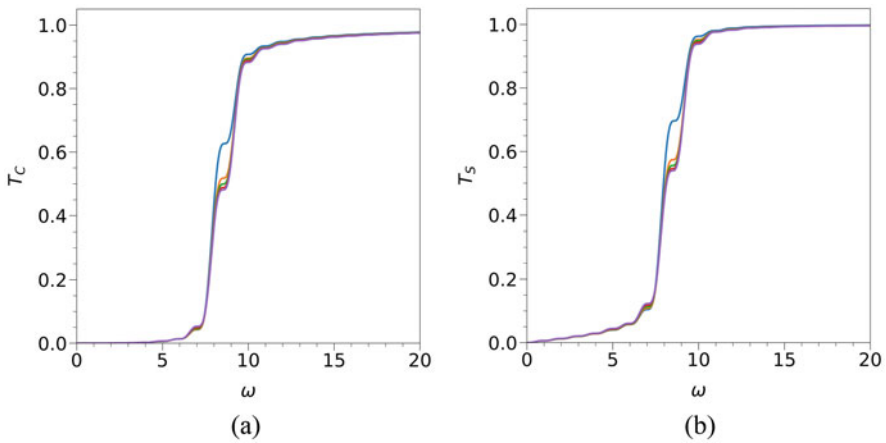


Fig. 3 Accumulated energy in frequency domain for different K_{nW} values. (a) “Cosine modes” and (b) “Sine modes”. — $K_{nW} = 0.003$, — $K_{nW} = 0.015$, — $K_{nW} = 0.03$, — $K_{nW} = 0.06$ and — $K_{nW} = 0.12$

where $q = m\pi$, $\xi = x/L$, with $0 \leq \xi \leq 1$, $m = 1$ and coefficients W^C , W^S are related with the cosine and sine modes, respectively. Using this seed solution, the modal solution derived through the perturbation method can be written as

$$\begin{aligned}
w = & \sum_{\beta=1,3} \sum_{i=7,8,9,10,24,25,26,27} \left\{ \left[W_{i,\beta}^C(\tau) \cos(i\theta) + W_{i,\beta}^S(\tau) \sin(i\theta) \right] \sin(\beta q\xi) \right\} \\
& + \sum_{i=0,1,16,17,18} \left\{ \left[W_{i,0}^C(\tau) \cos(i\theta) + W_{i,0}^S(\tau) \sin(i\theta) \right] \left[\frac{3}{4} - \cos(2q\xi) + \frac{1}{4} \cos(4q\xi) \right] \right\}
\end{aligned} \tag{10}$$

where $\tau = t\omega_0$. This solution takes into account the modal couplings arising from the quadratic and cubic nonlinear terms in Eq. (3).

To ensure convergence of the vibration amplitude up to twice the shell thickness 41 terms are used in Eq. (10). To obtain a consistent modal expansion for the u and v displacements, the procedure proposed by Silva [7] and Gonçalves et al. [8] is applied resulting in:

$$\begin{aligned}
u = & \sum_{\beta=1,3,5,7} \sum_{i=7,8,9,10,24,25,26,27} \left\{ \left[U_{i,\beta}^C(\tau) \cos(i\theta) + U_{i,\beta}^S(\tau) \sin(i\theta) \right] \cos(\beta q\xi) \right\} \\
& + \sum_{\beta=2,6} \sum_{i=0,1,2,15,16,17,18,19,32,33,34,35,36} \left\{ \left[U_{i,\beta}^C(\tau) \cos(i\theta) + U_{i,\beta}^S(\tau) \sin(i\theta) \right] \right. \\
& \quad \left. \times \left[\sin(\beta q\xi) - \frac{\beta}{\beta+2} \sin((\beta+2)q\xi) \right] \right\}
\end{aligned} \tag{11}$$

$$\begin{aligned}
v = & \sum_{\beta=1,3,5,7} \sum_{i=7,8,9,10,24,25,26,27} \left\{ \left[V_{i,\beta}^C(\tau) \cos(i\theta) + V_{i,\beta}^S(\tau) \sin(i\theta) \right] \sin(\beta q\xi) \right\} \\
& + \sum_{\beta=0,4} \sum_{i=0,1,2,15,16,17,18,19,32,33,34,35,36} \left\{ \left[V_{i,\beta}^C(\tau) \cos(i\theta) + V_{i,\beta}^S(\tau) \sin(i\theta) \right] \right. \\
& \quad \left. \times [\cos(\beta q\xi) - \cos((\beta+2)q\xi)] \right\}
\end{aligned} \tag{12}$$

These modal expansions satisfy the following boundary conditions for a simply supported cylindrical shell:

$$u = 0 \text{ at } x = \frac{L}{2}; \quad v, w = 0 \text{ at } x = 0, L. \tag{13}$$

Using the in-plane equilibrium equation in Eq. (3) together with the boundary conditions given by Eq. (13), the amplitudes U^C , U^S , V^C , and V^S are determined as a function of the transversal modal amplitude W^C and W^S through a standard Galerkin procedure. Then the resulting expressions are used to discretize the equation of motion in a transversal direction in Eq. (3), obtaining a system of second-order nonlinear equations in the time variable τ written in terms of W^C and W^S only.

4 Numerical Results

In this section, the physical and geometric parameters are the same defined in Sect. 3 and a non-dimensional value of the foundation stiffness $K_{nW} = 0.003$ is adopted.

To obtain resonance curves, a viscous damping $\eta_1 = 0.001$ ($\eta_2 = 0$) and a lateral harmonic pressure magnitude $P_L = 5000 \text{ N/m}^2$ are adopted. The function W_θ , given by:

$$W_\theta = [P_{8C} \cos(8\theta) + P_{8S} \sin(8\theta) + P_{9C} \cos(9\theta) + P_{9S} \sin(9\theta)] \quad (14)$$

with terms P_{8C} , P_{8S} , P_{9C} , and P_{9S} varying in the interval 0–1 are used here to excite the modes included in the initial (seed) expansion of the perturbation method. The geometrical parameters are chosen such that at least two natural frequencies are very close when considering a complete elastic base. These frequencies occur for vibration modes $(n,m) = (8,1)$ and $(n,m) = (9,1)$ where the natural frequencies are, respectively, 2985.62 rad/s and 3008.69 rad/s.

Figures 4 and 5 show the normalized maximum modal amplitude as a function of normalized frequency parameter (ω_1/ω_0) for the four main modes present in the seed solution of the perturbation method, considering two different driven modes. These resonance curves were obtained through a brute force method and exhibit, mainly in the resonance region, the excitation of all initial modes independent of the excited circumferential mode where it is observed an unstable region with quasi-periodic solution. Several bifurcation points, as Hopf, limit point, and torus, can be found in these complex resonance curves.

It is possible to observe in Fig. 6 a competition between a quasi-periodic solution (black phase portrait) and periodic solution (blue phase portrait) for a chosen frequency parameter of each case of excitation of circumferential mode. Figure 6a is related with Fig. 4, exciting directly the cosine mode (8,1), while Fig. 6b is related with Fig. 5, exciting directly the cosine mode (9,1). In these figures, Poincaré sections are marked in red to demonstrate the quasi-periodic solution and in blue for the periodic $1T$ solution. The chosen plane indicates a modal coupling between the basic modes of the initial solution of the perturbation method.

Due to modal coupling caused by the quadratic and cubic nonlinearities present into nonlinear equation motion of the FG cylindrical shell, a secondary resonance region is observed near $\omega_1/\omega_0 = 1.1$, as shown in Fig. 7. This modal amplitude $W_{10,1}^C$ appears in the modal solution, Eq. (10), as a result of the modal coupling of the seed solution and is excited in the main resonance region, creating this secondary resonant peak in the resonance curve for both driven modes. This second resonance peak can appear for other modal amplitudes as, for example, shown in zoomed regions of Figs. 4 and 5.

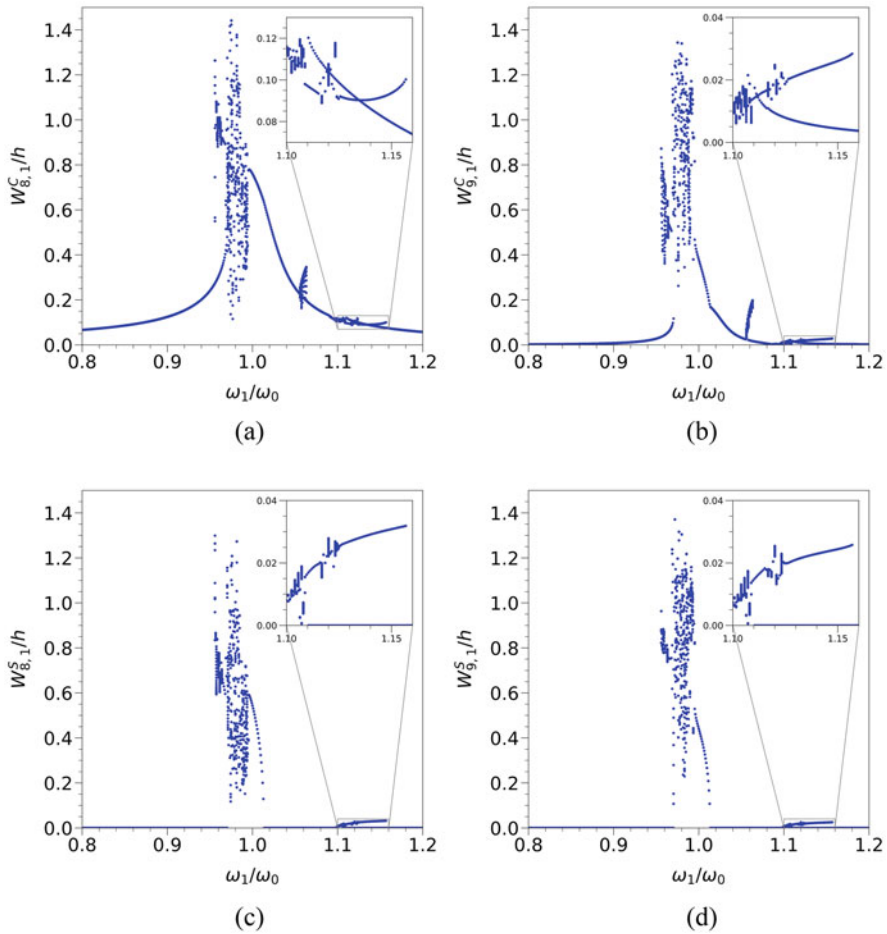


Fig. 4 Resonance curves for the modes (8,1) and (9,1) of the seed solution of transversal displacement field (a) $W_{8,1}^C$, (b) $W_{9,1}^C$, (c) $W_{8,1}^S$, (d) $W_{9,1}^S$. ($K_n W = 0.003$, $P_{8C} = 1$, $P_{8S} = P_{9C} = P_{9S} = 0$)

5 Conclusions

In this work, the nonlinear dynamic behavior of a FG cylindrical shell with a discontinuous elastic foundation in the circumferential direction is investigated. Applying Donnell's nonlinear shallow shell theory, the resultant nonlinear partial differential equation of motion is discretized as a set of nonlinear differential equations in time domain by the application of the standard Galerkin method. A fast Fourier transform is applied to obtain the main vibration modes later used as the seed solution of the perturbation method, which is used in turn to derive a consistent reduced-order nonlinear discrete model that represent the behavior

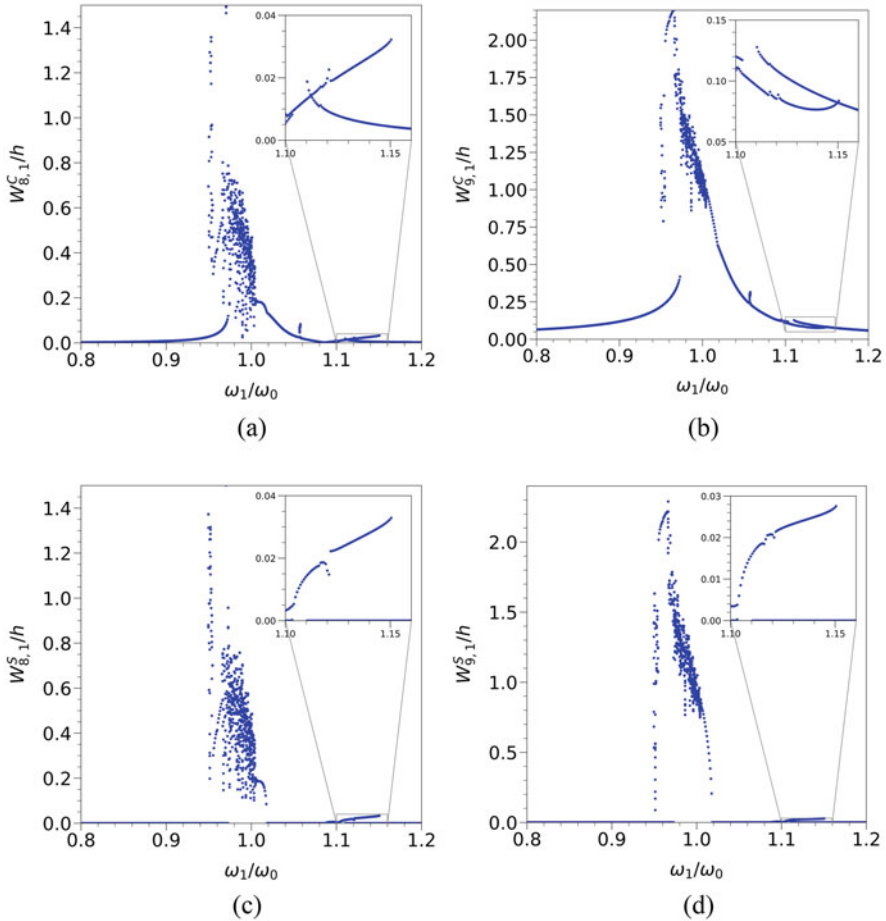


Fig. 5 Resonance curves for the modes (8,1) and (9,1) of the seed solution of transversal displacement field (a) $W_{8,1}^C$, (b) $W_{9,1}^C$, (c) $W_{8,1}^S$, (d) $W_{9,1}^S$. ($K_n W = 0.003$, $P_{9C} = 1$, $P_{8C} = P_{8S} = P_{9S} = 0$)

of the FG cylindrical shells. This allows a detailed nonlinear bifurcation analysis of the shell in the main resonance region. The results show the influence on the nonlinear resonance curves of the presence of circumferential discontinuity in the elastic foundation that leads to competition between periodic and quasi-periodic solutions and local bifurcations in resonance curves. Also, a secondary resonance region arises due to the discontinuity of the elastic foundation. It is associated with the frequency of higher modes of shell that arise due to modal coupling present in the displacement fields of the FG cylindrical shell.

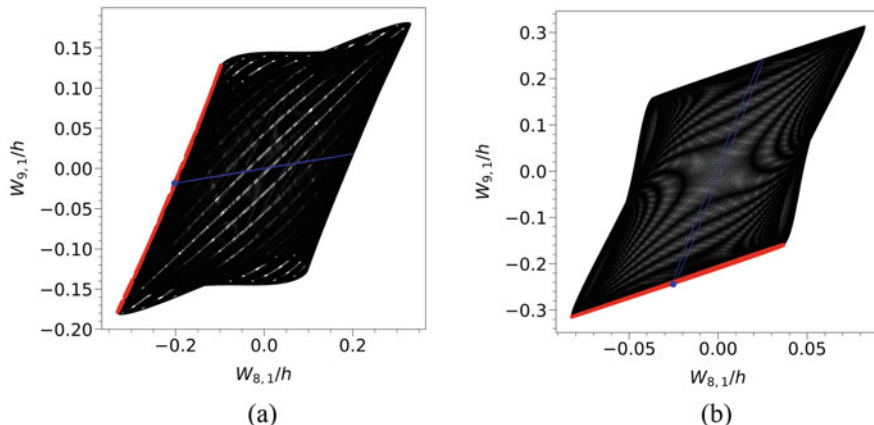


Fig. 6 Phase portraits with Poincaré map with $K_{nW} = 0.003$, $P_{8S}=P_{9S} = 0$: (a) $\omega_1/\omega_0 = 1.0616$ ($P_{8C} = 1, P_{9C} = 0$), (b) $\omega_1/\omega_0 = 1.0576$ ($P_{8C} = 0, P_{9C} = 1$)

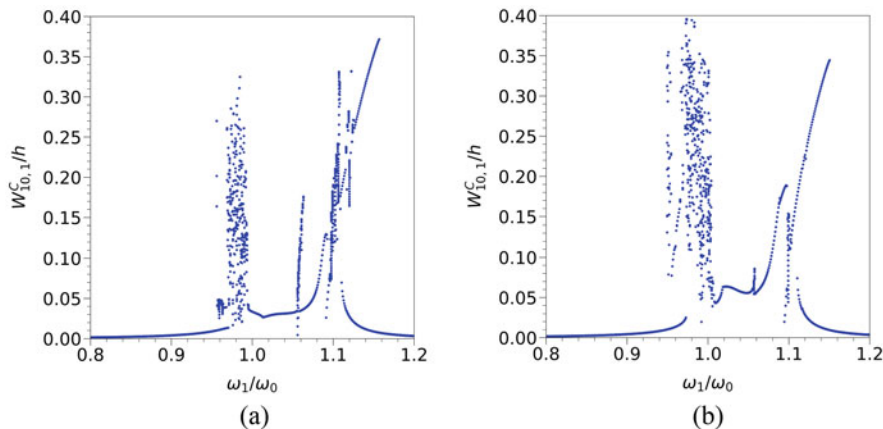


Fig. 7 Resonance curves for (a) $W_{10,1}^C$ ($P_{8C} = 1, P_{8S} = P_{9C} = P_{9S} = 0$), (b) $W_{10,1}^C$ ($P_{9C} = 1, P_{8S} = P_{8C} = P_{9S} = 0$). ($K_{nW} = 0.003$)

References

1. M. Amabili, G. Dalpiaz, Free vibrations of cylindrical shells with non-axisymmetric mass distribution on elastic bed. *Meccanica* **32**, 71–84 (1997)
2. H.G. Tj, T. Mikami, S. Kanie, M. Sato, Free vibrations of fluid-filled cylindrical shells on elastic foundations. *Thin-Walled Struct.* **43**(11), 1746–1762 (2005)
3. H.G. Tj, T. Mikami, S. Kanie, M. Sato, Free vibration characteristics of cylindrical shells partially buried in elastic foundations. *J. Sound Vib.* **290**(3–5), 785–793 (2006)
4. F.B. Nejad, S.M.M. Bideleh, Nonlinear free vibration analysis of prestressed circular cylindrical shells on the Winkler/Pasternak foundation. *Thin-Walled Struct.* **53**, 26–39 (2012)

5. P.C. Rodrigues, *Influence of Discontinuity of an Elastic Base in Resonance Curves of a Cylindrical Shell (in Portuguese)* (Universidade Federal de Goiás, Goiânia, 2019)
6. F.M.A. Silva, P.C. Rodrigues, P.B. Gonçalves, Nonlinear Oscillation of a FG Cylindrical Shell on a Discontinuous Elastic Foundation. In *New Trends in Nonlinear Dynamics – Proceedings of the First International Nonlinear Dynamics*
7. F.M.A. Silva, *Low Dimensional Models for Nonlinear Vibration Analysis and Stability of Cylindrical Shells (in Portuguese)* (Pontifícia Universidade Católica do Rio de Janeiro, Rio de Janeiro, 2008)
8. P.B. Gonçalves, F.M.A. Silva, Z.J.G.N. Del Prado, Low-dimensional models for the nonlinear vibration analysis of cylindrical shells based on a perturbation procedure and proper orthogonal decomposition. *J. Sound Vib.* **315**(3), 641–663 (2008)

The Effect of Boundary Conditions on Nonlinear Vibrations of Plates on a Viscoelastic Base via the Fractional Calculus Standard Linear Solid Model



Marina V. Shitikova  and Anastasiya I. Krusser 

1 Introduction

The dynamic response of plates on a viscoelastic foundation has been deeply investigated in the last few decades. In order to describe the properties of the foundation, different models of viscoelasticity are used [1]. Younesian et al. noted in their thorough review [1] that “new foundation models can be developed considering fractional nonlinearity and fractional damping”. Nowadays, the fractional calculus plays an important role in solving problems of structural mechanics [2], thereby the fractional derivative Winkler-type or Pasternak-type models of viscoelastic foundations are becoming increasingly widespread. Thus, a fractional derivative Kelvin–Voigt model of Winkler-type is proposed in [3] to examine the quasi-static problem of a rectangular plate rested on a viscoelastic foundation, which is subjected to uniformly distributed loads. The linear vibrations of elastic and viscoelastic Kirchhoff–Love plates on a fractional derivative Kelvin–Voigt foundation of the Pasternak type have been analyzed in [4, 5], respectively. Zhang et al. [6] applied the fractional derivative standard linear solid model to investigate the time-dependent behavior of a simply supported linear elastic plate on the viscoelastic Winkler-type foundation and compared numerical results with a classical model. The interaction between the simply supported linear elastic plate and viscoelastic Pasternak-type foundation described by the fractional Scott–Blair model has been considered in [7] to study the deflections and bending moments varying with time. Through theoretical and numerical results, the authors found that the fractional order has a dramatic influence on the deflection and bending moment, especially when the duration time is large. Praharaj et al. [8] studied the linear free vibration and

M. V. Shitikova (✉) · A. I. Krusser

Research Centre on Dynamics of Solids and Structures, Voronezh State Technical University, Voronezh, Russia

e-mail: mvs@vgasu.vrn.ru

the step-load-induced transient response of a thin plate on a fractional Kelvin–Voigt foundation for different types of boundary conditions. The same problem is solved for moving point load in [9]. The authors of [8, 9] have emphasized that the classical integer-order foundation model overestimates the damping of the foundation, thereby underestimates the dynamic deflection and the associated stresses. Hosseinkhani et al. [10] studied the vibration of a linear elastic Kirchhoff–Love plate based on the nonlinear foundation, the viscoelastic properties of which are described by the fractional Kelvin–Voigt model of the Winkler-type taking into account the nonlinear stiffness of foundation.

Reference to [3–10] clearly shows that all of the considered above papers are devoted to the analysis of linear Kirchhoff–Love plate vibrations. However, in the literature, there are reports on the research of the nonlinear vibrations of the von Karman plate in the viscoelastic medium, the damping properties of which are described by the Kelvin–Voigt model with fractional derivatives, accompanied by the internal resonance 2:1 [11]. This approach was later generalized for free vibrations of the plate in the viscoelastic medium for different types of the internal resonance [12]. The force-driven vibrations of fractionally damped plates subjected to primary and internal resonances were studied in [13]. The dynamic response of a rectangular nonlinear plate resting on a viscoelastic Winkler-type foundation, the damping features of which are described by the fractional derivative Kelvin–Voigt model, for the first time was considered in [14]. The standard linear solid model with fractional derivatives for defining the viscoelastic properties of the Winkler-type foundation was applied in [15]. But in these two papers, the boundary conditions of the plate are restricted to simply supported case, though there are known different combinations of simple boundary conditions in the literature for rectangular plates [16].

Thus, in the present paper, the influence of boundary conditions on the nonlinear vibrations of the “plate-foundation” system is studied for the case, when the properties of the foundation and of the surrounding medium are described by the fractional derivative standard linear solid model and Kelvin–Voigt model, respectively.

2 Problem Formulation

Let us consider nonlinear vibrations of a simply supported elastic plate in a viscoelastic medium, based on a viscoelastic foundation (Fig. 1), the dynamic response of which is described by the von Karman equation in terms of the plate’s lateral deflection $w = w(x, y, t)$ and the Airy’s stress function ϕ :

$$D\nabla^4 w + \rho h \frac{\partial^2 w}{\partial t^2} - \frac{\partial^2 w}{\partial x^2} \frac{\partial^2 \phi}{\partial y^2} - \frac{\partial^2 w}{\partial y^2} \frac{\partial^2 \phi}{\partial x^2} + 2 \frac{\partial^2 w}{\partial x \partial y} \frac{\partial^2 \phi}{\partial x \partial y} = q - F_1 - F_2 \quad (1)$$

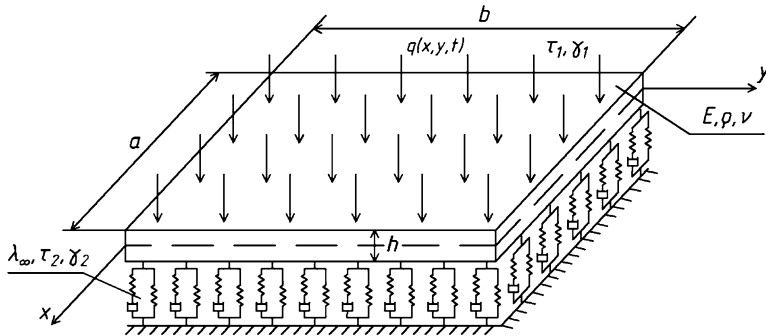


Fig. 1 Plate on a viscoelastic foundation modeled by the fractional derivative standard linear solid model

$$\nabla^4 \phi = Eh \left[\left(\frac{\partial w}{\partial x \partial y} \right)^2 - \frac{\partial^2 w}{\partial x^2} \frac{\partial^2 w}{\partial y^2} \right] \tag{2}$$

where $\nabla^4 = \partial^4/\partial x^4 + 2\partial^4/\partial x^2 \partial y^2 + \partial^4/\partial y^4$ is the biharmonic operator, q is the external load, $D = Eh^3/12(1 - \nu^2)$ is the plate's cylindrical rigidity, E and ν are the elastic modulus and Poisson's ratio of the plate's material, respectively, h and ρ are its thickness and density, t is the time, $F_2 = \tilde{\lambda}w$ is the reaction force of the viscoelastic foundation, $F_1 = \alpha_1 \tau_1^{\gamma_1} D_{0+}^{\gamma_1} w$ is the damping force of the viscoelastic medium possessing the retardation time τ_1 and damping coefficient α_1 , which is modeled by the viscoelastic Kelvin–Voigt model with the Riemann–Liouville derivative $D_{0+}^{\gamma_1}$ of the fractional order γ_1 ($0 < \gamma_1 \leq 1$) [17]:

$$D_{0+}^{\gamma} x(t) = \frac{d}{dt} \int_0^t \frac{x(t-t') dt'}{\Gamma(1-\gamma) t'^{\gamma}} \quad (0 < \gamma = \gamma_1 \leq 1) \tag{3}$$

and $\Gamma(1 - \gamma)$ is the Gamma function.

Let us assume, following [18], that the compliance operator of a viscoelastic foundation is described by the standard linear solid model with the Riemann–Liouville fractional derivative D_{0+}^{γ} (3) when $\gamma = \gamma_2$:

$$\tilde{\lambda} = \lambda_{\infty} \left[1 - \alpha_2 \nu_{\varepsilon} \frac{1}{1 + \tau_2^{\gamma_2} D_{0+}^{\gamma_2}} \right] \tag{4}$$

where λ_{∞} is the coefficient of instantaneous compliance of the foundation, $\nu_{\varepsilon} = \Delta \lambda \lambda_{\infty}^{-1}$, $\Delta \lambda = \lambda_{\infty} - \lambda_0$ is the defect of the compliance, i.e., the value characterizing the decrease in the compliance operator from its non-relaxed value λ_{∞} to its relaxed

Table 1 Plate mode shapes for different B.Cs

B.Cs.	$W_{m_i n_i}(x, y)$
SSSS	$\sin \frac{\pi m_1 x}{a} \sin \frac{\pi n_1 y}{b}$
CCCC	$\left(1 - \cos \frac{2\pi m_1 x}{a}\right) \left(1 - \cos \frac{2\pi n_1 y}{b}\right)$
CSCS	$\left(1 - \cos \frac{2\pi m_1 x}{a}\right) \sin \frac{\pi n_1 y}{b}$
CCSC	$\left(\cos \frac{3\pi m_1 x}{2a} - \cos \frac{\pi m_1 x}{2a}\right) \left(1 - \cos \frac{2\pi n_1 y}{b}\right)$

value λ_0 , and τ_2 and α_2 are the retardation time and damping coefficient of the viscoelastic foundation, respectively.

The following boundary conditions could be added to the set of Eqs. (1) and (2) at each edge:

1. Simply supported edges (S)

$$\text{at } x = 0 \text{ and } a, \quad w = \frac{\partial^2 w}{\partial x^2} = 0; \quad \text{at } y = 0 \text{ and } b, \quad w = \frac{\partial^2 w}{\partial y^2} = 0. \tag{5}$$

2. Clamped edges (C)

$$\text{at } x = 0 \text{ and } a, \quad w = \frac{\partial w}{\partial x} = 0; \quad \text{at } y = 0 \text{ and } b, \quad w = \frac{\partial w}{\partial y} = 0. \tag{6}$$

The following four types of boundary conditions (B.Cs) of the plate will be considered: all edges are simply supported (SSSS); all edges are clamped (CCCC); two opposite edges are clamped and other two edges are simply supported (CSCS), and one edge is simply supported and others are clamped (CCSC). In the abbreviation of B.Cs the letter symbols are used, for example, CSCS means a plate with edges $x = 0$ and $x = a$ clamped (C), $y = 0$ and $y = b$ simply supported (S).

In order to identify the possibility of the occurrence of the internal resonance during nonlinear vibrations of a plate based on a viscoelastic foundation and to carry out its subsequent analysis, suppose that only two natural modes of vibrations with numbers $m_1 n_1$ и $m_2 n_2$ are excited. Then the deflection of the plate could be represented in the following form:

$$w(x, y, t) = x_1(t)W_{m_1 n_1}(x, y) + x_2(t)W_{m_2 n_2}(x, y), \tag{7}$$

where $x_i(t)$ ($i = 1, 2$) are generalized displacements, and $W_{m_i n_i}(x, y)$ are the eigen functions. The mode shape functions for various B.Cs are presented in Table 1 [19].

Substituting the proposed solution (7) in (2), taking into account the boundary conditions to be considered for each specific case, and integrating with account for the orthogonality conditions of eigen functions yield the stress function. Thus, for the case of simply supported (SSSS) plate it has following form [15]:

$$\begin{aligned}
 \phi(x, y, t) = & \frac{Eh}{32\xi^2} \left(\frac{n_1^2}{m_1^2} \cos \frac{2\pi m_1 x}{a} + \xi^4 \frac{m_1^2}{n_1^2} \cos \frac{2\pi n_1 y}{b} \right) x_1(t)^2 \\
 & + \frac{Eh}{32\xi^2} \left(\frac{n_2^2}{m_2^2} \cos \frac{2\pi m_2 x}{a} + \xi^4 \frac{m_2^2}{n_2^2} \cos \frac{2\pi n_2 y}{b} \right) x_2(t)^2 \\
 & + \frac{Eh}{4} \left[\left(B^2 \cos \frac{\pi(m_1+m_2)x}{a} \cos \frac{\pi(n_1-n_2)y}{b} \right. \right. \\
 & \quad \left. \left. + C^2 \cos \frac{\pi(m_1-m_2)x}{a} \cos \frac{\pi(n_1+n_2)y}{b} \right) \beta_1^2 \right. \\
 & \quad \left. - \left(A^2 \cos \frac{\pi(m_1+m_2)x}{a} \cos \frac{\pi(n_1+n_2)y}{b} \right. \right. \\
 & \quad \left. \left. + D^2 \cos \frac{\pi(m_1-m_2)x}{a} \cos \frac{\pi(n_1-n_2)y}{b} \right) \beta_2^2 \right] x_1(t)x_2(t),
 \end{aligned} \tag{8}$$

where $\xi = b/a$, $\beta_1 = (m_1 n_2 + m_2 n_1)$, $\beta_2 = (m_1 n_2 - m_2 n_1)$, and coefficients A, B, C , and D are presented in [15].

The expressions for the stress function for the CCCC, CSCS, and CCSC types of B.Cs could be obtained in the same manner, but they are not presented here due to the cumbersomeness of the formulas.

Substituting the assumed two-term expansion for the deflection function of the plate (7) and the corresponding stress function in the equation of motion of the plate (1) resting on the viscoelastic Winkler-type foundation (4) yields the following set of nonlinear differential equations with respect to the generalized displacements:

$$\ddot{x}_1 + \Omega_1^2 x_1 + \frac{\lambda_\infty}{\rho h} \left[1 - \mathfrak{a}_2 v_\varepsilon \mathfrak{D}_\gamma^* (\tau_2^{\gamma_2}) \right] x_1 + \alpha_1 x_1^3 + \alpha_2 x_1 x_2^2 + \frac{\mathfrak{a}_1 \tau_1^{\gamma_1}}{\rho h} D_{0+}^{\gamma_1} x_1 = P_1(t), \tag{9}$$

$$\ddot{x}_2 + \Omega_2^2 x_2 + \frac{\lambda_\infty}{\rho h} \left[1 - \mathfrak{a}_2 v_\varepsilon \mathfrak{D}_\gamma^* (\tau_2^{\gamma_2}) \right] x_2 + \alpha_3 x_2^3 + \alpha_4 x_2 x_1^2 + \frac{\mathfrak{a}_1 \tau_1^{\gamma_1}}{\rho h} D_{0+}^{\gamma_1} x_2 = P_2(t), \tag{10}$$

where $P_i(t) = \frac{\int_0^a \int_0^b q(x, y, t) W_{m_i n_i}(x, y) dx dy}{\rho h \int_0^a \int_0^b [W_{m_i n_i}(x, y)]^2 dx dy}$, α_i are the coefficients depending both on the

vibration mode numbers and the type of B.Cs (which are not given here due to their bulky expressions), $\mathfrak{D}_\gamma^* (\tau_2^{\gamma_2}) = \frac{1}{1 + \tau_2^{\gamma_2} D_{0+}^{\gamma_2}}$ is the Rabotnov dimensionless fractional operator [20], and Ω_i^2 are the natural frequencies of the linear vibrations of the plate defined as

1. SSSS plate

$$\Omega_i^2 = \frac{E\pi^4 h^2}{12\rho(1 - \nu^2) b^4} \left(\xi^2 m_i^2 + n_i^2 \right)^2, \tag{11}$$

2. CCCC plate

$$\Omega_i^2 = \frac{4E\pi^4 h^2}{27\rho(1-\nu^2)b^4} \left(3\xi^4 m_i^4 + 2\xi^2 m_i^2 n_i^2 + 3n_i^4 \right), \quad (12)$$

3. CSCS plate

$$\Omega_i^2 = \frac{E\pi^4 h^2}{9\rho(1-\nu^2)b^4} \left(4\xi^4 m_i^4 + 2\xi^2 m_i^2 n_i^2 + 0.75n_i^4 \right), \quad (13)$$

4. CCSC plate

$$\Omega_i^2 = \frac{E\pi^4 h^2}{18\rho(1-\nu^2)b^4} \left(3.85\xi^4 m_i^4 + 5\xi^2 m_i^2 n_i^2 + 8n_i^4 \right). \quad (14)$$

Reference to Eqs. (11), (12), (13), and (14) shows that the fully clamped CCCC rectangular elastic plate has the greatest values of natural frequencies compared to other B.Cs, and after that in the descending order are the natural frequencies of CCSC, CSCS, and SSSS plates, respectively.

3 Method of Solution and Numerical Results

The set of two nonlinear Eqs. (9) и (10) could be solved by the generalized method of multiple time scales, which was proposed by Rossikhin and Shitikova [21, 22] in 1998 by involving the expansion of the fractional derivative in terms of different-order time scales in the traditional procedure of this method.

Expanding the Rabotnov dimensionless fractional operator \mathfrak{D}_γ^* ($\tau_2^{\gamma/2}$) in a Taylor series also in terms of new time scales [2], assuming damping coefficients \mathfrak{a}_i to be small values $\mathfrak{a}_i = \varepsilon^2 \mu_i$, where μ_i are finite values, and applying the procedure for eliminating the circular terms from the governing equations yield the solvability conditions, whence it follows that the one-to-one internal resonance is possible in the case when

$$\omega_1 = \omega_2, \quad (15)$$

where ω_1 and ω_2 are vibration frequencies of the mechanical system “plate – fractional derivative standard linear solid foundation”

$$\omega_i^2 = \Omega_i^2 + \frac{\lambda_\infty}{\rho h}. \quad (16)$$

Then the resolving nonlinear differential equations in the amplitudes $a_i = a_i(T_2)$ and phases $\varphi_i = \varphi_i(T_2)$ of nonlinear vibrations have the following form:

$$\left(a_1^2\right)^{\cdot} + s_1 a_1^2 = -\omega_1^{-1} \alpha_2 a_1^2 a_2^2 \sin \delta, \tag{17}$$

$$\left(a_2^2\right)^{\cdot} + s_2 a_2^2 = \omega_2^{-1} \alpha_4 a_1^2 a_2^2 \sin \delta, \tag{18}$$

$$\dot{\varphi}_1 = \frac{1}{2} \lambda_1 + \frac{3}{2} \alpha_1 \omega_1^{-1} a_1^2 + \alpha_2 \omega_1^{-1} a_2^2 + \frac{1}{2} \alpha_2 \omega_1^{-1} a_2^2 \cos \delta, \tag{19}$$

$$\dot{\varphi}_2 = \frac{1}{2} \lambda_2 + \frac{3}{2} \alpha_3 \omega_2^{-1} a_2^2 + \alpha_4 \omega_2^{-1} a_1^2 + \frac{1}{2} \alpha_4 \omega_2^{-1} a_1^2 \cos \delta, \tag{20}$$

where $\delta = 2(\varphi_2 - \varphi_1)$ is the phase difference, $\psi_i = \frac{1}{2} \pi \gamma_i \quad (i = 1, 2)$,

$$\begin{aligned} s_i &= \bar{\mu}_1 \tau_1^{\gamma_1} \omega_i^{\gamma_1-1} \sin \psi_1 + \lambda_{\infty} v_{\varepsilon} \bar{\mu}_2 \omega_i^{-1} R \sin \Phi, & R &= \sqrt{1 + 2(\tau_2 \omega_i)^{\gamma_2} \cos \psi_2 + (\tau_2 \omega_i)^{2\gamma_2}}, \\ \lambda_i &= \bar{\mu}_1 \tau_1^{\gamma_1} \omega_i^{\gamma_1-1} \cos \psi_1 - \lambda_{\infty} v_{\varepsilon} \bar{\mu}_2 \omega_i^{-1} R \cos \Phi, & \tan \Phi &= \frac{(\tau_2 \omega_i)^{\gamma_2} \sin \psi_2}{1 + (\tau_2 \omega_i)^{\gamma_2} \cos \psi_2}. \end{aligned} \tag{21}$$

and $\bar{\mu}_i = \frac{\mu_i}{\rho h} \quad (i = 1, 2)$.

The set of Eqs. (17), (18), (19) and (20) is the governing one for the amplitudes and phases of nonlinear free vibrations of the elastic plate for the different B.Cs on a viscoelastic Winkler-type foundation, damping features of which are defined by the fractional derivative standard linear solid model (4), when vibrations occur in a viscoelastic surrounding medium, properties of which are described by the fractional derivative Kelvin–Voigt model. Vibration frequencies and coefficients $\alpha_1 - \alpha_4$ in the expressions (17), (18), (19) and (20) depend on the type of boundary conditions.

Equations (17), (18), (19) and (20) are solved numerically using the procedure suggested in [13] for fractionally damped plates subjected to primary and internal resonances. A quadratic plate was considered as an example. Figure 2 clearly shows the energy exchange between interacting modes of undamped and damped vibration of the plate on the elastic and viscoelastic foundation via the fractional calculus standard linear solid model, respectively, at $\gamma_2 = 0$ (Fig. 2a) and $\gamma_2 = 0.1$ or $\gamma_2 = 0.25$ (Fig. 2b). With appearing of the damping properties of the environment $\gamma_1 \neq 0$ (Fig. 2a), in which the plate vibrates, the damping of the vibrations increases with the growth of the fractional parameter. Reference to Fig. 2b shows that the increase in the fractional parameter of the viscoelastic foundation results in a decrease in dimensionless amplitudes of nonlinear vibrations.

Reference to Fig. 3 shows the decrease in the dimensionless displacements X_1 and X_2 of the SSSS plate with the increase in fractional parameters of the surrounding viscoelastic medium and viscoelastic foundation.

Then knowing the generalized functions $x_i(t)$ and eigenmodes for the corresponding boundary conditions $W_{m_i n_i}(x, y)$ (see, Table 1), the final solution for the plate displacement $w(x, y, t)$ could be constructed via relationship (7).

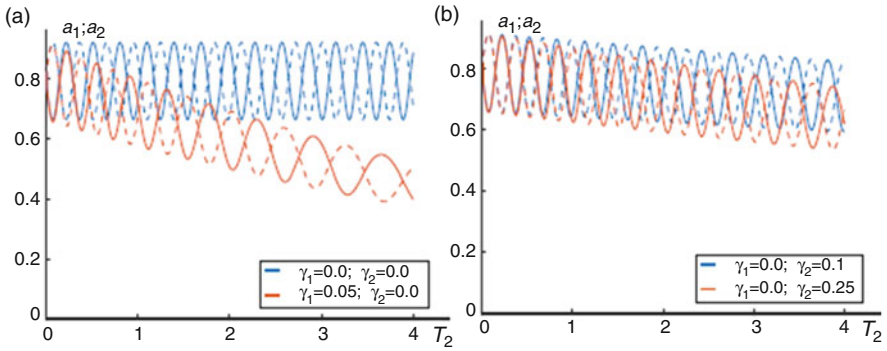


Fig. 2 The T_2 -dependence of the amplitudes of free vibrations for a simply supported rectangular plate in the case of 1:1 internal resonance: a_1 – dashed lines, a_2 – solid lines

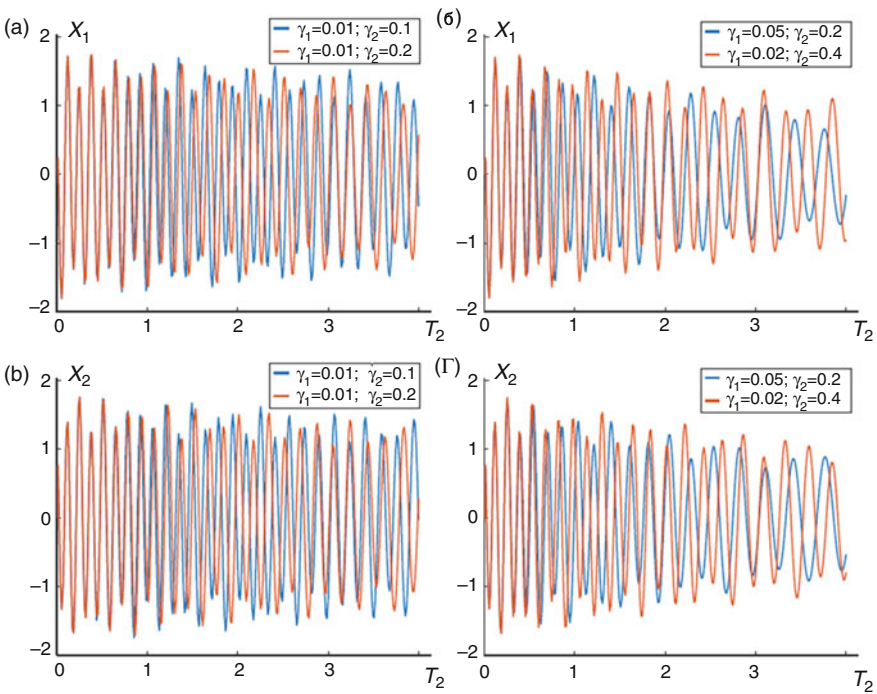


Fig. 3 The T_2 -dependence of the dimensionless displacements of the plate on a visco-elastic foundation described by the fractional derivative standard linear solid model

4 Conclusions

In the present paper, the influence of various boundary conditions on the free nonlinear vibrations of a von Karman elastic plate based on a viscoelastic Winkler-

type foundation is studied. The damping features of the viscoelastic foundation are described by the fractional derivative standard linear solid model, while the damping properties of the environment in which the vibrations occur are described by the Kelvin–Voigt viscoelastic model with the Riemann–Liouville fractional derivative. The governing equations of motion are presented in the general form with coefficients at nonlinear terms corresponding to each type of boundary conditions. The analysis of natural frequencies shows that the stiffer boundary conditions, the greater value of the frequency of vibrations. The CCCC rectangular elastic plate has the greatest value of natural frequency compared to other B.Cs.

The governing equations are obtained for determining nonlinear amplitudes and phases in the case of free vibrations, when the natural frequencies of the two dominant vibration modes are close to each other. The resulting set of equations allows one to control the damping properties of the external environment and the foundation by changing the fractional parameters from zero, what corresponds to an elastic medium and/or elastic foundation, to unit, what is in the agreement of the traditional standard linear solid model, resulting in the expansion of the range of applicability of the solution obtained. The obtained set of equations has been solved numerically for defining dimensionless amplitudes, as well as for calculating the values of dimensionless displacements for different values of fractional parameters.

Acknowledgement This research was supported by the Russian Foundation for Basic Research under the Grant No. 20-01-00443. The studies have been carried out using the facilities of the Collective Research Center named after Professor Yu. M. Borisov, Voronezh State Technical University, which is partly supported by the Ministry of Science and Education of the Russian Federation, Contract No 075- 15-2021-662.

References

1. D. Younesian, A. Hosseinkhani, H. Askari, E. Esmailzadeh, Elastic and viscoelastic foundations: A review on linear and nonlinear vibration modeling and applications. *Nonlinear Dynamics* **97**, 853–895 (2019)
2. Y.A. Rossikhin, M.V. Shitikova, Application of fractional calculus for dynamic problems of solid mechanics: Novel trends and recent results. *Appl. Mech. Rev.* **63**(1), Article ID 010801 (2010)
3. H. Zhu, L. Liu, X. Ye, Response of a loaded rectangular plate on fractional derivative viscoelastic foundation. *J. Basic Sci. Eng.* **19**(2), 271–278 (2011)
4. L. Kou, Response of rectangular plate on fractional derivative two-parameter viscoelastic foundation. *Chin. Q. Mech.* **34**(1), 154–160 (2013)
5. L. Kou, Y. Bai, Dynamic response of rectangular plates on two-parameter viscoelastic foundation with fractional derivatives. *J. Vib. Shock* **33**(8), 141–147 (2014)
6. C. Zhang, H. Zhu, B. Shi, L. Liu, Theoretical investigation of interaction between a rectangular plate and fractional viscoelastic foundation. *J. Rock Mech. Geotech. Eng.* **6**(4), 373–379 (2014)
7. W. Cai, W. Chen, W. Xu, Fractional modeling of Pasternak-type viscoelastic foundation. *Mech. Time-Depend. Mater.* **21**(1), 119–131 (2017)
8. R. Praharaj, N. Datta, On the transient response of plates on fractionally damped viscoelastic foundation. *Comput. Appl. Math.* **39**(4), Article ID 256 (2020)

9. R. Praharaaj, N. Datta, Dynamic response of plates resting on a fractional viscoelastic foundation and subjected to a moving load. *Mech. Based Design Struct. Mach.* (2020). <https://doi.org/10.1080/15397734.2020.1776621>
10. A. Hosseinkhani, D. Younesian, S. Farhangdoust, Dynamic analysis of a plate on the generalized foundation with fractional damping subjected to random excitation. *Math. Probl. Eng.* **2018**(2), 1–10 (2018)
11. Y. Rossikhin, M. Shitikova, Free damped nonlinear vibrations of a viscoelastic plate under two-to-one internal resonance. *Mater. Sci. Forum* **440-441**, 29–36 (2003)
12. Y.A. Rossikhin, M.V. Shitikova, J. Ngenzi, A new approach for studying nonlinear dynamic response of a thin plate with internal resonance in a fractional viscoelastic medium. *Shock. Vib.* **2015**, Article ID 795606 (2015)
13. M.V. Shitikova, V.V. Kandu, Force driven vibrations of fractionally damped plates subjected to primary and internal resonances. *Eur. Phys. J. Plus* **134**(9), Article ID 423 (2019)
14. M.V. Shitikova, V.V. Kandu, Analysis of the nonlinear vibrations of an elastic plate on a viscoelastic foundation in the presence of the one-to-one internal resonance (in Russian). *News of higher educational institutions. Construction* **3**, 5–22 (2020)
15. M.V. Shitikova, A.I. Krusser, Nonlinear vibrations of an elastic plate on a viscoelastic foundation modeled by the fractional derivative standard linear solid model. *EASD Proc. EURODYN*, 355–368 (2020)
16. A. Leissa, *Vibration of Plates* (Scientific and Technical Information Division, Office of Technology Utilization, NASA, Washington, D.C., 1969)
17. S. Samko, A. Kilbas, O. Marichev, *Fractional Integrals and Derivatives* (Theory and Applications. English translation by Gordon and Breach Science Publishers, Switzerland, 1993)
18. Y.A. Rossikhin, M.V. Shitikova, A new method for solving dynamic problems of fractional derivative viscoelasticity. *Int. J. Eng. Sci.* **39**, 149–176 (2001)
19. M. Kiasat, H. Zamani, M. Aghdam, On the transient response of viscoelastic beams and plates on viscoelastic medium. *Int. J. Mech. Sci.* **83**, 133–145 (2014)
20. Y.A. Rossikhin, M.V. Shitikova, Centennial jubilee of Academician Rabotnov and contemporary handling of his fractional operator. *Fract. Calc. Appl. Anal.* **17**, 674–683 (2014)
21. Y.A. Rossikhin, M.V. Shitikova, Application of fractional calculus for analysis of nonlinear damped vibrations of suspension bridges. *J. Eng. Mech.* **124**, 1029–1036 (1998)
22. M.V. Shitikova, The fractional derivative expansion method in nonlinear dynamic analysis of structures. *Nonlinear Dynam.* **99**, 109–122 (2020)

Augmented Perpetual Manifolds, a Corollary: Dynamics of Natural Mechanical Systems with Eliminated Internal Forces



Fotios Georgiades 

1 Introduction

Perpetual points (PPs) of a dynamical system have been defined recently by Prasad in [1]. They are the set of points that arise by setting the equations of accelerations and jerks equal to zero for nonzero velocities. By setting the accelerations zero then also the jerks are zero, but, at least for linear systems, the jerks are providing the additional equations needed for defining all the generalized coordinates and their velocities. The differential equations describing the motion of mechanical systems are of second order, therefore for zero accelerations (zero jerks too) and zero velocities, after writing the system in first order, lead to the fixed points of the system. With that view, the following can be said: the PPs are ‘generalizing’ the equilibrium points of mechanical systems for zero acceleration vectors but for nonzero velocities. The role of PPs in describing the dynamics of dynamical systems is ongoing research. In [2], experimental verification of the PPs, in a tilted pendulum, has been done. All the articles relative to PPs can be grouped in four research directions. The first one is about theoretical mathematical and experimental developments of PPs [1–4]. The second is to use PPs for identifications of hidden and chaotic attractors in nonlinear dynamical systems [5–13]. In [1], stated the

Although it is not typical practice for conference articles, in this challenging period with COVID-19, which is a ‘kind of attack’, through social physical distancing, towards personal relationships, people supporting socially the scientists have to be ‘acknowledged’. So this work is dedicated to my four best friends over this period, my two ‘sisters’ Anna and Marilena, my ‘brother’ Fanis, and my actual brother Andreas.

F. Georgiades (✉)

Center of Perpetual Mechanics & Centre of Nonlinear Systems, Centre for Nonlinear System,
Chennai Institute of Technology, Chennai, India
e-mail: fotiosgeorgiades@citchennai.net

possibility that the PPs to be used for identification for dissipative systems which is the third research direction [14–18]. In [19–21], the PPs of systems of differential equations, describing the motion of mechanical systems, have been examined with the view of mechanics which is the fourth group. In [19–20], with proved theorems declared, that the PPs, for linear mechanical systems, are associated with rigid body motions. The PPs corresponding to rigid body motions are not just a few points, but they are forming the perpetual manifolds [20]. The manifolds approach of PPs extended in [21], and new concepts have been defined, such as the perpetual mechanical systems and, the augmented perpetual manifolds. In [21], in a proved theorem, the conditions, that an N-degrees of freedom (dof) mechanical flexible system, with the application of external forces, can move as a rigid body, were defined. Otherwise stated, the system has a solution in the form of exact augmented perpetual manifolds.

This article is the continuation of the work done in [21], by examining the internal forces of the perpetual mechanical systems in augmented perpetual manifolds. The definitions and the theorem, that are in [21], recalled in Sect. 2.1. Then, by examining the internal forces of the perpetual mechanical systems, a corollary that is following the theorem of [21], in Sect. 2.2 is proven. In Sect. 3 with examples, the validity of the corollary, analytically in Sect. 3.1 and numerically in Sect. 3.2, is shown.

2 Theoretical Analysis

2.1 Introduction to the Theory

In this section, some definitions and the theorem will be recalled from [21]. In [21], the $2N$ dimensional exact perpetual manifolds of rigid body motions, which arise by examining the perpetual points of N-dof mechanical systems, have been defined as follows,

$$S = \{(q_s, \dots, q_s, \dot{q}_s, \dots, \dot{q}_s), (q_s, \dot{q}_s) \in \mathbb{R} \times \mathbb{R}^*\}. \quad (1)$$

The mechanical systems with sets of PPs that correspond to exact perpetual manifolds are called **perpetual mechanical systems** [21].

In [21], addressing the question ‘Is it possible in a mechanical system all accelerations to be equal but not necessarily zero’ the exact augmented perpetual manifolds can be defined as follows,

The $2N + 1$ dimensional exact augmented perpetual manifolds, e.g. X of a N-dof mechanical discrete system, with generalized coordinates q_i , that admits solutions of perpetual manifolds, arise when,

$$\ddot{q}_i(t) = \ddot{q}_a(t), \quad \text{for } i = 1, \dots, N, \quad \text{and } \ddot{q}_a(t) \in \mathbb{R}, \quad (2)$$

and the solutions of the system in state space, define them, as,

$$\mathbf{X} = \left\{ (t, q_a(t), \dots, q_a(t), \dot{q}_a(t), \dots, \dot{q}_a(t)) : (t, q_a(t), \dot{q}_a(t)) \in \mathbb{R}^3 \right\}. \quad (3)$$

Using the definitions above the following theorem in [21] has been proven,

Any $N(\geq 2)$ -degrees of freedom discrete mechanical system with generalized coordinates $q_i(t)$ that can be written as a perpetual mechanical system with external forcing that is described by the following system of differential equations,

$$\begin{aligned} & [\mathbf{M}_{i,j}(t, q_l(t), \dot{q}_m(t))] \times \{\ddot{q}_i(t)\} + [\mathbf{C}_{i,j}] \times \{\dot{q}_i(t)\} + [\mathbf{K}_{i,j}] \times \{q_i(t)\} \\ & + \left\{ F_i^{NL}(q_n(t), \dot{q}_o(t)) \right\} = \left\{ F_i(t, q_p(t), \dot{q}_q(t)) \right\}, \text{ for } i=1, \dots, N, \quad j=1, \dots, N, \\ & l, m, n, o, p, q \in \{1, 2, \dots, N\}, \text{ and } (q_i(t), \dot{q}_i(t), \ddot{q}_i(t)) \in \mathbb{R}^3, \end{aligned} \quad (4)$$

and admits unique solutions for the following matrices,

$[\mathbf{M}_{i,j}]$ is a real $N \times N$ inertia matrix with elements that can be, nonsmooth, nonlinear, time and state depended, functions but having at least one nonzero sum of k -row for all time instants,

$[\mathbf{K}_{i,j}]$ and $[\mathbf{C}_{i,j}]$, are real $N \times N$ constant, stiffness and proportional to velocity vector, matrices,

$\{F_i^{NL}\}$ is a $N \times 1$ vector of nonlinear internal forces with elements state depended nonlinear functions which can be nonsmooth but single-valued for rigid body motions, and $F_i^{NL}(q_s, 0) = 0$ for $q_s \in \mathbb{R}$,

$\{F_i\}$ is a real $N \times 1$ vector of external forces with elements, time and state dependent, maybe nonlinear and nonsmooth functions,

if the external forces (F_i) with the reference k -mass external force (F_k) are related as follows,

$$F_i(t, q_a(t), \dot{q}_a(t)) = \frac{\sum_{j=1}^N M_{i,j}(t, q_a(t), \dot{q}_a(t)) \cdot F_k(t, q_a(t), \dot{q}_a(t))}{\sum_{j=1}^N M_{k,j}(t, q_a(t), \dot{q}_a(t))},$$

$$\text{for } i, k \in \{1, 2, \dots, N\}, \text{ and } q_a(t) = q_i(t), \dot{q}_a(t) = \dot{q}_i(t), \quad (5)$$

then, the solution of any of the following differential equations,

$$\ddot{q}_a(t) = \frac{F_k(t, q_a(t), \dot{q}_a(t))}{\sum_{j=1}^N M_{k,j}(t, q_a(t), \dot{q}_a(t))} = G(t, q_a(t), \dot{q}_a(t)) \quad (6)$$

with vector field G , for the following set of initial conditions at the time instant t_0 ,

$$q_i(t_0) = q_a(t_0), \quad \text{for } i = 1, \dots, N, \text{ and } q_a(t_0) \in \mathbb{R}, \quad (7a)$$

$$\dot{q}_i(t_0) = \dot{q}_a(t_0), \quad \text{for } i = 1, \dots, N, \text{ and } \dot{q}_a(t_0) \in \mathbb{R}, \quad (7b)$$

is defining the generalized coordinates- q_i and their velocities in the exact augmented perpetual manifold,

$$\mathbf{X} = \left\{ (t, q_a(t), \dots, q_a(t), \dot{q}_a(t), \dots, \dot{q}_a(t)), (t, q_a(t), \dot{q}_a(t)) \in \mathbb{R}^3 \right\}. \quad (8)$$

The internal forces are comprised of all forces that can be in the left side of Eq. (4), and they are fulfilling the theorem requirements. The definition of physical boundaries of the perpetual mechanical system, whereas this is possible, can be done through the elements that correspond to the internal forces. In case that the overall system is not perpetual, the rest elements from the perpetual mechanical subsystem are considered as external forces and must fulfill the theorem requirements.

2.2 Corollary

Based on the above theorem that is proved in [21], the following corollary arises.

Corollary

The internal forces, of a perpetual natural nonlinear mechanical system and the underlying linear perpetual system, in the exact augmented perpetual manifolds are zero.

Proof

The equations of motion of a natural mechanical system arise by (4) when the inertia matrix is constant, and they are given by,

$$\begin{aligned} & [\mathbf{M}_{i,j}] \times \{\ddot{q}_i(t)\} + [\mathbf{C}_{i,j}] \times \{\dot{q}_i(t)\} + [\mathbf{K}_{i,j}] \times \{q_i(t)\} \\ & + \left\{ F_i^{NL}(q_n(t), \dot{q}_o(t)) \right\} = \left\{ F_i(t, q_p(t), \dot{q}_q(t)) \right\}, \quad \text{for } i=1, \dots, N, \quad j=1, \dots, N, \\ & n, o, p, q \in \{1, 2, \dots, N\}, \quad \text{and } (q_i(t), \dot{q}_i(t), \ddot{q}_i(t)) \in \mathbb{R}^3. \end{aligned} \quad (9)$$

In augmented perpetual manifolds, Eq. (9) is taking the form,

$$\begin{aligned}
 & \left[\mathbf{M}_{i,j} \right] \times \{ \ddot{q}_a(t) \} + \left[\mathbf{C}_{i,j} \right] \times \{ \dot{q}_a(t) \} + \left[\mathbf{K}_{i,j} \right] \times \{ q_a(t) \} + \left\{ F_i^{NL} (q_a(t), \dot{q}_a(t)) \right\} \\
 & = \{ F_i (t, q_a(t), \dot{q}_a(t)) \}, \text{ for } i = 1, \dots, N, \quad j = 1, \dots, N,
 \end{aligned}$$

$$\text{and } (q_a(t), \dot{q}_a(t), \ddot{q}_a(t)) \in \mathbb{R}^3. \tag{10}$$

The external forces are given by Eq. (5) and for constant inertia coefficients is taking the form,

$$F_i (t, q_a(t), \dot{q}_a(t)) = \frac{\sum_{j=1}^N M_{i,j} \cdot F_k (t, q_a(t), \dot{q}_a(t))}{\sum_{j=1}^N M_{k,j}}, \tag{11}$$

then, using Eq. (11) in Eq. (10) leads to,

$$\begin{aligned}
 & \left[\mathbf{M}_{i,j} \right] \times \{ \mathbf{1} \} \cdot \ddot{q}_a(t) + \left[\mathbf{C}_{i,j} \right] \times \{ \dot{q}_a(t) \} + \left[\mathbf{K}_{i,j} \right] \times \{ q_a(t) \} \\
 & + \left\{ F_i^{NL} (q_a(t), \dot{q}_a(t)) \right\} = \left\{ \sum_{j=1}^N M_{i,j} \right\} \cdot \frac{F_k (t, q_a(t), \dot{q}_a(t))}{\sum_{j=1}^N M_{k,j}}, \tag{12}
 \end{aligned}$$

and, considering Eq. (6) in Eq. (12) then, the following is true,

$$\begin{aligned}
 & \left\{ \sum_{j=1}^N M_{i,j} \right\} \cdot \ddot{q}_a(t) + \left[\mathbf{C}_{i,j} \right] \times \{ \dot{q}_a(t) \} + \left[\mathbf{K}_{i,j} \right] \times \{ q_a(t) \} \\
 & + \left\{ F_i^{NL} (q_a(t), \dot{q}_a(t)) \right\} = \left\{ \sum_{j=1}^N M_{i,j} \right\} \cdot \ddot{q}_a(t), \tag{13}
 \end{aligned}$$

that lead to,

$$\left[\mathbf{C}_{i,j} \right] \times \{ \dot{q}_a(t) \} + \left[\mathbf{K}_{i,j} \right] \times \{ q_a(t) \} + \left\{ F_i^{NL} (q_a(t), \dot{q}_a(t)) \right\} = \{ \mathbf{0} \}, \tag{14}$$

which means that the sum of all internal forces is zero. Regarding the underlying linear system Eqs. (10), (11), (12), (13), and (14) are still valid by omitting the nonlinear terms.

Noting that, in a document that the proof of the theorem is included, the above proof can be much more straightforward. The corollary is about the internal forces when the exact augmented perpetual manifolds are a solution of the perpetual

mechanical system. The augmented perpetual manifolds solution of a system admits zero velocity vectors which is excluded by the definition of the PPs. So it is not sufficient the requirement of the mechanical system to be only perpetual but, as the corollary states, needs also the existence of a solution in augmented perpetual manifolds that implies that for zero velocity vectors, as per theorem requirement, the nonlinear internal force, which is having any positions and velocities depended form, is zero. In case of zero velocities vector, the linear velocity-depended forces are zero.

3 Examples

On this section, the theory, in a 2-dof mechanical system with a configuration shown in Fig. 1, is applied. The analytical solutions, in the exact augmented perpetual manifolds, are also considered.

The equations of motion are given by,

$$\begin{aligned} & \begin{bmatrix} m_1 & 0 \\ 0 & m_2 \end{bmatrix} \times \begin{Bmatrix} \ddot{x}_1 \\ \ddot{x}_2 \end{Bmatrix} + \begin{bmatrix} k_l & -k_l \\ -k_l & k_l \end{bmatrix} \times \begin{Bmatrix} x_1 \\ x_2 \end{Bmatrix} + \begin{bmatrix} c_l & -c_l \\ -c_l & c_l \end{bmatrix} \times \begin{Bmatrix} \dot{x}_1 \\ \dot{x}_2 \end{Bmatrix} \\ & + \begin{Bmatrix} k_{nl} \cdot (x_1 - x_2)^3 + c_{nl} \cdot \tanh(b \cdot (\dot{x}_1 - \dot{x}_2)) + g_1 \cdot (x_1 - x_2)^4 \cdot (\dot{x}_1 - \dot{x}_2) \\ k_{nl} \cdot (x_2 - x_1)^3 + c_{nl} \cdot \tanh(b \cdot (\dot{x}_2 - \dot{x}_1)) + g_1 \cdot (x_2 - x_1)^4 \cdot (\dot{x}_2 - \dot{x}_1) \end{Bmatrix} \\ & = \begin{Bmatrix} f_1(t) \\ f_2(t) \end{Bmatrix} = \begin{Bmatrix} f_1(t) \\ m_2/m_1 \cdot f_1(t) \end{Bmatrix}. \end{aligned} \quad (15a)$$

The external forcing can be any function, and in this case the following form is considered,

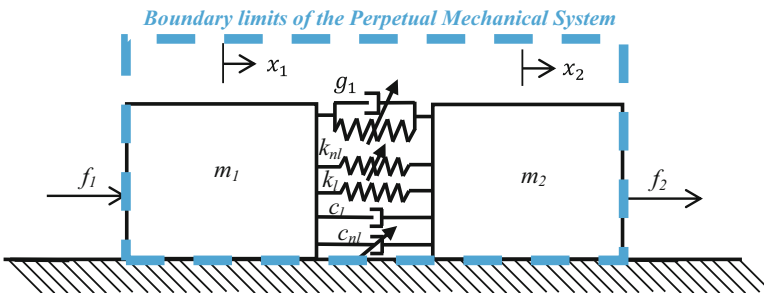


Fig. 1 The configuration of the 2-dof mechanical system

$$f_1(t) = A_{\text{ex}} \cdot \sin(\omega_{\text{ex}} \cdot t), \quad (15b)$$

and the internal forces are defined by,

$$\begin{aligned} \{F_{\text{int},i}\} = & \begin{bmatrix} k_l & -k_l \\ -k_l & k_l \end{bmatrix} \times \begin{Bmatrix} x_1 \\ x_2 \end{Bmatrix} + \begin{bmatrix} c_l & -c_l \\ -c_l & c_l \end{bmatrix} \times \begin{Bmatrix} \dot{x}_1 \\ \dot{x}_2 \end{Bmatrix} + \begin{Bmatrix} k_{\text{nl}} \cdot (x_1 - x_2)^3 \\ k_{\text{nl}} \cdot (x_2 - x_1)^3 \end{Bmatrix} \\ & + \begin{Bmatrix} c_{\text{nl}} \cdot \tanh(b \cdot (\dot{x}_1 - \dot{x}_2)) \\ c_{\text{nl}} \cdot \tanh(b \cdot (\dot{x}_2 - \dot{x}_1)) \end{Bmatrix} + \begin{Bmatrix} g_1 \cdot (x_1 - x_2)^4 \cdot (\dot{x}_1 - \dot{x}_2) \\ g_1 \cdot (x_2 - x_1)^4 \cdot (\dot{x}_2 - \dot{x}_1) \end{Bmatrix}. \end{aligned} \quad (15c)$$

The first two terms are well-known linear forces, the third term is corresponding to spring with cubic nonlinearity, the fourth term is smoothed dry friction force with b a constant having very high values to approximate ‘sudden jump’ in the vector field, and the fifth term is a generalized nonlinear force.

3.1 Analytical Solution

Neglecting the external forces in Eq. (15a) then the mechanical system can take the form,

$$\begin{aligned} & \begin{bmatrix} m_1 & 0 \\ 0 & m_2 \end{bmatrix} \times \begin{Bmatrix} \ddot{x}_1 \\ \ddot{x}_2 \end{Bmatrix} + \begin{bmatrix} k_l & -k_l \\ -k_l & k_l \end{bmatrix} \times \begin{Bmatrix} x_1 \\ x_2 \end{Bmatrix} + \begin{bmatrix} c_l & -c_l \\ -c_l & c_l \end{bmatrix} \times \begin{Bmatrix} \dot{x}_1 \\ \dot{x}_2 \end{Bmatrix} + \begin{Bmatrix} k_{\text{nl}} \cdot (x_1 - x_2)^3 \\ k_{\text{nl}} \cdot (x_2 - x_1)^3 \end{Bmatrix} \\ & + \begin{Bmatrix} c_{\text{nl}} \cdot \tanh(b \cdot (\dot{x}_1 - \dot{x}_2)) \\ c_{\text{nl}} \cdot \tanh(b \cdot (\dot{x}_2 - \dot{x}_1)) \end{Bmatrix} + \begin{Bmatrix} g_1 \cdot (x_1 - x_2)^4 \cdot (\dot{x}_1 - \dot{x}_2) \\ g_1 \cdot (x_2 - x_1)^4 \cdot (\dot{x}_2 - \dot{x}_1) \end{Bmatrix} = \begin{Bmatrix} 0 \\ 0 \end{Bmatrix}. \end{aligned} \quad (16)$$

Replacing the following,

$$x_1 = x_2 = x_a, \quad (17a)$$

$$\dot{x}_1 = \dot{x}_2 = \dot{x}_a, \quad (17b)$$

in Eq. (14) lead to,

$$\begin{bmatrix} m_1 & 0 \\ 0 & m_2 \end{bmatrix} \times \begin{Bmatrix} \ddot{x}_a \\ \ddot{y}_a \end{Bmatrix} = \begin{Bmatrix} 0 \\ 0 \end{Bmatrix} \implies \begin{Bmatrix} \ddot{x}_a \\ \ddot{y}_a \end{Bmatrix} = \begin{Bmatrix} 0 \\ 0 \end{Bmatrix}. \quad (18)$$

Therefore, when a solution given by Eq. (3) is considered, which is defining the exact rigid body motions, the accelerations are equal to zero.

Taking time derivative in Eqs. (14) then the system of jerk's equations arises as follows,

$$\begin{aligned}
 & \begin{bmatrix} m_1 & 0 \\ 0 & m_2 \end{bmatrix} \times \begin{Bmatrix} \ddot{\dot{x}}_1 \\ \ddot{\dot{x}}_2 \end{Bmatrix} + \begin{bmatrix} k_l & -k_l \\ -k_l & k_l \end{bmatrix} \times \begin{Bmatrix} \dot{x}_1 \\ \dot{x}_2 \end{Bmatrix} + \begin{bmatrix} c_l & -c_l \\ -c_l & c_l \end{bmatrix} \times \begin{Bmatrix} \ddot{x}_1 \\ \ddot{x}_2 \end{Bmatrix} \\
 & + \left\{ \begin{array}{l} 3 \cdot k_{nl} \cdot (x_1 - x_2)^2 \cdot (\dot{x}_1 - \dot{x}_2) + b \cdot c_{nl} \cdot \operatorname{sech}^2(b \cdot (\dot{x}_1 - \dot{x}_2)) \cdot (\ddot{x}_1 - \ddot{x}_2) \\ 3 \cdot k_{nl} \cdot (x_2 - x_1)^2 \cdot (\dot{x}_2 - \dot{x}_1) + b \cdot c_{nl} \cdot \operatorname{sech}^2(b \cdot (\dot{x}_2 - \dot{x}_1)) \cdot (\ddot{x}_2 - \ddot{x}_1) \end{array} \right\} \\
 & + \left\{ \begin{array}{l} 4 \cdot g_1 \cdot (x_1 - x_2)^3 \cdot (\dot{x}_1 - \dot{x}_2)^2 + g_1 \cdot (x_1 - x_2)^4 \cdot (\ddot{x}_1 - \ddot{x}_2) \\ -4 \cdot g_1 \cdot (x_2 - x_1)^3 \cdot (\dot{x}_2 - \dot{x}_1)^2 + g_1 \cdot (x_2 - x_1)^4 \cdot (\ddot{x}_1 - \ddot{x}_2) \end{array} \right\} = \begin{Bmatrix} 0 \\ 0 \end{Bmatrix}. \tag{19}
 \end{aligned}$$

In case, that the generalised coordinates and velocities are given by Eqs. (17a) and (17b), and considering Eq. (18), then the system of equations of jerks (Eq. 19) is taking the form,

$$\begin{bmatrix} m_1 & 0 \\ 0 & m_2 \end{bmatrix} \times \begin{Bmatrix} \ddot{\dot{x}}_a \\ \ddot{\dot{y}}_a \end{Bmatrix} = \begin{Bmatrix} 0 \\ 0 \end{Bmatrix} \implies \begin{Bmatrix} \ddot{\dot{x}}_a \\ \ddot{\dot{y}}_a \end{Bmatrix} = \begin{Bmatrix} 0 \\ 0 \end{Bmatrix}. \tag{20}$$

Therefore, also the jerks are equal to zero, and the system of Eq. (16) accepts as PPs the rigid body motions. The system of Eq. (16) corresponds to the mechanical system configuration shown in Fig. 1 by neglecting all the external forces. Considering that the external forces are given by Eq. (15a), all the requirements of the theorem are fulfilled, and the system has solutions in the exact augmented perpetual manifolds for equal initial displacements and equal initial velocities. Neglecting the nonlinearities in Eqs. (15) and (16) the associated linear system arises,

$$\begin{aligned}
 & \begin{bmatrix} m_1 & 0 \\ 0 & m_2 \end{bmatrix} \times \begin{Bmatrix} \ddot{x}_{L,1} \\ \ddot{x}_{L,2} \end{Bmatrix} + \begin{bmatrix} k_l & -k_l \\ -k_l & k_l \end{bmatrix} \times \begin{Bmatrix} x_{L,1} \\ x_{L,2} \end{Bmatrix} + \begin{bmatrix} c_l & -c_l \\ -c_l & c_l \end{bmatrix} \times \begin{Bmatrix} \dot{x}_{L,1} \\ \dot{x}_{L,2} \end{Bmatrix} \\
 & = \left\{ f_1(t) m_2 / m_1 \cdot f_1(t) \right\}, \tag{21}
 \end{aligned}$$

and, neglecting the external forces (equating right-hand side to zero), it is trivial to show, with a similar way, that it is a perpetual mechanical system. In both systems (linear and nonlinear systems) in the exact augmented perpetual manifolds, the solution for both masses is given by the solution of the following equation,

$$\ddot{x}_a = \frac{f_1(t)}{m_1}. \tag{22}$$

The internal forces defined by the Eq. (15c) in the exact augmented perpetual manifolds are given by,

$$\begin{aligned}
 \{F_{\text{int},a,i}\} &= \begin{bmatrix} k_l & -k_l \\ -k_l & k_l \end{bmatrix} \times \begin{Bmatrix} x_a(t) \\ x_a(t) \end{Bmatrix} + \begin{bmatrix} c_l & -c_l \\ -c_l & c_l \end{bmatrix} \times \begin{Bmatrix} \dot{x}_a(t) \\ \dot{x}_a(t) \end{Bmatrix} \\
 &+ \begin{Bmatrix} k_{nl} \cdot (x_a(t) - x_a(t))^3 \\ k_{nl} \cdot (x_a(t) - x_a(t))^3 \end{Bmatrix} + \begin{Bmatrix} c_{nl} \cdot \tanh(b \cdot (\dot{x}_a(t) - \dot{x}_a(t))) \\ c_{nl} \cdot \tanh(b \cdot (\dot{x}_a(t) - \dot{x}_a(t))) \end{Bmatrix} \\
 &+ \begin{Bmatrix} g_1 \cdot (x_a(t) - x_a(t))^4 \cdot (\dot{x}_a(t) - \dot{x}_a(t)) \\ g_1 \cdot (x_a(t) - x_a(t))^4 \cdot (\dot{x}_a(t) - \dot{x}_a(t)) \end{Bmatrix} = \begin{Bmatrix} 0 \\ 0 \end{Bmatrix}. \quad (23a)
 \end{aligned}$$

Therefore, the internal forces of the perpetual mechanical system in the exact augmented perpetual manifolds are all zero. The internal forces, of the underlying linear system, can be obtained by neglecting the nonlinear forces in Eq. (15c), and in the augmented perpetual manifolds are given by,

$$\{F_{\text{int},L,a,i}\} = \begin{bmatrix} k_l & -k_l \\ -k_l & k_l \end{bmatrix} \times \begin{Bmatrix} x_{L,a}(t) \\ x_{L,a}(t) \end{Bmatrix} + \begin{bmatrix} c_l & -c_l \\ -c_l & c_l \end{bmatrix} \times \begin{Bmatrix} \dot{x}_{L,a}(t) \\ \dot{x}_{L,a}(t) \end{Bmatrix} = \begin{Bmatrix} 0 \\ 0 \end{Bmatrix}. \quad (23b)$$

Considering the explicit form of external forces given by Eq. (15b) in Eq. (22), then, after direct integrations, the solution of the system in the exact augmented perpetual manifold is given by,

$$\begin{aligned}
 \dot{x}_1(t) &= \dot{x}_{L,1}(t) = \dot{x}_2(t) = \dot{x}_{L,2}(t) = \dot{x}_a(t) \\
 &= -\frac{A_{\text{ex}}}{m_1 \cdot \omega_{\text{ex}}} \cdot \cos(\omega_{\text{ex}} \cdot t) + \frac{A_{\text{ex}} \cdot \cos(\omega_{\text{ex}} \cdot t_0)}{m_1 \cdot \omega_{\text{ex}}} + \dot{x}_a(t_0), \quad (24a) \\
 x_1(t) &= x_{L,1}(t) = x_2(t) = x_{L,2}(t) = x_a(t) = -\frac{A_{\text{ex}}}{m_1 \cdot \omega_{\text{ex}}^2} \cdot \sin(\omega_{\text{ex}} \cdot t) \\
 &+ \left(\frac{A_{\text{ex}} \cdot \cos(\omega_{\text{ex}} \cdot t_0)}{m_1 \cdot \omega_{\text{ex}}} + \dot{x}_a(t_0) \right) \cdot (t - t_0) + \frac{A_{\text{ex}} \cdot \sin(\omega_{\text{ex}} \cdot t_0)}{m_1 \cdot \omega_{\text{ex}}^2} + x_a(t_0). \quad (24b)
 \end{aligned}$$

In the next section, the analytical findings with the numerical simulations are verified.

3.2 Numerical Solution

A car with mass $m_1 = 1500$ kg, coupled with a van of mass $m_2 = 1000$ kg are considered. The linear stiffness of coupler is $k_l = 5 \cdot 10^5$ N/m and the nonlinear stiffness is $k_{nl} = 3 \cdot 10^5$ N/m³. The linear modal analysis of the unforced system can be done by neglecting damping forces and setting as zero the right-hand side of Eq. (21), and leads to the following natural frequencies (ω_i); for the first mode $\omega_1 = 0$ rad/s and $\omega_2 = 28.87$ rad/s for the second mode with period $T_2 = 0.2176$ s. The damping coefficient is $c_l = 346.41$ N · s/m and, arises by considering 1% damping ratio for the second mode. The nonlinear damping coefficient has the same value $c_{nl} = 516.398$ N with $b = 10^6$ s/m (significantly high to approximate dry friction), and the generalized force coefficient is given by $g_1 = 5 \cdot 10^5$ N · s/m⁵. The simulations time interval is $4 \cdot T_2 = 0.8706237$ s. The excitation frequency is equal to the second natural frequency (ω_2) of the associated linear system. During the first half-time the excitation amplitude is $A_{ex,1} = 5 \cdot 10^6$ N and for the second half is $A_{ex,2} = -4.3301269 \cdot 10^6$ N. The initial conditions are $x_1(0) = x_{L,1}(0) = x_2(0) = x_{L,2}(0) = 1$ m and $\dot{x}_1(0) = \dot{x}_{L,1}(0) = \dot{x}_2(0) = \dot{x}_{L,2}(0) = 100$ m/s.

All the numerical simulations have been performed with Scilab 5.5.2 64-bit [22]. The solver is ‘Adams’ with time step $dt = T_2/1000 = 2.176 \cdot 10^{-4}$ s and, the relative and absolute tolerance are both of $3 \cdot 10^{-16}$.

In Fig. 2a, b, the transient responses (velocities) are depicted, which are obtained from the numerical simulations of both nonlinear and linear systems, the analytical solutions, given by Eqs. (24a, 24b), are also incorporated. It can be seen clearly that all the masses are having the same displacements and the same velocities.

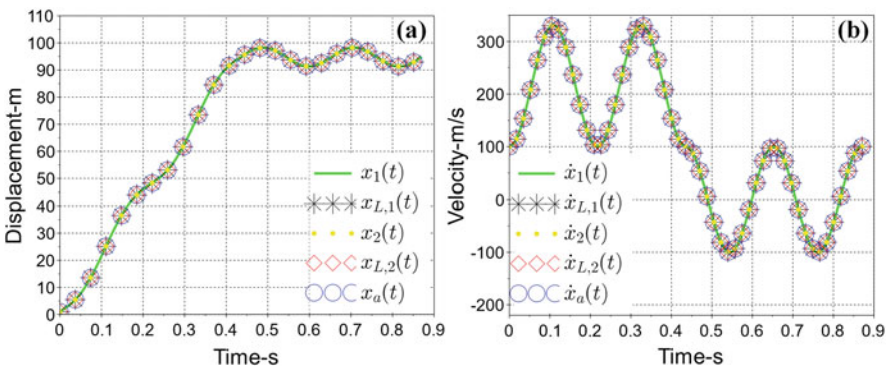


Fig. 2 (a) Displacements, (b) velocities

Table 1 The maximum absolute differences of the time series describing the dynamics

i	$\max x_i(t) - x_a(t) $ (m)	$\max x_{L,i}(t) - x_a(t) $ (m)	$\max \dot{x}_i(t) - \dot{x}_a(t) $ (m/s)	$\max \dot{x}_{L,i}(t) - \dot{x}_a(t) $ (m/s)
1	4.765×10^{-11}	1.450×10^{-12}	1.269×10^{-10}	4.868×10^{-12}
2	4.763×10^{-11}	1.506×10^{-12}	1.269×10^{-10}	3.752×10^{-12}

Table 2 The maximum absolute value of internal forces of the nonlinear and linear systems

$\max F_{\text{int}, a, 1}(t) $ (N)	$\max F_{\text{int}, L, a, 1}(t) $ (N)	$\max f_1(t) $ (N)
1.378×10^{-4}	4.966×10^{-8}	5.00×10^6

Moreover, in Table 1, the maximum absolute differences, of the responses and the velocities with the analytical solution, are shown. Their maximums of the maximums are of -10 order of magnitude, and considering that the actual values are greater than 1, these differences can be definitely attributed to numerical errors. This is further justified by the fact that these errors are much higher in the nonlinear system.

Therefore, the motion of the mechanical system is described by the exact augmented perpetual manifolds.

In Table 2 the maximum absolute values of the internal forces on the nonlinear system are shown, with maximum being -4 order of magnitude whereas the maximum of the excitation force is 10 orders of magnitude higher. The maximum value of the internal forces, on the underlying linear system, is of -8 order of magnitude. The nonzero values of the internal forces, since they are minimal with respect to the values of the actual forces in the equations of motion, and considering that they are much higher in the nonlinear system, can be attributed to numerical errors. These minimal values of internal forces are certifying the corollary of this article.

4 Discussion and Conclusions




In this article, a corollary is proved, stating that the perpetual natural mechanical systems, in the exact augmented perpetual manifolds, are internal forces-free. The corollary has been verified analytically and numerically in a 2-dof nonlinear system and the associated underlying linear system. The validity of this corollary is restricted only to natural mechanical systems, and the internal forces of unnatural mechanical systems can be discussed elsewhere. Also, in cases that the overall mechanical system is not perpetual, then the corollary is limited to the boundaries that define the perpetual mechanical subsystem. This corollary is rather significant in mechanics, since the internal forces of the mechanical systems are the main reason for failures.

References

1. A. Prasad, Existence of perpetual points in nonlinear dynamical systems and its applications. *Int. J. Bif. Chaos* **25**(2), 1530005 (2015)
2. P. Brzeski, L.N. Virgin, Experimental investigation of perpetual points in mechanical systems. *Nonlinear Dyn.* **90**, 2917–2928 (2017)
3. D. Dudkowsi, A. Prasad, T. Kapitaniak, Perpetual points and periodic perpetual loci in maps. *Chaos* **26**, 103103 (2016)
4. A. Prasad, A note on topological conjugacy for perpetual points. *Int. J. Nonlinear Sci.* **21**(1), 60–64 (2016)
5. D. Dudkowsi, A. Prasad, T. Kapitaniak, Perpetual points and hidden attractors in dynamical systems. *Phys. Lett. A* **379**(40–41), 2591–2596 (2015)
6. D. Dudkowsi, S. Jafari, T. Kapitaniak, N.V. Kuznetsov, G.A. Leonov, A. Prasad, Hidden attractors in dynamical systems. *Phys. Rep.* **637**, 1–50 (2016)
7. D. Dudkowsi, A. Prasad, T. Kapitaniak, Perpetual points: New tool for localization of coexisting attractors in dynamical systems. *Int. J. Bif. Chaos* **27**(4), 1750063 (2017)
8. F. Nazaimehr, B. Saaeidi, S. Jafari, J.C. Sprott, Are perpetual points sufficient for locating hidden attractors? *Int. J. Bif. Chaos* **27**(3) (2017)
9. F. Nazaimehr, S. Jafari, S.M.R.H. Golpayegani, J.C. Sprott, Categorizing chaotic flows from the viewpoint of fixed points and perpetual points. *Int. J. Bif. Chaos* **27**(2), 1750023 (2017)
10. D. Dudkowsi, A. Prasad, T. Kapitaniak, Describing chaotic attractors: Regular and perpetual points. *Chaos* **28**(3), 033604 (2018)
11. N.V. Kuznetsov, G.A. Leonov, T.N. Mokaev, A. Prasad, M.D. Shrimali, Finite-time Lyapunov dimension and hidden attractor of the Rabinovich system. *Nonlinear Dyn.* **92**, 267–285 (2018)
12. S.N. Chowdhury, D. Ghosh, Hidden attractors: A new chaotic system without equilibria. *Eur. Phys. J. Special Top.* **229**, 1299–1308 (2020)
13. F. Yu, Z. Zhang, L. Liu, H. Shen, Y. Huang, C. Shi, S. Cai, Y. Song, S. Du, Q. Xu, Secure communication scheme based on a new 5D multistable four-wing Memristive Hyperchaotic system with disturbance inputs. *Complexity* **2020**, 5859273 (2020)
14. S. Jafari, F. Nazaimehr, J.C. Sprott, S.M.R.H. Golpayegani, Limitation of perpetual points for confirming conservation in dynamical systems. *Int. J. Bif. Chaos* **25**, 1550182 (2015)
15. S. Cang, A. Wu, Z. Wang, Z. Chen, Four-dimensional autonomous dynamical systems with conservative flows: Two-case study. *Nonlinear Dyn.* **89**, 2495–2508 (2017)
16. P. Brzeski, L.N. Virgin, System identification of energy dissipation in a mechanical model undergoing high velocities: An indirect use of perpetual points. *Mech. Sys. Signal Proces.* **108**, 115–125 (2018)
17. A. Wu, S. Cang, R. Zhang, Z. Wang, Z. Chen, Hyperchaos in a conservative system with nonhyperbolic fixed points. *Complexity* **2018**, 9430637 (2018)
18. N. Wang, G. Zhang, H. Bao, Infinitely many coexisting conservative flows in a 4D conservative system inspired by LC circuit. *Nonlinear Dyn.* **99**, 3197–3216 (2020)
19. F. Georgiades, Theorem and observation about the nature of perpetual points in conservative mechanical systems, in *Exploiting NonLinear Dynamics for Engineering Systems, 'ENOLIDES'*, IUTAM Bookseries, ed. by I. Kovacic, S. Lenci, (Springer Nature, Cham, 2020), pp. 91–104
20. Georgiades, F.: Perpetual points in natural dissipative with viscous damping mechanical systems: a theorem and a remark. *Proc. of IMechE: Part-C J. of Mech. Eng. Sci.* (2020)
21. F. Georgiades, Augmented perpetual manifolds and perpetual mechanical systems-part I: definitions, theorem and corollary for triggering perpetual manifolds, application in reduced order modeling and particle-wave motion of flexible mechanical systems, *ASME. J. Comput. Nonlinear Dyn.* **16**(7), 19, 071005 (2021). <https://doi.org/10.1115/1.4050554>
22. The Scilab Team, version 5.5.2 (2015). <http://scilab.org>

Application of RFEM to Modelling Dynamics of Lattice-boom Offshore Cranes



Marek Metelski , Iwona Adamiec-Wójcik , Łukasz Drag ,
and Stanisław Wojciech 

1 Introduction

The development of offshore oil platforms and vessels, as well as offshore wind farms, requires the design and manufacture of specialized equipment for their maintenance. Cranes play an important role among such equipment, and those designed for offshore operations have to meet special requirements due to the sea environment in which they operate. Models used by offshore crane designers have to take into account motions of the base (vessel or platform) on which the crane is mounted, and complex conditions of lowering and lifting the loads such as waves and strong winds. Lattice booms are often used in practice because of two important characteristics: relatively light weight and high strength. The design of lattice-boom offshore cranes requires not only statics and linear vibration analysis, which can be performed using commercial software based on the finite element method. In many cases, in particular, those relating to the simulation of the overload protection systems such as AOPS (Active Overload Protection System), optimization calculations are needed. Those calculations require complex models of dynamics which take into consideration the base motion of the crane, wind influence or movements of the loads caused by the movement of supply vessels. These specialized dynamic calculations usually use authors' models tailored to specific needs and requirements of design companies.

In modelling crane dynamics some research does not take into account the flexibility of booms [1] but more often the flexibility is considered [2–5]. The

M. Metelski
Protea S.A., Gdańsk, Poland
e-mail: marek.metelski@protea.pl

I. Adamiec-Wójcik · Ł. Drag (✉) · S. Wojciech
University of Bielsko-Biała, Bielsko-Biała, Poland
e-mail: i.adamiec@ath.bielsko.pl; ldrag@ath.bielsko.pl; swojciech@ath.bielsko.pl

models created are based, among others, on the finite element method (FEM) [6, 7], the rigid finite element method (RFEM) [1, 2], and the modal method [8].

Authors' own models of cranes with lattice booms are relatively rarely encountered. This is especially because the structure of the boom is complex and the number of degrees of freedom describing deformations of the truss rods is very large; thus computer simulation time is long.

This paper presents an application of the rigid finite element method [9, 10] to modelling the flexibility of lattice booms in dynamics. Previous authors' works were concerned merely with statics [2]. The nodes at which the rods of the truss are connected are chosen as generalized coordinates. Validation of the boom model is carried out in the range of static analysis. Results of calculations concerning free and forced vibrations of the cranes with lattice booms are also presented.

2 Crane Model

Figure 1 shows lattice boom cranes with two types of slewing mechanism: cylinder and rope.

If the dynamics of the slewing mechanism are omitted, the two above cases can be included in the model presented in Fig. 2.

The following notation is assumed:

- { } – inertial coordinate system with axes x, y, z
- { }[~] – coordinate system assigned to the base vessel with axes $\tilde{x}, \tilde{y}, \tilde{z}$
- { }⁻ – coordinate system assigned to the rotary pedestal of the crane with axes $\bar{x}, \bar{y}, \bar{z}$.
- { }^s – coordinate system assigned to the supply vessel.

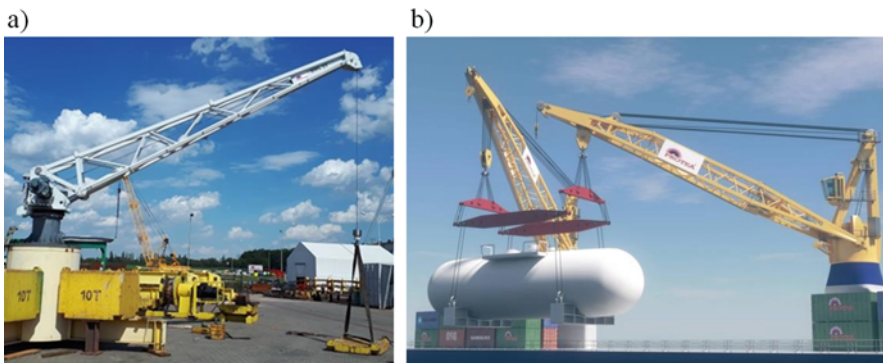


Fig. 1 Lattice boom cranes with (a) cylinder and (b) rope slewing mechanism

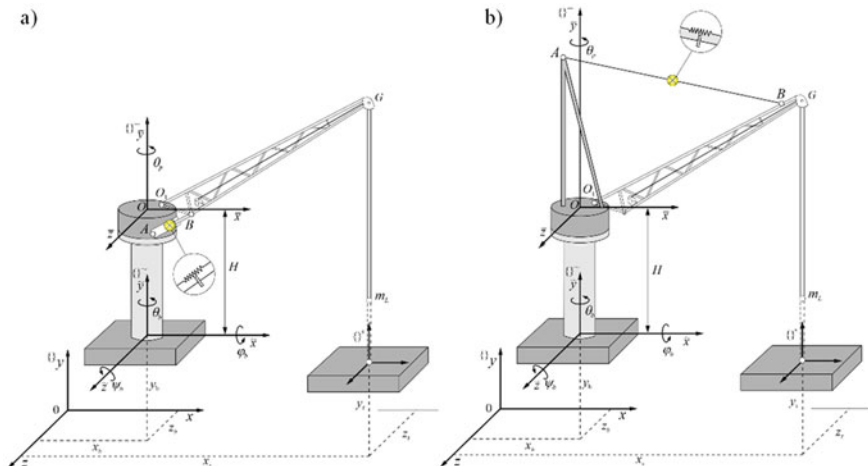


Fig. 2 General scheme of the crane with slewing mechanism (a) cylinder, (b) rope

It is assumed that the motion of the base vessel is known in the form of the following vector:

$$\mathbf{q}_b = \mathbf{q}_b(t) = [x_b(t) \ y_b(t) \ z_b(t) \ \psi_b(t) \ \theta_b(t) \ \varphi_b(t)]^T, \tag{1}$$

where functions $x_b(t), y_b(t), z_b(t)$ describe the position of a chosen point of the base vessel and $\psi_b(t), \theta_b(t), \varphi_b(t)$ are ZYX Euler angles defining the orientation of the base vessel with respect to the inertial coordinate system, namely orientation of axes $\tilde{x}, \tilde{y}, \tilde{z}$ of $\{\tilde{\cdot}\}$ in relation to axes x, y, z of $\{\cdot\}$.

Having used homogenous transformations, coordinates \mathbf{r}^\sim of system $\{\tilde{\cdot}\}$ can be expressed in the inertial frame $\{\cdot\}$ as follows:

$$\mathbf{r} = \mathbf{B}_b \mathbf{r}^\sim, \tag{2}$$

where $\mathbf{r} = [x \ y \ z \ 1]^T$ is the vector of coordinates in system $\{\cdot\}$, $\mathbf{r}^\sim = [\tilde{x} \ \tilde{y} \ \tilde{z} \ 1]^T$ is the vector of coordinates in system $\{\tilde{\cdot}\}$, $\mathbf{B}_b = \begin{bmatrix} \mathbf{R}_b & \mathbf{r}_b \\ 0 & 1 \end{bmatrix}$, $\mathbf{r}_b = [x_b \ y_b \ z_b]^T$, \mathbf{R}_b is the rotation matrix.

Coordinates from system $\{\tilde{\cdot}\}$ (assigned to the rotary part of the crane) can be transformed to the inertial coordinate system using the following formula:

$$\mathbf{r} = \mathbf{B}^{(p)} \bar{\mathbf{r}}, \tag{3}$$

where \mathbf{r} is defined by (1), $\bar{\mathbf{r}}$ is the vector of local coordinates in system $\{\tilde{\cdot}\}$,

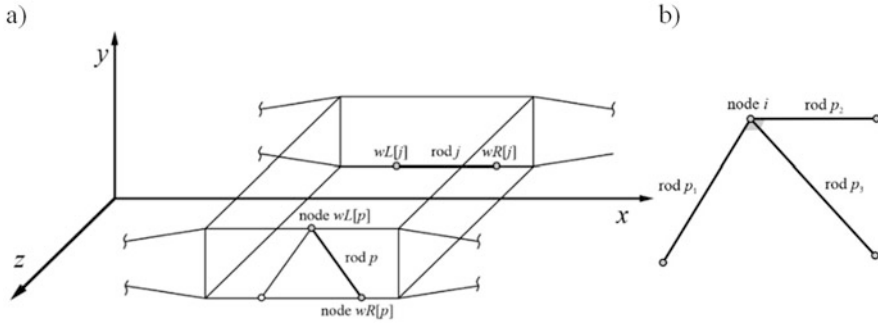


Fig. 3 Beam model of a lattice-boom (a) boom segment, (b) node with rods

$$\mathbf{P} = \begin{bmatrix} c\theta_P & 0 & s\theta_P & 0 \\ 0 & 1 & 0 & H \\ -s\theta_P & 0 & c\theta_P & 0 \\ 0 & 0 & 0 & 1 \end{bmatrix}$$

is the transformation matrix from system $\{ \}^-$ to

system $\{ \}^{\sim}$, $\mathbf{B}^{(p)} = \mathbf{B}_p \mathbf{P}$, θ_P is the angle of platform rotation.

In the above formula and further in the paper the following notation is used: $sa = \sin(a)$, $ca = \cos(a)$.

It is assumed that the main structure of the lattice-boom consists of boom sections connected consecutively. The boom section in general can be treated as a spatial truss (Fig. 3a) with a different number of members connecting the four main beams, which can also differ in mass and geometric parameters.

The members of the lattice section are treated as beams, which means that they undergo bending, shearing as well as longitudinal and torsional deformations. The rods (members of the lattice section) are firmly connected in a node (Fig. 3b), which means that the displacements of the rods p_1, p_2, p_3 in node i ($i = 1..n$) are the same. The initial position of all nodes before deformation of the lattice-boom is known in the following form

$$\bar{\mathbf{r}}_{i,0} = [\bar{x}_{i,0} \ \bar{y}_{i,0} \ \bar{z}_{i,0}]^T \text{ for } i = 1, \dots, n. \tag{4}$$

The coordinates of vectors (4) are defined in the reference system $\{ \}^-$. The position and configuration of each rod of the boom ($p = 1..m$) are defined by its left $wL[p]$ and right $wR[p]$ nodes. The orientation of the rods is defined using ZYX Euler angles and the geometry of the boom is described by means of homogenous transformations. The vector of generalized coordinates describing the displacements of the nodes consists of six components:

$$\mathbf{q}_i = [x_i \ y_i \ z_i \ \psi_i \ \theta_i \ \varphi_i]^T \text{ for } i = 1, \dots, n. \tag{5}$$

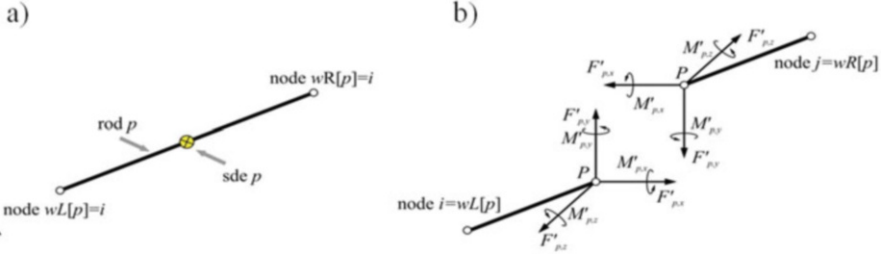


Fig. 4 (a) Discretization of rod p , (b) forces and moments acting at sde p

where x_i, y_i, z_i are translations in the $\bar{x}, \bar{y}, \bar{z}$ directions respectively in coordinate system $\{\bar{\cdot}\}$, $\psi_i, \theta_i, \varphi_i$ are the respective ZYX Euler angles.

Axes \bar{x}, \bar{y} are in the plane of the boom. The deviation of the \bar{x} -axis from \tilde{x} -axis defines angle θ_p of platform rotation.

It is assumed that axes of the local coordinate system connected with i node are parallel to the platform coordinate system $\{\bar{\cdot}\}$. When coordinate systems are chosen in such a way, the transformation of coordinates from the local system of node $\{i\}'$ to the global system $\{\bar{\cdot}\}$ can be performed according to the formula

$$\mathbf{r} = \mathbf{B}^{(p)} \mathbf{A}_i \mathbf{r}', \tag{6}$$

where $\mathbf{A}_i = \begin{bmatrix} c\psi_i c\theta_i & c\psi_i s\theta_i s\varphi_i - s\psi_i c\varphi_i & c\psi_i s\theta_i c\varphi_i + s\psi_i s\varphi_i & x_i \\ s\psi_i c\theta_i & s\psi_i s\theta_i s\varphi_i + s\psi_i c\varphi_i & s\psi_i s\theta_i c\varphi_i - s\psi_i s\varphi_i & y_i \\ -s\theta_i & c\theta_i s\varphi_i & c\theta_i c\varphi_i & z_i \\ 0 & 0 & 0 & 1 \end{bmatrix}$,

$\mathbf{B}^{(p)}$ is defined in (3).

Rod elements are discretized using the rigid finite element method [9], and respective forces and moments transferred by spring damping elements (sdes) (Fig. 4) of the rods are calculated.

Forces $\mathbf{F}'_{\mathbf{p}} = [F'_{p,x} \ F'_{p,y} \ F'_{p,z}]^T$ and moments $\mathbf{M}'_{\mathbf{p}} = [M'_{p,x} \ M'_{p,y} \ M'_{p,z}]^T$ transferred by spring-damping elements are derived and introduced into the equilibrium equations by means of generalized forces [9] at the end nodes of rod p .

The equations of motion are derived from the Lagrange equations of the second order. When calculating the kinetic energy, we consider masses and inertial moments of rods, the halves of which are connected in the nodes (Fig. 3b). If we assume that $\mathbf{\Omega}_p$ is the rotation matrix defining the position of rod p in system $\{\bar{\cdot}\}'$ before deformation, then the kinetic energy of node i is defined by the following expression:

$$E_i = \sum_{j=1}^{n_i} E_{i,j} = \frac{1}{2} \sum_{j=1}^{n_i} \int_{m_{p_{i,j}/2}}^{m_{p_{i,j}}} tr \left\{ \dot{\mathbf{r}}_i \dot{\mathbf{r}}_i^T \right\} dm \tag{7}$$

where n_i is the number of rods' halves meeting at node i , $\mathbf{r} = \mathbf{B}^{(p)} \mathbf{A}_i \mathbf{A}_{p_{i,j}} \mathbf{r}'_{p_{i,j}}$, $p_{i,j}$ is the number of rod j in global numbering, $\mathbf{r}'_{p_{i,j}}$ are local coordinates of rod $p_{i,j}$,

$$\mathbf{A}_{p_{i,j}} = \begin{bmatrix} \boldsymbol{\Omega}_{p_{i,j}} & 0 \\ 0 & 1 \end{bmatrix}.$$

Because matrices $\boldsymbol{\Omega}_{p_{i,j}}$ and $\mathbf{A}_{p_{i,j}}$ after transformation from the system of the rod to node system $\{i\}$ have constant elements, the expression for the kinetic energy can be presented in the form:

$$E_i = \frac{1}{2} tr \left\{ \dot{\mathbf{B}}_i \mathbf{H}_i \dot{\mathbf{B}}_i^T \right\} \tag{8}$$

where $\mathbf{B}_i = \mathbf{B}^{(p)} \mathbf{A}_i$, $\mathbf{H}_i = \sum_{j=1}^{n_i} \mathbf{A}_{p_{i,j}} \mathbf{H}_{p_{i,j}} \mathbf{A}_{p_{i,j}}^T$, $\mathbf{H}_{p_{i,j}}$ is the pseudo-inertial matrix of the halve of rod $p_{i,j}$ added to node i .

Having considered the load, winch and the rope system, the equations of motion of the crane can be written as follows:

$$\mathbf{M} \ddot{\mathbf{q}} = \mathbf{f} \tag{9}$$

where $\mathbf{M} = \begin{bmatrix} \mathbf{M}_0 & \dots & \mathbf{0} & \dots & \mathbf{0} & \mathbf{M}_{0r} & \mathbf{0} & \mathbf{0} \\ \vdots & \ddots & \vdots & & \vdots & \vdots & \vdots & \vdots \\ \mathbf{0} & \dots & \mathbf{M}_i & \dots & \mathbf{0} & \mathbf{M}_{ir} & \mathbf{0} & \mathbf{0} \\ \vdots & & \vdots & \ddots & \vdots & \vdots & \vdots & \vdots \\ \mathbf{0} & \dots & \mathbf{0} & \dots & \mathbf{M}_n & \mathbf{M}_{nr} & \mathbf{0} & \mathbf{0} \\ \mathbf{M}_{0r}^T & \dots & \mathbf{M}_{ir}^T & \dots & \mathbf{M}_{nr}^T & m_r & \mathbf{0} & \mathbf{0} \\ \mathbf{0} & \dots & \mathbf{0} & \dots & \mathbf{0} & \mathbf{0} & \mathbf{M}_L & \mathbf{0} \\ \mathbf{0} & \dots & \mathbf{0} & \dots & \mathbf{0} & \mathbf{0} & \mathbf{0} & I_D \end{bmatrix},$

$\mathbf{r}_L = \{x_L \ y_L \ z_L\}^T$ are coordinates of the load, θ_p is the rotation angle of the pedestal, φ_D is the rotation angle of the winch drum, \mathbf{q}_i is the coordinate vector of node i of the lattice.

The dynamic model and the computer program are applied to the analysis of a crane's strength characteristics for the wind platforms produced by the Protea company. The software elaborated is used by designers when selecting the individual crane components (boom construction, swing and/or winch type). In the first step, the static calculations are performed to confirm the correct selection of materials and boom rod cross-sections for the assumed load capacity to meet

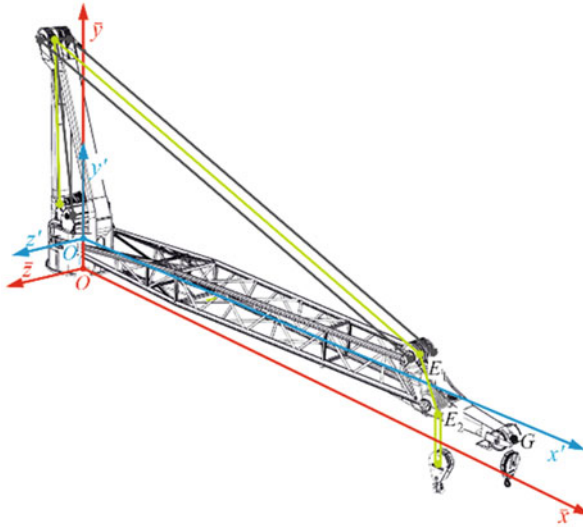


Fig. 5 Scheme of the crane

Table 1 Deflection of the boom at point G

Crane radius [m]	SWL [10^4 N]	RFEM model				ROBOT				δ [%]
		u_x [m]	u_y [m]	u_z [m]	u [m]	u_x [m]	u_y [m]	u_z [m]	u [m]	
2.7	268	77.99	-10.12	-10.59	79.4	78.0	-9.2	-11.0	79.3	0.06
17	460	59.64	-43.30	-10.00	74.4	58.5	-41.8	-11.0	72.7	2.21
30	460	16.18	-70.67	-5.69	72.7	16.6	-69.7	-6.6	72.0	1.06

the requirements of the regulatory bodies. In addition, dynamic calculations are performed in order to take into account the movement of the base vessel during typical seagoing service operations (lifting and lowering cargo, rotation of the crane) and emergency situations involving the activation of the overload system (AOPS), for example, when attaching a hook to the side of the delivery vessel.

Figure 5 shows the scheme of the crane used for verification of the model and computer programme. The authors’ own results concerned with statics are compared with the results of simulations carried out using the software package ROBOT.

For calculations, it is assumed that forces $F_x = 40 \cdot 10^4$ N, $F_y = -SWL$, $F_z = -40 \cdot 10^4$ N act at point E_2 of the boom end. The simulation results presented in Table 1 show good agreements of the static deflections. The error is smaller than 3%. Other results concerned with forces and stresses in selected rods and the rope are presented in [2].

The next section presents the results of the static and dynamic simulations for a light-service crane used on wind platforms, where the change of elevation is performed by means of a single cylinder.

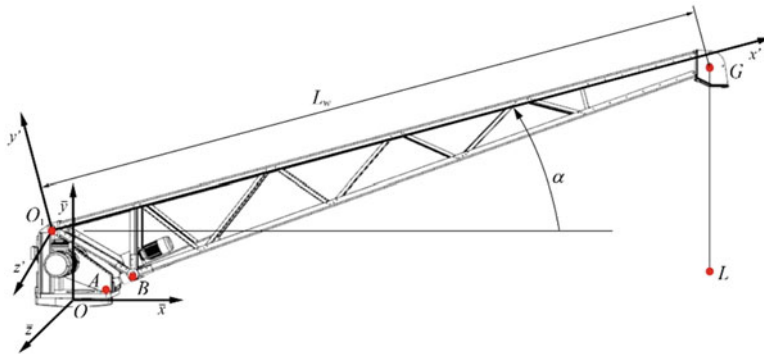


Fig. 6 Characteristic points of the service crane analysed

Table 2 Coordinates of the characteristic points of the crane

Point	Coordinates
Attachment of the boom – point $O_1 (\bar{x}_{O_1}, \bar{y}_{O_1})$ [m]	-0.19; 0.82
Connection of the cylinder with the pedestal – point $A (\bar{x}_A, \bar{y}_A)$ [m]	0.345; 0.102
Connection of the cylinder with the boom – point $B (x'_B, y'_B)$ [m]	0.683; -0.806
Calculation of loading, deflection – point $G(x'_G, y'_G)$ [m]	8.3; -0.111

3 Simulation Results

Simulations are carried out for a 2 mT service crane. Notations of attachment points for the boom and cylinder as well as the point for calculating deflections are presented in Fig. 6. It is assumed that the boom is mounted at point O_1 , and connections of the cylinder with the rotary pedestal and with the boom are denoted by points A and B . Point G marks the position on the boom in which the load is applied and deflections u_y and u_z of the boom are calculated (displacements of point G along axes OY and OZ).

The boom is constructed of 36 rods made of material of the same strength characteristics (Young modulus $E = 207$ GPa, Poisson number $\nu = 0.3$, material density $\rho = 7850$ kgm⁻³). The boom has four load-bearing beams connected by means of the rods. The beams have a closed square cross-section of 0.1m \times 0.1m with thickness 0.0065 m; the rods have a circular cross section with diameters of 0.0051 m and 0.004 m wall thickness. The total mass of the boom is 961 kg and its length is $L_w = 8.23$ m.

Table 2 presents the geometric data of the crane analysed, namely the coordinates of the characteristic points.

The crane extension mechanism has only one hydraulic cylinder. Cylinder geometry and its some other parameters are presented in Table 3.

At the beginning, horizontal static deflections of the boom and the lowest natural frequencies in xy and xz planes were calculated. Calculations were performed

Table 3 Cylinder parameters

Parameter	Value
Outer diameter of the cylinder D_{Cout} [m]	0.165
Inner diameter of the cylinder D_{Cin} [m]	0.14
Outer diameter of the rod d [m]	0.13
Minimal length of the boom L_{min} [m]	0.36
Extension of the cylinder L_{stroke} [m]	1.03

Table 4 Vertical U_y and horizontal U_z deflections of the boom, first natural frequencies ω_{xy} and ω_{xz}

Parameter	Value
Vertical deflection of the boom U_y [m]	-0.0203
Horizontal deflection of the boom U_z [m]	0.0065
First natural frequency in xy plane - ω_{xy} [Hz]	76.58
First natural frequency in xz plane - ω_{xz} [Hz]	40.74

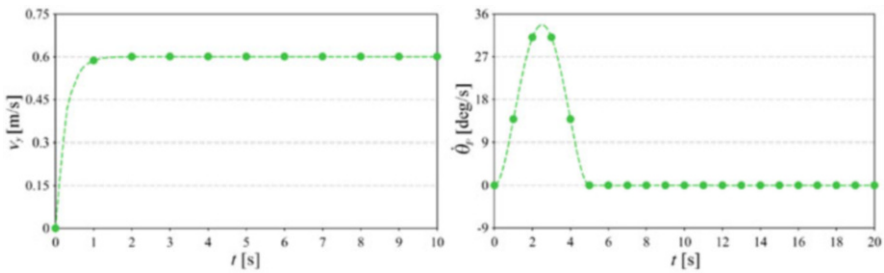


Fig. 7 Courses of vertical velocity v_y of the load and angular velocity $\dot{\theta}_P$ of crane pedestal rotation

assuming a load on the boom by means of these forces: vertical $F_y = 20,000$ N and horizontal $F_z = 2000$ N; gravitational load was also considered. Flexibility of the cylinder was taken into account. The calculation results including deflections of the crane and first natural frequencies are presented in Table 4.

The vertical velocity of the load (Fig. 7a) increases from zero up to nominal value $v_{nom} = 0.6$ m/s over 2 s. This causes relatively small vibrations of the boom with amplitude $a_{u,y} =$ approx. 0.006 m (Fig. 8a). The overload coefficient is defined as follows:

$$\eta = S/S_{nom} \tag{10}$$

where S – the force in the rope, $S_{nom} = m_L g / i_r$, i_r – transmission ratio of the rope system, does not exceed 1.23 (Fig. 8b). When rotation is considered with velocity increasing from zero to 34 deg/s (Fig. 7b), the deflections of the boom end and overload coefficient are larger ($a_{u,y} = 0.02$ m, $\eta = 1.35$).

Courses of deflections u_y and u_z of the crane and overload coefficient η in the rope obtained by simulating both tasks are presented in Figs. 8 and 9.

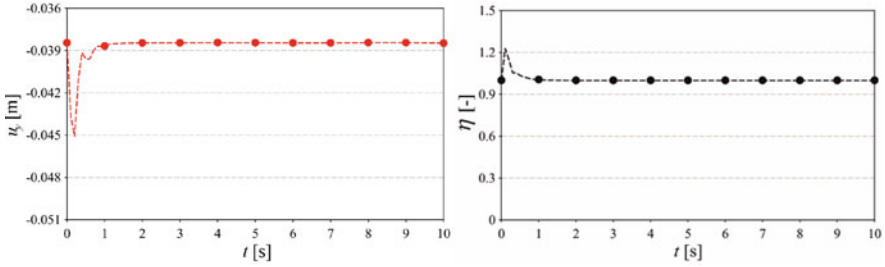


Fig. 8 Courses of vertical deflection u_y of the crane and overload coefficient η in the rope in the task of load lifting

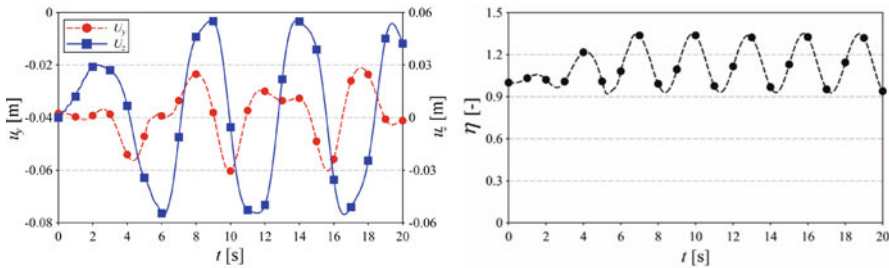


Fig. 9 Courses of vertical u_y and horizontal u_z deflections of the crane and overload coefficient η in the rope in the task of the crane rotation

4 Final Remarks

The model of lattice crane dynamics based on the rigid finite element method allows us to analyse the influence of base movements as well as winch and rotary drives on the behaviour of the crane. The simulation results indicate the correctness of the assumptions made and numerical effectiveness of the model presented. It is important to note that after its validation the software is used by the designers of Protea in everyday practice. The models developed are used in parallel with commercial packages. By adapting the interface to the needs of designers they are convenient for fast simulation of dynamics. Nor do they require as many input parameters as commercial packages mentioned.

An important feature of RFEM is that it is easy to attach lumped masses to any of the rods and/or nodes. Use of such rigid mass elements is a common practice in crane design. On the other hand, calculations of stresses using this method are subject to some errors, which is due to replacing flexible features of rods by SDEs with constant stiffness coefficients.

References

1. A. Cibicik, O. Egeland, Dynamic modelling and force analysis of knuckle boom crane using screw theory. *Mech. and Mach. Theory* **133**, 179–194 (2019)
2. I. Adamiec-Wójcik, Ł. Drag, S. Wojciech, M. Metelski, Application of the rigid finite element method to static analysis of lattice-boom cranes. *Int. J. Appl. Mech. Eng.* **23**(3), 803–811 (2018)
3. I. Adamiec-Wójcik, Ł. Drag, M. Metelski, K. Nadratowski, S. Wojciech, A 3D model for static and dynamic analysis of an offshore knuckle boom crane. *Appl. Math. Model.* **66**, 256–274 (2019)
4. A. Cibicik, E. Pedersen, O. Egeland, Dynamics of luffing motion of a flexible knuckle boom crane actuated by hydraulic cylinders. *Mech. and Mach. Theory* **143**, 103616 (2020)
5. X. Kong, Z. Qi, G. Wang, Elastic instability analysis for slender lattice-boom structures of crawler cranes. *J. Constr. Steel Res.* **115**, 206–222 (2015)
6. S. Heon-Jin, J. Chang-Kweon, J. Jong-Hoon, P. Sang-Hyeok, J. Yong-Gil, H. Sun-Chul, A safety evaluation of offshore lattice boom crane, in *International Conference CMSA, Advances in Intelligent Systems Research*, vol. 151, (Atlantis Press, 2018), pp. 275–280
7. G. Wang, Z. Qi, X. Kong, Geometrical nonlinear and stability analysis for slender frame structures of crawler cranes. *Eng. Struct.* **83**, 209–222 (2015)
8. A. Maczyński, S. Wojciech, Stabilization of load's position in offshore cranes. *J. Offshore Mech. Arct. Eng.* **134**, 1–10 (2012)
9. E. Wittbrodt, I. Adamiec-Wójcik, S. Wojciech, *Dynamics of Flexible Multibody Systems: Rigid Finite Element Method* (Springer, Berlin, 2006)
10. E. Wittbrodt, M. Szczotka, A. Maczyński, S. Wojciech, *Rigid Finite Element Method in Analysis of Dynamics of Offshore Structures* (Springer-Verlag, Berlin, 2013)

Dynamic Models of Cranes Applied to Offshore Wind Farm Service



Marek Metelski , Łukasz Drag , and Stanisław Wojciech 

1 Introduction

Growing demand for energy from renewable sources caused a growth in the number of wind platforms, particularly those which are situated remotely from residential areas. Offshore platforms, built at sea, at a certain distance from the shore, are also popular. In terms of service, the latter require specialist equipment, including small cranes designed for offshore applications. The users of these cranes expect their structure to be relatively simple, and their operating costs moderate. The machines are also expected to guarantee the safety of works conducted in difficult environmental conditions. In modelling these cranes, the movements of the base they are founded on (the platforms) and the movements of supply vessels, caused by sea waves, must be taken into account. Offshore service cranes include very important Automatic Overload Protection Systems (AOPS). Their design assumes the simulation of crane dynamics, considering the aforementioned operating conditions involving the impact of the marine environment (wind waves, sea currents, wind, etc.) and extraordinary events, such as the freezing of the lifted load to the ground, or hooking the lifted load onto elements on the supply vessel. Crane dynamic simulations should be carried out for the broadest scope of structural and operational parameters possible. Hence the importance of the effectiveness of the numeric model.

The models of statics and dynamics offshore cranes have been in use in offshore industries for many years. Due to the fact that these types of cranes are mounted on

M. Metelski
Protea S.A., Gdańsk, Poland
e-mail: marek.metelski@protea.pl

Ł. Drag (✉) · S. Wojciech
University of Bielsko-Biała, Bielsko-Biała, Poland
e-mail: ldrag@ath.bielsko.pl; swojciech@ath.bielsko.pl

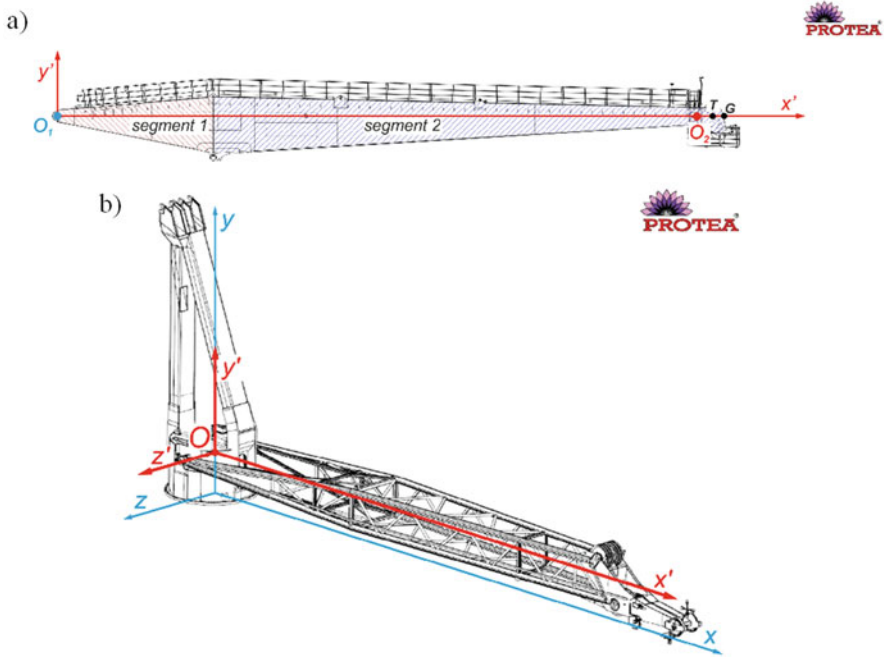


Fig. 1 Cranes with (a) box and (b) lattice booms

floating objects (ships, drill platforms), they take into account the influence of sea waves and wind conditions [1–3]. A number of research concern lifting operations performed under real operating conditions are investigated [2, 4, 5]. The box-type cranes were the subject of research in [1, 2, 4]. The statics of lattice boom cranes were analysed in [5, 6].

This paper presents a procedure which could be applied in creating a numerically effective substitute model for the crane. The proposed algorithm reflects the primary characteristics of a real crane. The basic differences which occur among individual crane types apply to the booms. The most popular boom types used in offshore cranes are box and lattice (Fig. 1).

The formulation of a substitute model for a crane requires knowledge of the design of a real crane, which could be used to calculate its mass parameters, analyse its static deflections and calculate the natural frequency. Models used for calculations in companies designing cranes applying commercial software (ROBOT, Abaqus, FemUp, etc.) or own software can be used for this purpose. The parameters that characterize the real objects are then input in the software which determines the parameters of the substitute (virtual) model, applying dynamic optimization methods. The substitute model, which is characterized by a relatively small number of degrees of freedom compared to full models, is developed applying the rigid finite element method (RFEM) [7].

2 Substitute (Virtual) Crane Model

The substitute crane model was developed on the basis of models described in detail in the paper [1]. However, certain simplifications were introduced to increase the overall effectiveness of calculations, as mentioned above. Figure 2 presents the adopted crane models.

The following notation is assumed:

- { } – global(inertial) coordinate system with axes x, y, z
- { } \sim – coordinate system assigned to the base vessel with axes $\tilde{x}, \tilde{y}, \tilde{z}$
- { } – coordinate system assigned to the rotating part with axes $\bar{x}, \bar{y}, \bar{z}$.
- { } s – coordinate system assigned to the supply vessel.

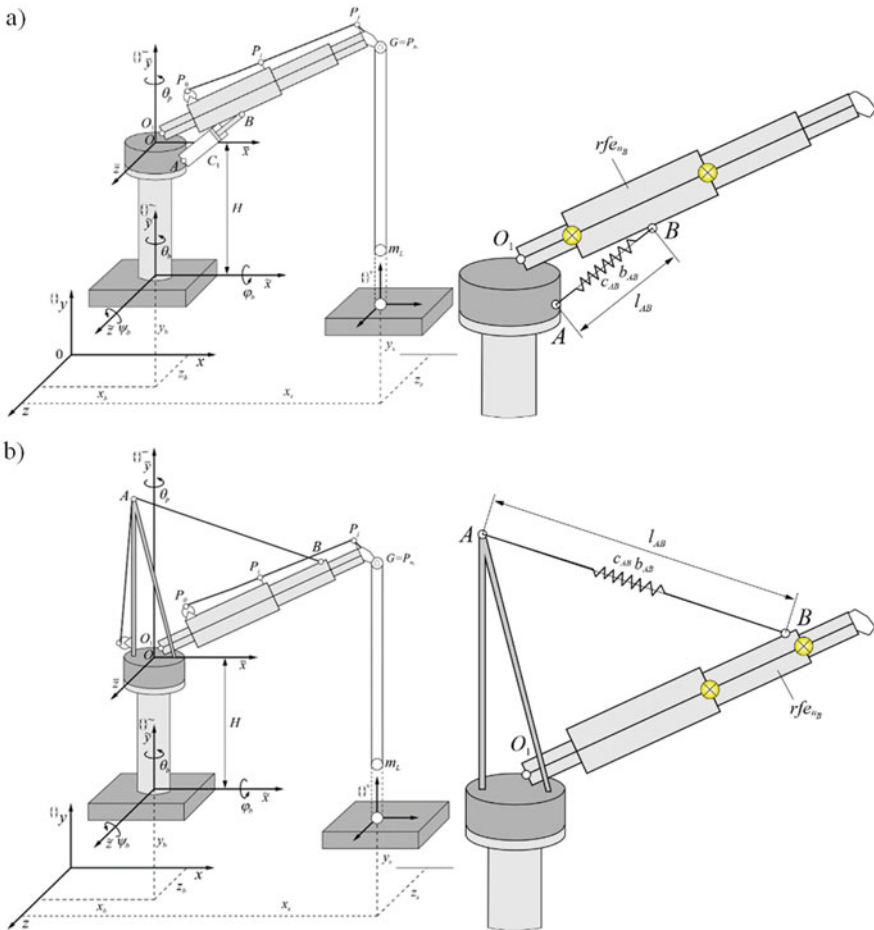


Fig. 2 General schemas of the crane with slewing mechanism (a) cylinder, (b) rope

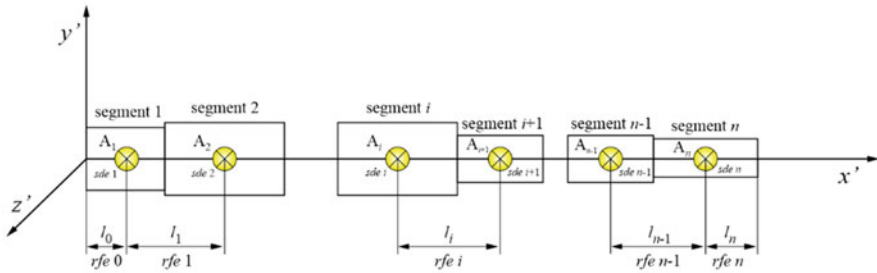


Fig. 3 Division of a boom into *rfe* and *sde*

It is assumed that the base vessel movement is known. The vector is therefore known:

$$\mathbf{q}_b = \mathbf{q}_b(t) = [x_b(t) \ y_b(t) \ z_b(t) \ \psi_b(t) \ \theta_b(t) \ \varphi_b(t)]^T, \tag{1}$$

where functions $x_b(t), y_b(t), z_b(t)$ determine the position of a selected point on the base vessel, a $\psi_b(t), \theta_b(t), \varphi_b(t)$ are ZYX Euler angles which determine the orientation of the base vessel relative to the base system, that is axes $\tilde{x}, \tilde{y}, \tilde{z}$ in $\{ \} \sim$ relative to axes x, y, z in $\{ \}$.

It is assumed that the substitute boom is a straight beam with stepwise variable rectangular cross-section, consisting of n segments. In the process of discretization, it is replaced by an $n + 1$ system of rigid finite elements (*rfe*) reflecting the mass (inertial) characteristics of the boom and n spring damping elements (*sde*) which are massless non-dimensional and reflect the bending and torsional susceptibilities of the boom (Fig. 3). Both *rfe* and *sde* are created through the division of segments.

Equations of motion were derived from second-order Lagrange equations, applying, among others, transformations described in the paper [7]. Generalized *rfe i* coordinates are therefore the vector components:

$$\mathbf{q}_i = \begin{bmatrix} \mathbf{r}_i \\ \phi_i \end{bmatrix}, \tag{2}$$

where: $\mathbf{r}_i = \begin{bmatrix} x_i \\ y_i \\ z_i \end{bmatrix}$ – coordinates of points A_i (translation coordinates),

$\phi_i = \begin{bmatrix} \psi_i \\ \theta_i \\ \varphi_i \end{bmatrix}$ – Euler angles (rotation coordinates).

The vector of generalized coordinates for the complete crane was defined in the following form:

$$\mathbf{q} = \left[\mathbf{q}_0^{(s)} \dots \mathbf{q}_i^{(s)} \dots \mathbf{q}_n^{(s)} \ \theta_P \ \mathbf{r}_L \ \varphi_D \right]^T, \tag{3}$$

where: $\mathbf{r}_L = \begin{bmatrix} x_L \\ y_L \\ z_L \end{bmatrix}$, φ_D – angle of rotation of the winch drum.

Equations of motion can be expressed in the following form:

$$\mathbf{M}\ddot{\mathbf{q}} = \mathbf{DR} + \mathbf{f}, \tag{4}$$

where:

\mathbf{M} – mass matrix,

\mathbf{q} – vector of generalized coordinates,

\mathbf{D} – matrix of reaction coefficients,

\mathbf{R} – vector of constraints reaction,

$\mathbf{f} = \mathbf{h} - \mathbf{h}_g - \mathbf{h}_s - \mathbf{h}^{(z)} - \mathbf{h}^{(L)} + \mathbf{T}$, \mathbf{f} – right side vector:

\mathbf{h} – from kinetic energy,

\mathbf{h}_g – from gravity,

\mathbf{h}_s – from the boom’s *sde* spring forces and dissipation energy,

$\mathbf{h}^{(z)}$ – from the luffing mechanism or the cylinder,

$\mathbf{h}^{(L)}$ – from rope deformation,

$$\mathbf{T} = \begin{bmatrix} \mathbf{0} \\ \vdots \\ \mathbf{0} \\ M_p \\ \mathbf{0} \\ M_D \end{bmatrix} \begin{matrix} -rfe\ 0 \\ \vdots \\ -rfe\ n \\ -\theta_p \\ -L \\ -\varphi_D \end{matrix}, \mathbf{D} = \begin{bmatrix} \mathbf{D}_w \\ 0\ 0 \\ \mathbf{0}\ \mathbf{0} \\ 0\ 0 \end{bmatrix} \begin{matrix} \\ -\theta_p \\ -L \\ -\varphi_D \end{matrix}.$$

These equations were supplemented by constraint equations in the accelerator form:

$$\mathbf{D}^T \ddot{\mathbf{q}} = \mathbf{G}. \tag{5}$$

The fourth order Runge-Kutta method with a constant integration step was applied in the integration of equations of motion.

3 Optimization Task

The boom is modelled as a variable-section beam (Figs. 4 and 5).

Let us assume that the aforementioned commercial or own software can be used to calculate the following values:

m_{ref} – boom mass,

S_{xref} – static moment of the boom in yz plane,

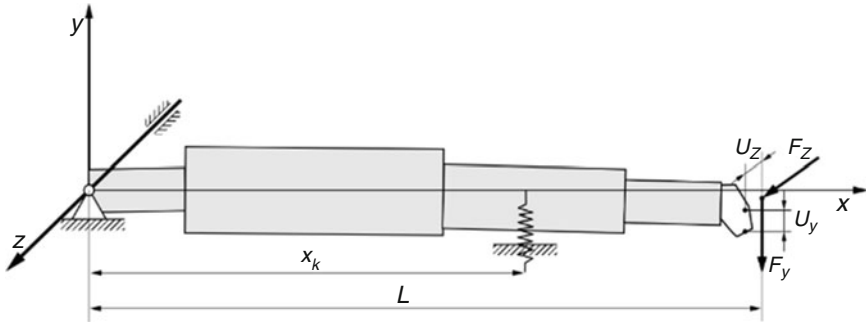


Fig. 4 Boom support

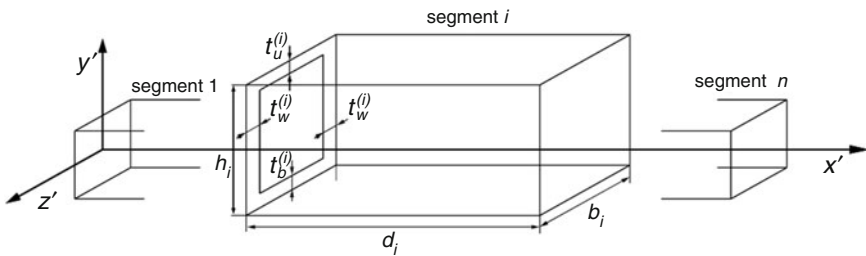


Fig. 5 Cross section of segment i

$U_{y,ref}, U_{z,ref}$ – deflections at the end of the boom loaded by forces $F_{y,ref}, F_{z,ref}$,
 ω_{1ref}^{xy} – first natural frequency of the boom in xy plane,
 ω_{1ref}^{xz} – first natural frequency of the boom in xz plane,

for boom support as presented in virtual models in Fig. 2, hence for a horizontal boom.

After designating:

m – mass of the virtual boom,

S_x – static moment of the virtual boom,

U_y, U_z – deflections of the substitute boom when loaded by forces F_y, F_z ,

ω_1^{xy} – first natural frequency of the virtual boom in xy plane,

ω_1^{xz} – first natural frequency of the virtual boom in xz plane,

then the optimization task is reduced to the selection of $4n$ parameters:

$$\begin{aligned}
 p_1 &= h_1 & p_{(i-1)+1} &= h_i & p_{4n-3} &= h_n \\
 p_2 &= b_1 & p_{(i-1)+2} &= b_i & p_{4n-2} &= b_n \\
 p_3 &= t_u^{(1)} = t_p^{(1)} & p_{(i-1)+3} &= t_u^{(i)} = t_p^{(i)} & p_{4n-1} &= t_u^{(n)} = t_p^{(n)} \\
 p_4 &= t_w^{(1)} & p_{(i-1)+4} &= t_w^{(i)} & p_{4n} &= t_w^{(n)} \\
 \vdots & & \vdots & & &
 \end{aligned} \tag{6}$$

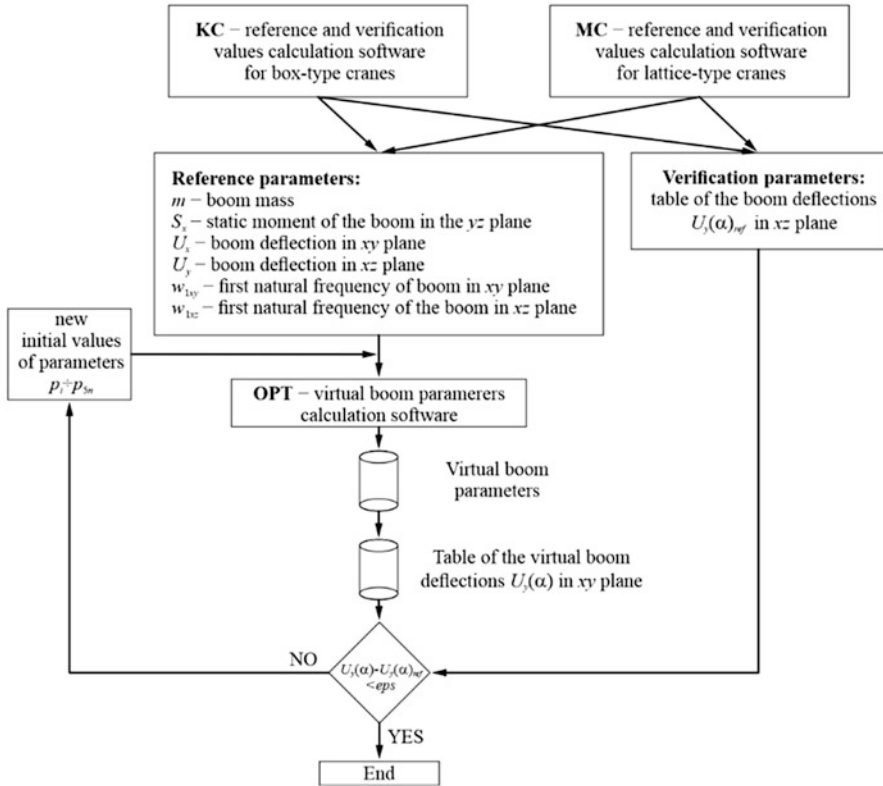


Fig. 6 Optimization algorithm based on table $U_j(\alpha)_{ref}$

and minimalizing the functional:

$$\Omega(p_1, \dots, p_{4n}) = \left[\frac{m - m_{ref}}{m_{ref}} \right]^2 + \left| \frac{S_x - S_{xref}}{S_{xref}} \right|^2 + \left[\frac{U_y - U_{yref}}{U_{yref}} \right]^2 + \left[\frac{U_z - U_{zref}}{U_{zref}} \right]^2 + \left[\frac{\omega_1^{xy} - \omega_{1ref}^{xy}}{\omega_{1ref}^{xy}} \right]^2 + \left[\frac{\omega_1^{xz} - \omega_{1ref}^{xz}}{\omega_{1ref}^{xz}} \right]^2, \tag{7}$$

which is the sum of squared relative deviation of reference and calculated values according to the substitute model. Initial calculations have shown that the optimization results are very sensitive to the selection of initial values. Therefore, a verification module, the idea for which is presented in Fig. 6, was involved into the optimization algorithm.

The purpose of the procedure is also to ensure the consistency of vertical deflection of the boom end, calculated according to the full model and according to the substitute model for various (defined) α , and not only for reference parameters when $\alpha = 0^\circ$. The process was practically carried out using the parallel calculation functionality offered by Delphi software.

4 Algorithm Applications

The proposed procedural algorithm was used to develop a virtual model of a crane manufactured by PROTEA. The crane is characterized by a high load capacity, and its boom is of the box type (Fig. 7).

The h_i , b_i , $t_u^{(i)}$, $t_w^{(i)}$, and $\rho^{(i)}$ values selected in the process of optimization for the selected division of the boom into *rfe* and *sde* allow such selection of mass and spring dumping parameters for each element that the virtual boom has managed to model the real boom with the highest possible accuracy. Limiting conditions specified in Table 1 were taken into account for the boom in the calculations.

Subsequent part of the paper presents the results of verification of the substitute crane model. The values of reference parameters were selected for a division of the boom into $n = 3$ elements. In calculating the reference values, the boom was loaded with the following forces: vertical $F_y=60,000g N$, horizontal $F_z=20,000g N$, and a gravitational load corresponding to gravity of $g = 9.80655 ms^{-2}$.

The values presented in Table 2 indicate that the optimization process was successfully completed. A very high level of compatibility of the reference value modelling in the virtual model was obtained. What is noteworthy, these values are determined for a horizontal boom configuration. Table 3 includes a comparison of boom deflection values for different lift angles, obtained in the full and virtual model.



Fig. 7 Box crane manufactured by Protea

Table 1 Limitation to h_i , b_i , $t_u^{(i)}$, $t_w^{(i)}$, and $\rho^{(i)}$ values, applied in the optimization process

Parameter	Values	
	Minimum	Maximum
Height of the boom cross section h_i [m]	0.1	3.5
Width of the boom cross section b_i [m]	0.1	3.5
Up and down flange thickness $t_u^{(i)}=t_b^{(i)}$ [m]	0.001	0.04
Web flange thickness $t_w^{(i)}$ [m]	0.001	0.04
Material density $\rho^{(i)}$ [kgm^{-3}] – constant	7850	7850

Table 2 Values of reference parameters determined in the full model (F) and after optimization process for the virtual model (V)

Parameter	Full model (F)	Virtual model (V)
Boom mass m [kg]	25941.46	25941.46
Static moment of the boom in the yz plane [kgm^2]	382578.35	382578.35
Boom deflection in the xy plane [m]	-0.1737	-0.1737
Boom deflection in the xz plane [m]	0.1319	0.1319
First natural frequency of the boom in the xy plane [Hz]	29.2464	29.2464
First natural frequency of the boom in the xz plane [Hz]	16.8296	16.8296

Table 3 Boom deflections U_y and U_z and their absolute $\Delta\delta_A$ and relative $\Delta\delta_R$ differences, calculated between the full model (F) and the virtual model (V)

α [°]	R[m]	Load [mT]	$U_{y, F}$ [m]	$U_{y, V}$ [m]	$\Delta\delta_A$ [m]	$\Delta\delta_R$ [%]
5	30.88	20.143	-0.062939	-0.063677	0.000738	1.17
25	28.1	23.877	-0.119381	-0.119898	0.000517	0.43
45	21.92	35.533	-0.168689	-0.168914	0.000225	0.13
65	13.1	60	-0.166956	-0.166911	-0.000044	0.03
85	2.7	60	-0.016844	-0.016808	-0.000036	0.21

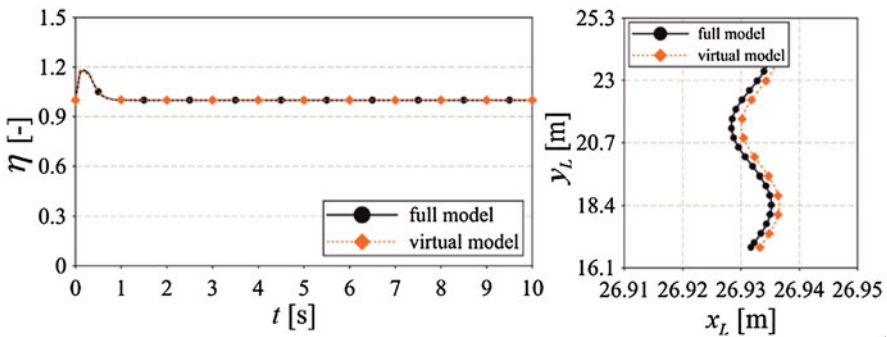


Fig. 8 Dynamic coefficient η of the rope system, trajectory of the load projected on plane xy

An analysis of the absolute $\Delta\delta_A$ and relative $\Delta\delta_R$ differences presented in Table 3 points to a conclusion that the boom parameters selected in the optimization process are correct. The relative difference in deflections between the full models and the virtual model does not exceed 1.2%.

Figure 8 presents the simulation results according to the full model, obtained for a division of the boom into $n = 10$ rigid finite elements and for the virtual model, for lifting a load from air using a winch at an initial speed of $v_{y, L} = 0$ m/s increased to $v_{y, L} = v_{nom}$.

The following assumptions were adopted in the calculations:

- the boom is inclined relative to the horizontal at: $\alpha = 30^\circ$,
- a load of $m_L = 30,000$ kg is connected to the end of the rope,

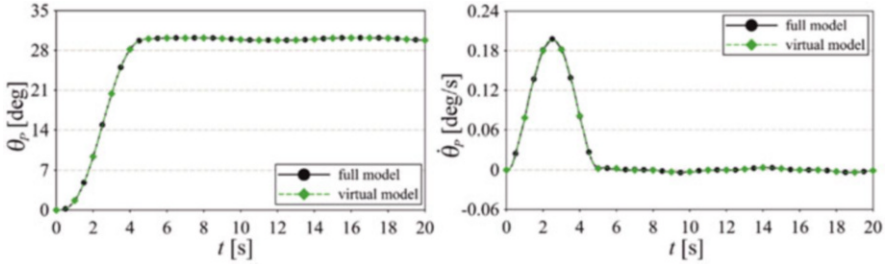


Fig. 9 Courses of the rotation angle θ_P and the angular rotation speed $\dot{\theta}_P$ of the crane column

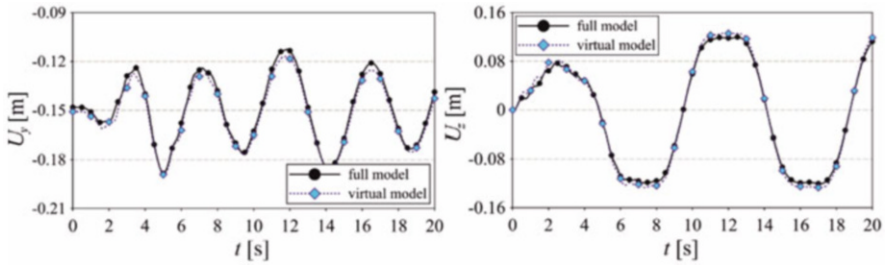
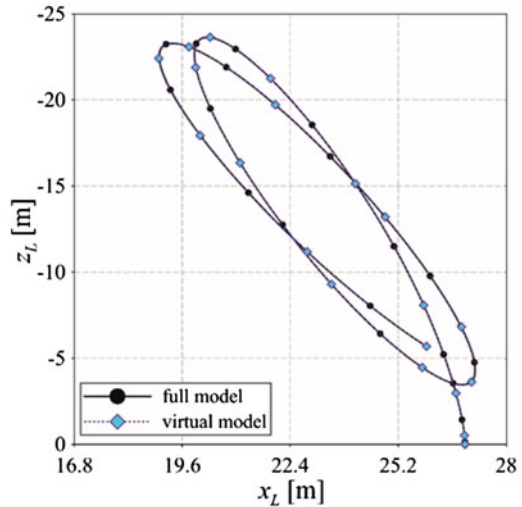


Fig. 10 Courses of the vertical U_y and horizontal U_z crane deflections

Fig. 11 Trajectory of the load projected on plane xz



- initially, the load is situated under point G , at a distance 20 m, respectively,
- the nominal speed of the load v_{nom} is 0.7 m/s.

In turn, Figs. 10 and 11 present the results of simulation of crane rotation according to the function in Fig. 9.

5 Conclusions

The paper presents models and procedural algorithms which, upon applying optimization methods, can be used to develop a virtual crane model. Formulated with the RFEM method, this model can be used towards the simulation of the crane dynamics, and is particularly useful AUTO 97: Continuation and Bifurcation Software for Ordinary Differential Equations for cranes designed for servicing wind platforms. For the proposed algorithm to work, the static deflection and boom vibrations must be determined with the use of their own models or commercially available software. In turn, the substitute (virtual) model allows to simulate the crane dynamic and emergency situations across changing conditions caused by waves and the movements of the supply vessel.

References

1. I. Adamiec-Wójcik, Ł. Drag, M. Metelski, K. Nadratowski, S. Wojciech, A 3D model for static and dynamic analysis of an offshore knuckle boom crane. *Appl. Math. Model.* **66**, 256–274 (2019)
2. H. Dae Suk, Y. Sung Won, Y. Hyun Sik, K. Myung Hyun, K. Sang Hyun, L. Jae Myung, Coupling analysis of finite element and finite volume method for the design and construction of FPSO crane. *Autom. Constr.* **20**(4), 368–379 (2011)
3. K. Ellermann, E.J. Kreuzer, M. Markiewicz, Nonlinear dynamics of floating cranes. *Nonlinear Dyn.* **27**(2), 107–183 (2002)
4. M.K. Bak, M.R. Hansen, Analysis of offshore knuckle boom crane – part one: modelling and parameter identification. *Model. Identif. Control.* **34**(4), 157–174 (2013)
5. S. Heon-Jin, J. Chang-Kweon, J. Jong-Hoon, P. Sang-Hyeok, J. Yong-Gil, H. Sun-Chul, A safety evaluation of offshore lattice boom crane, in *International Conference CMSA, Advances in Intelligent Systems Research*, vol. 151, (Atlantis Press, 2018), pp. 275–280
6. I. Adamiec-Wójcik, Ł. Drag, S. Wojciech, M. Metelski, Application of the rigid finite element method to static analysis of lattice-boom cranes. *Int. J. Appl. Mech. Eng.* **23**(3), 803–811 (2018)
7. E. Wittbrodt, I. Adamiec-Wójcik, S. Wojciech, *Dynamics of Flexible Multibody Systems: Rigid Finite Element Method* (Springer, Berlin, 2006)

Axisymmetric Nonlinear Free Vibration of a Conductive Annular Plate Under Toroidal Magnetic Field



Xu Haoran and Hu Yuda

1 Introduction

Thin conductive annular plate structures have a broad range of applications in many electromechanical devices such as superconducting electric machine motors, data storage drives, and turbomachinery. In these devices, annular plate structures under the action of non-uniform magnetic field may show complex dynamic behaviors combined with the influence of geometric nonlinearity, which may change the natural frequency of plates. Even if a little disturbance may lead to resonance and instability of annular plates, which represents the necessity of investigation on the magneto-elastic natural characteristics. The nonlinear vibration issue absorbed the attention of many researchers. The calculation for the displacement of annular and circular plate with different thicknesses and different internal and external diameter ratios under impact load was carried out by Shirmohammadi and Bahrami [1] to investigate the vibration by means of the spectral element method. Ma et al. [2, 3] presented the nonlinear oscillation characteristics of stiffened plate with boundary conditions by ANSYS analysis. Ansari et al. [4, 5] scrutinized the axisymmetric bending, buckling, and free vibration of FGM circular plate and annular plate, and discussed the influence of radius thickness ratio and material parameters on the natural frequency of plate. The free vibration of graphene foam annular plate was also presented, where natural frequencies of plate with different boundaries and foam coefficients were achieved by Wang et al. [6] utilizing the Chebyshev-Ritz method. Further, for plates with variable thickness, Žur et al. [8–10] proposed an

X. Haoran · H. Yuda (✉)

Yanshan University, Qinhuangdao, People's Republic of China

Hebei Key Laboratory of Mechanical Reliability for Heavy Equipment and Large Structures,

Yanshan University, Qinhuangdao, People's Republic of China

e-mail: huyuda03@163.com

iterative method to study the free vibration of circular plates with variable thickness, and obtained natural frequency of nonlinear free oscillation of circular plate. On the other hand, many valuable results have been obtained in the study of magnetoelastic problems of plate structures. Hu et al. [11] analyzed the magneto-elastic strong nonlinear subharmonic resonance and bifurcation of a thin strip plate by means of the improved multi-scale method, where the bifurcation diagram and the maximum Lyapunov exponent spectrum with different control parameters were used to reveal the complex dynamic behaviors. Arena et al. [12] showed the dynamic stability of a rotating magnetic levitation ring under radial magnetic forces, which reveals that at critical angular velocity, when critical mode becomes unstable, the loss of stability depends on stiffness of the ring and the symmetry/asymmetry of cross section. Hu and Li [13, 14] modeled the rotating circular plate and gave magneto-aeroelastic forced oscillation governing equations, which illustrates bifurcation and chaotic nonlinear dynamic behaviors of single mode and modal interaction characteristics. Yun and Ding [15, 16] introduce the three-dimensional magneto-electro-elastic theory to study magneto-electro-mechanics coupling mechanism of the axisymmetric bending of functionally graded annular plates made of piezoelectric, magneto-electro-elastic, and elastic material. Razavi et al. [17, 18] conducted nonlinear free oscillation and buckling of electromagnetic elastic rectangular plates under simply supported boundary condition, obtained analytical solutions and numerical results of frequency.

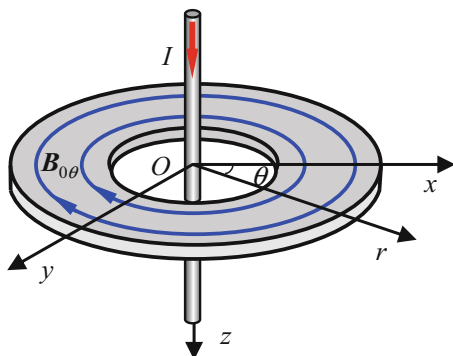
At present, it is noted that there are more researches on the magnetoelasticity of thin plates in the uniform magnetic field, researches on non-uniform ones are relatively less. In view of fact that the magnetic field induced by a current-carrying straight wire is a typically and widely existing and important non-uniform complex one, the magnetoelastic nonlinear free vibration of annular plates is analyzed. The expressions of natural frequency and electromagnetic force of plate are deduced respectively, and the influence of different control parameters on the oscillation characteristics of the system under non-uniform magnetic field environment is expounded in details.

2 The Induced Magnetic Field and Electromagnetic Forces

Consider the system consisted of isotropic conductive annular plate and the long straight current-carrying wire. The annular plate, whose located plane is perpendicular to the wire, is placed with its geometric center and wire coincided. This center is taken as the origin for the establishment of the cylindrical coordinates for the mechanical system, where r , θ , and z represent radial, circumferential, and transverse coordinate, respectively. The annular plate has outer radius R_a , internal radius R_b and uniform thickness h , and the straight current-carrying wire current intensity is I , as shown in Fig. 1.

Through the magnetoelastic theory, it can be obtained that the induced magnetic field is a toroidal magnetic field, and when the length of wire is long enough, the

Fig. 1 Mechanical model of annular plate with long straight current-carrying wire



magnetic induction intensity of a point with distance r from the wire is achieved as [19]:

$$B_{0\theta} = \frac{\mu_0 I}{2\pi r}, \quad B_{0r} = 0, \quad B_{0z} = 0 \tag{1}$$

where μ_0 is the permeability of vacuum. $B_{0\theta}$, B_{0r} , and B_{0z} are the toroidal, radial, and transverse components of the induced magnetic field vector, respectively.

For isotropic thin conductive annular plate in the non-uniform toroidal magnetic field induced by a long straight current-carrying wire, according to the magnetoelastic field theory, electrical conductors in the magnetic field are subjected to the Lorentz force. The transverse electromagnetic force and electromagnetic torque of the annular plate in the induced magnetic field are read as:

$$F_z = \int_{-\frac{h}{2}}^{\frac{h}{2}} f_z dz = -\sigma_0 h \left(\frac{\mu_0 I}{2\pi r} \right)^2 \frac{\partial w}{\partial t}, \quad m_r = \int_{-\frac{h}{2}}^{\frac{h}{2}} f_r \cdot z dz = \frac{\sigma_0 h^3}{12} \left(\frac{\mu_0 I}{2\pi r} \right)^2 \frac{\partial^2 w}{\partial r \partial t} \tag{2}$$

where σ_0 is the conductivity, w and t represent the transverse deflection and time variable, respectively.

3 Magnetoelastic Nonlinear Free Vibration

The nonlinear free vibration of annular plate in non-uniform toroidal magnetic field is presented, and the kinetic energy expression is achieved as:

$$T = \frac{1}{2} \rho \int_{-\frac{h}{2}}^{\frac{h}{2}} \int_{R_b}^{R_a} \int_0^{2\pi} \left[\left(-z \frac{\partial^2 w}{\partial r \partial t} \right)^2 + \left(\frac{\partial w}{\partial t} \right)^2 \right] r dr d\theta dz \tag{3}$$

where ρ is the mass density.

According to Kirchoff plate theory, the bending deformation potential energy of plate is approached as:

$$U_1 = \frac{1}{2} \int_{R_b}^{R_a} \int_0^{2\pi} (M_r \kappa_r + M_\theta \kappa_\theta) r dr d\theta \tag{4}$$

Considering the geometric nonlinearity, the strain potential energy U_2 of the mid-plane of plate is read as:

$$U_2 = \frac{1}{2} \int_{R_b}^{R_a} \int_0^{2\pi} (N_r \varepsilon_r + N_\theta \varepsilon_\theta) r dr d\theta \tag{5}$$

Here, M_r and M_θ represent bending moments, κ_r and κ_θ are the curvatures. N_r and N_θ are inertial forces in mid-plane, ε_r and ε_θ are line strains in mid-plane.

Expression of virtual work of electromagnetic force is:

$$\delta W_B = \frac{1}{2} \int_{R_b}^{R_a} \int_0^{2\pi} (F_z \delta w - m_r \delta u_r) r dr d\theta \tag{6}$$

where $u_r = \partial w / \partial r$ is angular displacement.

According to the Hamiltonian variational principle, we can get:

$$\int_{t_1}^{t_2} (\delta T - \delta U_1 - \delta U_2 + \delta W_B) dt = 0 \tag{7}$$

where t_1 and t_2 are fixed integral time domain.

Substituting Eqs. (3), (4), (5), and (6) into Eq. (7), perform the variational operation on displacement component w , and the integral expressions for δw can be obtained. Here, the axisymmetric transverse vibration is studied, to satisfy Eq. (7), the coefficient terms of δw in z direction are zero. Then we obtain the equation:

$$\begin{aligned} & D_M \left(\frac{\partial^4 w}{\partial r^4} + \frac{2}{r} \frac{\partial^3 w}{\partial r^3} - \frac{1}{r^2} \frac{\partial^2 w}{\partial r^2} + \frac{1}{r^3} \frac{\partial w}{\partial r} \right) - D_N \left[\frac{1}{2r} \left(\frac{\partial w}{\partial r} \right)^3 + \frac{3}{2} \left(\frac{\partial w}{\partial r} \right)^2 \frac{\partial^2 w}{\partial r^2} \right] + \\ & \sigma_0 h \left(\frac{\mu_0 I}{2\pi r} \right)^2 \cdot \frac{\partial w}{\partial t} - \frac{\sigma_0 h^3}{12} \left(\frac{\mu_0 I}{2\pi r} \right)^2 \cdot \left[\frac{\partial^3 w}{\partial r^2 \partial t} - \frac{1}{r} \frac{\partial^2 w}{\partial r \partial t} \right] + \rho h \frac{d^2 w}{dt^2} - \\ & \frac{\rho h^3}{12} \left[\frac{1}{r} \frac{d^2}{dt^2} \left(\frac{\partial w}{\partial r} \right) + \frac{d^2}{dt^2} \left(\frac{\partial^2 w}{\partial r^2} \right) \right] = 0 \end{aligned} \tag{8}$$

where $D_M = Eh^3/12(1 - \nu^2)$ and $D_N = Eh/(1 - \nu^2)$ represent flexural rigidity and tensile rigidity. E and ν represent Young's modulus and Poisson ratio, respectively.

For the axisymmetric vibration issue, the displacement solution satisfying the boundary conditions may be set in the following expansion form [7]:

$$w = T(t) \cdot W(r) \tag{9}$$

Then, the expression of mode function $W(r)$ is determined. Substituting Eq. (9) into Eq. (8), the Galerkin method is employed to derive the nonlinear free vibration differential equation:

$$a_{01}T''(t) + a_{02}T'(t) + a_{03}T(t) + a_{04}T^3(t) = 0 \quad (12)$$

where a_{01} , a_{02} , a_{03} , and a_{04} represent the coefficient expressions.

The method of multiple scales is applied to resolve nonlinear differential Eq. (12), and the frequency of natural vibration for the system is obtained [21]:

$$\omega = \omega_0 + \frac{3\eta}{8\omega_0} \frac{1}{Q^2} - \frac{\zeta^2}{8\omega_0} - \frac{15\eta^2}{256\omega_0^3} \frac{1}{Q^4} \quad (13)$$

where $Q = \sqrt{3\eta/(8\omega_0^2) + Ce^{\zeta t}}$, $\zeta = a_{02}/a_{01}$, $\omega_0^2 = a_{03}/a_{01}$, $\eta = a_{04}/a_{01}$, integral constant C is determined by initial conditions.

4 Numerical Example and Analysis

This section performs the numerical calculation and discussion for system composed of long straight current-carrying wire and aluminum conductive annular plate in wire's induced non-uniform magnetic field. The system is assumed with material properties: conductivity $\sigma_0 = 3.63 \times 10^7 (\Omega \cdot \text{m})^{-1}$, Young's modulus $E = 71$ GPa, mass density $\rho = 2670 \text{ kg/m}^3$, and Poisson's ratio $\nu = 0.34$ for plate. The straight wire is taken as superconducting wire that can carry large current [20]. The boundary S-C is analyzed.

4.1 Variation Law of Non-uniform Magnetic Field and Electromagnetic Force

Consider a long straight superconducting wire with stable current, the three-dimensional diagram of magnetic induction intensity $B_{0\theta}$ varying with current intensity I and radial position r is plotted as Fig. 2a. For Fig. 2a, take different I respectively and draw curves of $B_{0\theta} - I$, as Fig. 2b. Recalling Fig. 2 and Eq. (1) indicates that the smaller distance from wire, the stronger magnetic induction intensity. As distance from wire increases, $B_{0\theta}$ shows the nonlinear decrease with radial direction.

When $R_a = 0.2 \text{ m}$, $R_b = 0.1 \text{ m}$, $h = 0.0035 \text{ m}$, initial amplitude $a_0 = 0.001 \text{ m}$ and $I = 10 \text{ kA}$, Fig. 3 shows the three-dimensional diagram of electromagnetic force F_z varying with radial position r and time t . Through method of multiple scales, it is obtained that the analytical solution for $T(t)$ of Eq. (12) shows a simple

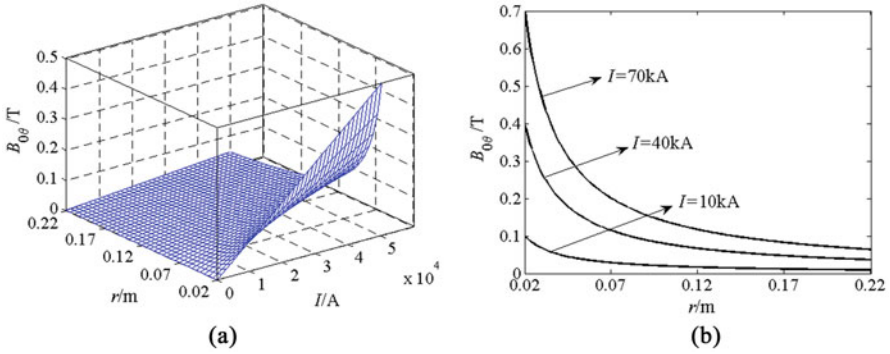


Fig. 2 Change law of $B_{0\theta}$. (a) Diagram of $B_{0\theta} - I - r$ (b) $B_{0\theta}$ varying with r in different I

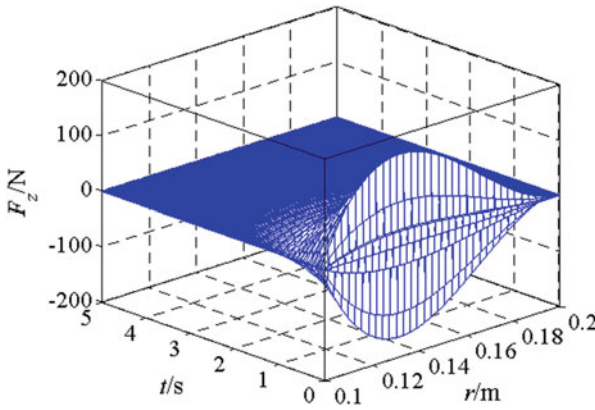


Fig. 3 Diagram of $F_z - t - r$

harmonic changing form. Since the current term exists in coefficient expression a_{02} , which means the induced magnetic field shows system. Recalling Eqs. (2), (9) and (12), it is noted that F_z decays with t . In r direction, F_z increases from zero at inner radius to global maximum at stagnation point $r = 0.6680 R_a$ with increasing slower rate, then it decreases with acceleration, until it reaches inflection point $r = 0.8390 R_a$, after which the decreasing trend is unobvious, then it decreases to zero at outer radius edge. According to Fig. 3, Fig. 4 shows the three-dimensional diagram of m_r varying with t and r . Combining with Eq. (2), it is shown that m_r decays with t . In r direction, m_r diminishes from global maximum at the inner radius to zero at point $r = 0.7265 R_a$ in an increasing unobvious trend, then grows inversely from zero to local maximum at $r = 0.8720 R_a$ with increasing slower rate, and finally drops to zero at outer radius edge with acceleration.

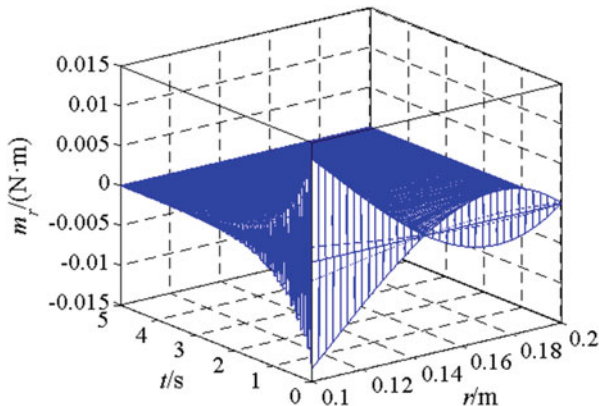


Fig. 4 Diagram of $m_r - t - r$

4.2 Variation Law of Natural Frequency

Variation of natural frequency with I In Fig. 5a, $R_a = 0.2$ m, $R_b = 0.1$ m, $h = 0.0035$ m and when $t = 1$ s. From Eq. (13) and curves of natural frequency ω varying with current I at different initial amplitudes a_0 , it is noted that $1/M^2$, $1/M^4$ and $-\zeta^2/(8\omega_0)$ decrease with increasing I , thus ω decreases with I . When I increases to a certain extent, ω tends to remain unchanged. Under the same I , for Fig. 6a, increasing a_0 causes the decrease of integral constant C , which increases fractions, as η_1 is positive, increasing a_0 increases the product of fraction including I , η and $-\eta^2$. So the larger a_0 , the larger ω . It is noted that ω is affected by initial value, which reflects typical nonlinear characteristics of system. However, when I increases to a certain degree, effect of a_0 becomes less obvious. As $R_a = 0.2$ m, $R_b = 0.1$ m and $a_0 = 0.001$ m and $t = 1$ s, Fig. 5b gives curves of ω varying with I under different h , which presents that ω shows the same changing law as Fig. 5a and increases significantly with h . In Fig. 5c, $R_b = 0.1$ m, $h = 0.0035$ m, $a_0 = 0.001$ m and $t = 1$ s, which represents curves of ω varying with I under different outer radiuses. Under the same current, the larger the outer radius, the smaller ω .

Variation of natural frequency with a_0 In the case of $R_a = 0.2$ m, $R_b = 0.1$ m, $h = 0.0035$ m and $I = 10$ kA, Fig. 6 gives three-dimensional diagram of ω varying with a_0 and t . Analyzing Fig. 6 and Eq. (13), we obtain that ω increases significantly as a_0 is larger. Thus, curves bend to the right namely the high-frequency side, which means the system exhibits hard characteristics. In addition, ω shows nonlinear characteristics due to the different initial values. In case of $R_a = 0.2$ m, $R_b = 0.1$ m, $h = 0.0035$ m and $t = 1$ s, Fig. 7 shows three-dimensional diagram of $\omega - a_0 - I$. It is found that the relationship between ω and a_0 is similar to Fig. 6. As I increases, bending trend of curves becomes less obvious, indicating that influence of a_0 on ω is weakened.

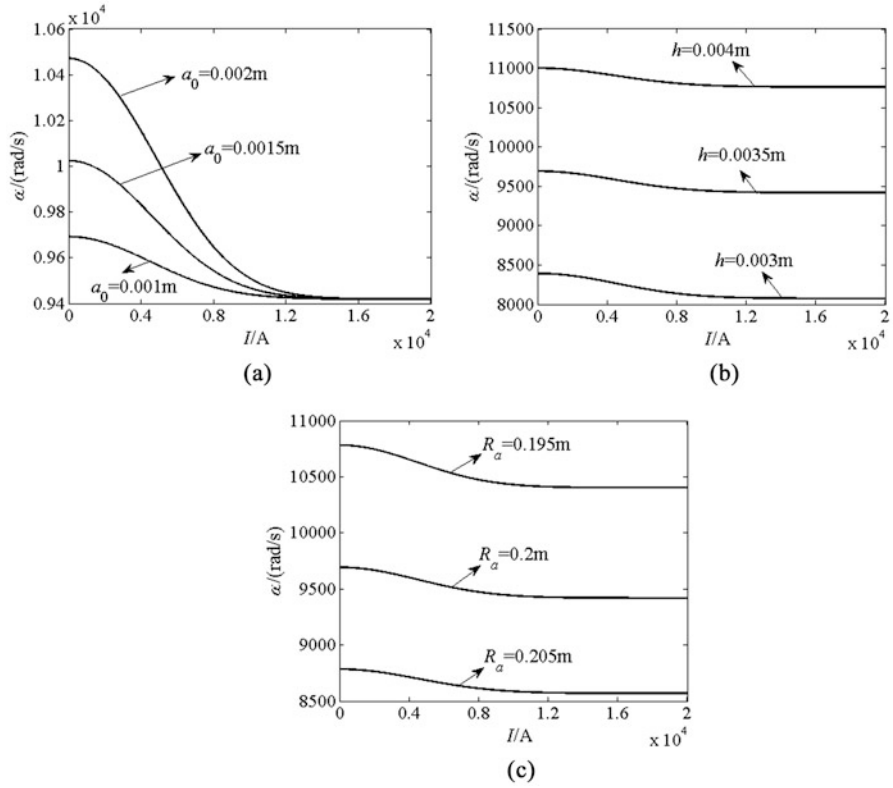


Fig. 5 Curves of $\omega - I$ under different parameters. (a) Different α_0 (b) Different h (c) Different R_a

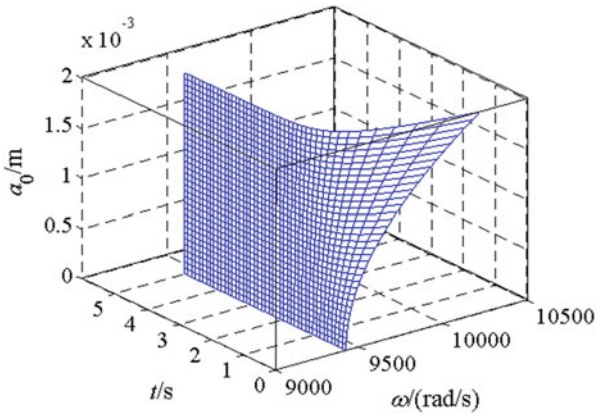


Fig. 6 Diagram of $\omega - \alpha_0 - t$

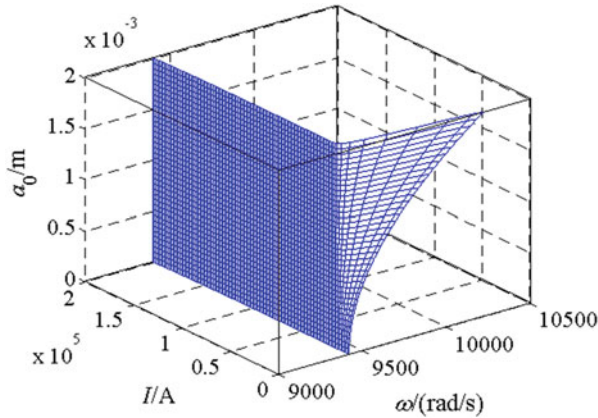


Fig. 7 Diagram of $\omega - \alpha_0 - I$

Variation of natural frequency with t In the case of $R_a = 0.2$ m, $R_b = 0.1$ m, $h = 0.0035$ m and $a_0 = 0.001$ m, Fig. 8 shows the curves of $\omega - t$ in different I . Considering Fig. 8a and Eq. (13), we obtain that, since t and I exist in the exponential function of denominator of expression ω , if wire is not carrying current, ω maintain a constant with t . Conversely, if wire carries current, ω declines with increase of t . Moreover, ω will not change with t when time increases to a certain extent. In addition, the curves of $\omega - t$ will converges fast and the value of ω will decrease with the increase of I , which tallies with the variation of ω with I in above figures.

In the case of $R_b = 0.1$ m, $I = 10$ kA, $h = 0.0035$ m and $a_0 = 0.001$ m, Fig. 8b gives the $\omega - t$ in different outer radiuses. It is obtained that Fig. 8b has the same change law as Fig. 8a. At the same time, ω decreases obviously when outer radius becomes larger, which also tallies with Fig. 5c. In the case of $R_a = 0.2$ m, $R_b = 0.1$ m, $I = 10$ kA and $h = 0.0035$ m, Fig. 8c represents the curves of $\omega - t$ in different a_0 . The natural frequency in Fig. 8c also shows the same varying law with time as Fig. 5a. At the same time, it may increase as initial amplitude increases, which also shows the same change law and the same hard characteristics consistent with Figs. 6 and 7.

5 Conclusions

In this article, the nonlinear free vibration of thin annular plates in non-uniform toroidal magnetic field of long straight current-carrying wire is approached. The expression of magnetic field and displacement function of plate under S-C boundary are obtained, the nonlinear differential equation of plates is deduced, which was solved through the method of multiple scales. The calculation examples present

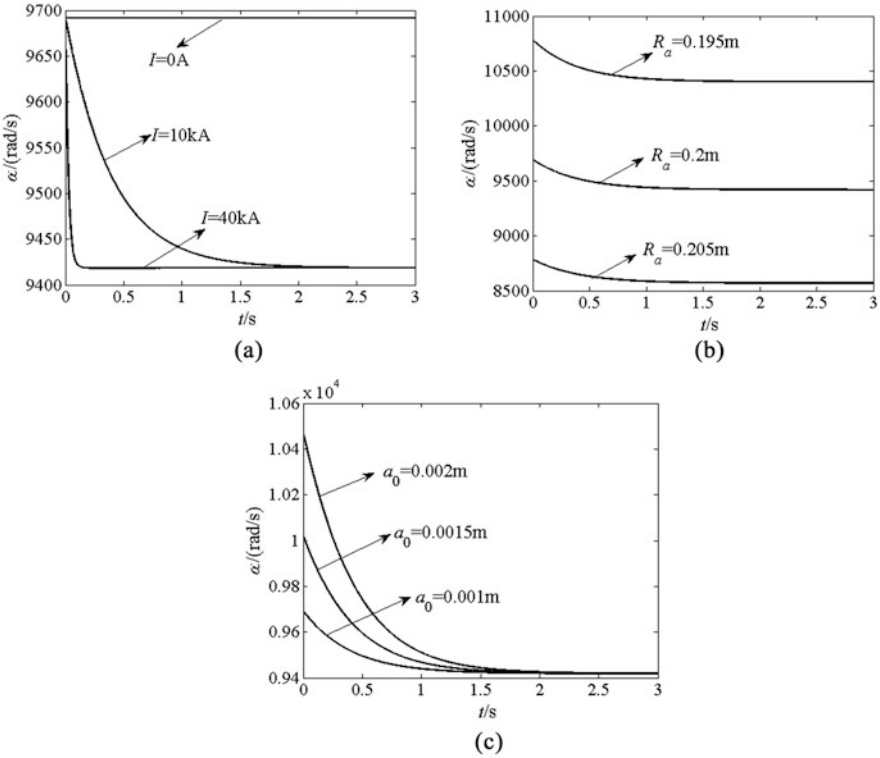


Fig. 8 Curves of $\omega - t$ under different parameters. (a) Different I (b) Different R_a (c) Different a_0

the natural frequency varying with different parameters. Results and discussions indicate that:

1. Under the S-C boundary condition, natural frequency declines and then remains constant with increasing current or time. In addition, natural frequency increases with increasing plate inner radius and thickness, but declines with increasing outer radius.
2. Natural frequency may be affected by the initial amplitude, which shows typical nonlinearity of system and that the system exhibits hard characteristics.
3. Electromagnetic force and torque decay with time, and show different variation in radial direction. In plane of plate, the induced non-uniform magnetic field declines nonlinearly along the radial direction.

Acknowledgments This project is supported by the National Natural Science Foundation of China (No. 12172321), Hebei Provincial Natural Science Foundation of China (No. A2020203007) and Hebei Provincial Graduate Innovation Foundation of China (No. CXZZBS2020041).

References

1. F. Shirmohammadi, S. Bahrami, Dynamic response of circular and annular circular plates using spectral element method. *App. Math. Model.* **53**, 156–166 (2018)
2. N. Ma, R. Wang, Nonlinear free vibration of stiffened plate with four edges clamped. *Chin. J. Theor. Appl. Mech.* **43**(5), 922–930 (2011)
3. N. Ma, R. Wang, P. Li, Geometrically nonlinear free vibration and internal resonance of a stiffened plate with four edges simply supported. *J. Vib. Shock.* **31**(24), 60–64 (2012)
4. R. Ansari, R. Gholami, M. Shojaei, V. Mohammadi, S. Sahmani, Bending, buckling and free vibration analysis of size-dependent functionally graded circular/annular microplates based on the modified strain gradient elasticity theory. *Eur. J. Mech. A-Solids.* **49**, 251–267 (2015)
5. S. Hosseini-hashemi, M. Derakhshani, M. Fadaee, An accurate mathematical study on the free vibration of stepped thickness circular/annular Mindlin functionally graded plates. *App. Math. Model.* **37**(6), 4147–4164 (2013)
6. Q. Wang, M. Teng, Vibration analysis of circular and annular plates made of 3D graphene foams via Chebyshev-Ritz method. *Aerosp. Sci. Technol.* **95**(105440), 1–12 (2019)
7. S. Chonan, T. Mikami, H. Ishikawa, The vibrations and critical speeds of rotating sawblades. *Japan. Soc. Mech. Eng.* **52**(478), 1805–1812 (1986)
8. K. Žur, Green's function for frequency analysis of thin annular plates with nonlinear variable thickness. *App. Math. Model.* **40**(5–6), 3601–3619 (2016)
9. J. Yuan, W. Chen, Exact solutions for axisymmetric flexural free vibrations of inhomogeneous circular Mindlin plates with variable thickness. *Appl. Math. Mech.* **38**(4), 505–526 (2017)
10. Z. Ye, Nonlinear vibration of circular plate with variable thickness. *J. Shanghai Univ.* **2**(1), 27–34 (1998)
11. Y. Hu, P. Hu, J. Zhang, Strongly nonlinear subharmonic resonance and chaotic motion of axially moving thin plate in magnetic field. *J. Comput. Nonlinear Dyn.* **3**(021010), 1–12 (2015)
12. A. Arena, W. Lacarbonara, On the stability of magnetically levitated rotating rings. *Int. J. Mech. Sci.* **131–132**, 286–295 (2017)
13. Y. Hu, W. Li, Study on primary resonance and bifurcation of a conductive circular plate rotating in air-magnetic fields. *Nonlinear Dyn.* **93**, 671–687 (2018)
14. Y. Hu, W. Li, Magnetoelastic axisymmetric multi-modal resonance and Hopf bifurcation of a rotating circular plate under aerodynamic load. *Nonlinear Dyn.* **97**, 1295–1311 (2019)
15. W. Yun, H. Ding, R. Xu, Three-dimensional analytical solutions for the axisymmetric bending of functionally graded annular plates. *App. Math. Model.* **40**(9–10), 5393–5420 (2016)
16. W. Yun, R. Xu, H. Ding, Axisymmetric bending of functionally graded circular magneto-electro-elastic plate. *Eur. J. Mech. A Solids* **30**(6), 999–1011 (2011)
17. S. Razavi, A. Shooshtari, Nonlinear free vibration of magneto-electro-elastic rectangular plates. *Compos. Struct.* **119**, 377–384 (2015)
18. K. Žur, M. Arefi, J. Kimc, J. Reddy, Free vibration and buckling analyses of magneto-electro-elastic FGM nanoplates based on nonlocal modified higher-order sinusoidal shear deformation theory. *Compos. Pt. B-Eng.* **12**(107601), 1–17 (2019)
19. T. Charitat, F. Graner, About the magnetic field of a finite wire. *Eur. J. Phys.* **24**(3), 267–270 (2003)
20. M. Takayasu, L. Chiesa, L. Bromberg, J. Minervini, HTS twisted stacked-tape cable conductor. *Supercond. Sci. Tech.* **25**(1), 014011 (2012)
21. Y. Hu, H. Xu, Nonlinear natural vibration of a circular plate in the non-uniform induced magnetic field. *J. Arch. Appl. Mech.* **91**, 2513–2533 (2021)

Modelling and Analysis of Vibrations on an Aerial Cable Car System with Moving Mass



Cesar Augusto Fonseca, Guilherme Rodrigues Sampaio,
Geraldo F. de S. Rebouças, Marcelo Pereira, and Americo Cunha Jr.

1 Introduction

Transporting persons and items by aerial cable cars, as seen in Fig. 1, has been in use over the last 100 years for many different applications. This type of transport is present in thousands of installations; Switzerland alone has more than 130 in operation. The study of cable car systems is an interesting subject in the modern literature, with many different aspects of the system approached, but published works on this topic are still only a few years old. Since it is a complex mechanical system with many bodies, flexibility, and subject to environmental perturbations, nonlinear phenomena may appear such as excitation of sub- and super-harmonics on the cable causing vibration to the traction mechanism, which can damage the machinery and endanger the operation.

The mechanical system studied consists of two cables, a supporting cable fixed in both ends and a variable-length traction cable. The car is modelled as a concentrated mass pulled by the traction cable and connected to the supporting cable through a spring. In this chapter, we analyze the effect of vibrations in the traction cable according to the speed of operation and position of the car. The coupling of the

C. A. Fonseca (✉)

Centro de Instrução Almirante Wanderkolk – CIAW, Rio de Janeiro, Brazil
e-mail: cesar.linhares@marinha.mil.br

G. R. Sampaio

RIO Analytics, Rio de Janeiro, Brazil

G. F. de S. Rebouças

Norwegian University of Science and Technology – NTNU, Trondheim, Norway
e-mail: geraldo.reboucas@ntnu.no

M. Pereira · A. Cunha Jr.

Rio de Janeiro State University – UERJ, Rio de Janeiro, Brazil
e-mail: marcelocpereira@globo.com; americo.cunha@uerj.br

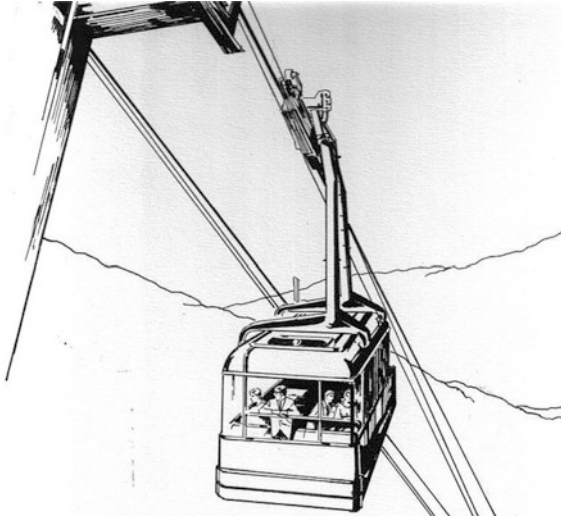


Fig. 1 Line art drawing of a typical aerial cable car system

two cables and a mass–spring system creates a very complex dynamic behaviour that causes a nonlinear movement and can even show some chaotic characteristics. Some references found in the literature such as the modelling of elevators show resemblance to the present study.

The work of Brownjohn [1] investigates the cable car that connects the island of Sentosa and Singapore’s main island through a vertical plane motion perspective. The article presents mathematical simulations representing the normal operation of the system, as well as free vibration, and the situation when the system is halted. Accelerometer measurements in the real system are used to obtain real vibrations for each operational condition. Investigation also includes a finite-element analysis of the system followed by the results analysis.

Terumichi et al. [2] analyze the non-stationary lateral vibration of a time-varying length string with a mass–spring system guided by rail, attached to the inferior end, a system similar to an elevator. A sinusoidal horizontal displacement at its upper end excites the string. An analysis of the influence of the string’s axial velocity on the vibrations is performed as well as an experimental setup investigation. Data generated by experiment and simulation are compared.

Bao et al. [3] analyze as well a vertical motion system similar to an elevator, focusing on lateral vibrations of the string. In this Chapter, the lateral motion of the mass, coming from imperfections on the rail guide, is the source of excitation. The Hamilton principle is used to obtain the string’s equations of motion. In the end, experimental test results are shown, and the results used validate the numerical simulations.

Lastly, Kaczmarczyk and Iwankiewicz [4] present a stochastic approach to the excitation of an elevator model. The stochastic parameters are the guide rail imper-

fections that excite the elevator car laterally. In order to do so, the imperfections are considered as a zero-mean stationary Gaussian process. Although the model proposed in this chapter uses a strict deterministic approach, the knowledge on time-scale separation shown is essential for solving the problem, as seen in another work of the same author [5].

Those works show that despite the presented cable vibration theories, there are still very few applications to aerial cable car systems, a common system around the world, where a failure can endanger many lives. Cable car systems differ significantly from elevators as the gravity acts transversely to the cable.

The main originality of this chapter is to develop a mechanical model of a cable car system, to investigate the influence of its parameters using numerical methods, and to explore some of its nonlinearities. This chapter is organized as follows: the mechanical–mathematical model for the system of interest is presented in Sect. 2, the numerical results and a brief discussion in Sect. 3, and finally the conclusions are made in Sect. 4.

2 Mechanical–Mathematical Model

The proposed mechanical system is illustrated in Fig. 2, where a pair of overhung cables has a constant value of tension and is fixed on both ends with density, circular cross-section, and constant length. The purpose of this cable is to provide support to the cable car and to serve as the rails, where the cable car slides on. Later, the rail cables are simplified as a single spring K attached to the cable car represented by the concentrated mass M . The car is pulled by another cable with a linear density ρ , cross-section A , and tension T . However, the length of the traction cable varies in time with constant velocity v , pulling the mass M to the origin, where the pulley is located.

To find the equivalent stiffness of the pair of supporting cables, a simple analytical approach is used. The car passing through the extent of the supporting cables is to be simplified as a concentrated load F travelling with constant velocity; then the solution of this problem is analytically solved and demonstrated in Hagedorn [6]. In this case, the cable deflection is given by

$$w(x, t) = -\frac{2FL_0}{\rho A\pi^2(c^2 - v^2)} \sum_{j=1}^{\infty} \frac{1}{j^2} \left(\sin \frac{j\pi vt}{L_0} - \frac{v}{c} \sin \frac{j\pi ct}{L_0} \right) \sin \frac{j\pi x}{L_0}, \quad (1)$$

where $c = \sqrt{T/\rho A}$ is a constant having the dimension of speed and the product ρA is the linear density of the cable. Then stiffness can be determined by taking the inverse of the deflection of the supporting cables.

The analytical solution of Eq. (1) is illustrated in Fig. 4 for different time instants using the mentioned parameters. It shows the deflection of the cable at different instants, while the load moves with velocity v . The parameters used to generate

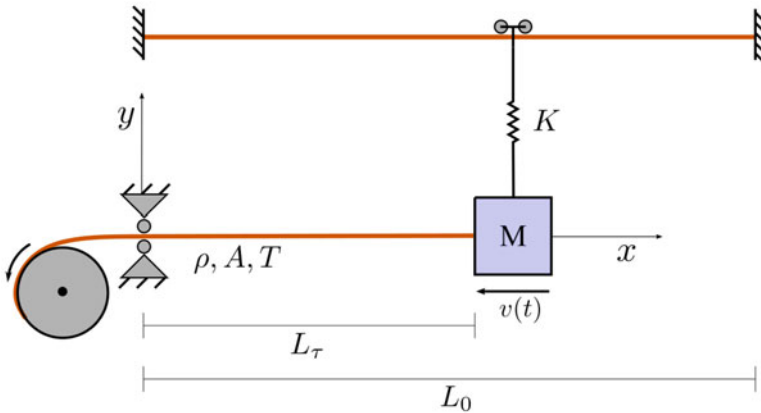


Fig. 2 Schematic representation of the mechanical system used to emulate the aerial cable car system: a variable-length cable coupled to a mass–spring oscillator

Table 1 Parameters used to model the rail cable and the traction cable

Supporting cables			Traction cables			
Parameter	Value	Unit	Parameter	Symbol	Value	Unit
Linear density	39.20	kg/m	Linear density	ρ	3.83	kg/m
Length	600	m	Initial length	L_0	600	m
Load	32.8	kN	Mass	M	6550	kg
Mean Tension	10.0	kN	Mean Tension	T	250	kN
Velocity	6.0	m/s	Stiffness	K	13.4	kN/m

these results are shown in Table 1. The deflection of the rope reaches its maximum value when the load is close to half of the length. Therefore, the rail cable equivalent stiffness value is estimated as

$$K = \frac{F}{w(L_0/2, L_0/2 v)}. \tag{2}$$

The following analysis does only concern with the mass being pulled by the cable. We begin by stating the kinetic \mathcal{T} and the potential energy of the rope and the mass. The total kinetic energy is

$$\mathcal{T} = \frac{1}{2} \int_0^{L(t)} \rho [\dot{v}^2 + (\dot{y} + v y')^2] dx + \frac{1}{2} M [\dot{v}^2 + (\dot{y} + v y')^2]_{x=L(t)}, \tag{3}$$

and the total potential energy \mathcal{U} is

$$\mathcal{U} = \frac{1}{2} \int_0^{L(t)} T y'^2 dx + \frac{1}{2} K y^2|_{x=L(t)}. \tag{4}$$

Here, y is the vertical displacement of the moving mass M attached to the pulling cable with linear density ρ and constant traction T . The dot represents the derivation in time and the $()'$ the spatial derivation.

For the traction cable, using the Hamilton principle with the adequate definition of the boundaries conditions and considering the variation of the length give the following initial-boundary value problem

$$\rho (\ddot{y} + 2v \dot{y} + v^2 y'') = T y'', \quad (5)$$

$$M (\ddot{y} + 2v \dot{y} + v^2 y') + K y = T y' \quad \text{at } x = L(t), \quad (6)$$

$$y = 0 \quad \text{at } x = 0. \quad (7)$$

The first boundary condition, given by Eq. (6), is not homogeneous. This term can be transferred to the differential equation of motion, Eq. (5), by considering the car's dynamic forces as a concentrated load at $x = L(t)$, rendering a simpler and more intuitive approach [7], given by

$$\rho (\ddot{y} + 2v \dot{y} + v^2 y'') + 2 [M(\ddot{y} + 2v \dot{y} + v^2 y' + g) + K y] \delta(x - L(t)) = T y'', \quad (8)$$

$$y = 0 \quad \text{at } x = 0, \quad (9)$$

$$T y' = 0 \quad \text{at } x = L(t), \quad (10)$$

where \dot{y} is the time derivative of y , and y' is the corresponding spatial derivative with respect to x .

To promote a separation of time scales in the problem, a slow time variation $\tau = \varepsilon t$ is introduced, in which $\varepsilon = v/\omega_0 L_0$, being ω_0 is the natural frequency of the cable without mass and spring, and L_0 the maximum extent of the cable, see [8, 9] for details.

Knowing that $L(t) = L_0 + vt$, so, $v = \dot{L} = \frac{\partial \tau}{\partial t} \frac{\partial L}{\partial \tau} = \varepsilon v$, where $v = \frac{\partial L}{\partial \tau}$. Therefore, we seek solutions of the form

$$y(x, t) \approx \sum_{i=1}^N \phi_i(x, \tau) q_i(t), \quad (11)$$

where $\phi_i(x, \tau) = \sin(\lambda_\tau^i x)$ and $q_i(t)$ are mode shapes and modal coordinates associated to the underlying eigenvalue problem, respectively. The term λ_τ^i is a slow variation in times of the natural frequency of the cable

$$\lambda_\tau^i = \frac{1}{2} \frac{(2i - 1) \pi}{L_\tau}. \quad (12)$$

Applying Eq. (11) into Eq. (8) multiplying by $\phi_j(x, \tau)$ and integrating between 0 and L_τ , it is possible to write the discrete dynamical equation of motion

$$\sum_{i=1}^N [\mathcal{M}_{ij} \ddot{q}_i(t) + \mathcal{G}_{ij} \dot{q}_i(t) + \mathcal{K}_{ij} q_i(t)] = 0, \quad (13)$$

where mass, gyroscopic, and stiffness operator components are, respectively, defined by the following expressions:

$$\begin{aligned} \mathcal{M}_{ij} &= \int_0^{L_\tau} \rho \phi_i \phi_j dx + M \phi_i(L_\tau) \phi_j(L_\tau) \\ \mathcal{G}_{ij} &= \int_0^{L_\tau} 2 \rho v \epsilon \phi_i' \phi_j dx + 2 M \epsilon v \phi_i'(L_\tau) \phi_j(L_\tau) \\ \mathcal{K}_{ij} &= \int_0^{L_\tau} (\rho v^2 \epsilon^2 - T) \phi_i' \phi_j' dx \\ &\quad + (M v^2 \epsilon^2 \phi_i''(L_\tau) + K \phi_i(L_\tau)) \phi_j(L_\tau). \end{aligned} \quad (14)$$

To construct the mass, gyroscopic, and stiffness matrices, the following orthogonality relationships are taken into account

$$\int_0^{L_\tau} \phi_j \phi_i dx = \frac{1}{2} L_\tau \delta_{ij}, \quad \int_0^{L_\tau} \phi_j \phi_i'' dx = -\frac{1}{2} \lambda_i^2 L_\tau \delta_{ij} \quad (15)$$

and that

$$\int_0^{L_\tau} \phi_j \phi_i' dx = -2 \frac{(i-1/2)(j-1/2)}{(i-1/2)^2 - (j-1/2)^2}, \quad (16)$$

where δ_{ij} is the Kronecker delta. As seen in Blevins [10], the result from Eq. (16) exists only when the sum $i+j$ is odd, otherwise it is zero. Also, one has $\phi_i = \sin(\frac{1}{2} \frac{(2i-1)\pi}{L_\tau} x)$ and $\phi_j = \sin(\frac{1}{2} \frac{(2j-1)\pi}{L_\tau} x)$.

Thus, for a two-mode approximation ($i = 1..2$ and $j = 1..2$), one gets

$$\begin{aligned} &\left(\frac{1}{2} \rho L_\tau + M\right) \ddot{q}_1(t) - M \ddot{q}_2(t) + \frac{3}{2} \rho v \epsilon \dot{q}_2(t) \\ &+ \frac{1}{8 L_\tau^2} \left[-2 \pi^2 \epsilon^2 v^2 \left(\frac{1}{2} \rho L_\tau + M\right) + L_\tau \pi^2 T + 8 K L_\tau^2 \right] q_1(t) \\ &+ \frac{1}{4 L_\tau^2} \left(M v^2 \pi^2 \epsilon^2 - 4 K L_\tau^2 \right) q_2(t) = 0, \quad (17) \\ &\times \left(\frac{1}{2} \rho L_\tau + M\right) \ddot{q}_2(t) - M \ddot{q}_1(t) - \frac{3}{2} \rho v \epsilon \dot{q}_1(t) \end{aligned}$$

$$\begin{aligned}
& + \frac{1}{4 L_\tau^2} \left(9 M v^2 \pi^2 \epsilon^2 - 4 K L_\tau^2 \right) q_1(t) \\
& + \frac{1}{8 L_\tau^2} \left[-18 \pi^2 \epsilon^2 v^2 \left(\frac{1}{2} \rho L_\tau + M \right) + 9 L_\tau \pi^2 T + 8 K L_\tau^2 \right] q_2(t) = 0,
\end{aligned} \tag{18}$$

which can be rewritten as

$$\begin{aligned}
& \ddot{q}_1(t) - \mu_\tau \ddot{q}_2(t) + \alpha_\tau \dot{q}_2(t) + \left[(-\beta_\tau - \eta_\tau + \sigma_\tau) + \omega_\tau^2 \right] q_1(t) + \\
& \left(\eta_\tau - \omega_\tau^2 \right) q_2(t) = 0
\end{aligned} \tag{19}$$

$$\begin{aligned}
& \ddot{q}_2(t) - \mu_\tau \ddot{q}_1(t) - \alpha_\tau \dot{q}_1(t) + \left(9 \eta_\tau - \omega_\tau^2 \right) q_1(t) + \\
& \left(9 (-\beta_\tau - \eta_\tau + \sigma_\tau) + \omega_\tau^2 \right) q_2(t) = 0,
\end{aligned} \tag{20}$$

where

$$\begin{aligned}
m_\tau &= \frac{1}{2} \rho L_\tau + M, \quad \mu_\tau = \frac{M}{m_\tau}, \quad \alpha_\tau = \frac{3}{2} \frac{\rho v}{m_\tau}, \quad \beta_\tau = \frac{\pi^2 \epsilon^2 v^2 \rho}{8 L_\tau m_\tau}, \\
\eta_\tau &= \frac{1}{4} \frac{\pi^2 \epsilon^2 v^2}{L_\tau^2} \mu_\tau, \quad \sigma_\tau = \frac{\pi^2 T}{8 L_\tau m_\tau}, \quad \text{and } \omega_\tau^2 = \frac{K}{m_\tau}.
\end{aligned} \tag{21}$$

The first term, m_τ , is the modal mass of the cable along with the cable car mass, which also brings the ratio μ_τ of the masses. The latter couples the system with its acceleration terms. The parameter α_τ represents the Coriolis, and β_τ and η_τ are the centripetal forces of the cable and the mass, respectively. The traction can now be written as σ_τ and the natural frequency from the attached spring as ω_τ . Each of these terms varies in the slow time τ as the pulling cable varies its length.

3 Numerical Results and Discussion

By inspecting the terms in (21), as well as Eqs. (19) and (20), it is possible to observe the overall dependency of the cable variation in the slow time τ . Moreover, some of them are proportional to $\mathcal{O}(1/L_\tau)$ like ω_τ^2 and η_τ ; others are proportional to $\mathcal{O}(1/L_\tau^2)$ like β_τ and σ_τ . It means that β_τ and σ_τ can become extremely high when the cable length is getting closer to zero. Although the effect is rather small for η and β_τ , it is usually not for σ_τ . It is worth pointing out that there is a set of values in which σ_τ surpasses the value of ω_τ^2 at a specific length of L_τ .

A numerical investigation is conducted, and a set of values are given for each of parameters from Eq. (21). Then, a simulation of Eqs. (19) and (20) using a 4th and

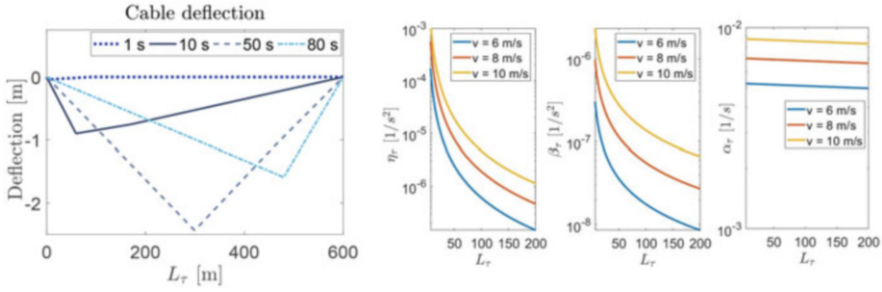


Fig. 3 Parameter variation of the first mode in relation to the length L_τ

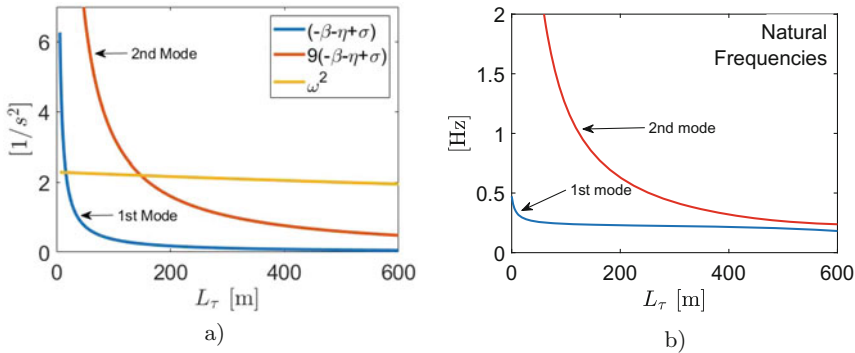


Fig. 4 In (a) The specific length where the natural frequencies depend more on the cable (blue and red) than on the rail stiffness (yellow). Travelling speed $v = 6$ m/s. In (b), variation of the natural frequencies as a function of the cable length

5th Runge–Kutta solver is done from initial condition of a fully extended length of cable to its almost entire retraction. The parameters used in the simulations match the ones from a real cable car installation, meaning that their values are completely feasible and the results may represent the behaviour of an actual situation (Fig. 3).

Figure 4 illustrates the variation of the parameters as the traction cable is being retracted by a constant velocity. Three different velocities are tested. Figure 4 shows that the parameters η_τ , β_τ , α_τ have little influence on the overall dynamics, albeit the increase of the travelling speed.

When comparing the parameters σ_τ and ω_τ^2 , one observes in Fig. 4a that there is a specific length of the cable that their values are equal, and as the cable car approaches the end, σ_τ becomes even higher that may be relevant to the dynamics. This results in Fig. 4b where it shows the variation of the natural frequencies as a function of the cable length.

To further investigate the proposed mechanical model, a harmonic force is added to the equation presented in Sect. 2 applied to the concentrated mass M . The nature of this force can be seen as an early approximation of the wind mean effect acting

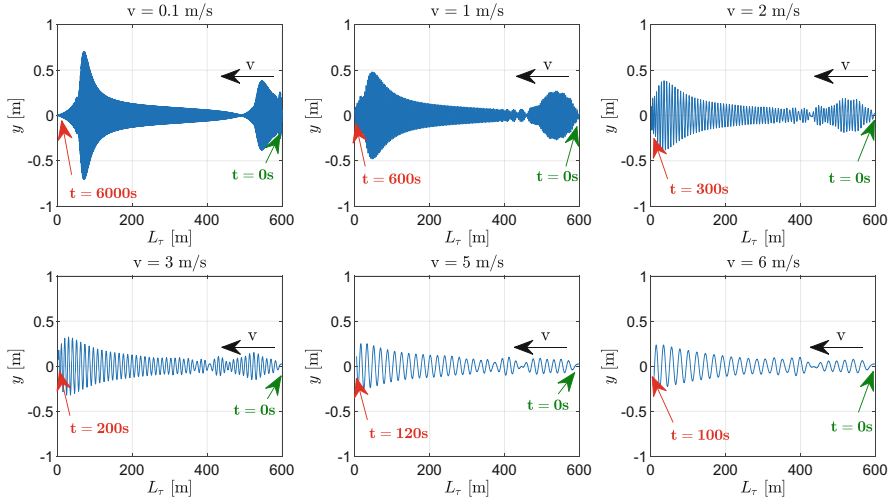


Fig. 5 Displacement for different velocities v of the cable car when the system is excited by a harmonic force at $F(t) = 300 \sin(\omega_f t)$ [N] at $x = L_\tau$

directly on the cable car. A Rayleigh model damping is also included to emulate the energy dissipation, which also prevents numerical instabilities.

A constant value for the external force frequency is chosen to be $\omega_f = 0.26$ Hz, because it has long period time compatible to the natural behaviour of the wind. Note in Fig. 4b that this becomes the resonance of the system twice as the cable retracts. The result can be seen in Fig. 5, which shows the cable car displacement time series $y(t)$. As expected, the cable car develops high amplitudes of oscillations twice as the cable gets shorter, and the maximum value of the amplitude gets smaller as the travelling velocity v is higher, due to the shorter period of time that the forcing frequency matches with one of the natural frequencies.

The presence of high-amplitude oscillations shown by the numerical simulation is in accordance with the real functioning cable car seen by the maintenance crew as it approaches the terminal station. These vibrations are mitigated by the breaking system changing the value of the travelling speed v . Also, the model has its own limitations, since by shortening the cable means that the mass M is reaching its boundary condition, which would lead to numerical instabilities or misrepresentation of the real phenomena.

4 Conclusions and Future Perspectives

This chapter presented a mechanical–mathematical model for a cable car system. First, the equations of motion are developed, and numerical analysis is conducted with parameters inspired by a real case. This analysis shows the changes of each

parameter as a function of the cable length, among them the increase of the stiffness parameter related to the cable.

This chapter paves the way for a series of different analyses, which may include the variation of the stiffness parameter related to the pair of supporting cables, the investigation of the influence of a harmonic forcing at the origin, which would represent the machinery responsible for actuating the whole system.

Results show that some points of the trajectory and some speeds present higher amplitude vibrations than others; this is an important nonlinear phenomenon that poses challenges to the operation of systems similar to the one modelled. The understanding of those phenomena, as well as its numerical modelling, is of high importance to the safe operation of aerial cable cars.

Another possibility is to include the presence of a random force concentrated at the mass, representing the wind or passengers moving inside the car. Lastly, these models can be compared to other numerical analyses with finite-element models or even with experimental data. This research can also be adapted to other mechanical equivalents found in installations such as in ski lifts.

Acknowledgments The fourth author would like to thank the financial support given to this research by the Brazilian agencies Coordenação de Aperfeiçoamento de Pessoal de Nível Superior—Brasil (CAPES)—Finance Code 001, and the Carlos Chagas Filho Research Foundation of Rio de Janeiro State (FAPERJ) under the following grants: 211.304/2015, 210.021/2018, 210.167/2019, and 211.037/2019.

References

1. J.M.W. Brownjohn, Dynamics of an aerial cableway system. *Eng. Struct.* **20**(9), 826–836 (1998)
2. Y. Terumichi, M. Ohtsuka, M. Yoshizawa, Y. Fukawa, Y. Tsujioka, Nonstationary vibrations of a string with time-varying length and a mass-spring system attached at the lower end. *Nonlinear Dyn.* **12**, 39–55 (1997)
3. J. Bao, P. Zhang, C. Zhu, Dynamic analysis of flexible hoisting rope with time-varying length. *Int. Appl. Mech.* **51**(6), 710–720 (2015)
4. S. Kaczmarczyk, R. Iwankiewicz, Dynamic response of an elevator car due to stochastic rail excitation. *Proc. Est. Acad. Sci.* **55**(1), 58–67 (2006)
5. S. Kaczmarczyk, The passage through resonance in a catenary–vertical hoisting cable system with slowly varying length. *J. Sound Vib.* **208**(2), 243–269 (1997)
6. P. Hagedorn, *Nonlinear Oscillations* (Oxford Sci. Publ., Oxford, 1988)
7. L. Meirovitch, *Fundamentals of Vibrations* (McGraw-Hill, New York, 2000)
8. A. Cunha Jr., C.A. Fonseca, G. Rodrigues, M. Pereira, Analysis of vibrations on an aerial cable car system with moving mass, in *Proceedings of the XV International Symposium on Dynamic Problems of Mechanics, DINAME 2019*, Buzios, 2019
9. D. Colón, A. Cunha Jr., S. Kaczmarczyk, J. Balthazar, On dynamic analysis and control of an elevator system using polynomial chaos and Karhunen-Loève approaches. *Proc. Eng.* **199**, 1629–1634 (2017)
10. R.D. Blevins, *Flow-Induced Vibration* (Van Nostrand Reinhold, 1990)

Influence of Model Nonlinearities on the Dynamics of Ring-Type Gyroscopes



Ibrahim F. Gebrel, Ligang Wang, and Samuel F. Asokanthan

1 Introduction

The linear and nonlinear dynamic response behavior of rotating rings has been studied in several recent articles. The nonlinear equations of motion considering only the in-plane vibrations of a ring were derived in [1]. The formulation of nonlinear equations of motion of ring-type gyroscope using two vibration modes has been performed employing Galerkin's procedure in [2]. The influence of rotation and flexible base on the natural frequencies and mode shapes have been investigated in detail in [3]. The modal behavior as well as stability of rotating rings in 3D under magnetic levitation has been studied via an analytical model and validated employing Finite Element Analysis [4]. The Coriolis forces induced in the ring gyroscope due to the ring's rotation cause the resonant mode to shift vibration into the next resonance mode, as described in [5].

The influences of extensional and shear deformation and inertia on natural frequency differences have been performed in [6]. The plane wave motion to solve the fixed deflection, natural frequency split, and mode contamination of the rotating ring-shaped periodic structures have been analytically examined [7].

In the present paper, the nonlinear dynamic behavior of rotating flexible rings for use in vibratory angular rate sensors has been studied via numerical simulations. A homogenous, isotropic ring is chosen as the resonator. The investigation of dynamic response analysis and the rotating macro ring gyroscope's stability behavior has been studied by [8] and Gebrel et al. [9] by considering the linearized model

I. F. Gebrel · S. F. Asokanthan (✉)

Department of Mech. and Matls. Engineering, The University of Western Ontario, London, ON, Canada

e-mail: sasokant@uwo.ca

L. Wang

Department of Mathematica, Harbin Engineering University, Harbin, Heilongjiang, China

associated with the second flexural modes. In [9], a theoretical model for generating nonlinear electromagnetic excitation forces is developed. The schematic of the rotating ring geometry used in the present study has been described in detail in [8, 9].

One of the most critical challenges in constructing ring-based vibratory gyroscopes is the requirement to operate at one of the highly resonant natural frequencies in order to maximize device sensitivity. However, large resonant amplitudes tend to bring out the undesirable nonlinear effects due to geometric as well as actuator nonlinearities. Consequently, the dynamic response of thin circular rings and consideration of input nonlinear actuator dynamics is warranted to gain a complete understanding of performance enhancements that can be achieved for this class of gyroscopes.

In the present paper, a mathematical model that represents the nonlinear dynamic behavior of a ring-type gyroscope is formulated. The nonlinear equations of motion are simplified by considering only the highly resonant second flexural mode the device utilizes and by ignoring the presence of extensional modes of vibration. Due to gyroscopic coupling present in the system and angular input rate, the natural frequency variations have been described in the prior study [9]. A suitable electromagnetic actuator model has been developed for the purposes of examining the nonlinear dynamic response.

2 Equation of Motion

In this study, the nonlinear equations of motion have been obtained by considering that the circumferential strain in the mid-surface is zero, and the equations of motion have been reduced to a suitable discrete form via Galerkin's procedure and the resulting equations permit the application of dynamic response analysis. The ring used for the present study is assumed to possess isotropic and homogenous material properties. Besides, under the Euler-Bernoulli theory, the transverse shear deformation influence is neglected since it is assumed that plane sections remain plane as well stay normal to the neutral surfaces after deformation [10]. Figure 1a shows the ring geometry and relevant parameters used in this paper. The stiffness components k_r and k_θ , respectively, denote the radial and circumferential components, while u_r and u_θ symbolize the transverse and circumferential displacements. The eight support springs considered to represent the flexible mounting are assumed to possess significantly low stiffness and are expected not to have an influence on the ring dynamics. A body-fixed set of axes X, Y, Z has been assigned to represent the angular motion of the ring with respect to an inertial frame R . In this formulation, the curvilinear surface coordinates α_1, α_2 , and α_3 are used for locating the neutral surface elements.

The second flexural mode shapes that possess identical natural frequencies for the ring are known as degenerate modes shapes and are separated by 45 degrees as shown in Fig. 1b. It may be noted that the presence of degenerate mode shapes is

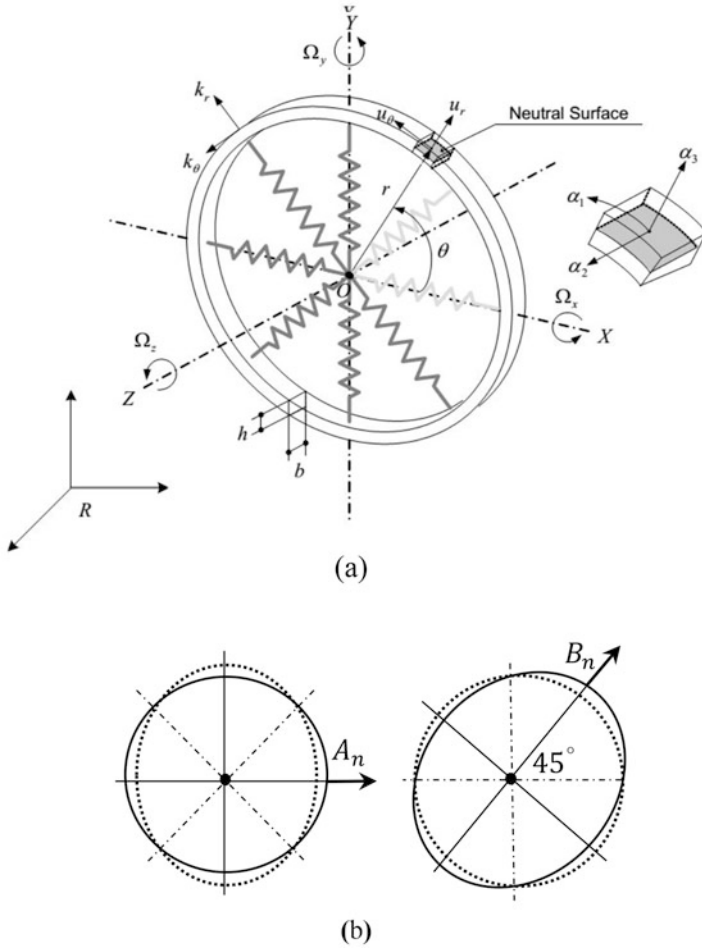


Fig. 1 (a) Ring geometry and parameters. (b) Degenerate second flexural mode shapes

due to the ring symmetry. The geometry and parameters used in the present paper have been described in detail in the prior research [9].

In this paper, the nonlinear equations of motion in terms of the generalized coordinates associated with the flexural coordinates A_n and B_n are developed to investigate a ring gyroscope's nonlinear dynamic behavior. As described in the previous study [9], the nonlinear governing equations for the rotating ring-type gyroscope with the consideration of in-extensional mid-surface when sinusoidal external electromagnetic forces in the radial direction are considered take the form:

$$\frac{EA}{br^2} \left(u_\theta' + u_r \right) - \frac{EI}{br^4} \left(u_\theta'''' - u_r'''' \right) + \rho h \Omega^2 \left(2u_\theta' - u_r'' \right) + k_r u_r + \rho h \left(\ddot{u}_r - \dot{\Omega} u_\theta - 2\Omega \dot{u}_\theta \right) = f_{Nem} (A_n, B_n, \theta_i) \cos(\omega t), \quad (1)$$

where $(\dot{\quad})$ represents time derivative while the spatial derivatives are denoted by $(\quad)'$. In Eq. (1), E represents the Young's modulus, I indicates area moment of inertia for ring cross-section, ρ is mass density, EI denotes flexural rigidity, A represents the cross sectional area of ring, b is the axial thickness of ring, h indicates radial thickness, r denotes the radius of the ring while ω is the excitation frequency. The term $f_{Nem}(A_n, B_n, \theta_i)$ represents sinusoidal nonlinear external electromagnetic force magnitude, while input angular rate and angular acceleration are, respectively, denoted by Ω and $\dot{\Omega}$.

In this study, the partial differential Eq. (1) is reduced to nonlinear ordinary differential equations by employing Galerkin's method. The general radial and circumferential displacements that satisfy the continuity conditions are employed in this discretization process. Under these conditions, considering the periodic nature of solutions, the deflection modes can be chosen as [2, 9].

$$u_r = A_n \cos(n\theta) + B_n \sin(n\theta) - \frac{n\gamma}{4r} \left[A_n^2(t) + B_n^2(t) \right] \quad (2)$$

$$u_\theta = -\frac{1}{n} \left[A_n \sin(n\theta) - B_n \cos(n\theta) \right] + \frac{\gamma}{8r} \left[A_n^2(t) + B_n^2(t) \right] \sin(2n\theta) - \frac{\gamma}{4r} A_n(t) B_n(t) \cos(2n\theta), \quad (3)$$

where the mode functions are observed to be composed of time-dependent generalized co-ordinates A_n and B_n , mode number n , ring radius r , and the nonlinear parameter γ . As seen from Eqs. (2) and (3) this parameter has an influence on both homogenous and the non-homogenous part of Eq. (1). Hence, the influence of the parameter γ which results from the in-extensionality of the middle surface is termed as system nonlinearity. In this paper, Eqs. (2) and (3) represent practically any transverse or circumferential deflection where nonlinear additive terms are incorporated in the mode function via the nonlinear term γ . In Eqs. (2) and (3), n takes the value 2 since only the second flexural modes are considered to contribute to the ring vibration. Galerkin's method is applied by employing Eqs. (2) and (3) in Eq. (1), multiplying by the appropriate weighting function associated with $A_n(t)$ and $B_n(t)$ and integrating with respect to θ from 0 to 2π . The resulting discretized set of nonlinear differential equations take the form:

$$\left[\rho h \pi + 2\rho h \pi \left(\frac{n\gamma}{2r} \right)^2 A_n^2 \right] \ddot{A}_n + 2\rho h \pi \left(\frac{n\gamma}{2r} \right)^2 A_n B_n \ddot{B}_n + 2\zeta \omega_0 \dot{A}_n + \left[\frac{EI}{br^4} (n^2 - 1) n^2 + \rho h \Omega^2 (n^2 - 2) + k_r \right] \pi A_n + \left[\frac{EA}{br^2} + k_r \right] (n\gamma/2r)^2 \left[A_n^2 + B_n^2 \right] \pi A_n + 2\rho h \pi (n\gamma/2r)^2 \left[\dot{A}_n^2 + \dot{B}_n^2 \right] A_n - \rho h \pi \dot{\Omega} \frac{1}{n} B_n - 2\rho h \pi \Omega \frac{1}{n} \dot{B}_n = f_{Nem} (A_n, B_n, \theta_i) \cos(\omega t) \quad (4)$$

$$\begin{aligned}
 & \left[\rho h \pi + 2 \rho h \pi \left(\frac{n\gamma}{2r} \right)^2 B_n^2 \right] \ddot{B}_n + 2 \rho h \pi \left(\frac{n\gamma}{2r} \right)^2 A_n B_n \ddot{A}_n + 2 \zeta \omega_0 \dot{B}_n + \left[\frac{EI}{br^4} (n^2 - 1) n^2 + \right. \\
 & \left. \rho h \Omega^2 (n^2 - 2) + k_r \right] \pi B_n + \left[\frac{EA}{br^2} + k_r \right] \left(\frac{n\gamma}{2r} \right)^2 \left[A_n^2 + B_n^2 \right] \pi B_n + 2 \rho h \pi \left(\frac{n\gamma}{2r} \right)^2 \\
 & \left[\dot{A}_n^2 + \dot{B}_n^2 \right] B_n + \rho h \pi \Omega^2 \frac{1}{n} A_n + 2 \rho h \pi \Omega \frac{1}{n} \dot{A}_n = 0,
 \end{aligned}
 \tag{5}$$

where the parameter ζ is the mechanical damping ratio, and n denotes the number of modes which is taken to be 2 in this study. A nonlinear electromagnetic force $f_{Nem}(A_n, B_n, \theta_i) \cos(\omega t)$ is considered to provide external sinusoidal excitation which is essential for the operation of the gyroscope where ω represents the excitation frequency. The angular position of electrostatic forces on the system is denoted by θ_i , $i = 1, 2, 3, 4$. Various configurations for the electromagnetic force are considered for the purposes of designing a ring gyroscope with effective second flexural resonant mode participation. Also, a suitable theoretical formulation of the electromagnetic force magnitude is developed considering the interactions between the electromagnet (*em*) and permanent magnets (*pm*) as shown in Fig. 2. The potential energy and force formulations are obtained from a dipole model by the law of Biot and Savart [11]. The expressions for nonlinear electromagnetic forces that affect the system from four positions are derived in the primary coordinate A_n as

$$\begin{aligned}
 f_{Nem}(A_n, B_n, \theta_i) = & \frac{\mu_0}{2\pi} k N i A M_A V_A \sum_{i=1}^2 \left(\cos(n\theta_i) - \frac{n\gamma}{2r} A_n \right) * \\
 & \left[\frac{3}{\left\{ d - A_n \cos(n\theta_i) - B_n \sin(n\theta_i) + \frac{n\gamma}{4R} \left[A_n^2 + B_n^2 \right]^4 \right\}} \right]
 \end{aligned}
 \tag{6}$$

where $\mu_0 = 4\pi \times 10^{-7} H/m$ represents the magnetic permeability of free space, $A = \pi R^2$ is the area of the loop, the number of coil turns is denoted by N while i , \tilde{R} , respectively, represent the coil current and radius of coil circular loop. M_a is the magnetization, and V_a represents the volume of the source magnet. In Eq. (6), consideration for the use of an iron core has been included via a relative permeability constant k . This equation has been employed for studying the effect of nonlinear actuator dynamics employing the system of Eqs. (4) and (5). The distance between electromagnetic (*em*) and the permanent magnet (*pm*) is designated as d as shown in Fig. 2.

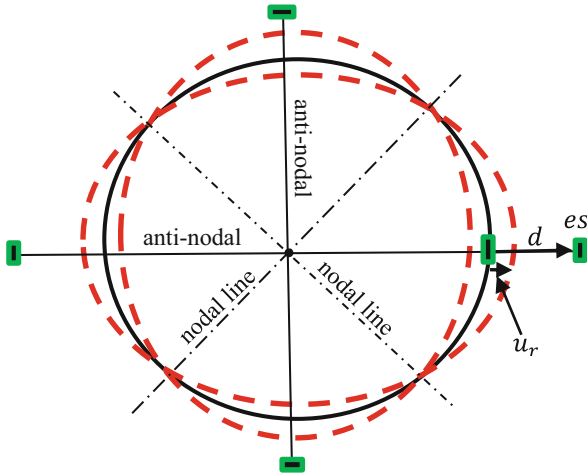


Fig. 2 Schematic representation of ring dynamics and actuator configurations

3 Results and Discussion

The dynamic response of the system when subjected to an external nonlinear actuator is examined via a numerical solution scheme in the present study. The mathematical model presented in Eqs. (4), (5), and (6) is employed for this purpose. Also, natural frequency variation due to rotation has been quantified and discussed in detail [9]. The operation of ring-based vibratory gyroscopes relies on nonlinear external excitation close to one of the resonant frequencies in order that device sensitivity may be maximized. To this end, variation of the second flexural natural frequency with the input angular rate is quantified using this model. It may be noted that as described in the studies [8, 9], the experimentally predicted natural frequencies agree with those predicted by the mathematical model presented in the present paper.

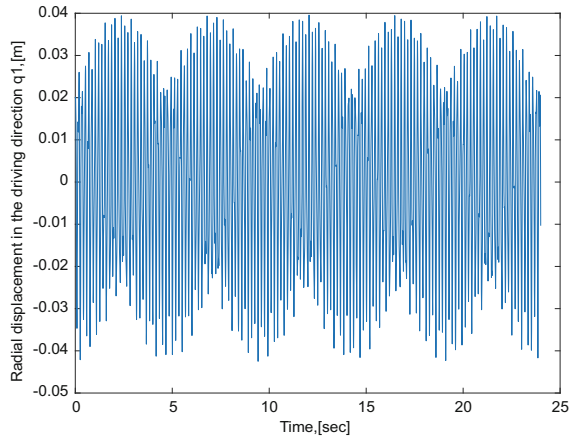
Furthermore, a nonlinear model which includes complex nonlinear inertia/stiffness terms, as well as a nonlinear electrometric force as depicted in Eqs. (4) and (5), have been employed. Equations (4) and (5) have been solved numerically to predict nonlinear response features of a ring gyroscope. At a nominal input angular rate of 2π rad/sec, the natural frequencies used in the present study have been evaluated as $\omega_1 = 58.6218$ rad/sec, and $\omega_2 = 64.8218$ rad/sec. In the absence of input angular rate of the ring, two identical natural frequencies are predicted and they take the values $\omega_1 = \omega_2 = 61$ rad/sec. The generalized coordinates $q_1 = A_n/h$, $q_2 = B_n/h$ have been used for the non-dimensional equations. The following typical ring design parameters: radius of $r = 92.5 \times 10^{-3}$ m, thickness of $h = 0.1016 \times 10^{-3}$ m, and a height of $b = 150 \times 10^{-3}$ m with Young's modulus of $E = 2.068 \times 10^{11}$ N/m² and the density of $\rho = 7833.41$ kg/m³ have been chosen in the present study. Besides, for all time as well as frequency response simulations,

a damping ratio, ζ of 0.01 has been assumed for the system. For all numerical simulations, a zero-velocity initial condition together with an initial displacement amplitude of $5 \times 10^{-3}m$ is imposed.

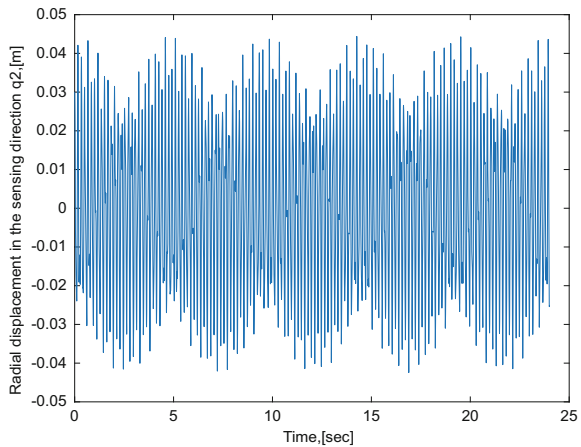
3.1 Nonlinear Dynamic Response in the Driving and Sensing Directions

The time history with long time records in the driving A_n and sensing B_n coordinates of a ring gyroscope shown in Fig. 3a, b are obtained using Eqs. (4), (5), and (6) in the presence of nonlinear term at an excitation frequency 60 rad/sec . The response

Fig. 3 Radial displacement for $\Omega = 2 \text{ rad/sec}$ in (a) driving and (b) sensing directions

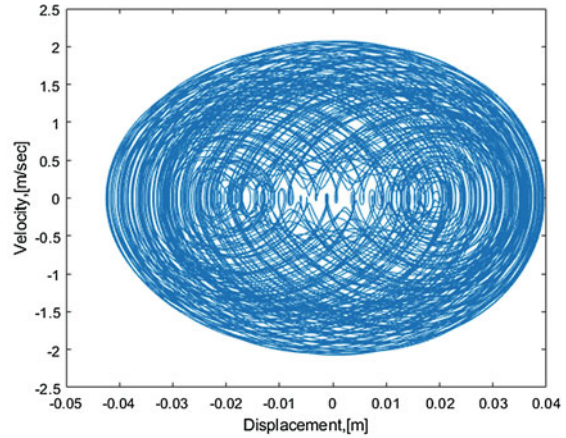


(a)

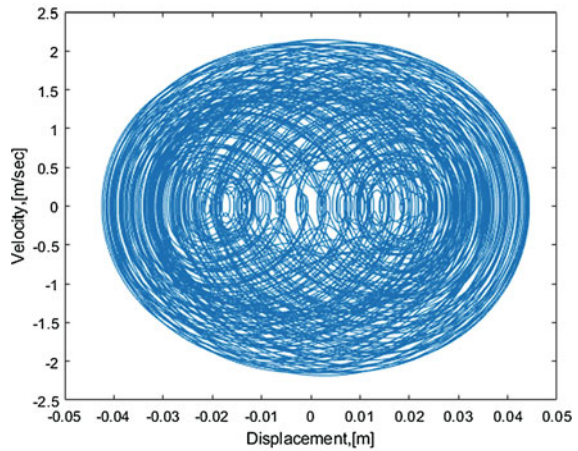


(b)

Fig. 4 Phase diagram in (a) driving and (b) sensing directions



(a)



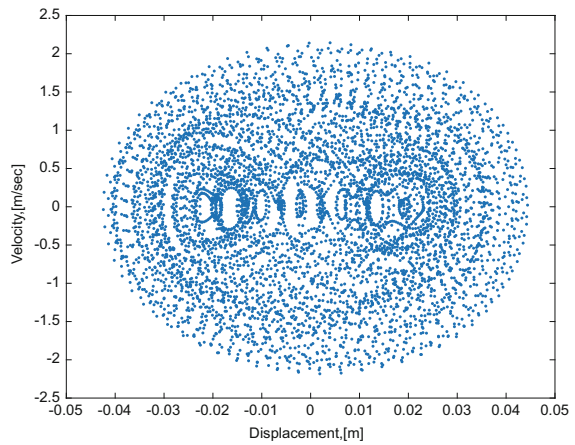
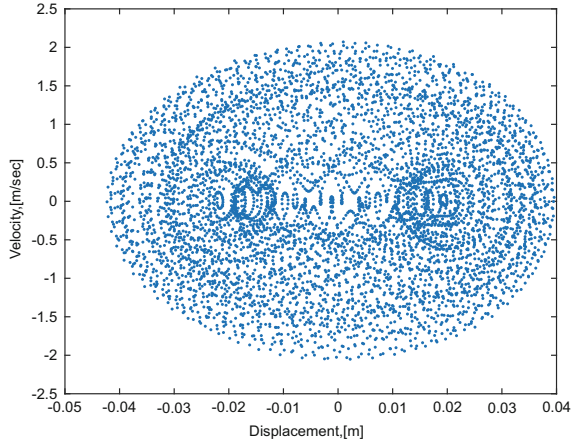
(b)

of the ring in the driving and the sensing directions, respectively, are displayed in Figs. 3a, b. This study concludes that due to the gyroscopic coupling present in the system, a transfer of energy takes place between the two modes in the presence of angular velocity input.

For the same system parameters and initial conditions, when the gyroscope is given an input angular rate of 2π rad/sec, the phase-plane trajectory based on the steady-state response in the driving and sensing directions, respectively, is shown in Fig. 4a, b.

Moreover, effects of nonlinearity can be seen in the Poincaré map plots in Fig. 5a, b and is indicated via multiple equilibrium points. Also, it can be observed that the resulting Poincaré map appears as a cloud of unorganized points due

Fig. 5 Poincare' map in (a) driving and (b) sensing directions



to the influence of the nonlinear term associated with the system as well as the electromagnetic force.

4 Conclusions

The nonlinear dynamic response of a macro ring-based gyroscope has been investigated for the purpose of quantifying the effects of system as well as actuator nonlinearities inherently present in such systems under operation. The device exhibits high nonlinearity in the presence of nonlinear term in the model which may be attributed to high vibration amplitudes. A suitable electromagnetic actuator model has been developed for the purposes of examining the nonlinear

dynamic response. The nonlinear dynamic response obtained via time-response, Phase portraits, and Poincare' maps indicates that the nonlinearity in the model and actuation play an essential role in shaping the dynamic ring behavior. Comparison with the linear model study [9], revealed that the inclusion of model nonlinearities in the presence of high vibration amplitudes has a strong influence and hence greatly demonstrates its significance.

References

1. D.A. Evensen, Nonlinear flexural vibrations of thin circular rings. PhD. Thesis, California Inst. Technol (1964)
2. D.A. Evensen, Nonlinear flexural vibrations of thin circular rings. *J. Appl. Mech.* **33**, 553–560 (1966)
3. S.C. Huang, W. Soedel, Effect of coriolis acceleration on the free and forced in-plane vibrations of rotating rings on elastic foundation. *J. Sound Vib.* **115**(2), 253–274 (1987)
4. A. Arena, W. Lacarbonara, On the stability of magnetically levitated rotating rings. *Int. J. Mech. Sci.* **131–132**(3), 286–295 (2017)
5. R. Eley, C.H.J. Fox, S. McWilliam, Coriolis coupling effects on the vibration of rotating rings. *J. Sound Vib.* **238**(3), 459–480 (2000)
6. W.B. Bickford, E.S. Reddy, On the in-plane vibrations of rotating rings. *J. Sound Vib.* **101**(1), 13–22 (1985)
7. D. Zhang, S. Wang, J. Liu, Analytical prediction for free response of rotationally ring-shaped periodic structures. *J. Vib. Acoust.* **136**(4), 12 (2014)
8. J. Cho, S.F. Asokanathan, Nonlinear instabilities in ring-based vibratory angular rate sensors. PhD. Thesis, Department of Mechanical Engineering, University of Western Ontario, Canada (2009)
9. I.F. Gebrel, L. Wang, S.F. Asokanathan, Dynamics of a ring-type macro gyroscope under electromagnetic external actuation forces. Proceedings of the ASME International Design Engineering, 86334, pp. V008T10A028. Technical Conferences IDETC/CIE, Quebec, Canada (2018)
10. S.F. Asokanathan, J. Cho, Dynamic stability of ring – based angular rate sensors. *J. Sound Vib.* **295**(3–5), 571–583 (2006)
11. W. Jearl, R. Halliday, Fundamentals of physics. 10th Edition, Cleveland State University, New Jersey, USA (2014)

Gravitational Dampers for Unloading Angular Momentum of Nanosatellites



Anton V. Doroshin 

1 Introduction

As it is well known, the problem of spacecraft attitude control implies the suppression of large values of the SC angular velocity after separation from the last stage of the space-rocket or unloading saturated reaction/momentum wheels. This assumes the large value of the angular momentum of the system (of the main body spacecraft and/or rotors-wheels) and its discharging. Therefore, the task of unloading the angular momentum is one of primary tasks of spacecraft attitude dynamics.

The angular momentum of reaction/momentum wheels can be transferred to the main spacecraft body using internal interaction [1, 2], and after this translation the angular momentum value can be decreased with the help of interaction with the external forces [3–13], e.g., central gravitational forces, which are acting on spacecraft moving along the orbit.

Due to the big importance of modern space missions with nanosatellites applying, it is very important to develop the simplest constructional schemes to the angular momentum unloading, which can be used basing on nanosatellites platforms.

In this work, the scheme of the gravitational unloading is proposed. This scheme (Fig. 1a) uses the internal body with different general inertia moments (Fig. 1c) placed in the spherical shell floating in the spherical cavity with viscous liquid (Fig. 1b). It is clear that at the motion along the orbit this internal body tries to rotate and to place the gravity-oriented spatial position, due to the properties of the gravitational stabilization principles. Therefore, the gravity forces initiate the internal angular motion of the internal sphere relative the cavity with viscous liquid.

A. V. Doroshin (✉)
Samara National Research University, Samara, Russia

At this internal rotation, the dissipative friction torques arise in the viscous fluid. This friction torque dissipates the kinetic energy and it acts on the main body of satellite and decelerates its angular motion. So, as the result, the angular momentum of satellite will decrease. The suggested spherical damper scheme is similar with the analogous construction of magnetic damper [3] interacting with geomagnetic field, where the internal spherical shell with permanent magnets was placed in the external sphere filled with bismuth: the internal sphere tries to rotate to coincide with the forces lines of geomagnetic field, and, therefore, this rotation relative the main body creates the dissipative torque due to the friction in bismuth.

This scheme allows to use this gravitational damper in cases of nanosatellites, especially if the nanosatellite has a symmetrical construction with three units (Fig. 2), one of which (e.g., central unit) contains this spherical damper.

2 Mathematical Model of the Attitude Motion

So, let us consider the orbital motion of the nanosatellite along the circle orbit: the system $CXYZ$ is orbital coordinates frame (Figs. 1 and 2), where the axis Z

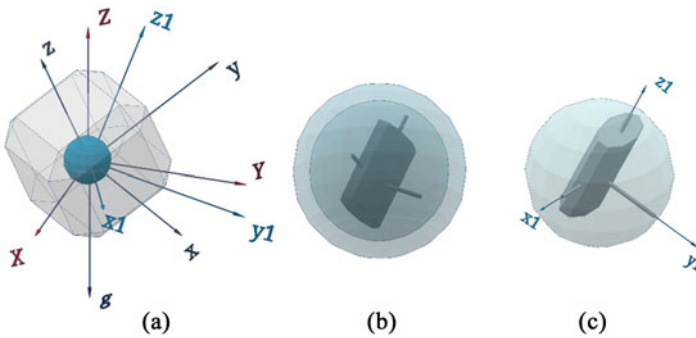
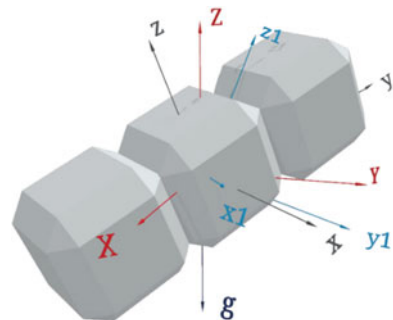


Fig. 1 A unit of a satellite with the internal spherical cavity (a) filled by a viscous fluid and the internal floating sphere (b) with the mounted gravitational body-damper (c)

Fig. 2 The nanosatellite with the central unit with the gravitational damper and corresponding coordinates systems



is directed from the gravity center to the orbital position of nanosatellite, axis Y is orthogonal to the orbital plane, and X represents the third right axis. The coordinates system $Cxyz$ is the central frame connected to the main body of nanosatellite, coinciding with its general axes of inertia; the system $Cx_1y_1z_1$ is the central frame connected to the general axes of the body-damper. In the case of nanosatellite construction with central damper-body unit (Fig. 2) let us to consider that the orbital system $CXYZ$ and connected systems $Cxyz$ and $Cx_1y_1z_1$ are central, i.e., the origin of all indicated systems is common, and it coincides with the center of mass of the satellite C .

The attitude position of the coordinates systems can be described by the well-known Euler's angles. For the system $Cxyz$ we will use three angles $\{\theta_1, \theta_2, \theta_3\}$ of subsequent rotations about the corresponding axes $x \rightarrow y \rightarrow z$ starting from the full coinciding with the system $CXYZ$. Then the following matrixes for subsequent rotations take place:

$$\Theta_1 = \begin{bmatrix} 1 & 0 & 0 \\ 0 & \cos \theta_1 & \sin \theta_1 \\ 0 & -\sin \theta_1 & \cos \theta_1 \end{bmatrix}; \Theta_2 = \begin{bmatrix} \cos \theta_2 & 0 & -\sin \theta_2 \\ 0 & 1 & 0 \\ \sin \theta_2 & 0 & \cos \theta_2 \end{bmatrix}; \Theta_3 = \begin{bmatrix} \cos \theta_3 & \sin \theta_3 & 0 \\ -\sin \theta_3 & \cos \theta_3 & 0 \\ 0 & 0 & 1 \end{bmatrix} \quad (1)$$

The complete matrix of transition from the orbital system $CXYZ$ to the connected system $Cxyz$ has form:

$$\Theta = \Theta_3 \cdot \Theta_2 \cdot \Theta_1 = \begin{bmatrix} \cos \theta_3 \cos \theta_2 & \sin \theta_3 \cos \theta_1 + \cos \theta_3 \sin \theta_2 \sin \theta_1 & \sin \theta_3 \sin \theta_1 - \cos \theta_3 \sin \theta_2 \cos \theta_1 \\ -\sin \theta_3 \cos \theta_2 & \cos \theta_3 \cos \theta_1 - \sin \theta_3 \sin \theta_2 \sin \theta_1 & \cos \theta_3 \sin \theta_1 + \sin \theta_3 \sin \theta_2 \cos \theta_1 \\ \sin \theta_2 & -\cos \theta_2 \sin \theta_1 & \cos \theta_2 \cos \theta_1 \end{bmatrix} \quad (2)$$

By the full analogy the system $Cx_1y_1z_1$ can be translated from the orbital system $CXYZ$ to the concrete final attitude with the help of subsequent rotations by angles $\{\psi_1, \psi_2, \psi_3\}$:

$$\Psi = \Psi_3 \cdot \Psi_2 \cdot \Psi_1 = \begin{bmatrix} \cos \psi_3 \cos \psi_2 & \sin \psi_3 \cos \psi_1 + \cos \psi_3 \sin \psi_2 \sin \psi_1 & \sin \psi_3 \sin \psi_1 - \cos \psi_3 \sin \psi_2 \cos \psi_1 \\ -\sin \psi_3 \cos \psi_2 & \cos \psi_3 \cos \psi_1 - \sin \psi_3 \sin \psi_2 \sin \psi_1 & \cos \psi_3 \sin \psi_1 + \sin \psi_3 \sin \psi_2 \cos \psi_1 \\ \sin \psi_2 & -\cos \psi_2 \sin \psi_1 & \cos \psi_2 \cos \psi_1 \end{bmatrix} \quad (3)$$

The kinematical equations for the angular velocity components of the main body $\omega = [p, q, r]^T$ and of the damper $\omega' = [p', q', r']^T$ in projections onto its own connected coordinates systems (xyz and $x_1y_1z_1$, correspondently) have the shape:

$$\begin{cases} p = \dot{\theta}_1 \cos \theta_2 \cos \theta_3 + \dot{\theta}_2 \sin \theta_3 + \omega_0 \Theta_{12} \\ q = -\dot{\theta}_1 \cos \theta_2 \sin \theta_3 + \dot{\theta}_2 \cos \theta_3 + \omega_0 \Theta_{22} \\ r = \dot{\theta}_1 \sin \theta_2 + \dot{\theta}_3 + \omega_0 \Theta_{32} \end{cases} \quad (4)$$

$$\begin{cases} p' = \dot{\psi}_1 \cos \psi_2 \cos \psi_3 + \dot{\psi}_2 \sin \psi_3 + \omega_0 \Psi_{12} \\ q' = -\dot{\psi}_1 \cos \psi_2 \sin \psi_3 + \dot{\psi}_2 \cos \psi_3 + \omega_0 \Psi_{22} \\ r' = \dot{\psi}_1 \sin \psi_2 + \dot{\psi}_3 + \omega_0 \Psi_{32} \end{cases} \quad (5)$$

where ω_0 is the value of the orbital angular velocity.

Let us consider the case when the inertia tensor of the main body of the satellite (without the damper) has in the connected system $Cxyz$ the central general diagonal form $\mathbf{J} = \text{diag}(A, B, C)$, and the inertia tensor of the damper-body also has the central general diagonal form $\mathbf{J}' = \text{diag}(A', B', C')$ in its connected frame $Cx_1y_1z_1$.

The dynamical equations of the attitude dynamics on the circle orbit can be written for the satellite main body and for damper-body as follows [14]:

$$\begin{cases} A\dot{p} + (C - B)qr = 3\omega_0^2(C - B)\Theta_{23}\Theta_{33} + M_x; \\ B\dot{q} + (A - C)pr = 3\omega_0^2(A - C)\Theta_{33}\Theta_{13} + M_y; \\ C\dot{r} + (B - A)pq = 3\omega_0^2(B - A)\Theta_{13}\Theta_{23} + M_z \end{cases} \quad (6)$$

$$\begin{cases} A'\dot{p}' + (C' - B')q'r' = 3\omega_0^2(C' - B')\Psi_{23}\Psi_{33} + M'_x; \\ B'\dot{q}' + (A' - C')p'r' = 3\omega_0^2(A' - C')\Psi_{33}\Psi_{13} + M'_y; \\ C'\dot{r}' + (B' - A')p'q' = 3\omega_0^2(B' - A')\Psi_{13}\Psi_{23} + M'_z \end{cases} \quad (7)$$

where $\{\Theta_{13}, \Theta_{23}, \Theta_{33}\}$, $\{\Psi_{13}, \Psi_{23}, \Psi_{33}\}$ – are components of matrixes (2) and (3) corresponding to the directional cosines of the gravitation direction (i.e., the orbital axis Z) in the connected frames. The vector $\mathbf{M} = [M_x, M_y, M_z]^T$ is the torque acting on the main body from the side of the damper-body due to liquid friction between the internal and internal spheres (Fig. 1). The vector $\mathbf{M}' = [M'_x, M'_y, M'_z]^T$ is the analogues torque acting on the damper-body from the side of the main body due to liquid friction.

The interaction of the bodies of the satellite due to liquid friction can be defined by the relative angular velocity of the damper (relative the main body). Then in projections onto the connected axes, the torques acting on the main body and on the damper are equal to the following vectors components:

$$\begin{aligned} \mathbf{M} &= \begin{bmatrix} M_x \\ M_y \\ M_z \end{bmatrix} = -\nu \left[\begin{bmatrix} p \\ q \\ r \end{bmatrix} - \Theta \cdot \Psi^{-1} \cdot \begin{bmatrix} p' \\ q' \\ r' \end{bmatrix} \right]; \\ \mathbf{M}' &= \begin{bmatrix} M'_x \\ M'_y \\ M'_z \end{bmatrix} = -\nu \left[\begin{bmatrix} p' \\ q' \\ r' \end{bmatrix} - \Psi \cdot \Theta^{-1} \cdot \begin{bmatrix} p \\ q \\ r \end{bmatrix} \right] \end{aligned} \quad (8)$$

where ν is the damping factor.

It is useful to add the kinematical equations for angles $\{\theta_1, \theta_2, \theta_3\}$ and $\{\psi_1, \psi_2, \psi_3\}$ in form resolved relative the derivatives:

$$\begin{cases} \dot{\theta}_1 = -\frac{1}{\cos \theta_2} (q \sin \theta_3 - p \cos \theta_3 + \cos \theta_3 \omega_0 \Theta_{12} - \sin \theta_3 \omega_0 \Theta_{22}); \\ \dot{\theta}_2 = q \cos \theta_3 + p \sin \theta_3 - \cos \theta_3 \omega_0 \Theta_{22} - \sin \theta_3 \omega_0 \Theta_{12}; \\ \dot{\theta}_3 = r + \operatorname{tg} \theta_2 (q \sin \theta_3 - p \cos \theta_3 + \cos \theta_3 \omega_0 \Theta_{12} - \sin \theta_3 \omega_0 \Theta_{22}) - \omega_0 \Theta_{32} \end{cases} \quad (9)$$

$$\begin{cases} \dot{\psi}_1 = -\frac{1}{\cos \psi_2} (q' \sin \psi_3 - p' \cos \psi_3 + \cos \psi_3 \omega_0 \Psi_{12} - \sin \psi_3 \omega_0 \Psi_{22}); \\ \dot{\psi}_2 = q' \cos \psi_3 + p' \sin \psi_3 - \cos \psi_3 \omega_0 \Psi_{22} - \sin \psi_3 \omega_0 \Psi_{12}; \\ \dot{\psi}_3 = r' + \operatorname{tg} \psi_2 (q' \sin \psi_3 - p' \cos \psi_3 + \cos \psi_3 \omega_0 \Psi_{12} - \sin \psi_3 \omega_0 \Psi_{22}) - \omega_0 \Psi_{32} \end{cases} \quad (10)$$

So, the Eqs. (6), (7), (8), (9), and (10) form the complete systems to modeling the angular motion of the satellite with the internal gravitational damper relative the orbital coordinates frame.

3 Modeling Results

Let us present the results of numerical modeling for the satellite with the internal gravitational damper with parameters indicated in Table 1.

As we see from the modeling results (Figs. 3, 4, 5, 6, 7, 8, and 9), the internal damper-body can effectively unload the initial angular momentum of the satellite. It follows from the fact that the equatorial angular velocity components (p , p' , r , r') take near-zero values after first 150,000 seconds (Figs. 3 and 5), and after we have decreasing oscillations with near-zero small amplitudes. The absolute values of q and q' will be finally equal to orbital angular velocity (Fig. 4).

The attitude of bodies is evolutionarily coming near to a position along the axes of the orbital frame, in full accordance with gravitational stabilization principle. The initial rotational motion relative the orbital frame, as we can see, is stopped due to the kinetic energy dissipation with the help liquid friction in the internal damper.

Table 1 The modeling parameters

Bodies parameters			
	Inertia tensor [kg*m ²]	Initial angular velocity [1/s]	Initial attitude [rad]
Main body	$\mathbf{J} = \operatorname{diag}(0.0045, 0.0055, 0.0035)$	$\boldsymbol{\omega}(0) = [0.0012, 0.001, -0.0025]$	$\{\theta_i\} = \{0.015, 0.01, 0.02\}$
Damper-body	$\mathbf{J}' = \operatorname{diag}(0.003, 0.004, 0.0015)$	$\boldsymbol{\omega}'(0) = [0.0022, 0.001, 0.0015]$	$\{\psi_i\} = \{0.015, 0.01, 0.02\}$
Orbital angular velocity ω_0 [1/s]		0.0012	
Damping factor ν [N*m*s]		0.00001	

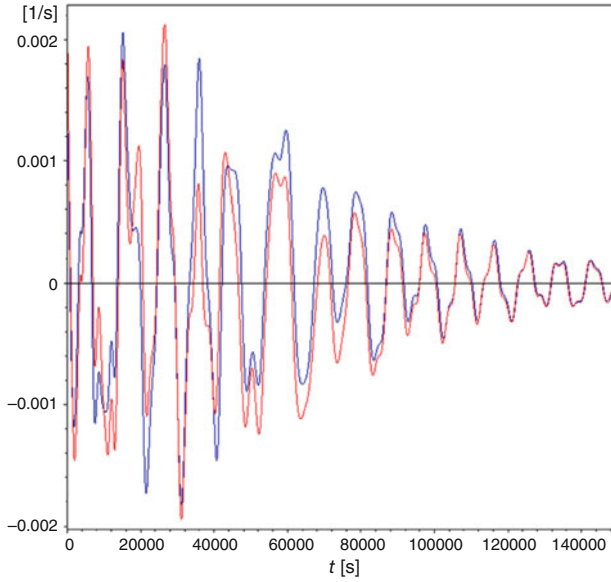


Fig. 3 The time-evolution of the angular velocities components p (blue) and p' (red) of the main body and the damper-body

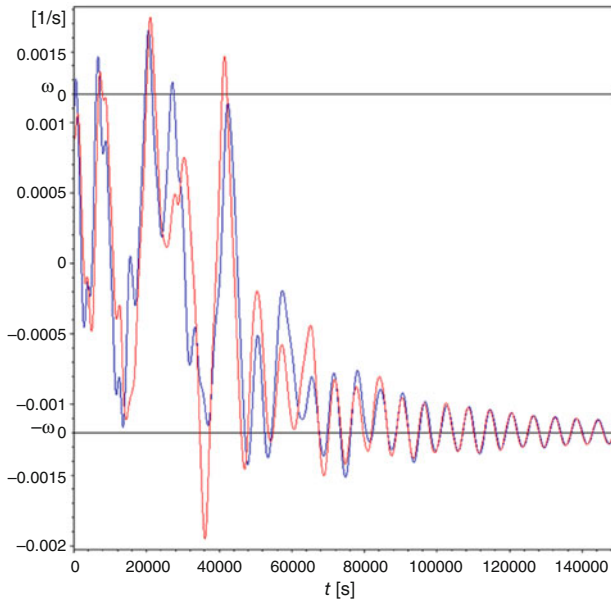


Fig. 4 The time-evolution of the angular velocities components q (blue) and q' (red) of the main body and the damper-body

Fig. 5 The time-evolution of the angular velocities components r (blue) and r' (red) of the main body and the damper-body

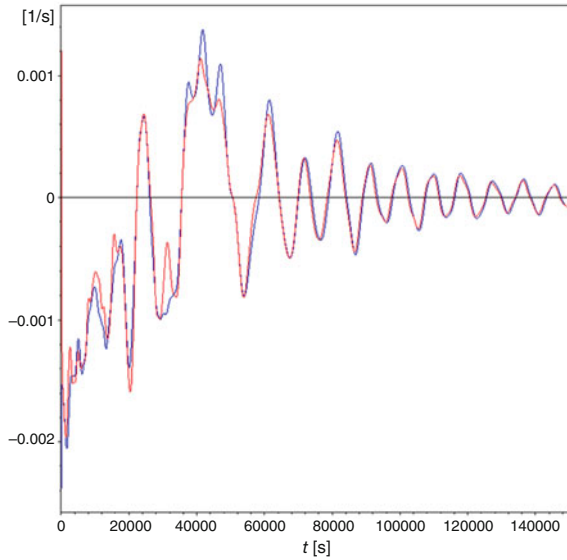
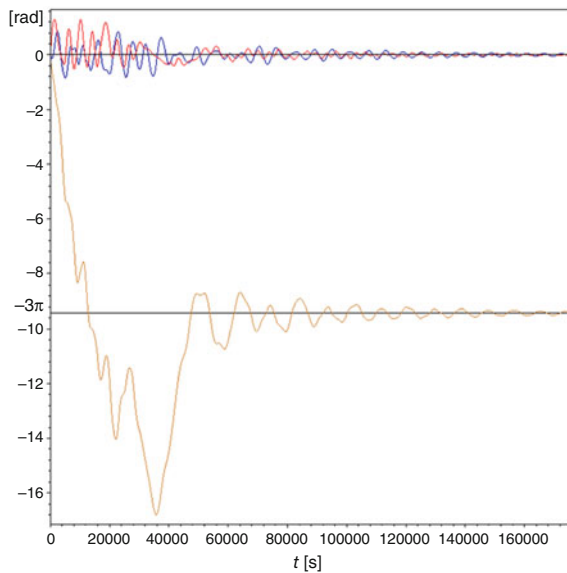


Fig. 6 The time-evolution of spatial angles θ_1 (red), θ_2 (blue), θ_3 (gold) of the attitude of the main body: the gravitational orientation is achieved (the main body is placed along the orbital axes)



4 Conclusions

The scheme of the satellite angular momentum unloading basing on the internal gravitational damper in the spherical cavity with viscous liquid was proposed. This scheme uses the external gravitational field to change the attitude of the internal damper-body relative the main body of the satellite, and to create, therefore,

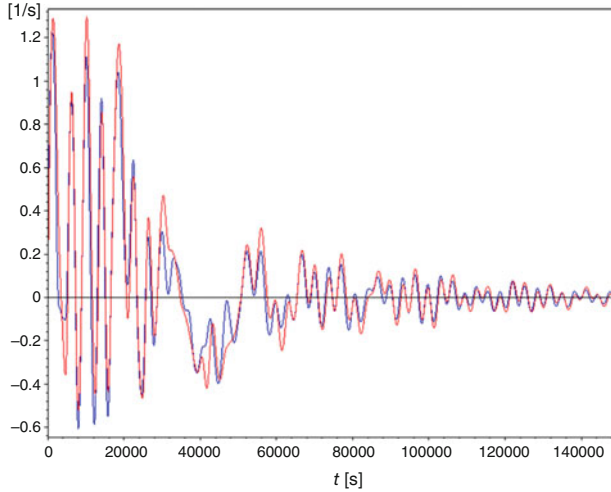


Fig. 7 The time-evolution of angles θ_1 (red) and ψ_1 (blue) of the attitude of the main body and the damper-body

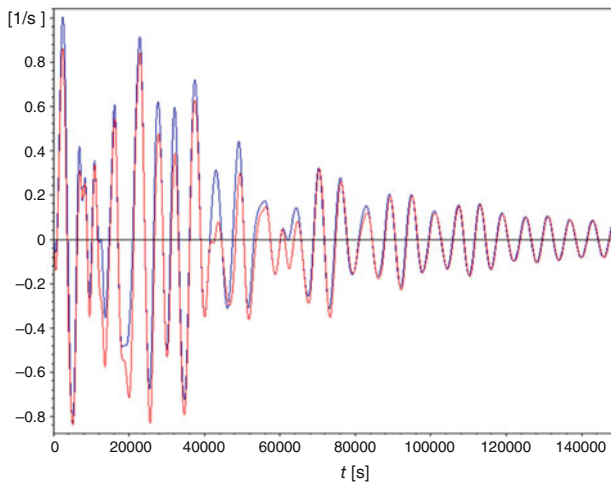


Fig. 8 The time-evolution of angles θ_2 (red) and ψ_2 (blue) of the attitude of the main body and the damper-body

dissipative torque of bodies' interaction due to the internal viscous friction, which unloads the angular momentum of the system.

The mathematical model of the attitude motion of satellites relative the orbital coordinates frame at the action of gravitational torques was constructed.

The numerical modeling was provided, that confirms the main suggested principle of the angular momentum unloading. As we can see from the modeling results,

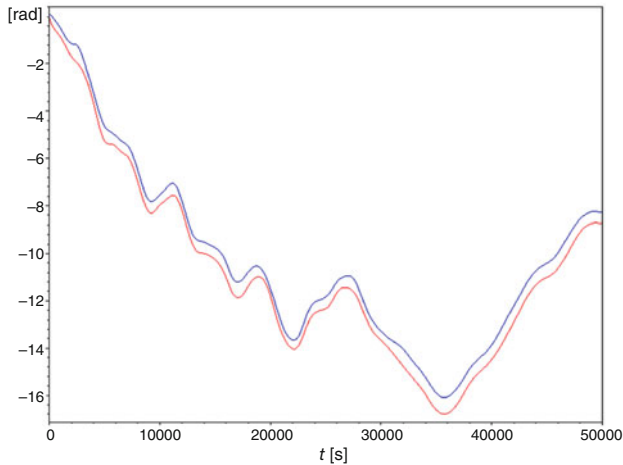


Fig. 9 The time-evolution of spatial angles θ_3 (red) and ψ_3 (blue) of the attitude of the main body and the damper-body: the angles have identical dynamics; they will coincide to 150,000 s

the process of the initial angular momentum unloading took about 150,000 seconds for parameters from Table 1.

Due to its simplicity, the studied scheme can be applied in cases of nanosatellites.

Acknowledgments The work is supported by the Russian Foundation for Basic Research (project # 19-08-00571 A).

References

1. A.V. Doroshin, Attitude control of spider-type multiple-rotor rigid bodies systems. Proceedings of the world congress on engineering 2009, London, U.K. Vol. II, pp. 1544–1549 (2009)
2. A.V. Doroshin, Homoclinic solutions and motion chaotization in attitude dynamics of a multi-spin spacecraft. *Commun. Nonlinear Sci. Numer. Simul.* **19**(7), 2528–2552 (2014)
3. L.K. Davis, “Motion damper” U.S. Patent No. 3,399,317. Washington, DC: U.S. Patent and Trademark Office (1968)
4. A.E. Sabroff, Advanced spacecraft stabilization and control techniques. *J. Spacecr. Rocket.* **5**(12), 1377–1393 (1968)
5. Y. Mashtakov, S. Tkachev, M. Ovchinnikov, Use of external torques for desaturation of reaction wheels. *J. Guid. Control Dynam.* **41**(8), 1663–1674 (2018)
6. D. Tong, Spacecraft momentum dumping using gravity gradient. *J. Spacecr. Rocket.* **35**(5), 714–717 (1998)
7. A. Skullestad, Modeling and control of a gravity gradient stabilised satellite. *Model. Identif. Control* **20**(1), 3–26 (1999)
8. B.K. Powell, Gravity-gradient momentum management. *J. Spacecr. Rocket.* **9**(6), 385–386 (1972)
9. S. Kedare, S. Ulrich, Formulation of torque-optimal guidance trajectories for a CubeSat with degraded reaction wheels. In *AIAA guidance, navigation, and control conference*, p. 0088 (2016)

10. T. Burns, H. Flashner, Adaptive control applied to momentum unloading utilizing the low earth orbital environment. *Guidance, Navigation and Control Conference*, 391–401 (1989)
11. T.F. Burns, H. Flashner, Adaptive control applied to momentum unloading using the low earth orbital environment. *J. Guid. Control Dynam.* **15**(2), 325–333 (1992)
12. Y.W. Jan, J.C. Chiou, Unloading law for a LEO spacecraft with two-gimbals solar array. *Acta Astronaut.* **51**(12), 843–854 (2002)
13. A.V. Bogachev, E.A. Vorob'eva, N.E. Zubov, E.A. Mikrin, M.S. Misrikhanov, V.N. Ryabchenko, S.N. Timakov, Unloading angular momentum for inertial actuators of a spacecraft in the pitch channel. *J. Comput. Syst. Sci. Int.* **50**(3), 483–490 (2011)
14. V.M. Morozov, V.I. Kalenova, Satellite control using magnetic moments: Controllability and stabilization algorithms. *Cosm. Res.* **58**, 158–166 (2020). <https://doi.org/10.1134/S0010952520030041>

Studies on the Liquid Sloshing and Rigid-Liquid-Flexible Coupling Dynamics of Spacecraft



Bole Ma, Baozeng Yue, Yong Tang, and Jiarui Yu

1 Introduction

Modern spacecraft typically carry a large amount of liquid fuel, and is also equipped with large flexible structures (e.g., solar panels, communication antenna, space manipulator). In the case of attitude and orbit motion, spacecraft are readily disturbed by liquid sloshing and flexible appendages vibrations. These problems have made critical the technologies of describing the rigid-liquid-flexible spacecraft coupling dynamics.

In microgravity (or low-gravity or zero-gravity) environment, note that the surface tension is dominant and the liquid volume takes an almost arbitrary orientation. Therefore, liquid sloshing is a complex, non-linear phenomena which is a difficult mathematical problem to solve analytically. At present, analytical solutions are limited to regular geometric tank shapes, such as cylindrical and rectangular [1, 2]. Accordingly, the equivalent mechanical models (EMMs) and the computational fluid dynamics (CFD) for predicting sloshing are developed, and good results have obtained. From the view of EMMs, the constraint-surface model [3, 4] and the moving pulsating ball model [5, 6] are gradually replacing spring–mass–damper model [7, 8] and pendulum models [9], which will be effective in predicting the behavior of liquid–spacecraft interaction. However, the combined EMMs–rigid-body model, although more concise, has some drawbacks from a precision point of view. On the other hand, CFD can be classified into three categories: Lagrangian methods, Eulerian methods (e.g., VOF and LS), and arbitrary Lagrangian–Eulerian (ALE) methods. ALE methods are intended to combine the respective advantages of both Lagrangian and Eulerian methods. A comprehensive book on nonlinear large-

B. Ma · B. Yue (✉) · Y. Tang · J. Yu
Beijing Institute of Technology, Beijing, China
e-mail: bzyue@bit.edu.cn

amplitude sloshing dynamics was compiled by Yue Baozeng, which ALE methods are described in detail [10]. This present work is based on a paper [11] that deals with the problem of liquid sloshing dynamics used improved ALE methods.

Meanwhile, most studies on spacecraft systems are focused on the rigid–liquid or rigid–flexible coupling dynamic. For example, Veldman [12] used the interface-capturing methods (VOF) to describe the process of liquid sloshing, and obtained the simulation results with rigid-liquid coupling system of liquid-filled spacecraft under attitude motion, which are verified by the experimental results of sloshsat Flevo satellite. Theureau [13] used CFD simulations (FLOW-3D) to predict the sloshing dynamics, and a spacecraft attitude controller is designed. However, there still exist large obstacle to the coupling system dynamics of spacecraft because of not considering coupling dynamics between liquid sloshing and the vibrations of flexible flexibles. Therefore, many methodologies have been developed to investigate the rigid-liquid-flexible coupling system of the spacecraft. Liu [14] investigated the slosh motion by a spherical pendulum, and a variable substitution method is proposed to apparently uncoupled mathematical model of the rigid-flexible-liquid spacecraft. Deng [15] represented large-scale liquid propellant motion by the moving pulsating ball model (MPBM), and the spacecraft attitude transition is carried out using a torqueum transfer technique. Gasbarri [16] investigated rigid-liquid-flexible coupling system of the spacecraft by a multibody method using a pendulum-like model for slosh and a beam-like model for flexibility. However, in order to reveal the complex coupling mechanism between the liquid, the rigid body, and the flexible appendages, it is still necessary to explore modeling and dynamics coupling of a liquid-filled flexible spacecraft.

The paper is outlined as follows: first, Section 2 deals with the numerical model of the rigid-liquid-flexible coupling system. The coupling effect is realized by exerting inertia forces to the liquid and flexible, and sloshing forces and torques to the rigid body. Once the model is presented, in Sect. 3 the calculation method is shown. The staggered algorithm is adopted to solve the liquid-sloshing module, the rigid body module, and the flexible appendages module in an iterative way. Section 4 presents the main analytical results dealing with the dynamics of the rigid-liquid-flexible coupling system. The system is simulated for a case and compared to the previous results, obtaining a reasonable match. Subsequently, the influences of the liquid sloshing on the coupling system are explored; some concluding remarks are drafted from the results obtained. Finally, concluding remarks are made in Sect. 5.

2 Dynamics Equation of a Liquid-Filled Flexible Spacecraft

As shown in Fig. 1, the spacecraft includes a rigid body, a partially filled spherical tank, and a beam-like appendage. It is necessary to consider the motion of liquid and flexible appendages in the dynamic reference system which is a rigid body fixed reference $Oxyz$ with its origin fixed at O . The effect of rigid body motion on liquid and flexible appendages is expressed as inertial forces. The rigid body dynamic

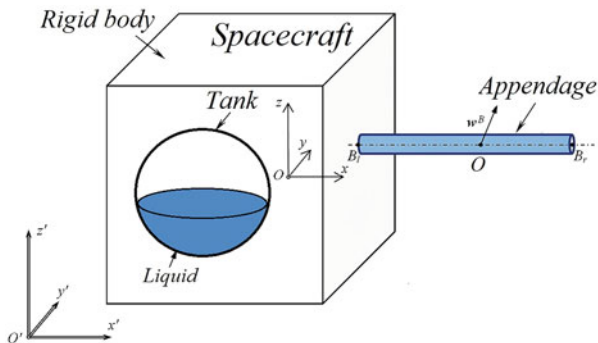


Fig. 1 Rigid-liquid-flexing system

equation considering the influences of liquid and flexible appendages is obtained. In addition, based on the dynamic equations of liquid and flexible appendages under reference frame of the main rigid, the forces and torques of liquid and flexible appendages on the main rigid body of the spacecraft are derived.

As shown in Fig. 1, the dynamics equation of the rigid body is given by

$$m_R \dot{v}_O + \dot{\omega} \times m_R r_R + \omega \times (\omega \times m_R r_R) = F^F + F^E + F^B \tag{1}$$

$$m_R r_R \times \dot{\omega} + J_R \cdot \dot{\omega} + \omega \times (J_R \cdot \omega) = T^F + T^E + T^B \tag{2}$$

where m_R is the mass of the rigid body; r_R is the position vector of the rigid body center of mass in $Oxyz$; J_R is the inertia tensor of the rigid body to O ; ω is the angular velocity of the $Oxyz$; v_O is the absolute velocities of O ; F^F , F^E , and F^B are respectively the force produced by liquid slosh, other external (e.g., gravity, control) and beam; T^F , T^E , and T^B are respectively the torque produced by liquid slosh, other external (e.g., gravity, control) and beam; The derivations of F^F , F^B , T^F , and T^B are discussed separately in the following sections.

2.1 The Forces and Torques of Liquid

The force F^F applied on the rigid body from the liquid can be expressed as

$$F^F = - \int_V (-pI + \tau) \cdot ndS \tag{3}$$

where p , τ , n , I , and V are the liquid pressure, the viscous stress tensor, the outer normal direction of a boundary unit, the unit tensor, and liquid region, respectively.

Based on the momentum equation of liquid and divergence theorem, the solution of Eq. (3) can be written

$$F^F = -m_L \dot{v}_O - \dot{\omega} \times m_L r_L - \omega \times (\omega \times m_L r_L) - \int_V \rho \left(\frac{Du}{Dt} + 2\omega \times u - f^{tru} \right) dV \quad (4)$$

where u denotes the velocity of the fluid relative to $Oxyz$, $\tau = \mu(\nabla u + (\nabla u)^T)$ is the deviatoric stress tensor, t is the time, μ is fluid viscosity coefficient, and p and ρ are the pressure and the fluid density, respectively. The first 3 terms are resulted from inertial force, and the last term caused by the real body force.

Similarly, the torque T^F applied on the rigid body from the liquid can be expressed as

$$T^F = -m_L r_L \times \dot{v}_O - J_L \cdot \dot{\omega}_L - \omega \times (J_L \cdot \omega) - \int_V r \times \left[\rho \left(\frac{Du}{Dt} + 2\omega \times u - f^{tru} \right) \right] dV \quad (5)$$

where J_L is the inertial tensor of O .

2.2 The Forces and Torques of Beam

The flexible appendages are modeled as a Bernoulli–Euler beam with uniform circular cross-section. Its axis is placed parallel to the x -axis. B_l and B_r are the left and right end of the beam, and are the position vector r_{OB_l} and r_{OB_r} in $Oxyz$, respectively. There exists an elastic displacement w^B . In $Oxyz$, $r_{OB_l} = [x_b \ y_b \ z_b]^T$, $r_{OB_r} = [x_b \ y_b \ z_b]^T$, $w^B = [0 \ w_y^B \ w_z^B]^T$ and there exist $r = r_{OB_l} + r_{Bl_Q} + w^B$. The inertial force of the beam is obtained as follows

$$f = - \left[\dot{v}_O + \dot{\omega} \times r + \omega \times (\omega \times r) + 2\omega \times \frac{\partial w^B}{\partial t} \right] \quad (6)$$

The transverse elastic vibration equations of the beam are expressed as follows:

$$\rho_B A_B \frac{\partial^2 w_y^B}{\partial t^2} = -EI \frac{\partial^4 w_y^B}{\partial x^4} - \rho_B A_{BCB} \frac{\partial w_y^B}{\partial t} + \rho_B A_B f_y \quad (7)$$

$$\rho_B A_B \frac{\partial^2 w_z^B}{\partial t^2} = -EI \frac{\partial^4 w_z^B}{\partial x^4} - \rho_B A_B c_B \frac{\partial w_z^B}{\partial t} + \rho_B A_B f_z \tag{8}$$

where c_B is the viscous damping coefficient of the beam structure; E_B , A_B , and ρ_B are the modulus of elasticity, the cross-sectional area, and the density of the beam, respectively; f_y and f_z are the components of the inertial force in the y - and z -directions.

The mode superposition method is used to discretize and solve Eqs. (7) and (8). The solution process of the rigid-flexible mode is omitted. Existing that $w_x^B = 0$, so the force F^b applied on the beam from the rigid body can be expressed as

$$\begin{aligned} F_x^b &= p_B A_B L_B \left[\dot{v}_{Ox} - (\omega_y^2 + \omega_z^2) x_b + (\omega_x \omega_y - \dot{\omega}_z) y_b \right. \\ &+ (\omega_x \omega_z + \dot{\omega}_y) y_b - \frac{1}{2} p_B A_B L_B^2 (\omega_y^2 + \omega_z^2) \\ &+ (\omega_x \omega_y - \dot{\omega}_z) \sum_{i=1}^{N_B} q_{yi} p_B A_B \int_0^{L_B} \varphi_{Bi} dx \\ &+ (\omega_x \omega_z + \dot{\omega}_y) \sum_{i=1}^{N_B} q_{yi} p_B A_B \int_0^{L_B} \varphi_{Bi} dx \\ &\left. - 2\omega_z \sum_{i=1}^{N_B} \frac{dq_{yi}}{dt} p_B A_B \int_0^{L_B} \varphi_{Bi} dx + 2\omega_y \sum_{i=1}^{N_B} \frac{dq_{zi}}{dt} p_B A_B \int_0^{L_B} \varphi_{Bi} dx \right] \end{aligned} \tag{9}$$

$$\begin{aligned} F_y^b &= E_B I_B \left. \frac{\partial^3 w_y^B}{\partial x^3} \right|_{x=0} = E_B I_B \sum_{i=1}^{N_B} q_{yi} \left. \frac{d^3 \varphi_{Bi}}{dx^3} \right|_{x=0} \\ &= -2E_B I_B \sum_{i=1}^{N_B} q_{yi} C_i \zeta_i^3 \frac{\text{ch} \zeta_i L_B + \cos \zeta_i L_B}{\text{sh} \zeta_i L_B + \sin \zeta_i L_B} \end{aligned} \tag{10}$$

$$\begin{aligned} F_z^b &= E_B I_B \left. \frac{\partial^3 w_z^B}{\partial x^3} \right|_{x=0} = E_B I_B \sum_{i=1}^{N_B} q_{zi} \left. \frac{d^3 \varphi_{Bi}}{dx^3} \right|_{x=0} \\ &= -2E_B I_B \sum_{i=1}^{N_B} q_{zi} C_i \zeta_i^3 \frac{\text{ch} \zeta_i L_B + \cos \zeta_i L_B}{\text{sh} \zeta_i L_B + \sin \zeta_i L_B} \end{aligned} \tag{11}$$

where L_B is the length of the beam; $\varphi_{Bi}(x)$ = i th transverse mode shape, $i = 1, \dots, N_B$; $q_{yi}(t)$ and $q_{zi}(t)$ are the corresponding modal coefficient of y and z , respectively; C_i is a constant that can be obtained by normalization; $\zeta_i L_B \approx (2i - 1) \pi/2$, ($i \geq 5$).

The torque T^b are presented below

$$\begin{aligned}
T_x^b &= \sum_{i=1}^{N_B} q_{yi} \frac{d^2 q_{zi}}{dt^2} - \sum_{i=1}^{N_B} q_{zi} \frac{d^2 q_{yi}}{dt^2} \\
&+ \left[\dot{v}_{Oz} + (\omega_x \omega_z - \dot{\omega}_y) (x_b) + (\omega_y \omega_z + \dot{\omega}_x) (y_b) - (\omega_x^2 + \omega_z^2) (z_b) \right] \\
&\sum_{i=1}^{N_B} q_{yi} \rho_B A_B \int_0^{L_B} \varphi_{Bi} x dx \\
&- \left[\dot{v}_{Oy} + (\omega_x \omega_y + \dot{\omega}_z) (x_b) - (\omega_x^2 + \omega_z^2) (y_b) + (\omega_y \omega_z - \dot{\omega}_x) (z_b) \right] \\
&\sum_{i=1}^{N_B} q_{zi} \rho_B A_B \int_0^{L_B} \varphi_{Bi} x dx + (\omega_y \omega_z - \dot{\omega}_x) \sum_{i=1}^{N_B} q_{yi} \rho_B A_B \int_0^{L_B} \varphi_{Bi} x dx \\
&- (\omega_x \omega_y + \dot{\omega}_z) \sum_{i=1}^{N_B} q_{zi} \rho_B A_B \int_0^{L_B} \varphi_{Bi} x dx + (\omega_y \omega_z + \dot{\omega}_x) \\
&\sum_{i=1}^{N_B} q_{yi}^2 - (\omega_y \omega_z - \dot{\omega}_x) \sum_{i=1}^{N_B} q_{zi}^2 + (\omega_z^2 - \omega_y^2) \sum_{i=1}^{N_B} q_{yi} q_{zi} + 2\omega_x \left(\sum_{i=1}^{N_B} q_{yi} \frac{dq_{yi}}{dt} + \sum_{i=1}^{N_B} q_{zi} \frac{dq_{zi}}{dt} \right)
\end{aligned} \tag{12}$$

$$T_y^b = E_B I_B \frac{\partial^2 w_z^B}{\partial x^2} \Big|_{x=0} = E_B I_B \sum_{i=1}^{N_B} q_{zi} \frac{d^2 \varphi_{Bi}}{dx^2} \Big|_{x=0} = 2E_B I_B \sum_{i=1}^{N_B} C_i \zeta_i^2 q_{zi} \tag{13}$$

$$T_z^b = -E_B I_B \frac{\partial^2 w_y^B}{\partial x^2} \Big|_{x=0} = -E_B I_B \sum_{i=1}^{N_B} q_{yi} \frac{d^2 \varphi_{Bi}}{dx^2} \Big|_{x=0} = -2E_B I_B \sum_{i=1}^{N_B} C_i \zeta_i^2 q_{yi} \tag{14}$$

Finally, the force F^B and torque T^B applied on the rigid body from the beam can be expressed as

$$F^B = -F^b, T^B = -T^b - r_{OB_i} \times F^b \tag{15}$$

3 Method of Solution

Based on the interleave method, the numerical simulation of the rigid-liquid-flexible coupling system of the spacecraft is established. This system has three modules, namely the liquid module, the rigid body module, and the flexible module. The iterative method is developed to solve the coupled model. Both the values of the liquid sloshing force F^F and torque T^F are calculated by the ALE method [11].

The absolute derivative term is written as the relative derivative in $Oxyz$.

$$\dot{v}_O = \dot{v}_O + \omega \times v_O, \quad \dot{\omega} = \dot{\omega} + \omega \times \omega = \dot{\omega} \tag{16}$$

$$m_s \dot{v}_O + \dot{\omega} \times m_s r_s = A \tag{17}$$

$$m_s r_s \times \dot{v}_O + J_s \cdot \dot{\omega} = B \tag{18}$$

$$\begin{bmatrix} m_s & 0 & 0 & 0 & m_s r_{sz} & -m_s r_{sy} \\ 0 & m_s & 0 & -m_s r_{sz} & 0 & m_s r_{sx} \\ 0 & 0 & m_s & m_s r_{sy} & -m_s r_{sx} & 0 \\ 0 & -m_s r_{sz} & m_s r_{sy} & J_{sxx} & -J_{sxy} & -J_{sxz} \\ m_s r_{sz} & 0 & -m_s r_{sx} & -J_{sxy} & J_{syy} & -J_{syz} \\ -m_s r_{sy} & m_s r_{sx} & 0 & -J_{sxz} & -J_{syz} & J_{szz} \end{bmatrix} \begin{bmatrix} \dot{v}_{Ox} \\ \dot{v}_{Oy} \\ \dot{v}_{Oz} \\ \dot{\omega}_x \\ \dot{\omega}_y \\ \dot{\omega}_z \end{bmatrix} = \begin{bmatrix} A_x \\ A_y \\ A_z \\ B_x \\ B_y \\ B_z \end{bmatrix} \tag{19}$$

$$\dot{y} = M^{-1}C = F \left(r_s(t), J_s(t), u(t), F^B(t), T^B(t), y \right) \tag{20}$$

Equation (20) can be solved numerically by the Runge-Kutta method.

4 Numerical Results

4.1 Response of Rigid-Flexible Coupled Spacecraft Under Step Excitation

For liquid sloshing, the used improved ALE methods [11] have been verified by published experimental. Therefore, to validate the method developed in the present work, the results obtained for 3D spacecraft models with rigid-flexible coupling system under step excitation are compared with previous results [17]. The tank is considered to be empty in a rigid-flexible coupling system. The cantilever beam has a length of $L_B = 1$ m, an inertia moment of $J_{Rxx} = J_{Ryy} = J_{Rzz} = 0.0448$ kg·m², a cross-sectional area of $A_B = 0.01$ m², a density of $\rho_B = 20.2$ kg/m³, and a flexural rigidity of $E_B I = 566.71$ N·m². The coordinates of fixed-end B_l points in the moving reference system are $r_{OBl} = [0.1 \ 0.0 \ 0.0]^T$ m.

A step external moment about the z -axis is as follows (Fig. 2):

$$T_z^E = \begin{cases} 30.0N \cdot m & t \leq 0.05s \\ -30.0N \cdot m & 0.1s \leq t \leq 0.15s \\ 0 & other \end{cases}$$

The time evolution curves in Fig. 2 presents the different responses of the rigid-flexible coupled spacecraft under step excitation; The curves (a), (b), and (c) in Fig. 2 correspond respectively to the numerical results of the flexible beam free end displacement w_y^B , the spacecraft angular velocity ω_z , and the rotation θ_z of the spacecraft around the z axis. For the flexible beam free end displacement, the results are very close to the analytical results; the peak amplitudes of the numerical results are a little smaller. The results of ω_z and θ_z are compared with previous results, and a good agreement is found.

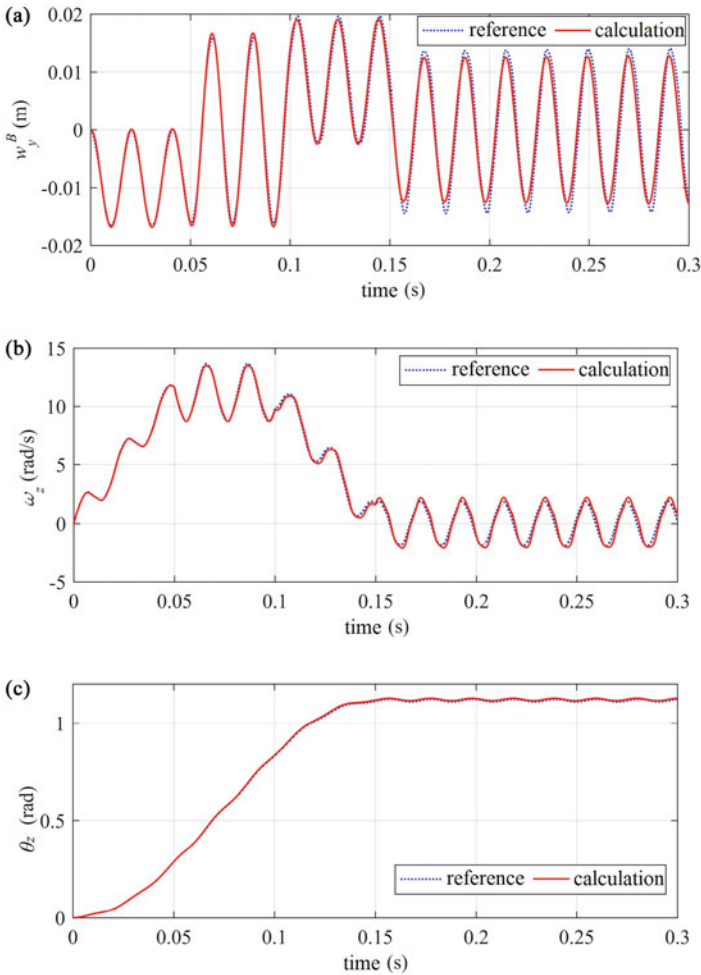


Fig. 2 Response of rigid-flexible coupled spacecraft: (a) w_y^B ; (b) ω_z ; (c) θ_z

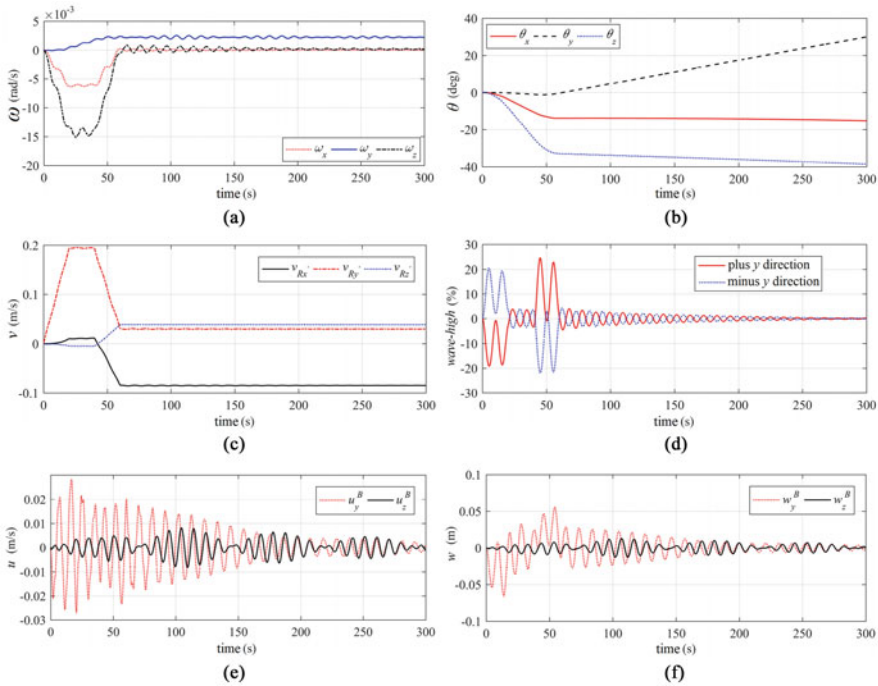


Fig. 3 Response of the rigid-liquid-flexible coupled spacecraft under the orbital driving force: (a) ω ; (b) θ ; (c) v ; (d) wave-high; (e) u ; (f) w

4.2 Response of the Rigid-Liquid-Flexible Coupled Spacecraft Under the Orbital Driving Force

The properties of spacecraft are given as follows:

Rigid part: $m_R = 400 \text{ kg}$, $J_{Rxx} = J_{Ryy} = 600 \text{ kg}\cdot\text{m}^2$, $J_{Rzz} = 800 \text{ kg}\cdot\text{m}^2$;

Liquid slug: The spherical tank radius $R = 0.4 \text{ m}$, the liquid-filling ratios is 40%, the surface tension coefficient $\sigma = 0.0725 \text{ N/m}$, the viscosity coefficient $\mu = 3 \times 10^{-6} \text{ Ns/m}^2$, $\rho = 1000 \text{ kg/m}^3$, the contact angle $\theta_0 = 5^\circ$, and the center coordinates of the container are $[0.1 \ 0.15 \ 0.0]^T \text{ m}$;

Flexible beam: $L_B = 11.4 \text{ m}$, $\rho_B = 177 \text{ kg/m}^3$, $A_B = 0.01 \text{ m}^2$, $E_{BI} = 407 \text{ N}\cdot\text{m}^2$, $c_B = 0.005$, $r_{OBI} = [1.428 \ 0.0 \ 0.0]^T \text{ m}$;

In micro-gravity environment, $g = 0.09 \text{ m/s}^2$. The orbital driving force about the y-axis is as follows:

$$F_y^E = \begin{cases} 5.0N \cdot m & t \leq 20s \\ -5.0N \cdot m & 40s \leq t \leq 60s \\ 0 & \text{other} \end{cases}$$

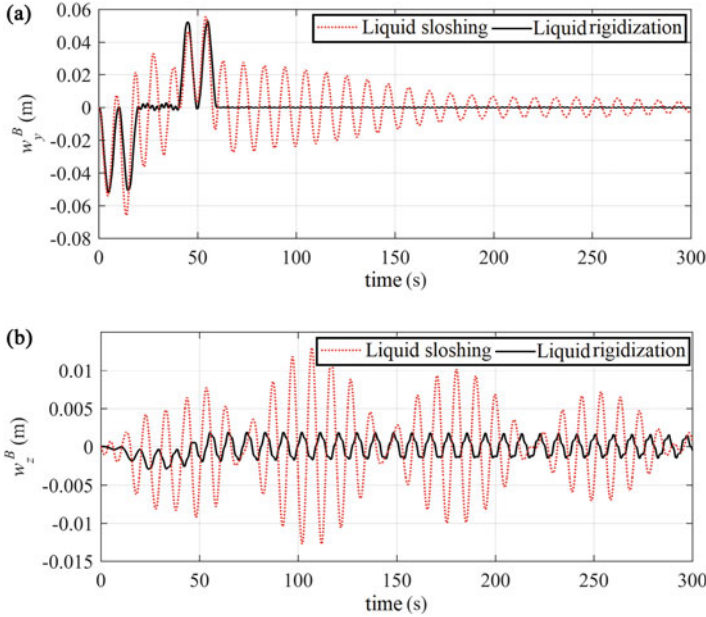


Fig. 4 Comparison of beam-ends displacement between liquid sloshing and liquid rigidization: (a) y -direction; (b) z -direction

Figure 3 presents the evolution over time of the different responses of the rigid-liquid-flexible coupled spacecraft under the orbital driving force. The curves (a), (b), and (c) in Fig. 3 correspond to numerical results with the angular velocity ω , the rotation angle θ and the centroid absolute velocity v of the rigid body, respectively. Although there is no driving force after 60s, the angular velocity ω still fluctuates. The reason is the influence of liquid sloshing and flexible appendages vibration. The curves (d), (e), and (f) in Fig. 3 correspond to numerical results with wave-high, flexible beam free end displacement u and velocity w , respectively.

Then we consider both cases with liquid sloshing and liquid rigidization. Liquid rigidization is assumed not to allow liquid sloshing. Figure 4 shows the displacement of beam end changes obviously in the form of vibration of amplitude and size under liquid rigidization. From Fig. 4 we can observe that there exists a big difference in the two results. The curves (a) in Fig. 4 show w_y^B decreases sharply after 60s. The curves (b) in Fig. 4 show w_z^B changes from beat vibration to vibration with higher harmonic components, and the descending of vibrating amplitude.

Figure 5 shows the angular velocity response of rigid body under liquid sloshing and liquid rigidization. A local magnification of the 50 s~250 s period on the right side of Fig. 5. We can observe that the fluid sloshing not only influences the shape of vibration output, but also changes the vibrating frequency and the vibrating amplitude of the angular velocity response of rigid body.

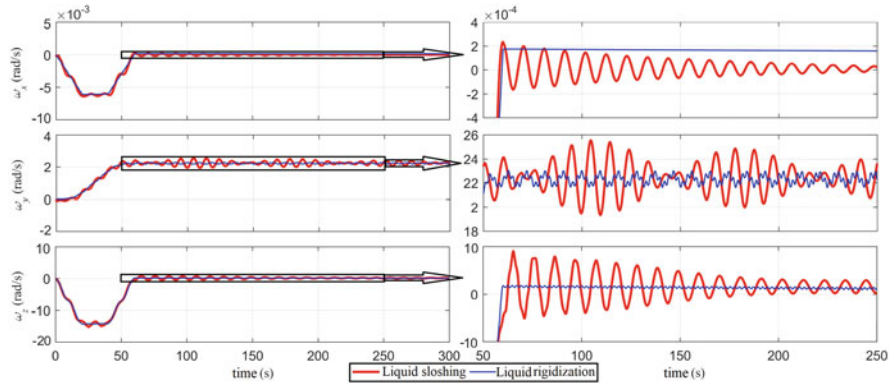


Fig. 5 Angular velocity response of rigid body under liquid sloshing and liquid rigidization

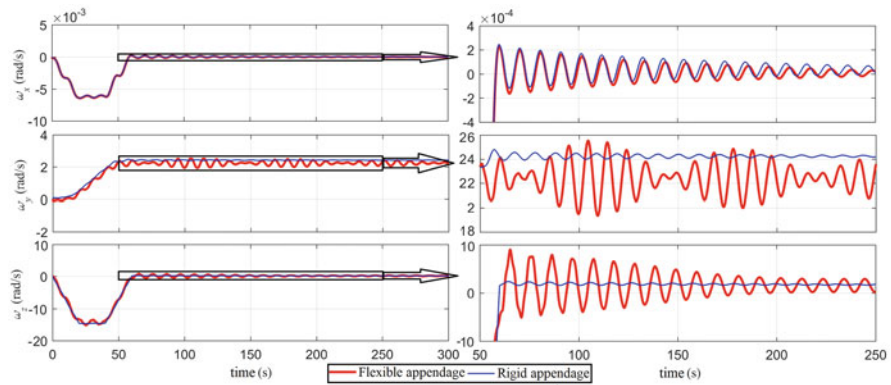


Fig. 6 Angular velocity response of the rigid body under the vibrations of flexible and rigid appendages

Fig. 6 shows the angular velocity response of the rigid body under the vibrations of flexible and rigid appendages. The vibration of rigid appendages is assumed not to allow deformation of appendages. A local magnification of the 50 s~250 s period is shown on the right of Fig.6. For rigid-liquid-flexible coupled spacecraft, the liquid sloshing and the vibrations of flexible flexibles can affect the angular velocity response of rigid body greatly.

It was found from Fig. 7 that the liquid wave-high amplitude and sloshing period were dependent on the vibrations of flexible and rigid appendages. That is, the maximum amplitude of the liquid wave-high was observed under the vibrations of flexible appendages, and it has a longer sloshing period.

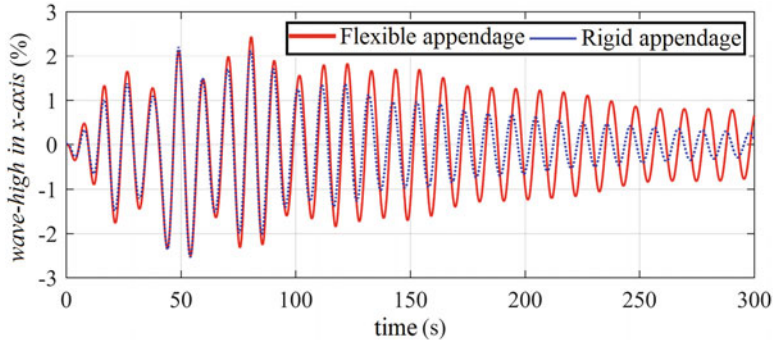


Fig. 7 Liquid wave-high under the vibrations of flexible and rigid appendages

5 Conclusions

To demonstrate the method developed in the present work, the results obtained for 3D spacecraft model with rigid-flexible coupling system under step excitation are compared with previous results, and a good agreement is found. The response of the rigid-liquid-flexible coupling spacecraft under orbital driving forces is studied. The influences of the liquid sloshing on the main rigid body and the flexible appendages are studied. Meanwhile, the vibrations of flexible appendages will also cause the main rigid body motion and liquid sloshing, respectively. Presented results show that there exists complex coupling mechanism among liquid sloshing, rigid body motion, and flexible appendages vibration.

References

1. R.A. Ibrahim, V.N. Pilipchuk, Recent advances in liquid sloshing dynamics. *Appl. Mech. Rev.* **54**(2), 133–199 (2001)
2. R.A. Ibrahim, *Liquid Sloshing Dynamics: Theory and Applications* (Cambridge University Press, Cambridge, 2005)
3. R.L. Berry, J.R. Tegart, Experimental study of transient liquid motion in orbiting spacecraft. NAS830690 (1975)
4. Z.C. Zhou, H. Huang, Constraint surface model for large amplitude sloshing of the spacecraft with multiple tanks. *Acta Astronaut.* **111**, 222–229 (2015)
5. J.P.B. Vreeburg, Dynamics and control of a spacecraft with a moving pulsating ball in a spherical cavity. *Acta Astronaut.* **40**(2–8), 257–274 (1997)
6. M. Deng, B.Z. Yue, Nonlinear model and attitude dynamics of flexible spacecraft with large amplitude slosh. *Acta Astronaut.* **133**, 111–120 (2017)
7. H.N. Abramson, Representation of fuel sloshing in cylindrical tanks by an equivalent mechanical model. *ARS J.* **31**(12), 1697–1705 (1961)
8. M. Farid, O.V. Gendelman, Response regimes in equivalent mechanical model of moderately nonlinear liquid sloshing. *Nonlinear Dyn.* **4**(92), 1517–1538 (2018)

9. H.F. Bauer, Nonlinear mechanical model for the description of propellant sloshing. *AIAA J.* **4**(9), 1662–1668 (2012)
10. B.Z. Yue, *Large Amplitude Liquid Sloshing Dynamics* (Science Press, Beijing, 2011)
11. Y. Tang, B.Z. Yue, Simulation of large-amplitude three-dimensional liquid sloshing in spherical tanks. *AIAA J.* **55**(6), 2052–2059 (2017)
12. A.E.P. Veldman, The numerical simulation of liquid sloshing on board spacecraft. *J. Comput. Phys.* **224**(1), 82–99 (2007)
13. D. Theureau, Integration of low g sloshing models with spacecraft attitude control simulators. In: *AIAA Guidance, Navigation, and Control (GNC) Conference*. Conference Boston, MA, USA (2013)
14. F. Liu, B.Z. Yue, Attitude dynamics and control of spacecraft with a partially filled liquid tank and flexible panels. *Acta Astronaut.* **143**(FEB.), 327–336 (2017)
15. M. Deng, Coupling dynamics of flexible spacecraft filled with liquid propellant. *J. Aerospace Eng.* **32**(5), 04019077 (2019)
16. P. Gasbarri, M. Sabatini, Dynamic modeling and stability parametric analysis of a flexible spacecraft with fuel slosh. *Acta Astronaut.* **127**(Oct–Nov), 141–159 (2016)
17. Y. Yan, B.Z. Yue, Analytical method for the attitude stability of partially liquid filled spacecraft with flexible appendage. *Acta Mechanica Sinica* **33**(1), 208–218 (2017)

Direct Sensitivity Analysis of Dynamic Responses for Nonlinear Structure



Zhifu Cao, Qingguo Fei, Dong Jiang, Rakesh K. Kapania, Hui Jin,
and Rui Zhu

1 Introduction

Different dynamic behaviors for nonlinear structures are affected by the varying of the structural parameters [1], such as quasi-periodic and chaotic vibrations [2]. Structural nonlinearity can be classified into three categories: geometrical, material, and contact nonlinearity [3, 4], are widespread in engineering structures and should not be neglected in modern engineering design. Dynamic performance of the system can be assessed by investigating how structural parameters affect the nonlinear responses, and sensitivity analysis of nonlinear dynamic response is a critical issue.

Sensitivity analysis plays an important role in many research fields such as optimization [5], model updating [6], and parameter identification [7]. The dynamic sensitivities of the responses with respect to parameters can be calculated using three methods: the perturbation method, adjoint variable method (AVM), and

Z. Cao

College of Aerospace Engineering, Chongqing University, Chongqing, China
e-mail: aezfcdo@cqu.edu.cn

Q. Fei (✉) · R. Zhu

Institute of Aerospace Machinery and Dynamics, Southeast University, Nanjing, China

School of Mechanical and Electronic Engineering, Nanjing Forestry University, Nanjing, China
e-mail: qgfei@seu.edu.cn

D. Jiang

School of Mechanical and Electronic Engineering, Nanjing Forestry University, Nanjing, China

R. K. Kapania

Kevin T. Crofton Department of Aerospace and Ocean Engineering, Virginia Polytechnic Institute and State University, Blacksburg, VA, USA

H. Jin

Department of Engineering Mechanics, Southeast University, Nanjing, China

direct differentiation method (DDM). The perturbation method is dependent on parameter perturbations to obtain the sensitivities, which can be using the real and/or imaginary perturbation formulation [8–10]. The finite difference method (FDM) is commonly used in sensitivity analysis, as it is easy to implement. Owing to the re-analysis for each parameter in perturbed response computation, the perturbation method suffers from the inefficiency of dynamic response sensitivity analysis. Given a time-dependent load to structure, e.g. impact, shock, and seismic loading, the vibration of structure often undesired. To optimize the performance of the structural vibration, the sensitivity analysis is needed for the dynamic response problems. In the AVM sensitivity analysis, independent adjoint terms are added to the sensitivity equations of objective function, and the sensitivities are computed in a manner analogous to the method of Lagrange multipliers [11]. The AVM, however, suffered from computational disadvantage for nonlinear dynamic problems. The AVM for nonlinear dynamic problems with initial conditions became a terminal-value problem where terminal conditions were prescribed for the adjoint equations. These equations must be integrated backward in time [11]. In this approach, the response and adjoint sensitivity cannot be computed simultaneously, and the storage costs can be large [12].

The DDM is an effective choice for forward time integration problem and can be successfully applied to sensitivity analysis. Scott and Azad [13] applied the DDM to a force-based element formulation with material and geometric nonlinearity to compute the response sensitivities. Ding et al. [14] developed the DDM to calculate the first and second derivatives of the dynamic response for non-viscously damped system. Akinlar [15] presented a staggered method to compute the response sensitivities for the Lorenz equations. The differentiation equation for normalized sensitivity analysis to different typical chaotic systems is derived in [16]. The DDM-based sensitivity analysis method is shown to be suitable for some systems with well-conditions of the sensitivity equations. Few attempts have been conducted on the problem of dynamic response sensitivity analysis for assembled structures, which contain nonlinearities localized in the connections.

In this paper, a direct sensitivity analysis method for nonlinear dynamic responses is proposed, in which the nonlinear dynamic response and corresponding sensitivity are synchronously determined. The paper is organized as follows. In Sect. 2, the direct sensitivity analysis method involving solutions of nonlinear dynamic response and direct differentiation formula are presented. In Sect. 3, the implementations of the nonlinear dynamic response sensitivity computation are verified by a Duffing oscillator considering chaotic and periodic vibrations. Finally, conclusions are presented in Sect. 4.

2 Methodology

2.1 Nonlinear Dynamic Response

The equation of motion for a nonlinear structure can be represented as

$$\mathbf{M}\ddot{\mathbf{x}}(t, \mathbf{p}) + \mathbf{C}\dot{\mathbf{x}}(t, \mathbf{p}) + \mathbf{K}\mathbf{x}(t, \mathbf{p}) + \mathbf{f}_{nl}(\mathbf{x}(t, \mathbf{p}), \dot{\mathbf{x}}(t, \mathbf{p}), \mathbf{p}) = \mathbf{f}(t) \quad (1)$$

where $\mathbf{M}, \mathbf{C}, \mathbf{K} \in \mathbb{R}^{N \times N}$ are the mass, damping, and stiffness matrix, respectively. $\mathbf{f}(t) \in \mathbb{R}^{N \times 1}$ represents the external excitation load. $\mathbf{x}(t), \dot{\mathbf{x}}(t), \ddot{\mathbf{x}}(t) \in \mathbb{R}^{N \times 1}$ are the displacement, velocity, and acceleration vector, respectively. $\mathbf{f}_{nl}(\mathbf{x}(t, \mathbf{p}), \dot{\mathbf{x}}(t, \mathbf{p}), \mathbf{p}) \in \mathbb{R}^{N \times 1}$ is the nonlinear restoring force, in which \mathbf{p} is the design parameters.

Dynamic responses can be computed from Eq. (1) using time integration method, such as Newmark procedure [17] used in this paper. The equation of motion of the system at time t_{n+1} can be written as the following nonlinear matrix algebraic equation in the unknowns $\ddot{\mathbf{x}}_{n+1}, \dot{\mathbf{x}}_{n+1}$, and \mathbf{x}_{n+1}

$$\Psi_{n+1} = \mathbf{f}_{n+1} - \mathbf{M}\ddot{\mathbf{x}}_{n+1} - \mathbf{C}\dot{\mathbf{x}}_{n+1} - \mathbf{K}\mathbf{x}_{n+1} - \mathbf{f}_{nl}(\mathbf{x}_{n+1}, \dot{\mathbf{x}}_{n+1}, \mathbf{p}) \quad (2)$$

where Ψ_{n+1} is the residual formula of the equation of motion. Using the Newmark- β [18] method, the Eq. (2) is rewritten as follows. The solution of Eq. (3) can be computed using Newton-Raphson algorithm.

$$\begin{aligned} \Psi_{n+1} = & \mathbf{f}_{n+1} + \mathbf{M} \left(\frac{1}{\beta(\Delta t)^2} \mathbf{x}_n + \frac{1}{\beta(\Delta t)} \dot{\mathbf{x}}_n - \left(1 - \frac{1}{2\beta}\right) \ddot{\mathbf{x}}_n \right) \\ & + \mathbf{C} \left(\frac{\gamma}{\beta(\Delta t)} \mathbf{x}_n - \left(1 - \frac{\gamma}{\beta}\right) \dot{\mathbf{x}}_n - (\Delta t) \left(1 - \frac{\gamma}{2\beta}\right) \ddot{\mathbf{x}}_n \right) \\ & - \left(\frac{1}{\beta(\Delta t)^2} \mathbf{M}\mathbf{x}_{n+1} + \frac{\gamma}{\beta(\Delta t)} \mathbf{C}\mathbf{x}_{n+1} + \mathbf{K}\mathbf{x}_{n+1} + \mathbf{f}_{nl}(\mathbf{x}_{n+1}, \dot{\mathbf{x}}_{n+1}, \mathbf{p}) \right) \\ = & \mathbf{0} \end{aligned} \quad (3)$$

2.2 Direct Sensitivity Analysis

The direct differentiation method (DDM) [19] is implemented in this paper to the computation of the nonlinear dynamic response sensitivity. Differentiating Eq. (1) directly with respect to the design parameters p_i ($i = 1, 2, \dots, q$), the derivatives of the algebraic equations of the sensitivity can be obtained,

$$\begin{aligned} & \mathbf{M} \frac{\partial \ddot{\mathbf{x}}(t, \mathbf{p})}{\partial p_i} + \mathbf{C} \frac{\partial \dot{\mathbf{x}}(t, \mathbf{p})}{\partial p_i} + \mathbf{K} \frac{\partial \mathbf{x}(t, \mathbf{p})}{\partial p_i} \\ & = - \frac{d\mathbf{f}_{nl}(\mathbf{x}(t, \mathbf{p}), \dot{\mathbf{x}}(t, \mathbf{p}), \mathbf{p})}{dp_i} \\ & = - \left(\frac{\partial \mathbf{f}_{nl}(\mathbf{x}(t, \mathbf{p}), \dot{\mathbf{x}}(t, \mathbf{p}), \mathbf{p})}{\partial \mathbf{x}} \frac{\partial \mathbf{x}(t, \mathbf{p})}{\partial p_i} + \frac{\partial \mathbf{f}_{nl}(\mathbf{x}(t, \mathbf{p}), \dot{\mathbf{x}}(t, \mathbf{p}), \mathbf{p})}{\partial \dot{\mathbf{x}}} \frac{\partial \dot{\mathbf{x}}(t, \mathbf{p})}{\partial p_i} + \frac{\partial \mathbf{f}_{nl}}{\partial p_i} \right) \\ & = - \left(\mathbf{J}_x \frac{\partial \mathbf{x}(t, \mathbf{p})}{\partial p_i} + \mathbf{J}_{\dot{\mathbf{x}}} \frac{\partial \dot{\mathbf{x}}(t, \mathbf{p})}{\partial p_i} + \frac{\partial \mathbf{f}_{nl}}{\partial p_i} \right) \end{aligned} \quad (4)$$

where the last term in the right-hand side of this expression represents an explicit dependence on variable p_i , and the first two terms show the implicit dependence through dynamic responses \mathbf{x} and $\dot{\mathbf{x}}$. The symbols $\mathbf{J}_{\mathbf{x}}$ and $\mathbf{J}_{\dot{\mathbf{x}}}$ are the Jacobian matrix of the nonlinear restoring force $\mathbf{f}_{nl}(\mathbf{x}(t, \mathbf{p}), \dot{\mathbf{x}}(t, \mathbf{p}), \mathbf{p})$ with respect to the displacement and velocity coordinates

$$\mathbf{J}_{\mathbf{x}} = \begin{bmatrix} \frac{\partial f_{nl1}}{\partial x_1} & \dots & \frac{\partial f_{nl1}}{\partial x_N} \\ \vdots & \ddots & \vdots \\ \frac{\partial f_{nlN}}{\partial x_1} & \dots & \frac{\partial f_{nlN}}{\partial x_N} \end{bmatrix}, \mathbf{J}_{\dot{\mathbf{x}}} = \begin{bmatrix} \frac{\partial f_{nl1}}{\partial \dot{x}_1} & \dots & \frac{\partial f_{nl1}}{\partial \dot{x}_N} \\ \vdots & \ddots & \vdots \\ \frac{\partial f_{nlN}}{\partial \dot{x}_1} & \dots & \frac{\partial f_{nlN}}{\partial \dot{x}_N} \end{bmatrix} \tag{5}$$

Introducing the following symbolic representation,

$$\mathbf{s}_i = \frac{\partial \mathbf{x}(t, \mathbf{p})}{\partial p_i}, \dot{\mathbf{s}}_i = \frac{\partial \dot{\mathbf{x}}(t, \mathbf{p})}{\partial p_i}, \ddot{\mathbf{s}}_i = \frac{\partial \ddot{\mathbf{x}}(t, \mathbf{p})}{\partial p_i} \tag{6}$$

the compact formula of the second-order ordinary differential equation of sensitivity can be rewritten as

$$\mathbf{M}\ddot{\mathbf{s}}_i + (\mathbf{C} + \mathbf{J}_{\dot{\mathbf{x}}})\dot{\mathbf{s}}_i + (\mathbf{K} + \mathbf{J}_{\mathbf{x}})\mathbf{s}_i + \frac{\partial \mathbf{f}_{nl}(\mathbf{x}(t, \mathbf{p}), \dot{\mathbf{x}}(t, \mathbf{p}), \mathbf{p})}{\partial p_i} = \mathbf{0} \tag{7}$$

With $\mathbf{x}(t, \mathbf{p})$ and $\dot{\mathbf{x}}(t, \mathbf{p})$ obtained from Eq. (1), the solution of the design sensitivities can be computed from Eq. (7) using again the Newmark method. The equilibrium equation of the nonlinear dynamic response sensitivity at t_{n+1} then can be derived as Eq. (8).

$$\begin{aligned} \Phi_{n+1} = & \mathbf{M} \left(-\frac{1}{\beta(\Delta t)^2} \mathbf{s}_{i,n} - \frac{1}{\beta(\Delta t)} \dot{\mathbf{s}}_{i,n} + \left(1 - \frac{1}{2\beta}\right) \ddot{\mathbf{s}}_{i,n} \right) \\ & + (\mathbf{C} + \mathbf{J}_{\dot{\mathbf{x}},n+1}) \left(-\frac{\gamma}{\beta(\Delta t)} \mathbf{s}_{i,n} + \left(1 - \frac{\gamma}{\beta}\right) \dot{\mathbf{s}}_{i,n} + (\Delta t) \left(1 - \frac{\gamma}{2\beta}\right) \ddot{\mathbf{s}}_{i,n} \right) \\ & + \frac{\partial \mathbf{f}_{nl}(\mathbf{x}(t_{n+1}, \mathbf{p}), \dot{\mathbf{x}}(t_{n+1}, \mathbf{p}), \mathbf{p})}{\partial p_i} + \left(\frac{1}{\beta(\Delta t)^2} \mathbf{M} + \frac{\gamma}{\beta(\Delta t)} (\mathbf{C} + \mathbf{J}_{\dot{\mathbf{x}},n+1}) + (\mathbf{K} + \mathbf{J}_{\mathbf{x},n+1}) \right) \mathbf{s}_{i,n+1} \\ = & \mathbf{0} \end{aligned} \tag{8}$$

The third term on the right-hand side of Eq. (8) represents the partial derivative of the restoring force vector, $\mathbf{f}_{nl}(\mathbf{x}(t, \mathbf{p}), \dot{\mathbf{x}}(t, \mathbf{p}), \mathbf{p})$, with respect to interest parameter p_i under the condition that the responses at time t_{n+1} are determined. The Jacobian matrix $\mathbf{J}_{\mathbf{x},n+1}$ and $\mathbf{J}_{\dot{\mathbf{x}},n+1}$ also should be determined using the responses at time t_{n+1} . This equation can be solved for the vector of unknowns $\mathbf{s}_{i,n+1}$. The dynamic response sensitivity with respect to other parameters can be determined using the same procedure.

It also can be noted that once the numerical response of the structure at t_{n+1} is known, the equilibrium equation of the nonlinear dynamic response sensitivity has several same structural matrix as Eq. (3) and is linear [20]. The advantage of

the DDM is that the response sensitivities can be synchronously computed with the calculation of the nonlinear dynamic responses, i.e., the computational procedure is more efficient compared with the FDM. Usually, the initial conditions of the displacement and velocity are given firstly, which lead to the sensitivities of the initial displacement and the velocity are zero. When the 2-norm of the residual function $\|\Psi_{n+1}^k\|_2$ satisfies the convergence criteria, the tolerance being set to 1.0×10^{-6} , the convergent nonlinear dynamic responses are applied to compute the responses directly at current time.

3 Duffing Oscillator

In this section, the proposed method will be demonstrated to dynamic response sensitivity analysis for nonlinear Duffing oscillator. The nondimensional Duffing oscillator with external forcing studied in this paper has the form,

$$\ddot{x} + c\dot{x} + kx + k_{nl}x^3 = B \cos \Omega t \quad (9)$$

where c , k are the linear damping and stiffness coefficients, respectively; k_{nl} is the cubic stiffness coefficient; B and Ω are the excitation amplitude and excitation frequency, respectively. These parameters are chosen to investigate the dynamic response and its sensitivity are listed in follows.

3.1 Effect of Secular Term

To verify the accuracy of the DDM-based sensitivity for the nonlinear dynamic response, the asymptotically analytical solution, and the finite difference solution of the dynamic response sensitivity for the free vibration of the undamped Duffing oscillator are considered. In this study, the parameters of the undamped Duffing oscillator with linear and cubic term are $k = 1$, $k_{nl} = 0.1$.

The Poincaré method (PCM) and Lindstedt-Poincaré method (LPM) [2], with initial displacement x_0 and zero velocity, are both applied to obtain the asymptotically analytical solution of the undamped Duffing oscillator. It is well known that the secular term $t \sin \omega_0 t$ appears in the PCM solution, which leads to response growing without bound as time increases. However, the effect of secular term can be avoided when using the LPM solutions [2]. The forward difference formula for the sensitivity of the response with respect to the nonlinear stiffness coefficient k_{nl} is given by

$$\mathbf{s}(t) = \frac{\mathbf{x}(t, k_{nl} + \Delta k_{nl}) - \mathbf{x}(t, k_{nl})}{\Delta k_{nl}} + \varepsilon \quad (10)$$

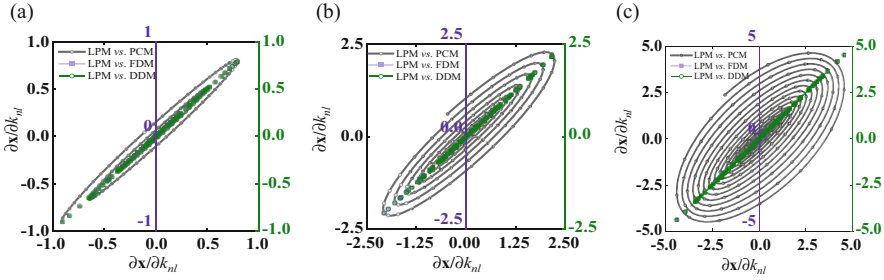


Fig. 1 Comparison of nonlinear displacement sensitivities among the four methods (x : LPM, y : PCM, FDM, DDM) with different time interval: (a) [0 20s]; (b) [0 50s]; (c) [0 100 s]

where $\varepsilon = \Delta k_{nl}/2|x''(k_{nl} + \Delta k_{nl})|$ is the truncation error, and $(*)''$ means the second-order derivative. The Δk_{nl} is the parameter perturbation in FDM-based sensitivity analysis [10]. The initial conditions are set to $x_0 = 0.5$ and $\dot{x}_0 = 0$, and the computation time spans are $0 < t \leq 20s$, $0 < t \leq 50s$, and $0 < t \leq 100 s$, respectively. Response sensitivities calculated using the LPM are applied as the reference in comparing the results obtained by the DDM, FDM, and PCM. For DDM- and FDM-sensitivity analysis, the relative convergence criterion tol , the time-step Δt , and the parameter perturbation Δk_{nl} are 10^{-10} , $10^{-3} s$ and $10^{-3} k_{nl}$, respectively.

Figure 1 illustrates the comparisons of nonlinear displacement sensitivities among the four methods with different time spans. When these displacement sensitivities match well, these points are located at the straight-line $y = x$. Otherwise, these points will be scattered around the straight-line. As shown in Fig. 1a–c, with the increase in the computational time, the differences between PCM and LPM-based response sensitivities are more obvious. In contrast, the blue and green straight lines show the consistency among the FDM, DDM, and LPM displacement sensitivities. It can also be concluded that the nonlinear dynamic responses computed using DDM procedure are not affected by the secular term, and the sensitivities obtained by DDM have high accuracy for the short-term and long-term sensitivity analyses when compared with the PCM procedure. The DDM procedure can be implemented for obtaining the long-term nonlinear dynamic response sensitivity.

3.2 Effect of Different Dynamic Behaviors

A special Duffing-type Ueda oscillator, which often exhibits periodic and chaotic dynamical behavior, is considered in this case. The Runge-Kutta method (RKM) [19], which can be implemented by MATLAB ODE solver (ode45), is compared for the sensitivity analysis for different dynamic behaviors in this subsection. The initial conditions of the Ueda oscillator for nonlinear dynamic response analysis are set to

Table 1 Different parameter sets of the Ueda oscillator

Parameters		Value			
		Set 1	Set 2	Set 3	Set 4
Damping coeff.	c	0.05	0.05	0.1	0.1
Linear stiffness coeff.	k	0	0	0	0
Cubic stiffness coeff.	k_{nl}	1	1	1	1
Force amplitude	B	1.4	7.5	12	14
Force frequency	Ω	1	1	1	1

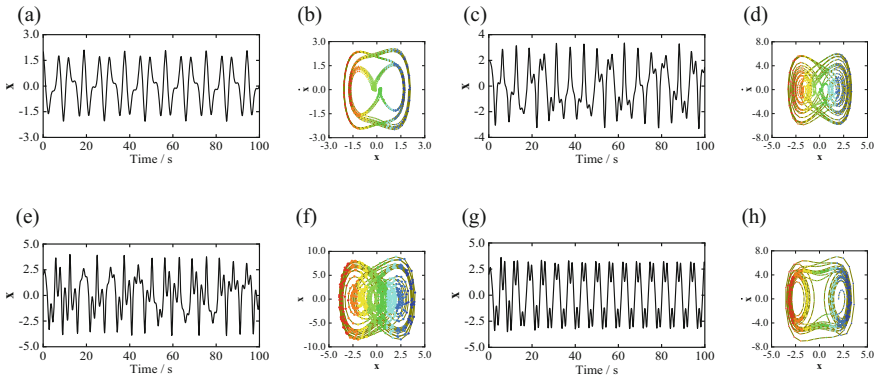


Fig. 2 Displacement and phase portraits for different sets using DDM procedure: (a, b) set 1, (c, d) set 2, (e, f) set 3, and (g, h) set 4

$x_0 = 0.5$ and $\dot{x}_0 = 0$, and the computation time span is $0 < t \leq 100$ s. For DDM- and FDM-sensitivity analysis, the relative convergence criterion tol , the time-step Δt , and the parameter perturbation Δk_{nl} are 10^{-10} , 10^{-3} s and $10^{-3}k_{nl}$, respectively.

Different physical states for quasi-periodic vibrations (*Sets 1 and 4*) and chaotic vibrations (*Sets 2 and 3*) are considered in Table 1. These three sensitivity analysis procedures are remarked as Method I (FDM-based procedure), Method II (DDM-based procedure), and Method III (RKM-based procedure).

The displacement and its sensitivity calculated using DDM with respect to the cubic stiffness coefficient are shown in Figs. 2 and 3, respectively. Figure 2 provides the time history of the displacement and the phase portraits for the four different parameter sets. The phase portraits of narrow band for *Sets 1 and 4* in Fig. 2b, h correspond to quasi-periodic vibrations. In contrast, Fig. 2d, f show the chaotic attractor, which is extremely sensitive to the initial conditions. The ‘aperiodic long-term behavior [2]’ in the chaotic vibration is shown in the time history of the displacement in Fig. 2c, e.

The time history of the displacement sensitivity with respect to the cubic stiffness coefficient is shown in Fig. 3a, c, e, g. Similar to the quasi-periodic vibration of the displacement, the displacement sensitivities oscillate periodically with time. The corresponding phase portraits (Fig. 3b, h) show that the sensitivities of the

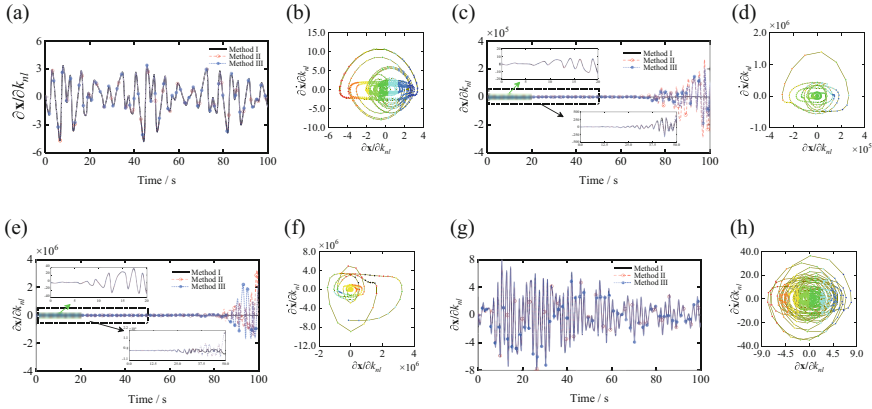


Fig. 3 Displacement response sensitivities with respect to cubic stiffness coefficient and its phase plot for different sets,—Method I, -o- Method II,---Method III: (a, b) set 1, (c, d) set 2, (e, f) set 3 and (g, h) set 4

quasi-periodic vibration sets 1 and 4 are bounded and settles into a regular region. By comparison, the response sensitivities of the chaotic vibration increase with an increase of time. In the chaotic region, the nonlinear dynamic response sensitivities are irregular.

As to the accuracy of the DDM-based long time response sensitivity computation, the results are reported by the comparison of the time history of the displacement sensitivities. As one could expect, for the quasi-periodic vibrations, the three sensitivity solutions compare almost perfectly for the sensitivity computation. In contrast, for the chaotic vibrations, the three solutions match well only for the short-term computation (Fig. 3c, e:0 ~ 20s). Compared with Method II and III sensitivities, the obvious differences appear for the Method I sensitivities in a long-term computation, as the FDM solutions are based on the parameter perturbation, which has a high sensitivity to the chaotical responses. The results show that the nonlinear dynamic response sensitivity solutions calculated by DDM are very close to the Method III solutions, whereas the FDM provides inconsistent sensitivity solutions for the long-term chaotic responses.

4 Conclusions

In this paper, a direct sensitivity analysis method for nonlinear dynamic responses is proposed. In this method, the nonlinear dynamic response and corresponding sensitivity are synchronously computed in the time integration scheme. The DDM sensitivity analysis method avoids the errors caused by the secular term in computation of long-term responses. For the special Duffing-type Ueda oscillator, the proposed method works well for computing the quasi-periodic response sensitivity,

which is bounded and settles into a regular region. For the chaotic vibration, the proposed method gives a similar result compared to the Runge-Kutta-based sensitivity solution.

Acknowledgements The authors would like to thank the support of the National Natural Science Foundation of China (No. 11602112, No. 11572086), and the Natural Science Foundation of Jiangsu Province (No. BK20170022). National Key Research and Development Program of China (2017YFC0805103).

References

1. A.X. Ni, Q.Q. Wang, Sensitivity analysis on chaotic dynamical systems by Non-Intrusive Least Squares Shadowing (NILSS). *J. Comput. Phys.* **347**, 56–77 (2017)
2. S.H. Strogatz, *Nonlinear dynamics and chaos* (CRC Press, Boca Raton, 2018)
3. Y.B. Li, S.B. Mulani, R.K. Kapania, et al., Nonstationary random vibration analysis of wing with geometric nonlinearity under correlated excitation. *J. Aircr.* **55**(5), 2078–2091 (2018)
4. S. Hernández, E. Menga, P. Naveira, et al., Dynamic analysis of assembled aircraft structures considering interfaces with nonlinear behavior. *Aerosp. Sci. Technol.* **77**, 265–272 (2018)
5. S. Dou, B.S. Strachan, S.W. Shaw, et al., Structural optimization for nonlinear dynamic response. *Phil. Trans. Royal Soc. A Math. Phys. Eng. Sci.* **373**(2051), 1–17 (2015)
6. Z.F. Cao, Q.G. Fei, D. Jiang, et al., Substructure-based model updating using residual flexibility mixed-boundary method. *J. Mech. Sci. Technol.* **31**(2), 759–769 (2017)
7. S. Hernández, E. Menga, S. Moledo, et al., Optimization approach for identification of dynamic parameters of localized joints of aircraft assembled structures. *Aerosp. Sci. Technol.* **69**, 538–549 (2017)
8. B.P. Wang, A.P. Apte, Complex variable method for eigensolution sensitivity analysis. *AIAA J.* **44**(12), 2958–2961 (2006)
9. J. Garza, H. Millwater, Multicomplex Newmark-Beta time integration method for sensitivity analysis in structural dynamics. *AIAA J.* **53**(5), 1188–1198 (2015)
10. Z. Cao, Q. Fei, D. Jiang, et al., Sensitivity analysis of nonlinear transient response based on perturbation in the complex domain. *J. Comput. Nonlinear Dyn.* **16**, 011001 (2021)
11. S.D. Trier, A. Marthinsen, O.I. Sivertsen, Design sensitivities by the adjoint variable method in nonlinear structural dynamics. in SIMS simulation conference. Trondheim, Norway (1996)
12. F.V. Keulen, R.T. Haftka, N.H. Kim, Review of options for structural design sensitivity analysis. part 1: linear systems. *Comput. Methods Appl. Mech. Eng.* **194**(30), 3213–3243 (2005)
13. M.H. Scott, V.J. Azad, Response sensitivity of material and geometric nonlinear force-based Timoshenko frame elements. *Int. J. Numer. Methods Eng.* **111**(5), 474–492 (2017)
14. Z. Ding, L. Li, G.M. Zou, et al., Design sensitivity analysis for transient response of non-viscously damped systems based on direct differentiate method. *Mech. Syst. Signal Process.* **121**, 322–342 (2019)
15. M.A. Akinlar, A new method for parameter sensitivity analysis of Lorenz equations. *Math. Probl. Eng.* **2013**, 1–7 (2013)
16. F. Shiraishi, Y. Hatoh, Dynamic sensitivities in chaotic dynamical systems. *Appl. Math Comput.* **186**(2), 1347–1359 (2007)
17. J.F. Doyle, *Nonlinear structural dynamics using FE methods* (Cambridge University Press, New York, 2015)
18. S.Y. Chang, Studies of Newmark method for solving nonlinear systems: (II) Verification and guideline. *J. Chin. Inst. Eng.* **27**(5), 663–675 (2004)

19. Z. Cao, Q. Fei, D. Jiang, et al., Dynamic sensitivity-based finite element model updating for nonlinear structures using time-domain responses. *Int. J. Mech. Sci.* **184**, 105788 (2020)
20. J.P. Conte, P.K. Vijalapura, M. Meghella, Consistent finite-element response sensitivity analysis. *J. Eng. Mech.* **129**(12), 1380–1393 (2003)

Perturbations for Non-Local Elastic Vibration of Circular Arches



Ugurcan Eroglu and Giuseppe Ruta

1 Introduction

Describing slender bodies as structured one-dimensional continua, i.e., deformable lines to which plane figures (cross-sections) following coarse kinematics are attached, is usual in structural mechanics, from the pioneering works of Bernoulli and Euler to the monographs by Love, Timoshenko, Antman (e.g., [1]). Modelling arches as curved beams led to many works on their response, following the evolution of the investigations on straight beams in several fields of applied mechanics. Among the rest, the effects of different inner constraints, kinematics of the cross-sections and constitutive prescriptions, plus multi-physical influences, inhomogeneous geometry and materials, and damage were investigated.

An interesting contemporary subject of one-dimensional formulations is the investigation of nano-sized structural members by continuum theories accounting for material organization and describing spatial dispersion properties (e.g., [2]). These non-classical theories may be classified as implicit/weak or explicit/strong, following [3, 4]. With respect to the usual theory of elasticity, implicit/weak theories add kinematical variables and work-conjugated stress measures; explicit/strong theories use the same kinematical variables and account for long-range interactions by integral or integral-differential operators; details are in [3, 5–7]. We use the well-established Eringen's model, initiated in [8] and enhanced in [9–12]: it suggests that the stress equals the convolution of the strain field and a suitable attenuation

U. Eroglu

Mechanical Engng. Dept., Izmir Univ. of Economics, Izmir, Turkey

e-mail: ugurcan.eroglu@izmirekonomi.edu.tr

G. Ruta (✉)

Structural and Geotechnical Engng. Dept., Univ. "La Sapienza"; National Group for Mathematical Physics, Roma, Italy

e-mail: giuseppe.ruta@uniroma1.it

function. The differential form in [13] is suitable only for infinite domains, since otherwise it leads to paradoxical results [14]. On the other hand, the integral form does not provide detectable solutions for problems of interest [15, 16], apart from special loading and boundary conditions [17, 18]. A two-phase version of Eringen's model [9] softens this mathematical problem but still requires additional boundary conditions, the physical interpretation of which is unavailable if solutions of applicative interest are searched [19].

We consider the simplest nano-sized curved beams of interest for applications in MEMS and NEMS, i.e., circular arches with rigid cross-sections. We suppose them to be shallow to simplify calculations and still account for the membrane actions. We use Eringen's two-phase model to account for size effects; we examine the influence of a non-linear static response and small geometric non-linearities on small-amplitude vibration. We consider finite kinematics and balance in the actual shape, pull them back to the reference one, and perturb them in terms of a scalar shape evolution parameter. To abstract from the material and geometrical actual values, suitable non-dimensional quantities yield a set of equations of real fields of real variables only. If arches are slender enough, shearing strain is negligible; experience and numerical results of the literature (among which our work [20]) suggest the relative orders of magnitude of the geometrical quantities involved, helping to limit the formal power series expansion to a suitable order. Eringen's two-phase model leads to an integral-differential system that is, on its turn, perturbed in terms of the fraction of non-local response [21]. This lets us find pattern solutions for benchmark problems at least at the lowest orders of the perturbation, which are thoroughly discussed and commented on.

2 Statics of Shallow Nano-Arches

The reference shape consists of a portion of circumference (the axis) and the copies of a compact plane figure attached orthogonally to the axis (the transverse cross-sections). Cartesian coordinates x, y have origin at the arch mid-span; a consistent unitary orthogonal basis is $\mathbf{e}_1, \mathbf{e}_2$. If f, R are the height of the arch and the radius of its axis, see Fig. 1, the position \mathbf{r}_0 of the axis is

$$\mathbf{r}_0(x) = x\mathbf{e}_1 + y(x)\mathbf{e}_2, \quad (y + R - f)^2 = R^2 - x^2. \quad (1)$$

The curvature $k = 1/R$ is uniform; if the span has length $2l$ and the arch is shallow, i.e., $f/l < 0.1$, easy calculations provide

$$\frac{l}{R} \approx 2\frac{f}{l}, \quad ds = |d\mathbf{r}_0(x)| = \frac{1}{\sqrt{1 - k^2x^2}}dx \approx dx. \quad (2)$$

By Eq. (2)₂, the Cartesian coordinate x very well approximates the curvilinear abscissa s ; all fields defined on the arch may be thus expressed in terms of $s \approx x$.

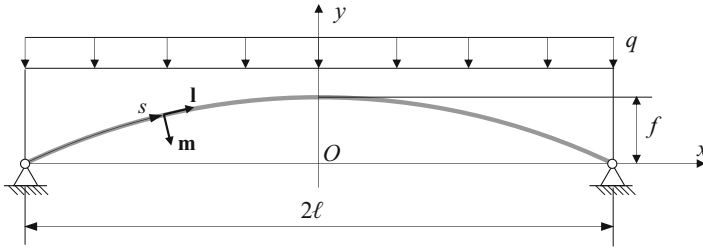


Fig. 1 A slender, shallow hinged circular arch under a uniform “vertical, dead” load

If a prime denotes $s \approx x$ -derivation, the unit tangents $\mathbf{l}(s)$ to the arch axis and their derivative, with magnitude $1/R$ and parallel to the axis normal \mathbf{m} , are

$$\mathbf{l}(s) = \mathbf{r}'_0(s), \quad \frac{\mathbf{m}(s)}{R} = \mathbf{l}'(s). \tag{3}$$

A new shape of the arch is given by the vector field $\mathbf{d}(s) = u(s)\mathbf{l}(s) + v(s)\mathbf{m}(s)$, the axis displacement, and the orthogonal tensor $\mathbf{R}(s)$, the cross-sections rotation, with the sole component φ about the normal to the plane of the arch. Finite strain measures pulled back to the reference shape are [22, 23]

$$\mathbf{u}(s) = \mathbf{R}^T(s) [\mathbf{r}_0(s) + \mathbf{d}(s)]' - \mathbf{l}(s), \quad \mathbf{U}(s) = \mathbf{R}^T(s)\mathbf{R}'(s). \tag{4}$$

The vector \mathbf{u} lists the axis elongation ε and the shearing γ between axis and cross-sections; the sole component of the skew-symmetric tensor \mathbf{U} is the axial curvature variation χ . If we skip the dependence of all fields on the place along the axis for simplicity of notation, the components of (4) are given by

$$\begin{aligned} \gamma &= -\sin \varphi (u' - kv + 1) + \cos \varphi (v' + ku), \\ \varepsilon &= \cos \varphi (u' - kv + 1) + \sin \varphi (v' + ku) - 1, \quad \chi = \varphi'. \end{aligned} \tag{5}$$

The external actions, along the axis and at its ends, are: vector-valued forces $\mathbf{b}(s), \mathbf{f}(-l), \mathbf{f}(l)$ spending power on the incremental axis displacement; skew-symmetric tensor-valued couples $\mathbf{B}(s), \mathbf{F}(-l), \mathbf{F}(l)$ spending power on the incremental cross-sections rotation. The contact actions among parts of the arch consist of a vector field $\mathbf{t}(s)$ and a skew-symmetric tensor field $\mathbf{T}(s)$, spending power on the incremental strains; their pull-back to the referential shape follows:

$$\mathbf{b} = \mathbf{R}\mathbf{a}, \quad \mathbf{B} = \mathbf{R}\mathbf{A}\mathbf{R}^T, \quad \mathbf{f} = \mathbf{R}\mathbf{g}, \quad \mathbf{F} = \mathbf{R}\mathbf{G}\mathbf{R}^T, \quad \mathbf{t} = \mathbf{R}\mathbf{s}, \quad \mathbf{T} = \mathbf{R}\mathbf{S}\mathbf{R}^T. \tag{6}$$

The virtual work principle and some algebra yield referential balance [22, 23]

$$\begin{aligned} \mathbf{s}' + \mathbf{U}\mathbf{s} + \mathbf{a} = \mathbf{0}, \quad \mathbf{S}' + \mathbf{U}\mathbf{S} - \mathbf{S}\mathbf{U} + \mathbf{u} \wedge \mathbf{s} + \mathbf{A} = \mathbf{0} \quad \forall x \in (-l, l) \\ \mathbf{s} = \mathbf{g}, \quad \mathbf{S} = \mathbf{G} \quad x = \pm l, \end{aligned} \tag{7}$$

where \wedge is the external product of vectors, providing skew-symmetric tensors; we introduce the decompositions $\mathbf{s} = N\mathbf{l} + V\mathbf{m}$ and $\mathbf{S} = M\mathbf{l} \wedge \mathbf{m}$, where N, V are the axial and shearing components of inner force and M is the bending couple.

Slender arches are almost shear-rigid; if we pose $\gamma = 0$ [1], its work conjugate V is constitutively unprescribed, given only by balance equations. Let the material response be linear elastic, consisting of a local and a non-local part, following Eringen’s two-phase model [9]. If A, B are the cross-sections axial and bending stiffnesses, the laws for the constitutively prescribed inner actions N, M are

$$N = A [(1 - \xi) \varepsilon + \xi K * \varepsilon], \quad M = B [(1 - \xi) \chi + \xi K * \chi], \tag{8}$$

where $0 \leq \xi < 1$ is the non-local fraction. Its contribution is the convolution of the relevant strain measure with a kernel function K

$$K * g = \int_{-l}^l K (|x - X|) g (X) dX. \tag{9}$$

Following the literature, K is an exponential in terms of a material property κ

$$K (|x - X|) = \frac{1}{2\kappa} \exp \left(\frac{|x - X|}{\kappa} \right) \tag{10}$$

and κ has the dimensions of a length, roughly providing the radius of non-local action.

If $\mathbf{a} = a_l\mathbf{l} + a_m\mathbf{m}$, we introduce the non-dimensional quantities

$$\begin{aligned} \bar{k} = \frac{l}{R}, \quad \alpha = \frac{f}{l}, \quad \bar{u} = \frac{u}{l}, \quad \bar{v} = \frac{v}{l}, \quad \theta = \varphi, \quad \bar{x} = \frac{x}{l} \approx \frac{s}{l}, \quad \bar{\kappa} = \frac{\kappa}{l} \\ \bar{N} = \frac{Nl^2}{B}, \quad \bar{V} = \frac{Vl^2}{B}, \quad \bar{M} = \frac{Ml}{B}, \quad \lambda = \sqrt{\frac{Al^2}{B}}, \quad \Theta_{m,l} = \frac{a_{m,l}l^3}{B} \end{aligned} \tag{11}$$

to abstract from particular geometrical and physical values; however, for simplicity, henceforth we omit overbars, implying that we deal only with the non-dimensional ratios in (11), except when confusion may arise.

Consider a shallow slender arch with pinned ends, loaded by a “vertical” uniform load; then, numerical (see, e.g., [20]) and experimental results suggest great simplifications of the field equations, since it is possible to estimate that

$$k = O(\alpha), \quad u = O(\alpha^2), \quad v = O(\alpha), \quad \theta = O(\alpha), \quad \lambda^{-1} = O(\alpha). \tag{12}$$

On physical bases, we admit that the values of the cross-section rotation at any place of the axis are influenced, though indirectly, by the shallowness ratio α . Thus, we expand the trigonometric functions in (5) in series up to $O(\alpha^2)$ and use (12). Following Mettler [24], $\varepsilon \ll 1$ and the normal force N are almost uniform with respect to $x \approx s$. Then, the field equations are

$$(1 - \xi) v'''' + \xi (K * v'')'' - (k + v'') N - \Theta_m = 0,$$

$$N = A [(1 - \xi) \varepsilon + \xi K * \varepsilon], \quad \varepsilon = u' - kv + \theta v' - \frac{\theta^2}{2} = u' - kv + \frac{(v')^2}{2}, \tag{13}$$

and the last equality in (13)₃ derives from the constraint of vanishing shearing strain. It turns then out that N shall be found imposing that the arch ends are fixed, yielding an integral-differential condition, contrary to the local case.

Always on physical bases, we admit that all the fields of interest in this problem regularly depend on the non-local fraction ξ . Any function g can then be approximated by a formal ξ -power series expansion up to order m

$$g \approx \sum_{i=0}^m \frac{\xi^i}{i!} \left. \frac{d^i g}{(d\xi)^i} \right|_{\xi=0} =: \sum_{i=0}^m \frac{\xi^i}{i!} g_i, \quad g_i := \left. \frac{d^i g}{(d\xi)^i} \right|_{\xi=0} \tag{14}$$

where the values at $\xi = 0$ are, for the physical meaning of ξ , those for a fully local elastic material. To mimic displacement-controlled mechanical tests, where the external load implicitly depends on the induced strain, we admit that also Θ_m has a non-local part and can thus be formally expanded in ξ -power series.

Inserting Eq. (14) into Eq. (13) provides a hierarchy of equations; limiting the expansion (14) to the first order, Eq. (13)₁ yields

$$v_0'''' - (k + v_0'') N_0 - \Theta_{m0} = 0,$$

$$v_1'''' - v_0'''' + (K * v_0'')'' - (k + v_0'') N_1 - v_1'' N_0 - \Theta_{m1} = 0, \tag{15}$$

while Eq. (13)_{2,3} yields, admitting that u vanishes at the ends at each order,

$$N_0 = \frac{\lambda^2}{2} \int_{-1}^1 \left(\frac{(v_0')^2}{2} - kv_0 \right) dx$$

$$N_1 = \frac{\lambda^2}{2} \int_{-1}^1 (v_0' v_1' - kv_1) dx - \int_{-1}^1 (N_0 - K * N_0) dx. \tag{16}$$

The solution to Eq. (15)₁ is obtained by Galërkin’s technique, using the same comparison functions as in [20]; following the results therein, in order to avoid static bifurcation we limit to $\alpha\lambda < \pi^3/8$ and get, c_1 being an arbitrary constant,

$$\begin{aligned}
 v_0 &= c_1 \cos \frac{\pi x}{2}, & N_0 &= \frac{c_1 \lambda^2 (\pi^3 c_1 - 64\alpha)}{16\pi}, \\
 \Theta_{m0} &= \frac{4c_1 \pi^6 + c_1^3 \pi^6 \lambda^2 - 96c_1^2 \pi^3 \alpha \lambda^2 + 2048c_1 \alpha^2 \lambda^2}{256\pi}.
 \end{aligned}
 \tag{17}$$

Inserting the ξ -0th-order solutions (17) into the ξ -1st-order field equations (15)₂, (16)₂ and using Gal erkin’s technique again with the same trial function, we get

$$\begin{aligned}
 N_1 &= -\frac{c_1 e^{-1/\kappa} \kappa \lambda^2 (\pi^3 c_1 - 64\alpha) \sinh(1/\kappa)}{16\pi} \\
 \Theta_{m1} &= -\frac{c_1 e^{-1/\kappa} \kappa}{256\pi} \left\{ \frac{4\pi^6 (\pi^4 \kappa^3 + 4\pi^2 \kappa + 32) \cosh(1/\kappa)}{(\pi^2 \kappa^2 + 4)^2} + \right. \\
 &\quad \left. + \frac{\sinh(1/\kappa)}{\pi^2 \kappa^2 + 4} \left[(\pi^2 \kappa^2 + 4) \lambda^2 (\pi^3 c_1 - 64\alpha) (\pi^3 c_1 - 32\alpha) + 4\pi^8 \kappa \right] \right\}.
 \end{aligned}
 \tag{18}$$

Remark that choosing the trial function (i.e., the field of axis deflection) at ξ -1st-order identical to that of ξ -0th-order (i.e., that of the local case) is reasonable only when the non-locality range is limited.

From Eq. (18)₁, we see that the introduction of a small amount of non-locality implies a reduction in the normal force, which is physically motivated because the long-range action is somehow weaker than the local one (see also the constitutive Eq. (8)). This softening effect also appears as a decrement in the value of the external load (see Eq. (18)₂) required to yield a given apex displacement.

Figure 2 shows: (a) the curves load vs. displacement of the apex for a non-local shallow and slender arch, with a limited non-local fraction; (b) the decrement of the

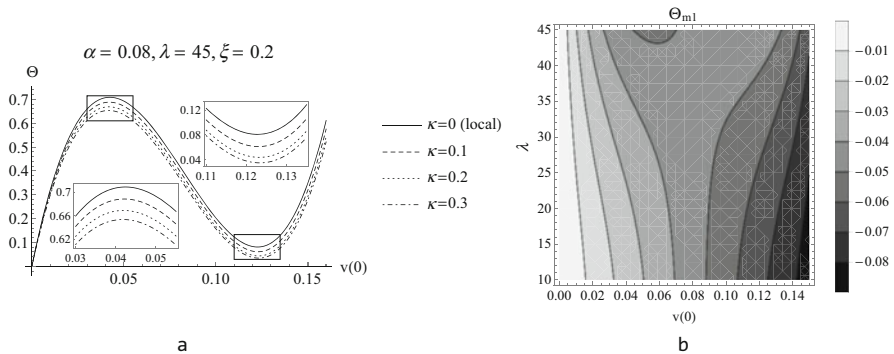


Fig. 2 (a) Equilibrium path for various non-local ratios κ ; (b) Decrement in the distributed load vs. the apex displacement and the slenderness ratio, $\alpha = 0.08, \kappa = 0.1$

external load required to maintain a given apex displacement. The softening effect due to long-range interactions is apparent in Fig. 2a, while Fig. 2b suggests that the same effect is more pronounced with the increase of the apex displacement and the decrease of the slenderness ratio. The first aspect is physically motivated by the fact that, all the rest left unchanged, the strain displacement of the apex increases if the arch is less stiff, hence if the non-locality effect (bringing softening) is more pronounced. The physical motivation of the second aspect is that, all the rest left unchanged, the slenderness ratio diminishes with the length of the axis; then, the physical domain is smaller and the non-locality, bringing a softening effect, affects the behaviour more remarkably.

A key remark is that this limited non-local fraction lets us still use symmetric trigonometric functions for the deformed shape. At higher ξ , the known boundary effect, due to missing neighbor at the boundaries, may considerably change the actual deformed shape and lead to early stage instability.

3 Small Vibration About Nonlinear Equilibria

If the mechanical fields regularly depend on a scalar evolution parameter, we may linearize Eqs. (5), (7), (8) in terms of it, getting two sets of equations: the first describes the reference configuration, the other provides small perturbations about it, as we did in [25]. If the reference shape is loaded with a uniform “vertical” load and deforms following the assumptions in the previous section, we obtain the non-linear equilibrium path described therein. A small-amplitude motion superposed on such equilibria obeys the equations

$$\begin{aligned} \hat{\gamma} &= \hat{v}' - \hat{\varphi} & \hat{N}' - (k + v'') \hat{V} - \hat{\chi} V + \hat{\Theta}_l &= 0 \\ \hat{\varepsilon} &= \hat{u}' - (k + v'') \hat{v} & \hat{V}' + (k + v'') \hat{N} + \hat{\chi} N + \hat{\Theta}_m &= 0 \\ \hat{\chi} &= \hat{\varphi}' & \hat{M}' + \hat{V} + \hat{\varepsilon} V &= 0, \end{aligned} \tag{19}$$

where functions with an overhat are non-dimensional first-order evolution increments (see Eq. (11)). The normal force may still be considered uniform, since the deformed arch remains shallow, and shearing strain is still negligible. If the only non-vanishing external distributed load is the transverse inertia of a harmonic motion with non-dimensional natural angular frequency Ω , Eq. (19) becomes

$$\begin{aligned} (1 - \xi) \hat{v}'''' + \xi (K * \hat{v}'')'' - (k + v'') \hat{N} - \hat{v}'' N + \hat{\varepsilon}' v''' + \hat{\varepsilon} v'''' - \Omega^2 \hat{v} &= 0 \\ \hat{N} &= \lambda^2 \{ (1 - \xi) [\hat{u}' - (k + v'') \hat{v}] + \xi K * [\hat{u}' - (k + v'') \hat{v}] \}. \end{aligned} \tag{20}$$

As for the static problem, we admit that all the fields regularly depend on the non-local fraction ξ and the ξ -linearization of Eq. (20) yields

$$\begin{aligned}
 \hat{v}_0'''' - (k + v_0'') \hat{N}_0 - \hat{v}_0'' N_0 + \hat{\varepsilon}_0 v_0'''' - \Omega_0^2 \hat{v}_0 &= 0 \\
 \hat{N}_0 &= -\frac{\lambda^2}{2} \int_{-1}^1 (k + v_0'') \hat{v}_0 dx, \\
 \hat{v}_1'''' - \hat{v}_0'''' + (K * \hat{v}_0'')'' - k \hat{N}_1 - v_0'' \hat{N}_1 - v_1' \hat{N}_0 - \hat{v}_0'' N_1 - \hat{v}_1'' N_0 + \\
 + \hat{\varepsilon}'_0 v_1'''' + \hat{\varepsilon}'_1 v_0'''' + \hat{\varepsilon}_0 v_1'''' + \hat{\varepsilon}_1 v_0'''' - \Omega_0^2 \hat{v}_1 - \Omega_1^2 \hat{v}_0 &= 0 \\
 \hat{\varepsilon}_0 &= \frac{\hat{N}_0}{\lambda^2}, \quad \varepsilon_0 = \frac{N_0}{\lambda^2}, \\
 \hat{\varepsilon}_1 &= \frac{\hat{N}_1}{\lambda^2} + \hat{\varepsilon}_0 - K * \hat{\varepsilon}_0, \quad \varepsilon_1 = \frac{N_1}{\lambda^2} + \varepsilon_0 - K * \varepsilon_0 \\
 \hat{N}_1 &= -\frac{\lambda^2}{2} \int_{-1}^1 [(k + v_0'') \hat{v}_1 + v_1' \hat{v}_0] dx - \frac{1}{2} \int_{-1}^1 [N_0 - K * N_0] dx.
 \end{aligned}
 \tag{21}$$

Remark that (21)_{1,2} coincides with those in [20], which was expected since the arch therein is fully local elastic. The remaining Eq. (21) provides the contribution of non-locality to the vibration of pre-loaded shallow arches, affecting both the response in the initial static loading and the superposed small vibration.

We tackle (21) by Galérkin’s technique, using a symmetric trial function, as in statics, of magnitude d_1 . Requiring that a non-trivial solution of (21)_{1,2} (i.e., for $d_1 \neq 0$) exists, we get the first non-dimensional natural angular frequency

$$\Omega_0^2 = \frac{4096\alpha^2\lambda^2 + \pi^6(6c_1^2\lambda^2 + 8) + \pi^8c_1^2 - (384\lambda^2 + 32\pi^2)\alpha\pi^3c_1}{128\pi^2} \tag{22}$$

affected, as expected, by the amplitude c_1 of the static response to the load Θ .

We may make considerations on the trial function similar to those for statics. Then, a non-trivial solution of the remaining Eq. (21) gives

$$\begin{aligned}
 \Omega_1^2 = -\frac{e^{-1/\kappa}\kappa}{128\pi^2} &\left[\sinh\left(\frac{1}{\kappa}\right) \left(\frac{128\pi^5\alpha c_1 + 8\pi^{10}\kappa^3 + 8\pi^8\kappa}{\pi^4\kappa^4 + 5\pi^2\kappa^2 + 4} \right) \right. \\
 + 2\lambda^2 &\left(2048\alpha^2 + 3\pi^6c_1^2 - 192\pi^3\alpha c_1 \right) - \frac{\pi^{10}c_1^2\kappa^2 + 4\pi^8c_1^2 - 32\pi^7\alpha c_1\kappa^2}{\pi^4\kappa^4 + 5\pi^2\kappa^2 + 4} \\
 + \frac{8\pi^6(\pi^4\kappa^3 + 4\pi^2\kappa + 32) \cosh\left(\frac{1}{\kappa}\right)}{(\pi^2\kappa^2 + 4)^2} &\left. \right]. \tag{23}
 \end{aligned}$$

If no initial load is present (i.e., $\Theta = 0$, $c_1 = 0$), the 0th (fully local response) and 1st (little fraction of non-local response) order frequencies reduce to

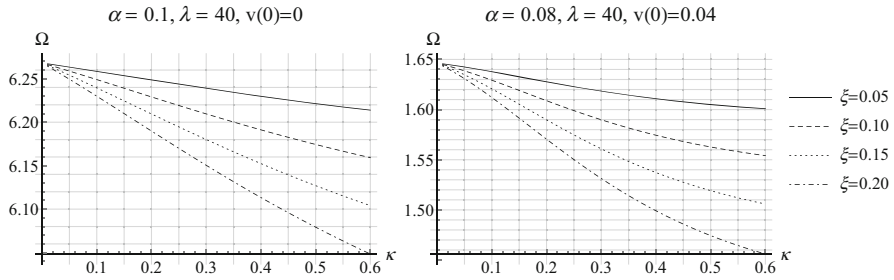


Fig. 3 Fundamental frequency vs. the non-local range ratio for undeformed (left) and deformed (right) shallow arches

$$\begin{aligned}
 \Omega_{0L}^2 &= \frac{8\pi^6 + 4096\alpha^2\lambda^2}{128\pi^2} \\
 \Omega_{1L}^2 &= -\frac{e^{-2/\kappa}\kappa}{16\pi^2(\pi^2\kappa^2 + 4)^2} \left[256\alpha^2(e^{2/\kappa} - 1)(\pi^2\kappa^2 + 4)^2\lambda^2 + \right. \\
 &\quad \left. + \pi^6(e^{2/\kappa}(\pi^4\kappa^3 + 4\pi^2\kappa + 16) + 16) \right] \tag{24}
 \end{aligned}$$

and provide the non-dimensional small-amplitude vibration natural angular frequency of symmetric mode shapes about the undeformed configuration.

Figure 3 shows the variation of the value of this frequency with the non-local range ratio κ for undeformed (i.e., previously unloaded) and deformed (i.e., preloaded by a uniform “vertical” load as in the previous section) arches. The softening effect of non-local elasticity, represented by the non-dimensional length of long-range interaction, is apparent in both cases and increases with the amount of the non-local fraction ξ . This is in accord with experimental evidence, at least for a certain class of nano-materials, and has a physical motivation that can be paraphrased by what already commented in the section on statics.

Figure 4 shows the variations of the square of the natural frequency and static apex displacement with the magnitude of the applied load; it is clearly seen, as we also showed in [20], that a snap bifurcation is possible and the non-local ratio always has a softening effect, once again as physically expected.

4 Conclusions

We examined small-amplitude vibration about non-linear equilibria of shallow non-local arches. The finite field equations are perturbed in terms of: the scalar evolution parameter of the detachment of the actual shape from the reference one and the scalar material parameter of the fraction of non-local elastic response

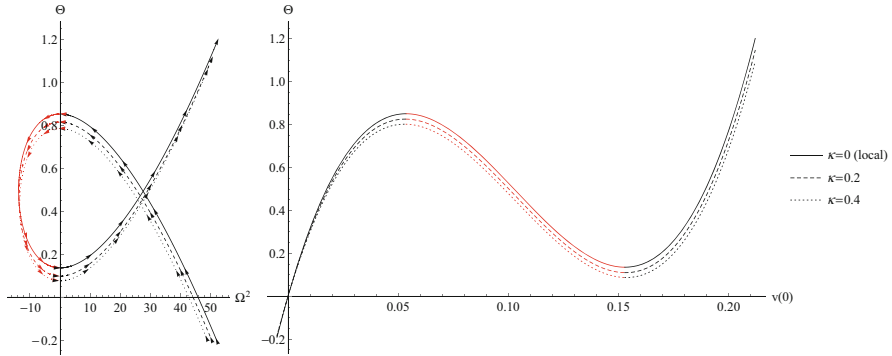


Fig. 4 Load-frequency (left) and load-displacement (right) graphs for $\alpha = 0.1$, $\lambda = 35$, $\xi = 0.2$ and various κ ; black: stable, red: unstable

according to Eringen's two-phase model. This two-term perturbation provides hierarchies of equations describing the influence of: geometrical non-linearities on kinematics and balance; and that of the long-range interaction on static and dynamic response. The perturbation procedure does not require additional and spurious boundary conditions, and the resulting equations are solved by Galërkin's technique, leading to original approximate solutions in closed form for the vibration frequencies, which may serve for material identification and validation studies for novel numerical/approximately exact solution techniques.

References

1. A.E.H. Love, *A Mathematical Treatise on the Mathematical Theory of Elasticity*, 2nd edn. (The University Press, Cambridge, 1906)
2. G.A. Maugin, *Generalized Continuum Mechanics: What Do We Mean by That?* Advances in Mechanics and Mathematics, vol. 21 (Springer, New York, 2010)
3. I.A. Kunin, *Elastic Media with Microstructure I: One-Dimensional Models* (Springer, Berlin, 1982)
4. P. Trovalusci, *Molecular Approaches for Multifield Continua: Origins and Current Developments*. Multiscale Modeling of Complex Materials: Phenomenological, Theoretical and Computational Aspects (Springer, Vienna, 2014), pp. 211–278
5. I.A. Kunin, *Elastic Media with Microstructure II: Three-Dimensional Models* (Springer, Berlin, 1983)
6. G.A. Maugin, Nonlocal theories or gradient-type theories: a matter of convenience. *Arch. Mech.* **31**(1), 15–26 (1979)
7. I.A. Kunin, On foundations of the theory of elastic media with microstructure. *Int. J. Eng. Sci.* **22**(8), 969–978 (1984)
8. A.C. Eringen, A unified theory of thermomechanical materials. *Int. J. Eng. Sci.* **4**(2), 179–202 (1966)
9. A.C. Eringen, Linear theory of nonlocal elasticity and dispersion of plane waves. *Int. J. Eng. Sci.* **10**, 425–435 (1972)
10. A.C. Eringen, Theory of nonlocal thermoelasticity. *Int. J. Eng. Sci.* **12**, 1063–1077 (1974)

11. A.C. Eringen, On nonlocal plasticity. *Int. J. Engng. Sci.* **19**(12), 1461–1474 (1981)
12. A.C. Eringen, D.G.B. Edelen, On nonlocal elasticity. *Int. J. Eng. Sci.* **10**, 233–248 (1972)
13. A.C. Eringen, Screw dislocation in non-local elasticity. *J. Phys. D: Appl. Phys.* **10**(5), 671–678 (1977)
14. J. Fernández-Sáez, R. Zaera, J.A. Loya, J.N. Reddy, Bending of Euler–Bernoulli beams using Eringen’s integral formulation: a paradox resolved. *Int. J. Eng. Sci.* **99**, 107–116 (2016)
15. G. Romano, R. Barretta, Comment on the paper exact solution of Eringen’s nonlocal integral model for bending of Euler-Bernoulli and Timoshenko beams by Meral Tuna and Mesut Kirca. *Int. J. Eng. Sci.* **109**, 240–242 (2016)
16. G. Romano, R. Barretta, M. Diaco, F.M. de Sciarra, Constitutive boundary conditions and paradoxes in nonlocal elastic nanobeams. *Int. J. Mech. Sci.* **121**, 151–156 (2017)
17. M. Tuna, M. Kirca, Exact solution of Eringen’s nonlocal integral model for bending of Euler-Bernoulli and Timoshenko beams. *Int. J. Eng. Sci.* **105**, 80–92 (2016)
18. M. Tuna, M. Kirca, Respond to the comment letter by Romano and Barretta on the paper exact solution of Eringen’s nonlocal integral model for bending of Euler-Bernoulli and Timoshenko beams. *Int. J. Eng. Sci.* **116**, 141–144 (2017)
19. R. Zaera, Ó. Serrano, J. Fernández-Sáez, On the consistency of the nonlocal strain gradient elasticity. *Int. J. Eng. Sci.* **138**, 65–81 (2019)
20. U. Eroglu, G. Ruta, Vibration of pre-loaded shallow circular arches, in *Nonlinear Dynamics of Structures, Systems and Devices*, ed. by W. Lacarbonara, B. Balachandran, J. Ma, J.A. Tenreiro Machado, G. Stepan (Springer, Cham, 2020), pp. 237–245
21. U. Eroglu, Perturbation approach to Eringen’s local/non-local constitutive equation with applications to 1-d structures. *Meccanica* **55**, 1119–1134 (2020)
22. S.S. Antman, *Nonlinear problems of elasticity* (Springer, New York, 1995)
23. M. Pignataro, N. Rizzi, G. Ruta, A beam model for the flexural-torsional buckling of thin-walled members. *Thin Wall. Struct.* **46**, 816–822 (2008)
24. E. Mettler, Dynamic buckling, in *Handbook of Engineering Mechanics*, ed. by Flugge (McGraw-Hill, New York, 1962)
25. U. Eroglu, G. Ruta, Fundamental frequencies and buckling in pre-stressed parabolic arches. *J. Sound Vib.* **435**, 104–118 (2018)

Two-Scale Curved Beam Model for Dynamic Analysis of Masonry Arches



Daniela Addessi, Paolo Di Re, Cristina Gatta, and Mariacarla Nocera

1 Introduction

Most of the historical masonry structures are based on arch systems. Hence, a large number of experimental studies were devoted to deeply understand response of masonry arches under static and dynamic loads [1–3]. Moreover, many numerical models, typically referring to limit analysis, discrete element approach, and finite element (FE) method, were proposed to predict structural behavior and safety conditions of arches [4, 5] and, in general, masonry structures [6–8]. Among various formulations, FE models result a flexible and effective tool for this purpose, as these permit a suitable representation of the inertia effects and accurately describe the evolution of degrading mechanisms and typical collapse modes of arches. In particular, multiscale approaches include the detailed geometric/mechanical modeling and, if properly formulated, can limit the computational efforts [9–11].

This chapter explores dynamic response of masonry arches built up with regular arrangement of bricks and mortar joints, by adopting a Timoshenko force-based curved beam FE. The model is an extension of the formulation presented in [5], originally proposed for static analysis, to the case of dynamic loading conditions. Proper cross-section displacement shape functions are derived to obtain a consistent form of the element mass matrix. To this end, the procedure presented in [12–14], based on the Unit Load Method, is applied to Timoshenko curved beam elements. Relying on a two-scale approach, the constitutive law for masonry material is derived via a homogenization procedure, linking the structural scale model to a repetitive masonry Unit Cell (UC) modeled at microlevel [15].

D. Addessi · P. Di Re · C. Gatta (✉) · M. Nocera
Department of Structural and Geotechnical Engineering, Sapienza University of Rome, Rome, Italy
e-mail: daniela.addessi@uniroma1.it; paolo.dire@uniroma1.it; cristina.gatta@uniroma1.it;
mariacarla.nocera@uniroma1.it

Numerical studies are performed to prove efficiency of the proposed model in describing dynamic behavior of masonry arches. First, modal decomposition analyses are conducted; then, response to earthquake excitation is investigated.

2 Force-Based Formulation for Dynamic Analysis

This section describes the curved beam FE used at the macroscopic scale. After introducing the fundamental element equations, the derivation of the consistent mass matrix to be used within the adopted force-based approach is presented.

2.1 Fundamental Element Equations and Flexibility Matrix

In the global reference system, six degrees of freedom (DOFs) govern the kinematics of the curved beam element, delimited by nodes I and J , corresponding to two translations and one in-plane rotation at each node. These are listed in the displacement vector $\mathbf{U} = (U_{X,I} \ U_{Y,I} \ \Theta_I \ U_{X,J} \ U_{Y,J} \ \Theta_J)^T$.

According to the equilibrated approach, the basic reference system in Fig. 1 is introduced. This is obtained from the local system (X, Y) , with X the direction going from I to J , through elimination of the element rigid body motions. In the basic configuration, only three deformation displacements are considered, that is the element elongation \tilde{U}_J and nodal rotations $\tilde{\Theta}_{I,J}$, collected in vector $\mathbf{V} = (\tilde{U}_J \ \tilde{\Theta}_I \ \tilde{\Theta}_J)^T$. The following kinematic relationship holds for \mathbf{V} :

$$\mathbf{V} = \mathbf{A}_g \mathbf{U} = \mathbf{A}_v \mathbf{A}_r \mathbf{U} \tag{1}$$

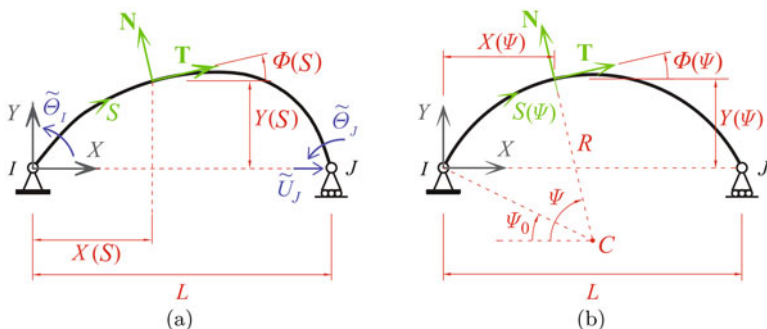


Fig. 1 Geometric parametrization in the basic reference system for the 2D element representing the axis of (a) arbitrarily curved and (b) circular arches

being \mathbf{A}_g the element compatibility matrix. This depends on the initial undeformed distance L between the abutments and the element orientation, by means of matrices \mathbf{A}_v , removing the element rigid body motions, and \mathbf{A}_r , rotating the DOFs from the global to the local reference system. Quantities work-conjugate to \mathbf{V} are contained in the basic element force vector $\mathbf{Q} = (N_J \ M_I \ M_J)^T$, being N_J the force parallel to X at J and $M_{I/J}$ the in-plane nodal moment at I/J .

According to the force-based formulation, equilibrium conditions are enforced along the element axis. To this end, a parametric representation of the 2D curve defining the beam axis \mathcal{L} is adopted, that is $\mathcal{L} \equiv [X = f(S); Y = g(S)]$, being S the arc-length abscissa, identifying the general element cross-section (Fig. 1a).

Considering the introduced parametric representation, the equilibrium conditions, relating the generalized stress vector $\boldsymbol{\Sigma}(S)$ to basic forces \mathbf{Q} and stress resultants $\boldsymbol{\Sigma}_q(S)$ due to distributed loads, are expressed as

$$\underbrace{\begin{pmatrix} N(S) \\ M(S) \\ T(S) \end{pmatrix}}_{\boldsymbol{\Sigma}(S)} = \underbrace{\begin{bmatrix} \cos \Phi(S) & -\frac{\sin \Phi(S)}{L} & -\frac{\sin \Phi(S)}{L} \\ Y(S) & \frac{X(S)}{L} - 1 & \frac{X(S)}{L} \\ -\sin \Phi(S) & -\frac{\cos \Phi(S)}{L} & -\frac{\cos \Phi(S)}{L} \end{bmatrix}}_{\mathbf{B}(S)} \underbrace{\begin{pmatrix} N_J \\ M_I \\ M_J \end{pmatrix}}_{\mathbf{Q}} + \underbrace{\begin{pmatrix} N_q(S) \\ M_q(S) \\ T_q(S) \end{pmatrix}}_{\boldsymbol{\Sigma}_q(S)}. \quad (2)$$

In Eq. (2), the equilibrium matrix $\mathbf{B}(S)$ is written in terms of coordinates $X(S)$, $Y(S)$ and the angle $\Phi(S)$ that the unit vector \mathbf{T} , tangent to the curve at S , forms with the local axis X (Fig. 1a).

The generalized section strain vector $\mathbf{E}(S)$, collecting the axial elongation $E(S)$, curvature $K(S)$, and shear strain $\Gamma(S)$, is related to $\boldsymbol{\Sigma}(S)$ by the section constitutive equation, which assumes the following incremental form:

$$\dot{\mathbf{E}}(S) = \boldsymbol{\Upsilon}(S) \dot{\boldsymbol{\Sigma}}(S) \quad (3)$$

being $\boldsymbol{\Upsilon}(S)$ the cross-section tangent flexibility matrix.

By imposing the virtual work equivalence and making use of Eqs. (2) and (3), the element tangent flexibility matrix \mathbf{F} is derived as

$$\mathbf{F} = \frac{\partial \mathbf{V}}{\partial \mathbf{Q}} = \int_0^{L_s} \mathbf{B}^T(S) \boldsymbol{\Upsilon}(S) \mathbf{B}(S) dS \quad (4)$$

where L_s is the length of the element axis. Equation (4) evaluates the exact flexibility matrix, as long as a closed solution of the integral can be evaluated.

In the special case of a circular arch with radius R , the arch-length abscissa S can be expressed as a linear function of the angle Ψ between the cross-section plane and the axis X (Fig. 1b), i.e., $S = R(\Psi - \Psi_0)$. Hence, by considering that $dS = R d\Psi$ and that geometric variable Ψ ranges between the abutment angles Ψ_0 and $\pi - \Psi_0$, the flexibility matrix in Eq. (4) is evaluated as

$$\mathbf{F} = R \int_{\Psi_0}^{\pi - \Psi_0} \mathbf{B}^T(\Psi) \boldsymbol{\Upsilon}(\Psi) \mathbf{B}(\Psi) d\Psi. \tag{5}$$

Matrix $\mathbf{B}(\Psi)$ in Eq. (5) can be easily determined from that in Eq. (2), considering that $\cos \Phi(\Psi) = \sin \Psi$ and $\sin \Phi(\Psi) = \cos \Psi$, while $X(\Psi) = R(\cos \Psi_0 - \cos \Psi)$ and $Y(\Psi) = R(\sin \Psi - \sin \Psi_0)$.

2.2 Consistent Element Mass Matrix

To evaluate the element mass matrix consistent with the force-based formulation, equivalent shape functions, interpolating the generalized cross-section displacements $\mathbf{U}_s(S)$ on the basis of the nodal displacements \mathbf{U} , are required [12, 13].

The procedure introduces generalized unit loads $\mathbf{P}_s = (F_X \ F_Y \ C)^T$, namely two forces F_X and F_Y and one couple C . Assuming loads \mathbf{P}_s as virtual forces applied at the general cross-section located at S , the virtual work equivalence is expressed as

$$\delta \mathbf{P}_s^T \mathbf{U}_s(S) = \int_0^{L_s} \delta \boldsymbol{\Sigma}^T(S, \xi) \mathbf{E}(\xi) d\xi \tag{6}$$

where symbol δ denotes the virtual variation of the variable and the variable ξ is introduced to evaluate the integral along the element axis. Hence, $\delta \boldsymbol{\Sigma}(S, \xi)$ collects the virtual section stresses at ξ due to the virtual unit loads applied at S . Considering the exact solution of the element equilibrium equations referred to the basic simply supported beam configuration, $\delta \boldsymbol{\Sigma}(S, \xi)$ results as

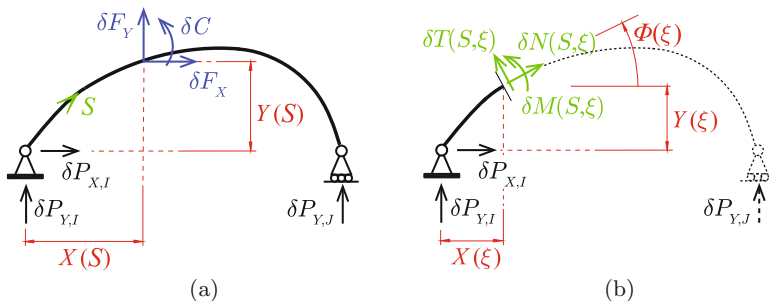


Fig. 2 Basic system with virtual forces applied at S : **(a)** element equilibrium, **(b)** section stresses for the element portion delimited by node I and cross-section at ξ .

$$\delta \boldsymbol{\Sigma}(S, \xi) = \mathbf{B}_r(\xi) \delta \mathbf{P}_r(S) = \mathbf{B}_r(\xi) \underbrace{\begin{bmatrix} -1 & 0 & 0 \\ -\frac{Y(S)}{L} & \frac{X(S)}{L} - 1 & \frac{1}{L} \\ \frac{Y(S)}{L} & -\frac{X(S)}{L} & -\frac{1}{L} \end{bmatrix}}_{\mathbf{B}_{r,s}(S)} \delta \mathbf{P}_s \quad (7)$$

where matrix $\mathbf{B}_{r,s}(S)$ evaluates the nodal reactions $\delta \mathbf{P}_r(S) = (\delta P_{X,I} \delta P_{Y,I} \delta P_{Y,J})^T$ due to unit loads applied at S (Fig. 2a), whereas matrix $\mathbf{B}_r(\xi)$ computes the section stresses at ξ given $\delta \mathbf{P}_r(S)$ (Fig. 2b). This assumes the following expression:

$$\mathbf{B}_r(\xi) = \begin{cases} \begin{bmatrix} -\cos \Phi(\xi) & -\sin \Phi(\xi) & 0 \\ -Y(\xi) & X(\xi) & 0 \\ \sin \Phi(\xi) & -\cos \Phi(\xi) & 0 \end{bmatrix} & \text{for } \xi < S \\ \begin{bmatrix} 0 & 0 & \sin \Phi(\xi) \\ 0 & 0 & L - X(\xi) \\ 0 & 0 & \cos \Phi(\xi) \end{bmatrix} & \text{for } \xi > S \end{cases} \quad (8)$$

Equation (7) can be introduced in Eq.(6) to obtain the relationship between generalized cross-section displacements and strains as:

$$\mathbf{U}_s(S) = \mathbf{B}_{r,s}^T(S) \int_0^{L_s} \mathbf{B}_r^T(\xi) \mathbf{E}(\xi) d\xi. \quad (9)$$

By including Eqs.(1)–(4) in Eq.(9) and considering the contribution of the element rigid body motions, the section displacements are expressed as a function of nodal displacements, and the shape function matrix $\mathbf{N}_s(S)$ is obtained, i.e.,

$$\mathbf{U}_s(S) = \underbrace{\left\{ \mathbf{B}_{r,s}^T(S) \left[\int_0^{L_s} \mathbf{B}_r^T(\xi) \boldsymbol{\Upsilon}(\xi) \mathbf{B}(\xi) d\xi \right] \mathbf{F}^{-1} \mathbf{A}_g + \mathbf{N}_r(S) \mathbf{A}_r \right\}}_{\mathbf{N}_s(S)} \mathbf{U} \quad (10)$$

where $\mathbf{N}_r(S)$ is the shape function matrix for element rigid body motions, which assumes the following form for arbitrarily curved beams:

$$\mathbf{N}_r(S) = \begin{bmatrix} 1 & \frac{Y(S)}{L} & 0 & 0 & -\frac{Y(S)}{L} & 0 \\ 0 & 1 - \frac{X(S)}{L} & 0 & 0 & \frac{X(S)}{L} & 0 \\ 0 & -\frac{1}{L} & 0 & 0 & \frac{1}{L} & 0 \end{bmatrix} \quad (11)$$

The computation of the shape function matrix $\mathbf{N}_s(S)$ allows to derive the element mass matrix \mathbf{M} in the global reference system as

$$\mathbf{M} = \int_0^{L_s} \mathbf{N}_s(S)^T \mathbf{m}_s(S) \mathbf{N}_s(S) dS \quad (12)$$

being $\mathbf{m}_s(S)$ the cross-section mass matrix.

If the circular beam axis case is considered and the parametrization in Fig. 1b is adopted, Eq. (10) becomes:

$$\mathbf{U}_s(\Psi) = \underbrace{\left\{ R \mathbf{B}_{r_s}^T(\Psi) \left[\int_{\Psi_0}^{\pi-\Psi_0} \mathbf{B}_r^T(\Psi_\xi) \mathbf{Y}(\Psi_\xi) \mathbf{B}(\Psi_\xi) d\Psi_\xi \right] \mathbf{F}^{-1} \mathbf{A}_g + \mathbf{N}_r(\Psi) \mathbf{A}_r \right\}}_{\mathbf{N}_s(\Psi)} \mathbf{U}. \quad (13)$$

To be noted is that, all the integrals over the element axis are evaluated through numerical integration procedures [5].

3 Two-Scale Model for Masonry Arches

The generalized constitutive law in Eq. (3), governing the response of the beam cross-section at the macroscale, is derived via a homogenization technique. The adopted procedure is detailed in [5, 15] and is briefly reviewed in the following.

Each quadrature cross-section located along the curved element axis is linked to a masonry Unit Cell made of a single brick (b) and a mortar layer (m). The UC is assumed as representative volume element and is modeled with a plane straight Timoshenko beam model. Setting a Cartesian reference system $(0, x, y)$ for the UC, with x aligned with the tangent axis \mathbf{T} of the structural beam, the generalized cross-section displacement fields at microlevel, $u(x)$, $v(x)$, and $\theta(x)$, are expressed as a function of the macroscopic deformations, $E(S)$, $K(S)$, and $\Gamma(S)$, and unknown periodic fluctuations, $u^*(x)$, $v^*(x)$, and $\theta^*(x)$, satisfying proper periodicity conditions. Accordingly, microscale axial, $\varepsilon_0(x)$, bending, $\kappa(x)$, and shear, $\gamma(x)$, strains are evaluated. The generalized stresses work-conjugate to $\varepsilon_0(x)$, $\kappa(x)$, and $\gamma(x)$, that is $n_{b/m}(x)$, $m_{b/m}(x)$, and $t_{b/m}(x)$, are determined assuming linear elastic constitutive law for bricks and a friction-damage model for mortar. Denoting with E_m and G_m the mortar Young's and shear moduli, with A , I , and A_s the area, inertia, and shear area of the beam cross-section, the following mortar generalized stress-strain relationship is adopted:

$$\begin{aligned} n_m(x) &= E_m A \varepsilon_0(x) - \int_A E_m \pi_\varepsilon(x, y) dA \\ m_m(x) &= E_m I \kappa(x) + \int_A E_m y \pi_\varepsilon(x, y) dA \\ t_m(x) &= G_m A_s \gamma(x) - \int_{A_s} G_m \pi_\gamma(x, y) dA \end{aligned} \quad (14)$$

where $\pi_\varepsilon(x, y) = D(x, y) H[\varepsilon(x, y)] \varepsilon(x, y)$ and $\pi_\gamma(x, y) = D(x, y) \gamma_p(x, y)$ are the normal and shear inelastic strains at a point of the mortar cross-section. These are expressed as a function of the normal strain, $\varepsilon(x, y) = \varepsilon_0(x) - y \kappa(x)$, the shear slip, $\gamma_p(x, y)$, and the damage variable $D(x, y) \in [0 - 1]$. The Heaviside function, $H[\bullet]$, is introduced in the definition of $\pi_\varepsilon(x, y)$ to model the stiffness recovery under cyclic loads. An irreversible evolution law is given for the damage variable ruled by an equivalent strain measure. This couples normal and shear strains, so accounting for mode I and II failure mechanisms, and depends on the fracture energies, G_{cI} and G_{cII} , the peak values of the normal, σ_0 , and shear, τ_0 , stresses. As for the flow of the inelastic slip γ_p , the Coulomb law is adopted, depending on the friction parameter μ . A detailed description is given in [5, 15].

Once the microscale quantities $n_{b/m}(x)$, $m_{b/m}(x)$ and $t_{b/m}(x)$ are evaluated, the upscaling process from micro- to macroscale is performed by computing the resultants $N(S)$, $M(S)$, and $T(S)$ as average components along the UC axis.

4 Dynamic Response of a Segmental Arch

The dynamic response of the segmental masonry arch in Fig. 3 is analyzed. The specimen consists of four rows of 39 brick units ($100 \times 75 \times 50 \text{ mm}^3$) arranged with lime mortar joints, resulting in a nominal span of 1900 mm, a nominal rise of 430 mm, and an out-of-plane width of 430 mm. The arch was experimentally tested in [3] by performing modal testing in the undamaged configuration and considering different damage scenarios. Here, results obtained in the virgin state are compared with those evaluated with the proposed model adopting a mesh of 6 equally spaced FEs, required to properly account for inertia effects, and the mechanical parameters contained in Table 1. Young’s moduli, $E_{b/m}$, Poisson ratios, $\nu_{b/m}$, and mass densities, $\rho_{b/m}$, are set according to [3].

Table 2 compares the experimental frequencies of the first four in-plane modes with their numerical counterpart, evaluated considering the initial undamaged arch

Fig. 3 Geometry and beam idealization of the analyzed arch (dimensions in mm)

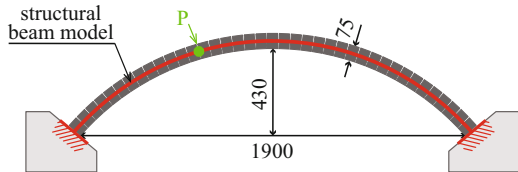


Table 1 Mechanical properties for bricks and mortar

	ρ [kg/m ³]	E [MPa]	ν [-]	σ_0 [MPa]	τ_0 [MPa]	G_{cI} [MPa]	G_{cII} [MPa]	μ [-]
Brick	1653.3	2500	0.2					
Mortar	1750.0	500	0.2	0.04	0.2	1.92E-05	1.15E-03	0.5

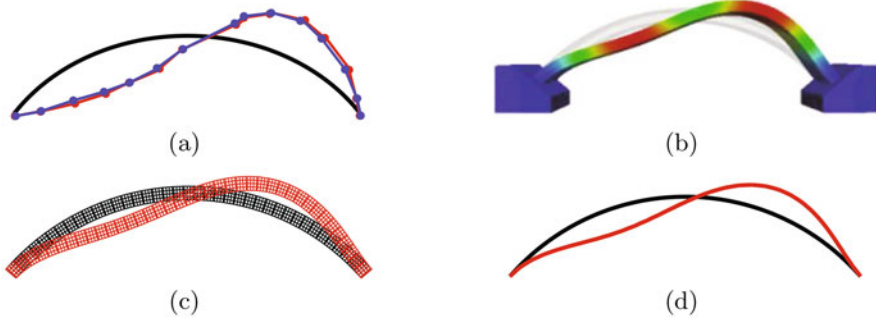


Fig. 4 Mode 1 deformed shape: (a) experimental [3], (b) 3D model [3], (c) 2D model, and (d) proposed beam model

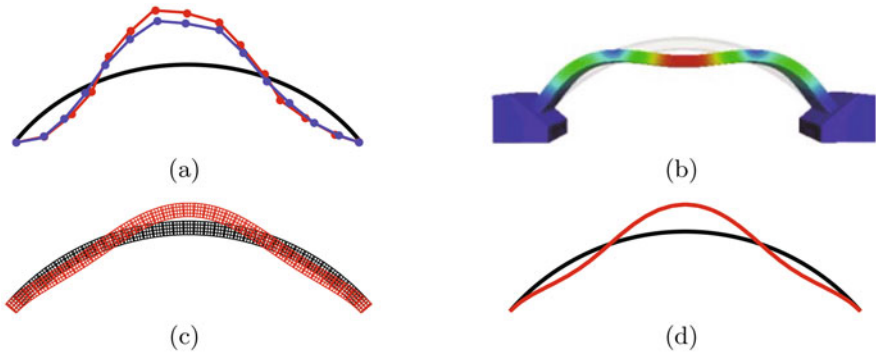


Fig. 5 Mode 2 deformed shape: (a) experimental [3], (b) 3D model [3], (c) 2D model, and (d) proposed beam model

configuration. In addition, two other sets of values are considered: the solution obtained with a 3D FE model reported in [3] and that obtained with a 2D plane stress FE model [16]. Both the 3D and 2D models discretize mortar and bricks separately resorting to a micro-modeling approach. From Table 2, it emerges that the beam eigenfrequencies very well agree with those derived from the micromechanical models and the experimental outcomes. Moreover, the first- and second-mode shapes are satisfactorily matched, as shown in Figs. 4 and 5, respectively. Conversely, for all numerical models, positions of third- and fourth-mode shapes are inverted with respect to the order resulting from the experimental test. This is probably due to slight variations in joint thickness, typical of manually assembled geometry, as also detected in [3].

Response of the arch to the WE acceleration history recorded during the 2009 L'Aquila earthquake is analyzed considering both linear elastic and nonlinear material assumptions. A scale factor of 2 is applied to the natural ground motion, attaining a peak ground acceleration of 6.47 m/s^2 . Rayleigh damping ratio is set equal to 1% [3] on the basis of the first two elastic frequencies. Focusing on the

Table 2 Experimental and numerical initial frequencies f [Hz] of the analyzed arch

	Mode 1	Mode 2	Mode 3	Mode 4
Experimental [3]	37.03	63.56	100.76	125.06
3D model [3]	36.55	65.87	114.34	124.08
2D model	37.81	67.91	118.19	128.09
Beam model	37.41	67.37	119.32	128.72

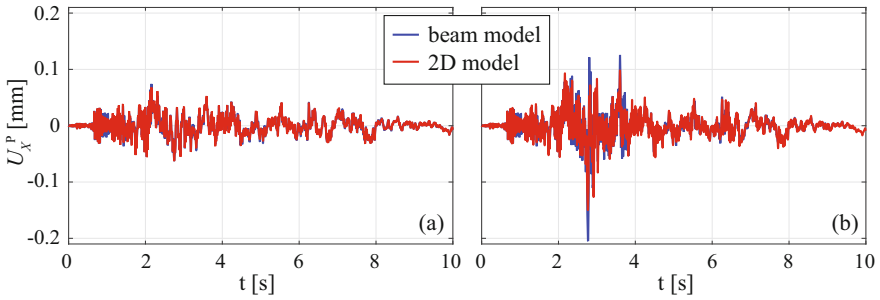


Fig. 6 Time histories of the horizontal relative displacement of point P under scaled L'Aquila earthquake: (a) linear elastic and (b) nonlinear responses

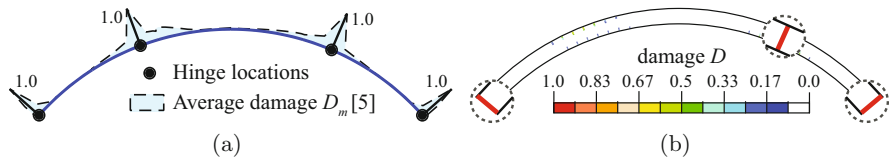


Fig. 7 Damage distribution at the end of the analyses for (a) beam and (b) 2D models

significant part of the response, Fig. 6a,b shows the time evolution of the horizontal relative displacement of point P, located as indicated in Fig. 3. Red lines represent the reference solution obtained with the 2D micromechanical model, whereas the blue curves refer to those evaluated with the proposed multiscale beam. Both models are based on the same constitutive assumptions (Table 1). Fracture energy and nonlocal integral regularizations are employed for beam and 2D formulations, respectively, to overcome pathological mesh dependency. In case of linear elastic constitutive assumption (Fig. 6a), identical responses are obtained. Good agreement also emerges in the nonlinear case (Fig. 6b), as both models predict displacement amplification with respect to the elastic response. This is caused by formation of damaged zones, typically constituting nonlinear hinges, which open and close during the loading history. Damage distribution at the end of the analyses is shown in Fig. 7 for both models, testifying similar hinge locations, although the beam model gives a more severe damage concentration as a consequence of the higher response amplification exhibited by the arch during the loading history (see Fig. 6b).

5 Conclusions

This chapter presented the formulation of a two-scale curved beam FE for nonlinear dynamic analysis of masonry arches. The model is defined according to the force-based approach, and a proper definition of the consistent element mass matrix is introduced. Numerical analysis of a segmental masonry arch showed the model accuracy in predicting the arch eigenfrequencies and its nonlinear response under earthquake excitation. Hence, the model represents an efficient computational tool to analyze large scale structures with low computational cost.

References

1. A. Gaetani, P.B. Lourenço, G. Monti, M. Moroni, Shaking table tests and numerical analyses on a scaled dry-joint arch undergoing windowed sine pulses. *Bull. Earthq. Eng.* **15**(11), 4939–4961 (2017)
2. P. Zampieri, N. Simoncello, C.D. Tetougueni, C. Pellegrino, A review of methods for strengthening of masonry arches with composite materials. *Eng. Struct.* **171**, 154–169 (2018)
3. M.G. Masciotta, D. Pellegrini, M. Girardi, C. Padovani, A. Barontini, P.B. Lourenço, D. Brigante, G. Fabbrocino, Dynamic characterization of progressively damaged segmental masonry arches with one settled support: experimental and numerical analyses. *Fract. Struct. Integr.* **51**, 423–441 (2020)
4. P. Roca, M. Cervera, G. Gariup, L. Pelà, Structural analysis of masonry historical constructions. Classical and advanced approaches. *Arch. Comput. Meth. Eng.* **17**, 299–325 (2010)
5. P. Di Re, D. Addessi, E. Sacco, A multiscale force-based curved beam element for masonry arches. *Comput. Struct.* **208**, 17–31 (2018)
6. C. Gatta, D. Addessi, F. Vestroni, Static and dynamic nonlinear response of masonry walls. *Int. J. Solids Struct.* **155**, 291–303 (2018)
7. E. Sacco, D. Addessi, K. Sab, New trends in mechanics of masonry. *Meccanica* **53**(7), 1565–1569 (2018)
8. A.M. D’Altri, V. Sarhosis, G. Milani, J. Rots, S. Cattari, S. Lagomarsino, E. Sacco, A. Tralli, G. Castellazzi, S. De Miranda, Modeling strategies for the computational analysis of unreinforced masonry structures: review and classification. *Arch. Comput. Methods Eng.* **27**, 1153–1185 (2020)
9. A. Anthoine, Homogenization of periodic masonry: plane stress, generalized plane strain or 3D modelling? *Commun. Numer. Methods Eng.* **13**, 319–326 (1997)
10. T.J. Massart, R.H.J. Peerlings, M.G.D. Geers, An enhanced multi-scale approach for masonry wall computations with localization of damage. *Int. J. Numer. Methods Eng.* **69**(5), 1022–1059 (2007)
11. D. Addessi, C. Gatta, S. Marfia, E. Sacco, Multiscale analysis of in-plane masonry walls accounting for degradation and frictional effects. *Int. J. Multiscale Comp. Eng.* **18**(2), 159–180 (2020)
12. R.M. De Souza, F.C. Filippou, A.M.B. Pereira, G.Y.R. Aranha, Force formulation of a non-prismatic Timoshenko beam finite element for dynamic analysis of frames, in *XXIV Iberian Latin-American Congress in Computational Methods in Engineering* (IEEE, Piscataway, 2003), pp. 789–813
13. Y. Shen, X. Chen, W. Jiang, X. Luo, Spatial force-based non-prismatic beam element for static and dynamic analyses of circular flexure hinges in compliant mechanisms. *Precis Eng.* **38**(2), 311–320 (2014)

14. P. Di Re, D. Addessi, A. Paolone, Mixed beam formulation with cross-section warping for dynamic analysis of thin-walled structures. *Thin-Walled Struct.* **141**, 554–575 (2019) <https://doi.org/10.1016/j.tws.2019.04.014>
15. D. Addessi, E. Sacco, Homogenization of heterogeneous masonry beams. *Meccanica* **53**(7), 1699–1717 (2018)
16. D. Addessi, E. Sacco, A. Paolone, Cosserat model for periodic masonry deduced by nonlinear homogenization. *Eur. J. Mech. A-Solids* **29**(4), 724–737 (2010)

Enriched Vlasov Beam Model for Nonlinear Dynamic Analysis of Thin-Walled Structures



Paolo Di Re, Daniela Addessi, and Cristina Gatta

1 Introduction

Thin-walled elements are widely adopted in standard constructions and often preferred to beams with compact cross-sections, as they are usually characterized by higher strength-to-weight ratios. However, nonlinear dynamic simulation of thin-walled structures is very challenging, as their behavior is strongly affected by multi-axial stress interaction and cross-section warping. Structural models for the analysis of large-scale structures are commonly made by beam finite elements (FE), because of their computational efficiency, and many enhanced formulations that include the effects of warping have been proposed in the last decades [1–3]. Extensive review of the literature is provided in [3, 4]. Additional research efforts have been made in the past 40 years, mainly applied to rotorcraft analysis [5]. However, only in few cases these models were focused on the analysis of large structures under dynamic loading conditions, e.g., [6].

This chapter proposes an enriched three-dimensional Vlasov beam FE model that accounts for torsion and shear cross-section warping under dynamic loading conditions. A displacement-based approach is adopted to define the element formulation, where supplementary degrees of freedom (DOFs) are introduced at the element nodes and used to describe the variation of the cross-section out-of-plane deformations. Some of these DOFs are also used to independently interpolate the cross-section shear strains along the beam axis, instead of the flexural rotations, so that shear locking is prevented [7]. The element governing equations that include inertia effects are derived from a Lagrangian functional, which also permits the derivation of the consistent element mass matrix [8].

P. Di Re (✉) · D. Addessi · C. Gatta

Department of Structural and Geotechnical Engineering, Sapienza University of Rome, Rome, Italy

e-mail: paolo.dire@uniroma1.it; daniela.addessi@uniroma1.it; cristina.gatta@uniroma1.it

Numerical tests on thin-walled structures are conducted to investigate the effect of cross-section warping on the dynamic response. Modal and nonlinear time-history analyses of a L frame are performed, and the influence of warping transmission at the joint is studied. The results obtained with the proposed model are compared with those provided by enhanced beam formulations, where richer warping descriptions are adopted [8, 9], and higher order shell FE models.

2 Beam Finite Element Formulation

In the proposed 3D beam FE formulation, called Enhanced Vlasov Displacement-based Element (EVDE), nine DOFs are introduced at each end node, i and j , that is the six standard translations and rotations, listed in vectors $\mathbf{u}_{i/j}$ and $\boldsymbol{\theta}_{i/j}$, respectively, and three additional DOFs used to represent cross-section warping (Fig. 1). These latter coincide with the end cross-section torsional curvature, $\chi_{xi/j}$, and shear strains, $\gamma_{yi/j}$ and $\gamma_{zi/j}$.

Hence, the nodal displacement vector results as

$$\mathbf{u} = \{u_i \ v_i \ w_i \ \theta_{xi} \ \theta_{yi} \ \theta_{zi} \ u_j \ v_j \ w_j \ \theta_{xj} \ \theta_{yj} \ \theta_{zj} \ \chi_{xi} \ \gamma_{yi} \ \gamma_{zi} \ \chi_{xj} \ \gamma_{yj} \ \gamma_{zj}\}^T \quad (1)$$

A reference basic configuration is introduced to remove the element rigid body motions. Hence, only twelve basic displacements are used to define the element behavior. These are listed in vector \mathbf{v} that results as

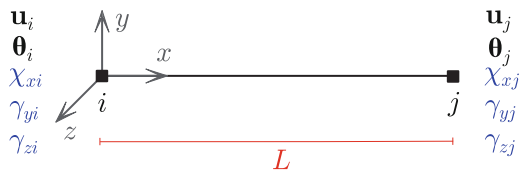
$$\mathbf{v} = \{u_j \ \theta_{zi} \ \theta_{zj} \ \theta_{xj} \ \theta_{yi} \ \theta_{yj} \ \chi_{xi} \ \gamma_{yi} \ \gamma_{zi} \ \chi_{xj} \ \gamma_{yj} \ \gamma_{zj}\}^T = \mathbf{a}_v \mathbf{u} \quad (2)$$

being \mathbf{a}_v the kinematic operator that removes the rigid body motions [4].

2.1 Cross-Section Response and Warping Representation

To account for cross-section warping, the out-of-plane deformations are introduced, yet assuming the cross-section as rigid in its plane. The displacements of the general material point are defined as the sum of the rigid body motions, $\mathbf{u}_r(x, y, z)$, and the warping out-of-plane deformation displacement field, $\mathbf{u}_w(x, y, z)$, i.e.,

Fig. 1 Nodal DOFs depicted in the local reference system



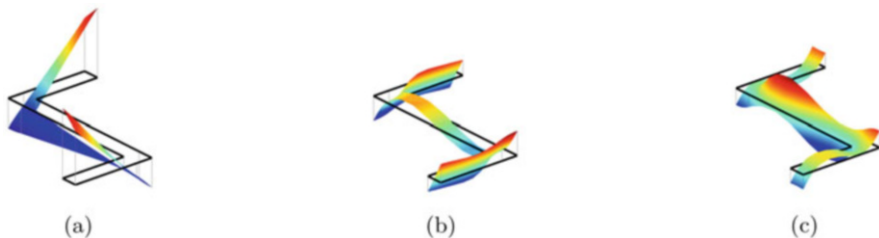


Fig. 2 Warping function shape for a S-shaped cross-section associated to (a) torsion, $M_{\eta_x}(y, z)$, (b) shear along y -axis, $M_{\eta_y}(y, z)$, and (c) shear along z -axis, $M_{\eta_z}(y, z)$

$$\mathbf{u}_m(x, y, z) = \mathbf{u}_r(x, y, z) + \mathbf{u}_w(x, y, z) = \begin{Bmatrix} u_r(x, y, z) \\ v_r(x, y, z) \\ w_r(x, y, z) \end{Bmatrix} + \begin{Bmatrix} u_w(x, y, z) \\ 0 \\ 0 \end{Bmatrix} \quad (3)$$

Vlasov's description of warping is assumed [10], properly enriched to include warping related to shear [11, 12]. Hence, the only non-zero warping field, $u_w(x, y, z)$, is written as the product of assumed warping functions, defined over the cross-section area, and generalized cross-section parameters, defined along the element axis, i.e.,

$$\begin{aligned} u_w(x, y, z) &= \mathbf{M}_\eta(y, z) \boldsymbol{\eta}_s(x) = \\ &= M_{\eta_x}(y, z) \chi_x(x) + M_{\eta_y}(y, z) \gamma_y(x) + M_{\eta_z}(y, z) \gamma_z(x) \end{aligned} \quad (4)$$

Warping functions, listed in row vector $\mathbf{M}_\eta(y, z)$, refer to out-of-plane deformations due to pure torsion and shear along y and z . The numerical procedure proposed in [4] is used for their evaluation, and the orthogonality conditions between $\mathbf{u}_r(x, y, z)$ and $\mathbf{u}_w(x, y, z)$ are satisfied. Figure 2 shows some examples of warping functions for a S-shaped cross-section.

Warping generalized parameters, listed in vector $\boldsymbol{\eta}_s(x)$, provide the amplitude of each component of $u_w(x, y, z)$ associated to each function $\mathbf{M}_\eta(y, z)$ and are assumed to coincide with the cross-section torsional curvature, $\chi_x(x)$, and shear strains, $\gamma_y(x)$ and $\gamma_z(x)$, respectively, according to Vlasov's theory.

Rigid body displacement fields, $\mathbf{u}_r(x, y, z)$, are related to the independent generalized cross-section displacements. These are listed in vector $\mathbf{u}_s(x)$ and are the three translations, $u(x)$, $v(x)$, and $w(x)$, the torsional rotation $\theta_x(x)$, and the two shear strains, $\gamma_y(x)$ and $\gamma_z(x)$, i.e.,

$$\mathbf{u}_s(x) = \{u(x) \ v(x) \ \theta_x(x) \ w(x) \ \gamma_y(x) \ \gamma_z(x)\}^T \quad (5)$$

Indeed, following the approach in [7], shear strains $\gamma_y(x)$ and $\gamma_z(x)$ are assumed as independent cross-section kinematic quantities, instead of the rotations $\theta_z(x)$ and

$\theta_y(x)$, to avoid shear locking. Hence, it results:

$$\mathbf{u}_r(x, y, z) = \boldsymbol{\alpha}(y, z) \mathbf{a}_u(x) \mathbf{u}_s(x) \quad (6)$$

where $\boldsymbol{\alpha}(y, z)$ and $\mathbf{a}_u(x)$ are the kinematic operators [4].

By enforcing the cross-section compatibility conditions, the generalized cross-section strain vector, $\mathbf{e}(x)$, is introduced. This collects the axial strain, $\varepsilon_G(x)$, flexural curvatures, $\chi_z(x)$ and $\chi_y(x)$, torsional curvature, $\chi_x(x)$, shear strains, $\gamma_y(x)$ and $\gamma_z(x)$, and additional warping strains, $\zeta_x(x) = \chi'_x(x)$, $\zeta_y(x) = \gamma'_y(x)$, $\zeta_z(x) = \gamma'_z(x)$, related to warping, i.e.,

$$\mathbf{e}(x) = \left\{ \varepsilon_G(x) \chi_z(x) \gamma_y(x) \chi_x(x) \chi_y(x) \gamma_z(x) \zeta_x(x) \zeta_y(x) \zeta_z(x) \right\}^T \quad (7)$$

where the apex denotes the derivative with respect to x . Thus, by introducing the compatibility differential operator $\mathbf{D}(x)$ [4], it results

$$\mathbf{e}(x) = \mathbf{D}(x) \mathbf{u}_s(x) \quad (8)$$

As null in-plane cross-section deformations are assumed, three strains are considered at the material point, i.e., axial elongation $\varepsilon_{xx}(x, y, z)$ and shear strains, $\gamma_{xy}(x, y, z)$ and $\gamma_{xz}(x, y, z)$. These are collected in vector $\boldsymbol{\varepsilon}_m(x, y, z)$ and expressed as the sum of rigid, $\boldsymbol{\varepsilon}_r(x, y, z)$, and warping strains, $\boldsymbol{\varepsilon}_w(x, y, z)$, as

$$\boldsymbol{\varepsilon}_m(x, y, z) = \boldsymbol{\varepsilon}_r(x, y, z) + \boldsymbol{\varepsilon}_w(x, y, z) = \hat{\boldsymbol{\alpha}}(y, z) \mathbf{e}(x) \quad (9)$$

where $\hat{\boldsymbol{\alpha}}$ indicates the cross-section compatibility operator [4].

Strains, $\boldsymbol{\varepsilon}_m(x, y, z)$, and stresses, $\boldsymbol{\sigma}_m(x, y, z)$, are related by the material constitutive law, and by enforcing the virtual work principle, the generalized section stresses, $\mathbf{s}(x)$, are defined. These result as

$$\begin{aligned} \mathbf{s}(x) &= \left\{ N(x) M_z(x) T_y^P(x) M_x^P(x) M_y(x) T_z^P(x) B_x(x) B_y(x) B_z(x) \right\}^T = \\ &= \int_{A(x)} \hat{\boldsymbol{\alpha}}^T(y, z) \boldsymbol{\sigma}_m(x, y, z) dA \end{aligned} \quad (10)$$

where $A(x)$ is the cross-section area, $N(x)$ is the axial stress, $M_z(x)$ and $M_y(x)$ are the bending moments, and $M_x(x)$ is the torsional moment. $B_x(x)$, $B_y(x)$, and $B_z(x)$ are the bi-moments, work-conjugate to $\zeta_x(x)$, $\zeta_y(x)$, $\zeta_z(x)$ [10, 12, 13], i.e.,

$$B_k(x) = \int_{A(x)} M_{\eta k}(y, z) \sigma_{xx}(x, y, z) dA, \quad \text{with } k = x, y, z \quad (11)$$

while quantities $M_x^P(x)$, $T_y^P(x)$, and $T_z^P(x)$ are the *primary* torsional moment and shear stresses.

2.2 Displacement-Based Approach

Polynomial interpolation is performed to express the variation of the generalized cross-section displacements, $\mathbf{u}_s(x)$, along the element axis. Linear axial displacement, $u(x)$, and shear strains, $\gamma_y(x)$ and $\gamma_z(x)$, are assumed, while cubic interpolation of transverse displacements, $v(x)$ and $w(x)$, and the torsional rotation, $\theta_x(x)$, are defined. It results

$$\mathbf{u}_s(x) = \mathbf{N}(x) \mathbf{v} \quad (12)$$

being $\mathbf{N}(x)$ the shape function matrix containing the polynomial functions with mentioned order [4]. By substituting Eq. (12) into Eq. (8), the relationship between cross-section strains and nodal displacements is derived, resulting as

$$\mathbf{e}(x) = \mathbf{D}(x) \mathbf{N}(x) \mathbf{v} = \mathbf{a}(x) \mathbf{v} \quad (13)$$

where $\mathbf{a}(x) = \mathbf{D}(x) \mathbf{N}(x)$ is the cross-section strain compatibility matrix.

2.3 Element Variational Formulation

The Lagrangian functional, $\mathcal{L} [\mathbf{u}_m(x, y, z), \dot{\mathbf{u}}_m(x, y, z)]$, is introduced to derive the element governing equations. This depends on the displacements, $\mathbf{u}_m(x, y, z)$, and velocities, $\dot{\mathbf{u}}_m(x, y, z)$, and results as the difference between the element kinetic, $T [\dot{\mathbf{u}}_m(x, y, z)]$, and potential energy, $\Pi [\mathbf{u}_m(x, y, z)]$, that is

$$\mathcal{L} [\mathbf{u}_m(x, y, z), \dot{\mathbf{u}}_m(x, y, z)] = T [\dot{\mathbf{u}}_m(x, y, z)] - \Pi [\mathbf{u}_m(x, y, z)] \quad (14)$$

Accounting for Eqs. (2), (9), (12), and (13), the potential energy is written as

$$\Pi = \int_L \mathbf{e}^T(x) \mathbf{s}(x) dx + \Pi_{ext} = \mathbf{u}^T \mathbf{a}_v^T \int_L \mathbf{a}^T(x) \mathbf{s}(x) dx + \Pi_{ext} \quad (15)$$

being Π_{ext} the external load potential. When element rigid body motions are included, Eq. (12) is extended and reads

$$\mathbf{u}_s(x) = \mathbf{N}(x) \mathbf{a}_v \mathbf{u} + \mathbf{N}_r(x) \mathbf{u} \quad (16)$$

where $\mathbf{N}_r(x)$ is the shape function matrix for rigid body displacements. Hence, by considering the nodal contribution, $\mathbf{u}^T \mathbf{p}$, and introducing vector $\mathbf{q}_s(x)$, denoting the distributed loads, the external load potential is expressed as

$$\Pi_{ext} = -\mathbf{u}^T \mathbf{p} - \mathbf{u}^T \mathbf{a}_v^T \int_L \mathbf{N}^T(x) \mathbf{q}_s(x) dx - \mathbf{u}^T \int_L \mathbf{N}_r^T(x) \mathbf{q}_s(x) dx \quad (17)$$

where the first integral corresponds to the element basic forces equivalent to distributed loads, namely \mathbf{q}_q , while the second integral corresponds to $-\mathbf{p}_{rq}$, this vector collecting the basic reaction forces due to distributed loads. The potential energy is finally written as

$$\Pi = \mathbf{u}^T \left\{ \mathbf{a}_v^T \left[\int_L \mathbf{a}^T(x) \mathbf{s}(x) dx - \mathbf{q}_q \right] - \mathbf{p} + \mathbf{p}_{rq} \right\} \quad (18)$$

The kinetic energy depends on the material mass density, $\rho(x, y, z)$, and velocity fields and is written by assuming $\dot{\mathbf{u}}_m(x, y, z)$ as the sum of the orthogonal rigid and warping velocities, $\dot{\mathbf{u}}_r(x, y, z)$ and $\dot{\mathbf{u}}_w(x, y, z)$, as for Eq. (3), i.e.,

$$T = \frac{1}{2} \int_V \rho(x, y, z) \left[\dot{\mathbf{u}}_r^T(x, y, z) \dot{\mathbf{u}}_r(x, y, z) + \dot{\mathbf{u}}_w^T(x, y, z) \dot{\mathbf{u}}_w(x, y, z) \right] dV \quad (19)$$

being V the element volume.

Vector $\dot{\mathbf{u}}_r(x, y, z)$ is related to the cross-section generalized velocities, namely $\dot{\mathbf{u}}_s(x)$, by expression similar to Eq. (6), while $\dot{\mathbf{u}}_w(x, y, z)$ contains as one non-zero component the warping velocity field $\dot{u}_w(x, y, z)$, which is assumed to depend on the generalized warping velocities, $\dot{\eta}_s(x)$, through the same warping functions introduced in Eq. (4). Hence, the kinetic energy is expressed as

$$T = \frac{1}{2} \int_L \dot{\mathbf{u}}_s^T(x) \mathbf{a}_u^T(x) \mathbf{m}_s^r(x) \mathbf{a}_u(x) \dot{\mathbf{u}}_s(x) dx + \frac{1}{2} \int_L \dot{\eta}_s^T(x) \mathbf{m}_s^w(x) \dot{\eta}_s(x) dx \quad (20)$$

where $\mathbf{m}_s^r(x)$ and $\mathbf{m}_s^w(x)$ are the cross-section rigid and warping mass matrices, respectively, resulting as

$$\mathbf{m}_s^r(x) = \int_{A(x)} \boldsymbol{\alpha}^T(y, z) \rho(x, y, z) \boldsymbol{\alpha}(y, z) dA \quad (21)$$

$$\mathbf{m}_s^w(x) = \int_{A(x)} \mathbf{M}_\eta^T(y, z) \rho(x, y, z) \mathbf{M}_\eta(y, z) dA \quad (22)$$

By considering Eqs. (4) and (8), the generalized warping velocities are expressed in terms of $\dot{\mathbf{u}}_s(x)$ as

$$\dot{\eta}_s(x) = \mathbf{a}_\eta(x) \dot{\mathbf{u}}_s(x), \quad \text{with} \quad \mathbf{a}_\eta(x) = \begin{bmatrix} 0 & 0 & \frac{d}{dx} & 0 & 0 & 0 \\ 0 & 0 & 0 & 0 & 1 & 0 \\ 0 & 0 & 0 & 0 & 0 & 1 \end{bmatrix} \quad (23)$$

Similarly to Eq. (16), $\dot{\mathbf{u}}_s(x)$ is related to the nodal velocities, $\dot{\mathbf{u}}$, as follows:

$$\dot{\mathbf{u}}_s(x) = \mathbf{N}(x) \mathbf{a}_v \dot{\mathbf{u}} + \mathbf{N}_r(x) \dot{\mathbf{u}} \quad (24)$$

Hence, the element kinetic energy finally results as

$$T = \frac{1}{2} \dot{\mathbf{u}}^T (\mathbf{m}^r + \mathbf{m}^w) \dot{\mathbf{u}} = \frac{1}{2} \dot{\mathbf{u}}^T \mathbf{m} \dot{\mathbf{u}} \quad (25)$$

where element rigid and warping mass matrices, \mathbf{m}^r and \mathbf{m}^w , are defined as

$$\mathbf{m}^r = \int_L \mathbf{N}_u^T(x) \mathbf{m}_s^r(x) \mathbf{N}_u(x) dx, \quad \mathbf{m}^w = \int_L \mathbf{N}_\eta^T(x) \mathbf{m}_s^w(x) \mathbf{N}_\eta(x) dx \quad (26)$$

being:

$$\mathbf{N}_u(x) = \mathbf{a}_u(x) \mathbf{N}(x) \mathbf{a}_v + \mathbf{a}_u(x) \mathbf{N}_r(x), \quad \mathbf{N}_\eta(x) = \mathbf{a}_\eta(x) \mathbf{N}(x) \mathbf{a}_v \quad (27)$$

and $\mathbf{m} = \mathbf{m}^r + \mathbf{m}^w$ the total element consistent mass matrix.

Equations (18) and (25) permit to express \mathcal{L} in terms of nodal quantities as

$$\mathcal{L}(\dot{\mathbf{u}}, \mathbf{u}) = \frac{1}{2} \dot{\mathbf{u}}^T \mathbf{m} \dot{\mathbf{u}} - \mathbf{u}^T \left\{ \mathbf{a}_v^T \left[\int_L \mathbf{a}^T(x) \mathbf{s}(x) dx - \mathbf{q}_q \right] - \mathbf{p} + \mathbf{p}_{rq} \right\} \quad (28)$$

and derive the element governing equations from the following condition:

$$\frac{d}{dt} \frac{\partial \mathcal{L}(\dot{\mathbf{u}}, \mathbf{u})}{\partial \dot{\mathbf{u}}} - \frac{\partial \mathcal{L}(\dot{\mathbf{u}}, \mathbf{u})}{\partial \mathbf{u}} = \frac{d}{dt} \frac{\partial T(\dot{\mathbf{u}})}{\partial \dot{\mathbf{u}}} + \frac{\partial \Pi(\mathbf{u})}{\partial \mathbf{u}} = \mathbf{0} \quad (29)$$

This gives the element equilibrium equations in the form:

$$\mathbf{m} \ddot{\mathbf{u}} + \mathbf{a}_v^T \left[\int_L \mathbf{a}^T(x) \mathbf{s}(x) dx - \mathbf{q}_q \right] + \mathbf{p}_{rq} = \mathbf{p} \quad (30)$$

When inertia forces are neglected, the element equilibrium equations state that the term in brackets must equal the basic nodal force vector, \mathbf{q} , work-conjugate to \mathbf{v} [4]. Hence, Eq. (30) assumes the following standard form:

$$\mathbf{m} \ddot{\mathbf{u}} + \mathbf{a}_v^T \mathbf{q} + \mathbf{p}_{rq} = \mathbf{p} \quad (31)$$

Notes and Comments Inertia terms associated to warping can produce spurious natural modes with low frequencies that increase computational effort. When cross-sections located at the element ends are free to warp, this likely occurs. Hence, for these cases, it is convenient to neglect term \mathbf{m}^w .

3 Numerical Validation

The dynamic response of the L frame in Fig. 3a is reproduced. The same specimen is analyzed in [13] under static loads. Rigid and warping displacements of ends A and E and displacement along y of the joint C are prevented. Material Young's modulus E_s and Poisson ratio ν_s are assumed as equal to 205000 MPa and 0.3, respectively.

A uniform mesh made of 10 and 14 proposed FEs for beam and column, respectively, is used to model the frame. Moreover, the standard force-based Timoshenko beam with rigid cross-section and the Enhanced Warping Mixed formulation beam Element (EWME) in [8] are used for comparison, adopting same mesh. For the latter, warping is assumed as parabolic along the element, parabolic and cubic along web and flanges, respectively, and linear across the thickness, on the basis of the findings reported in [3, 4, 8]. Same cross-section interpolation is also used to compute warping functions $M_\eta(y, z)$ for the proposed model. A FE model made of 2268 4-node Discrete Kirchhoff Quadrilateral shell element is used to compute the reference solution (see also Fig. 4).

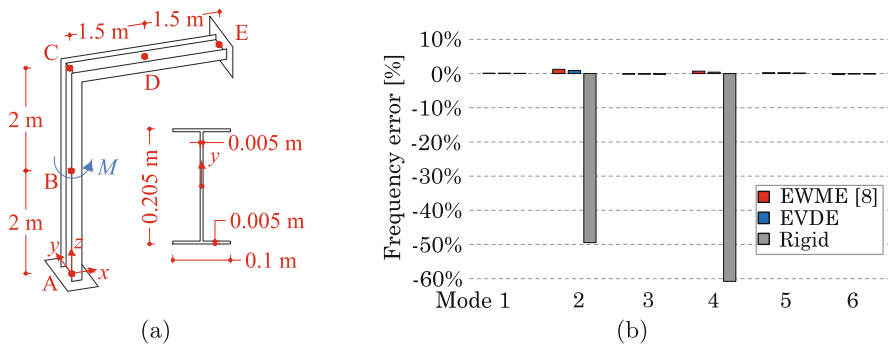


Fig. 3 L portal frame: (a) specimen geometry, (b) circular frequency errors obtained with respect to the shell solution (mode 1: 117.41 rad/s, mode 2: 167.57 rad/s, mode 3: 220.01 rad/s, mode 4: 288.53 rad/s, mode 5: 365.96 rad/s, mode 6: 389.73 rad/s)

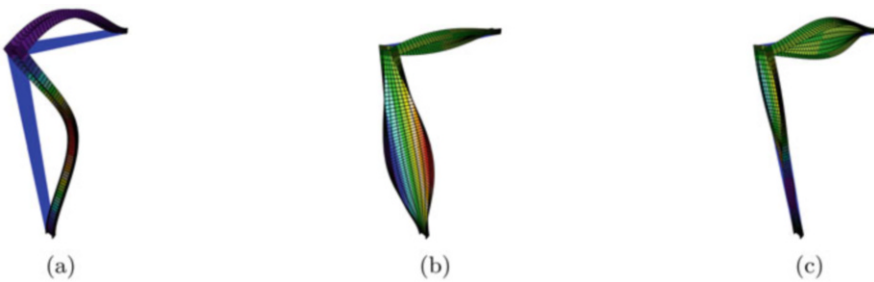


Fig. 4 L portal frame: deformed shape for mode (a) 1, (b) 2, and (c) 4

Figure 3b plots the errors obtained for the first 6 circular frequencies with the beam models with respect to the shell reference solution. The proposed beam and EWME give similar results. These perfectly agree with those obtained from the shell model. By contrast, the standard model based on rigid cross-section assumption provides correct solutions only for bending modes (1, 3, 5, and 6), while incorrect frequencies are given for modes 2 and 4 that involve torsion. Indeed, due to the particular orientation, end cross-sections of the members meeting at the joint undergo equal warping profile. Hence, when column twists, warping of the top cross-section produces warping in the beam, which twists as well. This effect is shown in Fig. 4, where the deformed shapes of mode 1 (bending), 2, and 4 (torsional) obtained with the shell model are depicted. In the proposed beam model, the additional nodal warping DOFs and element connectivity ensure warping continuity between column and beam [4, 8].

Nonlinear time-history analysis of the frame is performed under sinusoidal couple applied at mid-height of the column, assumed to vary according to: $M = \bar{M} \sin \bar{\omega}t$, being $\bar{M} = 1.0 \text{ kNm}$, $\bar{\omega} = 50 \text{ rad/s}$ and t the time variable.

Elasto-plastic material response is assumed, which is described through J2 plasticity model with linear kinematic hardening. $\sigma_y = 150 \text{ MPa}$ and $H_k = 0.01 E_s$ are assumed as yielding stress and hardening modulus, respectively.

Figures 5 and 6 plot the time evolution of the torsional rotation, θ_x , of (a) the mid-height cross-section of the column and (b) the mid-span cross-section of the beam, for linear elastic and elasto-plastic material response, respectively. Shell reference solution is represented with solid green curves. Dashed red and blue curves refer to those obtained with the EWME and proposed model (EVDE), respectively. Finally, dashed black curves indicate the response obtained with the standard beam. This latter does not consider boundary warping restraints and, thus, provides a significantly more flexible response. In addition, this does not account for warping transmission at the joint and, thus, provides null rotations for the beam (horizontal lines at zero in Figs. 5b and 6b). By contrast, EVDE correctly captures the beam torsional deformation and its solution perfectly matches those of the shell and EWME models.

Moreover, the standard beam model does not correctly simulate the evolution of the plastic effects in the material when elasto-plastic behavior is considered (Fig. 6). Due to warping constraints, torsion of the members induces significant shear-lag effects. Hence, at the first loading cycle, axial stress exceeds material yield stress, at both ends and mid-height of the column. Thus, plastic strains arise, affecting the remaining part of the time-history response. As opposed to the beam model formulations accounting for warping, the standard beam model does not capture shear-lag and shows yielding of the material caused by severe torsional shear stresses acting in the cross-section plane.

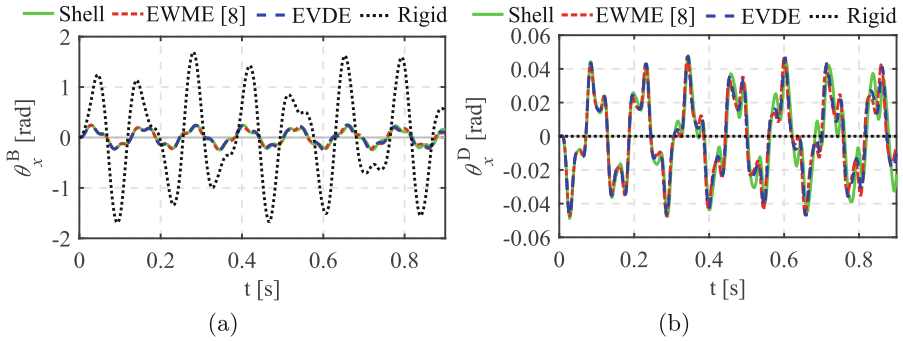


Fig. 5 L portal frame: torsional rotation of (a) mid-height cross-section of the column (point B) and (b) mid-span cross-section of the beam (point D) for linear elastic response

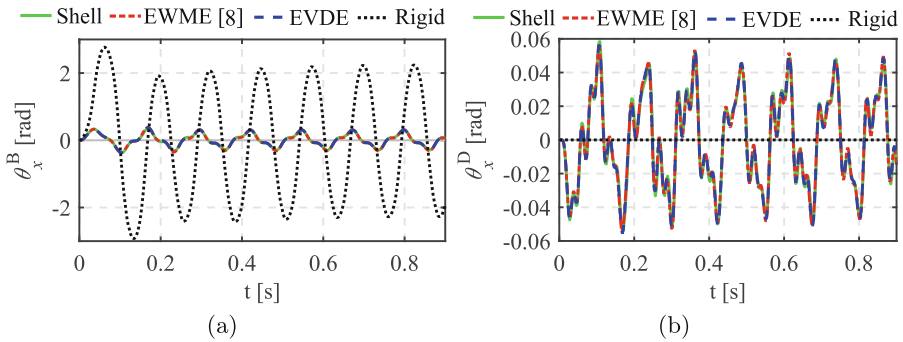


Fig. 6 L portal frame: torsional rotation of (a) mid-height cross-section of the column (point B) and (b) mid-span cross-section of the beam (point D) for nonlinear response

4 Conclusions

This chapter presented the formulation of a three-dimensional beam FE with cross-section warping for the analysis of thin-walled structures under dynamic loadings. The model is defined according to a displacement-based approach and referring to Vlasov’s theory, properly extended to include warping due to shear.

Numerical analysis of an L frame was presented. This showed that, as opposed to standard beam formulations based on rigid cross-section assumption, the proposed FE is highly accurate and is preferable to higher order shell or richer beam models for the analysis of large-scale structures, due to the lower computational cost it requires.

References

1. M. Pignataro, N. Rizzi, G. Ruta, V. Varano, The effects of warping constraints on the buckling of thin-walled structures. *J. Mech. Mater. Struct.* **4**(10), 1711–1727 (2009). <https://doi.org/10.2140/jomms.2009.4.1711>
2. P. Di Re, D. Addessi, A mixed 3D corotational beam with cross-section warping for the analysis of damaging structures under large displacements. *Meccanica* **53**(6), 1313–1332 (2018). <https://doi.org/10.1007/s11012--017-0749-3>
3. P. Di Re, D. Addessi, F.C. Filippou, Mixed 3D beam element with damage plasticity for the analysis of RC members under warping torsion. *J. Struct. Eng. ASCE* **144**(6), 04018064 (2018). [https://doi.org/10.1061/\(ASCE\)ST.1943-541X.0002039](https://doi.org/10.1061/(ASCE)ST.1943-541X.0002039)
4. D. Addessi, P. Di Re, G. Cimarello, Enriched beam finite element models with torsion and shear warping for the analysis of thin-walled structures. *Thin-Walled Struct.* **159**, 107259 (2021). <https://doi.org/10.1016/j.tws.2020.107259>
5. W. Yu, D.H. Hodges, V.V. Volovoi, E.D. Fuchs, A generalized Vlasov theory for composite beams. *Thin Walled Struct.* **43**(9), 1493–1511 (2005)
6. L. Librescu, O. Song, *Thin-Walled Composite Beams: Theory and Application*, vol. 131 (Springer, Berlin, 2006)
7. D. Thomas, J. Wilson, R. Wilson, Timoshenko beam finite elements. *J. Sound Vib.* **31**(3), 315–330 (1973). [https://doi.org/10.1016/S0022-460X\(73\)80276-7](https://doi.org/10.1016/S0022-460X(73)80276-7)
8. P. Di Re, D. Addessi, A. Paolone, Mixed beam formulation with cross-section warping for dynamic analysis of thin-walled structures. *Thin Wall Struct.* **141**, 554–575 (2019). <https://doi.org/10.1016/j.tws.2019.04.014>
9. P. Di Re, E. Lofrano, D. Addessi, A. Paolone, Enhanced beam formulation with cross-section warping under large displacements, in *Lecture Notes in Mechanical Engineering* (Springer, Cham, 2020), pp. 1217–1229. https://doi.org/10.1007/978-3-030-41057-5_99
10. V.Z. Vlasov, *Thin-Walled Elastic Beams* (National Technical Information Service, Springfield, 1984)
11. K. Saadé, B. Espion, G. Warzée, Non-uniform torsional behavior and stability of thin-walled elastic beams with arbitrary cross sections. *Thin Wall Struct.* **42**(6), 857–881 (2004). <https://doi.org/10.1016/j.tws.2003.12.003>
12. R. El Fatmi, Non-uniform warping including the effects of torsion and shear forces. Part I: a general beam theory. *Int. J. Solid Struct.* **44**(18–19), 5912–29 (2007). <https://doi.org/10.1016/j.ijsolstr.2007.02.006>
13. A. Genoese, A. Genoese, A. Bilotta, G. Garcea, A mixed beam model with non-uniform warping derived from the Saint Venant rod. *Comput. Struct.* **121**, 87–98 (2013). <https://doi.org/10.1016/j.compstruc.2013.03.017>

Part III
Computational Nonlinear Dynamics

Nonlinear Modal Analysis Through the Generalization of the Eigenvalue Problem: Applications for Dissipative Dynamics



Nidish Narayanaa Balaji and Matthew R. W. Brake

1 Introduction

The concept of nonlinear modal analysis (NMA) has become a very popular analytical as well as computational tool in the study of nonlinear structural systems. There have been several formulations of a computational procedure for this [1, 2], including time-domain [3] and frequency-domain methods [4]. Quasi-static approaches have also gained popularity in recent years, and this chapter considers such a formulation that is based on earlier work in [5].

Recent efforts by the authors [5] have indicated that a generalization of the constrained minimization of Rayleigh quotients provides an interesting nonlinear modal analysis approach (termed Rayleigh quotient-based NMA (RQNMA)) closely related to some of the other methods above. This chapter considers improvements to this formulation in three areas, namely: (1) modal analysis under dynamical operation; (2) forced response synthesis; and (3) investigation of modal coupling. A 1-dimensional (1D) finite element model of a bar with a frictional end will be used for numerical demonstration.

The rest of this chapter is organized as follows: Sect. 2 provides an overview of the methodologies including RQNMA and the chosen example; Sect. 3 presents results for nonlinear modal analysis, forced response synthesis, and an investigation of a case with modal coupling; and finally, Sect. 4 draws conclusions from the study.

N. N. Balaji (✉) · M. R. W. Brake

Department of Mechanical Engineering, William Marsh Rice University, Houston, TX, USA

e-mail: nb25@rice.edu; brake@rice.edu

2 Methodology

The current section provides an overview of the computational procedures involved in RQNMA and a description of the numerical benchmark that will be used for demonstrations in the rest of this chapter.

2.1 Rayleigh Quotient-Based Nonlinear Modal Analysis

Consider a (discrete, multiple degree-of-freedom) nonlinear dynamic system governed by the equations of motion,

$$\mathbf{M}\ddot{\bar{u}} + \mathbf{C}\dot{\bar{u}} + \mathbf{K}\bar{u} + \bar{f}_{nl}(\bar{u}, \dot{\bar{u}}, \dots) = \bar{f}_{ex}(t)$$

$$\mathbf{M}, \mathbf{C}, \mathbf{K} \in \mathbb{R}^{n \times n} \quad (1)$$

$$t \in \mathbb{R}_+; \bar{u}, \bar{f}_{ex} : \mathbb{R}_+ \rightarrow \mathbb{R}^n; \bar{f}_{nl} : \mathbb{R}^n \times \dots \rightarrow \mathbb{R}^n.$$

Here, n denotes the number of degrees of freedom (DoFs) in the system, and the solution, excitation, and nonlinearity are functions denoted above. The mass matrix (\mathbf{M}) is taken to be symmetric positive definite; the stiffness matrix (\mathbf{K}), symmetric positive semi-definite, and the damping matrix (\mathbf{C}), symmetric.

The definition for the nonlinear modes of this system used in [5] was the extremizing eigenpair of the corresponding eigenvector-dependent nonlinear eigenproblem (NEPv). Mathematically, this can be expressed as an algebraic system representing the first-order optimality conditions of the corresponding Rayleigh quotient extremization problem (constrained potential energy minimization),¹

$$\mathbf{K}\bar{u} + \bar{f}_{nl} - \lambda\mathbf{M}\bar{u} = 0$$

$$\bar{u}^T \mathbf{K}\bar{u} - \bar{u}^T \bar{f}_{nl} - \lambda q^2 = 0. \quad (2)$$

In the above algebraic system of equations, parameterized by the modal amplitude q , the multiplier λ was interpreted as the square of the natural frequency of the nonlinear mode under consideration. This interpretation presents certain difficulties in the applicability of the procedure for problems with even nonlinearities (nonlinear forces unsymmetric about the equilibrium). Furthermore, the relationship to dynamic operation is not very clear, introducing difficulties in the incorporation of nonlinear terms that are fundamentally dynamic such as rate-dependent friction models, etc. Although some preliminary efforts were undertaken in [5, 6], these aspects need to be investigated further.

¹Equation (2) is a restatement of the optimality conditions in [5], with the second equation modified to a form more suitable for numerical implementations.

This chapter explores an alternative interpretation of the multipliers λ , assessing its ramifications using a numerical example. Upon solving Eq. (2) for a range of modal amplitudes $q \in [-Q, Q]$, one obtains parametric relationships $\bar{u}(q)$ and $\lambda(q)$, denoting the deflection shape and multiplier (Rayleigh quotient), respectively. Note that hysteretic nonlinearities, at this stage, are only evaluated *quasi-statically* along the *modal backbone*.² These are interpreted to describe the terms in the equations of motion of the system at the modal level as

$$\ddot{q}(t) + \lambda(q(t))q(t) = 0. \tag{3}$$

This system, by construction, is conservative and does not possess any dissipative characteristics, even though the original system may be dissipative. The interpretation here is that this represents the conservative *part* of the complete system. Since $\lambda(q)$ is known from the above, this equation may be solved using any NMA technique applicable to conservative systems. For example, using a single (cosine-) harmonic expansion, an estimate of the modal natural frequency may be made. Assuming $q(t) = Q \cos(\omega_n(Q)t)$ (with natural frequency $\omega_n(Q)$ depending on the harmonic amplitude of the solution), one obtains

$$\omega_n(Q) = \sqrt{\frac{\mathcal{F}^{(c)}\{\lambda(q(t))q(t)\}}{Q}}, \tag{4}$$

where $\mathcal{F}^{(c)}(\cdot)$ denotes the discrete Fourier cosine transform. $\omega_n(Q)$ represents the *effective* natural frequency of an oscillation of the system that extremizes the nonlinear Rayleigh quotient *at each instant of oscillation*.

The effective mode shape of the nonlinear mode is taken to be the gradient of the solution $\bar{u}(q(t))$ with respect to q averaged over a cycle. This can be computed as the zeroth harmonic (denoted by $\mathcal{F}^{(0)}(\cdot)$) of the gradient,

$$\bar{\phi}(Q) = \mathcal{F}^{(0)} \left\{ \frac{\partial \bar{u}}{\partial q}(Q \cos(\omega_n t)) \right\}. \tag{5}$$

Here, $\omega_n(Q)$ and $\bar{\phi}(Q)$ denote the undamped natural frequency and the mode shape.

The dissipative characteristics of a mode can be estimated by obtaining an effective coefficient describing the non-conservative forces from a time-domain evaluation of the nonlinearities. Following the procedure above, assuming $q(t) = Q \cos(\omega_n t)$ allows for the definition of $\dot{q}(t)$, which can then be used to evaluate the nonlinear force in the modal domain ($f^{(m)}(t)$ below) as

$$\dot{u}(q(t)) = \frac{\partial \bar{u}}{\partial t}(Q \cos(\omega_n t))(-Q\omega_n \sin(\omega_n t)),$$

²Details on hysteretic evaluation are left out for brevity. The interested reader is directed to [5].

$$f^{(m)}(t) = \bar{\phi}^T(Q) \left(\mathbf{K}\bar{u}(q(t)) + \mathbf{C}\dot{\bar{u}}(q(t)) + \bar{f}_{nl}(\bar{u}, \dot{\bar{u}}, \dots) \right). \tag{6}$$

Introducing a damping term in the modal level of the form

$$\ddot{q}(t) + c(Q)\dot{q}(t) + \underbrace{\omega_n^2(Q)}_{\lambda(Q)} q(t) = 0 \tag{7}$$

allows the estimation of the coefficient $c(Q)$ through the sine harmonics of $f^{(m)}$ as

$$c(Q) = \frac{\mathcal{F}^{(s)}\{f^{(m)}(t)\}}{-Q\omega_n(Q)}. \tag{8}$$

This can also be used to estimate a ‘‘modal damping factor’’ given by $\zeta(Q) = c(Q)/(2\omega_n(Q))$, which is a quantity that is often used in system identification and modal testing practice.

The natural frequency ($\omega_n(Q)$), mode shape ($\bar{\phi}(Q)$), and damping coefficient ($c(Q)$) estimated above represent quantities that may be readily employed for systems operating close to the nonlinear resonance corresponding to the considered nonlinear mode. The forced response of the system can be *synthesized* in such regimes using the so-called single-mode theory [7], which will briefly be presented here for completeness. For a complex excitation of the form $\bar{f}_{ex}e^{i\Omega t}$ (with Ω and \bar{f}_{ex} being the excitation frequency and some complex amplitude), the solution is assumed to be of the form, $u(t) = Qe^{i\theta}e^{i\Omega t}$, with θ representing the phase of the response (assumed constant in time). Substituting this into the equations of motion and conducting an inner product with $\bar{\phi}(Q)$ will yield the complex algebraic equation in terms of unknown amplitude Q and phase θ

$$(\lambda(Q) - \Omega^2) + i(c(Q)\Omega) = \frac{\bar{\phi}^H(Q)\bar{F}_{ex}}{Q} e^{-i\theta}. \tag{9}$$

This can be solved analytically to yield,

$$\begin{aligned} \Omega^2 &= (\lambda(Q) - \frac{c^2(Q)}{2}) \pm \sqrt{\frac{c^4(Q)}{4} - \lambda(Q)c^2(Q) + \frac{|\bar{\phi}^H(Q)\bar{F}_{ex}|^2}{Q^2}} \\ \theta &= \text{Arg} \left(\frac{\bar{\phi}^T(Q)\bar{F}_{ex}}{Q} \right) - \tan^{-1} \frac{c(Q)\Omega}{\lambda(Q) - \Omega^2}, \end{aligned} \tag{10}$$

provided Ω is real. Note that $()^H$ indicates the Hermitian transpose in the above.

In the described approach, the requirement of solving a potentially large nonlinear system is only for solving the RQNMA equations (Eq. (2)), and all of the other steps only involve *post-processing* the RQNMA results through interpolation and single-time function evaluations, which are typically several orders of magnitude

faster than nonlinear equation solving. Further, the use of analytical gradients of the solutions of Eq. (2) with respect to q enables one to employ Hermite interpolants, improving accuracy of the post-processing steps.

In order to consider two modes concurrently, the following formulation is proposed (functional dependence on (Q_1, Q_2) is dropped for brevity of notation):

$$\begin{bmatrix} 1 & m_{12} \\ m_{12} & 1 \end{bmatrix} \begin{Bmatrix} \ddot{q}_1 \\ \ddot{q}_2 \end{Bmatrix} + \begin{bmatrix} c_{11} & c_{12} \\ c_{12} & c_{22} \end{bmatrix} \begin{Bmatrix} \dot{q}_1 \\ \dot{q}_2 \end{Bmatrix} + \begin{bmatrix} k_{11} & k_{12} \\ k_{12} & k_{22} \end{bmatrix} \begin{Bmatrix} q_1 \\ q_2 \end{Bmatrix} = \begin{Bmatrix} \bar{\phi}_1^T \bar{f}_{ex} \\ \bar{\phi}_2^T \bar{f}_{ex} \end{Bmatrix}. \quad (11)$$

Since nonlinear modes may not always be expected to be exactly orthogonal to each other, an off-diagonal mass matrix term m_{12} is included in the above (diagonal terms are 1 from definition). The terms $k_{ij}(Q_1, Q_2)$ and $c_{ij}(Q_1, Q_2)$ represent the nonlinear damping and stiffness terms and are assumed to be functions of the harmonic amplitudes of both the modes under consideration. The mode shapes $\bar{\phi}_1(Q_1)$ and $\bar{\phi}_2(Q_2)$ are, however, assumed to only be dependent on the amplitudes of their respective modes.

Given a pair of harmonic amplitudes (Q_1, Q_2) , the solution ansatz $u(t) = \sum_{i=1}^2 Q_i \bar{\phi}_i(Q_i) \cos(\omega_{n,i}(Q_i)t)$ will be used to evaluate the nonlinear forces in the system. Since $\omega_{n,1}/\omega_{n,2}$ need not be a rational fraction, one cannot use a periodic assumption here. Although multi-component Fourier techniques may be employed, they are avoided here since the evaluation of frictional nonlinearities is not very straightforward. Therefore, the nonlinear forces are generated over an *arbitrarily long* period of time (covering several cycles of each mode), and the parameters $c_{ij}(Q_1, Q_2), k_{ij}(Q_1, Q_2)$ are estimated using linear regression (iterations not necessary). Note that $m_{12}(Q_1, Q_2) = \bar{\phi}_1^T(Q_1) \mathbf{M} \bar{\phi}_2(Q_2)$ by definition.

2.2 Benchmark Model Description

The procedures described in Sect. 2.1 will be demonstrated using a nine-noded finite element model of a linear bar with a frictional end as shown in Fig. 1. The governing partial differential equations are

$$\rho A \frac{\partial^2 u}{\partial t^2} + \left(\alpha \frac{\partial u}{\partial t} - \beta \frac{\partial^3 u}{\partial x^2 \partial t} \right) - EA \frac{\partial^2 u}{\partial x^2} = f_{ex}(t) \delta(x - \ell) \quad x \in (0, \ell), \quad (12)$$

where $\delta(x)$ denotes the dirac delta distribution indicating excitation at the end. This is discretized using eight linear finite elements. The last node is connected to the ground using an elastic dry friction element [8] parameterized by the stiffness k_f and slip force μN . Two cases are considered:

1. $k_f = 2.5 \text{ MN m}^{-1}; \mu N = 0.75 \text{ MN}$.
2. $k_f = 6 \text{ MN m}^{-1}; \mu N = 0.75 \text{ MN}$.

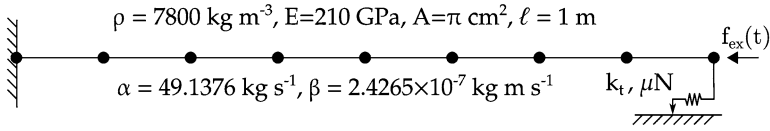


Fig. 1 Bar model

The parameters of case 2 are set in such a way as to highlight mode-coupling effects, whereas such effects are intentionally avoided in case 1.

3 Results

The current section presents the results of the application of the procedures described in Sect. 2.1 to the 1D bar model described above. The nonlinear modal analysis results are compared against frequency-domain references based on the periodic motion concept [4] (EPMC). All frequency-domain computations are conducted using the first five harmonics with harmonic balance.

3.1 Nonlinear Modal Analysis

Figure 2 presents the nonlinear modal characteristics for mode 1 of the system for both the cases. Case 1 (Fig. 2a) is a scenario where a single mode responds in an *isolated manner* around resonance, while case 2 (Fig. 2b) is a scenario where this is not so. A “tongue-like” projection typical of modal coupling in periodic motion backbones can be seen in the EPMC backbone in the boxed region in Fig. 2b. This feature is not captured by the RQNM formulation due to its fundamentally single modal definition.

Figure 3 depicts the frequency characteristics of the first mode and the 1/3rd frequency characteristics of the second mode, indicating a 1:3 internal resonance.

3.2 Synthesis of Frequency Responses

Figure 4 plots the frequency responses for the two cases (simulated using single harmonic forcing with different amplitudes solved using HBM), along with the nonlinear modal backbones from EPMC and RQNM. It can be seen that both the backbones follow the frequency response peaks closely.

The frequency response synthesis formulation in Eq. (10) can be traced back to classical multiple-scale approaches [9] and is presently employed to determine the

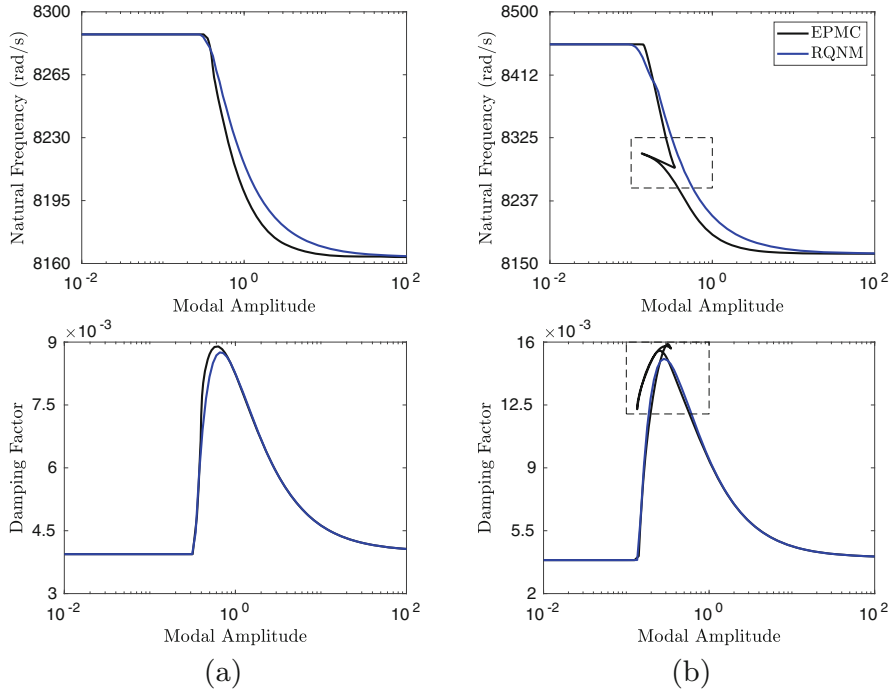


Fig. 2 The nonlinear frequency–amplitude and damping–amplitude relationship for (a) case 1 and (b) case 2. Boxed region(s) in (b) indicates relics of modal-coupling effects

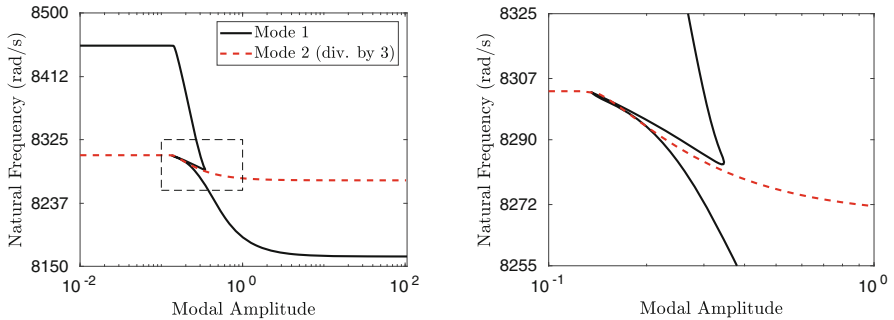


Fig. 3 The EPMC frequency–amplitude plot of mode 1 along with the mode 3 backbone (with frequency divided by 3) with an enlarged version

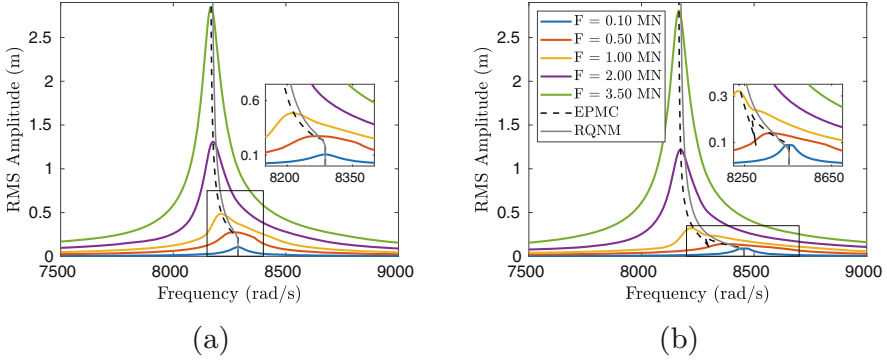


Fig. 4 The frequency response of the system in terms of the RMS displacement amplitude of the forcing node along with the modal backbones for (a) case 1, and (b) case 2

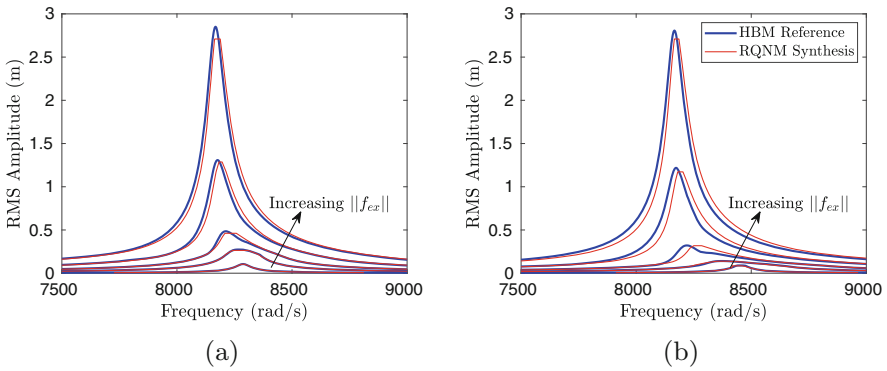


Fig. 5 Synthesis of forced responses: (a) case 1 and (b) case 2. See Fig. 4 for forcing amplitudes

accuracy of the developed reduced equations at the modal level. The accuracy of the synthesized responses can be taken to be indicative of the utility of the underlying nonlinear modal characteristics.

Figure 5 depicts the frequency responses (amplitudes) synthesized using Eq. (10) for the two cases under consideration. Although the synthesized responses follow the references closely, small discrepancies may be seen, especially for case 2. This is thought to be due to the internal resonance noted above.

3.3 Nonlinear Modal Modeling in the Presence of Modal Coupling

The possibility of using a multi-modal nonlinear expansion is explored here. Using harmonic amplitudes Q_1 and Q_2 for modes 1 and 2, respectively, the solution ansatz

that will be used is

$$\bar{u}(t) = \bar{\phi}_1(Q_1)Q_1 \cos(\omega_1(Q)t) + \bar{\phi}_2(Q_2)Q_2 \cos(\omega_2(Q)t). \tag{13}$$

Note that both modes are assumed to have only a cosine harmonic for simplicity. The next task will be to fit the parameters c_{ij} , k_{ij} to the internal forces of the system. As already mentioned, $\bar{u}(t)$ cannot be expected to be periodic for arbitrary Q_1 , Q_2 . Therefore, a time series is generated with $t \in (0, T)$ with an arbitrarily large T . Using this, the internal forces are evaluated and transformed to the *modal* domain to yield modal forces as follows:

$$\begin{aligned} f^{(m,1)}(t) &= \bar{\phi}_1^T(Q_1) (\mathbf{K}\bar{u}(t) + \mathbf{C}\dot{\bar{u}}(t) + \bar{f}_{nl}(t, \bar{u}, \dots)); \\ f^{(m,2)}(t) &= \bar{\phi}_2^T(Q_2) (\mathbf{K}\bar{u}(t) + \mathbf{C}\dot{\bar{u}}(t) + \bar{f}_{nl}(t, \bar{u}, \dots)). \end{aligned} \tag{14}$$

This is fit to parameters c_{ij} , k_{ij} by solving the linear regression problem

$$\begin{bmatrix} q_1(t) & q_2(t) & 0 & \dot{q}_1(t) & \dot{q}_2(t) & 0 \\ \vdots & \vdots & \vdots & \vdots & \vdots & \vdots \\ 0 & q_1(t) & q_2(t) & 0 & \dot{q}_1(t) & \dot{q}_2(t) \\ \vdots & \vdots & \vdots & \vdots & \vdots & \vdots \end{bmatrix} \begin{Bmatrix} k_{11} \\ k_{12} \\ k_{22} \\ c_{11} \\ c_{12} \\ c_{22} \end{Bmatrix} = \begin{bmatrix} f^{(m,1)}(t) \\ \vdots \\ f^{(m,2)}(t) \\ \vdots \end{bmatrix}. \tag{15}$$

Figure 6 depicts an example of the performance of such a fit (2D maps parameterized by Q_1 , Q_2). Note that this approach (along with the cosine assumption in Eq. (13)) is justified only for time-invariant nonlinearities. Some observations that may be made from the parameter estimates are:

- The parameters have non-trivial relationships to the modal amplitudes.
- The non-diagonal modal stiffness terms $k_{1,2}$ (which are zero in linear modal analysis) seem to play an appreciable role in at least some regimes.
- The $c_{2,2}$ damping term even takes negative values in the presence of small mode 2 and intermediate mode 1 amplitudes.

For frequency response synthesis, analytical approaches like in Eq. (10) are not trivial for multi-mode expansions. Therefore, a HBM implementation is developed that interpolates (using linear interpolants) the quantities $k_{ij}(Q_1, Q_2)$, $c_{ij}(Q_1, Q_2)$, $m_{12}(Q_1, Q_2)$, and $\bar{\phi}_i^T(Q_i)\bar{f}_{ex}$ to evaluate the internal forces. Since these quantities are estimated from the above regression over a uniform grid of (Q_1, Q_2) , the interpolation can be carried out in a very fast manner.³

³NLvib [10], an open-source MATLAB nonlinear vibration/continuation package, was used for the numerical continuation in this case.

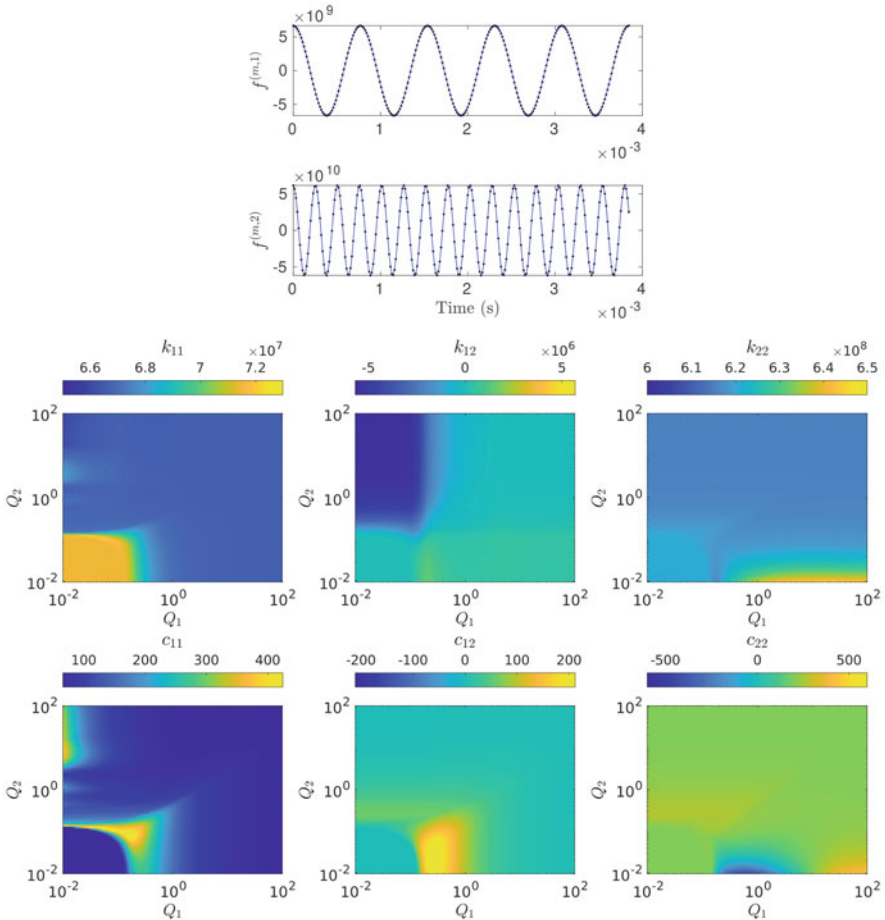


Fig. 6 (a) An example of the fitting procedure (case 1, $(Q_1, Q_2) = (100, 100)$). The dots depict the reference forces, and the continuous lines depict the fitted forces. (b) Parameter fits as functions of Q_1, Q_2 for case 2

Figure 7a, b plots the frequency response of the original system along with the synthesized frequency responses from the single-mode and two-mode expansions, and Fig. 7c, d shows the contributions of the individual modes in the response for the two cases. The two-mode expansion performs much better than the single-mode formulation in predicting the frequency responses, especially toward the higher amplitude regimes. However, the modal interaction features in case 2 are still not captured by this formulation. The reason is possibly due to the fact that such features may not be explained using just a single harmonic formulation. It will therefore be meaningful to explore multi-harmonic implementations of the modal analysis procedure outlined in Sect. 2.1, starting with obtaining multi-

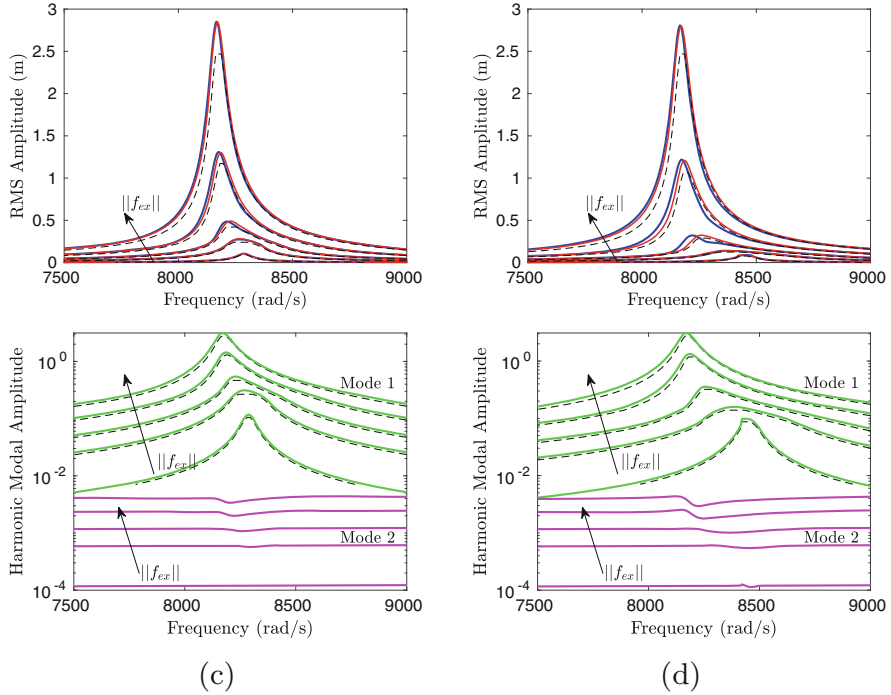


Fig. 7 The reference frequency response of the system (blue solid lines), single-mode synthesis (black dashed lines), and two-mode synthesis (red solid lines) for (a) case 1 and (b) case 2. Also plotted are the harmonic modal amplitudes for mode 1 (green) and mode 2 (magenta) along with the single-mode expansion (black dashed lines) for the two cases in (c), (d), respectively

harmonic mode shapes and/or natural frequency and damping estimates from a multi-harmonic approximation of Eq. (3) (see [7, 11], for instance).

4 Conclusions

An improved formulation of the Rayleigh quotient-based nonlinear modal analysis has been presented and its applicability demonstrated using a numerical benchmark.

Using a numerical multi-degree-of-freedom (MDoF) benchmark, response synthesis using single-mode and two-mode expansions has been compared, showing that the two-mode expansion offers superior overall accuracy. Both techniques, however, fail to detect nonlinear modal interaction/internal resonance phenomena. The results indicate that a multi-harmonic multi-modal expansion could yield better results. Time-domain (transient response) synthesis will require the extension of modal models of the form in Eq. (11), where the nonlinearities are dependent on the

harmonic amplitude and not on the instantaneous amplitude. Results and techniques from classical multiple time-scale approaches [9] are promising for such extensions.

The major advantage with the proposed approach comes from the fact that the computational requirements for large problems are minimized. The only nonlinear algebraic solution operations with sizes as large as the system are necessary in the initial NEPv stage. Further, evaluations of the nonlinear functions (which could be expensive in some cases) are only necessary for the modal model regression, which does not involve any further large nonlinear solutions. Therefore, the construction as well as utilization of the modal models is both relatively very cheap in comparison to evaluation of the full-order model.

References

1. G. Kerschen et al., Nonlinear normal modes, Part I: a useful framework for the structural dynamicist. *Mech. Syst. Signal Proc.* **23**(1), 170–194 (2009). ISSN: 08883270. <https://doi.org/10.1016/j.ymsp.2008.04.002>. <https://linkinghub.elsevier.com/retrieve/pii/S0888327008001015>
2. L. Renson, G. Kerschen, B. Cochelin, Numerical computation of nonlinear normal modes in mechanical engineering. *J. Sound Vib.* **364**, 177–206 (2016). ISSN: 0022460X. <https://doi.org/10.1016/j.jsv.2015.09.033>
3. G. Kerschen, Computation of nonlinear normal modes through shooting and pseudo-arclength computation, in *Modal Analysis of Nonlinear Mechanical Systems*, ed. by G. Kerschen (CISM International Centre for Mechanical Sciences, Vienna: Springer Vienna, 2014), pp. 215–250. ISBN: 978-3-7091-1791-0. https://doi.org/10.1007/978-3-7091-1791-0_5
4. M. Krack, Nonlinear modal analysis of nonconservative systems: extension of the periodic motion concept. *Comput. Struct.* **154**, 59–71 (2015). ISSN: 00457949. <https://doi.org/10.1016/j.compstruc.2015.03.008>. <http://linkinghub.elsevier.com/retrieve/pii/S0045794915000978>
5. N.N. Balaji, M.R.W. Brake, A quasi-static non-linear modal analysis procedure extending Rayleigh quotient stationarity for non-conservative dynamical systems. *Comput. Struct.* **230**, 106184 (2020). ISSN: 00457949. (2020). <https://doi.org/10.1016/j.compstruc.2019.106184>. <https://linkinghub.elsevier.com/retrieve/pii/S0045794919315160>
6. J.H. Porter et al., A quantitative assessment of the model form error of friction models across different interface discretization for jointed structures. *Mech. Syst. Signal Process.* (Under preparation)
7. M. Krack, L. Panning-von Scheidt, J. Wallaschek, A method for nonlinear modal analysis and synthesis: application to harmonically forced and self-excited mechanical systems. *J. Sound Vib.* **332**(25), 6798–6814 (2013). ISSN: 0022460X. <https://doi.org/10.1016/j.jsv.2013.08.009>. <https://linkinghub.elsevier.com/retrieve/pii/S0022460X13006664>
8. C. Siewert et al., Multiharmonic forced response analysis of a turbine blading coupled by nonlinear contact forces. *J. Eng. Gas Turbines Power* **132**(8), 082501 (2010). ISSN: 07424795. <https://doi.org/10.1115/1.4000266>
9. A.H. Nayfeh, D.T. Mook, *Nonlinear Oscillations*. en. Google-Books-ID: sj3ebg7jRaoC. (Wiley, London, 2008). ISBN: 978-3-527-61759-3
10. M. Krack, J. Gross, in *Harmonic Balance for Nonlinear Vibration Problems*. Mathematical Engineering (Springer, Cham, 2019). ISBN: 978-3-030-14022-9 978-3-030-14023-6. <https://doi.org/10.1007/978-3-030-14023-6>. <http://link.springer.com/10.1007/978-3-030-14023-6>
11. C. Joannin et al., A nonlinear component mode synthesis method for the computation of steady-state vibrations in non-conservative systems. *Mech. Syst. Signal Process.* **83**, 75–92 (2017). ISSN: 08883270. <https://doi.org/10.1016/j.ymsp.2016.05.044>

Continuation-Based Design of Self-Contacting Soft Robotic Manipulators



Christopher Marry, Harry Dankowicz, and Girish Krishnan

1 Introduction

Soft robots show great potential in applications requiring unique dexterity due to their ability to deform into complex shapes without the need for bulky and expensive motors as would be required in rigid robots. Soft robots have a higher strength-to-weight ratio than rigid robots of similar size and are also safer for applications involving interactions with humans [1]. On the flip side, soft robots present difficult design challenges: their actuation methods are coupled to their structures, and their static and dynamic deformation behavior is frequently nonlinear. As a consequence, the existing techniques for trajectory planning of rigid robots cannot be used directly for soft robots.

A fiber-reinforced elastomeric enclosure (FREE) [2, 3] is a type of pneumatic soft robotic manipulator that consists of an elastic tube wrapped with stiff fibers that constrain the ways the tube deforms when inflated. Design techniques for creating an initially straight single-segment FREE to match an arbitrary 2D curve when pressurized were presented in [4]. The problem of designing a multisegment FREE that can follow a desired 3D trajectory was considered in [5]. However, the technique presented there allowed for only a restricted class of FREE segment types and did not take gravitational effects into account. A more general technique for designing multisegment FREEs to match arbitrary 3D shapes was considered in Section 3.2 of [6]; their technique did account for gravity but did not consider the intermediate shapes of the manipulator during pressurization. Based on this technique, a design proposed for the task of forming a trefoil knot was found unable to complete the knot without manual intervention because of self-contact

C. Marry (✉) · H. Dankowicz · G. Krishnan
University of Illinois at Urbana-Champaign, Urbana, IL, USA
e-mail: cmarry2@illinois.edu; danko@illinois.edu; gkrishna@illinois.edu

that occurred at an intermediate configuration. A knotting actuator was also designed in [7] using a different pneumatic manipulator morphology that unfurls the manipulator as it is pressurized. However, if the manipulator was fully unfurled before deforming, self-contacts again prevented knotting from being achieved.

The onset of self-contact in slender elastic objects deformed through variations in boundary conditions is a well-known source of complex static equilibrium bifurcations. In [8], numerical continuation was used as a tool to study the equilibrium shapes of an elastic rod as its clamped ends were translated and rotated. It is found that buckling can cause bifurcations in which the rod suddenly forms planar loops. In [9], numerical continuation was used to show that a clamped elastic rod could attain a stable overhand knot configuration without any points of self-contact for narrow ranges of parameter values.

In this chapter, we use numerical continuation to overcome the lack of a design approach for multisegment FREEs that considers intermediate shapes and the potential onset of self-contact. Our approach allows the analysis to track continuous families of shapes under variations in the actuation pressure and other design parameters, while also accounting for the onset and persistence of self-contact. With the help of this tool, we present a preliminary investigation of the deformations of a six-segment manipulator in the presence of gravity under different initial orientations at the clamped end. An intriguing finding of our analysis is the possibility of several co-existing equilibrium configurations at the same actuation pressure, possibly associated with imperfect buckling of the manipulator due to its self-weight.

2 Design Principles

The basic building blocks of the soft robotic manipulators of interest here are elastomeric tubes wrapped with two families of stiff fibers that constrain the possible deformations of the tube during inflation, as represented schematically in Fig. 1a. For example, for fiber angles $\alpha = -\beta$, the tube extends or contracts with axial and radial stretch ratios λ_1 and λ_2 . In contrast, unequal fiber angles $\alpha \neq \beta$ result in an additional rotation about the tube axis by an angle δ , with λ_1 , λ_2 , and δ implicitly parameterized by the fiber angles and inflation pressure [2]. By adding a straight strain-limiting fiber along the length of the tube, the combined extension/contraction and rotation is converted into a helical deformation, as illustrated in Fig. 1b. In this case, $\kappa = (\lambda_1 - 1)/r(\lambda_1 + 1)$ and $\tau = \delta/l$ describe the intrinsic curvature κ and torsion τ of the tube in terms of the undeformed inner tube radius r and tube length l . For a given design, κ and τ are uniquely parameterized by the inflation pressure.

End-to-end concatenation of several helical FREEs creates a polyhelical shape under inflation. For a given number of segments, we may seek optimal choices of fiber angles and segment lengths to achieve a close approximation (in the absence of gravity) to a desired curve at some target pressure. To account for the influence of gravity, the design methodology in [6] introduces an intermediate target curve for

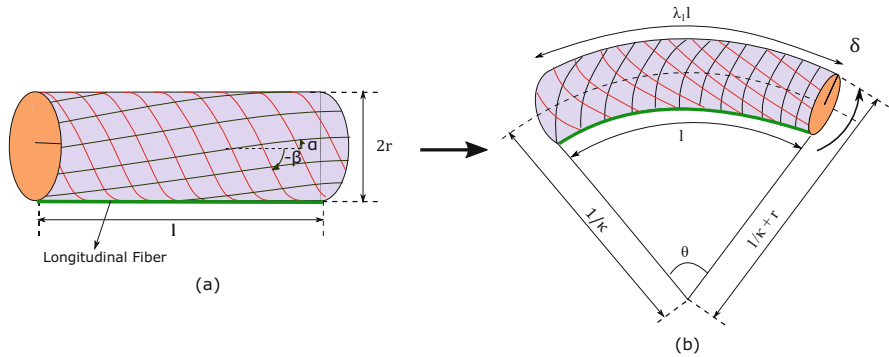


Fig. 1 (a) A FREE with $\alpha \neq \beta$ in an undeformed state. (b) The FREE of (a) under pressurization, which has deformed into a helix

Table 1 Construction parameters for the trefoil knot FREE

Segment	1	2	3	4	5	6
Length (mm)	77	67	82	80	59	69
κ (m^{-1})	5.0	42	17	27	37	9.6
τ (m^{-1})	0	-8.4	13	4.0	-2.4	56
α (deg)	58	74	71	72	74	86
β (deg)	-58	-78	-57	-69	-75	-26

this parameter optimization. This target curve is in turn obtained by solving for an equilibrium shape of an elastic Kirchhoff rod with intrinsic curvature and torsion equal to those of the desired curve, clamped-free boundary conditions with one end clamped to the position and orientation of the desired curve, and with elastic moduli identical to those of the FREEs, under a distributed load equal in magnitude but opposite in direction to gravity [10].

From [6], we obtain an example of such an analysis applied to a six-segment manipulator design and resulting in the parameter values shown in Table 1. Here, the desired curve in the presence of gravity is the trefoil knot with $x(t) = 30 \cos 4t$, $y(t) = 30 \sin 3t$, and $z(t) = 10 \sin 5t$ for $t \in [\pi/2, 3\pi/2]$ (shown in black in Fig. 2) translated, rotated, and shifted so that it starts at the origin, its initial tangent vector points in the negative z direction, and its total arclength is 434 mm. Here, the intermediate target curve, assuming gravity acting in the negative z direction, is closely approximated by the polyhelical curve [11] shown in color in this figure. Consistent with intuition, we see more pronounced deviations between the desired and target curves at arclengths further from the clamped end of the elastic rod.

This analysis is notably ignorant of the intermediate configurations that will result as gravity is successively introduced to the multisegment manipulator with equilibrium shape (in the absence of gravity) given by the polyhelical approximation to the natural curve. Indeed, from inspection of Fig. 2, it is clear that segment 6 must pass through segment 3 in order to achieve the desired shape, in violation of

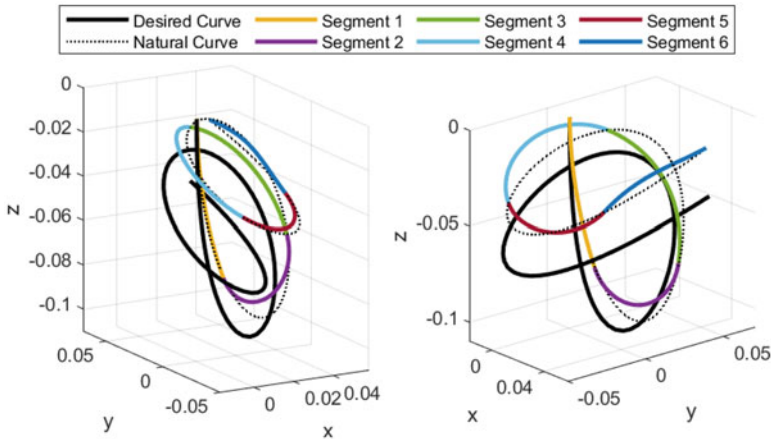


Fig. 2 The desired trefoil knot shape (black), its natural shape (dotted-line), and a 6-segment polyhelix approximant of its natural shape

the physical construction of the manipulator. In fact, as will be shown in Sect. 4, a self-contact also occurs between these segments during inflation from zero pressure in the persistent presence of gravity.

3 Mathematical Formalism

To enable implementation in a parameter continuation context and allow for the detection of self-contact, a multisegment FREE is here modeled as a segmented Kirchhoff rod [12] using an 18-dimensional nonlinear system of ODEs, with arclength as the dependent variable, and suitable segment boundary conditions. On each segment, the 18 states represent the projections of the centerline position vector \mathbf{r} , unit tangent vector \mathbf{t} , unit normal vectors \mathbf{n}_1 and \mathbf{n}_2 , internal force vector \mathbf{f} , and angular velocity vector $\mathbf{u} = \kappa_1 \mathbf{n}_1 + \kappa_2 \mathbf{n}_2 + \tau \mathbf{t}$ onto the axes of the inertial reference frame, such that

$$\mathbf{r}' = \mathbf{t}, \mathbf{t}' = \kappa_2 \mathbf{n}_1 - \kappa_1 \mathbf{n}_2, \mathbf{n}'_1 = -\kappa_2 \mathbf{t} + \tau \mathbf{n}_2, \mathbf{n}'_2 = \kappa_1 \mathbf{t} - \tau \mathbf{n}_1, \tag{1}$$

where $'$ denotes differentiation with respect to the arclength parameter.

Given the discussion in the previous section, we assume that each FREE segment has a intrinsic curvature vector $\mathbf{u}_0(p) := \kappa_{1,0}(p)\mathbf{n} + \tau_0(p)\mathbf{t}$, implicitly parameterized by the inflation pressure p and such that $\mathbf{u}_0(0) = \mathbf{0}$. The actual curvature vector \mathbf{u} is distinct from the intrinsic curvature vector \mathbf{u}_0 , as it also depends on gravitational and other external forces. The deviation $\tilde{\mathbf{u}} := \mathbf{u} - \mathbf{u}_0$ induces internal bending moments \mathbf{m} modeled here by the constitutive law

$$\mathbf{m} = EI (\tilde{\kappa}_1 \mathbf{n}_1 + \kappa_2 \mathbf{n}_2) + GJ \tilde{\tau} \mathbf{t}, \quad \tilde{\kappa}_1 = \kappa_1 - \kappa_{1,0}(p), \quad \tilde{\tau} = \tau - \tau_0(p) \quad (2)$$

in terms of the bending and shear material stiffnesses EI and GJ . Assuming material homogeneity, we obtain

$$\mathbf{m}' = EI (\kappa'_1 \mathbf{n}_1 + \kappa'_2 \mathbf{n}_2) + GJ \tau' \mathbf{t} + \mathbf{u} \times \mathbf{m}. \quad (3)$$

Static force and moment balance now yield

$$\mathbf{0} = \mathbf{f}' + \rho g \mathbf{e}_3, \quad \mathbf{0} = \mathbf{m}' + \mathbf{r}' \times \mathbf{f} = \mathbf{m}' + \mathbf{t} \times \mathbf{f}, \quad (4)$$

where g is the gravitational constant, ρ is the actuator density per unit length, and \mathbf{e}_3 is the direction of gravity. It follows that

$$\kappa'_1 = \frac{\mathbf{f} \bullet \mathbf{n}_2 - \mathbf{n}_1 \bullet (\mathbf{u} \times \mathbf{m})}{EI}, \quad \kappa'_2 = -\frac{\mathbf{f} \bullet \mathbf{n}_1 + \mathbf{n}_2 \bullet (\mathbf{u} \times \mathbf{m})}{EI}, \quad (5)$$

and

$$\tau' = -\frac{\mathbf{t} \bullet (\mathbf{u} \times \mathbf{m})}{GJ}. \quad (6)$$

Equations (1), (5), (6), and the first half of (4) govern the arclength dependence of the state variables for equilibrium configurations actuated by an inflation pressure and under the influence of gravity. Fast changes in the actuation pressure would require consideration of inertial effects, which are outside the scope of this chapter.

For a single-segment rod of length L , we supplement the governing differential equations with clamped-free boundary conditions, prescribing $\mathbf{r}(0)$, $\mathbf{t}(0)$, $\mathbf{n}_1(0)$, and $\mathbf{n}_2(0)$, and letting $\kappa_1(L) = \kappa_{1,0}(p)$, $\kappa_2(L) = 0$, $\tau(L) = \tau_0(p)$, and $\mathbf{f}(L) = \mathbf{0}$. For a multisegment model and in the absence of self-contact, we assume continuity of the position vector \mathbf{r} , frame vectors \mathbf{t} , \mathbf{n}_1 , and \mathbf{n}_2 , force vector \mathbf{f} , and deviation $\tilde{\mathbf{u}}$ across all internal boundaries.

In the presence of self-contact, we further segment our rod model so that the contact points remain at internal boundaries between two segments. In this case, we impose the additional boundary conditions

$$(\mathbf{r}_i(s_i) - \mathbf{r}_j(s_j)) \bullet \mathbf{t}_i(s_i) = (\mathbf{r}_i(s_i) - \mathbf{r}_j(s_j)) \bullet \mathbf{t}_j(s_j) = 0, \quad (7)$$

which ensures that the contact direction is perpendicular to the tangent direction at both contact points, parameterized by the to-be-determined arclengths s_i and s_j . We continue to assume continuity of \mathbf{r} , \mathbf{t} , \mathbf{n}_1 , \mathbf{n}_2 , and $\tilde{\mathbf{u}}$ across such boundaries but impose the jump conditions

$$\mathbf{f}_i(s_{i+}) = \mathbf{f}_i(s_{i+}) + \frac{\Delta \mathbf{f}}{D} (\mathbf{r}_i(s_i) - \mathbf{r}_j(s_j)), \quad (8)$$

$$\mathbf{f}_j(s_{j-}) = \mathbf{f}_j(s_{j+}) - \frac{\Delta f}{D} (\mathbf{r}_i(s_i) - \mathbf{r}_j(s_j)), \quad (9)$$

where the $+$ and $-$ subscripts refer to arclengths immediately before and after the self-contact. Here, D denotes the rod diameter and Δf is a to-be-determined normal contact force that is solved for as part of the overall boundary-value problem. Contact is maintained during the analysis as long as the force Δf remains positive. When Δf becomes zero, the contacting points are no longer being pushed together, and the force discontinuity and associated segmentation can be removed from the formulation.

Detection of the onset of self-contact during continuation (for example, during inflation) is handled through the monitoring of the relative positions of some discretized set of points along the manipulator. Self-contact occurs whenever two points on the i th and j th segments at overall arclengths s_i and s_j satisfy the condition $|\mathbf{r}_i(s_i) - \mathbf{r}_j(s_j)| - D = 0$. Unfortunately, neither the segments i and j nor the arclengths s_i and s_j are known a priori. In practice, we thus choose to monitor the minimum Euclidean distance between any two pairs of discretized points whose difference in arclength is greater than D . Once this minimum distance reaches D , approximate self-contact has been found, and the formulation required to handle sustained self-contact may be imposed.

4 Results and Discussion

We proceed to implement the multisegment boundary-value problem described in the previous section in the numerical continuation package COCO [13]. The differential equations are here discretized using orthogonal collocation with a uniform arclength mesh on each segment and interpolation using continuous, piecewise-polynomial interpolants. For the results reported below, we use 20 intervals per segment and polynomials of degree 4. The material properties used for all segments were $E = 1.8$ MPa, $G = 0.6$ MPa, and $D = 12.7$ mm.

4.1 Self-Contact

In the first example, illustrated in Fig. 3, continuation starts with the pressure set to 0, and the actuator hanging straight down, pointing in the direction of gravity. The panels of the figure show the manipulator shape at various intermediate pressures, as well as at the onset of the first and second self-contacts. As anticipated, the first self-contact occurs between segments 3 and 6 at approximately $p = 46.6$ psi. Another self-contact occurs between segments 1 and 4 at approximately $p = 47.2$ psi, at which pressure we chose to terminate continuation. Notably, both self-contacting

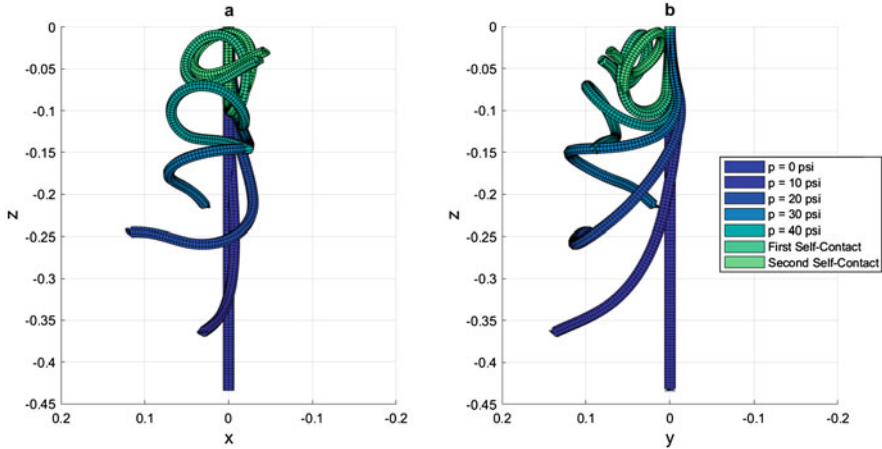


Fig. 3 Configuration of a FREE at various pressure values. The first self-contact occurs at approximately 46.6 psi, and the second at 47.2 psi

configurations are unknotted; in other words, if the ends were to be pulled in opposite directions, the manipulator would return to a straight configuration.

4.2 Buckling

The proposed methodology also allows for configurations to be tracked as other parameters are varied. For instance, if the initial orientation of the same manipulator as in Fig. 3 is quasi-statically inverted by rotation about the y-axis, followed by the pressurization of the manipulator, followed by a quasi-static rotation about the x-axis to a horizontal orientation, a qualitatively different configuration can be reached, as shown in Fig. 4. Notably, in this case, the free end of the manipulator has encircled its clamped base. No such encirclement occurred in Fig. 3. Here, inverting the manipulator causes it to buckle, and drastically increasing its curvature before pressurization is initiated. In this example, the buckling caused a positive curvature to be induced in the manipulator. However, if the initial rotation about the y-axis were to occur in the opposite direction, a negative curvature would have been induced, and subsequent pressurization would have resulted in a different configuration (remember that the FREE design induces a preferred helicity that breaks the rotational symmetry).

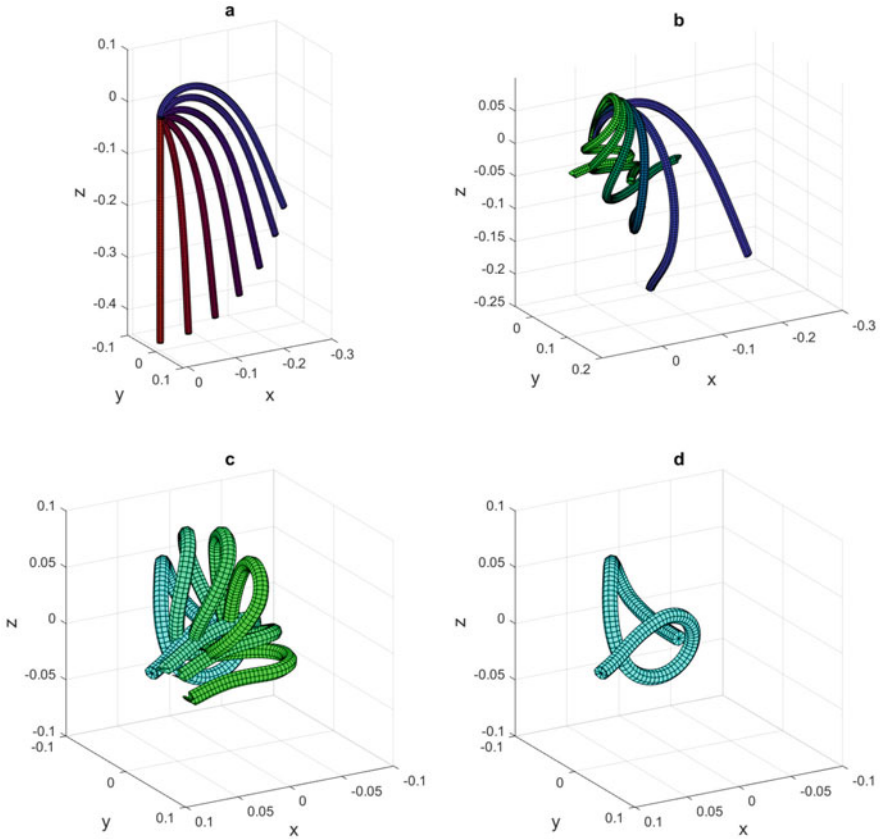


Fig. 4 A multi-step control sequence for a trefoil knot FREE. In **(a)**, gradient from red to blue shows rotation about the y-axis to an inverted orientation. Then in **(b)**, the gradient from blue to green shows the FREE being pressurized from 0 to 50 psi. In **(c)**, the green to cyan gradient shows the rotation about the x-axis to 90° , encountering a self-contact at 118° and again at 90° . **(d)** shows the configuration of the FREE at the onset of the second self-contact.

4.3 Co-existing Solutions

Finally, we consider the possibility of qualitative changes to the static bifurcation structure under variations in other design parameters. As an example, Fig. 5 shows one-parameter families of manipulator shapes, represented by the total twist of the curve, under variations in the inflation pressure and for different material densities (all other parameters are equal to those in Table 1). As seen in the figure, multiple equilibrium configurations co-exist in certain ranges of inflation pressures. Indeed, as the density is increased, the range of pressure values for which multiple solutions exist increases. Closer examination of the manipulator shape near these pressures

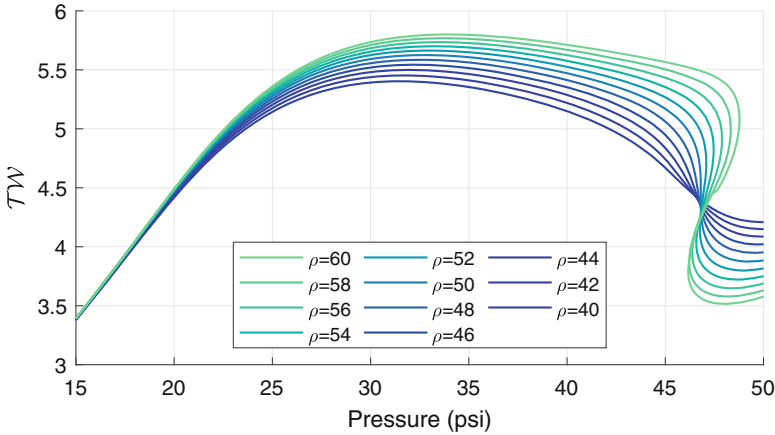


Fig. 5 Variations in pressure and twist (the integral of torsion with respect to arclength) along families of equilibrium shapes for different values of the density ρ . Geometric folds bound ranges of pressures in which three equilibrium configurations coexist

shows the part of the rod is nearly vertical, suggesting that the fold bifurcations seen here are examples of imperfect buckling bifurcations.

5 Concluding Discussion

This chapter presented a continuation-based design tool that allows for the computation of intermediate shapes of a multisegment fiber-reinforced elastomeric enclosure during inflation. Unlike other design methodologies, this tool is able to address the onset of self-contact and can continue to track configurational changes of the manipulator under further variations in pressure with sustained self-contact until such a time that contact is lost. The computational framework is generic enough to be used for other soft robotic actuators whose deformation is characterized by intrinsic curvatures that vary based on some actuated quantity. The tool also allows for a configuration to be studied in different loading scenarios, such as by reorienting the base. Indeed, by using both the actuation pressure and base orientation, the design space is extended to configurations that cannot be reached by solely controlling the pressure.

Among the results of particular interest is the existence of manipulator designs that exhibit multiple co-existing equilibrium configurations over ranges of pressure values bounded by geometric folds. At the extremes of these ranges, we anticipate that small changes in actuation pressure may result in large changes in the manipulator configuration. Designs that leverage such behavior could be utilized to make actuators that can rapidly deform when a critical pressure is reached, similar to those actuators studied in [14]. We anticipate that this bifurcation

structure is associated with non-symmetric buckling phenomena along portions of the manipulator. By analogy with other mechanical systems, we expect that intermediate branches of equilibrium configurations are unstable to perturbations. Future work will investigate the conditions for the existence of multiple solutions to the manipulator configuration, as well as control strategies (e.g., inspired by the control-based continuation paradigm) to attain such dynamically unstable shapes that could not be reached through the standard strategy of monotonically increasing the pressure.

The forward dynamics of FREE-based manipulator designs remains beyond the scope of this work and the parameter continuation framework, except for special choices of temporal boundary conditions, like periodic orbits. It is clear that intermittency of self-contact in such problems allows for highly complex behaviors.

References

1. D. Rus, M.T. Tolley, *Nature* **521**(7553), 467 (2015)
2. G. Singh, G. Krishnan, *Smart Mater. Struct.* **26**(6) (2017)
3. G. Krishnan, J. Bishop-Moser, C. Kim, S. Kota, *J. Mech. Robot.* **7**(4) (2015)
4. G. Singh, G. Krishnan, *Soft Robot.* **7**(1), 109 (2020)
5. F. Connolly, C. Walsh, K. Bertoldi, *Proc. Nat. Acad. Sci. U.S.A.* **114**(1), 51 (2017)
6. G. Singh, Modeling and design of fiber reinforced pneumatic actuators for soft robotics applications. Ph.D. thesis (2019)
7. L.H. Blumenschein, M. Koehler, N.S. Usevitch, E.W. Hawkes, D. Caleb Rucker, A.M. Okamura (2020). arXiv e-prints arXiv:2006.06117
8. G. Van der Heijden, S. Neukirch, V. Goss, J. Thompson, *Int. J. Mech. Sci.* **45**(1), 161 (2003)
9. D. Moulton, P. Grandgeorge, S. Neukirch, *J. Mech. Phys. Solids* **116**, 33 (2018)
10. F. Bertails-Descoubes, A. Derouet-Jourdan, V. Romero, A. Lazarus, *Proc. R. Soc. A Math. Phys. Eng. Sci.* **474**(2212) (2018)
11. A. Goriely, S. Neukirch, A. Hausrath, *Int. J. Bioinform. Res. Appl.* **5**(2), 118 (2009)
12. D.C. Rucker, R.J. Webster, G.S. Chirikjian, N.J. Cowan, *Int. J. Robot. Res.* **29**(10), 1263 (2010)
13. H. Dankowicz, F. Schilder, in *Recipes for Continuation*. Computational Science & Engineering, vol. 11 (Society for Industrial and Applied Mathematics (SIAM), Philadelphia, 2013)
14. J. Overvelde, T. Kloek, J. D'Haen, K. Bertoldi, *Proc. Nat. Acad. Sci. U.S.A.* **112**(35), 10863 (2015)

Bayesian Local Surrogate Models for the Control-Based Continuation of Multiple-Timescale Systems



Mark Blyth, Lucia Marucci, and Ludovic Renson

1 Introduction

Numerical continuation is an algorithm for exploring the bifurcation structure of a model. Numerical analysis allows one to learn about systems that would be excessively challenging to investigate analytically. Nevertheless, continuation tools are limited to cases where an easily evaluable model is available. Often, appropriate models are not available, for example in the climate sciences, where model evaluation is prohibitively slow; in agent-based modelling, where the dynamics cannot easily be reduced to a set of differential equations; or in experimental cases, where no model exists. Control-based continuation (CBC) is a method for defining continuation problems without the need for a model [1, 2]. It allows the experimenter to conduct a bifurcation analysis on black-box and physical systems and to determine the stability of dynamical features [3].

CBC has been used successfully to track equilibria and limit cycles in a range of physical systems, including a nonlinear energy harvester [4] and a multi-degree-of-freedom system with harmonically coupled modes [5], as well as to track fold bifurcations and backbone curves [6]. CBC is yet to be applied to problems such

M. Blyth
University of Bristol, Bristol, UK
e-mail: m.blyth@bristol.ac.uk

L. Marucci
University of Bristol, Bristol, UK

BrisSynBio, Bristol, UK
e-mail: lucia.marucci@bristol.ac.uk

L. Renson (✉)
Imperial College London, London, UK
e-mail: l.renson@imperial.ac.uk

as multiple-timescale oscillators, where the dynamics are strongly nonlinear, or chemical and biological systems, where measurements are subject to substantial noise. Here, we describe how surrogate regression models can be used to assist with the control-based continuation of such systems. We pay particular attention to multiple-timescale systems, as they are difficult to handle with currently available CBC methods.

Surrogate modelling is a technique whereby “real” data, such as experimental observations or simulation results, are replaced with closed-form models that approximate the data of interest. These surrogate models can be analysed in place of the original data, allowing the experimenter to shift computation away from an experiment and onto a computer. Uses of surrogates include the efficient emulation of computationally costly models [7] and performing hypothesis tests on physical systems [8, 9]. Surrogate modelling has seen some use in control-based continuation. A discretisation is a surrogate model of a signal, which allows the experimenter to perform calculations on finite-dimensional vectors instead of continuous functions. Furthermore, there exists a CBC method whereby Gaussian process regression is used to produce a local model of the bifurcation manifold of a system [10]. Standard numerical continuation procedures are used on this model, to numerically continue a fold bifurcation.

This chapter is structured as follows. Sections 1.1 and 1.2 introduce control-based continuation and motivate the uses of surrogate models within CBC. Next, Sect. 2 presents two different classes of surrogate models. Their performances are compared on synthetic data in Sect. 3. Section 4 concludes the work.

1.1 *Control-Based Continuation*

CBC defines a zero problem suitable for continuation, without the need for a model. It relies on finding and tracking noninvasive control targets—a control target that, when paired with a suitable controller, stabilises the limit cycles and equilibria of a system without changing their positions or existence. A continuation procedure is applied to the noninvasive targets, to track dynamical features across parameter values. CBC provides a method for finding noninvasive control, an algorithm for continuing the noninvasive targets, and a guarantee that the results represent the uncontrolled system dynamics.

The continuation scheme uses standard methods to solve for noninvasive control. Numerical solvers are not applied directly to the periodic signals, as the control input and system output are continuous functions. Instead, the signals are discretised. Fourier discretisation is used in all existing CBC applications. Here, the periodic signals are represented by the coefficients of their truncated Fourier series. Fourier discretisation works well for the systems that have currently been studied with CBC, as the output signals contain little noise or high-frequency energy. However, it becomes challenging to apply to signals with slowly decaying Fourier coefficients,

as the discretisation ceases to be noise-robust. We propose surrogate modelling as a method to help overcome this loss of robustness.

1.2 The Need for Surrogate Modelling

Fourier basis functions have global support. For an arbitrarily long signal, they will therefore average out any observation noise. In practice, signals are of finite, often short time duration, and may not be perfectly periodic as a result of stochastic effects. This greatly diminishes the noise-averaging capabilities of Fourier series and is further exacerbated when the signal contains large amounts of higher-frequency energy, as is typical with multiple-timescale systems. Numerical experiments indicate that on such signals, small numbers of harmonics cannot model the signal, and larger numbers will overfit the data, capturing both signal and noise. An example of this is shown in Fig. 1, where a truncated Fourier series of 60 harmonics is fitted to a signal, with and without noise. 60 harmonics is chosen as being the smallest number to provide a subjectively good fit; the noise-averaging ability decreases with the addition of more harmonics, so it is desirable to keep this number small. The Fourier model is seen to fit the noise-free signal to a reasonable degree of accuracy, albeit with some error close to the spikes. Nevertheless, when the signal becomes noise-corrupted, the Fourier model fails to average out the noise.

Simple low-pass filtering methods are undesirable for noise removal, as they do not discriminate between noise and signal, and as a result will remove valuable high-frequency information. This information is of great importance with slow-fast systems, as it captures the sporadic, rapid changes in the output. We propose a surrogate-based method, whereby recorded signals are replaced with a regression model chosen to represent the underlying, noise-free signal. The models retain

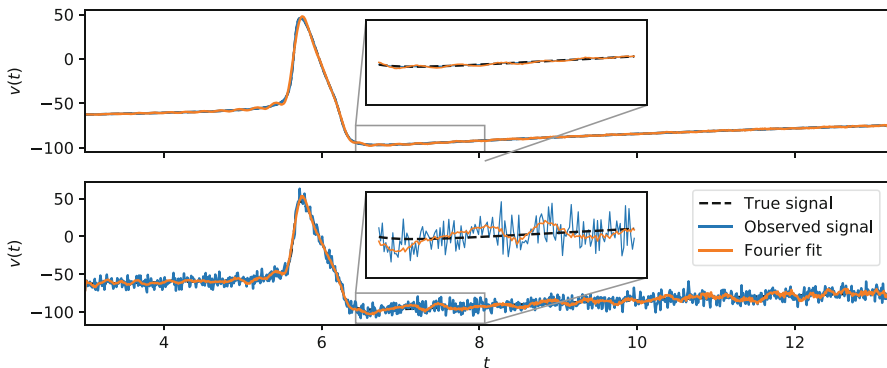


Fig. 1 Truncated Fourier series fitted to a clean (top) and a noisy (bottom) signal, obtained from the simulation of a Hodgkin–Huxley neuron. The Fourier series is observed as failing to properly average out observation noise

information about the high-frequency components of a signal whilst removing noise. Surrogates are chosen for their ability to separate the latent signal from the observation noise as accurately as possible, and therefore to faithfully reconstruct the true noise-free system output. The surrogate can then be analysed in place of the original data, to produce a more accurate discretisation of the signal.

A well-chosen surrogate gives a standalone, closed-form model that accurately describes the signal of interest and can be analysed as if it were an explicit system solution. Besides adaptive filtering, surrogates also allow one to correct issues with the recorded data. Provided the regressors faithfully represent the experimental recordings, they allow the resampling of measurements, which can both facilitate efficient numerical algorithms and simplify the initialisation of continuation methods. For example, when applying CBC to oscillatory systems where the signal period is not known a priori, one may choose to either define a phase-locked control target [11] or extract the period as an additional continuation parameter. In the latter case, it is necessary to determine the period of the signals used to initialise the continuation procedure. A typical estimation approach uses the zeros of the signal autocorrelation function [12]. This relies on uniform sampling intervals, which can be obtained by resampling from the surrogate model in cases where data points are missing or unevenly distributed.

Instead of a regressor, one may choose to use a physics-based surrogate model, the parameters of which are fitted during an experiment. This has the advantage of allowing the experimenter to incorporate prior physical knowledge into the continuation procedure. Nevertheless, accurate results would require the surrogate to capture the main physics of the system, which becomes challenging when studying non-trivial dynamics. In such cases, a regression-based surrogate or the standard model-free approaches are preferable.

Note that while CBC does not necessarily require a model of the system dynamics, it does require a model of the system output. This model defines the signal discretisation and specifies how to convert from a discretisation into a control target. Existing CBC methods use a truncated Fourier series; the Fourier series is therefore a surrogate, as well as a discretisation. An implicit assumption of control-based continuation is that the discretising model accurately represents the signal in question; however, this assumption is not generally tested. The use of novel surrogates offers a route for validating this assumption.

2 Surrogate Models for Multiple-Timescale Signals

Surrogate modelling follows a standard statistical regression procedure. Assume there exists some function $f(t)$, giving the “true” system output at time t . We only have access to a discrete set of noise-corrupted samples (t_i, x_i) for $i = \{0, 1, \dots, n\}$, where $x_i = f(t_i) + \varepsilon_i$ for some zero-mean i.i.d. nuisance variable ε_i . Given these samples, we seek a surrogate to reconstruct the latent function f . We consider Gaussian processes and Bayesian splines as candidate models.

2.1 Gaussian Process Regression

Gaussian processes generalise the multivariate Gaussian distribution to cases where the index set is of infinite dimension [13]. They can be interpreted as a distribution over functions. Given suitable function-space priors, one can use Bayesian methods to condition on observed data, to estimate the posterior value of the latent function at any given location.

The prior encodes our beliefs about the structure of the data, primarily by determining how similar two function outputs are, given their inputs. The prior implicitly represents a projection into a feature space of possibly infinite dimensionality; as such, it is called the kernel and is the source of the predictive power of Gaussian process regression. By definition, for a smooth function f , $|f(t_i) - f(t_j)|$ will be small if $|t_i - t_j|$ is small; loosely stated, the function outputs will be similar if their inputs are similar. The kernel specifies a prior belief over functions by encoding this neighbourhood of similarity, as well as the variance of the function. Kernels can also specify observation noise and long-term dependencies such as periodicity. One of the most commonly used kernels is the square-exponential, or radial basis function (RBF) kernel, defined for scalars as $k(t_i, t_j) = \sigma_f^2 \exp(-(t_i - t_j)^2/l^2)$ [13]. The hyperparameter l dictates the changeability of the function, by specifying how near two inputs must be for their outputs to be similar. Small l means the function can change rapidly over short intervals. σ_f^2 specifies the variance of the function, loosely interpreted as its amplitude. The Gaussian process model is fitted by selecting the kernel hyperparameters that maximise the model log-likelihood.

The RBF kernel represents a distribution over the set of C^∞ -smooth functions and generalises easily for multidimensional inputs. Other popular kernels include the Matern 3/2 and Matern 5/2, which encode C^1 and C^2 smoothness, respectively [13]. These kernels are stationary, meaning the statistical properties they encode are assumed to remain constant over the range of the data. Kernels can be made periodic by replacing their pointwise distance measure with an appropriate phase-based metric. Here, we consider Gaussian process regression with RBF, Matern 3/2, and Matern 5/2 kernels—three commonly used kernels—in addition to periodic RBF and periodic Matern 3/2 [13].

Gaussian process regression is an elegant approach to the statistical inference of f . Latent values are computed as a linear combination of inputs, weighted according to the kernel. Gaussian processes therefore act as a statistically optimal linear filter, for a given set of priors. They remove noise from a signal, whilst retaining the signal itself, making them an attractive method for surrogate modelling.

2.2 Bayesian Spline Regression

A spline curve is a composite curve made up of sections of polynomials. Each polynomial section connects to its neighbours at a knot point. Polynomial coefficients

are found by requiring each section to meet its neighbours smoothly at the knots and by imposing some boundary conditions.

BSplines reformulate spline curves into a more familiar regression setup. Spline curve basis functions, referred to as BSplines, are defined. Any spline can then be constructed as a weighted sum of these basis functions. BSplines are a popular method for regression and statistical smoothing [14].

The BSpline basis is constructed from a vector of scalar-valued knots, unlike traditional splines that are defined from a set of vector-valued knot points. The scalar knots must be placed in appropriate locations if the spline curve is to fit the data. Choice of knots is therefore important, but non-trivial, with typical approaches being optimisation—[15] or regularisation-based [14]. An alternative approach is to not select any single set of knots but to maintain a probabilistic distribution over all candidate knot sets. Such an approach is used in Bayesian free-knot splines [16, 17]. Here, a set of sensibly chosen priors are used to encode beliefs about form of the spline model. Bayes' rule is used to formulate a posterior distribution over possible knot sets, given data. Reversible-jump Markov chain Monte Carlo [18] is then employed to draw samples from the posterior distribution.

Free-knot splines provide a powerful, yet conceptually elegant method of choosing the best knots for any given data. Furthermore, Paciorek and Schervish found the method to outperform Gaussian process regression on a set of noisy scalar-valued example data [19]. This makes free-knot splines a good candidate for surrogate modelling. Here we use the Bayesian free-knot splines method of DiMatteo et al. [17] as implemented in [20], with a custom python wrapper.

3 Comparison of Surrogate Models

The surrogate models introduced in this chapter are tested on synthetic data obtained from the simulation of a van der Pol oscillator [21] and a Hodgkin–Huxley neuron [22].

The van der Pol oscillator is a nonlinear relaxation oscillator. Relaxation oscillators are able to model a wide variety of physical systems, making them an interesting target for control-based continuation. Nevertheless, as a result of their slow–fast dynamics, the system output shows abrupt, periodic changes. This abruptness makes the oscillators difficult to analyse using existing CBC procedures, which in turn means they are interesting as test models. Here we take the van der Pol system as presented in [21], with $\varepsilon = 5$. The output signal is taken as the position- or voltage-like variable $x(t)$.

The Hodgkin–Huxley model is chosen for being another example of a system producing abruptly changing outputs. The equations describe spiking dynamics in neurons, whereby a voltage-like variable alternates periodically between a slow, drifting change, and a sharp, rapid “spike”. To promote oscillatory behaviours, we use standard parameter values and $I = 1.75$. The output signal is taken as the voltage-like variable $v(t)$.

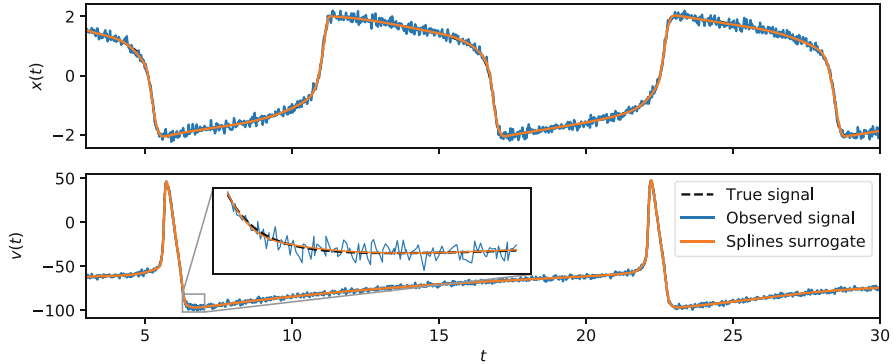


Fig. 2 Bayesian free-knot spline surrogate models, fitted to noisy signals from a simulated van der Pol oscillator (top) and Hodgkin–Huxley neuron (bottom)

Figure 2 shows an example of a free-knot splines surrogate model, fitted to noise-corrupted test data. The data are obtained by integrating the models; evaluating the solution at 1000 evenly spaced time points covering approximately three to five periods; noise corrupting the signal with i.i.d. Gaussian white noise; and then fitting a surrogate to the noise-corrupted samples. Visually, free-knot splines are seen to accurately reconstruct the true, noise-free signal. The surrogate is able to filter off noise without imparting a phase shift on the signal and without distorting it. Therefore, a Fourier discretisation obtained from the surrogate will be more accurate than one obtained from the raw data. Note that an inset axis is shown on the neuron signal. This shows the surrogate fit right at the end of a spike (100 extra data points are placed here for ease of illustration). Such regions are difficult to model accurately using surrogates, due to the rapid change in the statistical properties of the signal. Nevertheless, the surrogate is seen to accurately reconstruct the true signal even at this statistical change point, where one would typically expect the worst performance to be.

The goodness-of-fit of the tested surrogates is evaluated by calculating the mean-square error over a set of unseen test data. Solution data points are split deterministically into 25% test and 75% training points. The training data are noise-corrupted and then used to fit the surrogate. The surrogate predictions are compared against the true solution value at each test point, to compute the mean-square error. This is tested for various amounts of noise corruption and repeated 100 times to average out any randomness. The results are shown in Tables 1 and 2. The amount of noise is quantified both by the standard deviation σ of the noise and by the signal-to-noise ratio (SNR), given as the ratio of the signal energy to the noise energy.

It is found that periodic kernels almost always outperform non-periodic kernels. Any apparent exception to this likely arises as a result of difficulties in optimising the kernel hyperparameters. Besides this, no single kernel outperforms the other. Rather, the best kernel depends on the signal being studied. The tested Gaussian process kernels are stationary. This means that statistical properties are assumed to

remain constant across the entire signal. In particular, the kernels have a constant, fixed lengthscale. Where the signal changes regimes, such as between slow and fast dynamics, the lengthscale must be small to allow sufficient model flexibility to accommodate the changes. As stationary kernels cannot encode any changes in lengthscale, we are forced to choose the same small l across the whole signal. This means that, while the model is flexible enough to accommodate any rapid changes in the signal, it is also less able to discern between signal and noise. Noise corruption also causes rapid changes in the signal, and the small lengthscales mean the model is unable to filter out these perturbations accurately. Free-knot splines do not suffer from any such issues and outperform Gaussian process regression when both the stationarity assumption breaks down and the noise corruption is large. Where additional model flexibility is required, such as around regime changes in the signal, more knots are added. This allows the model more scope to adapt to the data. Tables 1 and 2 demonstrate this by showing Bayesian free-knot splines to outperform Gaussian process regression when the signals are more statistically nonstationary, as with the Hodgkin–Huxley signals, and when the amount of noise corruption is large.

Both Gaussian processes and free-knot splines are Bayesian methods. They rely on updating prior beliefs after seeing evidence. The quality of the surrogate prediction depends on both the amount of evidence available and the quality of these prior beliefs. In general, free-knot splines are significantly easier to work

Table 1 Mean-square prediction error of various surrogate models, as computed from surrogates fitted to a van der Pol signal with i.i.d. noise of standard deviation σ

SNR (dB)	$\sigma = 0$	$\sigma = 0.05$	$\sigma = 0.1$
–	–	30.0	24.0
Bayesian splines	2.11×10^{-4}	1.20×10^{-3}	3.00×10^{-3}
GPR: Periodic Matern 3/2	6.40×10^{-6}	5.63×10^{-4}	1.48×10^{-3}
GPR: Periodic RBF	3.60×10^{-7}	8.43×10^{-4}	2.92×10^{-3}
GPR: Matern 3/2	5.75×10^{-5}	2.40×10^{-3}	5.46×10^{-3}
GPR: Matern 5/2	3.59×10^{-5}	2.08×10^{-3}	5.27×10^{-3}
GPR: RBF	3.53×10^{-5}	2.09×10^{-3}	6.96×10^{-3}

Table 2 Mean-square prediction error of various surrogate models, as computed from surrogates fitted to a Hodgkin–Huxley signal with i.i.d. noise of standard deviation σ

SNR (dB)	$\sigma = 0$	$\sigma = 1$	$\sigma = 2$
–	–	37.4	31.4
Bayesian splines	8.00×10^{-2}	0.185	0.597
GPR: Periodic Matern 3/2	1.80×10^{-4}	0.213	0.641
GPR: Periodic RBF	3.36×10^{-2}	0.406	0.806
GPR: Matern 3/2	3.24×10^{-2}	0.759	1.82
GPR: Matern 5/2	1.72×10^{-2}	0.915	1.91
GPR: RBF	5.61×10^{-1}	1.78	2.60

with that Gaussian processes, as one can construct suitable splines priors much more simply than suitable kernels. Splines priors specify our beliefs about the form of the model, such as the number of knots, or the distribution of the noise. On the other hand, Gaussian process priors must encode our beliefs about candidate functions. While hyperparameter optimisation allows one to fit a kernel to data, it is not always obvious which kernels will work well, or why. Experience suggests that free-knot splines work out-of-the-box, whereas success with Gaussian processes requires considerable attention to kernel choice and hyperparameter optimisation. Nevertheless, free-knot splines require the implementation of a reversible-jump Markov chain Monte Carlo engine; Gaussian process regression is much simpler to implement, as it requires only linear algebra and a kernel function.

4 Conclusions

Control-based continuation is an experimental method for exploring the bifurcation structure of physical and black-box systems. Discretisation is a key part of control-based continuation. Existing CBC implementations use a truncated Fourier series to both remove noise from an experimentally derived signal and to discretise it. Numerical experiments indicate that Fourier series become less effective at filtering noise when large numbers of harmonics are required. Here, we investigate how Bayesian surrogate models can be used to remove noise from signals in such cases.

An adaptive filtering procedure is demonstrated using Bayesian surrogate models. These are shown to be effective at removing observation noise from synthetic signals. The resulting noise-free surrogate model can then be used in place of the recorded data, for discretising the system output.

Gaussian process regression is compared against Bayesian free-knot splines. Gaussian processes produce more accurate surrogates when signals are weakly nonlinear. Nevertheless, their predictive power is limited when stationary kernels are used. This means that the tested Gaussian process regressors give poor results when the amount of noise corruption and nonlinearity are large. In such cases, free-knot splines provide a more accurate model fit. Furthermore, free-knot spline models are easier to use than Gaussian processes, as their priors are simple and intuitive, and can easily be tuned to the data in question. Gaussian process kernels require careful hyperparameter optimisation to encode prior beliefs.

Acknowledgments M.B. was supported by an EPSRC DTP Scholarship, provided by the University of Bristol. L.M. was funded by the Engineering and Physical Sciences Research Council (EPSRC, grants EP/R041695/1 and EP/S01876X/1) and Horizon 2020 (CosyBio, grant agreement 766840). L.R. has received funding from the Royal Academy of Engineering (RF1516/15/11) that is gratefully acknowledged.

Conflict of Interest The authors declare that they have no conflict of interest.

References

1. J. Sieber, B. Krauskopf, Control based bifurcation analysis for experiments. *Nonlinear Dyn.* **51**(3), 365–377 (2008)
2. D.A. Barton, J. Sieber, Systematic experimental exploration of bifurcations with noninvasive control. *Phys. Rev. E* **87**(5), 052916 (2013)
3. D.A. Barton, Control-based continuation: Bifurcation and stability analysis for physical experiments. *Mech. Syst. Signal Process.* **84**, 54–64 (2017)
4. D.A. Barton, S.G. Burrow, Numerical continuation in a physical experiment: investigation of a nonlinear energy harvester. *J. Comput. Nonlinear Dyn.* **6**(1), 011010 (2011)
5. L. Renson, A. Shaw, D. Barton, S. Neild, Application of control-based continuation to a nonlinear structure with harmonically coupled modes. *Mech. Syst. Signal Process.* **120**, 449–464 (2019)
6. L. Renson, D.A. Barton, S.A. Neild, Experimental tracking of limit-point bifurcations and backbone curves using control-based continuation. *Int. J. Bifurcation Chaos* **27**(1), 1730002 (2017)
7. H. Mohammadi, P. Challenor, M. Goodfellow, Emulating dynamic non-linear simulators using Gaussian processes. *Comput. Stat. Data Anal.* **139**, 178–196 (2019)
8. J. Theiler, S. Eubank, A. Longtin, B. Galdrikian, J.D. Farmer, Testing for nonlinearity in time series: the method of surrogate data. *Phys. D: Nonlinear Phenom.* **58**(1–4), 77–94 (1992)
9. G. Lancaster, D. Iatsenko, A. Pidde, V. Ticcinelli, A. Stefanovska, Surrogate data for hypothesis testing of physical systems. *Phys. Rep.* **748**, 1–60 (2018)
10. L. Renson, J. Sieber, D. Barton, A. Shaw, S. Neild, Numerical continuation in nonlinear experiments using local Gaussian process regression. *Nonlinear Dyn.* **98**(4), 2811–2826 (2019)
11. K. H. Lee, D. A. W. Barton, and L. Renson. Reduced-order modelling of flutter oscillations using normal forms and scientific machine learning. arXiv preprint arXiv:2011.02041 (2020).
12. L. Rabiner, On the use of autocorrelation analysis for pitch detection. *IEEE Trans. Acoust. Speech Signal Process.* **25**(1), 24–33 (1977)
13. C.K. Williams, C.E. Rasmussen, *Gaussian Processes for Machine Learning*, vol. 2 (MIT Press Cambridge, Cambridge, 2006)
14. P.H. Eilers, B.D. Marx, Flexible smoothing with b-splines and penalties. *Stat. Sci.* **11**(2), 89–102 (1996)
15. O. Valenzuela, B. Delgado-Marquez, M. Pasadas, Evolutionary computation for optimal knots allocation in smoothing splines. *Appl. Math. Model.* **37**(8), 5851–5863 (2013)
16. M.J. Lindstrom, Bayesian estimation of free-knot splines using reversible jumps. *Comput. Stat. Data Anal.* **41**(2), 255–269 (2002)
17. I. DiMatteo, C.R. Genovese, R.E. Kass, Bayesian curve-fitting with free-knot splines. *Biometrika* **88**(4), 1055–1071 (2001)
18. P.J. Green, Reversible jump Markov chain Monte Carlo computation and Bayesian model determination. *Biometrika* **82**(4), 711–732 (1995)
19. C.J. Paciorek, M.J. Schervish, Nonstationary covariance functions for Gaussian process regression, in *Advances in Neural Information Processing Systems* (2004), pp. 273–280
20. G. Wallstrom, J. Liebner, R.E. Kass, An implementation of Bayesian adaptive regression splines (bars) in c with s and r wrappers. *J. Stat. Softw.* **26**(1), 1 (2008)
21. B. Van der Pol, Lxxxviii. On “relaxation-oscillations”. *Lond. Edinb. Dublin Philos. Mag. J. Sci.* **2**(11), 978–992 (1926)
22. A.L. Hodgkin, A.F. Huxley, A quantitative description of membrane current and its application to conduction and excitation in nerve. *J. Physiol.* **117**(4), 500–544 (1952)

Predicting the Type of Nonlinearity of Shallow Spherical Shells: Comparison of Direct Normal Form with Modal Derivatives



Yichang Shen, Nassim Kesmia, Cyril Touzé, Alessandra Vizzaccaro, Loïc Salles, and Olivier Thomas

1 Introduction

Reduced-order modelling (ROM) strategies dealing with geometrically nonlinear structures attract attention for a long time, and a number of methods have been proposed in the literature. In the recent years, a special emphasis has been put toward applications to finite element (FE) based models in order to extend the range of application to engineering structures with complex geometries. Also, numerous developments take into account both the *non-intrusive* characteristic of the method, that can be used with a standard (commercial) FE code without the need of entering inside the programs at the elementary level, and also on *simulation-free methods*, that can be used without the need of a priori, offline computations [1, 2].

The aim of this paper is to compare two different methods, namely the quadratic manifold (QM) built from modal derivatives (MD) [3, 4] and the direct normal form approach [5, 6], on a shell example. More particularly, the ability of the two methods in the prediction of the type of nonlinearity (hardening/softening behaviour) is investigated. In nonlinear vibrations, predicting the correct type of nonlinearity is the first characteristics that needs to be correctly given by a ROM since being a fundamental property of the nonlinear oscillations. The normal form approach,

Y. Shen · N. Kesmia · C. Touzé (✉)

IMSIA, Institut of Mechanical Sciences and Industrial Applications, ENSTA Paris, CNRS, EDF, CEA, Institut Polytechnique de Paris, Palaiseau, France

e-mail: yichang.shen@ensta-paris.fr; nassim.kesmia@ens-paris-saclay.fr; cyril.touze@ensta-paris.fr

A. Vizzaccaro · L. Salles

Vibration University Technology Centre, Imperial College London, London, UK

e-mail: a.vizzaccaro17@imperial.ac.uk; l.salles@imperial.ac.uk

O. Thomas

Arts et Métiers Institute of Technology, Lille, France

based on the invariant manifold theory, allows such a correct prediction [7]. On the other hand, QM does not rely on invariance property, and it has been shown recently that if a slow/fast assumption is not at hand, incorrect prediction can be formulated [8]. This general result is here illustrated on the specific case of a shallow spherical shell with increasing curvature. For that purpose, the von Kármán model, assuming shallowness, neglecting in-plane and rotary inertia and using an Airy stress function, is used [9].

In a second part, the validity of the von Kármán assumptions is verified by comparing the type of nonlinearity computed from a FE model. For that purpose, the direct normal form approach developed in [6] is used to get a direct access to the hardening/softening behaviour from the FE mesh.

2 Modelling

2.1 Analytical von Kármán Model for Shallow Spherical Shell

A free-edge spherical shell, made of a homogeneous isotropic material of density ρ , Poisson’s ratio ν and Young’s modulus E is considered, with the dimension of thickness h , radius of curvature R and outer diameter $2a$ (see Fig. 1). Large transverse deflections and moderate rotations are considered, so that the model is a generalization of von Kármán’s theory for large deflection of plates. The shell is assumed to be thin so that $h/a \ll 1$ and $h/R \ll 1$, and shallow: $a/R \ll 1$. Since we are interested in predicting the type of nonlinearity, damping and forcing are not considered. The equations of motion read [9]:

$$D\Delta\Delta w + \frac{1}{R}\Delta F + \rho h\ddot{w} = L(w, F), \tag{1a}$$

$$\Delta\Delta F - \frac{Eh}{R}\Delta w = -\frac{Eh}{2}L(w, w), \tag{1b}$$

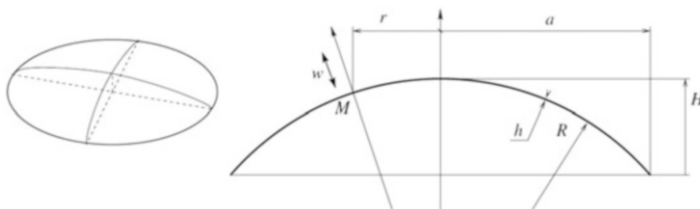


Fig. 1 Geometry of the free-edge shallow spherical shell

where w is the displacement, F the Airy stress function, Δ the Laplacian, L is a quadratic bi-linear operator and $D = Eh^3/12(1 - \nu^2)$ is the flexural rigidity, t indicates the time variable and the double dot ($\ddot{\bullet}$) the second derivative with respect to time. The problem is made nondimensional by introducing $r = a\bar{r}$, $t = a^2\sqrt{\frac{\rho h}{D}}\bar{t}$, $w = h\bar{w}$, and $F = Eh^3\bar{F}$. Thus, substituting the above definitions in equations of motion, Eq. (1), and dropping the overbars in the results, one obtains:

$$\Delta\Delta w + \varepsilon_q \Delta F + \ddot{w} = \varepsilon_c L(w, F), \tag{2a}$$

$$\Delta\Delta F - \sqrt{\kappa} \Delta w = -\frac{1}{2}L(w, w). \tag{2b}$$

where the two nondimensional coefficients are $\varepsilon_q = 12(1 - \nu^2)\sqrt{\kappa}$, and $\varepsilon_c = 12(1 - \nu^2)$, making also appear the aspect ratio κ of the shell as $\kappa = \frac{a^4}{R^2h^2}$.

The complete linear analysis has been tackled in [9]. As an important result, the behaviour of the eigenfrequencies with respect to the aspect ratio κ is shown in Fig. 2. One can observe in particular that purely asymmetric modes $(k, 0)$, with k nodal diameters and no nodal circle, show a very slight dependence upon κ . On the other hand, axisymmetric modes $(0, n)$ without nodal diameters, as well as mixed mode (k, n) with both $k \neq 0$ and $n \neq 0$, show a huge dependence on curvature. These results are important in order to analyse the type of nonlinearity, depending on the mode considered.

In order to predict the type of nonlinearity, Eqs. (2) are projected onto the natural basis of the eigenmodes. After projection, the semi-discretized equations of motion read [9]:

$$\ddot{X}_p + \omega_p^2 X_p + \sum_{i=1}^{+\infty} \sum_{j=1}^{+\infty} g_{ij}^p X_i X_j + \sum_{i=1}^{+\infty} \sum_{j=1}^{+\infty} \sum_{k=1}^{+\infty} h_{ijk}^p X_i X_j X_k = 0, \tag{3}$$

where X_p refers to the modal amplitude of the p th transverse mode, and ω_p its radian eigenfrequency. The nonlinear coupling coefficients write:

$$g_{ij}^p = -\varepsilon_q \iint_{\varphi_{\perp}} \phi_p L(\phi_i, \psi_j) dS - \frac{\varepsilon_q}{2} \sum_{b=1}^{+\infty} \frac{1}{\xi_b^4} \iint_{\varphi_{\perp}} L(\phi_i, \phi_j) \Upsilon_b dS \iint_{\varphi_{\perp}} \phi_p \Delta \Upsilon_b dS, \tag{4a}$$

$$h_{ijk}^p = \varepsilon_c \sum_{b=1}^{+\infty} \frac{1}{\xi_b^4} \iint_{\varphi_{\perp}} L(\phi_i, \phi_j) \Upsilon_b dS \iint_{\varphi_{\perp}} \phi_i L(\phi_k, \Upsilon_b) dS. \tag{4b}$$

ϕ_i refers to transverse eigenmodes while ψ_j are obtained from the diagonalization of the Airy stress function. ξ_n and eigenfunction Υ_n are zeros from the eigenproblem, the interested reader can find their detailed expression in [9]. φ_{\perp} is the domain defined by $(r, \theta) \in [0, 1] \times [0, 2\pi]$. Equations (3) describe the dynamics of the shell, and the trend of nonlinearity can be inferred from these equations.

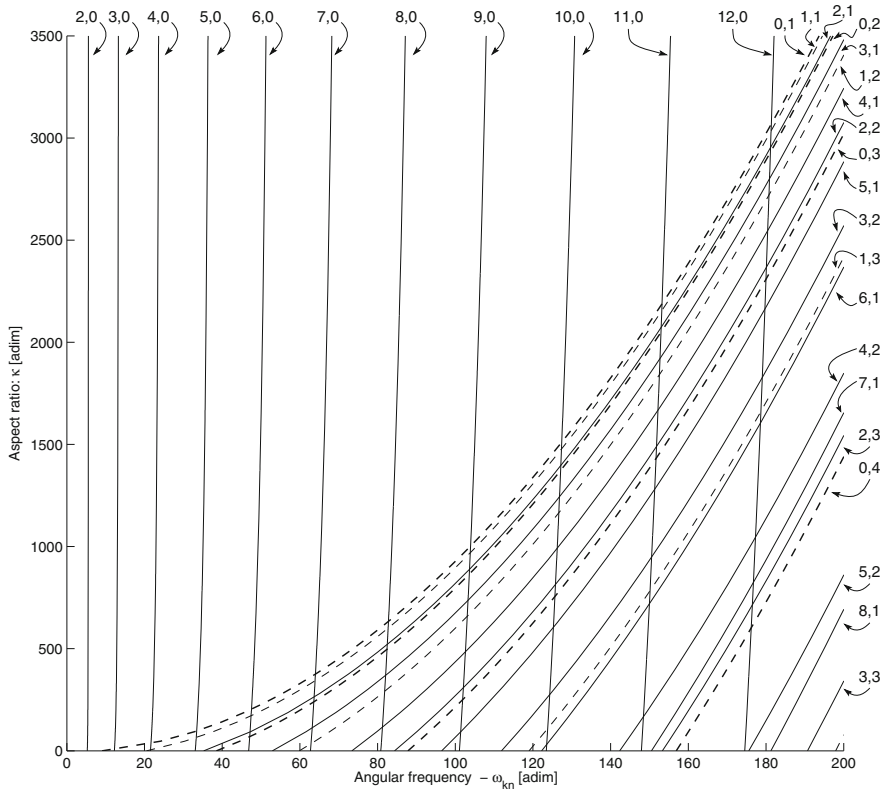


Fig. 2 Dimensionless natural frequencies ω_{kn} of the shell as a function of the aspect ratio κ (figure reprinted from [10]). $\kappa = 0$ corresponds to the flat plate case

2.2 Numerical Finite Element Model

In addition to the von Kármán model developed in the previous section, a FE procedure is also undertaken in order to analyse the type of nonlinearity of shallow spherical shells. For that purpose, the open source software `code_aster` [11] is used, and free-edge shallow shells have been meshed with both 2D shell elements and 3D brick elements. These meshes will be used in order to highlight the validity of von Kármán’s assumption in order to predict hardening/softening behaviour.

For the geometrically nonlinear structures, the equations of motion stemming from the FE discretization write:

$$\mathbf{M}\ddot{\mathbf{X}} + \mathbf{K}\mathbf{X} + \mathbf{G}(\mathbf{X}, \mathbf{X}) + \mathbf{H}(\mathbf{X}, \mathbf{X}, \mathbf{X}) = \mathbf{0}, \tag{5}$$

where \mathbf{X} is the vector of generalized displacements at the nodes, \mathbf{M} is the mass matrix, \mathbf{K} is the tangent stiffness matrix, and finally, $\mathbf{G}(\mathbf{X}, \mathbf{X})$ and $\mathbf{H}(\mathbf{X}, \mathbf{X}, \mathbf{X})$ represent quadratic and cubic nonlinear couplings.

3 Analytical Prediction of the Type of Nonlinearity

3.1 Analytical Results from the Three Reduction Methods

We first compare the prediction of the type of nonlinearity using the semi-analytical derivation obtained from von Kármán model. Three different predictions are contrasted. The first one is given by the normal form approach and has already been reported in [10]. As known from theoretical results [7], this prediction is correct thanks to the invariance property of nonlinear normal modes (NNMs). Two other solutions are compared to this reference solution, both obtained from the QM approach developed in [3, 4], the first one using full MD, and the second one static modal derivatives (SMD).

In each case, the dynamics is reduced to a single-degree of freedom equation from which one can infer the hardening/softening behaviour. Let p be the master mode of interest. Following [8], one can show that the reduced dynamics given by the three methods writes:

$$\ddot{R} + \omega_p^2 R_p + C_1 R_p^2 + C_2 \frac{\dot{R}_p^2}{\omega_p^2} + C_3 \frac{\ddot{R}_p R_p}{\omega_p^2} + C_4 R_p^3 + C_5 \frac{\dot{R}_p^2 R_p}{\omega_p^2} + C_6 \frac{\ddot{R}_p R_p^2}{\omega_p^2} = 0, \quad (6)$$

where the expression of C_1 to C_6 is different depending on the method and are recalled in Table 1.

A first-order perturbative development allows definition of the angular frequency of free oscillations ω_{NL} , connected to the natural frequency ω_p , as $\omega_{NL} = \omega_p (1 +$

Table 1 Table of coefficients of the reduced dynamics given by the three selected methods: MD for modal derivatives, SMD for static modal derivatives and NF for normal form

	C_1	C_2	C_3	C_4	C_5	C_6
MD	g_{pp}^p	0	0	$h_{ppp}^p - \sum_{\substack{s=1 \\ s \neq p}}^n \frac{2(g_{pp}^s)^2 (\omega_s^2 - 2\omega_p^2)}{(\omega_s^2 - \omega_p^2)^2}$	$-\sum_{\substack{s=1 \\ s \neq p}}^n \frac{4(g_{pp}^s)^2 \omega_p^2}{(\omega_s^2 - \omega_p^2)^2}$	$\sum_{\substack{s=1 \\ s \neq p}}^n \frac{4(g_{pp}^s)^2 \omega_p^2}{(\omega_s^2 - \omega_p^2)^2}$
SMD	$-2g_{pp}^p$	$-2g_{pp}^p$	$-4g_{pp}^p$	$h_{ppp}^p - \sum_{s=1}^n \frac{2(g_{pp}^s)^2}{\omega_s^2}$	$\sum_{s=1}^n \frac{4(g_{pp}^s)^2 \omega_p^2}{\omega_s^4}$	$\sum_{s=1}^n \frac{4(g_{pp}^s)^2 \omega_p^2}{\omega_s^4}$
NF	0	0	0	$h_{ppp}^p - \sum_{s=1}^n \frac{2(g_{pp}^s)^2 (\omega_s^2 - 2\omega_p^2)}{\omega_s^2 (\omega_s^2 - 4\omega_p^2)^2}$	$-\sum_{s=1}^n \frac{4(g_{pp}^s)^2 \omega_p^2}{\omega_s^2 (\omega_s^2 - 4\omega_p^2)^2}$	0

$T_p a^2$), where a is the amplitude of the response of the p th master coordinate and T_p the coefficient governing the type of nonlinearity. $T_p > 0$ indicates the hardening behaviour while $T_p < 0$ implies softening behaviour. The general expression for T_p with all the C_i coefficients reads as:

$$T_p = -\frac{1}{24\omega_p^4}(10C_1^2 + 10C_1C_2 + 4C_2^2 - 7C_2C_3 + C_3^2 - 11C_1C_3) + \frac{1}{8\omega_p^2}(3C_4 + C_5 - 3C_6). \quad (7)$$

As theoretically shown in [8], the MD and SMD method are awaited to give correct results only if a slow/fast assumption between master and slave coordinates is at hand. This slow/fast assumption has been quantified in [8]. Let ρ be the ratio between the smallest eigenfrequency of the slave modes and that of the master one labelled p . If $\rho > 4$, the slow/fast (S/F) assumption is fulfilled, while $\rho < 3$ means that QM method will probably fail. In order to analyse the fulfilment of this S/F, let us introduce ρ_p for spherical shells as:

$$\rho_p = \min_{n \in E_s} \left(\frac{\omega_n}{\omega_p} \right), \quad (8)$$

where E_s is the set of all the slave modes, i.e. all the modes except the master coordinate p .

3.2 Numerical Results for the Shallow Spherical Shell

The results are shown for 6 different master modes in Fig. 3. The first three cases are purely asymmetric modes, (2,0), (3,0) and (4,0); then the first two axisymmetric modes are considered, and finally a mixed mode (2,1) is selected. In the figures, the reference solution is given by the normal form approach (NNM) in magenta. The prediction given by QM MD is in red and QM SMD in yellow. The figures have two y-axis allowing to also report the variations of ρ_p for the mode of interest, as function of κ .

For mode (2,0), one can observe that MD and SMD methods fail to recover the 1:2 resonance leading to a change of behaviour of the type of nonlinearity. On the other hand, when κ is larger than 20, then ρ_p increases and is close to 4, the S/F assumption is retrieved and the three methods give the same results. Modes (3,0) and (4,0) show another important feature, already noted in [8]: the MD method has a divergence in the case of 1:1 resonance, which has no physical explanation and is interpreted as a failure of the method. For purely asymmetric modes, since they show a very slight dependence on curvature, this means that all the slave modes have strongly increasing eigenfrequencies with κ . Consequently, for all these modes

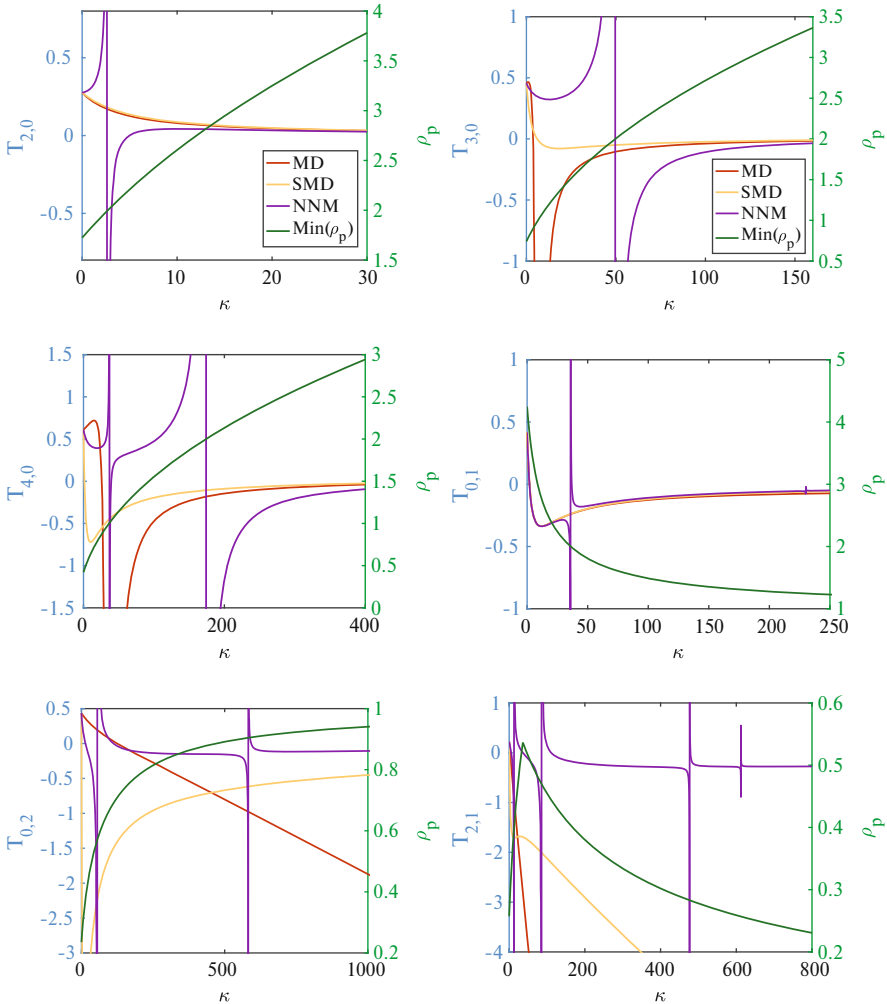


Fig. 3 Type of nonlinearity for 6 modes of the shell: modes (2,0), (3,0), (4,0), (0,1), (0,2), (2,1)

the S/F assumption is always finally retrieved, but sometimes at large values of curvature.

Mode (0,1) has the particularity to be very well predicted by using a single linear mode, as shown in [10]. Consequently the three methods behave correctly, even though ρ is decreasing with κ so that S/F does not hold. As a matter of fact, for all axisymmetric and mixed modes, the behaviour of their eigenfrequencies shown in Fig. 2 underlines that S/F assumption will never be met. Consequently, the prediction of the type of nonlinearity given by MD and SMD method completely fails.

4 FE Prediction on the Type of Nonlinearity

This section is devoted to compute the type of nonlinearity from FE models. For that purpose, one has first to select a number of specific cases of curvature since continuous increasing of κ is out of reach. Table 2 summarizes the selected case, where a constant value of radius $a = 0.15$ m has been retained. Varying the radius of curvature R and the thickness h gives rise to a number of κ values that can be directly compared with the predictions obtained in the previous section.

In the FE model, the material properties of the shell are the following: $\rho = 4400$ kg/m³, $E = 1.04e + 11$ Pa, $\nu = 0.3$. Two types of elements are used in the analysis. In the first case, DKT shell/plate element is used, and a mesh composed of 12,000 degrees of freedom (dofs) has been built, with three different thicknesses: 1, 3 and 5 mm. In the second case, quadratic 3D element is selected and a mesh composed of approximately 50,000 dofs, with the thickness 3 mm, has been created. A careful convergence study has underlined that the eigenfrequencies need to be finely computed in order to obtain a reliable result for the type of nonlinearity.

4.1 Direct Normal Form Approach

In order to predict the hardening/softening behaviour for the FE shell models, the direct normal form (DNF) introduced in [6] is used. The type of nonlinearity can be computed from \hat{T}_p that reads in this case:

$$\hat{T}_p = \frac{1}{8\hat{\omega}_p^2} \left[3 \left(\hat{A}_{ppp}^p + \hat{h}_{ppp}^p \right) + \hat{\omega}_p^2 \hat{B}_{ppp}^p \right]. \tag{9}$$

In this equation, \hat{h}_{ppp}^p is the nonlinear cubic coefficient that can be directly computed with a single STEP operation [1]. The other correcting terms \hat{A}_{ppp}^p and \hat{B}_{ppp}^p can be directly computed from the FE model thanks to the DNF approach, that allows to go directly from the physical space (nodes of the FE mesh) to the invariant-based span of the phase space, thanks to the nonlinear mapping given by the normal form approach. The complete expressions for leading these computations are explicit in [6], here we simply recall the values of the needed coefficients as given by:

Table 2 Dimensions of the selected shells for the FE analysis with the corresponding κ values

$a(m)$	0.15									
$R(m)$	3.5	2.5	1.5	0.9	0.8	0.7	0.6	0.5	0.4	0.3
$\kappa(h = 0.001 \text{ m})$	41.3	81.0	225.0	625	791	1033.16	1406.25	2025	3164.06	5625
$\kappa(h = 0.003 \text{ m})$	4.59	9	25	69.44	87.89	114.80	156.25	225	351.56	625.00
$\kappa(h = 0.005 \text{ m})$	1.65	3.24	9	25	31.64	41.32	56.25	81	126.56	225.00

$$\hat{A}_{ppp}^p = 2\phi_p^T \mathbf{G}(\phi_p, \bar{\mathbf{a}}_{pp}), \quad \hat{B}_{ppp}^p = 2\phi_p^T \mathbf{G}(\phi_p, \bar{\mathbf{b}}_{pp}), \quad (10)$$

where the expression of $\bar{\mathbf{a}}_{pp}, \bar{\mathbf{b}}_{pp}$ can be found in [6].

In order to draw out the comparison with the results obtained in the previous sections (von Kármán model) where a nondimensionalization was carried out, the relationship between the coefficient computed from FE model \hat{T}_p and dimensionless T_p is explicit as: $T_p = \hat{T}_p h^2 v^2$, where v is the mode shape scaling factor, which is chosen to obtain the same maximal amplitude for the analytical and FE mode shapes, i.e. $\hat{\phi}_p = \phi_p v$, with ϕ_p normalized by $\iint_{\varphi_{\perp}} \phi_p^2 dS = 1$ in analytical von Kármán model.

4.2 Results

Figure 4 compares the analytical result given by von Kármán model and normal form onto the analytical coefficients, to those obtained from the direct computation on the FE model, where again two different types of elements (DKT shell/plate element and 3D elements) have been used. The same mode as in Fig. 3 is used. A perfect matching is obtained between the two methods, underlining that the von Kármán model, even though relying on numerous assumptions, is sufficient in order to correctly predict the type of nonlinearity of shallow spherical shell. The results also underline the efficiency of the DNF approach for computing accurate ROMs for shell models.

5 Conclusions

The type of nonlinearity for free-edge shallow spherical shells has been studied with a special emphasis on comparing different models and methods. Two methods have been contrasted in their ability to correctly predict the type of nonlinearity: the normal form approach and the QM method based on modal derivatives. In that case, the von Kármán model has been used to illustrate how the two reduction methods can give different predictions. The results underline that modal derivatives approaches need a slow/fast assumption in order to yield a correct prediction. For numerous modes of the shallow spherical shell, the S/F assumption is never met so that both methods (using either MD or SMD) completely fail in predicting correctly the hardening/softening behaviour, whereas the normal form always gives the correct prediction. The second comparison is between the results given by von Kármán model and a finite element procedure. For that purpose, the DNF approach has been used, allowing to directly compute and predict the type of nonlinearity from FE models. Both models have been found to give the same predictions, underlining that the assumptions of the von Kármán model are well fulfilled so that the predictions given are correct.

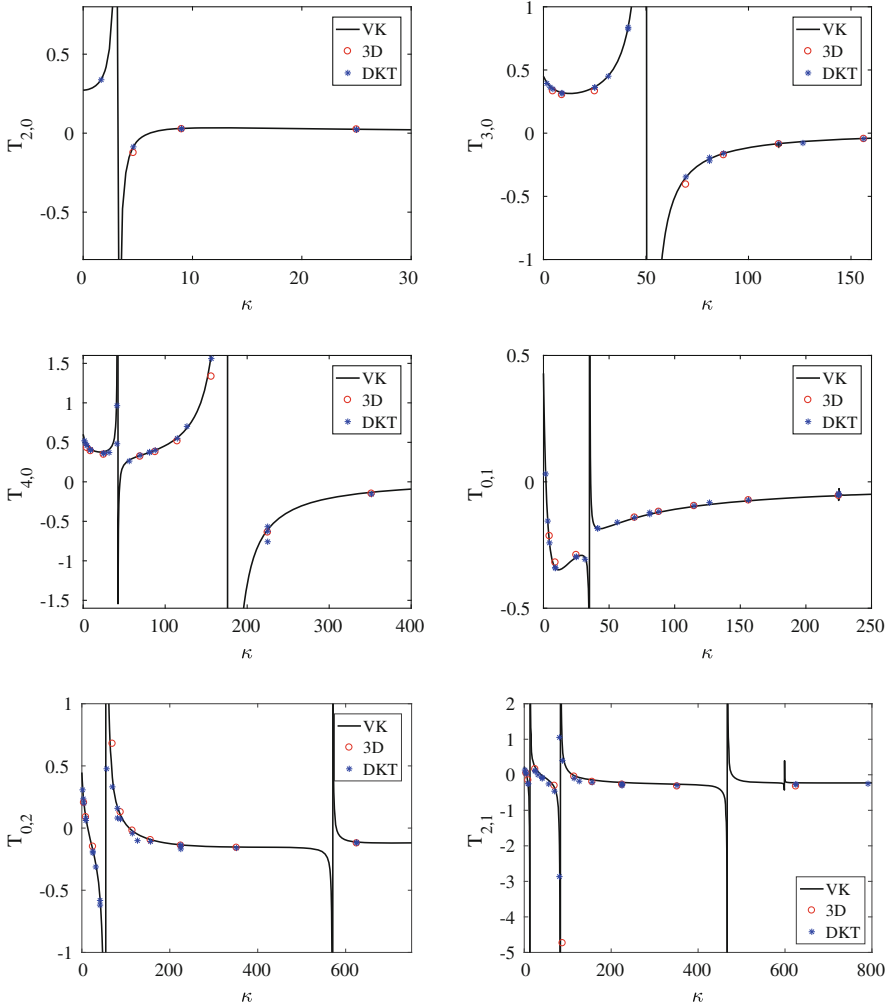


Fig. 4 Type of nonlinearity for 6 modes of the shell: modes (2,0), (3,0), (4,0), (0,1), (0,2), (2,1). Comparison of analytical results from von Kármán model (continuous lines) to numerical predictions obtained by combining FE procedure with DNF

References

1. A.A. Muravyov, S.A. Rizzi, Determination of nonlinear stiffness with application to random vibration of geometrically nonlinear structures. *Comput. Struct.* **81**, 1513–1523 (2003)
2. M.P. Mignolet, A. Przekop, S.A. Rizzi, S.M. Spottswood, A review of indirect/non-intrusive reduced order modeling of nonlinear geometric structures. *J. Sound Vib.* **332**, 2437–2460 (2013)
3. S. Jain, P. Tiso, J.B. Rutzmoser, D.J. Rixen, A quadratic manifold for model order reduction of nonlinear structural dynamics. *Comput. Struct.* **188**, 80–94 (2017)

4. J.B. Rutzmoser, D.J. Rixen, P. Tiso, S. Jain, Generalization of quadratic manifolds for reduced order modeling of nonlinear structural dynamics. *Comput. Struct.* **192**, 196–209 (2017)
5. C. Touzé, M. Amabili, Non-linear normal modes for damped geometrically non-linear systems: application to reduced-order modeling of harmonically forced structures, *J. Sound Vib.* **298**(4–5), 958–981 (2006)
6. A. Vizzaccaro, Y. Shen, L. Salles, J. Blahos, C. Touzé, Direct computation of normal form for reduced-order models of finite element nonlinear structures. *Comput. Method Appl. Mech. Engrg.*, 284, 113957, 2021.
7. C. Touzé, O. Thomas, A. Chaigne, Hardening/softening behaviour in non-linear oscillations of structural systems using non-linear normal modes. *J. Sound Vib.* **273**(1–2), 77–101 (2004)
8. A. Vizzaccaro, L. Salles, C. Touzé, Comparison of nonlinear mappings for reduced-order modelling of vibrating structures: normal form theory and quadratic manifold method with modal derivatives. *Nonlinear Dyn.* **103**, 3335–3370 (2021)
9. O. Thomas, C. Touzé, A. Chaigne, Non-linear vibrations of free-edge thin spherical shells: modal interaction rules and 1:1:2 internal resonance. *Int. J. Solids Struct.* **42**(11–12), 3339–3373 (2005)
10. C. Touzé, O. Thomas, Non-linear behaviour of free-edge shallow spherical shells: effect of the geometry. *Int J. Nonlinear Mech.* **41**(5), 678–692 (2006)
11. Électricité de France: Finite element *code_aster*, Analysis of Structures and Thermomechanics for Studies and Research (1989–2020). <https://www.code-aster.org/>

Parametric Model Order Reduction for Localized Nonlinear Feature Inclusion



Konstantinos Vlachas, Konstantinos Tatsis, Konstantinos Agathos,
Adam R. Brink, Dane Quinn, and Eleni Chatzi

1 Introduction

The ever increasing engineering and manufacturing demands require treatment of intricate nonlinear dynamical systems. By breaking down the system and addressing each component separately, the respective complexity can be reduced. This is referred to as dynamic substructuring [1]. The historical background behind the development of substructuring is discussed in detail in [2], where existing techniques are summarized and classified based on the coupling domain's characteristics and nature.

When the substructural formulation of real-life systems is investigated within a nonlinear context, additional treatment is required [3]. In tackling this, several alternative methodologies have been proposed. In [4], for instance, a formulation based on residual flexibility modes is employed to treat geometrically nonlinear systems. Other notable contributions include polynomial [5] or similar expansion-based approximations [6]. Representations augmented with modal derivatives have also been utilized for geometrically nonlinear systems in [7].

K. Vlachas (✉) · K. Tatsis · E. Chatzi
ETH Zurich, Zurich, Switzerland
e-mail: vlachas@ibk.baug.ethz.ch; chatzi@ibk.baug.ethz.ch; <https://chatzi.ibk.ethz.ch/>

K. Agathos
College of Engineering, Mathematics and Physical Sciences, University of Exeter, Exeter, United Kingdom
e-mail: K.Agathos@exeter.ac.uk

A. R. Brink
Sandia National Laboratories, Albuquerque, New Mexico, USA

D. Quinn
The University of Akron, Akron, OH, USA

In this context, the dominant approach appears to be the adoption of a nonlinear normal modes strategy. The notion gained increasing attention after the comprehensive formulation in [8], which describes a reduction framework able to capture a system's dynamics in a set of nonlinear modes. The approach's accurate performance has been demonstrated in several applications, including resonance prediction [9] and frequency response approximation [10].

When aiming to build a digital twin, substructuring may simplify the process of deriving accurate Reduced-Order Models (ROMs) by allowing individual reduction of components. To achieve this, Gruber et al. [11] employed a dual Craig-Bampton (CB) approach in a linear setting, whereas Lee [12] handles parametric dependencies via CB component modes interpolation on a suitable subspace. Within a nonlinear context, Joannin et al. [13] derived an accurate and efficient ROM via coupling of the nonlinear normal modes strategy with modal synthesis proposing a ROM scheme with more general applicability.

In the context of approximating nonlinear dynamical systems via a substructural ROM, this paper implements an alternative approach, aiming to remove any dependency on the derivation of nonlinear normal modes and address the parametric context of real-life systems. Further, the available literature in dynamic substructuring is strongly dominated by applications on geometrically nonlinear problems. A few additional contributions also exist in nonlinear damping [14] and contact modeling [15]. This paper instead focuses on reduced-order modeling for material nonlinearities in the form of plasticity.

Our approach derives a physics-based ROM through Proper Orthogonal Decomposition (POD) applied to nonlinear response snapshots. POD forms a powerful tool for approximating the reduced subspace spanning a component's response, thus assembling an accurate projection basis. It has already been applied in a substructuring context in [16] but only implemented in linear case studies without parametric dependencies. Similarly to our approach in some sense, Jin et al. [15] coupled CMS with POD in a two-stage methodology to address a dual rotor-bearing system with interface nonlinearities on the contact formulation. In this work, we couple the (multi)parametric ROM framework described in [17, 18] with the substructural formulation in [19, 20] to allow for separate reduction and treatment of individual components in a single step. The approach in [20] decomposes the response vector into a set of new coordinates, featuring an ideal and a deviatoric sub-system. This representation allows the pROM to integrate generalized nonlinear or damage features on interfaces or whole model entities and obtain response information in two ways: in a global scale through the reduction modes of the ideal system, namely the monolithic assembly without the presence of nonlinear features and in a localized scale of the individual components. Thus, the derived pROM can harvest information in a global structure level, contrary to CMS-based approaches that rely solely on component modes. Additionally, performing POD reduction in a component-wise manner produces deviatoric subspaces able to capture the local nonlinear behavior, thus waiving the need for mode expansion performed in [15].

2 Problem Statement

2.1 Substructuring for Nonlinear Feature Inclusion

We consider a dynamic structural system comprised of two linear components, termed “exterior regions,” which are identified as C_1 and C_2 respectively, and an internal component C_s , termed “isolated region.” While the components C_1 and C_2 are assumed to behave linearly, the localized internal component C_s accounts for nonlinearities represented by $\mathbf{G} \in \mathbb{R}^{n_s}$. Additionally, the system depends on m parameters, contained in the vector $\mathbf{p} = [p_1, \dots, p_m]^\top \in \Omega \subset \mathbb{R}^m$. Therefore, the governing equations describing the dynamic response of the system are:

$$\mathbf{M}(\mathbf{p})\ddot{\mathbf{u}}(t) + \mathbf{C}(\mathbf{p})\dot{\mathbf{u}}(t) + \mathbf{K}(\mathbf{p})\mathbf{u}(t) + \mathbf{G}_*(\mathbf{p}) = \mathbf{f}(t, \mathbf{p}), \tag{1}$$

$$\mathbf{u} = [\mathbf{u}_1 \quad \mathbf{u}_s \quad \mathbf{u}_2]^\top, \quad \mathbf{G}_* = [\mathbf{0} \quad \mathbf{G} \quad \mathbf{0}]^\top, \quad n = n_1 + n_s + n_2, \tag{2}$$

where $\mathbf{u}(t) \in \mathbb{R}^n$ represents the displacement, $\mathbf{M}, \mathbf{C}, \mathbf{K} \in \mathbb{R}^{n \times n}$ denote the mass, damping and stiffness matrices, and $\mathbf{f}(t, \mathbf{p}) \in \mathbb{R}^n$ the externally applied excitation. The order of the high fidelity system is n .

The localized response of the interior region \mathbf{u}_s is driven by the nonlinear nature of the component. We assume herein that $\mathbf{u}_s = \mathbf{x} + \mathbf{z}$, where \mathbf{x} represents an ideal system to be defined and \mathbf{z} the deviatoric response, capturing the difference between the ideal and the actual representation. This assumption implies that \mathbf{z} is dependent on the nonlinear terms \mathbf{G} . We further decompose the overall response $\mathbf{u}_x = [\mathbf{u}_1, \mathbf{x}_\alpha, \mathbf{x}_\gamma, \mathbf{x}_\beta, \mathbf{u}_2]^\top$, where the subscripts α, β denote the boundary variables between components C_1, C_2 , and C_s , respectively, and γ represents the inner variables of C_s . Thus, following Eq. (1):

$$\underbrace{\begin{bmatrix} \mathbf{M}_{11} & \mathbf{M}_{1\alpha} & \mathbf{0} & \mathbf{0} & \mathbf{0} \\ \mathbf{M}_{1\alpha}^\top & \mathbf{M}_{\alpha\alpha} & \mathbf{M}_{\gamma\alpha} & \mathbf{0} & \mathbf{0} \\ \mathbf{0} & \mathbf{M}_{\gamma\alpha}^\top & \mathbf{M}_{\gamma\gamma} & \mathbf{M}_{\gamma\beta} & \mathbf{0} \\ \mathbf{0} & \mathbf{0} & \mathbf{M}_{\gamma\beta}^\top & \mathbf{M}_{\beta\beta} & \mathbf{M}_{2\beta} \\ \mathbf{0} & \mathbf{0} & \mathbf{0} & \mathbf{M}_{2\beta}^\top & \mathbf{M}_{22} \end{bmatrix}}_{=\tilde{\mathbf{M}}} \begin{bmatrix} \ddot{\mathbf{u}}_1 \\ \ddot{\mathbf{x}}_\alpha \\ \ddot{\mathbf{x}}_\gamma \\ \ddot{\mathbf{x}}_\beta \\ \ddot{\mathbf{u}}_2 \end{bmatrix} + \tilde{\mathbf{C}}\dot{\mathbf{u}}_x + \tilde{\mathbf{K}}\mathbf{u}_x = \mathbf{f} + \mathbf{R}, \tag{3}$$

where the matrices $\tilde{\mathbf{C}}$ and $\tilde{\mathbf{K}}$ are expressed similar to $\tilde{\mathbf{M}}$, and \mathbf{R} is defined as:

$$\mathbf{R} = -[\mathbf{M}_{1\alpha}\ddot{\mathbf{z}}_\alpha + \mathbf{C}_{1\alpha}\dot{\mathbf{z}}_\alpha + \mathbf{K}_{1\alpha}\mathbf{z}_\alpha \quad \mathbf{0} \quad \mathbf{0} \quad \mathbf{0} \quad \mathbf{M}_{2\beta}^\top\ddot{\mathbf{z}}_\beta + \mathbf{C}_{2\beta}^\top\dot{\mathbf{z}}_\beta + \mathbf{K}_{2\beta}^\top\mathbf{z}_\beta]^\top \tag{4}$$

representing the deviatoric force terms on the exterior components that are driven by the internal response. This implies that coordinate \mathbf{x} describes the response under the additional excitation terms arising from \mathbf{R} . To complete the governing equations, the deviatoric terms are determined by:

$$\underbrace{\begin{bmatrix} \mathbf{M}_{\alpha\alpha} & \mathbf{M}_{\gamma\alpha} & \mathbf{0} \\ \mathbf{M}_{\gamma\alpha}^\top & \mathbf{M}_{\gamma\gamma} & \mathbf{M}_{\gamma\beta} \\ \mathbf{0} & \mathbf{M}_{\gamma\beta}^\top & \mathbf{M}_{\beta\beta} \end{bmatrix}}_{=\tilde{\mathbf{M}}_s} \begin{bmatrix} \ddot{\mathbf{z}}_\alpha \\ \ddot{\mathbf{z}}_\gamma \\ \ddot{\mathbf{z}}_\beta \end{bmatrix} + \tilde{\mathbf{C}}_s \dot{\mathbf{z}} + \tilde{\mathbf{K}}_s \mathbf{z} = \begin{bmatrix} -\mathbf{G}_\alpha(\mathbf{x}_\alpha + \mathbf{z}_\alpha, \mathbf{x}_\gamma + \mathbf{z}_\gamma) \\ -\mathbf{G}_\gamma(\mathbf{x} + \mathbf{z}) \\ -\mathbf{G}_\beta(\mathbf{x}_\gamma + \mathbf{z}_\gamma, \mathbf{x}_\beta + \mathbf{z}_\beta) \end{bmatrix} \quad (5)$$

where $\tilde{\mathbf{C}}_s$ and $\tilde{\mathbf{K}}_s$ are expressed similar to $\tilde{\mathbf{M}}_s$. The negative sign on Eq. (5) appears as the nonlinear terms \mathbf{G} of Eq. (1) have been transferred to the r.h.s. This way, the governing equations in Eq. (1) have been substituted by the mixed (ideal) system in Eq. (3) together with a set of nonlinear equations given in Eq. (5) to account for the deviatoric component $\mathbf{z} \in \mathbb{R}^{n_s}$.

2.2 POD-Based ROM in a Substructural Formulation

To derive a reduced representation of the problem described by Eq. (1), the response for a given operating parametric sample \mathbf{p}_j is assumed to span a low dimensional subspace $S \subset \mathbb{R}^n$. As such, the solution of Eq. (1) can be expressed in the form:

$$\mathbf{u}(t) = \mathbf{V}(\mathbf{p}_j)\mathbf{u}_r(t), \quad (6)$$

where $\mathbf{u}_r \in \mathbb{R}^r$, $r \ll n$ defines the components of the solution in the subspace S , represented by the projection basis $\mathbf{V}(\mathbf{p}_j)$. Thereafter, the system representation is obtained by means of a Galerkin projection, leading to an equivalent, low-order formulation of Eq. (1), where:

$$\mathbf{M}_r(\mathbf{p}_j) = \mathbf{V}(\mathbf{p}_j)^\top \mathbf{M}(\mathbf{p}_j) \mathbf{V}(\mathbf{p}_j) \quad \mathbf{G}_r(\mathbf{p}_j) = \mathbf{V}(\mathbf{p}_j)^\top \mathbf{G}(\mathbf{u}(t), \mathbf{p}_j). \quad (7)$$

The damping and stiffness matrices are projected similar to \mathbf{M}_r , whereas the force vector similar to \mathbf{G}_r . In this paper, we implement a POD-based approach that makes use of the substructural formulation presented in Sect. 2.1. By applying POD to collected time histories of the response, a solution manifold can be approximated for every parametric sample of a family of training realizations.

Here, two separate low-order subspaces are defined. First, based on Eq. (3), a projection basis is assembled from \mathbf{u}_x , responsible for approximating the solution manifold for the ideal system. The nonlinear component is treated in an isolated manner by deriving the respective subspace from the deviatoric component of the response \mathbf{z} , obtained through Eq. (5). The algorithmic procedure followed is presented in detail in Table 1.

For a new configuration, a projection basis is estimated utilizing a $k - NN$ clustering scheme. As indicated by Table 1, for an evaluation realization \mathbf{p}_q , the nearest training realizations are identified, and two local subspaces are assembled based on the respective approximated manifolds \mathbf{V}_x and \mathbf{V}_z of the training set. The

Table 1 Algorithmic process of the pROM

Notation:
 N_s : Number of training samples, N_T : Number of timesteps
 n : Full-order dimension, r : Reduced-order dimension

Input:
Parameter vector of training realizations $\mathbf{p} = [\mathbf{p}_1, \mathbf{p}_2, \dots, \mathbf{p}_{N_s}]$,
Realization \mathbf{p}_q to be approximated

Output: Quantity of interest for realization \mathbf{p}_q estimated with pROM

Training phase
*for $k=1, \dots, N_s$ do
–Simulate high fidelity model for $\mathbf{p} = \mathbf{p}_k$ and obtain displacement time histories
 $\mathbf{U}_{x,k} \in \mathbb{R}^{n \times N_T}$ (Eq. (3)) and $\mathbf{Z}_k \in \mathbb{R}^{n_s \times N_T}$ (Eq. (5))
–Perform POD to obtain local bases $\mathbf{V}_{x,k} \in \mathbb{R}^{n \times r_x}$ and $\mathbf{V}_{z,k} \in \mathbb{R}^{n_s \times r_z}$

Evaluation phase
*Identify neighboring training realizations on the parameter space
*Assemble neighboring local bases and perform POD to obtain $\mathbf{V}_{x,q}$ and $\mathbf{V}_{z,q}$
*Formulate the reduced-order matrices based on Eq. (7) for both
Eqs. (3) and (5) employing $\mathbf{V}_{x,q}$ and $\mathbf{V}_{z,q}$ respectively
*Evaluate the pROM approximation for quantity of interest \mathbf{Q}_q

pROM is then evaluated, and the resulting approximation is projected back to the original coordinates by Eq. (6).

3 Numerical Case Studies

In the following case studies, the parametric reduced-order model in a substructural formulation is denoted by pROM. The full-order model is based on a finite element analysis and is denoted as High Fidelity Model (HFM).

3.1 One-dimensional Rod

The finite discretization of a one-dimensional rod is considered first. We formulate our system in a nondimensionalized manner, dependent on the nominal parameters ρ , l , and EA representing the density, the overall length, and the axial rigidity of the rod, respectively. The M finite elements are spaced equally along the length, and variable $\xi = \frac{\text{position}}{l} \in [0, 1]$ denotes the nondimensionalized spatial position. We further assume an interior, nonlinear sub-region C_s , located in $\xi \in (\xi_1, \xi_2)$ with nonlinear interaction forces between all node pairs, formed as:

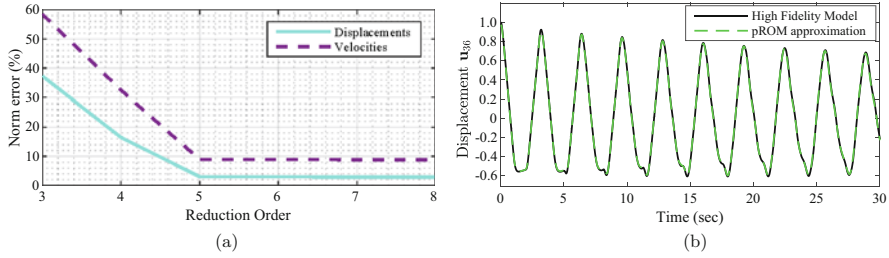


Fig. 1 Basis order study for reduction of the nonlinear component and response approximation with $r = 5$. High Fidelity denotes the full-order FEM. (a) Study on POD basis reduction order. (b) Example response approximation

$$g(w(t)) = r_1 * w(t) + r_2 * w^3(t) + r_3 * \dot{w}(t) + r_4 * \dot{w}^3(t) + h[w(t)], \quad (8)$$

where $w(t)$ denotes the relative displacement of the node pair and $h[w(t)]$ the forcing arising from hysteretic damping. This in turn is determined by:

$$\dot{h}(t) = (k_1 - k_2 \text{sign}(\dot{w}))h(t)\dot{w}. \quad (9)$$

We would like to note here that any hysteretic damping representation could be used in Eq. (9), including Bouc–Wen or Iwan models. A Bouc model is considered here for simplicity. Assuming the forcing between nodes i, j is defined as $g_{i,j}$, the nonlinearities in the boundary nodes α, β of C_s are of the form $\mathbf{G}_\alpha = g_{\alpha+1,\alpha}$, $\mathbf{G}_\beta = g_{\beta,\beta-1}$, whereas $\mathbf{G}_\gamma = -g_{i,i-1} + g_{i+1,i}$ with $i = \alpha + 1, \dots, \beta - 1$ corresponds to the internal ones.

We assume $\rho = 1, l = 1, EA = 1, r_1 = r_3 = 0.1M, r_2 = r_4 = 0.1M^3, k_1 = 0.5M$, and $(\xi_1, \xi_2) = (0.30, 0.40)$ for demonstration. We choose the initial conditions to excite the first mode of the linearized structure. The dependency pertains to parameter k_2 of the hysteretic model and the amplitude A of the excitation. This case study is similar to the one in [19]. To present our approach in a step-wise manner, in this example, we only apply POD in the interior C_s component (only assemble \mathbf{V}_z based on Table 1). The linear exterior regions are reduced based on modal decomposition, following the approach in [19]. For the evaluation phase, a 3 – NN scheme is employed.

To choose the reduction order of the projection basis \mathbf{V}_z , an example parametric domain is created with $M = 120, k_2 \in [4, 5]$ and $A \in [0.90, 1.10]$. The edge- and center-point of the domain represent the training realizations, whereas the validation set is chosen employing Latin hypercube sampling. Figure 1a depicts the average norm error across all validation samples. A reduction order of $r = 5$ is chosen to guarantee a robust and accurate performance. An example response approximation is provided in Fig. 1b for reference.

We evaluate the performance of the substructural pROM in a wide parametric domain as next. The k_2 variable controlling the hysteretic forcing ranges in

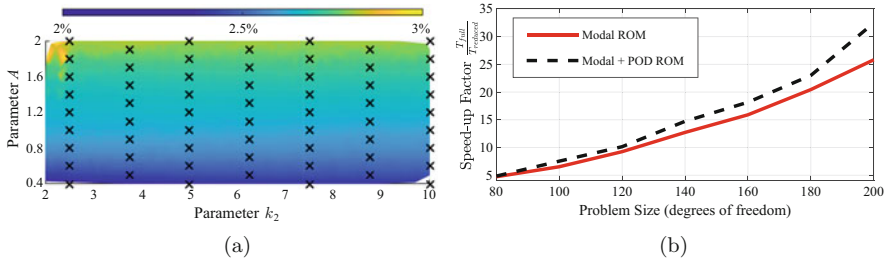


Fig. 2 Performance of the pROM. Training samples are indicated with black. Speed-up is compared to the Modal ROM [19] with an accuracy trade-off $\leq 0.5\%$. (a) Accuracy performance of the ROM. (b) Computational efficiency evaluation

[2.0, 10.0], whereas the amplitude term A in [0.40, 2.00]. The pROM performance is further compared to a global ROM, trained with all states of the training set, and the modal ROM formulated in [19]. The latter only reduces the linear regions employing modal decomposition. Thus, the accuracy is expected to be marginally better compared to our formulation that performs an additional POD reduction on the internal domain. The respective results are summarized in Fig. 2.

As depicted in Fig. 2a, the pROM delivers an accurate approximation across the whole domain of operation. These results imply that the ROM can capture the underlying dynamic phenomena in any region of the domain due to the local POD bases. As a comparison, the global ROM fails to provide an approximation with less than 20% error for any validation realization. The figure’s error pattern also indicates that an adaptive sampling of the training set might optimize the respective cost. Since large values of the A parameter lead to consistent higher errors, a refined sampling rate in that region might lead to an even more accurate approximation. In contrast, a coarser rate on the lower values might maintain accuracy while reducing computational resources.

In Fig. 2b, the computational efficiency of the pROM is depicted, compared against the savings from the modal ROM. The additional POD reduction of the nonlinear component leads to considerably greater speed-up, especially as the problem’s dimension increases. The trade-off remains acceptable, as the modal ROM delivers a maximum 0.5% more accurate representation in any case.

3.2 3D Cantilever Beam

Next, we consider a three-dimensional cantilever beam featuring plasticity, following a von Mises rule. The length l of the beam is 3000 mm; its height is 150 mm, whereas its width 300 mm. The beam is discretized using tetrahedral elements and assumes properties similar to steel: $E = 210$ GPa and $\rho = 8.050 \frac{\text{kg}}{\text{m}^3}$. The nonlinear component spans between [600 mm, 1200 mm].

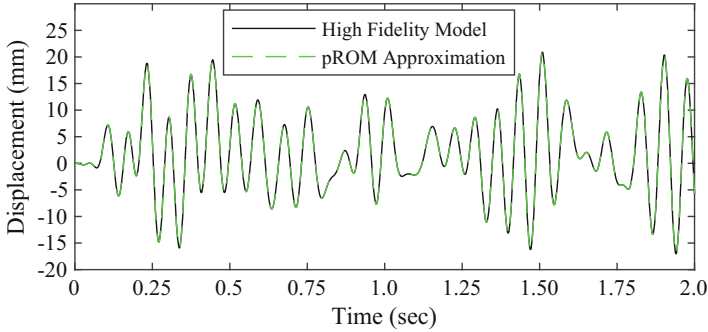


Fig. 3 Response approximation demonstrating the accuracy of the pROM for the 3D beam. The High Fidelity Model denotes the full-order FEM evaluation

A basis excitation is assumed. A low-pass filter is applied in a colored noise signal, and the resulting signal is multiplied by an amplitude factor. The excitation direction is assumed to be $\pi/4$. The colored noise includes components up to 200 Hz, spanning the case study's first four eigenmodes. Thus, the model is parameterized to the cut-off frequency ϕ , the amplitude term A , and the yield stress σ . This dependency formulation draws from actual operating systems' needs, where uncertainty may pertain to both the system properties and the excitation.

In this case, the complete algorithmic procedure of Table 1 is followed. Performing a study similar to Fig. 1a, the order of \mathbf{V}_x , \mathbf{V}_z reducing the exterior and internal components, is specified to be $r_x = 4$ and $r_z = 20$, respectively. The parametric domain of operation spans $[5.0, 100.0]$ for ϕ (Hz), $[1.0, 2.0]$ for A , and $[375, 425]$ for σ (MPa). Sampling is performed in a similar manner as previously and a 3-NN scheme is used for evaluation.

Figure 3 presents the quality of the pROM approximation on the nonlinear component's response. The respective time histories are almost identical, indicating an accurate reduction framework. Figure 4 further visualizes the precise approximation of the nonlinear terms of the case study, namely the stress state of the nonlinear component. The results indicate that the implemented pROM can reproduce the underlying response of the 3D beam accurately.

Table 2 summarizes the accuracy measures, indicating a robust pROM that manages to maintain a precise approximation across the whole parametric domain. Combined with the respective maximum threshold in estimating the nonlinear component's stress state, these findings suggest that the parametric dependencies are successfully infused into the low-order representation.

Regarding computational speed-up, the speed-up in Table 2 is relatively small compared to the computational toll reduction achieved for the 1D rod. This is attributed to the substantially increased dimension of the numerical example, and to the presence of nonlinearities in a constitutive level. These in turn create an efficiency bottleneck regarding the full-order evaluation of the nonlinear terms and require treatment with hyper-reduction techniques. Nonetheless, the focus of the

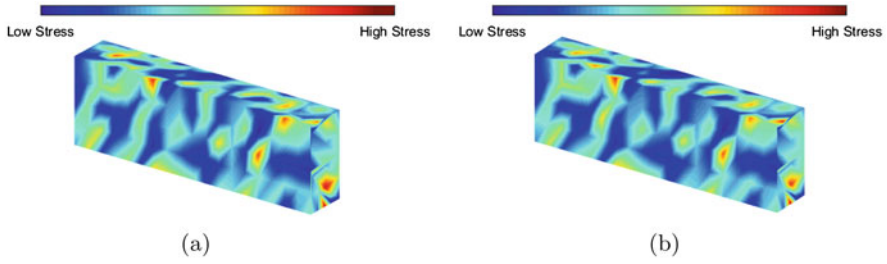


Fig. 4 Stress approximation performance of the pROM (Error 10%). The effective von Mises stress is visualized for the nonlinear component of the beam. (a) Stress visualization for the full model. (b) Stress approximation of pROM

Table 2 Evaluation of the pROM performance. Statistical measures of the error across the domain are presented along with the speed-up factor

Variable error norm	Mean (St. Dev.)	Maximum
Displacement— $\mathbb{R}E_{\mathbf{u}}$	<1%(0.15%)	<1%
Velocities— $\mathbb{R}E_{\mathbf{v}}$	<1%(0.10%)	1.04%
Nonlinear component stresses— $\mathbb{R}E_{\sigma}$	4.83%(3.75%)	14.75%

Speed-up factor of pROM evaluation $\frac{t_{HEM}}{t_{ROM}}$: 2.24

implemented substructural pROM formulation lies in providing a “proof of concept” example, and this remark can serve as a guideline for future research.

4 Conclusions

A physics-based pROM is derived in this study, capable of treating nonlinear components of complex systems separately. Contrary to CMS, the pROM couples the global system dynamics to the deviatoric localized phenomena introduced by the nonlinear features by manipulating the substructural formulation in [20]. The implemented pROM yields sufficient precision in approximating the component’s and system’s behavior across various parameters while substantially reducing the computational time.

However, certain limitations ought to be acknowledged. Firstly, efficiency needs to be further validated in larger-scale examples, where hyper-reduction techniques might be necessary. Additionally, future work should potentially address true-scale systems, comprising multiple components with nonlinearities of different natures, to generalize the applicability of the pROM.

Acknowledgments This research has been funded from the Sandia National Laboratories, the European Research Council, under the ERC Starting Grant WINDMIL (ERC-2015-StG #679843) on the topic of “Smart Monitoring, Inspection and Life-Cycle Assessment of Wind Turbines,”

and the European Union's Horizon 2020 research and innovation program under the Marie Skłodowska-Curie grant agreement No. 795917 "SiMAero, Simulation-Driven and On-line Condition Monitoring with Applications to Aerospace". Sandia National Laboratories is a multitechnology laboratory managed and operated by National Technology and Engineering Solutions of Sandia, LLC, a wholly owned subsidiary of Honeywell International Inc., for the U.S. Department of Energy's National Nuclear Security Administration under contract DE-NA0003525. This paper describes objective technical results and analysis. Any subjective views or opinions that might be expressed in the paper do not necessarily represent the views of the U.S. Department of Energy or the US Government.

References

1. K. Tatsis, V. Dertimanis, C. Papadimitriou, E. Lourens, E. Chatzi, A general substructure-based framework for input-state estimation using limited output measurements. *Mech. Syst. Signal Process.* **150**, 107223 (2021)
2. D. de Klerk, D.J. Rixen, S. Voormeeren, General framework for dynamic substructuring: history, review and classification of techniques. *AIAA J.* **46**(5), 1169–1181 (2008)
3. M.S. Allen, D. Rixen, M. Van der Seijs, P. Tiso, T. Abrahamsson, R.L. Mayes, *Substructuring in Engineering Dynamics* (Springer, Berlin, 2020)
4. M.K. Mahdiabadi, E. Buchmann, D. Xu, A. Bartl, D.J. Rixen, Dynamic substructuring of geometrically nonlinear finite element models using residual flexibility modes, in *Dynamics of Coupled Structures*, vol. 4 (Springer, 2017), pp. 215–223
5. R.J. Kuether, M.S. Allen, J.J. Hollkamp, Modal substructuring of geometrically nonlinear finite element models with interface reduction. *AIAA J.* **55**(5), 1695–1706 (2017)
6. F. Wenneker, P. Tiso, A substructuring method for geometrically nonlinear structures, in *Dynamics of Coupled Structures*, vol. 1 (Springer, Berlin, 2014), pp. 157–165
7. L. Wu, P. Tiso, K. K. Tatsis, E. Chatzi, F. van Keulen, A modal derivatives enhanced Rubin substructuring method for geometrically nonlinear multibody systems. *Multibody Syst. Dyn.* **45**(1), 57–85 (2019)
8. G. Kerschen, M. Peeters, J.C. Golinval, A.F. Vakakis, Nonlinear normal modes, part I: a useful framework for the structural dynamicist. *Mech. Syst. Signal Process.* **23**(1), 170–194 (2009)
9. R.J. Kuether, L. Renson, T. Detroux, C. Grappasonni, G. Kerschen, M.S. Allen, Nonlinear normal modes, modal interactions and isolated resonance curves. *J. Sound Vib.* **351**, 299–310 (2015)
10. M. Falco, M.K. Mahdiabadi, D.J. Rixen, Nonlinear substructuring using fixed interface nonlinear normal modes, in *Dynamics of Coupled Structures*, vol. 4 (Springer, Berlin, 2017), pp. 205–213
11. F.M. Gruber, D.J. Rixen, Dual Craig-Bampton component mode synthesis method for model order reduction of nonclassically damped linear systems. *Mech. Syst. Signal Process.* **111**, 678–698 (2018)
12. J. Lee, A parametric reduced-order model using substructural mode selections and interpolation. *Comput. Struct.* **212**, 199–214 (2019)
13. C. Joannin, F. Thouverez, B. Chouvion, Reduced-order modelling using nonlinear modes and triple nonlinear modal synthesis. *Comput. Struct.* **203**, 18–33 (2018)
14. T. Simpson, D. Giagopoulos, V. Dertimanis, E. Chatzi, On dynamic substructuring of systems with localised nonlinearities, in *Dynamic Substructures*, vol. 4 (Springer, 2020), pp. 105–116
15. Y. Jin, K. Lu, C. Huang, L. Hou, Y. Chen, Nonlinear dynamic analysis of a complex dual rotor-bearing system based on a novel model reduction method. *Appl. Math. Modell.* **75**, 553–571 (2019)
16. S. Im, E. Kim, M. Cho, Reduction process based on proper orthogonal decomposition for dual formulation of dynamic substructures. *Comput. Mech.* **64**(5), 1237–1257 (2019)

17. K. Vlachas, K. Tatsis, K. Agathos, A.R. Brink, E. Chatzi, A local basis approximation approach for nonlinear parametric model order reduction (2020). <https://arxiv.org/pdf/2003.07716.pdf>
18. K. Vlachas, K. Tatsis, K. Agathos, A.R. Brink, E. Chatzi, A physics-based, local pod basis approach for multi-parametric reduced order models, in *Conference Proceedings of ISMA-USD* (2020). <https://doi.org/10.3929/ethz-b-000442909>
19. D. Quinn, A. Brink, Global system reduction order modeling for localized feature inclusion. *J. Vib. Acoust.* **143**(4), 041006 (2021)
20. D.D. Quinn, Modal analysis of jointed structures. *J. Sound Vib.* **331**(1), 81–93 (2012)

Nonlinear Vibration of Functionally Graded Shallow Shells Resting on Elastic Foundations



Lidiya Kurpa, Tetyana Shmatko, and Jan Awrejcewicz

1 Introduction

Many elements of the modern constructions modelled by shallow shells resting on elastic foundations are fabricated of functionally graded materials (FGM). It is connected with essential advantages of the class composite materials such as continuous and smooth variation in properties in one or several directions. In addition, they are able to withstand high-temperature environments. The topic of dynamic analysis of FG plates and shells resting on elastic foundations draws continuously the attention of a lot of researchers [1–5]. There were developed different deformation theories and methods to solve technical problems that occur when behaviour of these plates and shells is studying [6–9]. Recent literature reviews concerning investigations of behaviour of FGM plates and shells resting on the elastic foundation are published in many works [2, 4, 10–13].

Despite a large number of the published papers and monographs devoted to this problem [2–7, 14, 15], there are many unsolved or insufficiently studied issues in the field of geometrically nonlinear vibrations. Among the problems, there is a problem of geometrically nonlinear vibrations of FG shallow shells. This is especially true for FG shells with a complex shape. In the present paper, we study the named problem. A distinctive feature of the work is the use of the R-functions method (RFM) [16]. Recently in the works [17–20], this method has been developed for the solution

L. Kurpa

Department of Applied Mathematics, National Polytechnic University “KhPI”, Kharkov, Ukraine

T. Shmatko (✉)

Department of Higher Mathematics, National Polytechnic University “KhPI”, Kharkov, Ukraine

J. Awrejcewicz

Department of Automation, Biomechanical and Mechatronics, Lodz University of Technology, Lodz, Poland

of the problems on the vibrations of FG laminated plates and shallow shells in the framework of the FSDT. In the work, the method is extended first time to shells resting on an elastic foundation using the higher order shell theory.

2 Mathematical Formulation and Solution Method

Shallow shells and plates made of functionally graded materials (mixture of metal and ceramics) resting on elastic foundations (Fig. 1) are considered. A planform of the shell can be complex and fixed by different ways.

It is assumed that the temperature is varied only in the thickness direction. Young’s modulus of ceramic and metal E_c , E_m depend on temperature according to law [13, 14]:

$$P_j(T) = P_0 \left(P_{-1}T^{-1} + 1 + P_1T + P_2T^2 + P_3T^3 \right), \tag{1}$$

where $P_0, P_{-1}, P_1, P_2, P_3$ are coefficients determined for each specific material. A table of values of these coefficients for some materials is presented in [2, 4, 14].

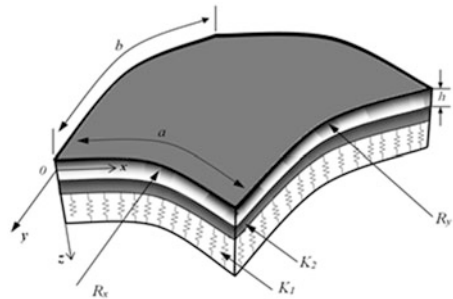
The effective material properties of the FGMs are calculated by Voigt’s model [13], provided that the Poisson’s ratio ν is a constant [1, 9]. The Young modulus E_f and density ρ of FG structure are defined as:

$$E_f(z, T) = (E_c(T) - E_m(T)) V_c + E_m(T), \tag{2}$$

$$\rho(z) = (\rho_c - \rho_m) V_c + \rho_m, \quad V_c = \left(\frac{2z + h}{2h} \right)^p. \tag{3}$$

In formulas (1, 2) z is the distance between the current point and the shell midsurface, the index p ($0 \leq p < \infty$) denotes the volume fraction exponent of ceramics V_c which is connected with volume fraction of metal V_m by relation $V_c + V_m = 1$. So effective module E_f (2) depends on constituent component of

Fig. 1 FGM shallow shell on elastic foundation



temperature T and applicate z . We consider shells with the same temperatures on the top and bottom of the object. By these assumptions, motion equations of plates and shells based on higher order shear deformation shell theory (HSDT) worked out by Reddy [21] and Reddy and Liu [22] can be written in the following form:

$$N_{11,x} + N_{12,y} - k_1 Q_1 = I_1 u_{,tt} + I_2 \psi_{x,tt} - c_1 I_4 w_{,xtt},$$

$$N_{12,x} + N_{22,y} - k_2 Q_2 = I_1 v_{,tt} + I_2 \psi_{y,tt} - c_1 I_4 w_{,ytt},$$

$$\begin{aligned} &Q_{1,x} + Q_{2,y} + (N_{11}w_{,x} + N_{12}w_{,y})_{,x} + (N_{12}w_{,x} + N_{22}w_{,y})_{,y} \\ &+ c_1 (P_{11,xx} + 2P_{12,xy} + P_{22,yy}) - c_2 (R_{1,x} + R_{2,y}) - K_W w + K_P \nabla^2 w = \\ &= I_1 w_{,tt} - c_1^2 I_7 (w_{,xx} + w_{,yy})_{,tt} + c_1 I_4 (u_{,x} + v_{,y})_{,tt} + c_1 I_5 (\psi_{x,x} + \psi_{y,y})_{,tt} \end{aligned}$$

$$M_{11,x} + M_{12,y} - Q_1 + c_2 R_1 - c_1 (P_{11,x} + P_{12,y}) = I_2 u_{,tt} + I_3 \psi_{x,tt} - c_1 I_5 w_{,xtt},$$

$$M_{12,x} + M_{22,y} - Q_2 + c_2 R_2 - c_1 (P_{12,x} + P_{22,y}) = I_2 v_{,tt} + I_3 \psi_{y,tt} - c_1 I_5 w_{,ytt},$$

where K_W and K_P are the Winkler and Pasternak parameters for elastic foundation, $N = \{N_{11}, N_{22}, N_{12}\}$ are the resultant forces in plane, $M = \{M_{11}, M_{22}, M_{12}\}$ are the bending and twisting moments, $P = \{P_{11}, P_{22}, P_{12}\}$ and $R = \{R_1, R_2\}$ are the higher order stress resultants, $Q = \{Q_1, Q_2\}$ are the resultant forces out of plane. These values are defined as

$$\begin{bmatrix} N \\ M \\ P \end{bmatrix} = \begin{bmatrix} A & B & E \\ B & D & F \\ E & F & H \end{bmatrix} \begin{bmatrix} \varepsilon^0 \\ k^0 \\ k^{(2)} \end{bmatrix}, \quad \begin{bmatrix} Q \\ R \end{bmatrix} = \begin{bmatrix} A & D \\ D & F \end{bmatrix} \begin{bmatrix} \varepsilon^0 \\ k^{(2)} \end{bmatrix}$$

where A_{ij}, B_{ij} , etc. are the shell stiffness, defined by

$$(A_{ij}, B_{ij} D_{ij}, E_{ij} F_{ij}, H_{ij}) = \int_{-h/2}^{+h/2} Q_{ij}(z, T) (1, z, z^2, z^3, z^4, z^6) dz, \quad i, j = 1, 2, 3$$

$$(A_{ij}, D_{ij}, F_{ij}) = \int_{-h/2}^{+h/2} Q_{ij}(z, T) (1, z^2, z^4) dz, \quad i, j = 4, 5$$

$$\{\varepsilon^0\} = \{\varepsilon_{11}^0, \varepsilon_{22}^0, \varepsilon_{12}^0\} = \left\{ u_{,x} - k_1 w + \frac{1}{2} w_{,x}^2, v_{,y} - k_2 w + \frac{1}{2} w_{,y}^2, u_{,y} + v_{,x} + w_{,x} w_{,y} \right\},$$

$$\varepsilon_{13}^0 = \psi_y + w_{,y}, \quad \varepsilon_{23}^0 = \psi_x + w_{,x}, \quad \{k^0\} = \{k_{11}^0, k_{22}^0, k_{12}^0\} = \{\psi_{x,x}; \psi_{y,y}; \psi_{x,y} + \psi_{y,x}\}$$

$$\{k^{(2)}\} = \{k_{11}^{(2)}, k_{22}^{(2)}, k_{12}^{(2)}\} = -c_1 \{(\psi_{x,x} + w_{,xx}); (\psi_{y,y} + w_{,yy}); (\psi_{x,y} + \psi_{y,x} + 2w_{,xy})\},$$

$$k_{13}^{(2)} = -c_2 (\psi_y + w_{,y}), \quad k_{23}^{(2)} = -c_2 (\psi_x + w_{,x}), \quad c_1 = \frac{4}{3h^2}; \quad c_2 = 3c_1$$

where $k_1 = 1/R_x$, $k_2 = 1/R_y$ are the principal curvatures of the shell along the coordinates x and y , respectively.

$$(I_1, I_2, I_3, I_4, I_5, I_7) = \int_{-h/2}^{+h/2} \rho(z) (1, z, z^2, z^3, z^4, z^6) dz,$$

$$Q_{11} = Q_{22} = \frac{E_f(z, T)}{1 - \nu_f^2}, \quad Q_{12} = \nu_f Q_{11}, \quad Q_{13} = Q_{23} = 0;$$

$$Q_{33} = Q_{44} = Q_{55} = \frac{E_f(z, T)}{2(1 + \nu_f)}.$$

If $c_1 = 0$, $c_2 = 0$ then we have motion equations corresponding to the first-order shear deformation theory (FSDT). Influence of the foundation is taken into account through relation [8] $p_0 = K_W w - K_P \nabla^2 w$.

3 Solution Method

Proposed method consists of three steps. Linear vibration problem is solved at the first step. To solve this problem the R-functions theory combined with variational Ritz’s method (RFM) is used. The main advantage of the R-functions theory is a possibility to build admissible functions in analytical form practically for an arbitrary domain. Application of Ritz’s method allows to use the admissible functions which satisfy the essential boundary conditions. Eigen values and eigen functions $w_1^{(e)}(x, y)$, $u_1^{(e)}(x, y)$, $v_1^{(e)}(x, y)$, $\psi_{x1}^{(e)}(x, y)$, $\psi_{y1}^{(e)}(x, y)$ found and presented in analytical form are applied in the second step. Auxiliary inhomogeneous task of elasticity problem type is solved by RFM also. Solution of this auxiliary problem allows to reduce the initial system of the differential equations to the following second-order nonlinear differential equation:

$$\ddot{y}(t) + \omega_L^2 y_1(t) + y_1^2(t)\beta + y_1^3(t)\gamma = 0. \tag{4}$$

Solution of Eq. (4) is carried out in the third step. Process of the proposed algorithm is the same to approach described in detail in works [17–19]. It should be mentioned that values for coefficients of Eq. (4) have been obtained in analytical form. They are expressed through the double integrals along the given domain [17].

Solution of Eq. (4) was found numerically using the classical 4-th order Runge-Kutta method.

4 Numerical Results

4.1 Test Problem. Shells with Rectangular Shape of Plan

Test 1 First, we validate the proposed approach on the problem about linear vibration of FG simply supported cylindrical panel with square planform made of Al/Al_2O_3 . The material properties are:

$$E_m=70GPa, \rho_m=2702\text{ kg/m}^3, E_c=380GPa, \rho_c=3800\text{ kg/m}^3, \nu_m = \nu_c=0.3.$$

Comparison of the dimensionless frequencies $\Lambda = \omega_L h\sqrt{\rho_c/E_c}$ calculated by the RFM with results obtained with the help of another methods [4, 23, 24] for different values of the gradient index p , curvatures a/R_x and thickness a/h is shown in Table 1.

Here we can see a good agreement of results obtained by the proposed approach with compared ones.

Test 2 As a second test example, we consider nonlinear vibration of FG simply supported cylindrical panel resting on elastic foundations with square planform. Geometrical parameters of the shallow shell are: $a/b = 1$; $2b/R = 0.8$; $2b/h = 20$; $h = 1$ mm. FG materials ($ZrO_2/Ti - 6Al - 4V$) is fabricated of metal $Ti - 6Al - 4V$ and ceramics Zirconia (ZrO_2). Poisson's ratio is assumed to be constant and put as 0.3. Young's modulus and density at the room temperature ($T_0 = 300$ K) are respectively:

$$E_m = 105.6981GPA, \quad \rho_m = 4427\text{ Kg/m}^3, \quad E_c = 168.0629\text{ GPA},$$

$$\rho_c = 3000Kg/m^3.$$

Table 1 Comparison of the dimensionless frequencies for FGM cylindrical panel

a/h	a/R_x	Method	$p = 0$	$p = 0.5$	$p = 1$	$p = 4$	$p = 10$
5	0.5	RFM(HSDT)	0.2141	0.1804	0.1607	0.1404	0.1329
		[4]	0.2169	0.1799	0.1589	0.1301	0.1204
		[23]	0.2153	0.1855	0.1678	0.1413	0.1328
		[24]	0.2113	0.1814	0.1639	0.1367	0.1271
5	1	RFM(HSDT)	0.2271	0.1945	0.1758	0.1476	0.1385
		[4]	0.2329	0.1944	0.1732	0.1402	0.1286
		[23]	0.2239	0.1945	0.1769	0.1483	0.1380
		[24]	0.2164	0.1879	0.1676	0.1394	0.1286

Table 2 Comparison of the present results for dimensionless frequency parameter of the cylindrical simply supported shells with corresponding results in [4]

(k_1, k_g)	T_t/T_b	Method	$p = 0$	$p = 0.5$	$p = 2$	$p = 5$
$k_w = 100 \quad k_g = 0$	$T_t = 400T_b = 400$	RFM (FSDT)	18.24	16.31	14.77	14.10
		RFM (HSDT)	18.45	16.50	14.93	14.28
		[4]	17.19	15.83	14.72	14.23
$k_w = 100 \quad k_g = 10$	$T_t = 400T_b = 400$	RFM (FSDT)	24.67	22.42	20.66	19.89
		RFM (HSDT)	24.82	22.57	20.78	20.02
		[4]	24.20	22.38	20.90	20.26

Table 3 Comparison of nonlinear to linear ratio ω_{NL}/ω_L with corresponding results in [4]

(k_w, k_g)	p	Method	Λ	W_{\max} / h				
				0.2	0.4	0.6	0.8	1
(100,0)	2	[4]	14.72	1.0040	1.0160	1.0356	1.0625	1.0961
		RFM	14.89	1.0023	1.0099	1.0240	1.0459	1.0765
(100,10)	0	[4]	24.20	1.0025	1.0101	1.0227	1.0399	1.0618
		RFM	24.47	1.0018	1.0073	1.0170	1.0313	1.0505
	0.5	[4]	22.38	1.0023	1.0091	1.0203	1.0358	1.0554
		RFM	22.42	1.0016	1.0068	1.0157	1.0289	1.0464
	2	[4]	20.905	1.0020	1.0080	1.0178	1.0315	1.0488
		RFM	20.747	1.0015	1.0062	1.0144	1.0262	1.0419
	5	[4]	20.26	1.0019	1.0074	1.0166	1.0294	1.0455
		RFM	20.03	1.0014	1.0059	1.0136	1.0248	1.0395

Earlier this problem was solved in article [4] by H-S Shen and H. Wang. Results obtained in the work for dimensionless frequency parameter $\Lambda = \Omega \ b^2 \sqrt{\rho_0/E_0}/h$ by both the theories (HSDT and FSDT) are compared with the results given in work [4] in Table 2. Note that E_0 and ρ_0 become E_m and ρ_m at the room temperature $T_0 = 300 \text{ K}$. Values k_{1w} , k_{2G} are defined as:

$$k_w = \overline{K}_{1w}(2b)^4 / (E_m h^3), \quad k_g = \overline{K}_{2G}(2b)^2 / (E_m h^3).$$

Comparison of the ratio nonlinear frequency to linear ω_{NL}/ω_L for the cylindrical panel at the temperature $T_b = T_t = 400 \text{ K}$ is shown in Table 3.

Test 2 demonstrates the results from the present method are in good agreement with the existing results.

4.2 Shells with a Complex Planform Resting on Elastic Foundation

New results for shallow shells with a complex planform were obtained. Let us consider the shallow shell resting on an elasticity foundation with planform shown in Fig. 2.

Suppose that shell is clamped completely including the cut-out. We will analyse two kinds of FGM: $Si_3N_4/SUS304$ and $ZrO_2/Ti - 6Al - 4V$. Geometrical dimensions are as follows:

$$T_b = T_t = 300 \text{ K}; k_1 = 0.2; k_2 = 0; 0.2; h/2a = 0.1; a_1/a = 0.2; a_1 = b_1; r/2a = 0.25.$$

Solution structure [16–20] for shells with complete clamped boundary can be taken as:

$$w = \omega\Phi_1, u = \omega\Phi_2, v = \omega\Phi_3, \psi_x = \omega\Phi_4, \psi_y = \omega\Phi_5 \tag{5}$$

where $\Phi_i, i = \overline{1,5}$ are indefinite components of structure [16] presented as an expansion in a series of some complete system (power polynomials, trigonometric polynomials, splines, etc.). Function $\omega(x, y)$ is constructed by the R-functions theory and vanished on whole boundary. In the given case this function has the following form:

$$\omega(x, y) = ((f_1 \wedge_0 f_2) \wedge ((f_3 \wedge_0 f_4) \wedge (f_5 \wedge_0 f_6))) \wedge_0 (f_7 \vee_0 f_8),$$

where symbols \wedge_0, \vee_0 denote the R-operations [16]. Functions $f_i, i = \overline{1,8}$ are defined as:

Fig. 2 Complex planform of FGM shallow shell

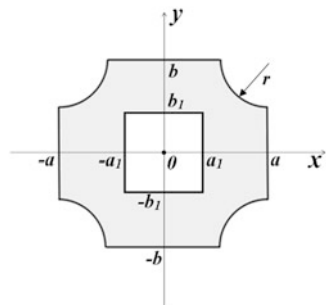


Table 4 Natural frequency parameter of the FGM ($Si_3N_4/SUS304$) clamped cylindrical shells (top) and spherical shells (bottom) resting on elastic foundation

p	$(k_w, k_g) (0,0)$	$(k_w, k_g) (100,0)$	$(k_w, k_g) (100,10)$	$(k_w, k_g) (100,100)$
Cylinder ($k_1 = 0.2; k_2 = 0$)				
0	75.301	77.512	91.098	166.912
0.5	52.148	53.901	64.548	117.595
1	45.610	47.245	57.099	102.590
2	40.680	42.228	51.475	90.837
5	36.676	38.162	46.951	81.226
10	34.930	36.400	45.052	77.371
Sphere ($k_1 = 0.2; k_2 = 0.2$)				
0	75.497	77.702	91.261	167.025
0.5	52.282	54.031	64.656	117.569
1	45.726	47.356	57.189	102.564
2	40.781	42.325	51.553	90.816
5	36.766	38.249	47.021	81.211
10	35.018	36.484	45.119	77.359

$$\begin{aligned}
 f_1 &= (a^2 - x^2) / 2a \geq 0, & f_2 &= (b^2 - y^2) / 2b \geq 0, \\
 f_{3,4} &= ((x \mp a)^2 + (y - b)^2 - r^2) / 2r \geq 0, & f_{5,6} &= ((x \pm a)^2 + (y + b)^2 - r^2) / 2r \geq 0, \\
 f_7 &= (x^2 - a_1^2) / 2a_1 \geq 0, & f_8 &= (y^2 - b_1^2) / 2b_1 \geq 0
 \end{aligned}$$

Indefinite components $\Phi_i, i = \overline{1, 5}$ of structures (5) were expanded in power series with account of problem symmetry [17–20]. To approximate indefinite component Φ_1 it was taken twenty-eight terms of the polynomials series and other indefinite components were approximated by fifteen terms. Variation of the natural frequency parameter for FGM ($Si_3N_4/SUS304$) cylindrical and spherical shells resting on elastic foundation with respect to volume fraction p and parameters of the foundation k_w, k_g is presented in Table 4.

As follows from Table 4 influence of curvatures is not essential for complete clamped shallow shells. More effect occurs with an increase of gradient index. The natural frequencies decrease while the gradient index increases as for cylindrical so for spherical shells. The results confirm that fundamental frequencies become higher when shallow shells are resting on elastic foundation. Effect of Winkler foundation stiffness on natural frequency is essentially lower than the influence of the shearing layer stiffness of the foundation.

In Fig. 3 behaviour of the backbone curves for clamped cylindrical shells made of (FGM $Si_3N_4/SUS304$) for fixed gradient index $p = 0.5$ and $p = 2$ and different values of the characteristics of the elastic foundations is shown.

As follows from Fig. 3 influence of characteristics of elastic foundation is more essential than value of the gradient index.

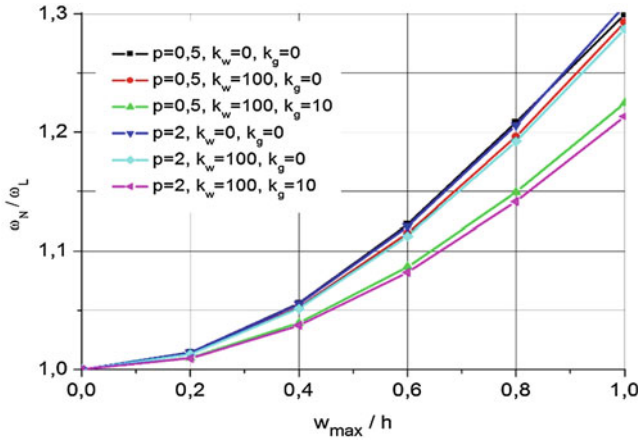


Fig. 3 Nonlinear to linear frequency ratio ω_{NL}/ω_L for ($Si_3N_4/SUS304$) clamped cylindrical shell resting on elastic foundation ($T_b = T_t = 300$ K, $k_1 = 0.5$; $k_2 = 0$; $h/2a = 0.1$; $a/b = 1$; $a_1 = b_1$; $a_1/a = 0.2$; $p = 0.5$; $p = 2$)

5 Conclusions

In this work, the R-functions method is used for the first time to study the free linear and geometrically nonlinear vibrations of functionally graded shallow shells with complex shape in plan resting on two-parameter elastic foundation. The material properties of FGMs are assumed to be temperature independent. Voight’s model is applied to calculate the effective material properties of FGMs. Mathematical model of the problem is carried out in the framework of two theories: FSDT and HSDT. Considered test problems confirm the validation of the proposed approach and developed software. New results for shells with a complex planform are presented and can be used by engineers in the design of the thin-walled elements of the modern constructions.

References

1. Z. Am, A.F. Radwan, On the simple and mixed first-order theories for functionally graded plates resting on elastic foundations. *Meccanica* **48**, 1501–1516 (2013)
2. M. Mohammadi, M. Arefi, R. Dimitra, F. Tornabene, Higher-order thermo-elastic analysis of FG-CNTR cylindrical vessels surrounded by Pasternak foundation. *Nanomaterials* **9**(1), 79, 1–21 (2019)
3. S.M. Ghumare, A.S. Sayyad, Analysis of functionally graded plates resting on elastic foundation and subjected to non-linear hygro-thermo-mechanical loading. *JMST Adv.* **1**, 233–248 (2019)
4. H.W. Hui-Shen, Nonlinear vibration of shear deformable FGM cylindrical panels resting on elastic foundations in thermal environments. *Composites Part B* **60**, 167–177 (2014)

5. M.H. Amini, M. Soleimani, A. Rastgoo, Three-dimensional free vibration analysis of functionally graded material plates resting on an elastic foundation. *Smart Mater. Struct.* **18**, 1–9 (2009)
6. P. Malekzadeh, Three-dimensional free vibration analysis of thick functionally graded plates on elastic foundations. *Compos. Struct.* **89**, 367–373 (2009)
7. H.-T. Thai, D.-H. Choi, A simple refined theory for bending, buckling and vibration of thick plates resting on elastic foundation. *Int. J. Mech. Sci.* **73**, 40–52 (2013)
8. H.-T. Thai, T.P. Vo, A new sinusoidal shear deformation theory for bending, buckling, and vibration of functionally graded plates. *App. Math. Model.* **37**, 3269–3281 (2013)
9. A. Hasani Baferani, A.R. Saidi, H. Ehteshami, Accurate solution for free vibration analysis of functionally graded thick rectangular plates resting on elastic foundation. *Compos. Struct.* **93**, 1842–1853 (2011)
10. A.S. Sayyad, Y.M. Ghugal, On the free vibration analysis of laminated composite and sandwich plates: A review of recent literature with some numerical results. *Compos. Struct.* **129**, 177–201 (2015)
11. D.K. Jha, T. Kant, R.K. Singh, A critical review of recent research on functionally graded plates. *Compos. Struct.* **96**, 833–849 (2013)
12. E. Carrera, S. Brischetto, Modeling and analysis of functionally graded beams, plates and shells-Part I. *Mech. Adv. Mater. Struct.* **17**(8), 585 (2010)
13. E. Carrera, S. Brischetto, Modeling and analysis of functionally graded beams, plates and shells-Part II. *Mech. Adv. Mater. Struct.* **18**(1), 1–2 (2011)
14. H.-S. Shen, *Functionally graded materials nonlinear analysis of plates and shells* (CRC Press, Boca Raton, 2009)
15. M. Amabili, *Nonlinear vibration and stability of shells and plates* (Cambridge University Press, Cambridge, 2008)
16. V.L. Rvachev, *The R-functions theory and its applications*. Kiev: Nauk.Dumka (in Russian) (1982)
17. J. Awrejcewicz, L. Kurpa, T. Shmatko, Investigating geometrically nonlinear vibrations of laminated shallow shells with layers of variable thickness via the R-functions theory. *J. Comp. Struct.* **125**, 575–585 (2015)
18. J. Awrejcewicz, L. Kurpa, T. Shmatko, Linear and nonlinear free vibration analysis of laminated functionally graded shallow shells with complex plan form and different boundary conditions. *J. Non-linear Mech.* **107**, 161–169 (2018)
19. L.V. Kurpa, T.V. Shmatko, Buckling and free vibration analysis of functionally graded sandwich plates and shallow shells by the Ritz method and the R-functions theory, *J. Mechanical Engineering Science, part C*, **0** (0) 1–12 (2020)
20. L.V. Kurpa, T.V. Shmatko, Investigation of free vibrations and stability of functionally graded three-layer plates by using the R-Functions theory and variational methods. *J. Math. Sci.* **249**(3), 496–520 (2020)
21. J.N. Reddy, A simple high-order theory for laminated composite plates. *J. Appl. Mech ASME* **51**, 745–752 (2003)
22. J.N. Reddy, C.F. Liu, A higher-order shear deformation theory of laminated elastic shells. *Int. J. Eng. Sci.* **23**, 319–330 (1985)
23. H. Matsunaga, Free vibration and stability of functionally graded shallow shells according to a 2-D higher-order deformation theory. *Compos Struct* **84**, 132–146 (2008)
24. M. Farid, P. Zahedinejad, P. Malekzaden, Three dimensional temperature dependent free vibration analysis of functionally graded material cylindrical panels resting on two parameter elastic foundation using a hybrid semianalytic, differential quadrature method. *Mater. DES* **31**, 2–13 (2010)

High-Order Approximation of Global Connections in Planar Systems with the Nonlinear Time Transformation Method



Bo-Wei Qin, Kwok-Wai Chung, Antonio Algaba,
and Alejandro J. Rodríguez-Luis

1 Introduction

Global connections (homoclinic and heteroclinic orbits) are important organizing centers in the dynamics of nonlinear systems. As it is very difficult to find exact connecting orbits (see, for instance, [1]), the Melnikov method is the most employed technique to guarantee their existence in planar systems [2, 3]. Several perturbation methods to approximate these bifurcations are frequently used [4–7]. Also for this task, the nonlinear time transformation (NTT) method, using trigonometric functions, was introduced in [8] and was successfully used in [9, 10].

The presence of global connections is guaranteed when a Takens–Bogdanov (double-zero eigenvalue with geometric multiplicity one) or a Hopf-zero bifurcation of equilibria appears [11, 12]. A very rich bifurcation scenario is expected in both cases (see, for instance, [13–20] for the Takens–Bogdanov and [21–26] for the Hopf-zero bifurcations, and the references therein).

B.-W. Qin

School of Mathematical Sciences, Fudan University, Shanghai, P.R. China
e-mail: boweiqin@fudan.edu.cn

K.-W. Chung

Department of Mathematics, City University of Hong Kong, Kowloon, Hong Kong, P.R. China
e-mail: makchung@cityu.edu.hk

A. Algaba

Departamento de Ciencias Integradas, Centro de Estudios Avanzados en Física, Matemática y Computación, Universidad de Huelva, Huelva, Spain
e-mail: algaba@uhu.es

A. J. Rodríguez-Luis (✉)

Departamento de Matemática Aplicada II, E.T.S. Ingenieros, Universidad de Sevilla, Sevilla, Spain
e-mail: ajrluis@us.es

The main purpose of this paper is the study, using the NTT method, of a homoclinic connection in a family of Rayleigh–Duffing oscillators (see Sect. 2.1). We also review its very recent application for obtaining a perturbation solution of a global connection up to any wanted order (both in the parameter space and in the phase plane). We illustrate that the NTT method is an efficient alternative to Melnikov method in the computation of the high-order coefficients of the Poincaré application near the global connection (because this calculation is impracticable due to the complicate integrals that appear in Melnikov method). Thus, important advancements have been made in approximating global bifurcations in the normal forms of the Takens–Bogdanov and Hopf-zero bifurcations [27–31]. Moreover, the NTT method is useful in the study of the canard explosion that occurs in singularly perturbed systems [32–34].

The rest of this work is organized as follows. We explain the application of the NTT method to perturbed Hamiltonian systems in Sect. 2. The case of perturbed non-Hamiltonian integrable systems and the study of the canard explosion are summarized in Sect. 3. Finally, some conclusions are provided.

2 Perturbing Hamiltonian Systems

In this section, we introduce the NTT method for obtaining the approximation of global connections, up to any desired order, in planar vector fields written as a perturbation of a Hamiltonian system (see details in [27–30]). Thus, we consider

$$\dot{x} = y, \quad \dot{y} = g(x) + \varepsilon [f(x, y) + \mu h(x, y)], \quad (1)$$

where $g(x)$, $f(x, y)$, and $h(x, y)$ are smooth functions, $|\varepsilon| \ll 1$ is a perturbation parameter, and μ is the control parameter. We assume that the unperturbed system possesses a global connection (a homoclinic orbit to a saddle equilibrium or a heteroclinic orbit connecting two saddles). Note that the well-known family of Liénard equations can be written in the form (1) with adequate scalings.

We introduce the nonlinear time transformation $\varphi(t, \varepsilon)$ of the form

$$\frac{d\varphi}{dt} = \Phi(\varphi, \varepsilon), \quad \Phi(\varphi + 2\pi, \varepsilon) = \Phi(\varphi, \varepsilon). \quad (2)$$

The function $\Phi(\varphi, \varepsilon)$ provides the relationship between the old time variable t and the new one φ . It will be considered as one unknown when the problem is solved. Throughout the scheme of the NTT method, its power series solution will be computed in an explicit manner. Moreover, we impose that Φ be periodic in φ in such a way that the global connection, which in the original time t evolves over an infinite interval, exists in a periodic interval. If $\varphi(t, \varepsilon) \rightarrow \varphi_{\pm}$ as $t \rightarrow \pm\infty$ for the global connection, then we have to impose that $\Phi(\varphi_{\pm}, \varepsilon) = 0$ for all ε , because this orbit has unbounded period. Then, system (1) is transformed into

$$x' \Phi = y, \quad y' \Phi = g(x) + \varepsilon[f(x, y) + \mu h(x, y)], \tag{3}$$

where the primes mean differentiation with respect to φ .

While system (1) has two unknowns, $x(t)$ and $y(t)$, the new system (3) has three, $x(\varphi, \varepsilon)$, $y(\varphi, \varepsilon)$, and $\Phi(\varphi, \varepsilon)$. Nevertheless, we can choose a smooth function $x(\varphi, \varepsilon)$ that satisfies the conditions of the connecting orbit. In this manner, by means of a perturbation scheme, we can compute $y(\varphi, \varepsilon)$ and $\Phi(\varphi, \varepsilon)$ from (3) and, at the same time, we can find an approximation of the value of μ for which the global bifurcation occurs. Three comments are relevant at this time. First, since it is a change of independent variable, choosing an appropriate function $x(\varphi, \varepsilon)$ is essential for the NTT method to allow us to obtain the approximations we are looking for. Unfortunately, we do not know of any general criteria to select $x(\varphi, \varepsilon)$ (its usefulness is seen a posteriori, depending on the result obtained with it; see below several examples). Second, the bifurcation value of μ found with the NTT method is independent of the function $x(\varphi, \varepsilon)$ chosen. This is because the existence and uniqueness of that value are guaranteed by Melnikov method and, at first-order, the NTT method coincides with Melnikov’s [8]. Third, trigonometric functions can be used for $x(\varphi, \varepsilon)$ because of the 2π -periodicity.

Once the function $x(\varphi, \varepsilon)$ is adequately chosen, we apply the perturbation method to approximate the global connection. We assume that the analytical solution can be expressed in terms of power series

$$y(\varphi, \varepsilon) = \sum_{i=0}^{\infty} \varepsilon^i y_i(\varphi), \quad \Phi(\varphi, \varepsilon) = \sum_{i=0}^{\infty} \varepsilon^i \Phi_i(\varphi), \quad \mu(\varepsilon) = \sum_{i=0}^{\infty} \varepsilon^i \mu_i, \tag{4}$$

where $\mu_i \in \mathbb{R}$ and $y_i(\varphi)$ and $\Phi_i(\varphi)$ are 2π -periodic functions in φ . Now we substitute the function $x(\varphi, \varepsilon)$ and (4) into (3), we expand the functions $g(x)$, $f(x, y)$ and $h(x, y)$ in the Taylor series about $\varepsilon = 0$, and we match the coefficients of like powers of ε . Thus, we first find the zero-order solution and, later, the i th-order solution with an iterative procedure. The smoothness of the functions found along this scheme, $y_i(\varphi)$ and $\Phi_i(\varphi)$, can be proved in each case [27–30].

In the rest of this section, we show the results obtained with the NTT method, first in a Rayleigh–Duffing oscillator; later we review them in several important unfoldings of the Takens–Bogdanov bifurcation.

2.1 Rayleigh–Duffing Oscillator

We consider the family of Rayleigh–Duffing mechanical oscillators

$$\ddot{x} + \alpha_1 \dot{x} + \alpha_2 x + x^3 + \dot{x}^3 = 0.$$

This model appears, for instance, in the field of planar flow-induced oscillations of slender rod-like continuous structures, after a discretization by one mode Galerkin approximation [35–37]. It is also present in the study of oscillations of pipes in heat exchangers [38]. This equation can be written in the form of the \mathbb{Z}_2 -symmetric system (invariant under the change $(x, y) \rightarrow (-x, -y)$)

$$\dot{x} = y, \quad \dot{y} = -\alpha_2 x - \alpha_1 y - x^3 - y^3, \tag{5}$$

whose equilibria are placed at $(0, 0)$ and $(\pm\sqrt{-\alpha_2}, 0)$. The origin exhibits a degenerate Takens–Bogdanov bifurcation. The principal feature of its bifurcation set appears because of the different stability between the supercritical Hopf bifurcations of the origin and the nontrivial equilibria and the repulsive homoclinic connection [39, 40]. This fact leads to the existence of a pair of saddle-node bifurcation curves of periodic orbits with hysteresis effect.

Our goal is to find the analytical approximation of the homoclinic bifurcation curve up to any desired order in the (α_1, α_2) -parameter plane, improving the existing first-order results [39]. Using the blow-up transformation

$$x = \epsilon^{\frac{1}{3}} X, \quad y = \epsilon^{\frac{2}{3}} Y, \quad \tau = \epsilon^{\frac{1}{3}} t, \quad \alpha_1 = -\epsilon^{\frac{4}{3}} \mu, \quad \alpha_2 = -\epsilon^{\frac{2}{3}}, \tag{6}$$

system (5) can be written as the perturbation of a Hamiltonian system

$$\dot{x} = y, \quad \dot{y} = x - x^3 + \epsilon(\mu - y^2)y. \tag{7}$$

For appropriateness in the notation, we have substituted $(X(\tau), y(\tau), \tau)$ with $(x(t), y(t), t)$ in (7). Then, using the nonlinear time transformation (2), we obtain

$$x' \Phi = y, \quad y' \Phi = x - x^3 + \epsilon(\mu - y^2)y. \tag{8}$$

Then, the following expression can be used to find the pair of \mathbb{Z}_2 -symmetric homoclinic orbits to the origin:

$$x(\varphi, \epsilon) = a(\epsilon) \sin \varphi = \sum_{i=0}^{\infty} \epsilon^i x_i(\varphi) = \sin \varphi \sum_{i=0}^{\infty} \epsilon^i a_i(\epsilon). \tag{9}$$

It describes the right homoclinic orbit (i.e. the orbit in the half plane $x > 0$) in a clockwise direction for $\varphi \in [0, \pi]$ and the left one in a counter-clockwise direction for $\varphi \in [\pi, 2\pi]$. Given this, it is enough to consider in our study $\varphi \in [0, \pi]$.

Substituting (9) and (4) into (8) and comparing the coefficient at each order of approximation, we obtain the following solution for the homoclinic orbit (for brevity we only show the first few terms; note also that we do not write the expression of $y(\varphi, \epsilon)$ since it can be found from $y = x' \Phi$)

$$\begin{aligned}
 x(\varphi, \varepsilon) &= \sqrt{2} \sin \varphi \left(1 - \frac{19}{2450} \varepsilon^2 + \frac{1,616,767}{1,260,525,000} \varepsilon^4 \right) + \mathcal{O}(\varepsilon^6), \\
 \Phi(\varphi, \varepsilon) &= \sin \varphi + \left(\frac{1}{70} \sin(2\varphi) + \frac{1}{28} \sin(4\varphi) \right) \varepsilon + \left(-\frac{361}{19,600} \sin \varphi \right. \\
 &\quad \left. - \frac{29}{39,200} \sin(3\varphi) + \frac{33}{7840} \sin(5\varphi) + \frac{1}{490} \sin(7\varphi) \right) \varepsilon^2 + \mathcal{O}(\varepsilon^3) \\
 \mu(\varepsilon) &= \frac{12}{35} - \frac{266,744}{16,506,875} \varepsilon^2 + \frac{79,870,390,898,976}{32,689,445,616,953,125} \varepsilon^4 + \mathcal{O}(\varepsilon^6). \quad (10)
 \end{aligned}$$

Thus, in the (α_1, α_2) -parameter plane the homoclinic curve is approximated by

$$\alpha_1 = -\frac{12}{35} \alpha_2^2 + \frac{266,744}{16,506,875} \alpha_2^5 - \frac{79,870,390,898,976}{32,689,445,616,953,125} \alpha_2^8 + \mathcal{O}(\alpha_2^{11}). \quad (11)$$

In Fig. 1 we compare the analytical results with the numerical ones obtained with AUTO and MatCont. In the case of the curve of homoclinic orbits in the parameter plane, the agreement is excellent in the interval $\alpha_1 \in [-0.7, 0]$.

In the following we will try to improve the accuracy by rewriting α_1 , $\Phi(\varphi, \varepsilon)$, and $a(\varepsilon)$ in continued fraction. In this way, we assume (as we observe that Φ_i contains odd (even, resp.) sine terms when i is even (odd, resp.)), this suggests that in the Φ expression we may group the odd-order terms to form a continued fraction and the even-order terms to form another)

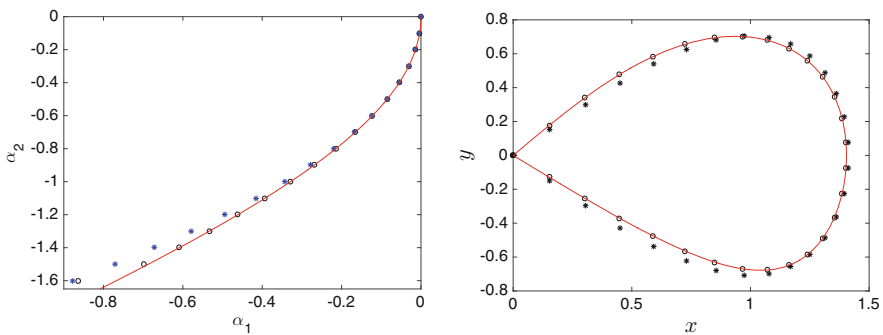


Fig. 1 For system (5), comparison between numerical continuation (solid) and analytical approximations (1st-order: star; 10th-order: empty circle) given in (10)–(11) for: (left) the curve of homoclinic connections; (right) homoclinic orbit for $\alpha_2 = -1$

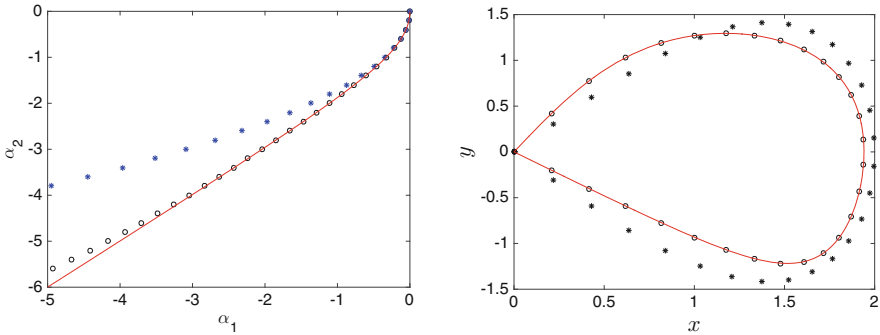


Fig. 2 For system (5), comparison between numerical continuation (solid) and analytical approximations (1st-order: star; 10th-order: empty circle) given in (12)–(14) for: (left) the curve of homoclinic connections; (right) homoclinic orbit for $\alpha_2 = -2$

$$\alpha_1 = -\alpha_2^2 \frac{b_1}{1 + \frac{b_2 \alpha_2^3}{1 + \frac{b_3 \alpha_2^3}{1 + \dots}}}, \quad a = \frac{a_0}{1 + \frac{a_2 \varepsilon^2}{1 + \frac{a_4 \varepsilon^2}{1 + \dots}}} \tag{12}$$

$$\Phi = \frac{\Psi_0}{1 + \frac{\Psi_2 \varepsilon^2}{1 + \frac{\Psi_4 \varepsilon^2}{1 + \dots}}} + \frac{\Psi_1}{1 + \frac{\Psi_3 \varepsilon^2}{1 + \frac{\Psi_5 \varepsilon^2}{1 + \dots}}}, \tag{13}$$

and obtain up to any wanted order (for brevity we only show the first few expressions)

$$b_1 = \frac{12}{35}, \quad b_2 = -\frac{66,686}{1,414,875}, \quad b_3 = -\frac{20,614,872,646,814}{198,092,767,747,875}, \quad a_0 = \sqrt{2},$$

$$a_2 = \frac{19}{2450}, \quad a_4 = \frac{81,103}{514,500}, \quad \Psi_0 = \sin(\varphi), \quad \Psi_1 = \frac{1}{70} \sin(2\varphi) + \frac{1}{28} \sin(4\varphi). \tag{14}$$

In Fig. 2 we can see the improvement achieved with these new approximations: A remarkable accordance is obtained in the interval $\alpha_1 \in [-3, 0]$.

2.2 Quadratic Takens–Bogdanov Bifurcation

In the study with the NTT method of the homoclinic bifurcation curve in the unfolding of the generic Takens–Bogdanov bifurcation [11, 12]

$$\dot{x} = y, \quad \dot{y} = \eta_1 + \eta_2 y + x^2 + xy, \tag{15}$$

we assume $x(\varphi, \varepsilon) = p(\varepsilon) \cos(2\varphi) + q(\varepsilon)$ and then, we are able to approximate the homoclinic curve in the parameter plane up to any desired order (see [27] for all the details). The first few terms are

$$\eta_1 = -\frac{49}{25}\eta_2^2 + \frac{144}{625}\eta_2^3 - \frac{345,168}{8,421,875}\eta_2^4 + \frac{7,223,269,392}{1,475,301,953,125}\eta_2^5 + \mathcal{O}(\eta_2^6). \tag{16}$$

2.3 Cubic Takens–Bogdanov Bifurcation

In the two-parameter unfolding of the Takens–Bogdanov normal form with cubic terms [11, 12]

$$\dot{x} = y, \quad \dot{y} = \eta_1 x + \eta_2 y + \sigma x^3 - x^2 y, \tag{17}$$

a pair of symmetric heteroclinic orbits exists when $\sigma = +1$ and of homoclinic connections when $\sigma = -1$. To apply the NTT method (see [28] for all the details), in the heteroclinic case we choose $x(\varphi, \varepsilon) = p(\varepsilon) \cos \varphi$, $p(\varepsilon) < 0$, and obtain the following approximation for the bifurcation curve:

$$\eta_2 = -\frac{1}{5}\eta_1 + \frac{16}{13,125}\eta_1^2 + \frac{5536}{103,359,375}\eta_1^3 + \frac{26,032,288}{8,953,505,859,375}\eta_1^4 + \mathcal{O}(\eta_1^5). \tag{18}$$

In the homoclinic case, it is adequate to use the expression of $x(\varphi, \varepsilon)$ given in (9). The approximation obtained for the bifurcation curve is

$$\eta_2 = \frac{4}{5}\eta_1 + \frac{184}{13,125}\eta_1^2 - \frac{21,664}{103,359,375}\eta_1^3 - \frac{15,742,432}{994,833,984,375}\eta_1^4 + \mathcal{O}(\eta_1^5). \tag{19}$$

2.4 Cuspidal Loop

In the unfolding

$$\dot{x} = y, \quad \dot{y} = \eta_1 + \eta_2 y + \eta_3 x^2 + \eta_4 xy - x^3 + x^2 y, \tag{20}$$

a cuspidal loop (a homoclinic orbit to a non-hyperbolic saddle undergoing a Takens–Bogdanov bifurcation [41]) to the origin occurs when $\eta_1 = \eta_2 = 0$. If we assume

that $x(\varphi, \varepsilon) = (\cos(2\varphi) - 1)p(\varepsilon)$, the application of the NTT method (see [29] for all the details) provides a perturbation solution of the cuspidal loop up to any wanted order (both in the parameter space and in the phase plane). The curve of cuspidal loops in the four-parameter space, in a neighborhood of the origin, is approximated by $\eta_1 = \eta_2 = 0$ together with (for brevity we only show the first few terms)

$$\eta_4 = -\frac{14}{15}\eta_3 - \frac{152}{84,375}\eta_3^3 + \frac{4,398,092}{209,302,734,375}\eta_3^5 + \mathcal{O}\left(\eta_3^7\right). \tag{21}$$

2.5 Takens–Bogdanov in Reversible Systems

The application of the NTT method to the study of global bifurcations in a codimension-three Takens–Bogdanov singularity in reversible systems is carried out in [30]. Specifically the system considered is [3]

$$\dot{x} = y, \quad \dot{y} = \varepsilon_1x + \varepsilon_2x^3 + \varepsilon_3xy + x^3y + \sigma x^5, \tag{22}$$

with $\sigma = \pm 1$. This system has up to five equilibria and exhibits a very rich bifurcation scenario for both values of σ . Several homoclinic and heteroclinic codimension-one and -two bifurcations are satisfactorily studied.

3 Other Applications of the NTT Method

3.1 Perturbing Non-Hamiltonian Integrable Systems

Recently, the NTT method has also been successfully applied to perturbations of non-Hamiltonian integrable systems of the form (see [31] for all the details)

$$\dot{x} = f(x, y) + \varepsilon [h_1(x, y) + \mu h_2(x, y)], \quad \dot{y} = g(x, y) + \varepsilon [h_3(x, y) + \mu h_4(x, y)], \tag{23}$$

where functions $g(x, y)$, $f(x, y)$, and $h_i(x, y)$, $i = 1, 2, 3, 4$, are smooth, $|\varepsilon| \ll 1$ and μ are perturbation and control parameters, respectively. Additionally, we assume that there exists a nonzero integrating factor $u(x, y)$ such that $(uf)_x + (ug)_y = 0$ (where the subscripts denote the partial derivatives with respect to the corresponding variables). Then the unperturbed system of (23) is integrable with the first integral $I(x, y)$ satisfying $I_y = -uf$ and $I_x = ug$. The heteroclinic connections that appear in the normal forms of the Hopf-zero and of the double-Hopf bifurcations can be successfully studied with the NTT method. In the case of the cubic parametric normal form for the Hopf-zero singularity [11, Sect. 7.4]

$$\dot{r} = \mu_1r + arz, \quad \dot{z} = \mu_2 - r^2 - z^2 + sz^3, \quad (a > 0, s \neq 0), \tag{24}$$

the heteroclinic curve in the parameter space is approximated as (for the sake of brevity we only show the first two nonzero terms)

$$\mu_1 = -\frac{3a^2s}{2(3a+2)}\mu_2 - \frac{9a^3s^3(360a^4 + 1134a^3 + 1341a^2 + 712a + 144)}{4(2a+1)(5a+2)(3a+2)^4}\mu_2^2 + \mathcal{O}(\mu_2^3).$$

In the case of a two-parametric unfolding of normal form system related to the non-resonant double-Hopf singularity (also valid for the Hopf-pitchfork bifurcation) in the case VIa [11, Sect. 7.5]

$$\dot{r}_1 = r_1(\mu_1 + r_1^2 + br_2^2), \quad \dot{r}_2 = r_2(\mu_2 + cr_1^2 - r_2^2) + kr_2^5, \tag{25}$$

with $c < 0 < b$, $A = -1 - bc > 0$ and $k < 0$, the heteroclinic curve is given by

$$\mu_2 = \left(\frac{c-1}{1+b}\right)\mu_1 - \frac{bk(c-1)^2(1-b+2bc)}{(1+b)^3(c-b+2bc)}\mu_1^2 + \mathcal{O}(\mu_1^3).$$

3.2 Canard Explosion

The canard explosion is a remarkable phenomenon that occurs in singularly perturbed systems [42]. It is an extremely fast transition from a periodic orbit with small amplitude (usually emerged in a Hopf bifurcation) to another one with large amplitude (relaxation oscillation). When the Melnikov method is applied, after a suitable rescaling [43], a perturbation of the non-Hamiltonian integrable system $\dot{x} = y - x^2, \dot{y} = -x$, appears. This system is integrable (with the integrating factor $u(x, y) = e^{-2y}$) and the first integral is given by $H(x, y) = e^{-2y} \left[x^2 - \left(y + \frac{1}{2} \right) \right]$. The parabola $y = x^2 - 1/2$ is an orbit of the integrable unperturbed system that corresponds to a homoclinic orbit, connecting a critical point at infinity on the Poincaré sphere. Thus, the application of the NTT method provides an excellent approximation to the canard explosion (all the details can be found in [32–34]).

4 Conclusions

In this work, we study homoclinic connections in a family of Rayleigh–Duffing mechanical oscillators [35–38]. The use of the NTT method provides high-order approximations (up to any desired order) for the locus in the parameter space where this global connection exists and, additionally, for the homoclinic orbit in the phase plane. This clearly ameliorates previous results [39]. It is remarkable that the introduction of continued fractions improves even more the agreement with the numerical results. Moreover, we survey the recent new results obtained by the NTT method in the study of homoclinic and heteroclinic connections, in planar

systems that are perturbations of Hamiltonian and of non-Hamiltonian integrable systems [27–34]. The formulas obtained in terms of several nonzero symbolic constant coefficients of the Takens–Bogdanov and Hopf-zero normal forms can be very useful in many bifurcation control engineering applications [20, 26]. The NTT method is a very effective alternative to Melnikov method in the computation of the high-order coefficients of the Poincaré application near the global connection (due to the intricate integrals that appear).

References

1. A. Algaba, E. Freire, E. Gamero, A.J. Rodríguez-Luis, An exact homoclinic orbit and its connection with the Rössler system. *Phys. Lett. A* **379**, 1114–1121 (2015)
2. L.M. Perko, *Differential Equations and Dynamical Systems* (Springer, New York, 2001)
3. A. Algaba, K.W. Chung, B.W. Qin, A.J. Rodríguez-Luis, Revisiting the analysis of a codimension-three Takens–Bogdanov bifurcation in planar reversible systems. *Nonlinear Dyn.* **96**, 2567–2580 (2019)
4. Y.Y. Chen, S.H. Chen, Homoclinic and heteroclinic solutions of cubic strongly nonlinear autonomous oscillators by the hyperbolic perturbation method. *Nonlinear Dyn.* **58**, 417–429 (2009)
5. M. Belhaq, B. Fiedler, F. Lakrad, Homoclinic connections in strongly self-excited nonlinear oscillators: the Melnikov function and the elliptic Lindstedt–Poincaré method. *Nonlinear Dyn.* **23**, 67–86 (2000)
6. M. Belhaq, M. Houssni, E. Freire, A.J. Rodríguez-Luis, Asymptotics of homoclinic bifurcation in a three-dimensional system. *Nonlinear Dyn.* **21**, 135–155 (2000)
7. Y.K. Cheung, S.H. Chen, S.L. Lau, A modified Lindstedt–Poincaré method for certain strongly nonlinear oscillators. *Int. J. Nonlinear Mech.* **26**, 367–378 (1990)
8. Y.Y. Cao, K.W. Chung, J. Xu, A novel construction of homoclinic and heteroclinic orbits in nonlinear oscillators by a perturbation-incremental method. *Nonlinear Dyn.* **64**, 221–236 (2011)
9. B.W. Qin, K.W. Chung, A. Fahsi, M. Belhaq, On the heteroclinic connections in the 1:3 resonance problem. *Int. J. Bifurcation Chaos* **26**, 1650143 (2016)
10. B.W. Qin, K.W., Chung, A.J. Rodríguez-Luis, M. Belhaq, Homoclinic-doubling and homoclinic-gluing bifurcations in the Takens–Bogdanov normal form with D_4 symmetry. *Chaos* **28**, 093107 (2018)
11. J. Guckenheimer, P.J. Holmes, *Nonlinear Oscillations, Dynamical Systems, and Bifurcations of Vector Fields* (Springer, New York, 1983)
12. Y.A. Kuznetsov, *Elements of Applied Bifurcation Theory* (Springer, New York, 2004)
13. E. Freire, A.J. Rodríguez-Luis, E. Gamero, E. Ponce, A case study for homoclinic chaos in an autonomous electronic circuit. A trip from Takens–Bogdanov to Hopf–Šil’nikov. *Phys. D* **62**, 230–253 (1993)
14. Y.A. Kuznetsov, S. Rinaldi, Remarks on food chain dynamics. *Math. Biosci.* **134**, 1–33 (1996)
15. A.D. Bazykin, *Nonlinear Dynamics of Interacting Populations* (World Scientific, Singapore, 1998)
16. A. Algaba, E. Freire, E. Gamero, A.J. Rodríguez-Luis, Analysis of Hopf and Takens–Bogdanov bifurcations in a modified van der Pol–Duffing oscillator. *Nonlinear Dyn.* **16**, 369–404 (1998)
17. A. Algaba, E. Gamero, A.J. Rodríguez-Luis, A bifurcation analysis of a simple electronic circuit. *Commun. Nonlinear Sci. Numer. Simulat.* **10**, 169–178 (2005)
18. E. Freire, L. Pizarro, A.J. Rodríguez-Luis, F. Fernández-Sánchez, Multiparametric bifurcations in an enzyme-catalyzed reaction model. *Int. J. Bifurcation Chaos* **15**, 905–947 (2005)

19. A. Algaba, M.C. Domínguez-Moreno, M. Merino, A.J. Rodríguez-Luis, Takens–Bogdanov bifurcations of equilibria and periodic orbits in the Lorenz system. *Commun. Nonlinear Sci. Numer. Simul.* **30**, 328–343 (2016)
20. M. Gazor, N. Sadri, Bifurcation controller designs for the generalized cusp plants of Bogdanov–Takens singularity with an application to ship control. *SIAM J. Control Optim.* **57**, 2122–2151 (2019)
21. B. Krauskopf, C. Rousseau, Codimension-three unfoldings of reflectionally symmetric planar vector fields. *Nonlinearity* **10**, 1115–1150 (1997)
22. A. Algaba, E. Freire, E. Gamero, A.J. Rodríguez-Luis, A three-parameter study of a degenerate case of the Hopf-pitchfork bifurcation. *Nonlinearity* **12**, 1177–1206 (1999)
23. A. Algaba, E. Freire, E. Gamero, A.J. Rodríguez-Luis, On a codimension-three unfolding of the interaction of degenerate Hopf and pitchfork bifurcations. *Int. J. Bifurcation Chaos* **9**, 1333–1362 (1999)
24. A. Algaba, E. Freire, E. Gamero, A.J. Rodríguez-Luis, A tame degenerate Hopf-pitchfork bifurcation in a modified van der Pol–Duffing oscillator. *Nonlinear Dyn.* **22**, 249–269 (2000)
25. A. Algaba, M. Merino, E. Freire, E. Gamero, A.J. Rodríguez-Luis, On the Hopf-pitchfork bifurcation in the Chua’s equation. *Int. J. Bifurcation Chaos* **10**, 291–305 (2000)
26. M. Gazor, N. Sadri, Bifurcation control and universal unfolding for Hopf-zero singularities with leading solenoidal terms. *SIAM J. Appl. Dyn. Syst.* **15**, 870–903 (2016)
27. A. Algaba, K.W. Chung, B.W. Qin, A.J. Rodríguez-Luis, A nonlinear time transformation method to compute all the coefficients for the homoclinic bifurcation in the quadratic Takens–Bogdanov normal form. *Nonlinear Dyn.* **97**, 979–990 (2019)
28. A. Algaba, K.W. Chung, B.W. Qin, A.J. Rodríguez-Luis, Computation of all the coefficients for the global connections in the \mathbb{Z}_2 -symmetric Takens–Bogdanov normal forms. *Commun. Nonlinear Sci. Numer. Simul.* **81**, 105012 (2020)
29. B.W. Qin, K.W. Chung, A. Algaba, A.J. Rodríguez-Luis, Analytical approximation of cuspidal loops using a nonlinear time transformation method. *Appl. Math. Comput.* **373**, 125042 (2020)
30. B.W. Qin, K.W. Chung, A. Algaba, A.J. Rodríguez-Luis, High-order analysis of global bifurcations in a codimension-three Takens–Bogdanov singularity in reversible systems. *Int. J. Bifurcation Chaos* **30**, 2050017 (2020)
31. B.W. Qin, K.W. Chung, A. Algaba, A.J. Rodríguez-Luis, High-order approximation of heteroclinic bifurcations in truncated 2D-normal forms for the generic cases of Hopf-zero and non-resonant double Hopf singularities. *SIAM J. Appl. Dynam. Syst.* **20**, 403–437 (2021)
32. A. Algaba, K.W. Chung, B.W. Qin, A.J. Rodríguez-Luis, Analytical approximation of the canard explosion in a van der Pol system with the nonlinear time transformation method. *Phys. D* **406**, 132384 (2020)
33. B.W. Qin, K.W. Chung, A. Algaba, A.J. Rodríguez-Luis, High-order study of the canard explosion in an aircraft ground dynamics model. *Nonlinear Dyn.* **100**, 1079–1090 (2020)
34. B.W. Qin, K.W. Chung, A. Algaba, A.J. Rodríguez-Luis, High-order analysis of canard explosion in the Brusselator equations. *Int. J. Bifurcation Chaos* **30**, 2050078 (2020)
35. W. Herfort, H. Troger, Robust modelling of flow induced oscillations of bluff bodies. *Math. Modelling Sc. Tech.* **8**, 251–255 (1987)
36. A.H. Nayfeh, D.T. Mook, *Nonlinear Oscillations* (Wiley, New York, 1979)
37. H. Troger, A. Steindl, *Nonlinear Stability and Bifurcation Theory* (Springer, Berlin, 1991)
38. H. Troger, Application of bifurcation theory to the solution of nonlinear stability problems in mechanical engineering, in *Numerical Methods for Bifurcation Problems*, ed. by T. Küpper et al. ISNM, vol. 70 (Birkhäuser, Basel, 1984), pp. 525–546
39. E. Freire, E. Gamero, A.J. Rodríguez-Luis, Study of a degenerate Bogdanov–Takens bifurcation in a family of mechanical oscillators. *Mech. Res. Commun.* **25**, 287–297 (1998)
40. H. Chen, L. Zou, Global study of Rayleigh–Duffing oscillators. *J. Phys. A* **49**, 165202 (2016)
41. F. Dumortier, R. Roussarie, J. Sotomayor, Bifurcations of cuspidal loops. *Nonlinearity* **10**, 1369–1408 (1997)
42. F. Dumortier, R. Roussarie, *Canard Cycles and Center Manifolds*, vol. 577 (Memoirs of the American Mathematical Society, 1996)
43. E. Freire, F. Gamero, A.J. Rodríguez-Luis, First-order approximation for canard periodic orbits in a van der Pol electronic oscillator. *Appl. Math. Lett.* **12**, 73–78 (1999)

Analytic Methods for Estimating the Effects of Stochastic Intermittent Loading on Fatigue-Crack Nucleation



Stephen Guth and Themistoklis Sapsis

1 Introduction

For many classes of structures, fatigue loads have a stochastic character with transient features that cannot be captured through a statistically stationary consideration. Examples include loads in wind turbines due to control and wind gusts, transitions between chaotic and regular responses in oil risers, and slamming loads in ship motions [1–3]. For such applications, traditional frequency domain approaches have difficulty predicting the fatigue effects of intermittent loading, as those are inherently connected to time-ordering and therefore cannot be captured by the spectral content of the load.

An alternative approach for the prediction of fatigue-crack nucleation relies on hysteretic cohesive-law models [4, 5]. This class of model has the advantage of applicability to arbitrary loading conditions, including random load cycling with transient spikes, but the disadvantage of requiring simulation of a large number of time histories, at enormous computational cost. Alternative approaches include statistical linearization [6–8], hierarchical modeling [9, 10], structured sampling methods [11], and optimal experimental design [12–16].

In this work, we first develop an efficient time-marching scheme for the fatigue model developed by Serebrinsky and Ortiz [4, 5] taking into account the time-ordering effects. Based on this model, we then derive analytical approximations for the probability mass function (pmf) of failure time in terms of the load probability density function (pdf) and the cohesive envelope [17].

S. Guth · T. Sapsis (✉)

Massachusetts Institute of Technology, Cambridge, MA, USA

e-mail: sguth@mit.edu; tsapsis@mit.edu

<http://sandlab.mit.edu/>

2 The Serebrinsky–Ortiz (SO) Model

In this work, we will consider a single material element with one dimensional loading, where the applied load is a random process given by $\sigma(t)$. The constitutive relation between $\sigma(t)$ and the corresponding displacement, $\delta(t)$, is given by the simple phenomenological model [4, 5]

$$\dot{\sigma} = \begin{cases} K^- \dot{\delta}, & \text{if } \dot{\delta} < 0, \\ K^+ \dot{\delta}, & \text{if } \dot{\delta} > 0, \end{cases} \quad (1)$$

where K^- and K^+ are the material stiffnesses associated with unloading and loading, respectively.

We assume fixed K^- (determined by the ray toward the origin), but evolve K^+ with the relation

$$\dot{K}^+ = \begin{cases} (K^+ - K^-) \frac{\dot{\delta}}{\delta_a}, & \text{if } \dot{\delta} < 0, \\ -K^+ \frac{\dot{\delta}}{\delta_a}, & \text{if } \dot{\delta} > 0. \end{cases} \quad (2)$$

Finally, we describe the *cohesive envelope* in the (δ, σ) plane, representing the maximum allowed strain deformation. When the curve $(\delta(t), \sigma(t))$ intersects the descending leg of the coherent envelope, crack initiation begins. A sample coherent envelope is given by

$$\sigma = \mathcal{F}(\delta) \triangleq e\sigma_c \frac{\delta}{\delta_c} e^{-\frac{\delta}{\delta_c}}, \quad (3)$$

where δ_c , σ_c , and δ_a are constants that characterize the material. We note that this model is designed for predictions on fatigue in elastic materials (metals) below the yield stress (approximately, σ_c from the cohesive envelope).

2.1 Time-Discretization of the SO Model

First, we assume that the loading function $\sigma(t)$ is a continuous random function with positive values. Second, we will replace the true continuous load with the piece-wise linear approximation

$$\dot{\sigma}(t) = \frac{\Delta\sigma_n^-}{\Delta t_n^-}, \quad t \in [\tau_{n-1}, \tau_{n-1} + \Delta t_n^-]$$

$$\dot{\sigma}(t) = \frac{\Delta\sigma_n^+}{\Delta t_n^+}, \quad t \in [\tau_{n-1} + \Delta t_n^-, \tau_{n-1} + \Delta t_n^- + \Delta t_n^+],$$

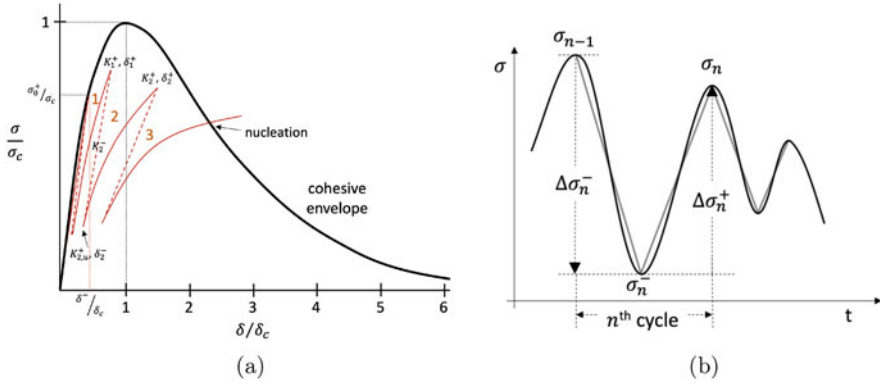


Fig. 1 (a) Schematic of the hysteretic cohesive-law and corresponding definition of fatigue-crack nucleation. The solid lines show loading and the dashed lines represent unloading. (b) Piece-wise linear approximation of the loading function $\sigma(t)$

where n is the number of cycle, $\Delta\sigma_n^-$ ($\Delta\sigma_n^+$) is the negative (positive) increment of the cycle, i.e. $\Delta\sigma_n^- < 0$ ($\Delta\sigma_n^+ > 0$), and Δt_n^- (Δt_n^+) is the corresponding duration (Fig. 1b). This piece-wise linear approximation allows us to integrate equations 1 and 2 with the following steps:

$$K_n^- = \frac{\sigma_{n-1}}{\delta_{n-1}} \tag{4}$$

$$K_{n,u}^+ = K_n^- - \exp\left(\frac{\Delta\sigma_n^-}{\delta_a K_n^-}\right) (K_n^- - K_{n-1}^+) \tag{5}$$

$$\delta_n - \delta_n^- = -\delta_a \log\left(1 - \frac{\Delta\sigma_n^+}{\delta_a K_{n,u}^+}\right). \tag{6}$$

If at any cycle, the point (δ_n, σ_n) lies above the cohesive envelope, one of two events will take place. First, if the stress–strain curve intersected the ascending leg, the strain δ_n may jump discontinuously to the ascending leg to fix the intersection. Otherwise, a crack will form. Crack nucleation at cycle N_f is thus associated with the condition

$$\sigma_{N_f}^+ \geq e\sigma_c \frac{\delta_{N_f}^+}{\delta_c} e^{-\frac{\delta_{N_f}^+}{\delta_c}} \quad \text{and} \quad \delta_{N_f}^+ > \delta_c. \tag{7}$$

A graphical summary of the described scheme is given in 1, and a sample evolution of K^+ is shown in Fig. 2. We observe that the evolution is typically linear except for certain discrete jumps. These jumps are associated with crossings of the ascending part of the coherent envelope due to intermittent loading events.

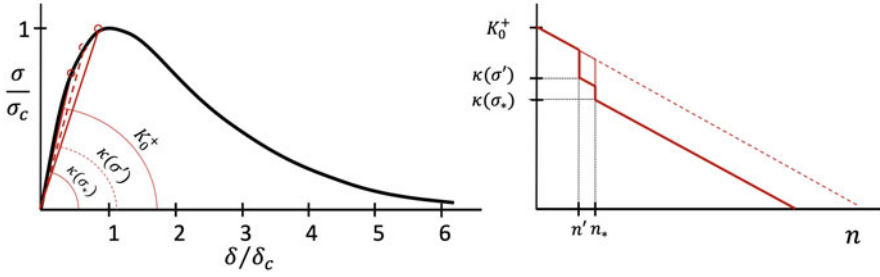


Fig. 2 Two loading scenarios shown in terms of the coherent envelope up-crossings and the stiffness in terms of the number of loading cycles

2.2 Simulation of a Loading Time Series Using the Probabilistic Decomposition-Synthesis Method

Here we formulate an approximation scheme for the failure time under arbitrary loading time series. We first decompose the loading signal into segments associated with extreme events and regular loading events. For segments of the loading time series where there is no up-crossing of the coherent envelope, we will show that the evolution of K^+ can be linearly approximated:

$$K_n^+ - K_{n-1}^+ \approx \Delta K, \tag{8}$$

where ΔK has a constant value that we will estimate later.

The remaining segments of the loading time series are associated with the discontinuous jumps in Fig. 2, corresponding to the intersections of the (σ, δ) curve with the ascending part of the coherent envelope. This breakdown of an intermittent process into a linear region and an extreme region parallels the probabilistic decomposition-synthesis framework developed in [18, 19].

Let the sequence $\{\sigma_n^+\}$ be the discretization of $\sigma(t)$ such that σ_n^+ is the n^{th} local maxima of $\sigma(t)$, and let $\hat{\sigma}$ be a fixed threshold. This sequence may be broken into two sets:

- $S_Q = \{n : \sigma_n^+ \leq \hat{\sigma}\}$ —the linear (quiescent) region
- $S_I = \{n : \sigma_n^+ > \hat{\sigma}\}$ —intermittent spikes

For points in the set S_Q , we will use the simplified update Eq. (8). For points in the set S_I , we will use the full SO update step as described in the previous section, regardless of whether the (σ, δ) curve actually crosses the coherent envelope. Finally, for technical reasons we will remove the first few peaks ($n \leq N_{\text{init}} \approx 5$) from S_Q and add them to S_I . This helps to initialize the algorithm for the case when there are otherwise few or no early spikes in the set S_I .

Estimation of the Slope ΔK We can directly estimate the slope ΔK in (8) from the SO model and the input signal statistics. From the piece-wise linear approximation, we have

$$\Delta K_n^+ = \left(1 - \exp\left(\frac{\Delta\sigma_n^-}{\delta_a K_n^-}\right)\right) (K_n^- - K_{n-1}^+) - \frac{\Delta\sigma_n^+}{\delta_a}. \quad (9)$$

We will assume that the quantity $\frac{\Delta\sigma_n^-}{\delta_a K_n^-}$ is very small, due to inverse dependence on δ_a , which will allow us to Taylor expand the exponential term. Additionally, we will also assume that the quantity $\left(\frac{K_{n-1}^+}{K_n} - 1\right)$ is small. When these approximations are made, we may relate the increments of K^+ to the increments of σ using the following expression:

$$\Delta K_n^+ = -\frac{\Delta\sigma_n^+}{\delta_a}. \quad (10)$$

For this problem, we will assume a known statistical distribution of the loading sufficient to compute $\mathbb{E}[\Delta K^+]$. We will give one such calculation, based on the joint pdf of the load $f(\sigma, \dot{\sigma})$ and the Rice Formula.

Suppose that $\sigma(t)$ is narrow-banded but not necessarily Gaussian. If the process is zero-mean, then we can rely on the amplitude of the positive peaks as a proxy for the amplitude of the jumps. The pdf of the peaks can be found as (for instance, as in [20]),

$$f_{\sigma^+}(a) = \frac{-1}{v_{\sigma^+}^+(0)} \frac{dv_{\sigma^+}^+(a)}{da}, \quad a \geq 0, \quad (11)$$

where $v_{\sigma^+}^+(a)$ is the a -up-crossing rate, given by the Rice formula:

$$v_{\sigma^+}^+(a) = \lim_{\Delta t \rightarrow 0} \frac{1}{\Delta t} \mathbb{E}[N^+(a, \Delta t)] = \int_0^\infty \dot{\sigma} f_{\sigma\dot{\sigma}}(a, \dot{\sigma}) d\dot{\sigma} \quad (12)$$

3 Analytical Approximation of the Failure Time pmf

If not for intersections between the $(\delta(t), \sigma(t))$ curve and the coherent envelope, the functional $N_f(\sigma)$ would be approximated by the linear relationship (see Eq. (8))

$$N_f = \frac{K_0^+}{\Delta K}, \quad (13)$$

where K_0^+ is the initial stiffness and ΔK is the expected change in K^+ over a typical cycle corresponding to the load distribution. However, the cohesive envelope changes things, by adding three effects: extreme terminal loads, intersections with the ascending part of the envelope, and intersection with the descending part of the envelope.

3.1 Setup

Cohesive Envelope We will write the cohesive envelope, introduced in Sect. 2, in the generic form $\sigma = \mathcal{F}(\delta)$, which has both a monotonic ascending and monotonic descending branch and two corresponding inverses: $\mathcal{F}_{asc}^{-1}(\sigma)$ and $\mathcal{F}_{des}^{-1}(\sigma)$.

Additionally, for what follows we define the functions:

$$\kappa(\sigma) \triangleq \frac{\sigma}{\mathcal{F}_{asc}^{-1}(\sigma)} \quad \text{and} \quad \eta(\sigma) \triangleq \frac{\sigma}{\mathcal{F}_{des}^{-1}(\sigma)} \quad (14)$$

which are assumed to be monotonic. These functions express the stiffness induced by an up-crossing with the ascending/descending part of the envelope and will be essential for our analysis. The monotonicity requirement is satisfied by typical cohesive envelopes (e.g. Eq. (3)).

Load Statistics We will assume that in the absence of envelope up-crossings the material stiffness, K_n^+ , evolves linearly with the number of cycles and with its gradient given by the mean value (see Eq. (10)). This is a valid assumption as long as the spread of values of $\Delta\sigma_n^+$ is not systematically large. If this is not the case, one can adopt a more complex model for the case of no envelope up-crossing using e.g. the Palmgren–Miner rule.

Further, we assume known pdf of local load maxima, σ_n^+ , as well as a known cumulative distribution $F_{\sigma^+}(\sigma)$.

Finally, we will assume the **independent spike hypothesis**: that the amplitude of local maxima is uncorrelated. This is *not* true in general for narrow-banded processes, but it *is* approximately true for “large enough” maxima, which is what is needed for our analysis. This will be a key assumption in determining the probability distribution for several intermediate quantities below.

3.2 Failure Time Distribution

Damage due to Terminal Loads Larger Than σ_c The maximum value of $\mathcal{F}(\delta)$ is given by σ_c , and is the maximum load the material can sustain. When the load on the material exceeds σ_c , it will fail no matter the fatigue history. We call these loads *terminal*. The failure cycle for this terminal mechanism is given by

$$n_x = \arg \min_{i>0} \{\sigma_i^+ > \sigma_c\}. \tag{15}$$

This is the expression for the first crossing time for the threshold σ_c . Following the independent spike hypothesis, the probability of seeing an extreme load above a given threshold may be modeled by sequential Bernoulli trials. In this case the pmf of the first cycle n_x when we have a spike of critical magnitude follows a geometric distribution

$$p_{N_x}(n) = (1 - p_c)^{n-1} p_c, \quad n = 1, 2, \dots \tag{16}$$

$$p_c = P[\sigma_i > \sigma_c] = \int_{\sigma_c}^{\infty} f_{\sigma^+}(s) ds. \tag{17}$$

Damage due to Up-crossings of the Ascending Part of the Envelope In general, the graph of (δ_n, σ_n) may have multiple intersections with the ascending part, leading to multiple discontinuous jumps in K_n^+ (Fig. 2). However, the total fatigue lifetime effect depends only on the cycle and magnitude of the *last* such intersection with the ascending part of the envelope, an intermediate result we can demonstrate geometrically by referring to Fig. 2.

We will use this idea to quantify this damage by defining the *damage quotient* $\phi(\sigma, n)$,

$$\phi(\sigma, n) \triangleq \frac{K_0^+ - \kappa(\sigma)}{\Delta K} - n, \tag{18}$$

which is meaningful only when it is positive, i.e. only when we have an up-crossing of the envelope. *The damage quotient essentially measures the magnitude of each jump on the material stiffness, expressed in a number of cycles lost due to this jump, every time we have an up-crossing.* For a generic loading sequence with peaks $\sigma_n^+, n = 1, 2, \dots$ the number of lost cycles due to up-crossing with the ascending part of the envelope will be given by the maximum of this quantity:

$$n_a \left(\{\sigma_i^+\}_{i=1}^{\infty} \right) = \arg \max_{0 \leq n < \infty} \phi(\sigma_n^+, n) = \arg \max_{0 \leq n < \infty} \left(\frac{K_0^+ - \kappa(\sigma_n^+)}{\Delta K} - n \right), \tag{19}$$

with the condition that this maximum is a positive number, i.e. we have at least one up-crossing with the ascending part of the envelope. If no up-crossing occurs, then $n_a = 0$.

To quantify the pmf for n_a , we will begin by using the pdf of the load peaks, $f_{\sigma^+}(a)$, and the monotonicity of function $\kappa(\sigma)$ to obtain the pdf for $\kappa(\sigma^+)$:

$$f_{\kappa}(a) = \frac{f_{\sigma^+}(\kappa^{-1}(a))}{|\kappa'(\kappa^{-1}(a))|}. \tag{20}$$

Based on this pdf, we now obtain the pdf and cdf for the damage quotient $\phi(\sigma_n^+, n)$:

$$f_{\phi_n}(a) = \Delta K f_{\kappa}(K_0^+ - n\Delta K - a\Delta K) \tag{21}$$

$$F_{\phi_n}(a) = 1 - F_{\kappa}(K_0^+ - n\Delta K - a\Delta K). \tag{22}$$

We can derive the probability distribution of the maximum argument of some set of random variables with a total probability argument (see [21]), which applied to our problem gives

$$p_{n_a}(n) = \int_{-\infty}^{\infty} Q_{\kappa}(x\Delta K) \frac{\Delta K f_{\kappa}(K_0^+ - n\Delta K - x\Delta K)}{1 - F_{\kappa}(K_0^+ - n\Delta K - x\Delta K)} dx, \quad n = 1, \dots, \tag{23}$$

where Q_{κ} is a function that is independent of n (i.e. it has to be computed once) and can be computed using an exponent-of-log manipulation, as well as the approximate limit $\Delta K \rightarrow 0$ to make a sum-to-integral substitution:

$$Q_{\kappa}(y) = \lim_{n \rightarrow \infty} \prod_{j=1}^n (1 - F_{\kappa}(K_0^+ - j\Delta K - y)) \tag{24}$$

$$= \exp\left(\frac{1}{\Delta K} \int_y^{\infty} \log(1 - F_{\kappa}(K_0^+ - z)) dz\right). \tag{25}$$

Substituting the above into (23) results in the pmf of the cycles until the last up-crossing of the ascending part of the envelope:

$$p_{n_a}(n_a) = \int_{-\infty}^{\infty} Q_{\kappa}(x\Delta K) W_{\kappa}(n_a\Delta K + x\Delta K) \Delta K dx, \quad n_a = 1, \dots, \tag{26}$$

$$W_{\kappa}(y) \triangleq \frac{f_{\kappa}(K_0^+ - y)}{1 - F_{\kappa}(K_0^+ - y)}.$$

Damage due to Up-crossings of the Descending Part of the Envelope Any intersection with the descending part of the coherent envelope will immediately cause material failure. As such, there can only be one such intersection. In order to quantify the statistics of this event, we define the *anticipation function* ψ :

$$\begin{aligned} \psi(\sigma_n, n) &\triangleq \eta(\sigma_n) - K_n^+, \\ K_n^+ &= K_{n_a}^+ - (n - n_a)\Delta K, \end{aligned} \tag{27}$$

where $\eta(\sigma) = \frac{\sigma}{\mathcal{F}_{des}^{-1}(\sigma)}$, K_n^+ is the material stiffness coefficient before cycle n , and $K_{n_a}^+ = \kappa(\sigma_{n_a})$. The material stiffness can be expressed in terms of the damage quotient (Eq. (18)) and its maximum value as follows:

$$K_n^+ = K_0^+ - (\phi_{n_a} + n)\Delta K, \quad (28)$$

where the pdf for ϕ_{n_a} is given by Eq. (21). The material failure time is given by the first zero up-crossing of the anticipation function:

$$N_f = \min\{n : \psi(\sigma_n, n) = \eta(\sigma_n) - K_0^+ + (\phi_{n_a} + n)\Delta K > 0\}. \quad (29)$$

We first compute the pdf for η . This will be given by:

$$f_\eta(a) = \frac{f_{\sigma^+}(\eta^{-1}(a))}{|\eta'(\eta^{-1}(a))|}. \quad (30)$$

Therefore, conditioning on $\xi = \phi_{n_a}\Delta K$, which expresses the maximum lost stiffness of the material due to an up-crossing with the ascending part of the envelope, and n_a , the cycle when this up-crossing occurs, we will have

$$F_{\psi_n}(a|\xi, n_a) = 1 - F_\eta(a + K_0^+ - \xi - n_a\Delta K). \quad (31)$$

To this end, the probability of having a material failure at N_f cycles is

$$p_{N_f}(n|\xi, n_a) = (1 - F_\eta(K_0^+ - \xi - n\Delta K)) \prod_{m=n_a+1}^{n-1} F_\eta(K_0^+ - \xi - m\Delta K),$$

$$n = n_a + 1, n_a + 2, \dots \quad (32)$$

where ξ follows the cdf $Q(\xi)$ (Eq. (25)), while n_a follows the pmf in Eq. (23). We will make the same logarithm substitution as before in Eq. (25) to give

$$p_{N_f}(n|\xi, n_a) = (1 - F_\eta(K_0^+ - \xi - n\Delta K)) V_\eta(n_a\Delta K + \xi, n\Delta K + \xi),$$

$$n = n_a + 1, n_a + 2, \dots \quad (33)$$

$$V_\eta(u, v) = \exp\left(\frac{1}{\Delta K} \int_u^v \log(F_\eta(K_0^+ - s)) ds\right).$$

Using Eq. (23) and assuming that probable n is much larger than the probable values of n_a (so we do not have to formally condition on $n > n_a$), as well as a small ΔK , we have

$$\begin{aligned}
p_{N_f}(n|\xi) &= \sum_{n_a=1}^{\infty} p_{N_f}(n|\xi, n_a) p(n_a) \\
&= \frac{1}{\Delta K} (1 - F_{\eta}(K_0^+ - \xi - n\Delta K)) \\
&\quad \times \int_{-\infty}^{\infty} \int_0^{\infty} Q_{\kappa}(y) V_{\eta}(\zeta + \xi, n\Delta K + \xi) W_{\kappa}(\zeta + y) d\zeta dy.
\end{aligned}$$

Finally, we integrate over the variable ξ after we multiply with the corresponding pdf $Q'_{\kappa}(\xi)$ to give the compact form:

$$\begin{aligned}
p_{N_f}(n) &= \frac{1}{\Delta K} \int_{-\infty}^{\infty} \int_0^{\infty} (1 - F_{\eta}(K_0^+ - \xi - n\Delta K)) \\
&\quad \times V_{\eta}(\zeta + \xi, n\Delta K + \xi) Q'_{\kappa}(\xi) S_{\kappa}(\zeta) d\zeta d\xi \quad (34)
\end{aligned}$$

$$S_{\kappa}(\zeta) \triangleq \int_{-\infty}^{\infty} Q_{\kappa}(y) W_{\kappa}(\zeta + y) dy. \quad (35)$$

Expression (34) together with the functions V_{η} (Eq. (33)), Q_{κ} (Eq. (25)), W_{κ} (Eq. (26)), and S_{κ} (Eq. (35)) consist of a full approximation of the cycles until material failure. These functions are given in terms of the coherent envelope shape and load peak statistics.

Combined Failure Time From Eqs. (17) and (34), we have expressions for the distribution of N_x and N_f , the failure times for the terminal-load case and quiescent-with-extremes-load pathways, respectively. To find the combined failure time, we simply check which comes first:

$$N_{\text{tot}} = \min\{N_x, N_f\} \quad (36)$$

$$p_{N_{\text{tot}}}(n) = p_{N_f}(n)(1 - F_{N_x}(n)) + p_{N_x}(n)(1 - F_{N_f}(n)), \quad (37)$$

where $F_{N_x}(n)$ and $F_{N_f}(n)$ are the cumulative probabilities corresponding to $p_{N_x}(n)$ and $p_{N_f}(n)$ (from Eqs. (17) and (34), respectively). In general, the terminal-load pathway may only contribute to the far left of the distribution (extremely early failure times), while the quiescent-with-extremes-load pathway controls the rest of the shape. However, in realistic applications it is very rare for a material to fail due to the terminal pathway as this mechanism can be easily accounted for in the design phase.

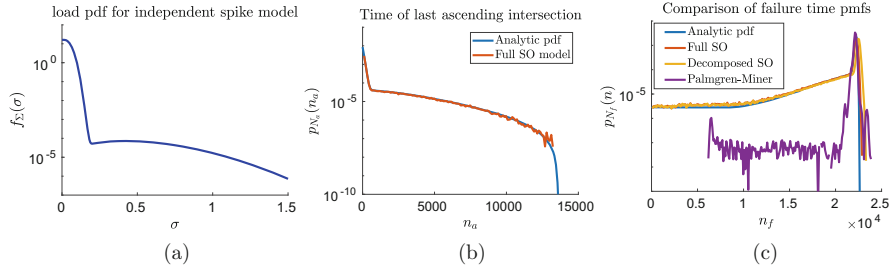


Fig. 3 Comparison of important distributions between the analytic framework and Monte Carlo simulation for $p_b = 1/20,000$. (a) The load peak (σ^+) pdf used for the independent spike model. (b) The pmf for the time of the last up-crossing, N_a , of the ascending branch of the coherent envelope. (c) The pmf for the time of fatigue-crack nucleation, N_f

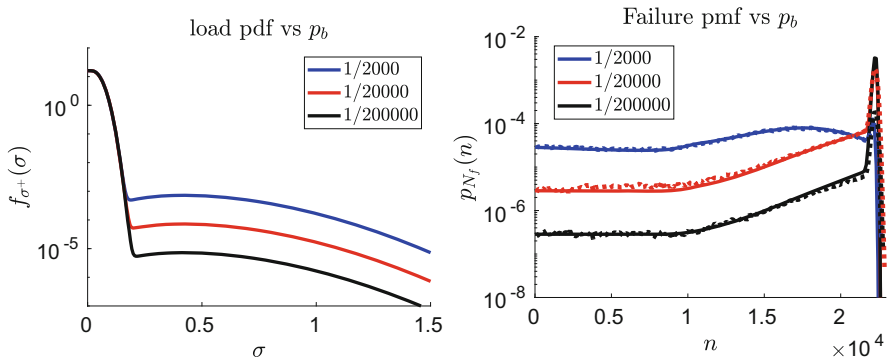


Fig. 4 Comparison of failure time pmf for different values of p_b in the independent spike model (a) Load peak (σ^+) probability density functions for different p_b . (b) Failure time distributions for different p_b . Analytical pmf is shown with solid curves and Monte Carlo simulations with dashed curves

3.3 Comparison of Analytic pmf with Monte Carlo Simulations

In order to compare the probabilistic framework developed in Sect. 3 to direct integration of the SO model, we employ the coherent envelope shape in Eq. (3) with scale parameters $\sigma_c = \delta_c = 1$ and $\delta_a = 300$. We consider realizations of a stochastic signal consisting of a zero-mean stochastic process superimposed with intermittent events.

Specifically, for each peak we first run a Bernoulli trial with success probability p_b . If this trial fails, then we have a non-extreme or *quiescent* peak, in which case we draw a sample from an absolute normal distribution with mean, $\mu_q = 0.03$, and standard deviation, $\rho_q = 0.03$. Note that for any broad-band stochastic process the peaks follow a Gaussian distribution [22]. If the Bernoulli trial succeeds, we instead draw an *extreme* sample from a Rayleigh distribution with scale parameter, $r = 0.42$. This results a probability density function for the load peak (σ^+) having

a sharp peak near $\sigma^+ = 0.03$ (i.e., much less than σ_c), but a long right tail with a small but finite probability mass corresponding to values of $\sigma > \sigma_c$ (Fig. 3a).

In Fig. 3b we present the comparison of the pmf for the cycle number associated with the last up-crossing of the ascending part of the envelope, p_{N_a} , while in Fig. 3c we compare the failure time distribution between the analytic framework and Monte Carlo simulations, based both on the fast decomposition-synthesis approximation and the full SO integration. Additionally, the predictions of the Palmgren–Miner rule are shown for reference. It is clear that the Palmgren–Miner rule underestimates the variance in failure time and cannot capture the heavy left tail.

To examine the effect of p_b (i.e., the density of intermittent loads) on the distribution of failure times, we repeat this experiment for three different values of p_b , given by $[1/2000, 1/20,000, 1/200,000]$. For the presented experiment, we use 1.2×10^6 , 1.9×10^6 , and 3.2×10^6 Monte Carlo realizations for increasingly small value of p_b . The corresponding load distributions, as well as failure time distributions, are displayed in Fig. 4. We emphasize the favorable agreement between the analytical approximation of the pmf and the direct Monte Carlo simulations. As extreme events become less likely, reduced left tail mass drives the distribution closer to the Palmgren–Miner rule.

4 Conclusions and Further Work

In this work, we developed both a time-marching integration and an approximate analytical solution for fatigue failure time in the SO model. We have shown how the SO model captures time-ordering effects discarded by other fatigue models, such as the Palmgren–Miner rule, and we showed how this model predicts a long left tail of early failure times under intermittent loading.

So far, we have limited ourselves to single element structures, with uniaxial loading. Real structures are much more complicated, with spatially distributed elements and loading. Application to real engineering problem will require interface with a structural model, such as a Finite Element Model (FEM), that can calculate the stresses across the entire structure. The attraction underlying such a combination would be the ability to locate specific structural elements at risk under intermittent loading, and to predict what sort of loads lead to heightened risk of early failure. At the same time, however, FEM integration will require a choice of mechanism to handle multi-axial loading (such as the von-Mises yield stress). Additionally, combining SO fatigue with FEM computations will require choices about the coupling between accumulated fatigue and changing material stiffness.

References

1. R.A. Khan, S. Ahmad, Dynamic response and fatigue reliability analysis of marine riser under random loads, in, *Structures, Safety and Reliability; Petroleum Technology Symposium of International Conference on Offshore Mechanics and Arctic Engineering*, vol. 2 (2007)
2. W. Hu, K.K. Choi, O. Zhupanska, J.H.J. Buchholz, Integrating variable wind load, aerodynamic, and structural analyses towards accurate fatigue life prediction in composite wind turbine blades. *Struct. Multidiscip. Optim.* **53**(3), 375–394 (2016)
3. P. Wolfsteiner, Fatigue assessment of non-stationary random vibrations by using decomposition in Gaussian portions. *Int. J. Mech. Sci.* **127**, 10–22 (2017)
4. S. Serebrinsky, M. Ortiz, A hysteretic cohesive-law model of fatigue-crack nucleation. *Scripta Mater.* **53**(1), 1193–1196 (2005)
5. S. Serebrinsky I. Arias, M. Ortiz, A phenomenological cohesive model of ferroelectric fatigue. *Acta Mater.* **54**, 975–984 (2006)
6. P.D. Spanos, I.A. Kougoumtzoglou, Harmonic wavelets based statistical linearization for response evolutionary power spectrum determination. *Probab. Eng. Mech.* **27**(1), 57–68 (2012). The IUTAM Symposium on Nonlinear Stochastic Dynamics and Control
7. M. Murata, H. Nagano, K. Kashino, Unscented statistical linearization and robustified Kalman filter for nonlinear systems with parameter uncertainties, in *2014 American Control Conference* (2014), pp. 5079–5084
8. K.R. Chernyshov, Information-theoretic statistical linearization. *Int. Fed. Autom. Control* **49**(12), 1797–1802 (2016)
9. E. Zio, N. Pedroni, Estimation of the functional failure probability of a thermal-hydraulic passive system by subset simulation. *Nucl. Eng. Design* **239**, 580–599 (2008)
10. W. Cousins, M.A. Mohamad, T.P. Sapsis, A probabilistic decomposition-synthesis method for the quantification of rare events due to internal instabilities. *J. Comput. Phys.* **322**, 288–308 (2016)
11. A. Olsson, G. Sandberg, O. Dahlblom, On Latin hypercube sampling for structural reliability analysis. *Struct. Saf.* **25**(1), 47–68 (2003)
12. *Exploring and Exploiting a Surrogate*, chapter 3 (Wiley, London, 2008), pp. 77–107
13. G. Malkomes, C. Schaff, R. Garnett, Bayesian optimization for automated model selection, in *Proceedings of the 2016 Workshop on Automatic Machine Learning, AutoML 2016, Co-Located with 33rd International Conference on Machine Learning (ICML 2016), New York City, NY, USA, June 24, 2016*, vol. 64 of *JMLR Workshop and Conference Proceedings*, ed. by F. Hutter, L. Kotthoff, J. Vanschoren (2016), pp. 41–47. [JMLR.org](http://jmlr.org)
14. K.K. Vu, C. D'Ambrosio, Y. Hamadi, L. Liberti, Surrogate-based methods for black-box optimization. *Int. Trans. Oper. Res.* **24**(3), 393–424 (2017)
15. X. Huan, Y.M. Marzouk, Simulation-based optimal Bayesian experimental design for nonlinear systems. *J. Comput. Phys.* **232**, 288–317 (2013)
16. S. Jiang, G. Malkomes, G. Converse, A. Shofner, B. Moseley, R. Garnett, Efficient nonmyopic active search, in *Proceedings of the 34th International Conference on Machine Learning - Volume 70, ICML'17* (2017), pp. 1714–1723. [JMLR.org](http://jmlr.org)
17. S. Guth, T.P. Sapsis, Probabilistic characterization of the effect of transient stochastic loads on the fatigue-crack nucleation time (2020)
18. M.A. Mohamad, T.P. Sapsis, Probabilistic description of extreme events in intermittently unstable dynamical systems excited by correlated stochastic processes. *SIAM/ASA J. Uncertainty Quantif.* **3**, 709–736 (2015)

19. H.K. Joo, M.A. Mohamad, T.P. Sapsis, Heavy-tailed response of structural systems subjected to stochastic excitation containing extreme forcing events. *J. Comput. Nonlinear Dyn.* **13**(9), 090914 (2018)
20. A. Naess, T. Moan, *Stochastic Dynamics of Marine Structures* (Cambridge University Press, Cambridge, 2013)
21. R. Habibi, Exact distribution of argmax (argmin). *Stoch. Quality Control* **26**(2), 155–162 (2011)
22. T.T. Soong, G. Mircea, *Random Vibrations of Mechanical and Structural Systems* (Prentice Hall, Englewood Cliffs, 1993)

Data-Driven Method for Real-Time Prediction of Fatigue Failure Under Stochastic Loading



Maor Farid

1 Introduction

Fatigue failure refers to the malfunctioning of a mechanical component due to the weakening of its material due to oscillatory loading below its ultimate tensile strength. The failure results in localized and progressive mechanical damage and cracks growth. Fatigue damage is cumulative over time, and even though it can be assessed by non-destructive tests (NDT) [1], it still can take place in unexpected timing, leading to hazardous consequences. Fatigue failure is one of the main reasons for mechanical failure in aerospace, offshore, and machine components. Hence, the accurate estimation of the current measure of cumulative damage and prediction of the time to failure of a given system is of major importance. Fatigue damage under an oscillatory loading is usually estimated by either time or frequency domain approaches. The most widely used time domain approach is based on the rainflow counting method for decomposing the stochastic signal to its underlying amplitudes and the corresponding number of cycles, followed by applying Miner's rule to assess the resulting cumulative damage. Frequency domain methods, such as those introduced by Dirlik [2] and Petrucci and Zuccarello [3], use probability density functions with parameters which are tuned with respect to the rainflow counting and Miner's method [4, 5]. Hence, and due to multiple observatory studies, rainflow counting and Miner's rule are considered as more reliable and accurate in comparison to the frequency domain methods. However, also time domain approaches are considered as inaccurate and limited in their ability to capture the underlying failure mechanisms. For example, it is well known that sudden changes

M. Farid (✉)

Massachusetts Institute of Technology, Cambridge, MA, USA

Technion—Israel Institute of Technology, Haifa, Israel

e-mail: faridm@mit.edu

in the loading amplitude lead to extensive cumulative damage, which is overlooked by Miner's rule. Thus, disagreements between theoretical and experimental results were broadly reported in literature [6], especially when dealing with broad-band stochastic loading. Machine learning (ML) algorithms and artificial neural networks (ANNs) in particular were proven to have a good ability to capture the underlying patterns and correlations in measured data, even when the underlying physical rules governing the system's behavior are obscure or unknown. Applying machine learning approaches for fatigue failure prediction based on measured data obtained from experiments, numerical simulations, or analytical analysis, is therefore a promising strategy for cumulative damage estimation. However, very limited results were reported in the literature about utilizing ML algorithms and ANNs for damage estimation [7–11]. Moreover, no study was done about predicting the time to failure (TTF) of a given mechanical component under stochastic loading.

The current paper presents an ANN-based approach for TTF prediction of a given mechanical component under statistically stationary stochastic loading. The method considers a wide range of possible material properties and loading characteristics. In other terms, the well-known generalization properties of an ANN are utilized for giving accurate predictions for a wide range of materials and loading characteristics. Moreover, the suggested method provides a quantified uncertainty measure, describing the confidence interval in which the true TTF value is most likely to be.

2 Theoretical Background

Miner's linear cumulative damage rule is given by the following equation:

$$D(t) = \sum_{i=1}^{N_k} \frac{n_i(t)}{N_{f,i}} \quad (1)$$

Here D is the damage fraction which quantifies the cumulative damage and the closeness to fatigue failure, which corresponds to $D = 1$. Hence, the failure time τ fulfills the following relation: $D(\tau) = 1$. The values $n_i(t)$ represent the number of cycles of the i th amplitude, i.e. $S_{a,i}$, that took place during the stochastic loading by time instance t , as obtained by the rainflow counting method. Parameter N_k is a user-defined hyper-parameter that represents the number of amplitudes considered in the rainflow counting method. $N_{f,i}$ is the number of loading cycles that will lead to a fatigue failure due to forcing with a single amplitude of $S_{a,i}$. The relation between $N_{f,i}$, $S_{a,i}$, the mean forcing amplitude S_m , and the mechanical properties of the component, is given by the following expression:

$$N_{f,i} = \left(\frac{S_{a,i}}{A\alpha} \right)^{\frac{1}{b}}, \alpha = 1 - \frac{S_m}{\sigma_{uts}} \quad (2)$$

Here A and b are the fatigue strength and fatigue exponent, respectively. Those are material properties which are obtained from literature of preliminary experiments. Parameter α is the Goodman's correction factor for non-zero mean stress, and σ_{ult} is the ultimate tensile strength of the material. It is noteworthy that the failure time and the dynamical response of a component subjected to oscillatory loading are heavily governed by its material properties. As one can see in Eq. (2), fatigue failure is not a time-dependent phenomenon, i.e. it is not dictated by the frequency content of the loading signal, but only by the amplitudes of its Fourier components. However, previous works pointed out that phenomena associated with rapid changes such as sudden gradients in the excitation amplitude, have a non-negligible effect on the cumulative damage, which is not captured by any time domain method. The loading signal is generated from a given power spectral density (PSD) function $G(f)$ that describes the frequency content of the possible stochastic loadings. A stochastic loading signal is generated from a given PSD $G(f)$ according to the following expression:

$$S(t) = S_m + \sum_{i=1}^{N_f} \sqrt{2G(f_i)\Delta f} \cos(2\pi f_i t + \phi_i) \quad (3)$$

Here, the phase angles, mean forcing amplitudes, and forcing frequencies are randomly drawn from uniform distributions above the following ranges: $\phi_i \sim \mathcal{U}[0, 2\pi]$, $S_m \sim \mathcal{U}[0, 250]$ MPa, and $f_i \sim \mathcal{U}[100, 200]$ Hz, respectively. The frequency resolution of the PSD is taken as $\Delta f = 0.1$ Hz. The sampling rate is taken as ten times the Nyquist frequency is chosen as $f_s = 2000$ Hz. The number of frequencies composing the loading signal is chosen as $N_f = 20$, and the number of amplitudes considered in the rainflow counting method is chosen as $N_k = 100$. The simulations were computed up to time $t_f = 120$ s with time step of $\Delta t = 1/f_s = 0.0005$ s. The chosen PSD function $G(f)$ is given by the following equation:

$$G(f) = A_G \exp - \frac{(f - \mu_G)^2}{2\sigma_G^2} \quad (4)$$

Here the parameters of the PSD are chosen as $\mu_G = 150$ Hz, $\sigma_G = 175$ Hz, and $A_G = 2500$ MPa²/Hz. The magnitude of the PSD function A_G was chosen such that the maximal amplitude of the loading signal will not exceed 85% of the ultimate tensile strength of the material σ_{ult} in order to avoid ultra-low cycle fatigue failure. Then, a data-set of $N = 2000$ loading signals were generated according to Eqs. (3)–(4), and their corresponding failure time τ was computed numerically using the rainflow counting method and Miner's rule in Eqs. (1)–(2). The data-set was divided into two parts with ratio of 75 : 25. The former, i.e. the training set, is used for optimizing the parameters of the predictive model during the learning process. The second portion, i.e. the test-set, is used for evaluating the accuracy of the predictions obtained by the model and its generalization abilities.

3 The Learning Problem

Artificial neural network (ANN) is a mathematical model that can fit a complex nonlinear function (called hypothesis function) to a given set of numerical examples called training set. The term learning refers to the process of optimization of the model's inner parameters in an iterative fashion. The problem of predicting a numerical value based on a given set of other numerical values is referred to as a regression problem.

In the current work, an ANN with three hidden layers is used as a predictive model. In order to reduce the dimensionality of the model's input, the loading signal is represented by the mean loading amplitude S_m and another characteristic amplitude, denoted by S_p . The latter is chosen as the p -percentile amplitude of the signal, which serves as an alternative to the maximal amplitude S_a suggested in literature for constant-amplitude loading. Preliminary analysis was conducted in order to estimate the correlation between the TTF τ , the mean amplitude S_m , and the percentile amplitude p for various values of parameter p . It was shown that for p values which are significantly larger or smaller than 90%, this correlation becomes more obscure (Fig. 1a–b), while for $p = 90\%$ the relation is sharper (Fig. 1c). The intuitive explanation to this fact is that in stochastic signals, the maximal amplitude S_a might be significantly larger than the rest of the peaks, which means that it is not a representative value of the entire signal. On the other hand, a parameter value which is too small might overlook multiple peaks which consist a significant portion of the signal's energy. Hence, $p = 90\%$ serves as a trade-off between both limiting cases.

Thus, the chosen input features vector \mathbf{x} consists of three material properties: fatigue strength A , fatigue exponent b , and ultimate tensile strength σ_{uts} , and two characteristic amplitudes: the mean value of the loading signal S_m , and the 90th percentile S_p amplitude.

$$\tau_{pred}(\mathbf{x}|\boldsymbol{\theta}) = NN_{\boldsymbol{\theta}}(\mathbf{x}), \mathbf{x} = \{A, b, \sigma_{uts}, S_m, S_p\} \quad (5)$$

Here, the output of the ANN is the predicted TTF τ_{pred} , which is a function of the features vector \mathbf{x} and the vector of the model's inner parameters, $\boldsymbol{\theta}$.

3.1 Creating the Training Set

Each mechanical component in the data-set corresponds to a vector in the features space, which includes the components shown in Eq. (5). The TTF that corresponds to the vector serves as its label or target variable, and denoted by $\tau(\mathbf{z})$. The properties vector that describes each example in the data-set is often referred to as a data-

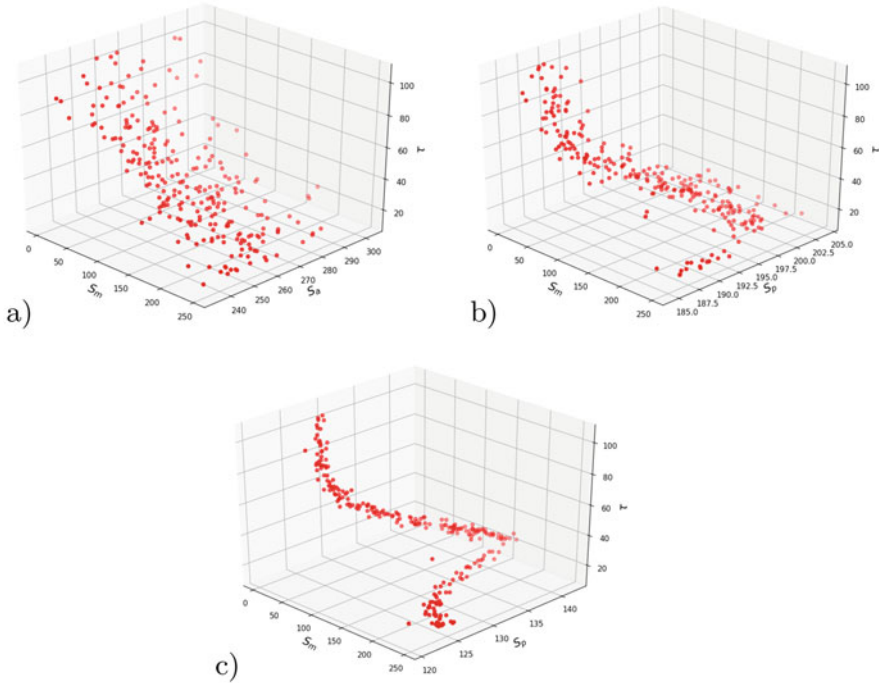


Fig. 1 The correlation between the failure time τ , the mean loading amplitude S_m , and the percentile amplitude S_p , for (a) $p = 100\%$ ($S_p = S_a$), (b) $p = 99.5\%$, (c) $p = 90\%$

point. Each data-point is randomly generated based on the following distributions: $S_m \sim \mathcal{U}[0, 250]$ MPa, $\sigma_{uts} \sim \mathcal{U}[500, 1000]$ MPa, $A \sim \mathcal{U}[1200, 1500]$ MPa, $b \sim \mathcal{U}[-0.2, -0.15]$. The forcing signals are then generated using Eqs. (3)–(4) for $N_f = 20$ frequencies which are randomly drawn from the following uniform distribution: $f_i \sim \mathcal{U}[100, 200]$ Hz. The resulting percentile amplitude is calculated numerically from the signal that was generated for $p = 90\%$. Finally, the TTF is estimated numerically for each feature vector \mathbf{z} using Eqs. (1)–(2). The data-set includes

$N = 1500$ data points.

It is noteworthy that neither the choice of Gaussian distribution nor using a particular fatigue simulation method leads to loss of generality. This is because the ANN can be trained on any given data-set and capture the underlying mapping between the system parameters and the resulting TTF. Generally, the data-set should include as many examples as possible, considering a vast range of possible system parameters and loading signals.

3.2 The Learning Model

After an iterative process of architecture optimization, we chose a fully connected artificial neural network (FC-ANN) as our learning model. We conduct an iterative architecture design by gradually increasing the complexity of the ANN, i.e. the number of its inner parameters, in order to minimize the chances for over-fitting by an overly complex learning model. The final architecture was chosen to contain three layers of five neurons in the input layer, twelve neurons in the hidden layer, and a single neuron in the output layer. We use a rectified linear unit (ReLU) activation function between the input and the hidden layer, and a linear activation function between the hidden to the output layer. This is a classical choice for regression problems with an unbounded output value. The values of the ANN parameters are initiated randomly. The model is trained for 10,000 iterations without mini-batches using the Adam optimizer with a learning rate of 0.01.

4 Offline Prediction

After the training process is completed, the ANN performances are validated on a test-set. The accuracy of the predictions is demonstrated by plotting each pair of predicted and GT TTF values on a single plane, i.e. $\tau_{pred} - \tau_{GT}$ plane. The closeness of the resulting point-cloud to the line of perfect prediction, i.e. $\tau_{pred} = \tau_{GT}$, serves as an accuracy measure for our predictive model, as shown in Fig. 2. As one can see, in Fig. 2, the points are tightly distributed around the line of perfect prediction $\tau_{GT} = \tau_{pred}$, indicating on a very good agreement between the predicted and the GT values. In order to quantify the quality of performances, the R-squared score is calculated, showing a very strong linear correlation between the predicted and GT values, i.e. ($R^2 = 0.986$).

Now, the trained predictive can generate further predictions for unseen feature vectors. However, in addition to a predicted TTF value, we are interested in having a corresponding confidence interval that quantifies the level of uncertainty of the model prediction τ_{pred} .

5 Uncertainty Quantification

In various engineering systems, immediate cessation might lead to severe implications in terms of both functionality and safety, such as emergency landing of an airplane in the midst of a commercial or operational military flight due to predicted fatigue failure in one of its critical components. Uncertainty quantification (UQ) is the scientific field of quantitative characterization of uncertainty. In the case of predicting TTF of critical components in real-time, UQ is of major importance for

decision making regarding taking immediate proper safety measures or operational actions.

In the current work, we introduce a methodology for quantifying the level of uncertainty in a given prediction using the results obtained by the trained predictive model on the test-set. The uncertainty of each TTF prediction is quantified using a time-variant probability density function (PDF), whose expected value and variance represent the estimated TTF and the corresponding confidence level, respectively.

$$P(t|\tau_{pred}(\mathbf{x}, \boldsymbol{\theta}), X^{test}) = g(\tau_{pred}(\mathbf{x}, \boldsymbol{\theta})|X^{test}) \quad (6)$$

The interval of values in which the TTF is estimated to be in a given statistical significance α is referred as confidence interval, and it is calculated according to the following expression:

$$\tau_{pred}^+, \tau_{pred}^-(\tau_{pred}(\mathbf{x})|X^{test}, \boldsymbol{\theta}) = \tau_{pred}(\mathbf{x}|\boldsymbol{\theta}) \pm \gamma \sqrt{\mathbb{E}[(T - \tau_{pred})^2]} \quad (7)$$

$$T \sim P(t|\tau_{pred}(\mathbf{x}, \boldsymbol{\theta}), X^{test})$$

Here γ is the number of standard deviations from the mean taken in the confidence interval. Selection of function $g(\tau_{pred})$ should embody the variance of point on the $\tau_{pred} - \tau_{GT}$ plane with respect to the line of perfect prediction. In the following sections, two alternative functions are discussed.

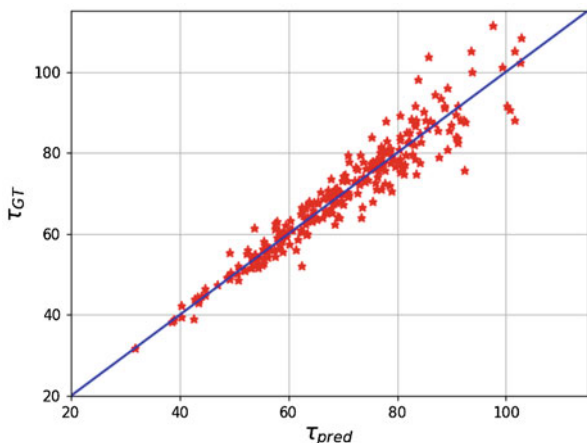


Fig. 2 GT vs. predicted TTF values obtained by the predictive model on the test-set (red dots) and the line of perfect prediction $\tau_{GT} = \tau_{pred}$ (blue line)

5.1 Bi-variate Normal Distribution

The first attempt to model the distribution of points on the $\tau_{pred} - \tau_{GT}$ plane is using a bi-variate normal (BVN) PDF, given by the expression in Eq. (8). We use this PDF because it is simple and convenient to apply. For example, for each predicted TTF $\tilde{\tau}_{pred}$, the BVN PDF generates a univariate normal distribution which is defined as the intersection between the BVN PDF and plane $\tau_{pred} = \tilde{\tau}_{pred}$.

$$\Phi(\mathbf{z}) = \frac{\exp\left(-\frac{1}{2}(\mathbf{z} - \boldsymbol{\mu})^T \boldsymbol{\Sigma}^{-1}(\mathbf{z} - \boldsymbol{\mu})\right)}{2\pi\sqrt{\beta}} \quad (8)$$

$$\boldsymbol{\mu} = \begin{pmatrix} \mu_x \\ \mu_y \end{pmatrix}, \quad \boldsymbol{\Sigma} = \begin{pmatrix} \sigma_x^2 & \sigma_{xy} \\ \sigma_{xy} & \sigma_y^2 \end{pmatrix}, \quad \beta = \det(\boldsymbol{\Sigma})$$

Here, $\mathbf{z} = \{\tau_{pred}, \tau_{GT}\}$ is a vector $\tau_{pred} - \tau_{GT}$ plane, $\boldsymbol{\mu}$ is the vector of means, and $\boldsymbol{\Sigma}$ is the covariance matrix of the PDF. In Eq. (6), the PDF obtained for a given TTF prediction $\tilde{\tau}_{pred}$ corresponds to the intersection between the BVN PDF and plane $\tau_{pred} = \tilde{\tau}_{pred}$:

$$P(t|\tilde{\tau}_{pred}) = \Phi(\tau_{pred} = \tilde{\tau}_{pred}, \tau_{GT} | \boldsymbol{\mu}(X^{test}), \boldsymbol{\Sigma}(X^{test})) \quad (9)$$

The confidence level α is associated with an elliptic iso-density locus on the PDF, which corresponds to $\Phi(\mathbf{z}) = \kappa$. Parameter κ is bounded to the following range: $\kappa \in (0, \kappa_{max})$ where $\kappa_{max} = 1/2\pi\sqrt{\beta}$. The level of confidence associated with a given ellipse is defined as the volume between the PDF and the area bounded by the ellipse, denoted by \mathcal{S} : ellipse of intersection between the PDF and a horizontal plane, i.e. iso-density locus $\Phi(\mathbf{z}) = \kappa$. The area in the $\tau_{pred} - \tau_{GT}$ plane which is bounded by the resulting ellipse is denoted by \mathcal{S} . The area between surface $\Phi(\mathbf{z})$ and region \mathcal{S} is considered as the confidence level α which related to height κ : $\alpha(\kappa) = \iint_{\mathcal{S}} \Phi(\mathbf{z}|X^{test}, \boldsymbol{\theta})$, where \mathcal{S} is the area bounded by ellipse $\mathcal{C} : \Phi(\mathbf{z}) = \kappa$. Hence, α is in fact the limit value of points bounded by the corresponding ellipse, assuming that the points are indeed normally distributed. In the absence of a close form solution of the integral in Eq. (8), the relation between the statistical significance α and parameter κ is evaluated numerically. The confidence boundaries are given explicitly according to the following expression:

$$\tau_{pred}^+, \tau_{pred}^-(\tau_{pred}(\mathbf{x})|X^{test}, \boldsymbol{\theta}) = \frac{\sigma_{xy}}{\sigma_x^2} \tau_{pred} \pm \frac{1}{\sigma_x} \sqrt{(\sigma_{xy}^2 - \sigma_x^2 \sigma_y^2) \tau_{pred}^2 + \rho\beta\sigma_x^2} \quad (10)$$

The bounding ellipse which is associated with $\alpha = 95\%$ is shown in Fig. 3a. As one can see, in contradiction to intuition, for predicted value which richer in points, i.e. near the mean of the PDF, the variance of the PDF is the largest, which it should be smaller due to greater amount of data points and hence greater confidence. Moreover, for extreme values where naturally there is smaller number of points, the variance of the PDF is very small. For some extreme values, no confidence interval

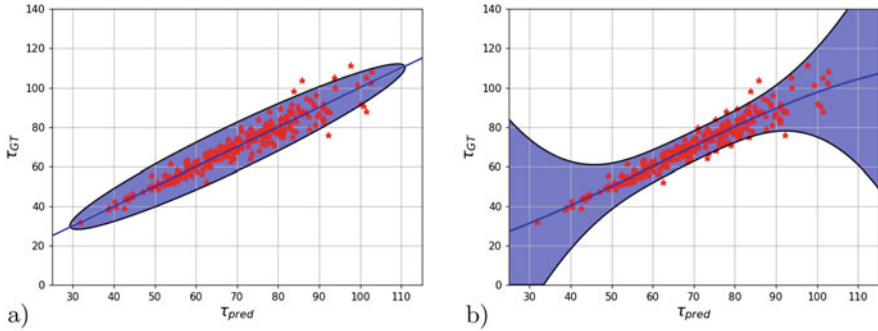


Fig. 3 Prediction of the trained model on the test-set X^{test} (red points), regression curve (blue line), confidence region (blue shade), and confidence boundaries (black lines) for statistical significance of $\alpha = 0.95$; (a) multivariate normal distribution, $\kappa = 1.3225E - 4$, (b) GPR with $\gamma = 1.96$ standard deviations

is defined. In conclusion, we are interested in a bi-variate PDF that allocates high variance for predicted TTFs for which there are fewer examples in the test-set and vice versa, and defines a confidence interval for any predicted TTF.

5.2 Gaussian Process Regression

Gaussian process regression (GPR) models are nonparametric kernel-based probabilistic models that fit the data with a set of possible curves that create a multivariate PDF. The resulting PDF has a larger variance for feature values with fewer examples, i.e. in ranges that lack in uncertainty. GPR models are considered as very flexible, and it was proven that the squared exponential covariance function corresponds to a Bayesian linear regression model with an infinite basis functions number of basis function. Moreover, it can be shown that GPR is equivalent to an FC-ANN with infinite number of neurons in its hidden layer [12]. As one can see in Fig. 3b, the bi-variate PDF generated by GPR maps predicted TTF values to narrow confidence intervals in ranges that contain an extensive amount of points, where that uncertainty level is low and vice versa.

6 Real-time Prediction

After the learning model was trained on the data-set, its prediction abilities of the ANN can be tested in real-time. The three material coefficients are known in advance, for example by a dedicated experiment, and the forcing-related features, i.e. S_m and S_p , are calculated in a desired rate. Then, the features vectors \mathbf{z} is fed

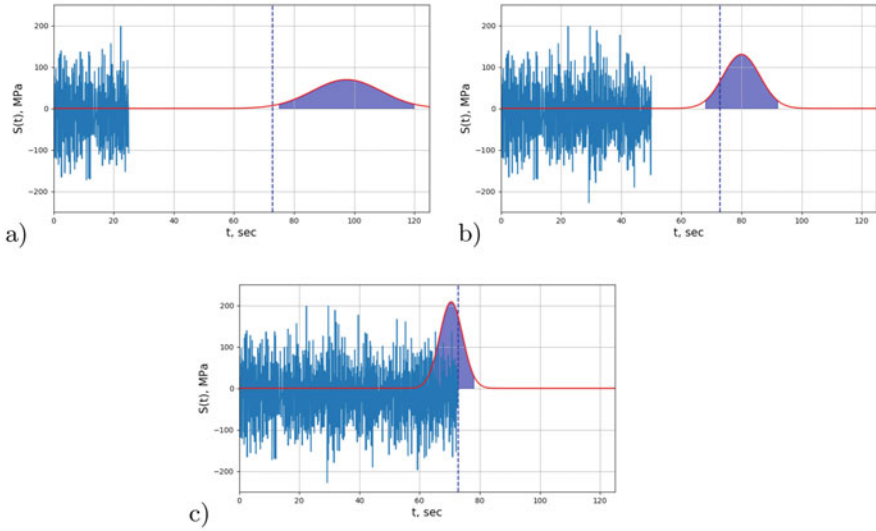


Fig. 4 Demonstration of real-time TTF prediction, in three consecutive instances, (a) $t = 5$ s, (b) $t = 25$ s, (c) $t = 45$ s. The measured loading signal (blue), GT TTF τ_{GT} (dashed blue), predicted TTF τ_{pred} (dashed red), and confidence interval corresponding to statistical significance of $\gamma = 75\%$ (purple shade)

to the pre-trained model to obtain the corresponding predicted TTF. This recursive process ensures that the predicted TTF is suitable for all the data that was read by the sensors. It is worth noting that all features in features vector \mathbf{z} have to match in their format and units to the features used in the training process. The corresponding confidence interval is obtained in accordance to Eq. (6) and using the GPR-based approach shown in the previous section.

As one can see in Fig. 4, the GT TTF (dashed-blue line) falls within the uncertainty gap obtained by the predictive model. Thus, under the assumption of statistically stationary stochastic loading, the TTF can be predicted in real-time during loading and obtain proper safety instructions before failure occurrence.

7 Concluding Remarks

In the current work, an FC-ANN-based approach was suggested for both offline and real-time failure time prediction. The prediction obtained by the machine learning model is based on the material properties of the mechanical component considered, the mean amplitude, and the percentile amplitude of the measured loading signal. The selection of those features is based on the assumption of statistically stationary loading. In addition to the predicted failure time, an uncertainty measure is obtained based on the tested performances of the model. The suggested method

paves the way toward a commercial predictive system, which is based on real-time measurements taken from motion sensors placed in informative locations on the mechanical component. Methodology for identification of most informative locations is suggested by Farid in another work. This method can give valuable safety instructions and operational suggestions, and serve as a life-saving predictive system.

Funding M.F. has been supported by the Fulbright Program, the ISEF Foundation, and the Israel Academy of Sciences and Humanities.

References

1. R.H. Tykot, Using nondestructive portable x-ray fluorescence spectrometers on stone, ceramics, metals, and other materials in museums: advantages and limitations. *Appl. Spectrosc.* **70**(1), 42–56 (2016)
2. T. Dirlik, *Application of Computers in Fatigue Analysis*. PhD thesis (University of Warwick, England, 1985)
3. G. Petrucci, B. Zuccarello, Fatigue life prediction under wide band random loading. *Fatigue Fract. Eng. Mater. Struct.* **27**(12), 1183–1195 (2004)
4. H.J. Sutherland, On the fatigue analysis of wind turbines. Technical report (Sandia National Labs, Albuquerque, 1999)
5. Y.-L. Lee, J. Pan, R. Hathaway, M. Barkey, *Fatigue Testing and Analysis: Theory and Practice*, vol. 13 (Butterworth-Heinemann, Oxford, 2005)
6. A. Antoniou, M. Vespermann, F. Sayer, A. Krimmer, Life prediction analysis of thick adhesive bond lines under variable amplitude fatigue loading, in *Proceedings of the 18th European Conference on Composite Materials (ECCM18)* (2018)
7. A.P. Vassilopoulos, E.F. Georgopoulos, V. Dionysopoulos, Artificial neural networks in spectrum fatigue life prediction of composite materials. *Int. J. Fatigue* **29**(1), 20–29 (2007)
8. J.F. Durodola, N. Li, S. Ramachandra, A.N. Thite, A pattern recognition artificial neural network method for random fatigue loading life prediction. *Int. J. Fatigue* **99**, 55–67 (2017)
9. S. Ramachandra, J.F. Durodola, N.A. Fellows, S. Gerguri, A. Thite, Experimental validation of an ANN model for random loading fatigue analysis. *Int. J. Fatigue* **126**, 112–121 (2019)
10. Y. Kim, H. Kim, I.-G. Ahn, A study on the fatigue damage model for Gaussian wideband process of two peaks by an artificial neural network. *Ocean Eng.* **111**, 310–322 (2016)
11. J.C.F. Pujol, J. M. Andrade Pinto, A neural network approach to fatigue life prediction. *Int. J. Fatigue* **33**(3), 313–322 (2011)
12. C.E. Rasmussen, Gaussian processes in machine learning, in *Summer School on Machine Learning* (Springer, Berlin, 2003), pp. 63–71

An Improved Formulation for Structural Optimization of Nonlinear Dynamic Response



Suguang Dou

1 Introduction

Nonlinear dynamics has been widely exploited in a wide range of applications concerning nonlinear micro-mechanical resonators [1]. Their applications include atomic force microscopy [2], micro-mass sensors [3, 4], micro-gyroscope [5], gravimeter [6], frequency division [7], and vibration energy harvester [8].

In recent years, there has been growing interest in the intentional design of nonlinearity for the purpose of tailoring the dynamic response. Many studies have investigated the applications of the shaped finger for comb drives. A few studies have applied the structural optimization techniques to tailor the mechanical nonlinearity, see e.g. [9–13]. In these studies, numerical optimization techniques were applied to tailor different aspects of the nonlinear dynamic responses, for example, the frequency–amplitude dependence or frequency–energy dependence [9, 10], the nonlinear forced resonances [11], and the internal resonances [12, 13].

In our previous study in [14], we proposed an efficient finite element based methodology for structural optimization of nonlinear micro-mechanical resonators with geometric nonlinearity described by Green stain. Later, the optimized designs were validated by using dynamic tests [15]. The fast optimization is achieved by using a direct finite element calculation of the nonlinear modal coupling coefficients [14, 16]. These nonlinear modal coupling coefficients can also be computed by using non-intrusive approaches [17]. When the structural geometry changes, these nonlinear modal coupling coefficients change accordingly, which further determine the change of the nonlinear dynamic response. The aim of this paper is to present an

S. Dou (✉)

DTU Wind Energy, Technical University of Denmark, Roskilde, Denmark

e-mail: sudou@dtu.dk

improved formulation for the optimization of nonlinear dynamic response through the nonlinear modal coupling coefficients.

2 Methods

The original methodology was proposed in [14] for the single-mode resonators and the multi-mode resonators with internal resonances. The methodology consists of nonlinear finite element modeling, eigenvalue analysis, direct finite element calculation of nonlinear modal coupling coefficients, and solving an optimization problem.

For brevity, the following description of the methodology is restricted to a single-mode beam resonator and its fundamental flexural mode whose eigen-frequency and eigenmode are denoted as ω and Φ , respectively.

2.1 Finite Element Model and Design Variables

The beam structure is discretized into a number of Euler–Bernoulli beam elements. In the optimization, the distribution of the in-plane width h of the beam is manipulated to tailor the nonlinear dynamic response, see Fig. 1. In order to ensure the effectiveness of the Euler–Bernoulli beam element, it is assumed that the distribution of the in-plane width varies continuously without drastic change. For the purpose of optimization, a large number of elements are used to enable a fine representation of the varying in-plane width. In order to ensure manufacturability and mechanical strength, it is reasonable to impose a lower bound h_{min} on the in-plane width. On the other hand, an upper bound h_{max} is also imposed on the in-plane width to suit the applicability of the beam theory. With the lower and upper bounds of the in-plane width, the design variables are defined as

$$h_e = h_{min} + \rho_e(h_{max} - h_{min}) \quad (1)$$

where $e = 1, \dots, N_e$ with N_e denoting the number of the beam elements.

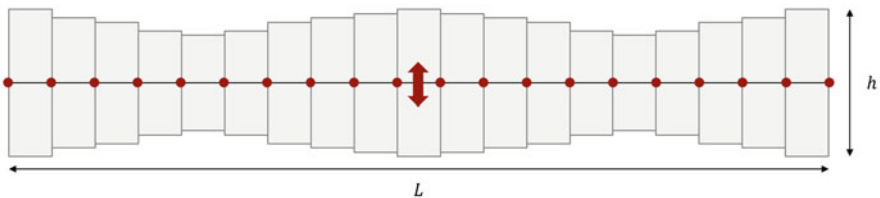


Fig. 1 Illustration of the varying in-plane width, the beam elements, and the direction of the in-plane vibration

2.2 Reduced-Order Model and Frequency–Amplitude Relation

Assume that the flexural vibration of the beam in its fundamental mode can be approximated by $\mathbf{u} = x \Phi$ with \mathbf{u} denoting the full-order displacement vector. The reduced-order model of the beam in its fundamental mode is described by the standard Duffing equation as follows:

$$\ddot{x} + 2\xi \omega \dot{x} + \omega^2 x + \alpha x^3 = f \cos(\Omega t) \tag{2}$$

where ξ is the modal damping ratio, ω is the eigen-frequency of the vibration mode, α is the coefficient of the cubic nonlinear stiffness term (Duffing nonlinearity), f and Ω are the amplitude and frequency of the external force, respectively.

The eigen-frequency ω is obtained by solving an eigenvalue problem

$$\mathbf{K}\Phi = \omega^2 \mathbf{M}\Phi \tag{3}$$

where \mathbf{M} and \mathbf{K} are the mass matrix and the stiffness matrix in the finite element model. Further, the eigenmode is normalized with respect to the mass matrix, i.e.

$$\Phi^T \mathbf{M}\Phi = 1 \tag{4}$$

In the reduced-order model in Eq. (2), the coefficient of the cubic nonlinearity is directly calculated in the finite element model as [14]

$$\alpha = 4 \sum_{e=1}^{N_e} \frac{EA(\rho_e)}{8L} \left(\mathbf{w}_e(\rho)^T \mathbf{K}_g \mathbf{w}_e(\rho) \right)^2 \tag{5}$$

where \mathbf{w}_e denotes an element-wise vector taken from the vibration mode Φ corresponding to the deflection of the beam element e . The matrix \mathbf{K}_g is given as [18]

$$\mathbf{K}_g = \frac{1}{30l} \begin{bmatrix} 36 & 3l & -36 & 3l \\ 3l & 4l^2 & -3l & -l^2 \\ -36 & -3l & 36 & -3l \\ 3l & -l^2 & -3l & 4l^2 \end{bmatrix} \tag{6}$$

where l is the length of the beam element e .

Note that Eq. (5) is derived for beam element with the nonlinearity arising from the mid-plane stretching effect existing in clamped–clamped beam and similar beam structures. This mid-plane stretching effect is not suitable to cantilever beam whose length can be seen as non-extensible. Alternatively, Eq. (5) can also be derived for the solid element with Green strain [14] which has a wider applicability.

The frequency of the resonance peak increases as the amplitude of the resonance peak increases, which is described as

$$\omega_p = \omega \left(1 + \gamma A_p^2 \right) \quad (7)$$

where ω_p and A_p denote the frequency and amplitude of the nonlinear forced resonance peak, respectively. The effective coefficient γ is given as

$$\gamma = \frac{3}{8} \frac{\alpha}{\omega^2} \quad (8)$$

It is emphasized that the above derivation of γ cannot fully reflect the change of the magnitude of the vibration mode Φ , and thus may to some extent bias the optimized design in the optimization as shown later in the numerical results.

In order to account for the change of the magnitude of the vibration mode, let $|\Phi|$ denote the magnitude of the vibration mode, and introduce a new coordinate $y = x |\Phi|$. The change of the coordinate from x to y corresponds to a change of the reduction basis from Φ to $\frac{\Phi}{|\Phi|}$. The reduced-order model in Eq. (2) can be re-written as

$$\ddot{y} + 2\xi\omega\dot{y} + \omega^2 y + \beta y^3 = g \cos \omega t \quad (9)$$

where

$$y = x |\Phi|, \quad \beta = \frac{\alpha}{|\Phi|^2}, \quad g = f |\Phi| \quad (10)$$

For the fundamental vibration mode of the clamped–clamped beam, its magnitude can be captured by the deflection at the midspan as

$$|\Phi| = \max(\Phi) = |\mathbf{L}^T \Phi| \quad (11)$$

where \mathbf{L} is a vector with all zeros but one non-zero component. The value of the non-zero component is one. Its index corresponds to the degree of freedom of the maximum deflection at the midspan of the beam.

From the reduced-order model in Eq. (9), the frequency–amplitude relation can be re-written as

$$\omega_p = \omega \left(1 + \Gamma B_p^2 \right) \quad (12)$$

where B_p is the amplitude of the resonance peak in the coordinate of y , and the effective coefficient Γ is given as

$$\Gamma = \frac{3}{8} \frac{\beta}{\omega^2} = \frac{3}{8} \frac{\alpha}{\omega^2 |\Phi|^2} = \frac{\gamma}{|\Phi|^2} \quad (13)$$

The effective coefficient in Eq. (13) is derived in the coordinate of y and the reduction basis $\frac{\Phi}{|\Phi|}$. Since the new reduction basis is normalized with its magnitude, the resulting effective coefficient Γ provides a fair comparison of the optimized designs in the numerical computation. This also implies that an alternative way to account for the change of the magnitude of the eigenmode is to use the eigenmode that is normalized with its magnitude. Specifically, one can replace Eq. (4) with

$$|\Phi_i| = 1 \quad (14)$$

In the following formulation and the numerical results, the normalization of the eigenmode with respect to the mass matrix in Eq. (4) is used, and the two effective coefficients in Eqs. (13) and (8) are compared in the context of optimization.

2.3 Optimization Problems and Sensitivities

First, the original formulation of the optimization problem to maximize the hardening behavior of a clamped–clamped beam resonator is

$$\begin{aligned} \max_{\rho} \quad & \bar{\gamma} = \frac{\alpha}{\omega^2} \\ \text{subject to:} \quad & (\mathbf{K} - \omega^2 \mathbf{M}) \Phi = \mathbf{0}, \\ & \Phi^T \mathbf{M} \Phi = 1, \\ & V(\rho) / V^* \leq 0.5, \\ & \mathbf{0} \leq \rho \leq \mathbf{1} \end{aligned} \quad (P_{old})$$

where the new objective function is defined in terms of γ in Eq. (8), and the constant factor $\frac{3}{8}$ is omitted in the objective function.

Based on the above formulation, the improved formulation of the same optimization problem is written as

$$\max_{\rho} \quad \bar{\Gamma} = \frac{\alpha}{\omega^2 |\Phi|^2} \quad (P_{new})$$

where the objective function is defined in terms of Γ in Eq. (13), and the constraints are the same as those in the problem P_{new} and therefore are omitted.

The two optimization problems are solved by using a gradient-based optimizer called the Method of Moving Asymptotes (MMA) [19], which is efficient and robust for solving structural optimization problems. The design sensitivities (i.e. gradients)

of the objective functions with respect to the design variables are calculated by using the adjoint method [20] as described in the following subsection.

2.4 Design Sensitivity Analysis Using the Adjoint Method

The derivation of the design sensitivity analysis is demonstrated by using the new objective function $\bar{\Gamma}$ in P_{new} .

First, two adjoint variables, λ and η , are introduced in order to apply the adjoint method in the design sensitivity analysis. The objective function is re-written as

$$\bar{\Gamma} = \bar{\Gamma} + \lambda^T (\mathbf{K} - \omega^2 \mathbf{M}) \Phi + \eta (\Phi^T \mathbf{M} \Phi - 1) \quad (15)$$

The gradients of the augmented objective function are derived as

$$\begin{aligned} \frac{d\bar{\Gamma}}{d\rho_e} &= \frac{\partial \bar{\Gamma}}{\partial \omega} \frac{d\omega}{d\rho_e} + \frac{\partial \bar{\Gamma}}{\partial \alpha} \left(\frac{\partial \alpha}{\partial \rho_e} + \frac{\partial \alpha}{\partial \Phi} \frac{d\Phi}{d\rho_e} \right) + \frac{\partial \bar{\Gamma}}{\partial |\Phi|} \frac{\partial |\Phi|}{\partial \Phi} \frac{d\Phi}{d\rho_e} \\ &+ \lambda^T \left[\left(\frac{\partial \mathbf{K}}{\partial \rho_e} - \omega^2 \frac{\partial \mathbf{M}}{\partial \rho_e} \right) \Phi - 2\omega \mathbf{M} \Phi \frac{d\omega}{d\rho_e} + (\mathbf{K} - \omega^2 \mathbf{M}) \frac{d\Phi}{d\rho_e} \right] \\ &+ \eta \left(\Phi^T \frac{\partial \mathbf{M}}{\partial \rho_e} \Phi + 2 \Phi^T \mathbf{M} \frac{d\Phi}{d\rho_e} \right) \end{aligned} \quad (16)$$

Collecting the terms of $\frac{d\Phi}{d\rho_e}$ and $\frac{d\omega}{d\rho_e}$, we have

$$\begin{aligned} \frac{d\bar{\Gamma}}{d\rho_e} &= \frac{\partial \bar{\Gamma}}{\partial \alpha} \frac{\partial \alpha}{\partial \rho_e} + \lambda^T \left(\frac{\partial \mathbf{K}}{\partial \rho_e} - \omega^2 \frac{\partial \mathbf{M}}{\partial \rho_e} \right) \Phi + \eta \Phi^T \frac{\partial \mathbf{M}}{\partial \rho_e} \Phi \\ &+ \left(\frac{\partial \bar{\Gamma}}{\partial \alpha} \frac{\partial \alpha}{\partial \Phi} + \frac{\partial \bar{\Gamma}}{\partial |\Phi|} \frac{\partial |\Phi|}{\partial \Phi} + \lambda^T (\mathbf{K} - \omega^2 \mathbf{M}) + 2\eta \Phi^T \mathbf{M} \right) \frac{d\Phi}{d\rho_e} \\ &+ \left(\frac{\partial \bar{\Gamma}}{\partial \omega} + \lambda^T (-2\omega \mathbf{M} \Phi) \right) \frac{d\omega}{d\rho_e} \end{aligned} \quad (17)$$

The values of the two adjoint variables can be chosen so that the two terms of $\frac{d\Phi}{d\rho_e}$ and $\frac{d\omega}{d\rho_e}$ vanish in the above equation, leading to a set of adjoint equations as

$$\begin{aligned} \frac{\partial \bar{\Gamma}}{\partial \alpha} \frac{\partial \alpha}{\partial \Phi} + \frac{\partial \bar{\Gamma}}{\partial |\Phi|} \frac{\partial |\Phi|}{\partial \Phi} + \lambda^T (\mathbf{K} - \omega^2 \mathbf{M}) + 2\eta \Phi^T \mathbf{M} &= \mathbf{0} \\ \frac{\partial \bar{\Gamma}}{\partial \omega} + \lambda^T (-2\omega \mathbf{M} \Phi) &= 0 \end{aligned} \quad (18)$$

The adjoint equations can be re-formulated into matrix form as

$$\begin{bmatrix} \mathbf{K} - \omega^2 \mathbf{M} & 2 \Phi^T \mathbf{M} \\ 2 \Phi^T \mathbf{M} & 0 \end{bmatrix} \begin{bmatrix} \lambda \\ \eta \end{bmatrix} = \begin{bmatrix} -\frac{\partial \bar{\Gamma}}{\partial \alpha} \frac{\partial \alpha}{\partial \Phi} - \frac{\partial \bar{\Gamma}}{\partial |\Phi|} \frac{\partial |\Phi|}{\partial \Phi} \\ \frac{1}{\omega} \frac{\partial \bar{\Gamma}}{\partial \omega} \end{bmatrix} \quad (19)$$

After solving the adjoint equations (19), the adjoint variables λ and η are determined. Then the sensitivities of the objective function are calculated as

$$\frac{d\bar{\Gamma}}{d\rho_e} = \frac{\partial \bar{\Gamma}}{\partial \alpha} \frac{\partial \alpha}{\partial \rho_e} + \lambda^T \left(\frac{\partial \mathbf{K}}{\partial \rho_e} - \omega^2 \frac{\partial \mathbf{M}}{\partial \rho_e} \right) \Phi + \eta \Phi^T \frac{\partial \mathbf{M}}{\partial \rho_e} \Phi \quad (20)$$

When the values of the adjoint variables λ and η are given, the right-hand side of Eq. (20) is cheap to compute for all design variables.

In each optimization iteration, the adjoint equations in Eq. (19) only need to be solved once and then the resulting values of the adjoint variables λ and η can be used in Eq. (20) to compute the sensitivities of the objective function with respect to all the design variables ρ_e with $e = 1, \dots, N_e$.

The adjoint method is more efficient than the direct differentiation method and the numerical finite difference approximation of the sensitivities, and thus allows a large number of design variables to be used in the optimization.

For the optimization problem *P_{old}*, the adjoint equations and the sensitivities of the objective function are given as

$$\begin{bmatrix} \mathbf{K} - \omega^2 \mathbf{M} & 2 \Phi^T \mathbf{M} \\ 2 \Phi^T \mathbf{M} & 0 \end{bmatrix} \begin{bmatrix} \lambda \\ \eta \end{bmatrix} = \begin{bmatrix} -\frac{\partial \bar{\gamma}}{\partial \alpha} \frac{\partial \alpha}{\partial \Phi} \\ \frac{1}{\omega} \frac{\partial \bar{\Gamma}}{\partial \omega} \end{bmatrix} \quad (21)$$

$$\frac{d\bar{\gamma}}{d\rho_e} = \frac{\partial \bar{\gamma}}{\partial \alpha} \frac{\partial \alpha}{\partial \rho_e} + \lambda^T \left(\frac{\partial \mathbf{K}}{\partial \rho_e} - \omega^2 \frac{\partial \mathbf{M}}{\partial \rho_e} \right) \Phi + \eta \Phi^T \frac{\partial \mathbf{M}}{\partial \rho_e} \Phi \quad (22)$$

3 Results

The improved optimization is applied to a micro-mechanical clamped–clamped beam in [14]. The evolution of the design is displayed in Fig. 2. The vibration mode of the final design is displayed in Fig. 3. For comparison, the old design and its fundamental flexural mode are displayed in Fig. 4.

Figure 2 shows that in the first 10 iterations, the optimizer distributes more material at two locations where the nonlinear strain energy is high [11]. In the following iterations, the optimizer begins to put more material at the midspan of the beam, yielding a central mass. The central mass was not shown in the design by using the original approach [14] and therefore is attributed to the improved

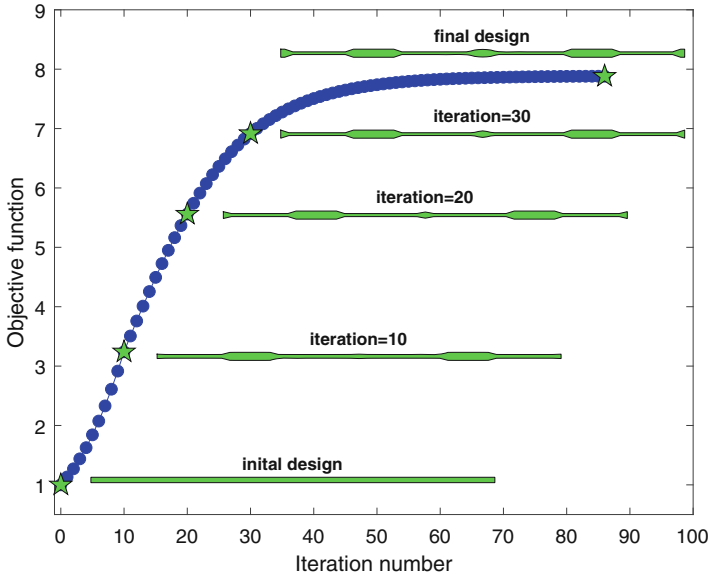


Fig. 2 The optimized design for maximizing the hardening behavior of the fundamental vibration mode of a clamped–clamped beam resonator. The objective function is normalized with its value of the initial design



Fig. 3 The fundamental flexural mode of the new design for maximizing the hardening behavior of a clamped–clamped beam. The color denotes the total displacement. The mode shape is obtained by using COMSOL Multiphysics 5.4 with 2D solid element



Fig. 4 The fundamental flexural mode of the design in [14] for maximizing the hardening behavior of a clamped–clamped beam. The color denotes the total displacement. The mode shape is obtained by using COMSOL Multiphysics 5.4 with 2D solid element. The image is re-used from [14]

optimization. Its occurrence is attributed to the improvement in the methodology, i.e. the change of the magnitude of the vibration mode is taken into account. The occurrence of central mass coincides with the fact that a central mass is used in ultra-wide bandwidth piezoelectric energy harvesting devices [8] and another result in topology optimization [21].

Further study is required to examine the applicability of the improved formulation of the optimization problem in a wider range of applications.

Table 1 shows a comparison of the two designs obtained by using the original objective function in P_{old} and the improved objective function in P_{new} . Note that

Table 1 Comparison of the two designs obtained by using the original objective function in P_{old} and the improved objective function in P_{new}

	P_{old}	P_{new}	ratio
$\frac{\gamma}{\gamma_0}$	13.35	10.11	0.757
$\frac{\Gamma}{\Gamma_0}$	7.56	8.05	1.064

γ_0 and Γ_0 are the corresponding values of the same initial design, while γ and Γ are the corresponding values of the two final designs. According to $\frac{\Gamma}{\Gamma_0}$, the new design obtained by using P_{new} has a larger value of Γ than the old design obtained by using P_{old} . However, when using the old objective function based on γ , this new design is a sub-optimal design because of the bias of the objective function. As discussed in Sect. 2 concerning the reduced-order models and frequency–amplitude relation, Γ provides a fair comparison of the optimized designs. This new design has a larger value of Γ . Consequently, this new design has a larger frequency shift for a given amplitude of the resonant peak than the old design. The improvement obtained by using the improved formulation in this example is 6.4%. In future work, the two optimized designs will be compared by using nonlinear frequency response and ring-down response.

4 Conclusions

This paper presents an improved formulation of the optimization problem for tuning the nonlinear dynamic response through the nonlinear modal coupling coefficients. For the hardening behavior of a clamped–clamped beam, the design obtained by using the improved formulation has a larger effective coefficient Γ than the design obtained by using the original formulation.

Further studies are required to extend this improved formulation of the optimization problem to multi-mode micro-mechanical resonators [14], topology optimization [21, 22], and optimization problems of micro-mechanical resonators with electrostatic actuation [23]. Additional studies are needed to examine the potential extension of the optimization frame to micro-mechanical cantilever-based structures with nonlinear inertial effects and nano-mechanical resonators where the non-local elastic effects prevail in the nonlinearity [24].

References

1. J.F. Rhoads, S.W. Shaw, K.L. Turner, Nonlinear dynamics and its applications in micro- and nanoresonators. *J. Dyn. Syst. Meas. Control* **132**, 034001 (2010)
2. B. Jeong, C. Pettit, S. Dharmasena, H. Keum, J. Lee, J. Kim, S. Kim, D.M. McFarland, L.A. Bergman, A.F. Vakakis, H. Cho, Utilizing intentional internal resonance to achieve multi-harmonic atomic force microscopy. *Nanotechnology* **27**, 125501 (2016)

3. W. Zhang, R. Baskaran, K.L. Turner, Effect of cubic nonlinearity on auto-parametrically amplified resonant MEMS mass sensor. *Sens. Actuator A Phys.* **102**, 139–150 (2002)
4. V.C. Meesala, M.R. Hajj, E. Abdel-Rahman, Bifurcation-based MEMS mass sensors. *Int. J. Mech. Sci.* **180**, 105705 (2020)
5. S.H. Nitzan, V. Zega, M. Li, C.H. Ahn, A. Corigliano, T.W. Kenny, D.A. Horsley, Self-induced parametric amplification arising from nonlinear elastic coupling in a micromechanical resonating disk gyroscope. *Sci. Rep.* **5**, 9036 (2015)
6. R.P. Middlemiss, A. Samarelli, D.J. Paul, J. Hough, S. Rowan, G.D. Hammond, Measurement of the Earth tides with a MEMS gravimeter. *Nature* **531**, 614–617 (2016)
7. K.R. Qalandar, B.S. Strachan, B. Gibson, M. Sharma, A. Ma, S.W. Shaw, K.L. Turner, Frequency division using a micromechanical resonance cascade. *Appl. Phys. Lett.* **105**, 244103 (2014)
8. A. Hajati, S.G. Kim, Ultra-wide bandwidth piezoelectric energy harvesting. *Appl. Phys. Lett.* **99**, 083105 (2011)
9. S. Dou, J.S. Jensen, Optimization of hardening/softening behavior of plane frame structures using nonlinear normal modes. *Comput. Struct.* **164**, 63–74 (2016)
10. T. Detroux, J. Noël, G. Kerschen, Tailoring the resonances of nonlinear mechanical systems. *Nonlinear Dyn.* **103**(4), 3611–3624 (2021). <https://doi.org/10.1007/s11071-020-06002-w>
11. S. Dou, J.S. Jensen, Optimization of nonlinear structural resonance using the incremental harmonic balance method. *J. Sound Vib.* **334**, 239–54 (2015)
12. A. Tripathi, A.K. Bajaj, Computational synthesis for nonlinear dynamics based design of planar resonant structures. *J. Vib. Acoust.* **135**, 051031 (2013)
13. A. Tripathi, A.K. Bajaj, Topology optimization and internal resonances in transverse vibrations of hyperelastic plates. *Int. J. Solids Struct.* **81**, 311–328 (2016)
14. S. Dou, B.S. Strachan, S.W. Shaw, J.S. Jensen, Structural optimization for nonlinear dynamic response. *Phil. Trans. R. Soc. A* **373**, 20140408 (2015)
15. L.L. Li, P.M. Polunin, S. Dou, O. Shoshani, B.S. Strachan, J.S. Jensen, S.W. Shaw, K.L. Turner, Tailoring the nonlinear response of MEMS resonators using shape optimization. *Appl. Phys. Lett.* **110**, 081902 (2017)
16. C. Touzé, M. Vidrascu, D. Chapelle, Direct finite element computation of non-linear modal coupling coefficients for reduced-order shell models. *Comput. Mech.* **54**, 567–580 (2014)
17. A. Frangi, G. Gobat, Reduced order modelling of the non-linear stiffness in MEMS resonators. *Int. J. Non Linear Mech.* **116**, 211–218 (2019)
18. S.H. Chen, Y.K. Cheung, H.X. Xing, Nonlinear vibration of plane structures by finite element and incremental harmonic balance method. *Nonlinear Dyn.* **26**, 87–104 (2001)
19. K. Svanberg, The method of moving asymptotes—a new method for structural optimization. *Int. J. Numer. Methods Eng.* **24**, 359–373 (1987)
20. F. Van Keulen, R.T. Haftka, N.H. Kim, Review of options for structural design sensitivity analysis. Part I: Linear systems. *Comput. Methods Appl. Mech. Eng.* **194**, 3213–3243 (2005)
21. S. Dou, J.S. Jensen, Analytical sensitivity analysis and topology optimization of nonlinear resonant structures with hardening and softening behavior, in *Proceedings of the 17th U.S. National Congress on Theoretical and Applied Mechanics, East Lansing* (2014). <https://orbit.dtu.dk/en/publications/analytical-sensitivity-analysis-and-topology-optimization-of-nonl>
22. J.S. Jensen, S. Dou, Topology optimization in nonlinear structural dynamics using direct computation of nonlinear coefficients, in *ECCOMAS Congress 2016: VII European Congress on Computational Methods in Applied Sciences and Engineering, Crete* (2016). <https://orbit.dtu.dk/en/publications/topology-optimization-in-nonlinear-structural-dynamics-using-dire>
23. J.S. Jensen, S. Dou, S.W. Shaw, Tailoring nonlinear dynamics of microbeam resonators with electrostatic actuation, in *Proceeding of 24th International Congress of Theoretical and Applied Mechanics*, vol. 1 (2016), pp. 148–149. <https://orbit.dtu.dk/en/publications/tailoring-nonlinear-dynamics-of-microbeam-resonators-with-electro>
24. M.A. Eltaher, M.E. Khater, S.A. Emam, A review on nonlocal elastic models for bending, buckling, vibrations, and wave propagation of nanoscale beams. *Appl. Math. Model.* **40**, 4109–4128 (2016)

An Improved Tensorial Implementation of the Incremental Harmonic Balance Method for Frequency-Domain Stability Analysis



Suguang Dou

1 Introduction

In recent years, there has been a renewed academic interest in the frequency-domain stability analysis of the time-periodic response of the dynamical systems [1–4]. The frequency-domain stability analysis is based on the Hill method, which combines the Floquet theory and the Fourier series expansion. One problem in frequency-domain stability analysis is related to spurious eigenvalues. In [1], Lazarus and Thomas proposed a criterion to sort the most converged eigenvalues, and validated it in a framework where the harmonic balance method (HBM) is combined with the asymptotic numerical method (ANM) for path-following or continuation of the response. However, even with a proper sorting criterion, Soykov and Ribeiro reported in [2] that an accurate frequency-domain stability analysis can require more harmonics than an accurate response analysis. This unaddressed problem has motivated the study in this work.

This study is performed in the framework of a tensorial implementation of the incremental harmonic balance (IHB) method. The original implementation was applied to structural optimization problems for tailoring the nonlinear resonances [5]. In a later study, the tensorial implementation of the IHB method is combined with the alternating frequency/time-domain method to study structural optimization problems for tuning the frequency–amplitude dependence of nonlinear normal modes in the context of frame structures [6]. Based on the existing tensorial implementation of the IHB method, the work in this paper investigates the frequency-domain stability analysis and suggests an important improvement in the implementation.

S. Dou (✉)

DTU Wind Energy, Technical University of Denmark, Roskilde, Denmark
e-mail: sudou@dtu.dk

2 Methodology

2.1 Time-Domain Equations of Motion

Consider a mechanical system with geometric nonlinearity. By using the nonlinear finite element models, the time-domain equations of motion can be written as

$$\mathbf{M} \frac{d^2 \mathbf{u}}{dt^2} + \mathbf{C} \frac{d\mathbf{u}}{dt} + \mathbf{g}(\mathbf{u}) = \mathbf{f}(\omega t) \quad (1)$$

where \mathbf{M} is the mass matrix, \mathbf{C} is the damping matrix, \mathbf{g} is a vector of the nonlinear internal forces which are nonlinear functions of \mathbf{u} , \mathbf{f} is a vector of the time-periodic external forces, t is the time, and $\omega = 2\pi/T$ is the circular frequency with T denoting the time period. Since the linear stiffness term is treated as a part of the nonlinear internal force \mathbf{g} , it is not explicitly shown in the above equation.

In the incremental harmonic balance method, a new scale of time is introduced as $\tau = \omega t = 2\pi(t/T)$. By using the new time scale τ , the time-domain equations of motion in Eq. (1) become

$$\omega^2 \mathbf{M} \frac{d^2 \mathbf{u}}{d\tau^2} + \omega \mathbf{C} \frac{d\mathbf{u}}{d\tau} + \mathbf{g}(\mathbf{u}) = \mathbf{f}(\tau) \quad (2)$$

2.2 Frequency-Domain Equations of Motion

The incremental harmonic balance method is applied to Eq. (2) through a few steps. First, a Fourier basis is introduced to project the time-domain response into the frequency domain as

$$\mathbf{u}(\tau) = \mathbf{s}(\tau) \mathbf{q} \quad (3)$$

where $\mathbf{s}(\tau)$ is a row vector of Fourier basis consisting of the sine and cosine functions, and \mathbf{q} is a column vector of Fourier coefficients which represent the frequency-domain response.

Substituting Eq. (3) into Eq. (2) and applying the Galerkin method, a system of nonlinear equations are obtained as [5]

$$\left(\omega^2 \overline{\mathbf{M}} + \omega \overline{\mathbf{C}} \right) \mathbf{q} + \overline{\mathbf{g}}(\mathbf{q}) = \overline{\mathbf{f}} \quad (4)$$

where $\overline{\mathbf{M}}$, $\overline{\mathbf{C}}$, $\overline{\mathbf{g}}$, and $\overline{\mathbf{f}}$ denote the frequency-domain counterpart of the mass matrix, the damping matrix, the internal force, and external force, respectively. For the convenience of communication, we refer to Eq. (4) as the frequency-domain governing equation. Equation (4) can also be written in a more general form as

$$\mathbf{r}(\mathbf{q}, \omega) = \mathbf{0} \quad (5)$$

where

$$\mathbf{r}(\mathbf{q}, \omega) = \left(\omega^2 \overline{\mathbf{M}} + \omega \overline{\mathbf{C}} \right) \mathbf{q} + \overline{\mathbf{g}}(\mathbf{q}) - \overline{\mathbf{f}} \quad (6)$$

2.3 Response Analysis

Since the frequency-domain governing equation is nonlinear, Newton–Raphson method is applied in the incremental harmonic balance method to solve the frequency-domain response. Consider a known solution represented by \mathbf{q}_0 and ω_0 . An unknown solution in the neighborhood of \mathbf{q}_0 and ω_0 can be expressed as

$$\mathbf{q} = \mathbf{q}_0 + \Delta\mathbf{q}, \quad \omega = \omega_0 + \Delta\omega \quad (7)$$

where $\Delta\mathbf{q}$ and $\Delta\omega$ are the increments of response and frequency, respectively. Substituting Eq. (7) into Eq. (5), we have

$$\mathbf{r}(\mathbf{q}_0 + \Delta\mathbf{q}, \omega_0 + \Delta\omega) = \mathbf{0} \quad (8)$$

Expanding Eq. (8) at \mathbf{q}_0 and ω_0 and retaining the first-order approximation, an incremental form of the frequency-domain governing equation is obtained as

$$\mathbf{K}_q \Delta\mathbf{q} + \mathbf{K}_\omega \Delta\omega = -\mathbf{r}(\mathbf{q}_0, \omega_0) \quad (9)$$

where

$$\mathbf{K}_q = \left. \frac{\partial \mathbf{r}(\mathbf{q}, \omega)}{\partial \mathbf{q}} \right|_{\mathbf{q}=\mathbf{q}_0, \omega=\omega_0}, \quad (10a)$$

$$\mathbf{K}_\omega = \left. \frac{\partial \mathbf{r}(\mathbf{q}, \omega)}{\partial \omega} \right|_{\mathbf{q}=\mathbf{q}_0, \omega=\omega_0}. \quad (10b)$$

Substituting Eq. (6) into Eqs. (11a) and (11b), we have

$$\mathbf{K}_q = \omega_0^2 \overline{\mathbf{M}} + \omega_0 \overline{\mathbf{C}} + \overline{\mathbf{K}}_t(\mathbf{q}_0) \quad (11a)$$

$$\mathbf{K}_\omega = 2\omega_0 \overline{\mathbf{M}} + \overline{\mathbf{C}} \quad (11b)$$

where

$$\bar{\mathbf{K}}_t(\mathbf{q}_0) = \left. \frac{\partial \bar{\mathbf{g}}(\mathbf{q})}{\partial \mathbf{q}} \right|_{\mathbf{q}=\mathbf{q}_0} \quad (12)$$

Eq. (9) can be solved with the quantities in Eqs. (11a)–(12), and a continuation approach such as the arc-length method [5].

2.4 Stability Analysis

The local stability of the obtained time-periodic response \mathbf{u}_0 is studied by adding a small disturbance δ :

$$\mathbf{u} = \mathbf{u}_0 + \delta \quad (13)$$

Substituting Eq. (13) into Eq. (2) and retaining the first-order approximation, the following equation is obtained as

$$\omega_0^2 \mathbf{M} \frac{d^2 \delta}{d\tau^2} + \omega_0 \mathbf{C} \frac{d\delta}{d\tau} + \mathbf{K}_t(\mathbf{q}_0) \delta = \mathbf{0} \quad (14)$$

In order to study the frequency-domain stability, the disturbance δ is assumed as

$$\delta = e^{\lambda \tau} \mathbf{s} \mathbf{p} \quad (15)$$

where λ and \mathbf{p} denote the Floquet exponent and vector, respectively.

The first- and second-order derivatives of δ are

$$\frac{d\delta}{d\tau} = \lambda e^{\lambda \tau} \mathbf{s} \mathbf{p} + e^{\lambda \tau} \frac{d\mathbf{s}}{d\tau} \mathbf{p} \quad (16a)$$

$$\frac{d^2 \delta}{d\tau^2} = \lambda^2 e^{\lambda \tau} \mathbf{s} \mathbf{p} + 2\lambda e^{\lambda \tau} \frac{d\mathbf{s}}{d\tau} \mathbf{p} + e^{\lambda \tau} \frac{d^2 \mathbf{s}}{d\tau^2} \mathbf{p} \quad (16b)$$

Substituting Eqs. (15)–(16b) into Eq. (14) and applying the Galerkin method, a quadratic eigenvalue problem is obtained as

$$\left(\mathbf{J}_2 \lambda^2 + \mathbf{J}_1 \lambda + \mathbf{J}_0 \right) \mathbf{p} = \mathbf{0} \quad (17)$$

where

$$\mathbf{J}_0 = \mathbf{K}_q(\mathbf{q}_0, \omega_0), \quad (18a)$$

$$\mathbf{J}_1 = 2\omega_0^2 \mathbf{M} \otimes \mathbf{h}^{(1)} + \omega_0 \mathbf{C} \otimes \mathbf{h}^{(2)}, \quad (18b)$$

$$\mathbf{J}_2 = \omega_0^2 \mathbf{M} \otimes \mathbf{h}^{(2)} \quad (18c)$$

Here the quantities of $\mathbf{h}^{(1)}$ and $\mathbf{h}^{(2)}$ are given in the following section. The quadratic eigenvalue problem in Eq.(17) can be directly solved. Alternatively, it can be re-written into a linear eigenvalue problem [2].

3 Tensorial Implementation

Let N_H denote the highest-order of the retained harmonics. The quantities $\mathbf{h}^{(0)}$, $\mathbf{h}^{(1)}$, and $\mathbf{h}^{(2)}$ are defined as

$$\mathbf{h}^{(0)} = -\frac{1}{2} \begin{bmatrix} 0 & \mathbf{0} & \mathbf{0} \\ \mathbf{0} & \widehat{\mathbf{I}} & \mathbf{0} \\ \mathbf{0} & \mathbf{0} & \widehat{\mathbf{I}} \end{bmatrix}, \quad \widehat{\mathbf{I}} = \begin{bmatrix} 1 & & \\ & \ddots & \\ & & N_H^2 \end{bmatrix}_{N_H \times N_H} \quad (19a)$$

$$\mathbf{h}^{(1)} = \frac{1}{2} \begin{bmatrix} 0 & \mathbf{0} & \mathbf{0} \\ \mathbf{0} & \mathbf{0} & \bar{\mathbf{I}} \\ \mathbf{0} & -\bar{\mathbf{I}} & \mathbf{0} \end{bmatrix}, \quad \bar{\mathbf{I}} = \begin{bmatrix} 1 & & \\ & \ddots & \\ & & N_H \end{bmatrix}_{N_H \times N_H} \quad (19b)$$

$$\mathbf{h}^{(2)} = \frac{1}{2} \begin{bmatrix} 2 & \mathbf{0} & \mathbf{0} \\ \mathbf{0} & \mathbf{I} & \mathbf{0} \\ \mathbf{0} & \mathbf{0} & \mathbf{I} \end{bmatrix}, \quad \mathbf{I} = \begin{bmatrix} 1 & & \\ & \ddots & \\ & & 1 \end{bmatrix}_{N_H \times N_H} \quad (19c)$$

The frequency-domain counterparts of the mass and damping matrices, and the internal and external forces are computed as

$$\bar{\mathbf{M}} = \mathbf{M} \otimes \mathbf{h}^{(0)}, \quad (20a)$$

$$\bar{\mathbf{C}} = \mathbf{C} \otimes \mathbf{h}^{(1)}, \quad (20b)$$

$$\bar{\mathbf{g}} = \begin{bmatrix} \mathbf{h}^{(2)} \mathcal{G}_1 \\ \vdots \\ \mathbf{h}^{(2)} \mathcal{G}_{N_{dof}} \end{bmatrix}, \quad (20c)$$

$$\bar{\mathbf{f}} = \begin{bmatrix} \mathbf{h}^{(2)} \mathcal{F}_1 \\ \vdots \\ \mathbf{h}^{(2)} \mathcal{F}_{N_{dof}} \end{bmatrix} \quad (20d)$$

where \otimes stands for Kronecker product, \mathcal{G}_i and \mathcal{F}_i denote the Fourier coefficients of the internal and external forces for the i th degree of freedom.

The frequency-domain counterpart of the tangent stiffness matrix $\bar{\mathbf{K}}_t$ is obtained with the assistance of a three-dimensional tensor $\mathbf{h}^{(3)}$ and the operation of tensor contraction as

$$\bar{\mathbf{K}}_t = \begin{bmatrix} \mathbf{h}^{(3)} : \mathcal{K}_{1,1} & \dots & \mathbf{h}^{(3)} : \mathcal{K}_{1,N_{dof}} \\ \vdots & \ddots & \vdots \\ \mathbf{h}^{(3)} : \mathcal{K}_{N_{dof},1} & \dots & \mathbf{h}^{(3)} : \mathcal{K}_{N_{dof},N_{dof}} \end{bmatrix} \quad (21)$$

where the symbol “:” denotes the tensor contraction operation, and $\mathcal{K}_{i,j}$ denotes a vector of Fourier coefficients corresponding to the component at the position (i, j) of $\mathbf{K}_t(\mathbf{u}(\tau))$.

In Eq. (21), $\mathbf{h}^{(3)}$ is a three-dimension tensor. Two specific forms of $\mathbf{h}^{(3)}$ are given in the following section for both the original and improved implementations. The tensor contraction operation of this three-dimension tensor $\mathbf{h}^{(3)}$ and a vector of Fourier coefficients $\mathcal{K}_{i,j}$ leads to a two-dimensional matrix of the size $(2N_H + 1) \times (2N_H + 1)$.

4 Numerical Implementation and Results

4.1 Three-Dimension Tensor

In the original numerical implementation [5], this three-dimension tensor is defined as

$$\mathbf{h}^{(3)}(i, j, k) = \frac{1}{2\pi} \int_0^{2\pi} \mathcal{S}_i(\tau) \mathcal{S}_j(\tau) \mathcal{S}_k(\tau) d\tau \quad (22)$$

where $\mathcal{S}_i(\tau)$ denote the i th function in a vector \mathcal{S} of cosine and sine functions sorted as

$$\mathcal{S} = [1 \quad \cos(\tau) \quad \dots \quad \cos(N_H \tau) \quad \sin(\tau) \quad \dots \quad \sin(N_H \tau)] \quad (23)$$

and the indices i, j, k are given as

$$i, j, k = 1, \dots, 2N_H + 1 \quad (24)$$

In the improved numerical implementation, this three-dimension tensor is defined as

$$\mathbf{h}^{(3)}(i, j, k) = \frac{1}{2\pi} \int_0^{2\pi} \mathcal{S}_i(\tau)\mathcal{S}_j(\tau)\widehat{\mathcal{S}}_k(\tau) d\tau \tag{25}$$

where $\widehat{\mathcal{S}}$ is given as

$$\widehat{\mathcal{S}} = [1 \ \cos(\tau) \ \dots \ \cos(2N_H\tau) \ \sin(\tau) \ \dots \ \sin(2N_H\tau)] \tag{26}$$

and the indices i, j, k are given as

$$i, j = 1, \dots, 2N_H + 1, \quad k = 1, \dots, 4N_H + 1 \tag{27}$$

Note that the size of the three-dimension tensor in Eq. (22) is $(2N_H + 1) \times (2N_H + 1) \times (2N_H + 1)$, whereas the three-dimension tensor in Eq. (25) is $(2N_H + 1) \times (2N_H + 1) \times (4N_H + 1)$.

One way to visualize the three-dimension tensor $\mathbf{h}^{(3)}$ is to project it into two-dimension plane, see Fig. 1. The harmonics in the first two dimensions are more thoroughly coupled in the improved tensor in Eq. (25) than in the original tensor in Eq. (22).

The operation of tensor contraction and a similar definition of the three-dimension tensor were also used in a recent study of the Galerkin averaging-incremental harmonic balance method [7].

The importance of this improvement can be seen from both theoretical and numerical points of view. From theoretical point of view, this improvement enables to accurately compute the frequency counterpart of the tangent stiffness matrix $\overline{\mathbf{K}}_t$

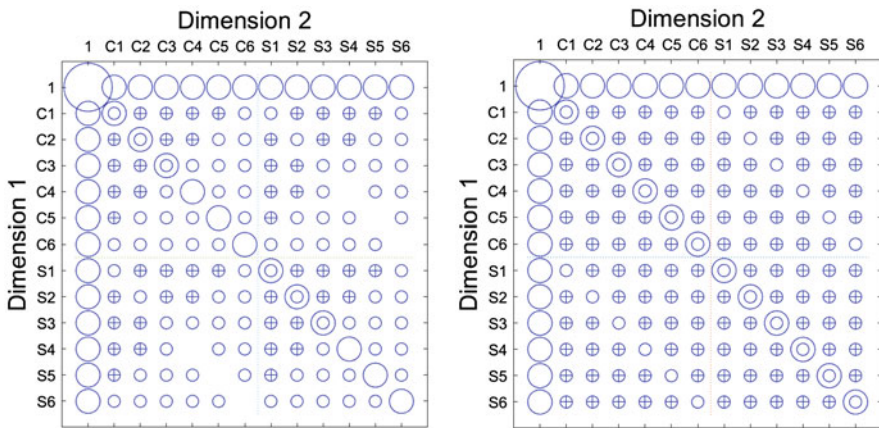


Fig. 1 Visualization of the original and the improved three-dimension tensor $\mathbf{h}^{(3)}$ in a two-dimension plane. $N_H = 6$. Left: the original tensor. Right: the improved tensor. A circle or a cross indicates there is a non-zero value along the third dimension. The size of the circle or cross is proportional to the magnitude of the value in the tensor. C_n and S_n denote the n th order cosine and sine function, respectively

for polynomial nonlinearity up to cubic order. For the cubic nonlinearity, its tangent stiffness is in quadratic form. When the harmonics of the response is up to the order of N_H , the harmonics of the tangent stiffness of the cubic nonlinearity is up to the order of $2N_H$. In the original implementation, the $2N_H$ harmonics in the tangent stiffness is truncated to the order of N_H . In the new implementation with the improvement, the $2N_H$ harmonics of the tangent stiffness are fully used in the computation without truncation. From numerical point of view, this reduces the number of harmonics required to achieve a converged and accurate analysis of response and stability. Without this improvement, the original implementation requires a large value of N_H , which is larger than the highest order of the significant harmonics in the response, to ensure the convergence and accuracy of the results. For the nonlinear finite element example shown later in the numerical results, the significant harmonic in the response is the fundamental harmonic. The original implementation without the improvement cannot converge with $N_H = 1$ around the resonance peak. However, the new implementation with the improvement can converge smoothly and efficiently with $N_H = 1$.

4.2 Stability Analysis

The improved implementation is applied to a finite element model of a clamped-clamped beam with geometric nonlinearity [5]. The beam is discretized into 20 Euler–Bernoulli beam elements. The quadratic and cubic nonlinearity is included to account for the midplane stretching effect [8]. The material properties are given as: Young’s modulus $E = 205$ Gpa, and mass density $\rho = 7800$ Kg/m³. The cross section is a solid square with $0.01\text{ m} \times 0.01\text{ m}$, and the beam length is $L = 150\sqrt{I/A}$, where A and I denote the area and the second moment of area, respectively. The damping matrix is proportional to the mass matrix, i.e. $\mathbf{C} = \alpha\mathbf{M}$, where $\alpha = 15.58$, leading to a modal damping ratio of 1% for the fundamental flexural mode. The load is applied at the three nodes around the midspan with a magnitude of 10.12 N.

In the stability analysis, a set of $4N_{dof}$ Floquet exponents with the imaginary parts of the smallest magnitudes are selected. The choice of using $4N_{dof}$ Floquet exponents instead of $2N_{dof}$ Floquet exponents is to ensure a full set of $2N_{dof}$ *fundamental* Floquet exponents are completely included. When the reliable Floquet exponents are determined, they are used to estimate the stability of the time-periodic response. A time-periodic response is unstable when there is at least one selected Floquet exponent whose real part is positive

$$\text{Re}(\lambda_i) > 0 \quad (28)$$

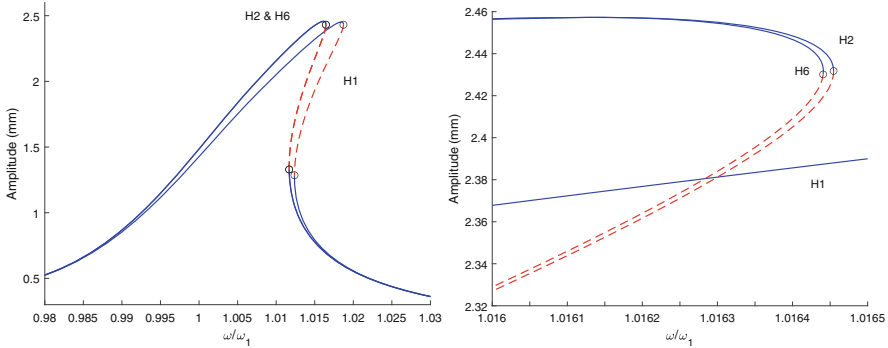


Fig. 2 Nonlinear frequency response of a nonlinear FE model of a clamped–clamped beam. Left: The resonance response at the lowest eigenfrequency. Right: Zoom of the resonance peaks. The solid and the dashed line indicate the stable and unstable response, respectively. The circles indicate the locations of bifurcations. The text hn indicates the number of harmonics

Figure 2 shows the response and stability computed by using the improved tensorial implementation. It can be seen that a small number of harmonics ($N_H \geq 2$) is sufficient to realize an accurate stability analysis. This efficiency is attributed to the proposed improvement in the tensorial implementation.

5 Conclusions

This paper presents an improved tensorial implementation of the incremental harmonic balance method in [5, 6]. The improvement enables an efficient and accurate frequency-domain stability analysis with a small number of harmonics. The proposed implementation is demonstrated by using a finite element model of a clamped–clamped beam with geometric nonlinearity.

The insight gained in this study may be used in other variants of the harmonic balance method. The essence of the proposed improvement is to account for the higher-order ($\geq N_H$) harmonics in the Jacobian matrix that may be truncated in the implementation. These higher-order harmonics are more important for the frequency-domain stability analysis than for the frequency-domain response analysis.

Further study is required to reduce the computational cost of the frequency-domain stability analysis by using advanced model order reduction techniques.

References

1. A. Lazarus, O. Thomas, A harmonic-based method for computing the stability of periodic solutions of dynamical systems. *C.R. Mec.* **338**, 510–517 (2010)
2. S. Stoykov, P. Ribeiro, Stability of nonlinear periodic vibrations of 3D beams. *Nonlinear Dyn.* **66**, 335–353 (2011)
3. F.L. Traversa, F. Bonani, Improved harmonic balance implementation of Floquet analysis for nonlinear circuit simulation. *Int. J. Electron. Commun.* **66**, 357–363 (2012)
4. T. Detroux, L. Renson, L. Masset, G. Kerschen, The harmonic balance method for bifurcation analysis of large-scale nonlinear mechanical systems. *Comput. Methods Appl. Mech. Eng.* **296**, 18–38 (2015)
5. S. Dou, J.S. Jensen, Optimization of nonlinear structural resonance using the incremental harmonic balance method. *J. Sound Vib.* **334**, 239–254 (2015)
6. S. Dou, J.S. Jensen, Optimization of hardening/softening behavior of plane frame structure using nonlinear normal modes. *Comput. Struct.* **164**, 63–74 (2016)
7. R. Ju, W. Fan, W. Zhu, An efficient Galerkin averaging-incremental harmonic balance method based on the fast Fourier transform and tensor contraction. *J. Acoust. Vib.* **142**(6), 061011 (2020)
8. S.H. Chen, Y.K. Cheung, H.X. Xing, Nonlinear vibration of plane structures by finite element and incremental harmonic balance method. *Nonlinear Dyn.* **26**, 87–104 (2001)

Statistical Analysis of an Iterative Algorithm Class for Dynamical Systems



Carlos Argáez, Peter Giesl, and Sigurdur Freyr Hafstein

1 Introduction

Dynamical systems are of fundamental importance in science and engineering because they offer a compact language to describe physical and other phenomena. In recent years, novel algorithms to construct complete Lyapunov functions describing the qualitative behaviour of dynamical systems have been introduced and improved [1–5]. The importance of Lyapunov functions lies in their ability to locate the systems' basins of attraction. They were introduced in 1893 by Lyapunov [6] to study the stability of equilibria of dynamical systems.

Let us consider

$$\dot{\mathbf{x}} = \mathbf{f}(\mathbf{x}), \quad (1)$$

where $\mathbf{x} \in \mathbb{R}^n$, $n \in \mathbb{N}$. A Lyapunov function for the system (1) is an auxiliary scalar-valued function, whose domain is a subset of the state-space and which is strictly decreasing along all solution trajectories in a neighbourhood of an attractor, such as an equilibrium or a periodic orbit.

A Lyapunov function is only defined in the neighbourhood of one attractor. A natural extension is a function defined on the whole state-space, a *complete Lyapunov function* (CLF), see [7–11]. A CLF allows for dividing the state-space into two disjoint areas: The area of gradient-like flow, where the solution trajectories flow through, and the chain-recurrent set, where infinitesimal perturbations can make the

C. Argáez (✉) · S. F. Hafstein
Science Institute, University of Iceland, Reykjavik, Iceland
e-mail: carlos@hi.is; shafstein@hi.is

P. Giesl
Department of Mathematics, University of Sussex, Falmer, UK
e-mail: p.a.giesl@sussex.ac.uk

system recurrent. On these two areas, the system behaves in fundamentally different ways. On the gradient-like part, a CLF V is strictly decreasing along solutions, whereas it is constant on the chain-recurrent set. For a sufficiently smooth CLF the orbital derivative $V'(\mathbf{x}) = \nabla V(\mathbf{x}) \cdot \mathbf{f}(\mathbf{x})$, i.e. the derivative along solutions, in these two areas is strictly negative or zero, respectively.

Although it is very difficult to construct Lyapunov functions for non-linear dynamical systems, there has been considerable progress in the last decades, see the review [12]. While there are several different approaches to computationally study dynamical systems, c.f. [13–16], in this paper we are mainly concerned with the methods from [1–5]. They allow for the computation of a (complete) Lyapunov function for any system described by an autonomous ordinary differential equation of the form (1).

Inspired by a method to compute classical Lyapunov functions for one stable equilibrium using Radial Basis Functions (RBFs), c.f. [5], the authors of this paper have developed a computationally efficient method to describe dynamical systems through the construction of a CLF and the subsequent localisation of the chain-recurrent set. The general idea is to find a CLF with $v'(\mathbf{x}) \leq 0$ by approximating a “solution” to the ill-posed problem $V'(\mathbf{x}) = -1$, where $V'(\mathbf{x}) = \nabla V(\mathbf{x}) \cdot \mathbf{f}(\mathbf{x})$ is the derivative along solutions of the ODE, i.e. the orbital derivative. A function v is computed using RBFs, a mesh-free collocation technique, such that $v'(\mathbf{x}) = -1$ is fulfilled at all points \mathbf{x} in a finite set X of collocation points.

The discretised problem of computing v is well-posed and possesses a unique solution. However, the computed function v cannot fulfil the PDE $v'(\mathbf{x}) = -1$ at all points of the chain-recurrent set, such as an equilibrium or a periodic orbit. This is the key component of our general algorithms to locate the chain-recurrent sets; to determine the chain-recurrent set, we use the area where $v'(\mathbf{x}) \approx 0$, c.f. [1–3].

In Sect. 2, we give more details about the algorithm to construct a CLF and to determine the chain-recurrent set, including an iterative method. Section 3 applies the method to an example and performs a detailed analysis with respect to two different evaluation grids used in the literature: We analyse the distribution of values in the evaluation grid and compare them using the median and the average in the iteration. We conclude in Sect. 4.

2 Description of the Algorithm

We will present the methodology introduced in [3], which is included in the freely distributed software LyapXool, see [4]. We first substitute the dynamical system (1) by

$$\dot{\mathbf{x}} = \hat{\mathbf{f}}(\mathbf{x}), \quad \text{where} \quad \hat{\mathbf{f}}(\mathbf{x}) = \frac{\mathbf{f}(\mathbf{x})}{\sqrt{\delta^2 + \|\mathbf{f}(\mathbf{x})\|^2}}, \quad (2)$$

with a small parameter $\delta > 0$ and where $\|\cdot\|$ denotes the Euclidean norm. Systems (1) and (2) have the same trajectories, but the speed of the solutions to (2) is nearly uniform. This was shown to deliver superior results, see [3].

2.1 Mesh-free Collocation

Mesh-free collocation methods, in particular with RBFs [5], are a powerful methodology for solving generalised interpolation problems. RBFs are certain real-valued functions, whose evaluation depends only on the distance from the origin; Gaussians, multiquadrics, and Wendland functions are examples of such functions.

Mesh-free collocation enables us to locally use a high resolution of collocation points to solve PDEs. In our work we use the compactly supported Wendland functions $\psi_{l,k}$ as RBFs, see [17]. They are positive definite functions that are polynomials on their compact support. We consider the RBF $\psi(\mathbf{x}) := \psi_{l,k}(\|\mathbf{x}\|)$, where $k \in \mathbb{N}$ is a smoothness parameter and l is fixed as $l = \lfloor \frac{n}{2} \rfloor + k + 1$. Our code uses the C++ tool from [18] to compute the Wendland functions. The Reproducing Kernel Hilbert Space (RKHS) corresponding to ψ contains the same functions as the Sobolev space $W_2^{k+(n+1)/2}(\mathbb{R}^n)$ and the spaces are norm equivalent.

Mesh-free collocation uses a finite set of collocation points $X = \{\mathbf{x}_1, \dots, \mathbf{x}_N\} \subset \mathbb{R}^n$, where the PDE is satisfied. We choose X as a subset of the following hexagonal grid with fineness-parameter $\alpha_{\text{Hexa-basis}} \in \mathbb{R}^+$:

$$\left\{ \alpha_{\text{Hexa-basis}} \sum_{k=1}^n i_k \omega_k : i_k \in \mathbb{Z} \right\}, \quad (3)$$

where $\omega_1 = (2\epsilon_1, 0, 0, \dots, 0)$, $\omega_2 = (\epsilon_1, 3\epsilon_2, 0, \dots, 0)$,

$$\dots, \omega_n = (\epsilon_1, \epsilon_2, \epsilon_3, \dots, (n+1)\epsilon_n) \text{ and } \epsilon_k = \sqrt{\frac{1}{2k(k+1)}}, \quad k \in \mathbb{N}.$$

This grid has been shown to optimally balance the opposing aims of a small fill distance, i.e. good error estimates, and a large separation distance of collocation points, i.e. small condition numbers of the collocation matrices, see [19]. All equilibria, i.e. points \mathbf{x} with $\mathbf{f}(\mathbf{x}) = \mathbf{0}$, need to be removed from the set of the collocation points X , since otherwise the collocation matrix would be singular.

The approximated v is the norm-minimal function in the corresponding RKHS that satisfies the PDE $v'(\mathbf{x}) = -1$ at all collocation points. Practically, we find v by solving a system of N linear equations, where N is the number of collocation points.

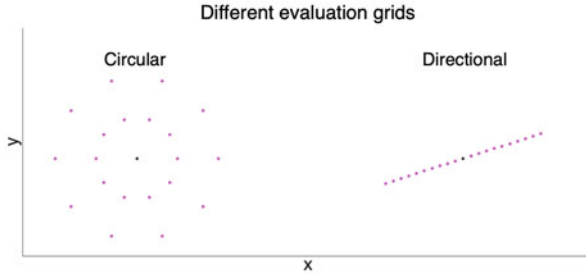


Fig. 1 Circular evaluation grid points around a collocation point (black) according to (4) and the directional evaluation grid points (5) around another collocation point (black)

To evaluate the computed CLF, several different evaluation grids have been proposed; in this paper we will focus on two different choices, see Fig. 1. The first one distributes points homogeneously in two circumferences of radius $r > 0$ and $r/2$, see [3].

$$Y_{\mathbf{x}_j} = \{\mathbf{x}_j + r\alpha_{\text{Hexa-basis}}(\cos(\theta), \sin(\theta))\} \cup \{\mathbf{x}_j + \frac{r}{2}\alpha_{\text{Hexa-basis}}(\cos(\theta), \sin(\theta))\} \quad (4)$$

where $\theta \in \{\pi/16, 2\pi/16, 3\pi/16, \dots, 2\pi\}$.

The grid (4) can be generalised to higher dimensions. However, the growth of the evaluation points cardinality is exponential in the dimension. To avoid that, we use evaluation points that are aligned along the flow of the ODE system at the collocation point in [2], see (5). Here, $r \in (0, 1)$ determines how far the evaluation points will be placed, and $m \in \mathbb{N}$ denotes the number of points on each side of the collocation points.

$$Y_{\mathbf{x}_j} = \left\{ \mathbf{x}_j \pm \frac{r \cdot k \cdot \alpha_{\text{Hexa-basis}} \cdot \hat{\mathbf{f}}(\mathbf{x}_j)}{m} : k \in \{1, \dots, m\} \right\}. \quad (5)$$

2.2 Algorithm

Since the PDE $V'(\mathbf{x}) = -1$ does not have a solution for all \mathbf{x} in the chain-recurrent set, we use an iterative algorithm to update the right-hand side in each step, using the results of the previous approximation; note that we only need to prescribe the value $V'(\mathbf{x}_j)$ at each collocation point \mathbf{x}_j . Our general algorithm to compute CLFs, given a set of collocation points X , is:

1. Compute the approximate solution v_0 to $V'(\mathbf{x}) = -1$; set $i = 0$
2. To approximate the chain-recurrent set by X^0 , for each collocation point \mathbf{x}_j , compute $v'_i(\mathbf{y})$ for all $\mathbf{y} \in Y_{\mathbf{x}_j}$, see (4) or (5). If $v'_i(\mathbf{y}) > \gamma$ for an $\mathbf{y} \in Y_{\mathbf{x}_j}$, then $\mathbf{x}_j \in X^0$, else $\mathbf{x}_j \in X^-$, where $\gamma \leq 0$ is a chosen critical value

3. Define $\tilde{r}_j = \left(\frac{1}{|Y_{x_j}|} \sum_{y \in Y_{x_j}} v'_i(\mathbf{y}) \right)_-$, where $x_- = x$ for $x \leq 0$ and $x_- = 0$ for $x > 0$
4. Define $r_j = \frac{N}{\sum_{i=1}^N |\tilde{r}_i|} \tilde{r}_j$
5. Compute the approximate solution v_{i+1} to $V'(\mathbf{x}_j) = r_j$
6. Set $i \rightarrow i + 1$ and repeat Steps 2–5 until some predefined criterion is reached

The aim of this paper is to investigate two aspects of the algorithm. Firstly, we investigate if using the average or the median in 3 is more appropriate for reiterating. Secondly, we compare the results using the circular or the directional evaluation grid. To enable a fair comparison, we use the same number of evaluation points in both grids.

3 Results

Let us consider system (1) with the right-hand side

$$f(x, y) = \begin{pmatrix} -x(x^2 + y^2 - 1/4)(x^2 + y^2 - 1) - y \\ -y(x^2 + y^2 - 1/4)(x^2 + y^2 - 1) + x \end{pmatrix}. \tag{6}$$

This system has an asymptotically stable equilibrium at the origin and two periodic circular orbits: an asymptotically stable periodic orbit at $\Omega_1 = \{(x, y) \in \mathbb{R}^2 \mid x^2 + y^2 = 1\}$ and a repelling periodic orbit at $\Omega_2 = \{(x, y) \in \mathbb{R}^2 \mid x^2 + y^2 = 1/4\}$.

The Wendland function used for computing a CLF to system (6) is $\psi_{5,3}$ with $c = 1$. The collocation points were set in the region $[-1.5, 1.5] \times [-1.5, 1.5] \subset \mathbb{R}^2$ and we used a hexagonal grid (3) with $\alpha_{\text{Hexa-basis}} = 0.09164$. We used both the circular grid with 10 different angles for two concentric circumferences and the directional grid (5) with parameters $m = 10$ and $r = 0.5$, resulting in 20 evaluation points per collocation point in both cases. We used $\delta^2 = 10^{-8}$, see (2), and the critical value $\gamma = -0.25$ in Step 2 of the Algorithm. For a plot of this CLF see [1].

3.1 Average and Median

For the average and the median, we use the classical definitions. The average is defined and used in the algorithm in Sect. 2.2. When using the median, the algorithm in Sect. 2.2 is modified accordingly. The median of numbers, assembled in a vector R in ascending order is defined as $\text{median}(R) = \frac{1}{2} \left(R_{\lfloor \frac{\#R+1}{2} \rfloor} + R_{\lceil \frac{\#R+1}{2} \rceil} \right)$. The median thus takes into account only the middle number(s).

3.2 Distribution

Let us consider the distribution of the values of the CLF’s orbital derivative for some random collocation points in iteration 0, using a circular evaluation grid, see Fig. 2. As none of these is Gaussian, the average value of the orbital derivative in Step 3 is not necessarily the optimal choice for a new value on the right-hand side in Step 5 in the algorithm for the next iteration.

We will now compare the distributions of the orbital derivatives when using circular and directional evaluation grids. In contrast to Fig. 2, we will now display the precise spatial distribution. We have chosen one random point in the chain-recurrent set (first two figures), and one random point, where the flow is gradient-like (last two figures), see Fig. 3.

For the chain-recurrent point with the circular grid (first figure), the values are random and vary between -1.3 and -0.1 ; the values for the gradient-like point (third figure) are negative between -1.5 and -1 . For the same collocation points, the results using the directional evaluation grid are very different. For the chain-recurrent point (second figure), the orbital derivative is clearly forced down to -1 at the collocation point, while being positive far away with maximum at 0.4 . The values have a distinct pattern with minimum at the collocation point with value -1 . Since the integral of the orbital derivative over the whole periodic orbit must be zero and we force it to be negative on some points, it has to be positive elsewhere. For the gradient-like point (fourth figure), the orbital derivative is between -1.1 and -0.7 .

While for points where the flow is gradient-like the difference between the circular and directional evaluation grids is not significant, it becomes clear that for points in the chain-recurrent set, the directional grid contains much more relevant information. The circular grid diffuses the information by considering many evaluation points out of the chain-recurrent set. The directional grid, however, only contains points which are of the same type as the collocation point (chain-recurrent/gradient-flow) and thus amplifies and clarifies the information: for points with gradient-like flow, the orbital derivative is close to -1 under the directional grid, while for points in the chain-recurrent set it displays a characteristic shape with a minimum at -1 and maxima at 0.4 for those points away from the collocation point.

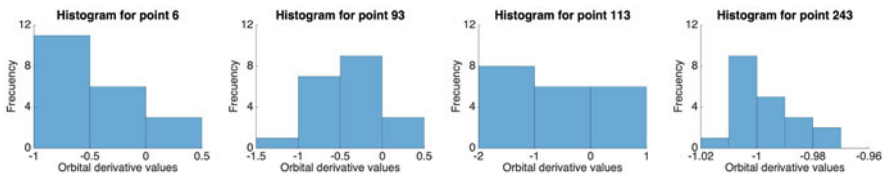


Fig. 2 Orbital derivative distribution around collocation points: circular evaluation grid. The points were chosen randomly. None of the distributions is Gaussian

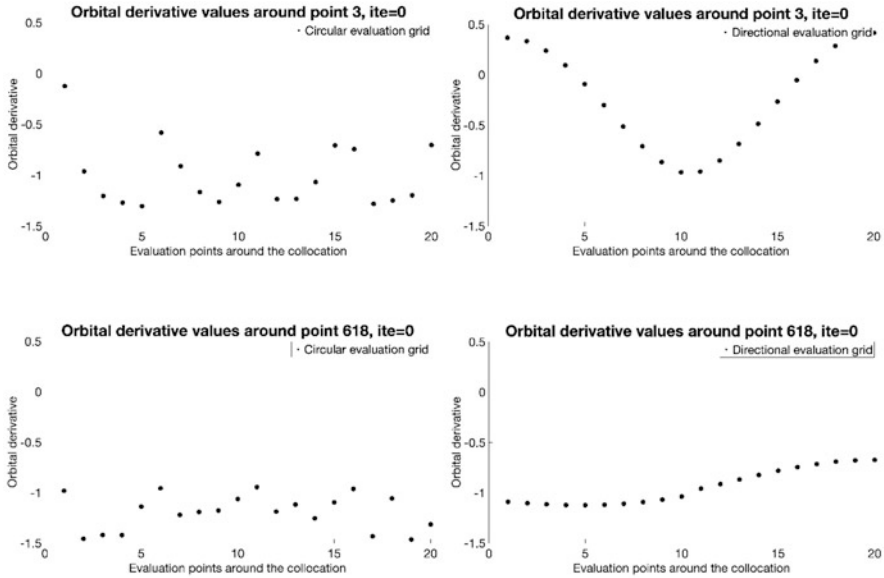


Fig. 3 Distribution of the orbital derivative around two collocation points in iteration 0. First: collocation point in chain-recurrent set, circular grid, second: collocation point in chain-recurrent set, directional grid, third: collocation point in gradient-like flow, circular grid, fourth: collocation point in gradient-like flow, directional grid

3.3 Iterations

Now we consider iterations: The goal of these iterations is to determine the right-hand side of the PDE used to construct the CLF. In particular, the right-hand side should become 0 for points in the chain-recurrent set, while it should stay strictly negative in the gradient-like flow. We use either the circular or the directional evaluation grids combined with either the average or the median. The results for iteration 4 are shown in Fig. 4 for the circular (upper row) and the directional (bottom row) evaluation grids.

Let us first consider a point in the chain-recurrent set (first column). While the circular evaluation grid (up) displays a large variation of values between -1.3 and -0.2 for the average values (column 1), and between -0.7 and -0.1 for the median values (column 2), the directional grid has a constant orbital derivative close to 0 for both average and median (bottom, columns 1 and 2) with values between 0 and 0.02 in both cases. The directional grid is thus better than the circular one; compared to iteration 0, the iterations have succeeded in identifying the correct right-hand side for the directional grid. When using the circular evaluation grid, the median gives better results than the average, as it has values closer to 0.

Let us now consider a point with gradient-like flow (columns 3 and 4). Again, the circular evaluation grid displays a larger variation of values, namely between

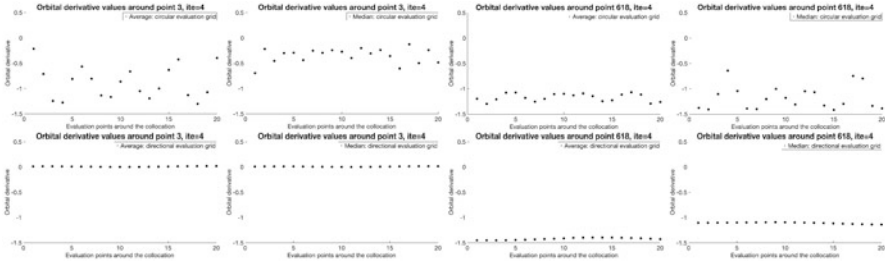


Fig. 4 Orbital derivative distribution around collocation points in iteration 4. Top row: circular, bottom row: directional evaluation grids. Column 1: chain-recurrent point, average, column 2: chain-recurrent point, median, column 3: gradient-like point, average, column 4: gradient-like point, median

−1.3 and −1 for the average values (up, column 3), and between −1.4 and −0.6 for the median value (up, column 4). The directional grid has a nearly constant orbital derivative at −1.4 for the average (bottom, column 3) and −1.1 for the median (bottom, column 4). The directional grid is again superior to the circular one; in this case the median results in a value closer to the original derivative at −1. For the circular evaluation grid, the average gives better results than the median as there is less variation; however, also the median delivers only negative values, i.e. classifying the collocation point correctly as gradient-like flow.

3.4 Determination of the Chain-Recurrent Set

Let us now investigate how the different methods manage to identify the chain-recurrent set after iterations 4 and 49. Figure 5 displays the approximation to the chain-recurrent set by plotting the collocation points $\mathbf{x}_j \in X^0$ (see Step 2 of the algorithm), i.e. \mathbf{x}_j where at least one point in corresponding evaluation grid $Y_{\mathbf{x}_j}$ satisfies $v'(\mathbf{x}) > \gamma$.

The results in Fig. 5 use the circular grid in the upper row. The figures in column 1 and 2 display the approximation to the chain-recurrent set in iterations 4 and 49, respectively, using a circular evaluation grid and the average. The two periodic orbits and the equilibrium at the origin are clear and completely displayed. However, they are over-approximated. In contrast, the figures in columns 3 and 4 showing the approximation to the chain-recurrent set in iterations 4 and 49, respectively, for the median and a circular grid, display gaps in the periodic orbits in iteration 49.

We continue with the directional grid in the bottom row. The figures in column 1 and 2, bottom row, display the approximation to the chain-recurrent set in iterations 4 and 49, respectively, using a directional evaluation grid and the average. The two periodic orbits and the equilibrium at the origin are clearly and completely displayed; however, they are slightly over-approximated in iteration 49. The figures

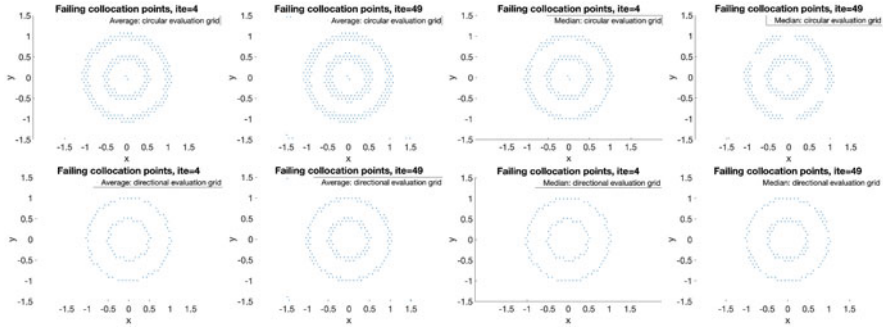


Fig. 5 Comparison of the chain-recurrent set in iterations 4 and 49. Top row: circular, bottom row: directional evaluation grids. Column 1: iteration 4, average, column 2: iteration 49, average, column 3: iteration 4, median, column 4: iteration 49, median

in columns 3 and 4, using a directional evaluation grid and the median, show a very similar picture with slightly less over-approximation.

3.5 Values on the Chain-Recurrent Set

Let us analyse the values of the orbital derivative on the circular periodic orbit with radius 1. In particular, we study their dependence on the circular and directional grids as well as using the average or the median for the iterations, see Fig. 6. The top figure shows the orbital derivative after iteration 0 on the orbit. It is plotted as a function of the angle on the positive x -axis, i.e. θ corresponds to the point $(\cos \theta, \sin \theta)$ on the orbit. After iteration 0 neither the evaluation grid nor the selection of average or median, matters. The values oscillate heavily between -1 and 0.7 .

The remaining four figures show the orbital derivative after iteration 49 on the orbit. In the left column, we used the circular evaluation grid and in the right column the directional evaluation grid. In both cases, we iterated using the average in the middle row and using the median in the bottom row. In all cases, we would like to achieve values of the orbital derivative close to zero. We clearly see that iterating using the average (middle row) is better as the orbital derivative is closer to zero. Further, the values oscillate much more if we use the circular evaluation grid. Indeed, if we use the directional evaluation grid and the average for iterations most of the values are between -0.02 and 0 , the only exceptions being two small spikes close to the angles 0 and π .

When using the circular evaluation grid and the median, we observe that the values oscillate considerably, and there are large areas, where the orbital derivative is entirely negative and below the threshold γ ; hence, they do not appear as failing in Fig. 5. Let us discuss why this can develop over the iterations: The circular grid

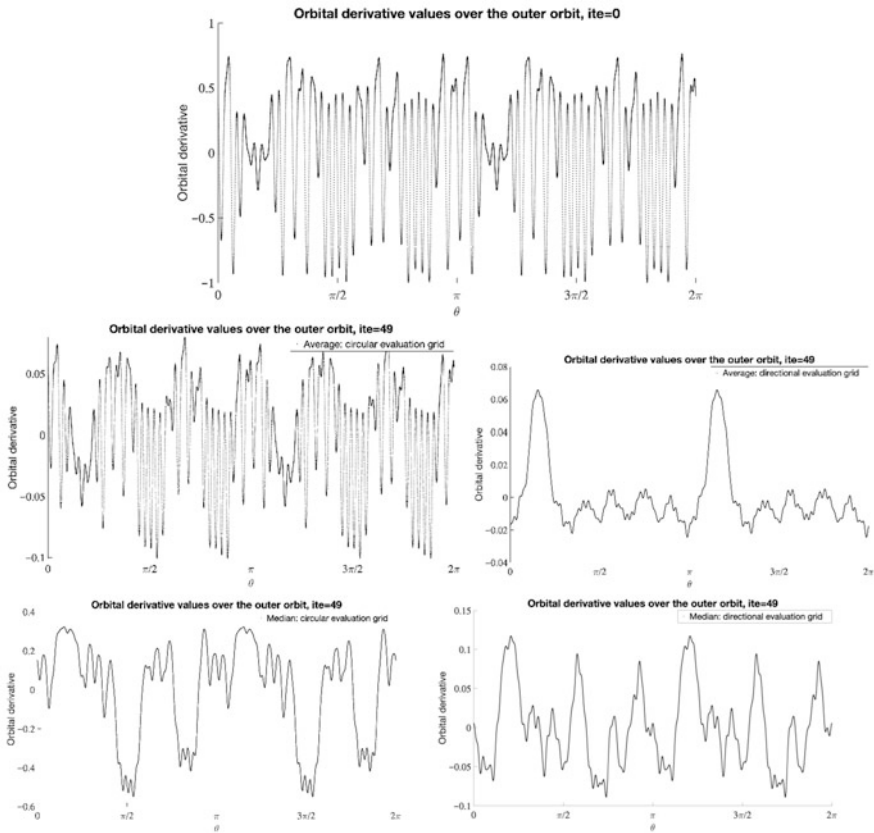


Fig. 6 Orbital derivative on the circular periodic orbit with radius 1. Top figure: iteration 0. All other figures: iteration 49. Left column: circular, right column: directional evaluation grid. Middle row: average, bottom row: median

takes adjacent points in the gradient-flow into account, which have negative orbital derivative, while the points of the directional evaluation grid lie on the periodic orbit with derivatives close to 0. While the average over the circular evaluation grid takes some positive values on the periodic orbit into account, the median just considers the middle number(s).

4 Conclusions

We have investigated the differences between using a circular or directional evaluation grid as well as those between employing the median or the average to the iterative process. We have found that the values of the orbital derivative around

a collocation point have no clear distribution; in particular, they are not Gaussian. Nevertheless, using the average provides better results in the iteration process for both types of evaluation grids. Further, the directional evaluation grid proved to be superior. This is presumably because the directional evaluation grid only considers points along the flow, which are of the same type as the collocation point; if the collocation point is on (or very close to) the chain-recurrent set, then so are the evaluation points. This improves the determination of the chain-recurrent set.

Summarising, using the directional evaluation grid with the average for iterations delivers the best results in localising the chain-recurrent set. For collocation points far from the chain-recurrent set, the graph is quite flat and its curvature will be (close to) zero, while it is non-zero for collocation points close to the chain-recurrent set. We anticipate that this criterion might perform better than the current one, namely that the orbital derivative is above a critical value.

References

1. C. Argáez, P. Giesl, S. Hafstein, Analysing dynamical systems: Towards computing complete Lyapunov functions, in *Proceedings of the 7th International Conference on Simulation and Modeling Methodologies, Technologies and Applications (SIMULTECH)*, Madrid, Spain (2017a), pp. 134–144
2. C. Argáez, P. Giesl, S. Hafstein, Computation of complete Lyapunov functions for three-dimensional systems, in *Proceedings of the 57th IEEE Conference on Decision and Control (CDC)*, Miami Beach, FL, USA (2018a), pp. 4059–4064
3. C. Argáez, P. Giesl, S. Hafstein, Computational approach for complete Lyapunov functions, in *Dynamical Systems in Theoretical Perspective*. Springer Proceedings in Mathematics and Statistics, ed. by J. Awrejcewicz, vol. 248 (2018b), pp. 1–11
4. C. Argáez, J.C. Berthet, H. Björnsson, P. Giesl, S.F. Hafstein, LyapXool—a program to compute complete Lyapunov functions. *SoftwareX* **10**, 100325 (2019)
5. P. Giesl, *Construction of Global Lyapunov Functions Using Radial Basis Functions*. Lecture Notes in Mathematical, vol. 1904 (Springer, Berlin, 2007)
6. A.M. Lyapunov, The general problem of the stability of motion. *Internat. J. Control* **55**(3), 521–790 (1992). Translated by A. T. Fuller from Édouard Davaux’s French translation (1907) of the 1892 Russian original
7. J. Auslander, Generalized recurrence in dynamical systems. *Contr. Diff. Equ.* **3**, 65–74 (1964)
8. C. Conley, Isolated Invariant Sets and the Morse Index, in *CBMS Regional Conference Series No. 38* (American Mathematical Society, New York, 1978)
9. C. Conley, The gradient structure of a flow I. *Ergodic Theory Dynam. Syst.* **8**, 11–26 (1988)
10. M. Hurley, Chain recurrence, semiflows, and gradients. *J. Dyn. Diff. Equation* **7**(3), 437–456 (1995)
11. M. Hurley, Lyapunov functions and attractors in arbitrary metric spaces. *Proc. Am. Math. Soc.* **126**, 245–256 (1998)
12. P. Giesl, S. Hafstein, Review of computational methods for Lyapunov functions. *Discrete Contin. Dyn. Syst. Ser. B* **20**(8), 2291–2331 (2015)
13. P. Ao, Potential in stochastic differential equations: novel construction. *J. Phys. A Math. Theor.* **37**(3), L25–L30 (2004)
14. M. Dellnitz, G. Froyland, O. Junge, The algorithms behind GAIO—Set oriented numerical methods for dynamical systems, in *Ergodic Theory, Analysis, and Efficient Simulation of Dynamical Systems*, ed. by B. Fiedler (Springer, Berlin, 2001), pp. 145–174

15. R. Yuan, X. Wang, Y. Ma, B. Yuan, P. Ao, Exploring a noisy van der Pol type oscillator with a stochastic approach. *Phys. Rev. E.* **87**(6), 062109 (2013)
16. X.-M. Zhu, L. Yin, P. Ao, Limit cycle and conserved dynamics. *Int. J. Mod. Phys. B* **20**(7), 817–827 (2006)
17. H. Wendland, Error estimates for interpolation by compactly supported Radial Basis Functions of minimal degree. *J. Approx. Theory* **93**, 258–272 (1998)
18. C. Argáez, P. Giesl, S. Hafstein, Wendland functions: A C++ code to compute them, in *Proceedings of the 7th International Conference on Simulation and Modeling Methodologies, Technologies and Applications (SIMULTECH)*, Madrid, Spain (2017b), pp. 323–330
19. A. Iske, *Perfect Centre Placement for Radial Basis Function Methods*. Technical Report TUM-M9809, TU Munich, Germany (1998)

WendlandXool: Simplified C++ Code to Compute Wendland Functions



Carlos Argáez, Peter Giesl, and Sigurdur Freyr Hafstein

1 Introduction

Wendland functions are compactly supported Radial Basis Functions (RBFs) widely used in (generalised) interpolation problems, including solving linear Partial Differential Equations (PDEs).

Let N points $\mathbf{x}_1, \dots, \mathbf{x}_N \in \mathbb{R}^n$ (collocation points), $\mathbf{x}_i \neq \mathbf{x}_j$ if $i \neq j$, and associated values $f_1, \dots, f_N \in \mathbb{R}$ be given. A classical interpolation problem consists of finding a function $f: \mathbb{R}^n \rightarrow \mathbb{R}$ satisfying $f(\mathbf{x}_j) = f_j$ for all $j = 1, \dots, N$. In a generalised interpolation problem, one prescribes the values of linear functionals applied to the function f . By prescribing the values of a linear differential operator, generalised interpolation problems can be used to numerically solve linear PDEs.

RBFs as kernels for Reproducing Kernel Hilbert Spaces (RKHS) provide a mighty machinery for solving interpolation and generalised interpolation problems in arbitrary dimensions [1–3]. Further, the error between the numerically computed interpolants and the true solution can be bounded above in terms of the fill distance, which is the proper measure of the density of the collocation points.

Another advantage of using RBFs and generalised interpolation problems for solving PDEs is that the collocation points do not have to be evenly distributed and no triangulation of the phase-space is needed. Such methods have been used in numerous different settings in areas as different as geography, image processing, various engineering applications, numerical integration [4], machine learning and

C. Argáez (✉) · S. F. Hafstein
Science Institute, University of Iceland, Reykjavik, Iceland
e-mail: carlos@hi.is; shafstein@hi.is

P. Giesl
Department of Mathematics, University of Sussex, Falmer, UK
e-mail: p.a.giesl@sussex.ac.uk

neural networks, cf. e.g. [4, 5]. The authors are mainly interested in RBFs methods for numerically solving PDEs [6], in particular in solving Zubov-like PDEs for the computation of (complete) Lyapunov functions in dynamical systems [7–10].

A (generalised) interpolation problem aims to select a function in a given function space, typically a RKHS, that optimally fulfils certain conditions. The Wendland functions are polynomials on their compact support and are well suited as kernels for RKHS. The structure of a particular Wendland function depends on two parameters and they can be defined in a recursive manner.

In this paper, we present a major revision of our first open-source code to compute Wendland functions [11] and give a new simplified algorithm implemented in C++ to explicitly compute any Wendland function. We have mentioned before in [11] the existence of different code, written in MAPLE [12, 13] as well as the C++ libraries libMesh [14] and FOAM-FSI [15] that can be used to evaluate and provide Wendland functions. Further, there is a code written in R that can be used to evaluate Wendland functions for given radial values [16]. However, these tools are limited to a predefined selection of Wendland functions or to the use of commercial computational packages. In [17] a program written in Python was presented, that generates C++ header files and code for Wendland functions, that can be included in C++ projects. In our code the use is somewhat simpler using classes and the evaluation of the Wendland functions and their auxiliary functions use the factorised form, that was shown in [18] to give much more exact results than when they are not factorised.

We present a C++ code that includes all necessary operations to compute any Wendland function and uses the *Armadillo C++ library* for linear algebra and scientific computing [19, 20], which is also distributed free of charge.

Further, as a new tool, our code produces a \LaTeX report in which all the operations to construct a Wendland function and auxiliary functions are summarised. This tool was introduced because the computation of Wendland functions and their auxiliaries requires the repeated application of several operations, that can be error prone in practice:

- Polynomial integration,
- Polynomial derivation,
- Polynomial factorisation.

Such a report provides a useful debugging tool and delivers the constructed Wendland functions and auxiliary functions in \LaTeX format, both factorised and expanded.

The new algorithm provides the coefficients of the polynomials of the Wendland functions as integers, which is the form in which Wendland functions are usually presented [7]. When Wendland functions are used to solve generalised interpolation problems, they appear linearly on both sides of linear equations and therefore they are essentially only defined up to a non-zero multiplicative constant. If the integer coefficients cannot be represented by built in integer types, then the program reports this. In fact, for practical computations Wendland functions are commonly used for

quite low parameters l, k , because otherwise the condition number of the collocation matrix is often very large.

2 Generalised Interpolation Using Wendland Functions

In this section, we sum up the most important aspects of generalised interpolation using Wendland functions. Consider a Hilbert space $H \subset C(\mathbb{R}^n, \mathbb{R})$ of continuous functions $f : \mathbb{R}^n \rightarrow \mathbb{R}$ and its dual H^* , i.e. the set of all linear and continuous functionals $\lambda : H \rightarrow \mathbb{R}$. In a RKHS the point evaluation functional $\delta_{\mathbf{x}_0}(f) = f(\mathbf{x}_0)$, evaluating the function at a point $\mathbf{x}_0 \in \mathbb{R}^n$, is in H^* . Given more regularity of the functions in H , differential operators evaluated at a point, e.g., $\lambda = \delta_{\mathbf{x}_0} \circ \frac{\partial}{\partial x_j}$, $j \in \{1, \dots, n\}$, are also in H^* .

Definition 1 (Generalised Interpolation Problem) Given N linearly independent functionals $\lambda_1, \dots, \lambda_N \in H^*$ and corresponding values $f_1, \dots, f_N \in \mathbb{R}$, a generalised interpolant $f \in H$ satisfies $\lambda_j(f) = f_j$ for all $j = 1, \dots, N$.

Note that the classical interpolation problem is a special case with $\lambda_j = \delta_{\mathbf{x}_j}$.

A norm-minimal generalised interpolant is an interpolant that is minimal in the norm of the Hilbert space H , i.e.

$$\arg \min_{f \in H} \{\|f\|_H : \lambda_j(f) = f_j, 1 \leq j \leq N\}.$$

The norm-minimal interpolant is unique and can be written as a linear combination of the Riesz representers $v_j \in H$ of the functionals, cf. e.g. [5], and if H is a RKHS the Riesz representers have a simple formula.

Recall that a RKHS is a Hilbert space H with a reproducing kernel $\Phi : \mathbb{R}^n \times \mathbb{R}^n \rightarrow \mathbb{R}$ such that

1. $\Phi(\cdot, \mathbf{x}) \in H$ for all $\mathbf{x} \in \mathbb{R}^n$
2. $g(\mathbf{x}) = \langle g, \Phi(\cdot, \mathbf{x}) \rangle_H$ for all $g \in H$ and $\mathbf{x} \in \mathbb{R}^n$

Here $\langle \cdot, \cdot \rangle_H$ is the inner product of H .

The Riesz representer of $\lambda_j \in H^*$ has the formula $v_j = \lambda_j^y \Phi(\cdot, \mathbf{y})$, i.e. λ_j applied to $\mathbf{x} \rightarrow \Phi(\mathbf{x}, \mathbf{y}) \in H$. Thus we can write the norm-minimal interpolant as $f(\mathbf{x}) = \sum_{j=1}^N \beta_j \lambda_j^y \Phi(\mathbf{x}, \mathbf{y})$, where the interpolation conditions $\lambda_j(f) = f_j$, $1 \leq j \leq N$, are used to fix the coefficients β_j .

RBF kernels are such that $\Phi(\mathbf{x}, \mathbf{y}) := \Psi(\|\mathbf{x} - \mathbf{y}\|)$ for a function $\Psi : [0, \infty) \rightarrow [0, \infty)$. There are numerous RBFs that can serve as kernels for RKHS and different RBFs will lead to different RKHSs.

The so-called Wendland functions [12, 21–24] have a compact support and are polynomials on their support. The corresponding RKHSs are norm-equivalent to Sobolev spaces, which together with the simple form of the Wendland functions make them well suited as kernels to solve linear PDEs.

The Wendland functions $\Psi_{l,k}^0$, where $l \in \mathbb{N}$ and $k \in \mathbb{N}_0$, can be defined recursively as follows, cf. [23].

Definition 2 (Wendland Function) The Wendland function $\Psi_{l,k}^0$, where $l \in \mathbb{N}$ and $k \in \mathbb{N}_0$, is defined recursively by

$$\begin{aligned} \Psi_{l,0}^0(r) &= (1-r)_+^l \\ \Psi_{l,j+1}^0(r) &= \int_r^1 t \Psi_{l,j}^0(t) dt \text{ for } j = 0, 1, \dots, k-1, \end{aligned} \tag{1}$$

where $x_+ = \max\{x, 0\}$ and $x_+^l := (x_+)^l$.

Hence

$$\Psi_{l,k}^0(r) = \underbrace{\int_r^1 t_k \int_{t_k}^1 t_{k-1} \cdots \int_{t_2}^1 t_1 \Psi_{l,0}^0(t_1)}_{k \text{ integrations}} \overbrace{dt_1 \cdots dt_k}^{k \text{ differentials}}. \tag{2}$$

Note that the support of the Wendland function $\Psi_{l,k}^0(r)$ is the interval $[0, 1]$ and thus, for a constant $c > 0$ the support of the function $\mathbf{x} \mapsto \Psi_{l,k}^0(c\|\mathbf{x} - \mathbf{x}_0\|)$ is a ball of radius c^{-1} , centred at \mathbf{x}_0 . In applications for dynamical systems, we deal with certain differential operators that require the following auxiliary functions, derived from the Wendland functions. They are also the reason, why it is advantageous to include a constant $c > 0$ in the definition of a Wendland function, i.e. consider the function $r \mapsto \Psi_{l,k}^0(cr)$ rather than $\Psi_{l,k}^0(r)$.

Definition 3 (Auxiliary Functions $\Psi_{l,k}^1$ and $\Psi_{l,k}^2$) For a fixed $c > 0$ and a given Wendland function $r \mapsto \Psi_{l,k}^0(cr)$, the auxiliary functions $r \mapsto \Psi_{l,k}^1(cr)$ and $r \mapsto \Psi_{l,k}^2(cr)$ are defined as follows for $r > 0$:

$$\Psi_{l,k}^1(cr) = r^{-1} \frac{d}{dr} \Psi_{l,k}^0(cr) \quad \text{and} \quad \Psi_{l,k}^2(cr) = r^{-1} \frac{d}{dr} \Psi_{l,k}^1(cr).$$

Remark 1 Auxiliary functions of higher order can be defined equivalently. The presented code can easily be adapted to compute them as well.

Remark 2 In case $\Psi_{l,k}^j(cr)$ can be continuously extended to $r = 0$, this is done and the function is also defined for $r = 0$.

3 Algorithm

As seen in (1), the parameters that define the polynomial's degree are k and l , where l denotes the degree of the initial polynomial and k is the number of iterative integrations.

An outline of the algorithm is as follows:

1. Compute the binomial expansion of $(1 - t_1)^l$. We do this by computing Pascal's triangle and expand the polynomial accordingly. The coefficients are stored in an array, starting with the coefficient for $t_1^0 := 1$ (left), then the coefficient for t_1^1 , etc.
2. After this, the iterative procedure starts. Remember that, according to (2), k is the number of integrations that will be performed. The operations performed by the algorithm are to multiply a polynomial with the free variable and to integrate, cf. (1). Both correspond to simple manipulations on the vector of coefficients of the polynomial.
 - (a) Multiplying with the free variable corresponds to shifting all elements to the right and put zero in the first position. After multiplying by t_j an integration is performed.
 - (b) Integration: We compute the following integral, with f as the polynomial from the last step, cf. (2).

$$\int_{t_{j+1}}^1 f(t_j) dt_j = F(1) - F(t_{j+1}). \quad (3)$$

Again this corresponds to shifting all elements to the right, but now the coefficient a_s of t_{j+1}^s in $F(t_{j+1})$ is multiplied with $1/s$. The first position, the coefficient for $t_{j+1}^0 := 1$, becomes the sum of the other coefficients. All other coefficients must then be multiplied by -1 , corresponding to $F(1) - F(t_{j+1})$. Notice that the new coefficients will in general not be integer numbers.

3. Once the for-loop ends at k , the remaining step is to compute the factor to convert all coefficients to integers. For this the algorithm keeps track of the least common denominator `lcd` and the greatest common factor `hcf` of the coefficients of the polynomials. If no overflow occurs the coefficients are multiplied by the factor `round(lcd/hcf)`, which makes all coefficients integers. If there is an overflow the execution is stopped and the user is warned.
4. The final polynomial $\Psi_{l,k}^0(cr)$ is of order $l + 1 + 2 \cdot k$ in $x = cr$ and is used to compute the auxiliary functions $\Psi_{l,k}^1(cr)$ and $\Psi_{l,k}^2(cr)$ as in Definition 3. For the efficient implementation, it is of use to note that in general for $j > 0$ the

function $\Psi_{l,k}^j(cr)/c^{2j}$ can be written as a rational function of $x = cr$, with the polynomial x^u , $u \in \mathbb{N}_0$, in the denominator. That is

$$\Psi_{l,k}^j(cr) = \sum_{i=-u}^v a_i(cr)^i c^{2j} = (cr)^{-u} c^{2j} \sum_{i=0}^{v+u} a_i(cr)^i$$

and the transformation from $\Psi_{l,k}^j(cr)$ to $\Psi_{l,k}^{j+1}(cr)$ is, once again, essentially just a simple manipulation of a vector of coefficients.

5. Finally, $\Psi_{l,k}^j(cr)$, $j = 0, 1, 2$, are factorised in the form

$$\Psi_{l,k}^j(cr) = c^{2j} (1 - cr)^s \frac{f_l(cr)}{(cr)^u},$$

where $f_l(cr) = \sum_{i=0}^t b_i(cr)^i$ is a polynomial in $x = cr$ of maximal degree. For this we use the fact that the coefficients in the polynomial, or polynomial numerator, of $\Psi_{l,k}^j$ have integer coefficients and thus, iterated polynomial synthetic division gives exact results and the polynomial $f_l(cr)$ also has integer coefficients.

6. Along the process the report in L^AT_EX is written.

Remark 3 Recall that when Wendland functions are used in generalised interpolation, they can be multiplied with a non-zero constant because they appear on both sides of linear equation. Therefore, they are most commonly presented with integer coefficients as in [7].

3.1 Evaluation

To evaluate the functions we use Horner's scheme. A few comments are in order: The evaluation routine is the same for all the functions, the Wendland function and all its auxiliary functions. In general we evaluate for $u, v \in \mathbb{N}_0$ and for $x = cr$, $0 < x < 1$, the expression

$$\Psi_{l,k}^j(x) = \sum_{k=-u}^v a_k(x)^k c^{2j} = c^{2j} (1 - x)^s \frac{f_l(x)}{x^u} = c^{2j} (1 - x)^s x^{-u} \sum_{i=0}^t b_i x^i$$

using Horner's scheme for the polynomial term $\sum_{i=0}^t b_i x^i$. For $x \geq 1$ the routine returns zero as expected. If $u = 0$ the function can be continuously extended to $x = 0$ and is evaluated as above, cf. e.g. Proposition 3.5 in [7].

4 How to Use/EXAMPLES

The program is found in <https://github.com/LyapXool/WendlandXool-V2> and consists of the files `wendland.cpp` and `wendland.hpp`.

Further, the file `WendlandExample.cpp` included, contains an example of its use. The class `WendRBF` delivers the interface to the Wendland functions to the user. To construct the Wendland function $\Psi_{l,k}^0(cr)$, for some constants $l \in \mathbb{N}$, $k \in \mathbb{N}_0$, and $c > 0$, together with its auxiliaries $\Psi_{l,k}^1(cr)$ and $\Psi_{l,k}^2(cr)$, the user can simply make it as an object using the constructor with the corresponding parameters:

```
WendRBF(int l, int k, double c, bool printreport)
```

If `printreport=true` then a detailed \LaTeX compilable report on the construction of the Wendland function and its auxiliaries is written in `wendlandreport.tex`. The default value is `false` and no report is written. After its initialisation/creation, the user can evaluate $\Psi_{l,k}^0(cr)$ at any $r \geq 0$ using

```
double WendRBF::operator()(double r)
```

Note that the argument should be r , not $x = cr$. To evaluate $\Psi_{l,k}^1(cr)$ at r one uses the member function `double WendRBF::aux1(double r)` and to evaluate $\Psi_{l,k}^2(cr)$ the member function `double WendRBF::aux2(double r)`. The routines that do the actual computations are in namespace `wendland`. An excerpt from the report when `WendRBF psi31(3,1,1.0,true)` is called follows:

Construction and all steps for the construction of the Wendland function.

Wendland function $\Psi_{3,1}^0$

First binomial $(1 - t_1)^3$

$$t_1^0 - 3t_1^1 + 3t_1^2 - t_1^3$$

Multiplying by t_1 :

$$0t_1^0 + t_1^1 - 3t_1^2 + 3t_1^3 - t_1^4$$

Computing integration: 1

Integrating from r **to** 1:

$$5 \times 10^{-2}r^0 + 0r^1 - 5 \times 10^{-1}r^2 + r^3 - 7.5 \times 10^{-1}r^4 + 2 \times 10^{-1}r^5$$

Using the factor 20 the Wendland function becomes for $0 \leq cr \leq 1$:

$$\Psi_{3,1}^0(cr) = 1 + 0c^1r^1 - 10c^2r^2 + 20c^3r^3 - 15c^4r^4 + 4c^5r^5$$

Construction and all steps for the construction of the auxiliary function.

Order: 1 Wendland function derivative $\Psi_{3,1}^1$.

Derive $\Psi_{3,1}^0(cr)$ by r and divide the result by r :

$$\Psi_{3,1}^1(cr) = -20c^2 + 60c^3r^1 - 60c^4r^2 + 20c^5r^3$$

For $0 < cr \leq 1$.

Construction and all steps for the construction of the auxiliary function.

Order: 2 Wendland function derivative $\Psi_{3,1}^2$.

Derive $\Psi_{3,1}^1(cr)$ by r and divide the result by r :

$$\Psi_{3,1}^2(cr) = 60c^3r^{-1} - 120c^4r^0 + 60c^5r^1$$

For $0 < cr \leq 1$.

Functions presented in a factorised form.

Next, we present the factorised version of the Wendland function.

$$\Psi_{3,1}^0(cr) = (1 - cr)_+^4 (1 + 4c^1r^1)$$

$$\Psi_{3,1}^1(cr) = (1 - cr)_+^3 c^2 (-20)$$

$$\Psi_{3,1}^2(cr) = (1 - cr)_+^2 c^3 (60r^{-1})$$

A graphical presentation of the function $\Psi_{3,1}^0(cr)$, $c = 1$, and its two auxiliary functions $\Psi_{3,1}^1(cr)$ and $\Psi_{3,1}^2(cr)$ can be seen in Fig. 1. For a table with the coefficients of the polynomials see Table 1.

5 Conclusions

We have upgraded our previous contribution [11] to compute Wendland's compactly supported Radial Basis Functions. The new code is more user-friendly and is presented in a clearer format through a class. Additionally, the evaluation of the Wendland functions and their auxiliaries has been optimised for numerical accuracy and, optionally, a detailed L^AT_EX compilable report on the generation of the Wendland functions and their auxiliaries can be generated.

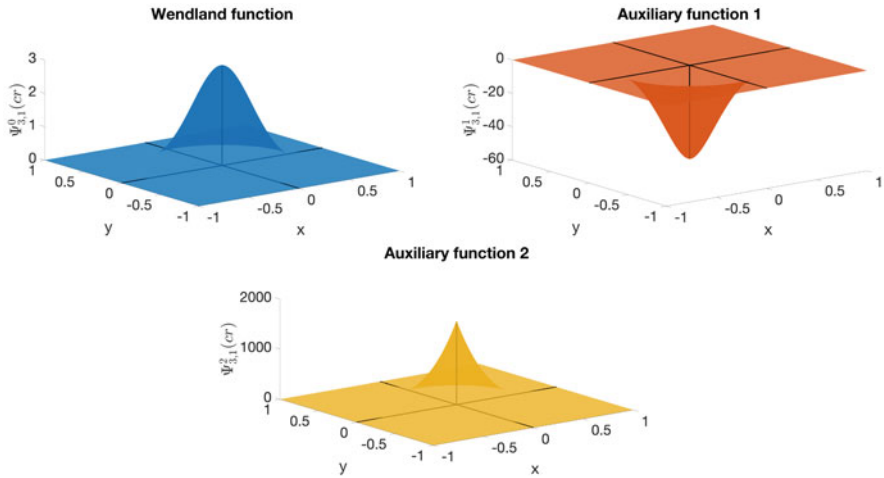


Fig. 1 Upper left: Wendland function $\Psi_{3,1}^0(\|(x, y)\|)$. Upper right: Auxiliary function 1. Lower: Auxiliary function 2

Table 1 Arrays presenting the results and their storage

	Wendland function $\Psi_{3,1}^0(cr)$					Function $\Psi_{3,1}^1(r)$				Function $\Psi_{3,1}^2(r)$			
Exponent k of r^k	0	1	2	3	4	5	0	1	2	3	-1	0	1
Coefficient a_k of $a_k r^k$	1	0	-10	20	-15	4	-20	60	-60	20	60	-120	60

References

1. M.D. Buhmann, *Radial Basis Functions: Theory and Implementations*. Cambridge Monographs on Applied and Computational Mathematics, vol. 12 (Cambridge University, Cambridge, 2003)
2. G. Fasshauer, *Meshfree approximation methods with MATLAB*. Number 6 in Interdisciplinary Mathematical Sciences (World Scientific, New York, 2007)
3. R. Schaback, H. Wendland, Kernel techniques: from machine learning to meshless methods. *Acta Numer.* **15**, 543–639 (2006)
4. J. Dick, F. Kuo, I. Sloan, High-dimensional integration: the quasi-Monte Carlo way. *Acta Numer.* **22**, 133–288 (2013)
5. H. Wendland, Scattered data approximation. *Cambridge Monographs on Applied and Computational Mathematics*, vol. 17 (Cambridge University, Cambridge, 2005)
6. B. Fornberg, N. Flyer, Solving PDEs with radial basis functions. *Acta Numer.* **24**, 215–258 (2015)
7. P. Giesl, *Construction of Global Lyapunov Functions Using Radial Basis Functions*. Lecture Notes in Mathematical 1904 (Springer, Berlin, 2007)
8. C. Argáez, S. Hafstein, Analysing dynamical systems towards computing complete Lyapunov functions, in *Proceedings of the 7th International Conference on Simulation and Modeling Methodologies, Technologies and Applications, Madrid, Spain* (2017), pp. 323–330
9. C. Argáez, P. Giesl, S. Hafstein, Computation of complete Lyapunov functions for three-dimensional systems, in *Proceedings of the 57rd IEEE Conference on Decision and Control (CDC)* (2018), pp. 4059–4064

10. C. Argáez, P. Giesl, S. Hafstein, Computational approach for complete Lyapunov functions. in *Dynamical Systems in Theoretical Perspective*. Springer Proceedings in Mathematics and Statistics, vol. 248, ed. by J. Awrejcewicz (2018), pp. 1–11
11. C. Argáez, S. Hafstein, P. Giesl, Wendland functions—a C++ code to compute them, in *Proceedings of the 7th International Conference on Simulation and Modeling Methodologies, Technologies and Applications* (2017), pp. 323–330
12. S. Zhu, Compactly supported radial basis functions: how and why? in *OCCAM Preprint Number 12/57* (University of Oxford, Oxford, 2012)
13. R. Schaback, The missing Wendland functions. *Adv. Comput. Math.* **34**, 67–81 (2011)
14. B. Kirk, J. Peterson, R. Stogner, G. Carey, `libMesh`: A C++ library for parallel adaptive mesh refinement/coarsening simulations. *Eng. Comput.* **22**(3–4), 237–254 (2006)
15. D. Blom, P. Cardiff, T. Gillebaart, E.t. Hofstede, V. Kazemi-Kamyab, FOAM-FSI project. Github. <https://github.com/davidsblom/FOAM-FSI>
16. D. Nychka, Wendland family of covariance functions and supporting numerical functions. Technical report. <https://www.rdocumentation.org/packages/fields/versions/11.6/topics/Wendland>
17. H. Bjornsson, S. Hafstein, Algorithm and software to generate code for wendland functions in factorized form, in *Proceedings of the 16th International Conference on Informatics in Control, Automation and Robotics (ICINCO)* (2019), pp. 156–162
18. H. Bjornsson, S. Hafstein, Verification of a numerical solution to a collocation problem, in *Proceedings of the 15th International Conference on Informatics in Control, Automation and Robotics (ICINCO)* (2018), pp. 587–594
19. C. Sanderson, R. Curtin, Armadillo: a template-based C++ library for linear algebra. *J. Open Source Softw.* **1**(2), 26 (2016)
20. C. Sanderson, R. Curtin, *Mathematical Software—ICMS 2018*. LNCS, vol. 10931. chapter A User-Friendly Hybrid Sparse Matrix Class in C++ (Springer, Berlin, 2018), pp. 422–430
21. Z. Wu, Compactly supported positive definite radial functions. *Adv. Comput. Math.* **4**(3), 283–292 (1995)
22. R. Schaback, Z. Wu, Operators on radial functions. *J. Comput. Appl. Math.* **73**(1-2), 257–270 (1996)
23. H. Wendland, Piecewise polynomial, positive definite and compactly supported radial functions of minimal degree. *Adv. Comput. Math.* **4**(4), 389–396 (1995)
24. H. Wendland, Error estimates for interpolation by compactly supported Radial Basis Functions of minimal degree. *J. Approx. Theory* **93**, 258–272 (1998)

Part IV
Analytical Techniques

Resonances of a Forced van der Pol Equation with Parametric Damping



Fatemeh Afzali, Ehsan Kharazmi, and Brian F. Feeny

1 Introduction

In this paper, we study the responses of an oscillator with van der Pol terms, parametric damping, and direct excitation. A potential application of this system is a vertical-axis wind-turbine blade, which can endure direct excitation and parametric damping [1, 2], as well as aeroelastic self-excitation, the mechanism of which can be loosely modeled with van der Pol-type nonlinearity [3, 4]. Here, the general behavior of this system is studied, rather than the specific responses of a specific model of an application system. As both parametric excitation and van der Pol nonlinearity can induce instabilities and oscillations, we seek to understand the combined effect of such terms in this system.

Parametric damping has been shown to generate instabilities [2, 5], similar to those of the Mathieu equation [3, 4], with period-1 or period-2 oscillation, and to decay with quasiperiodic dynamics when stable [2]. The study [2] used the Floquet solution combined with harmonic balance [6, 7].

Szabelski and Warminski [8] performed an analytical examinations on the system with three sources of vibration, parametric, self-excited, and inertial. Warminski [9] studied the nonlinear dynamics of a self, parametric, and externally excited oscillator with time delay analytically applying the method of multiple scales. Warminski also discussed the similarities and differences between the van der Pol and Rayleigh for regular, periodic, quasiperiodic, and chaotic oscillations.

F. Afzali (✉) · B. F. Feeny
Michigan State University, East Lansing, MI, USA
e-mail: afzalifa@msu.edu; feeny@egr.msu.edu

E. Kharazmi
Brown University, Providence, RI, USA
e-mail: ehsan_kharazmi@brown.edu

Parametric excitation has also been studied in the context of wind-turbine blades [10–13]. Luongo and Zulli [14] studied a self-excited tower under turbulent wind flow. The tower was assumed to be a nonlinear system where the stationary wind imposed the self-excitation, and the turbulent flow drove both parametric and external excitation. Combining parametric damping with self-excitation of nonlinear damping as in a van der Pol equation, with a particular choice of scaling and excitation frequencies, results in an equation given as

$$\ddot{x} + \epsilon(c_0 + c_1 \cos \omega t + x^2)\dot{x} + \omega_n^2 x = f_0 + f_1 \sin(\omega t), \quad (1)$$

where $\epsilon \ll 1$. The variables c_0 and c_1 are the mean damping and amplitude of the parametric damping, respectively, and f_0 and f_1 are mean and cyclic direct excitation amplitudes. The excitation frequency is ω and the natural frequency is ω_n . We will refer to this as the parametrically damped van der Pol (PDVDP) equation with external excitation.

In this work, we apply the first-order method of multiple scales [3, 15] to study an unforced and externally forced van der Pol equation with parametric damping at frequency ω . We study the sub-harmonic resonance of order $1/2$ as well as the nonresonant dynamics.

2 Perturbation Analysis: Method of Multiple Scales

The core of this study is the approximation of the solution to Eq. (1) based on the method of multiple scale (MMS) [3, 4]. Therefore, we expand the displacement as

$$x(T_0, T_1, \dots) = x_0(T_0, T_1, \dots) + \epsilon x_1(T_0, T_1, \dots) + \epsilon^2 x_2(T_0, T_1, \dots) + \dots, \quad (2)$$

where the time scales are $T_i = \epsilon^i t$, and $\epsilon \ll 1$. By using the chain rule, we obtain the derivatives for $n \in \mathbb{N}$ as $\frac{d^n}{dt^n}(\cdot) = (D_0 + \epsilon D_1 + \epsilon^2 D_2 + \dots)^n(\cdot)$, where $D_i = \frac{\partial}{\partial T_i}$. Here, we carry out the analysis up to the first order by considering the two time scales, $T_0 = t$ and $T_1 = \epsilon t$, and therefore expand the displacement as

$$x(T_0, T_1) \approx x_0(T_0, T_1) + \epsilon x_1(T_0, T_1). \quad (3)$$

By substituting the expansion (3) in Eq. (1) and using the derivatives, coefficients of similar powers of ϵ equate as

$$\epsilon^0 : D_0^2 x_0 + \omega_n^2 x_0 = f_0 + f_1 \sin(\omega t), \quad (4)$$

$$\epsilon^1 : D_0^2 x_1 + \omega_n^2 x_1 = -2D_0 D_1 x_0 - (c_0 + c_1 \cos \omega T_0 + x_0^2)(D_0 x_0). \quad (5)$$

The relationship between the excitation and the natural frequencies specifies different cases of resonance:

1. Nonresonant: no specific relationship between ω and ω_n
2. Primary resonance: $\omega \approx \omega_n$
3. Super-harmonic resonance: $\omega \approx \omega_n/m$ ($m \in \mathbb{N}$)
4. Sub-harmonic resonance: $\omega \approx m\omega_n$ ($m \in \mathbb{N}$)

In the next sections, we elaborate on this perturbation analysis for specific cases with and without external excitation, and apply other tools, to examine the dynamics with emphasis on secondary resonances.

3 Parametric Excitation Without External Excitation

We start with the case where there is no external forcing, i.e. $f_0 = f_1 = 0$. As a survey of the possible dynamics, Fig. 1 shows a frequency sweep from $\omega = 0$ to beyond $\omega = 2\omega_n$, when $\omega_n = 1$, $\epsilon = 0.1$, $c_0 = -1$, and $c_1 = 1$ (these parameters are dimensionless). The sweep, as a bifurcation diagram, is a plot of samples of the x variable of the nonwandering set in a Poincaré section [16] for various values of the frequency parameter. A Runge–Kutta method (Matlab ode45) is used to obtain numerical solutions of several periods to achieve steady-state. As the responses are typically quasiperiodic, the plots are generated by recording at each excitation frequency, 50 values of x at the downward $\dot{x} = 0$ crossing in the phase space.

We appeal to perturbation analysis to explain these responses. The solution to the leading-order Eq. (4) is

$$x_0(T_0, T_1) = A(T_1)e^{i\omega_n T_0} + \text{c.c.}, \tag{6}$$

where c.c. stands for the corresponding complex conjugate terms. We obtain the solvability conditions by substituting Eq. (6) into the right-hand-side of Eq. (5) and eliminating the “secular terms.” In MMS, the secular terms are defined as the terms that make the solution to grow without bound in time, and thus should be eliminated. By plugging Eq. (6) into Eq. (5), we obtain

$$D_0^2 x_1 + w_n^2 x_1 = (-2i\omega_n A' - ic_0\omega_n A - i\omega_n A^2 \bar{A})e^{i\omega_n T_0} - \frac{c_1}{2} \left(i\omega_n \bar{A} e^{i(\omega - \omega_n)T_0} \right) + \text{N.S.T.}, \tag{7}$$

where N.S.T stands for non-secular terms and $A' = D_1 A$. The homogeneous solution of Eq. (7) is of the form $e^{i\omega_n T_0}$ and therefore any right-hand-side term that is of the same form will become secular and cause x_1 to grow without bound. We seek the resonance cases that lead to additional secular terms. The right-hand-side of Eq. (7) merely shows the sub-harmonic resonance case. However, as shown in Fig. 1 as well as Eq. (7), the system has significant oscillatory behavior at the nonresonant

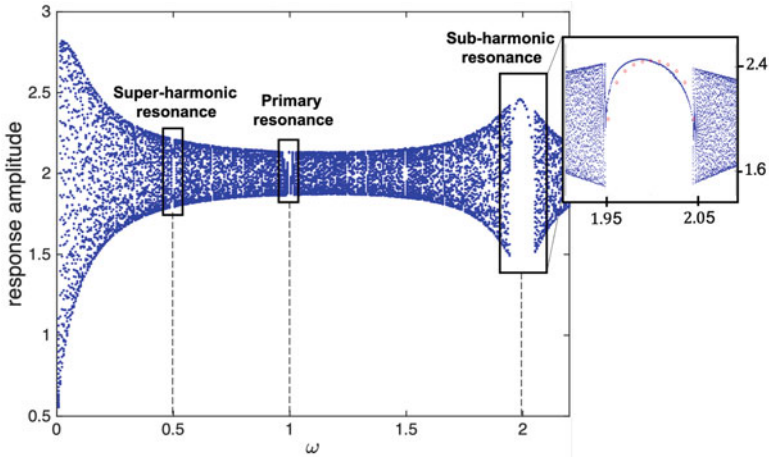


Fig. 1 PDVDP with parametric excitation only. The response amplitude versus the excitation frequency when $f_0 = f_1 = 0$, $\omega_n = 1$, $\epsilon = 0.1$, $c_0 = -1$, and $c_1 = 1$. The embedded sub-plot zooms in on the strong sub-harmonic resonance window. The circles are amplitudes predicted by the perturbation analysis

case, that is when there is no specific relationship between the excitation frequency ω and the natural frequency ω_n .

3.1 Nonresonant Case

We first consider the nonresonant case, where the solvability condition takes the form $2A' + c_0A + A^2\bar{A} = 0$. We recall that A is a complex function of T_1 . Writing it as $A(T_1) = \frac{1}{2}a(T_1)e^{i\beta(T_1)}$, the solvability condition becomes

$$a' + ia\beta' + \frac{1}{2}c_0a + \frac{1}{8}a^3 = 0. \tag{8}$$

By separating the real and imaginary parts, we obtain

$$a' + \frac{1}{2}c_0a + \frac{1}{8}a^3 = 0, \quad a\beta' = 0. \tag{9}$$

The response amplitude has steady-state values that depend on the parameter c_0 and are obtained by setting $a' = 0$. When $c_0 < 0$, there is a stable steady-state amplitude of $a = 2\sqrt{|c_0|}$. This amplitude and the solvability condition that leads to it are the same as in the regular van der Pol equation when $c_0 = -1$.

3.2 Sub-harmonic Resonance of Order 1/2

Here, we focus on the sub-harmonic resonance case, where the excitation frequency is tuned to be close to the double natural frequency, i.e. $\omega = 2\omega_n + \epsilon\sigma$. In this setting, the solvability condition is comprised of more terms and is given as $2A' + c_0A + A^2\bar{A} - \frac{c_1}{2}\bar{A}e^{i\sigma T_1} = 0$. By letting $A(T_1) = \frac{1}{2}a(T_1)e^{i\beta(T_1)}$, we obtain

$$a' + ia\beta' + \frac{1}{2}c_0a + \frac{1}{8}a^3 - \frac{1}{4}c_1ae^{i(\sigma T_1 - 2\beta)} = 0. \tag{10}$$

We separate the real and imaginary parts and then make the system autonomous via the change of variables $\gamma = \sigma T_1 - 2\beta$ to obtain the following governing equations of amplitude a and phase γ as

$$a' + \frac{1}{2}c_0a + \frac{1}{8}a^3 - \frac{1}{4}c_1a \cos(\gamma) = 0, \quad a\gamma' + \frac{1}{2}c_1a \sin(\gamma) - \sigma a = 0. \tag{11}$$

The response amplitude has steady-state values that depend on the parameters c_0 and c_1 and are obtained by setting $a' = \gamma' = 0$. By using the trigonometric identities, we remove γ and finally obtain the response amplitude as

$$a = 0, \quad \text{or} \quad a^2 = -4c_0 \pm 4\sqrt{\frac{c_1^2}{4} - \sigma^2}. \tag{12}$$

If $\frac{c_1^2}{4} - \sigma^2 > 0$, then Eq. (12) indicates that there are both zero and nonzero real-valued response amplitudes. Otherwise, the only steady-state amplitude is zero. Stability of these solutions is determined from the Jacobian of Eqs. (11).

Figure 2 shows the steady-state amplitude versus the excitation frequency $\omega = 2\omega_n + \epsilon\sigma$ for different values of c_0 and c_1 where $\epsilon = 0.1$ and $\omega_n = 1$. By slightly sweeping the detuning parameter σ , we keep the excitation frequency ω close to $2\omega_n$. We observe the emergence of a limit cycle at $\omega \approx 1.95$, whose amplitude grows and then disappears at $\omega \approx 2.05$. When $c_0 = -1$, a larger amplitude of parametric damping c_1 leads to a larger response amplitude; see the left panel in Fig. 2 where the inner and outer ellipses are associated with $c_1 = 0.2$ and $c_1 = 1$, respectively. An increase in the mean value of damping c_0 , however, decreases the response amplitude by moving down the ellipse till the horizontal axis $a = 0$, beyond which the lower branch of ellipse disappears; see the right panel in Fig. 2.

4 Parametric and External Excitation

In this case, the external forcing terms f_0 and f_1 are nonzero. Similar to the previous case, as a survey of the possible dynamics, Fig. 3 shows a frequency sweep from $\omega =$

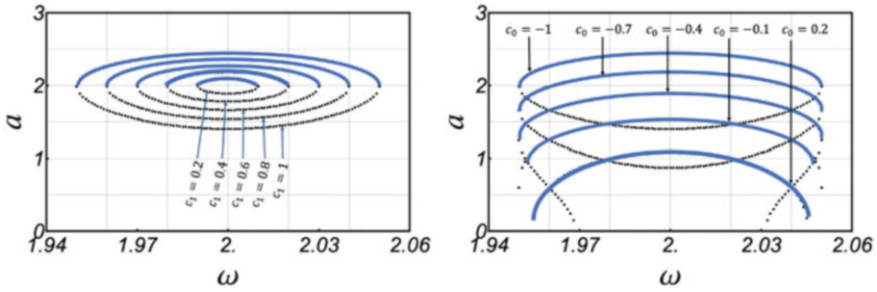


Fig. 2 PDVDP with parametric excitation only: nonzero steady-state response amplitude versus the excitation frequency in the case of sub-harmonic resonance. Left: $c_0 = -1$ and $c_1 = \{0.2, 0.4, 0.6, 0.8, 1\}$. Right: $c_1 = 1$ and $c_0 = \{-1, -0.7, -0.4, -0.1, 0.2\}$. Solid and dotted curves are stable and unstable branches

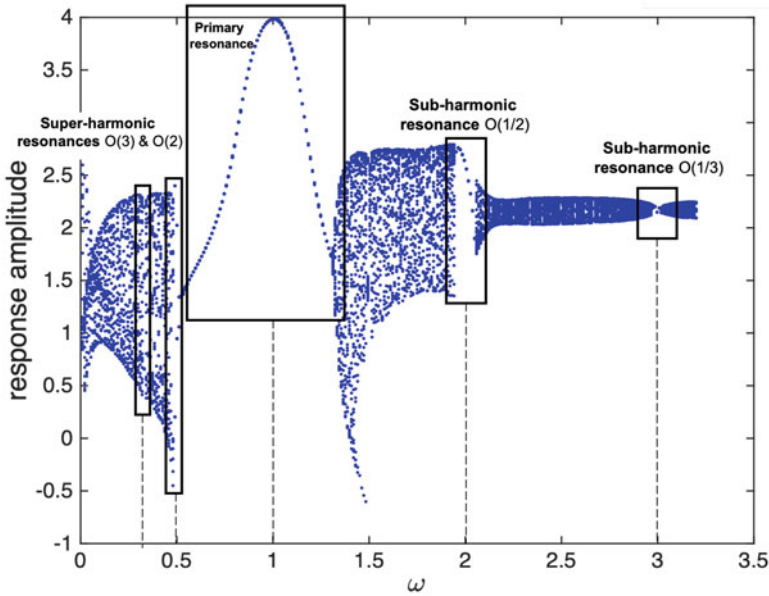


Fig. 3 PDVDP with parametric and external excitation. The response amplitude versus the excitation frequency ω where $f_0 = 0.2$, $f_1 = 1$, $\omega_n = 1$, $\epsilon = 0.1$, $c_0 = -1$, and $c_1 = 1$

0 to beyond $\omega = 3\omega_n$, with parameters $\omega_n = 1$, $c_0 = -1$, $c_1 = 1$, $f_0 = 0.2$, and $f_1 = 1$. The sweep is based on numerical simulations, and the steady-state response amplitudes are plotted. The plot shows that significant quasiperiodic dynamics occur for a large range of excitation frequencies with periodic windows around $\omega \approx \omega_n$, $\omega \approx 2\omega_n$, and $\omega \approx 3\omega_n$. The largest responses occur near the primary resonance range and then for sub-harmonic ones. Super-harmonic resonances are not apparent.

In this case, the particular solution to the leading order Eq. (4) is

$$x_0(T_0, T_1) = \Gamma + i\Lambda e^{i\omega T_0} + A(T_1)e^{i\omega_n T_0} - i\Lambda e^{-i\omega T_0} + \bar{A}(T_1)e^{-i\omega_n T_0}, \quad (13)$$

where $\Gamma = \frac{f_0}{\omega_n^2}$ and $\Lambda = \frac{f_1}{2(\omega^2 - \omega_n^2)}$. By plugging Eq. (13) in Eq. (5), we obtain

$$\begin{aligned} D_0^2 x_1 + \omega_n^2 x_1 = & \left(-2i\omega_n A' - ic_0\omega_n A - i\omega_n \Gamma^2 A - i\omega_n A^2 \bar{A} - 2i\omega_n \Lambda^2 A \right) e^{i\omega_n T_0} \\ & + \left(c_0\omega\Lambda + \omega\Gamma^2\Lambda + \omega\Lambda^3 + 2\omega A\bar{A}\Lambda \right) e^{i\omega T_0} \\ & + \left(\frac{c_1}{2}\omega\Lambda + 2i\omega\Gamma\Lambda^2 \right) e^{2i\omega T_0} \\ & - \omega\Lambda^3 e^{3i\omega T_0} + \left(i\frac{c_1}{2}\omega_n\bar{A} - 2\omega_n\Lambda\Gamma\bar{A} + 2\omega\Lambda\Gamma\bar{A} \right) e^{i(\omega - \omega_n)T_0} \\ & + i(2\omega - \omega_n)\Lambda^2\bar{A}e^{i(2\omega - \omega_n)T_0} + (\omega - 2\omega_n)\Lambda\bar{A}^2e^{i(\omega - 2\omega_n)T_0} \\ & + \text{c.c.} + \text{N.S.T.} \end{aligned} \quad (14)$$

The right-hand-side of Eq. (14) shows different cases of resonance; each can produce different secular terms. The cases are nonresonant, sub-harmonic resonance of orders 1/2 and 1/3, and super-harmonic resonance of order 2. Here we study the first two cases. The third case (super-harmonic of order 1/3) does not involve the parametric term, and others turn out to be of minimal significance. For the first two cases, we obtain the following solvability conditions:

- Nonresonant:

$$2A' + c_0A + \Gamma^2A + A^2\bar{A} + 2\Lambda^2A = 0 \quad (15)$$

- Sub-harmonic Resonance of Order 1/2 ($\omega \approx 2\omega_n$):

$$2A' + c_0A + \Gamma^2A + A^2\bar{A} + 2\Lambda^2A - \left(\frac{c_1}{2} - 2i\Lambda\Gamma \left(\frac{\omega}{\omega_n} - 1 \right) \right) \bar{A}e^{i\sigma T_1} = 0. \quad (16)$$

Although Fig. 3 indicates the primary resonance as a prominent case when $\omega \approx \omega_n$, the coefficient Λ becomes singular and would contradict the multiple-scales bookkeeping strategy. The analysis of primary resonance case requires weak excitation, as well as a second-order perturbation analysis to capture the parametric term, as in [17]. This will be analyzed in a separate study.

4.1 Nonresonant Case

The solvability condition in Eq. (15) is not affected by the parametric damping term, and hence the behavior is similar to the forced van der Pol equation [3, 4]. In this case, the phase equation becomes $\beta' = 0$, and hence the phase β is constant and does not influence the oscillation frequency. The amplitude equation yields the following steady-state solutions:

$$a = 0, \quad a = 2\sqrt{-c_0 - \Gamma^2 - 2\Lambda^2}, \tag{17}$$

where the zero solution is unstable and the nonzero solution exists and is stable when $\Gamma^2 + 2\Lambda^2 < -c_0$. Since $\Gamma^2 + 2\Lambda^2 > 0$, a negative value of c_0 is necessary (but not sufficient) for nonzero a . If the above condition is not satisfied, then the trivial solution $a = 0$ is stable.

Since the leading-order solution has the form

$$x_0 = \Gamma - 2\Lambda \sin \omega T_0 + a \cos(\omega_n T_0 + \beta) \tag{18}$$

when the condition $\Gamma^2 + 2\Lambda^2 < -c_0$ is satisfied, $a \neq 0$ and the response becomes quasiperiodic. Otherwise, with sufficient increase in the excitation (Λ and Γ), a is suppressed and the response becomes periodic; known as quenching [3, 4].

The parametric terms affect the first-order correction, x_1 , in the approximate solution $x(t) = x_0(t_0, T_1) + \epsilon x_1(T_0, T_1)$. In eliminating the secular terms, there are several contributions of different frequency components, including $2\omega, \omega - \omega_n, \omega + \omega_n$, from parametric excitation and van der Pol terms, and $2\omega_n, 3\omega_n, 3\omega, 2\omega - \omega_n, 2\omega + \omega_n, \omega - 2\omega_n$, and $\omega + 2\omega_n$, from the van der Pol terms. Thus the first-order solution can contribute two-frequency quasiperiodic effects, as the content of the total response has a linear combination of two frequencies.

4.2 Sub-harmonic Resonance of Order 1/2

In this case, the excitation and natural frequency form the relation $\omega = 2\omega_n + \epsilon\sigma$. We see from the solvability condition in Eq. (16) that in addition to the nonresonant secular terms in Eq. (15), the parametric damping and forcing appear. We substitute $A(T_1) = \frac{1}{2}a(T_1)e^{i\beta(T_1)}$ into the equation and let $\gamma = \sigma T_1 - 2\beta$. Then, the autonomous coupled system of governing equations of the amplitude a and phase γ becomes

$$\begin{aligned} a' + \frac{1}{8}a^3 + \left(\frac{c_0}{2} + \frac{\omega_n \Gamma^2}{2} + \Lambda^2 - \frac{c_1}{4} \cos \gamma + \Gamma \Lambda \left(1 - \frac{\omega}{\omega_n} \right) \sin \gamma \right) a &= 0, \\ a\gamma' - a\sigma + \frac{c_1}{2}a \sin \gamma + 2a\Gamma \Lambda \left(1 - \frac{\omega}{\omega_n} \right) \cos \gamma &= 0. \end{aligned} \tag{19}$$

The fixed points of Eq. (19) are obtained in the steady-state case when $a' = \gamma' = 0$, which admits $a = 0$ and a nontrivial solution. The equations for the nontrivial solution take the form $A_1 \sin \gamma + B_1 \cos \gamma = C_1$ and $A_2 \sin \gamma + B_2 \cos \gamma = C_2$ where the coefficients A_1, A_2, B_1, B_2, C_1 , and C_2 are functions of the parameters and the amplitude a . By solving for $\sin \gamma$ and $\cos \gamma$, and using the trigonometric identities, we remove the variable γ and form a parametric algebraic equation to

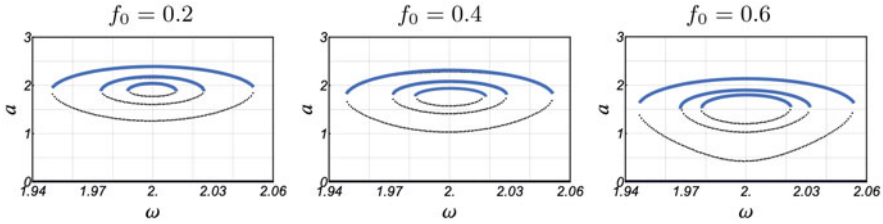


Fig. 4 PDVDP with parametric and external excitation in the case of sub-harmonic resonance where $c_0 = -1$ and $f_1 = 1$. The three plotted curves correspond to $c_1 = \{0.2, 0.5, 1\}$, and the panels are for $f_0 = \{0.2, 0.4, 0.6\}$. Solid and dotted curves are stable and unstable branches

obtain the steady-state amplitude a as,

$$a^4 + 8a^2(c_0 + 2\Lambda^2 + \Gamma^2) + 4(4c_0^2 + 16c_0\Lambda^2 - c_1^2 + 16\Lambda^4 + 4\sigma^2) + 16\Gamma^2 \left(2c_0 - 4\Lambda^2 \frac{\omega}{\omega_n} \left(\frac{\omega}{\omega_n} - 2 \right) + \Gamma^2 \right) = 0. \tag{20}$$

Solving for a^2 yields the steady-state response amplitude, which is valid if the square root in the quadratic-equation solution is real, and if $a^2 \geq 0$. The first criterion reduces to $4\sigma^2 < c_1^2 + 16\Gamma^2\Lambda^2$, when using $\omega - \omega_n \approx \omega_n$. Thus the frequency range of fixed amplitude solutions increases with c_1 , f_0 , and f_1 . For the case in which a and γ are fixed and stable, based on Eq. (13) and the definition of γ , the leading order solution takes the form

$$x_0 = \Gamma - 2\Lambda \sin(\omega T_0) + a \cos\left(\frac{\omega}{2}T_0 - \frac{\gamma}{2}\right), \tag{21}$$

which is a periodic (phase locked) response of fundamental frequency $\omega/2$. When a steady-state solution a does not exist, the response is in phase drift, and is quasiperiodic.

Figure 4 shows the steady-state response amplitude versus the excitation frequency for small value of detuning parameter, when $\epsilon = 0.1$ and $-0.5 < \sigma < 0.5$. Note that these figures show the amplitude a of one term in Eq. (21). The phase γ would affect peak-to-peak amplitudes. The mean damping and periodic forcing are set to be constant, $c_0 = -1$ and $f_1 = 1$, while different values of $c_1 = \{0.2, 0.5, 1\}$ are showing the ellipses. The larger values of c_1 are associated with the larger ellipses. We see that as the constant forcing term f_0 is varying between $\{0.2, 0.4, 0.6\}$, the ellipses are distorted and the limit cycle amplitude is increased. The sub-harmonic behavior of the parametric plus direct excitation is thus similar to that of the parametric excitation only, except that the solutions for the steady amplitudes are complicated and distorted by the direct excitation terms f_0 and f_1 .

5 Summary and Conclusions

In this paper, we studied the resonance of a forced and unforced van der Pol equation with parametric damping. Applications can include vertical-axis wind-turbine blade vibration, which can have parametric damping and van-der-Pol type terms in simplified models. The first-order method of multiple scales and numerical solutions were used.

The parametric damping with no external excitation demonstrated nonresonant and sub-harmonic resonance cases, where the system shows an oscillatory quasiperiodic behavior in the former case. In the latter resonance case, we found the steady-state amplitude versus the excitation frequency for different damping parameters. When $c_0 = -1$ (negative linear damping as with the van der Pol oscillator), the resonant response amplitude increases with the parametric damping c_1 . An increase in the mean value of damping c_0 , however, decreases the response amplitude.

We then studied van der Pol with parametric and direct excitation. In the nonresonant case the parametric damping term does not contribute in the solvability condition and therefore it showed the same behavior as the forced van der Pol. The nonresonant system can exhibit the quenching phenomenon when the excitation through the direct forcing is sufficiently large.

Our numerical studies showed the primary resonance as a dominant forced response case. The analysis of this case requires further investigation that will be done as a subsequent study with weak excitation. Based on previous studies on the cases with forcing and cyclic stiffness [17], we expect that a second-order multiple-scales analysis should be considered to correctly pull out the contribution of the parametric damping to the different resonance cases.

References

1. F. Afzali, O. Kapucu, B.F. Feeny, Vibrational analysis of vertical-axis wind-turbine blades, in *Proceedings of the ASME 2016 International Design Engineering Technical Conferences*. Paper number IDETC2016-60374, Charlotte, North Carolina, August 21–24 (2016)
2. F. Afzali, G.D. Acar, B.F. Feeny, A Floquet-based analysis of parametric excitation through the damping coefficient. *J. Vib. Acoust.* **143**(4), 041003 (2021)
3. A.H. Nayfeh, D.T. Mook, *Nonlinear Oscillations* (Wiley, New York, 2008)
4. R.H. Rand, *Lecture Notes on Nonlinear Vibrations* (2012). <https://ecommons.cornell.edu/handle/1813/28989>
5. Hartono, and A.H.P. Burgh, *An Equation Time-periodic Damping Coefficient: Stability Diagram and an Application* (Delft University of Technology, Delft, 2002)
6. G. Acar, B.F. Feeny, Floquet-based analysis of general responses of the Mathieu equation. *J. Vib. Acoust.* **138**(4), 041017(9 pages) (2016)
7. F. Afzali, B.F. Feeny, Response characteristics of systems with parametric excitation through damping and stiffness, in *In ASME International Design Engineering Technical Conferences and Computers and Information in Engineering Conference, American Society of Mechanical Engineers* (2020). paper number DETC2020-22457

8. K. Szabelski, J. Warmiński, Parametric self-excited non-linear system vibrations analysis with inertial excitation. *Int. J. Non Linear Mech.* **30**(2), 179–189 (1995)
9. J. Warminski, Nonlinear dynamics of self-, parametric, and externally excited oscillator with time delay: van der pol versus Rayleigh models. *Nonlinear Dyn.* **99**(1), 35–56 (2020)
10. V. Ramakrishnan, B.F. Feeny, Resonances of a forced Mathieu equation with reference to wind turbine blades. *J. Vib. Acoust.* **134**(6), 064501 (2012)
11. M.S. Allen, M.W. Sracic, S. Chauhan, M.H. Hansen, Output-only modal analysis of linear time-periodic systems with application to wind turbine simulation data. *Mech. Syst. Sig. Process.* **25**(4), 1174–1191 (2011)
12. T. Inoue, Y. Ishida, T. Kiyohara, Nonlinear vibration analysis of the wind turbine blade (occurrence of the superharmonic resonance in the out of plane vibration of the elastic blade). *J. Vib. Acoust.* **134**(3), 031009 (2012)
13. G.D. Acar, M.A. Acar, B.F. Feeny, Parametric resonances of a three-blade-rotor system with reference to wind turbines. *J. Vib. Acoust.* **142**(2), 021013(9 pages) (2020)
14. A. Luongo, D. Zulli, Parametric, external and self-excitation of a tower under turbulent wind flow. *J. Sound Vib.* **330**(13), 3057–3069 (2011)
15. A.H. Nayfeh, *Perturbation Methods* (Wiley, New York, 2008)
16. J. Guckenheimer, P. Holmes, *Nonlinear Oscillations, Dynamical Systems, and Bifurcations of Vector Fields* (Springer, New York, 1983)
17. V. Ramakrishnan, Analysis of wind turbine blade vibration and drivetrain loads. PhD thesis (Michigan State University, East Lansing, 2017)

Analysis of General Piecewise-Linear Non-Smooth Systems Using a Hybrid Analytical-Numeric Computational Method



Meng-Hsuan Tien and Kiran D'Souza

1 Introduction

The prediction and analysis of the dynamics of piecewise-linear (PWL) nonlinear systems, or bilinear systems in particular, are of importance in many fields including structural health monitoring of mechanical or aerospace systems [1–3], nonlinear circuit analysis for electrical systems [4, 5], and modeling gene regulatory networks in biological systems [6, 7]. The computation of the dynamic response of these systems is usually expensive since efficient linear techniques [8, 9] are not effective for analyzing these nonlinear dynamical systems or PWL nonlinear systems in particular. Moreover, the techniques that have been developed for nonlinear systems are usually much more computationally expensive than these traditional linear methods. Thus, developing efficient computational tools to predict the dynamics of bilinear systems has been drawing attention of researchers and engineers.

PWL nonlinearities are usually caused by discrete events in dynamical systems. For instance, the intermittent contact phenomenon in structural systems that result from cracks [10, 11], delamination [12–14], or interface among components [15] often creates PWL nonlinearity. Moreover, PWL nonlinearity is also observed in many electrical circuits when voltage- or current-dependent elements are employed to realize particular properties [4]. In order to accurately model the dynamics of these systems, a computational tool that can capture the nonlinearity is required. PWL nonlinear systems usually consist of multiple subsystems that can be modeled

M.-H. Tien (✉)

Department of Power Mechanical Engineering, National Tsing Hua University, Hsinchu, Taiwan
e-mail: mhtien@pme.nthu.edu.tw; tien.36@osu.edu

K. D'Souza

Department of Mechanical and Aerospace Engineering, The Ohio State University, Columbus, OH, USA
e-mail: dsouza.60@osu.edu

using linear techniques. However, traditional linear methods such as modal decomposition [16] are not able to predict the dynamics of the entire system since these systems can still exhibit strong nonlinear features [5, 17]. Numerical integration (NI) is the most common tool used to analyze nonlinear dynamical systems in a broad array of fields. However, NI requires a very small step size to capture the non-smooth evolution of state variables in PWL nonlinear systems. Thus, NI is usually computationally expensive for analyzing these systems. Another set of methods based on the harmonic balance (HB) method has also been widely used to predict the vibrational response of PWL nonlinear systems [18–20]. These methods compute the steady-state response of PWL nonlinear systems by approximating their periodic solutions using a truncated Fourier series. Numerical methods are then employed to solve for the unknown parameters in the assumed Fourier series. Although the HB-based methods are able to obtain the steady-state solution by skipping the time-consuming time marching process required by using NI, numerous harmonic terms are usually required to obtain an accurate solution, which still incurs a considerable computational cost. There has also been recent work in efficiently computing the transient and chaotic response of systems undergoing periodic excitation [21, 22]. This hybrid symbolic numeric computational (HSNC) method has been demonstrated to be more efficient than NI, but is not necessarily as efficient as HB-based methods in conducting parametric sweeps for systems that do reach a steady-state response. However, it should be noted that HSNC does work for responses that do not reach a steady state (i.e., transient, chaotic, non-stationary). This HSNC method works by using the analytical response of the system when it is in each linear regime and stitching the responses of the system together as it transitions from one regime to the next.

Recently, a new technique referred to as the bilinear amplitude approximation (BAA) method [23, 24] has been developed to compute the steady-state vibrational response of a subset of PWL nonlinear systems whose dynamic behavior can be approximated and modeled using bilinear oscillators. The BAA method is based on the idea that the vibrational cycle of a bilinear system can be obtained by combining the linear responses of the system in the distinct regions where the system behaves linearly. The method employs the analytical approach to determine these linear responses and incorporates a nonlinear optimization solver to numerically solve for the unknowns when coupling these PWL responses to obtain the nonlinear vibrational cycle. The computational cost of the BAA method can be reduced significantly since efficient linear techniques are used in the computation. However, the BAA method is only applicable to structural systems that are proportionally damped and hence limits its capability for analyzing general systems.

The goal of this paper is to extend the BAA method to general bilinear systems modeled using state-space representations. In the extended method, an analytical technique is used to express the responses of these systems in each of their linear regimes. Then a numerical tool is employed to solve for the parameters in the analytical expressions by applying appropriate compatibility conditions. Steady-state vibrational motion can then be obtained by combining the responses solved in each linear regime. The proposed hybrid method combines the analytical and

numerical approach to provide an efficient computational framework for capturing the vibrational response of nonlinear systems with bilinear elements. The remainder of the paper is organized as follows. First, the proposed method is introduced. Next, the results of applying the method for an electrical circuit with a voltage-dependent capacitor and a spring-mass mechanical oscillator are presented. Finally, conclusions are discussed.

2 Methodology

In this section, the BAA method [23, 24] developed for proportionally damped structural systems is extended to general bilinear systems modeled using state-space representations. In general the state-space model of physical systems can be represented as the following form:

$$\dot{\mathbf{u}} = \mathbf{A}(\mathbf{u})\mathbf{u}(t) + \mathbf{B}(\mathbf{u})\mathbf{q}(t), \quad (1)$$

where $\mathbf{A}(\mathbf{u})$ represents the state matrix and has the size of $n \times n$, $\mathbf{B}(\mathbf{u})$ represents the input matrix and has the size of $n \times p$, $\mathbf{u}(t) \in \mathbb{R}^n$ represents the state vector, and $\mathbf{q}(t) \in \mathbb{R}^p$ represents the input vector. In this paper, we consider a system where the system's behavior can be modeled using two distinct linear states

$$\mathbf{A}(\mathbf{u}) = \begin{cases} \mathbf{A}_1 & \text{if } u_n \geq 0 \\ \mathbf{A}_2 & \text{if } u_n < 0 \end{cases}, \quad (2)$$

$$\mathbf{B}(\mathbf{u}) = \begin{cases} \mathbf{B}_1 & \text{if } u_n \geq 0 \\ \mathbf{B}_2 & \text{if } u_n < 0 \end{cases},$$

where u_n represents the nonlinear state variable in the system, \mathbf{A}_1 and \mathbf{B}_1 represent the state matrix and the input matrix when the system is in the first linear state, and \mathbf{A}_2 and \mathbf{B}_2 represent the state matrix and the input matrix when the system is in the second linear state. Note that \mathbf{A}_1 , \mathbf{A}_2 , \mathbf{B}_1 , and \mathbf{B}_2 are all constant matrices. In order to obtain the analytical solutions of the system in each of its linear states, eigendecompositions of \mathbf{A}_1 and \mathbf{A}_2 are required. Since the state matrices \mathbf{A}_1 and \mathbf{A}_2 are generally non-symmetric, the eigenvalues of these matrices are not guaranteed to be real and the eigenvalues associated with \mathbf{A} and \mathbf{A}^T are not the same. The eigenvalue problem associated with the matrices \mathbf{A} 's can be expressed as

$$\mathbf{A}\mathbf{x} = \lambda\mathbf{x}. \quad (3)$$

The solution of Eq. (3) consists of eigenvalues λ_j and the right eigenvectors \mathbf{x}_j , where $j = 1, \dots, n$. Note that if λ_j is a complex eigenvalue, then the complex conjugate $\bar{\lambda}_j$ is also an eigenvalue. Moreover, the eigenvector \mathbf{x}_j associated with λ_j

is also complex and eigenvector $\bar{\mathbf{x}}_j$ associated with $\bar{\lambda}_j$ is the complex conjugate of \mathbf{x}_j . Next, the eigenvalue problem associated with the transposed matrices \mathbf{A}^T can be expressed as

$$\mathbf{A}^T \mathbf{y} = \lambda \mathbf{y}. \quad (4)$$

Note that \mathbf{A}^T and \mathbf{A} share the same eigenvalues, and \mathbf{x}_j 's are known as the right eigenvectors and the adjoint eigenvectors \mathbf{y}_j 's are known as the left eigenvectors. These eigenvectors satisfy the following biorthogonality:

$$\mathbf{y}_r^T \mathbf{A} \mathbf{x}_j = 0, \text{ if } \lambda_j \neq \lambda_r. \quad (5)$$

The eigenvectors can then be normalized by enforcing

$$\mathbf{y}_r^T \mathbf{x}_j = \delta_{jr}, \quad (6)$$

where δ_{jr} is the Kronecker delta. This yields

$$\mathbf{Y}^T \mathbf{A} \mathbf{X} = \mathbf{\Lambda}, \quad (7)$$

where $\mathbf{Y} = [\mathbf{y}_1, \dots, \mathbf{y}_n]$ is the matrix including all the left eigenvectors, $\mathbf{X} = [\mathbf{x}_1, \dots, \mathbf{x}_n]$ is the matrix including all the right eigenvectors, and $\mathbf{\Lambda} = \text{diag}[\lambda_1, \dots, \lambda_n]$ is the eigenvalue matrix. Next, by premultiplying Eq. (7) by \mathbf{X} and postmultiplying by \mathbf{Y}^T , Eq. (7) can be reformulated as

$$\mathbf{A} = \mathbf{X} \mathbf{\Lambda} \mathbf{Y}^T. \quad (8)$$

Equation (8) represents the modal decomposition of the matrix \mathbf{A} .

Next, by applying the state-space expansion theorem [16], the solution to Eq. (1) can be represented as a linear combination of the right eigenvectors

$$\mathbf{u}(t) = \mathbf{X} \boldsymbol{\xi}(t), \quad (9)$$

where $\boldsymbol{\xi}(t)$ are the modal coordinates. Then, inserting Eq. (9) into Eq. (1) and premultiplying by \mathbf{Y}^T , the following equation is obtained:

$$\mathbf{Y}^T \mathbf{X} \dot{\boldsymbol{\xi}}(t) = \mathbf{Y}^T \mathbf{A} \mathbf{X} \boldsymbol{\xi}(t) + \mathbf{Y}^T \mathbf{B} \mathbf{q}(t), \quad (10)$$

By using the orthogonormality relations from Eqs. (7) and (10) can be simplified to

$$\dot{\boldsymbol{\xi}}(t) = \mathbf{\Lambda} \boldsymbol{\xi}(t) + \mathbf{n}(t), \quad (11)$$

where $\mathbf{n}(t) = \mathbf{Y}^T \mathbf{B} \mathbf{q}(t)$. Note that Eq. (11) is a set of independent modal equations

$$\dot{\xi}_j(t) = \lambda_j \xi_j(t) + n_j(t), \quad (12)$$

where $j = 1, \dots, n$ and $n_j(t) = \mathbf{y}_j^T \mathbf{B} \mathbf{q}(t)$.

Next, the BAA method is modified to estimate the nonlinear forced response of the bilinear system. Assuming that the system is driven by harmonic excitation $\mathbf{q}(t) = \mathbf{q}_0 e^{i\alpha t}$, the modal response of the system in its linear states can be expressed as combinations of the linear transient response and the linear steady-state response:

$$\begin{aligned} \xi_{j,1}(t) &= c_{j,1} e^{\lambda_{j,1} t} + \frac{\mathbf{y}_{j,1}^T \mathbf{B}_1 \mathbf{q}_0}{i\alpha - \lambda_{j,1}} e^{i(\alpha t + \psi)}, \\ \xi_{r,2}(t) &= c_{r,2} e^{\lambda_{r,2} t} + \frac{\mathbf{y}_{r,2}^T \mathbf{B}_2 \mathbf{q}_0}{i\alpha - \lambda_{r,2}} e^{i(\alpha t + \psi)}, \end{aligned} \quad (13)$$

where $\xi_{j,1}(t)$ and $\xi_{r,2}(t)$ ($j = 1, \dots, n$ and $r = 1, \dots, n$) represent the modal coordinate of the system in the first and second linear states, respectively; $c_{j,1}, c_{r,2} \in \mathbb{C}$ are scalar complex coefficients of the linear transient response; $\alpha \in \mathbb{R}$ is the excitation frequency; $\psi \in \mathbb{R}$ reflects the phase difference between the excitation and the linear steady-state responses. Note that the additional phase angle ψ is included in the expressions to represent the phase shift caused by the nonlinearity [23]. Furthermore, if ξ_j is a complex coordinate associated with the right eigenvector \mathbf{x}_j , then the conjugate $\bar{\xi}_j$ is also a coordinate associated with the eigenvector $\bar{\mathbf{x}}_j$. Similarly, complex coefficients (c_j, \bar{c}_j) exist in conjugate pairs. The physical coordinates can be obtained by applying the coordinate transformation $\mathbf{u}_1(t) = \mathbf{X}_1 \boldsymbol{\xi}_1(t)$ and $\mathbf{u}_2(t) = \mathbf{X}_2 \boldsymbol{\xi}_2(t)$, where \mathbf{X}_1 represents the right eigenvector matrix of the system in the first linear state and \mathbf{X}_2 represents the right eigenvector matrix of the system in the second linear state.

The response of one steady-state vibrational cycle for the nonlinear state variable is schematically shown in Fig. 1. When $u_n \geq 0$, the system's behavior is governed by the first linear state; when $u_n < 0$, the system's behavior is governed by the second linear state. The time which the system spends in the first linear state is referred to as T_1 ; the time which the system spends in the second linear state is referred to as T_2 . The key idea of the proposed method is that the response of an entire nonlinear vibrational cycle can be obtained by combining the responses of the system in its two linear states. To this end, a set of compatibility conditions is enforced to solve for the unknowns $c_{j,1}, c_{r,2}$, and ψ in Eq. (13). These compatibility conditions are summarized as follows:

$$\begin{aligned} \mathbf{u}_1(T_1) &= \mathbf{u}_2(T_1), \\ \mathbf{u}_1(0) &= \mathbf{u}_2(T), \\ u_{n,1}(0) &= 0, \\ u_{n,1}(T_1) &= 0. \end{aligned} \quad (14)$$

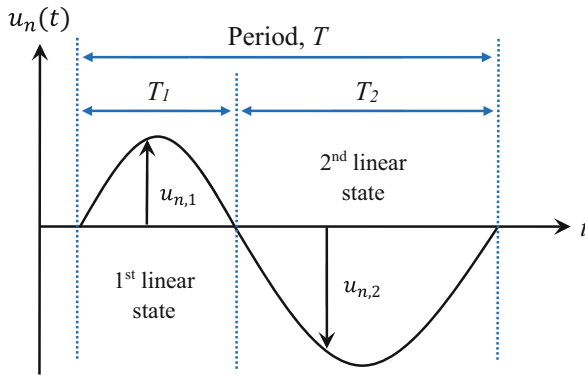


Fig. 1 One steady-state vibration cycle for the nonlinear state variable

The first and second equation in Eq. (14) represent the continuity condition that the state variables must satisfy at the moment when the system switches from one linear state to the other. The third and fourth equations represent the threshold value that the nonlinear state variable passes through when the system switches its linear state. Note that T is the period of the vibration cycle which can be calculated by $T = \frac{2\pi}{\alpha}$ and T_1 is an additional unknown that needs to be solved. Equation (14) can then be expressed in terms of modal coordinates as:

$$\begin{aligned}
 \mathbf{X}_1 \xi_1(T_1) - \mathbf{X}_2 \xi_2(T_1) &= \mathbf{0}, \\
 \mathbf{X}_1 \xi_1(0) - \mathbf{X}_2 \xi_2(T) &= \mathbf{0}, \\
 \mathbf{X}_{1,n} \xi_1(0) &= 0, \\
 \mathbf{X}_{1,n} \xi_1(T_1) &= 0,
 \end{aligned}
 \tag{15}$$

where $\mathbf{X}_{1,n}$ is the portion of the mode shapes corresponding to the nonlinear state variable $u_{n,1}$. The unknowns ($c_{j,1}$, $c_{r,2}$, ψ , T_1) in Eq. (15) can then be solved by employing a nonlinear optimization solver. In this work, the function “lsqnonlin” in MATLAB was used to find these parameters by minimizing the residual in Eq. (15). Once these parameters are obtained, a nonlinear vibrational cycle can be constructed by coupling the linear responses of each linear states.

The proposed method is developed for analyzing the steady-state dynamics of PWL systems, and is particularly beneficial when a parameter sweep is required. In the sweep process, the nonlinear optimization solver is given multiple random initial guesses at a starting parameter value. Since multiple local solutions might exist, only the one that has the minimum residual is chosen as the starting point for the parameter sweep. The parameter sweep can then be conducted efficiently by using the solution from the previous parameter value as the initial condition for computing the response at the next parameter point.

3 Results

Results of applying the methodology to a three degree-of-freedom (DOF) mechanical oscillator with contacting masses and a nonlinear analog circuit are discussed next.

3.1 Mechanical Oscillator with Contacting Elements

The proposed method is applied to analyze the nonlinear response of a three DOF mechanical oscillator with contacting masses as shown in Fig. 2a, where $m_1 = m_2 = 2.0$ kg, $m_3 = 10$ kg, $k_1 = 1.20$ N/m, $k_2 = 1.68$ N/m, $k_3 = 8.00$ N/m, $c_1 = 0.060$ kg/s, $c_2 = 0.0168$ kg/s, $c_3 = 0.400$ kg/s, and the initial gap $g = 0$ m. Note that the damping matrix is not proportional to the mass and stiffness matrices in this case study. The mass m_3 is excited by a harmonic force $F(t) = f_0 \cos(\omega t)$ with amplitude $f_0 = 0.01$ N and frequency ω . In order to analyze the intermittent contact behavior between m_1 and m_2 , the system’s dynamic behavior is modeled using two linear subsystems. The first sub-system represents the system’s first linear state when the gap is open, which is shown in Fig. 2b; the second sub-system represents the system’s second linear state when the gap is closed, which is shown in Fig. 2c. Note that a set of contact stiffness k^* and contact damping c^* is used to minimize the penetration between the contacting masses when the gap is in the closed state. The contact stiffness and damping are set to $k^* = 1000$ N/m and $c^* = 50$ kg/s in this work. The equations of motion of the system for its two linear states can be expressed as

$$\begin{aligned} \mathbf{M}_1 \ddot{\mathbf{x}}_1 + \mathbf{C}_1 \dot{\mathbf{x}}_1 + \mathbf{K}_1 \mathbf{x}_1 &= \mathbf{F}(t) \text{ if } x_1 - x_2 < 0, \\ \mathbf{M}_2 \ddot{\mathbf{x}}_2 + \mathbf{C}_2 \dot{\mathbf{x}}_2 + \mathbf{K}_2 \mathbf{x}_2 &= \mathbf{F}(t) \text{ if } x_1 - x_2 \geq 0, \end{aligned} \tag{16}$$

where the subscript 1 represents the first linear state when the gap is open, and the subscript 2 represents the second linear state when the gap is closed. The matrices can be expressed as

$$\begin{aligned} \mathbf{M}_1 = \mathbf{M}_2 &= \begin{bmatrix} m_1 & 0 & 0 \\ 0 & m_2 & 0 \\ 0 & 0 & m_3 \end{bmatrix}, \\ \mathbf{C}_1 &= \begin{bmatrix} c_1 & 0 & -c_1 \\ 0 & c_2 & -c_2 \\ -c_1 & -c_2 & c_1 + c_2 + c_3 \end{bmatrix}, \mathbf{C}_2 = \begin{bmatrix} c_1 + c^* & -c^* & -c_1 \\ -c^* & c_2 + c^* & -c_2 \\ -c_1 & -c_2 & c_1 + c_2 + c_3 \end{bmatrix}, \end{aligned} \tag{17}$$

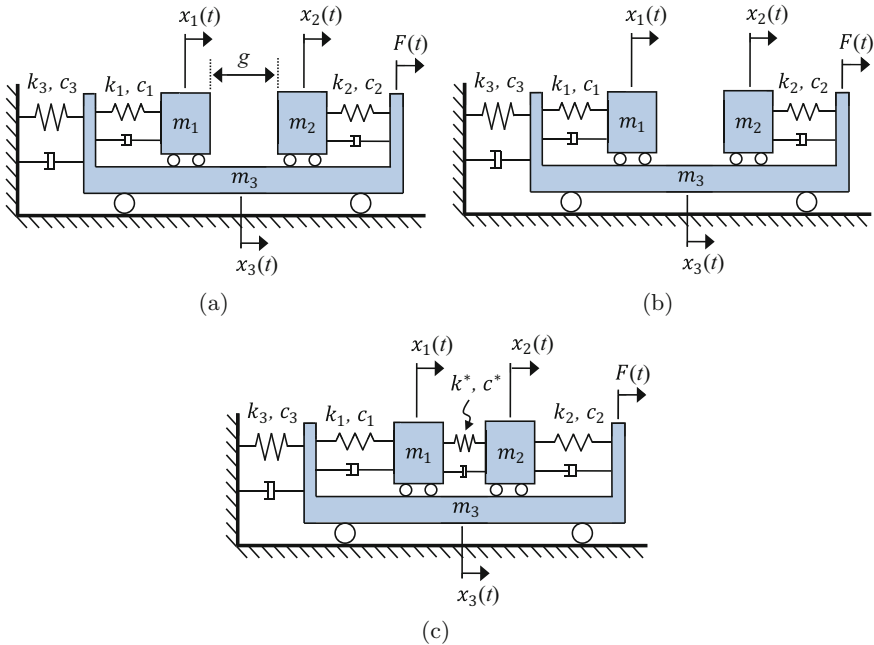


Fig. 2 (a) Three DOF mechanical oscillator with contacting masses. (b) The system in the open state. (c) The system in the closed state

$$\mathbf{K}_1 = \begin{bmatrix} k_1 & 0 & -k_1 \\ 0 & k_2 & -k_2 \\ -k_1 & -k_2 & k_1 + k_2 + k_3 \end{bmatrix}, \mathbf{K}_2 = \begin{bmatrix} k_1 + k^* & -k^* & -k_1 \\ -k^* & k_2 + k^* & -k_2 \\ -k_1 & -k_2 & k_1 + k_2 + k_3 \end{bmatrix}.$$

The coordinate $\mathbf{x} = [x_1, x_2, x_3]^T$ represents the displacements of m_1 , m_2 , and m_3 , respectively. Since the system is not proportionally damped, the state-space model is used to model its dynamics by expanding the coordinate system to $\mathbf{u} = [x_1, x_2, x_3, \dot{x}_1, \dot{x}_2, \dot{x}_3]$, where \dot{x}_1 , \dot{x}_2 , and \dot{x}_3 represent the velocity of the three masses. The state matrix and the input matrix of the state-space model can then be expressed as

$$\begin{aligned} \mathbf{A}_1 &= \begin{bmatrix} \mathbf{0} & \mathbf{I} \\ -\mathbf{M}_1^{-1}\mathbf{K}_1 & -\mathbf{M}_1^{-1}\mathbf{C}_1 \end{bmatrix}, \\ \mathbf{A}_2 &= \begin{bmatrix} \mathbf{0} & \mathbf{I} \\ -\mathbf{M}_2^{-1}\mathbf{K}_2 & -\mathbf{M}_2^{-1}\mathbf{C}_2 \end{bmatrix}, \\ \mathbf{B}_1 &= \begin{bmatrix} \mathbf{0} \\ \mathbf{M}_1^{-1} \end{bmatrix}, \end{aligned} \tag{18}$$

$$\mathbf{B}_2 = \begin{bmatrix} \mathbf{0} \\ \mathbf{M}_2^{-1} \end{bmatrix},$$

where \mathbf{I} represents the identity matrix.

Next, the proposed method is employed to compute the nonlinear response of the system. Note that the nonlinear state variable of this system is $u_n = x_1 - x_2$ since the system switches its state when $x_1 - x_2 = 0$. Furthermore only the real part in Eq. (15) is retained for the computation since the system is driven by $f_0 \cos \omega t$. The forced response obtained using the proposed method is compared with the one computed using numerical integration. The explicit Runge–Kutta method [25] and the event function in MATLAB [26] are used for performing numerical integration in this work. The comparison is shown in Fig. 3 with the solutions computed using the proposed method and numerical integration being in good agreement over the plotted frequency range. Furthermore, the average CPU time required by the proposed method to compute the forced response for a specific frequency using a Dell XPS 15 laptop (2.60 GHz) is 0.039 s. By contrast, numerical integration requires 2.557 s to obtain a steady-state response. The proposed method only requires 1.53% of the CPU time of numerical integration. The new method is expected to improve its computational performance with respect to NI as the system becomes more and more complex in the same way as BAA [27, 28].

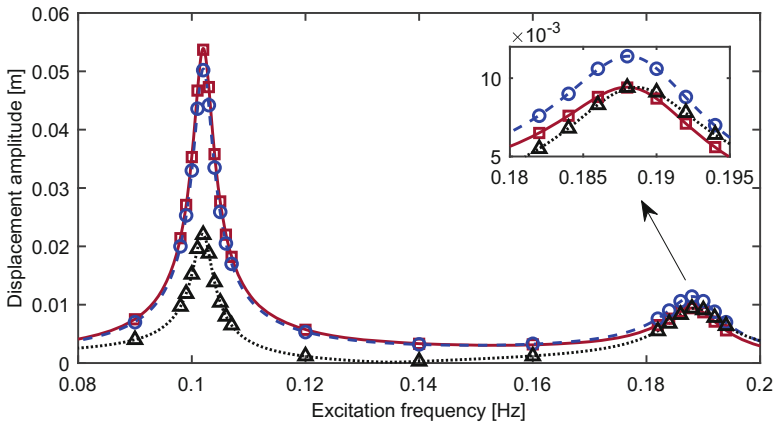
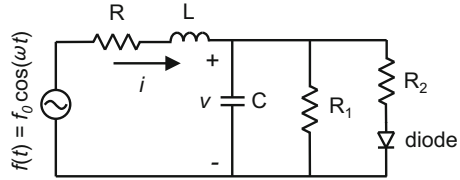


Fig. 3 Forced response of the three DOF mechanical oscillator. (—) represents the response of m_1 computed using the proposed method; (---) represents the response of m_2 computed using the proposed method; (···) represents the response of m_3 computed using the proposed method; (□) represents the response of m_1 computed using numerical integration; (○) represents the response of m_2 computed using numerical integration; (△) represents the response of m_3 computed using numerical integration

Fig. 4 A PWL nonlinear circuit with voltage-dependent resistance



3.2 Nonlinear Analog Circuit with a Voltage-Dependent Resistance

The proposed method is applied to analyze the dynamic response of a simple nonlinear circuit with a voltage-dependent resistance as shown in Fig. 4. This circuit is composed of several components including an inductor (L), a capacitor (C), a diode, and several resistors (R , R_1 , R_2). Note that the diode allows current to flow in only one direction and hence induces the PWL nonlinearity in the system. Furthermore, the system is driven by an AC voltage with amplitude f_0 and frequency ω . The state-space model of this circuit can be expressed as

$$\dot{\mathbf{u}} = \mathbf{A}(v)\mathbf{u}(t) + \mathbf{B} \cos(\omega t), \tag{19}$$

where $\mathbf{u}(t) = [v(t), i(t)]^T$. Note that v represents the voltage across the capacitor C and i represents the current across the resistor R and the inductor L . The state matrix and the input matrix of this system can be expressed as

$$\mathbf{A}(v) = \begin{cases} \begin{bmatrix} \frac{-R_1 R_2}{C(R_1 + R_2)} & \frac{1}{C} \\ \frac{-1}{L} & \frac{-R}{L} \end{bmatrix} & \text{if } v \geq 0 \\ \begin{bmatrix} \frac{-1}{C R_1} & \frac{1}{C} \\ \frac{-1}{L} & \frac{-R}{L} \end{bmatrix} & \text{if } v < 0 \end{cases}, \tag{20}$$

$$\mathbf{B} = \begin{bmatrix} 0 \\ \frac{f_0}{L} \end{bmatrix}.$$

The steady-state response of the system for a particular parameter set is computed using the proposed technique. The parameter values used in this case study are $R = 120 \, \Omega$, $L = 1.8 \times 10^{-2} \text{ mH}$, $C = 10^{-8} \text{ nF}$, $R_1 = 100 \, \Omega$, $R_2 = 10 \, \Omega$, and $f_0 = 1 \text{ V}$. Again, only the real part in Eq. (15) is retained for the computation since the system is driven by $f_0 \cos \omega t$. The phase plots of the system for $\omega = 500 \text{ Hz}$ computed using the proposed method and numerical integration are compared in Fig. 5a. Figure 5a shows that the proposed method is able to compute the system's response accurately. Next, the proposed method is used to perform a frequency sweep to validate its ability to capture the dynamics in a wide parameter

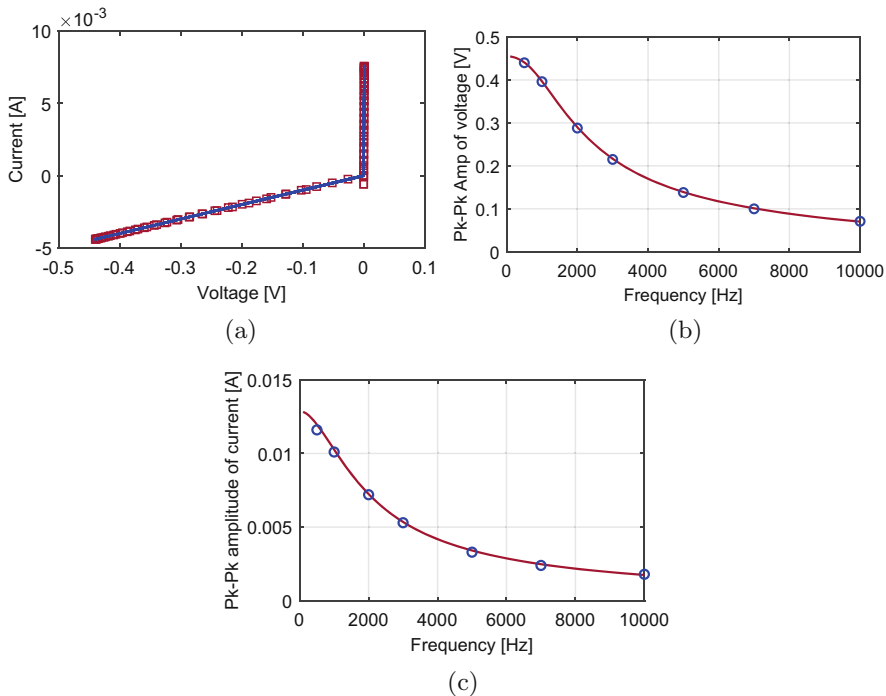


Fig. 5 (a) Phase plot of voltage and current computed using the proposed method (\square) and NI ($-$). (b) Peak-to-peak amplitude of voltage computed using the proposed method ($-$) and NI (\circ). (c) Peak-to-peak amplitude of current computed using the proposed method ($-$) and NI (\circ)

range. The peak-to-peak voltage and peak-to-peak current of the system for the excitation frequency range [100 Hz, 10,000 Hz] are shown in Fig. 5b,c, respectively. The response computed using the proposed method is compared with numerical integration in these plots. The forced response computed using the proposed method agrees well with the numerical integration solution in the plotted frequency range. The average CPU time required by the proposed method to analyze the steady-state response for a specific frequency is 0.08 s. By contrast, time integration requires 3.01 s to integrate to a steady-state response at each frequency. The proposed method only requires 2.7% of the CPU time of the numerical integration method. The speed-up of the proposed method will provide an efficient analysis tool for designing PWL circuits especially when the circuit is complex. Again, the new method is expected to improve its computational performance with respect to NI as the system becomes more and more complex in the same way as BAA [27, 28].

A key benefit of this new approach is that it enables a more thorough analysis of simple and complex nonlinear PWL systems. Next, the method will be used to conduct a multi-variable parametric study to investigate the dynamic properties of the circuit shown in Fig. 4. The excitation frequency and the resistance R are chosen as the control parameters in this parametric study. The peak-to-peak amplitude of

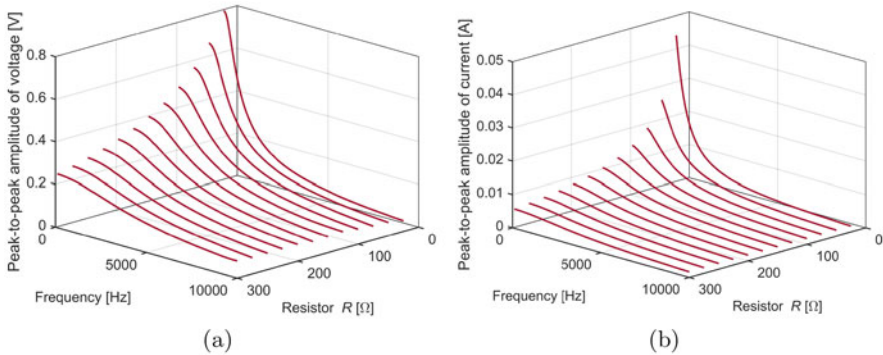


Fig. 6 (a) Global analysis of voltage using the proposed method. (b) Global analysis of current using the proposed method

voltage and current for the frequency range [100 Hz, 10000 Hz] and resistance range [25Ω , 300Ω] are efficiently computed and plotted in Fig. 6a,b, respectively. Figure 6 shows that the system exhibits the highest voltage and current when the frequency and resistance R are both small. This new method enables the accurate and efficient investigation of the global dynamic properties of PWL systems.

4 Conclusions

An efficient methodology for computing the steady-state vibration response of bilinear systems in general fields is introduced. The method extends the previous method referred to as the bilinear amplitude approximation method, which is developed for analyzing proportionally damped structural systems, to more general systems modeled using state-space representations. The new method utilizes the linear features of a state-space model in distinct linear regions to obtain the analytical solution for each linear sub-system. The nonlinear vibration response is then computed by applying appropriate compatibility conditions to couple the analytical solutions. The method uses the hybrid analytical-numeric approach to achieve efficient computation of the nonlinear dynamics.

The method is demonstrated on a three degree-of-freedom mechanical oscillator with contacting masses and an electrical circuit with voltage-dependent elements to show its broad application areas. The proposed method is validated by traditional numerical integration. Furthermore, the new method shows the capability of capturing the nonlinear response for a wide parameter range and is an efficient tool for conducting parametric studies for bilinear systems in a broad array of application areas.

Acknowledgments This paper is based on work partially supported by the National Science Foundation (United States) under Grant No. 1902408, program manager Dr. Robert Landers, and the Ministry of Science and Technology (Taiwan, R.O.C) under Grant No. MOST 109-2222-E-007-006-MY3. Any opinions, findings, and conclusions or recommendations expressed in this paper are those of the authors and do not necessarily reflect the views of the National Science Foundation and the Ministry of Science and Technology.

References

1. J.M.W. Brownjohn, A. De Stefano, Y.L. Xu, H. Wenzel, A.E. Aktan, Vibration-based monitoring of civil infrastructure: challenges and successes. *J. Civ. Struct. Health Monit.* **1**(3), 79–95 (2011). <https://doi.org/10.1007/s13349-011-0009-5>
2. S.W. Doebling, C.R. Farrar, M.B. Prime, A summary review of vibration-based damage identification methods. *Shock Vibr. Digest* **30**(2), 91–105 (1998)
3. K. D’Souza, B.I. Epureanu, Multiple augmentations of nonlinear systems and generalized minimum rank perturbations for damage detection. *J. Sound Vib.* **316**(1–5), 101–121 (2008). <https://doi.org/10.1016/j.jsv.2008.02.018>
4. N. Bajaj, G.T.C. Chiu, J.F. Rhoads, A megahertz-frequency tunable piecewise-linear electromechanical resonator realized via nonlinear feedback. *J. Sound Vib.* **425**, 257–274 (2018). <https://doi.org/10.1016/j.jsv.2018.02.053>. <http://www.sciencedirect.com/science/article/pii/S0022460X18301494>
5. T. Matsumoto, L. Chua, M. Komuro, The double scroll. *IEEE Trans. Circuits Syst.* **32**(8), 797–818 (1985)
6. J. Gebert, N. Radde, G.W. Weber, Modeling gene regulatory networks with piecewise linear differential equations. *Eur. J. Oper. Res.* **181**(3), 1148–1165 (2007). <https://doi.org/10.1016/j.ejor.2005.11.044>. <http://www.sciencedirect.com/science/article/pii/S0377221706001512>
7. L.G. Pabel Shahrear, Analysis of piecewise linear equations with bizarre dynamics. Ph.D. thesis (University of Bari ALDO MORO, Italy, 2015)
8. R. Allemang, Investigation of Some Multiple Input/Output Frequency Response Experimental Modal Analysis Techniques. PhD Thesis. Mechanical Engineering Department (University of Cincinnati, Cincinnati, 1980)
9. D.J. Ewins, *Modal Testing: Theory and Practice* (Research Studies Press, Taunton, 1984)
10. A.D. Dimarogonas, Vibration of cracked structures: A state of the art review. *Eng. Fract. Mech.* **55**(5), 831–857 (1996)
11. O.V. Shiiryayev, J.C. Slater, Detection of fatigue cracks using random decrement signatures. *Struct. Health Monit.* **9**(4), 347–360 (2010)
12. V.N. Burlayenko, T. Sadowski, Influence of skin/core debonding on free vibration behavior of foam and honeycomb cored sandwich plates. *Int. J. Non Linear Mech.* **45**(10), 959–968 (2009). <https://doi.org/10.1016/j.ijnonlinmec.2009.07.002>. <http://www.sciencedirect.com/science/article/B6TJ2-4WSRF6R-2/2/e819ff78d09436146a9e5fe36d39424>
13. C.N. Della, D. Shu, Vibration of delaminated composite laminates: A review. *Appl. Mech. Rev.* **60**(1), 1–20 (2007). <https://doi.org/10.1115/1.2375141>. <http://link.aip.org/link/?AMR/60/1/1>
14. H. Hein, L. Feklistova, Computationally efficient delamination detection in composite beams using Haar wavelets. *Mech. Syst. Sig. Process.* **25**(6), 2257–2270 (2011). <https://doi.org/10.1016/j.ymsp.2011.02.003>. <http://www.sciencedirect.com/science/article/pii/S0888327011000653>. Interdisciplinary Aspects of Vehicle Dynamics
15. A. Bilotta, C. Faella, E. Martinelli, E. Nigro, Indirect identification method of bilinear interface laws for FRP bonded on a concrete substrate. *J. Compos. Constr.* **16**(2), 171–84 (2012)
16. L. Meirovitch, *Fundamentals of Vibration* (Mcgraw-Hill Publication Company, New York, 2003). <https://books.google.com.tw/books?id=WJnpPAAACAAJ>

17. J.M.T. Thompson, A.R. Bokaian, R. Ghaffari, Subharmonic resonances and chaotic motions of a bilinear oscillator. *IMA J. Appl. Math.* **31**(3), 207–234 (1983). <https://doi.org/10.1093/imamat/31.3.207>
18. T.C. Kim, T.E. Rook, R. Singh, Super- and sub-harmonic response calculations for a torsional system with clearance nonlinearity using the harmonic balance method. *J. Sound Vib.* **281**(3–5), 965–993 (2005). <http://www.sciencedirect.com/science/article/B6WM3-4DJ4B15-4/2/2efc194126044a4307819c4fb6b3ecb8>
19. O. Poudou, Modeling and analysis of the dynamics of dry-friction-damped structural systems. Ph.D. thesis (The University of Michigan, Michigan, 2007)
20. A. Saito, M.P. Castanier, C. Pierre, O. Poudou, Efficient nonlinear vibration analysis of the forced response of rotating cracked blades. *ASME J. Comput. Nonlinear Dyn. Trans.* **4**(1), 011005 (2009)
21. M.H. Tien, K. D'Souza, Analyzing Bilinear systems using a new hybrid symbolic-numeric computational method. *J. Vib. Acoust.* **141**(3), 031008 (2019). <https://doi.org/10.1115/1.4042520>
22. M.H. Tien, K. D'Souza, Transient dynamic analysis of cracked structures with multiple contact pairs using generalized HSN. *Nonlinear Dyn.* **96**(2), 1115–1131 (2019). <https://doi.org/10.1007/s11071-019-04844-7>
23. C. Jung, K. D'Souza, B.I. Epureanu, Nonlinear amplitude approximation for bilinear systems. *J. Sound Vib.* **333**(13), 2909–2919 (2014)
24. M.H. Tien, K. D'Souza, A generalized bilinear amplitude and frequency approximation for piecewise-linear nonlinear systems with gaps or prestress. *Nonlinear Dyn.* **88**(4), 2403–2416 (2017). <https://doi.org/10.1007/s11071-017-3385-5>
25. J. Dormand, P. Prince, A family of embedded Runge-Kutta formulae. *J. Comput. Appl. Math.* **6**(1), 19–26 (1980). [https://doi.org/10.1016/0771-050X\(80\)90013-3](https://doi.org/10.1016/0771-050X(80)90013-3). <http://www.sciencedirect.com/science/article/pii/0771050X80900133>
26. MATLAB: version: R2019b (The MathWorks Inc., Natick, Massachusetts, 2019)
27. M.H. Tien, T. Hu, K. D'Souza, Generalized bilinear amplitude approximation and X-Xr for modeling cyclically symmetric structures with cracks. *J. Vib. Acoust.* **140**(4), 041012–041012-10 (2018). <https://doi.org/10.1115/1.4039296>
28. M.H. Tien, T. Hu, K. D'Souza, Statistical analysis of the nonlinear response of bladed disks with mistuning and cracks. *AIAA J.* **57**(11), 4966–4977 (2019). <https://doi.org/10.2514/1.J058190>

Analytical Approximation of Forced Oscillations of Nonlinear Helmholtz Resonator by Homotopy Analysis Method



Emmanuel Gourdon, Alireza Ture Savadkoohi, and Claude-Henri Lamarque

1 Introduction

Nonlinear acoustic HR can provide wide possibilities of practical applications, for example targeted nonlinear energy transfer in acoustics [1]. Nonlinear character of restoring characteristic and damping part can lead to substantial improvement of this element. So it becomes important to be able to describe and to predict the nonlinear amplitude-frequency response analytically to be able to optimize and to design the HR for practical applications. However, this kind of nonlinear resonator involves quadratic and cubic terms in their nonlinear restoring force which lead to different regimes (softening or hardening behavior) in function of amplitude of excitation. Those behaviors can be well predicted as shown in [2], but the methods usually require the use of a small parameter. So the problem is often solved as a weakly nonlinear system involving only small finite amplitudes or as strongly nonlinear system involving strong amplitudes. That is why we propose in the present study to use HAM to obtain the whole frequency response curves for various values of parameters. Indeed, HAM was introduced by Liao [3–8], and it is a nonperturbative analytical technique (a continuation method) for solving nonlinear differential equations. This method (more details about the HAM can be found in [9–11]) does not need to define and use a small (or large) parameter so it is well adapted to predict small as well as large amplitude oscillations of nonlinear systems. It has been applied recently with success in various domains to obtain approximate solutions to highly nonlinear problems [12–19]. We also have to take into account the mean of motion which cannot be disregarded because the damped system involves quadratic and cubic nonlinearities. This last point can be performed

E. Gourdon (✉) · A. Ture Savadkoohi · C.-H. Lamarque
LTDS, UMR CNRS 5513, ENTPE, Rue Maurice Audin, Vaulx-en-Velin, France
e-mail: emmanuel.gourdon@entpe.fr; Alireza.TURESAVADKOOHI@entpe.fr;
Claude-Henri.LAMARQUE@entpe.fr

following the work developed in [19]. In [19] authors proposed an example of application of HAM to a forced nonlinear vibratory system with quadratic and cubic nonlinearities in a nonlinear beam model.

The present paper is organized as follows. In the second section of this paper, we present governing equation of the considered system. Then, in section three we present the Homotopy Analysis Method and we apply the method with an example in section four.

2 Governing Equation of Helmholtz Resonator

We consider a classical HR [20] with a neck connected to a cavity. The walls are taken impervious. The air into the neck is considered as an incompressible mass (usual hypotheses when the Helmholtz number is small compared to one) and the air inside the cavity is supposed to be compressible. Classical hypotheses are taken: adiabatic transformations inside the acoustic resonator and the neck length is considered much smaller than cavity length. We have to take into account the restoring force due to the compression of the air in the cavity and the damping due to friction (air at high velocity) [21, 22]. We also take into account nonlinear terms for restoring and damping forces [22]. If we consider a displacement U of the air in the neck, it will induce a change of pressure Δp [22, 23]:

$$\Delta p = -\rho L \omega_0^2 \left(U - \frac{(\gamma + 1) S}{2V_0} U^2 + \frac{(\gamma + 1)(\gamma + 2) S^2}{6V_0^2} U^3 \right) \quad (1)$$

where ρ is the air density, L is the effective length of the neck as mentioned in [22], S is the cross section of the neck, V_0 is the volume in the cavity, γ is the specific heat ratio, and ω_0 is the linear resonance frequency of the resonator.

In the present paper, we take into account the cubic term of the restoring force function as it has been done in [1, 2]. This term can be taken into account when the vortex shedding is attenuated. We have also to introduce nonlinear damping (jet phenomenon [21, 24]). By considering the momentum equation, the conservation of mass, by combining the nonlinear restoring force, linear damping, the effective length, nonlinear damping, and the external pressure excitation p_e , the equation of motion with respect to time t reads as:

$$\frac{d^2 U}{dt^2} + \frac{\xi}{2L} \frac{dU}{dt} \left| \frac{dU}{dt} \right| + 2\delta \frac{dU}{dt} + \omega_0^2 U \left(1 - \alpha \frac{SU}{V_0} + \beta \left(\frac{SU}{V_0} \right)^2 \right) = -\frac{p_e}{\rho L} \quad (2)$$

where $\delta = \left(\frac{S}{2\rho L} \right) \Re(Z_{in} + Z_{vis})$, (where \Re stands for the real part of the complex number), $\alpha = \frac{(\gamma + 1)}{2}$, $\beta = \frac{(\gamma + 1)(\gamma + 2)}{6}$ and ξ is the total hydraulic-resistance

coefficient of the neck. Z_{in} is the acoustic impedance at inlet of HR, Z_{vis} is the friction acoustic impedance. We introduce dimensionless variables, $t^* = \omega_0 t$, $x = \frac{SU}{V_0}$, $c = \frac{2\delta}{\omega_0}$, $\sigma = \left(\frac{\xi}{2}\right) \left(\frac{V_0}{LS}\right)$ and we obtain:

$$\frac{d^2x}{dt^{*2}} + \sigma \frac{dx}{dt^*} \left| \frac{dx}{dt^*} \right| + c \frac{dx}{dt^*} + (x - \alpha x^2 + \beta x^3) = -p_e \tag{3}$$

The external excitation can be considered as a plane wave excitation with the form: $p_e = -f \cos(\omega t^* - \phi)$. Here a phase ϕ has been introduced just for convenience and this phase has to be determined. We suppose that the excitation frequency is close to the natural frequency of the system (so close to one here, see Eq. (3)).

Moreover, because of the quadratic nonlinearity in Eq. (3), the mean of motion $M = \frac{1}{T} \int_0^T x(t^*) dt^*$ can be nonzero, so after introducing a change of variables in time $\tau = \omega t^*$ we have to introduce a new variable $z(\tau)$ such as (as it has been done in [19]):

$$x(t^*) = M + z(\tau) \tag{4}$$

Then, we consider initial conditions (also by convenience) such as:

$$\frac{dx}{dt^*}(0) = 0, \quad x(0) = M + A \tag{5}$$

where $A = z(\tau = 0)$ being unknown.

Finally, we normalize variables by introducing $y(\tau)$ such as $z(\tau) = Ay(\tau)$. Thus, initial conditions for $y(\tau)$ are:

$$\frac{dy}{d\tau}(0) = 0, \quad y(0) = 1 \tag{6}$$

So the Eq. (3) becomes:

$$\omega^2 A \frac{d^2y}{d\tau^2} + \omega^2 \sigma A |A| \frac{dy}{d\tau} \left| \frac{dy}{d\tau} \right| + c \omega A \frac{dy}{d\tau} + (M + Ay(\tau)) - \alpha (M + Ay(\tau))^2 + \beta (M + Ay(\tau))^3 = f \cos(\tau - \phi) \tag{7}$$

The three unknown to be determined are $y(\tau)$, A , and M .

3 Application of Homotopy Analysis Method

The HAM refers to transform the nonlinear differential equation into an infinite number of linear differential equations and derive a family of solution series owing to a parameter ranging from zero to one. We have to define a linear operator $\mathcal{L}[Y(\tau, p)]$ and a nonlinear operator $\mathcal{N}[Y(\tau, p), D(p), \mu(p)]$ with the following zeroth-order equation (we have chosen the nonzero auxiliary function equals to 1 as done in lot of publications using HAM):

$$(1 - p)\mathcal{L}[Y(\tau, p) - y_0(\tau)] = ph\mathcal{N}[Y(\tau, p), D(p), \mu(p)] \tag{8}$$

where $p \in [0, 1]$ is the embedding parameter, $y_0(t)$ is the initial guess, and h is the convergence-control parameter (more details can be found in [19] where explanations have been given regarding the choice of this parameter; the methodology described in [19] is applied and used here for the governing equation of the present paper). It should be underlined that the analytical solution will be described with this unknown parameter h , and the solution will be expressed in series with a certain number of terms. However, in this paper we will just perform a first-order computation. This task does not require discussion about the convergence of the formal series since we are just interested (in this paper) in plotting amplitude-frequency response which is not dependent on h . The final solution will be dependent on h and it will be necessary to identify the value of h optimally. For $p = 0$ and $p = 1$ we obtain:

$$\begin{aligned} Y(\tau, 0) &= y_0(\tau) & Y(\tau, 1) &= y(\tau) \\ D(0) &= A_0 & D(1) &= A \\ \mu(0) &= M_0 & \mu(1) &= M \end{aligned} \tag{9}$$

The principle is that $Y(\tau, p)$ varies from the initial guess $y_0(\tau)$ to the desired solution as p varies from 0 to 1. Because the periodic solutions of Eq. (7) can be expressed in series of cosinus and sinus, we choose the following linear operator:

$$\mathcal{L}[Y(\tau, p)] = \omega^2 \left(\frac{\partial^2 Y(\tau, p)}{\partial \tau^2} + Y(\tau, p) \right) \tag{10}$$

Then we can define the nonlinear operator (owing to Eq. (7)):

$$\begin{aligned} &\mathcal{N}[Y(\tau, p), D(p), \mu(p)] && \tag{11} \\ &= \omega^2 D(p) \frac{\partial^2 Y(\tau, p)}{\partial \tau^2} + \sigma \omega^2 D(p) |D(p)| \frac{\partial Y(\tau, p)}{\partial \tau} \left| \frac{\partial Y(\tau, p)}{\partial \tau} \right| \\ &\quad + c\omega D(p) \frac{\partial Y(\tau, p)}{\partial \tau} + (\mu(p) + D(p)Y(\tau, p)) - \alpha (\mu(p) + D(p)Y(\tau, p))^2 \end{aligned}$$

$$+\beta (\mu(p) + D(p)Y(\tau, p))^3 - f_1 \cos(\tau) - f_2 \sin(\tau)$$

with:

$$f_1^2 + f_2^2 = f^2 \quad \phi = \arctan \frac{f_1}{f_2} \tag{12}$$

We use the Taylor expansions with respect to p :

$$Y(\tau, p) = y_0(\tau) + \sum_{k=1}^{+\infty} \underbrace{\left(\frac{1}{k!} \frac{\partial^k Y(\tau, p)}{\partial p^k} \Big|_{p=0} \right)}_{y_k(\tau)} p^k$$

$$D(p) = A_0 + \sum_{k=1}^{+\infty} \underbrace{\left(\frac{1}{k!} \frac{\partial^k D(p)}{\partial p^k} \Big|_{p=0} \right)}_{A_k} p^k, \quad \mu(p) = M_0 + \sum_{k=1}^{+\infty} \underbrace{\left(\frac{1}{k!} \frac{\partial^k \mu(p)}{\partial p^k} \Big|_{p=0} \right)}_{M_k} p^k \tag{13}$$

If the convergence-control parameter h is well chosen, then (13) converges when $p = 1$, such that:

$$y(\tau) = y_0(\tau) + \sum_{k=1}^{+\infty} y_k(\tau), \quad A = A_0 + \sum_{k=1}^{+\infty} A_k, \quad M = M_0 + \sum_{k=1}^{+\infty} M_k \tag{14}$$

As initial guess, we can choose $y_0(\tau) = \cos(\tau)$ which ensures that the initial conditions (6) are satisfied. Then, the methodology of HAM is the following: first, we differentiate Equation (8) k times with respect to p , secondly we divide it by $k!$ and finally we set $p = 0$ to obtain the k -th order equation:

$$\mathcal{L}[y_k(\tau) - \mathcal{X}_k y_{k-1}(\tau)] = h F_k \left(\underline{y}_{k-1}, \underline{A}_{k-1}, \underline{M}_{k-1} \right) \tag{15}$$

with zero initial conditions $y_k(0) = \frac{\partial y_k(0)}{\partial \tau} = 0$ where:

$$\begin{aligned} \mathcal{X}_k &= 0 \text{ if } k \leq 1 \text{ and } 1 \text{ if } k > 1, \\ \underline{y}_{k-1} &= [y_0(\tau), y_1(\tau), \dots, y_{k-1}(\tau)], \quad \underline{A}_{k-1} = [A_0, A_1, \dots, A_{k-1}], \\ \underline{M}_{k-1} &= [M_0, M_1, \dots, M_{k-1}] \end{aligned} \tag{16}$$

and

$$\begin{aligned}
 F_k \left(\underline{y}_{k-1}, \underline{A}_{k-1}, \underline{M}_{k-1} \right) &= \frac{1}{(k-1)!} \left. \frac{d^{k-1} \mathcal{N}[Y(\tau, p), D(p), \mu(p)]}{dp^{k-1}} \right|_{p=0} \\
 &= \omega^2 A_{k-1} \frac{\partial^2 y_{k-1}}{\partial \tau^2} + \sigma \omega^2 A_{k-1} |A_{k-1}| \frac{\partial y_{k-1}}{\partial \tau} \left| \frac{\partial y_{k-1}}{\partial \tau} \right| + c \omega A_{k-1} \frac{\partial y_{k-1}}{\partial \tau} \\
 &\quad + (M_{k-1} + A_{k-1} y_{k-1}) - \alpha \sum_{l=0}^{k-1} (M_l + A_l y_l) (M_{k-1-l} + A_{k-1-l} y_{k-1-l}) \\
 &\quad + \beta \sum_{l=0}^{k-1} \left(\sum_{m=0}^l (M_m + A_m y_m) (M_{l-m} + A_{l-m} y_{l-m}) \right) \cdot (M_{k-1-l} + A_{k-1-l} y_{k-1-l}) \\
 &\quad - (1 - \mathcal{X}_k) (f_1 \cos(\tau) + f_2 \sin(\tau)) \\
 &= a_{k,0} + \sum_{j=1}^{N(k)} a_{k,j} (\underline{y}_{k-1}, \underline{A}_{k-1}, \underline{M}_{k-1}) \cos(j\tau) + b_{k,j} (\underline{y}_{k-1}, \underline{A}_{k-1}, \underline{M}_{k-1}) \sin(j\tau)
 \end{aligned} \tag{17}$$

It should be noticed here that $a_{k,1}$ and $b_{k,1}$ have to be equal to zero otherwise secular terms (in $\tau \cos(\tau)$ and $\tau \sin(\tau)$) will appear in the solution which is impossible with the property of the linear operator. We can also conclude that $a_{k,0}$ has to be taken equal to zero otherwise a constant term will appear in the solution. The solution to Eq. (15) is:

$$y_k(\tau) = \mathcal{X}_k y_{k-1}(\tau) + \frac{h}{\omega^2} \sum_{j=2}^{N(k)} \frac{a_{k,j} \cos(j\tau) + b_{k,j} \sin(j\tau)}{1 - j^2} + E_1 \cos(\tau) + E_2 \sin(\tau) \tag{18}$$

where E_1 and E_2 are determined by zero initial conditions.

In the present paper, we are first interested to obtain steady-state solutions so as to obtain steady-state solutions of the mean motion M_0 , the amplitude A_0 , and the phase ϕ . It has been seen in different papers, especially in [19] that low-order approximations by HAM agree well with numerical simulations and it can be sufficient to consider the first-order approximation. That is why we present just the calculation of the first-order approximation in the following. So we obtain:

$$\begin{aligned}
 F_1 \left(\underline{y}_0, \underline{A}_0, \underline{M}_0 \right) &= -\omega^2 A_0 \cos(\tau) - \sigma \omega^2 A_0 |A_0| \sin(\tau) |\sin(\tau)| - c \omega A_0 \sin(\tau) \\
 &\quad + (M_0 + A_0 \cos(\tau)) - \alpha (M_0 + A_0 \cos(\tau))^2 + \beta (M_0 + A_0 \cos(\tau))^3 \\
 &\quad - f_1 \cos(\tau) - f_2 \sin(\tau)
 \end{aligned} \tag{19}$$

The nonlinear damping due to the jet phenomenon, expressed by the coefficient σ can usually be neglected for low level of sound pressure, but on high levels, σ must be present and is proportional to the ratio of cavity volume to that of the neck [22]. As done in [1, 2, 22], we can use the expansion in Fourier series of this term and keep just the first term because we can consider that those nonlinear terms have an order of magnitude smaller than the other terms. We have:

$$\begin{aligned} \sin(\tau)|\sin(\tau)| &= \sum_{n=1}^{+\infty} \frac{1}{\pi n(1 - \frac{n^2}{n^4})} (1 - (-1)^n) \sin(n\tau) \\ &= \frac{8}{3\pi} \sin(\tau) - \frac{8}{15\pi} \sin(3\tau) + \dots \end{aligned} \tag{20}$$

So, we obtain:

$$\begin{aligned} F_1 \left(y_0, A_0, M_0 \right) &= \left(1 + \frac{3}{2} \beta A_0^2 \right) M_0 - \alpha M_0^2 + \beta M_0^3 - \alpha \frac{A_0^2}{2} \\ &+ \left((1 - \omega^2) A_0 + 3\beta M_0^2 A_0 + \frac{3\beta}{4} A_0^3 - 2\alpha M_0 A_0 - f_1 \right) \cos(\tau) \\ &- \left(c\omega A_0 + f_2 + \sigma \omega^2 A_0 |A_0| \frac{8}{3\pi} \right) \sin(\tau) + \left(\frac{3}{2} \beta A_0^2 M_0 - \alpha \frac{A_0^2}{2} \right) \cos(2\tau) \\ &+ \frac{\beta}{4} A_0^3 \cos(3\tau) \end{aligned} \tag{21}$$

The three unknown M_0 , A_0 , and the phase ϕ can be obtained by imposing that the constant term and the coefficients of $\cos(\tau)$ and $\sin(\tau)$ be equal to zero as mentioned previously, so after some calculations, we get:

$$M_0 = G_1 - \frac{G_2}{G_1} + \frac{\alpha}{3\beta} \tag{22}$$

where:

$$\begin{aligned} G_1 &= \left(\frac{\sqrt{G_3}}{6^{3/2} \beta^2} + \frac{3\alpha A_0^2}{12\beta} - \frac{(3\beta A_0^2 + 2)\alpha}{12\beta^2} + \frac{\alpha^3}{27\beta^3} \right)^{1/3} \\ G_2 &= \left(\frac{3\beta A_0^2 + 2}{6\beta} - \frac{\alpha^2}{9\beta^2} \right) \\ G_3 &= (27A_0^4 \beta^2 + 54A_0^2 \beta + 36 - 18A_0^2 \alpha^2) A_0^2 \beta^2 + (8 - 24A_0^2 \alpha^2) \beta + 4A_0^2 \alpha^4 - 2\alpha^2 \end{aligned} \tag{23}$$

and

$$\begin{aligned} &\left((1 - \omega^2) A_0 + 3\beta M_0^2 A_0 + \frac{3\beta}{4} A_0^3 - 2\alpha M_0 A_0 \right)^2 \\ &+ \left(-c\omega A_0 - \sigma \omega^2 A_0 |A_0| \frac{8}{3\pi} \right)^2 = f^2 \\ \phi &= \arctan \frac{c\omega + \sigma \omega^2 |A_0| \frac{8}{3\pi}}{\omega^2 - 1 - 3\beta M_0^2 - \frac{3\beta}{4} A_0^2 - 2\alpha M_0} \end{aligned} \tag{24}$$

The previous equations are sufficient to plot the amplitude-frequency ($A_0, \omega/\omega_0$) curve (by solving the implicit function $F(A_0, \omega/\omega_0) = 0$ where F is a nonlinear function directly obtained by Eq. (24)) but it is also possible to obtain the general

solution by solving the first-order equation (according to Eq. (18) and by determining the two constants E_1 and E_2 with the zero initial conditions):

$$\begin{aligned} y_1(\tau) &= \frac{h}{\omega^2} \sum_{j=2}^{N(1)=2} \frac{a_{k,j} \cos(j\tau)}{1-j^2} + E_1 \cos(\tau) + E_2 \sin(\tau) \\ &= \frac{h}{\omega^2} \left(\left(\frac{1}{2}\beta M_0 - \frac{\alpha}{6} \right) A_0^2 (\cos(\tau) - \cos(2\tau)) + \frac{\beta}{32} A_0^3 (\cos(\tau) - \cos(3\tau)) \right) \end{aligned} \quad (25)$$

Finally, we obtain the desired solution:

$$\begin{aligned} x(t^*) &= M + Ay(\tau) \approx M_0 + A_0 (y_0(\tau) + y_1(\tau)) \\ &\approx M_0 + \frac{h}{\omega^2} \left(\left(\frac{\omega^2}{h} A_0 + \left(\frac{1}{2}\beta M_0 - \frac{\alpha}{6} \right) A_0^3 + \frac{\beta}{32} A_0^4 \right) \cos(\omega t^*) \right. \\ &\quad \left. + \left(\frac{\alpha}{6} A_0^3 - \frac{1}{2}\beta M_0 A_0^3 \right) \cos(2\omega t^*) - \frac{\beta}{32} A_0^4 \cos(3\omega t^*) \right) \end{aligned} \quad (26)$$

As already underlined, this approximation is only the first order and more terms are necessary to obtain a better approximation with determination of optimal h . In this paper, we are just interested in plotting amplitude-frequency response $(A_0, \omega/\omega_0)$ which is not dependent on h (see Eq. (24)). The final solution $x(t^*)$ will be dependent on h , and it will be necessary to identify the value of h optimally. The way to do it is the same as described in [19]. The optimal choice is obtained by minimizing the square residual of the governing equation for a given order of the approximation. For this, we have to consider the N th-order approximations of Eqs. (13). Then by inserting those N th-order approximations into Eq. (11) with $p = 1$, we can define the square residual error for the N th-order approximation as $E_N(h) = \int_0^1 (\mathcal{N}[y_N(\tau), A_N, M_N])^2 d\tau$. The solution series is convergent when $E_N(h) \rightarrow 0$ as $N \rightarrow \infty$. The optimal value of h for a given order N of approximation is obtained by the solution of the equation $\frac{dE_N}{dh} = 0$. As in [19] the results (they will be shown and analyzed in future works) show that low-order approximations agree well with numerical solutions and increasing orders of iterations increases the accuracy.

4 Simulation with an Example

In this section, we implement the previous calculations on an example, especially the steady-state solutions to obtain amplitude-frequency curve of the resonator. With classical multiple scales approach, we have to express all parameters in function

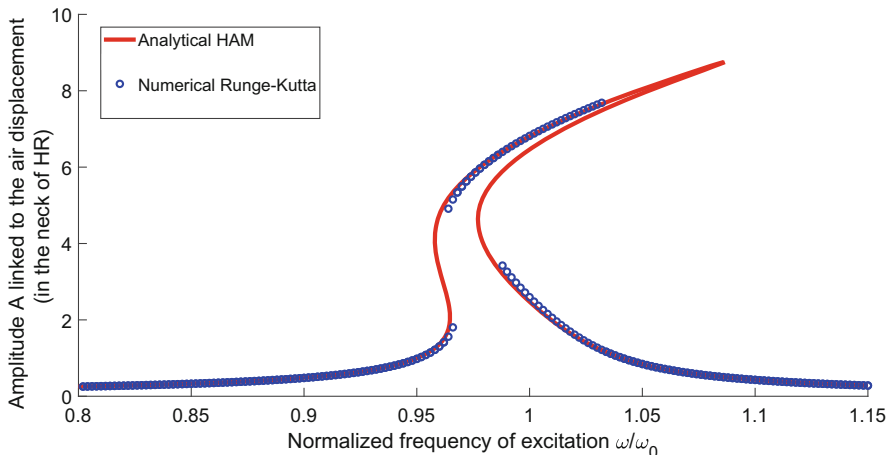


Fig. 1 Example of a nonlinear amplitude-frequency response obtained analytically by HAM showing softening and hardening behavior

of a small parameter (or a large one), and it is often not possible to obtain the amplitude-frequency curve of the resonator for intermediate values and without making hypotheses on the level of amplitudes (low or high amplitudes).

In the present paper, we can directly calculate the amplitude frequency-curve with no hypothesis on the parameters. To illustrate this point, we can choose an example with intermediate values showing softening and hardening behavior simultaneously (which was not possible to see with classical multiple scale approach as shown in [2]) with the following values for parameters:

$c = 0.1$; $\omega_0 = 10.5$; $\alpha = 14.4$; $\beta = 1.2$; $f = 10$ and we obtain the amplitude-frequency curve of Fig. 1 (the curves are not dependent on h). To obtain those classical amplitude-frequency curves $(A_0, \omega/\omega_0)$, which are the plot of A_0 in function of ω/ω_0 , we use the formula (24) and solve the implicit equation $F(A_0, \omega/\omega_0) = 0$ where F is a nonlinear function directly obtained by Eq. (24). Direct numerical integration of the initial governing equation has been done using a Runge–Kutta Scheme of order four to validate some analytical calculations for the amplitude A . Stationary solutions have been numerically computed and amplitude has been taken after a long time (numerical simulations have been computed from 0 to 200 s with a step of 0.01 s and the maximum x_{max} and minimum x_{min} values of x have been taken between 190 s and 200 s to obtain numerically $A = (x_{max} - x_{min})/2$ by increasing and decreasing ω/ω_0 by continuation). The figure shows a good agreement. Moreover, this figure shows that for this given set of parameters the resonator exhibits softening behavior ($\frac{\omega}{\omega_0} < 1$) for certain amplitudes and hardening ($\frac{\omega}{\omega_0} > 1$) behavior for higher amplitudes.

5 Conclusions

Applying Homotopy Analysis Method to the forced nonlinear Helmholtz Resonator has allowed to obtain nonlinear amplitude–frequency responses for the whole system taking into account nonlinear restoring force and nonlinear damping. Quadratic and cubic terms have been taken into account. Owing to the Homotopy Analysis Method which does not need to use a small or large parameter, it was possible to obtain different regimes (softening or hardening behavior) in one calculation and for intermediate oscillations. This was not possible with the classical multiple scales approach [25] where two regimes (low and high level) were calculated. We have also taken into account the mean of motion which cannot be disregarded because the damped system involves quadratic and cubic nonlinearities. The analytical approximations have been compared with a classical Runge–Kutta method on an example and the accuracy is good. It remains to study higher-orders to better study the influence of each parameter.

Acknowledgments This work was conducted in the framework of the LabEx CeLyA (ANR-10-LABX-0060) of Université de Lyon within the program “Investissement d’Avenir” (ANR-11-IDEX-0007) operated by the French National Research Agency (ANR).

References

1. E. Gourdon, A. Ture Savadkoohi, V. Alamo Vargas, Targeted energy transfer from one acoustical mode to an Helmholtz resonator with nonlinear behavior. *J. Vib. Acoust. Trans. ASME* **140**(6), art. no. 061005 (2018)
2. V. Alamo Vargas, E. Gourdon, A. Ture Savadkoohi, Nonlinear softening and hardening behavior in Helmholtz resonators for nonlinear regimes. *Nonlinear Dyn.* **91**(1), 217–231 (2018)
3. S.J. Liao, *Proposed Homotopy Analysis Techniques for the Solution of Nonlinear Problems*, Ph.D. Dissertation (Shanghai Jiao Tong University, Shanghai, 1992)
4. S. Liao, An approximate solution technique not depending on small parameters: a special example. *Int. J. Non-Linear Mech.* **30**(3), 371–380 (1995)
5. S. Liao, A.T. Chwang, Application of homotopy analysis method in nonlinear oscillations. *J. Appl. Mech. Trans. ASME* **65**(4), 914–922 (1998)
6. S. Liao, On the homotopy analysis method for nonlinear problems. *Appl. Math. Comput.* **147**(2), 499–513 (2004)
7. S. Liao, Notes on the homotopy analysis method: some definitions and theorems. *Commun. Nonlinear Sci. Numer. Simul.* **14**(4), 983–997 (2009)
8. S. Liao, Y. Tan, A general approach to obtain series solutions of nonlinear differential equations. *Stud. Appl. Math.* **119**(4), 297–354 (2007)
9. A.K. Alomari, F. Awawdeh, N. Tahat, F.B. Ahmad, W. Shatanawi, Multiple solutions for fractional differential equations: analytic approach. *Appl. Math. Comput.* **219**(17), 8893–8903 (2013)
10. A.K. Alomari, M.S.M. Noorani, R. Nazar, Comparison between the homotopy analysis method and homotopy perturbation method to solve coupled Schrodinger-KdV equation. *J. Appl. Math. Comput.* **31**(1–2), 1–12 (2009)
11. A.K. Alomari, M.I. Syam, N.R. Anakira, A.F. Jameel, Homotopy Sumudu transform method for solving applications in physics. *Results Phys.* **18**, 103265 (2020)

12. A. Mastroberardino, Homotopy analysis method applied to electrohydrodynamic flow. *Commun. Nonlinear Sci. Numer. Simul.* **16**(7), 2730–2736 (2011). <https://doi.org/10.1016/j.cnsns.2010.10.004>
13. A. Mohammadpour, E. Rokni, M. Fooladi, A. Kimiaefar, Approximate analytical solution for Bernoulli-Euler beams under different boundary conditions with non-linear Winkler type foundation. *J. Theor. Appl. Mech.* **50**(2), 339–355 (2012)
14. M. Mustafa, T. Hayat, A.A. Hendi, Influence of melting heat transfer in the stagnation-point flow of a Jeffrey fluid in the presence of viscous dissipation. *J. Appl. Mech. Trans. ASME* **79**(2), 024501 (5 pages) (2012)
15. T. Pirbodaghi, M.T. Ahmadian, M. Fesanghary, On the homotopy analysis method for non-linear vibration of beams. *Mech. Res. Commun.* **36**(2), 143–148 (2009)
16. S. Saha Ray, S. Sahoo, Traveling wave solutions to Riesz time-fractional Camassa-Holm equation in modeling for shallow-water waves. *J. Comput. Nonlinear Dyn.* **10**(6), 061026–1:5 (2015)
17. H.M. Sedighi, K.H. Shirazi, J. Zare, An analytic solution of transversal oscillation of quintic non-linear beam with homotopy analysis method. *Int. J. Non-Linear Mech.* **47**(7), 777–784 (2012)
18. J. Wen, Z. Cao, Sub-harmonic resonances of nonlinear oscillations with parametric excitation by means of the homotopy analysis method. *Phys. Lett. Sect. A Gen. Atomic Solid State Phys.* **371**(5–6), 427–431 (2007)
19. S. Shahlaei-Far, A. Nabarrete, J.M. Balthazar, Homotopy analysis of a forced nonlinear beam model with quadratic and cubic nonlinearities. *J. Theor. Appl. Mech.* **54**(4), 1219–1230 (2016)
20. H.V. Helmholtz, *Die Lehre von den Tonempfindungen als Physiologische Grundlage für die Theorie der Musik* (Braunschweig, Druck und Verlag von Friedrich Vieweg und Sons, Germany, 1863)
21. D. Singh, S. Rienstra, *A Systematic Impedance Model for Non-Linear Helmholtz Resonator Linear 19th AIAA/CEAS Aeroacoustics Conference, 27–29 May 2013, Berlin, Germany* (2013)
22. G.K. Yu, Y.D. Zhang, Y. Shen, Nonlinear amplitude-frequency response of a Helmholtz resonator. *J. Vib. Acoust.* **133**(2), 024502 (2011)
23. O. Richoux, V. Tourmat, T. Le Van Suu, Comportement non linéaire des bandes interdites dans un réseau acoustique unidimensionnel, in *Congrès Français d'Acoustique* (2006)
24. A. Hersh, B. Walker, in *Fluid Mechanical Model of the Helmholtz Resonator*. NASA Contractor Report, 1977, Washington, D.C., USA (1977)
25. A.H. Nayfeh, *Nonlinear Oscillation* (Wiley, New York, 1979)

Nonlinear Aspects of One-dimensional Supersymmetry



Eric Howard , Iftekher S. Chowdhury, and Ian Nagle

1 Introduction

Supersymmetry (SUSY) is an extension of the Standard Model and a conjectured fundamental symmetry between Bose and Fermi statistics, on the basis of \mathbb{Z}_2 -graded superalgebras, providing a natural mechanism for unification of gravity with electromagnetic, strong, and weak interactions, waiting for experimental confirmation. Supersymmetric models played a central role in many advances in theoretical physics since their discovery.

Supersymmetric quantum mechanics has been applied for solving challenging problems in theoretical and mathematical physics, providing a non-perturbative method to explore new iso-spectral quantum systems, study the supersymmetry breaking mechanism, discover new emergent hidden dynamical symmetries, and find exactly or quasi-exactly solvable problems in quantum mechanics. The intimate relationship between nonlinear supersymmetric systems and quasi-exactly solvability was initially discovered for one-dimensional quantum systems [1]. Supersymmetric Quantum Mechanics provide the algebraic form of complete or partial transformations associated with the spectral equivalence between dynamical systems with specific controllable energy spectra. Its development led to field and string theories with exceptional properties, such as superstring theory and supergravity, exceptional groups, and higher structures.

The Standard Model is a Poincaré-invariant gauge theory, with the gauge and fermion theory being constrained by internal symmetry principles, while the new

E. Howard (✉)
Macquarie University, Sydney, NSW, Australia
Griffith University, Brisbane, QLD, Australia
e-mail: eric.howard@mq.edu.au

I. S. Chowdhury · I. Nagle
Macquarie University, Sydney, NSW, Australia

physics beyond the Standard Model needs to find more relaxed features associated with new symmetries whose transformations do not commute with Poincaré transformations. Such task leads to a picture of supersymmetry as a possible solution to existing problems, such as gauge coupling unification, compactification, and the low-energy limit of string theories or the existence of dark matter. Various applications of supersymmetric quantum mechanics can be found in the dynamics of D-branes and black holes, M-theory and matrix models, or the theory of integrable systems and fluid mechanics. An interesting property of supersymmetry is that it manifests as a nonlinear symmetry of a bosonic system without fermion degrees of freedom. By employing generalized statistics [2], nonlinear supersymmetry can be developed without fermions, as a general case of linear supersymmetry [3].

Supersymmetric quantum mechanics admits several formulations in terms of bosonic degrees of freedom. A bosonized supersymmetry provides a good justification for several observed properties of the periodic quantum problem in many physical systems. Supersymmetric algebra was initially developed in field theories in terms of bosonic and fermionic fields, with the potential to apply to realizing a Grand-Unified Theory (GUT) for all four fundamental forces (strong, weak, electromagnetic, and gravitational). At the same time, supersymmetry and generalized statistics are intimately related in systems of parabosons with a nonlinear superalgebra. The hidden nature of these supersymmetries is an important characteristic of the conserved operators. Nonlinear supersymmetry (polynomial, n -fold) is associated to several systems such as the parabosonic [2] and parafermionic [4] oscillator models, the P , T -invariant models of planar fermions [5], Chern–Simons fields, or the symmetry of the fermion-monopoles [6].

Generalized statistics and supersymmetric systems find a common denominator in the hidden non-standard supersymmetric nature of pure parabosonic systems, exhibiting nonlinear properties. Parabosonic nonlinear supersymmetry can be generated by nontrivial corrections of the supersymmetric quantum mechanics. However, the quantization of nonlinear supersymmetry encounters the challenging problem of quantum anomalies. Our study is motivated by the existence of nonlinear supersymmetry in parabosonic systems, the hidden symmetries associated with their super-Hamiltonians, and the emergence of global quantum anomalies in supersymmetric quantum theories that break such symmetries.

In pure parabosonic systems with n -supersymmetry, the Hamiltonian and the associated supercharges have a nonlocal character. Consequently, the associated supercharges are nonlocal operators as infinite series in the operator. The nonlocal supercharges anticommute for a function of the Hamiltonian as a second order differential operator. The nonlinear supersymmetry algebra is quite similar to the finite W -algebras where the commutator of algebra generators is always proportional to an integrable (or finite order) polynomial. The symmetry generators are split into “even” (“bosonic”) and “odd” (“fermionic”) subsets, with “bosonic” and “fermionic” eigenstates of the Hamiltonian respectively.

In systems with supersymmetry, there are operators Q that together with the Hamiltonian form an algebra that is defined by both of the commutation and anticommutation relations, or a superalgebra. The nonlinear supersymmetry algebraic structure is described by the superalgebra [7]

$$[Q^\pm, H] = 0, \quad (Q^\pm)^2 = 0, \quad \{Q^+, Q^-\} = P_n(H), \quad (1.1)$$

where $P_n()$ is a polynomial of the n -th degree. The $+$ represent the states with even parity, while the $-$ describe states with odd parity.

The linear superalgebra (1.1) corresponds to $n = 1$ case and reduces to the supersymmetric quantum mechanics of Witten; however, the quantization of such nonlinear supersymmetry will generate a quantum anomaly [8]. Supersymmetric quantum mechanics were initially introduced by Witten as a natural toy model for studying the supersymmetry breaking mechanism as a solution to the hierarchy problem in particle physics. However, the “integrability conditions” and the existing nontrivial universal properties given by the Dolan–Grady relations [9] led to the development of holomorphic nonlinear supersymmetry algebra and extended versions of the superalgebra (1.1), containing several anomaly-free quantum mechanical systems, similar to the well-known exactly and quasi-exactly solvable systems [10–14]. In the present paper, we employ nonlinear supersymmetry algebra to analyze quantum anomalies naturally arising in supersymmetric one-dimensional systems.

2 Quantum Anomalies and Nonlinear Supersymmetry

Anomalies of symmetries play a significant role in quantum field theory and supersymmetry. A quantum anomaly occurs when a symmetry that is present in the classical theory is naturally broken in the corresponding quantum theory. A quantum anomaly that arises from the failure of a symmetry of the action in the classical theory is also a symmetry of any regularization of the full quantum theory. If a global symmetry exhibits anomalous properties, classical forbidden processes may occur as the selection rules in the classical theory are not respected any longer. This leads to quantum corrections during the quantization of classical nonlinear supersymmetric systems, connecting nonlinear supersymmetry to quasi-exactly solvable systems. The differences between linear and nonlinear supersymmetry mainly appear during the full quantization of the system. The existence of quantum anomalies led to natural generalizations of the linear and higher-derivative supersymmetry models such as the nonlinear holomorphic supersymmetry that quantizes classical one-dimensional systems with nonlinear supersymmetry of arbitrary order.

The quantum anomaly is present in linear quantum mechanical systems, taking a holomorphic form of the supersymmetric quantum mechanics and generating anomaly-free holomorphic operators. However, for some superpotentials, the integrals of motion admit quantum corrections that preserve the nonlinear supersymmetry at quantum level and avoid quantum anomalies.

Witten’s supersymmetric model [15] assumes the Hamiltonian of a quantum system as represented by a pair of Hamiltonians, where the energy eigenvalues are degenerate, in a graded Lie algebra with m charge operators and a Hamiltonian.

Witten’s supersymmetric quantum mechanics is given by the Hamiltonian

$$\mathcal{H} = p^2 + W^2 + W'm, \tag{2.1}$$

with the superpotential $m = \theta^+\theta^- - \theta^-\theta^+$, $W = W(x)$ and where x and p are even canonical variables, while $\{x, p\} = 1$, and $\theta^+, \theta^- = (\theta^+)^*$ are the Grassmann variables. The supersymmetry with two Grassmann variables can be used to implement the Dirac canonical quantization method. The Hamiltonian has integrals of motion that are even m , and odd $Q_+ = (W + ip)\theta^+$ and $Q_- = (Q^+)^*$, with a $\mathcal{N} = 2$ Poincaré supersymmetry algebra

$$\{Q^+, Q^-\} = -i\mathcal{H}, \quad \{\mathcal{H}, Q^\pm\} = 0, \quad \{m, \mathcal{H}\} = 0, \quad \{m, Q^\pm\} = \pm 2i Q^\pm. \tag{2.2}$$

If for any n integer, $W'm$ is replaced with $n\mathcal{W}'m$, the system has nonlinear supersymmetry of order n generated by the integrals of order n in momentum p $S_+ = (\mathcal{W} + ip)^n\theta^+$ and $S_- = (S_+)^*$ as supercharges. In this case, the Hamiltonian is

$$\mathcal{H} = p^2 + \mathcal{W}^2 + n\mathcal{W}'m. \tag{2.3}$$

Here, the Poisson bracket $\{S_+, S_-\} = -i(\mathcal{H})^n$ has the order n . The case $n = 1$ is linear, while for $n = 2, 3, \dots$, the canonical quantization of 2.6 leads to a quantum anomaly. The quantum analog of the integrals S_\pm does not commute with the quantum analog of 2.6, for any $n = 2, 3, \dots$ and any superpotential.

If the superpotentials with the form $\mathcal{W}(x)$ have the supercharge S_+ polynomial in $z = \mathcal{W} + ip$, the quantized system will be anomaly-free leading to a quasi-exactly solvable system. An n -supersymmetric system given by the superpotential $\mathcal{W}(x)$ is strongly connected to quasi-exactly solvability. A nonlinear n -supersymmetric harmonic oscillator with holomorphic supercharges and $W(x) = x$ will be described by the classical superalgebra $\{Q_n^+, Q_n^-\} = H^n$ is replaced with $\{Q_n^+, Q_n^-\} = H(H - \hbar)(H - 2\hbar) \dots (H - \hbar(n - 1))$. When $W(x) \neq ax + b$, the quantum analog of the oscillator and the Hamiltonian do not commute, $[Q_n^\pm, H_n] \neq 0$ and a quantum anomaly will appear. The canonical quantization of the system leads to a supersymmetric quantum system for any superpotential with associated quantum supercharges and Hamiltonian corresponding to a $\mathcal{N} = 2$ superalgebra where the quantum analog of m is a \mathbb{Z}_2 -grading operator $\Gamma = \sigma_3$ of the Lie superalgebra. The n -supersymmetric system will be anomaly-free in the corresponding quantized version of the system.

We consider the Lagrangian formalism for the construction of one-dimensional supersymmetric quantum mechanics systems with two Grassmann variables $\mathcal{N} = 2$ and holomorphic supersymmetric systems with supercharges as differential operators of order n . A supercharge with a polynomial form of order n behaves like an operator associated to a harmonic oscillator R^\pm such as

$$Q^\pm = (R^\mp)^n \theta^\pm + \sum_{k=0}^{n-1} q_{n-k} (R^\mp)^k \theta^\pm, \tag{2.4}$$

with q_k fixed real parameters.

For any classical system with the Lagrangian

$$L = \frac{1}{2}(\dot{x}^2 - W^2(x)) - gW'(x)\theta^+\theta^- + i\theta^+\dot{\theta}^-, \tag{2.5}$$

where θ^\pm , $(\theta^+)^* = \theta^-$ are the Grassmann variables, $W(x)$ is the superpotential, and g is the boson–fermion coupling constant, Witten supersymmetric quantum mechanics arises at $|g| = 1$ and can be associated to a Lie superalgebra of the integrals of motion. However, for $|g| = n$, $n = 2, 3, \dots$, the system has nonlinear supersymmetry. In the linear supersymmetric case, the Witten supersymmetric quantum mechanics is given by the classical Lie superalgebra of the Hamiltonian and supercharges.

For both fermion and boson particles, a symmetry is a transformation under which the Hamiltonian remains invariant and is consequently generated by an operator usually referred to as generator. The system possesses a symmetry if the Hamiltonian commutes with the generator of the symmetry transformation. Non-polynomial cases can also be developed via a limiting procedure applied to a polynomial supersymmetric algebra where the supercharges are pseudo-differential operators or by introducing complex-valued supercharges.

In higher-derivative (polynomial) supersymmetric algebra, for any integer values of the coupling constant $g = n$, the Lagrangian (2.5) is equivalent to the Hamiltonian

$$H = \frac{1}{2}(p^2 + W^2(x)) + nW'(x)\theta^+\theta^-, \quad n \in \mathbb{Z}, \tag{2.6}$$

with the Poisson–Dirac brackets $\{x, p\} = 1$, $\{\theta^+, \theta^-\} = -i$ in canonical approach and it is invariant under the transformations $g \rightarrow -g$, $W(x) \rightarrow -W(x)$.

The case of nonlinear supersymmetry brings an algebra that is quite different from a polynomial with nontrivial symmetry operators. The odd differential operators are exchanged with the associated non-polynomial functions of the Super-Hamiltonian in the Hilbert space spanned on its eigenfunctions. The Super-Hamiltonian can have nonlinear supersymmetric algebras of both polynomial and non-polynomial forms.

The Hamiltonian (2.6) has the odd integrals of motion

$$Q^+ = z^n \theta^+, \quad Q^- = (Q^+)^* = \bar{z}^n \theta^- \tag{2.7}$$

and can be translated into complex variables

$$z = W(x) + ip, \quad \bar{z} = z^* \tag{2.8}$$

taking the form

$$H = \frac{1}{2} (z\bar{z} + in\{z, \bar{z}\}\theta^+\theta^-), \tag{2.9}$$

where

$$\{Q^+, Q^-\} = -iH^n, \quad \{Q^+, Q^+\} = \{Q^-, Q^-\} = 0, \quad \{Q^\pm, H\} = 0. \tag{2.10}$$

The Hamiltonian has the form

$$\mathcal{H} = zz^* - \frac{C}{\mathcal{W}^2} + 4\mathcal{W}'m + c, \tag{2.11}$$

and the supercharges with a polynomial dependence on the momentum variable p are

$$S_+ = \left(z^2 + \frac{C}{\mathcal{W}^2}\right)\theta^+, \quad S_- = (S_+)^* \tag{2.12}$$

with the real constants a and C and satisfying the relation

$$\{S_+, S_-\} = -i \left((\mathcal{H} - c)^2 + C \right). \tag{2.13}$$

For any superpotential, the supersymmetry of (2.11), (2.12), and (2.13) is also preserved at quantum level if

$$\hat{\mathcal{H}} - c = -\hbar^2 \frac{d^2}{dx^2} + \mathcal{W}^2 - 2\hbar\sigma_3\mathcal{W}' - \frac{C}{\mathcal{W}^2} + \Delta(\mathcal{W}), \tag{2.14}$$

$$\hat{S}_+ = \hat{s}_+\sigma_+, \quad \hat{s}_+ = \left(\hbar \frac{d}{dx} + \mathcal{W}\right)^2 + \frac{C}{\mathcal{W}^2} - \Delta(\mathcal{W}), \tag{2.15}$$

$$\Delta(\mathcal{W}) = \frac{1}{2}\hbar^2 \left(\frac{\mathcal{W}''}{\mathcal{W}} - \frac{1}{2} \left(\frac{\mathcal{W}'}{\mathcal{W}} \right)^2 \right) = \hbar^2 \frac{1}{\sqrt{\mathcal{W}}} \left(\sqrt{\mathcal{W}} \right)'', \tag{2.16}$$

with $\sigma_+ = \frac{1}{2}(\sigma_1 + i\sigma_2)$ and $\Delta(\mathcal{W})$ a Schwarzian, $\Delta = -\frac{1}{2}\hbar^2 S(\omega(x))$, $S(\omega(x)) = (\omega''/\omega')' - \frac{1}{2}(\omega''/\omega')^2$, of $\omega(x) = \int^x dy/\mathcal{W}(y)$.

The projections of bosonic oscillator frequencies on the Grassmann algebra unit are z (\bar{z}), while the fermionic oscillator projections will be θ^+ (θ^-). For z and θ^+ , these projections are equal to $-W'(x)$ and $nW'(x)$, respectively. For $n = 0$, the odd integrals of motion satisfy $Q^\pm = \theta^\pm$, while the case $n = 1$ naturally leads to a linear supersymmetric behavior.

For polynomial orders $n \geq 2$, the Poisson superalgebra of the integrals of motion, the system has nonlinear supersymmetry.

When the system is quantized, for $\sigma_+ = \frac{1}{2}(\sigma_1 + i\sigma_2)$, the Hamiltonian can be written as

$$\hat{H} = \frac{1}{2} \left(-\hbar^2 \frac{d^2}{dx^2} + W^2(x) + n\hbar W'(x)\sigma_3 \right), \tag{2.17}$$

while the direct quantum supercharges become

$$\hat{Q}^+ = (\hat{Q}^-)^\dagger = \hat{z}^n \hat{\theta}^+ \quad \text{with} \quad \hat{z} = W(x) + \hbar \frac{d}{dx}, \quad \hat{\theta}^+ = \sqrt{\hbar} \sigma_+, \tag{2.18}$$

For any superpotential $W(x)$ and $n = 1$, the integrals of motion, $[\hat{Q}^\pm, \hat{H}] = 0$ are equal to the quantum supercharges (2.18), leading to a quantum analog superalgebra for (2.10) with $n = 1$. If $n = 2, 3, \dots$, any operator (2.18) will commute with the Hamiltonian (2.17) for any quadratic superpotential

$$W(x) = w_2 x^2 + w_1 x + w_0, \tag{2.19}$$

therefore for polynomials with the form $P_{n-1}(\hat{H})$ of order $n - 1$, the nonlinear superalgebra (2.10) becomes $[\hat{Q}^+, \hat{Q}^-]_+ = \hat{H}^n + P_{n-1}(\hat{H})$, The polynomials $P_{n-1}(\hat{H})$ have the coefficients $w_1^2 - 4w_0w_2$ and w_2^2 , and vanish for $\hbar \rightarrow 0$ [16].

If the supercharge \hat{Q}^+ has a holomorphic form that does not depend on \hat{z} but depends on \hat{z} , the supercharge will conserve if

$$n(n^2 - 1)\hbar \frac{d}{dx} (\hbar^2 W'' - \omega^2 W) = 0, \tag{2.20}$$

with ω^2 a constant. For any superpotential $[\hat{Q}^\pm, \hat{H}] \neq 0$, a quantum anomaly will be present but can be removed by introducing a quantum analog of the supercharges (2.7). In this case, the conservation is consistent with the quantum Hamiltonian (2.17) and therefore no anomaly is present. The Eq. (2.20) has a class of solutions

$$W(x) = w_+ e^{\omega x} + w_- e^{-\omega x} + w_0, \tag{2.21}$$

for $\omega \neq 0$, and a complementary solution (2.19) for $\omega = 0$, respectively. For different ω , ω_\pm , and ω_0 a full class of exactly and quasi-exactly solvable quantum mechanical systems is present.

Nonlinear supersymmetric systems of order n assume zero mode subspaces of the supercharges corresponding to the n -dimensional representations of the $SL(2, R)$ algebra. Nonlinear supersymmetric systems associated to (2.19) quadratic superpotentials correspond to quasi-exactly solvable systems with quartic potentials in PT-symmetric quantum mechanics.

The holomorphic quantum supercharges in classical n -supersymmetry are

$$Q^\pm = (A^\mp)^n \theta^\pm, \quad \text{where } A^\pm = \mp \hbar \frac{d}{dx} + W(x). \tag{2.22}$$

The corresponding holomorphic supercharges of the superpotentials admit a more general form if $[\hat{z}, \hat{\bar{z}}] = 2\hbar W'(x)$ and $[\hat{z}, \hat{\bar{z}}]_+ = 2(W^2(x) - \hbar^2 \frac{d^2}{dx^2})$. The operators \hat{z} and $\hat{\bar{z}}$ from Eq. (2.18) also admit a general form corresponding to the mutually conjugate operators Z and $\bar{Z} = Z^\dagger$.

The Hamiltonian and conservation condition for the supercharge will take the form

$$\mathcal{H}_n = \frac{1}{4} ([Z, \bar{Z}]_+ + n[Z, \bar{Z}]\sigma_3), \tag{2.23}$$

$$[Z, [Z, [Z, \bar{Z}]]] = \omega^2 [Z, \bar{Z}], \quad [\bar{Z}, [\bar{Z}, [Z, \bar{Z}]]] = \bar{\omega}^2 [Z, \bar{Z}], \tag{2.24}$$

with $\bar{\omega} = \omega^*$ equivalent to Dolan–Grady relations in spin integrable systems as a condition for an anomaly-free quantization of classical nonlinear holomorphic supersymmetric systems.

Anomaly-free quantization for systems with supersymmetry of order which is higher than two is less trivial and is not discussed here. The integrals of motion of the Hamiltonian (2.23) exist if

$$Q_n^+ = \prod_{k=0}^{n-1} \left(Z + \left(k - \frac{n-1}{2} \right) \omega \right) \cdot \sigma_+, \quad Q_n^- = (Q_n^+)^\dagger, \tag{2.25}$$

3 Discussion

Quasi-exactly solvable Hamiltonians assume a finite number of eigenstates and eigenvalues that correspond to a superalgebra. Indeed, such eigenstates span a finite-dimensional subspace with a representation of $SL(2, R)$ algebra. The dimension of the finite-dimensional representation is given by the Hamiltonian. Quantum analogues of classical systems exhibiting nonlinear supersymmetry have to account for the presence of quantum anomalies. A quantum anomaly is essentially the failure of a symmetry to be preserved at quantum level. Quantum anomalies exhibit a number of interesting features: an exact symmetry in the classical version of the theory, a divergence that appears in the quantum version of the theory, and a weak violation of the original symmetry that emerges in a regularized version of the quantum theory.

Such formalism can be a useful tool to engineer new collective properties of light–matter interaction, including novel nonlinear quantum mechanical systems, such as spin–orbit couplings and coherent excitation in Rydberg atom arrays as

well as understanding of the nonlinear evolution of soliton solutions in quantum optics and condensed matter physics, where supersymmetric Hamiltonians are becoming relevant. Additionally, this tool is a new avenue for quantum simulations of SUSY field theories, for better engineering and control of light–atom interactions. The quantization of systems that exhibit nonlinear supersymmetry properties is a nontrivial task due to the presence of quantum anomalies. The emergence of hidden symmetries is a natural property of supersymmetric algebra, closely related to the central charge. Supersymmetric quantum mechanics contains classes of potentials in super-Hamiltonians with hidden symmetries, associated with nonlinear momenta integrals of motion, where coordinates and momenta variables are mixed in the phase space, generating nonlinear W-type algebras. Nonlinear supersymmetry is mainly characterized by supercharges of higher order in bosonic momenta, and therefore it has the nature of a hidden symmetry.

4 Conclusions

We considered nonlinear supersymmetry of one-dimensional systems containing hidden symmetries generated by supercharges of higher order in momentum and study the quantum anomalies present in these systems. We investigated different aspects of one-dimensional systems with canonical form and nonlinear supersymmetry as well as their quantization and the presence of anomaly-free quantum systems with nonlinear supersymmetry.

References

1. E. Witten, Nucl. Phys. **B188**, 513–554 (1981)
2. M. Plyushchay, Int. J. Mod. Phys. **A23**, 3679–3698 (2000). hep-th/9903130
3. F. Cooper, A. Khare, U. Sukhatme, Phys. Rep. **251**, 267–385 (1995). hep-th/9405029
4. S. Klishevich, M. Plyushchay, Mod. Phys. Lett. **A14**, 2739–2752 (1999). hep-th/9905149
5. G. Grignani, M. Plyushchay, P. Sodano, Nucl. Phys. **B464**, 189–212 (1996). hep-th/9511072
6. F. De Jonghe, A.J. Macfarlane, K. Peeters, J.W. van Holten, Phys. Lett. **B359**, 114–117 (1995). hep-th/9507046
7. A.A. Andrianov, M.V. Ioffe, V.P. Spiridonov, Phys. Lett. **A174**, 273–279 (1993). hep-th/9303005
8. S. Klishevich, M. Plyushchay, Nucl. Phys. **B606**, 583–612 (2001). hep-th/0012023
9. L. Dolan, M. Grady, Phys. Rev. **D25**, 1587–1604 (1982)
10. A. Turbiner, Commun. Math. Phys. **118**, 467–474 (1988)
11. M.A. Shifman, Int. J. Mod. Phys. **A4**, 2897–2952 (1989)
12. A. Ushveridze, *Quasi-Exactly Solvable Models in Quantum Mechanics* (IOP Publishing, Bristol, 1994)
13. F. Finkel, A. Gonzalez-Lopez, N. Kamran, P.J. Olver, M.A. Rodriguez, *Lie Algebras of Differential Operators and Partial Integrability*. hep-th/9603139
14. C.M. Bender, G.V. Dunne, J. Math. Phys. **37**, 6–11 (1996). hep-th/9511138
15. E. Witten, Nucl. Phys. **B188**, 513 (1981)
16. S.M. Klishevich, M.S. Plyushchay, Nucl. Phys. B **606**, 583 (2001). [hep-th/0012023]

Global Stability Analysis of An Unemployment Model with Two Distributed Time Delays



Loredana Flavia Vesa, Eva Kaslik, and Mihaela Neamtu

1 Introduction

For the past tens of years, unemployment is one of the most challenging situation for any government to deal with. The root cause relies on the mismatch between the increase of the population with respect to the economy's ability to create new vacancies. This phenomena generate several unwanted side effects among which we can highlight the uncontrollable migration on one hand and on the other hand negative effect on mental state and behavior of the people. A long term unemployment usually leads to the depreciation of the professional skills and ability to perform according to the job requirements.

The government of a country plays one of the most important role in controlling and acting to improve the unemployment situation in order to have a healthy economy based on sustainable growth.

As a consequence, the unemployment requires attention and measures based on specific analysis of the diverse mathematical models.

The concepts used by Nikolopoulos and Tzanetis [1] for the housing allocation of homeless families due to the Athens 1999 earthquake, were developed later for the controllability of unemployment. Lately, [2] using some concepts from [1] took the

L. F. Vesa

Department of Mathematics, West University of Timisoara, Timișoara, Romania
e-mail: loredana.vesa@e-uvt.ro

E. Kaslik

Department of Mathematics and Computer Science, West University of Timisoara, Timișoara, Romania

M. Neamtu (✉)

Department of Economics and Economic Modelling, West University of Timisoara, Timișoara, Romania
e-mail: mihaela.neamtu@e-uvt.ro

next step for controlling the unemployment in developing countries. Furthermore, Pathan and Bhathawala [3] investigated the influence of the time delay on the action of the government and the private sector. Mirsa et al. [4] introduced an additional variable to account for the skill development programs, highlighting the link between the upgrade of workers' skills and unemployment reduction. Neamtu and Harding [5] further improved the mathematical model by introducing both the effect of migration and a distributed time delay. It is also important to mention that optimal control has been previously investigated in [6, 7].

The main motivation of this paper relies on the existing mathematical models which allow for the development of models of higher complexity, which takes into account two distributed time delays to reflect the past history of the investigated variables, extending previous results [8] which are concerned with a similar mathematical model with only one distributed time delay. Our main goal is to study and interpret the interaction between the unemployed and employed persons and vacancies which are newly created by both the government and the private sector, in terms of the qualitative theory of delay differential equations.

The paper is organized as follows. In Sect. 2, the mathematical model with two distributed time delays is described. The non-dimensional model, the existence of the equilibrium point, and the positivity and boundedness of solutions are presented in Sect. 3. Section 4 is concerned with the local stability analysis of the positive equilibrium. The global stability analysis is presented in Sect. 5. Numerical simulations are carried out and interpreted in Sect. 6 and finally the conclusions are drawn.

2 Mathematical Model

We consider the following variables: the number of unemployed persons which is denoted by $U(t)$, the number of employed persons denoted by $E(t)$, and the number of newly available vacancies $V(t)$, which are created by both the government and the private sector. We note that the new vacancies are made available by taking into consideration past unemployment levels, and therefore, distributed time delays are considered in the mathematical model.

The mathematical model with two distributed delays is written as follows:

$$\begin{cases} \dot{U}(t) = A - [a_1 \int_0^\infty k_1(s)V(t-s)ds + a_2]U(t) + a_3E(t) - b_1U(t) \\ \dot{E}(t) = [a_1 \int_0^\infty k_1(s)V(t-s)ds + a_2]U(t) - a_3E(t) - b_2E(t) \\ \dot{V}(t) = a_4 \int_0^\infty k_2(s)U(t-s)ds - b_3V(t) \end{cases} \quad (1)$$

where A is the constant growth rate of unemployed persons entering the labor market; a_1 , a_2 , and a_3 are positive constants of proportionality expressing the transfer rates between compartments, as described below: unemployed to employed with respect to new vacancies, unemployed to employed with respect to existing

jobs, and employed to unemployed, respectively; b_1 represents the death and migration rate of unemployed persons; b_2 is the death, retirement, and migration rate of employed persons; a_4 is the rate of appearance of new vacancies that are made available by the government and public sectors with respect to past unemployment levels; b_3 is the diminution rate of new vacancies.

The delay kernels $k_1, k_2 : [0, \infty) \rightarrow [0, \infty)$ are bounded and piecewise continuous probability density functions, such that:

$$\int_0^\infty k_1(s)ds = 1, \quad \tau_1 = \int_0^\infty sk_1(s)ds < \infty. \tag{2}$$

$$\int_0^\infty k_2(s)ds = 1, \quad \tau_2 = \int_0^\infty sk_2(s)ds < \infty. \tag{3}$$

Here, τ_1 is the average time delay for an unemployed person to get a previously created job, and τ_2 is the average time delay which is necessary for the creation of new vacancies based on unemployment levels from the past.

3 Construction of the Non-dimensional Model

With the aim of reducing the number of parameters from system (1), the following substitutions are considered:

$$x(t) = \frac{a_1 a_4}{a_3^2} U\left(\frac{t}{a_3}\right), \quad y(t) = \frac{a_1 a_4}{a_3^2} E\left(\frac{t}{a_3}\right), \quad z(t) = \frac{a_1}{a_3} V\left(\frac{t}{a_3}\right) \tag{4}$$

leading to the equivalent non-dimensional mathematical model:

$$\begin{cases} \dot{x}(t) = \gamma - \left[\int_0^\infty \hat{k}_1(s)z(t-s)ds + \alpha \right]x(t) + y(t) - \beta_1 x(t), \\ \dot{y}(t) = \left[\int_0^\infty \hat{k}_1(s)z(t-s)ds + \alpha \right]x(t) - y(t) - \beta_2 y(t), \\ \dot{z}(t) = \int_0^\infty \hat{k}_2(s)x(t-s)ds - \beta_3 z(t), \end{cases} \tag{5}$$

where the coefficients are expressed as

$$\gamma = \frac{a_1 a_4 A}{a_3^3}, \quad \alpha = \frac{a_2}{a_3}, \quad \beta_1 = \frac{b_1}{a_3}, \quad \beta_2 = \frac{b_2}{a_3}, \quad \beta_3 = \frac{b_3}{a_3}$$

and the delay kernels $\hat{k}_1(s) = \frac{1}{a_3} k_1\left(\frac{s}{a_3}\right)$, $\hat{k}_2(s) = \frac{1}{a_3} k_2\left(\frac{s}{a_3}\right)$ are probability density functions with the mean values $\hat{\tau}_1 = a_3 \tau_1$ and $\hat{\tau}_2 = a_3 \tau_2$, respectively.

Initial conditions which are taken into account for system (5) are

$$x(\theta) = \varphi(\theta), \quad y(\theta) = \psi(\theta), \quad z(\theta) = \xi(\theta), \quad \forall \theta \in (-\infty, 0],$$

with functions φ, ψ, ξ belonging to the Banach space $C_{0,\mu}(\mathbb{R}_-, \mathbb{R})$ (where $\mu > 0$) of continuous real valued functions on $(-\infty, 0]$ verifying $\lim_{t \rightarrow -\infty} e^{\mu t} \varphi(t) = 0$, endowed with the norm:

$$\|\varphi\|_{\infty,\mu} = \sup_{t \in (-\infty, 0]} e^{\mu t} |\varphi(t)|.$$

We refer to [9] for existence and uniqueness results for the solutions of initial value problems associated to systems of delay differential equations with distributed time delays such as (5), as well as the properties of continuous dependence of solutions of such systems on initial conditions.

The only positive equilibrium state for system (5) is:

$$S^+ := (x_0, y_0, z_0) = \left(\beta_3 z_0, \frac{\beta_3 z_0 (z_0 + \alpha)}{\beta_2 + 1}, z_0 \right).$$

For the positivity and boundedness of the solutions of the non-dimensional model (5), we refer to the following result which can be proved as in [5, 8]:

Theorem 1 *The open positive octant of \mathbb{R}^3 is invariant to the flow of system (5) and the set*

$$\Omega = \left\{ (x, y, z) : x \geq 0, y \geq 0, x + y \leq \frac{\gamma}{\beta_m}, 0 \leq z \leq \frac{\gamma}{\beta_m \beta_3} \right\},$$

where $\beta_m = \min(\beta_1, \beta_2)$ is a region of attraction for system (5), attracting all solutions initiating in the interior of the positive octant of \mathbb{R}^3 .

4 Local Stability Analysis

We linearize the system (5) about the equilibrium [10] to study the local stability of the positive equilibrium $S^+ = (x_0, y_0, z_0)$, by analyzing the distribution of the roots of the associated characteristic equation:

$$\det \begin{bmatrix} -z_0 - \alpha - \beta_1 - \lambda & 1 & -\beta_3 z_0 K_1(\lambda) \\ z_0 + \alpha & -1 - \beta_2 - \lambda & \beta_3 z_0 K_1(\lambda) \\ K_2(\lambda) & 0 & -\beta_3 - \lambda \end{bmatrix} = 0,$$

where $K_1(\lambda), K_2(\lambda)$ are the Laplace transforms of the delay kernels $\hat{k}_1(s), \hat{k}_2(s)$.

We obtain the following characteristic equation:

$$\beta_3 z_0 K_1(\lambda) K_2(\lambda) (\lambda + \beta_2) + P(\lambda) = 0, \tag{6}$$

where the polynomial $P(\lambda)$ is given by

$$P(\lambda) = (\lambda + \beta_3) [(\lambda + \beta_1)(\lambda + \beta_2 + 1) + (z_0 + \alpha)(\lambda + \beta_2)].$$

Using the Routh–Hurwitz criterion in the absence of time delays, we obtain:

Theorem 2 *If no time delays are present in system (5), the positive equilibrium state S^+ is locally asymptotically stable.*

Considering two arbitrary delay kernels $\hat{k}_1(s)$ and $\hat{k}_2(s)$ in system (5), we obtain the following result:

Theorem 3 *The positive equilibrium state S^+ of system (5) is locally asymptotically stable for any delay kernels $\hat{k}_1(s)$ and $\hat{k}_2(s)$.*

Proof Presuming the contrary, i.e. that the characteristic Eq. (6) has a root with positive real part $\Re(\lambda) \geq 0$, Eq. (6) can be written as:

$$\frac{\beta_3 z_0}{\lambda + \beta_3} K_1(\lambda) K_2(\lambda) = -(\lambda + \beta_1) \left(1 + \frac{1}{\lambda + \beta_2} \right) - (z_0 + \alpha). \tag{7}$$

Considering

$$Q(\lambda) = (\lambda + \beta_1) \left(1 + \frac{1}{\lambda + \beta_2} \right),$$

we observe that

$$\Re[Q(\lambda)] = \Re(\lambda) + \beta_1 + \frac{|\lambda|^2 + (\beta_1 + \beta_2)\Re(\lambda) + \beta_1\beta_2}{|\lambda + \beta_2|^2} > 0.$$

In Eq. (7) applying the absolute value we have

$$\frac{\beta_3 z_0}{|\lambda + \beta_3|} |K_1(\lambda)| |K_2(\lambda)| = |Q(\lambda) + z_0 + \alpha|. \tag{8}$$

As $\hat{k}_1(s)$ and $\hat{k}_2(s)$ are probability density functions and K_1, K_2 are their Laplace transforms, it follows that $|K_1(\lambda)| \leq 1$ and $|K_2(\lambda)| \leq 1$ for any $\lambda \in \mathbb{C}$ such that $\Re(\lambda) \geq 0$. Moreover, as $\Re(\lambda) \geq 0$ and $\beta_3 > 0$, we have $|\lambda + \beta_3| > \beta_3$. Hence, for the expression appearing in the left side of (8) we deduce:

$$\frac{\beta_3 z_0}{|\lambda + \beta_3|} |K_1(\lambda)| |K_2(\lambda)| \leq \frac{\beta_3 z_0}{\beta_3} = z_0.$$

Moreover, as $\Re[Q(\lambda)] \geq 0$, for the expression from the right side of (8) we have:

$$|Q(\lambda) + z_0 + \alpha| \geq z_0 + \alpha.$$

Therefore, the contradiction $\alpha \leq 0$ is obtained. Thus, all roots of (6) have strictly negative real part, and we finally deduce that S^+ is locally asymptotically stable, regardless of the delay kernels $\hat{k}_1(s)$ and $\hat{k}_2(s)$. \square

5 Global Stability Analysis

With the aim of analyzing the global asymptotic stability properties of the positive equilibrium state of system (5), a special type of Lyapunov function technique is utilized, based on a technique which has been successfully used in previous works such as [11–14].

Theorem 4 *The positive equilibrium S^+ of system (5) is globally asymptotically stable, for any choice of the delay kernels $\hat{k}_1(s)$ and $\hat{k}_2(s)$, if the following inequality is satisfied:*

$$z_0 \leq \min\{\beta_1, \alpha\beta_2\}. \tag{9}$$

Proof Using the substitution $u(t) = z(t) + \alpha$ in system (5), we obtain the equivalent system:

$$\begin{cases} \dot{x} = \gamma - D[u]x + y - \beta_1x \\ \dot{y} = D[u]x - (1 + \beta_2)y \\ \dot{u} = D[x] - \beta_3u + \alpha\beta_3, \end{cases} \tag{10}$$

where $D[u](t) = \int_0^\infty \hat{k}_1(s)u(t - s)ds$ and $D[x](t)x = \int_0^\infty \hat{k}_2(s)x(t - s)ds$

Considering the positive function $H(x) = x - 1 - \ln(x)$, the following positively definite Lyapunov function is constructed:

$$L(t) = L_1(t) + L_2(t) + L_3(t) \tag{11}$$

with

$$\begin{aligned} L_1(t) &= x_0H\left(\frac{x(t)}{x_0}\right) + \frac{\alpha}{u_0}y_0H\left(\frac{y(t)}{y_0}\right) + z_0u_0H\left(\frac{u(t)}{u_0}\right) \\ L_2(t) &= x_0z_0 \int_0^\infty \left(\hat{k}_2(s) \int_{t-s}^t H\left(\frac{x(r)}{x_0}\right) dr\right) ds \end{aligned}$$

$$L_3(t) = x_0 u_0 \int_0^\infty \left(\hat{k}_1(s) \int_{t-s}^t H\left(\frac{u(r)}{u_0}\right) dr \right) ds,$$

where $u_0 = z_0 + \alpha$.

In what follows, the derivatives of $L_1(t)$, $L_2(t)$, and $L_3(t)$ are computed.

$$\begin{aligned} L_1'(t) &= \dot{x} \left(1 - \frac{x_0}{x}\right) + \frac{\alpha}{u_0} \dot{y} \left(1 - \frac{y_0}{y}\right) + z_0 \dot{u} \left(1 - \frac{u_0}{u}\right) \\ &= (\gamma - D[u]x + y - \beta_1 x) \left(1 - \frac{x_0}{x}\right) + \frac{\alpha}{u_0} (D[u]x - (1 + \beta_2)y) \left(1 - \frac{y_0}{y}\right) \\ &\quad + z_0 (D[x] - \beta_3 u + \alpha \beta_3) \left(1 - \frac{u_0}{u}\right). \end{aligned}$$

At this stage, as (x_0, y_0, u_0) is the equilibrium of (10), we replace $\gamma = u_0 x_0 - y_0 + \beta_1 x_0$, $1 + \beta_2 = \frac{u_0 x_0}{y_0}$, and $\alpha \beta_3 = \beta_3 u_0 - x_0$ and by direct coefficient identification we obtain:

$$\begin{aligned} L_1'(t) &= -x_0(\beta_1 - z_0) \left(\frac{x}{x_0} + \frac{x_0}{x} - 2\right) \\ &\quad - (\alpha x_0 - y_0) \left(\frac{x_0}{x} + \frac{u_0}{u} + \frac{y}{y_0} + \frac{D[u]x y_0}{u_0 x_0 y} - \ln \frac{D[u]}{u} - 4\right) \\ &\quad - x_0 z_0 \left(2 \frac{x_0}{x} + \frac{u_0 D[x]}{u x_0} + \frac{D[u]x}{u_0 x_0} - \ln \frac{D[u]}{u} - \ln \frac{D[x]}{x} - 4\right) \\ &\quad - y_0 \left(\frac{x_0 y}{x y_0} + \frac{D[u]x y_0}{u_0 x_0 y} + \frac{u_0}{u} - \ln \frac{D[u]}{u} - 3\right) \\ &\quad - x_0 z_0 \ln \frac{D[x]}{x} - x_0 u_0 \ln \frac{D[u]}{u} + x_0 (D[u] - u) + z_0 (D[x] - x). \end{aligned}$$

Inequality $z_0 \leq \min\{\beta_1, \alpha \beta_2\}$ implies $\alpha x_0 - y_0 = \frac{\beta_3 z_0 (\alpha \beta_2 - z_0)}{1 + \beta_2} > 0$, and employing the inequality of means, the first four terms (denoted by $N(t)$ in what follows) in $L_1'(t)$ are negative, leading to:

$$L_1'(t) = N(t) - x_0 z_0 \ln \frac{D[x]}{x} - x_0 u_0 \ln \frac{D[u]}{u} + x_0 (D[u] - u) + z_0 (D[x] - x).$$

Moreover, we obtain

$$\begin{aligned} L_2'(t) &= x_0 z_0 \int_0^\infty \hat{k}(s) \left(H\left(\frac{x(t)}{x_0}\right) - H\left(\frac{x(t-s)}{x_0}\right) \right) ds \\ &= z_0 (x - D[x]) + x_0 z_0 \int_0^\infty \hat{k}_2(s) \ln \frac{x(t-s)}{x(t)} ds, \end{aligned}$$

and

$$\begin{aligned} L'_3(t) &= x_0 u_0 \int_0^\infty \hat{k}(s) \left(H \left(\frac{u(t)}{u_0} \right) - H \left(\frac{u(t-s)}{u_0} \right) \right) ds \\ &= x_0(u - D[u]) + x_0 u_0 \int_0^\infty \hat{k}_1(s) \ln \frac{u(t-s)}{u(t)} ds. \end{aligned}$$

Then we have

$$\begin{aligned} L'(t) &= L'_1(t) + L'_2(t) + L'_3(t) \\ &= N(t) - x_0 z_0 \ln \frac{D[x]}{x} - x_0 u_0 \ln \frac{D[u]}{u} + x_0 z_0 \int_0^\infty \hat{k}_2(s) \ln \frac{x(t-s)}{x(t)} ds \\ &\quad + x_0 u_0 \int_0^\infty \hat{k}_1(s) \ln \frac{u(t-s)}{u(s)} ds \\ &= N(t) - x_0 z_0 \left[\ln D[x] - \int_0^\infty \hat{k}_1(s) \ln(x(t-s)) ds \right] \\ &\quad - x_0 u_0 \left[\ln D[u] - \int_0^\infty \hat{k}_2(s) \ln(u(t-s)) ds \right]. \end{aligned}$$

Using Jensen’s inequality for probability density functions, as the logarithmic function is concave we obtain:

$$\ln \int_0^\infty \hat{k}_1(s) u(t-s) ds \geq \int_0^\infty \hat{k}_1(s) \ln(u(t-s)) ds.$$

Similarly,

$$\ln \int_0^\infty \hat{k}_2(s) x(t-s) ds \geq \int_0^\infty \hat{k}_2(s) \ln(x(t-s)) ds.$$

In conclusion:

$$L'(t) \leq 0 \quad , \quad \forall t \geq 0.$$

As $\{(x_0, y_0, u_0)\}$ is the largest invariant set of $\{(x, y, u) | L'(t) = 0\}$, employing the LaSalle invariance principle [15, 16], we deduce that the equilibrium (x_0, y_0, u_0) is globally asymptotically stable, and hence, the equilibrium S^+ of system (5) is also globally asymptotically stable. □

Remark 1 Based on the previous theorem and inequality (9), the following realistic upper bound for the growth rate of unemployed persons entering the labor market is obtained:

$$A \leq \frac{b_3}{a_1 a_4} \min \left\{ \frac{a_2 b_2 (a_2 b_2 + a_3 b_1)}{a_3^2}, b_1^2 + \frac{b_1 b_2 (b_1 + a_2)}{a_3 + b_2} \right\}, \tag{12}$$

which ensures the global stability of the positive equilibrium.

6 Numerical Simulations

The values of the system parameters considered for the numerical simulations are: $A = 5000, a_1 = 0.00002, a_2 = 0.4, a_3 = 0.01, a_4 = 0.007, b_1 = 0.04, b_2 = 0.05, b_3 = 0.05$. In this case, we emphasize that inequality (12) is satisfied, and hence, from Theorem 4 and Remark 1, we deduce that the positive equilibrium $(U^+, E^+, V^+) = (12427.6, 90057.9, 1739.86)$ is globally asymptotically stable, for any choice of the delay kernels $k_1(s)$ and $k_2(s)$ considered in system (1).

Figure 1 shows the evolution of $U(t), E(t),$ and $V(t)$, considering the initial condition $(U_0, E_0, V_0) = (14913.1, 99063.7, 1565.87)$, and several values for the two discrete delays $k_1(s) = \delta(s - \tau_1)$ and $k_2(s) = \delta(s - \tau_2)$, where δ denotes the Dirac function. Indeed, when $\tau_1 = 40$ is fixed, we notice that for positive values of the delay τ_2 , in the first phase, the unemployment levels drop below the equilibrium value U^+ . We notice that when the time delay τ_2 takes larger values, the unemployment level $U(t)$ reaches lower minimum values in the first phase, followed by the convergence to U^+ . At the same time, the employment level $E(t)$ first drops to a plateau level, followed by a further decrease to the equilibrium value E^+ in the second phase. Furthermore, the number of vacancies increases in the first phase to a maximum value larger than V^+ and then, decreases to V^+ in the second phase. Again, when τ_2 is larger, a slower convergence to the equilibrium values is observed.

On the other hand, when $\tau_2 = 40$ is fixed, for positive values of the delay τ_1 , in the first phase, the unemployment levels drop to a plateau level above the equilibrium value U^+ , followed by a decrease below the equilibrium value U^+ and later, converge to U^+ . Meanwhile, the employment level $E(t)$ first drops to a minimum level above the equilibrium value E^+ , followed by a small increase and then, convergence to E^+ . At the same time, the number of vacancies increases in the first phase to a maximum value larger than V^+ and then, in the second phase, it drops to the equilibrium value V^+ . Larger lags τ_1 imply a slower convergence to the equilibrium state.

In Fig. 2, the influence of the choice of initial conditions on the time evolution of state variables is visualized, with fixed values $\tau_1 = 30$ and $\tau_2 = 40$ of the time delays, showing the converge to the globally asymptotically stable equilibrium.

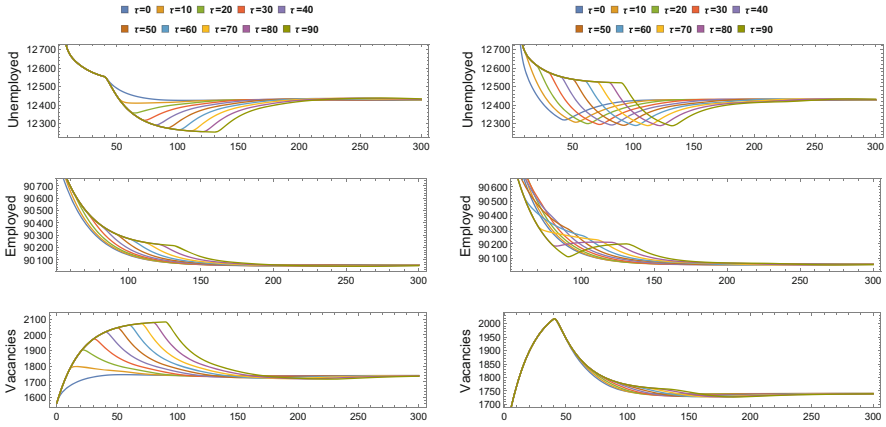


Fig. 1 Evolution of state variables $U(t)$, $E(t)$, and $V(t)$ of system (1) with discrete time delays considering $\tau_1 = 40$ fixed and $\tau_2 = \tau \in \{0, 10, \dots, 90\}$ (left) and $\tau_2 = 40$ fixed and $\tau_1 = \tau \in \{0, 10, \dots, 90\}$ (right) and the initial condition $(U_0, E_0, V_0) = (14913.1, 99063.7, 1565.87)$

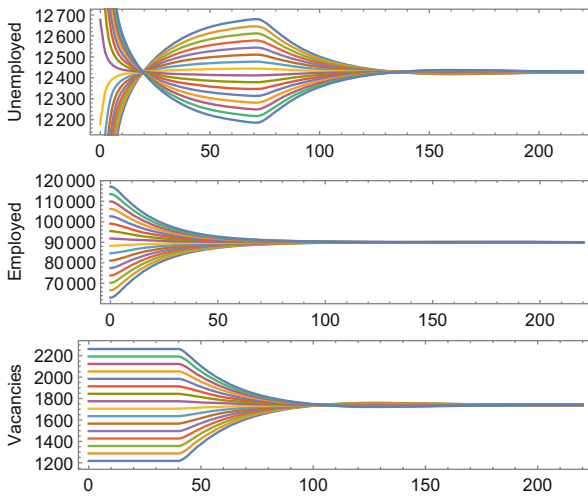


Fig. 2 Evolution of state variables $U(t)$, $E(t)$, and $V(t)$ of system (1) with discrete time delays considering $\tau_1 = 30$ and $\tau_2 = 40$, with different initial conditions

7 Conclusions

In this paper, we have carried out a local and global stability investigation for a mathematical model incorporating two distributed time delays illustrating the labor market. Our main result is the proof of global asymptotic stability properties of the unique positive equilibrium of the investigated system, guaranteed by a realistic upper bound for the growth rate of unemployed persons entering the labor market. Numerical simulations are presented to enhance the theoretical findings, also discussing the influence of the magnitude of the considered time delays on the behavior of the state variables.

References

1. C. Nikolopoulos, D. Tzanetis, A model for housing allocation of a homeless population due to a natural disaster. *Nonlinear Anal. Real World Appl.* **4**(4), 561–579 (2003)
2. A. Misra, A.K. Singh, A delay mathematical model for the control of unemployment. *Differ. Equations Dyn. Syst.* **21**(3), 291–307 (2013)
3. G. Pathan, P. Bhathawala, A mathematical model for unemployment control-an analysis with and without delay. *Int. J. Math. Appl.* **6**, 83–93 (2018)
4. A. Misra, A.K. Singh, P.K. Singh, Modeling the role of skill development to control unemployment. *Differ. Equations Dyn. Syst.*, 1–13 (2017). <https://doi.org/10.1007/s12591-017-0405-3>
5. L. Harding, M. Neamțu, A dynamic model of unemployment with migration and delayed policy intervention. *Comput. Econ.* **51**(3), 427–462 (2018)
6. U. Mallick, M. Biswas, Optimal analysis of unemployment model taking policies to control. *Adv. Model. Optim.* **20**(1), 303–312 (2018)
7. S. Munoli, S. Gani, S. Gani, A mathematical approach to employment policies: an optimal control analysis. *Int. J. Stat. Syst.* **12**(3), 549–565 (2017)
8. E. Kaslik, M. Neamțu, L.F. Vesa, Global stability analysis of an unemployment model with distributed delay. *Math. Comput. Simul.* **185**, 535–546 (2021)
9. V. Kolmanovskii, A. Myshkis, *Introduction to the Theory and Applications of Functional Differential Equations*, vol. 463 (Kluwer Academic, Dordrecht, The Netherlands, 1999)
10. O. Diekmann, M. Gyllenberg, Equations with infinite delay: blending the abstract and the concrete. *Int. J. Differ. Equations* **252**(2), 819–851 (2012)
11. G. Huang, A. Liu, A note on global stability for a heroin epidemic model with distributed delay. *Appl. Math. Lett.* **26**(7), 687–691 (2013)
12. A. Korobeinikov, Global properties of basic virus dynamics models. *Bull. Math. Biol.* **66**(4), 879–883 (2004)
13. C.C. McCluskey, Complete global stability for an SIR epidemic model with delay-distributed or discrete. *Nonlinear Anal. Real World Appl.* **11**(1), 55–59 (2010)
14. T. Kajiwara, T. Sasaki, Y. Takeuchi, Construction of Lyapunov functionals for delay differential equations in virology and epidemiology. *Nonlinear Anal. Real World Appl.* **13**(4), 1802–1826 (2012)
15. J.K. Hale, S.M.V. Lunel, *Introduction to Functional Differential Equations*, in *Applied Mathematics Science*, vol. 99 (Springer, New York, 1991)
16. H.L. Smith, *An Introduction to Delay Differential Equations with Applications to the Life Sciences*, vol. 57 (Springer, New York, 2011)

Estimating Generic Canard Explosions via Efficient Symbolic Computation



Bo-Wei Qin, Kwok-Wai Chung, Antonio Algaba,
and Alejandro J. Rodríguez-Luis

1 Introduction

In a large number of planar slow–fast systems, i.e., the systems with distinct time scales, a periodic orbit arising at the Hopf bifurcation can experience an extremely swift evolution in its amplitude and period. This rapid transition is usually named as canard explosion referring to the appearance of involving orbit in phase plane [1]. Over past several decades, many works have been devoted to study this phenomenon focusing on its existence and asymptotic behavior, see [2–5] and references therein. Besides, predicting the value of control parameter for its occurrence is also one of the significant issues that attracts lots of attentions.

It is time-consuming to locate a canard explosion with high accuracy via numerical tools, such as AUTO and MatCont, since it takes place through an exponentially small range of control parameters and cannot be identified and marked automatically. For this reason, an analytical estimation is crucial, and

B.-W. Qin
School of Mathematical Sciences, Fudan University, Shanghai, PR China
e-mail: boweiqin@fudan.edu.cn

K.-W. Chung
Department of Mathematics, City University of Hong Kong, Kowloon, Hong Kong, PR China
e-mail: makchung@cityu.edu.hk

A. Algaba
Departamento de Ciencias Integradas, Centro de Estudios Avanzados en Física, Matemática y Computación, Universidad de Huelva, Huelva, Spain
e-mail: algaba@uhu.es

A. J. Rodríguez-Luis (✉)
Departamento de Matemática Aplicada II, E.T.S. Ingenieros, Universidad de Sevilla, Sevilla, Spain
e-mail: ajrluis@us.es

several methods have been developed to do so, among which the classical iterative method [6] and the nonlinear time transformation (NTT) method [7] are two major approaches. Although it has been proved that the two methods can be applied to find high-order estimations, they still have limitations. If the system is relatively complicated, it may not be easy to find the exact value (even for the first term) using the classical iterative method. For instance, only the numeric value is provided in [8], and a quadratic fitting function is used to find the first term in [9] that is not straightforward. The NTT method is proved to be an effective approach for several systems [10, 11]. Nevertheless, its full generality has not been confirmed yet, and trigonometric functions are involved, which may lead to time-consuming computations. The aim of this chapter is to demonstrate a ready-to-use algorithm that can be applied to estimate the critical value for any system satisfying generic conditions. As we will see later, only polynomials are used to develop such an algorithm. It is therefore very efficient to compute the critical value, compared with aforementioned approaches. Let us first introduce the system in which a generic canard can occur.

In this chapter, we consider the system

$$\epsilon \dot{x} = f(x, y, \mu, \epsilon), \quad \dot{y} = g(x, y, \mu, \epsilon), \quad (1)$$

where f and g are sufficiently smooth functions, μ is a control parameter, and $0 < \epsilon \ll 1$ is the ratio of different time scales. By appropriate coordinate transformations, we can assume that the origin is an equilibrium of system (1) when $\mu = \epsilon = 0$, that is, $f(\mathbf{0}) = g(\mathbf{0}) = 0$, where $\mathbf{0}$ represents the point $(x, y, \mu, \epsilon) = (0, 0, 0, 0)$. The genericity of the canard explosion can be classified by the type of the turning point of the slow manifold. In this chapter, we consider only the generic canard, that is, the slow manifold given by $f(x, y, \mu, \epsilon) = 0$ possesses a non-degenerate turning point at the origin. We therefore follow the hypothesis provided in [5, Theorem 4]. For convenience, they are rewritten below.

Hypothesis 1 *System (1) satisfies the following conditions:*

$$(H1.1) \quad f_y(\mathbf{0}) \cdot g_x(\mathbf{0}) < 0.$$

$$(H1.2) \quad f_{xx}(\mathbf{0}) \neq 0.$$

$$(H1.3) \quad g_x \begin{vmatrix} f_y & f_\mu \\ f_{xy} & f_{x\mu} \end{vmatrix} - f_{xx} \begin{vmatrix} f_y & f_\mu \\ g_y & g_\mu \end{vmatrix} \neq 0 \text{ at } \mathbf{0}.$$

Here, subscripts stand for partial differentiation with respect to the corresponding variable. We remark that hypothesis (H1.1) immediately implies $f_y(\mathbf{0}) \neq 0$ and $g_x(\mathbf{0}) \neq 0$, which corresponds to two conditions that are not repeated here. With the above settings, according to Theorem 4 given in [5], the existence and uniqueness of formal power series for the canard explosion can be assured.

The rest of this chapter is organized as follows. We first demonstrate our approach for the generic canard and its theoretical ground in Sect. 2. Its implementation in

symbolic software will then be discussed in Sect. 3. In Sect. 4, two examples will be considered to reveal the advantages of our approach. Finally, some conclusions are provided in Sect. 5.

2 A General Procedure

We are now going to demonstrate our approach for computing the power series solutions to system (1). First, we define $k_1 = f_y(\mathbf{0})$, $k_2 = f_{xx}(\mathbf{0})/2$, and $k_3 = g_x(\mathbf{0})$, which are non-zero constants according to Hypothesis 1. Introducing

$$x = \sqrt{\epsilon}X, \quad y = \epsilon Y, \quad \mu = \epsilon\nu, \quad t = \sqrt{\epsilon}\tau, \tag{2}$$

we obtain the system in new variables as

$$\frac{dX}{d\tau} = \delta^{-2} f(\delta X, \delta^2 Y, \delta^2 \nu, \delta^2), \quad \frac{dY}{d\tau} = \delta^{-1} g(\delta X, \delta^2 Y, \delta^2 \nu, \delta^2), \tag{3}$$

where $\delta = \sqrt{\epsilon}$. Expanding system (3) in the Taylor series about $\delta = 0$ leads to

$$\begin{aligned} \frac{dX}{d\tau} &= k_1 Y + c\nu + d + k_2 X^2 + \delta \left(a_0 X + a_1 X\nu + a_2 XY + a_3 X^3 \right) + \sum_{i=2}^{\infty} \delta^i \bar{f}_i(X, Y, \nu), \\ \frac{dY}{d\tau} &= k_3 X + \delta \left(b_0 + b_1 \nu + b_2 Y + b_3 X^2 \right) + \sum_{i=2}^{\infty} \delta^i \bar{g}_i(X, Y, \nu), \end{aligned} \tag{4}$$

where \bar{f}_i and \bar{g}_i are polynomials of X, Y, ν , and other coefficients are given by

$$\begin{aligned} a_0 &= f_{x\epsilon}(\mathbf{0}), \quad a_1 = f_{x\mu}(\mathbf{0}), \quad a_2 = f_{xy}(\mathbf{0}), \quad a_3 = \frac{1}{6} f_{xxx}(\mathbf{0}), \quad c = f_{\mu}(\mathbf{0}), \\ b_0 &= g_{\epsilon}(\mathbf{0}), \quad b_1 = g_{\mu}(\mathbf{0}), \quad b_2 = g_y(\mathbf{0}), \quad b_3 = \frac{1}{2} g_{xx}(\mathbf{0}), \quad d = f_{\epsilon}(\mathbf{0}). \end{aligned}$$

System (4) can be further simplified by introducing a new variable as $Z = k_1 Y + c\nu + d$. We then have

$$\begin{aligned} \frac{dX}{d\tau} &= Z + k_2 X^2 + \delta \left[\left(a_0 - \frac{da_2}{k_1} \right) X + \left(a_1 - \frac{ca_2}{k_1} \right) X\nu + \frac{a_2}{k_1} XZ + a_3 X^3 \right] + \mathcal{O}(\delta^2) \\ &:= P(X, Z, \nu, \delta), \\ \frac{dZ}{d\tau} &= k_1 k_3 X + \delta \left[k_1 b_0 - b_2 d + (k_1 b_1 - cb_2)\nu + b_2 Z + k_1 b_3 X^2 \right] + \mathcal{O}(\delta^2) \\ &:= Q(X, Z, \nu, \delta). \end{aligned} \tag{5}$$

System (5) is now a summation of an integrable system (when $\delta = 0$) together with perturbation terms. Then, we look for a solution as

$$Z = \sum_{i=0}^{\infty} \delta^i Z_i(X) \quad \text{and} \quad v = \sum_{i=0}^{\infty} \delta^i v_i. \tag{6}$$

When $\delta = 0$, the system admits an integrating factor $U = \exp(-AZ_0)$, where $A = 2k_2/(k_1k_3) \neq 0$, and the first integral can be computed as $I(X, Z_0) = \exp(-AZ_0) \cdot (Z_0 + k_2X^2 + A^{-1})$. For a constant C in a certain interval, the level curves given by $I = C$ form a family of periodic orbits, whose limit is a homoclinic orbit connecting a point at infinity. This limiting curve is the zero-order solution of the slow manifold in blow-up coordinates, which is given by

$$Z_0(X) = -k_2X^2 - A^{-1}. \tag{7}$$

To solve the high-order solution, we eliminate time variable in (5) and obtain

$$Z'(X)P(X, Z, v, \delta) - Q(X, Z, v, \delta) = 0, \tag{8}$$

where prime denotes the differentiation with respect to X . Inserting (6) and (7) into (8) and extracting the coefficients of like powers of δ , one can obtain the equation for each order $\mathcal{O}(\delta^i)$ as

$$-A^{-1}Z'_i(X) - 2k_2XZ_i(X) + v_{i-1}(p_1 + p_2X^2) = R_i(X, Z_j, v_k)(X), \tag{9}$$

where $R_i(X)$ consists of remaining terms of each equation, which are already solved in previous orders, and $p_1 = cb_2 - k_1b_1$, $p_2 = 2k_2(ca_2 - k_1a_1)/k_1$. We point out that an equation like (9) is usually solved by introducing an integrating factor, see, for instance, Ref. [7]. Here, we will use a different approach that can be implemented in a symbolic software more easily. For this purpose, we need the following theorem.

Theorem 1 $\forall i \in \mathbb{N}_0$, $Z_i(X)$ can be uniquely determined as a polynomial.

Proof We prove it by mathematical induction. By (7), the statement is obviously true when $i = 0$. We assume that it holds for $i = 1, 2, \dots, m - 1$ and will show that $Z_m(X)$ can be uniquely solved from (9) as a polynomial. Denote by n the degree of $R_m(X)$. Then, we try the following ansatz:

$$Z_m(X) = \sum_{k=0}^j \zeta_k X^k \quad \text{with} \quad j = \begin{cases} 1, & \text{if } 0 \leq n \leq 2, \\ n - 1, & \text{if } n \geq 3. \end{cases} \tag{10}$$

Now, we need to show that the coefficients ζ_k can be uniquely determined. Substituting (10) into (9) and equating the coefficient of like powers of X yield a system of linear equations. We first consider the case when $n \geq 3$, for which the system is given by

$$\mathbf{M} \boldsymbol{\zeta} = \mathbf{R} \quad \text{with} \quad \mathbf{M} = \begin{pmatrix} \mathbf{M}_1 & \mathbf{M}_2 \\ \mathbf{M}_3 & \mathbf{M}_4 \end{pmatrix} \in \mathbb{R}^{(n+1) \times (n+1)}, \quad (11)$$

where \mathbf{R} is a column vector, whose first element and k th element are, respectively, the constant and coefficient of X^{k-1} in $R_m(X)$, the column vector $\boldsymbol{\zeta} = (\zeta_0, \zeta_1, \dots, \zeta_{n-1}, v_{m-1})^\top$ includes all the unknowns, $\mathbf{M}_1 = (0, -A^{-1}, 0, 0, \dots, 0)$, $\mathbf{M}_2 = p_1$, $\mathbf{M}_4 = (0, p_2, 0, 0, \dots, 0)^\top$. For \mathbf{M}_3 , all the elements on the diagonal are $-2k_2$, the element in the j th row and $(j + 2)$ th column is $-(j + 1)A^{-1}$ for all $j = 1, 2, \dots, n - 2$, and all remaining elements are zero. Then, the determinant of \mathbf{M} can be computed as

$$\det(\mathbf{M}) = (-2k_2)^{n-1} [c(2b_2k_2 - a_2k_3) - k_1(2b_1k_2 - a_1k_3)]. \quad (12)$$

It follows from Hypothesis (H1.2) and (H1.3) that $\det(\mathbf{M}) \neq 0$, which implies that (11) has one and only one solution. If $0 \leq n \leq 2$, the system of linear equations turns out to be

$$\begin{pmatrix} 0 & -A^{-1} & p_1 \\ -2k_2 & 0 & 0 \\ 0 & -2k_2 & p_2 \end{pmatrix} \begin{pmatrix} \zeta_0 \\ \zeta_1 \\ v_{m-1} \end{pmatrix} = \mathbf{R}, \quad (13)$$

where \mathbf{R} has the same definition as in (11). Analogously, (13) possesses one and only one solution since the determinant of the 3×3 matrix is non-zero. \square

The proof of Theorem 1 immediately yields the following corollary.

Corollary 1 $\forall i \in \mathbb{N}_0, v_i$ can be uniquely solved.

3 Implementation in Symbolic Software

In Sect. 2 we have demonstrated the theoretical ground of our approach, by which the existence and uniqueness of the solution can be assured. For practical application, in each order, once the vector \mathbf{R} and the square matrix in the system of linear equations (11) or (13) are found, the unknowns $Z_i(X)$ and v_{i-1} can be easily solved. Such a procedure can be easily implemented iteratively in a symbolic computational software. For instance, in this chapter, we use *Maple* to perform the computation. Once the system is in the form of (1) and satisfies the assumptions mentioned in Sect. 1, all subsequent manipulations can be executed with simple *Maple* codes. The pseudo-algorithm together with some *Maple* codes is given in Algorithm 1. Additionally, we find that the first-order solution for the critical value can be expressed in terms of the coefficients in (4) as

$$v_0 = \frac{1}{w} \left[d\alpha_2 - k_1\alpha_0 + \frac{1}{2A} \left(\alpha_2 + 2a_2 + \frac{k_1\alpha_3 - 2k_1a_3}{k_2} \right) \right], \quad (14)$$

where

$$w = k_1\alpha_1 - c\alpha_2 \quad \text{and} \quad \alpha_i = Ak_1b_i - a_i, \quad i = 0, 1, 2, 3.$$

To validate the proposed approach, we first consider the canard explosion in the van der Pol system [7] and an aircraft model [10, 12]. Recently, an algorithm based on the NTT method has been proposed to solve both problems. Our computation shows that the results obtained by the present method are the same as those in the literature. Compared with the NTT method, by which one needs to use trigonometric functions, it takes us much less time to apply Algorithm 1 (see Table 1). The reason is that only polynomials and matrices are involved here. In addition, the square matrices are known in advance.

Algorithm 1 Computing the power series of canard explosion in system (1)

Require: Functions f and g in system (1) and desired order m

Ensure: $Z_0(X)$, $Z_i(X)$ and v_{i-1} for $i = 1, 2, \dots, m$

- 1: Compute the constants: c, k_i, a_i and $b_i, i = 1, 2, 3$
 - 2: Apply the transformation $x := \delta * X, y := \delta^2 * Y$ and $\mu := \delta^2 * N$ # N represents ν
 - 3: $P :=$ Taylor series of f/δ^2 up to $\mathcal{O}(\delta^m)$; $Q :=$ Taylor series of g/δ up to $\mathcal{O}(\delta^m)$
 - 4: Apply substitution $Y := (Z - c * N)/k_1$ and update $Q := k_1 * Q$
 - 5: $EQ := dZ * P - Q$ #Here, dZ represents $Z'(X)$
 - 6: Define $Z := \sum_{i=0}^m \delta^i z[i]; dZ := \sum_{i=0}^m \delta^i dz[i]; N := \sum_{i=0}^m \delta^i v[i]$
 - 7: **for** i from 1 to m **do**
 - 8: $eq[i] :=$ coefficient of δ^i in EQ #Use code $coeff(\cdot, \cdot, \cdot)$ to collect the coefficients
 - 9: $R[i] := -eq[i]$ with $dz[i] = z[i] = v[i - 1] = 0$
 - 10: **end for**
 - 11: Assign the zero-order solution to $z[0]$ and compute $dz[0]$
 - 12: **for** i from 1 to m **do**
 - 13: $n :=$ degree of $R[i]$
 - 14: **if** $n \geq 3$ **then**
 - 15: Define the $(n + 1) \times (n + 1)$ matrix M given in (11) as M
 - 16: Collect the coefficient of $R[i]$ and define them as a vector named by CR
#Use code $CR := CoefficientVector(R[i], X)$
 - 17: **else**
 - 18: Define the square matrix and the column vector R in (13) as M and CR , respectively
 - 19: **end if**
 - 20: Solve the system of linear equations and define the vector of solution as ζ
 - 21: $v[i - 1] := \zeta[n + 1]$
 - 22: Assign $z[i]$ as a polynomial whose coefficients are stored in ζ in ascending order and compute $dz[i]$ #Use code $dz[i] := diff(z[i], X)$
 - 23: **end for**
-

Table 1 Computation time (in seconds) for the power series up to different orders

Case	van der Pol						Aircraft			
	5	10	20	30	40	50	5	10	15	20
NTT	0.422	1.094	3.859	10.625	26.078	60.360	0.531	2.765	10.109	28.656
Present	0.031	0.094	0.172	0.328	0.640	1.109	0.125	0.203	0.328	0.704

4 Comparisons with the Classical Method

Besides the efficiency of the present approach, another advantage is that one is able to find the power series up to any desired order, even if the functions f and g in (1) are complicated. We know that, if f and g are simple, the classical iterative method is also an efficient alternative to compute the high-order solution. Nevertheless, it is not a favorable method in some cases. This is because the classical iterative method is used under the original coordinates. To start with, one needs to obtain a zero-order solution of the slow manifold when $\epsilon = 0$, which is sometimes not an easy task if function f is too complex. We provide below two examples that are already considered by the classical method and compare the results with the ones obtained by the present approach.

4.1 Templator Model

The first one is the templator model that is analyzed in [8], and it reads as

$$\dot{X} = r - k_u X^2 - k_T X^2 T, \quad \dot{T} = k_u X^2 + k_T X^2 T - qT / (K + T), \tag{15}$$

where X and T are phase variables and all other symbols represent system parameters. Applying the same transformation given in [8], that is, $K = \epsilon \ll 1$, $r = q + \epsilon c$, $Q = T - X$, and $P = T + X$, and introducing a new time variable as $t = \epsilon \tau$, we obtain the system in new variables as¹

$$\begin{aligned} \epsilon \frac{dQ}{d\tau} &= \frac{(P - Q)^2}{4} [2k_u + k_T (P + Q)] - c\epsilon - \frac{2q(\epsilon + P + Q)}{2\epsilon + P + Q} := \bar{f}(Q, P, c, \epsilon), \\ \frac{dP}{d\tau} &= \left(c + \frac{2q}{2\epsilon + P + Q} \right) := \bar{g}(Q, P, c, \epsilon). \end{aligned} \tag{16}$$

We next find the equilibrium that is located at the local extremum of the slow manifold by solving $\bar{f}(Q_0, P_0, c_0, 0) = \bar{g}(Q_0, P_0, c_0, 0) = \bar{f}_Q(Q_0, P_0, c_0, 0) = 0$, which results in

¹We remark that there are two typos in (15a) of Ref. [8].

Table 2 Comparisons between numerical result and analytical estimations up to c_i

r^* (num.)	$i = 0$	$i = 1$	$i = 2$	$i = 3$	$i = 4$	$i = 5$
0.96755828	0.96773988	0.96758462	0.96756115	0.96755865	0.96755833	0.96755829

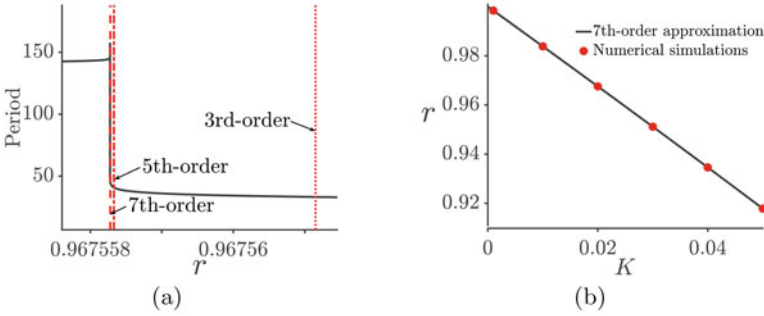


Fig. 1 Comparisons between analytical estimations and numerical results for the templator model. (a) Period versus r diagram (black) when $K = 0.02$ together with analytical predictions (red). (b) Critical value at different values of K

$$Q_0 = (1 - 2k_u\beta)/(k_T\beta), \quad P_0 = (2k_u\beta - 3)/(k_T\beta), \quad c_0 = qk_T\beta, \quad (17)$$

where $\beta = 2^{2/3}/[2^{2/3}k_u - (qk_T^2)^{1/3}]$. Then, we move the equilibrium and the parameter c to the origin so that the new system is in the form of (1) with $x = Q$, $y = P$, and $\mu = c$. Following the procedure given in Algorithm 1, the power series of the critical value can be easily obtained. Note that, in [8], using the classical iterative method, only the numeric value of the approximation is provided. On the contrary, with the present approach, the values of system parameters are not necessarily known a priori. The solution can be expressed in terms of symbolic parameters. Converting the parameter into original coordinates, the critical value r^* can be finally written as $r^* = q + \sum_{i=0}^{\infty} K^{i+1}c_i$, where c_i ($i = 1, 2, 3, 4$) are given in Appendix. To validate our result, we follow the system parameters used in [8], i.e., $q = k_T = 1$, $k_u = 0.01$, and $K = 0.02$. In Table 2, our estimations are compared with numerical result² that shows an excellent agreement. Besides, we show the associated bifurcation diagram in Fig. 1 (left panel), and in the right panel, comparisons for other values of K are also depicted.

²We also remark that the numerical result provided in Ref. [8] is inaccurate for higher significant digits.

4.2 Reduced Hodgkin–Huxley Model

As a second example, we consider now a more complex case, the reduced Hodgkin–Huxley (HH) model, whose equilibrium can only be computed numerically [9],

$$\begin{aligned}
 C\dot{V} &= I - \bar{g}_{Na}[\alpha_m(V)]^3[\alpha_m(V) + \beta_m(V)]^{-3}(0.8 - n)(V - V_{Na}) \\
 &\quad - \bar{g}_K n^4(V - V_K) - g_L(V - V_L), \\
 \dot{n} &= \alpha_n(V)(1 - n) - \beta_n(V)n,
 \end{aligned}
 \tag{18}$$

where

$$\begin{aligned}
 \alpha_m(V) &= \frac{0.1(V + 40)}{1 - \exp[-(V + 40)/10]}, & \beta_m(V) &= 4 \exp[-(V + 65)/18], \\
 \alpha_n(V) &= \frac{0.01(V + 55)}{1 - \exp[-(V + 55)/10]}, & \beta_n(V) &= 0.125 \exp[-(V + 65)/80].
 \end{aligned}$$

We take the same parameter values given in [9], namely $\bar{g}_{Na} = 120$, $\bar{g}_K = 36$, $g_L = 0.3$, $V_{Na} = 50$, $V_K = -77$, and $V_L = -54.4$. When the classical method is applied to this problem, the computation is not straightforward. The author used a quadratic fitting function with *Mathematica* to find the first-order approximation. Here, we apply our algorithm to this problem.

Again, we first find the location of the equilibrium and the critical value I_0 , at which the equilibrium is located at the local extremum of the slow manifold. We solve the three algebraic equations (two for the equilibrium and one for the local extremum) numerically. The results are $V_0 = -61.122882$, $n_0 = 0.378388$, and $I_0 = 6.522827$. We next move the equilibrium and parameter I to the origin and regard C as the perturbation parameter (i.e., ϵ in (1)). Now, the new system is in the form of (1) with $x = V$, $y = n$, and $\epsilon = C$. We then follow the aforementioned procedure to find the critical value. It is worth pointing out that, after Taylor expanding the two equations (see line 3 in Algorithm 1), the coefficients of each term are numerical values. But, the subsequent procedure still works when we implement it in *Maple* using the same code as before, and it takes only 1.519 s to solve the equation up to 20th order. The estimation for the critical value is finally provided as $I^* = \sum_{i=0}^{\infty} C^i I_i$, with

$$\begin{aligned}
 I_0 &= 6.522827, & I_1 &= -0.214573, & I_2 &= -0.0696026, & I_3 &= 0.0837185, \\
 I_4 &= 0.0859035, & I_5 &= 0.0133826, & I_6 &= -0.0748461, & I_7 &= -0.0910075, \\
 I_8 &= 0.0459785, & I_9 &= 0.271554, & I_{10} &= 0.189686, & I_{11} &= -0.755829.
 \end{aligned}$$

The approximation agrees well with numerical results, see Table 3 and Fig. 2. Different from the classical method, with which even the first-order approximation

Table 3 Comparison between numerical results and analytical estimations up to I_i

C	I^* (num.)	$i = 1$	$i = 2$	$i = 3$	$i = 4$	$i = 5$	$i = 6$	$i = 7$	$i = 8$	$i = 9$
0.2	6.477935	6.479913	6.477129	6.477799	6.477936	6.477940	6.477935	6.477934	6.477934	6.477935
0.1	6.500767	6.501370	6.500674	6.500758	6.500766	6.500767	6.500767	6.500767	6.500767	6.500767

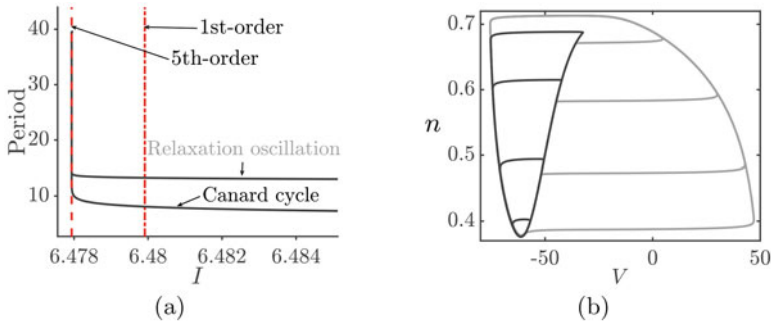


Fig. 2 Canard explosion in reduced HH model. (a) Period versus I diagram (black) when $C = 0.2$ together with analytical predictions (red) for canard explosion. (b) The evolution of periodic orbit from canard cycle to relaxation oscillation

cannot be solved easily, the present approach is able to obtain extremely high-order estimation.

5 Conclusions

In this chapter, we consider the canard explosion in a two-dimensional slow-fast system in which the slow manifold possesses a generic turning point. An efficient procedure for estimating the critical value for the canard explosion is demonstrated. Besides theoretical ground including existence and uniqueness of the solution, a pseudo-algorithm is also provided, whereby the present approach can be readily implemented in symbolic software *Maple*. To show the efficiency and efficacy of the present method, we apply it to several examples. Especially, for canard explosion in the templator model and reduced HH model, the existing approximations of the critical value are greatly improved with our approach. In addition to the examples considered here, the present method can be applied to any other system, as long as it satisfies the generic conditions.

Appendix: Coefficients c_i for the Templator Model

$$c_1 = qk_T\beta, \quad c_2 = -\frac{1}{9}qk_T^2\beta^2(9 + 3\omega - 3\omega^2 + 4\omega^3),$$

$$c_3 = -\frac{1}{972}qk_T^3\beta^3(972 + 864\omega - 972\omega^2 + 1637\omega^3 + 976\omega^4 - 336\omega^5 + 1728\omega^6),$$

$$c_4 = -\frac{1}{26244}qk_T^4\beta^4(26244 + 42444\omega - 50544\omega^2 + 106299\omega^3 + 153426\omega^4 - 21682\omega^5 + 383148\omega^6 + 213216\omega^7 + 149760\omega^8 + 364032\omega^9),$$

where $\omega = k_u\beta - 1$.

References

1. E. Benoît, L. Callot, F. Diener, M. Diener, Chasse au canards. *Collect. Math.* **31**, 37–119 (1981)
2. F. Dumortier, R. Roussarie, *Canard cycles and center manifolds*. *Mem. Am. Math. Soc.* **121** (1996). American Mathematical Society, Providence
3. M. Krupa, P. Szmolyan, Extending geometric singular perturbation theory to nonhyperbolic points-fold and canard points in two dimensions. *SIAM J. Math. Anal.* **33**, 286–314 (2001)
4. M. Krupa, P. Szmolyan, Relaxation oscillation and canard explosion. *J. Differ. Equ.* **174**, 312–368 (2001)
5. P.D. Maeschalck, F. Dumortier, Canard solutions at non-generic turning points. *Trans. Am. Math. Soc.* **358**, 2291–2334 (2005)
6. M. Brøns, An iterative method for the canard explosion in general planar systems. *Discrete Cont. Dyn. Syst.* **2013**(special), 1159–1180 (2013)
7. A. Algaba, K.W. Chung, B.W. Qin, A.J. Rodríguez-Luis, Analytical approximation of the canard explosion in a van der Pol system with the nonlinear time transformation method. *Physica D* **406**, 132384 (2020)
8. M. Brøns, Canard explosion of limit cycles in templator models of self-replication mechanisms. *J. Chem. Phys.* **134**, 144105 (2011)
9. J. Moehlis, Canards for a reduction of the Hodgkin-Huxley equations. *J. Math. Biol.* **52**, 141–153 (2006)
10. B.W. Qin, K.W. Chung, A. Algaba, A.J. Rodríguez-Luis, High-order study of the canard explosion in an aircraft ground dynamics model. *Nonlinear Dyn.* **100**, 1079–1090 (2020)
11. B.W. Qin, K.W. Chung, A. Algaba, A.J. Rodríguez-Luis, High-order analysis of canard explosion in the Brusselator equations. *Int. J. Bifurcation Chaos* **30**, 2050078 (2020)
12. J. Rankin, M. Desroches, B. Krauskopf, M. Lowenberg, Canard cycles in aircraft ground dynamics. *Nonlinear Dyn.* **66**, 681–688 (2011)

A Study of the Self-Oscillating Regime in the Problem of an Atomic Force Microscope in the Contact Mode



Pavel Udalov, Ivan Popov, and Alexey Lukin

1 Introduction

The atomic force microscope (AFM) uses a cantilever beam to measure the parameter of the surface (the distance between the tip and the sample). In the classical formulation of the AFM problem [6], the studied object is forced by a harmonic signal at the resonant frequency of the cantilever. Further, depending on which parameter is used to restore the parameter δ , two main AFM operation modes are distinguished – frequency and amplitude modulation [4]. In the first case, the surface topography is restored by changing the vibration frequency of the sample; on the other hand, the same is done according to the values of the amplitude of the AFM vibrations. The first version of the experiment is more attractive than the second one in that it exhibits smaller errors and inaccuracies in data acquisition [5, 6]. The only and most important problem of the experiment is that the resulting frequency response of this system is nonlinear [4], which makes it difficult to unambiguously determine the surface parameter of the object under study.

In this paper, we propose to consider the case of generalized nonlinear excitation, which depends on the generalized coordinates of a given system and to establish the possibility of the presence of a limit cycle and self-oscillations in a given system for a certain, given excitation force.

P. Udalov · I. Popov (✉) · A. Lukin

Department of Mechanics and Control Processes, Peter the Great St. Petersburg University, St. Petersburg, Russia

e-mail: udalov_pp@spbstu.ru; popov_ia@spbstu.ru; lukin_av@spbstu.ru

2 Mathematical Model

We study the motion of the contact-mode AFM shown in Fig. 1, where the probe is excited in flexural vibrations by a nonlinear motion of the sample in the z -direction. The probe is modelled as a linear cantilever beam [1] and the interaction between the tip and the sample is modelled as a pair of a nonlinear spring and a linear damper placed at the right end of the cantilever.

Unlike the classical AFM solution in the contact mode [3–5], in our formulation, the exciting force is not harmonic in the general case. And our goal is to select the law of excitation force which will take the expression for the limit cycles [5, 6]. Further, according to the characteristics of the limit cycle, it will be possible to receive surface information of the studied object.

2.1 Problem Formulation

We write the equation of motion of the Bernoulli-Euler beam [1] and boundary conditions governing the probe deflection as

$$EY \frac{\partial^4 w_d}{\partial x^4} = -\rho Y \frac{\partial^2 w_d}{\partial t^2}, \tag{1a}$$

$$w_d|_{x=0} = 0, \tag{1b}$$

$$\frac{\partial w_d}{\partial x} \Big|_{x=0} = 0, \tag{1c}$$

$$\frac{\partial^2 w_d}{\partial x^2} \Big|_{x=l} = 0, \tag{1d}$$

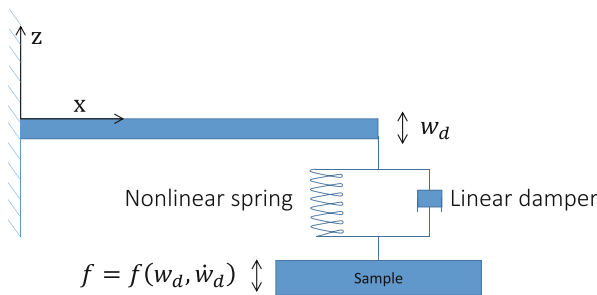


Fig. 1 Schematic view of the AFM

$$EY \frac{\partial^3 w_d}{\partial x^3} \Big|_{x=l} = \left[\mu \frac{\partial w_d}{\partial t} + F_H + f \left(w_d, \frac{\partial w_d}{\partial t} \right) \right] \Big|_{x=1}, \tag{1e}$$

where E and ρ are Young’s modulus and beam density, Y and A are the moment of inertia and cross-sectional area, w_d is the tip deviation near the equilibrium position, μ is the linear friction coefficient of the sample surface, F_H is the restoring force that occurs when the tip moves at the equilibrium position on the surface of the sample, $f \left(w_d, \frac{\partial w_d}{\partial t} \right)$ is excitation force transmitted from the sample to the tip.

$$F_H = \alpha_1 \left(\frac{w_d}{\delta} \right) - \alpha_2 \left(\frac{w_d}{\delta} \right)^2 - \alpha_3 \left(\frac{w_d}{\delta} \right)^3,$$

$$\alpha_1 = 2E^* \sqrt{R\delta^3}, \quad \alpha_2 = \frac{\alpha_1}{4}, \quad \alpha_3 = \frac{\alpha_1}{24},$$

where δ is the static indentation of the tip into the surface, R is the radius of the tip, E^* is the reduced elastic modulus defined as

$$\frac{1}{E^*} = \frac{1 - \nu_t^2}{E_t} + \frac{1 - \nu_s^2}{E_s},$$

and E_t, ν_t, E_s, ν_s are Young’s modulus and Poisson’s ratio of the tip and sample, accordingly.

We will characterize the function $f \left(w_d, \frac{\partial w_d}{\partial t} \right)$ as a by non-linearity of the Van der Pol type. This nonlinear term is responsible for energy pumping in a classical oscillator with nonlinear damping [5]:

$$f = f \left(w_d, \frac{\partial w_d}{\partial t} \right) = -\mu_f \left(\frac{w_d}{\delta} \right)^2 \frac{\partial w_d}{\partial t}.$$

We introduce the nondimensional quantities:

$$\hat{x} = \frac{x}{l}, \quad \hat{w} = \frac{w_d}{\delta}, \quad \hat{\alpha}_1 = \frac{\alpha_1 l^3}{EI\delta}, \quad \hat{t} = t \sqrt{\frac{EI}{\rho A l^4}},$$

$$\hat{\mu} = \mu \sqrt{\frac{l^2}{\rho A EI}}, \quad \hat{\mu}_f = \mu_f \sqrt{\frac{l^2}{\rho A EI}},$$

and rewrite Eq. (1) in nondimensional form as [3]

$$\hat{w}'''' + \hat{\ddot{w}} = 0, \tag{2a}$$

$$\hat{w}|_{\hat{x}=0} = 0, \quad (2b)$$

$$\hat{w}'|_{\hat{x}=0} = 0, \quad (2c)$$

$$\hat{w}''|_{\hat{x}=1} = 0, \quad (2d)$$

$$(\hat{w}''' - \hat{\alpha}_1 \hat{w})|_{\hat{x}=1} = \left(\hat{\mu} \hat{w} - \hat{\mu}_f \hat{w}^2 \dot{\hat{w}} - \hat{\alpha}_2 \hat{w}^2 - \hat{\alpha}_3 \hat{w}^3 \right)|_{\hat{x}=1}, \quad (2e)$$

where the prime indicates the derivative with respect to \hat{x} and the overdot indicates the derivative with respects to \hat{t} .

3 Perturbation Solution

We use the method of multiple scales [2] to find a uniformly valid second-order approximate solution of Eq. (2) and equation of the limit cycle in the form:

$$\hat{w} = \varepsilon \hat{w}_1(\hat{x}, \hat{T}_0, \hat{T}_1, \hat{T}_2) + \varepsilon^2 \hat{w}_2(\hat{x}, \hat{T}_0, \hat{T}_1, \hat{T}_2) + \varepsilon^3 \hat{w}_3(\hat{x}, \hat{T}_0, \hat{T}_1, \hat{T}_2), \quad (3)$$

where ε is small nondimensional bookkeeping parameter; $\hat{T}_0 = \hat{t}$, $\hat{T}_1 = \varepsilon \hat{t}$, $\hat{T}_2 = \varepsilon^2 \hat{t}$. We rescale effects of the damping as $\mu \rightarrow \varepsilon \mu$. Substituting Eq. (3) into Eq. (2) and balancing coefficients of like powers of ε , we obtain

order ε

$$\hat{w}_1'''' + D_0^2 \hat{w}_1 = 0, \quad (4a)$$

$$\hat{w}_1|_{\hat{x}=0} = 0, \quad (4b)$$

$$\hat{w}_1'|_{\hat{x}=0} = 0, \quad (4c)$$

$$\hat{w}_1''|_{\hat{x}=1} = 0, \quad (4d)$$

$$\hat{w}_1''' - \hat{\alpha}_1 \hat{w}_1|_{x=1} = 0. \quad (4e)$$

order ε^2

$$\hat{w}_2'''' + D_0^2 \hat{w}_2 = -2D_0 D_1 \hat{w}_1, \tag{5a}$$

$$\hat{w}_2|_{\hat{x}=0} = 0, \tag{5b}$$

$$\hat{w}_2'|_{\hat{x}=0} = 0, \tag{5c}$$

$$\hat{w}_2''|_{\hat{x}=1} = 0, \tag{5d}$$

$$\hat{w}_2''' - \hat{\alpha}_1 \hat{w}_2|_{\hat{x}=1} = -\hat{\alpha}_2 \hat{w}_1^2|_{\hat{x}=1}. \tag{5e}$$

order ε^3

$$\hat{w}_3'''' + D_0^2 \hat{w}_3 = -\left[2D_0 D_1 \hat{w}_2 + \left(D_1^2 + 2D_0 D_2\right) \hat{w}_1\right], \tag{6a}$$

$$\hat{w}_3|_{\hat{x}=0} = 0, \tag{6b}$$

$$\hat{w}_3'|_{\hat{x}=0} = 0, \tag{6c}$$

$$\hat{w}_3''|_{\hat{x}=1} = 0, \tag{6d}$$

$$\begin{aligned} & \left(\hat{w}_3'''' - \hat{\alpha}_1 \hat{w}_3\right)|_{\hat{x}=1} = \\ & = \left[\hat{\mu} D_0 \hat{w}_1 - 2\hat{\alpha}_2 \hat{w}_1 \hat{w}_2 - \left(\hat{\alpha}_3 + \hat{\mu}_f D_0\right) \hat{w}_1^3\right]|_{\hat{x}=1} \end{aligned} \tag{6e}$$

The first-order problem given by Eq. (4) is a linear eigenvalue problem. We express \hat{w}_1 [3] as

$$\hat{w}_1 = C_n \left(\hat{T}_1, \hat{T}_2\right) X_n(\hat{x}) e^{i\hat{\omega}_n \hat{t}} + c.c., \tag{7}$$

where $C_n \left(\hat{T}_1, \hat{T}_2\right)$ is a complex-value function which depends on parameters $\hat{T}_1, \hat{T}_2, X_n(\hat{x})$ is the n th natural mode shape determined by parameter $\hat{\omega}_n - n$ th nondimensional eigenfrequency and $c.c$ denotes the complex conjugate of the preceding terms.

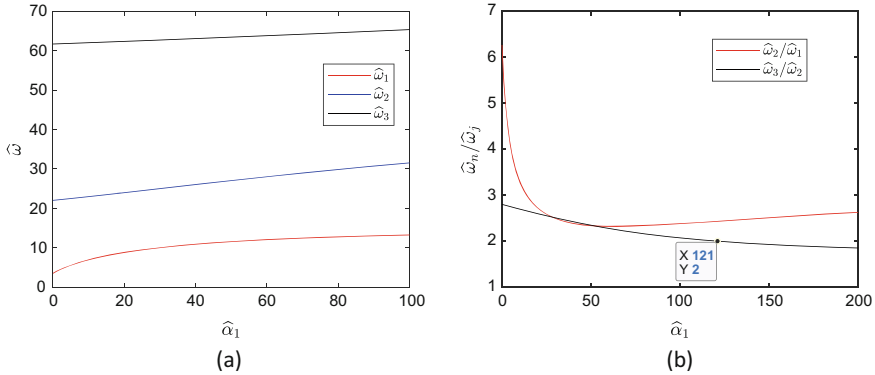


Fig. 2 The depends of quantities on the parameter $\hat{\alpha}_1$ the first, the second and the third natural frequency of the system (a) and the ratio of natural frequencies (b) $\hat{\omega}_2/\hat{\omega}_1$ (red line) and $\hat{\omega}_3/\hat{\omega}_2$ (black line)

Accordingly, we express $X_n(\hat{x})$ and $\hat{\omega}_n$ [3] as

$$X_n(\hat{x}) = -\frac{\sin h(b_n) + \sin(b_n)}{\cos h(b_n) + \cos(b_n)} (\cos h(b_n \hat{x}) - \cos(b_n \hat{x})) + (\sin(b_n \hat{x}) - \sin h(b_n \hat{x})), \tag{8}$$

and the natural frequencies $\hat{\omega}_n = b_n^2$ are solution of the characteristic equation

$$\mathcal{L}(b_n) = \hat{\alpha}_1 (\cos h b_n \sin b_n - \sin h b_n \cos b_n) + b_n^3 (1 + \cos b_n \cos h b_n) = 0. \tag{9}$$

Figure 2a shows the first, the second and the third $\hat{\omega}_1, \hat{\omega}_2, \hat{\omega}_3$ natural frequencies of the system as a function of linear stiffness $\hat{\alpha}_1$. When $\hat{\alpha}_1$ takes on value 121, $\hat{\omega}_3 \approx 2\hat{\omega}_2$. In this case, we can see the internal resonance between the second and the third modes [3].

Figure 2b shows the ratio of natural frequencies and it can be seen that in this case there is no internal resonance between first and second modes.

Substituting Eq. (7) into Eq. (5a), we obtain

$$\hat{w}_2'''' + D_0^2 \hat{w}_2 = -2D_0 D_1 \left[X_n(\hat{x}) C(\hat{T}_1, \hat{T}_2) e^{i\omega_n \hat{t}_0} + c.c \right], \tag{10}$$

and the solvability condition [5] for Eq. (10) demands that

$$D_1 C(\hat{T}_1, \hat{T}_2) = 0. \tag{11}$$

Substituting Eq. (11) into Eq. (5) and solving for \hat{w}_2 yields

$$\hat{w}_2 = C^2 \tilde{X}_n(\hat{x}) e^{2i\omega\hat{T}_0} + B\bar{C}C(\hat{x}^3 - 3\hat{x}^2) + c.c, \tag{12}$$

where

$$\tilde{X}_n(\hat{x}) = C_3 K_3(\sqrt{2}b_n \hat{x}) + C_4 K_4(\sqrt{2}b_n \hat{x}), \quad B = -\frac{\hat{\alpha}_2 X_n^2(1)}{6 + 2\hat{\alpha}_1}, \tag{13}$$

$$C_3 = \frac{\hat{\alpha}_2 X_n^2(1) K_2(\sqrt{2}b_n)}{\mathcal{L}(\sqrt{2}b_n)} \quad \text{and} \quad C_4 = \frac{-\hat{\alpha}_2 X_n^2(1) K_1(\sqrt{2}b_n)}{\mathcal{L}(\sqrt{2}b_n)}. \tag{14}$$

Substituting Eqs. (7), (12) into (6) and obtain solvability condition [5], we obtain

$$iC' = \frac{[2\hat{\alpha}_2(\tilde{X}_n(1)-2B)+3\hat{\alpha}_3 X_n^2(1)]X_n(1)}{2\Delta\omega_n} C^2 \bar{C} - \frac{i\hat{\mu}X_n(1)}{2\Delta} C + i\frac{3\hat{\mu}_f X_n^3(1)}{2\Delta\omega_n} C^2 \bar{C}, \tag{15}$$

where

$$\Delta = \int_0^1 X_n^2(\hat{x}) d\hat{x}. \tag{16}$$

The prime indicates the derivate with respect to \hat{T}_2 in Eqs. (15), (18), (19), (20), and (21).

When $X_n(1) = 0$, then

$$C = \text{Const.}$$

It means that in this case the tip becomes a node and there is no transfer of energy that occurs from the sample to the probe through the tip [3].

Substituting the Cartesian form [5]

$$C = a + i\gamma, \tag{17}$$

into Eq. (15) and separating the results into real and imaginary parts yields

$$a' = -\frac{\hat{\mu}X_n(1)}{2\Delta} a + \left(\frac{[2\hat{\alpha}_2(\tilde{X}_n(1)-2B)+3\hat{\alpha}_3 X_n^2(1)]X_n(1)}{2\Delta\omega_n} \gamma + \frac{3\hat{\mu}_f X_n^3(1)}{2\Delta\omega_n} a \right) \times (a^2 + \gamma^2), \tag{18}$$

$$\begin{aligned} \gamma' = & -\frac{\hat{\mu}X_n(1)}{2\Delta}\gamma + \\ & + \left(\frac{3\hat{\mu}_f X_n^3(1)}{2\Delta\omega_n}\gamma - \frac{[2\hat{\alpha}_2(\tilde{X}_n(1)-2B)+3\hat{\alpha}_3 X_n^2(1)]X_n(1)}{2\Delta\omega_n}a \right) \times \\ & \times (a^2 + \gamma^2). \end{aligned} \tag{19}$$

where a and γ are imaginary and real part of C .

To investigate the existence of a limit cycle we rewrite Eqs. (18) and (19) in polar coordinates $(a, \gamma) \rightarrow (\rho, \theta)$

$$\rho' = 2\rho^2 \left(\frac{3\hat{\mu}_f X_n^3(1)}{2\Delta\omega_n}\rho - \frac{\hat{\mu}X_n(1)}{2\Delta} \right) = \frac{X_n(1)}{\Delta}\rho^2 \left(\frac{3\hat{\mu}_f X_n^2(1)}{\omega_n}\rho - \hat{\mu} \right) \tag{20}$$

$$\theta' = -\frac{[2\hat{\alpha}_2(\tilde{X}_n(1) - 2B) + 3\hat{\alpha}_3 X_n^2(1)] X_n(1)}{2\Delta\omega_n}\rho, \tag{21}$$

The Eqs. (20), (21) for the radius ρ do not contain the variable θ . Therefore, the roots of the right side of the Eq. (20) will indicate the equilibrium in the system

$$\rho = 0, \quad \rho = \frac{\hat{\mu}\omega_n}{3\hat{\mu}_f X_n^2(1)}. \tag{22}$$

First point $\rho = 0$ denotes an unstable zero equilibrium and the second one denotes the amplitude of the stable limit cycle. To confirm these, we depict the phase plane in the Cartesian coordinates a and γ

Figure 3 shows that the limit cycle is stable because the phase curves on (a) and (b) are attracted from inside and outside to this equilibrium position of the system. Further, we show that in this system with a stable limit cycle, it is possible to perform amplitude and frequency modulation. For the first case, the implicit dependence of the amplitude of the limit cycle ρ in polar coordinates (ρ, θ) on the parameter $\hat{\alpha}_1$ is represented by the nontrivial case of the Eq. (22).

It was previously postulated that the system (18), (19) has an unstable equilibrium $(0, 0)$. As a mathematical justification we know, that the stability of the fixed point (a_0, γ_0) is determined by examining the eigenvalues of the Jacobian matrix of Eqs. (18) and (19), evaluated at the corresponding fixed point.

The linear part of (18)–(19) represents

$$a' = -\frac{\hat{\mu}X_n(1)}{2\Delta}a, \tag{23}$$

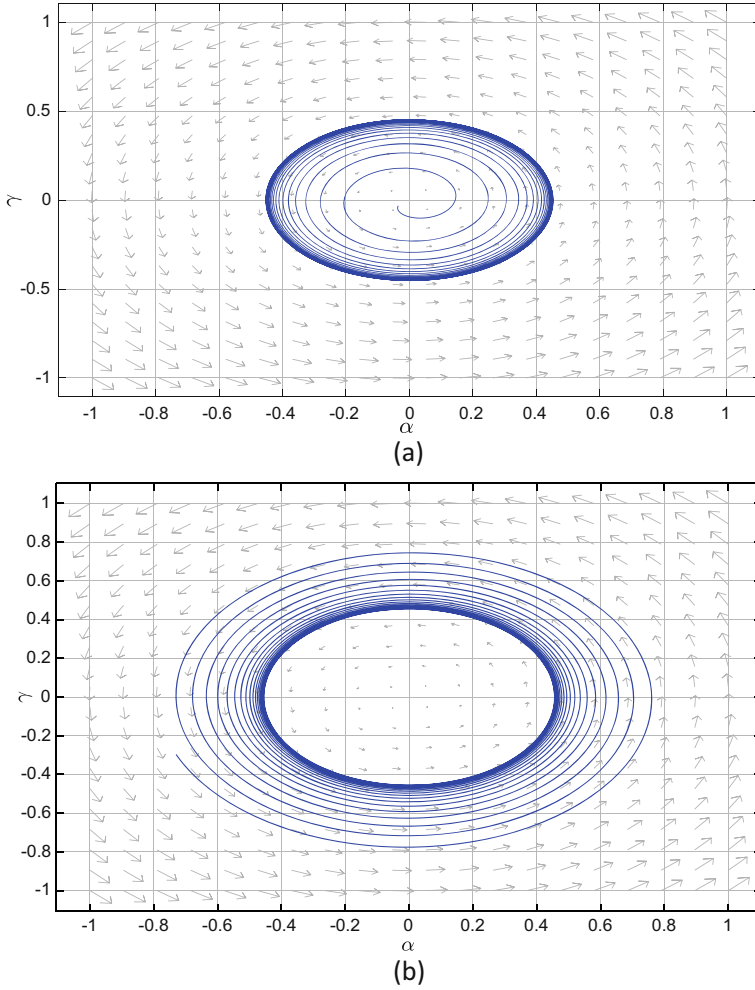


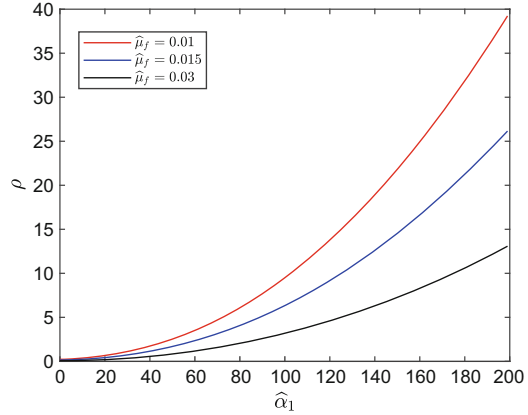
Fig. 3 System motion to self-oscillations under initial conditions (a) close to (0,0), (b) with sufficiently large initial conditions at $\hat{\mu} = 0.02$, $\hat{\mu}_f = 0.2$

$$\gamma' = -\frac{\hat{\mu} X_n(1)}{2\Delta} \gamma, \tag{24}$$

The expression for eigenvalues is

$$\lambda_{1,2} = -\frac{\hat{\mu} X_n(1)}{2\Delta}. \tag{25}$$

Fig. 4 The dependence of the polar radius ρ on the parameter $\hat{\alpha}_1$ when $\hat{\mu} = 0.015$, $\hat{\mu}_f = 0.01, 0.015, 0.03$



The eigenvalues of the Jacobian matrix (23), (24) depend explicitly on the form of free oscillations of the linear problem (2), in the case of the first mode $X_1(1)$ will be negative. Thus, the values in the equilibrium position $(0, 0)$ are positive, which gives rise to an unstable motion.

Figure 4 shows the dependence of the polar radius ρ on the parameter $\hat{\alpha}_1$, which characterizes the topography of the object. When the control parameter $\hat{\mu}_f$ increases, the polar radius ρ takes on large values. This is due to the fact that it is this parameter that is responsible for the amplitude of the effect, which directly relates to the AFM response.

Figure 5 shows the dependence of the eigenvalues λ of the linear system (23), (24) on the parameter $\hat{\alpha}_1$ for various values of the control factor $\hat{\mu}_f$, (a) depicts this dependence upon excitation of the first natural mode, (b) shows the excitation of the second natural mode. Depending on the sign of $X_n(\hat{x})$ at the right end of the AFM, a stable and unstable zero position of the linear system (23)–(24) will be determined. The zero-equilibrium position will be stable for all even forms, when the transition to the limit cycle will be observed with odd ones.

Substituting nontrivial part of Eq. (22) into Eq. (21) yields

$$\theta' = - \frac{\left[2\hat{\alpha}_2 \left(\tilde{X}_n(1) - 2B \right) + 3\hat{\alpha}_3 X_n^2(1) \right] \hat{\mu}}{6\Delta X_n(1) \hat{\mu}_f}. \tag{26}$$

We integrate the Eq. (26) within $\theta \in [0, 2\pi]$ and $t \in [0, T]$

$$T = - \frac{12\pi \Delta X_n(1)}{\left[2\hat{\alpha}_2 \left(\tilde{X}_n(1) - 2B \right) + 3\hat{\alpha}_3 X_n^2(1) \right] \hat{\mu}}, \tag{27}$$

where T – period of self-oscillations. And frequency of self-oscillation defines as

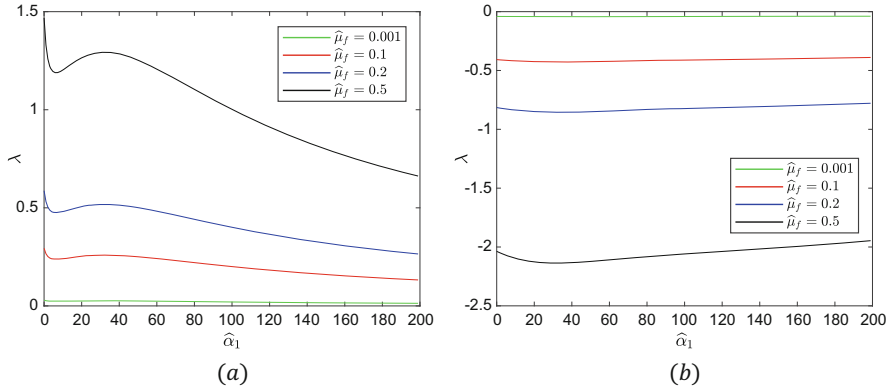


Fig. 5 The dependence of the eigenvalues λ on the parameter $\hat{\alpha}_1$ in the case of the excitation of the first (a) and second (b) modes when $\hat{\mu} = 0.015$, $\hat{\mu}_f = 0.1, 0.2, 0.3$

$$\nu = \frac{2\pi}{T} = -\frac{1}{6} \frac{\hat{\mu}}{\hat{\mu}_f} \frac{\left[2\hat{\alpha}_2 \left(\tilde{X}_n(1) - 2B \right) + 3\hat{\alpha}_3 X_n^2(1) \right]}{\Delta X_n(1)}. \tag{28}$$

It is interesting to obtain an explicit dependence of the polar radius ρ on the period of the limit cycle T . Substituting the nontrivial part of Eq. (22) into Eq. (27) yields

$$T\rho = -\frac{4\pi \Delta\omega_n}{\left[2\hat{\alpha}_2 \left(\tilde{X}_n(1) - 2B \right) + 3\hat{\alpha}_3 X_n^2(1) \right] X_n(1)}. \tag{29}$$

Figure 6 shows the dependence of period T (a) and frequency ν (b) of self-oscillations on the surface parameter $\hat{\alpha}_1$. These dependencies can be used for frequency modulation, which is quite accurate and promising in terms of minimizing interference and inaccuracies in taking time characteristics.

Figure 7 shows the relationship between the period T and the radius ρ of the limit cycle. This relationship may be useful for estimating noise with amplitude modulation.

The last step in this study will be to set the parameter $\hat{\mu}_f$ at which the frequency of the limit cycle will be equal to the natural frequency of the AFM. This is important because of depending on the frequency setting of the limit cycle, the zero position will be stable or unstable, that is, without an unstable zero equilibrium position, the limit cycle will not be observed.

For this we equate the Eq. (28) with natural frequency ω_n

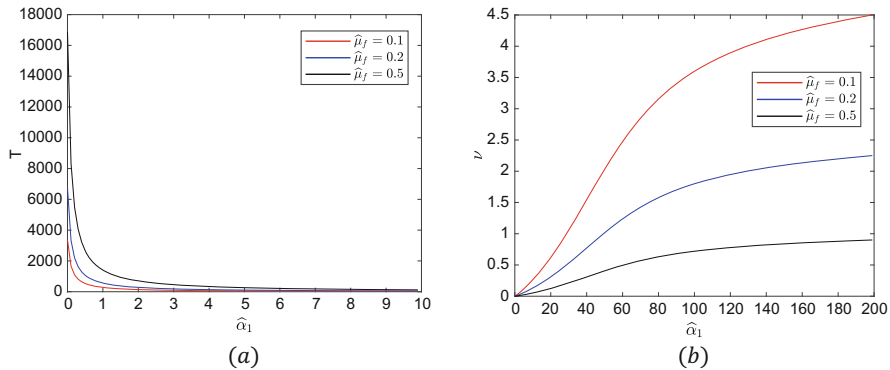


Fig. 6 The dependence of period T (a) and frequency ν (b) of the self-oscillation on the parameter $\hat{\alpha}_1$ when $\hat{\mu} = 0.015$, $\hat{\mu}_f = 0.1, 0.2, 0.3$

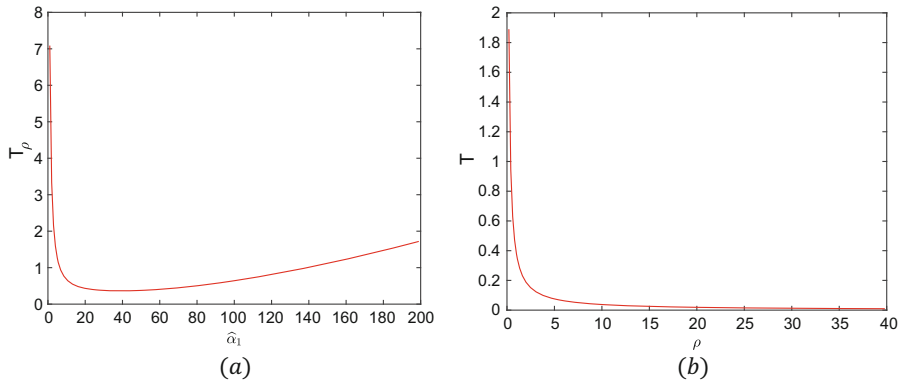


Fig. 7 The dependence of $T\rho$ on the parameter $\hat{\alpha}_1$ (a) and period T on the radius ρ of the self-oscillation in the case of the first natural mode

$$\nu = \omega_n \iff -\frac{1}{6} \frac{\hat{\mu}}{\hat{\mu}_f} \frac{\left[2\hat{\alpha}_2 \left(\tilde{X}_n(1) - 2B \right) + 3\hat{\alpha}_3 X_n^2(1) \right]}{\Delta X_n(1)} = \omega_n, \quad (30)$$

where do we find the value of the parameter $\hat{\mu}_f$

$$\hat{\mu}_f = -\frac{1}{6} \frac{\hat{\mu}}{\omega_n} \frac{\left[2\hat{\alpha}_2 \left(\tilde{X}_n(1) - 2B \right) + 3\hat{\alpha}_3 X_n^2(1) \right]}{\Delta X_n(1)}. \quad (31)$$

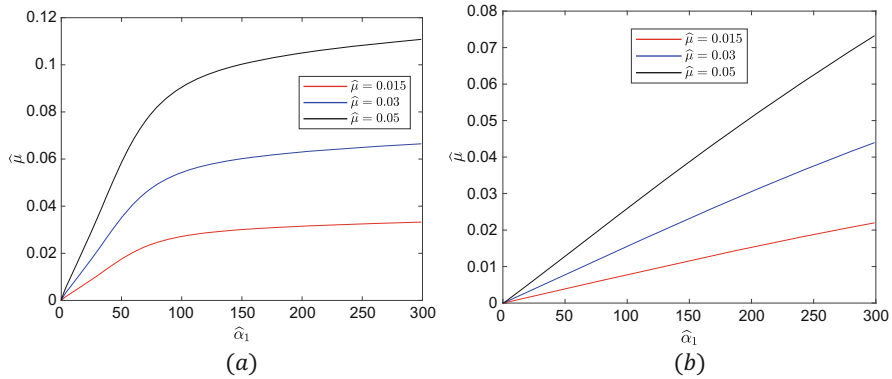


Fig. 8 The dependence of the control parameter $\hat{\mu}_f$ on the surface parameter $\hat{\alpha}_1$ in the case of the frequency of the limit cycle equal to (a) the first natural frequency and (b) the third natural frequency of AFM

Figure 8 shows the dependence of the control parameter $\hat{\mu}_f$ on the surface parameter $\hat{\alpha}_1$ in the case of the frequency of the limit cycle equal to the first and third eigenfrequencies of the AFM oscillation. Thus, it is possible to retrieve information about the surface of the object by the feedback signal of the parameter $\hat{\mu}_f$, which is adjusted to match the frequency of self-oscillations under the natural frequency of the AFM oscillations.

4 Conclusions

In this work, we study the dynamics of AFM in contact mode. In contrast to the standard harmonic excitation force acting on the sample, the generalized function of the degrees of freedom and time was considered. With a certain choice of this function, it is possible to organize a limit cycle in this system and use it to remove information about the object under study, which can take interest in the applied plan.

In addition, of special interest is the organization of a self-oscillating regime by acting on the tip of the AFM function which depends on generalized coordinates. Further, it becomes possible to explore the surface topography by changing the parameters of the limit cycle, which is more promising and more effective than the case of frequency modulation – because in the latter, as will be seen, the resonance curve is ambiguous, which makes it difficult to determine the amplitude maximum. Thus, the result of this work will be the construction of a solution for the case of the limit cycle and its qualitative study, and most importantly, comparison with other types of modulation in terms of speed and efficiency of data acquisition.

Acknowledgements The work was supported by the RFBR grant 20-01-00537.

References

1. V.L. Biderman, Theory of mechanical vibrations. M.: "Higher School", p. 149–160 (1980)
2. A.H. Nayfeh, Introduction to perturbation methods. M.: "World", p. 536 (1984)
3. E.M. Abdel-Rahman, A.H. Nayfeh, *Contact force identification using the subharmonic resonance of a contact-mode atomic force microscopy* (IOP Publishing Ltd, Blacksburg, 2005), pp. 199–207
4. R. Garcia, R. Perez, *Dynamic atomic force microscopy methods* (Elsevier Science B.V, Amsterdam, 2002), p. 301
5. A.H. Nayfeh, P.F. Pai, *Linear and nonlinear structural mechanics* (Wiley - VCH Publ, Mörlenah, 2004), p. 763
6. M.I. Younis, *MEMS linear and nonlinear statics and dynamics* (Springer Science + Business Media, New York, 2011), p. 453

Non-Rectification of Heat in Graded Si-Ge Alloys



S. Carillo, M. G. Naso, E. Vuk, and F. Zullo

1 Introduction

The thermal phenomenon that allows heat to be transferred in a suitable direction in a given material, while the flow is impeded in the opposite direction, is called thermal rectification [1, 2]. This is the analogue of the current rectification of the electronic diodes, and for this reason any device showing some thermal rectifying feature is called thermal diode. A homogeneous material possessing a constant thermal conductivity is known to possess no rectifying property [3]: the heat flows, under the same thermal gradient applied, equally in all possible directions. It follows that, if a material possesses a rectifying effect, then the thermal conductivity λ is a non-homogeneous function of the temperature. With non-homogeneous, we mean that the thermal conductivity also depends on the space variable \mathbf{x} . Despite to be necessary, this condition is however far from being sufficient: indeed, it has been shown [3] that, if the thermal conductivity is a separable function, i.e., if there exist two functions f and g such that $\lambda(T, \mathbf{x}) = f(T)g(\mathbf{x})$, then no rectifying effect can be observed in the material.

A practicable process to obtain non-homogeneous values of macroscopic properties, such as the thermal conductivity, is the manufacturing of functionally graded materials, i.e., materials with a specific gradation in the composition in order to

S. Carillo (✉)

Dipartimento di Scienze di Base e Applicate per l'Ingegneria, Università di Roma "LA SAPIENZA", Rome, Italy

I.N.F.N.—Sezione Roma1, Gr. IV—M.M.N.L.P., Rome, Italy

e-mail: sandra.carillo@uniroma1.it

M. G. Naso · E. Vuk · F. Zullo

DICATAM, Università degli Studi di Brescia, Brescia, Italy

e-mail: mariagrazia.naso@unibs.it; elena.vuk@unibs.it; federico.zullo@unibs.it

achieve particular performances or functions [4]. One of the most common examples of graded materials is binary alloys $A_c B_{1-c}$, where A and B are two different atomic species and c is the content of the species A (so that $c \in (0, 1)$). In this chapter we present a detailed analysis of the possibility to get a thermal diode with graded Si-Ge alloys. The investigation is mainly based on the results given in [1], where a systematic approach is introduced to find the optimal gradation of the species in order to maximize the efficiency of the fin. Our main assumptions are the following:

- The device is a wire of variable diameter D ; hence, the problem can be considered one-dimensional.
- The Fourier law describes accurately enough the temperature distribution within the device.
- The anharmonic, alloy, and boundary scattering of the phonons all give contributions to the value of the thermal conductivity.
- The concentration c and the diameter D are unknown variables and must be determined in order to optimize the rectifying effect.

This chapter is organized as follows: in Sect. 2 we introduce the main equations and the rectification coefficient R . Also, for the sake of clearness and completeness, we briefly describe the approach given in [1] to maximize this coefficient. In Sect. 3, we apply the formulae to a Si-Ge graded wire with variable diameter. An analytical formula for the thermal conductivity, mainly based on [5] (see also [6–8]), is presented and discussed. An example of evolutionary solution is also provided, and perspective developments in this direction are mentioned. In Sect. 4, we apply the results given in Sect. 2 to the obtained formula for the thermal conductivity. Finally, in the conclusions, the main aspects of this chapter are emphasized, under a constructive point of view. Indeed, even if it is true that our analysis seems to preclude the possibility to get significant values of the rectification coefficient, different perspectives that may indicate the methodology to achieve applicable results.

2 The Rectification Coefficient and Its Maximization

This section is mostly based on a work of Peyrard [2] and on a previous work of some of the co-authors [1] and introduces the main findings described in Sect. 3. In [2] it is shown that it is possible to get a rectifying effect from a device composed of two materials when at least one of them is characterized by a temperature-dependent thermal conductivity. When the temperature range considered is large, almost every metallic or semiconductor material has a temperature-dependent thermal conductivity. Furthermore, for graded materials, the thermal conductivity may also be a function of the gradation in composition: for example, for binary alloys $A_c B_{1-c}$, λ is a function of T and of the species content c (see, e.g., [9]). If the species content c is variable inside the material, i.e., $c = c(\mathbf{x})$, then the thermal conductivity becomes dependent on T and \mathbf{x} , $\lambda = \lambda(T, c(\mathbf{x}))$. In [1], a systematic

way to choose the spatial distribution of the composition $c(\mathbf{x})$ and the geometry of the device presenting the more interesting rectification performances has been introduced. Here, we recall the main findings for completeness and for the sake of readability of Sect. 3. By assuming that the Fourier law holds, the evolution of the temperature inside the device is governed by the following equation:

$$\rho(c(x))C(T, c(x))\frac{\partial T}{\partial t} = \frac{\partial}{\partial x} \left(\lambda(T, c(x))\frac{\partial T}{\partial x} \right), \tag{1}$$

where the density ρ can depend on the content c that may be a variable in x , and the specific heat capacity C in general depends on both T and c . The steady-state distribution of the temperature is described by the solution of the following equation:

$$\frac{dT}{dx} = -\frac{q}{\lambda(T, c(x))}. \tag{2}$$

In a steady-state situation, like the one we are considering, the heat flux q across the device is a constant (since it solves $\nabla \cdot \mathbf{q} = 0$). Then, the implicit solution of Eq. (2) is given by

$$T(x) = T(0) - q \int_0^x \frac{1}{\lambda(T(y), v(y))} dy, \tag{3}$$

giving

$$q = -\frac{T(L) - T(0)}{\int_0^L \frac{1}{\lambda(T(y), v(y))} dy}. \tag{4}$$

The efficiency of a thermal rectifier can be evaluated through the rectification coefficient, defined by the ratio of the heat flux in two opposite configurations, the “direct” and the “inverse”. To fix ideas, we take the two boundaries of the device at $x = 0$ and $x = L$ at the temperatures T_H and T_L , where $T_H > T_L$. In the direct configuration, the end $x = 0$ is at the temperature T_L and the end $x = L$ at the higher temperature T_H . In the reverse configuration, the boundary $x = 0$ is at the higher temperature T_H , whereas the end at $x = L$ is at the lower temperature T_L . From Eq. (3), if q_d and q_r are, respectively, the direct and reverse heat fluxes, the rectification coefficient R is defined as

$$R = \frac{|q_d|}{|q_r|} = \frac{\int_0^L \frac{1}{\lambda(\tau_r(y), c(y))} dy}{\int_0^L \frac{1}{\lambda(\tau_d(y), c(y))} dy}, \tag{5}$$

where τ_r and τ_d are the solutions of the steady Fourier equation (2) in the reverse and direct configurations, respectively, [1]. From (5), it is clear that if λ was a constant, the rectification constant would be equal to 1, i.e., the heat fluxes in the direct and inverse configurations are equal and no rectifying effect is observed. Notice that, if λ is constant, then the distribution of the temperatures in the two configurations is represented by the distributions of the temperatures T_d and T_r in the direct and reverse configurations, given, respectively, by

$$T_d = T_L + (T_H - T_L) \frac{x}{L}, \quad T_r = T_H - (T_H - T_L) \frac{x}{L}. \quad (6)$$

If we look at the plane (x, T) , these temperatures lie exactly on the diagonals of the rectangle with vertices in $(0, T_L)$, $(0, T_H)$, (L, T_L) , and (L, T_H) . According to [1], if λ is a regular continuous function of T and x , at steady state, the temperature profiles roughly will follow the same diagonals. Then, if the value that the thermal conductivity assumes on one of these diagonals is much greater than the value it assumes on the other diagonal, a considerable rectifying effect should be observed. Based on this reasoning, in [1], the following methodology is proposed to maximize the rectification coefficient (5):

1. Among the various possible geometries and distributions $c(x)$, look for the particular geometry and distribution $c_0(x)$ giving a saddle point to the function $\lambda(T, x)$ in the middle of the domain of interest. In the plane (x, T) , the saddle must present a maximum on one diagonal and a minimum on the other diagonal.
2. Among the various possible geometries and distributions $c(x)$, look for the particular geometry and the particular distribution $c_0(x)$ that maximizes the difference between the values that $\lambda(T, x)$ assumes on the vertices of the rectangle whose diagonals are given by (6). More precisely, if $T_A(x)$ denotes the values on one of the two diagonals and $T_B(x)$ the values on the other, maximize the differences $\lambda(T_A(0), 0) - \lambda(T_B(0), 0)$ and $\lambda(T_A(L), L) - \lambda(T_B(L), L)$.

In the next section, in order to apply the above line of reasoning to graded Si-Ge devices, we describe the dependence of the thermal conductivity on the temperature, gradation, and dimension of the section of the wire.

3 Si-Ge Alloys with Variable Section

The thermal conductivity of silicon-germanium alloys is in general lower than the corresponding thermal conductivities of the bulk materials. From a microscopic point of view, this is due to an additional scattering mechanism of the phonons inside the material, the so-called alloy scattering. The geometry of the material may also play a role in the determination of the thermal conductivity. Indeed, if the dimensions are small enough, the scattering of the phonons with the boundaries

of the material may become strong enough and contribute to a further lowering of the thermal conductivity. The properties of the Si-Ge alloys can be computed via first-principles approaches, like the density-functional perturbation theory (see, e.g., [10] for bulk materials with diffusive boundary conditions or [11] for disordered silicon-germanium alloys). As for the case of porous silicon, we need an analytical formulation of the thermal conductivity accurate enough and simple enough to be manipulated. In [5], the authors presented a theoretical, phenomenological formulation of the thermal conductivity of $\text{Si}_{1-c}\text{Ge}_c$ nanowire alloys, wherein the section of the wire is explicitly taken into account. This formulation is compared with experimental results: between a temperature range of (100, 400)K, the agreement seems to be good enough in order to be utilized here [5–7]. The thermal conductivity of a $\text{Si}_{1-c}\text{Ge}_c$ nanowire is then given by Wang and Mingo [5]

$$\lambda = \frac{k_B^4 T^3}{2\pi^2 v \hbar^3} \int_0^{\hbar w_c / k_B T} \frac{y^4 e^y}{(e^y - 1)^2} \frac{1}{\tau^{-1}} dy, \quad (7)$$

where k_B and \hbar are the Boltzmann's and reduced Planck's constants, the inverse scattering rate τ^{-1} is given, by the Matthiessen's rule, by the sum of three terms, i.e.,

$$\tau^{-1} = \tau_u^{-1} + \tau_a^{-1} + \tau_b^{-1},$$

where τ_u^{-1} , τ_a^{-1} , and τ_b^{-1} are, respectively, the contributions due to anharmonic, alloy, and boundary scattering. The anharmonic contribution is described by the weighted average between the Si and Ge terms, $\tau_u^{-1} = (1-c)\tau_{Si}^{-1} + c\tau_{Ge}^{-1}$, with τ_{Si}^{-1} proportional to $w^2 T e^{-C_{Si}/T}$ and τ_{Ge}^{-1} proportional to $w^2 T e^{-C_{Ge}/T}$ (C_{Si} and C_{Ge} are the constants and w is the frequency of the phonons). The alloy scattering term is approximated by a quadratic function of c , required to be zero for $c = 0$ and $c = 1$, giving $\tau_a^{-1} \sim c(1-c)w^4$ (see also [8] for the proportionality to the w^4 term). The boundary term is taken in [5] to be equal to $\tau_b^{-1} = v/D$, where D is the diameter of the wire and v is the average speed of sound, given by $v^{-2} = (1-c)v_{Si}^{-2} + cv_{Ge}^{-2}$ (v_{Si} and v_{Ge} are the average speeds of sound in silicon and germanium). The overall cutoff frequency w_c is given by $w_c = w_{cut}v/v_{Si}$, where $w_{cut} \sim 38.8$ THz [5].

Combining all together and taking the constants of proportionality from [5], we get

$$\lambda = \hat{\lambda}_0 T^3 \beta \int_0^{\Theta_c / \beta T} \frac{y^4 e^y (e^y - 1)^{-2}}{(1-c)y^2 T^3 e^{-C_{Si}/T} + q_1 c y^2 T^3 e^{-C_{Ge}/T} + q_2 c(1-c)T^4 y^4 + q_3 / (\beta D)} dy, \quad (8)$$

where $\hat{\lambda}_0 = 2.43 \text{Wm}^{-1} \text{K}^{-1}$, $\beta = \sqrt{1521 + 2575c}$, $\Theta_c = 1.1568 \cdot 10^4 \text{K}$, $C_{Si} = 139.8 \text{K}$, and $C_{Ge} = 69.34 \text{K}$. The three constants q_i are given by $q_1 = 1.93$, $q_2 = 3.41 \text{K}^{-1}$, $q_3 = 96.6 \text{K}^3 \text{m}$.

To get the evolution equation for the temperature (1), the values of the density and of the specific heat capacity are needed. In the case of $\text{Si}_{1-c}\text{Ge}_c$ alloys, the following formula that gives ρ as a function of c is given in [9] (the units are Kg/m^3):

$$\rho(c) = 2329 + 3493c - 499c^2. \quad (9)$$

The specific heat capacity, according to the well-known Debye formula, is

$$C = C_0 T^3 \int_0^{\Theta_c/\beta T} \frac{y^4 e^y}{(e^y - 1)^2} dy, \quad (10)$$

where C_0 is assumed to be $C_0 = (1 + c) \cdot 8.567 \cdot 10^{-5} \text{ J/K}^4 \text{ Kg}$. Note that the value of C_0 is chosen to fit the values of the specific heat capacity of the pure silicon (corresponding to $c = 0$), given by 710 J/Kg K at 300 K , and the value of the specific heat capacity of the germanium (corresponding to $c = 1$), given by 330 J/Kg K at 300 K .

The corresponding nonlinear, integro-differential equation describing the evolution of the temperature is given by

$$\rho C \frac{\partial T}{\partial t} = \frac{\partial}{\partial x} \left(\lambda \frac{\partial T}{\partial x} \right), \quad (11)$$

where ρ is given by Eq.(9), C by Eq.(10), and λ by (8). Note that, for graded materials, the species content c appearing in the formulae for λ , C , and ρ is a function of the space variable x , since it can vary along the wire. In general, the diameter D , in λ , may also depend on x .

Let us consider as a particular case (but interesting also under an applicative point of view) a material with constant values of the species content c and of the diameter of the wire D . In this case, both the heat capacity C (10) and the thermal conductivity (8) depend only on the temperature $T(x, t)$ for any fixed value of c and D . Equation (11) then becomes

$$\rho C(T) \frac{\partial T}{\partial t} = \frac{d\lambda(T)}{dT} \left(\frac{\partial T}{\partial x} \right)^2 + \lambda(T) \frac{\partial^2 T}{\partial x^2}. \quad (12)$$

Now, assume that the temperature $T(x, t)$ is a solution of the following implicit equation:

$$A_1 x + A_2 t + A_3 + \int_0^{T(x,t)} f(y) dy = 0, \quad (13)$$

where A_1 , A_2 , and A_3 are the three arbitrary constants and $f(y)$ is an unknown function to be determined. We also assume that $f(y)$ is always different from zero. The partial derivatives of the temperature can be expressed in terms of the function f and its derivative. Indeed, by differentiating equation (13), we get

$$\frac{\partial T}{\partial t} = -\frac{A_2}{f(T)}, \quad \frac{\partial T}{\partial x} = -\frac{A_1}{f(T)}, \quad \frac{\partial^2 T}{\partial x^2} = -\frac{A_1^2}{f(T)^2} \frac{df(T)}{dT}. \tag{14}$$

Substitution of the previous expression in (12) gives a differential equation in the unknown function $f(T)$:

$$\rho C(T)A_2 f(T)^2 + \frac{d\lambda(T)}{dT} A_1^2 f(T) - \lambda(T)A_1^2 \frac{df(T)}{dT} = 0 \tag{15}$$

that is a Bernoulli differential equation for f . It is known that the Bernoulli differential equation is linearizable through a change of the dependent variable. Indeed, if we set $f(T) = (w(T))^{-1}$, one has for $w(T)$:

$$\rho C(T)A_2 + \frac{d\lambda(T)}{dT} A_1^2 w(T) + \lambda(T)A_1^2 \frac{dw(T)}{dT} = 0 \tag{16}$$

and the further change of variables $w(T) = \frac{\tilde{w}(T)}{\lambda(T)}$ produces:

$$\rho C(T)A_2 + A_1^2 \frac{d\tilde{w}(T)}{dT} = 0, \tag{17}$$

which gives

$$\tilde{w}(T) = -\rho \frac{A_2}{A_1^2} \int_0^T C(y)dy + A_4, \tag{18}$$

where A_4 is a fourth arbitrary constant. Combining all together, we see that a particular family of solutions of Eq. (12), possessing four arbitrary constants, is given by the solution of the following implicit equation:

$$A_1 x + A_2 t + A_3 + \int_0^{T(x,t)} f(y)dy = 0, \quad f(y) = \frac{\lambda(y)}{A_4 - \rho \frac{A_2}{A_1^2} \int_0^y C(z)dz}. \tag{19}$$

We remember that the functions $\lambda(T)$ and $C(T)$ in (19) are the thermal conductivity and the heat capacity of the device.

Some remarks on the previous solution follow. The boundary conditions, assigned at $x = 0$ and $x = L$, are time-dependent. However, such solution may be unphysical, since, for suitable heat capacities and thermal conductivities, it may be unbounded as t goes to infinity. When a Taylor series approximation is adopted to express both heat capacity as well as the thermal conductivity, explicit integration of Eq. (19) is possible by a partial fraction decomposition. In this case also, it may be possible that the solution is unphysical. On the other hand, note that if the species content c and the diameter of the wire D are variable in space, Eq. (19) does not represent anymore the solution of Eq. (11), but still, if the coefficients A_1, A_2 , and

A_3 are suitably chosen variable in space, it is possible to get particular solutions for some special cases. In general, Eq. (11) is baffling, and it needs ad hoc strategies to be fully understood. We are developing a difference scheme in order to describe the evolution of the temperature inside the device corresponding to “ad hoc” initial and boundary conditions: this will be fully developed in a work in progress. In addition, a perturbative approach is currently under investigation to check whether on the introduction of ρ and λ as power series expansions in terms of small parameters that represent the difference of the current value with respect to its mean value (i.e., $\rho = \rho_0 + \epsilon\rho_1(x)$ and $\lambda = \lambda_0 + \epsilon\lambda_1(T, x)$) may produce physically meaningful results.

According to the methodology given in [1] and described in Sect. 2, it is sufficient here to describe the asymptotic (steady) solution of Eq. (11) in order to obtain the necessary information on the rectification coefficient (5). Actually, as stated by the items (1) and (2) at the end of Sect. 2, the function $\lambda(T, c)$ plays a fundamental role.

In Fig. 1, the plots of the value of the thermal conductivity for $T = 300$ K and for different values of D are reported. In the next subsection, we apply our methodology to the thermal conductivity (8): as we will see, in this case we find that it is not possible to obtain high values of the rectification coefficient (5) following our approach.

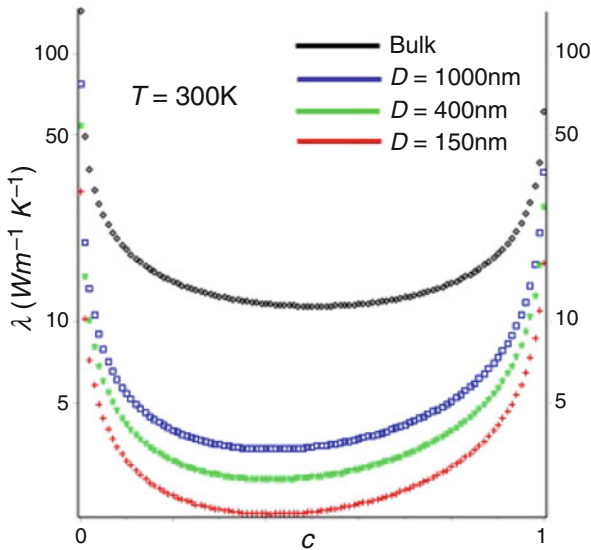


Fig. 1 The values of the thermal conductivity obtained from formula (8) with $T = 300$ K for $D = \infty$ (corresponding to a bulk alloy), $D = 1000$ nm, $D = 400$ nm, and $D = 150$ nm. A log scale has been used on the vertical axis

4 Analysis of the Thermal Conductivity (8) and the Corresponding Rectification Coefficient

This section is devoted to some remarks on the model under investigation aiming to stress are the main difficulties underlying the problem itself. According to the approach summarized in Sect. 2, if we are interested in obtaining sufficiently large values of the rectification coefficient, we need to require large values for the differences $\lambda(T_A(0), 0) - \lambda(T_B(0), 0)$ and $\lambda(T_A(L), L) - \lambda(T_B(L), L)$, where $T_A(x)$ defines the values of the temperatures on one of the two diagonals and T_B the values on the other. Indeed, such a choice is crucial, to follow *both* steps (1) and (2). However, to satisfy such conditions on $\lambda(T_A(0), 0) - \lambda(T_B(0), 0)$ and $\lambda(T_A(L), L) - \lambda(T_B(L), L)$, the function $\lambda(T, x = 0)$, when we consider its dependence on T in the domain (T_L, T_H) , is required to be *increasing* at least in some interval of the domain, whereas the function $\lambda(T, x = L)$ is required to be *decreasing* at least in some interval of the same domain. Since in formula (8) both the concentration c as well as the diameter D are assumed to depend on x , when $x = 0$ and $x = L$, these functions assume the values, say, $c(0)$, $c(L)$, $D(0)$, and $D(L)$. If, in some region of the variables c and D , the function $\lambda(T, c, D)$, as a function of T , is increasing and decreasing in some other regions, then suitably tuning the dependence of c and D on x , it would be possible to construct a thermal conductivity that exhibits an interesting rectification coefficient. However, in the range of temperatures (100, 400)K, the function $\lambda(T, c, D)$ does not satisfy the requested properties. Indeed, in the region $c = (0.05, 0.95)$ λ is almost flat for all values of T and for all the reasonable values of D , i.e., from 10 nm to $2 \cdot 10^4$ nm. In such a range of c , the values of λ are bounded in the interval $(1 - 25) \text{Wm}^{-1} \text{K}^{-1}$, as shown in Fig. 2, whereas in the full range of variation of c (i.e., $c \in (0, 1)$), the values of λ can reach values as large as $500 \text{Wm}^{-1} \text{K}^{-1}$. This behaviour suggests to choose values of c that correspond to almost pure silicon ($c \in (0, 0.05)$) or almost pure germanium ($c \in (0.95, 1)$). Nevertheless, in these ranges of variability, the thermal conductivity is always a *decreasing* function of the temperature, independently on the value of the concentration. The only exception is a very flat maxima, which correspond to fixed and small values of D (see the plots Fig. 3 for the dilute zones). This seems to preclude the possibility to tune the dependence of c and D on x in such a way to get an interesting value of the rectification coefficient. The above result can provide an explanation of the small values of R available in the literature for $\text{Si}_{1-c}\text{Ge}_c$ devices (see, e.g., [12]).

5 Conclusions

In this chapter, we systematically analysed the possibility to obtain a thermal diode for functionally graded Si-Ge alloys. We tried to get the particular spatial distribution of the species content c and the geometry of the wire giving reasonably

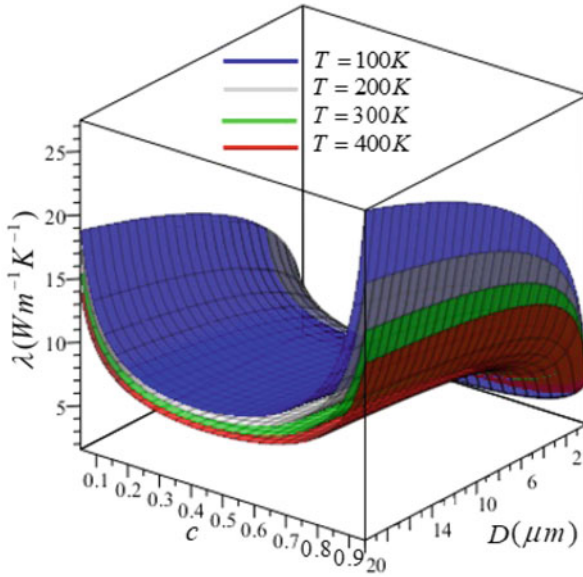


Fig. 2 The values of the thermal conductivity for $c \in (0.05, 0.95)$ for different values of the temperature

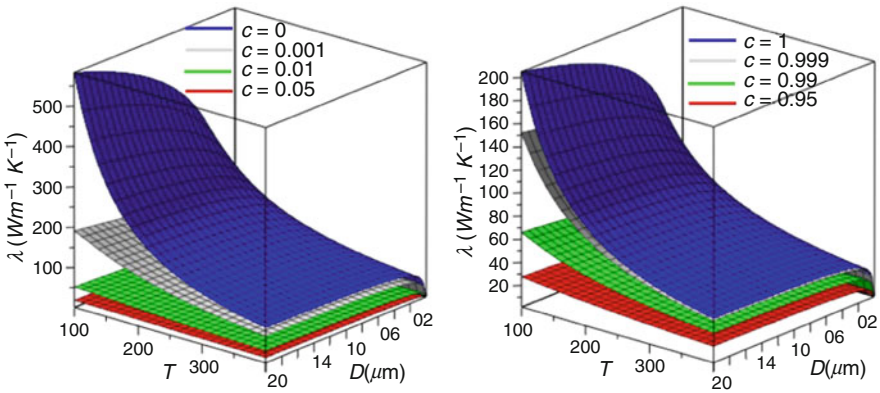


Fig. 3 The values of the thermal conductivity as a function of the temperature in the two dilute zones given by $c \in (0, 0.05)$ and $c \in (0.95, 1)$ for some values of c

high values of the rectification coefficient. This same methodology is applied to porous silicon materials in [1] showing the possibility to obtain a rectification coefficient equal to 3.15. The same approach applied to Si-Ge materials shows that a thermal diode with the characteristics here described has instead few chances to become a good heat rectifier. Clearly, this negative result only implies the impracticability to get a thermal diode with the above characteristics. The model here presented, although to be physical consistent and accurate, can be regarded as a first approximation to more complex approaches, and if new variables or different heat transfer laws are embedded in the model here considered, more satisfactory results can be achieved.

Acknowledgments Work performed under the auspices of the Gruppo Nazionale per la Fisica Matematica (GNFM-INdAM).

M.G.N., E.V., and F.Z. would like to acknowledge the financial support of the Università degli Studi di Brescia.

S.C. acknowledges the partial financial support of Università di Roma “LA SAPIENZA”.

S.C. and F.Z. would like to acknowledge the financial support of INFN.

References

1. M.G. Naso, E. Vuk, F. Zullo, On the optimization of heat rectification in graded materials. *Int. J. Heat Mass Trans.* **143**, 118520 (2019)
2. M. Peyrard, The design of a thermal rectifier. *EPL* **76**, 49 (2006)
3. D.B. Go, M. Sen, On the condition for thermal rectification using bulk materials. *J. Heat Transfer*. **132**, 124502 (4 pages) (2010)
4. M. Naebe, K. Shirvanimoghaddam, Functionally graded materials: a review of fabrication and properties. *Appl. Mater. Today* **5**, 223–245 (2016)
5. Z. Wang, N. Mingo, Diameter dependence of SiGe nanowire thermal conductivity. *Appl. Phys. Lett.* **97**, 101903 (2010)
6. R. Cheaito, J.C. Duda, T.E. Beechem, K. Hattar, J.F. Ihlefeld, D.L. Medlin, M.-A. Rodriguez, M.J. Campion, E.S. Piekos, P.E. Hopkins, Experimental investigation of size effects on the thermal conductivity of silicon-germanium alloy thin films. *Phys. Rev. Lett.* **109**, 195901 (2012)
7. J. Kim, E. Ou, D.P. Sellan, L. Shi, A four-probe thermal transport measurement method for nanostructures. *Rev. Sci. Instrum.* **86**, 044901 (2015). <https://doi.org/10.1063/1.4916547>
8. P.G. Klemens, The scattering of low-frequency lattice waves by static imperfections. *Proc. Phys. Soc. A* **68**, 1113 (1955)
9. F. Schaffler, in *Properties of Advanced Semiconductor Materials GaN, AlN, InN, BN, SiC, SiGe*, eds. by M.E. Levinshtein, S.L. Rumyantsev, M.S. Shur (Wiley, New York, 2001), pp. 149–188
10. W. Li, J. Carrete, N.I. A. Katcho, N. Mingo, ShengBTE: A solver of the Boltzmann transport equation for phonons. *Comput. Phys. Commun.* **185**(6) (2014). <https://doi.org/10.1016/j.cpc.2014.02.015>
11. J. Garg, N. Bonini, B. Kozinsky, N. Marzari, Role of disorder and anharmonicity in the thermal conductivity of Silicon-Germanium alloys: a first-principles study. *Phys. Rev. Lett.* **106**, 045901 (2011)
12. I. Carlomagno, V.A. Cimmelli, D. Jou, Heat flux rectification in graded $\text{Si}_c\text{Ge}_{1-c}$: longitudinal and radial heat flows. *Physica E* **90**, 149–157 (2017)

Expansion of Evolution Matrix and Lyapunov Exponents with Respect to Parameters



Anton O. Belyakov and Alexander P. Seyranian

1 Introduction

Computation of Lyapunov exponents (LEs) has been a topic for incentive study, see [1–5] and references therein. In this chapter, we analyze how approximate methods, such as method of averaging, can be implemented to facilitate the calculation of LE spectra.

This chapter is organized as follows. In the second section, we define LEs. In Sect. 3, we introduce approximate analytic calculation of evolution matrix with the use of averaging scheme that can yield analytical approximations of any order. In the end of the third section, we provide expression for the first-order expansion of LEs. Section 4 contains implementation of averaging to numeric computation of LEs with periodic QR factorization.

2 Definition of LEs

Let us consider the following linearization of a nonlinear system about its solution

$$\dot{p}(t) = \mathbf{J}(t) p(t),$$

A. O. Belyakov (✉)

Moscow School of Economics, Lomonosov Moscow State University, Moscow, Russia
National Research Nuclear University “MEPhI”, Moscow, Russia

Central Economics and Mathematics Institute, Russian Academy of Sciences, Moscow, Russia
e-mail: belyakov@mse-msu.ru

A. P. Seyranian

Institute of Mechanics, Lomonosov Moscow State University, Moscow, Russia
e-mail: seyran@imec.msu.ru

where $p(t) \in \mathbb{R}^n$ is the vector of state variable perturbations and $\mathbf{J}(t)$ is the piecewise continuous, integrable *Jacobian matrix* of the original nonlinear system. Solution of the matrix differential equation with the initial identity matrix

$$\dot{\mathbf{P}}(t) = \mathbf{J}(t) \cdot \mathbf{P}(t), \quad \mathbf{P}(0) = \mathbf{I} \tag{1}$$

yields *evolution matrix* $\mathbf{P}(t)$. LEs are defined as logarithms of eigenvalues of matrix

$$\Lambda = \lim_{t \rightarrow \infty} (\mathbf{P}'(t) \cdot \mathbf{P}(t))^{\frac{1}{2t}},$$

where \mathbf{P}' is the transposed matrix \mathbf{P} , and we assume that the finite limit exists (system is regular).

QR factorization of

$$\mathbf{P}(t) = \mathbf{Q}(t) \cdot \bar{\mathbf{R}}(t) \tag{2}$$

yields orthogonal matrix $\mathbf{Q}(t)$, upper triangular matrix $\bar{\mathbf{R}}(t)$ with positive diagonal elements, and expression for i -th LE as

$$\lambda^{(i)} = \lim_{t \rightarrow \infty} \frac{1}{t} \log |\bar{\mathbf{R}}^{(i,i)}(t)|, \tag{3}$$

where $i = 1, \dots, n$ and $^{(i,i)}$ denotes the i -th diagonal element.

3 Approximate Calculation of Evolution Matrix

We solve problem (1) approximately by the averaging method [6] in [7] assuming that the Jacobian matrix $\mathbf{J}(t)$ can be expanded into the series

$$\mathbf{J}(t) = \mathbf{J}_0(t) + \mathbf{J}_1(t) + \mathbf{J}_2(t) + \dots, \tag{4}$$

with the lower index denoting the order of smallness,¹ and that we know solution $\mathbf{P}_0(t)$ of the matrix initial value problem

$$\dot{\mathbf{P}}_0(t) = \mathbf{J}_0(t) \cdot \mathbf{P}_0(t), \quad \mathbf{P}_0(0) = \mathbf{I}. \tag{5}$$

Then, the change of variable

$$\mathbf{P}(t) = \mathbf{P}_0(t) \cdot \mathbf{Y}(t) \tag{6}$$

¹If $\mathbf{J}(t)$ differs from $\mathbf{J}_0(t)$ due to small change in the vector of parameters Δp , then $\mathbf{J}_1(t) = O(\|\Delta p\|)$, $\mathbf{J}_2(t) = O(\|\Delta p\|^2)$, and so on.

converts (15) into the standard form:

$$\dot{\mathbf{Y}}(t) = \mathbf{H}(t) \cdot \mathbf{Y}(t), \quad \mathbf{Y}(0) = \mathbf{I}, \quad (7)$$

where matrix $\mathbf{H}(t) := \mathbf{P}_0^{-1}(t) \cdot (\mathbf{J}(t) - \mathbf{J}_0(t)) \cdot \mathbf{P}_0(t)$ is small and can be written as

$$\mathbf{H}(t) = \mathbf{H}_1(t) + \mathbf{H}_2(t) + \dots \quad (8)$$

with $\mathbf{H}_j(t) := \mathbf{P}_0^{-1}(t) \cdot \mathbf{J}_j(t) \cdot \mathbf{P}_0(t)$ for all $j \geq 1$.

3.1 Averaging Scheme

Approximate solution of (7) can be found with *averaging method* in the form

$$\mathbf{Y}(t) = (\mathbf{I} + \mathbf{U}_1(t) + \mathbf{U}_2(t) + \dots) \cdot \exp((\mathbf{A}_1 + \mathbf{A}_2 + \dots)t), \quad (9)$$

where $\mathbf{U}_j(t)$ are the matrix functions, such that $\mathbf{U}_j(0) = 0$, $\lim_{t \rightarrow \infty} \frac{\mathbf{U}_j(t)}{t} = 0$. Matrices \mathbf{A}_j and \mathbf{U}_j can be found one by one with the scheme described, e.g., in [7]. The scheme includes substitution of (8) and (9) into (7), grouping terms of the same order of smallness, and solving resulting equations separately for each order. For the first-order approximation, we have $\dot{\mathbf{U}}_1(t) + \mathbf{A}_1 = \mathbf{H}_1(t)$ and we calculate \mathbf{A}_1 as the average of $\mathbf{H}_1(t)$, taking into account that $\mathbf{U}_1(0) = 0$ and $\lim_{t \rightarrow \infty} \frac{\mathbf{U}_1(t)}{t} = 0$:

$$\mathbf{A}_1 = \lim_{T \rightarrow \infty} \frac{1}{T} \int_0^T \mathbf{H}_1(t) dt = \lim_{T \rightarrow \infty} \frac{1}{T} \int_0^T \mathbf{P}_0^{-1}(t) \cdot \mathbf{J}_1(t) \cdot \mathbf{P}_0(t) dt. \quad (10)$$

For the second-order approximation, we have to calculate $\mathbf{U}_1(t)$ from $\dot{\mathbf{U}}_1(t) + \mathbf{A}_1 = \mathbf{H}_1(t)$, taking into account that $\mathbf{U}_1(0) = 0$:

$$\mathbf{U}_1(t) = \int_0^t (\mathbf{H}_1(\tau) - \mathbf{A}_1) d\tau, \quad (11)$$

and then from the equation for the second order $\dot{\mathbf{U}}_2(t) + \mathbf{A}_2 + \mathbf{U}_1(t) \cdot \mathbf{A}_1 = \mathbf{H}_2(t) + \mathbf{H}_1(t) \cdot \mathbf{U}_1(t)$, taking into account that $\mathbf{U}_2(0) = 0$ and $\lim_{t \rightarrow \infty} \frac{\mathbf{U}_2(t)}{t} = 0$, we get

$$\mathbf{A}_2 = \lim_{T \rightarrow \infty} \frac{1}{T} \int_0^T (\mathbf{H}_2(t) + \mathbf{H}_1(t) \cdot \mathbf{U}_1(t) - \mathbf{U}_1(t) \cdot \mathbf{A}_1) dt,$$

with the use of matrix \mathbf{A}_1 already obtained in (23). Similarly for the $n + 1$ -th-order approximation, one can derive that

$$\begin{aligned}
\mathbf{U}_n(t) &= \int_0^t (\mathbf{H}_n(\tau) - \mathbf{A}_n \\
&\quad + \mathbf{H}_{n-1}(\tau) \cdot \mathbf{U}_1(\tau) - \mathbf{U}_1(\tau) \cdot \mathbf{A}_{n-1} \\
&\quad \dots \\
&\quad + \mathbf{H}_1(\tau) \cdot \mathbf{U}_{n-1}(\tau) - \mathbf{U}_{n-1}(\tau) \cdot \mathbf{A}_1) d\tau, \tag{12}
\end{aligned}$$

$$\begin{aligned}
\mathbf{A}_{n+1} &= \lim_{T \rightarrow \infty} \frac{1}{T} \int_0^T (\mathbf{H}_{n+1}(t) \\
&\quad + \mathbf{H}_n(t) \cdot \mathbf{U}_1(t) - \mathbf{U}_1(t) \cdot \mathbf{A}_n \\
&\quad \dots \\
&\quad + \mathbf{H}_1(t) \cdot \mathbf{U}_n(t) - \mathbf{U}_n(t) \cdot \mathbf{A}_1) dt. \tag{13}
\end{aligned}$$

3.2 Expansion of Evolution Matrix

In the first-order approximation, we have from (9)

$$\mathbf{Y}(t) \approx \mathbf{I} + \mathbf{U}_1(t) + \mathbf{A}_1 t = \mathbf{I} + \int_0^t \mathbf{H}_1(\tau) d\tau,$$

where we took into account expression (11). From (6) and $\mathbf{H}_1(t) = \mathbf{P}_0^{-1}(t) \cdot \mathbf{J}_1(t) \cdot \mathbf{P}_0(t)$, we have the expansion of the evolution matrix till the first-order term for a short time scale

$$\mathbf{P}(t) \approx \mathbf{P}_0(t) \cdot \left(\mathbf{I} + \int_0^t \mathbf{P}_0^{-1}(\tau) \cdot \mathbf{J}_1(\tau) \cdot \mathbf{P}_0(\tau) d\tau \right),$$

which could also be valid for all $t \in [0, \infty)$ under additional conditions not assumed here, see, e.g., [6].

3.3 Expansion of LEs

Let us define symmetric matrix $\mathbf{M}(t) := \mathbf{P}'(t) \cdot \mathbf{P}(t)$. Then, we have its expansion $\mathbf{M}(t) = \mathbf{M}_0(t) + \mathbf{M}_1(t) + \dots$, where

$$\begin{aligned}
\mathbf{M}_0(t) &= \mathbf{P}'_0(t) \cdot \mathbf{P}_0(t), \\
\mathbf{M}_1(t) &= \left(\int_0^t \mathbf{P}_0^{-1}(\tau) \cdot \mathbf{J}_1(\tau) \cdot \mathbf{P}_0(\tau) d\tau \right)' \cdot \mathbf{M}_0(t)
\end{aligned}$$

$$+ \mathbf{M}_0(t) \cdot \left(\int_0^t \mathbf{P}_0^{-1}(\tau) \cdot \mathbf{J}_1(\tau) \cdot \mathbf{P}_0(\tau) \, d\tau \right).$$

First two terms of LE expansion $\lambda^{(i)} = \lambda_0^{(i)} + \lambda_1^{(i)} + \dots$ are

$$\lambda_0^{(i)} = \lim_{t \rightarrow \infty} \frac{\log(\mu_i(t))}{2t}$$

and

$$\lambda_1^{(i)} = \lim_{t \rightarrow \infty} \frac{1}{2t} \frac{\mathbf{v}'_i(t) \cdot \mathbf{M}_1(t) \cdot \mathbf{v}_i(t)}{\mu_i(t) (\mathbf{v}'_i(t) \cdot \mathbf{v}_i(t))},$$

where $\mathbf{v}_i(t)$ and $\mu_i(t)$ are the i -th eigenvector and the i -th eigenvalue of matrix $\mathbf{M}_0(t)$ so that

$$\mathbf{M}_0(t) \cdot \mathbf{v}_i(t) = \mathbf{v}_i(t) \mu_i(t).$$

Expression for $\lambda_1^{(i)}$ can be derived with the use of the derivative of LEs in [5], where \mathbf{J}_1 would be the derivative of \mathbf{J} w.r.t. a parameter.²

Notes and Comments The novelty here is in applying the averaging scheme that automatically removes in $\mathbf{M}_1(k)$ higher order terms that may appear in Taylor expansions [5, 8].

4 Calculation of LEs with Periodic QR Factorization

When the largest LE is positive, column vectors in matrix $\mathbf{P}(t)$ undergo exponential growth and become numerically linearly dependent as $t \rightarrow \infty$. That is why QR factorization is done periodically, as in [1], by the Gram–Schmidt algorithm, so that

²When parameters in matrix \mathbf{M} are perturbed $\mathbf{M}_0 \rightarrow \mathbf{M}$, then its eigenvalue $\mu \rightarrow \nu$ and corresponding eigenvector $\mathbf{v} \rightarrow \mathbf{u}$ are also changed, where $(\mathbf{M}_0 - \mathbf{I}\mu) \cdot \mathbf{v} = \mathbf{0}$ and $(\mathbf{M} - \mathbf{I}\nu) \cdot \mathbf{u} = \mathbf{0}$. We can write $\mathbf{v}' \cdot (\mathbf{M}_0 - \mathbf{I}\mu) \cdot \mathbf{v} = 0$ and $\mathbf{v}' \cdot (\mathbf{M} - \mathbf{I}\nu) \cdot \mathbf{u} = 0$. Due to smooth dependence of \mathbf{u} on parameters, we have vector $\mathbf{v} \approx \mathbf{u}$ and scalar $\mathbf{v}' \cdot (\mathbf{M} - \mathbf{I}\nu) \cdot \mathbf{v} \approx \mathbf{v}' \cdot (\mathbf{M} - \mathbf{I}\nu) \cdot \mathbf{u} = 0$. Hence, $\mathbf{v}' \cdot (\mathbf{M} - \mathbf{I}\nu) \cdot \mathbf{v} \approx 0$ yields

$$\nu \approx \frac{\mathbf{v}' \cdot \mathbf{M} \cdot \mathbf{v}}{\mathbf{v}' \cdot \mathbf{v}} = \frac{\mathbf{v}' \cdot (\mathbf{M}_0 + \mathbf{M}_1 + \dots) \cdot \mathbf{v}}{\mathbf{v}' \cdot \mathbf{v}} = \mu + \frac{\mathbf{v}' \cdot \mathbf{M}_1 \cdot \mathbf{v}}{\mathbf{v}' \cdot \mathbf{v}} + \dots,$$

$$\log \nu \approx \log \left(\mu + \frac{\mathbf{v}' \cdot \mathbf{M}_1 \cdot \mathbf{v}}{\mathbf{v}' \cdot \mathbf{v}} \right) = \log \mu + \log \left(1 + \frac{\mathbf{v}' \cdot \mathbf{M}_1 \cdot \mathbf{v}}{\mu \mathbf{v}' \cdot \mathbf{v}} \right) \approx \log \mu + \frac{\mathbf{v}' \cdot \mathbf{M}_1 \cdot \mathbf{v}}{\mu \mathbf{v}' \cdot \mathbf{v}}.$$

$$\mathbf{P}(t) = \mathbf{X}(t) \cdot \mathbf{Q}'(k - 1) \cdot \mathbf{P}(k - 1), \quad t \in (k - 1, k], \quad k = 1, 2, 3, \dots \quad (14)$$

with $\mathbf{X}(t)$ being the solution of the following matrix initial value problem:

$$\dot{\mathbf{X}}(t) = \mathbf{J}(t) \cdot \mathbf{X}(t), \quad \lim_{t \downarrow k-1} \mathbf{X}(t) = \mathbf{Q}(k - 1), \quad (15)$$

where $\mathbf{Q}(0) = \mathbf{P}(0) = \mathbf{I}$, while $\mathbf{Q}(k)$ is the result of Gram–Schmidt orthonormalization of column vectors in matrix $\mathbf{X}(k)$

$$\mathbf{X}(k) = \mathbf{Q}(k) \cdot \mathbf{R}(k), \quad (16)$$

and it is the next initial value (right-sided limit as $t \downarrow k$ meaning $t \rightarrow k + 0$) of matrix function \mathbf{X} . From substitution (16) in (14), we have $\mathbf{P}(k) = \mathbf{Q}(k) \cdot \mathbf{R}(k) \cdot \mathbf{Q}'(k - 1) \cdot \mathbf{P}(k - 1)$ recursion of which yields

$$\mathbf{P}(k) = \mathbf{Q}(k) \cdot \mathbf{R}(k) \cdot \mathbf{R}(k - 1) \cdot \dots \cdot \mathbf{R}(2) \cdot \mathbf{R}(1) = \mathbf{Q}(k) \cdot \prod_{j=k}^1 \mathbf{R}(j).$$

It follows from (2) that $\bar{\mathbf{R}}(k) = \prod_{j=k}^1 \mathbf{R}(j)$. Because $\mathbf{R}(k)$ is upper triangular, we have LE in (3) as

$$\lambda^{(i)} = \lim_{K \rightarrow \infty} \frac{1}{K} \sum_{k=1}^K \log \mathbf{R}^{(i,i)}(k). \quad (17)$$

4.1 Approximate Calculations of $\mathbf{X}(k)$

We solve problem (15) approximately by the averaging method [6] in [7] assuming that the Jacobian matrix $\mathbf{J}(t)$ can be expanded into the series (4) and that we know solution $\mathbf{X}_0(t)$ of the matrix initial value problem for $t \in (k - 1, k]$ with $k = 1, 2, 3, \dots$

$$\dot{\mathbf{X}}_0(t) = \mathbf{J}_0(t) \cdot \mathbf{X}_0(t), \quad \lim_{t \downarrow k-1} \mathbf{X}_0(t) = \mathbf{Q}_0(k - 1), \quad (18)$$

where $\mathbf{Q}_0(0) = \mathbf{I}$. Then the change of variable

$$\mathbf{X}(t) = \mathbf{X}_0(t) \cdot \mathbf{Y}(t) \quad (19)$$

converts (15) into the standard form:

$$\dot{\mathbf{Y}}(t) = \mathbf{H}(t) \cdot \mathbf{Y}(t), \quad \lim_{t \downarrow k-1} \mathbf{Y}(t) = \mathbf{I}, \quad (20)$$

where matrix $\mathbf{H}(t) := \mathbf{X}_0^{-1}(t) \cdot (\mathbf{J}(t) - \mathbf{J}_0(t)) \cdot \mathbf{X}_0(t)$ is small and can be written as

$$\mathbf{H}(t) = \mathbf{H}_1(t) + \mathbf{H}_2(t) + \dots \tag{21}$$

with $\mathbf{H}_j(t) := \mathbf{X}_0^{-1}(t) \cdot \mathbf{J}_j(t) \cdot \mathbf{X}_0(t)$ for all $j \geq 1$.

4.2 Averaging Scheme

Approximate solution of (20) for $t \in (k - 1, k]$ can be found with *averaging method* in the form

$$\mathbf{Y}(t) = (\mathbf{I} + \mathbf{U}_1(t) + \mathbf{U}_2(t) + \dots) \cdot \exp((\mathbf{A}_1(k) + \mathbf{A}_2(k) + \dots)(t - k + 1)), \tag{22}$$

where $\mathbf{U}_j(t)$ are the matrix functions, such that $\mathbf{U}_j(k) = \lim_{t \downarrow k-1} \mathbf{U}_j(t) = 0$. Matrices \mathbf{A}_j and \mathbf{U}_j can be found one by one with the scheme described, e.g., in [7]. The scheme includes substitution of (21) and (22) into (20), grouping terms of the same order of smallness, and solving resulting equations separately for each order. For the first-order approximation, we have $\dot{\mathbf{U}}_1(t) + \mathbf{A}_1(k) = \mathbf{H}_1(t)$, and we calculate \mathbf{A}_1 as the average of $\mathbf{H}_1(t)$, taking into account that $\mathbf{U}_1(k) = \lim_{t \downarrow k-1} \mathbf{U}_1(t) = 0$:

$$\mathbf{A}_1(k) = \int_{k-1}^k \mathbf{H}_1(t) dt = \int_{k-1}^k \mathbf{X}_0^{-1}(t) \cdot \mathbf{J}_1(t) \cdot \mathbf{X}_0(t) dt. \tag{23}$$

For the second-order approximation, we have to calculate $\mathbf{U}_1(t)$ from $\dot{\mathbf{U}}_1(t) + \mathbf{A}_1(k) = \mathbf{H}_1(t)$, taking into account that $\lim_{t \downarrow k-1} \mathbf{U}_1(t) = 0$:

$$\mathbf{U}_1(t) = \int_{k-1}^t (\mathbf{H}_1(\tau) - \mathbf{A}_1(k)) d\tau,$$

and then from the equation for the second order $\dot{\mathbf{U}}_2(t) + \mathbf{A}_2(k) + \mathbf{U}_1(t) \cdot \mathbf{A}_1(k) = \mathbf{H}_2(t) + \mathbf{H}_1(t) \cdot \mathbf{U}_1(t)$, taking into account that $\mathbf{U}_2(k) = \lim_{t \downarrow k-1} \mathbf{U}_2(t) = 0$, we get

$$\mathbf{A}_2(k) = \int_{k-1}^k (\mathbf{H}_2(t) + \mathbf{H}_1(t) \cdot \mathbf{U}_1(t) - \mathbf{U}_1(t) \cdot \mathbf{A}_1(k)) dt,$$

with the use of matrix \mathbf{A}_1 obtained in (23). Similarly for the $n + 1$ -th-order approximation, one can derive that

$$\begin{aligned}
\mathbf{U}_n(t) = & \int_{k-1}^t (\mathbf{H}_n(\tau) - \mathbf{A}_n(k) \\
& + \mathbf{H}_{n-1}(\tau) \cdot \mathbf{U}_1(\tau) - \mathbf{U}_1(\tau) \cdot \mathbf{A}_{n-1}(k) \\
& \dots \\
& + \mathbf{H}_1(\tau) \cdot \mathbf{U}_{n-1}(\tau) - \mathbf{U}_{n-1}(\tau) \cdot \mathbf{A}_1(k)) d\tau, \tag{24}
\end{aligned}$$

$$\begin{aligned}
\mathbf{A}_{n+1} = & \int_{k-1}^k (\mathbf{H}_{n+1}(t) \\
& + \mathbf{H}_n(t) \cdot \mathbf{U}_1(t) - \mathbf{U}_1(t) \cdot \mathbf{A}_n(k) \\
& \dots \\
& + \mathbf{H}_1(t) \cdot \mathbf{U}_n(t) - \mathbf{U}_n(t) \cdot \mathbf{A}_1(k)) dt. \tag{25}
\end{aligned}$$

Thus, (19) and (22) yield $\mathbf{X}(k) = \mathbf{X}_0(k) \cdot \exp(\mathbf{A}_1(k) + \mathbf{A}_2(k) + \dots)$.

4.3 Calculations of LEs

We expand the matrix-valued exponential function as follows:

$$\begin{aligned}
\mathbf{X}(k) = & \mathbf{X}_0(k) \cdot (\mathbf{I} + \mathbf{A}_1(k)) \\
& + \mathbf{X}_0(k) \cdot \left(\mathbf{A}_2(k) + \frac{1}{2}(\mathbf{A}_1(k))^2 \right) \\
& + \mathbf{X}_0(k) \cdot \left(\mathbf{A}_3(k) + \frac{1}{2}(\mathbf{A}_1(k)\mathbf{A}_2(k) + \mathbf{A}_2(k)\mathbf{A}_1(k)) + \frac{1}{6}(\mathbf{A}_1(k))^3 \right) \\
& + \dots
\end{aligned}$$

up to the required order of smallness. For example, the first-order approximation with the use of (23) takes the form

$$\mathbf{X}(k) \approx \mathbf{X}_0(k) \cdot \left(\mathbf{I} + \int_{k-1}^k \mathbf{X}_0^{-1}(\tau) \cdot \mathbf{J}_1(\tau) \cdot \mathbf{X}_0(\tau) d\tau \right). \tag{26}$$

Then, we make QR factorizations in (16) and calculate LEs via (17). Such approximate calculation could be numerically more robust than direct numerical solutions of (15), especially when $\mathbf{J}_1(\tau)$ is not smooth in time.

Notes and Comments In this section, we propose integration (26) based on known \mathbf{X}_0 instead of direct solution of matrix differential equation (15), since the latter can involve numerical issues.

5 Conclusions

We show the ways in which the method of averaging can be implemented for the calculation of LEs. The method of averaging gives analytic expansions of LEs w.r.t. parameters, and it can be useful in analysis of system dynamics facilitating numerical calculations. For investigation of the effectiveness of such approach, thorough numerical experiments are to be carried out.

Acknowledgments This work was supported by Russian Science Foundation, grant 19-11-00223.

References

1. G. Benettin, L. Galgani, A. Giorgilli, J.M. Strelcyn, Lyapunov exponents for smooth dynamical systems and for Hamiltonian systems: A method for computing all of them. *Meccanica* **15**, 9–20 (1980)
2. L. Dieci, C. Elia, SVD algorithms to approximate spectra of dynamical systems. *Math. Comput. Simul.* **79**(4), 1235–1254 (2008)
3. K. Ramasubramanian, M.S. Sriram, A comparative study of computation of Lyapunov spectra with different algorithms. *Physica D: Nonlinear Phenomena* **139**(1–2), 72–86 (2000)
4. A. Dabrowski, Estimation of the largest Lyapunov exponent-like (LLEL) stability measure parameter from the perturbation vector and its derivative dot product (part 2) experiment simulation. *Nonlinear Dyn.* **78**(3), 1601–1608 (2014)
5. A.P. Seyranian, Derivatives of an evolution matrix and Lyapunov exponents with respect to parameters. *Rep. NAS RA* **119**(4), 306–314 (2019)
6. N.N. Bogoliubov, Y.A. Mitropolsky, *Asymptotic Methods in the Theory of Non-Linear Oscillations* (Gordon and Breach, New York, 1961)
7. A.O. Belyakov, A.P. Seyranian, Stability Boundary Approximation of Periodic Dynamics, in *Nonlinear Dynamics of Structures, Systems and Devices* (2020), pp. 13–23. https://doi.org/10.1007/978-3-030-34713-0_2
8. A.P. Seyranian, A.A. Mailybaev, *Multiparameter Stability Theory with Mechanical Applications* (World Scientific, New Jersey, 2003)

Classification of a Family of Lorenz Knots with Reducible Symbolic Sequences



P. Gomes, N. Franco, and L. Silva

1 Introduction

Lorenz knots are the closed (periodic) orbits of the famous system of ODEs studied by E. N. Lorenz in [1]. *Lorenz links* are finite collections of (possibly linked) Lorenz knots.

In [2], Williams introduced a geometric model for the dynamics of the Lorenz system, which, together with Birman, he used to investigate Lorenz knots and links in [3]. The model, known as the *Lorenz template*, is a branched 2-manifold with an expanding semi-flow (Fig. 1). Tucker proved in [4] that Lorenz links are equivalent to links on the Lorenz template.

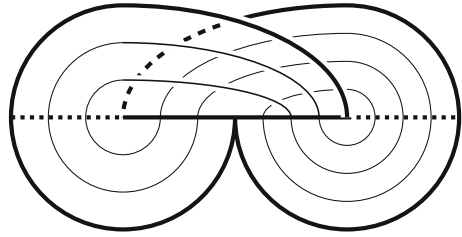
A torus knot is a closed curve on the surface of an unknotted torus T^2 . It is denoted by $T(p, q)$ where p and q are the number of times that it crosses a meridian and a longitude, respectively. Birman and Williams proved in [3] that all torus knots are Lorenz knots.

P. Gomes
Departmental Area of Mathematics, ISEL—Lisbon Superior Engineering Institute, Lisboa,
Portugal
e-mail: paulo.gomes@isel.pt

N. Franco
Department of Mathematics, University of Évora, Évora, Portugal
CIMA, Research Centre for Mathematics and Applications, Évora, Portugal
e-mail: nmf@uevora.pt

L. Silva (✉)
Departmental Area of Mathematics, ISEL—Lisbon Superior Engineering Institute, Lisboa,
Portugal
CIMA, Research Centre for Mathematics and Applications, Évora, Portugal
e-mail: luis.silva@isel.pt

Fig. 1 The Lorenz template with a Lorenz knot



A satellite knot is built by taking two nontrivial knots P (the pattern), contained in a solid unknotted torus T and not contained in a 3-ball in T , and C (the companion). The satellite knot is the image of P under an homeomorphism that takes the core of T onto C .

A knot is hyperbolic if its complement in S^3 is a hyperbolic 3-manifold. Thurston, in [5, 6], proved that a knot is hyperbolic *iff* it is neither a satellite knot nor a torus knot. In [7], Birman and Kofman observed that more than half of the hyperbolic knots whose complements can be constructed from seven or fewer ideal tetrahedra are Lorenz knots. However, Lorenz knots are rather scarce in tables of knots indexed by crossings (from the 1701936 prime knots having projections with less than 17 crossings, only 20 are Lorenz).

One of the goals of the study of Lorenz knots is their classification as *hyperbolic* or *non-hyperbolic*, possibly further distinguishing torus knots from satellites.

In [8], Dehornoy presents the following conjecture attributed to Morton:

Conjecture 1 (Morton) Every Lorenz satellite knot is a cable on a Lorenz knot, where a cable means a satellite where the pattern is a torus knot.

For our purposes, it is enough to assume a weaker form of this conjecture:

Conjecture 2 Every Lorenz satellite knot is a satellite of a Lorenz knot.

Birman and Williams showed in [3] that the satellites obtained as certain cables of Lorenz knots are also Lorenz knots. This was extended by El-Rifai,[9], who showed that the only way in which a Lorenz knot can be presented as the satellite of a Lorenz knot is if it is a cable on a Lorenz knot, possibly with additional twisting.

In [10], we derived an algorithm, based on [9], to obtain Lorenz satellite braids and their corresponding sequences from symbolic dynamics. This was a question raised by Birman in [11].

The horizontal solid line in Fig. 1 is designated as the *branch line* of the Lorenz template. Mapping the branch line onto $[-1, 1]$, the semi-flow's first return map f is a one-dimensional map from $[-1, 1] \setminus \{0\}$ onto $[-1, 1]$, with one discontinuity at 0 and strictly increasing and surjective in $[-1, 0[$ and $]0, 1]$. This map is called the *Lorenz map*.

Symbolic dynamics of the Lorenz map codify Lorenz knots, since the closed orbits in the semi-flow correspond to periodic orbits of the map. In [12], we introduced a geometric operation on Lorenz knots corresponding to the $*$ -product

defined in [12]. From [3, 13], we deduce that irreducible sequences with respect to the $*$ -product correspond to torus knots, so this geometric operation is a natural way of generating non-torus Lorenz knots.

In this chapter, we study an infinite family of Lorenz knots generated through $*$ -products that contains some of the hyperbolic Lorenz knots listed by Birman and Kofman in [7]. We prove that all these knots are not torus knots and that if the weaker form of Morton’s conjecture is true then they are not satellites either. We conclude that if the weaker form of Morton’s conjecture is true then all the knots from this family are hyperbolic.

2 Symbolic Dynamics

To each point $x \in [-1, 1]$, we associate its *symbolic address*, $ad(x) = L, 0, R$ accordingly, respectively, when $x < 0, x = 0$, or $x > 0$. Let $f^j = f \circ f^{j-1}$ be the j -th iterate of the Lorenz map f . The *itinerary* of a point x under f is the sequence of symbolic addresses $(i_f(x))_j = ad(x), ad(f(x)), ad(f^2(x)), \dots, ad(f^n(x))$, where $n \leq +\infty$ is the minimum index such that $f^n(x) = 0$. The *length* $|X|$ of $X = X_0 \dots X_{n-1}0$ is n . Fixing $L < 0 < R$, we induce the lexicographic order in the set Σ of sequences $X_0 \dots X_n$ such that $X_k \in \{L, R\}$ for all $k < n$ and $X_n = 0$ if $n < +\infty$.

Consider the shift map $s : \Sigma \setminus \{0\} \rightarrow \Sigma$.

Definition 1 A sequence $X \in \Sigma$ is *L-maximal* if $X_0 = L$ and for $k > 0, X_k = L \Rightarrow s^k(X) \leq X$, and *R-minimal* if $X_0 = R$ and for $k > 0, X_k = R \Rightarrow X \leq s^k(X)$.

It is straightforward to prove that a periodic word $(X_0 \dots X_{n-1})^\infty$ with least period n is *L-maximal* (resp. *R-minimal*) if and only if $X_0 \dots X_{n-1}0$ is *L-maximal* (resp. *R-minimal*). So there is a bijective correspondence between the *L-maximal* (resp. *R-minimal*) finite words and the cyclic permutation classes of periodic words.

Generalized Lorenz maps are boundary anchored maps, $g : [-1, 1] \setminus \{0\} \rightarrow [-1, 1]$, with one single discontinuity at 0, increasing in $[-1, 0[$ and in $]0, 1]$, not necessarily onto. These maps generate sub-Lorenz templates, see [14, 15], where all knots are Lorenz knots. The combinatorics of a generalized Lorenz map g are determined by the pair (X, Y) , where $X = Li_g(g(0^-))$ and $Y = Ri_g(g(0^+))$ are the critical itineraries.

For a pair of finite critical itineraries $(X, Y) \in \Sigma \times \Sigma$ and a word $S \in \Sigma$, define the $*$ -product $(X, Y) * S = \overline{S_0} \dots \overline{S_{|S|-1}}0$, where $\overline{S_j} = X_0 \dots X_{|X|-1}$ if $S_j = L$ and $\overline{S_j} = Y_0 \dots Y_{|Y|-1}$ if $S_j = R$.

The words $(X, Y) * S$ are the itineraries of points in the renormalization intervals of renormalizable Lorenz maps, and in [12], we studied the structure of their Lorenz knots as a geometric construction. From [3, 13], torus knots correspond to irreducible words with respect to the $*$ -product. Consequently, the hyperbolic and satellite Lorenz knots are generated by the $*$ -product through this geometric construction.

3 Lorenz Braids

Every knot and link on the Lorenz template is the closure of a *Lorenz braid*, obtained by cutting the template along the dotted lines in Fig. 1. A Lorenz braid has $n = p + q$ strings, where the p left strings cross over at least one of the q right strings, with no crossings between strings in each subset.

Each Lorenz braid has an associated permutation π that has k cycles iff the closure is a link with k components. Consequently, the braid's closure is a knot iff π has only one cycle.

For a finite sequence W , $n_L(W)$ and $n_R(W)$ denote, respectively, the number of symbols L and symbols R in W . If $W = (W_0 \dots W_{n-1})^\infty$ has least period n , then $n_L(W) = n_L(W_0 \dots W_{n-1})$ and $n_R(W) = n_R(W_0 \dots W_{n-1})$.

Given any periodic sequence W with least period n , we construct a Lorenz braid, whose closure is a Lorenz knot, on the following way, see Fig. 2: order the sequences $s(W), s^2(W), \dots, s^n(W) = W$ and associate them to startpoints, on the upper line, and endpoints, on the lower line, with points corresponding to words starting with L lying on the left half and points corresponding to words starting with R on the right half of each line. Now each string in the braid connects the startpoint corresponding to $s^k(W)$ to the endpoint corresponding to $s^{k+1}(W)$, such that all crossings are positive (the strings with startpoint on the left cross over the others).

We identify a periodic sequence $W = (W_0 \dots W_{n-1})^\infty$, by $W = W_0 \dots W_{n-1}$.

The *crossing number* of a knot K is the smallest number of crossings in any diagram of K . The *braid index* of a knot K is the smallest number of strings among braids whose closure is K . The *genus* of a link L , $g(L)$, is the minimal genus over all orientable surfaces S such that $\partial S = L$, where ∂S is the oriented boundary.

A *syllable* of a sequence is a subsequence of type $L^a R^b$ with maximal length.

The *trip number*, t , of a periodic sequence W with least period n is the smallest number of syllables of all its subsequences with length n .

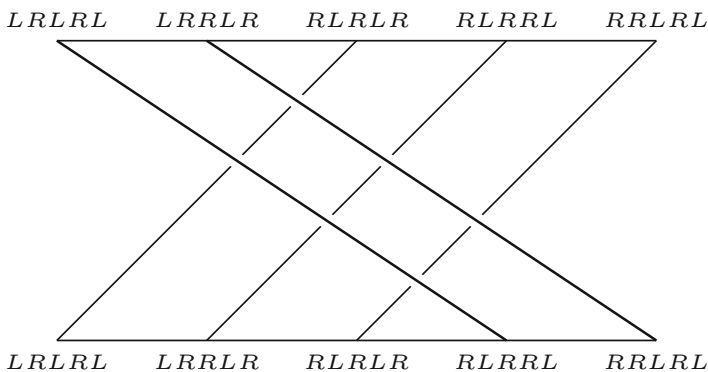


Fig. 2 Lorenz braid corresponding to $X = (LRRLR)^\infty$

Theorem 1 (Franks and Williams [16]) *Let K be a Lorenz knot with periodic word W ; then the braid index of K is equal to the trip number of W .*

The linking number $l(X, Y)$ of the link associated to (X, Y) is the number of crossings between strings from the braids corresponding to X and to Y .

Let X, Y be the two finite words corresponding to Lorenz knots and (X, Y) to a Lorenz link. Denote the Lorenz braid associated to $X (Y)$ by $\beta_X (\beta_Y)$. Identifying X and Y with the corresponding periodic words, for $Z \in \{X, Y\}$, define $L_Z = \{s^i(Z) : 0 \leq i < |Z| \text{ and } Z_i = L\}$ and $R_Z = \{s^i(Z) : 0 \leq i < |Z| \text{ and } Z_i = R\}$.

Let the images of these sets under the shift operator, ordered lexicographically, be, respectively, $s(L_Z)$ and $s(R_Z)$. Let $1 \leq i \leq n_L(X)$ ($1 \leq j \leq n_L(Y)$) be the position of each sequence in $s(L_X)$ ($s(L_Y)$). Finally, consider the ordered sets $s(L_X) \cup s(R_Y)$ and $s(L_Y) \cup s(R_X)$. Let $n_i, i = 1, \dots, n_L(X)$ be the position of the i th element of $s(L_X)$ in $s(L_X) \cup s(R_Y)$ and $m_j, j = 1, \dots, n_L(Y)$ the position of the j th element of $s(L_Y)$ in $s(L_Y) \cup s(R_X)$.

Lemma 1 *The linking number $l(X, Y)$ of the Lorenz link (X, Y) is given by $l(X, Y) = \sum_{i=1}^{n_L(X)} (n_i - i) + \sum_{j=1}^{n_L(Y)} (m_j - j)$, where n_i and m_j are defined as above.*

Proof The i th L string from β_X crosses over all the R strings from β_Y that have endpoints in the range $1, \dots, n_i - 1$. Since $i - 1$ L strings from X are also in this range, the i th L string from X crosses exactly $n_i - i$ R strings from Y . The total number of crossings between L strings of X and R strings of Y is therefore $\sum_{i=1}^{n_L(X)} (n_i - i)$. The same argument applies to the crossings between L strings of Y and R strings of X , so that the total number of crossings between these strings is $\sum_{j=1}^{n_L(Y)} (m_j - j)$. The linking number $l(X, Y)$ is therefore $\sum_{i=1}^{n_L(X)} (n_i - i) + \sum_{j=1}^{n_L(Y)} (m_j - j)$.

4 A Family of Lorenz Knots Defined by a $*$ -product

We will now classify the Lorenz knots corresponding to sequences of type

$$\left(LRL^k 0, RL^{k+2} (RL^{k+1})^n 0 \right) * LRL^m 0, \quad k, n > 0, \quad m \geq 0.$$

This family contains the knots $k4_3, k4_4, k5_5, k5_{14}, k6_5, k6_{11}, k6_{14}, k6_{17}, k7_{27}, k7_{30}, k7_{34}, k7_{37}$, and $k7_{63}$ from the list elaborated by Birman and Kofman in [7]. From now on, we will refer to these family of knots as *Family 0*.

Theorem 2 *Lorenz knots from Family 0 are not torus knots.*

Proof We compute the trip number and genus for the knots of Family 0 and show that there is no torus knot with the same pair of invariants.

From Prop. 5 of [12], with $X = LRL^k 0, Y = RL^{k+2} (RL^{k+1})^n 0, S = LRL^m 0,$

$$t((X, Y) * S) = n_L(S)t(X) + n_R(S)t(Y) = (m + 1) + (n + 1) = n + m + 2. \quad (1)$$

The genus g is computed from $2g = c - n + 1$ [3], where n is the string index and c is the number of crossings of a braid representative given by Lemma 2 of [12]

$$c((X, Y) * S) = c(X)n_L(S)^2 + c(Y)n_R(S)^2 + l(X, Y)n_L(S)n_R(S) - c(S).$$

Since the knots associated to X and S are trivial and Y is a torus knot,

$$\begin{aligned} c(X) &= n_L(X)n_R(X) = k + 1 \\ c(Y) &= n_L(Y)n_R(Y) = (k + 2 + n(k + 1))(n + 1) \\ c(S) &= n_L(S)n_R(S) = m + 1. \end{aligned}$$

To compute $l(X, Y)$, we use Lemma 1 above. We start by determining the number of crossings between the L strings of β_X and the R strings of β_Y :

$$\begin{aligned} s(L_X) &= \{L^k RL, L^{k-1} RL^2, \dots, LRL^k, RL^{k+1}\} \\ s(R_Y) &= \{L^{k+2}(RL^{k+1})^n R, L^{k+1}(RL^{k+1})^{n-1} RL^{k+2} R, \dots, \\ &\quad L^{k+1}(RL^{k+1})RL^{k+2}(RL^{k+1})^{n-2} R, L^{k+1} RL^{k+2}(RL^{k+1})^{n-1} R\}. \end{aligned}$$

All words in $s(R_Y)$ precede all words in $s(L_X)$; therefore, $n_i - i = n_R(Y) = n + 1$, $i = 1, \dots, k + 1$, and $\sum_{i=1}^{n_L(X)} (n_i - i) = (k + 1)(n + 1)$.

The crossings between the L strings of β_Y and the R strings of β_X are given by

$$\begin{aligned} s(L_Y) &= \{L^{k+1}(RL^{k+1})^n RL, L^k(RL^{k+1})^n RL^2, \dots, \\ &\quad L(RL^{k+1})^n RL^{k+1}, (RL^{k+1})^n RL^{k+2}, \\ &\quad L^k(RL^{k+1})^{n-1} RL^{k+2} RL, \dots, L(RL^{k+1})^{n-1} RL^{k+2} RL^k, \\ &\quad (RL^{k+1})^{n-1} RL^{k+2} RL^{k+1}, \dots, \\ &\quad L^k RL^{k+1} RL^{k+2}(RL^{k+1})^{n-2} RL, \dots, LRL^{k+1} RL^{k+2}(RL^{k+1})^{n-2} RL^k, \\ &\quad RL^{k+1} RL^{k+2}(RL^{k+1})^{n-1}, \\ &\quad L^k RL^{k+2}(RL^{k+1})^{n-1} RL, \dots, LRL^{k+2}(RL^{k+1})^{n-1} RL^k, \\ &\quad RL^{k+2}(RL^{k+1})^{n-1} RL^k\} \\ s(R_X) &= \{L^{k+1} R\}. \end{aligned}$$

The single word $L^{k+1}R$ in $s(R_X)$ precedes all the words in $s(L_Y)$ except the first, since $L^{k+1}(RL^{k+1})^n RL < L^{k+1}R$. We thus have $m_1 = 1$, $m_j = j + 1$, for $j = 2, \dots, n_L(Y) = (k + 1)(n + 1) + 1$ and $\sum_{j=1}^{n_L(Y)} (m_j - j) = (k + 1)(n + 1)$.

The linking number is therefore given by

$$l\left(LRL^k, RL^{k+2}(RL^{k+1})^n\right) = 2(k + 1)(n + 1)$$

, and the number of crossings of the Lorenz braids corresponding to the knots in Family 0 is

$$\begin{aligned} c((X, Y) * S) &= (k + 1)(m + 1)^2 + (n + 1)((k + 1)(n + 1) + 1) + \\ &\quad + 2(k + 1)(n + 1)(m + 1) - (m + 1) \tag{2} \\ &= (k + 1)(m + n + 2)^2 + n - m. \end{aligned}$$

The string index is $n((X, Y) * S) = (m + 1)(k + 2) + (n + 1)(k + 2) + 1$, and therefore, finally, the genus is given by

$$\begin{aligned} 2g &= (k + 1)(m + n + 2)^2 + n - m - (k + 2)(m + n + 2) \tag{3} \\ &= (k + 1)(m + n + 2)(m + n + 1) - 2(m + 1) \end{aligned}$$

The braid index (trip number) and genus of a torus knot $T(p, q)$, $1 < p < q$, p, q relatively prime, are given by $t = p$, $2g = (p - 1)(q - 1)$. So, if there is a torus knot with the same trip number and genus as a knot in this family, then

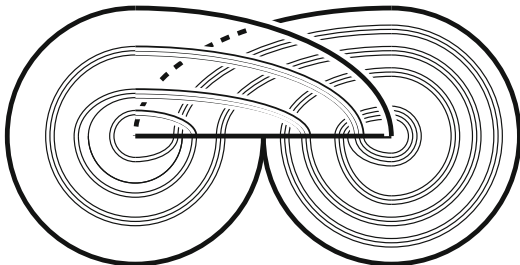
$$p = m + n + 2 \text{ and } (p - 1)(q - 1) = (k + 1)(m + n + 2)(m + n + 1) - 2(m + 1). \tag{4}$$

We will now show that there are no integers $k > 0, n > 0, m \geq 0$, and p, q satisfying the conditions above. Given $k, n > 0, m \geq 0$, assume there are p, q relatively prime, $1 < p < q$ satisfying 4. Then, $(p - 1)(q - 1) = (k + 1)p(p - 1) - 2(m + 1)$, so $(p - 1)(p(k + 1) - (q - 1)) = 2(m + 1)$ and $(p - 1) = m + n + 1$ must divide $2(m + 1)$. Since $(p - 1) > 0, 2(m + 1) > 0$, and $m + n > 1$, this means that there is an integer $\alpha > 0$ such that $2(m + 1) = \alpha(m + n + 1)$. This is equivalent to $(2 - \alpha)(m + 1) = \alpha(n + 1) - 2$. Since for $n > 0$ the second member is positive, $\alpha < 2$, so $\alpha = 1$ and $2(m + 1) = m + n + 1$, that is, $n = m + 1$.

From Eq. (4), $p = 2m + 3$ so $(p - 1)(q - 1) = (k + 1)p(p - 1) - (p - 1)$ and $q = (k + 1)p$, so p, q would not be relatively prime. Since there is no torus knot with the same braid index and genus as in Family 0, the proof is concluded.

El-Rifai, [9, 17], generalized a result from Birman and Williams, [3], obtaining the following theorem.

Fig. 3 Lorenz satellite knot



Theorem 3 (El-Rifai [17]) *The only way in which a Lorenz knot can be presented as a satellite of a Lorenz knot is when the pattern is a generalized k -twisted Lorenz knot, where k is the number of crossings in the Lorenz braid of the companion knot.*

Figure 1 shows the (torus) knot corresponding to the symbolic word $LRRLR$ on the Lorenz template. In Fig. 3, we exemplify El-Rifai’s construction of a satellite knot taking as companion the knot in Fig. 1.

In [10], we derived an algorithm, based on the work of El-Rifai, to obtain Lorenz satellite braids and their corresponding words. Using this algorithm, presented below, and Conjecture 2, we provide a criterion to decide whether a Lorenz knot is a satellite knot.

Definition 2 Let β be a Lorenz n -braid that closes to a knot and W the symbolic word associated to β . Consider the $n_L(W)$ L -started words in the orbit $s(W), \dots, s^n(W) = W$ of W , labeled as $l_1, \dots, l_{n_L(W)}$, and the $n_R(W)$ words starting with R labeled as $r_1, \dots, r_{n_R(W)}$, so that, under lexicographic order, $l_1 < \dots < l_{n_L(W)} < r_1 < \dots < r_{n_R(W)}$. The L -permutation associated to β , π_L^β , is defined on the L -points of β by $\pi_L^\beta(i) = j$ if l_j is the first L -started word in the orbit $s(l_i), \dots, s^n(l_i)$, for $i = 1, \dots, n_L(W)$. The R -permutation π_R^β on the R -points is likewise defined by $\pi_R^\beta(i) = j$ if r_j is the first R -started word in the orbit $s(r_i), \dots, s^n(r_i)$, for $i = 1, \dots, n_R(W)$.

Maps π_L^β and π_R^β are the first return maps of the shift map to the sets of L -started and R -started words, respectively.

Given three Lorenz braids α, β , and γ , all of them closing to knots, let π_R^α be the R -permutation of α and π_L^β be the L -permutation of β as in Definition 2. Let W_α, W_β and W_γ be symbolic words corresponding, respectively, to braids α, β , and γ . Let l_i and r_i be the words defined in Definition 2.

For W_β , define $m_R(i)$ as the number of R symbols between the first and second L in l_i , and $m_R(i) = 0$ whenever there are two consecutive L symbols, for $i = 1, \dots, k$. Likewise, for W_α , $m_L(i)$ will be the number of L symbols between the first and second R symbols in r_i , and $m_L(i) = 0$ if the first R is immediately followed by another R , for $i = 1, \dots, k$. To simplify the notation, we will write π_R for π_R^α and π_L for π_L^β .

Definition 3 Given a periodic word $W = (W_0 \dots W_{n-1})^\infty$ with minimal period n , we say that M is the maximal position if $s^M(W)$ is L -maximal and m is the minimal position if $s^m(W)$ is R -minimal.

The following algorithm returns the word W_δ corresponding to the satellite braid δ constructed from α , β , and γ through the procedure presented in [10]:

Algorithm 1

Input: Three periodic words $W_\alpha, W_\beta, W_\gamma$ with $n_R(W_\alpha) = n_L(W_\beta) = k$.

1. For $i = 1, \dots, k, W^i = W_\gamma$.
2. $j_1 = k$; insert $R^{m_R(j_1)}$ in W^1 immediately after its maximal position.
 $j_2 = \pi_L(j_1)$; insert $L^{m_L(j_2)}$ in W^1 immediately after its minimal position.
3. For $i = 2, \dots, k$:

$j_{2i-1} = \pi_R(j_{2i-2})$; insert $R^{m_R(j_{2i-1})}$ in W^i immediately after its maximal position.

$j_{2i} = \pi_L(j_{2i-1})$; insert $L^{m_L(j_{2i})}$ in W^i immediately after its minimal position.

4. $W_\delta = W^1 W^2 \dots W^k$

Output: The word W_δ , in L -maximal form, associated to the braid δ of the satellite knot generated through El-Rifai's construction with companion γ , left pattern α , and right pattern β , see [10].

Proposition 1 *If the satellite braid constructed as above from Lorenz braids α, β , and γ represents a knot, then its aperiodic word is obtained by the preceding algorithm.*

Theorem 4 *If Conjecture 2 is true, then Lorenz knots from Family 0 are not satellites.*

Proof Assuming Conjecture 1 or its weaker version 2 is true, if the knots associated to the words in the family were satellites, then they would have to be generated by Algorithm 1. The words in the family have the form

$$\left(LRL^k 0, RL^{k+2} (RL^{k+1})^n 0 \right) * LRL^m 0 = LRL^k RL^{k+2} (RL^{k+1})^n (LRL^k)^m 0 \tag{5}$$

with trip number $t = m + n + 2$. If a word W in this family could be generated by the algorithm above, there would be at least one pair of positive integers $1 < u, v < m + n + 2$ such that $t = uv$ and $W = W^1 \dots W^v$ where the trip number of each subword is $t(W^i) = u, i = 1, \dots, v$. Because each syllable in W (and each of the W^i) has only one R symbol, the satellite construction would have to be done with only two words and their corresponding Lorenz braids: a word W_C corresponding to the companion with trip number u , and a word W_A with v R symbols, corresponding to the left α braid. Notice that, under these conditions, the effect of the algorithm is to possibly add L symbols to a single syllable of each W^i (containing the minimal

position). Each W^i would thus differ from W_C only in the number of L symbols after the minimal position.

First take $u = 2$ (assuming $m+n$ even). Then, from Eq. (5) and the considerations above, we conclude that the first subword W^1 must have the form $W^1 = LRL^k RL^{k+1}$, while the last subword W^v ($v = \frac{m+n}{2} + 1 > 1$) must have one of the forms $W^v = LRL^{k+1} RL^{k+1}$ ($m = 0$) or $W^v = LRL^{k+2} RL^k$ ($m = 1$) or $W^v = LRL^{k+1} RL^k$ ($m > 1$). It is impossible to generate W^1 and any of the versions of W^v from the same 2-syllable word W by adding L symbols to a single syllable; therefore, no word of this family can be generated by the satellite construction algorithm starting from a 2-syllable word.

Suppose $u > 2$. Then, the first subword must have the form $W^1 = LRL^k RL^{k+2} R \dots$, and the last subword must have one of the forms $W^v = LRL^{k+1} RL^{k+1} R \dots$ or $W^v = LRL^{k+1} RL^{k+2} R \dots$ or $W^v = LRL^{k+2} RL^{k+1} R \dots$.

Again, W^1 and W^v cannot be generated from the same u -syllable word ($u > 3$).

Therefore, the words in family 0 cannot be generated by the satellite construction algorithm, and, assuming Conjecture 2 to be true, the knots associated to these words are not satellites.

Theorem 5 *If Conjecture 2 is true, then Lorenz knots from Family 0 are hyperbolic.*

Proof The knots in the family are not torus knots, by Theorem 2, and not satellite knots by Theorem 4. Thurston's theorem [5] implies that they are hyperbolic.

References

1. E. Lorenz, Deterministic non-periodic flow. *J. Atmos. Sci.* **20**, 130–141 (1963)
2. R. Williams, The structure of Lorenz attractors. *Publ. Math. I.H.E.S.* **50**, 73–99 (1979)
3. J. Birman, R. Williams, Knotted periodic orbits in dynamical systems—I: Lorenz's equations. *Topology* **22**, 47–82 (1983)
4. W. Tucker, A rigorous ODE solver and Smale's 14th problem. *Found. Comput. Math.* **2**, 53–117 (2002)
5. W. Thurston, Three-dimensional manifolds, Kleinian groups and hyperbolic geometry. *Bull. Am. Math. Soc. (N. S.)* **6**, 357–381 (1982)
6. W. Thurston, Hyperbolic structures on 3-manifolds I: deformation of acylindrical manifolds. *Ann. Math.* **124**, 203–246 (1986)
7. J. Birman, I. Kofman, A new twist on Lorenz links. *J. Topol.* **2**, 227–248 (2009)
8. P. Dehornoy, Les noeuds de Lorenz. arXiv:0904.2437 [math.GT]
9. E. El-Rifai, *Positive Braids and Lorenz Links*, PhD Thesis (University of Liverpool, Liverpool, 1988)
10. P. Gomes, N. Franco, L. Silva, Partial classification of Lorenz knots: syllable permutations of torus knots words. *Phys. D* **306**, 16–24 (2015)
11. J. Birman, Lorenz knots. arXiv:1201.0214 [math.GT]
12. N. Franco, L. Silva, Genus and braid index associated to sequences of renormalizable Lorenz maps. *Discrete Contin. Dyn. Syst. A* **32**, 565–586 (2012)
13. C. Tresser, R.F. Williams, Splitting words and Lorenz braids. *Phys. D* **62**, 15–21 (1993)

14. R. Ghrist, P. Holmes, M. Sullivan, *Knots and Links in Three-Dimensional Flows*. Lecture Notes in Mathematics, vol. 1654 (Springer, Berlin, 1997)
15. N. Franco, L. Silva, Zeta-functions of renormalizable sub-Lorenz templates. *Chaos, Solitons Fractals* **43**(2010), 47–56 (2010)
16. J. Franks, R. Williams, Braids and the Jones Polynomial. *Trans. Am. Math. Soc.* **303**, 97–108 (1987)
17. E. El-Rifai, Necessary and sufficient conditions for Lorenz knots to be closed under satellite construction. *Chaos, Solitons Fractals* **10**, 137–146 (1999)

An Algorithm to Determine the Exact Solution to Polynomial Semi-Definite Problems: Application to Structural Optimization



Laura Menini, Corrado Possieri, and Antonio Tornambe

1 Introduction

Polynomial models are ubiquitous in several applications such as: game theory [1], control systems [2], robotics [3], coding theory [4], optimization [5], system biology [6], and machine learning [7]. As an example in structural optimization, in [8], it has been shown that the optimum truss design problem involving constraints on the global stability and/or on the free vibration frequencies can be solved by determining the solution to a polynomial semi-definite problem.

The objective of this chapter is to show that the joint use of optimization techniques and algebraic geometry allows one to find closed-form solutions to this class of optimization problems. In particular, semi-definite problems are first recast in a classical polynomial form by exploiting conditions on the principal minors of the involved matrices. Second, algebraic geometry methods are used to determine the set of all the generalized critical points of the polynomial problem, which contains the infimum of the original problem. The main innovation of the procedure given herein with respect to other methods available in the literature (see, e.g., [9, 10]) is that it uses exact computations, thus allowing one to determine a closed-form expression for the optimal values of the problem.

L. Menini · A. Tornambe

Dipartimento di Ingegneria Civile e Ingegneria Informatica, Università di Roma “Tor Vergata”,
Roma, Italy

e-mail: laura.menini@uniroma2.it; tornambe@disp.uniroma2.it

C. Possieri (✉)

Istituto di Analisi dei Sistemi ed Informatica “A. Ruberti”, Consiglio Nazionale delle Ricerche,
Roma, Italy

e-mail: corrado.possieri@iasi.cnr.it

Organization of this Chapter Sections 2 and 3 contain an elaboration of material already present in the technical literature, whereas Sects. 4 and 5 contain original contributions. In particular, in Sect. 2, some algebraic geometry notions are reviewed following the exposition in [11]. In Sect. 3, a technique that allows one to determine candidate solutions to polynomial optimization problems in closed form is reviewed. In Sect. 4, it is shown how to recast a semi-definite optimization problem with polynomial matrices as a polynomial optimization problem. In Sect. 5, it is shown how to solve two classes of truss design problems using the methods reviewed in the previous sections. Finally, in Sect. 6, a discussion about the results given in this chapter is reported.

2 Notions and Results from Algebraic Geometry

Let \mathbb{C} , \mathbb{R} , \mathbb{Q} , and \mathbb{Z} , \mathbb{Q} , \mathbb{R} be the sets of complex, real, rational, and integer numbers, respectively. Let \mathbb{K} be any field, $\mathbb{Q} \subseteq \mathbb{K}$, and let $\mathbf{x} = [x_1 \dots x_n]^T$ be a vector of variables. A product of the form $\mathbf{x}^\alpha = x_1^{\alpha_1} \dots x_n^{\alpha_n}$, where the α_i 's are non-negative integers (α is referred to as *multi-index*), is a *monomial*. A *polynomial* is a finite linear combination of monomials. Let $\mathbb{K}[\mathbf{x}]$ denote the *ring* of all the polynomials in \mathbf{x} with coefficients in \mathbb{K} , and let $\mathbb{K}(\mathbf{x})$ be the *field* of all the rational functions in \mathbf{x} . A field \mathbb{K} is *algebraically closed* if every non-constant polynomial in $\mathbb{K}[\mathbf{x}]$ has at least one root in \mathbb{K} . The *algebraic closure* of a field \mathbb{K} , denoted as $\overline{\mathbb{K}}$, is the smallest algebraic extension of \mathbb{K} that is algebraically closed (e.g., \mathbb{C} is the algebraic closure of \mathbb{R}). Given $p_1, \dots, p_s \in \mathbb{K}[\mathbf{x}]$, the set

$$\langle p_1, \dots, p_s \rangle := \{ \sum_{i=1}^s q_i p_i, q_i \in \mathbb{K}[\mathbf{x}], i = 1, \dots, s \}$$

is the *ideal* generated by p_1, \dots, p_s , whereas the set

$$\mathbb{V}_{\mathbb{H}^n}(p_1, \dots, p_s) := \{ \mathbf{x} \in \mathbb{H}^n : p_i(\mathbf{x}) = 0, i = 1, \dots, s \}$$

is the *affine variety* (briefly, the *variety*) in \mathbb{H}^n generated by p_1, \dots, p_s . An ideal that can be generated by a single polynomial is *principal*; if z is a single variable, each ideal in $\mathbb{K}[z]$ is principal. Given ideals $\mathcal{I}_1 = \langle p_1, \dots, p_s \rangle$ and $\mathcal{I}_2 = \langle q_1, \dots, q_r \rangle$, the *sum of \mathcal{I}_1 and \mathcal{I}_2* is the ideal $\mathcal{I}_1 + \mathcal{I}_2 = \langle p_1, \dots, p_s, q_1, \dots, q_r \rangle$.

A *monomial order* in $\mathbb{K}[\mathbf{x}]$, denoted as $>$, is an ordering relation on the monomials such that: (i) either $\mathbf{x}^\alpha > \mathbf{x}^\beta$, $\mathbf{x}^\alpha < \mathbf{x}^\beta$, or $\mathbf{x}^\alpha = \mathbf{x}^\beta$; (ii) if $\mathbf{x}^\alpha > \mathbf{x}^\beta$, then $\mathbf{x}^{\alpha+\delta} > \mathbf{x}^{\beta+\delta}$ for any multi-index δ ; (iii) every non-empty set of monomials has a smallest element under $>$. Given $j \in \{1, \dots, n-1\}$, a monomial order $>$ *eliminates* x_1, \dots, x_j if $x_1^{\alpha_1} \dots x_j^{\alpha_j} > x_1^{\beta_1} \dots x_j^{\beta_j}$ implies $x_1^{\alpha_1} \dots x_j^{\alpha_j} \cdot x_{j+1}^{\alpha_{j+1}} \dots x_n^{\alpha_n} > x_1^{\beta_1} \dots x_j^{\beta_j} \cdot x_{j+1}^{\beta_{j+1}} \dots x_n^{\beta_n}$, for all non-negative integers $\alpha_{j+1}, \dots, \alpha_n, \beta_{j+1}, \dots, \beta_n$. The Lex monomial order (see [11] for its formal definition) eliminates x_1, \dots, x_j , $j \in \{1, \dots, n-1\}$.

Letting a monomial order $>$ be fixed, any $p \in \mathbb{K}[\mathbf{x}]$, $p \neq 0$, can be rewritten as $p = c_1 \mathbf{x}^{\alpha_1} + c_2 \mathbf{x}^{\alpha_2} + \dots$, with $c_1, c_2, \dots \in \mathbb{K}$, $c_1 \neq 0$, and $\mathbf{x}^{\alpha_1} > \mathbf{x}^{\alpha_2} > \dots$; the *leading term* $\text{LT}(p)$ of p is $c_1 \mathbf{x}^{\alpha_1}$. Given an ideal \mathcal{I} in $\mathbb{K}[\mathbf{x}]$, a finite set $\mathcal{G}_{\mathcal{I}} = \{p_1, \dots, p_s\}$ in $\mathbb{K}[\mathbf{x}]$ is a *Gröbner basis* of \mathcal{I} if $\langle \text{LT}(p_1), \dots, \text{LT}(p_s) \rangle = \langle \text{LT}(\mathcal{I}) \rangle$, where $\text{LT}(\mathcal{I}) := \{c\mathbf{x}^{\alpha} : \exists p \in \mathcal{I} \text{ such that } c\mathbf{x}^{\alpha} = \text{LT}(p)\}$. By Cox et al. [11, Ch. 2], each ideal in $\mathbb{K}[\mathbf{x}]$ has a Gröbner basis. Given an ideal \mathcal{I} in $\mathbb{K}[\mathbf{x}]$, the set $\mathcal{I}_j := \mathcal{I} \cap \mathbb{K}[x_{j+1}, \dots, x_n]$ is the *j-th elimination ideal* of \mathcal{I} , $j = 1, \dots, n - 1$.

Theorem 1 (Elimination Theorem [11]) *Let $j \in \{1, \dots, n - 1\}$ and $>$ be a monomial order that eliminates x_1, \dots, x_j . Let \mathcal{I} be an ideal in $\mathbb{K}[\mathbf{x}]$, and let $\mathcal{G}_{\mathcal{I}}$ be a Gröbner basis of \mathcal{I} . Then, $\mathcal{G}_{\mathcal{I}} \cap \mathbb{K}[x_{j+1}, \dots, x_n]$ is a Gröbner basis of \mathcal{I}_j .*

By Theorem 1, a basis of the j -th elimination ideal \mathcal{I}_j , $j \in \{1, \dots, n - 1\}$, can be determined by computing a Gröbner basis of \mathcal{I} with respect to an elimination order that eliminates x_1, \dots, x_j . A consequence of the elimination Theorem 1 is that eliminating the variables x_1, \dots, x_j from \mathcal{I} corresponds to project the variety $\mathbb{V}_{\mathbb{H}^n}(\mathcal{I})$, where either $\mathbb{H} = \mathbb{K}$ or $\mathbb{H} = \overline{\mathbb{K}}$, onto a lower-dimensional space.

Let \mathcal{I} be an ideal in $\mathbb{K}[\mathbf{x}]$. The polynomials p_1 and p_2 in $\mathbb{K}[\mathbf{x}]$ are *congruent modulo \mathcal{I}* , denoted by $p_1 = p_2 \text{ mod } \mathcal{I}$, if $p_1 - p_2 \in \mathcal{I}$. Congruence modulo \mathcal{I} is an *equivalence relation* on $\mathbb{K}[\mathbf{x}]$. Thus, given an ideal \mathcal{I} and p in $\mathbb{K}[\mathbf{x}]$, the *equivalence class of p modulo \mathcal{I}* is $\llbracket p \rrbracket_{\mathcal{I}} := \{q \in \mathbb{K}[\mathbf{x}] : p = q \text{ mod } \mathcal{I}\}$, whereas the *quotient of $\mathbb{K}[\mathbf{x}]$ modulo \mathcal{I}* is $\mathbb{K}[\mathbf{x}]/\mathcal{I} := \{\llbracket p \rrbracket_{\mathcal{I}}, p \in \mathbb{K}[\mathbf{x}]\}$. The multivariate division algorithm given in [11, Thm. 3, § 3, Ch. 2] can be used to find a standard representative for each class $\llbracket p \rrbracket_{\mathcal{I}}$. Namely, letting a monomial order $>$ be fixed and letting $\mathcal{G}_{\mathcal{I}}$ be a Gröbner basis of \mathcal{I} , the remainder of the division of p by $\mathcal{G}_{\mathcal{I}}$, denoted by $p \% \mathcal{G}_{\mathcal{I}}$, is a standard representative of $\llbracket p \rrbracket_{\mathcal{I}}$. Therefore, the set $\mathfrak{A} := \mathbb{K}[\mathbf{x}]/\mathcal{I}$ is an algebra over \mathbb{K} .

Theorem 2 (Finiteness Theorem [11]) *Let a monomial order $>$ be fixed, and let $\mathcal{G}_{\mathcal{I}}$ be a Gröbner basis of the ideal \mathcal{I} in $\mathbb{K}[x]$. Consider the following conditions:*

- (i) *The algebra $\mathfrak{A} = \mathbb{K}[x]/\mathcal{I}$ is finite-dimensional over \mathbb{K} .*
- (ii) *$\exists m_i \in \mathbb{Z}$, $m_i \geq 1$, and $g_i \in \mathcal{G}_{\mathcal{I}}$ such that $x_i^{m_i} = \text{LT}(g_i)$, $i = 1, \dots, n$.*
- (iii) *The variety $\mathbb{V}_{\mathbb{K}^n}(\mathcal{I})$ is a finite set.*

Conditions (i)–(ii) are equivalent and imply (iii). Furthermore, if \mathbb{K} is algebraically closed, then (i)–(iii) are all equivalent.

If an ideal \mathcal{I} satisfies either condition (i) or (ii) of Theorem 2, then it is *zero-dimensional*. Given $q \in \mathbb{K}[\mathbf{x}]$ and an ideal \mathcal{I} in $\mathbb{K}[\mathbf{x}]$, let $m_q^{\mathfrak{A}} : \mathfrak{A} \rightarrow \mathfrak{A}$, $m_q^{\mathfrak{A}}(\llbracket p \rrbracket_{\mathcal{I}}) := \llbracket q \rrbracket_{\mathcal{I}} \llbracket p \rrbracket_{\mathcal{I}} = \llbracket q p \rrbracket_{\mathcal{I}} \in \mathfrak{A}$. If \mathcal{I} is zero-dimensional, then $m_q^{\mathfrak{A}}$ can be represented via a matrix $M_q^{\mathfrak{A}}$. By using the matrices $M_q^{\mathfrak{A}}$, $q \in \{x_1, \dots, x_n\}$, and combining the methods given in [14, Thm. 2.6] and [12], the computational Algorithms 2 and 4 have been given in [13] to determine, if any, a solution to a system of polynomial equalities and inequalities.

3 Solution to Polynomial Optimization Problems

Consider the following *minimization problem* (briefly, *MP*):

$$\left\{ \begin{array}{l} \text{minimize } f(\mathbf{x}), \\ \text{with } g_i(\mathbf{x}) \leq 0, \quad i = 1, \dots, r, \\ \quad \quad \quad h_j(\mathbf{x}) = 0, \quad j = 1, \dots, p, \end{array} \right. \tag{1}$$

where $f, g_1, \dots, g_r, h_1, \dots, h_p \in \mathbb{R}[\mathbf{x}]$. Note that the Ω_p set of problem (1) a semi-algebraic set,

$$\Omega_p := \{\mathbf{x} \in \mathbb{R}^n : \mathbf{g}(\mathbf{x}) \leq \mathbf{0}, \mathbf{h}(\mathbf{x}) = \mathbf{0}\}, \tag{2}$$

where $\mathbf{g} = [g_1 \dots g_r]^\top \in \mathbb{R}^r[\mathbf{x}]$ and $\mathbf{h} = [h_1 \dots h_p]^\top \in \mathbb{R}^p[\mathbf{x}]$, and the relations in (2) have to be understood component-wise. Let \mathcal{O}_p° be the set of all the solutions \mathbf{x}° to the MP (1), if any, and let $\mathcal{O}_v^\circ = f(\mathcal{O}_p^\circ)$ be the *optimal value*.

Example 1 Consider the MP (1), with $f(x_1, x_2) = x_1^2 x_2^2 + x_1^2 - 2x_1 x_2 + 1$ in $\mathbb{R}[x_1, x_2]$ and $\Omega_p = \mathbb{R}^2$. A *critical point* for this problem is any pair (x_1^*, x_2^*) such that $\frac{\partial f}{\partial x_i} \Big|_{(x_1, x_2) = (x_1^*, x_2^*)} = 0, i = 1, 2$. The value attained by f at a critical point \mathbf{x}^* , $f^* = f(x_1^*, x_2^*)$, is a *critical value*. The set of all critical values of the MP (1) can be determined using the elimination Theorem 1. In particular, define $\mathcal{I} = \langle \frac{\partial f}{\partial x_1}, \frac{\partial f}{\partial x_2}, z - f \rangle$, where z is an additional variable. Since z is a single variable, the elimination ideal $\mathcal{I} \cap \mathbb{R}[z]$ is principal. Therefore, there exists $q \in \mathbb{R}[z]$ such that $\mathcal{I} \cap \mathbb{R}[z] = \langle q \rangle$. Hence, the critical values, if any, are among the real roots of $q(z)$, and if the MP (1) admits a minimum value f° , then $q(f^\circ) = 0$. The Gröbner basis of \mathcal{I} , with respect to the Lex monomial order with $x_1 > x_2 > z$, is $\{z - 1, x_2, x_1\}$. Therefore, since $q(z) = z - 1$, one has that $z_1^* = 1$ is the only critical value and $(x_1^*, x_2^*) = (0, 0)$ is the corresponding critical point. Now, the objective is to determine whether $z_1^* = 1$ is the minimum value of f . Since $f(x_1, x_2) = x_1^2 + (1 - x_1 x_2)^2$, it results that $f(\mathbf{x}) \geq 0$ for all $\mathbf{x} \in \mathbb{R}^2$. Moreover, considering the sequence $(x_1^\ell, x_2^\ell) = (\frac{1}{\ell}, \ell)$, one has $f(x_1^\ell, x_2^\ell) = \frac{1}{\ell^2}, \lim_{\ell \rightarrow +\infty} f(x_1^\ell, x_2^\ell) = 0$. Thus, the greatest lower bound of f is $f^* = 0$, which shows that $z_1^* = 1$ is actually not the minimum value of f over \mathbb{R}^2 : f does not attain a minimum over \mathbb{R}^2 but only a finite *infimum value*. \blacktriangle

The following definition is taken from [15], where it has been shown that the critical values are candidates to be minima, whereas the generalized critical values are the candidates to be infima.

Definition 1 Consider the MP (1), with $\Omega_p = \mathbb{R}^n$. Thus:

- (i) f^* is a *critical value* of the MP (1) if there exists a *critical point* $\mathbf{x}^* \in \mathbb{R}^n$ such that $f^* = f(\mathbf{x}^*)$ and $\frac{\partial f}{\partial \mathbf{x}} \Big|_{\mathbf{x} = \mathbf{x}^*} = \mathbf{0}$.

- (ii) f^{**} is a *generalized critical value* of the MP (1) if there exists a sequence $\mathbf{x}^\ell \in \mathbb{R}^n$ such that $\lim_{\ell \rightarrow +\infty} f(\mathbf{x}^\ell) = f^{**}$, $\lim_{\ell \rightarrow +\infty} \|\mathbf{x}^\ell\| = +\infty$ and $\lim_{\ell \rightarrow +\infty} \|\mathbf{x}^\ell\| \cdot \left\| \frac{\partial f}{\partial \mathbf{x}} \Big|_{\mathbf{x}=\mathbf{x}^\ell} \right\| = 0$.
- (iii) Let C_p^* and be the sets of all critical points \mathbf{x}^* .
- (iv) Let C_v^* be the set of all the critical values f^* , and let C_v^{**} be the set of all generalized critical values.
- (v) The union $\mathcal{E}_v^* = C_v^* \cup C_v^{**}$ is referred to as the set of all *generalized extremal values*; elements of \mathcal{E}_v^* are represented by the superscript $*$. \circ

The interested reader is referred to [15–17] for some polynomials admitting both critical values and generalized critical values in \mathbb{R}^n . By Jelonek and Kurdyka [18], sets containing C_v^* and \mathcal{E}_v^* can be determined via algebraic geometry. As for C_v^* , define the ideal \mathcal{I} in $\mathbb{R}[\mathbf{x}, z]$, $\mathcal{I} = \langle \frac{\partial f(\mathbf{x})}{\partial \mathbf{x}}, z - f(\mathbf{x}) \rangle$, where z is an additional single variable. Since the elimination ideal $\mathcal{I} \cap \mathbb{R}[z]$ is principal, there exists $q \in \mathbb{R}[z]$ such that

$$\mathcal{I} \cap \mathbb{R}[z] = \langle q \rangle. \tag{3}$$

Letting $\Omega_p = \mathbb{R}^n$, the critical values of the MP (1) are real roots of $q(z)$ (i.e., $C_v^* \subseteq \mathbb{V}_{\mathbb{R}}(q)$), although there may exist real root of $q(z)$ that are not critical values of the MP (1). In fact, it may result that the corresponding critical point is non-real (i.e., the sets C_v^* and $\mathbb{V}_{\mathbb{R}}(q)$ need not coincide). The points in $\mathcal{CC}_v^* := \mathbb{V}_{\mathbb{R}}(q)$ are referred to as *candidate critical values* and $\mathcal{CC}_v^* \supseteq C_v^*$.

In order to determine the generalized extremal values, define the ideal

$$\begin{aligned} \mathcal{I} = \langle & \frac{\partial f(\mathbf{x})}{\partial x_1} - F_1, \dots, \frac{\partial f(\mathbf{x})}{\partial x_n} - F_n, x_1 \frac{\partial f(\mathbf{x})}{\partial x_1} - G_{1,1}, \dots, \\ & x_1 \frac{\partial f(\mathbf{x})}{\partial x_n} - G_{1,n}, \dots, x_n \frac{\partial f(\mathbf{x})}{\partial x_n} - G_{n,n}, z - f(\mathbf{x}) \rangle; \end{aligned}$$

in $\mathbb{R}[x_1, \dots, x_n, F_1, \dots, F_n, G_{1,1}, \dots, G_{n,n}, z]$, where, F_i , $G_{i,j}$, and z are the auxiliary variables that denote the values attained by $\frac{\partial f(\mathbf{x})}{\partial x_i}$, $x_i \frac{\partial f(\mathbf{x})}{\partial x_j}$, and $f(\mathbf{x})$, respectively, $i = 1, \dots, n$, $j = 1, \dots, n$, as \mathbf{x} varies in \mathbb{R}^n . Thus, compute

$$\mathcal{I}_a = \mathcal{I} \cap \mathbb{R}[F_1, \dots, F_n, G_{1,1}, \dots, G_{n,n}, z], \tag{4a}$$

$$\mathcal{I}_b = \mathcal{I}_a + \langle F_1, \dots, F_n, G_{1,1}, \dots, G_{n,n} \rangle,$$

$$\mathcal{I}_c = \mathcal{I}_b \cap \mathbb{R}[z]. \tag{4b}$$

By Cox et al. [11], the variety $\mathbb{V}_{\mathbb{C}^{n^2+n+1}}(\mathcal{I}_a)$ is the projection onto \mathbb{C}^{n^2+n+1} of the values attained by $\frac{\partial f(\mathbf{x})}{\partial x_i}$, $x_i \frac{\partial f(\mathbf{x})}{\partial x_j}$, and $f(\mathbf{x})$ as \mathbf{x} varies in \mathbb{C}^n , whereas the variety $\mathbb{V}_{\mathbb{C}^{n^2+n+1}}(\mathcal{I}_b)$ is the intersection of such a projection with $\bigcap_{i=1}^n \mathbb{V}_{\mathbb{C}^{n^2+n+1}}(F_i) \cap \bigcap_{i=1}^n \mathbb{V}_{\mathbb{C}^{n^2+n+1}}(G_{i,j})$. Thus, the variety $\mathbb{V}_{\mathbb{C}}(\mathcal{I}_c)$ is the projection of this intersection onto \mathbb{C} . Note that \mathcal{I}_c need not coincide with $\mathcal{I}_a \cap \mathbb{R}[z]$. Since \mathcal{I}_c is principal, there

exists $q_c \in \mathbb{R}[z]$ such that $\mathcal{I}_c = \langle q_c \rangle$. Letting $\Omega_p = \mathbb{R}^n$, the generalized extremal values of the MP (1) are real roots of $q_c(z)$ (i.e., $\mathcal{E}_v^* \subseteq \mathbb{V}_{\mathbb{R}}(q_c)$); the points in $\mathbb{V}_{\mathbb{R}}(q_c) =: \mathcal{CE}_v^*$ are referred to as *candidate generalized extremal values*, which include the critical values and the generalized critical values, i.e., $\mathcal{CE}_v^* \supseteq \mathcal{E}_v^*$.

Consider the MP (1), (2), with Ω_p given by (2). Letting

$$\Theta := \{\emptyset, \{1\}, \dots, \{r\}, \{1, 2\}, \dots, \{1, \dots, r\}\}, \tag{5}$$

be the set of all the subsets of $\{1, \dots, r\}$, for each $\theta \in \Theta$, define

$$f_\theta = f + \sum_{j=1}^p \gamma_j h_j + \sum_{k \in \theta} \lambda_k g_k, \tag{6}$$

where $\boldsymbol{\gamma} = [\gamma_1 \dots \gamma_p]^\top$ and $\boldsymbol{\lambda} = [\lambda_1 \dots \lambda_r]^\top$ are the Karush–Kuhn–Tucker (briefly, KKT) multipliers [19, 20]; as in the unconstrained case, the ideal $\mathcal{I}_{\theta,c} = \langle q_{\theta,c}(z) \rangle$ is such that the roots of its generator $q_{\theta,c}(z)$ are candidate generalized extremal values of the extended MP

$$\left| \begin{array}{l} \text{minimize } f_\theta(\mathbf{x}, \boldsymbol{\lambda}, \boldsymbol{\gamma}), \\ \text{with } (\mathbf{x}, \boldsymbol{\lambda}, \boldsymbol{\gamma}) \in \Omega_p \times \mathbb{R}^r \times \mathbb{R}^p, \end{array} \right.$$

which is analogous to the MP (1) in the variables $\mathbf{x}, \boldsymbol{\lambda}, \boldsymbol{\gamma}$. Let $q_d(z) \in \mathbb{R}[z]$ be the least common multiple of $q_{\theta,c}(z), \theta \in \Theta$. Thus,

$$\bigcap_{\theta \in \Theta} \mathcal{I}_{\theta,c} = \langle q_d(z) \rangle. \tag{7}$$

Thus, for all $\theta \in \Theta$, let $\tilde{f}_\theta := \sum_{j=1}^p \gamma_j h_j + \sum_{k \in \theta} \lambda_k g_k$ and define

$$\begin{aligned} \mathcal{N}_{a,\theta} := & \langle \frac{\partial \tilde{f}_\theta(\mathbf{x}, \boldsymbol{\lambda}, \boldsymbol{\gamma})}{\partial x_1} - F_1, \dots, \frac{\partial \tilde{f}_\theta(\mathbf{x}, \boldsymbol{\lambda}, \boldsymbol{\gamma})}{\partial \gamma_r} - F_{n+r+p}, x_1 \frac{\partial \tilde{f}_\theta(\mathbf{x}, \boldsymbol{\lambda}, \boldsymbol{\gamma})}{\partial x_1} - G_{1,1}, \dots, \\ & \gamma_r \frac{\partial \tilde{f}_\theta(\mathbf{x}, \boldsymbol{\lambda}, \boldsymbol{\gamma})}{\partial \gamma_r} - G_{n+r+p,n+r+p}, \sum_{j=1}^p \gamma_j^2 + \sum_{k \in \theta} \lambda_k^2 - 1, z - f(\mathbf{x}) \rangle, \end{aligned}$$

where $F_1, \dots, F_{n+r+p}, G_{1,1}, \dots, G_{n+r+p,n+r+p}, z$ are the auxiliary variables, whose role is the same as of the ones employed in (4b). Thus, let $\mathcal{N}_{b,\theta} = \mathcal{N}_{a,\theta} \cap \mathbb{R}[F_1, \dots, F_{n+r+p}, G_{1,1}, \dots, G_{n+r+p,n+r+p}, z], \mathcal{N}_{c,\theta} = \mathcal{N}_{b,\theta} + \langle F_1, \dots, F_{n+r+p}, G_{1,1}, \dots, G_{n+r+p,n+r+p} \rangle$, and $\mathcal{N}_{d,\theta} = \mathcal{N}_{b,\theta} \cap \mathbb{R}[z]$, for all $\theta \in \Theta$. Therefore, since the ideal $\mathcal{N}_{d,\theta}$ is principal, for each $\theta \in \Theta$, let $\tilde{q}_{\theta,c}(z) \in \mathbb{R}[z]$ be such that $\mathcal{N}_{d,\theta} = \langle \tilde{q}_{\theta,c} \rangle$ and let \tilde{q}_d be the least common multiple of $\tilde{q}_{\theta,c}(z), \theta \in \Theta$. One has the next lemma [21].

Lemma 1 *Using the construction given above, it results that, for the MP (1), (2),*

$$\mathcal{O}_v^\circ \subseteq \mathcal{CE}_v^* = \mathbb{V}_{\mathbb{R}}(q_d) \cup \mathbb{V}_{\mathbb{R}}(\tilde{q}_d).$$

By Lemma 1, if the MP (1), (2), admits a minimum value f° , then f° belongs to the finite set \mathcal{CE}_v^* . Therefore, let

$$\mathcal{CE}_v^* = \{f_1^*, f_2^*, \dots, f_\sigma^*\},$$

where $f_1^* < f_2^* < \dots < f_\sigma^*$, and the f_i^* 's are the candidate generalized extremal values. Let $f_0^* = -\infty$ and $f_{\sigma+1}^* = +\infty$.

The proof of the following theorem follows from [21].

Theorem 3 Take $\sigma + 1$ arbitrary numbers $F_1, \dots, F_{\sigma+1} \in \mathbb{R}$ ordered as follows: $f_0^* < F_1 < f_1^* < F_2 < \dots < f_\sigma^* < F_{\sigma+1} < f_{\sigma+1}^*$. Then, apply Algorithm 4 of [13] to the system of equalities and inequalities

$$f = F, \quad \mathbf{g} \leq \mathbf{0}, \quad \mathbf{h} = \mathbf{0}, \tag{8}$$

for each $F \in \{F_1, f_1^*, F_2, f_2^*, \dots, F_{\sigma+1}\}$.

- (3.1) If system (8) admits at least a solution for $F = F_j$, for some $j \in \{1, \dots, \sigma\}$, then it admits at least a solution for each $F \in (f_{j-1}^*, f_j^*)$.
- (3.2) If system (8) admits at least a solution for $F = F_1$, then f is unbounded from below over Ω_p .
- (3.3) Let $j \in \{1, \dots, \sigma\}$ be such that system (8) does not admit a solution for $F = F_j$ and system (8) admits at least a solution for $F = F_{j+1}$. Then, f_j^* is the greatest lower bound of f over Ω_p ; in addition, if system (8) admits at least a solution for $F = f_j^*$, then $f^\circ = f_j^*$ is the minimum value of f over Ω_p .
- (3.4) Let f_i^* be the smallest critical value (not necessarily the smallest candidate critical value). Letting ε be a sufficiently small positive number such that there is no generalized critical value in $[f_i^* - \varepsilon, f_i^*]$, if system (8) does not admit a solution for $F = f_i^* - \varepsilon$, then $f^\circ = f_i^*$ is the minimum value of f ; otherwise, there does not exist a minimum.

Example 2 Consider the following MP:

$$\left| \begin{array}{l} \text{minimize } x_1^2 + x_2x_3 - x_3^3 \\ \text{with } x_1 + x_2 + x_3 = 0, \\ 5 - x_3 \leq 0, \quad x_1 \leq 0. \end{array} \right.$$

Let $\Theta = \{\emptyset, \{1\}, \{2\}, \{1, 2\}\}$, and, for each $\theta \in \Theta$, define f_θ as follows:

$$\begin{aligned} f_\emptyset &= x_1^2 + x_2x_3 - x_3^3 + \gamma_1(x_1 + x_2 + x_3), & f_{\{1\}} &= f_\emptyset + \lambda_1(5 - x_3), \\ f_{\{2\}} &= f_\emptyset + \lambda_2(x_1), & f_{\{1,2\}} &= f_{\{1\}} + \lambda_2(x_1). \end{aligned}$$

Hence, one can compute:

$$\mathcal{I}_{\emptyset,c} = \langle z \rangle, \quad \mathcal{I}_{\{1\},c} = \langle 225 + 4z \rangle, \quad \mathcal{I}_{\{2\},c} = \langle z \rangle, \quad \mathcal{I}_{\{1,2\},c} = \langle 50 + z \rangle.$$

The least common multiple of the generators of $\mathcal{I}_{\emptyset,c}$, $\mathcal{I}_{\{1\},c}$, $\mathcal{I}_{\{2\},c}$, and $\mathcal{I}_{\{1,2\},c}$ is $q_d(z) = z(z + 50)(4z + 225)$. Thus, if the MP has a minimum value f° , then

$$f^\circ \in \mathcal{CE}_v^* = \left\{ -\frac{225}{4}, -50, 0 \right\}.$$

Letting $F_1 = -60 < f_1^*$ and using Algorithm 4 of [13], one obtains that (8) admits one solution for $F = F_1$, and then f is unbounded from below over Ω_p . ▲

4 Converting Semi-Definite Problems into Polynomial Optimization Problems

Consider the following *semi-definite problem* (briefly, *SDP*):

$$\left| \begin{array}{l} \text{minimize } f(\mathbf{x}), \\ \text{with } M_i(\mathbf{x}) \geq 0, \quad i = 1, \dots, s, \\ \quad \quad \quad h_j(\mathbf{x}) = 0, \quad j = 1, \dots, p, \end{array} \right. \tag{9}$$

where $f \in \mathbb{R}[\mathbf{x}]$, $M_1(\mathbf{x}), \dots, M_s(\mathbf{x})$ are the polynomial mappings from \mathbb{R}^n to the space of symmetric $m_i \times m_i$ -dimensional matrices and $h_1(\mathbf{x}), \dots, h_p(\mathbf{x})$ are the given scalar polynomial functions. By classical semi-definite results [22], the matrix $M_i(\mathbf{x})$ is positive semi-definite if and only if all its principal minors are non-negative. Therefore, letting $\wp_1(\mathbf{x}), \dots, \wp_r(\mathbf{x})$ be all the principal minors of matrices $M_1(x), \dots, M_s(x)$, which are in $\mathbb{R}[\mathbf{x}]$ due to the properties of minors, determining a solution to the SDP (9) is equivalent to solve the MP

$$\left| \begin{array}{l} \text{minimize } f(\mathbf{x}), \\ \text{with } -\wp_i(\mathbf{x}) \leq 0, \quad i = 1, \dots, q, \\ \quad \quad \quad h_j(\mathbf{x}) = 0, \quad j = 1, \dots, p, \end{array} \right. \tag{10}$$

that is in the form of (1). Therefore, the techniques given in Sect. 3 can be used to determine the solution to the SDP (9).

5 Application to Truss Optimization

In this section, the results given in Sects. 3 and 4 are used to solve truss optimization problems. The setting of this section is the same as in [8]. A truss is understood as an assemblage of pin-jointed uniform straight bars. The bars can only carry axial tension and compression when the truss is loaded at the joints. A truss is determined

by positions of nodes and volumes of bars, i.e., by vectors $\mathbf{y} \in \mathbb{R}^m$ and $\mathbf{x} \in \mathbb{R}^n$. The response of the truss to the vector of nodal forces $\mathbf{u} \in \mathbb{R}^m$ is measured by the vector of nodal displacements $\mathbf{d} \in \mathbb{R}^n$. The *global stiffness* and *geometry matrices* of the truss are denoted by $A(\mathbf{x})$ and $G(\mathbf{x}, \mathbf{d})$, respectively (see [8] for their formal definition). Given the vector of nodal positions \mathbf{y} , these matrices can be computed in symbolic form by interfacing the MATLAB package `fminsdp` [23] with the MATLAB Symbolic Toolbox.

5.1 Truss Design with Global Stability Constraints

Following the construction in [8], the truss design problem with global stability constraints reduces to determine a solution to the following SDP:

$$\left\{ \begin{array}{l} \text{minimize } \sum_{i=1}^n x_i, \\ \text{with } A(\mathbf{x}) + G(\mathbf{x}, \mathbf{d}) \succeq 0, \\ \quad \begin{bmatrix} c & \mathbf{u}^\top \\ \mathbf{u} & A(\mathbf{x}) \end{bmatrix} \succeq 0, \\ \quad x_i \geq 0, \quad i = 1, \dots, n, \end{array} \right. \quad (11)$$

with $\mathbf{d} = A^{-1}(\mathbf{x})\mathbf{u}$. This problem has the form (9), and hence, it can be solved by using the techniques given in Sects. 3 and 4 as shown in the following example.

Example 3 Consider the truss depicted in Fig. 1a.

Assuming unitary values of the mechanical parameters, it results that

$$A(\mathbf{x}) = \begin{bmatrix} \frac{x_2}{4} + x_4 + \frac{16x_5}{25} & \frac{x_2}{4} - \frac{8x_5}{25} \\ \frac{x_2}{4} - \frac{8x_5}{25} & \frac{x_2}{4} + \frac{4x_5}{25} \end{bmatrix},$$

$$G(\mathbf{x}, \mathbf{d}) = \begin{bmatrix} \frac{54x_2x_5}{-125x_2x_4+80x_5x_4+180x_2x_5} & \frac{18x_2x_5}{-125x_2x_4+80x_5x_4+180x_2x_5} \\ \frac{18x_2x_5}{-125x_2x_4+80x_5x_4+180x_2x_5} & \frac{-125x_2x_4-80x_5x_4-126x_2x_5}{125x_2x_4+80x_5x_4+180x_2x_5} \end{bmatrix}.$$

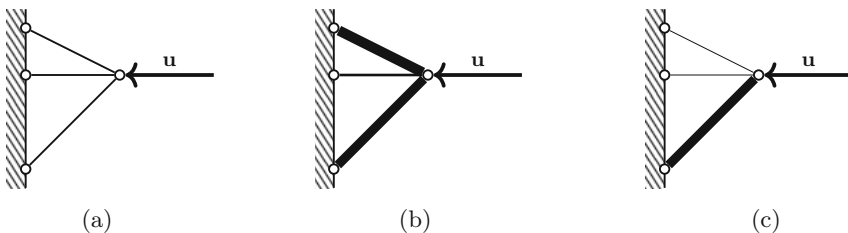


Fig. 1 The considered truss and solutions to the optimal truss design problem with constraints on the global stability and on the free vibration frequencies. (a) A truss. (b) Solution to (11). (c) Solution to (12)

Hence, letting $c = 0.5$, the SDP (11) has been first converted into an MDP of the form (1) as shown in Sect. 4, and the algebraic geometry technique given in Sect. 3 has been used to determine the set of all the candidate optimal values, which is constituted by 45 real values whose explicit expression has been omitted for brevity. Letting \bar{F} be the third smallest real root of the polynomial $573696z^8 + 147845760z^7 - 10923471088z^6 + 251692143168z^5 - 1376295300920z^4 - 9707873025112z^3 + 25572262462105z^2 + 101605679900136z - 28107941625776$, since for $F \leq \bar{F}$ there does not exist any solution of (8), whereas for $F = \bar{F}$ such a problem admits a solution, whose numerical expression is $\mathbf{x}^\circ = [0 \ 1.97442 \ 0 \ 0.40004 \ 1.73649]^\top$, the optimal value of (11) is $f^\circ = \bar{F}$, and \mathbf{x}° is the corresponding optimal solution; see Fig. 1(b). It is worth noticing that the numerical evaluation of the exact solution given above matches with the output of the solver `fmindsp` to four decimal places. ▲

5.2 Truss Design with Constraints on the Free Vibration Frequencies

The technique outlined in Sect. 5.1 can be easily adapted to deal with the optimization of trusses with constraints on the free vibration frequencies. In particular, following [8], the compliance constraint such that the lowest eigenfrequency is bigger than or equal to the value $\bar{\sigma}$ can be rewritten as

$$\left\{ \begin{array}{l} \text{minimize } \sum_{i=1}^n \mathbf{x}_i, \\ \text{with } A(\mathbf{x}) - \bar{\sigma} M(\mathbf{x}) \geq 0, \\ \begin{bmatrix} c & \mathbf{u}^\top \\ \mathbf{u} & A(\mathbf{x}) \end{bmatrix} \geq 0, \\ \mathbf{x}_i \geq 0, \quad i = 1, \dots, n, \end{array} \right. \tag{12}$$

where $M(\mathbf{x}) = M_0 + M_s(\mathbf{x})$ is the mass matrix of the truss: M_0 is the part corresponding to nonstructural mass, whereas the (lumped) structural mass matrix $M_s(\mathbf{x})$ is defined as $M_s(\mathbf{x}) = \sum_{i=1}^n \mathbf{x}_i M_i$, where $M_i = \frac{\rho}{2} I$, I denotes the identity matrix of suitable dimensions, and ρ is the material density. The SDP (12) can be solved as in the previous section, as shown in the following example.

Example 4 Consider again the truss of Example 3. Letting $c = 0.5$, $\bar{\sigma} = 1$, and $\rho = 1$, the SDP (12) has been first converted into an MDP of the form (1) as shown in Sect. 4 and the algebraic geometry technique given in Sect. 3 has been used to determine the set of all the candidate optimal values, which is constituted by 27 real values whose explicit expression has been omitted for brevity. Letting $\bar{F} = \frac{1}{16}(79 + 7\sqrt{74})$, since for $F < \bar{F}$ there does not exist any solution of (8), whereas for $F = \bar{F}$ such a problem admits the solution $\mathbf{x}^\circ = [0 \ 7.96035 \ 0 \ 0.0987429 \ 0.641925]^\top$, the optimal value of (11) is $f^\circ = \bar{F}$, and \mathbf{x}° is the corresponding optimal solution; see Fig. 1c.

6 Results and Discussion

The main contribution of this chapter is twofold. First, it is shown how to recast a polynomial SDP into a polynomial optimization problem that can be solved by using classical techniques. Second, it is shown how algebraic geometry methods can be used to determine a closed-form expression for the solution to the polynomial problem. The main innovation of the procedure given herein with respect to other methods available in the literature is that it uses exact computations, thus allowing one to determine a closed-form expression for the optimal values.

The proposed technique has validated and corroborated via application to some structural optimization problems involving constraints on the global stability of the structure and on the free vibration frequencies.

References

1. C. Possieri, M. Sassano, *Automatica* **74**, 23 (2016)
2. L. Menini, C. Possieri, A. Tornambe, *IEEE Trans. Autom. Control* **61**(5), 1362 (2016)
3. D.A. Cox, J.B. Little, D. O’Shea, *Using Algebraic Geometry* (Springer, Berlin, 1998)
4. J.H. Van Lint, *Introduction to Coding Theory*, vol. 86 (Springer, New York, 2012)
5. D.E. Kirk, *Optimal Control Theory: An Introduction* (Courier Corporation, Honolulu, 2012)
6. Z. Szallasi, J. Stelling, V. Periwal, *System Modeling in Cellular Biology* (MIT Press, New York, 2006)
7. Y.S. Abu-Mostafa, M. Magdon-Ismael, H.T. Lin, *Learning from Data* (AMLBook, New York, 2012)
8. M. Kočvara, *Struct. Multidiscip. Optim.* **23**(3), 189 (2002)
9. A. Wächter, L.T. Biegler, *Math. Prog.* **106**(1), 25 (2006)
10. I.S. Duff, *ACM Trans. Math. Soft.* **30**(2), 118 (2004)
11. D. Cox, J. Little, D. O’Shea, *Ideals, Varieties, and Algorithms* (Springer, Berlin, 2015)
12. B. Sturmfels, *Solving Systems of Polynomial Equations* (American Mathematical Society, Providence, 2002)
13. B.D.O. Anderson, R.W. Scott, *Proc. IEEE* **65**(6), 849 (1977)
14. L. Menini, C. Possieri, A. Tornambe, *Asian J. Control* **20**(2), 1 (2018)
15. K. Kurdyka, P. Orro, S. Simon, et al., *J. Differ. Geom.* **56**(1), 67 (2000)
16. M.S. El Din, in *International Symposium Symbolic Algebraic Computer* (2008), pp. 71–78
17. F. Guo, M.S. El Din, L. Zhi, in *International Symposium Symbolic Algebraic Computer* (2010), pp. 107–114
18. Z. Jelonek, K. Kurdyka, *Discrete Comput. Geom.* **34**(4), 659 (2005)
19. W. Karush, *Minima of functions of several variables with inequalities as side conditions*. Master’s thesis (University of Chicago, Chicago, 1939)
20. H.W. Kuhn, A.W. Tucker, in *Proceedings Berkeley Symposium Mathematical Statistics and Probability* (University California, Berkeley, 1951)
21. L. Menini, C. Possieri, A. Tornambe, *IEEE Trans. Autom. Control* **63**(12), 4188 (2018)
22. C. Possieri, M. Sassano, in *54th IEEE Conference Decision Control* (2015), pp. 5197–5202
23. C.-J. Thore, *fminsdp* (2021) (<https://www.mathworks.com/matlabcentral/fileexchange/43643-fminsdp>), MATLAB Central File Exchange. Retrieved September 24, 2021

Semi-Analytical Approaches for Solving Duffing Oscillator with Multi-Frequency Excitation



Aalokeparno Dhar and I. R. Praveen Krishna

1 Introduction

A large domain of physical systems in the world can be modeled as a second-order dynamical system, and this explains the need for its study [1]. There are many second-order dynamical systems that exhibit different steady-state phase portraits depending on the value of their nonlinear parameters. Duffing oscillator is one such mostly studied oscillator [2]. Till date, there are more than two thousand papers discussing the dynamics of the Duffing oscillator. This is because, in many engineering fields, the nonlinear governing differential equations can be reduced to the form of Duffing equation [3]. The Duffing equation consists of the cubic term in the stiffness, which causes quasi-periodicity and chaotic behavior in the response to a simple harmonic or biharmonic excitation. This equation is further modified by introducing higher-order terms in stiffness (such as quintic Duffing oscillator [4]) or nonlinearities even in the viscous damping term. Furthermore, analysis of Duffing equation is extended with other nonlinear systems superimposed in it, such as Rayleigh–Duffing oscillator [5], Helmholtz–Duffing oscillator [6], Duffing–van der Pol oscillator [7, 8].

The response of dynamical systems is often explained through their steady-state phase portraits. Finding a steady-state solution to obtain phase portraits for these nonlinear dynamical systems is an interesting and challenging topic. Numerical integration is an easy but very time-consuming process to reach a steady-state solution. So different methods are developed to solve these types of nonlinear differential equations. One of these methods is the Harmonic Balance Method (HBM) [9, 10]. It is a frequency-domain method where the response is approximated

A. Dhar · I. R. Praveen Krishna (✉)
Department of Aerospace Engineering, Indian Institute of Space Science and Technology,
Thiruvananthapuram, India

by a truncated Fourier series. But simple HBM cannot predict quasi-periodicity as in quasi-periodicity the solution consists of frequencies that are not a direct integer multiple of each other. Multi-Harmonic Balance Method (MHBM) [11, 12] is an extension of HBM where the approximated solution consists of more than one frequency corresponding to the multiple independent time series for the system. Guskov and Thouverez [13] discussed the evolution of HBM and MHBM for solving quasi-periodic solutions. They applied MHBM and adjusted HBM (AHBM) to solve the Duffing equation. In adjusted HBM, the multi-harmonic excitation is approximated to the mono-dimensional case. It concludes that both methods end up in the same solution, where MHBM is more time efficient in it.

Another method that is recently introduced by Rook [14] is Time Variational Method (TVM). Unlike the HBM approach where the system is solved in the frequency domain, TVM solves it in the time domain itself. The reason is that in HBM, the solution is expressed in the form of Fourier functions, but in TVM it is expressed in the form of periodic basis functions that are distributed in the time domain. This reduces the effort and computation of the AFT (Alternate Time Frequency) process in each iteration. In Rook's paper, the convergence of the solution with different basis functions is analyzed. It finds better compactness and convergence of cubic spline function than other basis functions for solving a variety of nonlinear models. Also, its comparison with other methods available in the literature (HBM, shooting method) is also shown. Krishna and Padmanabhan [10] extended this method to solve for reduced-order nonlinear systems with multi-DOF. Prabith and Krishna [15] used the TVM method (with cubic spline basis function) in a multiple-frequency excited system by approximating it in a single time scale. So far, this method is not extended to multiple time scale formulations like MHBM.

In this chapter, an MHBM equivalent multi-frequency time variational technique (MTVM) is formulated. MTVM (using cubic spline as the basis function) along with MHBM is used for obtaining phase portrait of quasi-periodically excited single DOF Duffing oscillator. MTVM is found to be more time efficient than MHBM for solving this system. A continuation algorithm is applied to both of the methods, and the response is observed by varying excitation amplitude of one of the excitation frequencies. All the results are compared with numerically integrated solutions.

2 Methodology

2.1 MHBM Formulation

General single DOF equation of motion can be expressed as

$$m\ddot{x} + c\dot{x} + kx + f_{nl}(x, \dot{x}) = f(t), \quad (1)$$

where m is the mass, c is the stiffness, and k is the stiffness of the system. In this chapter, $f(t)$ is assumed to have two independent time scales, i.e., the excitation frequency is having a maximum of two independent fundamental frequencies ($f(t) = f_1 \sin(\omega_1 t + \psi_1) + f_2 \sin(\omega_2 t + \psi_2)$).

For now in this formulation, the equation is scaled in two time domains, $\tau_1 = \omega_1 t$, $\tau_2 = \omega_2 t$. (Some cases require to take $\tau_1 = \frac{\omega_1 t}{I}$, where I is an integer if sub-harmonics are present in the response). Then, the time derivatives of x can be expressed as

$$\begin{aligned}\dot{x} &= \omega_1 \frac{\partial x}{\partial \tau_1} + \omega_2 \frac{\partial x}{\partial \tau_2} \\ \ddot{x} &= \omega_1^2 \frac{\partial^2 x}{\partial \tau_1^2} + 2\omega_1 \omega_2 \frac{\partial^2 x}{\partial \tau_1 \partial \tau_2} + \omega_2^2 \frac{\partial^2 x}{\partial \tau_2^2}\end{aligned}$$

The solution of x is approximated as a truncated second-order Fourier series

$$\hat{x} = A_1 + \sum_{i=1}^{N_h} (A_i \cos(\mathbf{k}_i, \boldsymbol{\tau}) + B_i \sin(\mathbf{k}_i, \boldsymbol{\tau})) \quad (2)$$

$$(\mathbf{k}_i, \boldsymbol{\tau}) = (\mathbf{k}_i, \boldsymbol{\omega})t = k_{1i} \tau_1 + k_{2i} \tau_2$$

Here, $\boldsymbol{\omega}$ is the vector containing two frequency bases, $\boldsymbol{\tau}$ is the vector containing time scales. \mathbf{k}_i contains k_{1i} and k_{2i} , which are harmonic indexes corresponding to ω_1 and ω_2 . (\mathbf{a}, \mathbf{b}) denotes the dot product between any two vectors \mathbf{a} and \mathbf{b} of equal size. Here for a given number of harmonics N , the truncation of Fourier terms is considered from the paper by Sun, et al. [12], leading to

$$\hat{x} = A_0 + \sum_{j=1}^N (A_{0j} \cos(j\tau_2) + B_{0j} \sin(j\tau_2)) + \sum_{i=1}^N \sum_{j=-N}^N (A_{ij} \cos(i\tau_1 + j\tau_2) + B_{ij} \sin(i\tau_1 + j\tau_2))$$

So correspondingly N_h mentioned in Eq. (2) will become

$$N_h = \frac{(2N + 1)^2 + 1}{2}$$

This precisely denotes that N harmonics in two independent frequency basis systems consists of total N_h numbers of different dependent or independent frequencies where i th frequency is denoted by $(\mathbf{k}_i, \boldsymbol{\omega})$.

Now \hat{x} can be substituted into Eq. (1), and it leads to

$$r = \mathbf{n}^T (\mathbf{J}\mathbf{x} + f_{nl} - f_{ex}). \tag{3}$$

Where \mathbf{n} is the vector containing the Fourier functions, \mathbf{x} is the vector containing the Fourier coefficients. \mathbf{J} can be interpreted as the linear part of the Jacobian matrix. The right-hand side need not be zero as \hat{x} is only an approximation.

$$\mathbf{J} = \begin{bmatrix} k & 0 & 0 \\ 0 & k - m(\mathbf{k}_i, \boldsymbol{\omega})^2 & c(\mathbf{k}_i, \boldsymbol{\omega}) \\ 0 & -c(\mathbf{k}_i, \boldsymbol{\omega}) & k - c(\mathbf{k}_i, \boldsymbol{\omega})^2 \end{bmatrix}$$

$$\mathbf{x} = \begin{Bmatrix} A_0 \\ A_i \\ B_i \end{Bmatrix}$$

$$\mathbf{n} = \begin{Bmatrix} 1 \\ \cos(\mathbf{k}_i, \boldsymbol{\tau}) \\ \sin(\mathbf{k}_i, \boldsymbol{\tau}) \end{Bmatrix}$$

f_{nl} is the Fourier coefficient of the nonlinear term. Applying Galerkin’s weighted residual approach, it leads to

$$\mathbf{r}_1 = \frac{1}{4\pi^2} \int_{\tau_2=0}^{2\pi} \int_{\tau_1=0}^{2\pi} \mathbf{n}^T (J_1 \mathbf{x}_1 + f_{nl} - f_{ex}) \mathbf{n} d\tau_1 d\tau_2.$$

Due to the orthogonality property of the Fourier shape functions, it reduces to

$$\mathbf{r} = \mathbf{J}\mathbf{x} + f_{nl} - f_{ex}, \tag{4}$$

which is a nonlinear algebraic system of equations and can be solved using iterative methods such as Newton–Raphson method

$$\mathbf{x}_{n+1} = \mathbf{x}_n - \frac{\partial \mathbf{r}}{\partial \mathbf{x}}^{-1} \mathbf{r}_{x_n}.$$

The Jacobian

$$\frac{\partial \mathbf{r}}{\partial \mathbf{x}} = \mathbf{J} + \frac{\partial f_{nl}}{\partial \mathbf{x}}$$

$$\frac{\partial f_{nl}}{\partial \mathbf{x}} = \frac{1}{4\pi^2} \frac{\partial}{\partial \mathbf{x}} \int_0^{2\pi} \int_0^{2\pi} f_{nl} \mathbf{n} d\tau_1 d\tau_2 = \frac{1}{4\pi^2} \int_0^{2\pi} \int_0^{2\pi} \frac{\partial f_{nl}}{\partial \mathbf{x}} \mathbf{n} d\tau_1 d\tau_2. \quad (5)$$

As $\frac{\partial f_{nl}}{\partial \mathbf{x}}$ is a nonlinear function of x, \dot{x} , this can be evaluated using AFT (Alternating Frequency Time) method [16]. But the accuracy of this process depends on the number of sampling points considered in the time domain [17]. More the number of points is computationally expensive, but less points introduce aliasing error.

2.2 MTVM Formulation

Here also the same single-DOF equation of motion (Eq. (1)) is considered, and the time scaling τ_1 and τ_2 is applied.

If a time-varying function is approximated in terms of basis functions corresponding to one time scale, then the solution is approximated as

$$x(\tau) = \mathbf{n}(\tau)^T \mathbf{x} = \sum_{i=1}^{N_p} n_i(\tau) x_i$$

Here, \mathbf{n} vector contains wavelet functions or finite element shape functions evaluated in the discrete time points distributed in the fundamental time period. Similar way, if a time-varying function is approximated in terms of basis functions corresponding to two time scale, then it would be

$$x(\tau_1, \tau_2) = \mathbf{n}(\tau_1)^T \mathbf{X} \mathbf{n}(\tau_2) = \sum_{i=1}^{N_p} \sum_{j=1}^{N_p} n_i(\tau_1) n_j(\tau_2) x_{ij}. \quad (6)$$

Applying this approximation to the governing equation leads to

$$\begin{aligned} r = & m[\omega_1^2 \mathbf{n}''(\tau_1)^T \mathbf{X} \mathbf{n}(\tau_2) + 2\omega_1 \omega_2 \mathbf{n}'(\tau_1)^T \mathbf{X} \mathbf{n}'(\tau_2) + \omega_2^2 \mathbf{n}(\tau_1)^T \mathbf{X} \mathbf{n}''(\tau_2)] \\ & + c[\omega_1 \mathbf{n}'(\tau_1)^T \mathbf{X} \mathbf{n}(\tau_2) + \omega_2 \mathbf{n}(\tau_1)^T \mathbf{X} \mathbf{n}'(\tau_2)] + k \mathbf{n}(\tau_1)^T \mathbf{X} \mathbf{n}(\tau_2) \\ & + \mathbf{n}(\tau_1)^T \mathbf{F}_{nl} \mathbf{n}(\tau_2) - \mathbf{n}(\tau_1)^T \mathbf{F}_{ex} \mathbf{n}(\tau_2). \end{aligned}$$

Now Galerkin’s weighted residual method is applied by multiplying the equation with $\mathbf{n}_l(\tau_1)$ and $\mathbf{n}_m(\tau_2)^T$ and doing double cyclic integration with respect to τ_1 and τ_2 , respectively. This results in

$$\begin{aligned} \mathbf{R} = & m[\omega_1^2 \mathbf{D}^{(2)} \mathbf{X} \mathbf{D}^{(0)} + 2\omega_1 \omega_2 \mathbf{D}^{(1)} \mathbf{X} \mathbf{D}^{(1)} + \omega_2^2 \mathbf{D}^{(0)} \mathbf{X} \mathbf{D}^{(2)}] \\ & + c[\omega_1 \mathbf{D}^{(1)} \mathbf{X} \mathbf{D}^{(0)} + \omega_2 \mathbf{D}^{(0)} \mathbf{X} \mathbf{D}^{(1)}] + k \mathbf{D}^{(0)} \mathbf{X} \mathbf{D}^{(0)} \end{aligned} \quad (7)$$

$$+ \mathbf{D}^{(0)} \mathbf{F}_{nl} \mathbf{D}^{(0)} - \mathbf{D}^{(0)} \mathbf{F}_{ex} \mathbf{D}^{(0)},$$

where $\mathbf{D}^{(0)} = \langle \mathbf{n}^T \mathbf{n} \rangle$, $\mathbf{D}^{(1)} = \langle \mathbf{n}'^T \mathbf{n} \rangle$, $\mathbf{D}^{(2)} = \langle \mathbf{n}''^T \mathbf{n} \rangle$, and $\langle \mathbf{a}^T \mathbf{b} \rangle = \frac{1}{2\pi} \int_0^{2\pi} \mathbf{a}^T \mathbf{b} d\tau$. These matrices are known as differentiation matrices [15]. Differentiation matrices contain all the information of the basis functions used in the formulation. For example, if one considers \mathbf{n} to be Fourier functions instead of basis functions distributed around discrete time points, then $\mathbf{D}^{(0)}$ will become a diagonal matrix due to the orthogonality of Fourier functions, and this formulation will transform into an MHBM formulation (though the calculation of the nonlinear functions will not be the same for both methods as explained at the end of this section).

Equation (7) is a 2-dimensional matrix equation, and it is required to transform into a vector form to solve the system of equations. Now the vector form can be obtained using the Kronecker product by the rule $\text{vec}(\mathbf{AXB}) = (\mathbf{B}^T \otimes \mathbf{A}) \text{vec}(\mathbf{X})$. This leads to

$$\begin{aligned} \mathbf{r} = & \left[m(\omega_1^2 \mathbf{D}^{(2)T} \otimes \mathbf{D}^{(0)} + 2\omega_1 \omega_2 \mathbf{D}^{(1)T} \otimes \mathbf{D}^{(1)} + \omega_2^2 \mathbf{D}^{(0)T} \otimes \mathbf{D}^{(2)}) \right. \\ & \left. + c(\omega_1 \mathbf{D}^{(1)T} \otimes \mathbf{D}^{(0)} + \omega_2 \mathbf{D}^{(0)T} \otimes \mathbf{D}^{(1)}) + k \mathbf{D}^{(0)T} \otimes \mathbf{D}^{(0)} \right] \text{vec}(\mathbf{X}) \\ & + \mathbf{D}^{(0)T} \otimes \mathbf{D}^{(0)} \text{vec}(\mathbf{F}_{nl}) - \mathbf{D}^{(0)T} \otimes \mathbf{D}^{(0)} \text{vec}(\mathbf{F}_{ex}). \end{aligned}$$

\mathbf{r} is the residual vector, absolute of which should be minimized by finding the \mathbf{X} that is going to be the solution. Same as MHBM, here also the residual can be solved using iterative methods. The convergence rate depends on the choice of basis function that forms the differentiation matrix of the residual system. Now both TVM and MTVM use the same differentiation matrices $\mathbf{D}^{(0)}$, $\mathbf{D}^{(1)}$, and $\mathbf{D}^{(2)}$, and only difference is that MTVM uses the product of their combinations. So the nature of convergence is going to depend on the basis functions in the same way it depends for TVM.

For using gradient-based iterative methods like Newton–Raphson method, one needs to find the Jacobian. So again there is a requirement to find \mathbf{F}_{nl} and $\frac{\partial \mathbf{F}_{nl}}{\partial \mathbf{X}}$ from \mathbf{X} in each iteration. The nonlinear coefficient can be approximated as the function of \mathbf{x} same as that of the original nonlinear function, i.e., i th term of $\text{vec}(\mathbf{F}_{nl})$ is calculated as f_{nl} of i th term of $\text{vec}(\mathbf{X})$ and $\text{vec}(\dot{\mathbf{X}})$. (From \mathbf{X} , $\dot{\mathbf{X}}$ can be directly found as $\dot{\mathbf{X}} = \mathbf{D}^{(0)-1} [\omega_1 \mathbf{D}^{(1)} \mathbf{X} \mathbf{D}^{(0)} + \omega_2 \mathbf{D}^{(0)} \mathbf{X} \mathbf{D}^{(1)}] \mathbf{D}^{(0)-1}$.) This is the advantage of TVM over the AFT (Alternating Time Frequency) methods because in AFT methods the solution from each iteration needs to be transformed from frequency domain to time domain and vice versa. Figures 1 and 2 show the comparison between two methods.

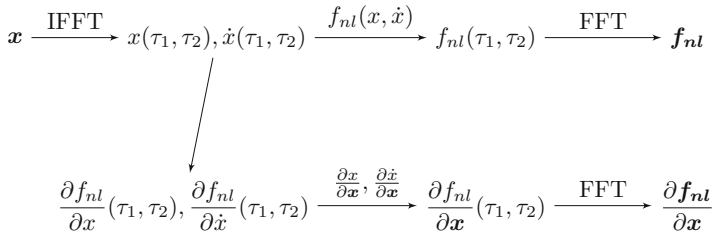


Fig. 1 Obtaining nonlinear function in HBM–AFT method

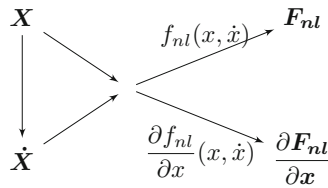


Fig. 2 Obtaining nonlinear function in TVM method

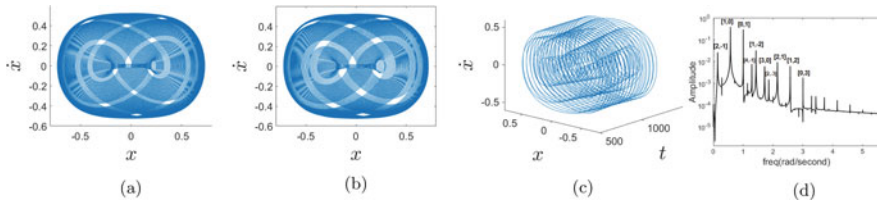


Fig. 3 Duffing oscillator under quasi-periodic excitation: $\alpha = 1.0286$, $\zeta = .005$, $\omega_1 = 0.572$, $\omega_2 = 1$, $F_1 = 0.385$, $F_2 = 0.1$. (a) Response obtained from MHBM. (b) Response obtained from MTVM. (c) 3d plot showing the response with time progress. (d) Frequency-domain plot

3 Results

In this chapter, the MTVM method is applied to the nonlinear systems consists of cubic spline basis function. The choice of this basis function is made from the result and analysis in the paper written by Rook [14], which concludes that for TVM, cubic spline has a good convergence rate compared to other basis functions like hat, sinc, or linear spline functions. It also requires a fewer number of time points to approximate the response, which makes the residual and Jacobian matrix smaller and the system computationally less expensive. The response of a quasi-periodically excited Duffing oscillator is shown in Fig. 3. The computation time to obtain this kind of system by MTVM is found to be lesser than MHBM. The number of iterations is more in MTVM than MHBM, but the computation time per iteration is less for MTVM, which makes the overall elapsed time lesser.

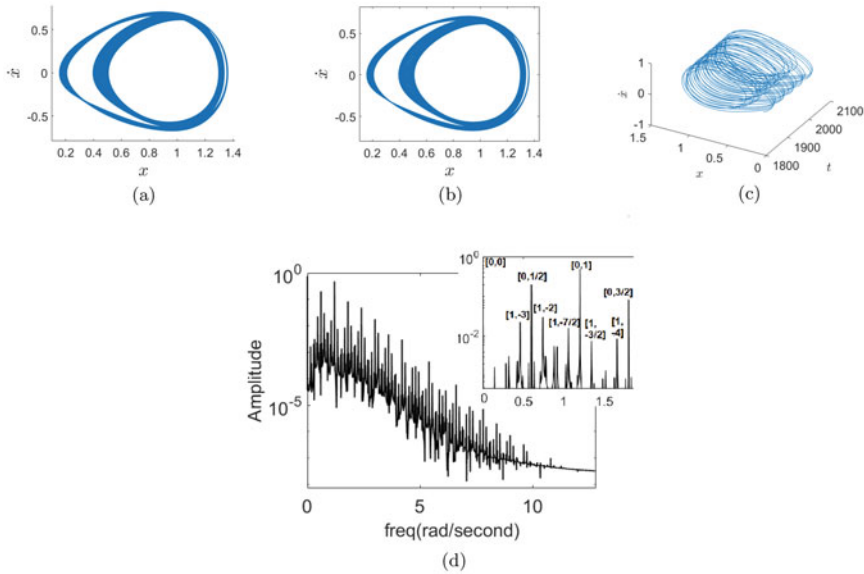


Fig. 4 Duffing oscillator under quasi-periodic excitation: $\alpha = 1$, $\zeta = 0.15$, $\omega_1 = \pi$, $\omega_2 = 1.2$, $F_1 = 0.05$, $F_2 = 0.28$. (a) Response obtained from MHBM. (b) Response obtained from MTVM. (c) 3d plot showing the response with time progress. (d) Frequency-domain plot

The frequency response (Fig. 3d) shows a good number of principle peaks corresponding to the harmonics of the excitation frequencies $\omega_1 = 0.572$ rad/s and $\omega_2 = 1$ rad/s. Although the major two peaks correspond to the harmonics [1,0], and [0,1], there exist other super-harmonic combinations like [1,-2], [2,-1], [2,1], [3,0], etc. marked in Fig. 3d, where harmonic $[i, j]$ corresponds to the response frequency $i\omega_1 + j\omega_2$ of the system that gets excited. Similar harmonic components are found in the second example as well, shown in Fig. 5. In Fig. 4, the sub-harmonic components are also found along with the super-harmonic components. To obtain this response, the time scaling in both the formulation is done as $\tau_1 = \omega_1 t$, $\tau_2 = \omega_2 t/2$. This enables the system to find the resonance of the second sub-harmonic of the second fundamental frequency ω_2 , its multiples, and combinations with other frequencies in the system. Harmonic combinations like [0,1/2], [1,3/2], [1,-7/2] have significant amplitudes in frequency-domain plot (Fig. 4d). Also, in the phase portrait, one can find the offset of the response from the (0,0) point.

The case shown in Fig. 5 is again investigated by varying one of the excitation amplitudes, shown in Fig. 6. It is found that the region of response covers the non-overlapping part of two circles, each with radius $2(F_1 + F_2)$ and offset between their center is $2F_1$ along the x axis. Though, this trend breaks down after certain value of F_2 ($F_2 > .4$).

After F_2 nearby 0.4, the solution amplitude jumps suddenly. For a linear system, the solution amplitude is supposed to vary linearly with F_2 . To identify the nonlinear

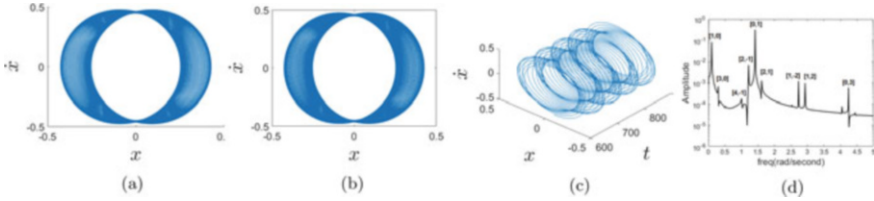


Fig. 5 Duffing oscillator under quasi-periodic excitation: $\alpha = 1$, $\zeta = 0.005$, $\omega_1 = 0.1$, $\omega_2 = \sqrt{2}$, $F_1 = 0.1$, $F_2 = 0.3$. (a) Response obtained from MHBM. (b) Response obtained from MTVM. (c) 3d plot showing the response with time progress. (d) Frequency-domain plot

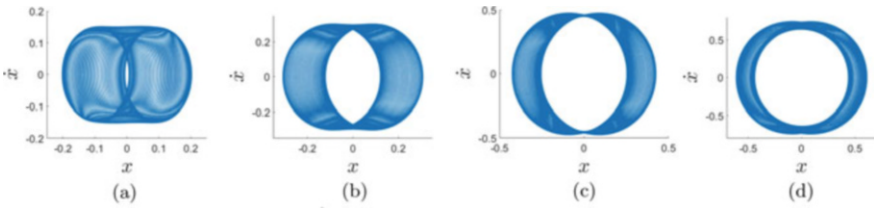


Fig. 6 Duffing oscillator under quasi-periodic excitation: $\alpha = 1$, $\zeta = .005$, $\omega_1 = .1$, $\omega_2 = \sqrt{2}$, $F_1 = .1$; phase portrait comparison with varying F_2 . (a) $F_2 = .1$. (b) $F_2 = .2$. (c) $F_2 = .3$. (d) $F_2 = .4$

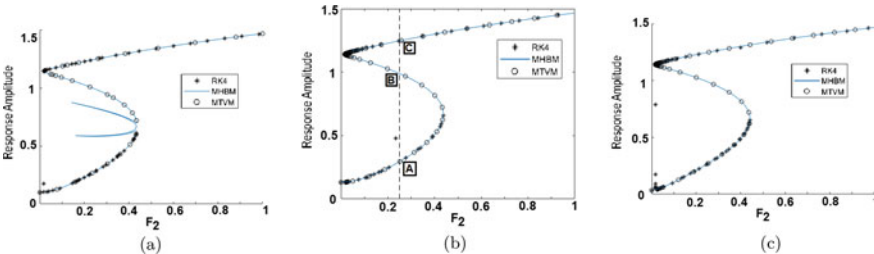


Fig. 7 Duffing oscillator under quasi-periodic excitation: $\alpha = 1$, $\zeta = 0.005$, $\omega_2 = \sqrt{2}$, $F_1 = 0.1$; continuation plot with F_2 varying and for four different values of ω_1 . (a) $\omega_1 = 0.01$. (b) $\omega_1 = 0.5$. (c) $\omega_1 = 2$

phenomena, a continuation method is applied with F_2 as the varying parameter. Hypersphere algorithm [10] is used for this purpose.

Figure 7 shows that in the range for F_2 between 0 and 0.4, the system shows at least three solutions, and after that only one solution is possible for each F_2 . Figure 8 shows an example of three different responses for the same parameter values. The phase portrait shown in Fig. 6 corresponds to the lowest branch of the 3-solution region. The continuation curve remains more or less the same for $\omega_1 > 0.35$. Figure 7b,c are examples of such curve. In fact, this trend is the same for the periodically excited Duffing oscillator if the response amplitude is plotted against excitation amplitude. But when ω_1 is at the vicinity of ω_2 , the continuation curve shows a different trend, shown in Fig. 9. At $\omega_1 = 1.5$ rad/s

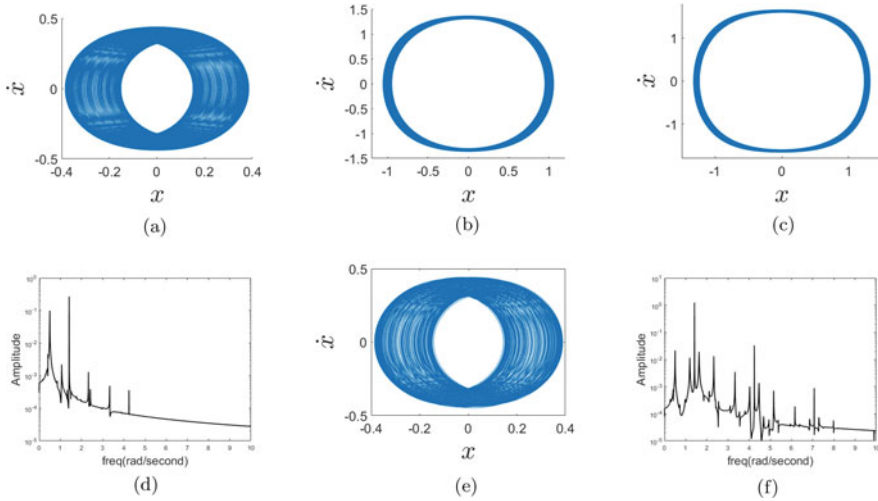


Fig. 8 Three different solutions obtained from Fig. 7b at $F_2 = 0.25$, marked as A, B, and C. (a). Phase portrait of A. (b) Phase portrait of B (unstable). (c) Phase portrait of C. (d) Frequency plot of A. (e) Stable solution of B using RK4. (f) Frequency plot of C

which is nearby $\omega_2 = \sqrt{2}$, it is capable of showing more than 10 different solutions at the same input parameters and forcing functions. The continuation curve also cuts $F_2 = 0$ at three different amplitudes. $F_2 = 0$ indicates a periodic excitation with frequency $\omega_1 = 1.5$ rad/s. The frequency response of Duffing oscillator under periodic excitation shows 3-solutions in a fixed region of frequency, and in the rest of the frequency domain, it has a single-phase portrait solution [18]. Figure 9 shows that the system has multiple solutions when periodically excited with frequency 1.5 rad/s.

Change in system behavior by changing excitation frequency can be better analyzed by observing response by frequency continuation method. Similar to the force continuation algorithm, one can apply continuation in one excitation frequency keeping the other frequency constant. For MHBm, it can cause some problems if the varying frequency tries to cross the constant frequency. This is because, if both of the excitation frequencies are the same, one cannot any more assume that the system consists of two independent time scales. Moreover, if one can obtain the complete frequency response in a $\omega_1 \times \omega_2$ domain that covers the resonance region common to both excitation frequencies, one can find that the cross-section of that surface cut through one of the frequency axes contains multiple non-connected branches. So continuation in one frequency will not give the full picture of the system response. Instead, one can use continuation in both ω_1 and ω_2 and keeping their ratios constant. Now for different ratios, different continuation curves can be obtained; combining all of them, one can obtain the frequency response in the 2D frequency domain.

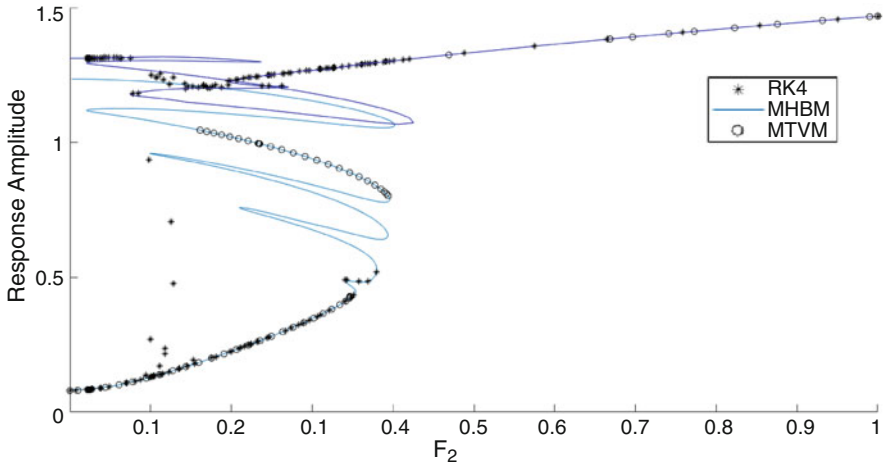


Fig. 9 Continuation plot for the system mentioned in Fig. 7 with $\omega_1 = 1.5$, which is in the vicinity of $\omega_2 = \sqrt{2}$

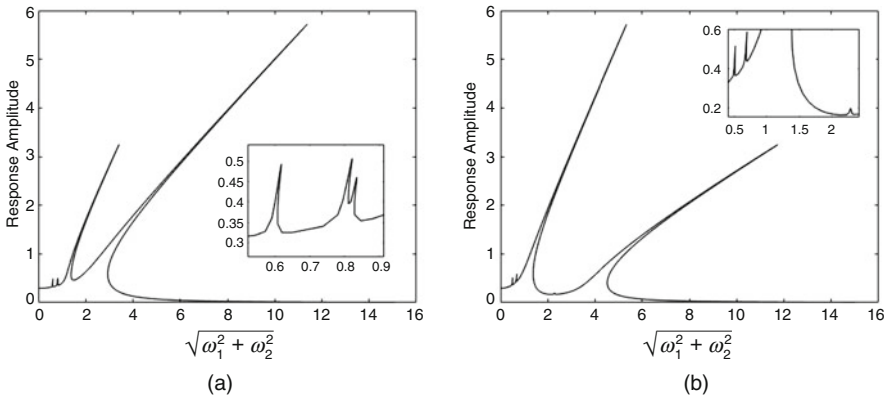


Fig. 10 Continuation plot by varying norm of excitation frequency with different frequency ratios, obtained from MHBM ($F_1 = 0.1, F_2 = 0.3$). (a) $\frac{\omega_2}{\omega_1} = 0.5095$. (b) $\frac{\omega_2}{\omega_1} = 3.7321$

In Fig. 10, two such continuation plots are shown. If the continuation plots are analyzed by changing $\tan^{-1} \frac{\omega_2}{\omega_1}$ from 0° to 90° , one can find that initially, two major peaks will be converging to each other. They will join and become a single peak when the ratio $\frac{\omega_2}{\omega_1}$ becomes 1, which is expected as it will become a periodically excited system. Again if the angle is increased, it will divide into two peaks and move away from each other. These two peaks correspond to the resonance of the system with each of the excitation frequencies, respectively. During this whole process, both of the peaks will have their peak values constant, which are approximately 5.717 (for the larger peak) and 3.247 (for the shorter peak), and these values depend on the amplitudes of the excitation frequencies,

respectively. But when they join together at the frequency ratio of unity, the peak value jumps to approximately 6.609. Other than these two major peaks, one can find some more peaks with much smaller amplitude. In Fig. 10a where frequency ratio $\frac{\omega_2}{\omega_1} = 0.5095$, there exist three such peaks at the excitation frequency $(\omega_1, \omega_2) = (0.5512, 0.2808)$, $(0.7327, 0.3733)$, and $(0.7446, 0.3794)$ respectively, all in *rad/s*. These peaks correspond to resonance in the harmonic components [1,2], [0,3], and [2,-1], respectively. The frequency-domain response at these small peak points is observed, which revealed these harmonic components with maximum response amplitudes. In Fig. 10b, also one can find peaks with similar kinds of resonances.

4 Conclusions

The proposed MTVM method is found to be a useful tool for obtaining quasi-periodic responses of nonlinear dynamical systems. Both super-harmonic and sub-harmonic combinations were found in the response of the Duffing oscillator. The response obtained from the proposed MTVM approach shows a good match with that of MHBM and numerical integration. MTVM effectively captures the quasi-periodic responses in this study identified by MHBM and numerical integration. In comparison with MHBM, MTVM is found to be more time efficient and computationally less rigorous in the stepwise calculation for Duffing kind of systems. In the force continuation, there exist some regions in the solution where MTVM was not able to continue and restarting of the calculation was required to obtain different segments of the continuation curve, whereas MHBM did not have such problems. Using force and frequency continuation, a good idea of the nonlinear behavior of the Duffing oscillator is obtained, and migration of their behavior is observed with changing the parameters of excitation. To conclude about the proposed method, MTVM can be considered as a good extension of TVM to the multi-frequency domain. Although the rigorous study is still required with different nonlinear models to analyze its overall performance, one can expect same kind of behavior of MTVM as that of TVM in the case of convergence and accuracy. So same kind of relationship one can establish between MTVM and MHBM similar to the existing relationship between TVM and HBM.

References

1. S.H. Strogatz, *Nonlinear Dynamics and Chaos: With Applications to Physics, Biology, Chemistry, and Engineering*. Studies in Nonlinearity (Avalon Publishing, New York, 2014)
2. I. Kovacic, M.J. Brennan, Background: on Georg Duffing and the Duffing equation, in *The Duffing Equation: Nonlinear Oscillators and their Behaviour* (2011), pp. 1–23
3. M.J. Brennan, I. Kovacic, Examples of physical systems described by the Duffing equation, in *The Duffing Equation: Nonlinear Oscillators and their Behaviour* (2011), pp. 25–53

4. M.S.H. Chowdhury, M.d. Alal Hosen, K. Ahmad, M.Y. Ali, A.F. Ismail, High-order approximate solutions of strongly nonlinear cubic-quintic Duffing oscillator based on the harmonic balance method. *Results Phys.* **7**, 3962–3967 (2017)
5. C.H. Miwadinou, A.V. Monwanou, L.A. Hinvi, A.A. Koukpededji, C. Ainamon, J.B. Chabi Orou, Melnikov chaos in a modified Rayleigh–Duffing oscillator with ϕ 6 potential. *Int. J. Bifurcation Chaos* **26**(05), 1650085 (2016)
6. A.Y.T. Leung, Z. Guo, Homotopy perturbation for conservative Helmholtz–Duffing oscillators. *J. Sound Vib.* **325**(1-2), 287–296 (2009)
7. L. Zhou, F. Chen, Chaotic motions of the Duffing-van der Pol oscillator with external and parametric excitations. *Shock Vib.* **2014**, 1–5 (2014)
8. L. Ravisankar, V. Ravichandran, V. Chinnathambi, Prediction of horseshoe chaos in Duffing-van der Pol oscillator driven by different periodic forces. *Int. J. Eng. Sci.* **1**(5), 17–25 (2012)
9. M.S. Alam, Md. A. Razzak, Md. A. Hosen, Md. R. Parvez, The rapidly convergent solutions of strongly nonlinear oscillators. *SpringerPlus* **5**(1), 1–16 (2016)
10. I.R. Praveen Krishna, C. Padmanabhan, Improved reduced order solution techniques for nonlinear systems with localized nonlinearities. *Nonlinear Dyn.* **63**(4), 561–586 (2011)
11. M. Guskov, J.-J. Sinou, F. Thouverez, Multi-dimensional harmonic balance applied to rotor dynamics. *Mech. Res. Commun.* **35**(8), 537–545 (2008)
12. C. Sun, Y. Chen, L. Hou, Steady-state response characteristics of a dual-rotor system induced by rub-impact. *Nonlinear Dyn.* **86**(1), 91–105 (2016)
13. M. Guskov, F. Thouverez, Harmonic balance-based approach for quasi-periodic motions and stability analysis. *J. Vib. Acoust.* **134**(3), 031003 (11 pages) (2012)
14. T. Rook, An alternate method to the alternating time-frequency method. *Nonlinear Dyn.* **27**(4), 327–339 (2002)
15. K. Prabith, I.R. Praveen Krishna, A time variational method for the approximate solution of nonlinear systems undergoing multiple-frequency excitations. *J. Comput. Nonlinear Dyn.* **15**(3), 031006 (2020)
16. Y.-B. Kim, S.T. Noah, Quasi-periodic response and stability analysis for a non-linear Jeffcott Rotor. *J. Sound Vib.* **190**(2), 239–253 (1996)
17. E.G. Williams, *Fourier Acoustics: Sound Radiation and Nearfield Acoustical Holography* (Academic Press, New York, 1999)
18. M.J. Brennan, I. Kovacic, A. Carrella, T.P. Waters, On the jump-up and jump-down frequencies of the Duffing oscillator. *J. Sound Vib.* **318**(4–5), 1250–1261 (2008)

Part V
Bifurcation and Dynamic Instability

Bifurcation and Triggers of Coupled Singularities in the Dynamics of Generalized Rolling Pendulums



Katica R. (Stevanović) Hedrih

1 Introduction

Let's start with the definition of what a trigger of coupled singularities is. If in a phase portrait, which shows the nonlinear dynamics of a system with one-degree-of-freedom movement, there are three singular points, two types of stable centers, and one type of unstable saddle, which are surrounded by a homoclinic orbit-separatrix phase trajectory in the form of number "eight", if it intersects at an unstable point of the saddle type, then the set of these elements represents the trigger of the coupled singularities (see References [1, 2–6]). One look at the contents of articles on the rolling of bodies along surface and lines in real space $Rn3$ written by other authors give as following: The problem of qualitative analysis of rolling motion without slipping of a homogeneous ball and homogeneous disk on a horizontal plane was studied by S.A. Chaplygin (1903, 1911), D.Korteweg (1900), and P.Appel (1900) (see References [7, 8]). In his dictatorial dissertation [9] from 1923, Demmckenko V. studied rolling, without sliding, the ball in which the gyroscope was placed. From the numerous literatures on rolling without sliding heavy bodies on planes, on surfaces of various shapes, as well as on straight or curvilinear paths, we will point out only some of the latest ones, in which real systems are studied. In this paper, for brief illustrations, we cite the following References [10–12]. Rolling without sliding heavy bodies on planes, on surfaces of different shapes, as well as on straight or curved paths are systems with one-sided constraints. Theoretical analyzes and

K. R. (Stevanović) Hedrih (✉)

Department of Mechanics, Mathematical Institute of Serbian Academy of Science and Arts, Belgrade, Serbia

Faculty of Mechanical Engineering at University of Niš, Niš, Serbia

e-mail: katicah@mi.sanu.ac.rs; khedrih@sbb.rs

results can be found in a series of works by Kozlov and co-authors, and among them we cite references [13] explicate talk about it.

In a series of author's published articles, between them and papers [6, 14–16], some partially obtained particular results of studying the dynamics of rolling pendulums along curvilinear paths in stationary or rotating vertical planes around a vertical axis at a constant angular velocity, with corresponding phase portraits, are presented. A series of phase portraits with different structures of singular points and phase trajectories, especially those of separatrix, are presented. In the last manuscript [2], special attention is paid to the occurrence of bifurcation of stable equilibrium positions and the existence of triggers of coupled singularities.

2 Trigger of Coupled Singularities in the Dynamics of Generalized Rolling Pendula Along Curvilinear Route in the Stationary Vertical Plane

In the series of References [4, 14, 15] of the authors of this paper, the results of research nonlinear dynamics of special cases of generalized rolling pendulums on stationary curvilinear trace in the vertical plane and a series of phase portraits in phase planes (independent generalized coordinate and its derivative) are presented. Each of these phase portraits contains at least one trigger of coupled singularities, consisting of an unstable saddle type singular point, and two stable center type singular points, surrounded by a single (separatrix) phase trajectory in the form of number “eight”, which intersects at an unstable saddle-type singular point. In such a system there is no bifurcation phenomenon [7, 8], because the trigger of coupled singularities is a property of nonlinear dynamics of such systems and in such a system there is no parameter with whose change such a trigger of coupled singularities would disappear, which is caused by the properties of the curvilinear line extremums in a set of one maximum and two minimums of the curvilinear trajectory in the vertical plane.

By analyzing the shape of the paths along which the body of a generalized rolling pendulum rolls, without slipping, and also structures of different phase trajectory portraits of different particular examples it is possible to formulate the following a general definition and theorem on the stationary trigger of coupled singularities:

Definition Suppose that a curvilinear route is given by a pair function of a shape $y = f(x)$, for which it holds $f(x) = f(-x)$, and which has at the points for extreme values: the minimums $C_s(x_s, y_s = f(x_s))$ for $\dot{f}(x_s) = 0, f''(x_s) > 0$, and the maxima $S_s(x_s, y_s = f(x_s))$ for $\dot{f}(x_s) = 0, f''(x_s) < 0$. The number of maxima of a function defined in this way is odd, if one of the maxima is at zero coordinate, and the number of minima is even, if it is not the only one with zero coordinates, so the total number of extremes of such a function is always odd.

Theorem 1 In the phase portrait of the dynamics of a generalized rolling pendulum, whose heavy body rolls along a curvilinear trajectory in the stationary vertical plane and in the Earth's gravitational field, each maximum of the rolling path corresponds to one singular point of the unstable saddle type, while for each minimum of the curvilinear trajectory, one singular point of the stable center type corresponds to the stable position of the pendulum equilibrium on the trajectory. As the curvilinear path is defined by a pair function, and if the number of maxima is one and the number of minima is two, then one trigger of coupled singularities is present in the phase portrait. This trigger consists of three coupled singular points and one homoclinic separatrix (a phase trajectory) in the form of the number “eight”, which intersects at a singular point corresponding to the maximum of the curvilinear trajectory. If the number of maxima is odd, and the number of minima of the curvilinear path is even, then in the phase portrait there are coupled triggers of coupled singularities and separatrix in the form of a multiple multiplied number “eight”.

3 Bifurcation and Trigger of Coupled Singularities in the Dynamics of Generalized Rolling Pendula Along the Curvilinear Route in a Rotating Vertical Plane at a Constant Angular Velocity About a Vertical Axis

In a series of References [2, 6, 16] the results of research of nonlinear dynamics of special cases of generalized rolling pendulums on curvilinear line in a rotating vertical plane, at a constant angular velocity Ω around the vertical axis are presented, and a given series of phase trajectory portraits in phase planes. Each of these phase portraits contains at least one trigger of coupled singularities, consisting of a singular point of the unstable saddle type, and two singular points of the stable center type, surrounded by a single-separator phase trajectory in the form of number “eight”, which intersects at a singular point of the unstable saddle type. The angular velocity Ω of rotation of the vertical plane around the vertical axis appears as a bifurcation parameter, whose change can achieve the disappearance of the trigger of coupled singularities, or the appearance of that trigger in the phase portrait, or the appearance of bifurcation [7, 8] of a stable type singular position, and two new singular points of the stable center type appear around it, and in the phase portrait a separatrix phase trajectory in the form of a number of “eight” that surrounds them and self-intersect at a singular point which has lost stability and bifurcated into unstable saddle-type singular point. In such a system, there is now a phenomenon of a bifurcation [1, 2, 6–8, 16], because the trigger of coupled singularities is now in results caused by the property of nonlinearity in the form of bifurcation and nonlinear dynamics of such a system. And with the existence of a bifurcation parameter with the change of which the trigger of coupled singularities appears or disappears.

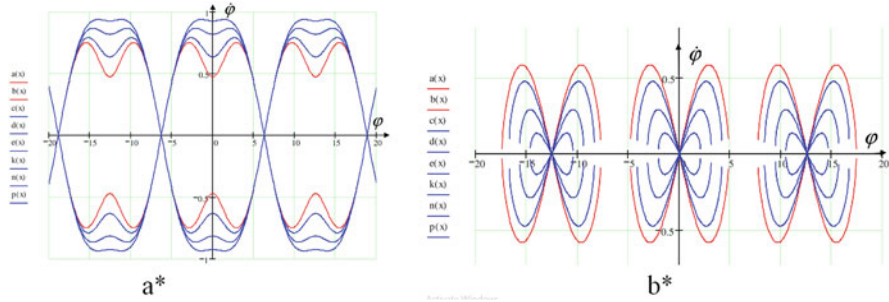


Fig. 1 Graphic representation of the transformation, by changing the bifurcation parameter λ , of the separatrix phase trajectories of the phase portrait

For example, the ordinary nonlinear differential equation of non-linear rolling dynamics, non-slip, heavy homogeneous thin disk, radius r , in a circle, radius R , in a rotating vertical plane at a constant angular velocity Ω about the vertical Central axis, is: $\ddot{\varphi} + \frac{\Omega^2}{\kappa} (\lambda - \cos \varphi) \sin \varphi = 0$, which φ is generalized independent coordinate, $\kappa = 1 + \frac{I_2^2}{r^2}$ is the coefficient of disk rolling and $\lambda = \frac{g}{(R-r)\Omega^2}$ is the bifurcation parameter (see References [1, 6, 7, 16] for details).

In Fig. 1, a^* and b^* , it is shown graphic representation of the transformations, by changing the bifurcation parameter λ , of the separatrix phase trajectories of the phase portrait of the non-linear rolling dynamics of a heavy homogeneous thin disk, radius r , in a circle, radius R , in a rotating vertical plane at a constant angular velocity Ω around the vertical Central axis. These graphs are also presentation continuous process of bifurcations followed by the change of bifurcation parameter λ .

3.1 Main Results – Existence of Bifurcations and Triggers of Coupled Singular Points and Characteristic Equation of Nonlinear Dynamics of a Generalized Rolling Pendulum Along Trajectory in the Rotating Vertical Plane at a Constant Angular Velocity About Vertical Axis

In this paper, main attention is paid to a more detailed analysis of *the characteristic equation* of dynamics of the generalized rolling pendulum, along trajectory in the rotate vertical plane at a constant angular velocity about vertical axis, which was performed in [2] in the form:

$$f'(x) \left\{ 1 - r \frac{f''(x)}{[1 + [f'(x)]^2]^{\frac{3}{2}}} \right\} - \frac{2\kappa}{3g} \Omega^2 \left\langle x - \frac{rf'(x)}{\sqrt{1 + [f'(x)]^2}} \right\rangle \left\langle 1 - \frac{rf''(x)}{[1 + [f'(x)]^2] \sqrt{1 + [f'(x)]^2}} \right\rangle = 0 \tag{1}$$

and in which: $y = f(x)$ in general, or in particular cases $y = f(x) = kx^2(x^2 - a^2)^2$ or $y = f(x) = kx^2(x^2 - a^2)^2(x^2 - b^2)$ is equation of the curvilinear path, where a , b , and k are known constants, and with the following relation $a < b$, κ , $\kappa = 1 \frac{r^2}{R^2}$ the rolling coefficient, r the radius of the circle of the body of the pendulum by which the pendulum rolls along curvilinear paths, Ω the angular velocity of rotation of the vertical plane about the vertical axis, and in which the curvilinear rolling route of the generalized rolling pendulum. A series of graphs of characteristic Eq. (1) was made, which shows the existence of triggers of coupled singularities, as well as a set of different separatrix – separating phase trajectories. An analysis of the stability of singular points is given, as well as the relative equilibrium positions of the generalized rolling pendulum on the rotate curvilinear path. The different types of periodic rolling of the generalized rolling pendulum along the rotate curvilinear path, as well as the dependence of the period of periodic rolling on the initial conditions of the dynamics of the generalized rolling pendulum, are evident.

The singular point center type, which corresponds to stable equilibrium position and point of the minimum at curvilinear route, loses stability and turns into an unstable singular point of the saddle type, and two new singular points of the type of stable centers appear around it. Triggers of coupled three singular points also appear in the phase portrait, and with that to the existence of separatrix – phase trajectory, in the shape of the number “eight”, which are not present in the dynamics when that vertical plane is at rest.

It is pointed out that there is a mathematical and qualitative analogy of the properties of the dynamics of a generalized rolling pendulum with the movement of a heavy material point along a smooth curvilinear path in a rotating vertical plane around a vertical axis at a constant angular velocity Ω .

In Figs. 2 and 3, graphics of the curvilinear route, as well as the frequency characteristic functions (1) of the nonlinear rolling dynamics of a rigid heavy thin disk, in a rotating vertical plane with a constant angular velocity around the vertical axis defined by the equation $y = f(x) = kx^2(x^2 - a^2)$ and $y = f(x) = kx^2(x^2 - a^2)^2(x^2 - b^2)$ respectively, are presented.

In Fig. 2, a detail of the graph of the frequency characteristic function (1) of nonlinear rolling dynamics of a rigid heavy thin disk, along a curvilinear path in a rotating vertical plane with a constant angular velocity around the vertical axis, defined by the equation $y = f(x) = kx^2(x^2 - a^2)$: detail shows the phenomenon of bifurcation of a stable singular point center type into unstable saddle-type and

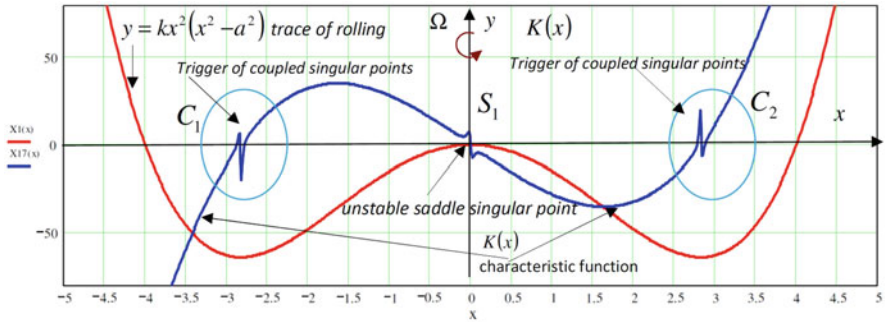


Fig. 2 Graphs of the curvilinear route, as well as the frequency characteristic functions (1) of the nonlinear rolling dynamics of a rigid heavy thin disk, in a rotating vertical plane with a constant angular velocity around the vertical axis defined by the equation $y = f(x) = kx^2(x^2 - a^2)$

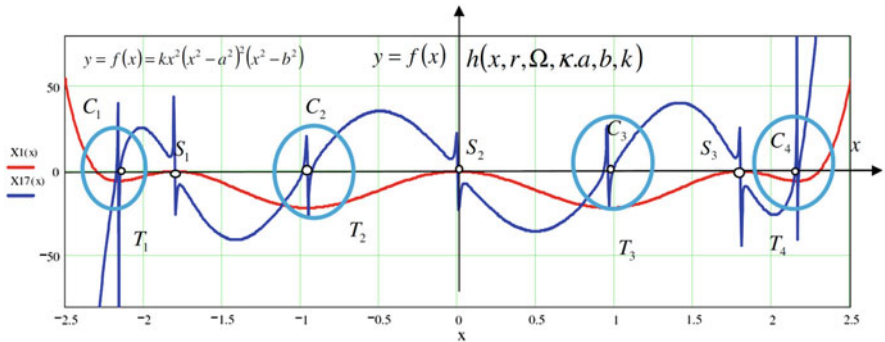


Fig. 3 Graphs of the curvilinear route, as well as the frequency functions of the nonlinear rolling dynamics of a rigid heavy thin disk, in a rotating vertical plane with a constant angular velocity around the vertical axis defined by the equation $y = f(x) = kx^2(x^2 - a^2)^2(x^2 - b^2)$

appearance of two new stable singular points center type around - appearance of a trigger of coupled singularities, are visible.

In Fig. 4, a detail of the graph of the frequency characteristic function (1) of nonlinear rolling dynamics of a rigid heavy thin disk, along a curvilinear path in a rotating vertical plane with constant angular velocity around the vertical axis, defined by the equation $y = f(x) = kx^2(x^2 - a^2)^2(x^2 - b^2)$: detail shows the phenomenon of bifurcation of a stable singular point center type into unstable saddle-type point and appearance of two new stable singular points center type around - appearance of a trigger of coupled singularities are visible.

By analyzing the shape of the paths along which the body of the generalized rolling pendulum rolls, without slipping, as well as by analyzing a series of phase portraits and the structure of singular points in them, as well as structural stability and sensitivity to changes in the system's bifurcation parameters, based on series published author's References [4, 14, 15], as well as a large number of numerical

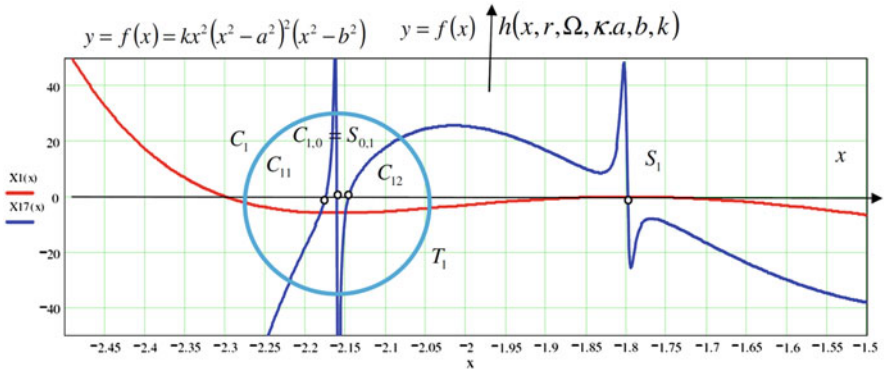


Fig. 4 Detail of the graph of the frequency function of nonlinear rolling dynamics of a rigid heavy thin disk, along a curvilinear path in a rotating vertical plane with constant angular velocity around the vertical axis, defined by the equation $y = f(x) = kx^2(x^2 - a^2)^2(x^2 - b^2)$; detail shows the phenomenon of bifurcation of a stable singular point center type into unstable saddle-type brush and basket of two new stable singular points center type around – appearance of a trigger of coupled singularities

experiments and obtained different graphs of nonlinear phenomena in nonlinear dynamics of generalized rolling pendulum, a new theorem of bifurcation and of trigger of coupled singularities can be defined in the following formulation:

Theorem on bifurcation and on the trigger of coupled singularities in the dynamics of generalized rolling pendulums along curvilinear routes in a rotating vertical plane around a vertical axis at a constant angular velocity: Let the curved line, given with $y = f(x)$, for which it is valid $f(x) = f(-x)$, and which has at the points for extreme values $EX_s(x_s, y_s = f(x_s))$ $\exists a \dot{f}(x_s) = 0$, the minimums $C_s(x_s, y_s = f(x_s))$ for $\dot{f}(x_s) = 0, f''(x_s) > 0$, and the maxima $S_s(x_s, y_s = f(x_s))$ for $\dot{f}(x_s) = 0, f''(x_s) < 0$, the curvilinear route, along which rolls, without slipping, a heavy homogeneous thin disk, of radius $r > 0$, and let it located in the Earth's gravitational field, and in the vertical plane, which rotates around the vertical axis, at a constant angular velocity $\Omega > 0$. The characteristic equation for determining the singular points, as well as the position of the relative equilibrium of the disk on the curvilinear path, in the vertical rotating plane around the vertical axis at a constant angular velocity $\Omega > 0$, is of the form:

$$K(x) = f'(x) \left\{ 1 - r \frac{f''(x)}{[1 + [f'(x)]^2]^{\frac{3}{2}}} \right\} - \frac{2\kappa}{3g} \Omega^2 \left\langle x - \frac{rf'(x)}{\sqrt{1 + [f'(x)]^2}} \right\rangle \left\langle 1 - \frac{rf''(x)}{[1 + [f'(x)]^2] \sqrt{1 + [f'(x)]^2}} \right\rangle = 0 \quad (2)$$

or in the form

$$K(x) = \left\{ 1 - r \frac{f''(x)}{[1 + [f'(x)]^2]^{\frac{3}{2}}} \right\} \left\{ f'(x) - \frac{2\kappa}{3g} \Omega^2 \left\langle x - \frac{rf'(x)}{\sqrt{1 + [f'(x)]^2}} \right\rangle \right\} = 0 \tag{3}$$

in which it is $\kappa = \frac{\mathbf{J}_p}{Mr^2} = \frac{i_p^2}{r^2} = \frac{i_c^2}{r^2} + 1 = \kappa$, that is $\kappa^{\frac{3}{2}}$, the rolling coefficient of the disk, because is $\mathbf{J}_{Cz} = \sigma \frac{r^4}{4} \pi = M \frac{r^2}{4}$ and $\mathbf{J}_P = \mathbf{J}_c + Mr^2 = \frac{3}{2}Mr^2$, and g the acceleration of the Earth gravity. Around each extremum of the curvilinear trajectory, which is the minimum defined by $C_s(x_s, y_s = f(x_s))$ for $\dot{f}(x_s) = 0$, $f'(x_s) > 0$, in the dynamics of thin dick rolling, bifurcation and trigger of conjoined singularities appear, and around each extremum, which is maximum defined with $S_s(x_s, y_s = f(x_s))$ for $\dot{f}(x_s) = 0$, $f'(x_s) < 0$, there is no bifurcation and trigger of coupled singularities (see Figs. 2, 3, and 4).

Proof In order to prove the claims from the previous theorem on bifurcation and on triggers of coupled singularities, in addition to the approach to graphical paths through graphs of characteristic algebra nonlinear equation $K(x) = 0$, we can also do it analytically. To prove by the analytical method, it is first necessary to determine the minima $C_s(x_s, y_s = f(x_s))$ for $\dot{f}(x_s) = 0$, $f'(x_s) > 0$, and the maxima $S_s(x_s, y_s = f(x_s))$ for $\dot{f}(x_s) = 0$, $f'(x_s) < 0$, of the curvilinear route of generalized pendulum rolling, by which we analytically defined the curvilinear trajectory. We will then develop a characteristic function (2), in the neighborhood around each local extremum, the minimum $C_s(x_s, y_s = f(x_s))$ for $\dot{f}(x_s) = 0$, $f'(x_s) > 0$, or the maximum $S_s(x_s, y_s = f(x_s))$ for $\dot{f}(x_s) = 0$, $f'(x_s) < 0$, the curvilinear path, in Taylor’s series, and examine the conditions under which there are three real roots in the local neighborhood of the same. The absence of three zeros in the local neighborhood of the maximum $S_s(x_s, y_s = f(x_s))$ for $\dot{f}(x_s) = 0$, $f'(x_s) > 0$ of the curvilinear path gives a conclusion about the non-existence of bifurcation and triggers of coupled singularities, and the existence of three real zeros in the local environment of the minimum of the curvilinear path gives a conclusion about the occurrence of bifurcation and the existence of triggers of coupled singularities.

In order to develop the function of the characteristic Eq. (2) in the local environment of the singular point $C_s(x_s, y_s = f(x_s))$ for $\dot{f}(x_s) = 0$, $f'(x_s) > 0$, the minimum $C_s(x_s, y_s = f(x_s))$ for $\dot{f}(x_s) = 0$, $f'(x_s) > 0$ of this function $y = f(x)$, we will use the shift $x_s \rightarrow x_s + x$ on the basis of which we wrote the following approximation:

$K(x_s)_{x_s \rightarrow x_s+x} \approx K(x_s) + \frac{1}{1!} K'(x_s)x + \frac{1}{2!} K''(x_s)x^2 + \frac{1}{3!} K'''(x_s)x^3 + \dots$ in the form cubic polynomial and we add the terms to the cube, so that we get the cube equation, whose roots need to be examined.

Then it is necessary to solve the first three derivatives $K(x_s)$, $K'(x_s)$, $K''(x_s)$, $K'''(x_s)$ of the characteristic function $K(x)$ at the extreme value points – of any singular point that corresponds to the minimum of the function $y = f(x)$ which

defines the curvilinear path of rolling. These $K(x_s)$, $K'(x_s)$, $K''(x_s)$, $K'''(x_s)$ would be the coefficients of the cubic equation of approximation of the characteristic equation $K(x) = 0$ (2) of the nonlinear dynamics of the rolling pendulum along that path in a rotating vertical plane around the vertical axis at a constant angular velocity.

Then, for each analytical approximation of the characteristic equation $K(x) = 0$ of nonlinear dynamics of the rolling pendulum in the vicinity of the extremum, the conditions for the existence of three real roots and the conditions when they occur, as well as the intervals of system parameters in which they occur or disappear. Such parameters are bifurcation parameters and occurrence intervals of triggered singularity triggers.

4 Concluding Remarks

The paper presents an analogy of the nonlinear dynamics of a heavy material point along curvilinear paths in a vertical stationary, as well as, in a rotating vertical plane, at a constant angular velocity, around a vertical axis and the nonlinear dynamics of a generalized rolling pendulum along the same curvilinear paths in both these cases. Two theorems are defined. One is about the existence of triggers of coupled singularities as a consequence of the existence of the extremums-minimums of the curvilinear rolling routes in the stationary vertical plane. The second theorem describes the process of bifurcation and occurrence and disappearance of triggers of coupled singularities in the local environment of the minimum of curvilinear paths in rotating vertical planes, at a constant angular velocity around the vertical axis, caused by the angular velocity of rotation of the vertical plane in which the curvilinear path is. This angular velocity is a bifurcation parameter. Based on a numerical experiment with various curvilinear rolling routes, a large number of graphs of the characteristic function of nonlinear dynamics of generalized rolling pendulum, were obtained, such as phase trajectory portraits of nonlinear dynamics of a generalized rolling pendulum along curvilinear paths in a rotating vertical plane at different values of constant angular velocity about a vertical axis, based on when the theorem of occurrence of triggers of coupled singularities, its properties, and disappearance, in the nonlinear dynamics of generalized rolling pendulums was formulated. From a large number of obtained graphics, the most characteristic examples were selected and presented in the paper. The results of previous published author's references for particular examples of the shape of curvilinear paths along which the body of a generalized rolling pendulum rolls were also used. The analytical method of proving the definition of the theorem is also presented.

We can conclude that, in the observed case of characteristic function presented in Fig. 3, in the phase trajectory portrait, three types of separatist phase trajectories – homoclinic orbits in the shape of the number “eight” are observed: the first type of separatrix phase trajectories surrounds only three coupled singular points; the

second type of separatrix phase trajectories surrounds two triggers of coupled singularities and only intersects at one singular point of the unstable saddle type between them; the third type of third-order homoclinic orbits surrounds one second-order homoclinic orbit, as well as two first-order homoclinic orbits.

References

1. A.A. Andronov, A.A. Vitt, S. Haykin, *Teoriya kolebaniy (Theory of oscillations)* (Nauka, Moskva, 1981), p. 568. (In Russian)
2. K.R. Hedrih (Stevanović), Dynamics of a rolling heavy thin disk along rotate curvilinear trace on vertical plane about vertical axis, Proceedings, of the 7th International Congress of the Serbian Society of Mechanics, (32th Yugoslav Congress) 24–16 June 2019, Sremski Karlovci, Serbia, pp. 96–97; ISBN 978-86-909973-7-4; <http://www.ssm.org.rsm>
3. K.R. Hedrih (Stevanović), A trigger of coupled singularities. *Meccanica*, **39**(3), pp. 295–314 (2004). <https://doi.org/10.1023/B:MECC.0000022994.81090.5f>
4. K.R. Hedrih (Stevanović), Vibro-impact dynamics in systems with trigger of coupled three singular points: Collision of two rolling bodies. The 24th International Congress of Theoretical and Applied Mechanics (IUTAM ICTAM 2016), Montreal, Canada, 21–26 August, 2016, Book of Papers, pp. 212–213. IUTAM permanent site. ISBN: NR16-127/2016E-EPUB; Catalogue Number: 978-0-660-05459-9
5. K.R. Hedrih (Stevanović), *Nonlinear Dynamics of a Heavy Material Particle along a Circle Which Rotates and Optimal Control*, Chapter in Book IUTAM Symposium on Chaotic Dynamics and Control of Systems and Processes in Mechanics, Editors: G. Rega, and F. Vestroni, Volume 122 of the series Solid Mechanics and its Applications, (Kluwer and Springer, 2003), pp 37–45. SBN: 978-1-4020-3267-7 (Print) 978-1-4020-3268-4 (Online)
6. K.R. Hedrih (Stevanović), in *Rolling heavy disk along rotating circle with constant angular velocity, Computer Algebra Systems, in Teaching and Research, Chapter 2*. ed. by A.N. Prokopenya, M. Jakubiak. Problems of Classical Mechanics, vol. V (Siedlce University of Natural Sciences and Humanities, Siedlce 2015) pp. 293–304. © Copyright Uniwersytet, Przyrodniczo-Humanistyczny w Siedlcach, Siedlce 2015, ISSN 2300-7397; ISBN 978-83-7051-779-3
7. J. Guckenheimer, H. Ph, *Nonlinear Oscillations, Dynamical Systems, and Bifurcations of Fields* (Springer, New York, 1983), p. 461
8. J. Gerard, J. Daniel, *Elementary Stability and Bifurcation Theory* (Springer, New York, 1980)
9. V. Demč3nko, Kotrljanje bez klizanja giroskopske lopte po sferi (Rolling without slipping, a gyroscopic ball on a sphere), Doctoral dissertation, University of Belgrade, November 15, 1923, (1924), pp. 1–94.
10. C. Le Saux, R.I. Leine, C. Glocker, Dynamics of a rolling disk in the presence of dry friction. *J. o Nonlinear Sci.* **15**, 27–61 (2005)
11. D.P. Rašković, *Teorija oscilacija (Theory of oscillatins)*. Book. Naučna knjiga, First Edition 1952., Second Edition, 1965. <http://elibrary.matf.bg.ac.rs/search>; <http://elibrary.matf.bg.ac.rs/handle/123456789/3778>
12. M. Rehan, M. Reyhanoglu, Control of rolling disk motion on an arbitrary smooth surface. *IEEE Control Syst Lett* **2**(3), 357–362 (2018)
13. V.V. Kozlov, On the dynamics of systems with one-sided non-integrable constraints. *Theor. Appl. Mech.* (2019). <https://doi.org/10.2298/TAM190123005K>
14. K.R. Hedrih (Stevanović), Non-linear phenomena in vibro-impact dynamics: Central collision and energy jumps between two rolling bodies. Dedicated to memory of Professor and important scientist Ali Nayfeh (December 21, 1933-March 27, 2017). *Nonlinear Dyn.* **91**(3), 1885–1907 (2018). <https://doi.org/10.1007/s11071-017-3988-x>.

15. K.R. Hedrih (Stevanović), Rolling heavy ball over the sphere in real R^3 space. *Nonlinear Dyn.*, **97**, 63–82 (2019). <https://doi.org/10.1007/s11071-019-04947-1>.
16. K.R. Hedrih (Stevanović), Vibro-impact dynamics of two rolling heavy thin disks along rotate curvilinear line and energy analysis. *J. Nonlinear Dynam.*, **98**(4), 2551–2579. <https://doi.org/10.1007/s11071-019-04988-6>.

Parametric Instability and Bifurcation of Thin-Walled Axially Compressed Long FRP Columns



Julio C. Coaquira, Daniel C. T. Cardoso , Paulo B. Gonçalves , and Diego Orlando 

1 Introduction

There is a growing interest in the application of thin-walled beams of composite materials in several engineering fields. Their advantages have been corroborated by numerous researches and by applications in real structures. Among the composite materials used in engineering structures, there is a growing interest in those obtained by combining fibers immersed in a polymeric matrix, especially those produced by the pultrusion process (fiber-reinforced polymers – FRP) [1, 2]. Examples of the use of FRPs in civil construction are found worldwide, from components in buildings, pedestrian walkways, or bridges for vehicles with limited spans, railways, and other civil engineering infrastructure works, to geotechnical applications [1, 2].

As practical applications show, most FRP structural elements are thin-walled. Thus, FRP structural elements are generally light and slender, have a low damping coefficient [3] and Young's modulus. In this scenario, failures generally occur due to buckling instead of material strength limitations. Therefore, slender FRP structural elements may exhibit instability under static and dynamic loads, in addition to excessive vibrations.

The instability analysis of open section profiles has traditionally been investigated using the theory proposed by Vlasov [4] and, since then, various nonlinear formulations have been proposed, derived from Vlasov's hypotheses. Here, the geometrically nonlinear formulation proposed by Mohri et al. [5] for the analysis of the global behavior of open section beams is adopted. This formulation has been

J. C. Coaquira · D. C. T. Cardoso · P. B. Gonçalves
Pontifical Catholic University of Rio de Janeiro, Rio de Janeiro, Brazil

D. Orlando (✉)
State University of Rio de Janeiro, Resende, Brazil

successfully used in [6, 7] to study the static stability and natural frequencies of steel profiles.

Since the critical load that leads to failure in thin-walled structures is generally determined by their stability, the loss of stability of thin-walled structures subjected to static loads has been widely investigated in the technical literature. However, their instability under dynamic axial loads is largely unknown. The straight configuration of a column can become unstable under dynamic axial load magnitudes much lower than the static critical load. For a column under harmonic axial excitation, this occurs if there are certain relationships between the frequency of the applied load and the natural frequencies of the column in the transversal direction. In this case, the so-called parametric resonance can occur and even infinitesimal lateral disturbances can lead to large amplitude lateral vibrations.

The dynamic instability of thin-walled axially loaded metal columns under harmonic and pulse loads has been the subject of a series of works in the past [8]. However, most contributions, even in recent years, are restricted to the determination of critical excitation frequencies/loads by the Bolotin method [9], which allows the derivation of the parametric instability boundaries through a linear formulation. Only a few contributions investigate the nonlinear behavior of these structures. In this context, the local parametric instability of FRP short columns has been recently studied by Coaquira et al. [10] and a detailed analysis of the local and global behavior of FRP columns under axial load is presented in [11].

This article analyzes the parametric instability of an FRP column with a channel section under axial harmonic forcing. Using a global formulation, the regions of parametric instability are obtained as a function of the frequency and magnitude of the harmonic excitation. Bifurcation diagrams are obtained using continuation techniques and the brute force method and the stability of the solutions is subsequently investigated using the Floquet theory. The bifurcation analysis allows identification of the bifurcations associated with the parametric instability boundaries in the force control space, as well as the existence of coexisting solutions. Then, the evolution of the basins of attraction of the coexisting solutions is investigated as a function of the forcing magnitude, in order to assess the dynamic integrity of the desired stable solution (trivial solution). The present numerical approach based on the nonlinear equations does not depend on the assumption of small excitation magnitude, non-linearity, and damping frequently used in the literature, when solving through perturbation methods and the Mathieu-Hill's equations [12, 13].

2 Formulation and Results

Figure 1 shows the channel section geometry, displacement field, and global coordinate system. This geometry has low torsional stiffness, and flexural-torsional coupling is one of the main concerns in their design. The nonlinear equations of motion of the thin-walled column are here derived in terms of the two flexural displacements and the torsion angle [5]. Consider a simply supported beam with

warping unconstrained at the ends. Using as interpolation functions the flexural and torsional free vibration modes and applying the Galerkin method, a system of coupled nonlinear ordinary differential equations of motion is obtained. For each number of axial half-wave n there are three eigenvalues. The lowest natural frequencies and bifurcation loads are associated with one half-wave in the axial direction. Adopting $n = 1$, the following system is obtained [11]:

$$\begin{aligned} & \frac{mL}{2} \left(\frac{d^2}{dt^2} v + z_c \frac{d^2}{dt^2} \theta_x \right) + 2\xi\omega_o \frac{d}{dt} v + EI_z \frac{\pi^4}{2L^3} \left[v + \frac{\pi^2}{8L^2} v^3 \right] \\ & - P(t) \frac{\pi}{L} \left[\frac{\pi}{2} (v + z_c \theta_x) + \frac{2}{3} y_c \theta_x^2 \right] + (EI_z - EI_y) \frac{\pi^3}{L^3} \left(\frac{4}{3} w \theta_x - \frac{3}{8} \pi v \theta_x^2 \right) = 0 \end{aligned} \tag{1}$$

$$\begin{aligned} & \frac{mL}{2} \left(\frac{d^2}{dt^2} w - y_c \frac{d^2}{dt^2} \theta_x \right) + 2\xi\omega_o \frac{d}{dt} w + EI_y \frac{\pi^4}{2L^3} \left[w + \frac{\pi^2}{8L^2} w^3 \right] \\ & - P(t) \frac{\pi}{L} \left[\frac{\pi}{2} (w - y_c \theta_x) + \frac{2}{3} z_c \theta_x^2 \right] + (EI_z - EI_y) \frac{\pi^3}{L^3} \left(\frac{4}{3} v \theta_x + \frac{3}{8} \pi w \theta_x^2 \right) = 0 \end{aligned} \tag{2}$$

$$\begin{aligned} & \frac{mL}{2} \left(I_o \frac{d^2}{dt^2} \theta_x + z_c \frac{d^2}{dt^2} v - y_c \frac{d^2}{dt^2} w \right) + 2\xi\omega_o \frac{d}{dt} \theta_x + \frac{1}{2} \frac{\pi^4}{L^3} EI_w \theta_x \\ & + \frac{1}{2} \frac{\pi^2}{L} GJ \theta_x + \frac{3}{16} \frac{\pi^4}{L^3} EI_t \theta_x^3 + EI_z \frac{\pi^4}{2L^3} \left[v + \frac{\pi^2}{8L^2} v^3 \right] \\ & - P(t) \frac{\pi}{L} \left[\frac{\pi}{2} I_o \theta_x - y_c \left(\frac{\pi}{2} w - \frac{4}{3} v \theta_x \right) + z_c \left(\frac{\pi}{2} v + \frac{4}{3} w \theta_x \right) \right] \\ & + (EI_z - EI_y) \frac{\pi^3}{L^3} \left[\frac{4}{3} v w - \frac{3}{8} \pi (v^2 \theta_x - w^2 \theta_x) \right] = 0 \end{aligned} \tag{3}$$

where v and w are the transversal displacements in the Y and Z directions, respectively, θ_x is the torsion angle, as illustrated in Fig. 1, $P(t)$ is the axial load, $m = \rho A$ is the mass per unit length, E is the longitudinal Young’s modulus, G is the shear modulus, I_z is the moment of inertia in relation to the Z axis, I_y is the moment of inertia in relation to the Y axis, J is the Saint Venant torsion constant, and y_c and z_c are the shear center (SC) coordinates of the section. In addition, ξ is the dimensionless viscous damping coefficient and ω_o is the lowest natural frequency. These coupled nonlinear equations with time-dependent (periodic) coefficients can be solved using numerical methods or by perturbation techniques.

The linearization of Eqs. (1, 2, and 3) forms a system of Mathieu-Hill equations [12, 13]. The linearized system presents a stable trivial solution for forcing

Fig. 1 Channel section geometry, displacement field, and global coordinate system. SC shear center, CG center of gravity

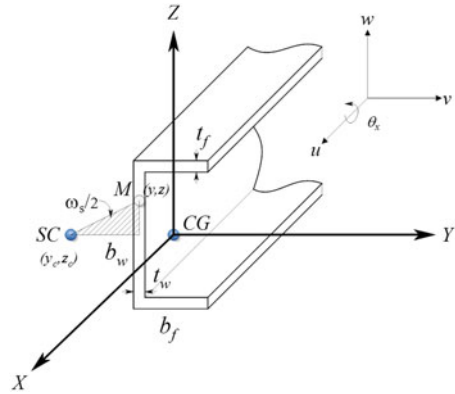


Table 1 Material properties of the orthotropic and isotropic materials

Properties	M1	M2	M3	M4	M5	ISO
E_1 (kN/mm ²)	20.0	20.0	28.0	20.1	15.89	28.0
E_2 (kN/mm ²)	10.0	5.0	19.3	8.62	7.75	28.0
G_{12} (kN/mm ²)	5.0	2.2	2.6	2.47	3.13	11.38
ν_{12}	0.23	0.23	0.23	0.23	0.32	0.23
ν_{21}	0.115	0.0575	0.1585	0.098	0.0735	0.23

values lower than the dynamic critical load, which becomes unstable giving rise to oscillatory solutions whose amplitude grows exponentially. For the nonlinear system, the solution can be trivial or periodic for load levels lower than the critical load and periodic or aperiodic of various types above the critical value, as shown subsequently.

Here, the nonlinear oscillations and parametric instability of a harmonically excited long FRP simply supported column with a channel section with dimensions $b_f = 10\text{cm}$, $b_w = 20\text{cm}$, $t_f = t_w = 5\text{mm}$ is adopted. The shear center (SC) coordinates of the monosymmetric section are: $y_c = -60.8\text{mm}$ and $z_c = 0.0$. For the following parametric analysis, five orthotropic materials (M1 to M5) and one isotropic material (ISO), used as a reference, are adopted. The relevant constants of these materials, based on values obtained from catalogs and experimental values, are shown in Table 1 [11]. In Eqs. (1, 2, and 3) $E = E_1$ and $G = G_{12}$. The mass density, based on the average experimental value, is $\rho = 1850 \text{ kg/m}^3$ [11].

Table 2 shows the three lowest natural frequencies and static bifurcation loads for the six analyzed materials, considering a column with length $L = 4.0\text{m}$, where F designates the flexural natural frequency and bifurcation load (around the minor axis) and FT the two flexural-torsional frequencies and loads. For this length, the lowest natural frequency and the lowest static bifurcation load (static critical load) is related to a flexural-torsional mode for all materials. It is also observed that the third natural frequency and bifurcation load are much higher than the first two [11].

Table 2 Static bifurcation loads and natural frequencies of the unloaded beam as a function of the material properties for $L = 4.0m$ [11]

Mode →	FT		F		FT	
	P (kN)	ω_0 (rad/s)	P (kN)	ω_0 (rad/s)	P (kN)	ω_0 (rad/s)
M1	20.967	59.876	23.865	63.881	241.412	203.299
M2	17.071	54.027	23.865	63.881	239.149	202.218
M3	23.222	63.015	33.412	75.585	334.377	239.114
M4	17.520	54.734	23.985	64.041	240.578	202.821
M5	15.494	51.472	18.961	56.940	191.261	180.842
ISO	33.412	75.785	35.301	77.692	342.561	242.022

One axial half wave

The results confirm the strong influence of the material properties on both the static critical load and fundamental frequency.

In the study of the dynamic stability of the column, an axial load of the form $P(t) = P_d \sin(\Omega_f t)$ is considered, where Ω_f is the excitation frequency and P_d is the magnitude of the harmonic excitation. Dividing the applied load by the static critical load, P_{cr} , and considering a non-dimensional time parameter $\tau = \omega_{01} t$, where ω_{01} is the lowest natural frequency, the non-dimensional axial excitation takes the form:

$$Q(\tau) = Q_d \sin(\delta \tau) \tag{4}$$

where $Q_d = P_d/P_{cr}$ is the load ratio and $\delta = \Omega_f/\omega_{o1}$ is the frequency ratio.

Figure 2a shows the parametric instability boundaries (transition boundaries from stable to unstable trivial solution) for the six materials under analysis, considering $L = 4.0m$ and $\xi = 1.45\%$. These instability boundaries are obtained by the continuation method in conjunction with Floquet theory. The longitudinal Young’s modulus, E_1 (Table 1) has a strong influence on the instability boundaries. As E_1 decreases the fundamental frequency also decreases, shifting the transition boundaries to the left. The parametric stability boundaries associated with the same longitudinal modulus, E_1 , are superimposed (see Table 1). For example, M3 and ISO materials have the same stability boundary, as do M1, M2, and M4 materials.

Figure 2b shows the nondimensional parametric instability boundaries obtained by dividing the excitation frequency by the lowest natural frequency (fundamental frequency) of each material, $\delta = \Omega_f/\omega_{o1}$, and the magnitude of excitation by the respective static critical load (Table 2), $Q_d = P_d/P_{cr}$. The lowest dynamic critical load, around $\Omega_f = 2\omega_{01}$, for the six materials is practically the same, decreasing slightly with E_1 . The effect of E_1 increases in the following regions to the left. For the isotropic material (ISO) the instability regions (tongues) emanate from the points $\delta = \Omega_f/\omega_o = 2/n$ with $n = 1, 2, 3 \dots$. Thus, the main parametric resonance region occurs in the vicinity of $\delta = 2.0$ and the fundamental resonance region in the vicinity of $\delta = 1.0$, which are the most relevant in structural dynamics, where the dynamic critical load is much lower than the static critical load (straight dashed black horizontal line). For example, in the case of the isotropic material

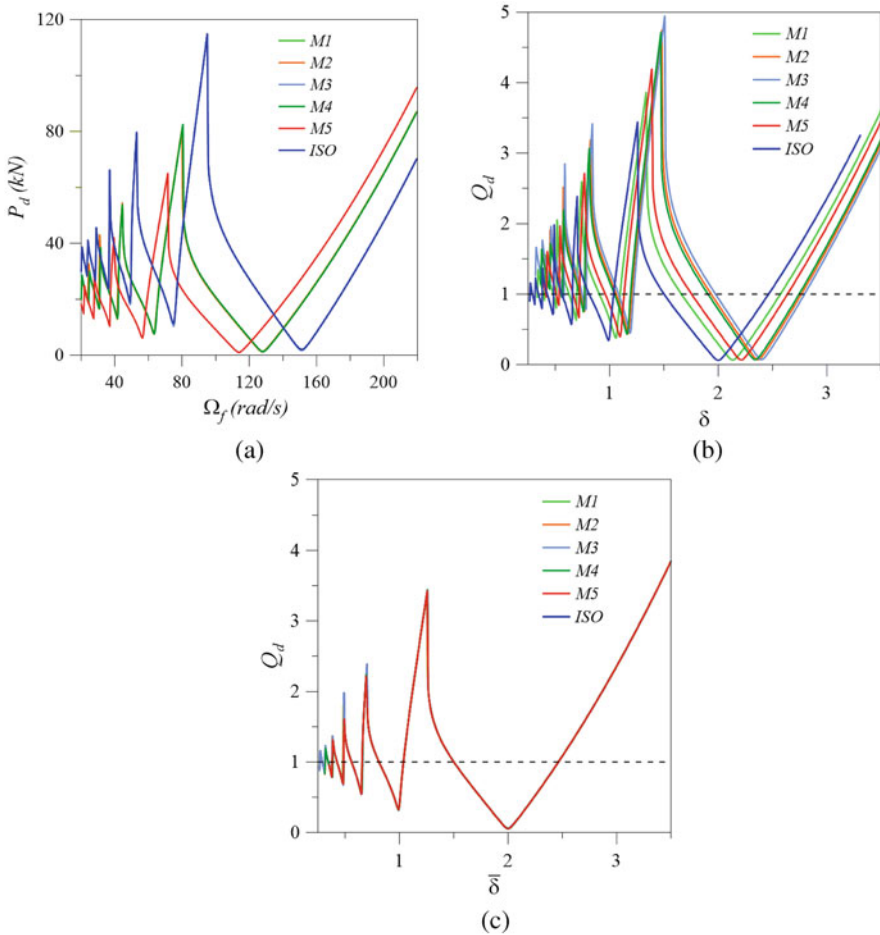


Fig. 2 Parametric instability boundaries for different materials, $L = 4.0m$ and $\xi = 1.45\%$. (a) without normalization; (b) excitation frequency normalized as a function of the fundamental frequency; (c) excitation frequency normalized as a function of the lowest flexural frequency

for $\xi = 1.45\%$, the dynamic critical load is only 6% of the static critical load. In the case of orthotropic materials (M1 to M5), the instability regions emanate from different values of δ . As the natural frequency decreases, they move to the right due to the adopted normalization of the excitation frequency. On the other hand, if the frequency associated with the bending mode, which is the second lowest frequency, is used as a reference in the adimensionalization process ($\bar{\delta} = \Omega_d/\omega_{02}$), all curves overlap as shown in Fig. 2c. This shows that the parametric instability boundary is associated with the excitation of the flexural vibration mode associated with the minimum moment of inertia.

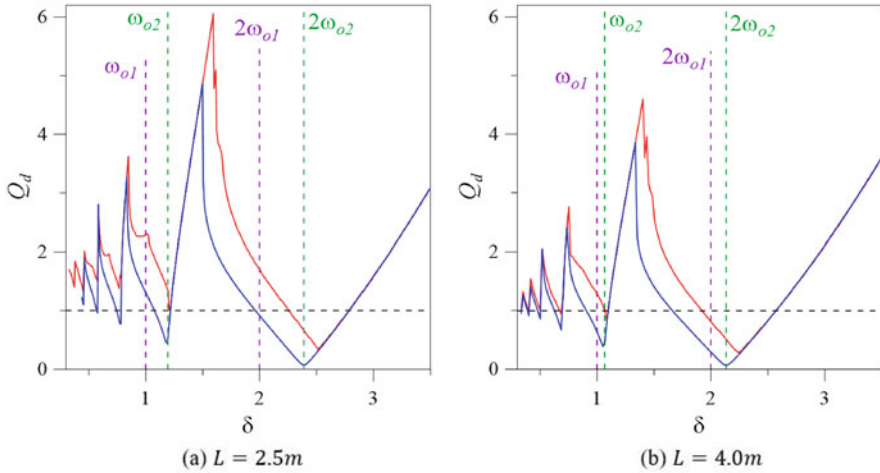


Fig. 3 Normalized stability boundaries for two-column lengths. Material M1 and $\xi = 1.45\%$

In addition to the parametric instability boundary, in certain structures under a harmonic axial load, there can be for each excitation frequency parameter, δ , a maximum load, Q_e , where the displacements increase indefinitely and the time response goes to infinity, known as escape boundary [14]. The escape and parametric instability boundaries for material M1 and different values of column length are shown in Fig. 3. In addition to the static critical load, the two lowest natural frequencies and their double are also shown as a reference (vertical dashed lines). The escape boundary is always superimposed on or above the parametric instability boundary. When the escape (red) and parametric instability (blue) boundaries are superimposed it means that the parametric instability load, Q_d , and the escape load, Q_e , have the same value, indicating the presence of an unstable bifurcation. On the other hand, when the escape boundary is above the parametric instability boundary, the column undergoes a stable bifurcation, with the ensuing non-trivial periodic solution remaining stable up to escape. In the main parametric resonance region, around $\Omega_f = 2\omega_{o2}$, the escape loads are much lower than the static critical load. Thus special care must be taken in design to prevent the collapse of the structure. The minimum values in each instability tongue are associated with the flexural frequency while the escape load is due to the excitation of the flexural-torsional mode.

To illustrate the bifurcations connected to the parametric and escape boundaries, bifurcation diagrams are shown in Figs. 4 and 5. They are here obtained using both continuation and brute force techniques. The continuous lines represent stable solutions and the dashed lines represent unstable solutions. Figure 4 shows the bifurcation diagrams, having as a control parameter the forcing magnitude Q_d , for $L = 4.0m$ and $\delta = 2.08$ (close to the lowest dynamic critical load). The trivial solution becomes unstable by means of a supercritical flip bifurcation (FSP),

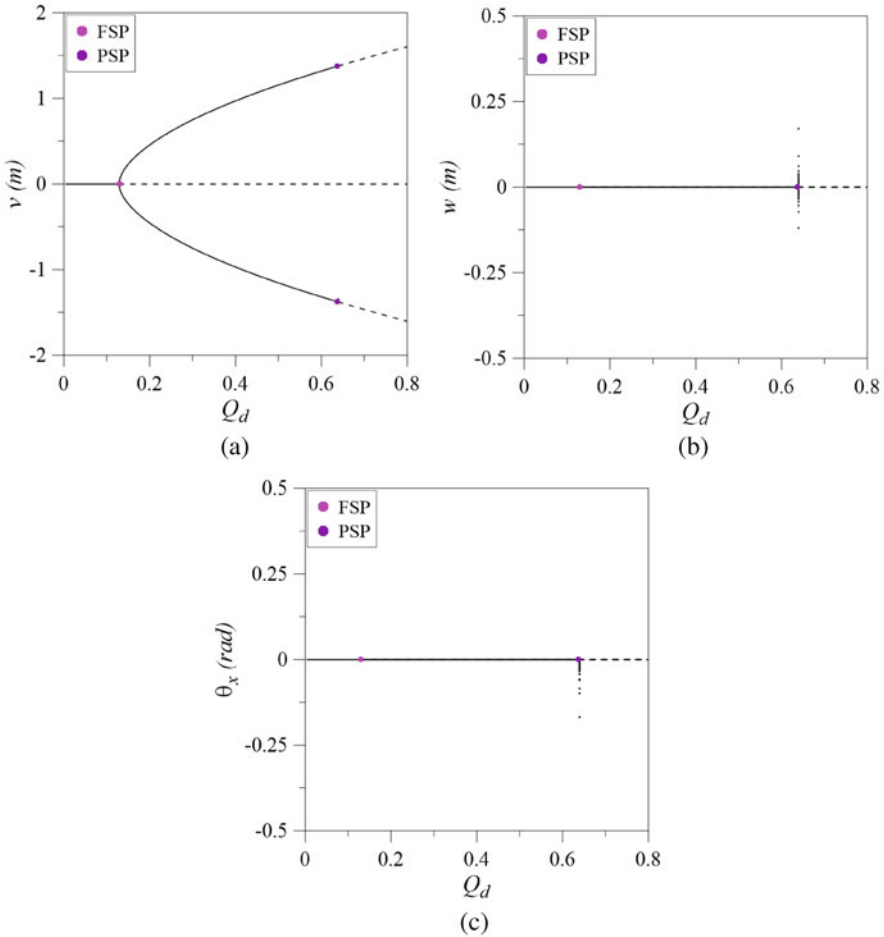


Fig. 4 Bifurcation diagrams for $L = 4.0m$ and $\delta = 2.08$. Material M1. $\xi = 1.45\%$

giving rise to a stable 2T periodic solution, which becomes unstable through a supercritical pitchfork bifurcation (PSP) and immediately afterward the escape occurs. As observed here, the displacements w and θ_x , associated with the flexural-torsional mode are excited and start to increase just after the supercritical flip bifurcation, indicating that the escape is triggered by the excitation of the flexural-torsional mode.

Figure 5 shows four bifurcation diagrams for selected values of the frequency parameter δ in the two main resonance regions. For $\delta = 1.00$ the trivial solution becomes unstable due to a supercritical pitchfork bifurcation, giving rise to two stable solutions of period 1 T. Each of these solutions becomes unstable due to a new supercritical pitchfork bifurcation and, shortly after, escape occurs. For $\delta = 1.10$ the trivial solution becomes unstable due to a subcritical pitchfork bifurcation (PSB),

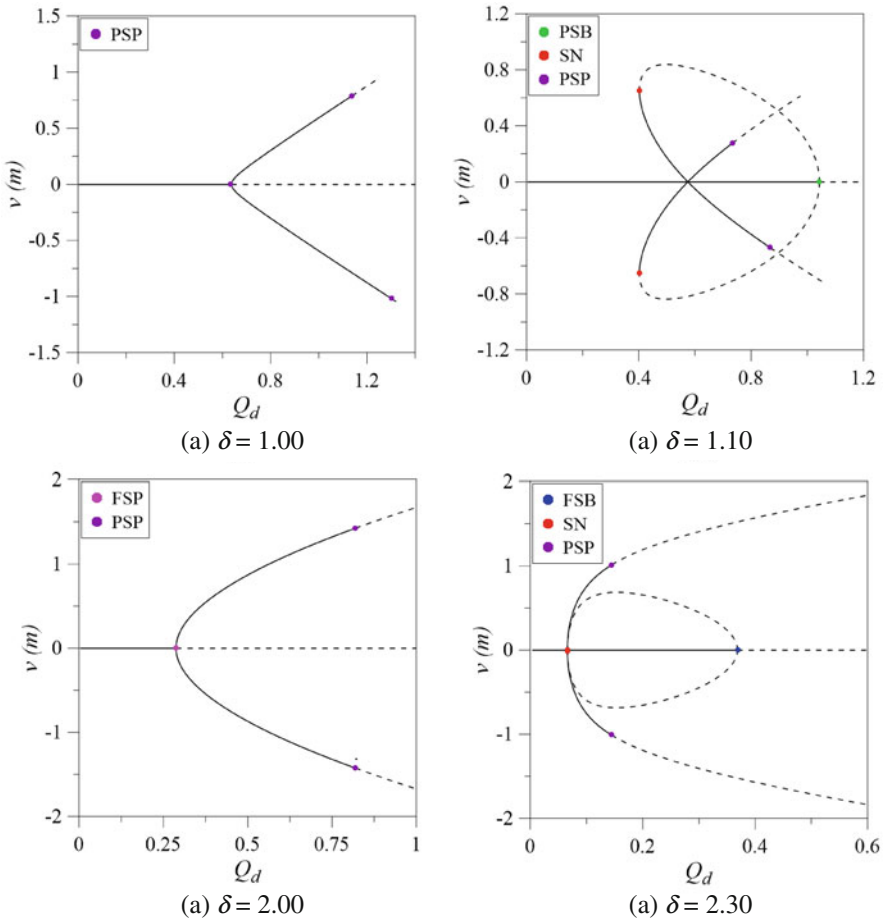


Fig. 5 Bifurcation diagrams for $L = 4.0m$ and selected values of δ . Material M1. $\xi = 1.45\%$

giving rise to two unstable solutions of period $1T$. Each of these solutions becomes stable due to a saddle-node bifurcation (SN), giving rise to a region where different stable solutions coexist for load levels lower than the dynamic buckling load. For finite disturbances after the SN bifurcation, the steady-state solution is a function of the initial conditions. These solutions become unstable through a supercritical pitchfork bifurcation (PSP), after which only the stable trivial solution remains up to the critical value. For $\delta = 2.00$ the structure becomes unstable due to a supercritical flip bifurcation (FSP), giving rise to a stable $2 T$ periodic solution, which becomes unstable due to a supercritical flip bifurcation after which escape occurs. For $\delta = 2.30$ the trivial solution becomes unstable due to a subcritical flip bifurcation (FSB), giving rise to an unstable $2 T$ period solution that becomes stable due to a saddle-node bifurcation. To illustrate the sensitivity to initial conditions and

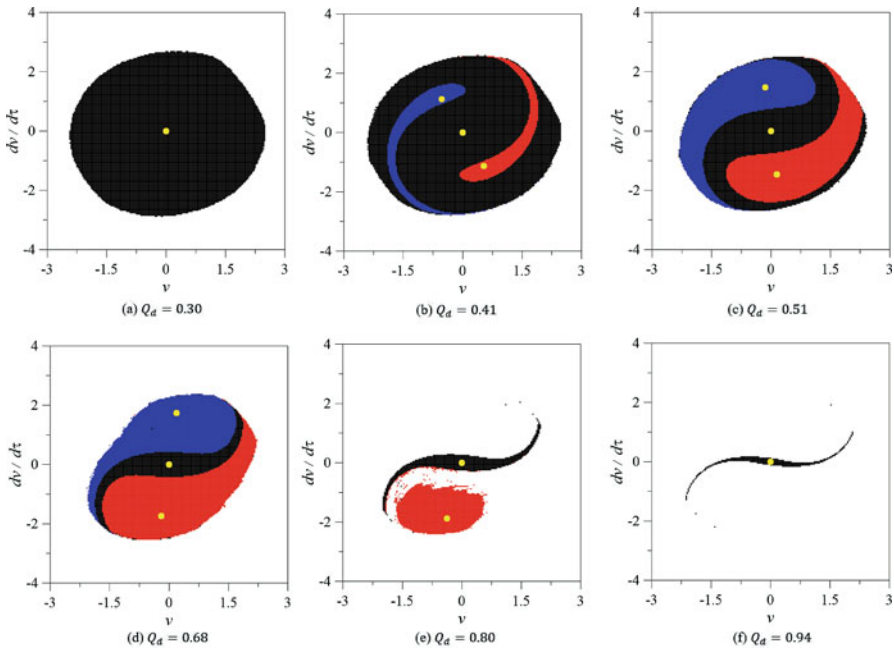


Fig. 6 Basins of attraction for $L = 4.0m$ and $\delta = 1.10$. Material M1. $\xi = 1.45\%$

the influence of coexisting solutions, including escape, Fig. 6 shows the evolution of the basins of attraction (plane v vs. $dv/d\tau$) for $\delta = 1.10$. The black region corresponds to the trivial solution, the blue and red regions to the two 1 T periodic solutions, while the white region corresponds to the initial conditions that lead to the escape (flexural-torsional excitation). The results show that, for high load levels, although the trivial solution is still mathematically stable (eigenvalues within the unit circle), small disturbances may lead to escape due to the erosion of the safe basin. This highlights the importance of analyzing the evolution and erosion of the basins of attraction in nonlinear dynamical systems with coexisting attractors [15].

3 Conclusions

The results highlight the influence of the orthotropy of the FRP material on the static buckling loads and natural frequencies, leading to a substantial decrease in static critical load and fundamental frequency when compared with the isotropic material. This decrease is due to the FRP’s low resistance in the transversal direction and low shear modulus. In addition, the parametric instability load and the escape load are much lower than the static critical load in the main resonance regions even at high damping ratios. The parametric instability is triggered by the excitation of

the flexural mode while escape by the excitation of the flexural-torsional mode. The nonlinearity leads to a qualitatively rich dynamics with coexisting solutions, leading to basins of attraction with a complex topology. The parametric instability of the pultruded column is of design concern as it causes the stable vertical equilibrium position to bifurcate into large-amplitude solutions and initiates a process that may lead the failure and the loss of its load-carrying capacity.

Acknowledgments The authors acknowledge the financial support of the Brazilian research agencies, CNPq, FAPERJ-CNE, FAPERJ-ARC, and CAPES.

References

1. A. Zaman, S.A. Gutub, M.A. Wafa, A review on FRP composites applications and durability concerns in the construction sector. *J. Reinf. Plast. Compos.* **32**(24), 1966–1988 (2013)
2. Vedernikov, A., Safonov, A., Tucci, F., Carlone, P., Akhatov, I. Pultruded materials and structures: A review. *J. Composite Mater.* 0021998320922894 (2020)
3. X. Wei, J. Russell, S. Živanović, J.T. Mottram, Measured dynamic properties for FRP footbridges and their critical comparison against structures made of conventional construction materials. *Compos. Struct.* **223**, 110956 (2019)
4. V.Z. Vlasov, *Thin-walled Elastic Beams*, 2nd edn. (Israel Program for Scientific Translation, Jerusalem, 1961)
5. F. Mohri, L. Azrar, M. Potier-Ferry, Flexural–torsional post-buckling analysis of thin-walled elements with open sections. *Thin-Walled Struct.* **39**(11), 907–938 (2001)
6. R.C. Mancilla, P.B. Gonçalves, E.C. Carvalho, Non-linear dynamics analysis and stability of thin-walled beams with monosymmetric channel-section. In: ICASS 2015 eighth international conference on advanced in steel structures, Lisbon (2015)
7. J.C. Coaquira, P.B. Gonçalves, E.C. Carvalho, Dynamic instability of cantilever beams with open cross-section. In: ASME 2016 international mechanical engineering congress and exposition. ASME digital collection, Charlotte (2016)
8. T. Yabuki, Y. Arizumi, F. Akamine, L.W. Lu, Nonlinear effect on instability of steel columns under dynamic axial loads. *J. Struct. Eng.* **131**(12), 1832–1840 (2005)
9. V.V. Bolotin, *The Dynamic Stability of Elastic Systems*. Holden-Day, USA (1964)
10. J.C. Coaquira, D.C.T. Cardoso, P.B. Gonçalves, D. Orlando, Parametric instability and nonlinear oscillations of an FRP channel section column under axial load. *Nonlinear Dyn.* (2020). <https://doi.org/10.1007/s11071-020-05663-x>
11. J.C. Coaquira, Nonlinear Analysis of the Instability and Vibration of a Pultruded Columns Reinforced with Fibers. Ph.D. Dissertation, Civil Engineering Department, PUC-Rio, Brazil (2020). (in Portuguese)
12. W.C. Xie, *Dynamic Stability of Structures* (Cambridge University Press, Cambridge, UK, 2006)
13. I. Kovacic, R. Rand, S. Mohamed Sah, Mathieu’s equation and its generalizations: Overview of stability charts and their features. *Appl. Mech. Rev.* **70**(2), 020802 (2018)
14. J.M.T. Thompson, Y. Ueda, Basin boundary metamorphoses in the canonical escape equation. *Dyn. Stab. Syst.* **4**(3–4), 285–294 (1989)
15. S. Lenci, G. Rega, *Global Nonlinear Dynamics for Engineering Design and System Safety* (Springer, Cham, 2019)

Analysis of Nonlinear Behaviors in Active Magnetic Bearing-Rotor System



Xiaoshen Zhang, Zhe Sun, Wolfgang Seemann, Lei Zhao, Zhao Jingjing, and Zhengang Shi

1 Introduction

The active magnetic bearing (AMB)-rotor system is inherently nonlinear. During operation, most components may show nonlinear characteristics, such as the nonlinearity of electromagnetic force (the nonlinear relationship of electromagnetic force with respect to rotor displacement and currents) [1, 2], saturation nonlinearities [3], hysteresis [4], and rotor nonlinearities including the internal friction [5] and rotor crack [6]. If the operating condition is harsh, some of nonlinear factors will be prominent and exert influences on the systems.

Nonlinear factors can lead to unexpected behaviors. For example, the nonlinearity of electromagnetic force could cause jump phenomenon, period doubling, quasi-periodic motion, and chaos. The nonlinearity of electromagnetic force is common in the AMB-rotor system. Its effects have been discussed in [2, 7, 8]. Other nonlinear factors can also lead to complicated behaviors. Refs. [9, 10] considered both current saturation and nonlinearity of electromagnetic force and found supercritical pitchfork bifurcation in an AMB-rotor system. Generally, these nonlinear behaviors have negative influences. It is necessary to investigate them and thereby propose effective measures to prevent them.

The approximate analytical methods are effective and common in nonlinear analyses of AMB-rotor systems. Ref. [2] utilized the method of multiple scales to obtain analytical solutions describing dynamic characteristics in main resonance

X. Zhang · Z. Sun (✉) · L. Zhao · Z. Jingjing · Z. Shi
Institute of Nuclear and New Energy Technology, The Key Laboratory of Advanced Reactor Engineering and Safety, Ministry of Education, Beijing, China
e-mail: zxs16@mails.tsinghua.edu.cn; sun_zhe@tsinghua.edu.cn; zhaolei@tsinghua.edu.cn; zhao-jj@tsinghua.edu.cn; shizg@tsinghua.edu.cn

W. Seemann

Institut für Technische Mechanik, Karlsruher Institut für Technologie, Karlsruhe, Germany

region. The jump phenomenon was found. The harmonic balance method can also be used to analyze nonlinear behaviors in main and harmonic resonance regions [11]. These analytical analyses of AMB-rotor systems usually focused on the vibration characteristics. The approximate solutions obtained only contain the vibration amplitude and phase. There were some limitations. The suspension characteristics that are also important to the system were not mentioned.

During operation of the AMB-rotor system, the rotor suspends without contact with the stator. This brings some advantages, such as no mechanical wear and low maintenance cost. But it also means that mechanical clearance between the rotor and stator is much larger than those of mechanical bearings, and the rotor can move in a relatively large physical space. The rotor may suspend steadily in different positions for different conditions. The steady suspension position of the rotor is called static equilibrium. Due to large mechanical clearance of AMBs, the static equilibrium can make contributions to the rotor displacement that is defined with respect to the reference position. In the AMB-rotor system, the rotor displacement depends on both vibration amplitude and static equilibrium. Therefore, the researches that only focused on the rotor vibration amplitude and phase [2, 7, 8, 11] cannot obtain the comprehensive dynamic characteristics. However, the effects of static equilibrium on system performance and stability were only discussed in a few researches [12], which needs to be explored further.

In this research background, this chapter analyzed both effects of rotor vibration and static equilibrium analytically. Compared with the method of multiple scales adopted in [12] that can only get static equilibrium and vibration amplitude but no vibration phase, the harmonic balance method adopted in this chapter can obtain approximate solutions including all of them. Nonlinear behaviors of the system were further investigated based on the solutions.

2 Mathematical Model

As Fig. 1 shows, an AMB-rotor system consists of the sensor, controller, power amplifier, electromagnets, and rotor. During operation, once the rotor deviates from the reference position, its displacement is measured by the sensor, and the measurement signal is transmitted to the controller. The controller gives the control command based on its control law. Thereby, the power amplifier outputs currents, which generate electromagnetic forces in the actuator to act on the rotor and return it to the reference position. By this way, AMBs can support the rotor without contact force.

However, some nonlinear factors exist in the system. The current output from the power amplifier has extreme limits. The electromagnetic force generated in the electromagnet is inherently nonlinear. The AMB-rotor system with current saturation and nonlinear electromagnetic force has been introduced in [9, 12]. The same model is adopted in this chapter.

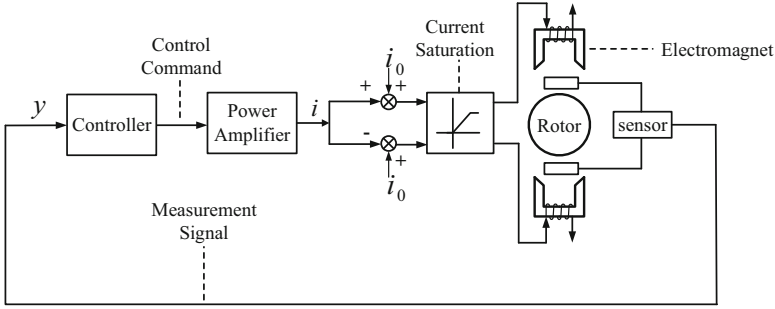


Fig. 1 System diagram of AMB-rotor system

This chapter only focuses on the direction where unexpected behaviors happen, and the high-order actual controller is simplified into a PD controller equivalently. By considering the nonlinearity of electromagnetic force and current saturation, a single degree-of-freedom model can be obtained. To facilitate subsequent analysis, the model has been transformed into a non-dimensional one.

Under the action of PD controller, the control current can be expressed as

$$i = K_p y + K_d \dot{y}, \tag{1}$$

where y is the rotor displacement, \dot{y} is its first derivative with respect to time, and K_p, K_d are proportional and differential gains of PD controller, respectively.

The electromagnetic force is generated by control current i and bias current i_0 together. But limited by output capacity of power amplifier, system currents i_{\pm} in opposite electromagnets have extremum values, which are formulated in

$$i_{\pm} = \text{med} (0, i_0 \pm i, 1), \tag{2}$$

where “med” means taking the median value among three values in the bracket and the bias current is $i_0 = 0.5$.

According to [1], the electromagnetic force F can be formulated as

$$F = K_F \left(\left(\frac{i_+}{1+y} \right)^2 - \left(\frac{i_-}{1-y} \right)^2 \right), \tag{3}$$

where K_F is the force coefficient determined by the system structure, whose value is 0.0097.

Under the action of unbalance excitation, the motion differential equation is

$$\ddot{y} = -F + f \cos (\Omega t), \tag{4}$$

where f is the amplitude of unbalance excitation, while Ω is the excitation frequency, namely the rotor speed.

Equations (1)–(4) make up the nonlinear model. However, the fraction expression of electromagnetic force (3) brings challenges to subsequent analysis. In order to get analytical solutions, the approximation of electromagnetic force is obtained in the possible operating region of the system. A polynomial fitting of the electromagnetic force F_f with respect to i and y is performed. The fitting model is obtained as follows:

$$\ddot{y} = -F_f + f \cos(\Omega t). \quad (5)$$

In this equation, the fitting electromagnetic force can be expressed as

$$F_f = \sum_{1 \leq m+n \leq 11} k_{m,n} y^m \dot{y}^n, \quad (6)$$

where $k_{m,n} = 0$ if $m + n$ is even number; otherwise, $k_{m,n}$ are relational expressions about controller parameters K_p , K_d . The nonlinearity of electromagnetic force and current saturation are approximated by fitting electromagnetic force to this polynomial. Subsequent analysis is conducted based on polynomial model (5).

3 Analytical Analysis

The harmonic balance method is a common one of approximate analytical methods to do dynamic analyses of nonlinear systems. In this chapter, it is used to study both effects of rotor vibration and static equilibrium on dynamic characteristics of the AMB-rotor system. The solving procedure is as follows.

This chapter only focuses on the first-order approximate solution. The solution of polynomial model (5) is set as

$$y = C + a \cos(\Omega t + \phi), \quad (7)$$

where a and ϕ are the vibration amplitude and phase, respectively, while C represents the static equilibrium. All of them need to be determined.

Substitution of (7) into (5) leads to a polynomial equation with C , a , and ϕ , which contains a constant term, a first-order harmonic term, and high-order harmonic terms. By neglecting high-order harmonic terms and collecting the similar terms according to constant term, $\cos(\Omega t)$ and $\sin(\Omega t)$, respectively, we can obtain three algebraic equations,

$$G_1(a, \phi, C) = 0, \quad (8)$$

$$G_2(a, \phi, C) = 0, \quad (9)$$

$$G_3(a, \phi, C) = 0, \tag{10}$$

where $G_1(a, \phi, C)$, $G_2(a, \phi, C)$, and $G_3(a, \phi, C)$ are the polynomial expressions whose coefficients depend on system parameters including K_p , K_d , and Ω .

Solving algebraic equations (8), (9), and (10), the static equilibrium C , vibration amplitude a , and vibration phase ϕ can be obtained. Then, the periodic solution y shown in (7) is determined.

The stability of periodic solutions can be analyzed by the Floquet theory.

Introduce state variables $x_1 = \dot{y}$, $x_2 = y$, and $x_3 = \Omega t$, and transform polynomial model (5) into an autonomous one,

$$\dot{\mathbf{x}} = \begin{bmatrix} \dot{x}_1 \\ \dot{x}_2 \\ \dot{x}_3 \end{bmatrix} = \begin{bmatrix} -F_f(x_1, x_2) + f \cos(x_3) \\ x_1 \\ \Omega \end{bmatrix} = \mathbf{G}(\mathbf{x}). \tag{11}$$

Equation (11) is a periodic function whose period is $T = \frac{2\pi}{\Omega}$. According to [13], its monodromy matrix can be calculated by

$$\begin{aligned} \frac{d\mathbf{M}(t)}{dt} &= \left. \frac{\partial \mathbf{G}(\mathbf{x})}{\partial \mathbf{x}} \right|_{\mathbf{x}_0} \mathbf{M}(t), \\ \mathbf{M}(0) &= \mathbf{I}, \end{aligned} \tag{12}$$

where \mathbf{x}_0 is the corresponding periodic solution of (11). Integrate (12) in a period T and obtain monodromy matrix $\mathbf{M}(T)$. Then, the stability of each periodic solution can be determined by eigenvalues of the monodromy matrix.

4 Results and Discussions

4.1 Supercritical Pitchfork Bifurcation

In this chapter, the system parameters are chosen as $K_p = 1.904$, $K_d = 4.801$, and $\Omega = 1$. The approximate solutions and their stability can be obtained through above analysis procedure. It is found that the number and stability of solutions may change for different excitations. The coexistence of multiple solutions leads to nonlinear behaviors.

In the AMB-rotor system, the rotor displacement can intuitively show effects of nonlinear factors and indicate the system performance. Under the influences of nonlinearity of electromagnetic force and current saturation, the rotor displacement exhibits complicated behaviors, as shown in Fig.2. There are three different solutions that are represented by y_1 , y_2 , and y_3 , respectively. It is the extremum values of rotor displacement that affect system performance and stability. Therefore, the maximum and minimum values are marked. During operation, the rotor can

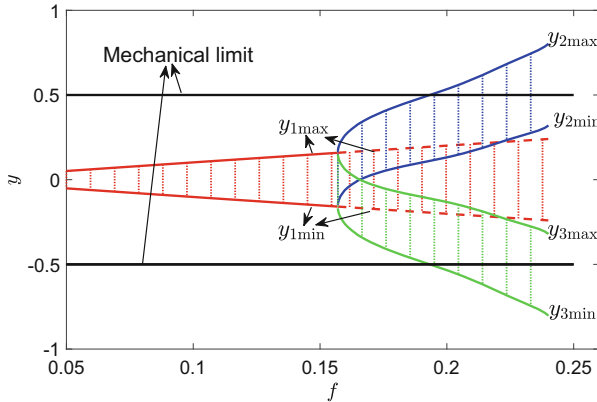


Fig. 2 Rotor displacement with respect to excitation amplitude: black line—mechanical limit, red line— y_1 , blue line— y_2 , green line— y_3 , solid line—stable solution, dashed line—unstable solution, dotted line—range of motion of rotor

move in the range of motion limited by maximum and minimum displacements. The dotted line represents the range of motion.

It can be seen that there is only one periodic solution y_1 for small f . The maximum and minimum displacements $y_{1\max}$, $y_{1\min}$ are symmetric around the reference position, namely the zero displacement point in Fig. 2. As f increases in a certain range, y_1 increases nearly linearly (see $y_{1\max}$). No unexpected behaviors occur. However, as f increases to a critical value, namely $f = 0.156$, nonlinear factors become prominent and complicated behaviors occur. The trivial solution y_1 still exists, but its stability changes. Namely, the trivial solution y_1 becomes unstable. In addition, two other solutions y_2 and y_3 appear. In this situation, three solutions coexist, but only one of the stable solutions, namely y_2 or y_3 , can be exhibited in actual system. This is a bifurcation of rotor displacement with respect to excitation amplitude. After bifurcation, the absolute values of $y_{2\max}$ and $y_{3\min}$ are much larger than $y_{1\max}$.

The bifurcation of rotor displacement will affect the system performance and stability. There are auxiliary bearings in the system, which can avoid damage to the rotor and stator during a touchdown process. But auxiliary bearings also create mechanical limits for the rotor, which are defined as the relative positions of auxiliary bearings from the reference position and marked in Fig. 2. If the rotor displacement exceeds mechanical limits, it will collide with auxiliary bearings that will lead to instability. Before bifurcation, maximum and minimum displacements $y_{1\max}$, $y_{1\min}$ are acceptable. However, after bifurcation, difference values of $y_{2\max}$ or $y_{3\min}$ to mechanical limits become much smaller. The rotor approaches the auxiliary bearings much closer. This will weaken the capacity of resisting to a disturbance. Under the effect of disturbance, the possibility of collision between rotor and stator increases. The system performance deteriorates. As f is further increased to 0.195,

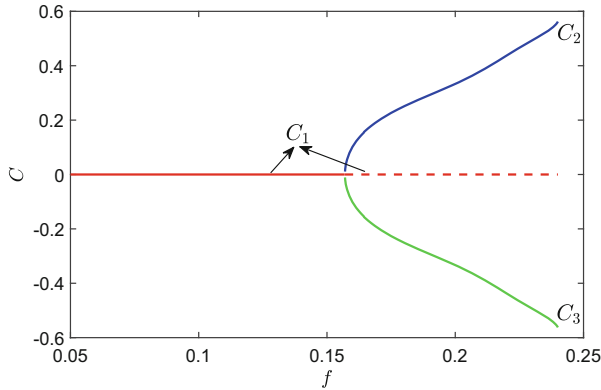


Fig. 3 Static equilibrium with respect to excitation amplitude: solid line—stable solution, dashed line—unstable solution

y_{2max} and y_{3min} will exceed the mechanical limits and the system cannot keep stable even if there is no disturbance.

It should also be noted that unexpected behaviors appearing in the system are not only about the dynamic characteristics of vibration. After bifurcation, for y_2 and y_3 that can be exhibited during operation, the range of motion of the rotor is not symmetric around the reference position. It means that the static equilibrium does not coincide with the reference position all the time.

It can also be known from analytical results that all of C , a , and ϕ in solution (7) have multiple values. The static equilibrium C , vibration amplitude a , and phase ϕ are illustrated, respectively, to explain their effects on rotor displacement.

Figure 3 shows the relationship between the static equilibrium C and f . The stability of static equilibrium can be determined as follows: the static equilibria in stable periodic solutions are thought to be stable, and that in unstable periodic solution is thought to be unstable. The static equilibrium exhibits complicated characteristics. As f is small, there is only one static equilibrium, namely the stable trivial equilibrium. It coincides with the reference position. However, as f is increased to 0.156, where the bifurcation of rotor displacement occurs, both number and stability of static equilibrium change. The trivial equilibrium loses its stability. And two stable nontrivial equilibria appear. The nontrivial equilibria are symmetric around the reference position and increase gradually with the further increase of f . The relatively large mechanical clearance makes existence of nontrivial equilibria physically possible. The phenomenon is called pitchfork bifurcation. The branch solution and unstable trivial solution locate in the same side of the critical point. Therefore, the bifurcation is a supercritical one.

To make clear the role of rotor vibrations in nonlinear behaviors of the AMB-rotor system, the vibration amplitude a and phase ϕ are obtained and shown in Fig. 4. There is a one-to-one correspondence between a and ϕ . For small f , there is one solution for vibration amplitude and phase. However, after bifurcation point of

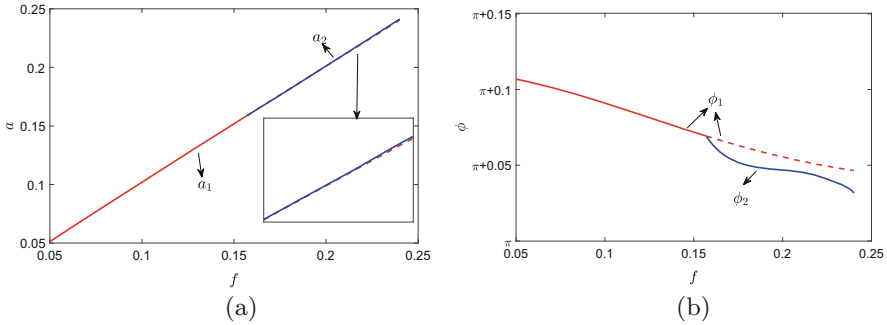


Fig. 4 Vibration amplitude and phase with respect to excitation amplitude: solid line—stable solution, dashed line—unstable solution

the rotor displacement, there are two solutions for vibration amplitude and phase, while there are three solutions for rotor displacement and static equilibrium. And a_1 , ϕ_1 are the vibration amplitudes in solution y_1 . The vibration amplitude and phase in solution y_2 and y_3 are the same, and they are a_2 and ϕ_2 . It can be seen that values of a_1 and a_2 , ϕ_1 and ϕ_2 have slight differences. They hardly have influences on the rotor displacement.

It can be concluded that the complicated behaviors reflected in the rotor displacement are caused by the bifurcation of static equilibrium. The dynamic characteristics of vibration are not complicated. Under influences of the nonlinearity of electromagnetic force and current saturation, the number and stability of static equilibrium will be different for different conditions. The relatively large mechanical clearance creates physical conditions for the existence of nontrivial equilibria. As a result, the supercritical pitchfork bifurcation of static equilibrium occurs in the AMB-rotor system.

Looking back to Fig. 2, as f is small, the bifurcation of static equilibrium has not appeared and the rotor vibrates around the trivial equilibrium. With the gradual increase of f , the static equilibrium remains zero. The maximum rotor displacement increases because the vibration amplitude increases. At this stage, the maximum rotor displacement is exactly the vibration amplitude. However, after bifurcation of static equilibrium, the trivial equilibrium loses its stability. The rotor deviates from the reference position and starts to vibrate around one of nontrivial equilibria. The maximum rotor displacement is the sum of vibration amplitude and absolute value of the static equilibrium. The supercritical pitchfork bifurcation of static equilibrium results in the fact that the maximum rotor displacement increases dramatically. Although the bifurcation of static equilibrium does not cause instability in mathematics, it can make system performance deteriorate and even lose stability during actual operation.

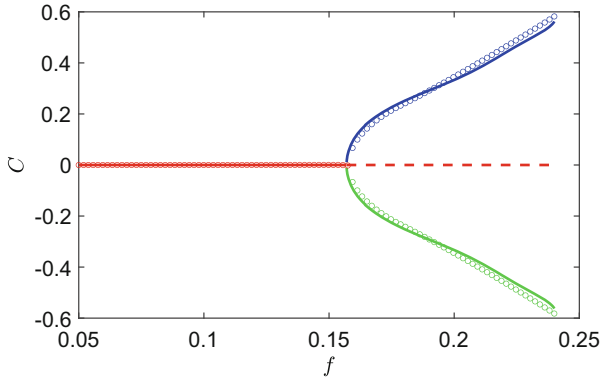


Fig. 5 Comparison of numerical and analytical results: solid line—stable analytical solution, dashed line—unstable analytical solution, circle—numerical solution, note: the same color represents same solution

4.2 Numerical Validation

The analysis results obtained through harmonic balance method are validated numerically in this section.

The bifurcation of static equilibrium is also obtained through numerical method. The numerical integration can obtain the stable equilibria but no unstable equilibria. The comparison of analytical and numerical results is shown in Fig. 5. It can be seen that the analytical and numerical results are generally in agreement.

To illustrate the bifurcation, the time-domain responses before and after bifurcation are shown in Fig. 6a,b, respectively. For $f = 0.1$, the rotor vibrates slightly around the trivial equilibrium. There is only one stable analytical solution. The numerical results and analytical solution are highly consistent. For $f = 0.2$, the nonlinear characteristics of the AMB-rotor system become prominent and multiple solutions coexist. There is one unstable solution and two stable solutions. In the numerical simulation, the stable solution can be exhibited, while the unstable cannot. Two time-domain responses are obtained for two different initial conditions and are consistent with two stable analytical solutions after entering the steady state. There is no numerical solution corresponding to the unstable solution.

The analytical solutions obtained through harmonic balance method and their stability results are proved to be correct and accurate.

5 Conclusions

The dynamic characteristics of the AMB-rotor system were analyzed by considering the nonlinearity of electromagnetic force and current saturation. The analytical

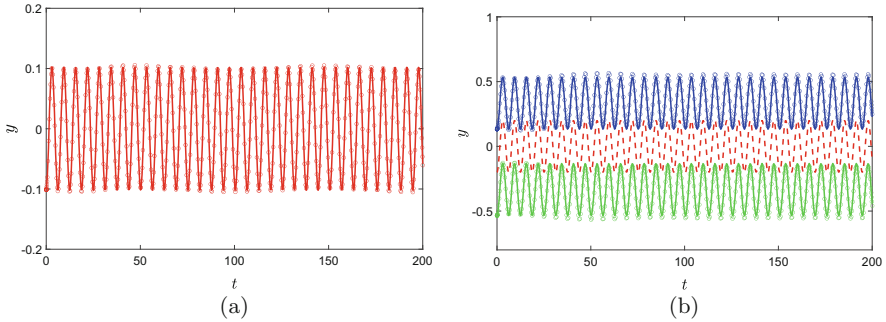


Fig. 6 Time-domain responses: solid line—stable analytical solution, dashed line—unstable analytical solution, circle—numerical solution, note: the same color represents the same solution. (a) $f = 0.1$. (b) $f = 0.2$.

solutions containing both information of rotor vibration and suspension were obtained through the harmonic balance method, and nonlinear dynamic analysis was performed based on the solutions. It was found there might be multiple solutions for the rotor displacement. During actual operation, the rotor may vibrate around a position deviating from the reference position. The system performance deteriorates and even instability may happen. Through further analysis, it is found that the unexpected behaviors are mainly caused by a supercritical pitchfork bifurcation of the static equilibrium. In other words, the effects of nonlinear are reflected in the static equilibrium rather than vibration amplitude and phase. At last, the accuracy and stability of the solutions were validated.

Acknowledgments This work was supported by the National Key R&D Program of China [2018YFB2000100] and the National S&T Major Project (Grant No. ZX069).

References

1. G. Schweitzer, E.H. Malsen, *Magnetic Bearings: Theory, Design and Application to Rotating Machinery* (Springer, Berlin, 2009)
2. N.A. Saeed, M. Eissa, W.A. El-Ganini, Nonlinear oscillations of rotor active magnetic bearings system. *Nonlinear Dyn.* **74**(1–2), 1–20 (2013)
3. K. Kang, A. Palazzolo, Homopolar magnetic bearing saturation effects on rotating machinery vibration. *IEEE Trans. Magn.* **48**(6), 1984–1994 (2012)
4. C. Cristache, I. Valiente-Blanco, E. Diez-Jimenez, M. Alvarez-Valenzuela, N. Pato, J. Perez-Diaz, Mechanical characterization of journal superconducting magnetic bearings: Stiffness, hysteresis and force relaxation. *J. Phys. Conf. Ser.* **507**(PART 3), 032012 (2014). DOI 10.1088/1742-6596/507/3/032012
5. F. Sorge, Stability analysis of rotor whirl under nonlinear internal friction by a general averaging approach. *J. Vib. Control* **23**(5), 808–826 (2017). DOI 10.1177/1077546315583752
6. L. Hou, Y. Chen, Z. Lu, Z. Li, Bifurcation analysis for 2:1 and 3:1 super-harmonic resonances of an aircraft cracked rotor system due to maneuver load. *Nonlinear Dyn.* **81**(1–2), 531–547 (2015)

7. J.I. Inayat-Hussain, Geometric coupling effects on the bifurcations of a flexible rotor response in active magnetic bearings. *Chaos Solitons Fractals* **41**(5), 2664–2671 (2009)
8. M.J. Jang, C.K. Chen, Bifurcation analysis in flexible rotor supported by active magnetic bearing. *Int. J. Bifurcation Chaos* **11**(8), 2163–2178 (2001). DOI 10.1142/S0218127401003437
9. X. Zhang, T. Fan, Z. Sun, L. Zhao, X. Yan, J. Zhao, Z. Shi, Nonlinear analysis of rotor-AMB system with current saturation effect. *Appl. Comput. Electromagn. Soc. J.* **34**(4), 557–566 (2019)
10. Z. Sun, X. Zhang, T. Fan, X. Yan, J. Zhao, L. Zhao, Z. Shi, Nonlinear dynamic characteristics analysis of active magnetic bearing system based on cell mapping method with a case study. *Mech. Syst. Sig. Process.* **117**, 116–137 (2019)
11. A. Leung, Z. Guo, Resonance response of a simply supported rotor-magnetic bearing system by harmonic balance. *Int. J. Bifurcation Chaos* **22**(6) (2012). DOI 10.1142/S0218127412501362
12. X. Zhang, Z. Sun, L. Zhao, X. Yan, J.X. Zhao, Z. Shi, Analytical analysis of supercritical pitchfork bifurcation in active magnetic bearing-rotor system with current saturation. *Nonlinear Dyn.* **104**(1), 103–123 (2021)
13. Lust, K.: Improved numerical floquet multipliers. *Int. J. Bifurcation Chaos Appl. Sci. Eng.* **11**(9), 2389–2410 (2001). DOI 10.1142/S0218127401003486

Characterizing Fundamental, Superharmonic, and Subharmonic Resonances Using Phase Resonance Nonlinear Modes



Martin Volvert and Gaëtan Kerschen

1 Introduction

Modal analysis has been, and continues to be, the dominant dynamical method used in structural design. The goal of modal analysis is to find the vibration modes, resonance frequencies, and damping ratios of the considered system [1]. One key assumption of modal analysis is linearity, which, however, real-world structures violate because they may feature advanced materials, friction, and contact [2]. The theory of nonlinear normal modes (NNMs) was developed to generalize the concept of a vibration mode to nonlinear systems [3]. In direct analogy to a linear mode, Rosenberg defined a NNM as a synchronous vibration of the undamped, unforced system for which all points reach their extreme values or pass through zero simultaneously [4, 5]. This definition is only valid for multi-point, multi-harmonic forcing, which is not always used in practice. The focus of this chapter is on phase resonances for fundamental resonances of harmonically forced, damped systems as well as for superharmonic and subharmonic resonances. For these latter resonances, the phase lag between the harmonic of interest of the displacement and the forcing may not necessarily be equal to $\pi/2$, unlike fundamental resonances. In this context, we propose herein a generalization of phase resonance of nonlinear systems for which the corresponding structural deformation is termed a phase resonance nonlinear mode (PRNM). These PRNMs are applied to the well-known Duffing oscillator.

M. Volvert (✉) · G. Kerschen

Space Structures and Systems Laboratory, Department of Aerospace and Mechanical Engineering, University of Liège, Liège, Belgium

e-mail: m.volvert@uliege.be; g.kerschen@uliege.be

2 Resonances of the Duffing Oscillator

The Duffing oscillator comprises a mass attached to linear and cubic springs and a linear damper. The governing equation of motion of the harmonically forced Duffing oscillator is

$$\ddot{x}(t) + 0.01\dot{x}(t) + x(t) + x^3(t) = f \sin \omega t, \quad (1)$$

where f is the forcing amplitude, whereas ω is the excitation frequency.

Considering the Fourier decomposition of the displacement, where the positive integer ν takes into account the subharmonics of the excitation frequency ω ,

$$x(t) = \frac{c_0}{\sqrt{2}} + \sum_{k=1}^{\infty} \left(s_k \sin \left(k \frac{\omega}{\nu} t \right) + c_k \cos \left(k \frac{\omega}{\nu} t \right) \right) \quad (2)$$

shows that many resonances exist in this simple system. Specifically, each harmonic component of the displacement can trigger a resonance as long as the relation $\frac{k}{\nu}\omega$ corresponds to the frequency of the fundamental resonance of the system. When the ratio $\frac{k}{\nu}$ is lower (greater) than 1, the resonance is said to be subharmonic (superharmonic) and is located after (before) the fundamental resonance. In this chapter, the resonances are divided into four categories, namely:

- Fundamental resonance ($k = 1, \nu = 1$)
- Superharmonic resonance $k:\nu$ ($k > \nu, \nu = 1$)
- Subharmonic resonance $k:\nu$ ($\nu > k, k = 1$)
- Other superharmonic and subharmonic resonances $k:\nu$ ($k > 1, \nu > 1$)

Superharmonic and subharmonic resonances can further be divided into subcategories depending on the parity of k and ν .

The goal of this section is to analyze carefully the resonant response of the Duffing oscillator, as previously achieved in [6]. To this end, the system is analyzed considering four different forcing amplitudes f , i.e., 0.01N, 0.25N, 1N, and 3N. The nonlinear frequency response curves (NFRCs) are depicted in Fig. 1. For a forcing amplitude of 0.01N in Fig. 1a, the only nonlinear effect appearing in the NFRC is the hardening of the fundamental resonance. At 0.25N in Fig. 1b, 3:1 superharmonic and 1:3 subharmonic resonance branches appear before and after the fundamental resonance, respectively. It should be noted that the subharmonic resonance is isolated from the main curve. Additional branches corresponding to 2:1, 4:1, 5:1, and 7:1 superharmonic and 1:2 subharmonic resonances arise in Fig. 1c at 1N. Finally, as the forcing continues to increase, new resonances, for which both k and ν can be different from 1, start to appear, first as isolated singular point solutions and then as growing isolated branches. When the forcing amplitude is 3N, some of these resonances, such as the 7:3, 3:2, 4:3, 7:2, 2:3, 3:4, 5:7, and 3:5 resonances, can be observed in Fig. 1d. A close-up on these specific superharmonic and subharmonic resonances is made in Fig. 1e,f, respectively. The main resonances are examined

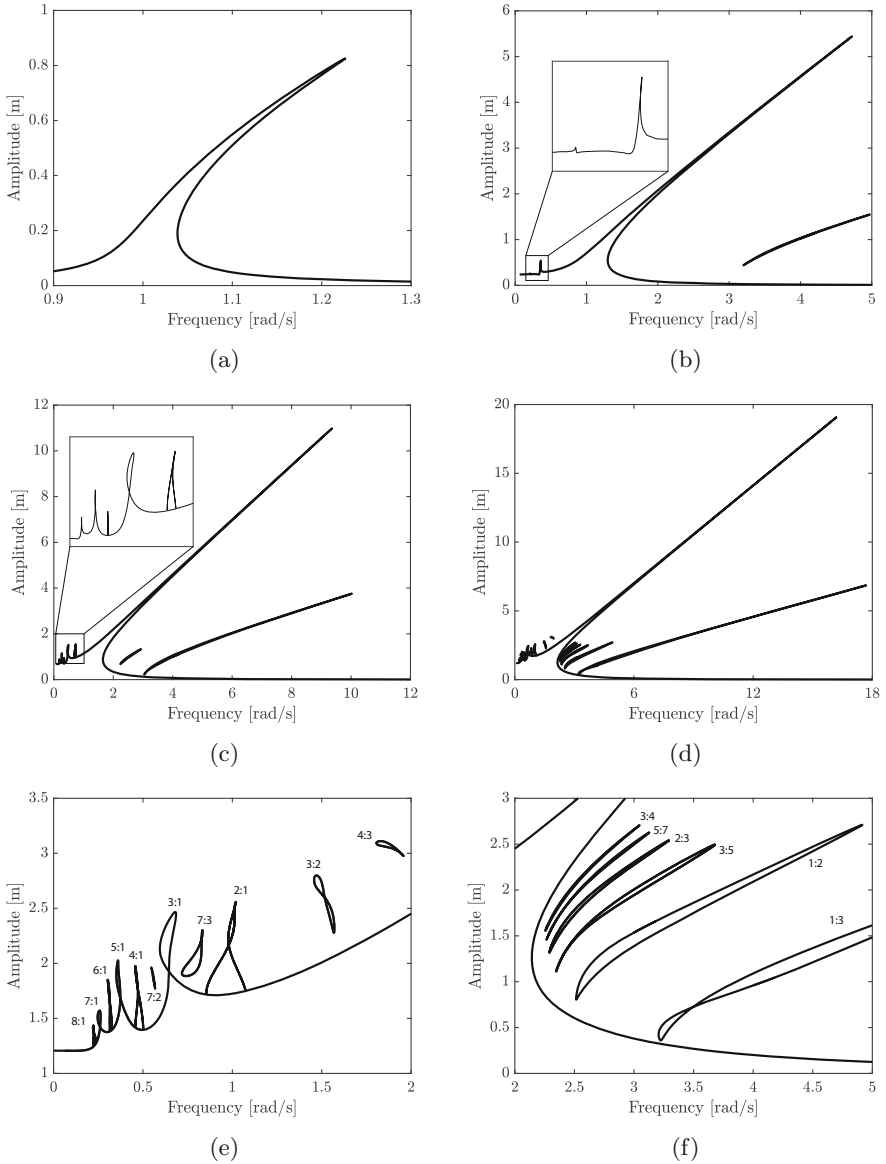


Fig. 1 NFRCs of the Duffing oscillator: (a) $f = 0.01N$, (b) $f = 0.25N$, (c) $f = 1N$, and (d) $f = 3N$, (e) close-up on the superharmonic resonances, (f) close-up on the subharmonic resonances

in greater detail hereafter. Particular attention is devoted to the phase difference between the dominant harmonic component of the displacement and the harmonic excitation.

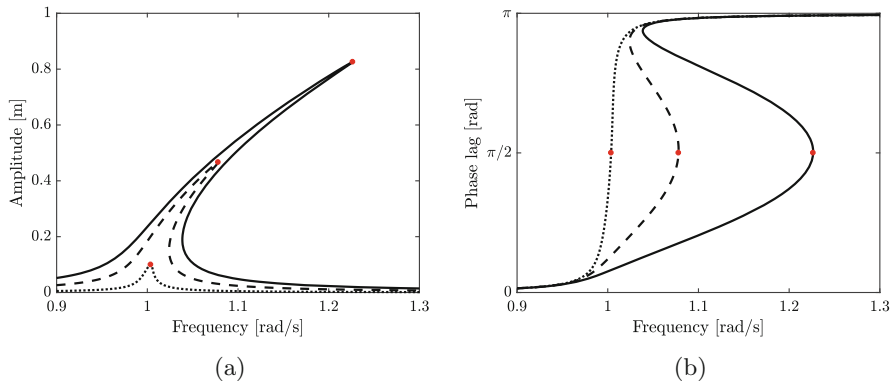


Fig. 2 NFRCs of the fundamental resonance of the Duffing oscillator for $f = 0.001N$ (\cdots), $f = 0.005N$ ($-\ -$), and $f = 0.01N$ ($—$): (a) amplitude and (b) phase lag of the first harmonic component. The red dots correspond to phase resonance

2.1 Fundamental Resonance

The amplitude and phase lag of the first harmonic component of the displacement in the neighborhood of the fundamental resonance are displayed in Fig. 2a,b, respectively. The phase lag varies between 0 and π and passes through $\pi/2$ at resonance.

2.2 Superharmonic Resonances ($k > \nu$, $\nu = 1$)

In the case of superharmonic resonances, the ratio $\frac{k}{\nu}$ is greater than one, and the resonance peaks are located before the fundamental resonance. The phase lags of the 3/1 and 2/1 harmonic components of the 3 : 1 and 2 : 1 resonances are depicted in Fig. 3a,b, respectively.

2.2.1 Odd Superharmonic Resonances (k is Odd)

The phase lag of the 3/1 harmonic component of the 3:1 resonance is comprised between 0 and π and, as for the fundamental resonance, passes through $\pi/2$ at resonance. The same observation holds for the 5 : 1 and 7 : 1 superharmonic resonances. These results suggest that phase quadrature between the forcing and the dominant harmonic component exists at resonance for odd superharmonic branches.

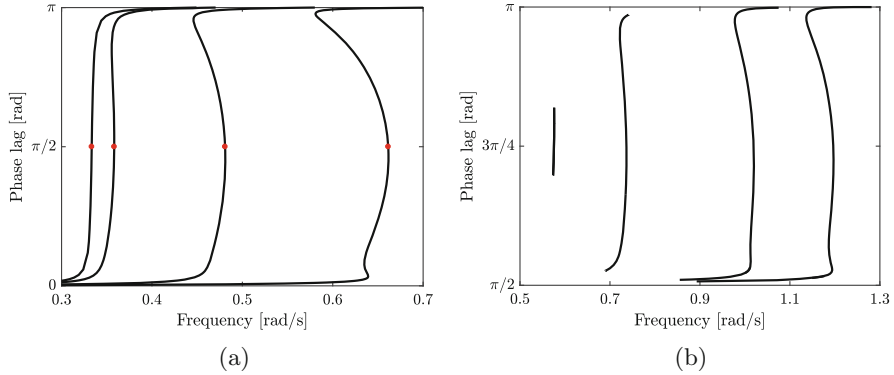


Fig. 3 Phase lags of the 3:1 and 2:1 superharmonic resonances for 4 forcing amplitudes: (a) 3:1 and (b) 2:1. The points where the phase lag is equal to $\pi/2$ are marked by red dots

2.2.2 Even Superharmonic Resonances (k is Even)

The phase lag of the 2/1 harmonic component of the 2:1 resonance is comprised between $\pi/2$ and π and passes through $3\pi/4$ at resonance. The same observation holds for the 4:1, 6:1, and 8:1 resonances. It can be noted that these resonances bifurcate out of the main NFRC.

2.3 Subharmonic Resonances ($\nu > k, k = 1$)

The ratio $\frac{k}{\nu}$ is lower than one, and the resonance branches are located beyond the fundamental resonance. The phase lags of the 1/3 and 1/2 harmonic components for the 1 : 3 and 1 : 2 resonances are depicted in Fig. 4a,b, respectively.

2.3.1 Odd Subharmonic Resonances (ν is Odd)

The corresponding phase lag for the 1/3 harmonic component is bounded by $\pi/3$ and $2\pi/3$. Since the branch is isolated, the phase lag is twice equal to $\pi/2$, which happens at the extremities of the isolated branch. For higher-order 1 : ν subharmonic resonances, the phase lag of the $1/\nu^{th}$ harmonic component is located within the interval $[\pi/2 \pm \pi/2\nu]$.

2.3.2 Even Subharmonic Resonances (ν is Even)

As for even superharmonic resonances, the phase lag of even subharmonic resonances is not centered around $\pi/2$. Specifically, for the 1:2 resonance, it is

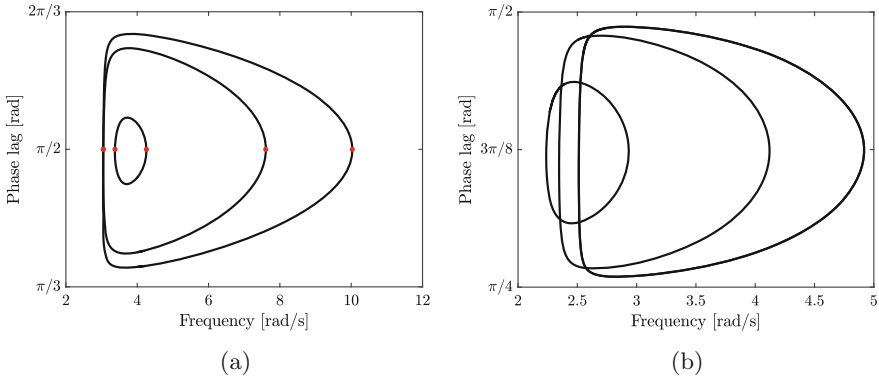


Fig. 4 Phase lags of the 1:3 and 1:2 subharmonic resonances for 3 forcing amplitudes: **(a)** 1:3 and **(b)** 1:2

Table 1 Phase lag of the k/ν harmonic component of the $k : \nu$ resonance

	$k \ \& \ \nu$ are odd	k or ν is even
Phase lag at resonance	$\pi/2$	$3\pi/4\nu$
Phase lag interval	π/ν	$\pi/2\nu$

centered around $3\pi/8$ and comprised between $\pi/4$ and $\pi/2$. For higher-order $1 : \nu$ resonances, the phase lag interval is $\pi/2\nu$ and centered around $3\pi/4\nu$.

2.4 Other Superharmonic and Subharmonic Resonances ($k > 1, \nu > 1$)

Resonances for which neither k nor ν is equal to 1 (see Fig. 1e,f) can also be studied based on the parity of k and ν . Specifically, for the $k : \nu$ resonance, if either k or ν is even, the phase lag of the k/ν harmonic component at resonance is $3\pi/4\nu$ as for even superharmonic and subharmonic resonances, and $\pi/2$ when both k and ν are odd as for odd superharmonic and subharmonic resonances. These results are summarized in Table 1.

3 Phase Resonance Nonlinear Modes

For linear systems, phase resonance takes place when the single-point harmonic forcing and the displacement at the forcing location are in quadrature, i.e., the phase is locked at $\pi/2$ [7]. As illustrated in Fig. 2, this linear definition extends to the fundamental resonances of nonlinear systems.

The results in the previous section allow us to generalize the concept of phase resonance to superharmonic and subharmonic resonances of nonlinear systems. Indeed, they demonstrate that the phase lag can still be used as a robust criterion to track the locus of their resonance peaks, as carried out for fundamental resonances in [8]. The key finding is that phase quadrature between k/ν harmonic component of the $k : \nu$ branch and the forcing is no longer necessarily achieved for such resonances, but depends on the parity of k and ν as indicated in Table 1.

3.1 A New Nonlinear Mode Definition

Considering the unforced linear oscillator

$$m\ddot{x}(t) + c\dot{x}(t) + kx(t) = 0, \tag{3}$$

velocity feedback can be considered to drive the system into resonance [9, 10]:

$$m\ddot{x}(t) + c\dot{x}(t) + kx(t) - \mu\dot{x}(t) = 0, \tag{4}$$

where the feedback term $\mu\dot{x}(t)$ plays the role of *virtual forcing*. Because this virtual forcing and the velocity are collinear, phase quadrature with the displacement $x(t)$, and, hence, phase resonance, is naturally enforced when $\mu = c$.

Phase resonance nonlinear modes (PRNMs) further extend Eq. (4) and take into account superharmonic and subharmonic resonances of nonlinear systems:

The PRNMs of the $k : \nu$ resonance correspond to the periodic responses obtained by feeding back the T -periodic velocity of the harmonic component k/ν shifted by the delay $\nu\alpha/k\omega$ into the autonomous system.

Mathematically, the following equation is to be solved for the Duffing oscillator:

$$m\ddot{x}(t) + c\dot{x}(t) + kx(t) + k_{nl}x^3(t) - \mu\dot{x}_{\frac{k}{\nu}, T}\left(t - \frac{\nu}{k}\frac{\alpha}{\omega}\right) = 0, \tag{5}$$

where ω is the frequency at which the PRNMs are to be calculated, and T is the corresponding period. $\alpha = \pi/2 - \delta$ where δ is the phase lag at resonance given in Table 1. For instance, $\alpha = 0$ for all resonances for which k and ν are odd. The ratio $\frac{\nu}{k}$ in the delay accounts for the fact that the period of the fundamental harmonic component is k/ν times that of the k/ν harmonic component.

Considering the 1:2 subharmonic resonance ($k = 1, \nu = 2$) as an illustrative example, Fig. 5 shows the three steps to calculate the velocity feedback from the original velocity $\dot{x}(t)$ shown in Fig. 5a:

1. Filtering out all the harmonic components of $\dot{x}(t)$ that are different from k/ν to obtain the $\frac{\nu}{k}T$ -periodic signal: $\dot{x}_{\frac{k}{\nu}, \frac{\nu}{k}T}(t)$ (Fig. 5b)
2. Transforming $\dot{x}_{\frac{k}{\nu}, \frac{\nu}{k}T}(t)$ into a T -periodic signal: $\dot{x}_{\frac{k}{\nu}, T}(t)$ (Fig. 5c)

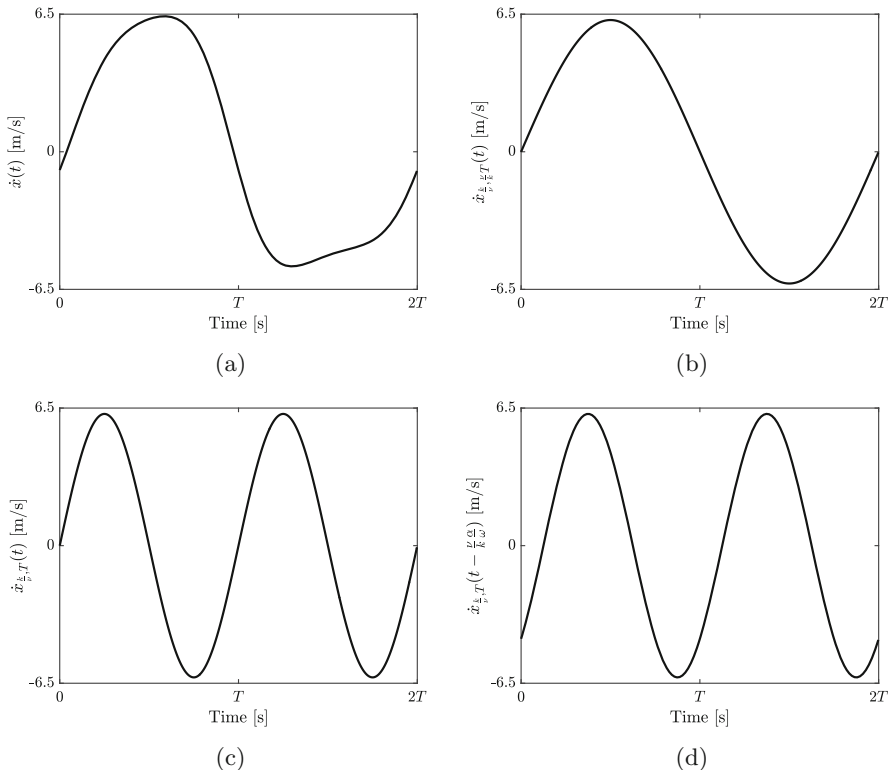


Fig. 5 Calculation of the velocity feedback: **(a)** original velocity, **(b)** after step 1 (filtering), **(c)** after step 2 (T -periodic), and **(d)** after step 3 (delay)

3. Delaying $\dot{x}_{\frac{k}{v},T}(t)$ by the angle $\frac{v}{k}\alpha$, i.e., $\pi/4$ for the 1:2 resonance: $\dot{x}_{\frac{k}{v},T}(t - \frac{v}{k}\frac{\alpha}{\omega})$ (Fig. 5d)

For multi-degree-of-freedom systems, the velocity feedback is applied at the degree of freedom where the external forcing is located.

3.2 PRNMs of the Duffing Oscillator

3.2.1 Fundamental Resonance

The PRNM backbone of the fundamental resonance is superposed to the NFRCs of the Duffing oscillator in Fig. 6. As anticipated, the backbone goes exactly through the $\pi/2$ phase lag points in Fig. 6b and traces very closely the locus of the resonance peaks of the different NFRCs in Fig. 6a.

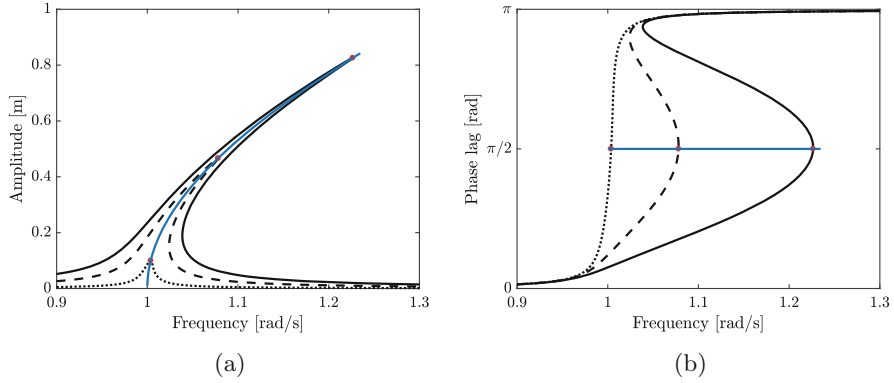


Fig. 6 NFRCs and PRNMs of the fundamental resonance of the Duffing oscillator: (a) amplitude and (b) phase lag. Black: NFRC; blue: PRNM

3.2.2 Superharmonic Resonances

For odd and even superharmonic resonances, the phase lags are $\pi/2$ and $3\pi/4$, respectively. The PRNM backbones corresponding to 3:1 and 2:1 resonances are shown in Fig. 7a,b, respectively. These figures confirm the relevance of the PRNMs for the characterization of superharmonic resonances.

3.2.3 Subharmonic Resonances

The PRNMs of the 1:3 and 1:2 subharmonic resonances are represented in Fig. 8, where the phase lags at resonance are $\pi/2$ and $3\pi/8$, respectively. An important remark is that a critical forcing amplitude is required to activate these resonances. Below this forcing, the isolated resonance branch, and, hence, the PRNM, does not exist.

3.2.4 Other Superharmonic and Subharmonic Resonances

The PRNMs of the remaining superharmonic and subharmonic resonances can also be computed based on the results from Table 1.

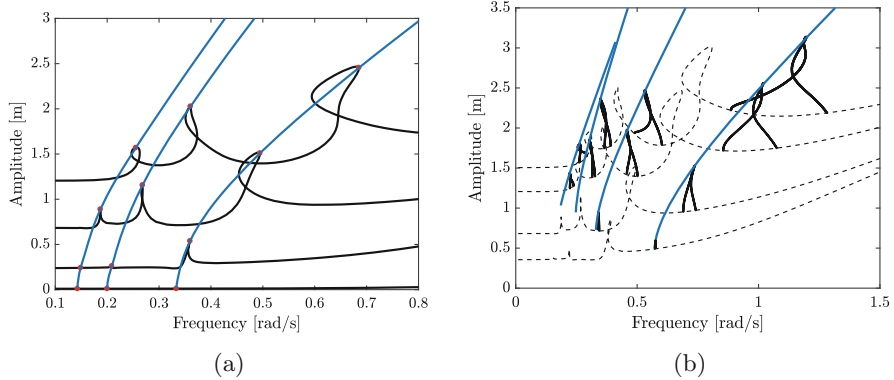


Fig. 7 NFRCs and PRNMs of the 3:1 and 2:1 superharmonic resonances for 4 forcing amplitudes: (a) 3:1 and (b) 2:1. Black: NFRC; blue: PRNM

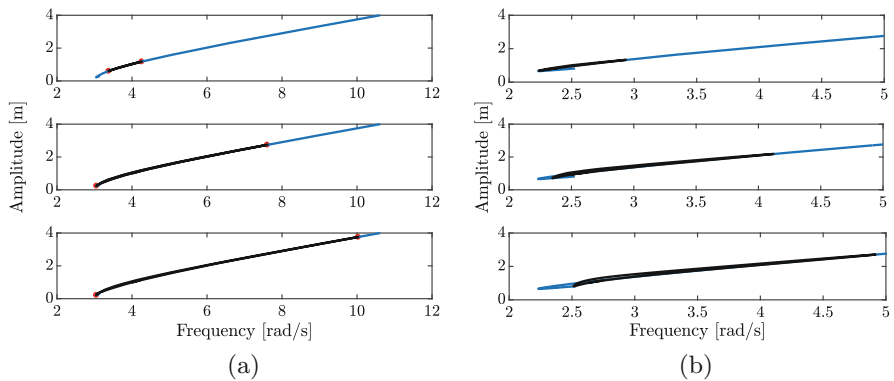


Fig. 8 NFRCs and PRNMs of the 1:3 and 1:2 subharmonic resonances for 3 forcing amplitudes: (a) 1:3 and (b) 1:2. Black: NFRC; blue: PRNM

4 Conclusions

The objective of this chapter was to carry out a detailed study of the phase lags associated with superharmonic and subharmonic resonances of the Duffing oscillator. The study has revealed that phase quadrature still holds for $k : \nu$ resonances when k and ν are both odd. Otherwise, resonance occurs for a phase lag equal to $3\pi/4\nu$. Based on these results, the PRNMs of the $k : \nu$ resonance correspond to the periodic responses obtained by feeding back the delayed velocity of the harmonic component k/ν into the autonomous system at the point where the external forcing is located.

References

1. D.J Ewins, *Modal Testing: Theory, Practice, and Application*, 2nd edn. (Research Studies Press, Philadelphia, 2000)
2. G. Kerschen, K. Worden, A.F. Vakakis, J.-C. Golinval, Past, present and future of nonlinear system identification in structural dynamics. *Mech. Syst. Sig. Process.* **20**(3), 505–592 (2006)
3. A.F. Vakakis, L.I. Manevitch, Y.V. Mikhlin, V.N. Pilipchuk, A.A. Zevin, *Normal Modes and Localization in Nonlinear Systems* (Wiley, New York, 1996)
4. R.M. Rosenberg, Normal modes of nonlinear dual-mode systems. *J. Appl. Mech.* **27**(2), 263–268 (1960)
5. R.M. Rosenberg, The normal modes of nonlinear n-degree-of-freedom systems. *J. Appl. Mech.* **29**(1), 7–14 (1962)
6. U. Parlitz, W. Lauterborn, Superstructure in the bifurcation set of the Duffing equation. *Phys. Lett.* **107A**, 351–355 (1985)
7. F. De Veubeke, *A Variational Approach to Pure Mode Excitation using Characteristic Phase Lag Theory*. Technical report (1956)
8. L. Renson, A. Gonzalez-Buelga, D.A.W. Barton, S.A. Neild, Robust identification of backbone curves using control-based continuation. *J. Sound Vib.* **367**, 145–158 (2016)
9. M. Krack, Nonlinear modal analysis of nonconservative systems: Extension of the periodic motion concept. *Comput. Struct.* **154**, 59–71 (2015)
10. I. Sokolov, V. Babitsky, Phase control of self-sustained vibration. *J. Sound Vib.* **248**, 725–744 (2001)

An Adaptive Sub-Cells Interpolation Method to Enhance Computational Efficiency for Global Attractors of Nonlinear Dynamical Systems



Xi Wang, Jun Jiang, and Ling Hong

1 Introduction

There are a plenty of nonlinear problems in a variety of disciplines. These problems are hard to be described by linear dynamical systems. It is seldom to solve these nonlinear dynamical systems analytically; therefore, several numerical methods are widely utilized in system dynamics.

The cell mapping method is prominent for global analysis of nonlinear dynamical systems. The first version of cell mapping methods called the simple cell mapping method (SCM) is presented by Hsu in 1980s [1]. The SCM method was applied to study long-term system responses such as equilibrium states, periodic motions, and domains of attraction [2]. Some methods are developed to reduce this flaw, such as the point mapping under cell reference method [3–5]. The generalized cell mapping method (GCM) was later presented by Hsu [6]. The GCM with the subdomain-to-subdomain method was applied for global transient analysis by Hsu in 1992 [7]. The GCM was widely applied to deal with crisis bifurcation [8–11] and hyperchaotic crisis [12]. Moreover, Hong et al. presented the fuzzy generalized cell mapping (FGCM) method for the global analysis of fuzzy dynamical system [13–15]. However, when the GCM method is applied in high-dimensional systems, the computational cost immediately soars to a prohibitive magnitude.

One extension of cell mapping methods is the set-oriented method with the subdivision technique to reduce the computational cost [16]. An adaptive subdivision algorithm was developed for the existence of multiple different cell sizes [17].

The interpolation cell mapping (ICM) method based on the SCM method was developed by Tongue and Gu [18]. The ICM method is more accurate than the SCM

X. Wang · J. Jiang · L. Hong (✉)

State Key Laboratory for Strength and Vibration, Xi'an Jiaotong University, Xi'an, China
e-mail: wangxi5@stu.xjtu.edu.cn; jun.jiang@mail.xjtu.edu.cn; hongling@mail.xjtu.edu.cn

method, while they both have nearly the same amount of computational cost [19, 20]. The error of linear interpolation in the ICM method is of order $O(h^2)$, while the error of the SCM method is of order $O(h)$, where h is the cell size [21]. Another application of interpolation in cell mapping is the generalized cell mapping with sampling-adaptive interpolation (GCMSAI). The GCMSAI method based on the GCM method is proposed by Liu et al. [22]. The GCMSAI method could be applied in the observations of boundary metamorphoses [23]. The subdivision technique is incorporated with an interpolation sampling method, which can further enhance the efficiency over the set-oriented method for global analysis of nonlinear dynamical systems [24].

In this chapter, a previous adaptive interpolation sampling method for enhancing the subdivision technique is further improved in both efficiency and adaptability. The performance of the second-order interpolation with a given error criterion is applied to measure the complexity of the dynamic behavior within a cell, and more objective criteria are set up in order to choose the number of sub-cells to be divided in a cell that does not meet the error criterion. The second-order interpolation lattice based on Taylor expansion is applied to each of the sub-cells so as to minimize the sampling computational cost in the cell, and thus the overall computational cost. A three-dimensional system is taken as an example to illustrate the performance of the proposed method.

This chapter is organized as follows. In Sect. 2, the main content of the previous method in [24] is recalled and an index of computational efficiency is defined. In Sect. 3, the performance of interpolation can be used to measure the complexity of dynamic behavior. In Sect. 4, an adaptive sub-cells interpolation method is presented to enhance computational efficiency for global attractors of nonlinear dynamical systems. In Sect. 5, a three-dimensional system is taken as examples to demonstrate the adaptive sub-cells interpolation method. Finally, the conclusion will be presented within the last section.

2 Recall of the Previous Method

The method presented in [24] is an efficient one for finding global attractor of nonlinear dynamical systems. For the convenience of comparison, this method is first briefly reviewed.

2.1 Process of the Previous Method

The main algorithm steps of the previous method are as follows:

Algorithm 1 The subdivision algorithm

Require: Iteration times $maxiter$, refinement partition sub , sampling numbers N_s cell space partition N , underlying dynamics \mathbf{F}

Ensure: Invariant cell set S_{inv}

```

 $iter \leftarrow 0$ 
 $S_c \leftarrow N$ 
 $\mathbf{G} \leftarrow$  mapping creation ( $S_r, \mathbf{F}, N_s$ )
while  $iter < maxiter$  do
     $S_r \leftarrow$  refine ( $S_c, N, sub$ )
    Improve cell space resolution  $N \leftarrow N \times sub$ 
     $\mathbf{G} \leftarrow$  mapping creation ( $S_r, \mathbf{F}, N_s$ )
     $S_c \leftarrow$  backward searching ( $S_r, \mathbf{G}$ )
     $iter \leftarrow iter + 1$ 
end while
    
```

2.2 Second-Order Interpolation Lattice with Error Estimation

In the process of constructing one-step mappings, a second-order interpolation lattice with error estimation is adopted separately in cells to enhance the computational efficiency. With the application of interpolation, a plenty of calculations of numerical integration could be replaced by calculation of interpolation, and a considerable cost of computation could be saved.

In an N-dimensional system, this interpolation lattice based on the second-order Taylor expansion is shown as follows:

$$\begin{aligned}
 \mathbf{x}(T) = & \mathbf{x}^c(T) + \sum_{l=1}^N \left. \frac{\partial \mathbf{x}(T)}{\partial x_l} \right|_{\mathbf{x}=\mathbf{x}^c} (x_l - x_l^c) + \\
 & \frac{1}{2!} \sum_{l=1}^N \sum_{m=1}^N \left. \frac{\partial^2 \mathbf{x}(T)}{\partial x_l \partial x_m} \right|_{\mathbf{x}=\mathbf{x}^c} (x_l - x_l^c)(x_m - x_m^c) + \mathbf{O}(\|\Delta \mathbf{x}\|_2^3),
 \end{aligned}
 \tag{1}$$

where $\mathbf{x} = [x_1, \dots, x_n]$ is a sampling point in a cell z , $\mathbf{x}(T)$ is the image point of \mathbf{x} , $\mathbf{x}^c = [x_1^c, \dots, x_n^c]$ is the center point of this cell z , and besides, the first partial derivatives $\left. \frac{\partial \mathbf{x}(T)}{\partial x_l} \right|_{\mathbf{x}=\mathbf{x}^c} (x_l - x_l^c)$ and second partial derivatives $\left. \frac{\partial^2 \mathbf{x}(T)}{\partial x_l \partial x_m} \right|_{\mathbf{x}=\mathbf{x}^c} (x_l - x_l^c)$ can be estimated by several interpolation nodes in this cell z . There are 3^N interpolation nodes selected at an equal interval in a cell.

Since the true error is one order smaller than the order of the Taylor expansion, the error between interpolation and numerical integration can be estimated roughly by the second-order term. Let the remainder term $\mathbf{R}(\mathbf{x}) = [r_1, \dots, r_n]$ equal the second-order term:

$$\mathbf{R}(\mathbf{x}) = \frac{1}{2!} \sum_{l=1}^N \sum_{m=1}^N \left. \frac{\partial^2 \mathbf{x}(T)}{\partial x_l \partial x_m} \right|_{\mathbf{x}=\mathbf{x}^c} (x_l - x_l^c)(x_m - x_m^c). \tag{2}$$

In order not to influence the subsequent analysis, the error bound is fixed as a half of the cell size $\mathbf{H} = [H_1, \dots, H_n]$, the corresponding criterion is given as follows:

$$\begin{cases} \forall r_l \leq \frac{H_l}{2}, \text{ interpolation is permitted.} \\ \exists r_l > \frac{H_l}{2}, \text{ direct numerical integration instead,} \end{cases} \tag{3}$$

where $l = 1, \dots, n$. If the criterion is satisfied, the image point $\mathbf{x}(T)$ could be obtained by interpolation Eq. (2), otherwise, by numerical integration instead.

It should be noted that since the interpolation method is applied to the cell mapping method, the interpolation result of each sampling point does not need to be very close to the integration result. The error criterion can ensure that the image cell set obtained by interpolation is close to the image cell set obtained by integration, thereby ensuring that the following process will not deviate too much.

2.3 The Interpolation Accuracy and the Computational Efficiency

In an iteration process, the number of remaining cells that cover the global attractor is assumed to be N_c . The number of sampling points in each cell is assumed to be N_s , and the number of interpolation nodes in each cell is assumed to be N_i where $N_i = 3^N$ in the second-order interpolation lattice. The time of a process of numerical integration completed by the fourth-order Runge–Kutta method is assumed to be T_{RK} . The time of a process of interpolation is assumed to be T_{Ip} . Besides, let η denote the proportion of integration samples to the total number of samples:

$$\eta = \frac{\text{integration samples}}{\text{total samples}}, \tag{4}$$

where $\eta = 100\%$ for the worst situation while $\eta = 0\%$ for the best situation. When η is small, it means most of the interpolation errors satisfy the error criterion, which also means the interpolation results are pretty accurate. Thus, η could be used as an index to measure the interpolation accuracy.

The computational cost in an iteration process could be shown as follows:

$$T = \eta \times N_c \times N_s \times T_{RK} + (1 - \eta) \times N_c \times N_s \times T_{Ip} + N_c \times N_i \times T_{RK}. \tag{5}$$

The computational cost of T_{RK} is several hundred times of that of T_{Ip} ; therefore, the computational cost of interpolation could be ignored. Let $\zeta = \eta + N_I/N_s$; then Eq. (5) could be rewritten as

$$T = \zeta \times N_c \times N_s \times T_{RK}. \quad (6)$$

3 The Interpolation Adaptability

To further enhance the computational efficiency in this circumstance, the performance of the second-order interpolation with the given error criterion is adopted to measure the complexity of the dynamic behavior within a cell. The interpolation shape of the cell is only related to the derivatives of each order. Besides, the performance of the second-order interpolation with the given error criterion is only related to the second-order derivatives. Each second-order partial derivative could be regarded as a geometric feature; then the remainder term in Eq. (2) can be rewritten as

$$\begin{cases} r_1(x, y, z) = d_{11}^1 x^2 + d_{22}^1 y^2 + d_{33}^1 z^2 + d_{12}^1 xy + d_{13}^1 xz + d_{23}^1 yz \\ r_2(x, y, z) = d_{11}^2 x^2 + d_{22}^2 y^2 + d_{33}^2 z^2 + d_{12}^2 xy + d_{13}^2 xz + d_{23}^2 yz \\ r_3(x, y, z) = d_{11}^3 x^2 + d_{22}^3 y^2 + d_{33}^3 z^2 + d_{12}^3 xy + d_{13}^3 xz + d_{23}^3 yz, \end{cases} \quad (7)$$

where $d_{ii}^k = \frac{\partial^2 x_k(T)}{2\partial x_i^2} \Big|_{\mathbf{x}=\mathbf{x}^c}$, $d_{ij}^k = \frac{\partial^2 x_k(T)}{\partial x_i \partial x_j} \Big|_{\mathbf{x}=\mathbf{x}^c}$, $x = (x_1 - x_1^c)$, $y = (x_2 - x_2^c)$, $z = (x_3 - x_3^c)$.

We can further analyze the criterion satisfaction in each cell from the perspective of probability theory. Introduce random variables X, Y, Z to represent the projection of the distance between the sample point \mathbf{x} and the center point \mathbf{x}^c in three dimensions. In addition, introduce a random variable $[R_1, R_2, R_3]$ to represent the projection of the remainder term $\mathbf{R}(\mathbf{x}) = [r_1, r_2, r_3]$ in three dimensions. Then, the distribution of the remainder term can be expressed as follows:

$$\begin{cases} R_1 = d_{11}^1 X^2 + d_{22}^1 Y^2 + d_{33}^1 Z^2 + d_{12}^1 XY + d_{13}^1 XZ + d_{23}^1 YZ \\ R_2 = d_{11}^2 X^2 + d_{22}^2 Y^2 + d_{33}^2 Z^2 + d_{12}^2 XY + d_{13}^2 XZ + d_{23}^2 YZ \\ R_3 = d_{11}^3 X^2 + d_{22}^3 Y^2 + d_{33}^3 Z^2 + d_{12}^3 XY + d_{13}^3 XZ + d_{23}^3 YZ, \end{cases} \quad (8)$$

where X, Y, Z satisfy the uniform distribution of $U(-H_1/2, H_1/2)$, $U(-H_2/2, H_2/2)$, $U(-H_3/2, H_3/2)$, respectively. Next, the random variable W is introduced to indicate the status where the points in the cell satisfy the criterion of Eq. (3), which can be expressed as follows:

$$W = \max\{|R_1/H_1|, |R_2/H_2|, |R_3/H_3|\}. \quad (9)$$

Then, the probability of satisfying the criterion of the cell can be expressed as:

$$P\{W < 0.5\}. \quad (10)$$

Let $\iota = 1 - P\{W < 0.5\}$. ι is a parameter related to each second-order derivative, which means it is also a geometric feature. Obviously, if the dynamic behavior of this region is very complicated, the error of the interpolation result is more difficult to satisfy the criterion. Therefore, ι would become very high in this cell. Thus, ι could be applied to measure the complexity of the dynamic behavior within a cell.

All cells can fall into three types according to their ι : excellent cells, good cells, bad cells. The ι of excellent cells is less than 10%, the ι of good cells is between 10% and 40%, and the ι of bad cells is greater than 40%.

4 Adaptive Sub-Cells Interpolation Method

For the third-order interpolation lattice, it is difficult to propose a corresponding error criterion. However, it provides an idea to improve the simulated shape by appropriately increasing the density of interpolation nodes. Increasing the density of interpolation nodes can divide the cell into several smaller sub-cells. Based on the idea of piecewise interpolation, a new sub-cells interpolation lattice is presented.

For each cell, m^N interpolation nodes are selected at equal intervals. Let $\mathbf{h} = [h_1, \dots, h_N] = \mathbf{H}/(m - 1)$ denote the interval of interpolation nodes. In a case $N = 3$, the distribution of interpolation nodes can be shown as follows:

$$\mathbf{x}_{\mathbf{IP}}^{(i,j,k)} = \mathbf{x}_{\mathbf{IP}}^{(0,0,0)} + i \times [h_1, 0, 0]^T + j \times [0, h_2, 0]^T + k \times [0, 0, h_3]^T, \quad (11)$$

where $i, j, k = -(m - 1)/2, -(m - 3)/2, \dots, 0, \dots, (m - 3)/2, (m - 1)/2$ and $\mathbf{x}_{\mathbf{IP}}^{(0,0,0)}$ denotes the center point of the cell. These interpolation nodes are located inside the cell or on the cell boundary. It could be calculated that there are $(m - 2)^N$ interpolation nodes located inside the cell and they are represented by $\mathbf{x}_{\mathbf{IP}}^{(i,j,k)}$, $i, j, k = -(m - 3)/2, \dots, 0, \dots, (m - 3)/2$. Other interpolation nodes are located on the cell boundary.

For any sampling point \mathbf{x} in this cell, the nearest interpolation node located in the cell is chosen as the expansion point of the Taylor expansion. If $\mathbf{x}_{\mathbf{IP}}^{(i,j,k)}$ is the expansion point for this sampling point \mathbf{x} , its image point $\mathbf{x}(T)$ could be calculated as follows:

$$\mathbf{x}(T) = \mathbf{T}_0(\mathbf{x}) + \mathbf{T}_1(\mathbf{x}) + \mathbf{T}_2(\mathbf{x}) + \mathbf{O}(\|\Delta\mathbf{x}\|_2^3), \quad (12)$$

where $\mathbf{T}_0(\mathbf{x})$, $\mathbf{T}_1(\mathbf{x})$, and $\mathbf{T}_2(\mathbf{x})$ represent the constant term, the first-order term, and the second-order term in the Taylor expansion, respectively. And the criterion is the same as Eqs. (3)–(4).

For any sampling point \mathbf{x} in this cell, the nearest interpolation node located in the cell is chosen as the expansion point of the Taylor expansion. There are $(m - 2)^N$ interpolation nodes located inside the cell. Naturally, all sampling points are divided into $(m - 2)^N$ mutually exclusive subsets according to their different expansion points. Therefore, the cell is divided into $(m - 2)^N$ sub-cells. According to the Taylor expansion in Eq. (2), the approximate estimate of the error of interpolation can be reduced from $O(H^3)$ to $O(H/(m-2)^N) = O(H^3)/(m-2)^N$, which means the accuracy has been greatly improved.

Due to the self-similarity of strange attractors, the geometric features of each sub-cell are similar to the geometric features of the cell. The simulated shape of sub-cells interpolation lattice is actually a combination of several similar small shapes like a jigsaw. Besides, the second-order interpolation lattice in Sect. 2 is actually a special case of sub-cells interpolation at $m = 3$.

In Sect. 3, the cells of the global attractor can fall into three kinds according to their complexity of dynamic behavior ι . However, for each cell, it is difficult to quickly obtain ι of this cell by Eqs. (9)–(10). Some numerical methods such as Monte Carlo method can be applied to obtain ι of this cell. Different interpolation lattices can be applied according to the ι of the cell, as follows:

$$\begin{cases} \iota < 10\%, m = 3 \\ 10\% \leq \iota \leq 40\%, m = 5 \\ \iota > 40\%, m = 7. \end{cases} \quad (13)$$

The error of interpolation would be particularly large when the resolution of the global attractor is not high, thus, in the first k iterations, numerical integration is applied, and the interpolation is started to be used in the later iteration process.

5 Examples of Applications

We consider a problem in three-dimensional Lorenz system that can be written as

$$\begin{cases} \dot{x}_1 = \sigma(x_2 - x_1) \\ \dot{x}_2 = \gamma x_1 - x_2 - x_1 x_3 \\ \dot{x}_3 = x_1 x_2 - b x_3. \end{cases} \quad (14)$$

The system parameters are $\sigma = 10$, $\gamma = 18$, $b = \frac{8}{3}$. The domain of interest in the state space is $D = [-21, 21] \times [-21, 21] \times [-6, 30]$. The integration time to compute one-step mappings is π . $15 \times 15 \times 15$ points are sampled in each cell. In

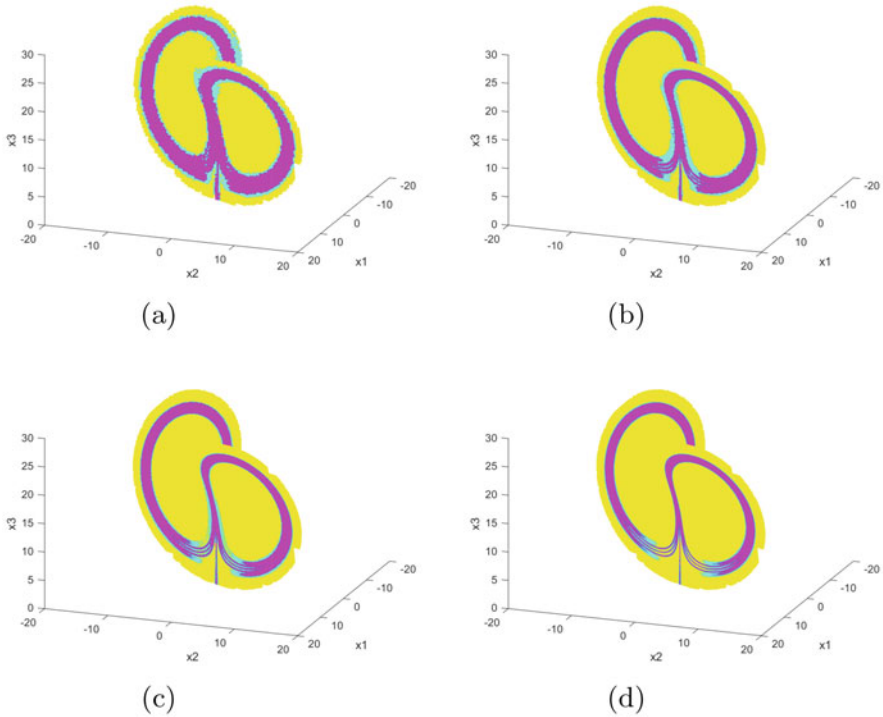


Fig. 1 The global attractor of the Lorenz system made up of cells with three sub-cells interpolation lattices. Yellow denotes cells applied by the sub-cells interpolation lattice with $m = 3$. Cyan denotes cells applied by the sub-cells interpolation lattice with $m = 5$. Magenta denotes cells applied by the sub-cells interpolation lattice with $m = 7$. (a) Iteration=19. (b) Iteration=22. (c) Iteration=25. (d) Iteration=28

the first 18 iterations of subdivision, numerical integration is used for calculating the one-step mappings from all the sampling points.

Figure 1 shows the global attractor in different resolutions obtained by the present method. It could be found that the structure of the invariant sets is fractal that two parallel stripes gradually split into four stripes as the resolution of cell state space increases.

Figure 2 illustrates the total computational cost of the present method in comparison with the set-oriented method and the previous method.

6 Conclusions

In [24], the subdivision is incorporated with an interpolation sampling method, which can further enhance the efficiency over the set-oriented method. In this chapter, it is further improved in both efficiency and adaptability. In this way, a cell is actually divided into smaller sub-cells with smaller interpolation area,

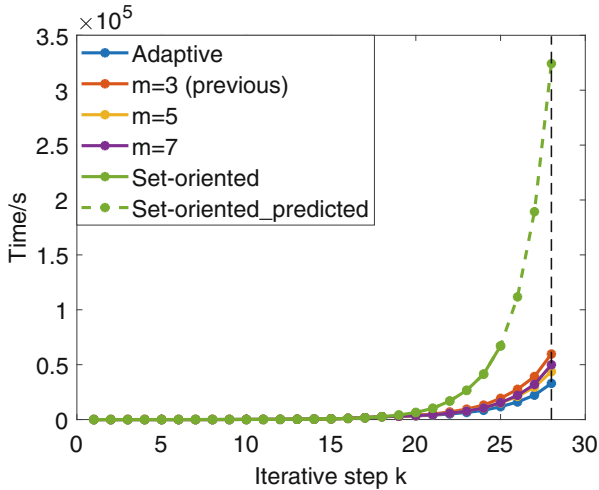


Fig. 2 The computational cost of the Lorenz system in different iterations. Since the set-oriented method consumes too much time to finish after 25 iterations, the time taken by the set-oriented method after 25 iterations is given in a predictive broken line

which is similar to piecewise interpolation lattice and thus with higher accuracy of interpolation. So the overall computational cost will be significantly reduced. A familiar three-dimensional dynamical system is taken as an example to illustrate the effectiveness of the proposed method.

As can be seen, each cell could still be processed independently in the present adaptive interpolation method. Thus, it is promising to incorporate the present method with GPU parallel computing in order to substantially further enhance the computational efficiency in the global analysis of nonlinear dynamical systems. In addition, it is interesting to note that the interpolation performance has a closer relationship with the complexity of the local dynamics in cells, and therefore, this can be further explored in the future work.

Acknowledgments This work was supported by the National Natural Science Foundation of China (Grant Nos. 11972274, 11772243, 11672218).

References

1. C.S. Hsu, A theory of cell-to-cell mapping dynamical-systems. *J. Appl. Mech. Trans. ASME* **47**(4), 931–939 (1980)
2. C.S. Hsu, R.S. Guttalu, An unravelling algorithm for global analysis of dynamical-systems—an application of cell-to-cell mappings. *J. Appl. Mech. Trans. ASME* **47**(4), 940–948 (1980)
3. J. Jiang, J.X. Xu, A method of point mapping under cell reference for global analysis of nonlinear dynamical-systems. *Phys. Lett. A* **188**(2), 137–145 (1994)

4. J. Jiang, J.X. Xu, An iterative method of point mapping under cell reference for the global analysis of non-linear dynamical systems. *J. Sound Vib.* **194**(4), 605–621 (1996)
5. J. Jiang, J.X. Xu, An iterative method of point mapping under cell reference for the global analysis: theory and a multiscale reference technique. *Nonlinear Dyn.* **15**(2), 103–114 (1998)
6. C.S. Hsu, A probabilistic theory of non-linear dynamical-systems based on the cell state-space concept. *J. Appl. Mech. Trans. ASME* **49**(4), 895–902 (1982)
7. C.S. Hsu, Global analysis by cell mapping. *Int. J. Bifurcation Chaos* **2**(4), 727–771 (1992)
8. L. Hong, J.X. Xu, Crises and chaotic transients studied by the generalized cell mapping digraph method. *Phys. Lett. A* **262**(4–5), 361–375 (1999)
9. L. Hong, J.X. Xu, Discontinuous bifurcations of chaotic attractors in forced oscillators by generalized cell mapping digraph (GCMD) method. *Int. J. Bifurcation Chaos* **11**(3), 723–736 (2001)
10. L. Hong, J.X. Xu, Chaotic saddles in Wada basin boundaries and their bifurcations by the generalized cell-mapping digraph (GCMD) method. *Nonlinear Dyn.* **32**(4), 371–385 (2003)
11. L. Hong, J.X. Xu, Double crises in two-parameter forced oscillators by generalized cell mapping digraph method. *Chaos Solitons Fractals* **15**(5), 871–882 (2003)
12. L. Hong, Y.W. Zhang, J. Jiang, A hyperchaotic crisis. *Int. J. Bifurcation Chaos* **20**(4), 1193–1200 (2010)
13. L. Hong, J.Q. Sun, Bifurcations of forced oscillators with fuzzy uncertainties by the generalized cell mapping method. *Chaos Solitons Fractals* **27**(4), 895–904 (2006)
14. L. Hong, J.Q. Sun, Bifurcations of a forced Duffing oscillator in the presence of fuzzy noise by the generalized cell mapping method. *Int. J. Bifurcation Chaos* **16**(10), 3043–3051 (2006)
15. L. Hong, J. Jiang, J.Q. Sun, Fuzzy responses and bifurcations of a forced Duffing oscillator with a triple-well potential. *Int. J. Bifurcation Chaos* **25**(1) (2015)
16. M. Dellnitz, A. Hohmann, A subdivision algorithm for the computation of unstable manifolds and global attractors. *Numer. Math.* **75**(3), 293–317 (1997)
17. R. Guder, M. Dellnitz, E. Kreuzer, An adaptive method for the approximation of the generalized cell mapping. *Chaos Solitons Fractals* **8**(4), 525–534 (1997)
18. B.H. Tongue, On obtaining global nonlinear-system characteristics through interpolated cell mapping. *Physica D* **28**(3), 401–408 (1987)
19. B.H. Tongue, K. Gu, Interpolated cell mapping of dynamical-systems. *J. Appl. Mech. Trans. ASME* **55**(2), 461–466 (1988)
20. B.H. Tongue, K.Q. Gu, A theoretical basis for interpolated cell mapping. *SIAM J. Appl. Math.* **48**(5), 1206–1214 (1988)
21. W.K. Lee, C.S. Hsu, A global analysis of an harmonically excited spring-pendulum system with internal resonance. *J. Sound Vib.* **171**(3), 335–359 (1994)
22. X.M. Liu, J. Jiang, L. Hong, D.F. Tang, Studying the global bifurcation involving Wada boundary metamorphosis by a method of generalized cell mapping with sampling-adaptive interpolation. *Int. J. Bifurcation Chaos* **28**(2), 1830003 (2018)
23. X.M. Liu, J. Jiang, L. Hong, D.F. Tang, Wada boundary bifurcations induced by boundary saddle-saddle collision. *Phys. Lett. A* **383**(2-3), 170–175 (2019)
24. X. Wang, J. Jiang, L. Hong, Enhancing subdivision technique with an adaptive interpolation sampling method for global attractors of nonlinear dynamical systems. *Int. J. Dyn. Control* **8**(4), 1147–1160 (2020)

Birth of the Neimark–Sacker Bifurcation for the Passive Compass-Gait Walker



Essia Added and Hassène Gritli

1 Introduction

To properly analyze the walking phenomenon, it is necessary to use a biped robot which seems like to the human being. The compass-gait biped robot is proposed to be the simplest possible model that can imitate the human walking [1–6]. It is a biped model without knees, without ankles, and with punctual ground contact. It has been known so far that it is characterized by a passive dynamic walking, which is modeled by an impulsive hybrid nonlinear system [5, 7, 8]. Passive dynamic walking is a series of cyclical and symmetrical movements with the alternation of the impact of the feet on the walking surface and the oscillations by descending a slightly deep inclined surface without any force as an active controller. It is characterized by the step length, the step period, the stride, the pace of walking, the speed of movement, and the initial conditions just after or before the walk step.

Many researches have been done on the development of walking bipeds based on the principle of passive dynamic walking [7, 8]. The pioneer Tad McGeer proposed in [9] that the simplest passive walker could serve as an alternate point of departure for the synthesis of passive bipedal walking. It has been shown in [5], using mainly the Poincaré map and the bifurcation diagrams, that the passive motion of the compass robot exhibits for the first time a cascade of period-doubling bifurcations (PDB) as a route to chaos, which explored the passive bipedal walking using mainly bifurcation diagrams with reference to some variation in its geometrical and inertial parameters. After that, several authors have studied chaos and bifurcations of the

E. Added · H. Gritli (✉)

Higher Institute of Information and Communication Technologies, University of Carthage, Tunis, Tunisia

Laboratory of Robotics, Informatics and Complex Systems (RISC Lab-LR16ES07), National Engineering School of Tunis, University of Tunis El Manar, Tunis, Tunisia

passive motion of the compass-gait biped model and other related models [7, 10–14]. Authors in [15, 16] showed the appearance of the cyclic-fold bifurcation (CFB) in the passive behavior of the compass-gait model. Moreover, it was shown the appearance of the Neimark–Sacker bifurcation (NSB) in the controlled compass-gait walker [17] and another more complicated biped robot under control [18, 19]. Several other complex phenomena were also reported in [20, 21] for the compass robot under the OGY-based state-feedback control. These research works are primarily an analysis of the properties of the passive walk of biped robots like stability, limit cycles, periodicity, and so on.

The objective of this work is to present a further investigation of the passive motion of the compass-gait biped walker as it goes down an inclined surface and by varying some parameter, which was not considered in previous works. Using mainly the bifurcation diagrams, we will show the exhibition of the PDB and its route to chaos. We will show also, and for the first time, the birth of the NSB, and hence the generation of quasi-periodic passive gaits. Furthermore, the goal of this work is to demonstrate that the passive dynamic models such as the compass-gait biped walker has the ability to model the chaotic behavior of the human locomotion with certain modifications.

The remaining of this work is organized as follows: The compass-like biped passive dynamic walker and its impulsive hybrid nonlinear dynamics are presented in Sect. 2. The Poincaré map approach and stability analysis of the fixed point are presented in Sect. 3. Analysis of and discussion about the results of numerical simulation of the biped robot's properties in order to reveal its behaviors by varying its parameters are reported in Sect. 4. The conclusion and future works are finally given in Sect. 5.

2 The Passive-Dynamics Biped Walker

Wabot-1 is the first biped robot walker. It was created by Waseda University (Japan) in 1973. The Wabot-1 comes from the laboratory of Professor Takanishi [22]. The compass-like biped is the simplest model of walkers that imitate humans [5]. It is easy to model it and analyze its walking results and then its control.

2.1 Model Description

As shown in Fig. 1, the model of the passive-dynamics compass-gait biped robot is modeled as a two-link mechanism. The point mass m_h at the hip represents the upper body, while m_s and m_{ns} stand for the masses of the stance leg and the swing leg, respectively. The length of the stance leg is equal to the length of the swinging one with $l = a + b$, where a (resp. b) designates the distance from the tip of the leg (resp. the hip) to the center-of-mass of the leg. The configuration variables of the

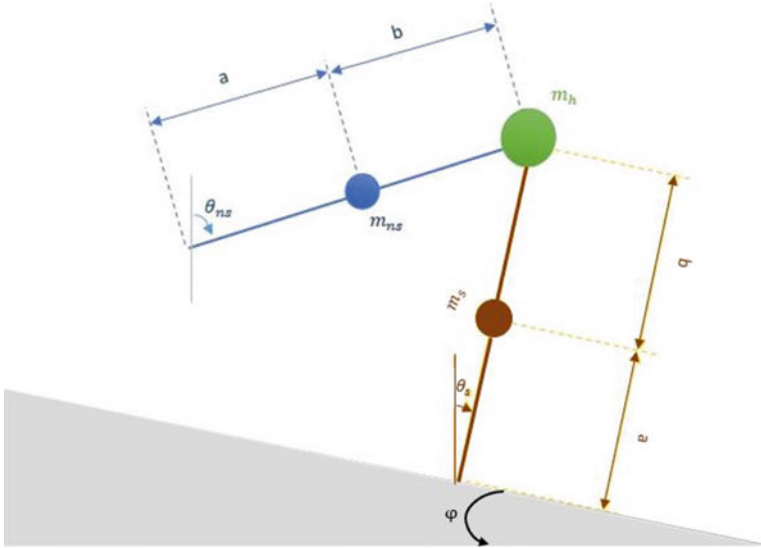


Fig. 1 The model of the compass-like passive-dynamics biped robot on the walking surface of slope φ

biped robot are mainly described by the two angles θ_s and θ_{ns} , respectively, of the stance leg and the swing leg. Note that the positive angles of these two variables θ_s and θ_{ns} are computed counterclockwise with respect to the associated vertical lines.

For the simulation of the compass-gait biped walker, we will take the values of the different inertial parameters: $a = 0.5$ [m], $b = 0.5$ [m], $l = 1$ [m], $m = 5$ [Kg], and $m_h = 10$ [Kg]. Moreover the gravitational constant is $g = 9.8$ [ms^{-2}].

Remark 1 The compass-gait walker is known to possess passive gaits that are almost similar to the human walking [1, 2]. Far from the analysis of human locomotion, the compass-gait walker was used also for investigating the animal locomotion. The compass model might reasonably provide a template for analyzing the motions in the sagittal plane of the center-of-mass of some diverse species, namely the six-legged trotters (such as cockroaches), the four-legged trotters (such as dogs), the two-legged runners (such as birds), and the hoppers (such as kangaroos) [23]. Other examples of animals are the palaeognathae, the running crab, the trotting dogs, and the bouncing kangaroo rats [24]. Successful walkers and runners have bird-like legs and were called in [25] as bipedal birds. By varying the position of the center-of-mass of the two legs, the compass-gait walker approaches some kinds of running birds as the palaeognathae.

2.2 Model of the Walking Dynamics

The motion model of the compass-gait robot contains a swing phase described by a continuous-time nonlinear ordinary differential equation, and a collision stage described by a discrete-time algebraic equation [26, 27]. One step of the motion cycle starts from the swing phase and ends when the collision of the swing leg with the ground occurs, and then ends with the collision phase.

The motion during the swing phase can be formulated typically using the Euler-Lagrange formulation, by the following expression:

$$J(q)\ddot{q} + C(q, \dot{q})\dot{q} + G(q) = Bu \quad (1)$$

where $J(q)$ is the inertia matrix, $C(q, \dot{q})$ is the centrifugal forces' matrix, $G(q)$ is the vector of gravitational torques, B is the control matrix, and u is the control input. Expressions of the previous matrices can be found, for example, in [28].

There are some standard assumptions for the impact event: (1) it is perfectly inelastic, (2) it is instantaneous, and (3) there is no slip on the ground. Then, the impact results in an instantaneous jump in speeds, while the position variables continue throughout the impact [26, 28, 29].

The angular momentum is usually denoted as $Q(q)\dot{q}$. At the impact, there is a conservation of the angular momentum as follows [5]:

$$Q(q)_+\dot{q}^+ = Q(q)_-\dot{q}^- \quad (2)$$

The superscripts $-$ and $+$ indicate situations just before and after the impact, respectively. Expression of the two matrices $Q(q)_+$ and $Q(q)_-$ can be found in [28].

The impact phase occurs when the swing leg of the biped robot touches the ground. Under the previous assumptions, the impact happens when the following condition is satisfied:

$$\theta_{ns} + \theta_s + 2\varphi = 0 \quad (3)$$

where here, and as indicated in Fig. 1, φ is the slope angle.

Posing $x = [q^T \dot{q}^T]^T$ as the state vector. Using the previous expressions (1), (2), and (3), the complete dynamics of the compass robot is expressed by the following impulsive hybrid nonlinear system:

$$\dot{x} = f(x) + g(x)u \quad \text{if} \quad x \notin \Gamma \quad (4a)$$

$$x^+ = h(x^-) \quad \text{if} \quad x \in \Gamma \quad (4b)$$

where $f(x) = \begin{bmatrix} \dot{q} \\ -J(q)^{-1} (H(q, \dot{q})\dot{q} + G(q)) \end{bmatrix}$, $g(x) = \begin{bmatrix} 0 \\ J(q)^{-1} B \end{bmatrix}$, $h(x) = \begin{bmatrix} Rq \\ S(q)\dot{q} \end{bmatrix}$, where the two matrices R and S are defined respectively as: $R = \begin{bmatrix} 0 & 1 \\ 1 & 0 \end{bmatrix}$ and $S(q) = Q(q)_+^{-1} Q(q)_-$. In addition, the control input u in (4a) is considered to be zero in this work, i.e. the compass-type bipedal robot is completely uncontrolled ($u = 0$) while walking down the inclined surface. Moreover, the set Γ in the system (4) is expressed as follows:

$$\Gamma = \{ x \in \mathbb{R}^4 : Cx + 2\varphi = 0 \} \tag{5}$$

where $C = [1 \ 1 \ 0 \ 0]$.

3 Poincaré Map, Fixed Point, and Stability Analysis

The Poincaré map is a classic technique for the discretization of a continuous-time dynamic system. It is useful for reducing the order of the system and bridging the gap between continuous and discrete systems [16, 28, 30]. In general, a K -periodic limit cycle must return to the initial state x_0 after K intersections. Successive intersection states of the flow ϕ with the Poincaré section define the following Poincaré map:

$$x_{k+1} = P(x_k) = \phi(\tau_r(x_k), x_k) \tag{6}$$

where $\tau_r(x_k)$ is the return time to the Poincaré section and $\phi(t, x)$ stands for the flow of the hybrid system (4).

For our case of the compass-gait biped robot, the Poincaré section is chosen to be the set Γ defined by expression (5). Moreover, for a passive walk, we take $u = 0$ in the hybrid system (4).

To study the stability of the passive compass-gait biped robot, we must first find the fixed point of the Poincaré map (6), which presents the initial condition of departure for the passive locomotion. For this task, we have chosen to use the Poincaré map method and the Shooting method [31, 32] to find the period- K fixed point x_\star , by numerically solving the following equation:

$$\phi(\tau_r(x_\star), x_\star) - x_\star = 0 \tag{7}$$

For further details, we refer our reader to [32]. The stability of the period- K fixed point is evaluated via the eigenvalues of the following Jacobian matrix $DP(x_\star)$ of the Poincaré map (6):

$$DP(x_\star) = \left(I_n - \frac{f(x_\star)C}{Cf(x_\star)} \right) \Phi(\tau_r(x_\star), x_\star) \quad (8)$$

where I_n is the $(n \times n)$ -identity matrix and $\Phi(\tau_r(x_\star), x_\star)$ is the monodromy matrix [32].

If all the eigenvalues of the Jacobian matrix $DP(x_\star)$ are inside the unit circle, then the K -periodic fixed point x_\star is stable. Otherwise, it is unstable.

4 Numerical Simulation

In this section, we will analyze the passive motion of the compass robot under the variation of the parameter “ a ,” which is the length of the lower segment of a leg. Via bifurcation diagrams and through the tendency of the eigenvalues of the Jacobian matrix of the Poincaré map, we will reveal the exhibition of the NSB. It is important to note that this choice of the parameter a as the bifurcation parameter was not considered in the literature. In [5], the length ratio was defined as $\beta = \frac{b}{a}$. In the literature and for the compass-gait robot, only the period-doubling route to chaos was reported. In the sequel, only the parameter a will be varied, while all the other parameters are kept constant.

4.1 Limit Cycle Computation

A limit cycle is the attractor of a periodic behavior. It is a closed trajectory $\phi(\tau_r(x_0), x_0)$, where x_0 is the initiation condition belonging to some selected Poincaré section. Each fixed point x_\star of the Poincaré map corresponds to a point (a state) of the limit cycle of the continuous-time dynamic system. A limit cycle corresponds to a fixed point on the Poincaré section. Thus, the computation of a K -periodic limit cycle returns to the determination of the K -periodic fixed point x_\star of the Poincaré map.

By solving the nonlinear function (7) and by selecting the periodicity number K , the numerical results of the Poincaré map are organized in Table 1 for different values of the parameter a . The adopted slope angle of the walking surface is $\varphi = 5.1^\circ$. In this table, x_\star is the fixed point of the Poincaré map, $\tau_r(x_\star)$ is the return time or is the step period of the bipedal walking, and K is the periodicity number of the fixed point x_\star . It is worth to note that we have only presented in Table 1 the stable fixed points of period K .

Table 1 Some numerical results of the Poincaré map obtained for the slope angle $\varphi = 5.1^\circ$

a	x_\star^T	$\tau_r(x_\star)$	K
0.9	[9.4973699 – 19.69737 – 462.83168 – 112.02359]	0.35187130	1
0.7	[12.467649 – 22.667649 – 197.24258 – 106.05712]	0.57792570	1
0.58	[13.539178 – 23.739178 – 142.88053 – 105.7622]	0.67951066	2
	[58.000000 12.869681 – 23.069681 – 160.98869]	0.69980887	
0.56	[14.070625 – 24.270625 – 122.33799 – 106.24581]	0.67830010	2
	[12.431829 – 22.631829 – 166.86743 – 103.73518]	0.73153079	
0.54	[14.359646 – 24.559646 – 108.61565 – 106.33997]	0.68285110	2
	[12.22787 – 22.427870 – 166.97703 – 103.18352]	0.75700318	
0.51	[14.513951 – 24.713951 – 104.72653 – 106.43770]	0.70993425	4
	[11.846687 – 22.046687 – 1.65.16622 – 101.98528]	0.79155306	
	[14.642066 – 24.842066 – 85.655845 – 105.92070]	0.68219092	
	[12.437935 – 22.637935 – 160.78174 – 103.60024]	0.78831673	
0.5071	[14.451018 – 24.651018 – 108.23360 – 106.41090]	0.71800684	8
	[11.876948 – 22.076948 – 163.63368 – 101.97145]	0.79293892	
	[14.664376 – 24.864376 – 85.429475 – 105.95284]	0.68497855	
	[12.360433 – 22.560433 – 161.12870 – 103.39413]	0.79219593	
	[14.579353 – 24.779353 – 101.21745 – 106.44476]	0.70805590	
	[11.786268 – 21.986268 – 165.70061 – 101.86121]	0.79601784	
	[14.645779 – 24.845779 – 82.818192 – 105.78372]	0.68073782	
	[12.575223 – 22.775223 – 158.85084 – 103.91522]	0.78981806	

4.2 Period-Doubling Route to Chaos and Birth of the NSB

As noted previously, we choose the length of the lower leg segment a as the bifurcation parameter. The angle of the slope of the walking surface was kept constant to $\varphi = 5.1^\circ$ (where φ is the angle between the horizontal walking surface and the inclined walking surface). Then, by varying the parameter a , we obtained the bifurcation diagrams in Fig. 2. Figure 2a presents the classical scenario of successive period-doubling bifurcations as a route to chaos, revealing then the behavior of the bipedal robot while varying the value of a and then as a decreases. Figure 2b presents a pattern which will be repeated until reaching chaos, which is more evident in Fig. 2c. Figure 2b shows very well the first PDB from which the 1-periodic behavior becomes 2-periodic. In Fig. 2c, we see a second and a third PDB from a 2-periodic gait to a 4-periodic one and then to a 8-periodic gait. The period doubling continues until reaching the chaotic regime represented in Fig. 2d. A further decrease of the parameter a leads to the sudden fall of the compass robot.

In order to better observe the cascade of period-doubling bifurcations and their route to chaos more precisely and then to resolve attractors existing in quite different ranges, we have modified the scale of the two axes. Let \hat{a} be the rescaled bifurcation parameter a , and let $\hat{\tau}$ be the rescaled step period. Then, in order to have a period-doubling route to chaos more evident and then the approximate self-similarity

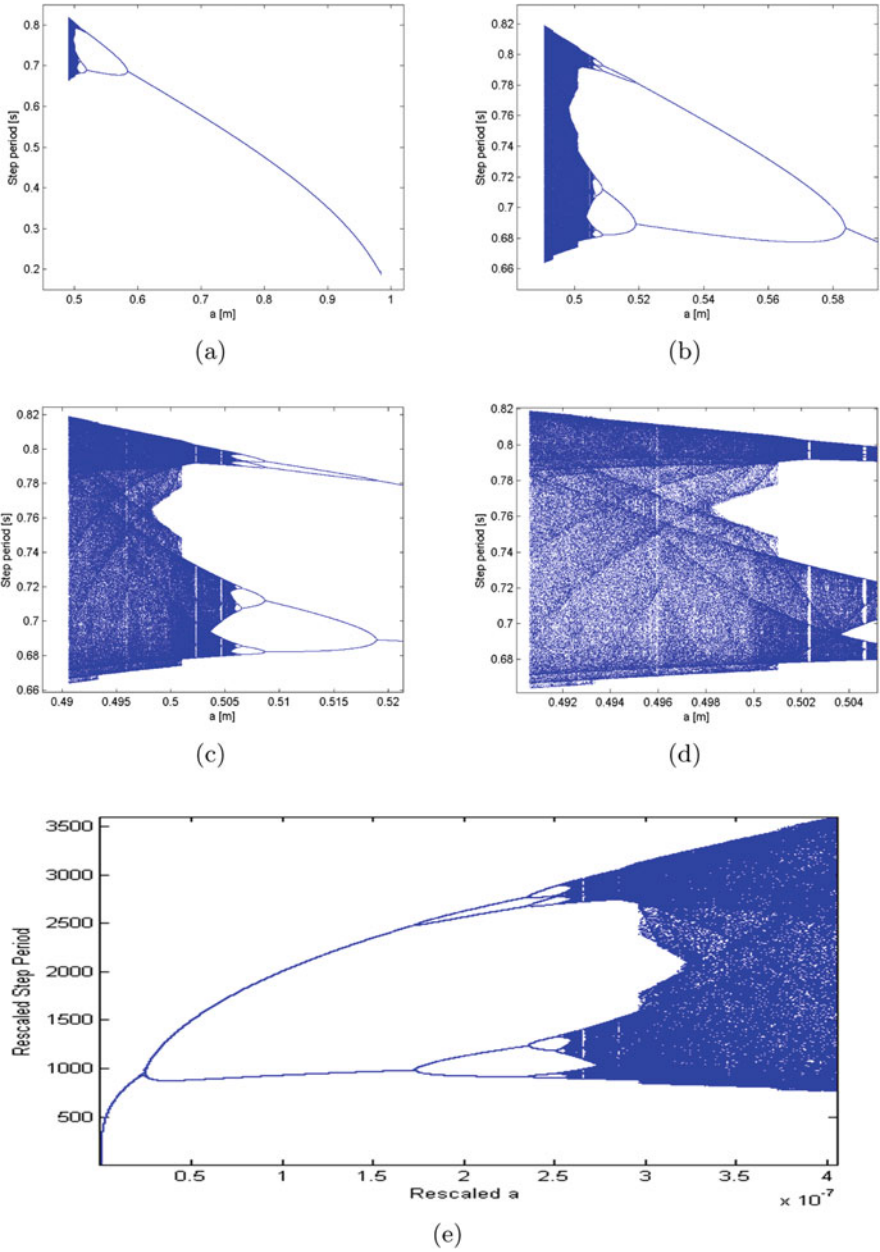


Fig. 2 Bifurcation diagram plotted for the slope angle $\varphi = 5.1^\circ$ and by varying the parameter a , showing the first PDB (a), the second PDB (b), the third PDB (c), and chaos (d). The portrait in (e) shows a rescaled bifurcation diagram of that in (a) according to the two rescaling functions in (9)

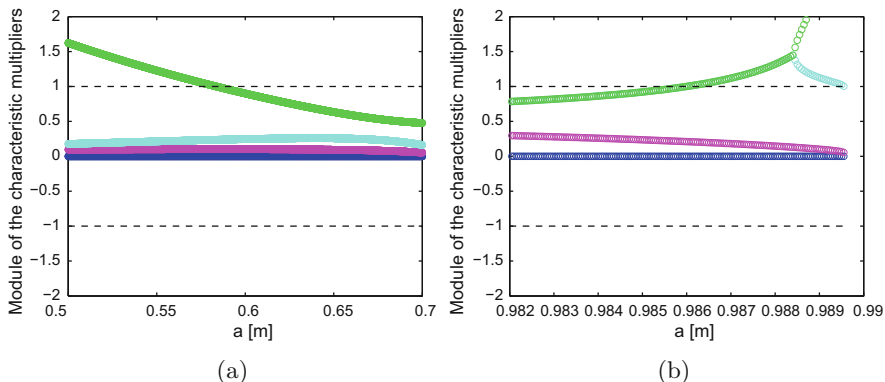


Fig. 3 Variation of the characteristic multipliers for $\varphi = 5.1^\circ$ and as a varies. (a) shows variation of the real part of the characteristic multipliers and reveals occurrence of the PDB (intersection with -1). (b) depicts variation of the module of the characteristic multipliers revealing occurrence of the NSB (intersection with $+1$)

becomes more apparent, we have minimized the window of the period-1 motions and then enlarged the window of such road to chaos by adopting the following two rescaling functions:

$$\hat{a} = e^{-a \times 30} \qquad \hat{\tau} = e^{\tau \times 10} \qquad (9)$$

where here τ is the step period of the bipedal walking. By allying then these rescaling functions in (9) on the bifurcation diagram in Fig. 2a, we obtained hence the bifurcation diagram represented in Fig. 2e. The transition from period-1 gaits to chaotic ones via successive PDBs is now very clear.

Figure 3 shows variation of the eigenvalues, the characteristic multipliers, and of the Jacobian matrix $DP(x_*)$ of the Poincaré map, which is present in Eq. (8), by varying the bifurcation parameter a . Figure 3a reveals the real part of the characteristic multipliers, whereas Fig. 3a shows their module. Each intersection of these characteristic multipliers with the horizontal lines ± 1 presents a bifurcation. The results in Fig. 3b demonstrate the occurrence of the PDB at the value $a = 0.5830$. Notice that in Fig. 3a, we have four curves for the eigenvalues. However, in Fig. 3b and as a increases, we have three eigenvalues. This happens because we have two complex-conjugate eigenvalues and that become real and different as a increases, as shown at the right part of Fig. 3b. This phenomenon reveals then the existence of the NSB, which occurs at the value $a \approx 0.98414$. Such phenomenon appears for the first time, and in this work, for the passive dynamic walking of the compass robot.

Actually, the NSB is present in the bifurcation diagram of Fig. 2, but it is not clear there. Figure 4b is the result of zooming in of the region encircled by the red circle in Fig. 4a. This figure shows two new behaviors. The first one is the 1-periodic unstable limit cycle (p1-ULC), which continues to appear even after the robot falls

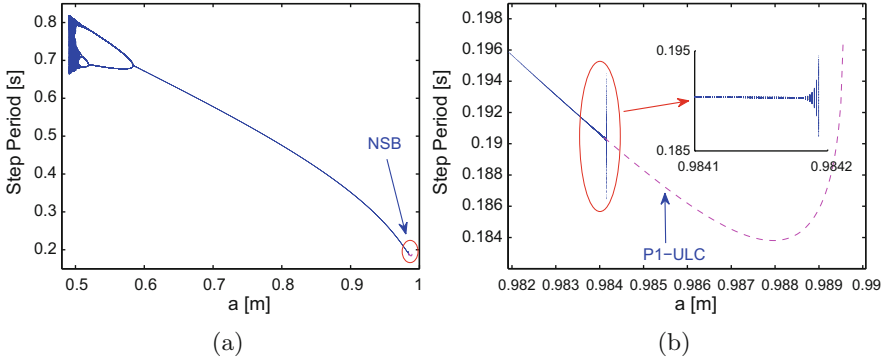


Fig. 4 Bifurcation diagram for $\varphi = 5.1^\circ$ showing the birth of the NSB (a), which is more evident in (b). Here (b) is an enlargement of (a)

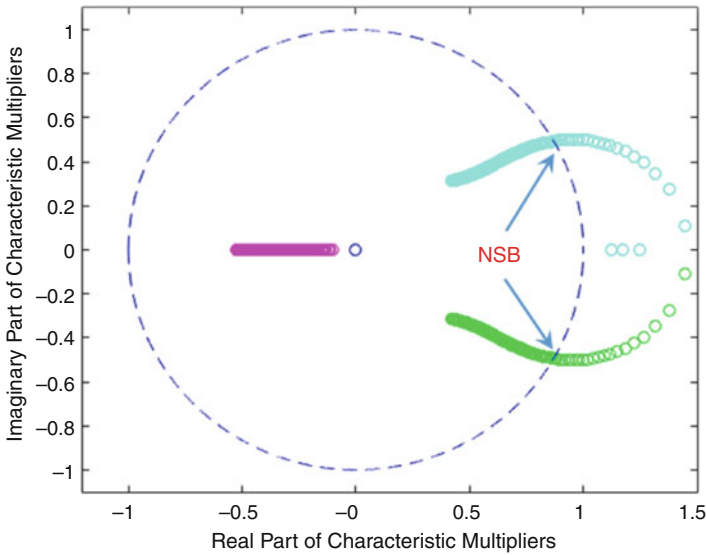


Fig. 5 Loci of the characteristic multipliers as varying a and for $\varphi = 5.1^\circ$

down. The second behavior is the birth of the NSB, which has just appeared for values of the parameter a very close to 1 ($a \approx 0.98414$). By increasing a further, such new behavior ends up at the value $a = 0.984157$ and then causing the fall of the compass robot.

Figure 5 shows the variation of the characteristic multipliers in the unit circle by varying the bifurcation parameter a around the region of values that shows the NSB. It is clear that two complex-conjugate eigenvalues, presented by green and cyan colors, leave the unit circle as a varies. This behavior reveals and confirms therefore the birth of the NSB.

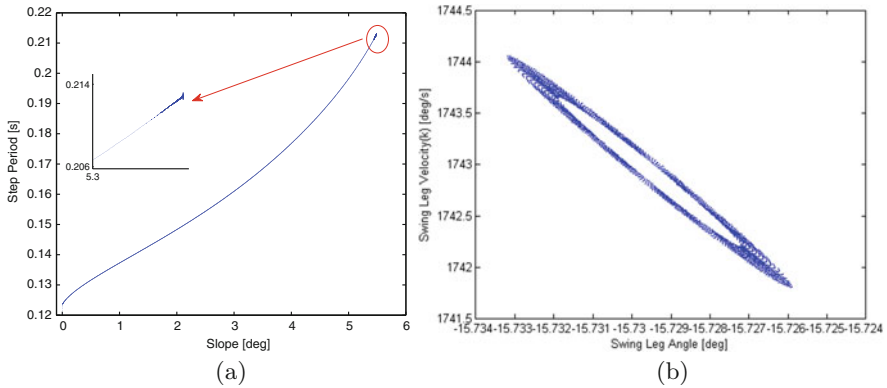


Fig. 6 (a) shows a bifurcation diagram obtained for $a = 0.9841$ and by varying φ , and Poincaré section (b) generated for $\varphi = 5.1^\circ$ and $a = 0.984155$

As noted before, the Neimark–Sacker Bifurcation (NSB) occurs for $\varphi = 5.1^\circ$ at $a = 0.98414$. Then, to more understand this phenomenon, we have analyzed the behavior of the compass-type bipedal robot by setting the value of a to 0.9841 and we have varied the slope φ of the walking surface as illustrated in Fig. 6a. We observed that the period-doubling sequence disappears and only the change from a 1-periodic behavior to a quasi-periodic behavior remains, and which reflects hence the exhibition of the NSB.

By simulating the intersection of the trajectory of the hybrid system (4) with the Poincaré section Γ defined in (5), we obtained the portrait in Fig. 6b, which illustrates the quasi-periodic behavior of the bipedal robot for $a = 0.984155$, that is for a value of a just after the NSB.

It is worth noting that the quasi-periodic motion of a general nonlinear system is represented in the Poincaré section by a closed invariant circle. We obtained an almost similar form represented in Fig. 6b. Note that this distribution of points around the closed circle in Fig. 6b occurs because the selected parameter (a in Fig. 4 or φ in Fig. 6a) for which we have a quasi-periodic behavior is very close to the NSB.

Remark 2 Notice that just after the NSB, the quasi-periodic behavior appears in a very small interval either of the bifurcation parameter a in Fig. 4 or of the bifurcation parameter φ in Fig. 6a. Therefore, just after this interval, the biped robot suddenly falls down. Hence, we have not observed the transition phenomenon from quasi-periodic motions to chaos in the passive gaits of the compass-gait walker by varying the parameter a and also by varying the parameter φ . However, Gritli and Belghith have observed chaos after the quasi-periodic motions in the compass-gait model under the OGY-based state-feedback control [17], and also in the dynamic walking of the torso-driven biped robot under also this same controller [18, 19]. In all these previous references, the interval of the bifurcation parameter within which the quasi-periodic motions and their subsequent chaotic motions occur, is considerably large.

In contrast, in this paper, and for the compass-gait walker (without control), we observed and for the first time the NSB and the quasi-periodic motions, which are found to be displayed in a very small interval of the adopted bifurcation parameters.

Remark 3 Generally, in nonlinear systems, and after the occurrence of the NSB, one would expect to observe a quasi-periodic motion, which eventually becomes chaotic as some bifurcation parameter varies. It is worth to note that such transition in the behavior of the dynamical system can be observed in general systems that have no constraint on their validity and saying on their simulation/execution. Thus, we can execute the nonlinear system and hence observe its outputs by varying (increasing or decreasing) the bifurcation parameter as needed while there is no condition that stops its execution.

However, the compass-gait walker, as a nonlinear dynamical system, is not the case. The biped robot can walk down/on the ground and can also fall down. In this second situation, we cannot talk about a system and then its execution is not valid. Then, when the biped robot falls down, the execution of the program for simulating its walking, which is defined by the impulsive hybrid nonlinear system (4), is stopped. Therefore, by varying the bifurcation parameter, and when simulating such system (4), we monitor the falling condition of the compass-gait walker. If this condition is fulfilled, then we stop the simulation, and a further increase/decrease of the bifurcation parameter will not show other valid motions, since from any initial condition, the biped robot will fall down and no limit set (attractor) exists.

Moreover, recall that for the passive compass-gait walker, the conventional phenomenon displayed in its motion by varying some bifurcation parameter, is the period-doubling route to chaos. See for example [5, 15, 16] and the review paper [7]. Gritli and his co-workers showed in [15] that the compass-gait robot reveals the cyclic-fold bifurcation, and in [16] that such bifurcation leads to the appearance of the double-boundary crisis, that causes in consequence the abrupt destruction of the chaotic motion and hence no other motion exists and only unstable solutions exist. Such crisis occurs at the slope $\varphi = 5.21^\circ$, and just after this value, the biped robot falls down from any initial conditions. Hence, there is no steady gait generated in the bipedal walking of the compass-gait walker and then no attractor was observed in the bifurcation diagram for $\varphi > 5.21^\circ$.

Note that the bifurcation diagram and its period-doubling route to chaos observed for the compass-gait biped walker in [5, 15, 16] are almost similar to that in Fig. 2. Just after the chaotic regime, the biped robot falls down and then we cannot execute the impulsive hybrid nonlinear dynamics (4) and then its simulation is stopped. Thus, in this Fig. 2 and also in the other bifurcation diagrams, the blue attractor means that the biped robot walks indefinitely (without falling down) and then the nonlinear system (4) is here simulated for $t \rightarrow +\infty$. However, the white regions at the right and at the left of the bifurcation diagram mean that no steady gait exists and hence the biped robot falls down after some steps and then after some defined instant $t < +\infty$, depending on the selected initial condition. Thus, in Fig. 2 (or Fig. 4), by decreasing the bifurcation parameter a , we observed the period-doubling route to chaos. The chaotic phase was terminated at the parameter $a = 0.49073$.

Then, just after, that is for $a = 0.49074$, the compass robot falls down and no further simulation of the nonlinear system (4) was achieved.

For the NSB, the problem is the same. Indeed, in Fig. 2 or Fig. 4, by increasing the bifurcation parameter a , we observe the period-1 motion and then the transition to the quasi-periodic behavior via the NSB. As noted previously in Remark 2, the quasi-periodic motions were found to exist in a very small interval of the bifurcation parameter a in Fig. 4 and the bifurcation parameter φ in Fig. 6a. Then, at some value of this bifurcation parameter near the NSB, the compass biped walker falls down and hence no steady solution/gait was observed. As explained before, the numerical simulation of the hybrid nonlinear system (4) was completely stopped.

5 Conclusions and Future Works

In this work, we investigated the passive gait of the planar biped robot with a compass-like motion. We presented some numerical results with respect to the bifurcation parameter a , which is the length of the lower segment of the leg. We showed also by means of bifurcation diagrams that the value of a can change the whole behavior of our bipedal robot, and therefore its stability. We revealed the appearance of the classical period-doubling route to chaos as a decreases. Moreover, we showed the birth, and for the first time, of the Neimark–Sacker bifurcation as a increases.

As a future work, we aim at analyzing the passive motion of the compass-gait walker using the explicit analytical expressions of the Poincaré map [28, 30] and in order to prove existence of the NSB. Our idea is to determine, via the center manifold theorem, the analytical expression of the Lyapunov coefficients and at least of the first one. This approach will lead to characterize the type of the NSB to be either subcritical or supercritical, and then to judge whether the quasi-periodic motion is initially stable or unstable.

Acknowledgments The authors would like to thank the Ministry of Higher Education and Scientific Research (Ministère de l'Enseignement Supérieur et de la Recherche Scientifique (MESRS)), Tunisia, for technical and financial support (Project no. 20PEJC~06-02).

References

1. U.D. Croce, P.O. Riley, J.L. Lelas, D. Kerrigan, A refined view of the determinants of gait. *Gait Posture* **14**(2), 79–84 (2001)
2. A.D. Kuo, The six determinants of gait and the inverted pendulum analogy: a dynamic walking perspective. *Hum. Mov. Sci.* **26**(4), 617–656 (2007)
3. M. Garcia, A. Chatterjee, A. Ruina, Efficiency, speed, and scaling of two-dimensional passive-dynamic walking. *Dyn. Stab. Syst.* **15**(2), 75–99 (2000)

4. M. Garcia, A. Chatterjee, A. Ruina, M. Coleman, The simplest walking model: stability, complexity, and scaling. *J. Biomech. Eng.* **120**(2), 281–288 (1998)
5. A. Goswami, B. Thuilot, B. Espiau, Study of the passive gait of a compass-like biped robot: Symmetry and chaos. *Int. J. Robot. Res.* **17**, 1282–1301 (1998)
6. M. Fathizadeh, H. Mohammadi, S. Taghvaei, A modified passive walking biped model with two feasible switching patterns of motion to resemble multi-pattern human walking. *Chaos Solitons Fractals* **127**, 83–95 (2019)
7. S. Iqbal, X.Z. Zang, Y.H. Zhu, J. Zhao, Bifurcations and chaos in passive dynamic walking: a review. *Robot. Auton. Syst.* **62**(6), 889–909 (2014)
8. S. Gupta, A. Kumar, A brief review of dynamics and control of underactuated biped robots. *Adv. Robot.* **31**(12), 607–623 (2017)
9. T. McGeer, Passive dynamic walking. *Int. J. Robot. Res.* **9**(2), 62–68 (1990)
10. Q. Li, X.S. Yang, New walking dynamics in the simplest passive bipedal walking model. *Appl. Math. Model.* **36**(11), 5262–5271 (2012)
11. Q. Li, J. Guo, X.S. Yang, New bifurcations in the simplest passive walking model. *Chaos An Interdisciplinary J. Nonlinear Sci.* **23**, 043110 (2013)
12. M. Fathizadeh, S. Taghvaei, H. Mohammadi, Analyzing bifurcation, stability and chaos for a passive walking biped model with a sole foot. *Int. J. Bifurcation Chaos* **28**(9), 1850113 (2018)
13. S. Montazeri Moghadam, M. Sadeghi Talarposhti, A. Niaty, F. Towhidkhal, S. Jafari, The simple chaotic model of passive dynamic walking. *Nonlinear Dyn.* **93**(3), 1183–1199 (2018)
14. M. Nourian Zavareh, F. Nazarimehr, K. Rajagopal, S. Jafari, Hidden attractor in a passive motion model of compass-gait robot. *Int. J. Bifurcation Chaos* **28**(14), 1850171 (2018)
15. H. Gritli, N. Khraeif, S. Belghith, Period-three route to chaos induced by a cyclic-fold bifurcation in passive dynamic walking of a compass-gait biped robot. *Commun. Nonlinear Sci. Numer. Simul.* **17**(11), 4356–4372 (2012)
16. H. Gritli, S. Belghith, N. Khraeif, Cyclic-fold bifurcation and boundary crisis in dynamic walking of biped robots. *Int. J. Bifurcation Chaos* **22**(10), 1250257 (2012)
17. H. Gritli, S. Belghith, Walking dynamics of the passive compass-gait model under OGY-based state-feedback control: Rise of the Neimark-Sacker bifurcation. *Chaos Solitons Fractals* **110**, 158–168 (2018)
18. H. Gritli, S. Belghith, Displayed phenomena in the semi-passive torso-driven biped model under OGY-based control method: Birth of a torus bifurcation. *Appl. Math. Model.* **40**(4), 2946–2967 (2016)
19. H. Gritli, S. Belghith, Bifurcations and chaos in the semi-passive bipedal dynamic walking model under a modified OGY-based control approach. *Nonlinear Dyn.* **83**(4), 1955–1973 (2016)
20. H. Gritli, S. Belghith, Walking dynamics of the passive compass-gait model under OGY-based control: Emergence of bifurcations and chaos. *Commun. Nonlinear Sci. Numer. Simul.* **47**, 308–327 (2017)
21. H. Gritli, S. Belghith, Walking dynamics of the passive compass-gait model under OGY-based state-feedback control: Analysis of local bifurcations via the hybrid Poincaré map. *Chaos Solitons Fractals* **98**, 72–87 (2017)
22. N.G. Tsagarakis, Z. Li, J. Saglia, D.G. Caldwell, The design of the lower body of the compliant humanoid robot “ccub”, in *Proceedings of the 2011 IEEE International Conference on Robotics and Automation* (IEEE, New York, 2011), pp. 2035–2040
23. R.M. Ghigliazza, R. Altendorfer, P. Holmes, D. Koditschek, A simply stabilized running model. *SIAM J. Appl. Dyn. Syst.* **2**(2), 187–218 (2003)
24. D.E. Koditschek, R.J. Full, M. Buehler, Mechanical aspects of legged locomotion control. *Arthropod Struct. Dev.* **33**(3), 251–272 (2004). *arthropod Locomotion Systems: from Biological Materials and Systems to Robotics*
25. D. Kar, K. Kurien Issac, K. Jayarajan, Gaits and energetics in terrestrial legged locomotion. *Mech. Mach. Theory* **38**(4), 355–366 (2003)
26. J.W. Grizzle, G. Abba, F. Plestan, Asymptotically stable walking for biped robots: analysis via systems with impulse effects. *IEEE Trans. Autom. Control* **46**, 51–64 (2001)

27. E.R. Westervelt, J.W. Grizzle, C. Chevallereau, J.H. Choi, B. Morris, *Feedback Control of Dynamic Bipedal Robot Locomotion* (CRC Press, New York, 2018)
28. W. Znegui, H. Gritli, S. Belghith, Design of an explicit expression of the Poincaré map for the passive dynamic walking of the compass-gait biped model. *Chaos Solitons Fractals* **130**, 109436 (2020)
29. H. Gritli, S. Belghith, N. Khraeif, OGY-based control of chaos in semi-passive dynamic walking of a torso-driven biped robot. *Nonlinear Dyn.* **79**(2), 1363–1384 (2015)
30. W. Znegui, H. Gritli, S. Belghith, A new Poincaré map for investigating the complex walking behavior of the compass-gait biped robot. *Appl. Math. Model.* **94**, 534–557 (2021)
31. I.A. Hiskens, M.A. Pai, Trajectory sensitivity analysis of hybrid systems. *IEEE Trans. Circuits Syst. I* **47**, 204–220 (2000)
32. H. Gritli, S. Belghith, *Identification, Stability and Stabilization of Limit Cycles in a Compass-Gait Biped Model via a Hybrid Poincaré Map* (Springer, Cham, 2016), pp. 259–289

A Degenerate Takens–Bogdanov Bifurcation in a Normal form of Lorenz’s Equations



Antonio Algaba, M. Cinta Domínguez-Moreno, Manuel Merino,
and Alejandro J. Rodríguez-Luis

1 Introduction

In the world of dynamical systems, the first known and most famous chaotic one is the Lorenz system [1]

$$\dot{x} = \sigma(y - x), \quad \dot{y} = \rho x - y - xz, \quad \dot{z} = -bz + xy, \quad \sigma, \rho, b \in \mathbb{R}. \quad (1)$$

The study of its riveting and intricate dynamical behavior has been carried out in multitude of works (see the recent papers [2–15] and references therein).

One way to obtain important information on the organizing centers of the dynamics in system (1) is by means of the study of local bifurcations of equilibria. Whereas the Hopf and Takens–Bogdanov bifurcations have been fully studied in Lorenz system [9, 10], the Hopf-pitchfork bifurcation (a pair of imaginary eigenvalues and the third one zero; it occurs when $\sigma = -1$, $b = 0$, $\rho > 1$) and the triple-zero bifurcation (a triple-zero eigenvalue; it arises if $\sigma = -1$, $b = 0$, $\rho = 1$) cannot be analyzed by the standard procedures because non-isolated equilibria appear when $b = 0$.

To avoid this problem, in this paper we consider a three-parameter unfolding, that is close to the normal form of the triple-zero bifurcation exhibited by Lorenz system, given by Algaba et al. [16]

A. Algaba · M. Cinta Domínguez-Moreno (✉) · M. Merino
Departamento de Ciencias Integradas, Centro de Estudios Avanzados en Física, Matemática y Computación, Universidad de Huelva, Huelva, Spain
e-mail: algaba@uhu.es; mcinta.dominguez@dmat.uhu.es; merino@uhu.es; merino@dmat.uhu.es

A. J. Rodríguez-Luis
Departamento de Matemática Aplicada II, E.T.S. Ingenieros, Universidad de Sevilla, Sevilla, Spain
e-mail: ajrluis@us.es

$$\dot{x} = y, \quad \dot{y} = \varepsilon_1 x + \varepsilon_2 y + Axz + Byz, \quad \dot{z} = \varepsilon_3 z + Cx^2 + Dz^2, \tag{2}$$

where $\varepsilon_1, \varepsilon_2, \varepsilon_3 \approx 0$ and A, B, C, D are real parameters. System (2) exhibits a triple-zero bifurcation when $\varepsilon_1 = \varepsilon_2 = \varepsilon_3 = 0$. These equations are also invariant under the change $(x, y, z) \rightarrow (-x, -y, z)$. We remark that several systems studied in the literature appear as particular cases of (2) for certain parameter choices [17–22]. Without loss of generality [16], we can take $A = -1, C = 1$

$$\dot{x} = y, \quad \dot{y} = \varepsilon_1 x + \varepsilon_2 y - xz + Byz, \quad \dot{z} = \varepsilon_3 z + x^2 + Dz^2. \tag{3}$$

System (3) can have up to four equilibria, namely $E_1 = (0, 0, 0), E_2 = (0, 0, -\varepsilon_3/D)$ if $D \neq 0$ and $E_{3,4} = (\pm\sqrt{-\varepsilon_1(\varepsilon_3 + D\varepsilon_1)}, 0, \varepsilon_1)$ if $\varepsilon_1(\varepsilon_3 + D\varepsilon_1) < 0$. Note that E_1 and E_2 are placed on the z -axis, which is an invariant set.

The characteristic polynomial of the Jacobian matrix of system (3) at the origin E_1 is given by $P(\lambda) = \lambda^3 + p_1\lambda^2 + p_2\lambda + p_3$, where $p_1 = -(\varepsilon_2 + \varepsilon_3), p_2 = \varepsilon_2\varepsilon_3 - \varepsilon_1, p_3 = \varepsilon_1\varepsilon_3$. Therefore, the origin exhibits the following bifurcations:

- (a) A pitchfork bifurcation when $\varepsilon_1 = 0, \varepsilon_2 \neq 0, \varepsilon_3 \neq 0$. The nontrivial equilibria E_3 and E_4 appear when $-\varepsilon_1(\varepsilon_3 + D\varepsilon_1) > 0$.
- (b) A transcritical bifurcation (involving also E_2) when $\varepsilon_3 = 0, \varepsilon_1 \neq 0, \varepsilon_2 \neq 0, D \neq 0$.
- (c) A Hopf bifurcation when $\varepsilon_1 < 0, \varepsilon_2 = 0, \varepsilon_3 \neq 0$.
- (d) A Takens–Bogdanov bifurcation (nondiagonalizable double-zero eigenvalue) when $\varepsilon_1 = 0, \varepsilon_2 = 0, \varepsilon_3 \neq 0$. It is of homoclinic-type when $\varepsilon_3 < 0$ and of heteroclinic-type if $\varepsilon_3 > 0$.
- (e) A Hopf-zero bifurcation when $\varepsilon_2 = 0, \varepsilon_3 = 0, \varepsilon_1 < 0$.
- (f) A double-zero bifurcation (a diagonalizable double-zero eigenvalue) when $\varepsilon_1 = 0, \varepsilon_3 = 0, \varepsilon_2 \neq 0$ (see [16]).
- (g) A triple-zero bifurcation when $\varepsilon_1 = \varepsilon_2 = \varepsilon_3 = 0$.

We show now that all the information on the equilibrium E_2 can be obtained from the analysis of E_1 . To study E_2 we translate it to the origin by means of the change $x = \tilde{x}, y = \tilde{y}, z = \tilde{z} - \varepsilon_3/D$, that transforms system (3) into

$$\dot{\tilde{x}} = \tilde{y}, \quad \dot{\tilde{y}} = (\varepsilon_1 + \frac{1}{D}\varepsilon_3)\tilde{x} + (\varepsilon_2 - \frac{B}{D}\varepsilon_3)\tilde{y} - \tilde{x}\tilde{z} + B\tilde{y}\tilde{z}, \quad \dot{\tilde{z}} = -\varepsilon_3\tilde{z} + \tilde{x}^2 + D\tilde{z}^2, \tag{4}$$

with $\varepsilon_3, D \neq 0$.

Since system (3) is symmetric to the change

$$(x, y, z, t, \varepsilon_1, \varepsilon_2, \varepsilon_3, B, D) \rightarrow \left(x, y, z - \frac{\varepsilon_3}{D}, t, \varepsilon_1 + \frac{\varepsilon_3}{D}, \varepsilon_2 - \frac{B\varepsilon_3}{D}, -\varepsilon_3, B, D\right), \tag{5}$$

it is direct to obtain the stability and bifurcations of E_2 from the stability and bifurcations of E_1 . Thus, it is enough to study the bifurcations exhibited by E_1 .

2 Takens–Bogdanov Bifurcations of the Origin

The Takens–Bogdanov bifurcation of E_1 occurs when $p_2 = p_3 = 0$, $p_1 \neq 0$, that is, when $\varepsilon_1 = \varepsilon_2 = 0$, $\varepsilon_3 \neq 0$. For these values, the Jacobian matrix has a nondiagonalizable double-zero and a nonzero eigenvalue. Thus, system (3) reads

$$\dot{x} = y, \quad \dot{y} = -xz + Byz, \quad \dot{z} = \varepsilon_3 z + x^2 + Dz^2. \tag{6}$$

By means of the second-order approximation to the center manifold, we obtain the third-order reduced system and compute its normal form

$$\dot{x} = y, \quad \dot{y} = a_3x^3 + b_3x^2y, \quad \text{with } a_3 = 1/\varepsilon_3, b_3 = (2 - \varepsilon_3 B)/\varepsilon_3^2. \tag{7}$$

Its unfolding is given by

$$\dot{x} = y, \quad \dot{y} = \varepsilon_1 x + \varepsilon_2 y + a_3x^3 + b_3x^2y. \tag{8}$$

By means of the rescaling

$$x \rightarrow \frac{|\varepsilon_3| \sqrt{|\varepsilon_3|}}{2 - B\varepsilon_3} \bar{x}, \quad y \rightarrow \frac{\varepsilon_3^2 \sqrt{|\varepsilon_3|}}{(2 + B\varepsilon_3^2)} \bar{y}, \quad t \rightarrow \frac{2 - B\varepsilon_3}{|\varepsilon_3|} \tau, \tag{9}$$

system (8) is transformed into

$$\dot{\bar{x}} = \bar{y}, \quad \dot{\bar{y}} = \frac{\varepsilon_1(2 - B\varepsilon_3)^2}{\varepsilon_3^2} \bar{x} + \frac{\varepsilon_2(2 - B\varepsilon_3)}{|\varepsilon_3|} \bar{y} + \text{sgn}(\varepsilon_3) \bar{x}^3 - \bar{x}^2 \bar{y}. \tag{10}$$

Thus, the Takens–Bogdanov bifurcation is of heteroclinic case when $\varepsilon_3 > 0$ and of homoclinic case if $\varepsilon_3 < 0$. Note that if $\varepsilon_3 = 0$ a triple-zero bifurcation is present. Moreover, when $(\varepsilon_1, \varepsilon_2, \varepsilon_3) = (0, 0, 2/B)$, with $B \neq 0$, a degenerate Takens–Bogdanov bifurcation occurs. This case will be analyzed below.

In the homoclinic case, when $\varepsilon_3 < 0$, the equilibria of system (10) are $(0, 0)$ and $(\pm(2 - B\varepsilon_3)\sqrt{-\varepsilon_1/\varepsilon_3}, 0)$, $\varepsilon_3 \neq 2/B$, $\varepsilon_1 > 0$. From the Takens–Bogdanov singularity, the curves corresponding to the following bifurcations emerge [23–25]: (a) A pitchfork bifurcation of the origin is present when $\varepsilon_1 = 0$. (b) A subcritical Hopf bifurcation of the origin if $\varepsilon_2 = 0$, $\varepsilon_1 < 0$. (c) A supercritical Hopf bifurcation of the nontrivial equilibria when $\varepsilon_2 \approx (2 - B\varepsilon_3)\varepsilon_1/\varepsilon_3$, for $\varepsilon_1 > 0$. (d) A homoclinic connection to the origin for $\varepsilon_2 \approx 4(2 - B\varepsilon_3)\varepsilon_1/(5\varepsilon_3)$, with $\varepsilon_1 > 0$. Since the third eigenvalue ($\varepsilon_3 < 0$) determines the behavior outside the center manifold, these homoclinic connections are attractive. (e) A saddle-node bifurcation of symmetric periodic orbits when $\varepsilon_2 \approx c\varepsilon_1(2 - B\varepsilon_3)/\varepsilon_3$, where $\varepsilon_1 > 0$, $c \approx 0.752$.

In the heteroclinic case, when $\varepsilon_3 > 0$, the equilibria of system (10) are $(0, 0)$ and $(\pm(2 - B\varepsilon_3)\sqrt{-\varepsilon_1/\varepsilon_3}, 0)$, $\varepsilon_3 \neq 2/B$, $\varepsilon_1 < 0$. The following curves are present [23–25]: (a) A pitchfork bifurcation of the origin for $\varepsilon_1 = 0$. (b) A subcritical

Hopf bifurcation of the origin for $\varepsilon_2 = 0, \varepsilon_1 < 0$. (c) A heteroclinic connection to nontrivial equilibria if $\varepsilon_2 \approx (2 - B\varepsilon_3)\varepsilon_1/(5\varepsilon_3), \varepsilon_1 < 0$. As the third eigenvalue ($\varepsilon_3 > 0$) determines the behavior outside the center manifold, these heteroclinic connections are repulsive.

2.1 Codimension-Three Takens–Bogdanov

The normal form coefficient b_3 , given in (7), vanishes when $\varepsilon_3 = 2/B, B \neq 0$.

Thus, considering the fourth-order approximation to the center manifold we obtain the fifth-order reduced system on the center manifold

$$\dot{x} = y, \quad \dot{y} = a_3x^3 + a_5x^5 + b_5x^4y. \tag{11}$$

Multiplying system (11) by $(1 - (a_5/a_3)x^2)$, the x^5 -term can be eliminated

$$\dot{x} = y + \frac{-a_5}{a_3}x^2y, \quad \dot{y} = a_3x^3 + b_5x^4y, \quad \text{with } a_3 = \frac{1}{\varepsilon_3}, \quad b_5 = \frac{-B^4}{8}(5B + 3D). \tag{12}$$

An unfolding is given by

$$\dot{x} = y, \quad \dot{y} = \mu_1x + \mu_2y + a_3x^3 + \mu_3x^2y + b_5x^4y, \tag{13}$$

with $\mu_1 = \varepsilon_1, \mu_2 = \varepsilon_2, \mu_3 = (2 - B\varepsilon_3)/\varepsilon_3^2$.

To analyze this Takens–Bogdanov, we use the rescaling

$$x \rightarrow \sqrt[6]{\frac{|a_3|}{b_5^2}} u, \quad y \rightarrow b_5 \sqrt[6]{\frac{|a_3|^5}{b_5^{10}}} v, \quad t \rightarrow \sqrt[3]{\frac{b_5}{|a_3|^2}} \tau,$$

and then system (13) is transformed into

$$\dot{u} = v, \quad \dot{v} = \tilde{\mu}_1u + \tilde{\mu}_2v + \text{sgn}(a_3)u^3 + \tilde{\mu}_3u^2v + u^4v, \tag{14}$$

where

$$\tilde{\mu}_1 = \frac{\varepsilon_1}{4} \sqrt[3]{\varepsilon_3^4 B^8 (5B + 3D)^2}, \quad \tilde{\mu}_2 = \frac{-\varepsilon_2}{2} \sqrt[3]{-B^4 \varepsilon_3^2 (5B + 3D)}, \quad \tilde{\mu}_3 = \frac{-2(2 - B\varepsilon_3) \sqrt[3]{\varepsilon_3}}{\sqrt[3]{B^4 (5B + 3D)}}.$$

The analysis of this three-parameter family can be found in [26, 27]. In the parameter space several codimension-two bifurcation curves emerge from the point $(0, 0, 2/B)$.

In the homoclinic case ($\text{sgn}(a_3) < 0$, i.e., $\varepsilon_3 < 0$):

- A nondegenerate Takens–Bogdanov for $\tilde{\mu}_1 = \tilde{\mu}_2 = 0, \tilde{\mu}_3 \neq 0$, i.e., $\varepsilon_1 = \varepsilon_2 = 0, \varepsilon_3 \neq 2/B$.
- A degenerate Hopf bifurcation of the origin for $\tilde{\mu}_2 = \tilde{\mu}_3 = 0, \tilde{\mu}_1 < 0$, i.e., $\varepsilon_2 = 0, \varepsilon_3 = \frac{2}{B}, \varepsilon_1 < 0$.
- A degenerate Hopf bifurcation of the nontrivial equilibria when $\tilde{\mu}_2 = -\tilde{\mu}_1^2, \tilde{\mu}_3 = 0$, i.e., $\varepsilon_3 = \frac{2}{B}, \varepsilon_2 = \frac{-1}{2}\varepsilon_1^2 B^2(5B + 3D), \varepsilon_1 > 0$.
- A degenerate (zero-trace) homoclinic connection to the origin when $\tilde{\mu}_2 = 0, \tilde{\mu}_3 = \frac{-8\tilde{\mu}_1}{7}, \tilde{\mu}_1 > 0$, i.e., $\varepsilon_2 = 0, \varepsilon_1 = \frac{7(2-B\varepsilon_3)}{B^4\varepsilon_3(5B+3D)} > 0$.
- A cusp of saddle-node bifurcations of periodic orbits when $\tilde{\mu}_2 = c_3\tilde{\mu}_1^2, \tilde{\mu}_3 = c_4\tilde{\mu}_1, \tilde{\mu}_1 > 0$, with $c_3 \approx 1.5713, c_4 \approx -3.3484$. That is, for $\varepsilon_2 = \frac{2c_3(2-B\varepsilon_3)^2}{c_4^2 B^2(5B+3D)}, \varepsilon_1 = \frac{-8(2-B\varepsilon_3)}{c_4\varepsilon_3 B^4(5B+3D)} > 0$.

In the heteroclinic case ($\text{sgn}(a_3) > 0$, i.e., $\varepsilon_3 > 0$):

- A nondegenerate Takens–Bogdanov bifurcation when $\tilde{\mu}_1 = \tilde{\mu}_2 = 0, \tilde{\mu}_3 \neq 0$, i.e., $\varepsilon_1 = \varepsilon_2 = 0, \varepsilon_3 \neq 2/B$.
- A degenerate Hopf bifurcation of the origin for $\tilde{\mu}_2 = \tilde{\mu}_3 = 0, \tilde{\mu}_1 < 0$, i.e., $\varepsilon_2 = 0, \varepsilon_3 = 2/B, \varepsilon_1 < 0$.
- A degenerate (zero-trace) heteroclinic connection when $\tilde{\mu}_2 = 0, \tilde{\mu}_3 \approx \frac{3}{7}\tilde{\mu}_1, \tilde{\mu}_1 < 0$, i.e., $\varepsilon_2 = 0, \varepsilon_1 \approx -\frac{7}{3}(2 - B\varepsilon_3)^3$.

We end this section with two useful comments for Sect. 3. On the one hand, the information on the Takens–Bogdanov bifurcation exhibited by E_2 can be easily obtained from the above results by using the symmetry (5): it is of homoclinic-type if $\varepsilon_3 > 0$ and of heteroclinic-type when $\varepsilon_3 < 0$. On the other hand, the (diagonalizable) double-zero bifurcation exhibited by the origin has been analyzed in [16]. There, the following expression is obtained for the curve of heteroclinic connections between E_1 and E_2 (in the nondegenerate case $B \neq 2\Delta - \Delta^3\varepsilon_1$)

$$\varepsilon_1 \approx -\frac{1}{2D}\varepsilon_3 + \frac{a^2(-2\Delta + B)}{4D(3a + 2)(-\Delta^2\varepsilon_1 + 1)}\varepsilon_3^2, \text{ where } \Delta = \frac{1}{\varepsilon_2}, a = \frac{\Delta^3\varepsilon_1 - \Delta}{D} > 0.$$

3 Numerical Study

With the information provided in Sect. 2, we are going to perform a numerical study of system (3) with the continuation software AUTO [28]. Specifically, we will draw bifurcation sets in the $(\varepsilon_1, \varepsilon_3)$ -parameter plane, in a neighborhood of the degeneracies DZ (diagonalizable double-zero) and TB (Takens–Bogdanov). We will fix $\varepsilon_2 = -1, B = -0.1 < 0$, and $D = 0.01 > 0$ according to the values used in [22].

First we draw, in Fig. 1a,b, partial bifurcation sets with the bifurcation curves related to the degeneracies DZ (of the origin) and TB (of E_2) in the fourth and second quadrants, respectively. We can observe the curves h (Hopf bifurcation of the equilibria $E_{3,4}$) and He (heteroclinic cycle between the equilibria E_1 and E_2). Both curves emerge from the point where the double-zero degeneracy of the origin occurs, $DZ = (0, 0)$ in the $(\varepsilon_1, \varepsilon_3)$ -parameter plane. Moreover, three straight lines intersect at the double-zero point DZ, namely P^1 (pitchfork bifurcation of the origin, $\varepsilon_1 = 0$), P^2 (pitchfork bifurcation of E_2 , $\varepsilon_3 = -0.01\varepsilon_1$) and T (transcritical bifurcation between E_1 and E_2 , $\varepsilon_3 = 0$). Note that in these pitchfork bifurcations the equilibria $E_{3,4}$ emerge. Fixed a value of ε_3 in a neighborhood of the point DZ, the periodic orbit emerged from h is attractive and, increasing the value of ε_1 , it disappears in a heteroclinic cycle He .

This cycle He is formed by two heteroclinic connections, one is structurally stable (since it goes from E_1 to E_2 on the invariant z -axis) and the other one is more relevant (because it is placed outside the z -axis). To show the differences that exist between the heteroclinic cycles of Fig. 1a,b we draw their projections

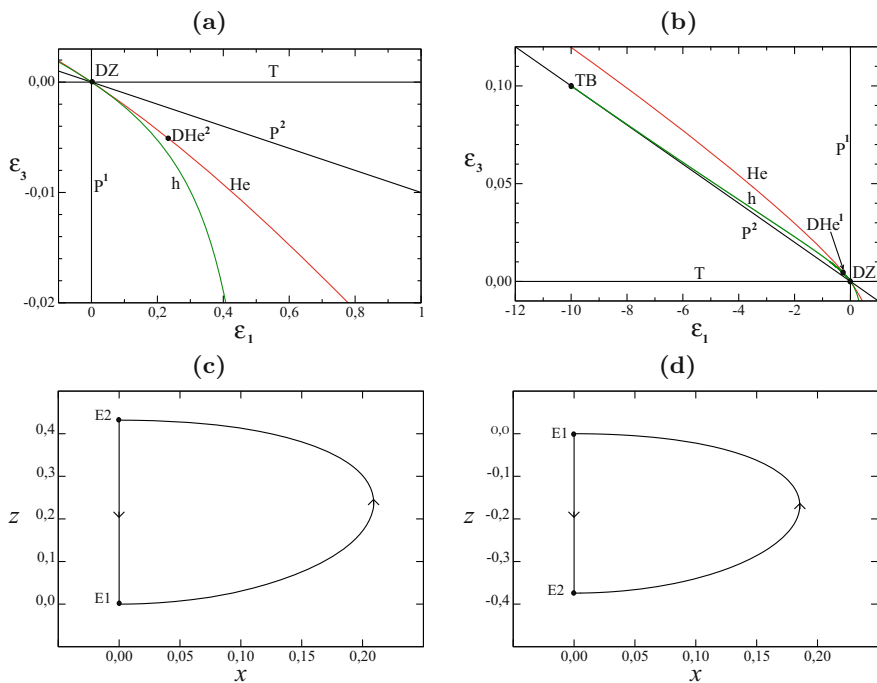


Fig. 1 For $\varepsilon_2 = -1, B = -0.1, D = 0.01$ partial bifurcation set in a neighborhood of the point DZ: (a) in the fourth quadrant; (b) in the second quadrant. (c) Projection onto the (x, z) -plane of the heteroclinic cycle He of panel (a) that exists when $(\varepsilon_1, \varepsilon_3) \approx (0.2, -0.0043175)$. (d) Projection onto the (x, z) -plane of the heteroclinic cycle He of panel (b) that exists when $(\varepsilon_1, \varepsilon_3) \approx (-0.2, 0.0037414)$

onto the (x, z) -plane in Fig. 1c,d, respectively. Remark that throughout this work, with the aim of simplifying the notation, we will label the heteroclinic cycle (in fact, due to the symmetry, a pair of heteroclinic cycles exist) and the heteroclinic bifurcation with the same symbol, although they are two different objects. Also, when necessary, we will use superscripts to indicate the equilibria that are involved in a certain bifurcation or in its degeneration.

Such heteroclinic cycles are attractive when they emerge from DZ since the saddle quantities in the fourth quadrant $\delta_{E_1} = |\max(\lambda_1, \lambda_3)/\lambda_2|$ and $\delta_{E_2} = |\lambda_2^*/\lambda_3^*|$ satisfy $\delta_{E_1}\delta_{E_2} > 1$. Here we denote the eigenvalues of the Jacobian matrix at the origin E_1 as $\lambda_3 = \varepsilon_3$, $\lambda_{2,1} = [\varepsilon_2 \pm \sqrt{\varepsilon_2^2 + 4\varepsilon_1}]/2$, and the eigenvalues of the Jacobian matrix at $E_2 = (0, 0, -100\varepsilon_3)$ as $\lambda_3^* = -\varepsilon_3$, $\lambda_{2,1}^* = [\varepsilon_2 - \frac{B}{D}\varepsilon_3 \pm \sqrt{(\varepsilon_2 - \frac{B}{D}\varepsilon_3)^2 + 4(\varepsilon_1 + \frac{\varepsilon_3}{D})}]/2$.

As seen in Fig. 1a,b, on each of the curves He, there is a point DHe where the heteroclinic cycle is degenerate. In fact, when $\varepsilon_1 > 0$, the equilibrium E_1 is always a real saddle along the curve He but E_2 , that is also a real saddle when it arises from DZ, becomes a saddle-focus from the point $\text{DHe}^2 \approx (0.2328879, -0.0050898)$. In the case of the branch located in the second quadrant, when $\varepsilon_1 < 0$, the equilibrium E_2 is always a real saddle along the curve He, whereas the equilibrium E_1 , that emerges from DZ as a real saddle, becomes a saddle-focus from $\text{DHe}^1 \approx (-0.25, 0.004611)$.

The change in the configuration of E_1 (resp. E_2) on the curve of the heteroclinic connections He in the second (resp. fourth) quadrant implies the appearance of an infinity of bifurcation curves, which arise from the aforementioned point DHe^1 (resp. DHe^2) on the He curve.

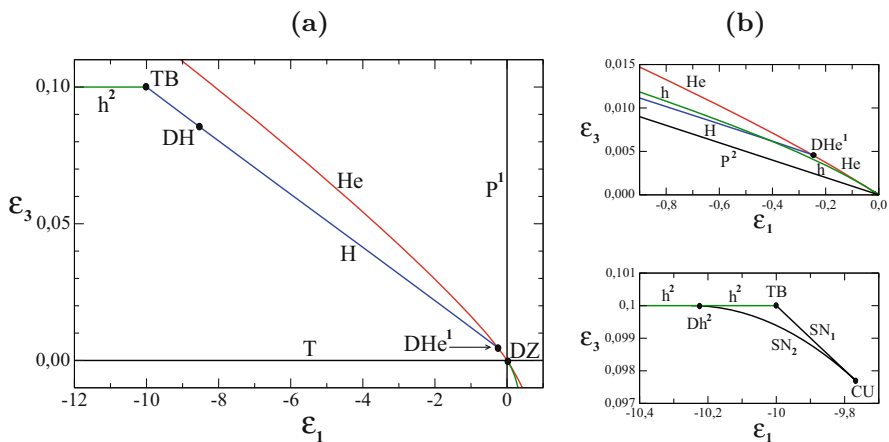


Fig. 2 For $\varepsilon_2 = -1, B = -0.1, D = 0.01$ partial bifurcation set: (a) in the second quadrant; (b) zoom of panel (a) in the vicinity of the points $\text{DH}\circ^{E_1}$ (upper panel) and TB (lower panel)

Specifically, in Fig. 2a,b, we can see the curve H (of homoclinic connections to the equilibrium E_2) that emerges from the point DHe^1 . In a vicinity of DHe^1 , a saddle periodic orbit emerges from H (since $\delta_{E_2} < 1$ at the points of such a neighborhood). A degenerate point DH appears on H when $(\varepsilon_1, \varepsilon_3) \approx (-8.5339606, 0.0855365)$ because $\delta_{E_2} = 1$. The curve H ends at the point $TB = (-10, 0.1)$ where E_2 undergoes a Takens–Bogdanov bifurcation. This is in agreement with the theoretical results of Sect. 2 that guarantee, for these parameter values, that the Takens–Bogdanov bifurcation of E_2 is of homoclinic-type.

In the second quadrant, the Hopf bifurcation h of the nontrivial equilibria $E_{3,4}$ is always supercritical and this curve connects the points DZ and TB (see Fig. 1b). In addition to the homoclinic connection curve H, other curves emerge from TB, namely a curve h^2 of Hopf bifurcation of E_2 ($\varepsilon_3 = 0.1$ when $\varepsilon_1 < -10$) and a curve SN_1 of saddle-node bifurcation of periodic orbits. The Hopf bifurcation h^2 is subcritical when it emerges from TB and it becomes supercritical because a degeneracy occurs at $Dh^2 \approx (-10.2487498, 0.1)$ as the first Lyapunov coefficient vanishes. A new curve SN_2 of saddle-node bifurcations of symmetric

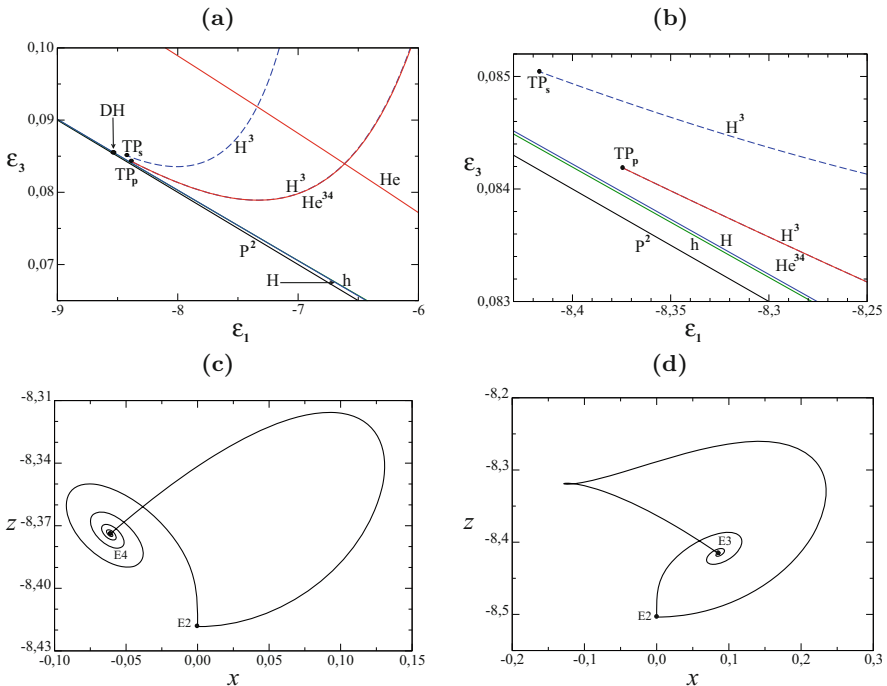


Fig. 3 For $\varepsilon_2 = -1$, $B = -0.1$, $D = 0.01$: (a) partial bifurcation set in the second quadrant. (b) Zoom of panel (a). Projection onto the (x, z) -plane of T-point heteroclinic loops connecting E_2 and the equilibria $E_{3,4}$ (note that because of the symmetry, a pair of the corresponding orbits exists): (c) principal T-point for $(\varepsilon_1, \varepsilon_3) \approx (-8.3738877, 0.0841835)$; (d) secondary T-point when $(\varepsilon_1, \varepsilon_3) \approx (-8.4159326, 0.0850368)$

periodic orbits emerges from Dh^2 . A cusp bifurcation of periodic orbits $CU \approx (-9.7715876, 0.0977398)$ occurs when SN_1 and SN_2 collapse (see lower panel of Fig. 2b). The cusp CU is the first one of an infinite sequence of cusps that accumulate to the point DH [24].

Close to the degeneracy DH , other bifurcation curves can be seen in Fig. 3a,b. Specifically from the point $TP_P \approx (-8.3738877, 0.0841835)$ (where a T-point heteroclinic loop between E_2 and $E_{3,4}$ exists and whose projection in the (x, z) -plane can be seen in Fig. 3c) three curves of global connections arise, namely He^{34} (heteroclinic connection between E_3 and E_4), H^3 (homoclinic connection to $E_{3,4}$), and a curve of homoclinic connections to E_2 (not included in Fig. 3) that ends at DHe^1 (see Fig. 2a,b) [6, 29–31]. The curve H^3 ends in a secondary T-point between E_2 and $E_{3,4}$ for $TP_S \approx (-8.4159326, 0.0850368)$ whose projection on the (x, z) -plane appears in Fig. 3d.

The presence in the second quadrant of the degenerations analyzed (and the bifurcation curves that arise from them) determines the existence of regions where chaotic attractors exist (see Fig. 4a,b). We note that these attractors, obtained for $\varepsilon_3 = 0.085$, are structurally stable when the value of ε_1 is varied. Moreover, as observed in these figures, their size increases when ε_1 augments along the interval $[-8, -6.3]$.

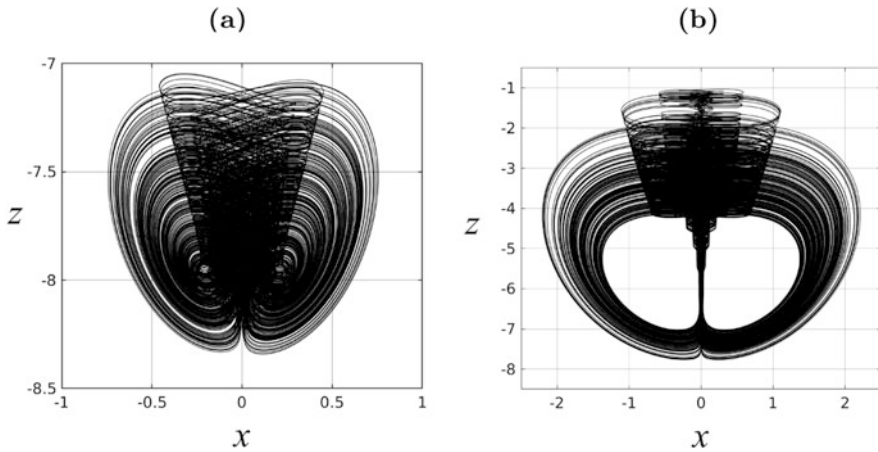


Fig. 4 For $\varepsilon_2 = -1, \varepsilon_3 = 0.085, B = -0.1, D = 0.01$ chaotic attractor when: (a) $\varepsilon_1 = -8$, with initial conditions $(x_0, y_0, z_0) = (0, 0.1, -8)$. (b) $\varepsilon_1 = -6.3$, with initial conditions $(x_0, y_0, z_0) = (0, 0.1, -7)$

4 Conclusions

In this work we consider an unfolding of a normal form of the Lorenz system near a triple-zero singularity. The combination of analytical and numerical tools allows to obtain partial interesting information on the complicated dynamics exhibited by system (3) related to a Takens–Bogdanov bifurcation and a diagonalizable double-zero degeneracy. Specifically, a degenerate heteroclinic connection, among other global connections, gives rise to infinite homoclinic orbits that will lead to the existence of chaos. Completing in the future the analysis of system (3) will shed new light on the behavior of the Lorenz system near its triple-zero singularity.

References

1. E.N. Lorenz, Deterministic non-periodic flows. *J. Atmos. Sci.* **20**, 130–141 (1963)
2. E.J. Doedel, B. Krauskopf, H.M. Osinga, Global invariant manifolds in the transition to preturbulence in the Lorenz system. *Indagationes Math.* **22**, 222–240 (2011)
3. R. Barrio, F. Blesa, S. Serrano, Global organization of spiral structures in biparameter space of dissipative systems with Shilnikov saddle-foci. *Phys. Rev. E* **84**, 035201 (2011)
4. R. Barrio, A.L. Shilnikov, L. Shilnikov, Kneadings, symbolic dynamics and painting Lorenz chaos. *Int. J. Bifurcation Chaos* **22**, 1230016 (2012)
5. A. Algaba, F. Fernández-Sánchez, M. Merino, A.J. Rodríguez-Luis, Centers on center manifolds in the Lorenz, Chen and Lü systems. *Commun. Nonlinear Sci. Numer. Simul.* **19**, 772–775 (2014)
6. A. Algaba, F. Fernández-Sánchez, M. Merino, A.J. Rodríguez-Luis, Analysis of the T-point-Hopf bifurcation in the Lorenz system. *Commun. Nonlinear Sci. Numer. Simul.* **22**, 676–691 (2015)
7. J.L. Creaser, B. Krauskopf, H.M. Osinga, α -flips and T-points in the Lorenz system. *Nonlinearity* **28**, R39–R65 (2015)
8. E.J. Doedel, B. Krauskopf, H.M. Osinga, Global organization of phase space in the transition to chaos in the Lorenz system. *Nonlinearity* **28**, R113–R139 (2015)
9. A. Algaba, M.C. Domínguez-Moreno, M. Merino, A.J. Rodríguez-Luis, Study of the Hopf bifurcation in the Lorenz, Chen and Lü systems. *Nonlinear Dynam.* **79**, 885–902 (2015)
10. A. Algaba, M.C. Domínguez-Moreno, M. Merino, A.J. Rodríguez-Luis, Takens–Bogdanov bifurcations of equilibria and periodic orbits in the Lorenz system. *Commun. Nonlinear Sci. Numer. Simul.* **30**, 328–343 (2016)
11. A. Algaba, E. Gamero, M. Merino, A.J. Rodríguez-Luis, Resonances of periodic orbits in the Lorenz system. *Nonlinear Dynam.* **84**, 2111–2136 (2016)
12. A. Algaba, M. Merino, A.J. Rodríguez-Luis, Superluminal periodic orbits in the Lorenz system. *Commun. Nonlinear Sci. Numer. Simul.* **39**, 220–232 (2016)
13. J.L. Creaser, B. Krauskopf, H.M. Osinga, Finding first foliation tangencies in the Lorenz system. *SIAM J. Appl. Dyn. Syst.* **16**, 2127–2164 (2017)
14. H.M. Osinga, Understanding the geometry of dynamics: the stable manifold of the Lorenz system. *J. Roy. Soc. New Zeal.* **48**, 203–214 (2018)
15. A. Algaba, M.C. Domínguez-Moreno, M. Merino, A.J. Rodríguez-Luis, A review on some bifurcations in the Lorenz system, in *Nonlinear Systems*, vol. 1, ed. by V. Carmona, J. Cuevas-Maraver, F. Fernández-Sánchez, E. García-Medina. *Understanding Complex Systems* (Springer, Cham, 2018)

16. A. Algaba, M.C. Domínguez-Moreno, M. Merino, A.J. Rodríguez-Luis, Double-zero degeneracy and heteroclinic cycles in a perturbation of the Lorenz system. Preprint (2020)
17. T. Shimizu, N. Morioka, On the bifurcation of a symmetric limit cycle to an asymmetric one in a simple model. *Phys. Lett. A* **76**, 201–204 (1980)
18. A.L. Shil'nikov, On bifurcations of the Lorenz attractor in the Shimizu-Morioka model. *Physica D* **62**, 338–346 (1993)
19. A.M. Rucklidge, Chaos in a low-order model of magnetoconvection. *Physica D* **62**, 323–337 (1993)
20. C. Liu, T. Liu, L. Liu, K. Liu, A new chaotic attractor. *Chaos Soliton Fract.* **22**, 1031–1038 (2004)
21. L.F. Mello, M. Messias, D.C. Braga, Bifurcation analysis of a new Lorenz-like chaotic system. *Chaos Soliton Fract.* **37**, 1224–1255 (2008)
22. H. Kokubu, R. Roussarie, Existence of a singulary degenerate heteroclinic cycle in the Lorenz system and its dynamical consequences: Part I. *J. Dyn. Differ. Equ.* **16**, 513–557 (2004)
23. J. Guckenheimer, P.J. Holmes, *Nonlinear Oscillations, Dynamical Systems, and Bifurcations of Vector Fields* (Springer, New York, 1983)
24. S. Wiggins *Introduction to Applied Dynamical Systems and Chaos* (Springer, New York, 2003)
25. Y.A. Kuznetsov, *Elements of Applied Bifurcation Theory* (Springer, New York, 2004)
26. C. Li, C. Rousseau, Codimension 2 symmetric homoclinic bifurcations and application to 1:2 resonance. *Can. J. Math.* **42**, 191–212 (1990)
27. A.J. Rodríguez-Luis, E. Freire, E. Ponce, On a codimension 3 bifurcation arising in an autonomous electronic circuit, in *Bifurcation and Chaos: Analysis, Algorithms, Applications*, ed. by R. Seydel et al. International Series of Numerical Mathematics, vol. 97 (Birkhäuser, Basel, 1991), pp. 301–306
28. E.J. Doedel, et al. *AUTO-07P: Continuation and Bifurcation Software for Ordinary Differential Equations*. Technical report (Concordia University, Concordia, 2012)
29. P. Glendinning, C. Sparrow, T-points: a codimension two heteroclinic bifurcation. *J. Statist. Phys.* **43**, 479–488 (1986)
30. F. Fernández-Sánchez, E. Freire, A.J. Rodríguez-Luis, T-Points in a \mathbb{Z}_2 -symmetric electronic oscillator. *Nonlinear Dynam.* **28**, 53–69 (2002)
31. F. Fernández-Sánchez, E. Freire, A.J. Rodríguez-Luis, Analysis of the T-point–Hopf bifurcation. *Physica D* **237**, 292–305 (2008)

Numerical Studies on the Nonlinear Dynamics of the Ziegler Column under Pulsating Follower Force



Guilherme Rosa Franzini and Carlos Eduardo Nigro Mazilli

1 Introduction

The response of the Ziegler column subjected to a follower force is a classical problem that has received studies in the last seven decades (see, for example, [1–3]). Despite its apparent simplicity, it reveals a number of intricate aspects, including dynamic instability (flutter) and possible mode localization [4]. Recently, [5] and [6] investigated the dynamic response of the Ziegler’s column considering the piezoelectric effects for both control of vibration and energy harvesting, respectively.

An interesting (sometimes referred to a “paradox”) regarding the response of the Ziegler’s column is the decrease in the critical value of the follower force when damping is included in the mathematical model. In [7], the author discusses the effects of nonlinearities associated with the torsional springs of the column and addresses non-periodic post-critical responses for the undamped column.

Reference [8] focuses on the effects of the nonlinear damping according to a van der Pol model on the post-critical response of the Ziegler’s column under follower force. Among other findings, the authors highlight that the Hopf bifurcation can be either supercritical or subcritical, which had already been anticipated in [9].

In [10], the authors readdress the influence of the linear damping on the dynamics of the Ziegler’s column under follower force. By using the multiple scale method and numerical integration of the mathematical model, they discuss, among other aspects, the post-critical responses.

If the follower force is further harmonically varying with time, parametric excitation also appears. Yet, it is remarkable that the interaction of the two instability

G. R. Franzini (✉) · C. E. N. Mazilli
Escola Politécnica, University of São Paulo, São Paulo, Brazil
e-mail: gfranzini@usp.br; cenmazzi@usp.br

mechanisms has not been previously addressed in the literature, as far as the authors are aware of. Therefore, they believe this is a novel aspect of the ongoing research herein reported. In this paper, focus is placed on the stability maps obtained in the plane of parameters that define the parametric excitation and on examples of post-critical time-histories.

The paper is organized as follows. Section 2 presents the mathematical models. The analysis methodology is detailed in Sect. 3. Section 4 brings the results and the corresponding discussions. The conclusions are addressed in Sect. 5.

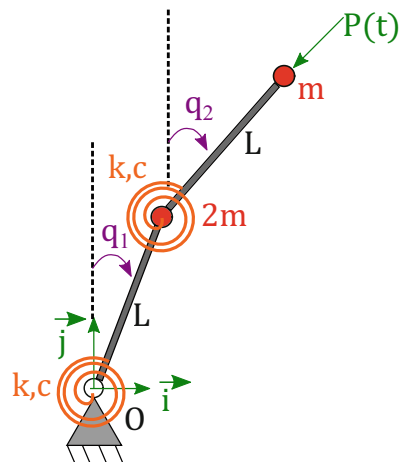
2 Mathematical Model

The model studied here is composed of two identical massless rigid bars of length L , connected by means of two torsional visco-elastic springs of stiffness k and damping constant c . Lumped masses $2m$ and m are included at mid-span and tip, respectively. A pulsating compressive follower force $P(t) = \bar{P} + \Delta P \sin \Omega t$ is applied to the tip of the column. The angular coordinates q_1 and q_2 are measured with respect to the line that characterizes the straight column, and no gravitational effects are considered. Figure 1 illustrates the investigated problem.

The equations of motion are obtained using the Euler–Lagrange’s equation. For the sake of conciseness, the intermediate steps are not herein detailed and the final mathematical model is given, in its dimensional form, by Eqs. (1) and (2).

$$\begin{aligned}
 mL^2(3\ddot{q}_1 + \cos(q_1 - q_2)\ddot{q}_2 + \sin(q_1 - q_2)\dot{q}_2^2) + c(2\dot{q}_1 - \dot{q}_2) + k(2q_1 - q_2) = \\
 = (\bar{P} + \Delta p \sin(\Omega t))L \sin(q_1 - q_2)
 \end{aligned}
 \tag{1}$$

Fig. 1 Ziegler’s column under pulsating follower force



$$mL^2(\cos(q_1 - q_2)\ddot{q}_1 + \ddot{q}_2 - \sin(q_1 - q_2)\dot{q}_1^2) + c(-\dot{q}_1 + \dot{q}_2) + k(-q_1 + q_2) = 0 \quad (2)$$

Aiming at generalizing the discussion, the mathematical model is rewritten in dimensionless form. For this, consider the reference frequency $\omega = \sqrt{\frac{k}{mL^2}}$ and the dimensionless quantities defined in Eq. (3).

$$\bar{p} = \frac{\bar{P}L}{k}, \Delta p = \frac{\Delta PL}{k}, n = \frac{\Omega}{\omega}, \zeta = \frac{c}{2mL^2\omega}, \tau = t\omega \quad (3)$$

Defining $(\)' = \frac{d}{d\tau}(\)$, the governing dimensionless system of differential equations reads:

$$3q_1'' + \cos(q_1 - q_2)q_2'' + 4\zeta q_1' - 2\zeta q_2' + \sin(q_1 - q_2)(q_2')^2 + 2q_1 - q_2 + (\bar{p} + \Delta p \sin(n\tau)) \sin(q_1 - q_2) \quad (4)$$

$$\cos(q_1 - q_2)q_1'' + q_2'' - 2\zeta q_1' + 2\zeta q_2' - \sin(q_1 - q_2)(q_1')^2 - q_1 + q_2 = 0 \quad (5)$$

3 Analysis Methodology

The equations of motion are numerically integrated using DifferentialEquations.jl package programmed in Julia, version 1.5.1. This package is able to choose the proper numerical solver. A standard notebook (i7–10th gen processor, 8 Gb RAM) has been employed for the numerical integrations using a single core.

Analyses with both the linearized (around $q_1 = q_2 = 0$) and the nonlinear models are carried out. Firstly, the linearized and autonomous form of the mathematical model is used for the modal analyses. The linearized model is also useful for studying the stability of the straight configuration of the column under pulsating follower force. Similarly to what has been done in [11] for a chain of articulated rigid pipes ejecting fluid under support excitation, the stability analysis is presented in the form of colormaps showing the maximum absolute value of the Floquet's multipliers (ρ^*) as function of the amplitude and frequency of the parametric excitation (Δp and n , respectively) for different values of averaged follower force \bar{p} and structural damping ratio ζ . The reader interested in details regarding the Floquet's theory is referred to [12].

The analyses with the nonlinear model are developed as follows. The mathematical model is integrated using initial conditions $q_1(0) = q_1'(0) = q_2'(0) = 0$ and $q_2(0) = 0.05$ during 1500 parametric excitation periods $\bar{\tau} = 2\pi/n$. Then, time-histories $q_1(\tau)$ and $q_2(\tau)$ are presented with the corresponding amplitude spectra. In the amplitude spectra, ω^* is the frequency normalized with respect to ω .

4 Results and Discussions

For the sake of organization, the results are discussed in two subsections. The natural modes and the stability maps are addressed in Sect. 4.1. Time-histories and maps of post-critical responses obtained with the nonlinear equations of motion are presented in Sect. 4.2.

4.1 Results from the Linearized Model

Modal analysis with the undamped Ziegler’s column ($\zeta = 0$) with $\bar{p} = 2$, which is slightly smaller than the critical load $\bar{p}_{cr} = 2.09$ for the column with the non-pulsating follower force [9], results in $\lambda_1 = i0.707$, $\lambda_2 = \lambda_1^*$, $\lambda_3 = i$ and $\lambda_4 = \lambda_3^*$ as eigenvalues, $()^*$ representing the complex conjugate and i the imaginary unit. Hence, the natural frequencies are $\omega_1 = 0.707$ and $\omega_2 = 1$. The corresponding mode shapes are illustrated in Fig. 2. It is worth noting that the second mode is localized.

Figure 3 brings the stability maps obtained at $\bar{p} = 2$. These maps plot, in a color scale, the variation of ρ^* (the maximum modulus of the Floquet’s multipliers) with the amplitude and frequency of parametric excitation (Δp and n , respectively). Each map is generated using a 2000×2000 grid in approximately half hour. The regions of stability are those characterized by $\rho^*(n; \Delta p) \leq 1$. On the other hand, unbounded solutions appear if $\rho^*(n; \Delta p) > 1$.

Figure 3a illustrates the stability map obtained for the undamped column. This map reveals two vertices of the instability region (i.e., the region shaded in red) arising at $n \approx 1.4$ and $n \approx 2$, corresponding to twice the undamped natural frequencies of the column and, consequently, to the principal parametric instabilities of the vibration modes. Besides the region associated with the principal parametric

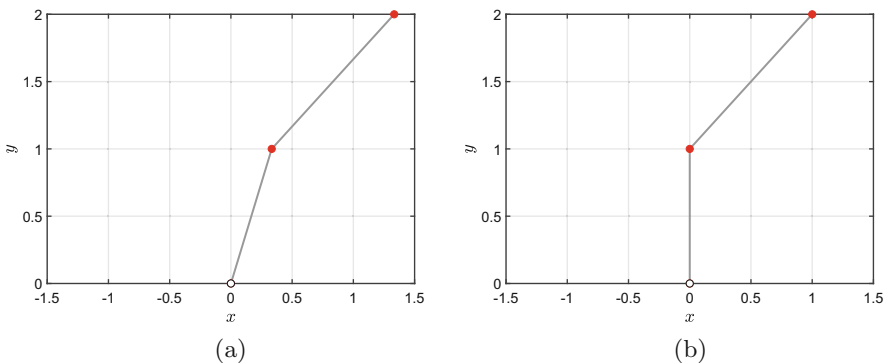


Fig. 2 Modal analysis— $\zeta = 0$ and $\bar{p} = 2$. (a) Mode 1— $\omega_1 = 0.707$. (b) Mode 2— $\omega_2 = 1$

instability, Fig. 3a also shows the existence of another region of the plane of control parameters $(n; \Delta p)$ associated with unbounded solutions. This secondary region of parametric instability is observed for low values of parametric excitation frequency n , with a vertex at $n \approx 0.29$, possible “unfavorable” combination resonance $(\omega_2 - \omega_1)$. Instability here would denote the system leaving the basin of attraction of the trivial equilibrium configuration, due to the closeness to the unstable subcritical Hopf bifurcation of the classical constant follower force problem. Notice that with the increasing of the damping, Fig. 3b–f, $\bar{p} = 2$ becomes supercritical and the trivial equilibrium configuration becomes unstable, thus explaining the growing of the response amplitudes.

As seen in Fig. 3b, a slight increase in the structural damping to $\zeta = 0.005$ decreases the size of the region of stability. The same figure reveals the appearance of a well defined region of stability at $n \approx 1.7$ (possible “favorable” combination resonance $(\omega_2 + \omega_1)$) and $0.03 \leq \Delta p \leq 0.18$ (see the region shaded in light blue). Notice that the increase of damping leads to $\bar{p} = 2$ being supercritical with respect to the follower force problem, but the stable supercritical Hopf bifurcation indicates the possibility of a stable periodic attractor, which has been captured here. Further increase in the values of ζ enlarges the region of parametric instability, shifting the isolated region of bounded responses (see the region shaded in blue) to larger values of parametric excitation amplitude Δp ; see Fig. 3d–f.

From the qualitative point of view, the enlargement of the region of the plane of control parameters $(n; \Delta p)$ associated with unbounded responses (parametric instability) indicates that the presence of structural damping plays a destabilizing role on the parametric excitation of the Ziegler’s column under pulsating follower force. This result goes in line with the “counter-intuitive” and well-known fact that the presence of structural damping decreases the critical load for the stability of the trivial equilibrium configuration of the column (see, for example, [10]). At least to the best of the authors’ knowledge, the stability of the straight configuration of the Ziegler’s column under pulsating follower force has not been previously addressed in the literature and consists a novelty feature of the present study.

4.2 Results from the Nonlinear Model

Firstly, we discuss the time-histories $q_1(\tau)$ and $q_2(\tau)$ and the corresponding amplitude spectra obtained at $n = 2$, $\bar{p} = 2$, three values of parametric excitation amplitude ($\Delta p = 0$, $\Delta p = 0.10$, and $\Delta p = 0.30$) and two values of dimensionless damping, namely $\zeta = 0$ and $\zeta = 0.05$. Notice that $n = 2$ is a favorable scenario for the parametric instability of the column with respect to the second mode, provided the natural frequency of the localized mode of the undamped column is $\omega_2 = 1$. For the sake of brevity, the results from the case with $n = 2\omega_1 = \sqrt{2}$ are not shown here.

Figure 4 presents the time-histories obtained for the undamped column. The illustrated responses reveal that the responses $q_2(\tau)$ oscillate with much larger

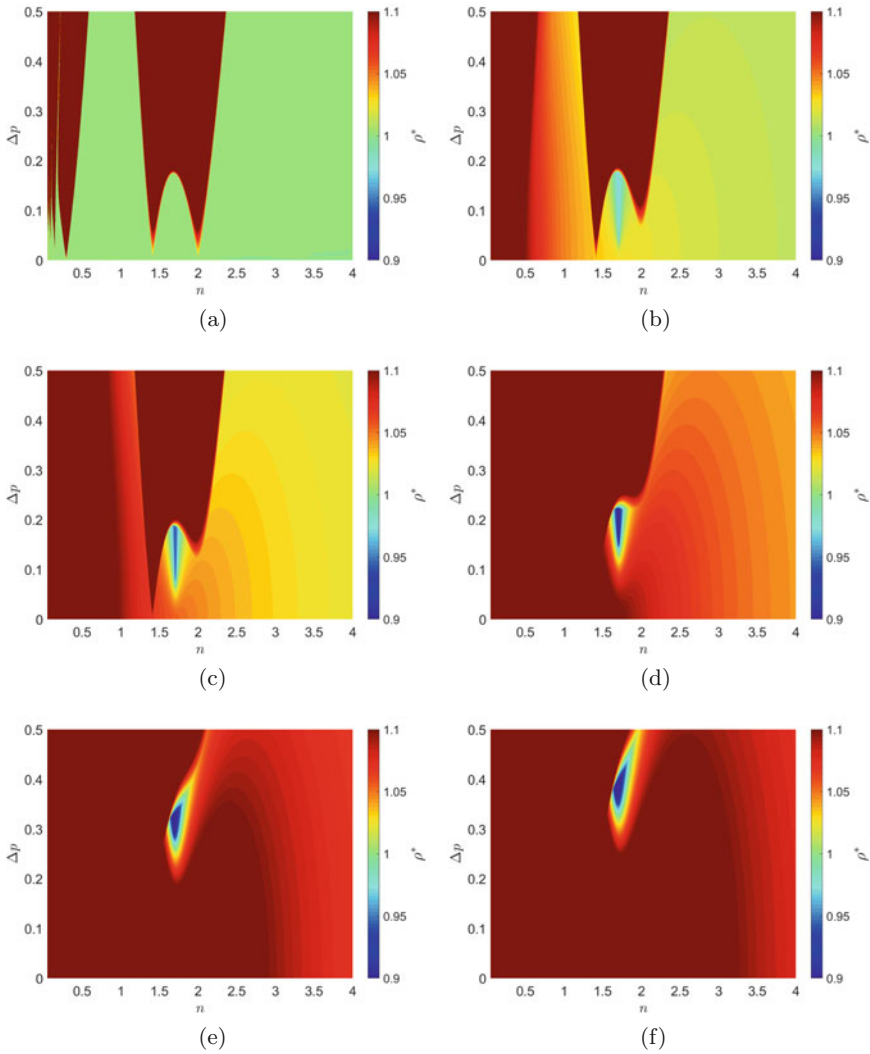


Fig. 3 Stability maps $\bar{p} = 2$. (a) $\zeta = 0.00$. (b) $\zeta = 0.005$. (c) $\zeta = 0.01$. (d) $\zeta = 0.02$. (e) $\zeta = 0.04$. (f) $\zeta = 0.05$

amplitude if compared to $q_1(\tau)$. This indicates that the parametric resonance with the second undamped mode, in spite of the nonlinear modal coupling, still keeps essentially the character of a localized forced response.

As seen in Fig. 4a,b, the response of the autonomous problem (i.e., the one with $\Delta p = 0$) is characterized by narrow-banded amplitude spectra, with well defined peaks at the undamped natural frequencies ω_1 and ω_2 .

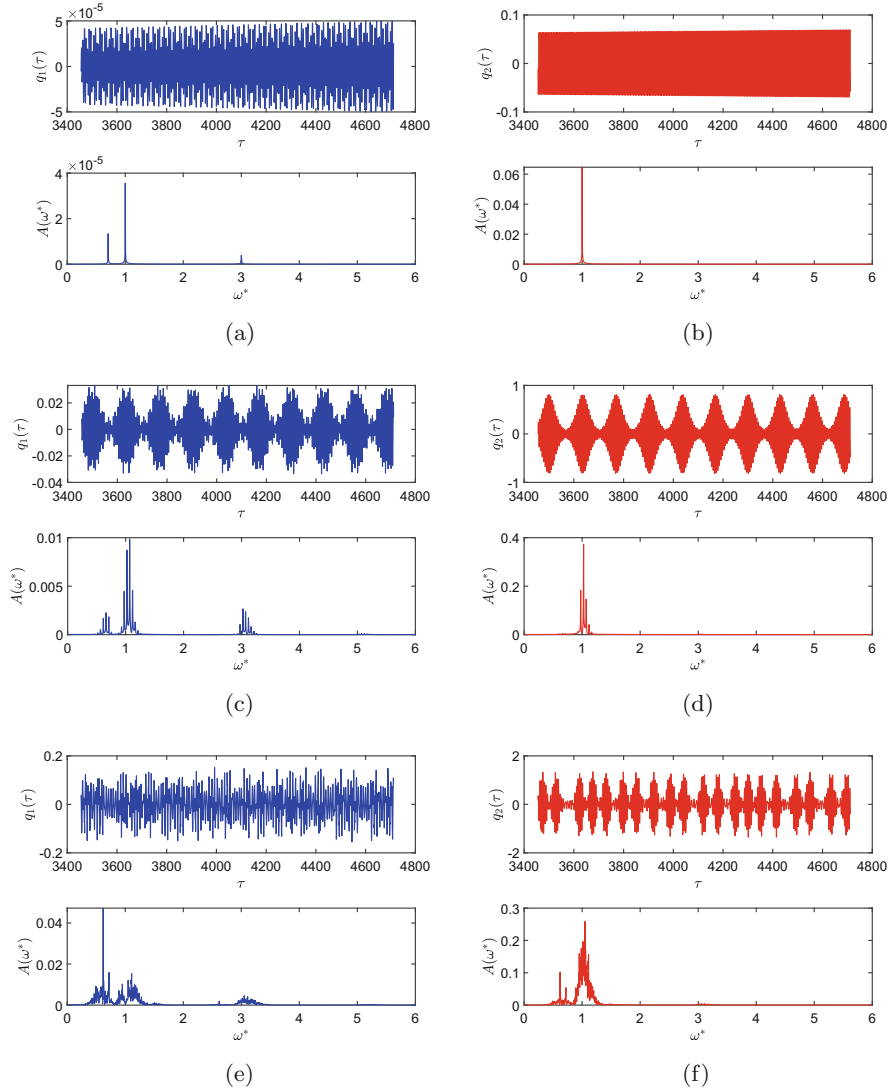


Fig. 4 Time-histories and amplitude spectra for $\zeta = 0$, $n = 2$, and $\bar{p} = 2$. **(a)** $q_1(\tau)$, $\Delta p = 0$. **(b)** $q_2(\tau)$, $\Delta p = 0$. **(c)** $q_1(\tau)$, $\Delta p = 0.10$. **(d)** $q_2(\tau)$, $\Delta p = 0.10$. **(e)** $q_1(\tau)$, $\Delta p = 0.30$. **(f)** $q_2(\tau)$, $\Delta p = 0.30$

When the amplitude of the dynamic component of the follower force is $\Delta p = 0.10$, Fig. 4c,d indicate the presence of amplitude-modulated responses, basically because of lack of damping that is essential for reaching a possible steady state. Particularly, the amplitude spectrum presented in Fig. 4c reveals the presence of the frequency components around ω_1 , ω_2 , and $3\omega_2$, the latter a subharmonic of the second natural frequency. Finally, Fig. 4e,f show irregular responses of the undamped column when $\Delta p = 0.30$. The amplitude spectra present larger bands than those for $\Delta p = 0.10$ (Fig. 4c,d).

Time-histories $q_1(\tau)$ and $q_2(\tau)$ and their amplitude spectra obtained with $\zeta = 0.05$ are shown in Fig. 5. When compared to the undamped case, the presence of structural damping decreases the amplitude modulations and increases the maximum responses. Notice, also, that the characteristic oscillation amplitudes of $q_1(\tau)$ and $q_2(\tau)$ have the same order of magnitude, indicating that the presence of damping breaks down the localized vibrations.

Despite the parametric excitation being a favorable scenario for oscillations in the second mode, all the amplitude spectra illustrated in Fig. 5 have a well defined dominant frequency around $\omega^* = 0.707$, corresponding to the first undamped vibration mode. Also counter-intuitive is the fact that the increase in the parametric excitation amplitude Δp leads to a decrease in the characteristic oscillation amplitudes of $q_1(\tau)$ and $q_2(\tau)$. On the other hand, as expected, the presence of damping leads to smaller amplitude modulations in the response the Ziegler's column.

Aiming at improving the understanding of the response, Fig. 6 plots some of the trajectories already discussed in Figs. 4 and 5 in the form of colored 3D curves, the color being associated with the value of \dot{q}_2 . The projections of the trajectories onto the phase-planes $q_1(\tau) \times q_2(\tau)$, $q_1(\tau) \times \dot{q}_1(\tau)$, and $q_2(\tau) \times \dot{q}_1(\tau)$ are also depicted.

While the trajectories obtained for the undamped case exhibit irregular behaviors, those from the simulations with $\zeta = 0.05$ offer useful insights into the dynamics of the Ziegler's column. For $\Delta p = 0$, Fig. 6b indicates a closed curve, corresponding to a periodic attractor (as foreseen by the stable supercritical Hopf bifurcation). When the parametric excitation amplitude is increased, this curve becomes "broader," which might perhaps be interpreted as a quasi-periodic attractor (see Fig. 6d,f).

A multiple-scales analysis has been performed, but its detailing is avoided here for brevity. It revealed that, for the case $n = 2$, any added damping, however small, completely erases the second (localized) mode in spite that it is parametrically excited, fact that is confirmed by the numerical results of Fig. 5, while the fully undamped system does show an important second mode contribution, the lack of dissipation leading to a sort of "beating" pattern in both modes. This result is further illustrated by the Poincaré's section of Fig. 7, using the stroboscopic period $\tau_{sb} = 2\pi/n$ and $\Delta p = 0.30$.

Hence, besides providing the well-known decrease in the critical follower force, damping also wipes out the localized mode. It is also to be noticed that other harmonic contributions arise, as shown in Figs. 5 and 6, due to the particular

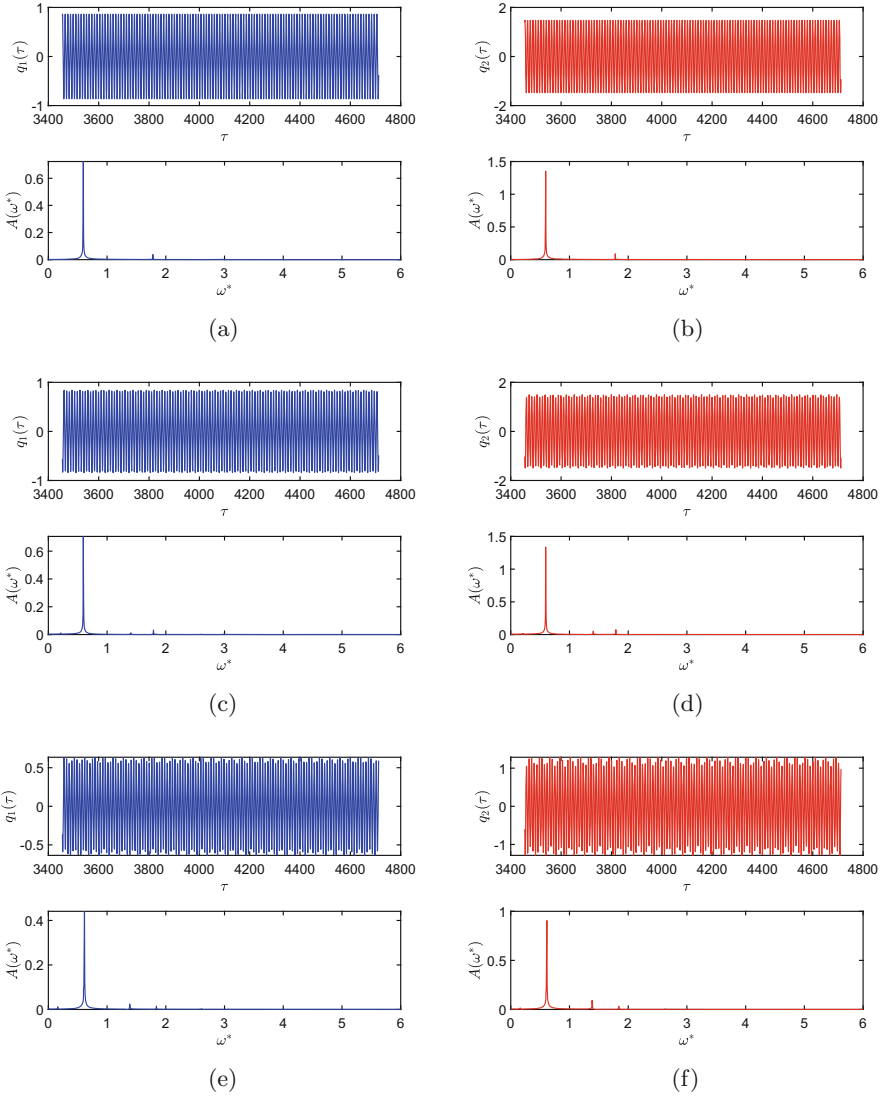


Fig. 5 Time-histories and amplitude spectra for $\zeta = 0.05$, $n = 2$, and $\bar{p} = 2$. (a) $q_1(\tau)$, $\Delta p = 0$. (b) $q_2(\tau)$, $\Delta p = 0$. (c) $q_1(\tau)$, $\Delta p = 0.10$. (d) $q_2(\tau)$, $\Delta p = 0.10$. (e) $q_1(\tau)$, $\Delta p = 0.30$. (f) $q_2(\tau)$, $\Delta p = 0.30$

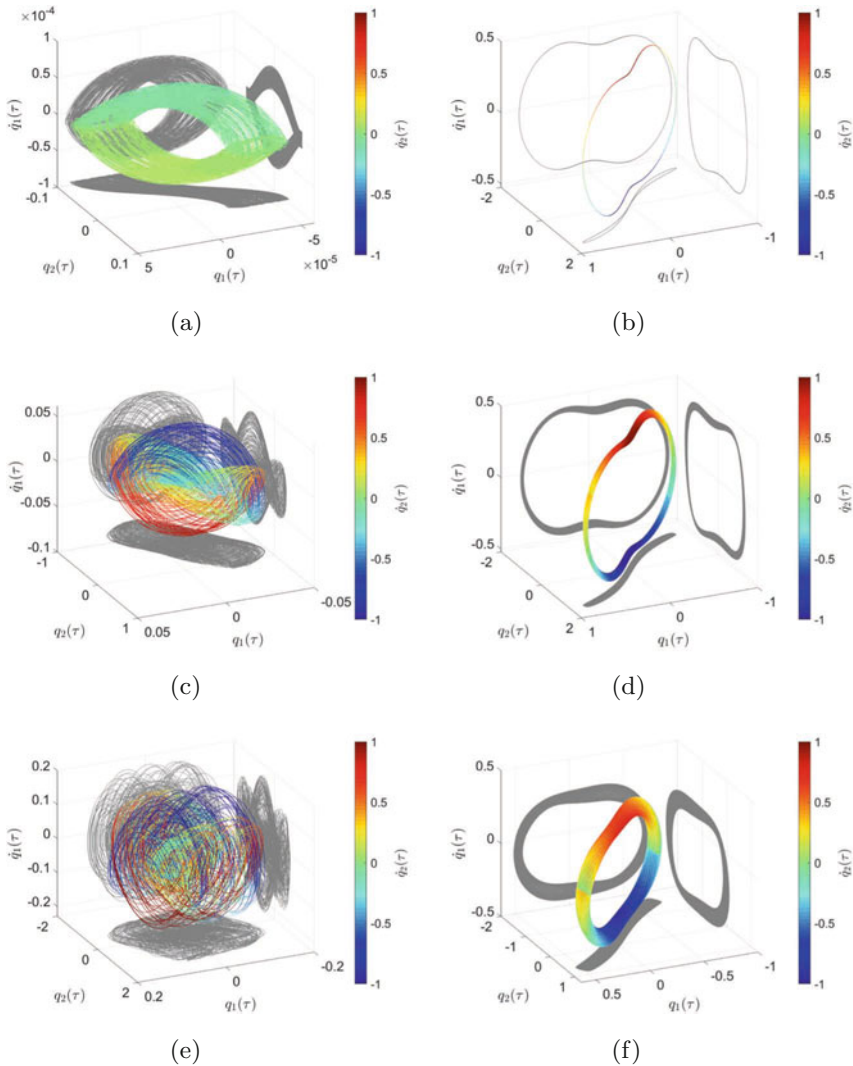
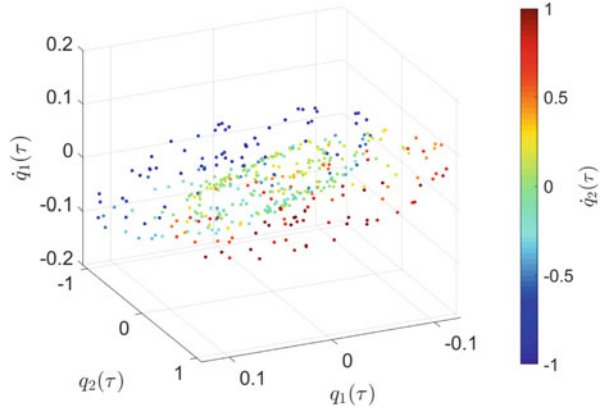


Fig. 6 Projections of phase trajectories. (a) $\zeta = 0, \Delta p = 0$. (b) $\zeta = 0.05, \Delta p = 0$. (c) $\zeta = 0, \Delta p = 0.10$. (d) $\zeta = 0.05, \Delta p = 0.10$. (e) $\zeta = 0, \Delta p = 0.30$. (f) $\zeta = 0.05, \Delta p = 0.30$

solutions associated with non-secular terms. Other scenarios, such as those of $n = 2\omega_1 = \sqrt{2}$ (principal parametric excitation of the first mode) or $n = \omega_1 + \omega_2 = \sqrt{2}/2 + 1$ (combination resonance of modes 1 and 2) could be further explored but were not included here due to lack of space.

Fig. 7 Points in the Poincaré's section. $\Delta p = 0.30$, $n = 2$, and $\zeta = 0$



5 Conclusions

In this paper, the authors addressed the Ziegler column problem, yet with a pulsating follower force, which constitutes a novelty, to the best of their knowledge. The interplay between two instability phenomena, namely, flutter and parametric resonance, plus the destabilizing effect of damping and the response localization are also discussed in this essentially numerical investigation.

The stability maps revealed that the presence of damping decreased the region of the plane of parameters that govern the parametric excitation associated with bounded solutions. Additionally, examples of post-critical time-histories exhibited amplitude modulations associated with the pulsating follower force. Other studies focusing on the nonlinear response of the parametrically excited Ziegler column will be addressed in the near future. Hence, it is reckoned that further analysis is still needed to fully explore the system complex dynamics.

Acknowledgments The authors acknowledge the support of the Brazilian Scientific Research Council (CNPq), under the projects 305945/2020-3 and 301050/2018-0. São Paulo Research Foundation (FAPESP) is acknowledged for the grant 2019/27855-2.

References

1. H. Ziegler, Die Stabilitätskriterien der Elastomechanik. *Ing.-Arch* **20**, 49–56 (1952)
2. H. Herrmann, I.C. Jong, On nonconservative stability problems of elastic systems with slight damping. *J. Appl. Mech.* **33**, 125–133 (1966)
3. P. Hagedorn, On the destabilizing effect of non-linear damping in non-conservative systems with follower forces. *Int. J. Non-Lin. Mech.* **5**(2), 341–358 (1970)
4. S. Lenci, C.E.N. Mazzilli, Asynchronous free oscillations of linear mechanical systems: a general appraisal and a digression on a column with a follower force. *Int. J. Non-Lin. Mech.* **94**, 223–234 (2017)

5. F. D'Annibale, F. Rosi, A. Luongo, Controlling the limit-cycle of the Ziegler column via a tuned piezoelectric damper. *Math Prob. in Eng.* **2015**, 1–9 (2015)
6. C.E.N. Mazzilli, G.R. Franzini, Parametric excitation of an asynchronous Ziegler's column with a piezoelectric element, in *Proceedings of the 10th European Nonlinear Dynamics Conference—ENOC2020+1* (2021)
7. A.N. Kounadis, On the paradox of the destabilizing effect of damping in non-conservative systems. *Int. J. Non-Linear Mech.* **27**(4), 597–609 (1992)
8. A. Luongo, F. D'Annibale, M. Ferretti, Hard loss of stability of Ziegler's column with nonlinear damping. *Meccanica* **51**, 2647–2663 (2016)
9. C.E.N. Mazzilli, Nonlinear dynamics and stability: a formulation for systems subjected to support excitation and non-conservative loading, in *Habilitation Thesis (in Portuguese)* (University of São Paulo, São Paulo, 1988)
10. F. D'Annibale, M. Ferretti, On the effects of linear damping on the nonlinear Ziegler's column. *Nonlinear Dyn.* **103**(4), 3149–3164 (2020)
11. I.M. Lourenço, R.M.M. Orsino, G.R. Franzini, Dynamics of an articulated chain of rigid pipes discharging fluid under concomitant support excitation: a numerical analysis. *J. Braz. Soc. Mech. Sci. Eng.* **42**(581), 1–15 (2020)
12. A. Nayfeh, B. Balachandran, *Applied Nonlinear Dynamics—Analytical, Computational and Experimental Methods* (Wiley, New York, 1995)

Hidden Regularity of Stability Boundaries in Two-step Hill's Equations



Emilio Freire, Manuel Ordóñez, and Enrique Ponce

1 Introduction

Following [1], even there were preliminary studies, after the work on the motion of the lunar perigee by G. W. Hill in 1877, the term “Hill’s equation” is associated with a class of homogeneous, linear, second-order differential equations with real, periodic coefficients. Such equations have a lot of applications in engineering and physics, including problems in mechanics, astronomy, and the theory of electric circuits, just to mention a few. The Hill’s equation has the general form

$$\ddot{x}(t) + V(t)x(t) = 0, \quad (1)$$

where the potential V is a T -periodic function. The specific case $V(t) = a_0 + a_1 \cos t$ is usually called Mathieu’s equation, see [2] for a general overview, while the case of piecewise constant periodic potential is named Meissner’s equation, firstly studied by E. Meissner in 1918 and later by H. Hochstadt in the 1960s, see Chapter 8 in [1]. Recently, the nonlinear version of Meissner’s equation with the stiffness term of the form $V(t) \sin x(t)$ has been considered in [3, 4] for the study of pendulum systems.

We are interested in the analysis of Hill’s equation with a two-step piecewise constant function as T -periodic potential; our motivation comes from the original model established by R. de L. Kronig and W. G. Penney in 1931 for the study of electrons in crystal lattices [5], where the width of the two steps is not equal, namely

E. Freire · M. Ordóñez · E. Ponce (✉)
E.T.S. Ingeniería, Sevilla, Spain
e-mail: efrem@us.es; mordonez@us.es; eponcem@us.es

$$\ddot{x}(t) + V(t)x(t) = 0, \quad V(t) = \begin{cases} a, & 0 \leq t \leq \tau, \\ b, & \tau \leq t \leq T. \end{cases} \tag{2}$$

There are few recent works in the subject; excepting the one by S. Gan and M. Zhang [6], based on the study of rotation numbers, other papers studying Eq. (2), as in [7, 8] and very recently in [9], assume for the potential V to be a square wave, that is, $T = 2\tau$. Here, we study the general situation by analyzing first the elliptic–elliptic case ($a, b > 0$) in a three-parameter setting; the remaining cases will be addressed elsewhere.

Obviously, after setting $y = \dot{x}$, we can write Eq. (2) as

$$\begin{pmatrix} \dot{x} \\ \dot{y} \end{pmatrix} = \begin{pmatrix} 0 & 1 \\ -V(t) & 0 \end{pmatrix} \begin{pmatrix} x \\ y \end{pmatrix} = A(t) \begin{pmatrix} x \\ y \end{pmatrix}, \tag{3}$$

where $A(t)$ is T -periodic. Notice that the matrix $A(t)$ can be written as

$$A(t) = J \begin{pmatrix} V(t) & 0 \\ 0 & 1 \end{pmatrix}, \quad J = \begin{pmatrix} 0 & 1 \\ -1 & 0 \end{pmatrix}, \tag{4}$$

a feature of general linear periodic Hamiltonian problems, which can be written in the form

$$\dot{\mathbf{x}} = JS(t)\mathbf{x}, \quad \mathbf{x} \in \mathbb{R}^2, \tag{5}$$

where J is as given before, and $S(t)$ is a 2×2 symmetric T -periodic matrix.

We recall that for a linear system with periodic coefficients,

$$\dot{x} = A(t)x(t), \tag{6}$$

with $A(t + T) = A(t)$, for all $t \in \mathbb{R}$, $T > 0$, and $x \in \mathbb{R}^n$, if $X(t)$ is a fundamental matrix of solutions with $X(0) = I$, then $X(t + T)$ is also a fundamental matrix and there exists a non-singular matrix C such that $X(t + T) = X(t)C$ for all t . This fact implies that

$$X(t + T) = X(t)X(T). \tag{7}$$

From (7) we obtain

$$X(nT) = X(T)^n. \tag{8}$$

Thus, the so-called *monodromy matrix* $X(T)$ contains all the information to characterize the whole dynamics, i.e., the stability of the null solution, the existence of periodic solutions and so on. The eigenvalues of $X(T)$ are the *characteristic multipliers* or *Floquet multipliers*.

Clearly, if $\mu \in \mathbb{R}$ and $v \in \mathbb{R}^n$ are such that $X(T)v = \mu v$, then the solution $\psi(t) = X(t)v$, with $\psi(0) = v$, verifies

$$\psi(t + T) = X(t + T)v = X(t)X(T)v = X(t)\mu v = \mu\psi(t),$$

so that the existence of *T-periodic* solutions is associated with the existence of a multiplier $\mu = 1$ because if $X(T)v = v$, then $\psi(t) = X(t)v$ is *T-periodic*. On the other hand, if $\mu = -1$ is an eigenvalue of $X(T)$ and v is an associated eigenvector, then we have that the solution $\psi(t) = X(t)v$, with $\psi(0) = v$ is *2T-periodic*. Obviously, from the linear and homogeneous character, any periodic solution is not isolated, since it belongs to a linear one-dimensional manifold of periodic solutions.

In practice, although the system is linear and homogeneous, it turns out difficult to compute the fundamental matrix $X(t)$. From Liouville's formula

$$\det X(T) = \exp\left(\int_0^T \text{trace } A(s)ds\right),$$

it can be concluded that $\prod_{i=1}^n \mu_i > 0$, where $\mu_i \in \mathbb{C}$ are the Floquet multipliers of $X(T)$. In our bi-dimensional case, we have that $\text{trace}(A) = 0$, for all t , and so the determinant of the monodromy matrix is equal to 1. This entails that for the two characteristic multipliers, say μ_1, μ_2 , we have $\mu_1, \mu_2 = 1$, so that they are the roots of the quadratic

$$\mu^2 - \text{trace } X(T)\mu + 1 = 0.$$

Consequently, when $-2 < \text{trace } X(T) < 2$ both multipliers are complex numbers, forming a conjugate pair on the unit circle of the complex plane. Therefore, the stability of all the solutions is guaranteed in such a case. On the other hand, when $|\text{trace } X(T)| > 2$, it is easy to conclude that both multipliers are real but one of them with modulus greater than one, so that there are unbounded solutions and the system becomes unstable. Thus, our goal is to describe for Eq. (2) the parametric stability boundaries given by the surfaces $\text{trace } X(T) = \pm 2$.

2 The Elliptic–Elliptic Case ($a > 0, b > 0$)

We only consider in this work the elliptic–elliptic case where $a > 0$ and $b > 0$, while the remaining cases will be studied elsewhere. Thus, we can take $\omega_a > 0$ and $\omega_b > 0$ such that $a = \omega_a^2$ and $b = \omega_b^2$, so that

$$V(t) = \begin{cases} \omega_a^2, & t \in [0, \tau] \\ \omega_b^2, & t \in [\tau, T] \end{cases} \tag{9}$$

where T , the period of $V(t)$, is given. Here, it is not difficult to compute the monodromy matrix $M = X(T)$, which depends on the three parameters $(\omega_a, \omega_b, \tau)$, namely

$$M(\omega_a, \omega_b, \tau) = \exp \begin{pmatrix} 0 & T - \tau \\ -(T - \tau)\omega_b^2 & 0 \end{pmatrix} \cdot \exp \begin{pmatrix} 0 & \tau \\ -\tau\omega_a^2 & 0 \end{pmatrix}. \tag{10}$$

The following symmetry result is natural, since it says that the order of the two steps in the periodic interval is not essentially relevant. Its proof is straightforward by observing that the change $(\omega_a, \omega_b, \tau) \longleftrightarrow (\omega_b, \omega_a, T - \tau)$ makes to appear in $M(\omega_b, \omega_a, T - \tau)$ the product of the same exponential matrices in reverse order.

Lemma 1 *The monodromy matrix $M(\omega_b, \omega_a, T - \tau)$ is similar to the monodromy matrix $M(\omega_a, \omega_b, \tau)$.*

Using the explicit computations

$$\exp \begin{pmatrix} 0 & \tau \\ -\tau\omega_a^2 & 0 \end{pmatrix} = \cos(\omega_a\tau)I + \frac{\sin(\omega_a\tau)}{\omega_a} \begin{pmatrix} 0 & 1 \\ -\omega_a^2 & 0 \end{pmatrix} \tag{11}$$

and

$$\exp \begin{pmatrix} 0 & T - \tau \\ -(T - \tau)\omega_b^2 & 0 \end{pmatrix} = \cos(\omega_b(T - \tau))I + \frac{\sin(\omega_b(T - \tau))}{\omega_b} \begin{pmatrix} 0 & 1 \\ -\omega_b^2 & 0 \end{pmatrix}, \tag{12}$$

where I stands for the identity matrix, a straightforward algebraic manipulation leads to the expression

$$\text{trace } M = 2 \cos(\omega_a\tau) \cos(\omega_b(T - \tau)) - \frac{\omega_a^2 + \omega_b^2}{\omega_a\omega_b} \sin(\omega_a\tau) \sin(\omega_b(T - \tau)).$$

The above expression was already reported by Meissner in 1918, and we look for a deeper insight into the parameter regions corresponding to the stability boundaries $\text{trace } M = 2$ and $\text{trace } M = -2$, which determine the complicated known structure of resonance pockets.

In what follows, we substitute the interval length parameter τ by the ratio $r \in (0, 1)$, where $\tau = rT$, assuming also without loss of generality that $T = 2\pi$. Thus, we can start our analysis by studying the parametric surfaces

$$\cos(2\pi r\omega_a) \cos(2\pi(1 - r)\omega_b) - \frac{\omega_a^2 + \omega_b^2}{2\omega_a\omega_b} \sin(2\pi r\omega_a) \sin(2\pi(1 - r)\omega_b) = \pm 1, \tag{13}$$

corresponding to the stability boundaries $\text{trace } M = 2$ (for the + sign) and $\text{trace } M = -2$ (for the - sign), which determine the bifurcation set of the problem. Effectively, if by moving parameters one crosses some of the above parametric surfaces, the system passes from being stable to unstable or vice versa.

Clearly, when $\omega_a = \omega_b = \omega$ Eq. (13) reduces to $\cos(2\pi\omega) = \pm 1$, so that the stability boundaries contain the lines

$$\Sigma_n = \left\{ (\omega_a, \omega_b, r) : \omega_a = \omega_b = \frac{n}{2}, r \in (0, 1) \right\}, \tag{14}$$

for any natural number n . The situation for $\omega_a \neq \omega_b$ is much more involved.

Before considering the problem in its generality, it is very interesting to look for the special cases $M = I$ (all the solutions are T -periodic) and $M = -I$ (all the solutions are $2T$ -periodic). For instance, to study the case when $M = I$, it suffices to impose for the matrices in (11)–(12) to be inverse one of each other, getting the conditions

$$\begin{aligned} \cos(2\pi r\omega_a) &= \cos(2\pi(1-r)\omega_b), \\ \frac{\sin(2\pi r\omega_a)}{\omega_a} &= -\frac{\sin(2\pi(1-r)\omega_b)}{\omega_b}, \end{aligned} \tag{15}$$

$$\omega_a \sin(2\pi r\omega_a) = -\omega_b \sin(2\pi(1-r)\omega_b).$$

Two cases arise. First, if the sides of the last two equations do not vanish, then after dividing such two equations we get the trivial case $\omega_a = \omega_b$, for which we get the reduced conditions

$$\begin{aligned} \cos(2\pi r\omega_a) &= \cos(2\pi(1-r)\omega_a), \\ \sin(2\pi r\omega_a) &= -\sin(2\pi(1-r)\omega_a), \end{aligned} \tag{16}$$

that is, $2\pi r\omega_a + 2\pi(1-r)\omega_a = 2\pi\omega_a = 2k\pi$, for some $k \in \mathbb{N}$. In short, we have that when $\omega_a = \omega_b = k$ for some $k \in \mathbb{N}$, then $M = I$. Second, when the sides of the last two equations vanish, we have $2\pi r\omega_a = k\pi$ and $2\pi(1-r)\omega_b = m\pi$ for some natural numbers k and m ; to fulfill the first condition we need k and m to be of the same parity.

A parallel argument applies for the case $M = -I$, and so we can state our first main result, which gives the structure of the skeleton for the bifurcation set of Eq. (2).

Proposition 1 Consider Eq. (2) with $a = \omega_a^2$, $b = \omega_b^2$, $T = 2\pi$, and $\tau = rT$ for $(\omega_a, \omega_b, r) \in \mathbb{R}^+ \times \mathbb{R}^+ \times (0, 1)$. For the parameter values corresponding to the points belonging to the lines Σ_n given in (14) and to the denumerable family of curves

$$\Gamma_{k,m} = \left\{ (\omega_a, \omega_b, r) : \omega_a = \frac{k}{2r}, \omega_b = \frac{m}{2(1-r)}, r \in (0, 1) \right\}, \tag{17}$$

the monodromy matrix of Eq. (2) satisfies $M = I$ when $k + m$ or n are even, while $M = -I$ if $k + m$ or n are odd.

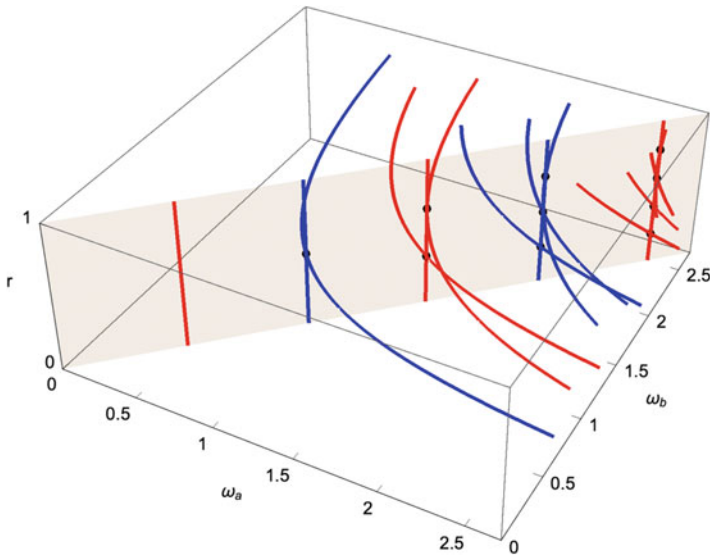


Fig. 1 The first lines corresponding to $M = I$ (blue) and $M = -I$ (red). Observe the vertical segments Σ_1 to Σ_5 , all contained in the plane $\omega_a = \omega_b$ which are alternatively associated with $M = -I$ and $M = I$, and some Γ -curves intersecting Σ_n for $n \geq 2$

Any point $P_{k,m}$ of $\Gamma_{k,m}$ with $(k + m)r = k$ belongs to the parametric plane $\omega_a = \omega_b$, so that it is also in Σ_n for $n = k + m$, and constitutes one of the highest co-dimension points of the bifurcation set, see Fig. 1.

Note that if we project the $\Gamma_{k,m}$ curves in (17) on the plane (ω_a, ω_b) by eliminating r , after some standard manipulations, we get the first quadrant branches of the family of hyperbolas $(2\omega_a - k)(2\omega_b - m) = km$, with parallel asymptotes to the axes, namely $\omega_a = k/2$ and $\omega_b = m/2$.

Starting from expression (13), we can try to visualize (typically, by implicit plotting in 3D) the surfaces that organized by the lines given in Proposition 1 in the parameter set $(\omega_a, \omega_b, r) \in \mathbb{R}^+ \times \mathbb{R}^+ \times (0, 1)$, determine the full bifurcation set of our problem. For instance, for $0 < \omega_a, \omega_b < 3$ you obtain the configuration of Fig. 2. We observe how both surfaces trace $M = 2$ and trace $M = -2$ are organized in pairs of leaves that intersect each other along the lines of Proposition 1. The points $P_{k,m}$ of Proposition 1, namely

$$P_{k,m} = \left(\frac{k + m}{2}, \frac{k + m}{2}, \frac{k}{k + m} \right),$$

turn out to be the highest co-dimension points (co-dimension 3) of the bifurcation set, and their local study deserves further consideration.

To fully understand the observed structure, in the next section we introduce new parameters that not only simplify very much the analysis but also provide a deeper insight into the bifurcation set.

3 Discovering the Hidden Regularity of the Bifurcation Set

In order to get a better knowledge of the intricate structure of stability boundaries in Fig. 2, we consider the *mean frequency* ω , the *global discrepancy between frequencies* δ , and their *relative discrepancy* ϱ , namely

$$\omega = r\omega_a + (1 - r)\omega_b, \quad \delta = r\omega_a - (1 - r)\omega_b, \quad \varrho = \frac{\omega_a - \omega_b}{\omega_a + \omega_b}. \tag{18}$$

Note that, by definition, these parameters satisfy $\omega > 0$, $\delta \in (-\omega, \omega)$, and $\varrho \in (-1, 1)$. Straightforward computations give the inverse relations to recover the original parameters, namely

$$\omega_a = \frac{\omega - \delta\varrho}{1 - \varrho}, \quad \omega_b = \frac{\omega + \delta\varrho}{1 + \varrho}, \quad r = \frac{(\omega + \delta)(1 - \varrho)}{2(\omega - \delta\varrho)}, \tag{19}$$

and if one computes the Jacobian of the transformation, one gets

$$\left| \frac{\partial(\omega_a, \omega_b, r)}{\partial(\omega, \delta, \varrho)} \right| = \frac{1}{1 - \varrho^2},$$

so that the change is regular in its whole domain.

A first virtue of this parameter transformation is that they straighten the lines where $M = \pm I$, now becoming orthogonal, because we have

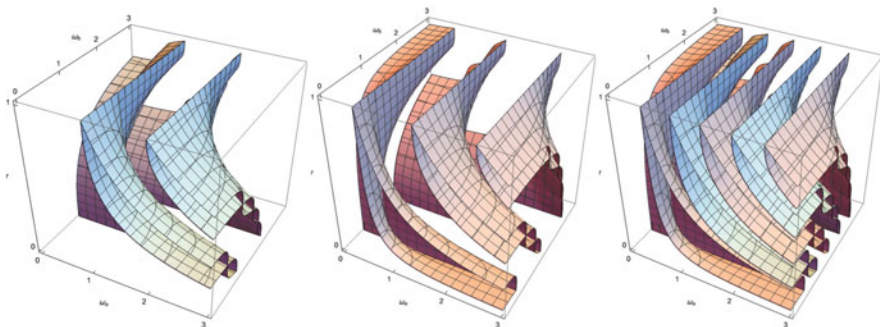
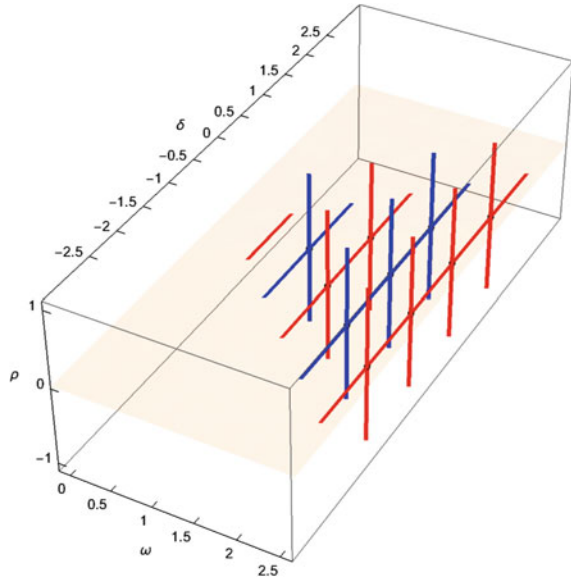


Fig. 2 The first surfaces corresponding to trace $M = 2$ (light blue), trace $M = -2$ (light red), and all of them. We observe 3D pockets where Eq. (2) becomes unstable along with intricate parameter regions between surfaces where the equation is stable

Fig. 3 The first lines corresponding to $M = I$ (blue) and $M = -I$ (red) in the new parameter set $(\omega, \delta, \varrho)$. Observe that the segments Σ_1 to Σ_5 are now contained in the plane $\varrho = 0$. They become orthogonal to the Γ -lines, which appear as bounded vertical segments



$$\Sigma_n = \left\{ (\omega, \delta, \varrho) : \omega = \frac{n}{2}, \delta \in \left(-\frac{n}{2}, \frac{n}{2}\right), \varrho = 0 \right\}, \tag{20}$$

and

$$\Gamma_{k,m} = \left\{ (\omega, \delta, \varrho) : \omega = \frac{k+m}{2}, \delta = \frac{k-m}{2}, \varrho \in (-1, 1) \right\}, \tag{21}$$

which now are finite segments, see Fig. 3.

The convenience of introducing these new parameters is natural after observing that in (13) the product of cosines (respectively, sines) can be written as

$$\frac{1}{2} [\cos(2\pi(r\omega_a \pm (1-r)\omega_b)) \pm \cos(2\pi(r\omega_a \mp (1-r)\omega_b))].$$

Therefore, Eq. (13) becomes

$$\frac{1}{2} [\cos(2\pi\omega) + \cos(2\pi\delta)] - \frac{\omega_a^2 + \omega_b^2}{4\omega_a\omega_b} [\cos(2\pi\delta) - \cos(2\pi\omega)] = \pm 1,$$

or equivalently, $(\omega_a + \omega_b)^2 \cos(2\pi\omega) - (\omega_a - \omega_b)^2 \cos(2\pi\delta) = \pm 4\omega_a\omega_b$. If in this last expression with the plus sign (the minus sign) we make use of the trigonometric identity $\cos(2\theta) = 1 - 2 \sin^2 \theta$ (the identity $\cos(2\theta) = 2 \cos^2 \theta - 1$, respectively) and we introduce our third new parameter ϱ , then it is immediate to state our final main result, as follows.

Theorem 1 *In terms of the new parameters $(\omega, \delta, \varrho)$ given in (18), the analytical expressions for the parametric surfaces trace $M = 2$ and trace $M = -2$ (the stability boundaries) are given by*

$$\sin^2(\pi\omega) - \varrho^2 \sin^2(\pi\delta) = 0,$$

and

$$\cos^2(\pi\omega) - \varrho^2 \cos^2(\pi\delta) = 0,$$

respectively, where the set of admissible parameter values is

$$\{(\omega, \delta, \varrho) : \omega > 0, \delta \in (-\omega, \omega), \varrho \in (-1, 1)\}.$$

The advantages of the new expressions for the stability boundaries are rather obvious. Apart from its simplicity, we realize that in addition to the symmetry stated in Lemma 1, which translates now to the invariance of the stability boundaries in the parameter space $(\omega, \delta, \varrho)$ under the change

$$(\omega, \delta, \varrho) \longleftrightarrow (\omega, -\delta, -\varrho),$$

there appear the new elementary symmetries

$$(\omega, \delta, \varrho) \longleftrightarrow (\omega, -\delta, \varrho),$$

and

$$(\omega, \delta, \varrho) \longleftrightarrow (\omega, \delta, -\varrho),$$

and so we can restrict our attention to the parametric regions with non-negative values of δ and ϱ , as done in Fig. 4. Furthermore, we can take advantage of the 1-periodicity of the surfaces both with respect to parameters ω and δ .

We also note that the expressions for the stability boundaries provided by Theorem 1 admit the trivial factorizations

$$[\sin(\pi\omega) + \varrho \sin(\pi\delta)] \cdot [\sin(\pi\omega) - \varrho \sin(\pi\delta)] = 0$$

and

$$[\cos(\pi\omega) + \varrho \cos(\pi\delta)] \cdot [\cos(\pi\omega) - \varrho \cos(\pi\delta)] = 0,$$

which explain the interleaving property of the family, organized in pairs of oscillating surfaces that define the resonance regions. Moreover, these factorizations allow to determine in a rigorous way the shape and size of such regions; the details of such analysis will appear elsewhere.

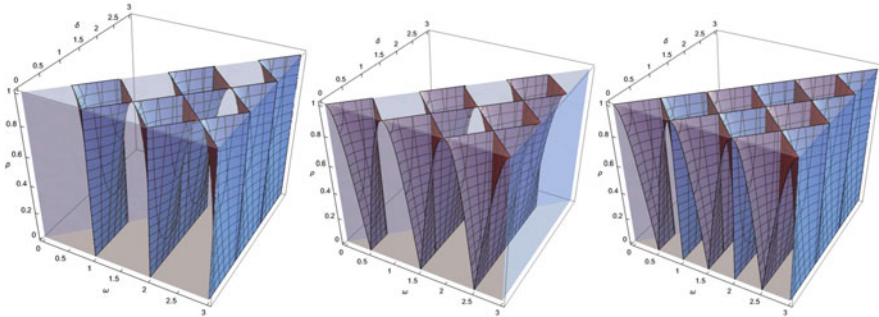


Fig. 4 The new first surfaces associated with trace $M = 2$ (light blue), trace $M = -2$ (light red), and the ensemble of them. Thanks to its symmetry, we only need to plot the part corresponding to non-negative values of δ and ϱ

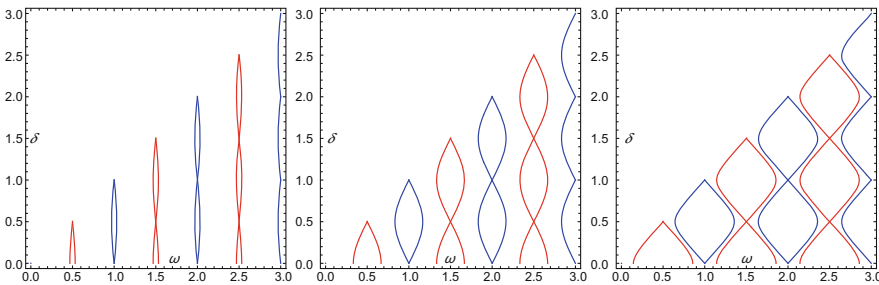


Fig. 5 From left to the right, sections for positive δ of the bifurcation set of Fig. 4 when $\varrho = 0.1$, $\varrho = 0.5$, and $\varrho = 0.9$. The resonance pockets become greater and greater as ϱ approaches 1. The shape and size of these pockets can be completely justified thanks to Theorem 1, by using the trivial factorizations of the analytical expressions for the surfaces trace $M = \pm 2$

Thus, thanks to Theorem 1, we have achieved to discover the hidden regularity of the bifurcation set, see Figs. 4 and 5. The resonance regions, when we take different sections with a fixed value of ϱ , appear organized in pockets around the lines $\omega = (2k - 1)/2$ and $\omega = k$, and there appear $2k - 1$ and $2k$ of them, respectively. They become wider and wider as $|\varrho|$ approaches the unity and degenerate into segments without area when $\varrho = 0$. Thus, this relative discrepancy ϱ between frequencies seems to play the most important role regarding the magnitude of resonance pockets.

4 Concluding Remarks

In this work, the study of Hill's equations with two-step potentials has been revisited, and a new approach based upon a suitable choice of new parameters has been shown to be very powerful, not only gaining in simplicity of the analysis, but also providing a deeper insight into the bifurcation set. The hidden regularity

of such a set has been unveiled, exhibiting new symmetries and periodicities. The local study of the highest co-dimension bifurcation points is now a simple task, to be done in a future work, where the remaining cases, namely the elliptic–parabolic configuration ($a > 0$, $b = 0$), and the elliptic–hyperbolic one ($a > 0$, $b < 0$) will also be addressed.

Acknowledgments This work has been realized thanks to Consejería de Economía y Conocimiento de la Junta de Andalucía (P12-FQM-1658 grant), Spanish Ministerio de Ciencia, Innovación y Universidades—Agencia Estatal de Investigación (MTM2016-77278-P (FEDER) and PGC2018-096265-B-I00 grants).

References

1. W. Magnus, S. Winkler, *Hill's Equations* (Wiley, New York, 1966)
2. I. Kovacic, R. Rand, S.M. Sah, Mathieu's equation and its generalizations: overview of stability charts and their features. *Appl. Mech. Rev.* **70**(1–22), 020822 (2018)
3. A.A. Burov, V.I. Nikonov, On the nonlinear Meissner equation. *Int. J. Nonlinear Mechanics* **110**, 26–32 (2019)
4. A. Markeev, Stability of an equilibrium position of a pendulum with step parameters. *Int. J. Nonlinear Mech.* **73**, 12–17 (2015)
5. R. de L. Kronig, W.G. Penney, Quantum mechanics in crystal lattices. *Proc. R. Soc. Lond.* **130**, 499–513 (1931)
6. S. Gan, M. Zhang, Resonance pockets of Hill's equations with two-step potentials. *SIAM J. Math. Anal.* **32**(3), 651–664 (2000)
7. H. Broer, M. Levi, Geometrical aspects of stability theory for Hill's equations. *Arch. Rational Mech. Anal.* **131**, 225–240 (1995)
8. H. Broer, C. Simó, Resonance tongues in Hill's equations: a geometric approach. *J. Differ. Equ.* **166**, 290–327 (2000)
9. Y. Yamanaka, N. Yamaoka, Oscillation and nonoscillation theorems for Meissner's equation. *Appl. Math. Comput.* **388**(1–13), 125526 (2021)

Bifurcation Studies of a Nonlinear Mechanical System Subjected to Multi-Frequency-Quasi-Periodic Excitations



K. Prabith and I. R. Praveen Krishna

1 Introduction

The engineering systems such as electronic circuits, vehicle suspensions, gears, and multi-spool gas turbines are often subjected to multi-frequency-quasi-periodic excitations during their operation period. The presence of nonlinearities in the system adds complexity to the analysis and makes the system response unpredictable sometimes. It requires an extensive nonlinear dynamic analysis of such systems to prevent their unwanted failure during the worse operating conditions. Generally, the numerical integration schemes are employed to solve the nonlinear differential equations representing the system [1]. However, it is very time-consuming for the multi-degree of freedom (DOF) models since all the transients need to die out for obtaining a steady-state response. Some researchers [2–4] have used the multi-harmonic balance method (MHBM) to acquire the frequency responses which is found to be very effective compared to numerical integrations. An alternating frequency-time (AFT) scheme [5] is incorporated with the MHBM for the efficient calculation of the Jacobian matrix. In addition to the calculation of periodic responses, the MHBM-AFT can be used for the tracking of quasi-periodic branches as well [6].

The response curves and their associated bifurcations can provide a clear picture of the system dynamics. Bifurcations can be identified by performing the stability analysis and then, checking the values of the Floquet exponents. The detection of bifurcation points is very important since it can cause dramatic changes in the response. For example, a limit point (LP) bifurcation can lead to a sudden jump in the response as the parameter is varied. The influence of parameters on the overall dynamics of the system is very significant, and it can result in different kinds

K. Prabith · I. R. Praveen Krishna (✉)

Indian Institute of Space Science and Technology, Thiruvananthapuram, India

of bifurcations. As a result, the designer has to be very cautious in selecting the system parameters. Establishing a bifurcation map for determining the boundaries of the dynamic regimes may assist the designers in the appropriate selection of parameters. It can be achieved by performing the parametric analysis and collecting all the detected bifurcations to plot the bifurcation map. Using the harmonic balance method (HBM), some authors [7–10] have performed the bifurcation tracking for single-frequency excitation problems. However, bifurcation studies for the multi-frequency-quasi-periodic excitation problems are rare in the literature.

Generally, the multi-frequency-quasi-periodic excitation problems are solved using numerical integration schemes. But, they are very time-consuming when the model is of large DOF. Later, the MHBMAFT technique has been introduced; however, it has some limitations when more than two-frequency excitations come into the picture. In such cases, the AFT procedure becomes cumbersome and its programming becomes complex. The time variational method (TVM) does not have such problems since it operates in the time domain only. However, it cannot solve the quasi-periodic problems directly, since the formulation of TVM is based on periodicity. As a result, it is extended to more than two-frequency excitation problems by expressing the governing equations in terms of a frequency that is the common divisor of the approximated frequency components [11]. Now, the problem becomes periodic and it can be solved using the TVM. Hence, in this paper, the TVM is employed for performing bifurcation studies of a mechanical system undergoing multi-frequency-quasi-periodic excitations.

2 Methodology Formulation

The governing differential equation of an N DOF, nonlinear mechanical system undergoing multi-frequency-quasi-periodic excitation can be expressed as,

$$\mathbf{M}\ddot{\mathbf{x}} + \mathbf{C}\dot{\mathbf{x}} + \mathbf{K}\mathbf{x} + \mathbf{f}_n(\mathbf{x}, t) = \mathbf{f}_{ext}(\omega_1, \omega_2, \dots, \omega_n, t) \quad (1)$$

where \mathbf{M} , \mathbf{C} , and \mathbf{K} are the mass, damping, and stiffness matrices respectively, of order $N \times N$. \mathbf{f}_{ext} and \mathbf{f}_n are the external and nonlinear force vectors respectively, of order $N \times 1$. $\dot{\mathbf{x}}$ and $\ddot{\mathbf{x}}$ are the first and second derivatives of \mathbf{x} with respect to time t . $\omega_1, \dots, \omega_n$ are the excitation frequencies that may be the irrational multiples of each other. As a result, the system response will include the linear combinations of all these frequencies and it will be quasi-periodic in nature. For analyzing such quasi-periodic systems, the periodic solution methodologies such as the harmonic balance method (HBM) and time variational method (TVM) cannot be useful. However, it can be made periodic by expressing the excitation frequencies in terms of their common divisor as given below,

$$\omega_0 = \frac{\tilde{\omega}_j}{p_j}, \quad j = 1, 2, \dots, n \quad p_j \in \mathbf{N} \quad (2)$$

where $\tilde{\omega}_j$ is the approximated value of ω_j obtained by approximating the irrational frequency ratios to rational. As a result, the response will be approximate and its accuracy is highly dependent on how close the approximated ratios are with the actual ones. By using the transformation $\tau = \omega_0 t$, Eq. (1) is modified as,

$$\omega_0^2 \mathbf{M} \mathbf{x}'' + \omega_0 \mathbf{C} \mathbf{x}' + \mathbf{K} \mathbf{x} + \mathbf{f}_n(\mathbf{x}, \tau) = \mathbf{f}_{ext}(\tau) \quad (3)$$

where \mathbf{x}' and \mathbf{x}'' are the first and second derivatives of \mathbf{x} with respect to τ . Now, Eq. (3) can be solved using the TVM by expressing the response, nonlinear function, and external force as,

$$\mathbf{x}(\tau) = \hat{\mathbf{X}} \cdot \chi(\tau) \quad \mathbf{f}_n(\tau) = \hat{\mathbf{F}}_n \cdot \chi(\tau) \quad \mathbf{f}_{ext}(\tau) = \hat{\mathbf{F}}_{ext} \cdot \chi(\tau) \quad (4)$$

where $\chi(\tau)$ is the basis function that may be a wavelet scaling function or a finite element shape function. $\hat{\mathbf{X}}$, $\hat{\mathbf{F}}_n$, and $\hat{\mathbf{F}}_{ext}$ are the displacement, nonlinear force, and external force matrices, respectively, of order $N \times N_p$, where N_p is the discrete-time points taken for the analysis [11]. By substituting Eq. (4) in Eq. (3) and following the Galerkin procedure, the resulting weak form residual is expressed as,

$$\begin{aligned} \mathbf{R}(\hat{\mathbf{x}}) = & [\omega_0^2(\mathbf{M} \otimes \mathbf{D}^{(2)}) + \omega_0(\mathbf{C} \otimes \mathbf{D}^{(1)}) + (\mathbf{K} \otimes \mathbf{D}^{(0)})] \hat{\mathbf{x}} \\ & + (\mathbf{I} \otimes \mathbf{D}^{(0)})(\hat{\mathbf{f}}_n(\hat{\mathbf{x}}) - \hat{\mathbf{f}}_{ext}) = 0 \end{aligned} \quad (5)$$

where $\hat{\mathbf{x}} = \text{vec}(\hat{\mathbf{X}})$, $\hat{\mathbf{f}}_n = \text{vec}(\hat{\mathbf{F}}_n)$, and $\hat{\mathbf{f}}_{ext} = \text{vec}(\hat{\mathbf{F}}_{ext})$. $\text{vec}(\cdot)$ is a function which stacks the columns of the matrix operated upon. \otimes is the Kronecker product and $\mathbf{D}^{(m)}$ are the differentiation matrices of order $m = 0, 1, 2$. The differentiation matrices are derived from the basis function and its expressions are given in Ref. [12]. The Newton–Raphson method is used to solve Eq. (5), and an arc-length continuation method is also incorporated to obtain the periodic unstable branches.

2.1 Stability Analysis

In this paper, the local stability of the solution points is determined using the Floquet theory [12]. For performing the analysis, the system is perturbed periodically from its equilibrium point and the resulting variational equation is converted into a quadratic eigenvalue problem by using the relation,

$$\epsilon(\tau) = e^{\lambda\tau} \phi(\tau) \quad (6)$$

where $\epsilon(\tau)$ is the periodic perturbation function. λ and $\phi(\tau)$ are the eigenvalues and eigenfunctions of the perturbed system, respectively. Now, by using the relation $\phi(\tau) = \hat{\Phi} \cdot \chi(\tau)$, the quadratic eigenvalue problem is expressed in the discrete-time domain and is solved for λ . Even though the solution process provides $2NN_p$ eigenvalues, the first $2N$ eigenvalues with the smallest imaginary parts in modulus will be useful for the stability analysis. The system is asymptotically stable when the real parts of those eigenvalues are negative and is unstable when at least one of them is positive.

3 Mathematical Model

In order to perform the nonlinear analysis, a Duffing oscillator undergoing multi-frequency excitation is utilized. The parameters of the model are listed in Table 1. Mainly two cases of external excitations are applied at the mass center: The first one is a two-frequency excitation and the latter is a three-frequency excitation. The excitation frequency ratios for the given model are expressed below,

$$\begin{aligned} \frac{\omega_1}{\omega_2} &= \sqrt{2} && \text{for case 1} \\ \frac{\omega_1}{\omega_2} &= \sqrt{2}, \quad \frac{\omega_1}{\omega_3} = 0.625 && \text{for case 2} \end{aligned} \tag{7}$$

Table 1 System parameters of the Duffing oscillator

Properties	Value
Mass (Kg)	m = 10
Damping (Ns/m)	c = 20
Stiffness (N/m)	k = 4000
<i>Nonlinear function</i>	
$f_n = \alpha x^3$	$\alpha = 0$ to 20000
<i>Excitation force</i>	
$f_{ext} = f_1 \cos(\omega_1 t) + f_2 \cos(\omega_2 t)$	$f_1 = 1000, f_2 = 1000,$
$f_{ext} = f_1 \cos(\omega_1 t) + f_2 \cos(\omega_2 t) + f_3 \cos(\omega_3 t)$	$f_1 = 1000, f_2 = 1000, f_3 = 1000$

4 Results and Discussions

4.1 Case 1: Two-frequency Excitation

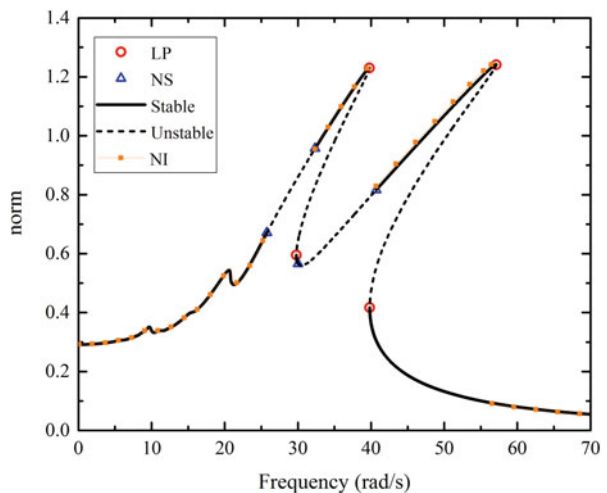
In order to employ the TVM, the irrational frequency ratio is approximated and the common divisor is calculated as given below,

$$\frac{\tilde{\omega}_1}{\tilde{\omega}_2} = \frac{10}{7} = 1.429 \approx \sqrt{2} \qquad \omega_0 = \frac{\tilde{\omega}_1}{10} = \frac{\tilde{\omega}_2}{7} \qquad (8)$$

The number of time points, N_p is taken as 1000 for the analysis. Figure 1 shows the stability diagram of the Duffing oscillator when nonlinear stiffness $\alpha = 10000$. In Fig. 1, the stable response is indicated by a solid line whereas the unstable part is shown by the dashed line. The stable part of the responses is validated using numerical integration (NI) and a good agreement is obtained, as shown in Fig. 1. Limit point (LP) and Neimark–Sacker (NS) bifurcations are observed in the system response, and they are represented using the circle and triangle markers, respectively.

The response is stable until $\omega = 25.76$ rad/s and then it undergoes NS bifurcation at $\omega = 25.76$ rad/s. It is identified by checking the Floquet exponents as shown in Fig. 2a. An NS bifurcation is detected when a pair of Floquet exponents crosses the imaginary axis as a pair of complex conjugates [7, 8]. Generally, an NS bifurcation indicates a transition from periodic to the quasi-periodic regime. However, in the case of quasi-periodic excitation problems, the response is already quasi-periodic. Hence, the NS bifurcation represents a transition from quasi-periodic to another quasi-periodic regime. It can be understood from Fig. 3, in which the motions before and after the NS bifurcation are obtained using numerical integration and are

Fig. 1 Stability diagram of the Duffing oscillator subjected to two-frequency excitations when $\alpha = 10000$



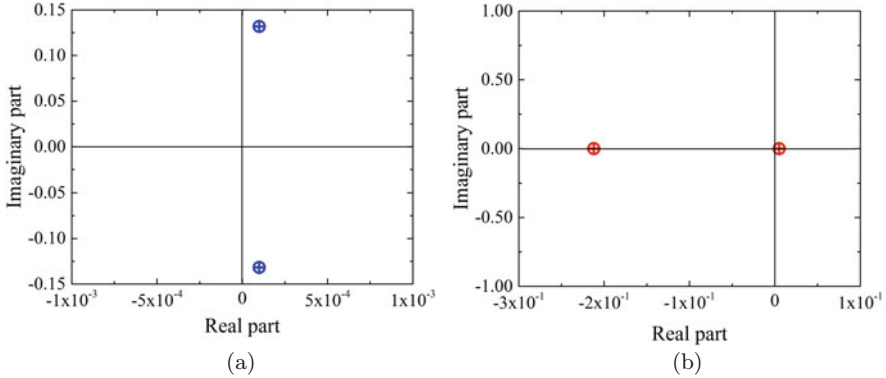


Fig. 2 Floquet exponents in the vicinity of NS and LP bifurcations. **(a)** NS at $\omega = 25.76$ rad/s. **(b)** LP at $\omega = 39.77$ rad/s

compared. Since the Poincaré maps of both motions are closed curves, the motions are said to be quasi-periodic in nature. Now, the fast Fourier transform (FFT) of the responses are analyzed to determine the frequency contents. It is found that the motion before the NS bifurcation contains the frequency components that are the linear combinations of the excitation frequencies. Hence, this kind of motion is predictable using the current solution method. However, the motion after the NS bifurcation includes certain frequency components that are not known before the methodology formulation. Hence, the determination of such a quasi-periodic branch is difficult using the proposed method, since the frequency components are a priori unknown.

Beyond the NS bifurcation point, the response is unstable until $\omega = 32.36$ rad/s. When the frequency is increased again, the response becomes stable in the range of $32.36 < \omega < 39.77$ rad/s. Later, a sudden jump is observed at $\omega = 39.77$ rad/s that indicates the occurrence of LP bifurcation. It is confirmed by checking the Floquet exponents as shown in Fig. 2b, where one of the Floquet exponents crossed the imaginary axis along the real axis. Similar to the first peak, NS and LP bifurcations are observed for the second peak as well.

In order to find the bifurcation map of NS bifurcations, a parametric analysis is conducted. Figure 4 shows the NS bifurcation tracking for the variation of nonlinear stiffness. Mainly, two NS boundaries are noticed and they are shown in Fig. 5. They represent the bifurcation map of NS bifurcations, inside which a new quasi-periodic regime exists. From Fig. 5, it is observed that the NS1 bifurcation disappears below $\alpha = 5670$ whereas the NS2 bifurcation continues to exist till $\alpha = 1115$. In addition, the co-existence of different quasi-periodic responses is also noticed in Fig. 5. The bifurcation map of LP bifurcations is not included in this paper.

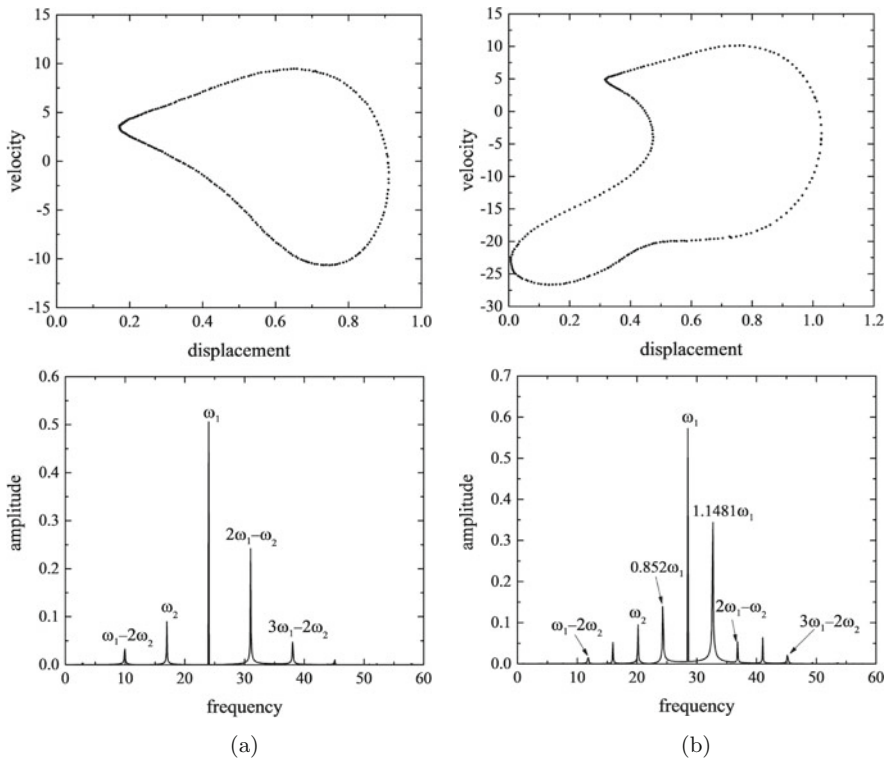


Fig. 3 Poincaré map and FFT of the responses, (a) before NS bifurcation, (b) after NS bifurcation

4.2 Case 2: Three-Frequency Excitation

The approximated frequency ratios and the common divisor of the three-frequency excitation problem can be obtained as,

$$\frac{\tilde{\omega}_1}{\tilde{\omega}_2} = \frac{10}{7} = 1.429 \approx \sqrt{2} \quad \frac{\tilde{\omega}_1}{\tilde{\omega}_3} = \frac{10}{16} = 0.625 \quad \omega_0 = \frac{\tilde{\omega}_1}{10} = \frac{\tilde{\omega}_2}{7} = \frac{\tilde{\omega}_3}{16} \quad (9)$$

The number of time points required to solve the problem is taken as 3000. An increase in the time points leads to an increase in the computation time as well. However, it is very less compared to the numerical integration schemes. In addition, the TVM does not require an alternate transformation between the time and frequency domains during the calculation of the Jacobian matrix as compared to the HBM. The Jacobian matrix can be directly obtained by taking the partial derivatives of the nonlinear function with respect to the state variables and calculating them at the time points. It makes the programming very simple even though the computation time is inferior to the HBM.

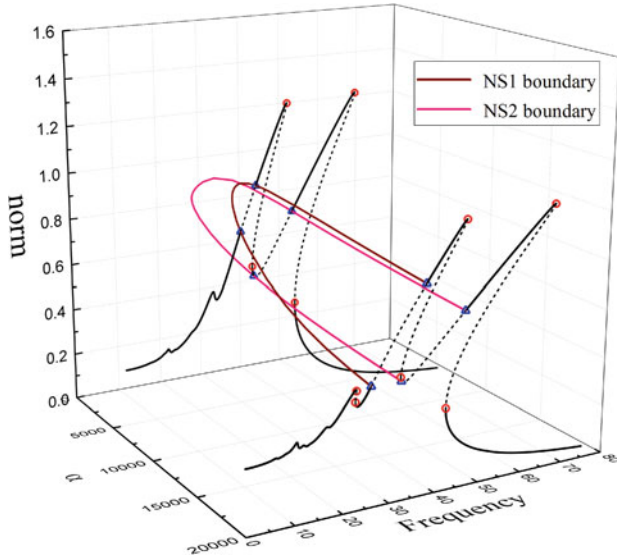


Fig. 4 NS bifurcation tracking for the variation of nonlinear stiffness

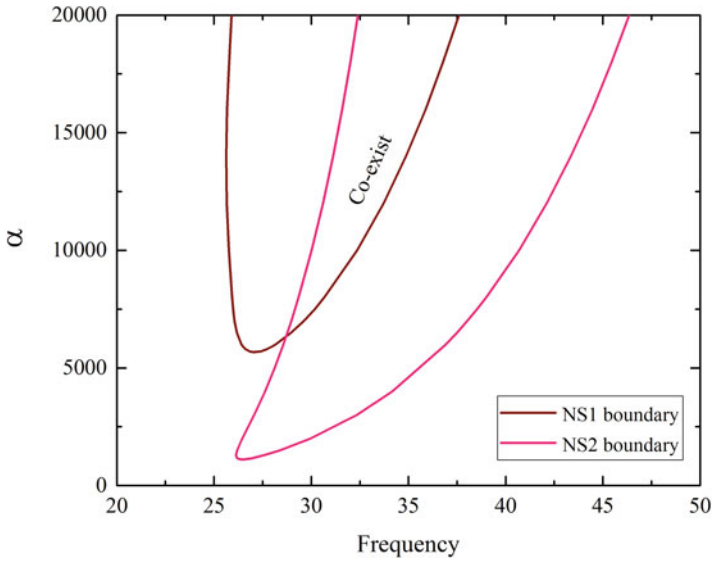


Fig. 5 Bifurcation map of NS bifurcation for the variation of nonlinear stiffness

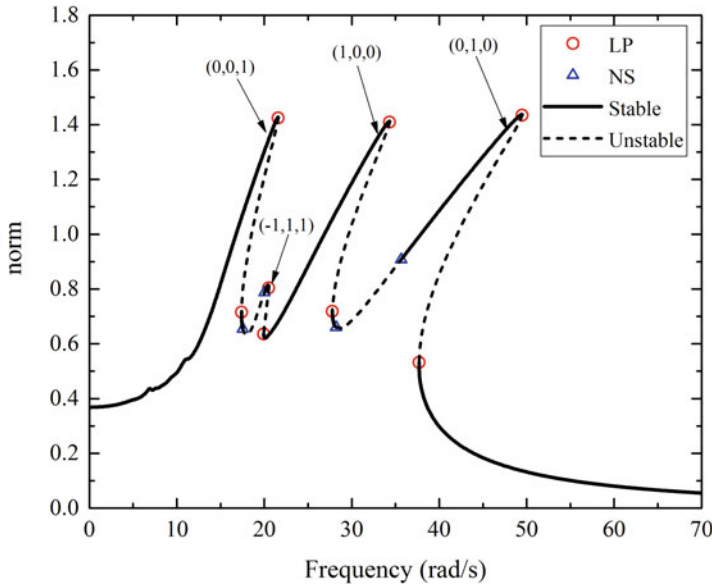


Fig. 6 Stability diagram of the Duffing oscillator subjected to three-frequency excitations when $f_1 = 1000$, $f_2 = 1000$, $f_3 = 1000$, and $\alpha = 5000$

The stability diagram of the three-frequency excitation problem is shown in Fig. 6. The system response contains the linear combinations of excitation frequencies which is generally expressed as $i\omega_1 + j\omega_2 + k\omega_3$. For simplicity, it can be denoted using (i, j, k) , where i, j , and k are integers. In Fig. 6, three principal resonance peaks are noticed corresponding to the three excitation frequencies. They are denoted as $(1,0,0)$, $(0,1,0)$, and $(0,0,1)$, respectively. In addition, a small peak is also observed which corresponds to the combination $(-1,1,1)$.

As observed earlier, LP and NS bifurcations are seen in the response at different frequencies. In order to determine the boundaries of NS bifurcation with respect to the excitation force, a parametric analysis is conducted and a bifurcation map is plotted as shown in Fig. 7. Mainly, three NS boundaries are noticed and its width is increasing as the magnitude of excitation force is increasing. The co-existence of different dynamic regimes is also possible at higher values of the excitation force.

5 Conclusions

In this paper, the bifurcation studies of a nonlinear mechanical system subjected to multi-frequency-quasi-periodic excitation are performed using the TVM. A Duffing oscillator undergoing two and three-frequency excitations is used for the analysis. An arc-length continuation method is incorporated with the TVM to track the

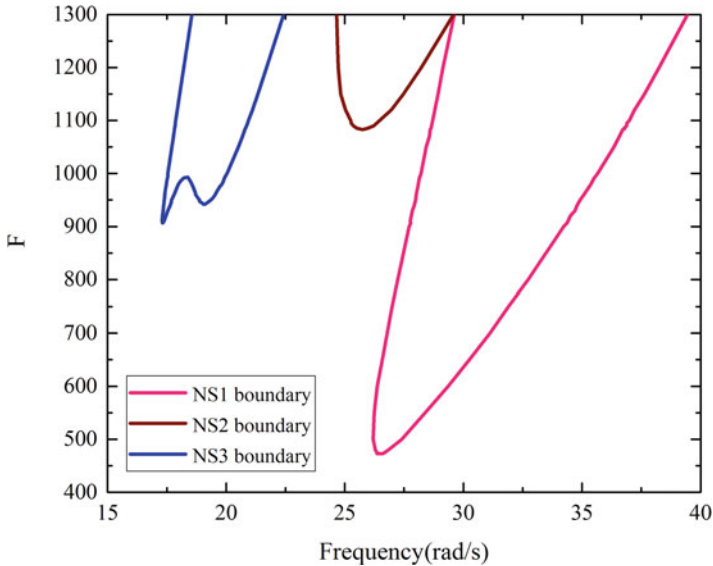


Fig. 7 Bifurcation map of NS bifurcation for the variation of excitation force

unstable periodic branches. The local stability of the solution points is determined using the Floquet theory, and the associated bifurcation points are detected using the Floquet exponents. From the analysis, it is observed that two bifurcations, namely LP and NS bifurcations are seen in the frequency response. The onset points of these bifurcations are mainly dependent on the values of the system parameters such as nonlinear stiffness and excitation force. In order to find the boundaries of NS bifurcations, a parametric analysis is conducted and detected the locations of NS bifurcation for different values of the system parameters. Then, a bifurcation map is plotted connecting all the detected NS bifurcation points. The bifurcation map represents the boundary where a transition from one motion to another happens. It will be useful for designers while selecting the parameters of the system. However, conducting the parametric analysis to determine the bifurcation map is very time-consuming. An efficient method will be performing the parametric continuation to track the path of bifurcation which is suggested as future work.

References

1. Z. Zhu, Z. Liu, Strange nonchaotic attractors of chua's circuit with quasiperiodic excitation. *Int. J. Bifurcation Chaos* **7**(01), 227–238 (1997)
2. M. Guskov, F. Thouverez, Harmonic balance-based approach for quasi-periodic motions and stability analysis. *J. Vib. Acoust.* **134**(3), 031003_1–11 (2012)
3. L. Hou, H. Chen, Y. Chen, K. Lu, Z. Liu, Bifurcation and stability analysis of a nonlinear rotor system subjected to constant excitation and rub-impact. *Mech. Syst. Signal Process.* **125**, 65–78 (2019)

4. C. Sun, Y. Chen, L. Hou, Steady-state response characteristics of a dual-rotor system induced by rub-impact. *Nonlinear Dyn.* **86**(1), 91–105 (2016)
5. T. Cameron, J.H. Griffin, An alternating frequency/time domain method for calculating the steady-state response of nonlinear dynamic systems. *J. Appl. Mech.* **56**(1), 149–154 (1989)
6. L. Peletan, S. Baguet, M. Torkhani, G. Jacquet-Richardet, Quasi-periodic harmonic balance method for rubbing self-induced vibrations in rotor–stator dynamics. *Nonlinear Dyn.* **78**(4), 2501–2515 (2014)
7. L. Xie, S. Baguet, B. Prabel, R. Dufour, Bifurcation tracking by harmonic balance method for performance tuning of nonlinear dynamical systems. *Mech. Syst. Signal Process.* **88**, 445–461 (2017)
8. T. Detroux, L. Renson, L. Masset, G. Kerschen, The harmonic balance method for bifurcation analysis of large-scale nonlinear mechanical systems. *Comput. Methods Appl. Mech. Eng.* **296**, 18–38 (2015)
9. T. Detroux, L. Renson, L. Masset, G. Kerschen, The harmonic balance method for bifurcation analysis of nonlinear mechanical systems, in *Nonlinear Dynamics*. Proceedings of the 33rd IMAC, A Conference and Exposition on Structural Dynamics, vol. 1 (Springer, Berlin, 2015), p. 65
10. B. Santhosh, S. Narayanan, C. Padmanabhan, Periodic response and bifurcations of a smooth and discontinuous oscillator by harmonic balance method. *Adv. Vib. Eng.* **12**(5), 401–412 (2013)
11. K. Prabith, I. Praveen Krishna, A time variational method for the approximate solution of nonlinear systems undergoing multiple-frequency excitations. *J. Comput. Nonlinear Dyn.* **15**(3) (2020)
12. T. Rook, An alternate method to the alternating time-frequency method. *Nonlinear Dyn.* **27**(4), 327–339 (2002)

Part VI
Rotating Systems

A Novel Balancing Method of the Rotor System Using Load Identification and FIR Filter-Based Force Estimation Technique



Shibo Zhao, Xingmin Ren, Kuan Lu, Yongfeng Yang, Lihui Li, and Chao Fu

1 Introduction

Excessive vibration of the rotor system must be solved in the process of aero-engine development. The rotor operated with stable condition is an important guarantee to reduce the vibration and improve the safety, reliability, and service life of aero-engine. A series of works have focused on the evaluations of the dynamic characteristics of rotor system [1–3]. Identifying the unbalance of rotor system is a key factor for balancing rotating machinery. Modal Balancing Method (MBM) [4] and Influence Coefficient Method (ICM) [5] are two classical methods used in rotor balancing field along with identification of unbalanced parameters with steady-state responses under the circumstances of a series of selected rotating speeds. Meanwhile, transient balancing methods [6, 7] during acceleration are also mentioned by some research with the condition of several test runs with trial weights. However, the balancing effect of MBM and ICM are easily affected by the factors that influence the condition of the rotational speed which cannot be ignored, such as rotational speed fluctuation and low-frequency noise in actual operation process. Meanwhile, the above two balancing methods require the rotor system to operate with constant rotational speed. There is no doubt that balancing without considering the condition of rotational speeds would make sense in field balancing.

Another disadvantage of conventional techniques of balancing is the requirement of a number of test runs, which is always not convenient for large rotating machines. The dynamic balancing method requires test run without trial weights [8, 9] is put forward and the central idea is to estimate the rotor unbalance without adding trial weights, which will omit the process of test run with trial weights, avoid problems

S. Zhao · X. Ren · K. Lu (✉) · Y. Yang · L. Li · C. Fu

Institute of Vibration Engineering, Northwestern Polytechnical University, Xi'an, People's Republic of China

e-mail: lukuan@nwpu.edu.cn

that trial weights may lead to, e.g., excessive vibration response of the structure, and make the balancing process more convenient and safe. The best approach of balancing without trial weights is identifying unbalance by optimized balancing technology [10].

In this chapter, we identify the unbalance of the rotor system by deducing the relationship between the unbalance excitation force and vibration response, which is the other effective way of balancing without trial weights [11]. As a matter of fact, some deterministic-stochastic techniques have been introduced to rotating dynamics for unknown input force estimation [12, 13]. An FIR filter-based force estimation technique is proposed in this chapter to eliminate the errors of the preliminary excitation forces calculated by the load identification technique, and then the unbalance parameters are identified by analyzing the amplitudes and phases of the excitation forces estimated by FIR filter. The proposed method does not require test runs with trial weights and succeeds in identifying the unbalance parameters without the limitation of the rotational speed conditions. The balancing results of double discs rotor system demonstrate the accuracy and the effectiveness of the proposed method.

TMM is introduced in Sect. 2, which is used to obtain the dynamical equations of rotor system, and then the balancing process of the proposed method is demonstrated in detail. The balancing procedure of double-disc rotor system is introduced in Sect. 3 to verify the accuracy of the proposed method with the conditions whatever variable rotational speeds or constant rotational speeds. The results of the whole balancing procedures are discussed in Sect. 4.

2 Modeling and Balancing Method

2.1 The TMM

The TMM is vastly utilized to derive the general equations of motion of the rotor machines because of its high precision in calculation and convenience to programming. As shown in Fig. 1, the TMM requires the shaft of the rotor system to be divided by the distribution of discs, and the rotor system with N discs is divided into $N + 1$ segments. Each segment consists of several sub-structures and different sub-structures corresponding to certain pattern of transfer matrices. When the physical parameters are given, these transfer matrices are determined.

By considering the boundary conditions at both ends of the shaft, the general motion equation of the rotor system can be obtained using the TMM as follows:

$$\mathbf{M}\ddot{\mathbf{U}}(t) + \mathbf{C}\dot{\mathbf{U}}(t) + \mathbf{K}\mathbf{U}(t) = \mathbf{F}(t) \quad (1)$$

where \mathbf{M} , \mathbf{C} , and \mathbf{K} are the mass matrix, damping matrix, and stiffness matrix of rotor system which are equivalent to the matrices of $4N \times 4N$, respectively.

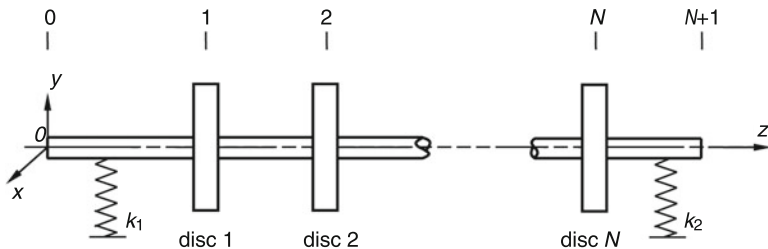


Fig. 1 Academic model of the rotor system with N discs

$\mathbf{U}(t)$, $\dot{\mathbf{U}}(t)$, $\ddot{\mathbf{U}}(t)$ are the displacement, velocity, and acceleration vectors, and each owns $4N$ elements, respectively. $\mathbf{F}(t)$ denotes the excitation forces corresponding to the mass unbalance on the discs, which owns $4N$ elements as well.

2.2 The Balancing Process of the Proposed Method

2.2.1 The Load Identification Technique

The unbalance excitation force is considered as the external input of the rotor system which is required to be calculated in the balancing procedure. The unbalance response of the rotor system is considered as the output that is produced by the external input and can be obtained by analyzing the general equation of motion of the rotor system. In the meantime, the Frequency Response Function (FRF) of the rotor system consists of the critical speed and modal parameters of the rotor system which can be obtained through the homogeneous solution of differential equation of rotor system when $\dot{\varphi} = \dot{\varphi}_c$, $\dot{\varphi}_c$ is the angular velocity corresponding to the critical rotational speed. In this way, the process of the load identification technique is to preliminarily calculate the unbalance excitation force of the rotor system by the unbalance response and the FRF of the rotor system.

The relationship between the input and output of the general system can be expressed as follows:

$$\mathbf{U}(\omega) = \mathbf{H}(\omega) \mathbf{F}(\omega) \tag{2}$$

where $[\mathbf{U}(\omega)]_{L \times 1}$ is the dynamic response vector, L represents the total number of measurement points of the dynamic response, $[\mathbf{F}(\omega)]_{P \times 1}$ is the unbalance excitation force vector, P represents the total number of the unbalance excitation force while $L \geq P$ in general, and $[\mathbf{H}(\omega)]_{L \times P}$ is the FRF of the system.

The relationship between modal FRF matrix and FRF matrix is as follows:

$$\mathbf{H}(\omega) = \Phi \mathbf{H}_q(\omega) \Phi^T$$

where $\mathbf{H}_q(\omega) = \text{diag}[\mathbf{H}_1(\omega), \mathbf{H}_2(\omega), \dots, \mathbf{H}_r(\omega), \dots, \mathbf{H}_N(\omega)]$, $\mathbf{H}_r(\omega)$ is the r th modal FRF of the system which can be expressed as:

$$\mathbf{H}_r(\omega) = \frac{1}{M_r(\omega_r^2 - \omega^2 + 2j\omega\omega_r\xi_r)}, \quad (r = 1, 2, \dots, N)$$

where M_r , ω_r , and ξ_r are the r th modal mass, modal frequency, and modal damping ratio of the system, respectively. ω is time-varying frequency.

For non-proportional damping system, the unbalance excitation force can be expressed as:

$$\mathbf{F}(\omega) = (\{\Phi^*\} \{\Phi^*\}^T)^{-1} \{\Phi^*\} \mathbf{M}_r (\omega_r^2 - \omega^2 + 2j\omega\omega_r\xi_r) (\{\Phi^T\} \{\Phi\})^{-1} \{\Phi^T\} \mathbf{U}(\omega) \quad (3)$$

where \mathbf{M}_r , ω_r , and ξ_r are the diagonal matrix composed of modal mass, modal frequency, and modal damping ratio, respectively. ω is the diagonal matrix composed of the time-varying frequency, $\{\Phi\} = \{[\phi]_1, [\phi]_2, \dots, [\phi]_r, \dots, [\phi]_N\}$, $[\Phi^*] = \{[\phi^*]_1, [\phi^*]_2, \dots, [\phi^*]_r, \dots, [\phi^*]_N\}$, ($r = 1, 2, \dots, N$) are the complex modal matrices of the rotor system, and $[\phi]_r$, $[\phi^*]_r$ are the complex modal vectors.

2.2.2 The FIR Filter-Based Force Estimation Technique

In the work discussed in this chapter, the FIR filter-based input estimation technique is used for the estimation of unbalance excitation force of a rotating machinery. The theory, algorithm, and implementation of the FIR filter system are systematically introduced by Hu [14]. The process of the FIR filter system is that the calculated force \mathbf{F} passes through the FIR filter system \mathbf{p} , so that the output \mathbf{F}' no longer contains the frequency component of $|f| > |f_c|$, but the component of $|f| \leq |f_c|$ remains lossless, where f_c is the cutoff frequency of filter. In the meantime, the finite length of \mathbf{p} and the input do not contain the feedback from the output to the input, making the FIR filter system always stable. The relationship between the input and output of FIR filter system in frequency domain while $z = e^{j\omega}$ is expressed as, $\mathbf{F}'(e^{j\omega}) = \mathbf{P}(e^{j\omega})\mathbf{F}(e^{j\omega})$, where $\mathbf{F}'(e^{j\omega})$, $\mathbf{F}(e^{j\omega})$, and $\mathbf{P}(e^{j\omega})$ are the Fourier transform of $\mathbf{F}'(n)$, $\mathbf{F}(n)$, and $\mathbf{p}(n)$, respectively. It is important to note that $\mathbf{F}(e^{j\omega})$ is equivalent to the unbalance excitation force $\mathbf{F}(\omega)$ calculated by Eq. 3.

2.2.3 The Unbalance Parameters Identification Procedure

The excitation force vectors consist of the unbalance excitation forces of the discs in time domain which are expressed as follows:

$$\begin{cases} [\mathbf{F}_x(t)]_{N \times 1} = [F_{x1}(t), F_{x2}(t), \dots, F_{xi}(t), \dots, F_{xN}(t)] \\ [\mathbf{F}_y(t)]_{N \times 1} = [F_{y1}(t), F_{y2}(t), \dots, F_{yi}(t), \dots, F_{yN}(t)] \end{cases}$$

where N is the number of discs. The elements of the excitation force vectors can be rewritten as follows:

$$\begin{cases} F_{xi}(t) = m_i e_i A(t) \cos [B_x(t) + \varphi_{ei}] \\ F_{yi}(t) = m_i e_i A(t) \sin [B_y(t) + \varphi_{ei}] \end{cases} \tag{4}$$

where $m_i e_i A(t)$ is the term of amplitude, m_i, e_i represent the mass and eccentricity of i th disc, $A = \sqrt{\dot{\varphi}^4(t) + \alpha^2}$, and $\dot{\varphi}(t), \alpha$ are the angular velocity and acceleration of the disc. $\dot{\varphi}(t) = \dot{\varphi}(t_0) + \alpha t$, $\dot{\varphi}(t_0)$ is the initial angular velocity. $B_x(t)$ and $B_y(t)$ are the terms of phases; $B_x(t) = \varphi(t) + \psi_x(t)$, $B_y(t) = \varphi(t) + \psi_y(t)$, and $\varphi(t)$ are the rotational angles of the disc; and $\varphi(t) = \varphi(t_0) + \dot{\varphi}(t)t + \frac{1}{2} \alpha t^2$ $\varphi(t_0)$ are the initial angles of the disc. Generally, we assume that $\varphi(t_0) = 0$, $\psi_x(t)$ and $\psi_y(t)$ can be expressed as follows:

$$\begin{cases} \psi_x(t) = \arctan -\frac{\alpha}{\dot{\varphi}^2(t)} \psi_x(t) \in (-\frac{\pi}{2}, 0) \\ \psi_y(t) = \arctan -\frac{\alpha}{\dot{\varphi}^2(t)} \psi_y(t) \in (-\frac{\pi}{2}, 0) \end{cases} \tag{5}$$

With regard to the rotor system operating with constant rotational speed, $\dot{\varphi}(t_0)$ is a fixed value, $\alpha = 0$, $\varphi(t) = \dot{\varphi}(t_0)t$, $\psi_x(t) = \psi_y(t) = 0$. Because the rotor system operates with variable rotational speeds, we assume $\dot{\varphi}(t_0) = 0$, α is a fixed value.

The corresponding amplitudes, phases, and time points of each data of the unbalance force estimated by FIR filter are given in Eqs. 4 and 5, and the unbalance parameters (eccentricities and azimuths) of the discs can be calculated by Eqs. 4 and 5.

Therefore, the whole balancing procedure is present as follows: the unbalance excitation forces of the discs are preliminarily obtained by Eq. 3. After that, the ultimate unbalance forces are estimated by FIR filter while the frequency component of $|f| \leq |\dot{\varphi}(t)/2\pi|$ remains lossless. The corresponding amplitudes, phases, and time points of the estimated unbalance forces are introduced in Eq. 4, and the unbalance parameters (eccentricities and azimuths) of the discs can be obtained by the amplitudes and phases of the corresponding unbalance forces estimated by FIR filter.

3 Simulation Balancing of the Double-Disc Rotor System

In this section, we will investigate the balancing effect and accuracy of the proposed method on double-disc rotor system. The unbalance parameters will be identified in the situation of constant rotational speed and variable rotational speeds. The displacements and the modal parameters of the model will be calculated first and will be regarded as the known quantities of the system. It should be noted that the displacements can be directly measured by displacement sensors in experiment. The modal parameters of the system can be obtained by finite element analysis [15]

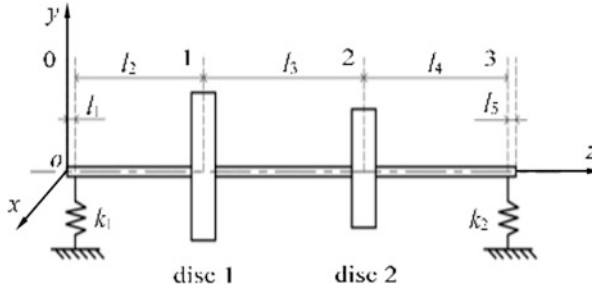


Fig. 2 Academic model of the rotor system with double discs

Table 1 Value of physical parameters of the double-disc rotor system

Unit	Parameter and value
Shaft	$l_1 = l_5 = 0.01$ m, $l_2 = 0.16$ m, $l_3 = 0.2$ m, $l_4 = 0.18$ m, Diameter of shaft: $d = 0.01$ m
Disc	Mass: $m_1 = 4$ kg, $m_2 = 2.5$ kg, diameter: $h_1 = 0.15$ m, $h_2 = 0.12$ m, Damping: $c_1 = c_2 = 20$ N·s/m Unbalance parameters: $e_1 \angle \varphi_1 = 4 \times 10^{-5}$ m $\angle 210^\circ$, $e_2 \angle \varphi_2 = 6 \times 10^{-5}$ m $\angle 180^\circ$
Young's modulus of elasticity	$E = 2.1 \times 10^{11}$ Pa
Stiffness of support	$k_1 = 5.5 \times 10^5$ N/m, $k_2 = 5.0 \times 10^5$ N/m

while the model can be established by analytic method. Liu et al. [16] obtained the modal parameters of the rotor system by software Samcef Rotor. For complex model, the combination of analytical and experimental modal analysis is an effective way to obtain modal parameters. After that, the validity of calculating the unbalance force and the estimation of the unbalance force by FIR filter will be analyzed. The unbalance parameters are identified through the estimated unbalance force. The results of the whole balancing procedures are discussed afterward.

The model of the isotropic double-disc rotor system is shown in Fig. 2 and the physical parameters of the rotor system are given in Table 1.

3.1 Calculating Transient Response and Modal Parameters by the TMM

In this section, the TMM is used to calculate the transient unbalance response and modal parameters of the double-disc rotor system.

For the double-disc rotor system shown in Fig. 2, **M**, **C**, **K** in Eq. 1 are equivalent to the matrices of 8×8 , **U**(*t*), **U**'(*t*), **U**''(*t*), **F**(*t*) are the column vectors each owns 8 elements. It should be noted that **U**(*t*) = [$x_1, \beta_1, y_1, \gamma_1, x_2, \beta_2, y_2, \gamma_2$], where $x_1, \beta_1, y_1, \gamma_1$ and $x_2, \beta_2, y_2, \gamma_2$ are the displacement and slope angle of the respective cross-section within the *XOZ* plane and *YOZ* plane of each disc, respectively.

Table 2 The modal parameters of the double-disc rotor system

Modal shape				Critical speed (r/min)		Modal frequency (rad/s)		Modal mass	
ϕ_1	$\phi_{11} = 1$	ϕ_2	$\phi_{12} = 1$	1st	809.59	1st	84.78	1st	6.64
	$\phi_{21} = 1.03$		$\phi_{22} = -1.57$	2nd	2832.32	2nd	296.60	2nd	10.16

Through multi modal analysis of the rotor system as shown in Eq. 1, the eigenvalues-based algorithms are introduced to obtain the eigenvalues and the eigenvectors, which are the modal frequency and the modal shapes of the rotor system, respectively. The modal frequency $\omega = [\omega_1, \omega_2]^T$, the modal shapes $\Phi_r = [\phi_{1r} \ \phi_{2r}]^T$, ($r = 1, 2$), and the modal mass matrix $M_r = \text{diag}[M_1, M_2]$ of double-disc rotor system are tabulated in Table 2. Meanwhile, the first critical speed is 809.59 r/min and the second critical speed is 2832.32 r/min. With regard to the isotropic double-discs rotor system, the modal shapes are the function of the displacements of x -axis of discs. Meanwhile, the modal shapes correspond to each order modal frequency.

3.2 The Balancing of the Rotor System with Constant Rotational Speed

The rotor system that operates at a speed of 600 r/min, 810 r/min, 1800 r/min, and 2832 r/min are analyzed to investigate and verify the balancing effect and accuracy of the proposed method. The balancing process of the constant rotational speed of 1800 r/min is selected as an example, the calculated forces of x -axis of the discs are preliminarily obtained by the steady-state displacements of x -axis of the discs and the modal parameters shown in Table 2. The unbalance forces estimated by FIR filter are shown in Fig. 3. The exact forces used to analyze the accuracy of the calculated forces of the discs are shown in Fig. 3.

Figure 3 shows that the main frequency of the calculated forces and the exact excitation forces are basically in agreement while the rotor system operates at 1800 r/min. Further, the amplitude of the calculated results are slightly less than the exact results; the relative errors of the amplitude between the exact and calculated forces of disc 1 and disc 2 in frequency domain are 1.07% and 6.32%, as shown in Fig. 3, respectively.

The unbalance parameters identified by the estimated steady-state forces and Eq. 4 are given in Table 3. By adding counterweight $3.85 \times 10^{-5} \text{ m} \angle 33.00^\circ$ and $5.39 \times 10^{-5} \text{ m} \angle 0.11^\circ$ to the corresponding discs of the rotor system, the x -axis displacements of each disc are greatly reduced at an operating speed of 1800 r/min as shown in Fig. 4. The results obtained and the balancing effect of the proposed method at rotor speeds of 600 r/min, 810 r/min, and 2832 r/min are given in Table 3.

It should be noted that the balancing effect at an operating speed of 810 r/min is worse than that at other rotational speeds. The preliminary conclusion of the

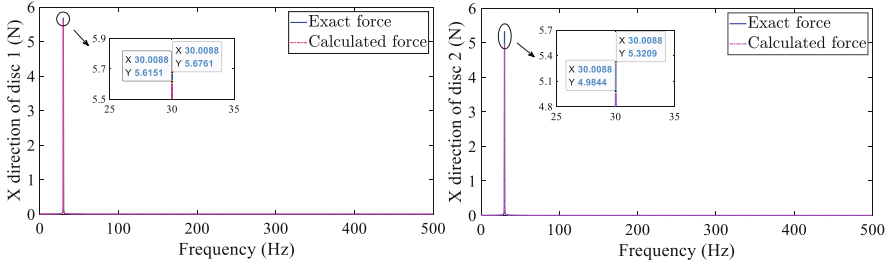


Fig. 3 Comparison of exact and calculated forces of x-axis in frequency domain

Table 3 The balancing results of the double discs rotor system

Rotational speed (r/min)	Disc	Identified unbalance parameters	Identified error	Amplitude (m)	
		Eccentricity/Azimuth	Eccentricity/Azimuth	Before/After balancing	Amplitude decrease
600	1	3.97×10^{-5} m/200.21°	0.75%/-9.79	6.40×10^{-5} / 9.00×10^{-6}	85.94%
	2	6.22×10^{-5} m/174.11°	3.67%/-5.89	6.70×10^{-5} / 1.00×10^{-5}	85.07%
810	1	2.75×10^{-5} m/173.14°	31.25%/-36.86	4.35×10^{-4} / 2.18×10^{-4}	49.89%
	2	5.85×10^{-5} m/159.25°	2.5%/-20.75	4.49×10^{-4} / 2.25×10^{-4}	49.89%
1800	1	3.85×10^{-5} m/213.00°	3.75%/3.00°	5.90×10^{-5} / 6.00×10^{-6}	89.83%
	2	5.39×10^{-5} m/180.11°	10.17%/0.11°	5.05×10^{-5} / 3.00×10^{-6}	94.06%
2832	1	3.89×10^{-5} m/206.35°	2.75%/-3.65°	2.31×10^{-4} / 2.30×10^{-5}	90.04%
	2	5.88×10^{-5} m/174.66°	2.00%/-5.34	4.68×10^{-4} / 4.60×10^{-5}	90.17%

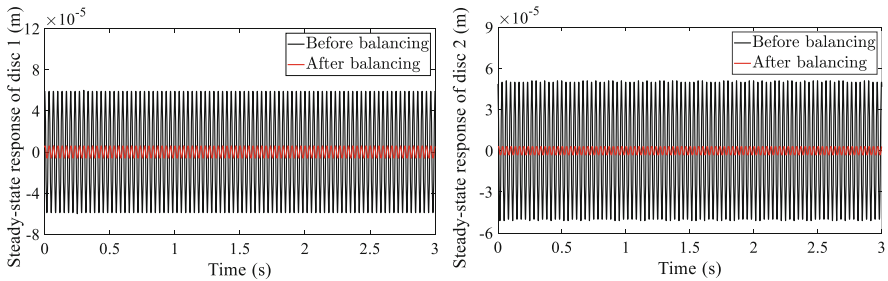


Fig. 4 X-axis displacements of the discs before and after balancing with the rotational speed of 1800 r/min

above phenomenon is that the calculated results of the excitation force while the rotor operating at 810r/min are not in line with the exact excitation force, while 810r/min is near the first critical speed. However, the balancing effect of operating at 600 r/min and 1800 r/min is better than that at 810 r/min. Therefore, the balancing rotational speed before and after the first critical speed should be selected for the secondary steady-stated balancing of the rotor system if the balancing accuracy near the first order fails to reach the required balancing standard.

3.3 The Balancing of the Rotor System with Variable Rotational Speeds

With regard to the variable rotational speeds with constant angular acceleration of 20 rad/s^2 , the x -axis calculated forces of the discs are preliminarily obtained by the x -axis transient displacements of the discs and the modal parameters. The unbalance forces estimated by FIR filter are shown in Fig. 5. The exact excitation forces used for analyzing the accuracy of the calculated forces of the discs are shown in Fig. 5.

The unbalance parameters derived by Eq. 4 and the unbalance forces estimated by FIR filter are tabulated in Table 4. The identified errors of the eccentricities are within 10% and the unbalance azimuths errors are much lower, which show a high precision in unbalance identification. By adding counterweight $3.85 \times 10^{-5} \text{ m} \angle 31.40^\circ$ and $5.61 \times 10^{-5} \text{ m} \angle 0.03^\circ$ to the corresponding discs, the deflections of each disc are greatly reduced in the whole operation as shown in Fig. 6. The transient response data before and after balancing are shown in Table 4.

The balancing results given in Tables 3 and 4 verify the effectiveness of the proposed method in balancing field of rotor system. The vibration responses of each disc are greatly reduced in the balancing procedures of different constant speeds, which show that the identifications of unbalance parameters are robust with respect to the constant rotational speed. However, Table 4 shows that the maximum amplitudes of the double discs rotor system decrease by more than 90% in general while balancing based on variable rotational speeds.

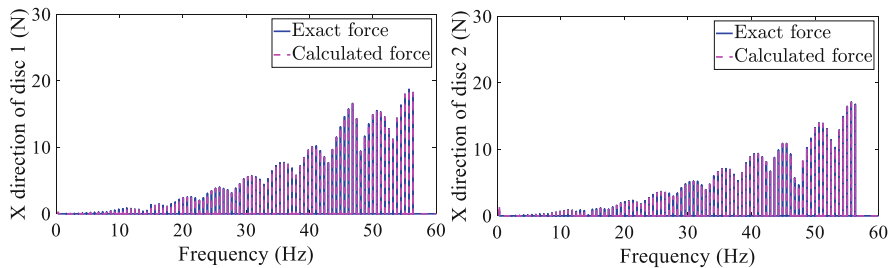


Fig. 5 Comparison of exact and calculated forces of x -axis in frequency domain

Table 4 The balancing results of the double discs rotor system

Disc	Identified unbalance parameters/Identified error		1st order		2nd order	
			Maximum deflection (m)	Maximum deflection decrease	Maximum deflection (m)	Maximum deflection decrease
	Eccentricity	Azimuth	Before/After balancing		Before/After balancing	
1	$3.85 \times 10^{-5} \text{ m}/3.75\%$	$211.40^\circ/1.40^\circ$	$5.06 \times 10^{-4}/2.88 \times 10^{-5}$	94.31%	$3.86 \times 10^{-4}/2.73 \times 10^{-5}$	92.93%
2	$5.61 \times 10^{-5} \text{ m}/6.50\%$	$180.03^\circ/0.03^\circ$	$5.23 \times 10^{-4}/2.95 \times 10^{-5}$	94.36%	$7.22 \times 10^{-4}/4.60 \times 10^{-5}$	93.63%

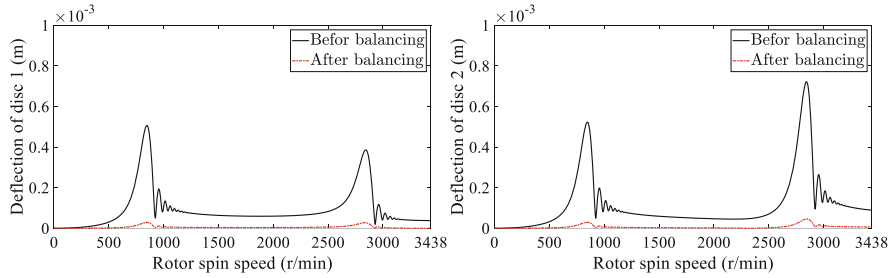


Fig. 6 Deflections of the discs before and after balancing

It can also be concluded from the balancing results that errors existed in the unbalance parameters identification. It is deduced that the main reason for the above errors is the difference in details between the excitation forces estimated by FIR filter and exact forces (Figs. 3 and 5). Specifically, the amplitudes of calculated forces are slightly smaller than that of exact forces. The reason for the above phenomena could be the calculation errors caused by the finite register length effects in the FIR filter process. However, using more memory units to reduce the calculation errors will undoubtedly increase the cost of hardware design, which is not cost-effective for the balancing process because of high precision of the proposed method before improvement.

4 Conclusions

In this chapter, we present a novel technique in the balancing field of rotating machinery. The proposed method is divided into two steps. The unbalance force is preliminarily calculated based on load identification technique and unbalance force is then estimated based on the FIR filter. Further, we identify the unbalance parameters (eccentricity and azimuth) by the unbalance force estimated by FIR filter. The numerical simulations have been carried out for a double-disc rotor system, while the unbalance parameters are identified based on both constant rotational speed and variable rotational speeds. The balancing results proves that the dynamic balancing process is robust with respect to the rotational speed.

The work discussed in this chapter is a part of an ongoing research on model-based techniques for unbalance identification, and this approach can be easily extended for unbalance identification of other rotor-disk-coupling bearing systems. A general approach for dynamic balancing with experimental verification remains as a future work.

References

1. Y.F. Yang, Q.Y. Wu, Y.L. Wang, et al., Dynamic characteristics of cracked uncertain hollow-shaft. *Mech. Syst. Signal Process.* **124**, 36–48 (2019)
2. H. Ma, J. Zeng, R.J. Feng, et al., Review on dynamics of cracked gear systems. *Eng. Fail. Anal.* **55**, 224–245 (2015)
3. K. Lu, Y.L. Jin, et al., Review for order reduction based on proper orthogonal decomposition of application in mechanical systems. *Mech. Syst. Signal Process.* **123**, 264–297 (2019)
4. R.E.D. Bishop, G.M.L. Gladwell, The vibration and balancing of an unbalanced flexible rotor. *J. Mech. Eng. Sci.* **1**(1), 66–77 (1959)
5. T.P. Goodman, A least-square method for computing balance corrections. *J. Eng. Ind. Trans. ASME* **86**(3), 273–279 (1964)
6. S.Y. Zhou, J.J. Shi, Optimal one-plane active balancing of rigid rotor during acceleration. *J. Sound Vib.* **249**(1), 196–205 (2001)
7. C. Yue, *Research on Multi-order and Multiplane Balancing of High Speed Rotor* (Northwestern Ploytechnical University, Xi'an, 2015)
8. R. Ramlau, J. Niebsch, Imbalance estimation without test masses for wind turbines. *J. Solar Energy Eng. Trans. ASME* **131**(1), 011010 (2009)
9. B. Xu, L. Qu, R. Sun, The optimization technique-based balancing of flexible rotors without test runs. *J. Sound Vib.* **238**(5), 877–892 (2000)
10. G.F. Bin, X.J. Li, J.G. Wu, et al., Virtual dynamic balancing method without trial weights for multi-rotor series shafting based on finite element model analysis. *J. Renew. Sustain. Energy* **6**, 042014 (2014)
11. S.B. Zhao, X.M. Ren, et al., A transient characteristic-based balancing method of rotor system without trail weights. *Mech. Syst. Signal Process.* **148**, 107117 (2021)
12. M.H. Lee, T.C. Chen, Intelligent fuzzy weighted input estimation method for the forces generated by an operating rotating machine. *Measurement* **44**(5), 917–926 (2011)
13. A. Shrivastava, A.R. Mohanty, Estimation of single plane unbalance parameters of a rotor-bearing system using Kalman filtering based force estimation technique. *J. Sound Vib.* **418**, 184–199 (2018)
14. G.S. Hu, *Digital Signal Processing: Theory, Algorithm and Implementation*, 3rd edn. (Tsinghua University Press, Beijing, 2012)
15. Y.E. Zhong, Y.Z. He, Z. Wang, et al., *Rotor Dynamics*, 1st edn. (Tsinghua University Press, Beijing, 1987)
16. G.Q. Liu, L.X. Zheng, Q. Mei, et al., Balancing method of flexible rotor across second order without trail weights. *Acta Aero. Astro. Sinica* **35**(4), 1019–1025 (2014)

Post-Resonance Backward Whirl Analysis of Accelerating Cracked Overhung Rotor System Using Fatigue Crack Model



Tariq Alzarooni and Mohammad A. AL-Shudeifat

1 Introduction

Overhung rotor systems (OH) cover a wide range of engineering applications including heavy-duty aerospace and industrial systems such as aircraft engines, helicopter shafts, turbines, compressors, pumps, and so forth. Therefore, the development of early fault detection methodologies to avoid catastrophic and costly breakdowns have captured interests of many researchers these days. The propagation of transversal breathing cracks in OH is one of the major causes of damages in rotordynamic systems. Accordingly, studying the dynamic behavior of cracked OH in presence of isotropic and anisotropic bearings forms the focal point of the subject paper.

Breathing crack has been studied by many researchers since 1980s. Many of those early researchers have mathematically modulated the breathing crack mechanism by simulating stiffness variation via using simple cosine function [1–19]. Alternatively, other researchers have employed Fourier series expansion to simulate breathing crack mechanism by varying moment of inertia for the cracked element [20–22]. Thus, an accurate time-varying stiffness matrix of the cracked element is simulated.

Whirl orbit analysis were also exploited for significant vibration characteristics that implies presence of breathing crack phenomena [2, 14, 15, 21–26]. In [2] the offset in pre-resonance synchronous forward whirl (FW) and backward whirl (BW) frequencies was reviewed in accounting for multiple transverse cracks. It was reported that their relevant frequencies and critical speeds decrease with increasing cracks depth. In [22] the quantity and shape of loops were reviewed against pre-

T. Alzarooni (✉) · M. A. AL-Shudeifat

Department of Mechanical Engineering, Khalifa University of Science and Technology, Abu Dhabi, UAE

e-mail: tariq.alzarooni@ku.ac.ae

resonance BW and FW frequencies. Pairs of subcritical peaks were noticed at $1/2^f$, $1/3^{rd}$, and $1/4^{th}$ of the fundamental critical zone. FW was observed to occur before BW at each subcritical peak. Whirl orbit shape has been deeply studied in [15] using numerical analysis followed by experimental verification. It was reported that pre-resonance backward whirl frequency precedes forward whirl frequency within subcritical speed range which is in line with the vast majority of published literature. Nevertheless, this contradicts finding reported in [22] where subcritical FW speed was inferred to precede subcritical BW speed. More details regarding shaft's whirl shifts, using breathing crack model, at near critical speed range is studied in [24]. It was reported that an interim whirl reversal from FW to BW precession occurs at near resonance speed which was mainly attributed to crack propagation. In [27], finite element program was employed to calculate complex eigenvalues of an overhung rotor having asymmetrical bearing support. It was reported that bearings asymmetry has resulted in two pre-resonance BW excitations corresponding to two BW critical speeds. The result of which was mainly attributed to unbalance excitations forces. By comparison, the second pre-resonance critical BW was not reported in isotropic bearings conditions. An extensive review was made in [28] to investigate the existence of the simultaneous pre-resonance FW and BW zones by employing complex modal analysis for JC rotor supported on anisotropic bearings with two disks. A parametric analysis was conducted by incorporating various unbalance force magnitude on two disks, their relative angular positions, bearings damping, and disk locations. It was reported that the capturing of simultaneous pre-resonance BW and FW motions is strongly affected by the aforementioned parameters. It was also reported that whirl transitions are followed by the sharp reduction in whirl amplitude. Similar studies have also been performed in [29] considering imbalanced OH rotor supported by flexible anisotropic bearings. The unbalance mass and shaft bow were simulated at different sections of the rotor which has resulted in simultaneous pre-resonance BW and FW precessions. Such phenomena were reported to be influenced by damping, bearing anisotropy, forcing functions magnitudes, and most importantly their angular orientations. The influence of gravity, friction, rotor-stator rub was studied on OH rotor in [30, 31] using 2-DOF lumped mass method. In [30], it was reported that the gravity factor influences Rotor Stiffening which results in a complete rubbing effect that induces shift in pre-resonance BW and FW frequencies. In [31] it was reported that pre-resonance BW zones expand with increased eccentricity and coefficient of friction. It was further instigated that frequency contents of pre-resonance BW zones increases due to increased stiffness as a result of high friction contact. The impact of snubbing effect on Pr-BW and Po-BW precessions that is associated with isotropic and anisotropic bearings conditions has been studied in [32] for transient rotor system. It was reported that Po-BW zones are more intensified and recurrent for active snubbing cases. Further, an important finding was also reported that BW frequency contents tend to be the same for all cases including Pr-BW and Po-BW although their excitations are reported at various rotary speeds. A few parametric studies have been performed recently in [33–36] by considering single- and double-

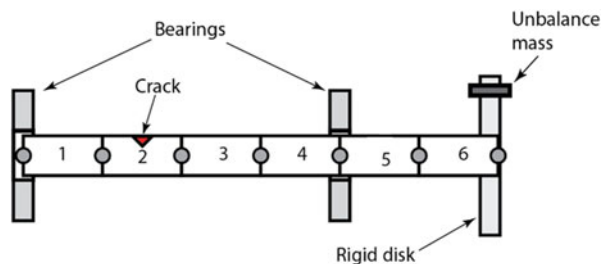
disk systems with an open crack model. An interesting findings were made in [36] on Pr-BW and Po-BW excitation zones using different angular acceleration rates backed up by experimental analysis.

In the present work, the novelty is pursued by analyzing BW and FW precession on cracked overhung rotor using breathing crack function and undergoing the transient operation. The overarching goal is to study the impact of conducting such parametric analysis on asymmetric rotor configuration such as OH rotor in view of directional whirl analysis particularly on Pr-BW and Po-BW precessions. The breathing crack model of [21, 22] is employed in the analysis considering the most realistic approach for resembling crack behavior. Finite Element Model is used to develop Linear-Time-Variant (LTV) equations of motions of the cracked rotor systems along with considering different bearings condition scenarios for accelerated overhung rotor system. The same will also be established on an intact-rotor system in order to map dynamical variation on the behavior of Pr-BW and Po-BW phenomena. In addition, the full spectrum analysis (FSA) is also employed to verify the existence of these BW zones.

2 Rotor Overhung System Modelling with Breathing Crack

The breathing crack model, proposed in [21, 22], is considered here where the transverse crack of depth h is normalized by the radius of the shaft R , which results in the non-dimensional representation of the crack depth $\mu = h/R$. The orientation of the unbalance force vector is located at angle β with respect to the crack opening direction assuming that the crack opening direction is initially in the negative y -axis. Detailed information of breathing crack functions can be found in [21, 22]. In the context of mathematical modeling using the FE approach, the element containing the breathing crack will undergo variation in stiffness based on centroidal and neutral axis changes during rotation, whereas the remaining elements shall be treated as intact shaft elements based on Euler-Bernoulli beam with circular cross-section. The following schematic plot shown in Fig. 1 represents the FE model of the considered overhung rotor. The crack is introduced into the second element and the transverse displacements is measured near to the second node from the right side of the shaft.

Fig. 1 Schematic diagrams of the finite element disk-shaft-bearing-rotor system



The rotor of mass M and length L is divided into finite N -elements with $N + 1$ nodes and the finite element equation of motion is described as follows:

$$\mathbf{M} \ddot{\vec{q}} + \hat{\mathbf{C}} \dot{\vec{q}} + \mathbf{K}(t) \vec{q} = \vec{\mathbf{F}}_u(t) + \vec{\mathbf{F}}_g \tag{1}$$

where \mathbf{M} , $\hat{\mathbf{C}}$ and \mathbf{K} are $4(N + 1) \times 4(N + 1)$ global mass, damping and gyroscopic, and stiffness matrices, respectively. \mathbf{M} resembles the addition of rotor’s classical mass and inertial matrices. $\hat{\mathbf{C}}$ resembles the rotor’s total gyroscopic and proportional damping matrices as $\hat{\mathbf{C}} = \Omega(t) \mathbf{G} + \mathbf{C}$, where $\Omega(t)$ is rotor’s angular speed and \mathbf{C} is a proportional damping matrix obtained via $\mathbf{C} = \gamma \mathbf{M} + \zeta \mathbf{K}$ where $\gamma = 0.0005 \text{ s}^{-1}$ and $\varepsilon = 0.00005 \text{ s}$. More details regarding mass, stiffness, and gyroscopic matrices formulation can be found in [37, 38]. The overall system unbalance force vector $\vec{\mathbf{F}}_u(t)$ has a size of $4(N + 1) \times 1$. For the shaft angular displacement and velocity $\theta(t) = \alpha t^2/2$ and $\Omega(t) = \alpha t$, respectively, the unbalance force vector will have two components at the i -th node, where they are added according to the following relations:

$$f_i = [f_i^u \quad f_i^v \quad 0 \quad 0] \tag{2}$$

$$f_i^u(t) = me\alpha^2 t^2 \cos(\alpha t^2/2 + \beta) + me\alpha \sin(\alpha t^2/2 + \beta) \tag{3}$$

$$f_i^v(t) = me\alpha^2 t^2 \sin(\alpha t^2/2 + \beta) - me\alpha \cos(\alpha t^2/2 + \beta) \tag{4}$$

where the product me represents the unbalance (m is the unbalance mass, e unbalance mass eccentricity), and β is the orientation angle of the unbalance force vector with respect to the transversal crack direction. Therefore, the elements of $\mathbf{F}_u(t)$ at the node corresponding to the disc location are given in Eqs. (3 and 4), while other nodal unbalance forces are set equal to zero. The gravity force vector is also included in \mathbf{F}_g . Bearings were included in the model through the addition of stiffness and damping at the corresponding nodes.

The cracked element stiffness matrix of the cracked element with a breathing crack model is obtained as in [35] as:

$$\mathbf{k}(t) = \frac{E}{l^3} \begin{bmatrix} 12I_{\bar{Y}}(t) & 12I_{\bar{X}\bar{Y}}(t) & -6I_{\bar{X}\bar{Y}}(t) & 6I_{\bar{Y}}(t) & -12I_{\bar{Y}}(t) & -12I_{\bar{X}\bar{Y}}(t) & -6I_{\bar{X}\bar{Y}}(t) & 6I_{\bar{Y}}(t) \\ 12I_{\bar{X}\bar{Y}}(t) & 12I_{\bar{X}}(t) & -6I_{\bar{X}}(t) & 6I_{\bar{X}\bar{Y}}(t) & -12I_{\bar{X}\bar{Y}}(t) & -12I_{\bar{X}}(t) & -6I_{\bar{X}}(t) & 6I_{\bar{X}\bar{Y}}(t) \\ -6I_{\bar{X}\bar{Y}}(t) & -6I_{\bar{X}}(t) & 4I_{\bar{X}}^2(t) & -4I_{\bar{X}\bar{Y}}^2(t) & 6I_{\bar{X}\bar{Y}}(t) & 6I_{\bar{X}}(t) & 2I_{\bar{X}}^2(t) & -2I_{\bar{X}\bar{Y}}^2(t) \\ 6I_{\bar{Y}}(t) & 6I_{\bar{X}\bar{Y}}(t) & -4I_{\bar{X}\bar{Y}}^2(t) & 4I_{\bar{Y}}^2(t) & -6I_{\bar{Y}}(t) & -6I_{\bar{X}\bar{Y}}(t) & -2I_{\bar{X}\bar{Y}}^2(t) & 2I_{\bar{Y}}^2(t) \\ -12I_{\bar{Y}}(t) & -12I_{\bar{X}\bar{Y}}(t) & 6I_{\bar{X}\bar{Y}}(t) & -6I_{\bar{Y}}(t) & 12I_{\bar{Y}}(t) & 12I_{\bar{X}\bar{Y}}(t) & 6I_{\bar{X}\bar{Y}}(t) & -6I_{\bar{Y}}(t) \\ -12I_{\bar{X}\bar{Y}}(t) & -12I_{\bar{X}}(t) & 6I_{\bar{X}}(t) & -6I_{\bar{X}\bar{Y}}(t) & 12I_{\bar{X}\bar{Y}}(t) & 12I_{\bar{X}}(t) & 6I_{\bar{X}}(t) & -6I_{\bar{X}\bar{Y}}(t) \\ -6I_{\bar{X}\bar{Y}}(t) & -6I_{\bar{X}}(t) & 2I_{\bar{X}}^2(t) & -2I_{\bar{X}\bar{Y}}^2(t) & 6I_{\bar{X}\bar{Y}}(t) & 6I_{\bar{X}}(t) & 4I_{\bar{X}}^2(t) & -4I_{\bar{X}\bar{Y}}^2(t) \\ 6I_{\bar{Y}}(t) & 6I_{\bar{X}\bar{Y}}(t) & -2I_{\bar{X}\bar{Y}}^2(t) & 2I_{\bar{Y}}^2(t) & -6I_{\bar{Y}}(t) & -6I_{\bar{X}\bar{Y}}(t) & -4I_{\bar{X}\bar{Y}}^2(t) & 4I_{\bar{Y}}^2(t) \end{bmatrix} \tag{5}$$

The cross-sectional moments of area $I_{\bar{X}}(t)$, $I_{\bar{Y}}(t)$ and $I_{\bar{X}\bar{Y}}(t)$ are calculated using the breathing functions given in [21, 22].

The rotordynamic transient whirl response is obtained by the numerical simulation based on a constant angular acceleration rate. The resultant whirl amplitude is calculated from $z = \sqrt{u^2 + v^2}$ at the second node in the FE model where u and v represent the horizontal and vertical vibration whirl amplitudes, respectively. In addition, both isotropic and anisotropic bearing stiffness conditions are considered in the analysis. The ratio of the vertical stiffness k_{yy} to the horizontal stiffness k_{xx} in the bearings is expressed as $\rho = k_{yy}/k_{xx}$.

3 Simulation Results and Discussion

Bearing anisotropy and gyroscopic factors are well established in the literature to have impact on Pre-resonance Backward Whirl (Pr-BW) of any typical rotor system. The influence of the same on the recently discovered Post-Resonance Backward Whirl (Po-BW) in [33] for accelerated single and double disk rotor system is yet to be demonstrated in accelerated overhung rotor system along with using breathing crack function. Therefore, the influence of bearings anisotropy, gravity force, and the gyroscopic effect on the Po-BW is first studied here for the crack-free (intact) overhung rotor system. In Fig. 2, VCP approach is used to capture these Po-BW zones at various angular acceleration rates of intact overhung rotor. The description of full system in Fig. 2a is associated with incorporation of the gyroscopic, gravity, and bearings anisotropy effects. It is clear that there are substantial changes in the Po-BW zones for the gyroscopic-free system in Fig. 2b and the gravity-free and gyroscopic-free system in Fig. 2c if compared with full system. However, there are hardly any changes on Po-BW zones for gyroscopic-free in Fig. 2b, and gyroscopic and gravity-free in Fig. 2c plots. Therefore, it can be concluded that the Po-BW for the intact overhung rotor system is most likely affected by the bearing anisotropy, gyroscopic effect, and the angular acceleration rate rather than the gravity effect.

Nevertheless, it is observed that Pr-BW precession does not appear in crack-free simulation for all range of rotor's angular acceleration rates. The influence of breathing crack propagation at $\alpha = 25 \text{ rad/s}^2$ on the Po-BW excitation for isotropic and anisotropic bearings conditions is addressed in Fig. 3a and Fig. 3b, respectively. The gyroscopic effect is also incorporated in the model considering its evident impact on crack-free rotor as highlighted in the previous context. It is interesting to point out that for the case of isotropic supports ($\rho = 1$), the appearance of breathing cracks excites both Pr-BW and Po-BW zones where their recurrence and extent are strongly affected at higher crack depths. A nearly similar findings have been reached for anisotropic bearings case ($\rho = 7$) in terms of intensity and recurrence of Pr-BW and Po-BW zones at high crack depth ratio; however, more Po-BW recurrence is captured at low crack depth ratio range. An important insight is that this special characteristic of Po-BW zones can be utilized to distinguish between the impact of bearing anisotropy, and crack propagation in the rotor system.

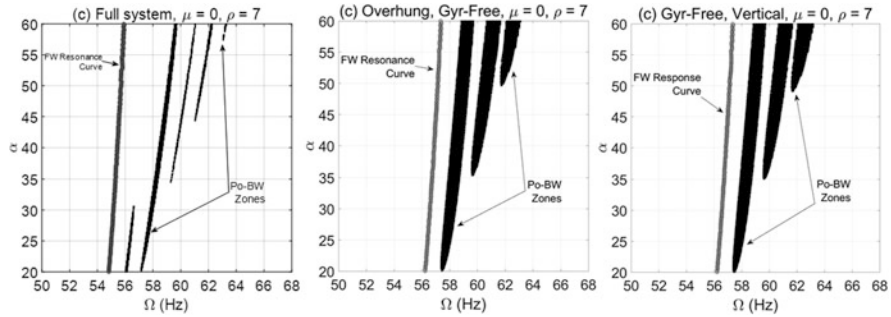


Fig. 2 Po-BW zones of rotational speeds at varying angular acceleration rate of overhung intact rotor system with anisotropic bearings including gravity and gyroscopic effects in (a); gyroscopic-free system including gravity effect in (b); and gravity-free and gyroscopic-free system in (c)

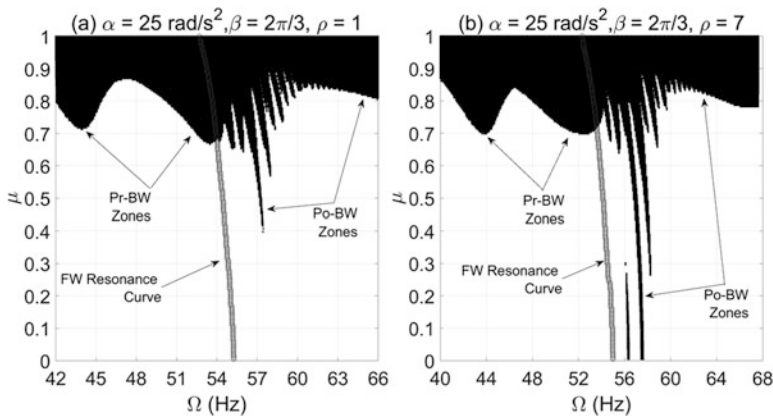


Fig. 3 BW zones of rotational speeds at $\alpha = 25 \text{ rad/s}^2$ of the cracked overhung rotor system with isotropic bearings in (a) and anisotropic bearings in (b)

Analysis of rotor behavior at higher angular acceleration rate of $\alpha = 50 \text{ rad/s}^2$ for isotropic and anisotropic bearing conditions is shown in Fig. 4a and Fig. 4b, respectively, where the gravity and gyroscopic effects are still incorporated. It is observed that more or less similar profile of Pr-BW is captured, however with slightly more intensity for anisotropic bearings case ($\rho = 7$). Nevertheless, for Po-BW it is observed that more recurrence is captured which can be solely attributed to increased rotor acceleration rate.

One important finding, which is common for all cases, is that the transition from Pr-BW to Po-BW is swept through the fundamental FW resonance curve as shown in Fig. 3 and Fig. 4. The zones of Po-BW are further investigated using FSA plots for anisotropic bearings conditions chosen at $\mu = 0.69$ from Fig. 3 and Fig. 4. Accordingly, the FSA plots for the whirl response accurately captures and verifies the Po-BW zones in the whirl response for a cracked overhung rotor as illustrated

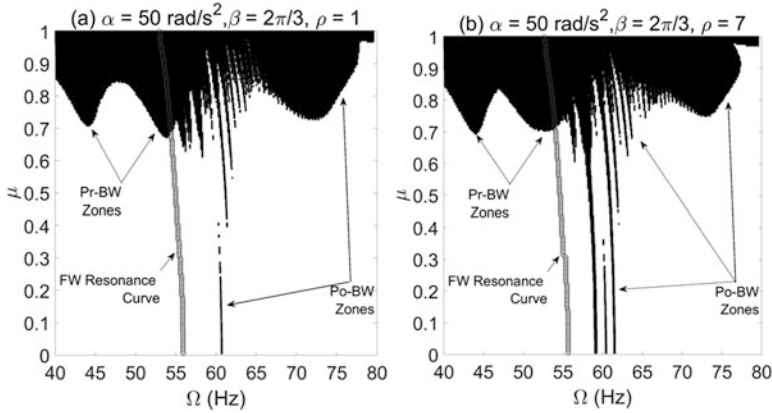


Fig. 4 BW zones of rotational speeds at $\alpha = 50 \text{ rad/s}^2$ of the cracked overhung rotor system with isotropic bearings in (a) and anisotropic bearings in (b)

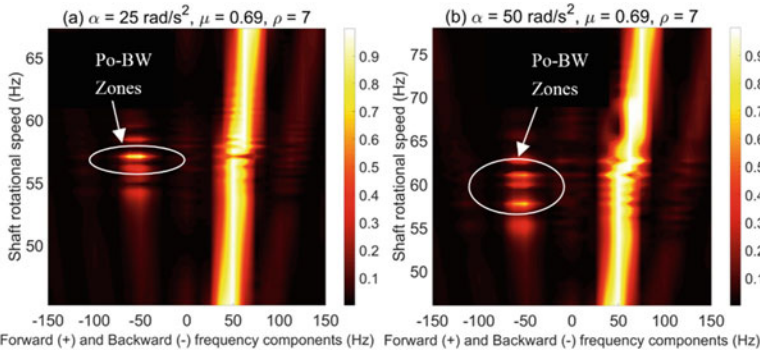


Fig. 5 FSA plot for cracked OH rotor at $\alpha = 25 \text{ rad/s}^2$ (a), and at $\alpha = 50 \text{ rad/s}^2$ (b)

in Fig. 5. For instance, in the case of $\alpha = 25 \text{ rad/s}^2$, Po-BW frequency zones are observed to be in the range of 55–8.5 Hz according to Fig. 5a of FSA plot. This confirms findings obtained via whirl response plot for Po-BW zones of Fig. 5b at $\mu = 0.69$ circa. Similarly, Po-BW frequencies are observed to be in the range of 56–63 Hz for $\alpha = 50 \text{ rad/s}^2$ according to the FSA plot in Fig. 5b. This confirms findings obtained via whirl plot of Fig. 4b at roughly similar crack depth ratio.

4 Conclusions

The BW phenomenon is studied here in accelerated intact and cracked overhung rotor systems using a breathing crack model. The study is purely based on numerical simulation using FEM equations of motion for startup rotor operation. The time-

varying stiffness matrix of the cracked element was superimposed in the FE model to simulate the breathing behavior of the crack. The obtained linear-time-varying EOMs were numerically integrated to compute the whirl response of the cracked rotor system during startup operation. Whirl behavior is analyzed in the range of the critical FW speed zones using VCP and FSA plots. For the intact rotor system with anisotropic bearings, it was found that Po-BW precession is substantially affected by gyroscopic effect. However, it was also found that the whirl behavior is independent of gravity. For the cracked overhung rotor system with breathing crack model, a new type of BW, which has been named as Po-BW in recent literature, was captured at supercritical speed zone that is centered about the minima of critical FW resonance and subsequent local peaks. These zones are found to be affected by bearing anisotropy, rotor angular acceleration rate, and crack depth. The effectiveness of FSA in capturing these Po-BW zones were also demonstrated. This brings about the high potentiality of using FSA as a tool for capturing these phenomena that could certainly help advance vibration health monitoring regime for accelerated rotor system.

References

1. B. Grabowski, The vibrational behaviour of a rotating shaft containing a transverse crack. *Dyn. Rotors.*, 423–465 (1984)
2. D. Gayen, D. Chakraborty, R. Tiwari, Finite element analysis for a functionally graded rotating shaft with multiple breathing cracks. *Int. J. Mech. Sci.* **134**(June), 411–423 (2017)
3. H. Khorrami, S. Rakheja, R. Sedaghati, Vibration behavior of a two-crack shaft in a rotor disc-bearing system. *Mech. Mach. Theory* **113**, 67–84 (2017)
4. M.J. Gómez, C. Castejón, J.C. García-Prada, Crack detection in rotating shafts based on 3 × energy: Analytical and experimental analyses. *Mech. Mach. Theory* **96**, 94–106 (2016)
5. A.A. Cavalini, L. Sanches, N. Bachschmid, V. Steffen, Crack identification for rotating machines based on a nonlinear approach. *Mech. Syst. Signal Process.* **79**, 72–85 (2016)
6. Z. Kulesza, J.T. Sawicki, Damping by parametric excitation in a set of reduced-order cracked rotor systems. *J. Sound Vib.* **354**, 167–179 (2015)
7. Z. Kulesza, Dynamic behavior of cracked rotor subjected to multisine excitation. *J. Sound Vib.* **333**(5), 1369–1378 (2014)
8. R. Toni Liong, C. Proppe, Application of the cohesive zone model for the evaluation of stiffness losses in a rotor with a transverse breathing crack. *J. Sound Vib.* **332**(8), 2098–2110 (2013)
9. R. Ricci, P. Pennacchi, Discussion of the dynamic stability of a multi-degree-of-freedom rotor system affected by a transverse crack. *Mech. Mach. Theory* **58**, 82–100 (2012)
10. M.-C. Wu, S.-C. Huang, Vibration and crack detection of a rotor with speed-dependent Bearings. *Int. J. Mech. Sci.* **40**(6), 545–555 (1998)
11. D.J. Han, Vibration analysis of periodically time-varying rotor system with transverse crack. *Mech. Syst. Signal Process.* **21**(7), 2857–2879 (2007)
12. J.J. Sinou, B. Faverjon, The vibration signature of chordal cracks in a rotor system including uncertainties. *J. Sound Vib.* **331**(1), 138–154 (2012)
13. J.T. Sawicki, M.I. Friswell, Z. Kulesza, A. Wroblewski, J.D. Lekki, Detecting cracked rotors using auxiliary harmonic excitation. *J. Sound Vib.* **330**(7), 1365–1381 (2011)
14. L. Cheng, N. Li, X.F. Chen, Z.J. He, The influence of crack breathing and imbalance orientation angle on the characteristics of the critical speed of a cracked rotor. *J. Sound Vib.* **330**(9), 2031–2048 (2011)

15. M.A. Al-Shudeifat, E.A. Butcher, C.R. Stern, General harmonic balance solution of a cracked rotor-bearing-disk system for harmonic and sub-harmonic analysis: Analytical and experimental approach. *Int. J. Eng. Sci.* **48**(10), 921–935 (2010)
16. J.J. Sinou, Detection of cracks in rotor based on the $2\times$ and $3\times$ super-harmonic frequency components and the crack-unbalance interactions. *Commun. Nonlinear Sci. Numer. Simul.* **13**(9), 2024–2040 (2008)
17. J.J. Sinou, A.W. Lees, A non-linear study of a cracked rotor. *Eur. J. Mech. A/Solids* **26**(1), 152–170 (2007)
18. J.J. Sinou, Effects of a crack on the stability of a non-linear rotor system. *Int. J. Non. Linear. Mech.* **42**(7), 959–972 (2007)
19. J.J. Sinou, A.W. Lees, The influence of cracks in rotating shafts. *J. Sound Vib.* **285**(4–5), 1015–1037 (2005)
20. C. Guo, M.A. Al-Shudeifat, J. Yan, L.A. Bergman, D.M. McFarland, E.A. Butcher, Stability analysis for transverse breathing cracks in rotor systems. *Eur. J. Mech. A/Solids* **42**, 27–34 (2013)
21. C. Guo, M.A. Al-Shudeifat, J. Yan, L.A. Bergman, D.M. McFarland, E.A. Butcher, Application of empirical mode decomposition to a Jeffcott rotor with a breathing crack. *J. Sound Vib.* **332**(16), 3881–3892 (2013)
22. M.A. Al-Shudeifat, E.A. Butcher, New breathing functions for the transverse breathing crack of the cracked rotor system: Approach for critical and subcritical harmonic analysis. *J. Sound Vib.* **330**(3), 526–544 (2011)
23. Q. Han, J. Zhao, W. Lu, Z. Peng, F. Chu, Steady-state response of a geared rotor system with slant cracked shaft and time-varying mesh stiffness. *Commun. Nonlinear Sci. Numer. Simul.* **19**(4), 1156–1174 (2014)
24. O.S. Jun, M.S. Gadala, Dynamic behavior analysis of cracked rotor. *J. Sound Vib.* **309**(1–2), 210–245 (2008)
25. A.K. Darpe, K. Gupta, A. Chawla, Transient response and breathing behaviour of a cracked Jeffcott rotor. *J. Sound Vib.* **272**(1–2), 207–243 (2004)
26. A.D. Nembhard, J.K. Sinha, A. Yunusa-Kaltungo, Experimental observations in the shaft orbits of relatively flexible machines with different rotor related faults. *Meas. J. Int. Meas. Confed.* **75**, 320–337 (2015)
27. O.J. Bearings, W. Lund, K.K. Thomsen, T. Technical, Forward and backward critical speeds and forced response of an overhung rotor with asymmetrical bearing supports, no. December, 1993
28. J.M. Dias, R.J. Allemang, Some insights into the simultaneous forward and backward whirling of rotors. *Proc. Int. Modal Anal. Conf. – IMAC 2*, 1257–1263 (2001)
29. A. Muszynska, Forward and backward precession of a vertical anisotropically supported rotor. *J. Sound Vib.* **192**(1), 207–222 (1996)
30. E. Chipato, A.D. Shaw, M.I. Friswell, Effect of gravity-induced asymmetry on the nonlinear vibration of an overhung rotor. *Commun. Nonlinear Sci. Numer. Simul.* **62**, 78–89 (2018)
31. E. Chipato, A.D. Shaw, M.I. Friswell, Frictional effects on the nonlinear dynamics of an overhung rotor. *Commun. Nonlinear Sci. Numer. Simul.* **78**, 104875 (2019)
32. M.A. AL-Shudeifat, M. Friswell, O. Shiryavev, C. Nataraj, On post-resonance backward whirl in an overhung rotor with snubbing contact. *Nonlinear Dyn.* **101**, 741–754 (2020)
33. M.A. Al-shudeifat, New backward whirl phenomena in intact and cracked rotor systems. *J. Sound Vib.* **443**, 124–138 (2018)
34. M. Al-shudeifat, O. Shiryavev, T. Alzarooni, C. Nataraj, Full spectrum analysis for studying the backward whirl in accelerated rotor systems. 15th international conference in dynamical systems – theory and applications. Łódź, Poland (5th December 2019)
35. T. Alzarooni, M. Al-shudeifat, O. Shiryavev, On backward whirl excitation in linear-time-variant intact and cracked rotor systems. 15th international conference in dynamical systems – theory and applications. Łódź, Poland (5th December 2019)

36. M.A. AL-Shudeifat, O. Shiryayev, F. Al Hammadi, T. Alzarooni, C. Nataraj, Post-resonance backward whirl in accelerating cracked rotor systems. *Eur. J. Mech. A/Solids* (2020). <https://doi.org/10.1016/j.euromechsol.2020.104039>
37. M.I. Friswell, J.E.T. Penny, S.D. Garvey, A.W. Lees, Dynamics of rotating machines. *Dyn. Rotat. Mach.*, 1–526 (2015)
38. M.A. Al-Shudeifat, On the finite element modeling of the asymmetric cracked rotor. *J. Sound Vib.* **332**(11), 2795–2807 (2013)

Stochastic Resonances and Antiresonances in Rotating Mechanisms



Eugen Kremer 

1 Introduction

The effect of high-frequency stochastic excitation of dynamic systems on their low-frequency behaviour is well-known. A special manifestation of this effect is so-called stochastic resonance—a resonance-like response of a system to the level of a random excitation. This effect was originally discovered in climatology and later applied in many fields of natural sciences and engineering [1].

In earlier works, stochastic resonance was considered as a pure stochastic phenomenon and only for the systems with two-well potential. Further development made it clear that this effect is relevant for a wider class of dynamical systems and that it can be effectively considered within the frame of the concept of vibrational mechanics, which was originally proposed by I. I. Blekhman [2]. The main idea of this concept consists in the replacement of the original equations for fast motions by equations for the averaged, slow motion. These averaged equations content some additional slow, so-called vibrational forces. Within the framework of vibrational mechanics, it was possible not only to give an effective and compact description of numerous amazing effects [2] but also to provide engineers with a calculation methodology and tools which allowed the development of essential new solutions in vibration technology and to improve a number of processes and machines [3–5].

Application of this approach to the systems with high-frequency stochastic excitation was developed in [6, 7].

In this study, the basic method of the concept of vibrational mechanics—the method of direct separation of motion—is applied with some modifications to obtaining averaged equations of a rotating mechanism with high-frequency stochastic component in the rotation speed of the carrier disc. This problem is of

E. Kremer (✉)

Institute for Problems in Mechanical Engineering of Russian Academy of Sciences,
St. Petersburg, Russia

interest for many engineering applications where stochastic excitation from impact vapours in gearboxes, processed material, etc. takes place and where the frequency characteristics of the mechanism are important (for example in vibration absorbers and regulators).

2 Averaged Equations of the Rotating Mechanisms with Stochastic Excitation

2.1 Formulation of Problem

A rotating multi-body mechanism with one degree of freedom is described. The mechanism consists of n kinematically coupled solids performing a flat motion relative to the rotating disc. The disc rotates with an angular velocity

$$\Omega = \Omega_0 (1 + \xi(t)), \quad (1)$$

oscillating near its average value Ω_0 where $\xi(t)$ is some stochastic process described by its canonical expansion [5, 6]:

$$\xi = \int_{\omega_0}^{\infty} (\xi_s(\omega) \sin\omega t + \xi_c(\omega) \cos\omega t) d\omega. \quad (2)$$

Here, $\xi_s(\omega)$ and $\xi_c(\omega)$ are mutually independent and stochastically orthogonal random functions. It is assumed that the spectrum of the random process ξ does not contain frequencies lower than ω_0 , and $q = \frac{\omega_0}{\Omega_0} \gg 1$. Therefore, any realisation of this random process can be considered subsequently as a function of only a fast time $\theta = \omega_0 t$. Probabilistic characteristics of the functions $\xi_s(\omega)$ and $\xi_c(\omega)$ have the following properties:

$$E(\xi_s(\omega)) = E(\xi_c(\omega)) = 0, \quad E(\xi_s(\omega) \xi_c(\omega)) = 0,$$

$$E(\xi_s(\omega_i) \xi_s(\omega_j)) = E(\xi_c(\omega_i) \xi_c(\omega_j)) = S(\omega_i) \delta(\omega_i - \omega_j). \quad (3)$$

Here, E denotes the mathematical expectation, $\delta(\omega)$ is the δ -function, and $S(\omega)$ is the spectral density of the process.

The considered kinematics are presented in Fig. 1. Here, one of the bodies of the mechanism with number j is depicted in two positions: the initial ($\psi = 0$) and the current with the generalised coordinate ψ .

The kinetic energy of the system is calculated as

$$T = \frac{1}{2} A \dot{\psi}^2 + B \dot{\psi} \Omega + \frac{1}{2} C \Omega^2. \quad (4)$$

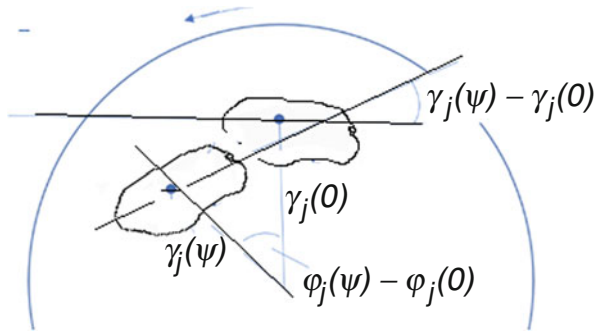


Fig. 1 The kinematics of the rotating mechanism

Here, the dot means differentiation by time, and the values A , B and C are functions of the generalised coordinate ψ and are calculated as

$$A = \sum_{j=1}^n \left(m_j \left(r_j'^2 + \varphi_j'^2 r_j^2 \right) + J_j \gamma_j'^2 \right), \tag{5}$$

$$B = \sum_{j=1}^n \left(m_j \varphi_j' r_j^2 + J_j \gamma_j' \right), \tag{6}$$

$$C = \sum_{j=1}^n \left(m_j r_j^2 + J_j \right), \tag{7}$$

where the prime denotes differentiation by the generalised coordinate ψ , m_j and J_j are masses and central moments of inertia, $r_j(\psi)$ and $\varphi_j(\psi)$ are polar coordinates of the gravity centres of the bodies in the rotating reference system, and $\gamma_j(\psi)$ is the rotation angle of the bodies relative to the rotating disc. Potential energy $\Pi(\psi)$ as a function of the generalised coordinate ψ and the dissipative function $\Phi(\psi)$ are assumed to be predetermined.

Unlike the usual definition assumed in vibrational mechanics, we use the averaging definition introduced in the paper [6]. The averaging, generalised to stochastic systems, is also denoted by $\langle \dots \rangle$, but it is understood that it means the successive application of the usual averaging over the fast time $\theta = \omega_0 t$ on a period equal to 2π and calculating the mathematical expectation. Thus, for some function f we consider the operation

$$\langle f \rangle = \frac{1}{2\pi} E \left(\int_0^{2\pi} f d(t\omega_0) \right) = \frac{1}{2\pi} \int_0^{2\pi} E(f) d(t\omega_0). \tag{8}$$

In accordance with this definition, $\langle \xi \rangle = 0$.

The aim of the study is obtaining the equation for the averaged variable

$$\Psi(t) = \langle \psi \rangle. \tag{9}$$

2.2 Equation of the Fast Motions

Next, the complete motion of the system is described by the following Lagrange equation:

$$A\ddot{\psi} + \frac{1}{2}A'\dot{\psi}^2 + B\Omega_0\dot{\xi} - \frac{1}{2}C'\Omega_0^2(1 + \xi)^2 + \Pi'(\psi) - \frac{\partial\phi}{\partial\dot{\psi}} = 0. \tag{10}$$

The aim of the further consideration is the reduction of this equation to the equation for a slow motion.

2.3 Equation of the Slow Motions

Following the concept of vibrational mechanics, we consider the generalised coordinate ψ as depending on slow time $\tau = \Omega_0 t$ and fast time $\theta = q\tau$. Further, it can be presented as $\psi(\tau, \theta) = \Psi(\tau) + \zeta(\tau, \theta)$, where Ψ is the result of averaging ψ introduced by Eq. (9), and $\langle \zeta \rangle = 0$. In dimensionless variables, we have

$$\Psi(\tau) = E \left(\frac{1}{2\pi} \int_0^{2\pi} \psi(\tau, \theta) d\theta \right), \tag{11}$$

$$\langle \zeta \rangle = E \left(\frac{1}{2\pi} \int_0^{2\pi} \zeta(\tau, \theta) d\theta \right) = 0. \tag{12}$$

Using Expression (1) for Ω , we bring Eq. (4) to the standard form used in [5]:

$$\ddot{\psi} = F(\psi, \dot{\psi}) + B_1(\psi, \dot{\psi})\xi_1 + B_2(\psi, \dot{\psi})\xi_2 + B_3(\psi, \dot{\psi})\xi_3 \tag{13}$$

with

$$F = \frac{1}{A} \left(-\frac{1}{2}A'\dot{\psi}^2 + \frac{1}{2}C'\Omega_0^2(1 + \langle \xi^2 \rangle) - \Pi'(\psi) + \frac{\partial\phi}{\partial\dot{\psi}} \right),$$

$$\xi_1 = \dot{\xi}, \xi_2 = \xi, \xi_3 = \xi^2 - \langle \xi^2 \rangle$$

$$B_1 = -\frac{B\Omega_0}{A}, B_2 = \frac{\Omega_0^2 C'}{A}, B_3 = \frac{\Omega_0^2 C'}{2A}. \tag{14}$$

It should be noted that although the dimensionless time $\tau = \Omega_0 t$ is considered to be a slow time, differentiation by it, still denoted by a dot, implies full differentiation taking into account the dependence of the generalised coordinate on both slow and fast time by the rule

$$\dot{\psi} = \frac{\partial \psi}{\partial \tau} + q \frac{\partial \psi}{\partial \theta}, \ddot{\psi} = \frac{\partial^2 \psi}{\partial \tau^2} + 2q \frac{\partial^2 \psi}{\partial \tau \partial \theta} + q^2 \frac{\partial^2 \psi}{\partial \theta^2}. \tag{15}$$

In accordance with the concept of the vibrational mechanics [1], the equation for the slow motion can be presented in the form

$$\ddot{\Psi} = F(\Psi, \dot{\Psi}) + V(\Psi, \dot{\Psi}) \tag{16}$$

with an additional slow term V which is known as the vibrational force. The method of direct separation of motions in the interpretation of the paper [6] provides the general expression of the vibrational force for the equation of the type (13) with an error of the order of $\frac{1}{q^2}$ for arbitrary dependences of F, B_1, B_2 and B_3 on ψ and $\dot{\psi}$. In the considered case of the dependence of B_1, B_2 and B_3 only on ψ , this expression has the form

$$V = \frac{1}{2} \left(\frac{\partial^2 F}{\partial \dot{\psi}^2} (\kappa_1 B_1^2 + \kappa_2 B_2^2 + \kappa_3 B_3^2) - (\kappa_1 B_1^2 + \kappa_2 B_2^2 + \kappa_3 B_3^2)' \right). \tag{17}$$

Here, the values κ_j ($j = 1,2,3$) are integral characteristics of the stochastic processes ξ_1, ξ_2, ξ_3 which are calculated from their spectral density S_j as.

$$\kappa_j = \int_{\omega_0}^{\infty} S_j(k) k^{-2} dk. \tag{18}$$

Substituting the functions F, B_1, B_2 and B_3 from (7) in (10), we obtain the following specification of Eq. (9) for the slow motion:

$$\ddot{\Psi} = \frac{1}{A} \left(-\frac{1}{2} A' \dot{\Psi}^2 + \frac{1}{2} C' \Omega_0^2 (1 + \langle \xi^2 \rangle) - \Pi(\Psi) + \frac{\partial \phi}{\partial \dot{\Psi}} \right) + V \tag{19}$$

with

$$V = \frac{\Omega_0^2}{2A} \left(H \frac{\partial^3 \phi}{\partial \dot{\Psi}^3} - (AH)' \right), \tag{20}$$

$$H = \frac{1}{A^2} \left(\kappa_1 B^2 + \Omega_0^2 (\kappa_2 + \kappa_3/4) C'^2 \right). \tag{21}$$

Since $q \gg 1$, it is possible to limit the expression (21) to the first member with sufficient precision:

$$H \approx \frac{\kappa_1 B^2}{A^2}.$$

The averaged Eqs. (19, 20, and 21) can also be presented in the form

$$A\ddot{\Psi} + \frac{1}{2}A'\dot{\Psi}^2 - \frac{1}{2}C'_{eff}\Omega_0^2 + \Pi' - \frac{\partial\phi_{eff}}{\partial\dot{\Psi}} = 0 \quad (22)$$

with

$$C_{eff} = C \left(1 + \langle \xi^2 \rangle \right) - AH, \quad \Phi_{eff} = \Phi + \frac{1}{2}\Omega_0^2 \frac{d^2\Phi}{d\dot{\Psi}^2} H, \quad (23)$$

Equation (22) with the averaged coordinate Ψ is similar to the Lagrange Eq. (10) with $\xi = 0$, i.e. without stochastic excitation. It differs from Eq. (10) by replacing the oscillating angular velocity Ω with its mean value Ω_0 , and by introducing the values C_{eff} and Φ_{eff} instead of C and Φ . The effective characteristics of the slow dynamics C_{eff} and Φ_{eff} are calculated with formulas (23) and differ from the inertial coefficient C and the dissipative function Φ by the terms which consider the effect of high-frequency excitation on the slow motion.

This difference determines in general the dependence of the equilibrium positions, eigenfrequency, and dissipation on the intensity of high-frequency excitation.

The problem of the transformation of low-frequency characteristics under the action of high-frequency stochastic excitation is of special interest for mechanisms whose operating performance is sensitive to misalignment in their eigenfrequency. To these mechanisms belong, for example, different vibration absorbers with self-adjustment to rotation speed, such as centrifugal pendulum absorbers [8–10]. Focusing on this class of applications, we will further restrict ourselves to considering the case of the pure inertial rotating mechanism ($\Pi' \equiv 0$) without dissipation ($\Phi = 0$).

3 Low-Frequency Behaviour Near the Equilibrium Position

3.1 Equilibrium Position of the Slow Motion

The position of the relative equilibrium in the absence of the high-frequency excitation is assumed to correspond to $\psi = 0$. This can always be provided by the corresponding definition of this generalised coordinate. From Eq. (10), it follows from $\Pi' \equiv 0$ and $\xi = 0$ that.

$$C'(0) = 0. \quad (24)$$

The position of the relative equilibrium for the slow motion $\Psi = \Psi_0$ is defined from Eq. (22):

$$C'_{eff}(\Psi_0) = 0 \quad (25)$$

and can differ in general from 0. The value of Ψ_0 for small relative amplitude of the angular velocity λ can be obtained approximately as

$$\Psi_0 = \kappa_1 \frac{2B(0)B'(0)A(0) - B^2(0)A'(0)}{(1 + \langle \xi^2 \rangle) C''(0)A^2(0)}. \quad (26)$$

This expression is obtained from Eq. (25) after its linearisation by Ψ_0 and considering Eq. (23).

This vibro-mechanical modification of the equilibrium position due to the high-frequency stochastic excitation needs some asymmetry of the system relative to the point $\psi = 0$. In other words, it needs that $B'(0) \neq 0$ or $A'(0) \neq 0$.

3.2 Eigenfrequency of the Slow Motion

Another vibro-mechanical effect is the shift of the eigenfrequency. This effect also takes place for the symmetric systems, for which $\Psi_0 = 0$, because for them $B'(0) = 0$ and $A'(0) = 0$. We will consider this case, since it is of most interest for the practice and by the same token gives a more transparent and compact expression as a non-symmetrical case.

The eigenfrequency ω is obtained from Eq. (22), which, after its linearisation, has the form

$$\ddot{\Psi} + \omega^2 \Psi = 0 \quad (27)$$

with

$$\omega = \omega_0 \sqrt{\frac{C''_{eff}(0)}{C''(0)}} = \omega_0 \sqrt{1 - \eta}. \quad (28)$$

Here, ω_0 is the eigenfrequency of the original system without high-frequency excitation, which is calculated as

$$\omega_0 = \Omega_0 \sqrt{-\frac{C''(0)}{2A(0)}}, \quad (29)$$

and the coefficient η is the dimensionless parameter, which determines the effect of high-frequency excitation on the eigenfrequency of the slow motion and is calculated as

$$\eta = (A''(0)H(0) + H''(0)A(0)) / C''(0) - \langle \xi^2 \rangle. \tag{30}$$

The expression (30) can be transformed with Eq. (21) to the form

$$\eta = \frac{\kappa_1 B(0)}{2Q_0^2 A^3(0)} (A''(0)B(0) - 2B''(0)A(0)) + 4Q_0^2 \Omega_0^2 (\kappa_2 + \kappa_3/4) - \langle \xi^2 \rangle. \tag{31}$$

3.3 Application Example: Centrifugal Pendulum Absorber

This result can be applied to the centrifugal pendulum absorber which is described, for example, in Den Hartog’s classic textbook [8]. This absorber has been used effectively since the 1930s, first in aircraft and in recent years in the automotive industry [9, 10]. This type of absorber allows us to provide its eigenfrequency proportional to the rotational speed and thus to keep it equal to the frequency of the torque irregularity of a reciprocating engine, whose frequency also increases linearly with engine speed. Due to a special design of this hanging, rather complex kinematics can be achieved even for a one-mass pendulum.

Although this device has found wide application and has been the subject of many studies, the effects associated with additional stochastic influences, as far as we know, have not yet been considered.

Here, we will consider only the simplest principle kinematics presented in Fig. 2.

Here, a pendulum with mass m and central moments of inertia J is pivotally mounted at the point P located at a distance L from the centre of rotation O of the

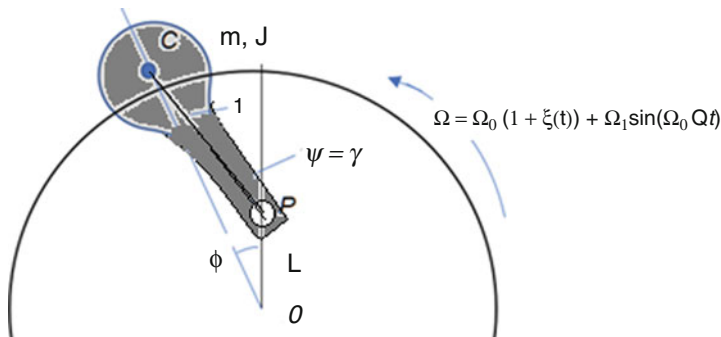


Fig. 2 Vibrational mechanics transformation of the rotating mechanism with stochastic excitation

carrier disc with moments of inertia J_D . The distance between the pivot and the centre of gravity of the pendulum is l . The angular velocity Ω of the carrying disc oscillates in accordance with the equation

$$\Omega = \Omega_0 (1 + \xi(t)) + \Omega_s(t), \tag{32}$$

where the last term represents the forced low-frequency oscillation of the disc. This vibration of the angular velocity is caused by a low-frequency oscillating torque $M_s = M_m \sin(\Omega_0 Q t)$ with amplitude M_m and so-called excitation order Q acting on the disc. The additional equation for this slow motion can be obtained as the averaged Lagrange equation for the rotation angle of the disc, for which the variable Ω is the generalised velocity. This equation in the linearised approximation is

$$C(0)\dot{\Omega}_s + B(0)\ddot{\Psi} = M_m \sin(\Omega_0 Q t). \tag{33}$$

Considering the low-frequency oscillation of Ω leads also to some modification of Eq. (27), which now takes the form

$$\ddot{\Psi} + \omega^2 \Psi + \frac{B(0)}{A(0)} \dot{\Omega}_s = 0. \tag{34}$$

We will look for a solution of Eqs. (33) and (34) in the form.

$$\Omega_s = \Omega_m \cos(\Omega_0 Q t), \Psi = \Psi_m \sin(\Omega_0 Q t) \tag{35}$$

Thus, the amplitudes Ω_m and Ψ_m are obtained from the algebraic equations

$$-C(0)\Omega_0 Q \Omega_m - B(0)(\Omega_0 Q)^2 \Psi_m = M_m, \tag{36}$$

$$-\frac{B(0)}{A(0)} \Omega_0 Q \Omega_m + \left(-(\Omega_0 Q)^2 + \omega^2\right) \Psi_m = 0. \tag{37}$$

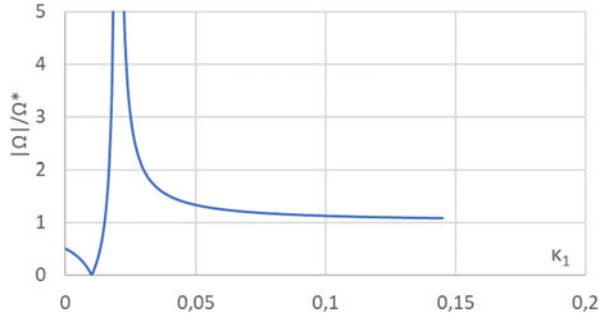
The solution of Eqs. (36) and (37) is

$$\begin{aligned} \Psi_m &= -\frac{\lambda}{(-Q^2 + Q_0^2(1 - \eta) + \lambda)} \frac{M_m}{B(0)(\Omega_0 Q)^2}, \\ \Omega_m &= -\frac{-Q^2 + Q_0^2(1 - \eta)}{(-Q^2 + Q_0^2(1 - \eta) + \lambda)} \frac{M_m}{C(0)\Omega_0 Q} \end{aligned} \tag{38}$$

with

$$\lambda = \frac{B^2(0)Q^2}{A(0)C(0)}, Q_0^2 = \frac{\omega^2}{Q_0^2} = -\frac{C''(0)}{2A(0)}. \tag{39}$$

Fig. 3 Amplitude development with changing the intensity of stochastic excitation



Now, we will specify these expressions for the case of the simple pendulum presented in Fig. 2, taking the rotation angle γ as the generalised coordinate ψ and considering the following geometrical relationships for the polar coordinates r and φ of the the pendulum centre of gravity:

$$r = \sqrt{L^2 + l^2 + 2Ll\cos\psi}, \tan\varphi = \frac{l\sin\psi}{L + l\cos\psi} \tag{40}$$

Thus, the values $A, B, C, A''(0), B''(0)$ and Q_0^2 take the form

$$\begin{aligned} A(0) &= ml^2 + J, B(0) = ml(l + L) + J, C(0) \\ &= m(l + L)^2 + J + J_D, A''(0) = 0, B''(0) = -ml, Q_0^2 = \frac{mlL}{ml^2 + J}L. \end{aligned} \tag{41}$$

Then, the amplitude of the angular velocity of the disc Ω_m can be obtained from Eq. (38) in the form $\Omega_m = -\frac{1-(Q/Q_0)^2-\eta}{(1-(Q/Q_0)^2-\eta+\lambda/Q_0^2)} \frac{M_m}{C^{(0)}\Omega_0 Q}$.

The correction factor η to the eigenfrequency in the approximation of Eq. (22) has an especially simple form, $\eta = \kappa_1/k$ with $k = \frac{(ml^2+J)}{(ml(l+L)+J)}$. So, the expression (42) can be transformed as

$$\Omega_m = -\Omega_* \frac{\kappa_{1A} - \kappa_1}{\kappa_{1R} - \kappa_1} \tag{42}$$

with $\Omega_* = \frac{M_m}{C^{(0)}\Omega_0 Q}, \kappa_{1A} = k(1 - \nu), \kappa_{1R} = k\left(1 - \nu + \frac{\nu B^2(0)}{A(0)C(0)}\right), \nu = \left(\frac{Q}{Q_0}\right)^2$.

The expression (42) shows: increasing the intensity of stochastic excitation leads first to decreasing of the disc velocity amplitude $|\Omega_m|$ to 0 (stochastic antiresonance) and then to resonance-like increasing this amplitude to very big values (stochastic antiresonance). This scenario always takes place if $\nu < 1$ (excitation order is smaller than the nominal absorber order). The corresponding curve of amplitude development with changing the intensity of stochastic excitation κ_1 is presented in Fig. 3 for one example of rather realistic values of parameters: $\kappa_{1A} = 0.01$ and $\kappa_{1A} = 0.02$.

4 Conclusions

The main results of the work are as follows:

- For the first time, the general equation for the averaged equation of a rotating multi-mass mechanism with one degree of freedom is obtained in the presence of high-frequency stochastic oscillations of the carrier. This equation is similar to the initial equation in the absence of excitation with a modified inertial coefficient and dissipative function, which depend on the intensity of the random process.
- The general expressions for the position of the equilibrium point and for eigenfrequency of the slow motions near this point are obtained.
- As an example, a standard centrifugal pendulum absorber with a simplest kinematics was considered. It is shown that changing the intensity of the stochastic excitation manifests itself first in the fall of the disc velocity amplitude to 0 (stochastic antiresonance) and then to resonance-like increasing this amplitude to very big values (stochastic antiresonance). This takes places if the excitation order is smaller than the nominal absorber order.

References

1. L. Gammaitoni, P. Hänggi, P. Jung, Stochastic resonance. *Rev. Mod. Phys.* **70**(1), 223–287 (1998). <https://doi.org/10.1103/RevModPhys.70.223>
2. I. Blekhman, *Vibrational Mechanics: Nonlinear Dynamic Effects, General Approach, Applications* (World Scientific, Singapore, 2000)
3. I. Blekhman, L. Vaisberg, D. Indeitsev, Theoretical and experimental basis of advanced vibrational technologies. *Vib. Prob. ICOVP* (2011). https://doi.org/10.1007/978-94-007-2069-5_18
4. L. Vaisberg, Vibration technology research achievements of the Mekhanobr scientific school and their practical implementation. *Vibroengineering Procedia* **25**, 76–82 (2019). <https://doi.org/10.21595/vp.2019.20820>
5. И.И. Блехман, Л.А. Вайсберг, Б.П. Лавров, В.Б. Васильков, К.С. Якимова, Универсальный вибрационный стенд: опыт использования в исследованиях, некоторые результаты. *Научно-технические ведомости СПбГТУ* **3**(33), 224–227 (2003). Russian. (LIBRARY ID: 24675872)
6. E. Kremer, Low-frequency dynamics of systems with modulated high-frequency stochastic excitation. *J. Sound Vib.* **437**, 422–436 (2018)
7. I. Blekhman, E. Kremer, Stochastic resonance as the averaged response to random broadband excitation and its possible applications. *Proc. IMechE.. Pt. C J. Mech Eng Sci* **233**(23–24), 7445–7446 (2019)
8. J.P. Den Hartog, *Mechanical Vibrations* (McGraw-Hill, New York, 1956)
9. A. Kooy, A. Gillmann, J. Jäckel, M. Bosse, *DMFW – Nothing new? , 6. LuK Symposium, 2002* (LuK GmbH & Co, Bühl/Baden, 2002)
10. T. Krause, E. Kremer, P. Movlazada, Theory and simulation of centrifugal pendulum absorber with trapezoidal suspension, in: *Vibration Problems ICOVP 2011: 10th International Conference on Vibration Problems, Prague* (2011)

Internal Resonances of a Rotating Pre-deformed Blade Under a Harmonic Gas Pressure



Bo Zhang, Hu Ding, and Li-Qun Chen

1 Introduction

The rotating blade plays a key role in the turbomachine. The research works on the dynamics of beam rotating about a fixed axis are pioneered in the late 1940s by Sutherland [1]. Engineers design the turbine blades properly to make them operate away from their natural frequencies. However, the blades' vibration failure is still a dominant type in turbine failure [2]. Hence, researchers should investigate the further resonance mechanisms of such a structure. The central axis of the blades could be deformed by the huge thermal gradient inside the turbine machine. Further, from the view of the equation of motion of the blade, the quadratic nonlinearities are produced by the pre-deformation. From Nayfeh's monograph, one can find that if some of the natural frequencies of the blade are commensurable, energy can exchange among these modes. This phenomenon is often called internal resonance.

Pesheck, Pierre, and Shaw [3] presented a reduced-order model for rotating beams and obtained the nonlinear normal modes of the rotating beam. In 2012, Lacarbonara et al. [4] calculated the critical rotating speeds for the 1:1, 2:1, 3:1, and 3:2 internal resonances for a rotating blade. After that, more and more researchers [5–14] reported the different types of resonances based on various nonlinear models of rotating blade. Zhang and Li [15] built the nonlinear dynamic model for a pre-deformed blade considering the effects of the thermal gradient environment. Based on this dynamic model of pre-deformed rotating blade, there

B. Zhang

School of Mechanics and Engineering Science, Shanghai University, Shanghai, China

School of Science, Chang'an University, Shaanxi, China

H. Ding · L.-Q. Chen (✉)

School of Mechanics and Engineering Science, Shanghai University, Shanghai, China

e-mail: lqchen@shu.edu.cn

exist several research papers investigating the nonlinear dynamic behavior for the different resonances, such as primary resonance [16, 17] and harmonic resonance [18, 19], separately. However, the systematic comparisons and discussions on different internal resonances of the blade model are rare in the literature. This is the motivation here. In the present study, ten different types of resonance of the blade are identified together with the method of multiple scales (MMS). Similarities and differences of the stabilities and response curves are discussed.

2 Mathematic Model and Theoretical Analysis

Considering a rotating blade under harmonic gas pressure P_{gas} under a thermal gradient environment g_y and g_z , as shown in Fig. 1. The symbol γ denotes the nondimensional rotating speed of the disk. The symbols θ and ψ denote the pre-twisted angle and the setting angle, respectively. The nondimensional viscous damping coefficient is assumed as c_d .

After the derivation process of formulas in the studies [15, 16], the equations of motion in the modal space could be obtained as follows:

$$\ddot{\tilde{q}}_i + c_d \dot{\tilde{q}}_i + \omega_i^2 \tilde{q}_i = \tilde{f}_i \cos(\omega t) + \sum_{j=1}^{n_2+n_3} \sum_{k=1}^{n_2+n_3} \eta_{ijk} \tilde{q}_j \tilde{q}_k + \sum_{j=1}^{n_2+n_3} \sum_{k=1}^{n_2+n_3} \sum_{l=1}^{n_2+n_3} \xi_{ijkl} \tilde{q}_j \tilde{q}_k \tilde{q}_l \quad (i = 1, \dots, n_2 + n_3) \quad (1)$$

where \tilde{q}_i, \tilde{f}_i are the displacement vector and the excitation vector in the modal space, ω is the excitation frequency, η_{ijk}, ξ_{ijkl} are the quadratic nonlinear coefficients and the cubic nonlinear coefficients, respectively. n_2 and n_3 are the number of trial functions assumed in chordwise and the flapwise displacement, respectively. A nondimensional small parameter ε is defined to describe the weakness of system response. Hence, the modal displacements are scaled as $\tilde{q}_i \leftrightarrow \varepsilon \tilde{q}_i$. In the following subsection, compared with the order of modal displacement, three different cases

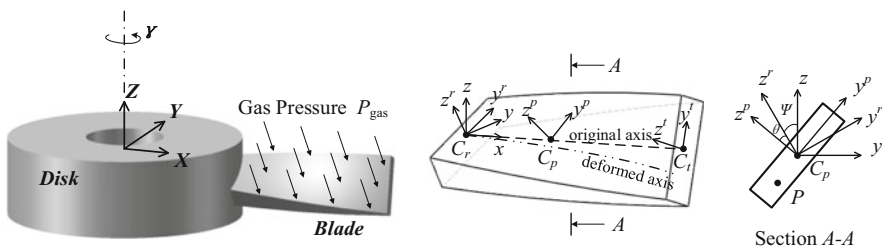


Fig. 1 The sketch of the rotating blade model

of the modal force order will be discussed: strong, medium, weak. To solve the nonlinear dynamic equation of the rotating blade via MMS, three time-scales $T_0 = t$, $T_1 = \varepsilon t$, and $T_2 = \varepsilon^2 t$ are introduced. The modal displacements are assumed to take the following form:

$$\tilde{q}_i(t) = \tilde{q}_{i0}(T_0, T_1, T_2) + \varepsilon \tilde{q}_{i1}(T_0, T_1, T_2) + \varepsilon^2 \tilde{q}_{i2}(T_0, T_1, T_2) + O(\varepsilon^3) \tag{2}$$

As it is demonstrated in the reference [16], in 2:1 internal resonance, the analytical results have good accuracy with only the first two time-scales T_0 and T_1 , and ξ_{ijkl} have little effects on the dynamic response. From the reference [17], it can be found that the steady-state response is only dependent on the time-scales T_0 and T_2 in 3:1 internal resonance.

2.1 Strong Forced Vibration: \tilde{f}_i Is of the Same Order as \tilde{q}_i

In this case, the following rescale [18, 19] is used:

$$c_d \leftrightarrow \varepsilon c_d, \quad \tilde{f}_i \leftrightarrow \varepsilon \tilde{f}_i \tag{3}$$

The equation of motion is cast into

$$\ddot{\tilde{q}}_i + \omega_i^2 \dot{\tilde{q}}_i = \tilde{f}_i \cos(\omega t) + \varepsilon \left(-c_d \dot{\tilde{q}}_i + \sum_{j=1}^{n_2+n_3} \sum_{k=1}^{n_2+n_3} \eta_{ijk} \tilde{q}_j \tilde{q}_k \right) + O(\varepsilon^2, \varepsilon^3 \dots) \tag{4}$$

Substitute the first-order approximate solution into Eq. (4) and compare the coefficients of ε^0 and ε^1 . One can obtain the zero-order and the first-order equation as

$$D_0^2 \tilde{q}_{i0} + \omega_i^2 \tilde{q}_{i0} = \tilde{f}_i \cos(\omega T_0) \tag{5}$$

$$D_0^2 \tilde{q}_{i1} + \omega_i^2 \tilde{q}_{i1} = -2D_0 D_1 \tilde{q}_{i0} - c_d D_0 \tilde{q}_{i0} + \sum_{j=1}^{n_2+n_3} \sum_{k=1}^{n_2+n_3} \eta_{ijk} \tilde{q}_{j0} \tilde{q}_{k0} \tag{6}$$

The general solution form of the zero-order Eq. (5) could be written as

$$\tilde{q}_{i0} = A_i(T_1) \exp(i\omega_i T_0) + B_i \exp(i\omega T_0) + cc \tag{7}$$

Substitute Eq. (7) into Eq. (6). One can obtain the following first-order equation

$$\begin{aligned}
 D_0^2 \tilde{q}_{i1} + \omega_i^2 \tilde{q}_{i1} = & -i\omega_i (2D_1 A_i + c_d A_i) \exp(i\omega_i T_0) - i\omega c_d B_i \exp(i\omega T_0) \\
 & + \sum_{j=1}^{n_2+n_3} \sum_{k=1}^{n_2+n_3} \eta_{ijk} \cdot \{A_j A_k \exp(i(\omega_j + \omega_k) T_0) + A_j B_k \exp(i(\omega_j + \omega) T_0) \\
 & + B_j A_k \exp(i(\omega_k + \omega) T_0) + B_j B_k \exp(2i\omega T_0) + A_j \bar{A}_k \exp(i(\omega_j - \omega_k) T_0) \\
 & + \bar{A}_j B_k \exp(i(\omega - \omega_j) T_0) + B_j \bar{A}_k \exp(i(\omega - \omega_k) T_0)\} + cc
 \end{aligned} \tag{8}$$

From the analysis of the potential secular terms, we could find a series of resonance types in 2:1 internal resonance.

1. When $2\omega \approx \omega_1$, the term $B_j B_k \exp(2i\omega T_0)$ acts as the secular terms of the first mode. This corresponds to the super-harmonic resonance of first mode and is recorded as Resonance I in the present paper for short.
2. When , the term $B_j B_k \exp(2i\omega T_0)$ acts as the secular terms of the second mode. This corresponds to the super-harmonic resonance of second mode and is recorded as Resonance II in the present paper for short.
3. When $\omega \approx 2\omega_1$, the term $\bar{A}_j B_k \exp(i(\omega - \omega_j) T_0)$ acts as the secular terms of the first mode. This corresponds to the sub-harmonic resonance of first mode and is recorded as Resonance III in the present paper for short.
4. When $\omega \approx 2\omega_2$, the term $\bar{A}_j B_k \exp(i(\omega - \omega_j) T_0)$ acts as the secular terms of the second mode. This corresponds to the sub-harmonic resonance of second mode and is recorded as Resonance IV in the present paper for short.
5. When $\omega \approx \omega_1 + \omega_2$, the term $\bar{A}_j B_k \exp(i(\omega - \omega_j) T_0)$ acts as the secular terms of the first mode and the secular terms of the second mode in the same time. This corresponds to the combination resonance of summed type and is recorded as Resonance V in the present paper for short.
6. When $\omega \approx \omega_2 - \omega_1$, the term $A_j B_k \exp(i(\omega_j + \omega) T_0)$ acts as the secular terms of the second mode. This corresponds to the combination resonance of difference type and is recorded as Resonance VI in the present paper for short.

2.2 Medium Forced Vibration: \tilde{f}_i Is of One Order Higher than \tilde{q}_i

In this case, the following rescale [15, 16] is used: $c_d \leftrightarrow \varepsilon c_d$, $\tilde{f}_i \leftrightarrow \varepsilon^2 \tilde{f}_i$. After the similar derivation process of Sect. 2.1, the first-order equation could be obtained as follows:

$$\begin{aligned}
 D_0^2 \tilde{q}_{i1} + \omega_i^2 \tilde{q}_{i1} = & \frac{\tilde{f}_i}{2} \exp(i\omega T_0) - i\omega_i (2D_1 A_i + c_d A_i) \exp(i\omega_i T_0) + \\
 & \sum_{j=1}^{n_2+n_3} \sum_{k=1}^{n_2+n_3} \eta_{ijk} [A_j A_k \exp(i(\omega_j + \omega_k) T_0) + A_j \bar{A}_k \exp(i(\omega_j - \omega_k) T_0)] + cc
 \end{aligned} \tag{9}$$

From the analysis of the potential secular terms, we find the following resonance possibilities in 2:1 internal resonance.

7. When $\omega \approx \omega_1$, the term $\tilde{f}_i \exp(i\omega T_0) / 2$ acts as the secular terms of the first mode. This corresponds to the primary resonance of first mode and is recorded as Resonance VII in the present paper for short.
8. When $\omega \approx \omega_2$, the term $\tilde{f}_i \exp(i\omega T_0) / 2$ acts as the secular terms of the second mode. This corresponds to the primary resonance of second mode and is recorded as Resonance VIII in the present paper for short.

2.3 Weak Forced Vibration: \tilde{f}_i Is of Two Order Higher than \tilde{q}_i

In this case, the order of the damping coefficient must be turn up to balance the effect of the excitation. Hence, the following rescale [17] is used: $c_d \leftrightarrow \varepsilon^2 c_d$, $\tilde{f}_i \leftrightarrow \varepsilon^3 \tilde{f}_i$. After the similar derivation process of Sect. 2.1, the second-order equation could be obtained as Eq. (10)

$$\begin{aligned}
 D_0^2 \tilde{q}_{i2} + \omega_i^2 \tilde{q}_{i2} = & -i\omega_i (2D_2 A_i + c_d A_i) \exp(i\omega_i T_0) + \frac{\tilde{f}_i}{2} \exp(i\omega T_0) \\
 & + 2 \sum_{j=1}^{n_2+n_3} \sum_{k=1}^{n_2+n_3} \sum_{m=1}^{n_2+n_3} \sum_{n=1}^{n_2+n_3} \eta_{ijk} \eta_{kmn} \cdot \left[\frac{A_m A_n A_j}{\omega_k^2 - (\omega_m + \omega_n)^2} \exp(i(\omega_j + \omega_m + \omega_n) T_0) \right. \\
 & + \frac{A_m \bar{A}_n A_j}{\omega_k^2 - (\omega_m - \omega_n)^2} \exp(i(\omega_j + \omega_m - \omega_n) T_0) \\
 & + \frac{A_m A_n \bar{A}_j}{\omega_k^2 - (\omega_m + \omega_n)^2} \exp(i(-\omega_j + \omega_m + \omega_n) T_0) + \left. \frac{\bar{A}_m A_n A_j}{\omega_k^2 - (\omega_n - \omega_m)^2} \exp(i(\omega_j - \omega_m + \omega_n) T_0) \right] \\
 & + \sum_{j=1}^{n_2+n_3} \sum_{k=1}^{n_2+n_3} \sum_{l=1}^{n_2+n_3} \xi_{ijkl} [A_j A_k A_l \exp(i(\omega_j + \omega_k + \omega_l) T_0) + A_j A_k \bar{A}_l \exp(i(\omega_j + \omega_k - \omega_l) T_0) \\
 & + A_j \bar{A}_k A_l \exp(i(\omega_j - \omega_k + \omega_l) T_0) + \bar{A}_j A_k A_l \exp(i(-\omega_j + \omega_k + \omega_l) T_0)] + cc
 \end{aligned} \tag{10}$$

From the analysis of the potential secular terms, we find the following resonance possibilities in 3:1 internal resonance.

9. When $\omega \approx \omega_1$, the term $\tilde{f}_i \exp(i\omega T_0) / 2$ acts as the secular terms of the first mode. This corresponds to the primary resonance of first mode and is recorded as Resonance IX in the present paper for short.
10. When $\omega \approx \omega_2$, the term $\tilde{f}_i \exp(i\omega T_0) / 2$ acts as the secular terms of the second mode. This corresponds to the primary resonance of second mode and is recorded as Resonance X in the present paper for short.

For the sake of consistency, the symbol σ_1 , the internal detuning parameter, is defined to measure the nearness to the complete 2:1 or 3:1 internal resonance. For the first 8 cases of 2:1 internal resonance, $\omega_2 = 2\omega_1 + \varepsilon\sigma_1$. For the last 2 cases of 3:1 internal resonance, $\omega_2 = 3\omega_1 + \varepsilon^2\sigma_1$. The symbol σ_2 , the external detuning

parameter, is defined to measure the nearness between the excitation frequency ω and the certain critical value for different resonance types.

For the 10 different resonance types above, eliminating the corresponding secular terms will lead to the corresponding solvability conditions, respectively. After that, the different averaged equations can be obtained for the different resonance types. Due to limited space, the averaged equations will not be recorded here. Solving the equilibrium point of average equation can reveal the steady-state response in the corresponding resonance. The response stabilities can be determined by calculating the eigenvalues of the Jacobian matrix of the average equation.

3 Results and Discussion

A series of numerical examples are presented and the dynamic responses of the rotating blade in different resonance cases are compared. The blade parameters are set as the reference [16]. The setting angle $\Psi = 10^\circ$, the total pre-twisted angle $\Theta = 10^\circ$, the ratio between the two principle moment of inertia for the blade section $\kappa = 0.25$, the ratio of the disk radius to the blade length $\delta = 0$, the thermal gradient $g_y = 0$ and $g_z = 0.032$, the slenderness ratio $\eta = 200$. The variations of the first three natural frequencies and their multiples are displayed in Fig. 2 of the reference [17]. The figure demonstrates the possibilities of the 2:1 internal resonance and the 3:1 internal resonance at rotating speed $\gamma = 6.5798$ and 19.7026 , respectively. To verify the accuracy of the analytical results obtained via MMS, the dynamic system obtained after rescaling is integrated numerically with the aid of Runge-Kutta method. The frequency responses obtained by the two methods are compared for different resonance cases in Fig. 2. In the figure, the lines denote the results obtained from theoretical analysis, and the markers represent those obtained from the numerical integration. As shown in Fig. 2, the analytical results are in accordance with those obtained from the numerical integrations.

Figure 3 shows the variation of the frequency response curves with the thermal gradient for the 10 different types of resonance cases. The multi-valued phenomenon exists in all resonance cases. Thermal gradient has different effects on the dynamic behavior (concluding the response peaks and the unstable region size) for different resonance types. For all the 2:1 internal resonance, the blade experiences double jumping under excitation sweeps. This phenomenon indicates that the system experiences an evolution from softening to hardening behavior when the blade passes through the 2:1 internal resonance, and the frequency responses of primary resonance of the first mode in the case of 3:1 internal resonance bend to the right similar to the case without internal resonance [12]. For some resonance cases, the frequency response curves are quite similar to each other. For example, in 2:1 internal resonance, the frequency response curves of the primary resonance of the first mode are similar to those of super-harmonic resonance of the first mode. The

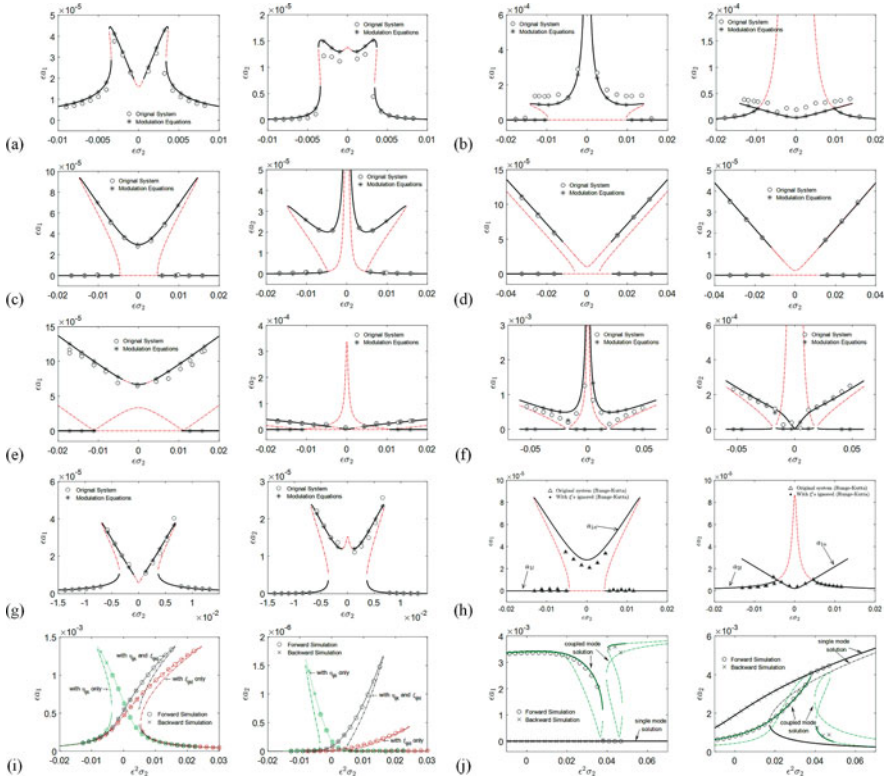


Fig. 2 The comparison of frequency responses obtained by the theoretical analysis and the numerical integrations for different resonance cases: (a) ~ (j) denote the case of Resonance I to Resonance X, respectively

frequency response curves of the sub-harmonic resonance of the first mode are similar to those of the primary resonance of the second mode. For the resonance cases shown in Fig. 3b–e, h, j, there exist single-mode solutions for the steady-state response.

Figure 4 shows the effects of σ_1 and σ_2 on the force response curves for different resonance cases. The hysteresis phenomenon can be found in the primary resonance of the first mode in both cases of 2:1 internal resonance and 3:1 internal resonance. Two limit points exist on the force response curves for both resonance cases. The effects of the external detuning parameter σ_2 on both resonance cases are similar. The first limit points [15] are delayed remarkably by σ_2 . In contrast, the second limit points change slightly with the variation of σ_2 . Hence the unstable region is enlarged by σ_2 . The effects of the internal detuning parameter σ_1 seem to be different on the two resonance cases. The first limit points change remarkably with

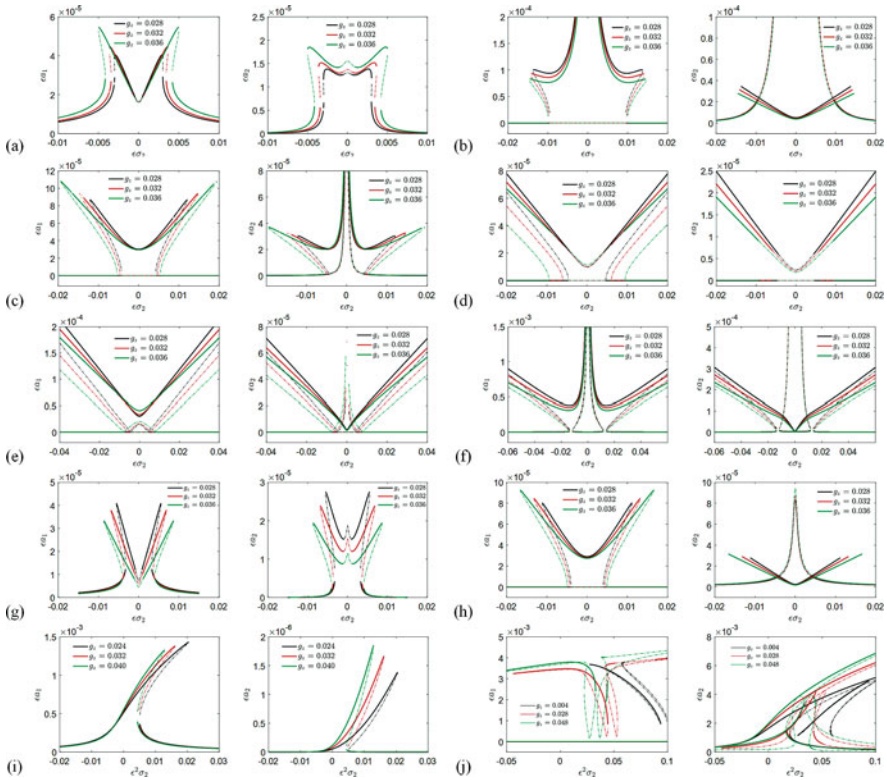


Fig. 3 The effects of thermal gradient on the frequency response curves for different resonance cases: (a) ~ (j) denote the case of Resonance I to Resonance X, respectively

the variation of σ_1 . Figure 5 demonstrates the saturation phenomenon [9, 16] exists both in the primary resonance of second mode and sub-harmonic resonance of second mode in the case of 2:1 internal resonance. Figure 6 illustrates the quasi-saturation phenomenon found in the combination resonance cases in 2:1 internal resonance. The saturation or quasi-saturation phenomenon cannot be found in 3:1 internal resonance.

As shown in Fig. 7, the coupled-mode solutions are detected in both 2:1 internal resonances and 3:1 internal resonances. The unstable regions are always surrounded by stable regions in both cases. The coupled-mode solution exists in the whole excitation plane in both cases of 2:1 internal resonance, while the coupled-mode solution is invalid in region E in the 3:1 internal resonance. The single-mode solution always exists with at least one stable solution for the 3:1 internal resonance. The stable regions in excitation parameters plane of super-harmonic resonance of the second mode are similar to those of the primary resonance of the second mode in the case of 2:1 internal resonance. In contrast, the stable regions of 3:1 internal resonances are quite different.

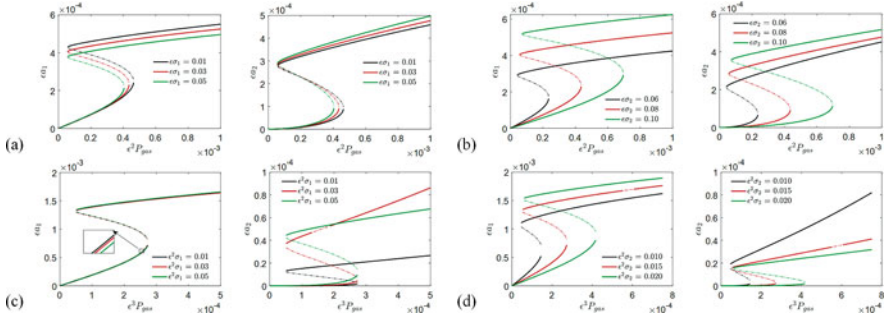


Fig. 4 The effects of internal detuning parameter σ_1 and external detuning parameter σ_2 on the force response curves for different resonance cases: (a, b) Resonance VII, (c, d) Resonance IX

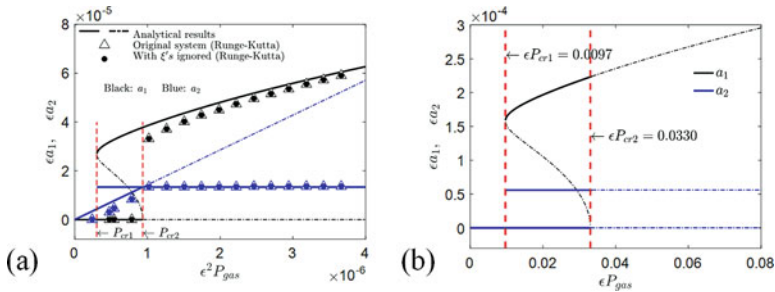


Fig. 5 The saturation phenomenon in some resonance cases: (a) Resonance VIII, (b) Resonance IV

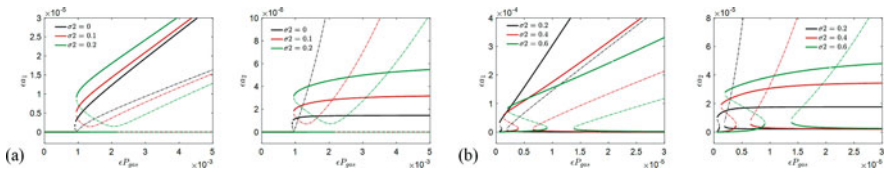


Fig. 6 The quasi-saturation phenomenon in some resonance cases: (a) Resonance V, (b) Resonance VI

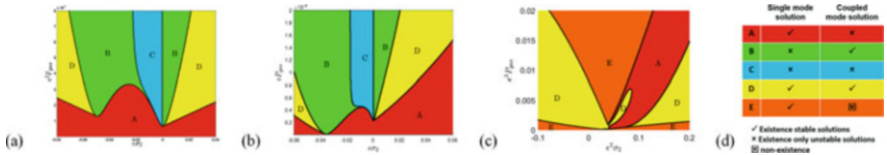


Fig. 7 The stability ranges of different solutions in the excitation plane ($\sigma_2 - P_{gas}$) (a) Resonance VIII, (a) Resonance VIII, (b) Resonance II, (c) Resonance X, (d) the explanatory legend

4 Conclusions

The possibilities of 10 different types of resonances of a rotating blade are determined with the aid of MMS. The dynamic responses of the rotating blade are compared for 10 different resonance cases. The following conclusion can be drawn.

1. Strong and medium excitations lead to 2:1 internal resonance, and weak excitation leads to 3:1 internal resonance.
2. The double jumping and the saturation/quasi-saturation exist only in the 2:1 internal resonances, while multi-valuedness exists in all resonances.
3. Both coupled- and single-mode solutions exist unconditionally in 2:1 internal resonances, but only single-mode solutions exist unconditionally in 3:1 internal resonances. Single-mode solutions are unconditionally stable in 3:1 internal resonance, while stable coupled- and single-mode solutions may coexist in both resonances.
4. The 2:1 internal resonances depend only on quadratic terms, while the 3:1 internal resonances depend on both cubic and quadratic terms.
5. The thermal gradient affects differently on response peaks and unstable regions of different types of resonance.

Acknowledgments This project is supported by National Natural Science Foundation of China (Grant Nos. 11702033 and 11872159), the Fundamental Research Funds for the Central Universities, CHD (Grant No. 300102120106), Innovation Program of Shanghai Municipal Education Commission (No. 2017-01-07-00-09-E00019).

References

1. R.L. Sutherland, Bending vibration of a rotating blade vibrating in the plane of rotation. *ASME J. Appl. Mech.* **16**(4), 389–394 (1949)
2. M. Rafiee, F. Nitzsche, M. Labrosse, Dynamics, vibration and control of rotating composite beams and blades: A critical review. *Thin Wall Struct* **119**, 795–819 (2017)
3. E. Pesheck, C. Pierre, S.W. Shaw, Modal reduction of a nonlinear rotating beam through nonlinear normal modes. *ASME J. Vib. Acoust.* **124**(2), 229–236 (2002)
4. W. Lacarbonara, H. Arvin, F. Bakhtiari-Nejad, A geometrically exact approach to the overall dynamics of elastic rotating blades-part 1: Linear modal properties. *Nonlinear Dyn.* **70**(1), 659–675 (2012)
5. S. Sina, G. Kerschen, H. Haddadpour, Nonlinear normal modes of axial-torsional vibrations of rotating thin walled composite beam. *Proceedings of International Conference on Noise and Vibration Engineering (Isma2012) / International Conference on Uncertainty in Structural Dynamics (Usd2012)*, 2547–2561 (2012)
6. S.A. Sina, H. Haddadpour, H.M. Navazi, Nonlinear free vibrations of thin-walled beams in torsion. *Acta Mech.* **223**(10), 2135–2151 (2012)
7. M. Shahgholi, S.E. Khadem, Internal, combinational and sub-harmonic resonances of a nonlinear asymmetrical rotating shaft. *Nonlinear Dyn.* **79**(1), 173–184 (2015)
8. M.H. Yao, Y. Niu, W. Zhang, Nonlinear resonance behaviors of rotating pretwisted cylindrical panels. *Proceedings of the Asme International Design Engineering Technical Conferences and Computers and Information in Engineering Conference, 2018*, **6** (2018)

9. W. Zhang, G. Liu, B. Siriguleng, Saturation phenomena and nonlinear resonances of rotating pretwisted laminated composite blade under subsonic air flow excitation. *J. Sound Vib.* **478** (2020)
10. X.X. Bian, F.Q. Chen, F.X. An, Global dynamics of a compressor blade with resonances. *Math. Probl. Eng.* **2016** (2016)
11. Reddy, B.S., Ghosal, A.: Nonlinear dynamics of a rotating flexible link. *J. Comput. Nonlinear Dyn.* **10**(6) (2015)
12. O. Thomas, A. Senechal, J.F. Deu, Hardening/softening behavior and reduced order modeling of nonlinear vibrations of rotating cantilever beams. *Nonlinear Dyn.* **86**(2), 1293–1318 (2016)
13. D. Wang, Y.S. Chen, M. Wiercigroch, Q.J. Cao, Bifurcation and dynamic response analysis of rotating blade excited by upstream vortices. *Appl Math Mech-Engl* **37**(9), 1251–1274 (2016)
14. D. Wang, Z.F. Hao, Y.S. Chen, Y.X. Zhang, Dynamic and resonance response analysis for. A turbine blade with varying rotating speed. *J Theor App Mech-Pol* **56**(1), 31–42 (2018)
15. B. Zhang, Y.M. Li, Nonlinear vibration of rotating pre-deformed blade with thermal gradient. *Nonlinear Dyn.* **86**(1), 459–478 (2016)
16. B. Zhang, Y.-L. Zhang, X.-D. Yang, L.-Q. Chen, Saturation and stability in internal resonance of a rotating blade under thermal gradient. *J. Sound Vib.* **440**(3), 34–50 (2019)
17. B. Zhang, H. Ding, L.Q. Chen: Three to one internal resonances of a pre-deformed rotating beam with quadratic and cubic nonlinearities. *Int. J. Non Linear Mech.* **126** (2020)
18. B. Zhang, H. Ding, L.Q. Chen, Super-harmonic resonances of a rotating pre-deformed blade subjected to gas pressure. *Nonlinear Dyn.* **98**(4), 2531–2549 (2019)
19. B. Zhang, H. Ding, L.Q. Chen, Subharmonic and combination resonance of rotating pre-deformed blades subjected to high gas pressure. *Acta Mech. Solida Sin.* **33**(5), 635–649 (2020)

Part VII
Modal Interactions and Energy Transfer

Investigation of Quasi-Periodic Solutions in Nonlinear Oscillators Featuring Internal Resonance



Giorgio Gobat, Attilio Frangi, Cyril Touzé, Louis Guillot, and Bruno Cochelin

1 Motivation

Nonlinear dynamical phenomena in coupled oscillators are connected with the emergence of complex features that have no counterpart in linear theory. In this context, one can cite for example jump phenomena, hysteretic behaviours, quasi-periodic solutions, and chaotic vibrations [1–3]. In recent years, a number of investigations highlighting the occurrence of the so-called *frequency combs* (FCs) in the observed dynamical solutions have been reported in the literature on Micro-Electro Mechanical Systems (MEMS). These dynamical behaviours are characterized by the appearance of numerous frequency peaks in the Fourier transform of the vibration data, organized with repeating patterns and constant interspace between the spectral peaks (see Fig. 1). For instance, FCs have important applications in optics and can be used for measurement purposes, see, e.g., [4, 5].

In MEMS devices, FCs have been experimentally reported, e.g. in [6, 7], where a resonator with strong nonlinear coupling between bending and torsional modes is addressed. Other examples are provided in [8], where a tunable FC is considered, or in [9] where a 1:2 internal resonance in a MEMS arch resonator is investigated.

G. Gobat · A. Frangi
Politecnico di Milano, Milano, MI, USA
e-mail: giorgio.gobat@polimi.it; attilio.frangi@polimi.it

C. Touzé (✉)
Institute of Mechanical Sciences and Industrial Applications, Institut Polytechnique de Paris,
CNRS – ENSTA Paris – EDF – CEA, Palaiseau, France
e-mail: cyril.touze@ensta-paris.fr

L. Guillot · B. Cochelin
Laboratoire de Mécanique et d'Acoustique, LMA – UMR 7031 AMU – CNRS – Centrale
Marseille, Marseille, France
e-mail: guillot@lma.cnrs-mrs.fr; bruno.cochelin@centrale-marseille.fr

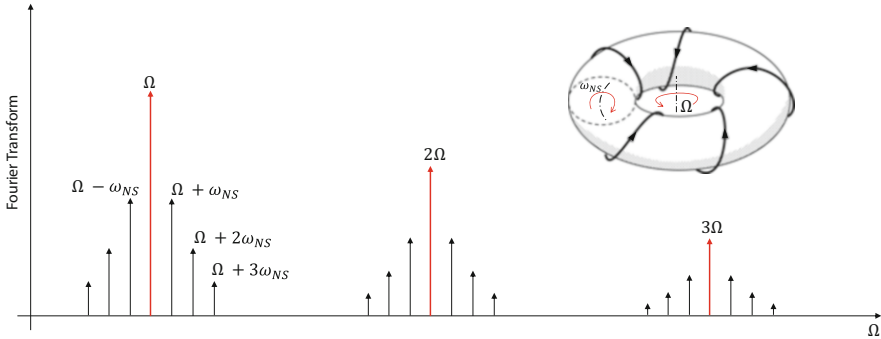


Fig. 1 Schematic representation of a frequency comb induced by a Neimark–Sacker bifurcation. The bifurcation introduces in the system response a new incommensurate frequency ω_{NS} such that the Fourier transform of the system shows peaks at the forced frequency Ω multiples and at each combination $m\Omega \pm n\omega_{NS}$ with m and n integers. This corresponds to a motion of the orbits on a torus in the phase space (qualitative representation in the top-right corner).

Another option to achieve FC is through contact phenomena inducing period-doubling bifurcations, as in [10].

Through the analysis of the experiments available in the literature, a direct relationship between a FC and a quasi-periodic (QP) regime can be argued. When a FC is established, the response is characterized by an amplitude modulation in time, and an incommensurate frequency ω_{NS} appears along with the driving frequency Ω . Due to nonlinearities, ω_{NS} and Ω combine according to the rule $m\Omega \pm n\omega_{NS}$ with m and n integers, and each combination corresponds to a peak in the Fourier transform, see Fig. 1.

This chapter focuses on nonlinear oscillators featuring 1:2 and 1:3 internal resonances (IR) and on the appearance of QP solutions as the consequence of Neimark–Sacker bifurcations. In this case, the emergence of QP regimes and FCs can be easily predicted if the locus of Neimark–Sacker bifurcation points is available [11, 12]. Numerical evaluation of the boundary curves of specific bifurcation points, as parameters are varied, is currently an active research topic in the literature. For example, numerical continuation methods can be adapted with few additional constraints to follow the locus of a specific bifurcation point in the parameter space, see, e.g., [13] for recent examples in nonlinear oscillations.

Even though NS bifurcation points have been identified in these systems for a long time, see, e.g., [14, 15] and references therein, new results are reported in this document. An analytical expression of the Neimark–Sacker boundary curve is provided for the 1:2 IR case, and a numerical continuation method is developed for the systematic computation of the NS boundary curve. The latter method is also applied to the case of a 1:3 IR.

This chapter is organized as follows. Section 2 presents the reference nonlinear systems considered in the investigation, while Sect. 3 derives the analytical expres-

sion of the Neimark–Sacker boundary for the case of the 1:2 IR. Then in Sect. 4, the comparison between the analytical and numerical solutions in the systems considered is discussed. Finally, in Sect. 5, we summarize the outcomes of the work.

2 Reference Systems

This chapter considers a system of two coupled nonlinear oscillators featuring 1:2 and 1:3 IR. The former one is described through its second-order normal form [1], while the latter considers a simplified system. The equations of motion of the former system read

$$\ddot{q}_1 + \omega_1^2 q_1 + 2\mu_1 \dot{q}_1 + \alpha_{12}^{(1)} q_1 q_2 = F \cos(\Omega t), \quad (1a)$$

$$\ddot{q}_2 + \omega_2^2 q_2 + 2\mu_2 \dot{q}_2 + \alpha_{11}^{(2)} q_1^2 = 0, \quad (1b)$$

in which q_i , ($i = 1, 2$) is the displacement of the i -th oscillator and ω_i are the two eigenfrequencies, hereafter assumed to fulfil the relation $\omega_2 \approx 2\omega_1$. Two quadratic coefficients $\alpha_{12}^{(1)}$ and $\alpha_{11}^{(2)}$ are introduced. In the mechanical context with conservative loads, one has $\alpha_{11}^{(2)} = \alpha_{12}^{(1)}/2$. The linear damping coefficients are μ_i , $i = 1, 2$, and an external harmonic forcing with angular frequency Ω and amplitude F is applied to the first oscillator.

For the 1:3 IR, the focus in this contribution is put on a system that is simplified as compared to the complete normal form for a 1:3 internal resonance, following the example selected and analysed in [6, 7]. The equations of motion read

$$\ddot{q}_1 + \omega_1^2 q_1 + \mu_1 \dot{q}_1 + \beta_{111}^{(1)} q_1^3 + \beta_{112}^{(1)} q_1^2 q_2 = F \cos(\Omega t), \quad (2a)$$

$$\ddot{q}_2 + \omega_2^2 q_2 + \mu_2 \dot{q}_2 + \beta_{111}^{(2)} q_1^3 = 0. \quad (2b)$$

In this system, $\beta_{ik}^{(j)}$ are the nonlinear coupling coefficients. Since we are interested in the 1:3 IR, the eigenfrequencies are such that $\omega_2 \approx 3\omega_1$. The monomial terms that are not herein considered as compared to the normal form of the system are the following: $q_1 q_2^2$ on the first oscillator; q_2^3 and $q_2 q_1^2$ on the second oscillator. Also in this case, if we consider a mechanical context with conservative loads, one has $\beta_{111}^{(2)} = \beta_{112}^{(1)}/3$.

3 Neimark–Sacker Analytical Boundary for 1:2 Resonance

This section investigates the frequency response functions (FRF) of the oscillators described by Eq. (1). The appearance of QP solutions was documented, e.g., in

[14, 16], although the expression of the Neimark–Sacker boundary curve was not detailed. Following the multiple scales (MS) method [17, 18], we introduce two different time scales $T_0 = t$ and $T_1 = \varepsilon t$, with ε a small bookkeeping parameter. A linear expansion of the system response as $q_i = q_{i0} + \varepsilon q_{i1}$ is assumed, while the damping is modelled as $\mu_i = \varepsilon \xi_i$, the forcing term as $F = \varepsilon f$, and finally the nonlinear coefficients as $\alpha_{12}^{(1)} = \varepsilon \bar{\alpha}_{12}^{(1)}$, $\alpha_{11}^{(2)} = \varepsilon \bar{\alpha}_{11}^{(2)}$. Under these assumptions, we rewrite (1) as

$$\ddot{q}_1 + \omega_1^2 q_1 = \varepsilon[-2\xi_1 \dot{q}_1 - \bar{\alpha}_{12}^{(1)} q_1 q_2 + f \cos(\Omega t)], \tag{3a}$$

$$\ddot{q}_2 + \omega_2^2 q_2 = \varepsilon[-2\xi_2 \dot{q}_2 - \bar{\alpha}_{11}^{(2)} q_1^2]. \tag{3b}$$

The forcing frequency Ω is close to the first eigenfrequency ω_1 ($\omega_2 \approx 2\omega_1$), and detuning parameters σ_1 and σ_2 are introduced to quantify the mismatches as $\omega_2 = 2\omega_1 + \varepsilon\sigma_1$ and $\Omega = \omega_1 + \varepsilon\sigma_2$. Following a classical path, the solution of the first-order system can be expressed in the form $q_{i0} = A_i(T_1) \exp(i\omega_i T_0) + c.c.$, with $A_i(T_1) = a_i(T_1)/2 \exp(i\theta_i(T_1))$. When q_{i0} is inserted in the second-order system, secular terms arise. Forcing them to vanish (solvability conditions), a set of four differential equations are obtained. The resulting system is made autonomous by introducing the angular variables:

$$\gamma_1 = \theta_1 - \sigma_2 T_1, \quad \gamma_2 = 2\theta_1 - \theta_2 - \sigma_1 T_1. \tag{4}$$

The dynamics of the first-order solution a_i and γ_i with respect to slow time scale T_1 is governed by

$$a_1' = \frac{a_1 \left(\bar{\alpha}_{12}^{(1)} a_2 \sin(\gamma_2) - 4\xi_1 \omega_1 \right) - 2f \sin(\gamma_1)}{4\omega_1}, \tag{5a}$$

$$\gamma_1' = \frac{\bar{\alpha}_{12}^{(1)} a_1 a_2 \cos(\gamma_2) - 2f \cos(\gamma_1)}{4a_1 \omega_1} - \sigma_2, \tag{5b}$$

$$a_2' = -\frac{\bar{\alpha}_{11}^{(2)} a_1^2 \sin(\gamma_2) + 4\xi_2 a_2 \omega_2}{4\omega_2}, \tag{5c}$$

$$\gamma_2' = -\frac{f \cos(\gamma_1)}{a_1 \omega_1} - \sigma_1 + \frac{1}{2} \cos(\gamma_2) \left(\frac{\bar{\alpha}_{12}^{(1)} a_2}{\omega_1} - \frac{\bar{\alpha}_{11}^{(2)} a_1^2}{2a_2 \omega_2} \right). \tag{5d}$$

The fixed point solutions, associated to forced oscillations of constant amplitudes, can be expressed as a function of a_1 and a_2 only. The amplitude equations, employing the physical parameters of Eq. (2), finally read:

$$\begin{aligned}
a_2^3 + \frac{8\omega_1 \Gamma}{\alpha_{12}^{(1)}} ((\Omega - \omega_1)(\omega_2 - 2\Omega) + \mu_1 \mu_2) a_2^2 + \frac{16\omega_1^2}{\alpha_{12}^{(1)2}} ((\Omega - \omega_1)^2 + \mu_1^2) a_2 \\
- \frac{\Gamma \alpha_{11}^{(2)} F^2}{\alpha_{12}^{(1)2} \omega_2} = 0, \quad a_1 = \sqrt{\frac{4\omega_2 a_2}{\alpha_{11}^{(2)} \Gamma}},
\end{aligned} \tag{6}$$

where $\Gamma = \sqrt{\frac{1}{\mu_2^2 + (\omega_2 - 2\Omega)^2}}$.

We now focus on the definition of the Neimark–Sacker (NS) boundary curve. The stability of the solutions depends on the eigenvalues λ of the Jacobian matrix of system (5). The NS bifurcation requires that a pair of complex conjugate eigenvalues crosses the imaginary axis. Furthermore, the same eigenvalues must satisfy transversality and nondegeneracy conditions [19]. Imposing these constraints in the characteristic polynomial of Eqs. (5), one can express the NS boundary as a polynomial in a_2 :

$$b_1 a_2^4 + b_2 a_2^3 + b_3 a_2^2 + b_4 a_2 + b_5 = 0, \tag{7}$$

where the expression of each coefficient is reported in Appendix A. For fixed values of the system parameters $\mu_1, \mu_2, \alpha_{12}^{(1)}, \omega_2, \omega_1$ and spanning the values of Ω , one gets the boundary curve for the NS bifurcation as a function $a_2(\Omega)$.

4 Neimark–Sacker Boundary Curve: Numerical Results

In this section, the NS boundaries associated with the system of Eqs. (1) and (2) are investigated numerically and, in the former case, compared to the analytical prediction developed in the previous section.

The numerical continuation procedure has been implemented in the software MANLAB [20, 21]. The procedure is based on the standard augmented system method here briefly introduced, using the general dynamical system notations used in [22]. Let $\mathbf{x}(t)$ be a n -dimensional vector and \mathbf{f} the nonlinear smooth mapping defining the dynamical system

$$\dot{\mathbf{x}} = \mathbf{f}(\mathbf{x}(t), \boldsymbol{\alpha}), \tag{8}$$

where $\boldsymbol{\alpha}$ is the parameter vector of the system. Let us assume that, for a given value of $\boldsymbol{\alpha}$, a period-1 limit cycle emerges from a NS bifurcation, such that $\mathbf{x}(0) = \mathbf{x}(1)$ (phase condition).

The goal is to follow the locus of NS bifurcation points as $\boldsymbol{\alpha}$ is varied. To this purpose, we parametrize the critical multipliers $\lambda_{1,2}$ by means of a scalar variable θ as: $\lambda_{1,2} = e^{\pm i\theta}$. Let us introduce a complex eigenfunction $\mathbf{w}(t)$ of system (8). The

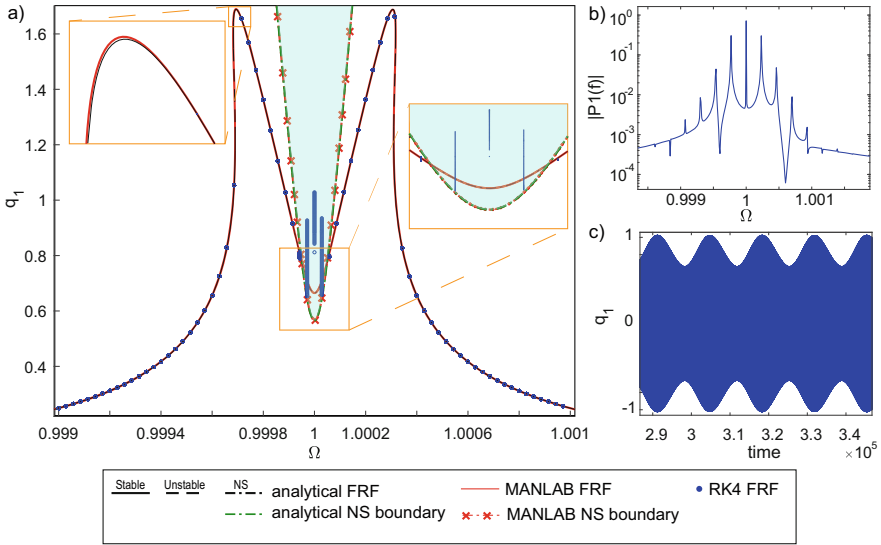


Fig. 2 q_1 as a function of the excitation frequency Ω for system (1) with 1:2 IR. Selected parameters are: $\alpha_{12}^{(1)} = 2 \cdot 10^{-3}$, $\alpha_{11}^{(2)} = 1 \cdot 10^{-3}$, $\mu_1 = \mu_2 = 1 \cdot 10^{-4}$, $F = 5 \cdot 10^{-4}$, and $\sigma_1 = 0$. In (a), black lines represent the FRF of the multiple scale system from Eq. (6) (a continuous line denotes a stable branch, dashed unstable, dash dotted marks the quasi-periodic regime). The red continuous line represents the FRF of the system Eq. (1) computed through numerical continuation in MANLAB (10 harmonics). The red dot dashed line is the NS boundary obtained with numerical continuation methods (10 harmonics). The dark green dashed line is the analytical NS boundary. The light blue filled region highlights where a QP regime is expected. The blue circle markers represent the RK4 direct time-marching solution (Poincaré sections). A cloud of points arises from the QP regime. Two enlarged views close to the peak and to the NS region allow appreciating the small differences between the solutions. In (b) and (c), results for the value $\Omega = 1$ are reported. (b) is the Fourier transform of the time history represented in (c). The frequency comb and the amplitude modulation are clearly visible

system that allows the continuation of NS boundary consists of Eqs. (8) along with the phase condition [22]:

$$\dot{\mathbf{w}} - \mathbf{f}_{\mathbf{x}}(\mathbf{x}(t), \boldsymbol{\alpha})\mathbf{w}(t) = \mathbf{0}, \tag{9a}$$

$$\mathbf{w}(1) - e^{i\theta}\mathbf{w}(0) = \mathbf{0}, \tag{9b}$$

$$\int_0^1 \mathbf{w}^T(t)\mathbf{w}_0(t)dt - 1 = 0, \tag{9c}$$

where $\mathbf{w}_0(t)$ is a complex-valued reference eigenfunction at a nearby point on the solution branch and $\mathbf{f}_{\mathbf{x}}$ is the Jacobian of Eq. (8). Equation (9) is solved with MANLAB that implements the Harmonic Balance Method for the computation of periodic solutions and applies Hill’s method to evaluate the stability of the system (see [23]). This approach was demonstrated to be extremely efficient and reliable for the analysis of nonlinear systems. To this aim, the augmented system (9) must be converted in the frequency domain using a Floquet–Hill formulation.

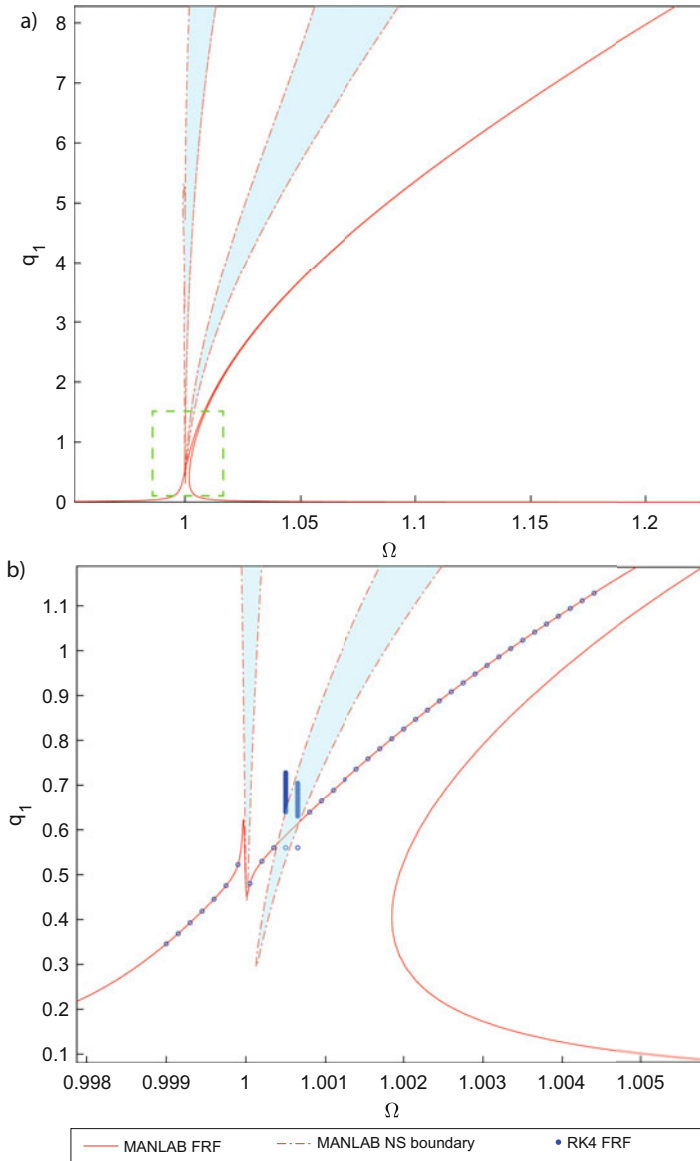


Fig. 3 q_1 as a function of the excitation frequency Ω for system (2) obtained with the continuation method (10 harmonics). Selected parameters: $\beta_{111}^{(1)} = 1 \cdot 10^{-2}$, $\beta_{112}^{(1)} = 2 \cdot 10^{-2}$, $\beta_{111}^{(2)} = 6.66 \cdot 10^{-3}$, $\mu_1 = \mu_2 = 1 \cdot 10^{-4}$, $F = 1 \cdot 10^{-3}$, and $\omega_2 = 3\omega_1$. **(a)** Complete FRF, **(b)** enlarged view close to the NS bifurcations. The red lines represent the FRF of the system. The red dash dotted lines are the NS boundaries achieved with numerical continuation methods. The light blue colouring highlights the regions in the parameter space enveloped in the NS boundary. The blue circle markers represent the RK4 direct time-marching solution (Poincaré sections). A cloud of points arises from the QP regime.

Figure 2 shows the results obtained in the case of the 1:2 IR, where the analytical prediction given by Eq. (6) and Eq. (7) is compared to the numerical one obtained by continuation of Eq. (1) with MANLAB and direct time-marching Runge–Kutta 4 (RK4) method. The three approaches provide the same result in the periodic regions, and only small differences can be observed close to the resonance peaks between the analytical and continuation approaches. The NS boundary encloses a connected domain centred on the resonance frequency ω_1 . Here, the time-marching approach reveals the quasi-periodic regime and the FC. A nearly perfect match between analytical and numerical NS boundaries is found, thus validating the overall procedure.

For the 1:3 IR case, only the numerical solution of Eqs. (2) is reported in Fig. 3. One can observe a more complex pattern with two different tongues of instability regions. More specifically, the NS boundary crosses the frequency response function in two different portions, thus creating two narrow regions with QP solutions, one centred on ω_1 , the other being shifted to higher frequencies. The local existence of two different regions is a noteworthy difference with respect to the 1:2 IR case. Moreover, it is worth stressing that capturing the narrow and close instability tongues is quite difficult with standard continuation methods. In the proposed example, we also show results obtained with a RK4 direct integration close to the unstable regions. The two results have a perfect agreement in the periodic regions, and as expected, the RK4 integration detects the QP regime within the NS boundary.

5 Conclusions

In this chapter, we have obtained an analytical expression of the Neimark–Sacker boundary for a system of two coupled oscillators with 1:2 internal resonance. The analytical formula has been validated with an ad hoc developed numerical continuation of bifurcation points. The numerical method has also been used to compute the NS boundaries for two oscillators featuring 1:3 internal resonance showing that two distinct instability regions exist. These regions have the shape of narrow tongues and are difficult to detect only with direct integration schemes and other standard numerical tools.

Appendix A: Coefficient of NS Boundary Polynomial

$$b_1 = \frac{\alpha_{12}^{(1)4} \mu_1 \mu_2}{64\omega_1^4} \quad (\text{A.1a})$$

$$b_2 = -\frac{\alpha_{12}^{(1)3} (\mu_1 + \mu_2)^2 \sqrt{\mu_2^2 + (\omega_2 - 2\Omega)^2}}{8\omega_1^3} \quad (\text{A.1b})$$

$$b_3 = -\frac{\alpha_{12}^{(1)2}}{2\omega_1^2} \mu_1 \mu_2 \cdot (\mu_1^2 + \mu_2^2 + 2\mu_1 \mu_2 - 2\omega_1 \Omega + 4\omega_2 \Omega + \omega_1^2 - \omega_2^2 - 3\Omega^2) \quad (\text{A.1c})$$

$$b_4 = \frac{2\alpha_{12}^{(1)}}{\omega_1} (\mu_1 + \mu_2)^2 \sqrt{\mu_2^2 + (\omega_2 - 2\Omega)^2} \cdot (\mu_1^2 + 2\mu_2 \mu_1 + \mu_2^2 + (\omega_1 + \omega_2 - 3\Omega)^2) \quad (\text{A.1d})$$

$$b_5 = 4 \left((\mu_1 (\mu_2^2 + (\omega_2 - 2\Omega)^2) + \mu_2 (\Omega - \omega_1)^2 + \mu_2 \mu_1^2) \cdot (\mu_1 (4\mu_2^2 + (\Omega - \omega_1)^2) + \mu_2 (\mu_2^2 + (\omega_2 - 2\Omega)^2) + \mu_1^3 + 4\mu_2 \mu_1^2) - (\mu_1 + \mu_2)^2 (\mu_1^2 + (\Omega - \omega_1)^2) \times (\mu_2^2 + (\omega_2 - 2\Omega)^2) \right) \quad (\text{A.1e})$$

References

1. J. Guckenheimer, P. Holmes, *Nonlinear Oscillations, Dynamical Systems, and Bifurcations of Vector Fields*, vol. 42 (Springer, Berlin, 2013)
2. A.H. Nayfeh, B. Balachandran, *Applied Nonlinear Dynamics: Analytical, Computational, and Experimental Methods* (Wiley, London, 2008)
3. G. Rega, W. Lacarbonara, A.H. Nayfeh, C.-M. Chin, Multiple resonances in suspended cables: direct versus reduced-order models. *Int. J. Non-Linear Mech.* **34**(5), 901–924 (1999)
4. A. Ganesan, C. Do, A. Seshia, Phononic frequency comb via intrinsic three-wave mixing. *Phys. Rev. Lett.* **118**(3), 033903 (2017)
5. J. Ye, S.T. Cundiff, *Femtosecond Optical Frequency Comb: Principle, Operation and Applications* (Springer, Berlin, 2005)
6. D.A. Czaplewski, C. Chen, D. Lopez, O. Shoshani, A.M. Eriksson, S. Strachan, S.W. Shaw, Bifurcation generated mechanical frequency comb. *Phys. Rev. Lett.* **121**(24), 244302 (2018)
7. D.A. Czaplewski, S. Strachan, O. Shoshani, S.W. Shaw, D. López, Bifurcation diagram and dynamic response of a MEMS resonator with a 1:3 internal resonance. *Appl. Phys. Lett.* **114**(25), 254104 (2019)
8. I. Mahboob, R. Dupuy, K. Nishiguchi, A. Fujiwara, H. Yamaguchi, Hopf and period-doubling bifurcations in an electromechanical resonator. *Appl. Phys. Lett.* **109**(7), 073101 (2016)
9. A. Hajjaj, F. Alfossail, M.I. Younis, Two-to-one internal resonance of MEMS arch resonators. *Int. J. Non-Linear Mech.* **107**, 64–72 (2018)

10. A. Guerrieri, A. Frangi, L. Falorni, An investigation on the effects of contact in MEMS oscillators. *J. Microelectromech. Syst.* **27**(6), 963–972 (2018)
11. J. Neimark, *On Some Cases of Periodic Motions Depending on Parameters* Dokl. Akad. Nauk SSSR, vol. 129 (1959), pp. 736–739
12. R.J. Sacker, On invariant surfaces and bifurcation of periodic solutions of ordinary differential equations: Chapter ii: Bifurcation-mapping method. *J. Differ. Equ. Appl.* **15**(8–9), 759–774 (2009)
13. L. Xie, S. Bagnuet, B. Prabel, R. Dufour, Bifurcation tracking by harmonic balance method for performance tuning of nonlinear dynamical systems. *Mech. Syst. Signal Process.* **88**, 445–461 (2017)
14. A.H. Nayfeh, D.T. Mook, *Nonlinear Oscillations* (Wiley, London, 1979)
15. J.W. Miles, Resonantly forced motion of two quadratically coupled oscillators. *Phys. D* **13**, 247–260 (1984)
16. S. Lenci, G. Rega, Axial–transversal coupling in the free nonlinear vibrations of Timoshenko beams with arbitrary slenderness and axial boundary conditions. *Proc. R. Soc. A Math. Phys. Eng. Sci.* 472(2190), 20160057 (2016)
17. A.H. Nayfeh, *Perturbation Methods* (Wiley, London, 2008)
18. S.H. Strogatz, *Nonlinear Dynamics and Chaos with Student Solutions Manual: With Applications to Physics, Biology, Chemistry, and Engineering* (CRC Press, Boca Raton, 2018)
19. Y.A. Kuznetsov, *Elements of Applied Bifurcation Theory*, vol. 112 (Springer, Berlin, 2013)
20. L. Guillot, B. Cochelin, C. Vergez, A Taylor series-based continuation method for solutions of dynamical systems. *Nonlinear Dyn.* **98**(4), 2827–2845 (2019)
21. L. Guillot, P. Vigué, C. Vergez, B. Cochelin, Continuation of quasi-periodic solutions with two-frequency harmonic balance method. *J. Sound Vib.* **394**, 434–450 (2017)
22. W.-J. Beyn, A. Champneys, E. Doedel, W. Govaerts, Y.A. Kuznetsov, B. Sandstede, Numerical continuation, and computation of normal forms, in *Handbook of Dynamical Systems III: Towards Applications* (2001)
23. L. Guillot, A. Lazarus, O. Thomas, C. Vergez, B. Cochelin, A purely frequency based Floquet-Hill formulation for the efficient stability computation of periodic solutions of ordinary differential systems. *J. Comput. Phys.* (**416**), 109477 (2020)

Theoretical Investigations on an Internally Resonant Piezoelectric Energy Harvester



Aravindan Muralidharan and Shaikh Faruque Ali

1 Introduction

Vibration energy harvesting has become the need of the hour for realizing autonomous systems in fields such as structural health monitoring without relying much on the hazardous and exhaustible batteries. Among all the mechanisms available for harnessing vibration from the environment, piezoelectric energy harvesting is the most sought after one, which is mainly due to its higher power densities [1]. Harvesters based on linear resonance work efficiently only when the excitation frequency is in close proximity to the natural frequency. This makes the linear harvester susceptible to the uncertain variations in the ambient environment. Introducing deliberate nonlinearities into the harvesting system as a means to harvest power over a broadband of frequencies has garnered more attention in the recent times as it aids in overcoming the major shortcoming of the linear harvester [2].

Harvesters with intentional nonlinearities have been reported to display improved bandwidth of power in comparison to the linear harvesters under both deterministic and random excitation (Litak [3] and Friswell [4]). Also, several works in the literature demonstrate the potential of exciting multiple modes of piezoelectric system for broadband performance [5]. Internal resonance can occur in multi-modal nonlinear harvesters when the natural frequencies of the system are commensurable [6]. Energy transfer occurs between the modes under internal resonance, and this phenomenon can be made use of to harvest electrical power over a broad band of frequencies.

A. Muralidharan · S. Faruque Ali (✉)
Indian Institute of Technology Madras, Chennai, India
e-mail: sfali@iitm.ac.in

Geometrically, nonlinear beams are commonly idealized as cubic oscillators with symmetric potential wells. For such oscillators, significant energy transfer between the modes is found to occur when their corresponding natural frequencies are tuned to the ratio of 1:3 [6]. The dynamics of such systems boast modulated responses in the vicinity of the primary resonances [7]. The experimental work carried out by Guillot et al. [8] on a piezoelectric system with 1:3 internal resonance under harmonic excitation demonstrated the possibility of using internal resonance toward broadband energy harvesting.

The motivation of carrying out this work comes from the prospect of utilizing large responses of 1:3 resonant systems near the fundamental resonance for wideband power extraction. To this end, studies are carried out in the present work to characterize the performance of a piezoelectric harvester with 1:3 internal resonance under harmonic excitation.

2 Harvester Model

The schematic representation of the harvester is shown in Fig. 1. An inverted cantilever beam of length L_b constitutes the harvester system. The material properties, namely the density and the modulus of elasticity of the beam, are represented by ρ_b and E_b , respectively. The width and thickness of the beam are correspondingly taken to be b_b and d_b . A concentrated mass M_t with a corresponding mass moment of inertia I_t is lumped at a distance L_t from the fixed end of the beam. Piezoelectric patches of length L_p , width b_p , and thickness d_p are attached onto both faces of the beam. The cross-sectional area as well as the second moment area of the beam and piezoelectric patch are denoted as $[A_b, A_p]$ and $[I_b, I_p]$, respectively. The geometrical and electrical properties of the piezoelectric patches considered in the study are taken from [9]. The damping ratios of the first two modes are represented by ξ_1 and ξ_2 , respectively. The harvester system is set to steady-state motion by a harmonic base displacement of the form $z = z_0 \cos(\Omega t)$.

Let u_p and v_p be the vertical and horizontal displacements of any given point P at a distance s from the fixed end along the neutral axis of the beam as shown in Fig. 1. In addition to these displacements, the cross-section of the beam also undergoes rotation at point P that is denoted by ϕ_p the corresponding curvature of which is represented as κ_p . Assuming the beam to be inextensible, ϕ_p , κ_p , and u_p can be expressed in terms of v_p as given in [4]. This chapter employs Galerkin discretization to obtain an approximate solution for the horizontal displacement at any point, v_p along the beam that is given by

$$v_p(s, t) = \sum_{h=1}^N q_h(t) \left[\Phi_h^c(s) H_c(s) + \Phi_h^b(s) H_b(s) \right], \quad (1)$$

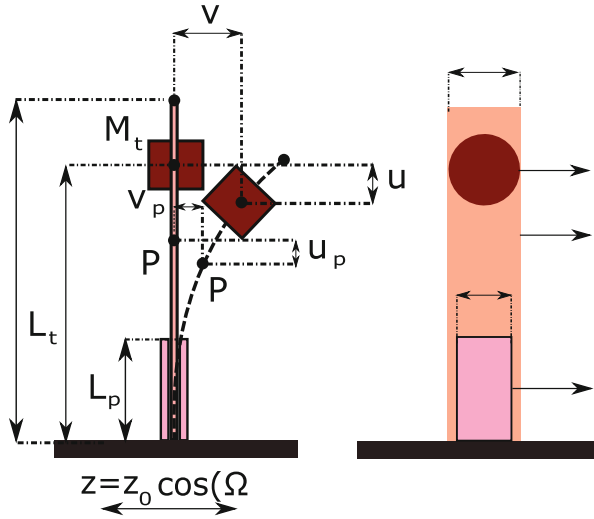


Fig. 1 Schematic representation of the harvesting system

where $\Phi_h^c(s)$ and $\Phi_h^b(s)$ are the cantilever beam modes of the piezoelectric and non-piezoelectric domains of the harvester, respectively. N corresponds to the total number of modes considered for the analysis. $q_h(t)$ denotes the generalized coordinate of the h^{th} mode. $H_c(s)$ and $H_b(s)$ correspond to the piezoelectric and non-piezoelectric regions.

Using the expressions given in [4] for the kinetic as well as potential energies and the work done by harvester in extracting electrical power, the following governing mechanical equation can be obtained.

$$\alpha_{hh}\ddot{q}_h + c_h\dot{q}_h + \gamma_{hh}q_h + \sum_{i,j,k,l=1}^N \beta_{ijkl} \left(q_k q_l \ddot{q}_i + q_j \dot{q}_k \dot{q}_l \right) + \left(\lambda_{ijhl} q_i q_l + \lambda_{hjkl} q_k q_l \right) q_j - \Theta_{1,h} V - \frac{1}{2} \sum_{i,j,k=1}^N \left(\Theta_{2,hjk} q_j q_k + 2\Theta_{2,ijh} q_i q_j \right) V = \Psi_h \ddot{z} \quad h = 1, 2, \dots, N, \quad (2)$$

where

$$\alpha_{hj} = \rho_c A_c \Delta_{hj}^c + \rho_b A_b \Delta_{hj}^b + M_t \psi_{hj} + I_t N_{hj} \quad (3a)$$

$$\gamma_{hj} = E_b I_c \mu_{hj}^c + E_b I_b \mu_{hj}^b - \rho_c A_c g \Gamma_{hj}^c - \rho_b A_b g \Gamma_{hj}^b - M_t g \chi_{hj} \quad (3b)$$

$$\beta_{ijkl} = \rho_c A_c \Lambda_{ijkl}^c + \rho_b A_b \Lambda_{ijkl}^b + M_t \sigma_{ijkl} + I_t \Xi_{ijkl} \quad (3c)$$

$$\lambda_{ijkl} = E_b I_c \eta_{ijkl}^c + E_b I_b \eta_{ijkl}^b \quad (3d)$$

$$\Psi_h = -(\rho_c A_c v_h^c + \rho_b A_b v_h^b + M_t \tau_h). \quad (3e)$$

The constants in Eq. (3) are functions of the mode shapes integrated from 0 to L_b . For the definition of constants in Eq. (3), the reader can refer to [10]. The harvester takes the monostable configuration if $M_t < M_{tb}$ and bistable configuration if $M_t > M_{tb}$ where M_{tb} is the buckling mass. In this chapter, studies are carried out to probe the behavior of monostable harvester in the presence of internal resonance.

Similarly, the governing differential equation of the electrical front of the harvester is obtained to be

$$C_p \dot{V} + \frac{V}{R_L} + \sum_{i=1}^N \Theta_{1,i} \dot{q}_i + \frac{1}{2} \sum_{i,j,k=1}^N \Theta_{2,ijk} \left(2q_i \dot{q}_j q_k + \dot{q}_i q_j q_k \right) = 0, \quad (4)$$

where Θ_1 and Θ_2 are the electromechanical coupling coefficients obtained as a function of the mode shape of the piezoelectric patch. R_L is the load resistance.

3 Approximate Solutions Using Perturbation Approach

In order to understand the performance of the harvester near its fundamental resonance, the system Eqs. (2) and (4) with weak nonlinearities ($\beta_{h_jkl} \rightarrow \epsilon \beta_{h_jkl}$, $\lambda_{h_jkl} \rightarrow \epsilon \lambda_{h_jkl}$) and damping ($c_h \rightarrow \epsilon c_h$) under soft excitation ($z \rightarrow \epsilon z$) is analyzed where ϵ is a perturbation constant that is very small.

Solutions for q and V are assumed to be of the following asymptotic form [6]:

$$q_h(t; \epsilon) = q_{h0}(T_0, T_1) + \epsilon q_{h1}(T_0, T_1) + O(\epsilon^2) \quad (5a)$$

$$V(t; \epsilon) = V_0(T_0, T_1) + \epsilon V_1(T_0, T_1) + O(\epsilon^2), \quad (5b)$$

where $T_0 = t$, $T_1 = \epsilon t$ are the time scales used in the present work. The temporal derivatives in the governing equations can be written in terms of T_0 and T_1 as

$$\frac{d}{dt} = D_0 + \epsilon D_1 + O(\epsilon^2); \quad \frac{d^2}{dt^2} = D_0^2 + 2\epsilon D_0 D_1 + O(\epsilon^2), \quad (6)$$

where $D_0 = \frac{\partial}{\partial T_0}$; $D_1 = \frac{\partial}{\partial T_1}$.

The zeroth-order solution of q_h is given by

$$q_{h0} = C_h(T_1) e^{i\omega_h T_0} + C_h^*(T_1) e^{-i\omega_h T_0}. \quad (7)$$

The two terms in the above solution represent the complex conjugate pair, where C_h is the complex amplitude to be found out and its complex conjugate term is represented by (*) in the superscript. Using q_{h0} , the zeroth-order solution of the generated voltage, V_0 , can be obtained as

$$V_0 = \tilde{V}_0 + \tilde{V}_0^*. \quad (8)$$

The term \tilde{V}_0 in Eq. (8) is obtained to be

$$\tilde{V}_0 = \sum_{i=1}^N R_i \Theta_{1,i} C_i e^{i\omega_i T_0}, \quad (9)$$

where $R_i = -\alpha_{ii} \frac{\left(\omega_i^2 C_p R_L^2 + i\omega_i R_L \right)}{1 + \omega_i^2 C_p^2 R_L^2}$.

This chapter only considers the first two primary modes commensurable with a ratio of 1:3. To denote the proximity of ω_2 to $3\omega_1$ and Ω to ω_1 , the following terms are defined.

$$\omega_2 = 3\omega_1 + \epsilon\sigma_0, \quad \Omega = \omega_1 + \epsilon\sigma_1, \quad (10)$$

where σ_0 and σ_1 are the internal detuning parameters. Making use of the above relation, the $O(\epsilon)$ term of the excitation force is given by

$$O(\epsilon) : \psi_h \ddot{z} = -\omega_h^2 z_0 \psi_h \cos(\omega_1 T_0 + \sigma_1 T_1). \quad (11)$$

Eliminating the secular terms of $O(\epsilon)$ to zero and setting the temporal derivatives with respect to T_1 to zero, the following stationary equations for amplitudes and phases when $\Omega \approx \omega_1$ are obtained.

$$\begin{aligned} 8\omega_1 a_1 (\sigma_1) + 4\text{Re}(Z_1) a_1 + [\text{Re}(W_{12}) \cos \eta_1 - \text{Im}(W_{12}) \sin \eta_1] a_1^2 a_2 + a_1 \sum_{i=1}^2 \text{Re}(W_{ii}) a_i^2 \\ = -4\psi_1 \omega_1^2 z_0 \cos \eta_2 \end{aligned} \quad (12)$$

$$\begin{aligned} 4\text{Im}(Z_1) a_1 + [\text{Im}(W_{12}) \cos \eta_1 + \text{Re}(W_{12}) \sin \eta_1] a_1^2 a_2 + a_1 \sum_{i=1}^2 \text{Im}(W_{ii}) a_i^2 \\ = 4\psi_1 \omega_1^2 z_0 \sin \eta_2 \end{aligned} \quad (13)$$

$$\begin{aligned} 8\omega_2 a_2 (3\sigma_1 - \sigma_0) + 4\text{Re}(Z_2) a_2 + [\text{Re}(P_{21}) \cos \eta_1 + \text{Im}(P_{21}) \sin \eta_1] a_1^3 \\ + a_2 \sum_{i=1}^2 \text{Re}(P_{ii}) a_i^2 = 0 \end{aligned} \quad (14)$$

$$4\text{Im}(Z_2)a_2 + [\text{Im}(P_{21}) \cos \eta_1 - \text{Re}(P_{21}) \sin \eta_1]a_1^3 + a_2 \sum_{i=1}^2 \text{Im}(P_{ii})a_i^2 = 0, \tag{15}$$

where a_1 and a_2 are the modal amplitudes. $\eta_1 = \varphi_2 + \sigma_0 T_1 - 3\varphi_1$ and $\eta_2 = \sigma_1 T_1 - \varphi_1$ are the phase shifts of the second modal response and excitation frequency with respect to the first modal response, respectively.

To obtain the steady-state solutions of the amplitudes and phases, the terms \dot{a}_i and $\dot{\varphi}_i$ are set to be equal to 0 in Eqs. (12)–(15).

The harvested power, P , is given by

$$P = \frac{|V_0|^2}{R_L}, \tag{16}$$

where the expression for V_0 is given in Eq. (8).

4 Results and Discussion

Table 1 provides the values of the parameters for which the numerical simulations are carried out in this work. The value of ϵ is taken to be 0.01 in this chapter. The lumped mass, M_t , is varied to realize 1:3 internal resonance in the harvesting system. The critical value of lumped mass ($M_{cr}=19.1$ g) corresponds to the value at which commensurability of the natural frequencies is realized. The first two natural frequencies pertaining to M_{cr} are 16.51 rad/s and 49.52 rad/s, respectively. The internal detuning parameter, σ_0 , is negative for $M_t > M_{cr}$ and positive for $M_t < M_{cr}$. Stable and unstable branches of the stationary solutions are represented by solid and dashed lines, respectively. Solid dot markers and black colored asterisk in the responses represent the Hopf (HP) and Saddle-Node (SN) points, respectively.

The frequency responses of first two modal amplitudes (a_1, a_2) and harvested power, P , for $\sigma_0 = 0$ under different excitation amplitudes are shown in Fig. 2. Despite a_2 taking a non-zero value, the frequency response of a_1 resembles a single-mode response for an excitation amplitude (z_0) of 2 mm. Loops emerge

Table 1 Description of parameters used in the model

Parameter	Value	Parameter	Value
ρ_b	7800 kg/m ³	ρ_p	5440 kg/m ³
A_b	4 mm ²	A_p	3 mm ²
d_b	0.25 mm	d_p	0.3 mm
L_b	300 mm	L_p	35 mm
L_t	100 mm	L_c	28 mm
E_b	210 GPa	E_p	15.857 GPa
$\xi_{1,2}$	0.02	C_p	15.11 nF

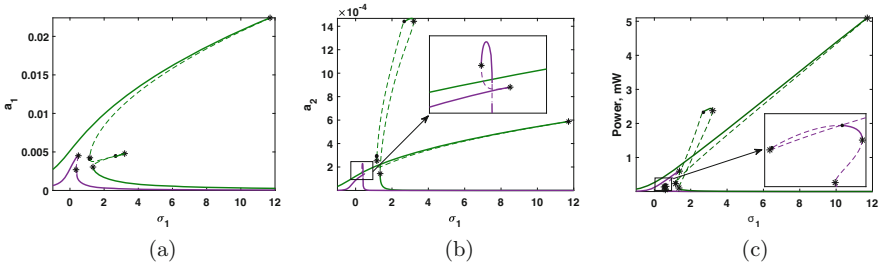


Fig. 2 Frequency response curves of modal amplitudes and harvested power when $\Omega \approx \omega_1$, $\sigma_0 = 0$, $R_L = 1 \text{ M}\Omega$. Violet and green lines correspond to $z_0 = 2 \text{ mm}$ and 15 mm , respectively

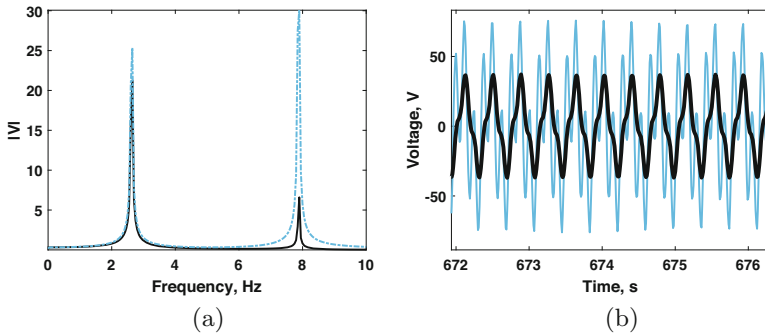


Fig. 3 Frequency spectra and time histories of generated voltage, V , for $z_0 = 15 \text{ mm}$, $R_L = 1 \text{ M}\Omega$, $\sigma_0 = 0$. Black and blue lines denote responses at $\sigma_1 = 1.8$ and $\sigma_1 = 2.5$, respectively

in the frequency response of a_2 indicating the existence of internal resonance in the system [6]. The amplitude of the loop-like branch increases considerably with increase in z_0 , which can be observed from Fig. 2b. This gives rise to an additional coexistent stable branch in the power curve ($2.4 \leq \sigma_1 \leq 3.2$ for $z_0 = 15 \text{ mm}$). The influence of higher mode response on the harvested power can be perceived from the observation that the magnitude of harvested power due to loop-like branch ($P \approx 2.5 \text{ mW}$) is of the same order as that of the primary hardening branch ($P \approx 5 \text{ mW}$) in the range of σ_1 considered for this chapter as can be seen from Fig. 2c.

For $z_0 = 15 \text{ mm}$, the time histories and frequency spectra obtained using fast Fourier transform (FFT) plots of voltage corresponding to $\sigma_0 = 0$, $R_L = 1 \text{ M}\Omega$ at two different values of σ_1 (1.8, 2.5) are shown in Fig. 3. Two frequencies dominate the responses, and expectedly, those frequencies pertain to first ($f_1 = 2\pi/\omega_1$) and second ($f_2 = 3f_1 = 2\pi/\omega_2$) natural frequencies of the system. The predominant contribution to the voltage from the first modal response, a_1 , is clearly evident for the case of $\sigma_1 = 2.5$, which could be observed from the FFT plot given in Fig. 3a. The significant energy transfer between the modes can be observed when $\sigma_1 = 2.5$

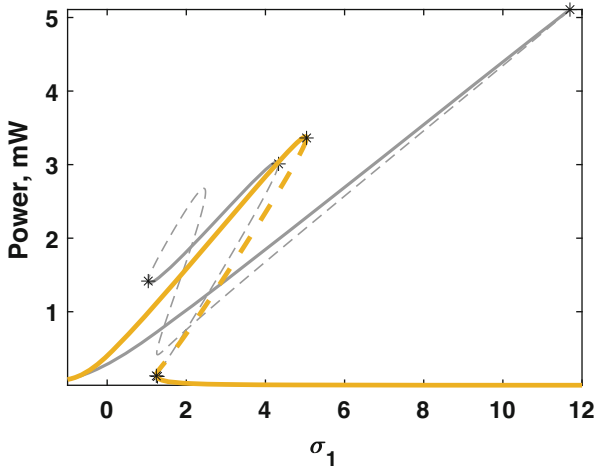


Fig. 4 Variation of the harvested power with σ_0 when for $R_L = 1 \text{ M}\Omega$ and $z_0 = 15 \text{ mm}$. Gray and orange lines denote the responses for $\sigma_0 = -10$ and $\sigma_0 = -20$, respectively

where the voltage generation due to loop-like branch surpasses that of a_1 although $\Omega \approx \omega_1$ as can be observed from the time history in Fig. 3b.

The variation of harvested power with detuning parameter, σ_0 , is shown in Fig. 4. For $\sigma_0 = -10$, the frequency response of P boasts a loop-like branch existing over a broader frequency range ($0.45 \leq \sigma_1 \leq 4.1$) with an appreciable magnitude of power as compared to other coexisting stable branches. The magnitude of power decreases tremendously when σ_0 is not very close to 0. This inference is well supported by the observation of the absence of loop-like branches when $\sigma_0 = -20$. Thus, the stable branch yielding higher power output can be realized by the appropriate tuning of internal detuning parameter (σ_0).

To understand the feasibility of activating higher power yielding branches, basins of attraction are studied when $\sigma_0 = -10$ and $z_0 = 15 \text{ mm}$, which are presented in Fig. 5. The power outputs of 2.35 mW, 1.12 mW, and 32 μW are represented by yellow, cyan, and violet basins, respectively, as shown in Fig. 5a. Similarly, violet and yellow basins in Fig. 5b denote the power outputs of 20 μW and 4.28 mW, respectively. The complex loop response is realized at $\sigma_1 = 3$ only if the initial values of a_2 are significantly large for values of a_1 belonging to the range $3.6e-3 \leq a_1 \leq 7.7e-3$. Yellow basin is preferred for a small set of initial conditions when $\sigma_1 = 6$ where a_1 is markedly larger than a_2 . Figure 5b demonstrates that the magnitude of power is significantly low for low values of a_1 . Hence, the harvesting efficiency in the required frequency band can be improved by operating the harvester with externally perturbed initial conditions.

The role of excitation amplitude on influencing the energy transfer between the modes, and consequently, the harvested power is shown in Fig. 6 when $\sigma_1 = 1.8$. A monotonic increase in the magnitude of harvested power is observed when $\sigma_0 = 0$

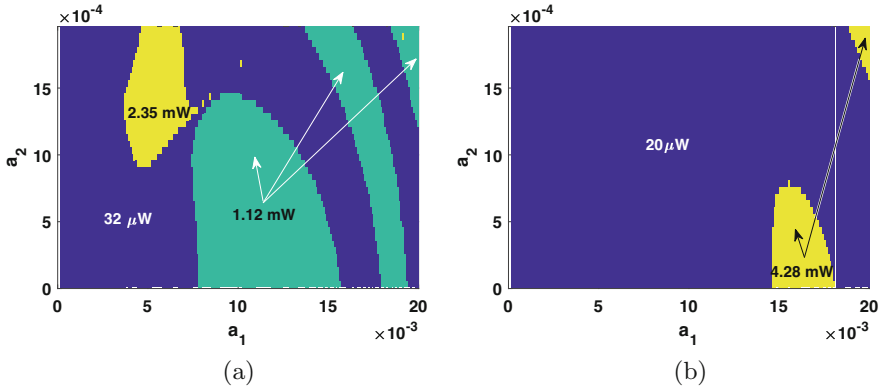


Fig. 5 Basins of attraction of harvested power for $z_0 = 15$ mm and $\sigma_0 = -10$ at (a) $\sigma_1 = 3$, (b) $\sigma_1 = 6$

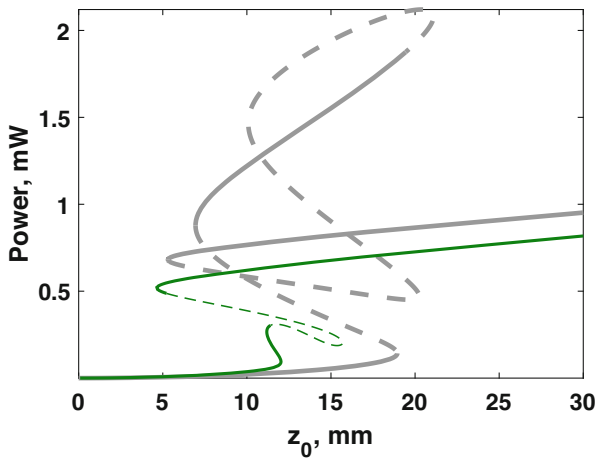


Fig. 6 Effect of excitation amplitude on harvested power at $\sigma_1 = 1.8$. Green and gray lines correspond to the responses when $\sigma_0 = 0$ and $\sigma_0 = -10$

with an increase in z_0 . In contrast to the above, three stable branches coexist in the range $6.4 \leq z_0 \leq 19.5$ when $\sigma_0 = -10$. The magnitude of power harvested can be increased notably by activating higher stable branch in the above specified amplitude range through suitable initial conditions. Saturation in the magnitude of power can be observed beyond a particular value of z_0 as seen in Fig. 6.

5 Conclusions

This chapter studies the role of 1:3 internal resonance toward broadband piezoelectric energy harvesting. The method of multiple scales is employed to obtain the asymptotic solutions of the governing equations in the neighborhood of fundamental resonance. Results presented in this chapter show that the higher mode positively influences the magnitude and bandwidth of power generation near the fundamental resonance. The work also reports the effect of suitable tuning of the lumped mass in amplifying the energy transfer between the modes that in turn enhances the power output. The outcomes of the present study demonstrate that the performance of piezoelectric harvester can be significantly improved by realizing 1:3 internal resonance between the first two modes.

Acknowledgments The authors are thankful to the Department of Science and Technology, India, for funding the research work (Project No. DST-YSS/2014/000336).

References

1. A. Erturk, D.J. Inman, *Piezoelectric Energy Harvesting* (Wiley, London, 2011)
2. F. Cottone, H. Vocca, L. Gammaitoni, Nonlinear Energy Harvest. Phys. Rev. Lett. **102**(8), 080601 (2009)
3. G. Litak, M. Friswell, S. Adhikari, Magnetopiezoelectric energy harvesting driven by random excitations. Appl. Phys. Lett. **96**(21), 214103 (2010)
4. M.I. Friswell, S.F. Ali, O. Bilgen, S. Adhikari, A.W. Lees, G. Litak, Non-linear piezoelectric vibration energy harvesting from a vertical cantilever beam with tip mass. J. Intell. Mater. Syst. Struct. **23**(13), 1505–1521 (2012)
5. M. Rajarathinam, S. Ali, Energy generation in a hybrid harvester under harmonic excitation. Energy Convers. Manag. **155**, 10–19 (2018)
6. A.H. Nayfeh, D.T. Mook, *Nonlinear Oscillations* (Wiley, London, 2008)
7. S.A. Emam, A.H. Nayfeh, Non-linear response of buckled beams to 1:1 and 3:1 internal resonances. Int. J. Non-Linear Mech. **52**, 12–25 (2013)
8. V. Guillot, A. Givois, M. Colin, O. Thomas, A. Ture Savadkoohi, C.-H. Lamarque, Theoretical and experimental investigation of a 1: 3 internal resonance in a beam with piezoelectric patches. J. Vib. Control. <https://doi.org/10.1177/1077546320910536>
9. Smart Material GmbH, MFC Types specifications. <https://www.smart-material.com/MFC-product-P2.html>
10. S.A. Mousavi Lajimi, M.I. Friswell, Energy harvesting from a non-linear standing beam–mass system: two-versus one-mode approximations. J. Intell. Mater. Syst. Struct. **28**(8), 1010–1022 (2017)

On Learning the Impact Dynamics of a Physical Beam Structure Coupled to a Multi-Stable Continuum



Ioannis T. Georgiou

1 A Bottom-Up Synthesis of a Class of Complex Flexible Structures for Irreversible Energy Flow

In this article we report preliminary results in regard to an effort to discover, by means of pure data-driven exploration of paradigmatic physical models, mechanical structural systems exhibiting nonlinear phenomena underlined by the irreversible flow of mechanical energy among its parts. Augmenting a flexible structure by embedding within it a flexible continuum with multiple static equilibria is a quite promising way to discover such systems [1–3]. Established nonlinear dynamics knowledge [4] and revised-updated classical mechanics [5] to include bifurcations and chaos as fundamental knowledge motivates research efforts aimed at exploring the use and design of nonlinearities for technology innovations. Herein presented is a bottom-up design of a class of complex mechanical structural systems to form a dynamics environment for the occurrence of processes (vibrations, waves) underlined by irreversible mechanical energy flow. Term complexity refers to both the geometry features of the system domain and the possible mathematical complexity (bifurcations, chaos) of the hosted dynamical processes. Current state-of-the-art sensor and data acquisition technologies render handling, in terms of acquiring high-quality data, this two-fold system complexity much more effective by means of an actual, physical model rather than by a mathematical one, the usual approach. Figure 1 depicts a physical continuum modified by embedding within it a multi-stable continuum to trigger interactions among slow invariant manifolds of waves-vibrations and the broad spectrum of manifolds of fast vibrations-waves

I. T. Georgiou (✉)
National Technical University of Athens, Athens, Greece
Purdue University, West Lafayette, IN, USA
e-mail: georgiou@central.ntua.gr

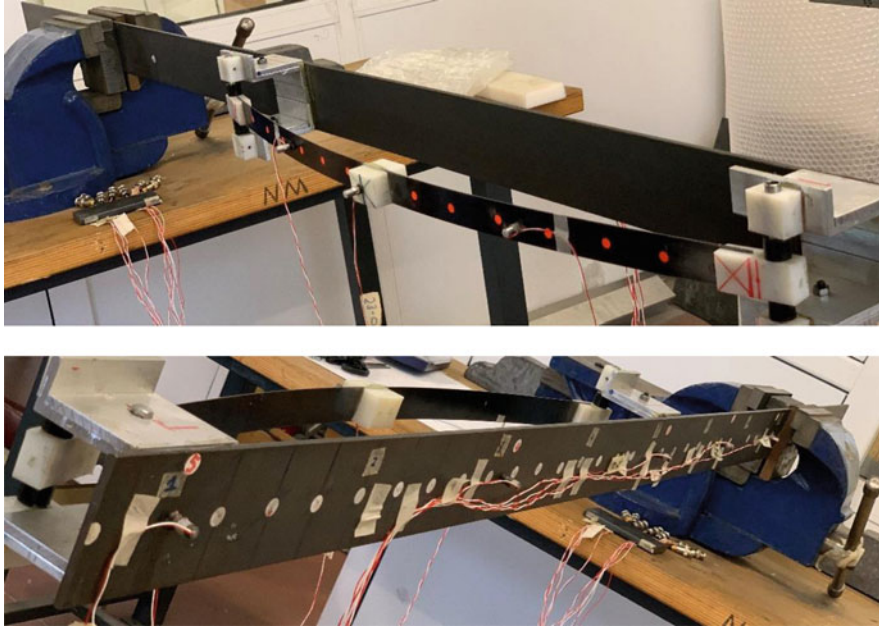


Fig. 1 Lab set-up of a two-beam coupled structure composed of a steel beam (core) and imbedded thin steel beam possessing at least three static equilibria (continuum level nonlinearity). Eight evenly distributed accelerometers sample simultaneously the transverse component of the acceleration vector field

(transversal fast fibers) supported by the continuum nature of the coupled system [3]. Slow-fast dynamics interactions in the presence of coexisting multiple static equilibria may infer irreversible energy flow between the two beams.

An interesting paradigmatic system is that synthesized by attaching at the free tip of a cantilevered elastic beam a planar rigid pendulum [6]: observed (for the first time) was the drain of vibration energy from the flexible continuum to the embedded multi-equilibria nonlinear oscillator. This phenomenon was attributed to bifurcation interactions of the slow invariant manifold of motions, contributed by the pendulum oscillator, with the transverse fast motions contributed by the flexible continuum. This interaction appears as an internal resonance between slow and fast oscillations at critical energy levels. It approaches the well-known internal 1:2 resonance occurring when the fast dynamics have evolved into the slow dynamics [7]. *Replacing the nonlinear oscillator with a multi-stable flexible continuum opens promising directions to discover potential exploitable nonlinear phenomena.* A related limiting slow-fast continuum system was analyzed in work [1, 2]. Therein emphasized is the role of the bifurcation of the slow invariant manifold and its interaction with fast vibrations [2]. The slow invariant manifold of a system is an equilibrium for all its fast time scales. Various known and unknown bifurcations may occur, thus enabling interactions with possible irreversible energy flow characteristics. The

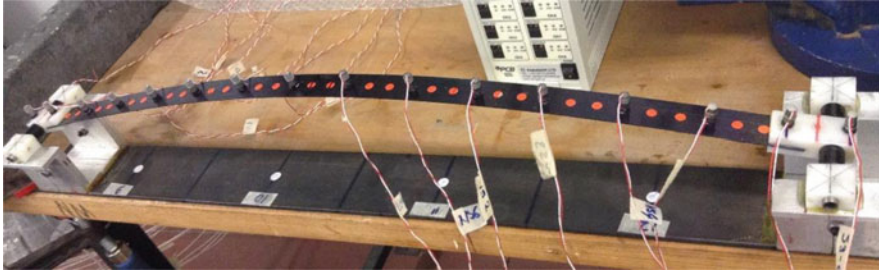


Fig. 2 A lab multi-stable flexible continuum of high-strength steel material. In previous work [20] 16 sensors were used to sample its motions at the bending acceleration level

challenge of discovering this interesting class of complex mechanical systems can be potentially met by means of synthesis of actual physical models. The physical model is attractive given the sensory data-and-machine learning potentiality. To this end, the physical dynamics of the two-beam system are sampled by a set of sensors detecting the transversal acceleration field in local time-and-space varying coordinates [8], in line with the modern considerations of geometric mechanics where natural coordinates are used to derive the equations of motions [9–11]. The advanced proper orthogonal decomposition (POD) transform [12–16] reduces the physical data cloud, the dataset geometric object, of the typical motion into essential low-dimensional modal dynamics (principal signals). The geometry of the physical data is the natural playground where correlations in simultaneous measurements shall form with indirect reference to the system complexity. The data cloud implicit topology is the bridge connecting mechanics available in raw datasets to the actual physics in the complex system. The role of the physical data cloud as a means to capture correlations in distributed sensing is emphasized along with the *axiom* that advanced POD computes its intrinsic geometric properties.

1.1 The Nature of the Embedded Multi-stable Flexible Continuum

Figure 2 depicts a thin beam continuum with a multitude of coexisting static equilibria induced-controlled by boundary conditions in the axial direction. It is a continuum level kind of geometric nonlinearity inferring strong coupling of three fields of motion: main bending without shearing, stretching without shearing, and minor lateral bending with significant shearing. The number of static equilibria can be increased by controlling the amount of axial displacement [9]. It allows ultra-fast dissipation of initially stored in bending strain energy [3, 20, 21]. This occurs because of the bifurcations-interactions of the slow dynamics with a sequence of fast coupled vibrations. In Fig. 1, this multi-stable continuum is embedded within in a larger-scale structure to explore: (1) whether it can absorb strain

energy initially stored in the latter; and (2) whether it can function as a vibration absorbing shield for the core structure in the sense energy stored initially in does not leak into the core continuum. We are searching for the existence of nonlinear phenomena characterized by irreversible energy flow from the core structure into the embedded multi-stable continuum. We shall potentially discover them, if they exist, by understanding its impact-induced response on the basis of sensory vibration data. The complexity of the structure domain enters the picture in the sense of how to distribute the sensors. It has been discovered that nonlinear mechanical structural systems with coexisting multiple static equilibria may admit dynamical processes with irreversible energy flow [6, 20–22]. A large volume of works is limited to very elementary two coupled oscillator systems [22]. Definitely, a continuum lever mechanics approach takes into account various complexity factors that can occur in an actual physical system. *Flexible continua with multiple static equilibria offer an unexplored topic to search for nonlinear phenomena underlined by irreversible energy flow* [21].

Experimental Procedure The two-beam structure, Fig. 1, is excited by means of a modal hammer to induce elastic wave propagation motions that eventually settle down to stationary waves or natural free vibrations. The dynamics developed in the complex structure domain are sampled at eight points by ultralight accelerometers. Motions are induced by controlled impact at sites over the multi-stable continuum as well as at sites over the core support continuum. The sensors provide the local coordinate resolution of the transverse acceleration field. This is a geometrically consistent measurement along natural local coordinates [8]. Modern geometric mechanics are formulated in coordinates which are consistent with shape and deformation [9–11] and thus geometry consistent sensing is a natural choice. So datasets collected by geometry consistent sensors need to be processed appropriately to detect redundant information and thus extract the essential dynamics. The data cloud plays an important role here. It allows comparing motions on the basis of only datasets [23]. Figure 3 presents the projection of the physical data cloud, embedded into an eight-dimensional Euclidean space, into a natural three-dimensional space that accommodates any triad of sensors. The complexity of the geometry of the data cloud is turned into analytic low-dimensional essential information by the advanced proper orthogonal decomposition transform.

Data quality The acquired digital data of acceleration are of high quality. The sensors are state-of-the-art ultra-light piezoelectric accelerometers with sensitivity near 1 mV/m/s^2 . The sampling rate is high at 48000 Hz accompanied by AD conversion resolution at 18 bits with a small discretization error at $10/2^{18}$. The signal/noise ratio is quite high, in the order of 500.

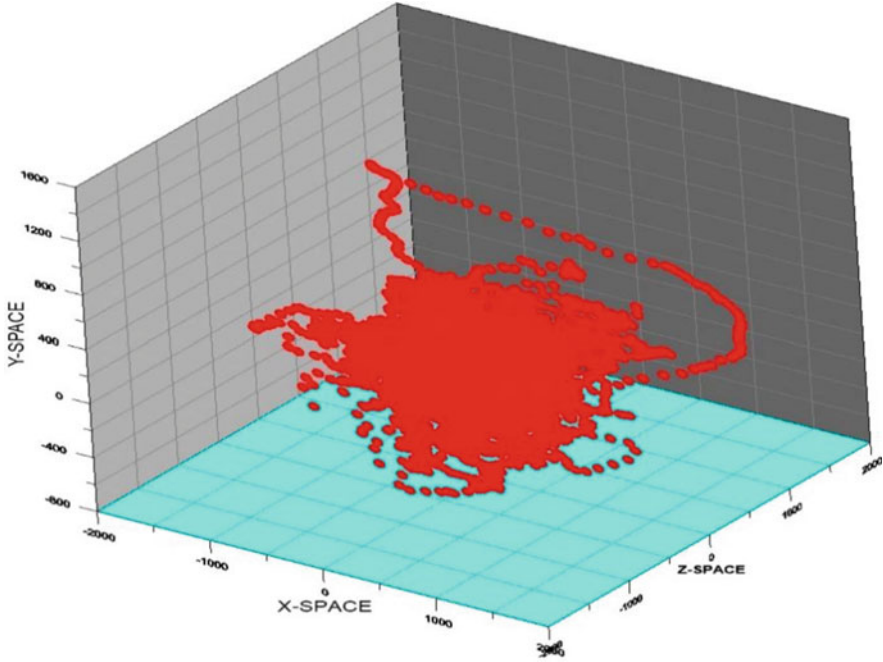
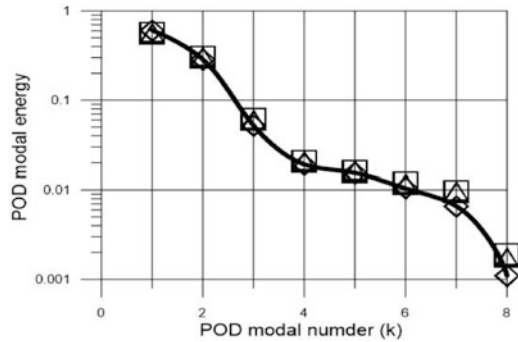


Fig. 3 Viewing the multi-channel simultaneous measurement as a collection of data points, the physical data cloud, in the appropriate Euclidean space is pivotal since hidden correlations give rise to implicit characteristic directions running through the data cloud. Shown above is the projection of an eight-dimensional data cloud into a three-dimensional space. The implicit characteristic directions, not easily discerned, govern the whole dataset

2 Physical Data Cloud Reduction Analysis

In this work, we emphasize the importance of the geometric structure of a multi-channel simultaneous measurement by sensors covering the whole structure. We have installed five sensors in the core structure and three in the multi-stable continuum. The typical multi-channel simultaneous measurement of the acceleration vector is viewed as a time sequence of snapshot points in the eight-dimensional Euclidean space. Important now is the multi-directional features of the data cloud, such as stationary directions about which the data are concentrated, Fig. 3. Passing from differential geometry [24] to functional analysis mathematical physics [25], these directions are necessarily normal to each other and they are identified by proper orthogonal decomposition (POD) transform computations [8, 16]. In machine learning classical POD [17–20] is known as PCA. Here we are using the advanced POD transform for dimension reduction computations since it is related to linear modal analysis philosophy aimed to characterize the physics of nonlinear processes in a reduced order, modal-like framework. The geometry of the data cloud is formed accordingly to the inherent relations among the sensor observers. To show

Fig. 4 Advanced POD-based computation of the ICDs size spectrum curve, identified with the POD energy spectrum curve, of three free motions, system in Fig. 1, at different energy levels. Motions excited by impacting the embedded multi-stable continuum



in the results that the multi-stable continuum is embedded in the core structure, we augment the eight-channel dataset to nine channels, where the added column is a copy of the data stream from sensor no. 3. This augmentation does not affect the implicit properties of the data cloud.

2.1 Results

This complex structure, Fig. 1, both in physical geometry and dynamics features, possesses a complicated wave function: free response to point-localized initial conditions. Just as in linear systems, prediction of the wave function is a central issue in nonlinear structural dynamics. It is a challenge for physical complex structures. To sample the unknown wave function, free motions were induced by impacting the two-beam structure at several points, located at the core and the embedded multi-stable continuum. In particular, for a specified point of excitation and when the structure was at one of the stable equilibria, families of motions were excited and parameterized by the impact magnitude: local and global waves-vibrations were excited.

Using advanced POD transform computation tools, a set of sensory data clouds were fused, decomposed, and projected into their intrinsic characteristic directions (ICDs). The fusion operation amounts to the collapse of the data cloud into the spectrum sequence of auto-correlation energies (eigenvalues). Figure 4 reveals that three such motions, with distant energy levels, have very similar energy spectrum curves. Figure 5 reveals that the dominant ICDs are realized as localized shapes over the nonlinear continuum. Certainly, these are remarkable results given the complexity of the structure and the exactly extracted reduced one-dimensional, thus modal-like, dynamics.

Are the localized data cloud modal shapes over the embedded nonlinear continuum vibration properties of the complex structure? To explore this issue, free motions are induced by impacting the core structure in a region close to the attached continuum nonlinearity. Figure 6 reveals that the sensory data cloud forms

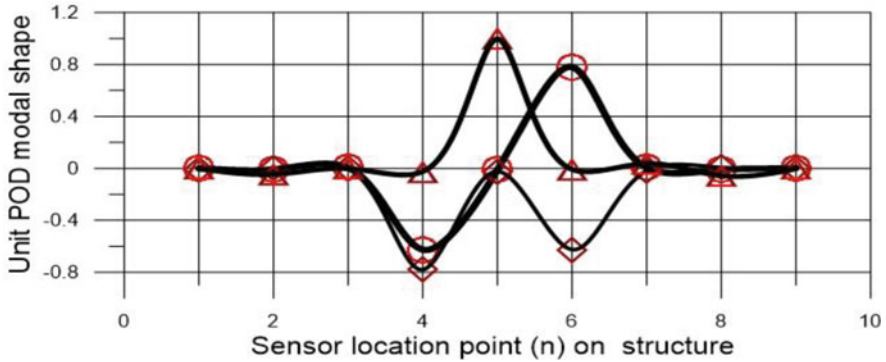


Fig. 5 Data cloud modal reduction of typical motion excited by impacting the embedded multi-stable continuum: Computed modal shapes of the dominant ICDs (first three data points, Fig. 4), localized over the nonlinear continuum domain (points: 4–6), core structure domain (points 1–3, and 7–9)

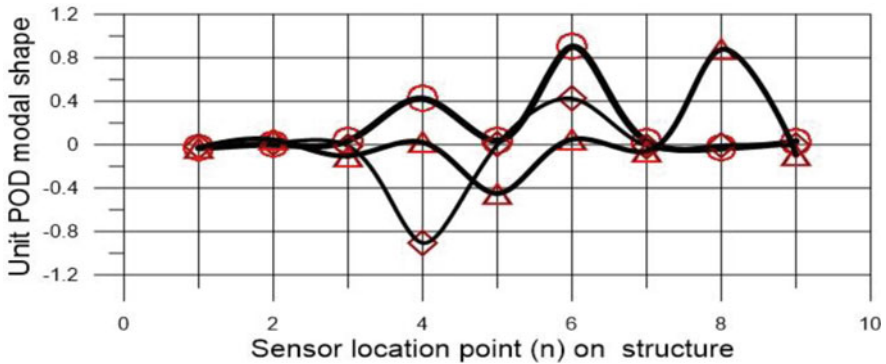


Fig. 6 Data cloud modal reduction of typical motion excited by impacting the embedded multi-stable continuum: Computed modal shapes of the dominant ICDs (first three data points, Fig. 4), localized over the nonlinear continuum domain (points: 4–6), core structure domain (points 1–3, and 7–9)

dominant directions localized as POD modal shapes over the multi-stable continuum domain. They are quite similar to the ones characterizing motions induced over the multi-stable continuum. It seems that the localization is insensitive to the location of the impact keeping in mind that impact dynamics of colliding bodies is not trivial mechanics [26]. This indicates that sensory data cloud implicit characteristic directions capture correlations due to localization and thus point directly to the existence of localized over the nonlinear continuum modal motions. But these data modal motions have very complicated waveforms as furnished by the principal signals frequency content: a range of slow vibrations interacting with a range of fast vibrations.

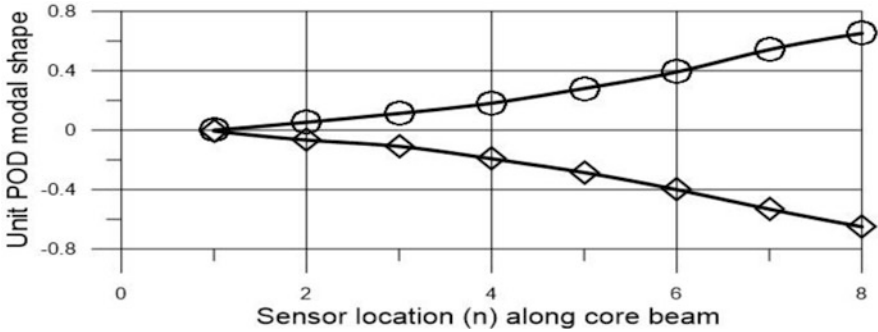


Fig. 7 The modal shapes of the dominant ICDs of two physical data clouds of the transverse acceleration field developed in the core cantilevered beam, Fig. 8. Identical ICDs accompanied by a common principal signal, which is a single frequency vibration at 1.64795 Hz

Verification of physics interpretation-the pivotal role of the cantilevered beam structure. The physical data cloud modal analysis method is verified by a reference, or benchmark, experiment where the physical data cloud geometry is related to modal properties of vibrations in a continuum whose modes are computed analytically by a reduced model. We remove the nonlinear continuum and we are left with the core structure, a cantilevered beam with two concentrated masses, Fig. 8. Two free motions are excited by separate impacts at nearby points. The collected physical data clouds are restricted over settled free vibrations, or standing waves, to avoid uncertainties due to interactions of propagating waves and anomalies in the structure. Figure 7 reveals that the two sensory data clouds share the same single dominant intrinsic characteristic direction. It is identified with the shape of the lowest or fundamental, normal mode of vibration of a cantilevered linear elastic beam with two concentrated masses. Here we have used the concept of intersections of variations of data clouds [23]. This reference experiment establishes the merit of the physical data cloud approach and its natural decomposition and physics interpretation by the advanced POD transforms. The reduced model is the Euler Bernoulli beam.

The Euler Bernoulli reduced model of a uniform cross-section beam structure is the bridge connecting the projection of the physical data cloud onto its implicit characteristic directions (ICD) to actual normal mode vibration physics. Admitting axiomatically a thorough decomposition by POD, the data cloud geometry is the needed generic feature allowing us to step into the generic nonlinear regime, the trade-off being the challenging issue of a physics interpretation of the data cloud ICDs and the companion principal signals. As presented here, this issue is addressed in first steps by determining whether the physical data clouds of a properly generated family of motions are intersected as geometric objects [23]. On one hand, strong intersection of physical data clouds seems to extract vibration modal physics, Fig. 7. On the other hand, weak intersection, extracts wave and vibration modal physics surrounded by a cloud of uncertainty [23].

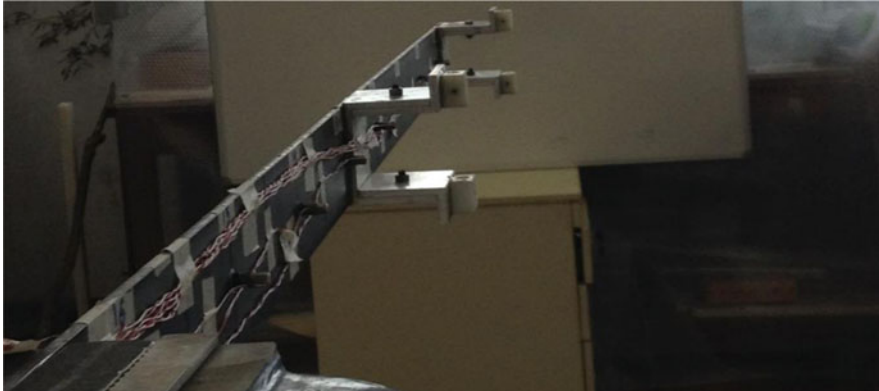


Fig. 8 The core cantilevered beam without the embedded multi-stable continuum. The slow dynamics should be governed by the classical Euler Bernoulli beam model, considered as reduced model of three-dimensional elasticity, modified by two masses. Sharp intersection of at least two physical data clouds over ICDs verifies this fact, Fig. 7

3 Discussion and Conclusions

We have learned some remarkable properties of the impact-induced free dynamics of a two-beam flexible structure explored as an interesting modification of a core cantilevered beam by embedding within it a multi-stable flexible beam. Previous experimental works [3, 20, 21] reveal that, when uncoupled, the specific multi-stable continuum exhibits ultra-fast decay of free vibrations. It is conjectured that this is due to the fact that the slow invariant manifold-initially dominated by bending slow motions-slaves, when multiple equilibria are present, the stretching motions, and the lateral bending with considerable shearing. Nonlinear coupling extends the slow invariant manifold to cover axial and lateral vibration motions. Slow invariant manifold bifurcation mechanisms precipitate interactions between slow and fast vibrations accompanied by ultra-fast decay.

When the multi-stable nonlinear continuum is attached to a specific flexible continuum, the core substructure, we are discovering several remarkable facts, thanks to the physical data cloud approach: learn the essential behavior of a complex system only from sensory datasets. The data cloud analysis reveals the following. Whenever a free motion is initiated by impact at a point on the embedded multi-stable continuum, the physical data cloud is dominated by three ICDs, POD data modes, with physical shapes localized strongly over the embedded multi-stable continuum. They contain more than 96% of the motion auto-correlation energy. A tiny amount of energy does leak into the core structure. The rest of the POD modes are localized over the core structure. For free motions initiated by impact at points on the core continuum, the physical data cloud is dominated by three ICDs which are very similar to the ones present in data clouds of motions excited by impact on the multi-stable continuum. The POD modes are properties of the geometry of the

physical data cloud and cannot be connected directly to normal modes of vibration. However, since they express the intrinsic characteristic directions of the data cloud geometry – formed naturally as a result of modal physics correlations in a continuum structure, we conjecture that the localized POD modal shapes indicate directly the presence of localized normal modes of vibration of the complex structure. We have the following consequence: The fact that vibration data localization occurs over the domain of the multi-stable continuum indicates that mechanical energy initially stored in the core structure eventually shall flow irreversibly into the embedded multi-stable continuum to naturally form localized motions.

The main issue considered was to learn how an impact-induced motion evolves from an elastic wave, excited locally, into settled free vibrations in the presence of multiple static equilibria in a complex structure. The geometric complexity of the structures along with the global multiple static equilibria presents an environment that renders this dynamical process a challenge to understand on the basis of pure sensor-based datasets. The impact-induced free motions carry a wealth of information: the genesis of an elastic wave, its interactions with anomalies, and its final attraction or transformation into free-standing waves, the eigenstates, or normal modes of vibration. Our experimental observations as analyzed by POD-based reduction indicate that, after the irreversible energy flow from the core structure into the multi-stable continuum, slow invariant manifold bifurcations (unexplored) push further irreversibly captured mechanical energy from multiple slow time scales into multiple fast time scales, and thus expediting the natural irreversible flow, dissipation, of mechanical energy into heat.

References

1. I.T. Georgiou, *Nonlinear Dynamics and Chaotic Motions of a Singularly Perturbed Nonlinear Viscoelastic Beam*. PhD Dissertation, Purdue U. Aero & Astro School, West Lafayette, Indiana (1993)
2. I.T. Georgiou, M.J. Corless, A.K. Bajaj, Dynamics of nonlinear structures with multiple equilibria: A singular perturbation-invariant manifold approach. *Zeitschrift fur angewandte Mathematic und Phyzic ZAMP* **50**, 892–924 (1999)
3. Georgiou, I.T.: A Physical Model-based Orthogonal Decomposition Approach in Exploiting Continuum Nonlinearities: Multiple Equilibria and Ultra-Fast Decaying Vibrations. In: 1st International Nonlinear Dynamics Conference (NODYCON19) Proceedings, Rome, Italy (2019)
4. J. Guckenheimer, P. Holmes, *Nonlinear Oscillations, Dynamical Systems, and Bifurcations of Vector Fields* (Springer, New York, 1983)
5. H. Goldstein, C.P. Poole, J. Safko, *Classical Mechanics*, 3rd edn. (Addison Wesley, San Francisco, 2002)
6. I.T. Georgiou, I.B. Schwartz, M. Emaci, A.F. Vakakis, Interaction between slow and fast oscillations in an infinite degree-of-freedom linear system coupled to a nonlinear subsystem: Theory and experiment. *ASME J. Appl. Mech.* **66**, 448–459 (1999)
7. I.T. Georgiou, On the global geometric structure of the dynamics of the elastic pendulum. *Nonlinear Dyn.* **18**, 51–68 (1999)

8. I.T. Georgiou, A single pair-of-sensors technique for geometry consistent sensing of acceleration vector fields in beam structures: Damage detection and dissipation estimation by POD modes. *Meccanica* **50**, 1303–1330 (2015)
9. B. Gabutti, P. Lepora, G. Merlo, A bifurcation problem involving the Elastica. *Meccanica* **15**, 154–165 (1980)
10. M.B. Rubin, *Cosserat Theories: Shells, Rods and Points* (Kluwer Academic, Dordrecht, 2000)
11. G. Romano, R. Barrette, M. Disco, Geometric continuum mechanics. *Meccanica*, **49** (1), 111–133 (2014)
12. I.T. Georgiou, I.B. Schwartz, A Proper Orthogonal Decomposition Approach to Coupled Structural-Mechanical Dynamical Systems. In: ASME-IMECE Symposium on Nonlinear Dynamics and Controls, DE-Vol. 91, 7–12, Atlanta, Georgia, USA (1996).
13. I.T. Georgiou, J. Sansour, Analyzing the finite element dynamics of nonlinear in-plane rods by the method of proper orthogonal decomposition, in *CIMNE: Computational Mechanics*, ed. by S. Adelson, E. Onate, E. Dvorkin, (New Trends and Applications, Barcelona, 1998)
14. I.T. Georgiou, I.B. Schwartz, Dynamics of large scale coupled structural-mechanical systems: A singular perturbation-proper orthogonal decomposition approach. *SIAM J. Appl. Math.* **59**(4), 1178–1207 (1999)
15. I.T. Georgiou, Advanced proper orthogonal decomposition tools: Using reduced order models to identify normal modes of vibration and slow invariant manifolds in the dynamics of planar nonlinear rods. *Nonlinear Dyn.* **41**, 69–110 (2005)
16. I.T. Georgiou, Advanced Time-and-Space POD Transform Computational Frameworks for Natural Reduction Analysis of Computational Nonlinear Continuum Mechanics: Understanding the Coupled-Tensor Field Dynamics of Flexible Rods, Unpublished, 2020.
17. M.M. Loeve, *Probability theory*, Van Nostrand (1955)
18. L. Sirovich, Turbulence and the dynamics of coherent structures. Pt.1. *Quart. Appl. Math.* **45**, 561–571 (1987)
19. N. Aubrey, P. Holmes, L.J. Lumley, E. Stone, The dynamics of coherent structures in the wall region of a turbulent boundary layer. *J. Fluid Mech.* **192**, 115–173 (1988)
20. I.T. Georgiou, A.K. Bajaj, Experimental nonlinear phenomena in structures with multiple equilibria controlled by boundary displacements: Ultra-fast decay of coupled vibrations. In: 9th European Nonlinear Dynamics Conference (ENOC2017) Proceedings. Budapest (2017).
21. I.T. Georgiou, Energy flow considerations in nonlinear systems on the basis of interesting experiments with three paradigmatic physical Systems in Engineering, in *IUTAM Symposium on Exploiting Nonlinear Dynamics for Engineering Systems. ENOLIDES 2018. IUTAM Book Series*, ed. by I. Koranic, S. Lenci, vol. 37, (Springer, Cham, 2020). https://doi.org/10.1007/978-3-030-23692-2_10
22. G. Kerchen, Y.S. Lee, A.F. Vakakis, D.M. McFarland, L.A. Bergman, Irreversible passive energy transfer in coupled oscillators with essential nonlinearities. *SIAM. J. Appl. Math.* **66**, 648–679 (2006)
23. I.T. Georgiou, Big data in experimental structural dynamics by synchronous ensembles of collocated acceleration signals (CAS): The reciprocity principle failure and advanced diagnostics for composite structures, in *IWSHM2019: Enabling Intelligence Life-Cycle Health Management for Industry Internet of Things (IIOT)*, ed. by F.-H. Chang, F. Kopsaftopoulos, (DEStech Publishing Inc., Lancaster, 2019)
24. M.W. Boothby, *An Introduction to Differentiable Manifolds and Riemannian Geometry* (Academic Press, INC., San Diego, California, 1986)
25. E.A. Taylor, C.D. Lay, *Introduction to Functional Analysis* (Robert E. Krieger Publishing Company, Malabar, Florida, 1980)
26. W. Goldsmith, *Impact: The Theory and Physical Behaviour of Colliding Solids* (Dover ed, New York, 2001)

Part VIII
Non-smooth Systems

Vibration Analysis of a Multi-DOF Impact Oscillator with Multiple Motion Constraints



Wei Dai  and Jian Yang 

1 Introduction

Impact oscillator models are widely used for studying the vibro-impact behaviour of many engineering dynamic systems such as tooling machineries [1, 2], drilling systems [3, 4], rotary machines [5] and robot joints [6]. Those systems usually consist of a main linear system and a single constraint or multiple constraints. When the displacement of the main system exceeds the constraint clearance, the main system may be engaged with the constraint. The inclusion of rigid or elastic constraint in a system can bring in non-smooth stiffness nonlinearities, resulting in complex nonlinear behaviour in the dynamic response including bifurcations and chaotic motions [7]. The elastic constraint may also alter the vibration transmission characteristics between sub-structures of the integrated system [8]. While much research has been conducted focusing on the dynamics of the single-degree-of-freedom (SDOF) impact oscillator with a single elastic or rigid constraint [9–11], there have been very limited studies on the dynamics of multi-degree-of-freedom (MDOF) impact oscillator systems with multiple motion constraints [12]. Such a study can then enable the investigation of the vibration transmission mechanisms and power flow characteristics, which can benefit the designs of vibration attenuation systems to obtain an improved performance [8, 12–20].

In this paper, the dynamics and vibration behaviour of a 3DOF impact oscillator with multiple linear motion constraints is studied. The mathematical model is firstly presented. Both the frequency-domain approximation method and the time-domain numerical method are then employed to determine the steady-state response of the system. The influence of the stiffness of the linear constraints on the response of the impact oscillator system is examined.

W. Dai · J. Yang (✉)

University of Nottingham Ningbo China, Ningbo, PR China

e-mail: jian.yang@nottingham.edu.cn

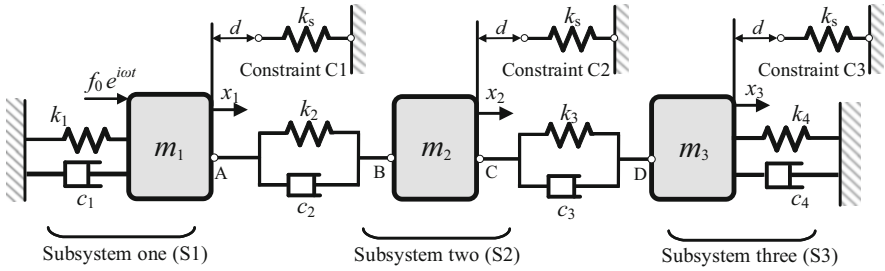


Fig. 1 Schematic of the 3DOF impact oscillator system with multiple constraints

2 Impact Oscillator Modelling with Multiple Constraints

Figure 1 shows the MDOF impact oscillator system model. Three masses are coupled via springs and dampers to form a chain oscillator, the motion of which is restrained by three springs as motion constraints. The SDOF subsystem one (S1) on the left is subjected to a harmonic force excitation with the amplitude of f_0 and frequency of ω . The static equilibrium positions of the three masses, where $x_1 = x_2 = x_3 = 0$ and the springs k_1, k_2, k_3, k_4 are un-stretched, are set as a reference. Three linear constraints C 1, C 2 and C 3 with identical stiffness k_s are for the masses m_1, m_2 and m_3 , respectively. When the springs in three constraints are un-stretched and the masses are in equilibrium, i.e. $x_1 = x_2 = x_3 = 0$, the left-hand-side terminals of the three linear constraints are placed at a distance of d to the right of masses m_1, m_2 and m_3 , respectively.

Based on Newton’s 2nd law, the governing equations of the impact oscillator can be obtained and presented in a matrix form as

$$\begin{aligned}
 & \begin{bmatrix} m_1 & 0 & 0 \\ 0 & m_2 & 0 \\ 0 & 0 & m_3 \end{bmatrix} \begin{Bmatrix} \ddot{x}_1 \\ \ddot{x}_2 \\ \ddot{x}_3 \end{Bmatrix} + \begin{bmatrix} c_1 + c_2 & -c_2 & 0 \\ -c_2 & c_2 + c_3 & -c_3 \\ 0 & -c_3 & c_4 + c_3 \end{bmatrix} \begin{Bmatrix} \dot{x}_1 \\ \dot{x}_2 \\ \dot{x}_3 \end{Bmatrix} \\
 & + \begin{bmatrix} k_1 + k_2 & -k_2 & 0 \\ -k_2 & k_2 + k_3 & -k_3 \\ 0 & -k_3 & k_4 + k_3 \end{bmatrix} \begin{Bmatrix} x_1 \\ x_2 \\ x_3 \end{Bmatrix} + \begin{Bmatrix} f_{C1} \\ f_{C2} \\ f_{C3} \end{Bmatrix} = \begin{Bmatrix} f_0 e^{i\omega t} \\ 0 \\ 0 \end{Bmatrix}, \quad (1)
 \end{aligned}$$

where $f_{C1} = k_s(x_1 - d)U(x_1 - d)$, $f_{C2} = k_s(x_2 - d)U(x_2 - d)$ and $f_{C3} = k_s(x_3 - d)U(x_3 - d)$ are the nonlinear forces applied by the constraints C1, C2 and C3 to the mass m_1, m_2 and m_3 , respectively, and $U(\delta)$ in those expressions represents the Heaviside step function of a displacement variable δ defined by

$$U(\delta) = \begin{cases} 0, & \text{when } \delta \leq 0, \\ 1, & \text{when } \delta > 0. \end{cases} \quad (2)$$

For the later parametric study, the following parameters can be introduced as

$$\omega_1 = \sqrt{\frac{k_1}{m_1}}, \omega_2 = \sqrt{\frac{k_4}{m_3}}, \zeta_1 = \frac{c_1}{2m_1\omega_1}, \zeta_2 = \frac{c_4}{2m_3\omega_2}, l_0 = \frac{m_1 g}{k_1},$$

$$X_1 = \frac{x_1}{l_0}, X_2 = \frac{x_2}{l_0}, X_3 = \frac{x_3}{l_0}, \lambda = \frac{k_s}{k_1}, \gamma = \frac{\omega_2}{\omega_1}, \mu = \frac{m_2}{m_1}, \rho = \frac{m_3}{m_1},$$

$$\kappa = \frac{k_2}{k_1}, \alpha = \frac{c_2}{c_1}, \epsilon = \frac{k_3}{k_1}, \beta = \frac{c_3}{c_1}, F_0 = \frac{f_0}{l_0 k_1}, \Omega = \frac{\omega}{\omega_1}, \tau = \omega_1 t, \eta = \frac{d}{l_0},$$

where ω_1 and ω_2 denote the natural frequencies of the linear oscillator in subsystem-1 (S1) and subsystem-3 (S3) without the constraints, respectively, ζ_1 and ζ_2 represent the damping ratios of the individual oscillators in S1 and S3, respectively, l_0 is the characteristic length, X_1, X_2 and X_3 are the dimensionless response displacements for mass m_1, m_2 and m_3 , respectively, λ is the stiffness ratio of the linear constraint, γ is the undamped natural frequency ratio between the oscillators in S1 and S3, μ and ρ are the mass ratios, κ and α are the non-dimensional stiffness and damping ratios for the interfacial spring and damper between m_1 and m_2 , respectively, ϵ and β are the non-dimensional stiffness and damping ratios for the spring and damper between m_1 and m_3 , respectively, F_0 and Ω are the non-dimensional excitation amplitude and frequency, respectively, τ is the dimensionless time and η is the gap width ratio. By using these parameters, the governing equation of Eq. (1) can be transformed into a non-dimensional form as

$$\begin{bmatrix} 1 & 0 & 0 \\ 0 & \mu & 0 \\ 0 & 0 & \rho \end{bmatrix} \begin{Bmatrix} X_1'' \\ X_2'' \\ X_3'' \end{Bmatrix} + \begin{bmatrix} 2\zeta_1(1 + \alpha) & -2\zeta_1\alpha & 0 \\ -2\zeta_1\alpha & 2\zeta_1(\alpha + \beta) & -2\zeta_1\beta \\ 0 & -2\zeta_1\beta & 2(\rho\zeta_2\gamma + \zeta_1\beta) \end{bmatrix} \begin{Bmatrix} X_1' \\ X_2' \\ X_3' \end{Bmatrix} + \begin{bmatrix} 1 + \kappa & -\kappa & 0 \\ -\kappa & \kappa + \epsilon & -\epsilon \\ 0 & -\epsilon & \rho\gamma^2 + \epsilon \end{bmatrix} \begin{Bmatrix} X_1 \\ X_2 \\ X_3 \end{Bmatrix} + \begin{Bmatrix} F_{C1} \\ F_{C2} \\ F_{C3} \end{Bmatrix} = \begin{Bmatrix} F_0 e^{i\Omega\tau} \\ 0 \\ 0 \end{Bmatrix}, \quad (3)$$

where $F_{C1} = \lambda(X_1 - \eta)U(X_1 - \eta)$, $F_{C2} = \lambda(X_2 - \eta)U(X_2 - \eta)$ and $F_{C3} = \lambda(X_3 - \eta)U(X_3 - \eta)$ are the dimensionless nonlinear forces applied by the constraints C1, C2 and C3, respectively. To obtain the steady-state response of the system, numerical integration method with time discretization, i.e. the Runge-Kutta Dormand-Prince (RKDP) method with adaptive time-step size, and the harmonic balance method with alternating-frequency-time scheme (HB-AFT) are used to solve the Eq. (3). To implement HB-AFT for the current system, the steady-state dimensionless displacement responses of the masses are firstly approximated by a truncated N -order Fourier series with the fundamental frequency of Ω , and

the corresponding velocity and acceleration response can be obtained by the differentiation of the displacement response. The time histories of the dimensionless constraints forces F_{C1} , F_{C2} and F_{C3} , can then be obtained and Fourier transformed to find the Fourier coefficients of the constraints forces. By substituting those expressions into Eq. (3) and balancing the corresponding harmonic terms, a total number of $(6N + 3)$ nonlinear algebraic equations can be obtained. A combination use of Newton-Raphson method and numerical arc-length continuation method can be used to determine the roots for those equations [21–23].

3 Results and Discussions

Here the effects of the stiffness ratio λ of the linear motion constraints on the steady-state maximum displacement X_{1_max} of the mass m_1 , X_{2_max} of the mass m_2 and X_{3_max} of the mass m_3 are investigated and shown in Figs. 2, 3 and 4, respectively. Four different values of stiffness ratio λ are considered with $\lambda = 0, 0.5, 1$ and 1.5 , of which the case with $\lambda = 0$ is the un-constrained system used for comparison purpose. The system parameters are set as $\zeta_1 = \zeta_2 = 0.01$, $\gamma = 1$, $\mu = 1$, $\rho = 1$, $\kappa = 1$, $\epsilon = 1$, $\alpha = 1$, $\beta = 1$, $\eta = 0.1$ and $F_0 = 0.1$. The results obtained by the 7th order HB-AFT method are plotted in different lines while those obtained by RKDP method are denoted by symbols.

Figure 2 shows that three main peaks are observed in each steady-state frequency response curve of the mass m_1 . By conducting modal analysis on the corresponding un-constrained linear system with $\lambda = 0$, it is found that at the first peak near $\Omega = 0.75$, the motions of the three masses are in-phase, i.e. the relative phase angle between the responses of three masses is zero. When the system is excited at the second peak near $\Omega = 1.4$, the displacement responses of the mass m_1 and the mass m_3 are out of phase, i.e. the relative phase angle is π , while the response amplitude

Fig. 2 Effects of stiffness ratio λ of the constraints on the steady-state maximum displacement X_{1_max} of the mass m_1 . The solid line and circles, dashed line and triangles, dotted line and squares, dash-dot line and rhombuses are for $\lambda = 0, 0.5, 1.0$ and 1.5 , respectively

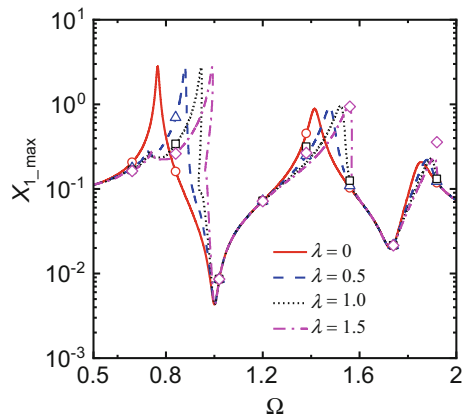


Fig. 3 Effects of stiffness ratio λ of the constraints on the steady-state maximum displacement X_{2_max} of the mass m_2 . The solid line and circles, dashed line and triangles, dotted line and squares, dash-dot line and rhombuses are for $\lambda=0, 0.5, 1.0$ and 1.5 , respectively

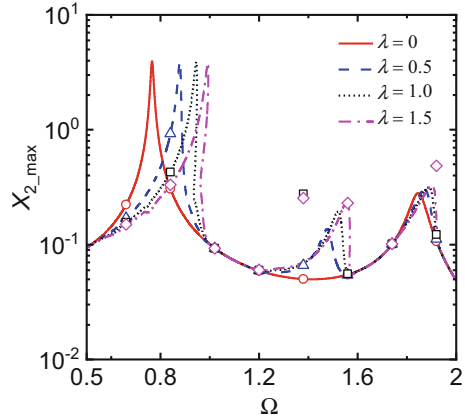
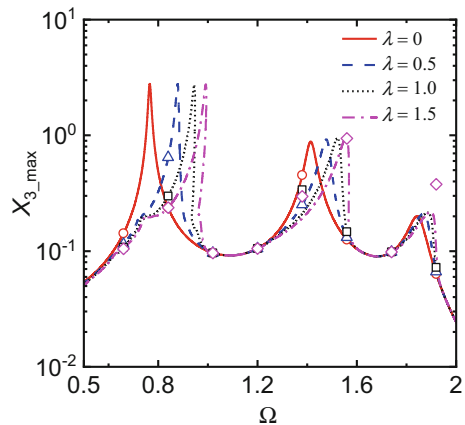


Fig. 4 Effects of stiffness ratio λ of the constraints on the steady-state maximum displacement X_{3_max} of the mass m_3 . The solid line and circles, dashed line and triangles, dotted line and squares, dash-dot line and rhombuses are for $\lambda=0, 0.5, 1.0$ and 1.5 , respectively



of the mass m_2 is relatively small. As for $\Omega \approx 1.85$, the motions of the mass m_2 and mass m_3 are in-phase but the response of the mass m_1 has a phase difference of $\pi / 2$ to that of the mass m_2 as well as the mass m_3 . Figure 2 also shows that with the introduction of linear constraints, all three peaks of the X_{1_max} curves bend to the high-frequency range. Multiple solutions can be found near the resonant frequencies. The reason is that the response displacement magnitude of the mass m_1 exceeds the gap width η between the constraint and the mass, therefore the mass m_1 is engaged with the constraint C1 near the peak frequencies. The linear constraint can increase the system stiffness during the intermittent contact with the mass and lead to a hardening effect on the response of the mass m_1 . It was also found that there is a local maximum point in the X_{1_max} curve when $\Omega \approx 0.7$. This is due to the super-harmonic response component of the mass m_1 , to be shown later. When the constraint stiffness ratio λ increasing from 0 to 0.5, to 1 and to 2, the three peaks in the X_{1_max} curves bend more to the right. Moreover, the first peak value shows

little variation while there are slight increases in the second peak and the third peak values with the increasing λ .

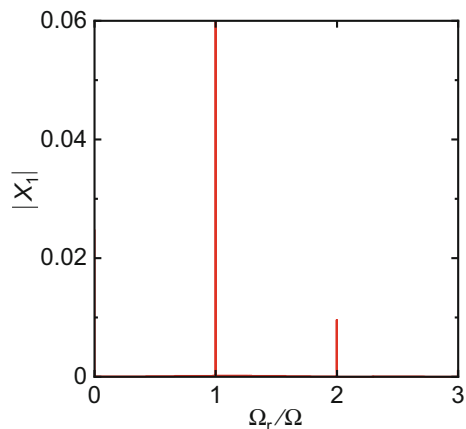
Figure 3 shows that for the un-constrained system with $\lambda = 0$, there are only two peaks in the frequency response curve of the mass m_2 . An extra peak can be found near $\Omega = 1.4$ when the linear constraint is considered. It also shows that with the increase of the constraint stiffness ratio λ from 0 to 0.5, then to 1.0 and finally to 1.5, the first peak and the third peak of X_{2_max} are bending to the right with only minor differences in the first peak but a slight increase in the third peak value. The second peak also shows a bending to the right with a substantial growth on the peak value. However, it is noticed that there are relatively large discrepancies between the HB-AFT result and the numerical integration results near the second and the third peak frequency when the stiffness ratio λ of the constraints are relatively high, i.e. $\lambda = 1$ and 1.5. This phenomenon will be further explored later.

Figure 4 shows that by a comparison between the un-constrained case with stiffness ratio $\lambda = 0$ and the linear constraint cases, all three peaks of the steady-state response curves X_{3_max} of the mass m_3 extend to the high frequencies due to the interaction between the masses and the corresponding linear constraints. With the increase of λ from 0 to 0.5, to 1.0 and to 1.5, more bending on all three peaks to the high frequency range can be observed. Slight increase can be found on the second and third peak of the X_{3_max} curve. In contrast, there is a small reduction on the first peak value. Figure 4 also shows a difference between HB-AFT result and numerical integration result in the case of $\lambda = 1.5$ when the system is excited near the third peak. This phenomenon is further discussed in later content.

Figure 5 presents the frequency spectra of the response of the mass in S1 in the case of $\lambda = 1.5$ when excited at $\Omega = 0.7$. It shows that there exists a super-harmonic response component at $\Omega_r = 2\Omega$, which is corresponding to the local maximum point in the frequency response of the mass m_1 in S1 near $\Omega = 0.7$ shown in Fig. 2.

Figure 6 further explores the reasons for the differences between HB-AFT approximation results and numerical integration results observed in Figs. 2, 3

Fig. 5 Frequency spectra of the displacement response of the mass m_1 in S1 at the excitation frequency of $\Omega = 0.7$.



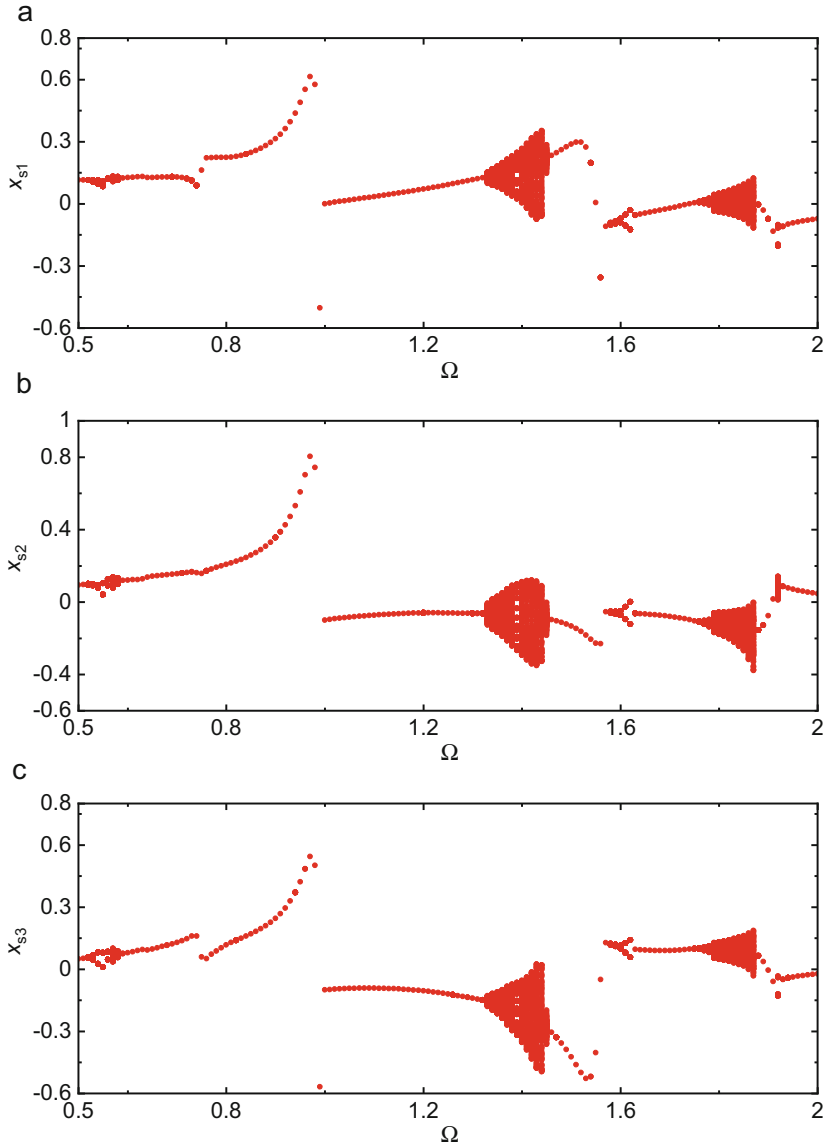


Fig. 6 Bifurcation diagrams with a low-to-high frequency sweep for (a) x_{s1} of the mass m_1 , (b) x_{s2} of the mass m_2 and (c) x_{s3} of the mass m_3 .

and 4 by studying the system with parameters set as $\lambda = 1.5$, $\zeta_1 = \zeta_2 = 0.01$, $\gamma = 1$, $\mu = 1$, $\rho = 1$, $\kappa = 1$, $\epsilon = 1$, $\alpha = 1$, $\beta = 1$, $\eta = 0.1$ and $F_0 = 0.1$. Figure 6a–c shows the bifurcation diagrams for each mass by using a low-to-high frequency sweep, respectively. The steady-state time histories of the dimensionless

displacement of each mass obtained by RKDP method are sampled using a sampling period of $T = 2\pi/\Omega$. The samplings of the dimensionless displacement x_{s1} of m_1 , x_{s2} of m_2 and x_{s3} of m_3 from a starting time of $256 T$ and to $356 T$ at each pre-described excitation frequency in the range of $0.5 \leq \Omega \leq 2$ are recorded and plotted, respectively. It shows that the bifurcations occur on the boundaries of the frequency ranges of $0.5 < \Omega < 0.6$, $1.3 < \Omega < 1.45$ and $1.55 < \Omega < 1.65$ as well as $1.75 < \Omega < 1.9$. Non-periodic responses can be observed at particular frequency bands of $1.3 < \Omega < 1.45$ and $1.75 < \Omega < 1.85$. This behaviour suggests that in these frequency ranges, even little variations in the parameter values of the system can lead to significant changes in the response of the masses. The HB method based on the assumption of periodic responses cannot capture the non-periodic responses that occurred in these frequency bands, resulting in the discrepancies between the HB-AFT results and numerical integration results. It may be summarized that a large stiffness ratio of the linear constraints may lead to bifurcations when the excitation frequency is in the vicinity of the three resonant frequencies. This phenomenon is related to the stronger stiffness nonlinearities introduced by the constraints into the oscillating system when increasing the stiffness λ of the linear constraints. For the systems with a smaller value of λ , there is weaker stiffness nonlinearity introduced by the constraints into the oscillating system and hence a reduced nonlinear effect. With the responses of the systems obtained, further analysis on vibration transmission in terms of force transmissibility and vibration power flow can be conducted to reveal the effects of motion constraints on vibration suppression performance.

4 Conclusions

This paper studied the dynamic responses of an MDOF impact oscillator with multiple linear spring constraints. The equations of motion of the impact oscillator system subjected to harmonic force excitation were firstly obtained and solved by HB-AFT approximation and time-marching method. The influence of the stiffness ratio of the linear constraints on the response behaviour of the oscillator system was studied. The results show that the inclusion of the linear constraints can lead to rich nonlinear phenomena including super-harmonic responses and multiple solution branches. The resonance peaks in the curves of the steady-state displacement response of the masses bend to the high-frequencies and an extra peak may appear in the frequency response curve of the second mass in the middle. An increase of the stiffness ratio of the linear constraints may introduce a stronger hardening nonlinear effect on the system such that all the peaks in the frequency response curves twist further to the right. Bifurcations can occur near the resonance peaks of the response of each mass when the stiffness of the constraints is high.

Acknowledgments This work was supported by the National Natural Science Foundation of China (Grant number 12172185).

References

1. M. Wiercigroch, A.M. Krivtsov, Frictional chatter in orthogonal metal cutting. *Philos. Trans. Royal Soc. A Math Phys. Eng. Sci.* **359**(1789), 2629–2629 (2001)
2. P. Wahi, A. Chatterjee, Self-interrupted regenerative metal cutting in turning. *Int. J. Non-Linear Mech.* **43**, 111–123 (2008)
3. M. Wiercigroch, J. Wojewoda, A.M. Krivtsov, Dynamics of ultrasonic percussive drilling of hard rocks. *J. Sound Vib.* **280**, 739–757 (2005)
4. E. Pavlovskaja, D.C. Hendry, M. Wiercigroch, Modelling of high frequency vibro-impact drilling. *Int. J. Mech. Sci.* **91**, 110–119 (2015)
5. J. Hong, P. Yu, D. Zhang, Y. Ma, Nonlinear dynamic analysis using the complex nonlinear modes for a rotor system with an additional constraint due to rub-impact. *Mech. Syst. Signal Proc.* **116**, 443–461 (2019)
6. S. Yin, J. Ji, G. Wen, Complex near-grazing dynamics in impact oscillators. *Int. J. Mech. Sci.* **156**, 106–122 (2019)
7. A.B. Nordmark, Non-periodic motion caused by grazing incidence in an impact oscillator. *J. Sound Vib.* **145**, 279–297 (1991)
8. W. Dai, J. Yang, B. Shi, Vibration transmission and power flow in impact oscillators with linear and nonlinear constraints. *Int. J. Mech. Sci.* **168**, 105234 (2020)
9. H. Jiang, A.S.E. Chong, Y. Ueda, M. Wiercigroch, Grazing-induced bifurcations in impact oscillators with elastic and rigid constraints. *Int. J. Mech. Sci.* **127**, 204–214 (2017)
10. M. Wiercigroch, S. Kovacs, S. Zhong, D. Costa, V. Vaziri, M. Kapitaniak, E. Pavlovskaja, Versatile mass excited impact oscillator. *Nonlinear Dyn.* **99**, 323–339 (2020)
11. J. Ing, E. Pavlovskaja, M. Wiercigroch, S. Banerjee, Bifurcation analysis of an impact oscillator with a one-sided elastic constraint near grazing. *Phys. D Nonlinear Phenom.* **239**, 312–321 (2010)
12. W. Dai, J. Yang, Vibration transmission and energy flow of impact oscillators with nonlinear motion constraints created by diamond-shaped linkage mechanism. *Int. J. Mech. Sci.* **194**, 106212 (2020)
13. J. Yang, Y.P. Xiong, J.T. Xing, Dynamics and power flow behaviour of a nonlinear vibration isolation system with a negative stiffness mechanism. *J. Sound Vib.* **332**, 167–183 (2013)
14. J. Yang, Y.P. Xiong, J.T. Xing, Nonlinear power flow analysis of the duffing oscillator. *Mech. Syst. Signal Proc.* **45**, 563–578 (2014)
15. J. Yang, Y.P. Xiong, J.T. Xing, Power flow behaviour and dynamic performance of a nonlinear vibration absorber coupled to a nonlinear oscillator. *Nonlinear Dyn.* **80**, 1063–1079 (2015)
16. J. Yang, Y.P. Xiong, J.T. Xing, Vibration power flow and force transmission behaviour of a nonlinear isolator mounted on a nonlinear base. *Int. J. Mech. Sci.* **115–116**, 238–252 (2016)
17. J. Yang, B. Shi, C. Rudd, On vibration transmission between interactive oscillators with nonlinear coupling interface. *Int. J. Mech. Sci.* **137**, 238–251 (2018)
18. B. Shi, J. Yang, C. Rudd, On vibration transmission in oscillating systems incorporating bilinear stiffness and damping elements. *Int. J. Mech. Sci.* **150**, 458–470 (2019)
19. J. Yang, J.Z. Jiang, S.A. Neild, Dynamic analysis and performance evaluation of nonlinear inerter-based vibration isolators. *Nonlinear Dyn.* **99**, 1823–1839 (2019)
20. C. Zhu, J. Yang, C. Rudd, Vibration transmission and power flow of laminated composite plates with inerter-based suppression configurations. *Int. J. Mech. Sci.* **190**, 106012 (2020)
21. G. Von Groll, D.J. Ewins, The harmonic balance method with arc-length continuation in rotor/stator contact problems. *J. Sound Vib.* **241**, 223–233 (2001)
22. A.H. Nayfeh, B. Balachandran, *Applied nonlinear dynamics: analytical, computational, and experimental methods* (Wiley, New York, 2008)
23. R. Seydel, *Practical bifurcation and stability analysis*, 3rd edn. (Springer, Heidelberg, 2010)

Design of NARX Model for Dry Friction System of the Three-Piece Bogie



Dali Lyu, Qichang Zhang, and Shuying Hao

1 Introduction

Dry friction occurs in all actual mechanical systems, in which surfaces are in contact with each other and can slide freely between each other [1]. The characteristic of the dry friction plays a significant role in the dynamic system. In some scenarios, friction plays advantageous effects, such as the application of automobile tires, clutches, brake pads, bogie wedges, and various dampers. Friction also has disadvantageous effects, such as abnormal vibration and noise caused by friction. Therefore, the study of friction dynamics has very important theoretical and practical significance. The dynamic behavior of dry friction belongs to the category of non-smooth dynamics. The research of non-smooth dynamic systems involves many fields such as machinery, aerospace, control, power, and neural networks [2]. The first mathematical friction model was proposed by Coulomb, which depends on the relative velocity direction. The magnitude of the friction force is constantly proportional to the normal contact force, as shown in Fig. 1. Stribeck effect [3] ensures that the friction force changes during a continuous function of the velocity,

D. Lyu

Department of Mechanics, School of Mechanical Engineering, Tianjin University, Tianjin, China

Tianjin Key Laboratory of Nonlinear Dynamics and Control, Tianjin University, Tianjin, China

Tianjin Internal Combustion Engine Research Institute, Tianjin University, Tianjin, China

Q. Zhang (✉)

Department of Mechanics, School of Mechanical Engineering, Tianjin University, Tianjin, China

Tianjin Key Laboratory of Nonlinear Dynamics and Control, Tianjin University, Tianjin, China

e-mail: qzhang@tju.edu.cn

S. Hao

Tianjin Key Laboratory of Advanced Electromechanical System Design and Intelligent Control,

Tianjin University of Technology, Tianjin, China

Fig. 1 Representation of Coulomb friction

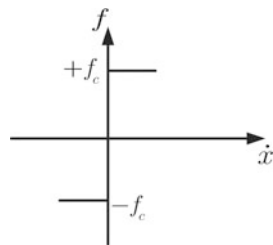


Fig. 2 Representation of the Stribeck curve

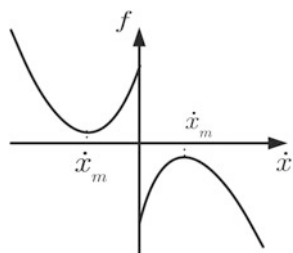
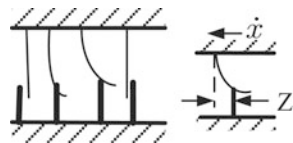


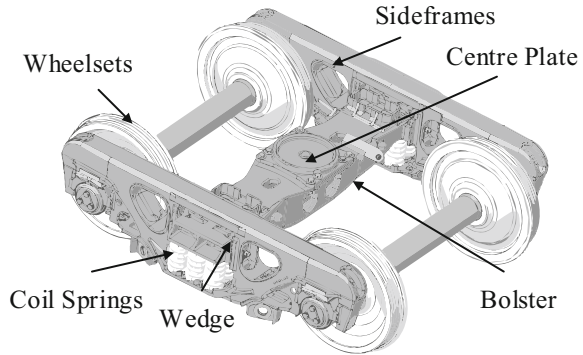
Fig. 3 The physical interpretation of LuGre model



as shown in Fig. 2. The LuGre model [4] was considered as a derivation from the Dahl model. The model containing Stribeck and static friction effects describes the friction as the result of the interaction of surface bristles and establishes the average bristle deflection, as shown in Fig. 3. But so far, friction is a complex phenomenon depending on many physical parameters and working conditions, and none of the available models can claim general validity.

The three-piece bogies were first developed by the USA and the Soviet Union in the 1930s, comprised of one bolster, two sideframes, and two wheelsets. As shown in Fig. 4, the bolster is seated in the sideframes through a set of springs and wedge friction dampers. The characteristic of dry friction plays a significant role in the dynamic system. The modeling of the friction force in the system depends on several environmental factors including sliding speed, temperature, and normal load. The suspension system is highly complex and time-consuming due to the dry friction.

The neural network has a good ability to approximate any function, with the advantages of self-learning, generalization, and robustness. Therefore, it has been widely used in all areas. A time-delay recurrent neural network (TDRNN) was employed and trained to predict the pitch angle of the system, where two types of structural nonlinearity were studied, cubic-spring, and friction [5]. Taqvi used a NARX model to detect the internal and external faults in a distillation column, this model was adequate for the representation of system behavior by using the sensor noise and zero mean normal distributed noise for training [6]. NARX was used to

Fig. 4 Bogie structure

model the helicopter flight dynamics system, which has complexity and interaction between various subsystems. Previous research has proven that the NARX method is a feasible way to establish the dynamic model of a system. However, the basis for the selection of NARX model parameters is not stated, and it is impossible to determine the parameters with a unified standard. The literature [7] tested 101 various criteria to determine the number of hidden neurons in the Neural Networks model. The number of hidden neurons obtained is very different according to the 101 criteria. The common method for determining the number of input parameters is based on trial and error. It was observed that overfitting was avoided for a network having 6 neurons in a single processing layer. Swarm intelligence has been proved as a technique that can solve non-deterministic polynomial-time computational problems. It is gaining popularity in solving different optimization problems. As of 2018, the most commonly used algorithm particle swarm optimization (PSO) was used in almost 47% of cases in the literature [8]. PSO algorithm takes up less memory and learns faster, compared with genetic algorithm (GA) and imperial competition algorithm (ICA). The purpose of this paper is to study the parameter setting method of the NARX model based on the PSO method for railway freight car bogies with dry friction model.

2 Methodology

2.1 NARX Method

NARX model defined in the literature [9] is:

$$f(t) = h(y(t-1), y(t-2), \dots, y(t-q), f(t-1), f(t-2), \dots, f(t-q)), \quad (1)$$

some nonlinear mapping $h: \mathbb{R}^{2q} \rightarrow \mathbb{R}$ exists whereby the present value of the output $f(t)$ is uniquely defined in terms of its past values $f(t-1), f(t-2), \dots, f(t-q)$

and its past values of the input $y(t - 1), y(t - 2), \dots, y(t - q)$. q is the number of the delay units of output and input.

For the case of the Coulomb friction with discontinuous features, an AVD (acceleration, velocity, and displacement) model is proposed to simulate [10].

$$f(t) = h\left(y(t - 1), y(t - 2), \dots, y(t - q_d), \dot{y}(t - 1), \dot{y}(t - 2), \dots, \dot{y}(t - q_v), \ddot{y}(t - 1), \ddot{y}(t - 2), \dots, \ddot{y}(t - q_a), f(t - 1), f(t - 2), \dots, f(t - q_f)\right) \tag{2}$$

$\dot{y}(t), \ddot{y}(t)$ are the sampled velocity and acceleration signals which are usually obtained from the measured displacement by a numerical differentiation method. q_d, q_v, q_a are the numbers of the delay units of displacement, velocity, and acceleration respectively.

A general single-degree-of-freedom nonlinear system was established, and the relationship between input and output was obtained by the finite difference method [10].

$$f(t) = b\ddot{y}(t) + a_1\ddot{y}(t - 1) + a_2\ddot{y}(t - 2) + a_3\left[3y^2(t - 1)\ddot{y}(t - 1) + 6y(t - 1)\dot{y}^2(t - 1)\right] - 2f(t - 1) + f(t - 2), \tag{3}$$

where a_1, a_2, a_3 are the coefficients of the input. As shown in Eq. (3), the displacement and velocity data must be used with acceleration data to obtain the correct nonlinear term. It is necessary to include the present value in the input information because the NARX network architecture is consistent with the theoretical model to better describe physical phenomena. The current value must be included in the input information, because the NARX network architecture is consistent with the theoretical model and can better describe physical phenomena.

Based on the Eqs. (1) and (2) of the NARX model, the NARX model used in this paper is:

$$f(t) = h\left\{ [y(t), \dot{y}(t), \ddot{y}(t)], [y(t - 1), \dot{y}(t - 1), \ddot{y}(t - 1)], \dots, [y(t - q), \dot{y}(t - q), \ddot{y}(t - q)], f(t - 1), \dots, f(t - q) \right\}, \tag{4}$$

Equation (4) is simplified to eq. (5) as:

$$f(t) = h(Y(t), Y(t - 1), \dots, Y(t - q), f(t - 1), \dots, f(t - q)), \tag{5}$$

where $Y(t) = \{y(t), \dot{y}(t), \ddot{y}(t)\}$.

The NARX learns to predict one-time series given past values of the same time series and the external or exogenous time series. The NARX consists of input, hidden, and output layers. The input consists of the time delays data of the

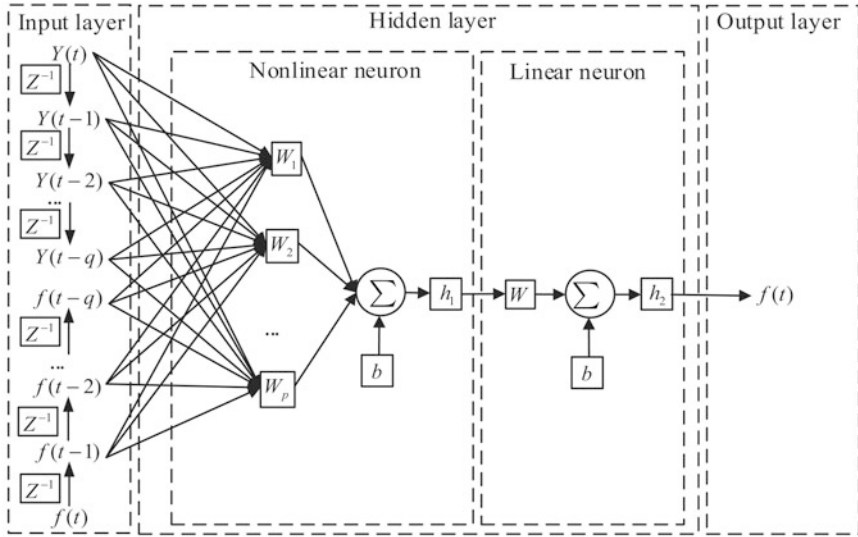


Fig. 5 NARX network displacement prediction model with the secondary suspension system

input signal and output signal transmitted through the hidden layer, this output is transmitted through the last connection multiplies the weight. The structure of the NARX is shown in Fig. 5.

The mean square error (MSE) of the training data is used to evaluate the performance of the NARX model, which is defined as:

$$MSE = \frac{1}{N} \sum_{t=1}^N (\hat{f}(t) - f(t))^2, \tag{6}$$

where $\hat{f}(t)$ is the estimated value of the NARX, $f(t)$ is the real value of the friction system, which is obtained from the friction experiment. N is the number of calculated data values.

2.2 PSO-NARX Method

In order to find the optimal network structure, particle swarm searches for the best suitable global position (gbest) and best personal position (pbest). In the particle swarm optimization modeling process, the particles will move to find the best position (also known as gbest and pbest) in each iteration of the system. At this time, the speed and position of all particles can be attained as follows:

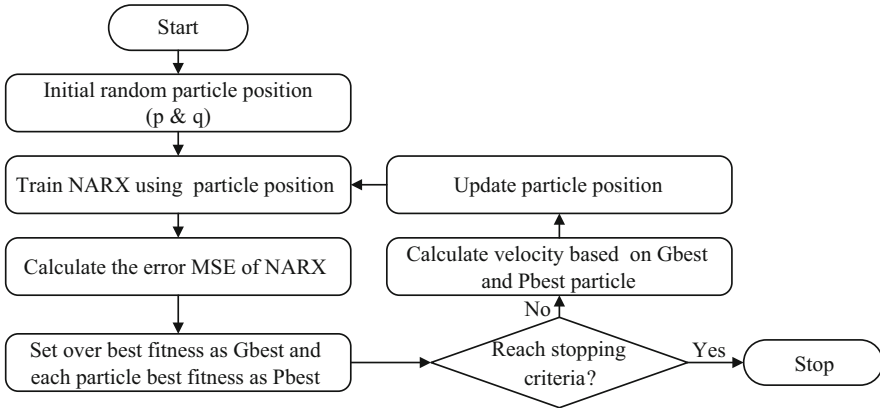


Fig. 6 PSO-NARX learning process

$$\begin{aligned}
 V_d^{k+1} &= \omega V_d^k + c_1 r_1 (P_{id}^k - X_d^k) + c_2 r_2 (P_{gd}^k - X_d^k), \\
 X_d^{k+1} &= X_d^k + V_d^{k+1}
 \end{aligned}
 \tag{7}$$

where X_d^k and X_d^{k+1} represent the current and next position of the particle. V_d^k and V_d^{k+1} represent the current and next speed of the particle, respectively. P_{id}^k and P_{gd}^k are the most suitable global position and best personal position, respectively. Usually, two positive acceleration constants c_1 and c_2 are selected from the operator to optimize the network output. r_1 and r_2 are both random numbers in the form of values (0,1). The determined acceleration factors (c_1 and c_2) are 2. ω is called inertia weight in the range [0.9,1.2]. ω is a linear decreasing variable from an initial value (ω_{max}) to a final value (ω_{min}) for improving the performance as the iteration according to the following equation:

$$\omega(t) = \omega_{max} - \frac{\omega_{max} - \omega_{min}}{T_{max}} t,
 \tag{8}$$

where t is the number of the current iteration of the PSO algorithm and T_{max} is the maximum number of iterations [11].

Figure 6 demonstrates the training process of networks in the hybrid PSO-NARX model. The initial values of the number of the delay units (q) and the hidden layer neurons (p) are randomly set. In the next step, having the initial step of particles, the PSO-NARX model network will be trained. The next step is to check the convergence of the trained network based on the MSE between the predicted and actual values. Reduce the error by changing the position of the particles to obtain the lowest error or reach the set maximum number of iterations. This process continues until one of the stopping criteria is met.

3 Results and Discussion

3.1 Experiment Set-up

The friction damping performance of the three-piece bogie is mainly produced by the main friction surface between the wedge and the side frame, and the pressure on the friction surface is exerted by the weight of the car body through the bolster. In order to obtain the friction characteristics of the main friction pair, an experimental device for the main friction pair was established. The structure size and material of the friction pair adopt the actual structure of the bogie friction pair, and the side pressure is loaded by the hydraulic device to simulate the side pressure of the friction pair. Figure 7 shows a schematic and test photo of the dry friction test system. The objective is to measure the dynamic friction force in the sliding interface between the fixed block and the moving block. The instrument can be roughly divided into two parts: the loading part containing components vertical actuator, displacement sensor, force sensor, and hydraulic device, the friction part containing components fixed block, and moving block.

The displacement load is applied to the bottom of the moving block as the system excitation, and the force signal collected on the top of the fixed block is used as the system response. The input of the experimental data consists of a quasi-periodic signal displacement filtered with a 100 Hz cut-off, while the output is composed of the time series of the friction force, the sampling frequency is at 1000 Hz.

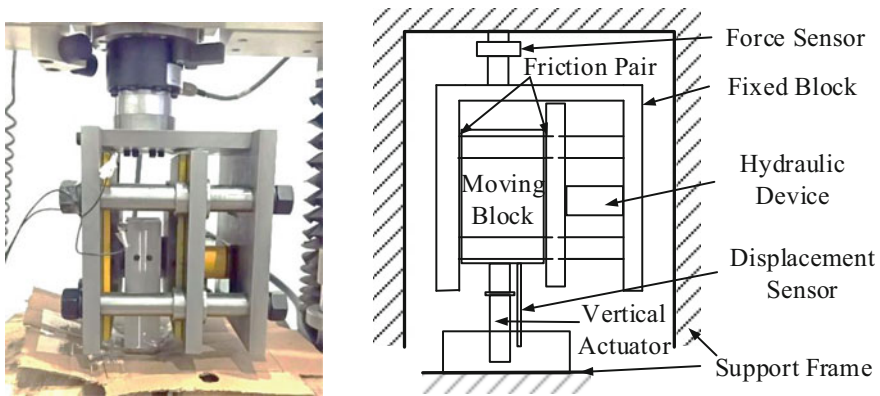


Fig. 7 The dry friction test system: (a) test photo; (b) schematic diagram

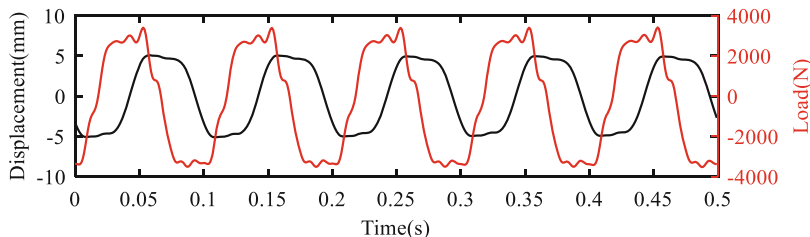


Fig. 8 Experimental time series of load force of output and displacement of input vs time

3.2 Testing Data and Results

The experiment was conducted over three excitation frequencies to simulate the changes in the frequency components of the excitation energy at different vehicle speeds. This is done to determine a model that can work well under different operating conditions. Therefore, there are three data sets: low-frequency (1 Hz) data, medium-frequency (5 Hz) data, and high-frequency (10 Hz) data. The objective is to predict the pulling force based on the information of the excitation displacement, velocity, and acceleration. Figure 8 shows the experimentally measured time series of load force of the output and displacement of the input used for modeling in the high-frequency data sections. The velocity and acceleration data are generated by the differentiation of displacement.

Initially, the datasets were used to perform NARX training. In this analysis, approximately 70% of datasets are selected for training, 15% for validation, and 15% are left for testing of NARX neural network. The validation phase was performed during the training procedure for weights and bias adjustment while the test datasets were used for final validation. The maximum value of the number of the delay units (q) and hidden layer neurons (p) is set to 20. The p and q in the NARX model are set to maximum. The hidden units use the tangent-sigmoid activation function while the output unit uses the linear activation function. Subsequently, the prediction method based on PSO-NARx model is further used to perform the system identification of the dry friction system. The network architecture PSO-NARX is the same as the conventional NARX, except that the number of the delay units and hidden layer neurons is determined by the PSO method. The p and q in the PSO-NARX model are set to any integer between 1 and 20. The process continues until the stopping condition is that the maximum number of iterations is 50 times.

The model prediction output of the NARX and PSO-NARX models is shown in Fig. 9. Table 1 shows the ensemble model performance for the different excitation frequencies. The prediction accuracy of the PSO-NARX model is approximately 10 times higher than the NARX method. The fitting accuracy of the NARX architecture is not the best when the delay units ($q = 20$) and hidden layer neurons ($p = 20$) are set the maximum value. It is necessary and feasible to use the PSO method to select the number of delay units and hidden layer neurons to improve the fitting accuracy.

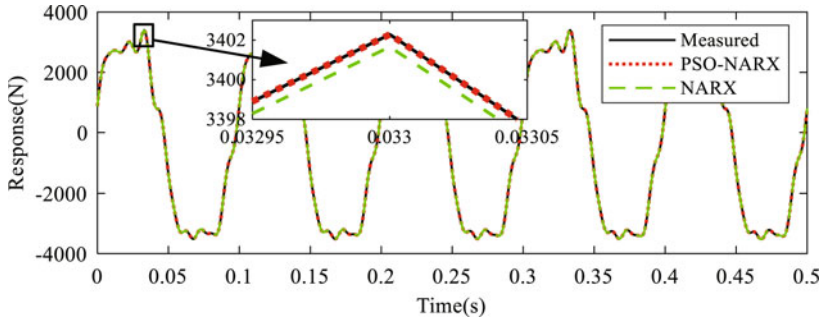


Fig. 9 Comparison between the measured and estimated output of the validation set for high-frequency excitations

Table 1 Predicted results using PSO-NARX and traditional NARX

Training data sets	NARX	PSO-NARX		
	MSE	q	p	MSE
Low-frequency	0.863	15	20	0.0346
Medium-frequency	0.555	9	18	0.0541
High-frequency	0.534	9	18	0.0369

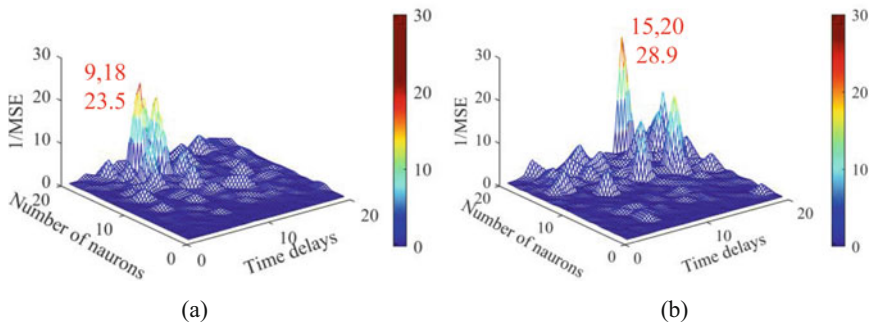


Fig. 10 The MSE value of NARX is calculated using the exhaustive method. (a) High-frequency. (b) Low-frequency

The PSO method can get the optimal solution, but it may also fall into the local optimal and cannot reach the global optimal. Therefore, the exhaustive method is used to obtain the error conditions of the NARX model for the number of delay units and neurons.

As shown in Fig. 10, the exhaustive method is used under high-frequency and low-frequency. The numbers of delay units and neurons are respectively set as 9 and 18, 15 and 20. The error values are 0.0369 and 0.0346 respectively, which is expressed as 1/MSE. Compared with the PSO-NARX calculation results in Table 1, it is found that the error values are the same, and the number of delay units and neurons are also consistent. It shows that the PSO-NARX method is feasible and the optimal solution of the system can be obtained.

Table 2 Predicted results using PSO-NARX and traditional NARX without the present unit of input $Y(t)$

Training data sets	NARX	PSO-NARX		
	MSE	q	p	MSE
Low-frequency	0.069	9	20	0.053
Medium-frequency	1.094	17	17	0.1216
High-frequency	2.321	8	18	0.0425

The NARX and PSO-NARX models are used to calculate the error MSE of the prediction result excluding the present unit of input $Y(t)$. From the comparison of NARX and PSO-NARX in Table 2, it can be seen from Table 2 that the q and p will change when the fitting accuracy MSE is the highest. The fitting accuracy of PSO-NARX is higher than NARX, the prediction accuracy of the PSO-NARX model is approximately 10 times higher than the NARX method. By comparing the data in Table 1 and Table 2, the PSO-NARX model improves the fitting accuracy more than 20% when the external input delay term $Y(t)$ is added. This shows that it is necessary to increase the external input $Y(t)$.

4 Conclusions

A new element type based on nonlinear autoregressive with exogenous input (NARX) is proposed to establish the bogie suspension with dry friction system. The number of delay units and the hidden layer neurons in NARX cannot be calculated by a fixed expression. However, the PSO method can be used to obtain more accurate recognition accuracy. An experimental model for bogie dry friction is designed. The displacement, velocity, acceleration, and load obtained from the test are used as the input and output data of the NARX. The results show that the PSO-NARX can be well established as the dynamic model of the dry friction system. The prediction accuracy of the PSO-NARX is approximately 10 times higher than the NARX. Adding the present unit of the input of the NARX and the PSO-NARX improves the fitting accuracy more than 20%. Therefore, the prediction results of experimental data with different characteristics prove that the PSO-NARX neural network has good generalization performance for dry friction dynamic systems. The PSO-NARX can accurately predict the dynamic behavior of the system. The present unit of input data should be added in the establishment of PSO-NARX. The PSO-NARX established in this paper can be used to model the dry friction system and provide a new method for vehicle state monitoring.

References

1. S.W. Shaw, On the dynamic response of a system with dry friction. *J. Sound Vib.* **108**(2), 305–325 (1986)

2. D. Qian, Z. Hongmei, The advance in researches of friction dynamics in mechanics system. *Adv. Mech.* **43**(01), 112–131 (2013)
3. R. Stribeck, Die wesentlichen eigenschaften der gleitund rollenlager-the key qualities of sliding and roller bearings. *Zeitschrift des Vereines Seutscher Ingenieure.* **46**(38,39), (1342–1348, 1432–1437) (1902)
4. C.O.H. Canudas de Wit, K.J. Astrom, P. Lischinsky, A new model for control of systems with friction. *J IEEE Trans. Automatic Control* **40**(3), 419–425 (1995)
5. B. Zhang, J.L. Han, H.W. Yun, X.M. Chen, Nonlinear aeroelastic system identification based on neural network. *Appl. Sci-Basel.* **8**(10), 1916 (2018)
6. S.A. Taqvi, L.D. Tufa, H. Zabiri, A.S. Maulud, F. Uddin, Fault detection in distillation column using narx neural network. *Neural. Comput. Appl.* **32**(8), 3503–3519 (2020)
7. K.G. Sheela, S.N. Deepa, Review on methods to fix number of hidden neurons in neural networks. *Math. Probl. Eng.* **2013**(425740) (2013)
8. L. Brezočnik, I. Fister, V. Podgorelec, Swarm intelligence algorithms for feature selection: A review. *J Appl. Sci.* **8**(9), 1521 (2018)
9. S. Haykin, *Neural networks: A comprehensive foundation.* McMaster University; Person Education, (1998)
10. Q. Chen, G. Tomlinson, R. J. M. S., Processing S. A new type of time series model for the identification of non-linear dynamical systems. **8**(5), 531–549 (1994).
11. H. Liu, X.W. Zhang, L.P. Tu, A modified particle swarm optimization using adaptive strategy. *Expert Syst. Appl.* **152**, 113353 (2020)

A Generalized Solution Scheme Using an Implicit Time Integrator for Piecewise Linear and Nonlinear Systems



Huimin Zhang, Runsen Zhang, Andrea Zaroni, and Pierangelo Masarati

1 Introduction

Piecewise linear and nonlinear systems, such as gap-activated springs in vibrating machines [1, 2], gear backlashes [3], structures with damage or clearance [4], and drag torques [5], are commonly used in civil engineering, aerospace, mechanical engineering, and infrastructures. Because of the piecewise linear or nonlinear characteristics, these systems exhibit very complex and diverse dynamic behavior. However, this kind of nonlinearity brings difficulties to the accurate prediction of dynamic responses. For single-degree-of-freedom (SDOF) systems, some traditional methods, including the averaging method [6], the perturbation method [7], and the harmonic balance method [8], can be employed to look for analytical solutions, but the application range of these analytical methods is very limited, and they become tedious and time-consuming when the number of degrees of freedom increases. Therefore, for such problems, numerical integration is a more general choice and sometimes the only one to simulate their dynamic response.

Time integration methods for semi-discrete motion equations have been well developed in the field of structural dynamics and are simply reviewed. These methods can be divided into two categories: explicit and implicit. Explicit methods, such as the central difference method, the explicit generalized- α method [9], and the Noh–Bathe method [10], are easy to implement, but they are all conditionally

H. Zhang (✉) · R. Zhang

School of Aeronautic Science and Engineering, Beihang University, Beijing, China

Dipartimento di Scienze e Tecnologie Aerospaziali, Politecnico di Milano, Milan, Italy

e-mail: huimin.zhang@polimi.it; runsen.zhang@polimi.it

A. Zaroni · P. Masarati

Dipartimento di Scienze e Tecnologie Aerospaziali, Politecnico di Milano, Milan, Italy

e-mail: andrea.zaroni@polimi.it; pierangelo.masarati@polimi.it

stable, which means that their time step sizes are limited by the highest frequency of the system to be solved. As a result, explicit methods are more commonly used in wave propagation and impact problems, where the time step size required by the stability limit is of the same order of that needed to capture the physics of the problem. Implicit methods, including the Newmark method [11], the generalized- α method [12], the Bathe method [13], and many others, can be designed to be unconditionally stable at least for linear problems, so that their time step size only depends on the desired solution accuracy, at the cost of greater computational effort. When applied to linear systems, implicit methods require the factorization of the effective stiffness matrix; for nonlinear systems, an iterative solution approach is inevitable. A comprehensive review about time integration methods can be found in [14].

Focusing on piecewise linear and nonlinear systems, some attempts have been made to provide solution approaches using time integration methods. Yu [15] and Fadaee et al. [16] transformed the piecewise linear problem in an equivalent linear complementarity problem (LCP) [17], which can be solved using the Lemke algorithm, and adopted the Bozzak–Newmark method [18] to integrate the dynamic equations. A similar concept was also employed by He et al. [19], based on the precise integration method (PIM) [20] and the Lemke algorithm. These methods, referred to as the LCP-based schemes in that context, are applicable when the piecewise linear characteristic is the only nonlinearity in the dynamics equations. They have been successfully applied to simulate the dynamic response of multi-degree-of-freedom (MDOF) systems [4, 21, 22]. Another approach is to adopt an explicit integrator [3, 23], which first updates the displacement at the current step by the known state variables and guarantees that the piecewise linear or nonlinear characteristic is taken into account. However, as mentioned above, the drawback of explicit methods is their conditional stability, which limits their step size and can make the results unreliable for nonlinear systems.

From the above review, the existing LCP-based schemes can handle piecewise linear problems, whereas only explicit integrators can be employed if other nonlinearities are present. As a further attempt, this chapter aims at providing a more elegant and versatile formulation of piecewise linear and nonlinear systems by using projection functions, and at presenting a generalized solution procedure based on the generalized- α method [12] and the semi-smooth Newton iteration [24]. The projection function [25, 26] has been used to deal with discontinuities caused by impacts and frictions. It is also introduced here to model the piecewise linear and nonlinear characteristics. Compared with the LCP-based schemes, the advantages of the proposed scheme are that it can be directly extended to general piecewise nonlinear systems, since the dynamic equations involving the projection function can be solved by the semi-smooth Newton iteration. Meanwhile, the proposed scheme shows obvious efficiency advantages for systems with a large number of piecewise features, due to the fast convergence rate of the Newton iteration. Several numerical examples are simulated to show the numerical performance of the proposed scheme.

This chapter is organized as follows. In Sect. 2, the dynamics equations for piecewise linear and nonlinear systems are presented using the projection functions. The computational procedures are provided in Sect. 3, based on the generalized- α method and the semi-smooth Newton iteration. Numerical experiments are implemented in Sect. 4, and finally, conclusions are drawn in Sect. 5.

2 Formulation

For illustrative purposes, the piecewise linear SDOF system shown in Fig. 1 is discussed first. Its elastic restoring force can be formulated as

$$K(x) = \begin{cases} k_1 x, & x \leq \Delta \\ k_1 x + k_2(x - \Delta), & x > \Delta, \end{cases} \quad (1)$$

where $K(x)$ is the elastic force, x is the displacement of the cart, Δ is the initial clearance, and k_1 and k_2 are the stiffness values. With this simple piecewise linear model, the basic idea of previous LCP-based schemes is reviewed here. From Eq. (1), the complementarity relationship is established by introducing two auxiliary variables g and y , as

$$g = y - x + \Delta, \quad y \geq 0, \quad g \geq 0, \quad y \cdot g = 0. \quad (2)$$

Using the variable y , Eq. (1) can be equivalently transformed into

$$K(x) = k_1 x + k_2 y. \quad (3)$$

After applying the time integration schemes, the numerical displacement x_k at time t_k satisfies

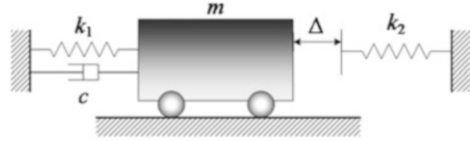
$$k^* x_k + k_2 y_k = r_k^*, \quad (4)$$

where k^* is the effective stiffness value, which is a constant for linear systems; r_k^* is the effective external load, which needs to be updated per step. Combining Eqs. (2) and (4), one obtains

$$y_k = (k^* + k_2)^{-1} k^* g_k + (k^* + k_2)^{-1} (r_k^* - k^* \Delta), \quad y_k \geq 0, \quad g_k \geq 0, \quad y_k \cdot g_k = 0. \quad (5)$$

At each step, y_k can be obtained by solving the LCP in Eq. (5) via the Lemke algorithm. Then, x_k is computed as $g_k = y_k - x_k + \Delta$, and other state variables are updated according to the time integration scheme. The above procedure can be easily extended to solve MDOF systems. However, the LCP-based schemes are designed only for piecewise linear systems, due to the lack of an efficient solver for nonlinear complementarity problems. To our knowledge, so far no numerical

Fig. 1 Piecewise linear SDOF system



solution scheme is available in the literature using implicit integrators for piecewise nonlinear systems.

To fill this gap, this chapter employs the projection function to formulate more general forms of piecewise linear and nonlinear characteristics. From convex analysis, the projection of a point w in a convex set C is the closest point in C to w , defined as

$$\text{proj}_C(w) = \arg \min_{z \in C} |w - z|. \tag{6}$$

It follows that if $w \in C$, $\text{proj}_C(w) = w$, and otherwise, $\text{proj}_C(w)$ is the nearest boundary point of C to w . Using the projection function, Eq. (1) can be transformed into

$$K(x) = k_1x + k_2\text{proj}_{\mathbb{R}_0^+}(x - \Delta). \tag{7}$$

It can be seen that the projection function in Eq. (7) can play the role of the auxiliary variable y of the LCP-based schemes in Eq. (3). For general multi-stage piecewise linear systems, as

$$K(x) = \begin{cases} k_1x + z_1, & x \leq x_1 \\ k_2x + z_2, & x_1 < x \leq x_2 \\ \dots & \\ k_nx + z_n, & x > x_{n-1} \end{cases} \tag{8}$$

where $K(x)$ should be continuous at x_1, x_2, \dots, x_{n-1} by setting proper constants z_1, z_2, \dots, z_n , the equivalent form using the projection function can be written as

$$K(x) = k_1x + z_1 + \sum_{i=2}^n (k_i - k_{i-1})\text{proj}_{\mathbb{R}_0^+}(x - x_{i-1}). \tag{9}$$

When extended to piecewise nonlinear systems, such as

$$K(x) = \begin{cases} \sum_{j=1}^{p_1} k_{1,j}x^{m_{1,j}} + z_1, & x \leq x_1 \\ \sum_{j=1}^{p_2} k_{2,j}x^{m_{2,j}} + z_2, & x_1 < x \leq x_2 \\ \dots & \\ \sum_{j=1}^{p_n} k_{n,j}x^{m_{n,j}} + z_n, & x > x_{n-1}, \end{cases} \tag{10}$$

where p_1, p_2, \dots , and p_n are the positive integers, and the equivalent form using the projection function is

$$\begin{aligned}
 K(x) = & \sum_{j=1}^{p_1} k_{1,j} x^{m_{1,j}} + z_1 \\
 & + \sum_{i=2}^n \left(\sum_{j=1}^{p_i} k_{i,j} \left(\text{proj}_{[x_{i-1}, +\infty)}^{m_{i,j}}(x) - x_{i-1}^{m_{i,j}} \right) \right. \\
 & \left. - \sum_{j=1}^{p_{i-1}} k_{i-1,j} \left(\text{proj}_{[x_{i-1}, +\infty)}^{m_{i-1,j}}(x) - x_{i-1}^{m_{i-1,j}} \right) \right). \tag{11}
 \end{aligned}$$

As can be seen, the projection function provides a more elegant, versatile, and flexible manner to express the piecewise linear and nonlinear characteristics. Its solution can be included in the solution program of nonlinear systems, without additional computational procedures, as discussed in more detail in the next section. Since polynomial stiffness functions can cover most situations in structural dynamics, other possible forms, which can also be expressed using the projection functions by selecting proper projected functions and convex sets, are not discussed here one by one.

To present a general formulation of piecewise linear and nonlinear MDOF systems, an auxiliary variable $\mathbf{y} \in \mathbb{R}^{q \times 1}$ is introduced as

$$\mathbf{y} = \mathbf{P}(\mathbf{x}) = \begin{bmatrix} \text{proj}_{C_1}(w_1(\mathbf{x})) \\ \text{proj}_{C_2}(w_2(\mathbf{x})) \\ \dots \\ \text{proj}_{C_q}(w_q(\mathbf{x})), \end{bmatrix} \tag{12}$$

where $\mathbf{x} \in \mathbb{R}^{s \times 1}$ is the displacement vector, and $\mathbf{w}(\mathbf{x}) = [w_1(\mathbf{x}), w_2(\mathbf{x}), \dots, w_q(\mathbf{x})]^T$ are defined as functions of \mathbf{x} . Then, the general form of the dynamics equations can be expressed as

$$\mathbf{M}\ddot{\mathbf{x}} + \mathbf{C}\dot{\mathbf{x}} + \mathbf{K}(\mathbf{x}, \mathbf{y}, t) = \mathbf{R}(t), \tag{13}$$

where $\mathbf{M} \in \mathbb{R}^{s \times s}$ and $\mathbf{C} \in \mathbb{R}^{s \times s}$ are the mass and damping matrices, assumed constant for simplicity, the over dots indicate derivation with respect to time t , $\mathbf{K}(\mathbf{x}, \mathbf{y}, t) \in \mathbb{R}^{s \times 1}$ is the elastic force vector, and $\mathbf{R}(t) \in \mathbb{R}^{s \times 1}$ is the external load vector. Equations (12–13) constitute the dynamics equations that need to be solved.

3 Computational Procedure

In representation of methods of the same class, the generalized- α method [12] is employed to illustrate the step-by-step computational procedure. Its improved scheme [27], which holds second-order accuracy for displacement, velocity, and acceleration, is adopted. It introduces an acceleration-like variable \mathbf{a} as

$$(1 - \alpha)\mathbf{a}_{k+1} + \alpha\mathbf{a}_k = (1 - \delta)\ddot{\mathbf{x}}_{k+1} + \delta\ddot{\mathbf{x}}_k, \mathbf{a}_0 = \ddot{\mathbf{x}}_0, \tag{14}$$

where the subscript k denotes the state variables of step k , and α and δ are the parameters of the algorithm. Using the acceleration-like variable \mathbf{a} , the displacement and velocity of step $k + 1$ are updated according to

$$\begin{aligned} \mathbf{x}_{k+1} &= \mathbf{x}_k + h\dot{\mathbf{x}}_k + \frac{h^2}{2}((1 - 2\beta)\mathbf{a}_k + 2\beta\mathbf{a}_{k+1}) \\ \dot{\mathbf{x}}_{k+1} &= \dot{\mathbf{x}}_k + h((1 - \gamma)\mathbf{a}_k + \gamma\mathbf{a}_{k+1}), \end{aligned} \tag{15}$$

where h is the time step size, and β and γ are the additional parameters of the algorithm. The generalized- α method embraces some well-known single-step schemes. For instance, when $\alpha = \delta = 0$, it reduces to the Newmark method [11]; when $\alpha = \delta = 0, \gamma = 1/2, \beta = 1/4$, it reduces to the trapezoidal rule (TR). From linear spectral analysis, a set of optimal parameters, controlled by the spectral radius ρ_∞ at the high-frequency limit, is

$$\alpha = \frac{2\rho_\infty - 1}{\rho_\infty + 1}, \delta = \frac{\rho_\infty}{\rho_\infty + 1}, \beta = \frac{1}{(\rho_\infty + 1)^2}, \gamma = \frac{3 - \rho_\infty}{2(\rho_\infty + 1)}, \rho_\infty \in [0, 1]. \tag{16}$$

A smaller ρ_∞ denotes worse accuracy and stronger numerical damping. To avoid excessive loss of accuracy, $\rho_\infty \geq 0.6$ is recommended for general purpose integration, and for stiff problems and large finite element systems, a smaller ρ_∞ can be used to filter out the inaccurate high-frequency modes.

At each step, the stage variables need to satisfy the discrete dynamic equations, as

$$\mathbf{g}(\mathbf{x}_{k+1}) = \mathbf{M}\ddot{\mathbf{x}}_{k+1} + \mathbf{C}\dot{\mathbf{x}}_{k+1} + \mathbf{K}(\mathbf{x}_{k+1}, \mathbf{y}_{k+1}, t_{k+1}) - \mathbf{R}_{k+1}, \tag{17}$$

where $\mathbf{y}_{k+1} = \mathbf{P}(\mathbf{x}_{k+1}), \dot{\mathbf{x}}_{k+1}$, and $\ddot{\mathbf{x}}_{k+1}$ can be expressed as functions of \mathbf{x}_{k+1} using Eqs. (14) and (15), as

$$\ddot{\mathbf{x}}_{k+1} = \frac{1 - \alpha}{(1 - \delta)\beta h^2}(\mathbf{x}_{k+1} - \mathbf{x}_k) - \frac{1 - \alpha}{(1 - \delta)\beta h}\dot{\mathbf{x}}_k - \frac{\delta}{1 - \delta}\ddot{\mathbf{x}}_k - \frac{1 - \alpha - 2\beta}{2\beta(1 - \delta)}\mathbf{a}_k \tag{18}$$

$$\begin{aligned}\dot{\mathbf{x}}_{k+1} &= \frac{\gamma}{\beta h}(\mathbf{x}_{k+1} - \mathbf{x}_k) - \frac{\gamma - \beta}{\beta} \dot{\mathbf{x}}_k - \frac{\gamma - 2\beta}{2\beta} h \mathbf{a}_k \\ \mathbf{a}_{k+1} &= \frac{1 - \delta}{1 - \alpha} \ddot{\mathbf{x}}_{k+1} + \frac{\delta}{1 - \alpha} \ddot{\mathbf{x}}_k - \frac{\alpha}{1 - \alpha} \mathbf{a}_k.\end{aligned}$$

The Jacobi matrix of $\mathbf{g}(\mathbf{x}_{k+1})$ with respect to \mathbf{x}_{k+1} can be expressed as

$$\begin{aligned}\mathbf{G}(\mathbf{x}_{k+1}) &= \frac{1 - \alpha}{(1 - \delta)\beta h^2} \mathbf{M} + \frac{\gamma}{\beta h} \mathbf{C} + \mathbf{K}_x(\mathbf{x}_{k+1}, \mathbf{y}_{k+1}, t_{k+1}) \\ &\quad + \mathbf{K}_y(\mathbf{x}_{k+1}, \mathbf{y}_{k+1}, t_{k+1}) \mathbf{A}(\mathbf{x}_{k+1}) \mathbf{W}(\mathbf{x}_{k+1}),\end{aligned}\quad (19)$$

where

$$\mathbf{K}_x(\mathbf{x}, \mathbf{y}, t) = \frac{\partial \mathbf{K}(\mathbf{x}, \mathbf{y}, t)}{\partial \mathbf{x}^T}, \mathbf{K}_y(\mathbf{x}, \mathbf{y}, t) = \frac{\partial \mathbf{K}(\mathbf{x}, \mathbf{y}, t)}{\partial \mathbf{y}^T}, \mathbf{W}(\mathbf{x}) = \frac{d\mathbf{w}(\mathbf{x})}{d\mathbf{x}^T} \quad (20)$$

and

$$\mathbf{A}(\mathbf{x}) = \text{diag}(\lambda_{C_i}(w_i(\mathbf{x}))), \lambda_C(w) = \begin{cases} 0, & \text{if } w \notin C \\ 1/2, & \text{if } w \in \partial C \\ 1, & \text{else.} \end{cases} \quad (21)$$

The iterative scheme is

$$\mathbf{x}_{k+1}^{l+1} = \mathbf{x}_{k+1}^l - \left(\mathbf{G}(\mathbf{x}_{k+1}^l)\right)^{-1} \mathbf{g}(\mathbf{x}_{k+1}^l). \quad (22)$$

Until the convergence condition is satisfied, the state variables of step $k + 1$ are obtained. Other implicit integrators can also be employed in a similar manner. The LCP-based schemes have not yet been applied to solve the piecewise nonlinear problems, which cannot be translated to equivalent LCPs. Therefore, the available solution scheme of implicit integrators for such problems is first developed in this chapter. Its numerical performance is checked by some numerical examples in Sect. 4.

4 Numerical Examples

Two illustrative examples, including a MDOF case and a piecewise nonlinear case, are simulated in this section. The linear case is employed to show the computational efficiency, and the nonlinear case is used to demonstrate the effectiveness for piecewise nonlinear systems. The simulations were run on an Intel i5-8265U CPU @ 1.60 GHz with 8.00 GB RAM.

4.1 MDOF Case

First, the MDOF cases, as

$$\mathbf{M} = \begin{bmatrix} m & & & & \\ & m & & & \\ & & m & & \\ & & & \ddots & \\ & & & & m \end{bmatrix}, \mathbf{K}_x = \begin{bmatrix} 2k_1 & -k_1 & & & \\ -k_1 & 2k_1 & -k_1 & & \\ & -k_1 & \ddots & \ddots & \\ & & \ddots & 2k_1 & -k_1 \\ & & & -k_1 & k_1 \end{bmatrix}, \tag{23}$$

$$\mathbf{K}_y = \begin{bmatrix} k_2 & & & & \\ & k_2 & & & \\ & & k_2 & & \\ & & & \ddots & \\ & & & & k_2 \end{bmatrix}, \mathbf{y} = \mathbf{P}(\mathbf{x}) = \begin{bmatrix} \text{proj}_{\mathbb{R}_0^+}(x_1) \\ \text{proj}_{\mathbb{R}_0^+}(x_2) \\ \text{proj}_{\mathbb{R}_0^+}(x_3) \\ \vdots \\ \text{proj}_{\mathbb{R}_0^+}(x_s) \end{bmatrix}, \mathbf{R}(t) = \begin{bmatrix} A_0 + A \sin(2\pi ft) \\ A_0 + A \sin(2\pi ft) \\ A_0 + A \sin(2\pi ft) \\ \vdots \\ A_0 + A \sin(2\pi ft) \end{bmatrix},$$

$$\mathbf{C} = 0.1\mathbf{M} + 0.01\mathbf{K}_x, \mathbf{K}(\mathbf{x}, \mathbf{y}, t) = \mathbf{K}_x\mathbf{x} + \mathbf{K}_y\mathbf{y}$$

with a different number of DOFs, are simulated. The number of piecewise characteristics is set as the same as the number of DOFs. The system parameters are assumed as $m = 1 \text{ kg}$, $k_1 = 1000 \text{ N/m}$, $k_2 = 2000 \text{ N/m}$, $f = 100 \text{ Hz}$, $A_0 = 1 \text{ N}$, $A = 10 \text{ N}$. The initial displacements satisfy static equilibrium.

Since the accuracy of numerical solutions depends on the time integrator, the proposed scheme and the LCP-based scheme will give the same results if they employ the same integrator and step size. For this reason, only the computational efficiency of these two schemes is compared. Based on the TR with $h = 0.001 \text{ s}$, the transient response within $[0, 1 \text{ s}]$ is tracked, and the required CPU time for these two schemes is listed in Table 1. It follows that as the number of piecewise characteristics increases, the new method gradually exhibits a significant efficiency advantage. During the numerical experiments, the Newton iteration can always reach convergence in no more than 5 iterations, but the number of pivoting required by the Lemke algorithm increases rapidly with the number of piecewise characteristics. In the worst case, the Lemke method needs exponential complexity, which means that it requires up to 2^q pivot steps to reach the final result. Therefore, the proposed scheme is more efficient for systems with a large number of piecewise features.

4.2 Piecewise Nonlinear Time-Varying Oscillator

In this case, the piecewise nonlinear time-varying oscillator investigated in Ref. [28] is simulated. The motion equation in dimensionless form is

Table 1 Required CPU time (s) of the proposed scheme and the LCP-based scheme

Number of piecewise characteristics	TR/Newton iteration	TR/Lemke's algorithm
10	0.1834	0.1024
50	1.0867	1.0722
100	4.0558	6.5924
1000	654.6712	22489.3308

$$\ddot{x} + 2\xi\dot{x} + r(t)k(x) = f(t), \tag{24}$$

where $\xi = 0.05$, $f(t) = 0.5$, and

$$r(t) = 1 + 0.3 \sin \omega t + 0.15 \sin 2\omega t + 0.1 \sin 3\omega t \tag{25}$$

$$k(x) = \begin{cases} (x - 1) + 0.1(x - 1)^2 + 0.2(x - 1)^3, & x > 1 \\ 0, & -1 \leq x \leq 1 \\ (x + 1) - 0.1(x + 1)^2 + 0.2(x + 1)^3, & x < -1. \end{cases} \tag{26}$$

Using the projection function, $k(x)$ can be equivalently converted into

$$k(x, y) = (x - y) + 0.1y(x - y)^2 + 0.2y^2(x - y)^3, \quad y = \text{proj}_{[-1,1]}(x). \tag{27}$$

According to the results in Ref. [28], different stable solutions may exist for a certain ω . When a stable solution satisfies $|x| > 1$, it is called no-impact (NI) motion; when $x_{\max} > 1$ and $-1 < x_{\min} < 1$ ($x_{\min} < -1$ and $-1 < x_{\max} < 1$), it is called single-side impact (SSI) motion; when $x_{\max} > 1$ and $x_{\min} < -1$, it is called double-side impact (DSI) motion.

Three values of ω , 0.4, 0.8, and 1.2, are assumed, and the corresponding phase diagrams of steady-state response in $[900T, 1000T]$ ($T = 2\pi/\omega$) are computed using TR with $h = T/210$, as shown in Fig. 2. By trying different initial conditions, all possible stable solutions for a certain ω are presented. They are consistent with the analytical solutions [28] from the harmonic balance method. For example, when $\omega = 0.8$, three stable motions, NI, SSI, and DSI, are all possible. Therefore, the implicit integration schemes proposed here can be used to study the impact dynamics behaviors and more complex nonlinear systems.

5 Conclusions

This chapter provides a general solution scheme using implicit integrators for simulating the dynamic response of piecewise linear and nonlinear systems. The developed scheme employs the projection function to express the piecewise characteristics, instead of converting them into equivalent LCPs. Compared with the existing LCP-based schemes, the newly developed scheme possesses two benefits. It

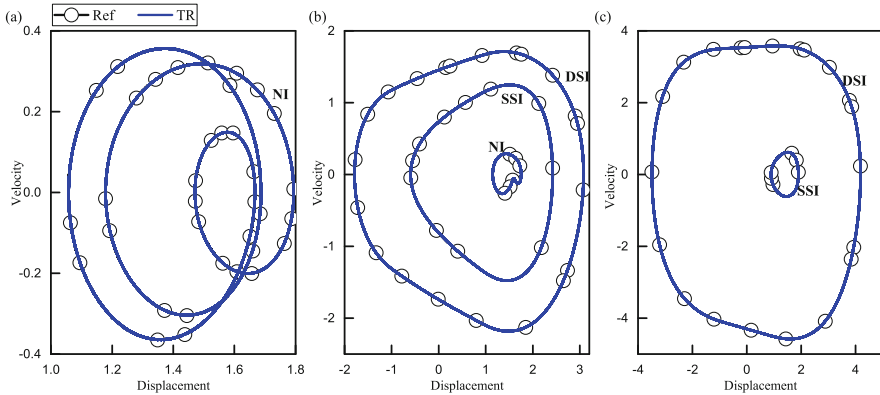


Fig. 2 Phase diagrams of steady-state responses: (a) $\omega = 0.4$; (b) $\omega = 0.8$; (c) $\omega = 1.2$

can be easily extended to general piecewise nonlinear systems, because the discrete nonlinear equations containing the projection functions can be solved uniformly by the semi-smooth Newton method. Moreover, due to the fast convergence rate of the Newton iteration, the proposed scheme is more efficient than LCP-based schemes for systems with a large number of piecewise features. The computational procedure is presented, based on the generalized- α method and the semi-smooth Newton iteration. Other implicit integrators can also be utilized in a similar manner. Numerical experiments demonstrate that the Newton iteration is more efficient than the Lemke algorithm, especially when the system has a lot of piecewise features. When applied to piecewise nonlinear problems, the numerical solutions present a high consistency with the analytical ones.

References

1. Y.L. Ma, S.D. Yu, D.L. Wang, *J. Vib. Control* **22**(7), 1808 (2016)
2. C. Si, R. Tian, J. Feng, X. Yang, *Adv. Mech. Eng.* **9**(12), 1687814017742313 (2017)
3. S. Boere, A. Shukla, R. Fey, H. Nijmeijer, *J. Comput. Nonlinear Dyn.* **5**(2) (2010)
4. D. Joglekar, M. Mitra, *J. Sound Vib.* **344**, 242 (2015)
5. J.Y. Yoon, H. Lee, *Proc. Inst. Mech. Eng. C J. Mech. Eng. Sci.* **229**(8), 1399 (2015)
6. A.H. Nayfeh, *Introduction to Perturbation Techniques* (Wiley, London, 2011)
7. A. Narimani, M. Golnaraghi, G.N. Jazar, *J. Vib. Control* **10**(12), 1775 (2004)
8. R.J. Comparin, R. Singh, *J. Sound Vib.* **142**(1), 101 (1990)
9. J. Chung, J.M. Lee, *Int. J. Numer. Methods Eng.* **37**(23), 3961 (1994)
10. G. Noh, K.J. Bathe, *Comput. Struct.* **129**, 178 (2013)
11. N.M. Newmark, *J. Eng. Mech. Div.* **85**(3), 67 (1959)
12. J. Chung, G. Hulbert, *J. Appl. Mech.* **60**, 371 (1993)
13. G. Noh, K.J. Bathe, *Comput. Struct.* **212**, 299 (2019)
14. K.K. Tamma, J. Har, X. Zhou, M. Shimada, A. Hoitink, *Arch. Comput. Methods Eng.* **18**(2), 119 (2011)
15. S. Yu, *Nonlinear Dyn.* **71**(3), 493 (2013)

16. M. Fadaee, S. Yu, *Int. J. Mech. Sci.* **131**, 218 (2017)
17. R.W. Cottle, J.S. Pang, R.E. Stone, *The Linear Complementarity Problem* (SIAM, 2009)
18. W. Wood, M. Bossak, O. Zienkiewicz, *Int. J. Numer. Methods Eng.* **15**(10), 1562 (1980)
19. D. He, Q. Gao, W. Zhong, *Nonlinear Dyn.* **94**(3), 2059 (2018)
20. W. Zhong, F. Williams, *Proc. Inst. Mech. Eng. C J. Mech. Eng. Sci.* **208**(6), 427 (1994)
21. M. Fadaee, S. Yu, *J. Mech. Sci. Tech.* **31**(4), 1551 (2017)
22. X. Zhang, X. Kong, B. Wen, C. Zhao, *Nonlinear Dyn.* **82**(1–2), 987 (2015)
23. Q. Bi, X. Chen, J. Kurths, Z. Zhang, *Nonlinear Dyn.* **85**(4), 2233 (2016)
24. L. Qi, J. Sun, *Math. Program.* **58**(1–3), 353 (1993)
25. R.T. Rockafellar, *Math. Oper. Res.* **1**(2), 97 (1976)
26. P. Alart, A. Curnier, *Comput. Methods Appl. Mech. Eng.* **92**(3), 353 (1991)
27. M. Arnold, O. Brüls, *Multibody Syst. Dyn.* **18**(2), 185 (2007)
28. Q. Ma, A. Kahraman, *J. Sound Vib.* **284**(3–5), 893 (2005)

Dynamics of Discontinuous Nonlinear Oscillators with Compliant Contacts Subjected to Combined Harmonic and Random Loadings



Pankaj Kumar, S. Narayanan, and Sayan Gupta

1 Introduction

Vibro-impact systems, with piecewise smooth (PWS) characteristics, can mathematically model a range of physical systems that involve moving components with amplitude constraint motion [1, 2]. In many cases, bodies that collide have some compliance, and hence, impact is not perfectly rigid. Soft impacting systems are modeled using continuous functions of force-deformation relations during contacts [3]. The strong non-smooth nonlinearities generated at the discontinuity induce complex response behavior that is specific to non-smooth systems [2, 4]. One of the foremost challenges in investigating PWS systems is in developing algorithms that include prediction of time and location of non-smooth events as accurately as possible [5]. This has led to the development of various event-driven and time stepping methods to locate the switching points. However, most of available event detection routines are specific to deterministic systems [5].

The largest Lyapunov exponent (LLE) is usually the most important metric to interpret bifurcation and stability characteristics. However due to the difficulty in evaluation of Jacobian matrix at discontinuities, the classical methods developed for smooth dynamical systems cannot be directly applied. Müller [6] has extended Wolf's algorithm [7] for the calculation of LEs for non-smooth dynamical systems

P. Kumar (✉)

Dynamic Analysis Group, Bharat Heavy Electricals Limited, Nagpur, India

S. Narayanan

Mechanical Engineering, Indian Institute of Technology Madras, Chennai, India

e-mail: narayans@iitm.ac.in

S. Gupta

Applied Mechanics, Indian Institute of Technology Madras, Chennai, India

e-mail: sayan@iitm.ac.in

with discontinuity. An alternative approach to stochastic bifurcation analysis is to use the joint probability density function (jpdf) of state variables for P-bifurcation analysis. Estimating the response pdf of a discontinuous system can be obtained by solving the corresponding Fokker–Planck (FP) equation. Numerical solution of the FP equation is possible [8] but the presence of discontinuity creates challenges.

This chapter focuses on the development of a methodology for the response analyses of a stochastically excited non-smooth oscillator with soft impacts. An adaptive time stepping scheme is implemented for the path-wise solution of discontinuous stochastic differential equations (SDEs) to precisely locate the discontinuity event. In order to ensure that the correct Brownian path is traversed, Brownian tree structure [9] is used for adopting the new Brownian increments, conditioned on the previous increments. The proposed method is used for bifurcation analysis of a noisy Duffing–van der Pol (DVDP) oscillator having one- and two-sided impact barriers.

2 Problem Statement

Consider an elastic impact oscillator subjected to combined harmonic and Gaussian white noise excitations; see Fig. 1a. The governing equation of motion can be written in the general form as

$$\ddot{X} + f(X, \dot{X}) + g(q, \dot{q}) = \sigma W(t) + F \sin(\omega t), \quad (1)$$

where $f(X, \dot{X})$ is a general nonlinear function, $g(q, \dot{q})$ represents the impact force, \ddot{X} , \dot{X} , and X are, respectively, the acceleration, velocity, and displacement of the mass, q and \dot{q} represent the relative penetration (indention) and velocity between the colliding bodies, F and ω are, respectively, the amplitude and frequency of harmonic excitation, $W(t)$ is a stationary, zero-mean Gaussian white noise, and σ represents its intensity. In this chapter, the contact force is modeled following [10–12] and is given by

$$g(q, \dot{q}) = k_h q^n (1 + c_h \dot{q}), \quad (2)$$

where k_h is the contact stiffness, c_h is the damping coefficient, and n is a power exponent that depends on materials under impact.

3 Piecewise Smooth System Dynamics

Due to the presence of bilateral barriers on both sides of the equilibrium position, two different regimes of oscillations occur—(a) when the oscillator is in contact with the barrier and (b) when it is not. Hence, the phase space of the system dynamics is

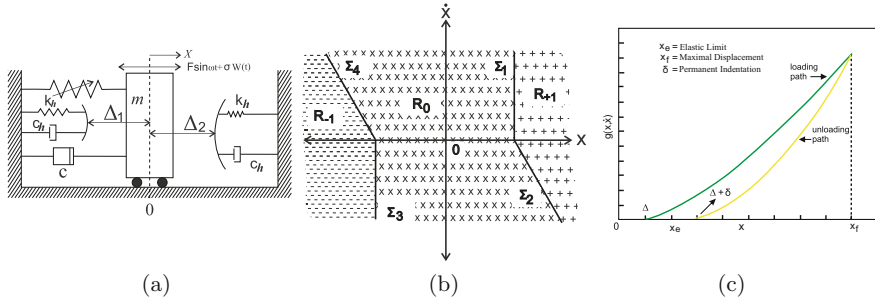


Fig. 1 (a) Schematic of a vibro- impact oscillator with discontinuous support (b) subspaces of the linear impact model (c) constitutive relationship for inelastic impact

divided into three possible subspaces; see Fig. 1b. Hence, Eq. (1) actually represents three different governing equations depending on whether the mass is without contact with any barrier or with contact with the right or the left barrier:

$$\ddot{X} + f(X, \dot{X}) = \sigma W(t) + F \sin(\omega t); [X, \dot{X}] \in R_0, \tag{3}$$

$$\ddot{X} + f(X, \dot{X}) + k_h(X - \Delta_2)^n(1 + c_h \dot{X}) = \sigma W(t) + F \sin(\omega t); [X, \dot{X}] \in R_{+1}, \tag{4}$$

$$\ddot{X} + f(X, \dot{X}) + k_h(X + \Delta_1)^n(1 + c_h \dot{X}) = \sigma W(t) + F \sin(\omega t); [X, \dot{X}] \in R_{-1}. \tag{5}$$

Numerical investigations of piecewise smooth SDE system, such as given in Eqs.(3)–(5), are faced with a challenging task in determining the exact time instances at which the oscillating mass hits the barriers. Hence, the first step is to define the switches where the transition from R_i to R_j occurs. Proper definition of switches in the case of inelastic impacts is complicated due to the different loading and unloading paths as shown in Fig. 1c. For example, when $X > 0, \dot{X} > 0$, the contact between the moving mass and the right barrier occurs if $X = \Delta_2$. However during unloading, the mass will lose the contact with the barrier when the contact force vanishes. Therefore, two different algebraic indicator functions given by

$$\begin{aligned} I_1(X, \dot{X}) &= X - \Delta_2 = 0, \\ I_2(X, \dot{X}) &= g(X - \Delta_2, \dot{X}) = 0, \end{aligned} \tag{6}$$

are used to define the loading and unloading phases. Hence, the discontinuity boundaries between R_0 and R_{+1} are defined by Σ_1 and Σ_2 as

$$\begin{aligned} R_0 \rightarrow R_{+1} &\equiv \Sigma_1 = \{I_1(X(t^*)) = 0, I_2(X(t^*), \dot{X}(t^*)) \geq 0\} : \text{loading}, \\ R_{+1} \rightarrow R_0 &\equiv \Sigma_2 = \{I_1(X(t^*)) \geq 0, I_2(X(t^*), \dot{X}(t^*)) = 0\} : \text{unloading}, \end{aligned} \tag{7}$$

where t^* is the time at which the discontinuity surface is reached. Similarly, the indicator functions between R_0 and R_{-1} , during loading and unloading, are defined as

$$\begin{aligned} I_3(X, \dot{X}) &= X + \Delta_1 = 0, \\ I_4(X, \dot{X}) &= g(X + \Delta_1, \dot{X}) = 0. \end{aligned} \tag{8}$$

The switches between the discontinuity boundaries between R_0 and R_{-1} are defined by Σ_3 and Σ_4 as

$$\begin{aligned} R_0 \rightarrow R_{-1} &\equiv \Sigma_3 = \{I_3(X(t^*)) = 0, I_4(X(t^*), \dot{X}(t^*)) \leq 0\} : \text{loading}, \\ R_{-1} \rightarrow R_0 &\equiv \Sigma_4 = \{I_3(X(t^*)) \leq 0, I_4(X(t^*), \dot{X}(t^*)) = 0\} : \text{unloading}. \end{aligned} \tag{9}$$

4 Response Statistics Using Fokker–Planck Equation

Assuming Gaussian white noise excitation, the state-space vector $\mathbf{X} = [X_1, X_2]$ for the impact oscillator can be assumed to be approximately Markovian. Consequently, the evolution of the jpdf of the state variables is governed by the FP equation. However, the discontinuity at $X = \Delta_1, \Delta_2$, poses challenges in formulating the FP equation. To incorporate Eqs. (3)–(5) due to two-sided barrier into a single equation, the auxiliary functions

$$H_1 = H(X - \Delta_2), \quad H_2 = H(X + \Delta_1), \tag{10}$$

are defined, where $H(X)$ is the Heaviside unit step function. This enables rewriting Eqs. (3)–(5) as a single equation of the form

$$\ddot{X} + f(X, \dot{X}) + H_1 k_h (X - \Delta_2)^n (1 + c_h \dot{X}) + H_2 k_h (X + \Delta_1)^n (1 + c_h \dot{X}) = \sigma W(t). \tag{11}$$

Moreover, the FE solution of the corresponding FP equation requires that the activation function to be differentiable in order to comply with the C^0 continuity condition [8]. This difficulty can be circumvented by approximating the Heaviside unit step function as $H(X - \Delta) \approx \frac{1}{1 + e^{-\theta(X - \Delta)}}$, where the parameter θ can be suitably adjusted [2].

The corresponding FP equation for the pdf $p(\mathbf{X}; t)$ is given by

$$\frac{\partial p}{\partial t} = -X_2 \frac{\partial p}{\partial X_1} - \frac{\partial}{\partial X_2} \{-f(X_1, X_2) + \psi(X_1, X_2)\} p + \frac{\sigma^2}{2} \frac{\partial^2 p}{\partial X_2^2}, \tag{12}$$

where $\psi(X_1, X_2) = -\frac{1}{1 + e^{-\theta(X_1 - \Delta_2)}} k_h (X_1 - \Delta_2)^n (1 + c_h X_2) - \frac{1}{1 + e^{-\theta(X_1 + \Delta_1)}} k_h (X_1 + \Delta_1)^n (1 + c_h X_2)$ and p is the jpdf of the state variables \mathbf{X} . Numerical solution

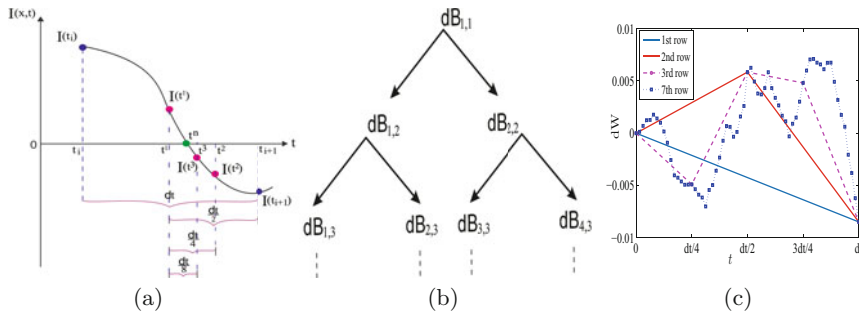


Fig. 2 (a) Bisection scheme, (b) Brownian tree, (c) sample of Brownian tree

for the FP equation is obtained using a finite-element (FE)-based method [8]. Due to the presence of the discontinuity, a differential meshing is adopted whose size varies from 0.01 to 0.001. It is observed that the FE grid with element size smaller than 0.0075 gives solution with reasonable accuracy when benchmarked in terms of the Kullback–Leibler entropy measure [8]. Any further refinement in mesh size increases the computational time with no significant increase in the accuracy.

5 Adaptive Time Stepping Procedure

Path-wise solution of the noisy discontinuous oscillator demands precise location of time and position of discontinuity. Hence in order to accurately locate the discontinuity event t^* , the bisection technique is adopted in numerical integration. Here, once the solver detects the sign change in indicator function, *i.e.*, $\mathbf{I}(\mathbf{X}(t_i), t_i)\mathbf{I}(\mathbf{X}(t_{i+1}), t_{i+1}) < 0$, bisection scheme is used to find the discontinuity point t^i and is given by (Fig. 2a)

$$t^i = t^{i-1} + \text{sgn}(I(\mathbf{X}, t_i)I(\mathbf{X}, t^{i-1})) \frac{dt}{2^i}. \tag{13}$$

The bound for the number of iterations is taken as $|\mathbf{I}(\mathbf{X}(t^N), t^N)| < \epsilon$, where ϵ is a predefined number close to zero. The discontinuity point $t^* = t^N$ is approximated after a sufficient number of iterations.

An important prerequisite while implementing adaptive step-size scheme for path-wise solution of the SDEs is that when a point of discontinuity is detected and the original time step is discarded, the numerical solution should continue on the original Brownian path, so that the correct statistics of the numerical solution should be maintained. Hence, for implementing the bisection algorithm during numerical simulation, one should not reject the Wiener increments for the previous time steps dB_j , and compute new dB_j proportional to the reduced time step. This would lead to a poor approximation or even a biased numerical solution. To ensure that

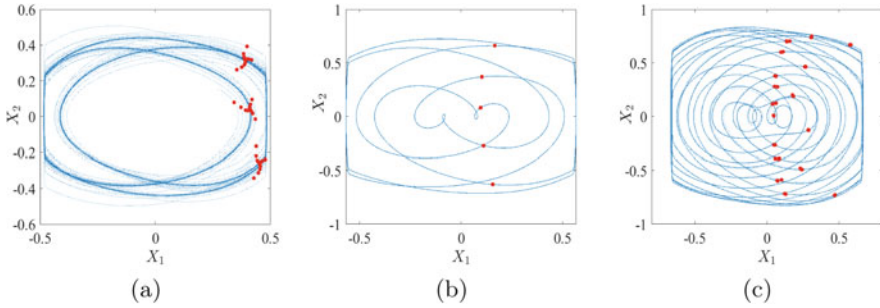


Fig. 3 Phase plane and its Poincaré section for different offset positions. (a) $\Delta_1 = -0.475, \Delta_2 = 0.475$, (b) $\Delta_1 = -0.55, \Delta_2 = 0.55$, and (c) $\Delta_1 = -0.65, \Delta_2 = 0.65$

numerical solution is directed along the correct Brownian path trajectory, during the recursive generation of reduced time steps, the Wiener increments for a level (say $m + 1$) conditioned on the previous level m can be obtained by using the concept of Brownian tree [9] and given by

$$dB_{2l-1,m+1} = \frac{1}{2}dB_{l,m} + \phi_{l,m}, \quad dB_{2l,m+1} = \frac{1}{2}dB_{l,m} - \phi_{l,m}, \quad (14)$$

where $\phi_{l,m}$ are normally distributed random variables with mean zero and variance 2^{-m} , $m = 1, 2, \dots$ number of rows and $l = 1, 2, \dots, 2^{m-1}$ denotes the number of nodes. More precisely, a tree structure will be generated with each node having two downstream branches (Fig. 2b), which pass through each intermediate points generated through variable time integration (Fig. 2c). Proposed adaptive time stepping procedure (ATSP) is also used for the computation of the LLE using the Wolf’s algorithm [7] in combination with Müller’s procedure [6].

6 Numerical Results

A DVDP oscillator with $f(x, \dot{x}) = -\alpha x - c\dot{x} + \beta_0 x^3 - \beta_1 x^2 \dot{X} + \beta_2 x^4 \dot{X}$ (Fig. 1a) is considered. Here, α and c denote the linear stiffness and damping terms, and $\{\beta_i(t)\}_{i=0}^2$ define the nonlinear stiffness and damping. The following parameters are fixed at $\beta_0 = 0.5, \beta_1 = \beta_2 = 1, n = 3/2$.

The influence of the control parameter Δ on the non-smooth dynamics is considered for $c = -0.1, F = 0.42, \omega = 1, \sigma = 0$. The phase plane plots and the associated Poincaré maps (red points) for three different values of offset positions are presented in Fig. 3, which show period-3, period-5, and multi-periodic responses, respectively. For barrier position $\Delta_1 = -0.475, \Delta_2 = 0.475$, the effect of noise ($\sigma = 0.01$) on system response is presented in Fig. 4a. Notice that noise causes perturbations in the system dynamics and the period-3 orbit loses

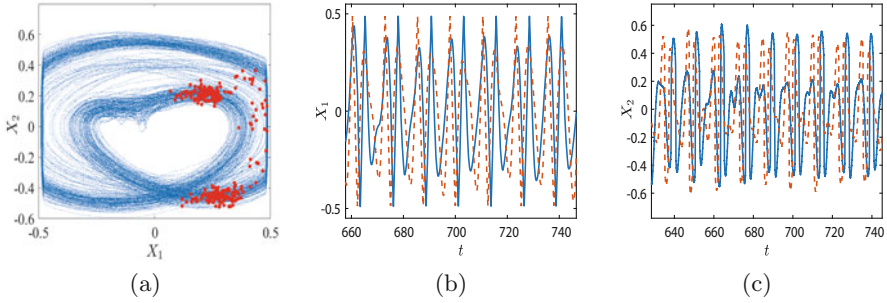


Fig. 4 (a) Phase plane and its Poincaré section, (b) time series of displacement, (c) time series of velocity, (ATPS (solid line), constant time step (dashed line))

its periodic behavior. The time histories of displacement as well as velocity, for $\Delta_1 = -0.475, \Delta_2 = 0.475, \sigma = 0.01$, as obtained using the Milstein method in combination with the proposed ATSP, are shown in Fig. 4b, c. For comparison, the time histories obtained through the Milstein method but using fixed time step $dt = 0.0025$ are also presented; significant deviation between the two time histories is observed. A comparison of system dynamics with and without elastic barriers is presented in Fig. 5 assuming $c = -0.1, F = 0.42, \omega = 1, \sigma = 0.0025$. Note that without impact, the system response is of chaotic nature (Fig. 5a), while there is a period-3 orbit with impact (Fig. 5b). Figure 5c presents the LLE variation as a function of α . Figure 6 presents the bifurcation diagrams for smooth as well as non-smooth systems, respectively. Results depict a considerable region with chaotic behavior in case of smooth system, while for non-smooth system LLE is negative for the given range of linear stiffnesses α . Hence, we conclude that elastic impact suppresses chaos.

In order to obtain further insights, on the combined influence of dry friction and impacts on the dynamics of the system, parametric investigations are carried out, which are summarized in Fig. 7. Figure 7a depicts that without elastic impact, but with dry friction having friction coefficients $f_s = 0.02$, system dynamics is of period-1 orbit about one of the fixed points of the oscillator. System response with impact, but without friction, results in a period-3 orbit (Fig. 7b). However, the combined effect of impact and friction leads to chaotic orbits (Fig. 7c).

Next, solving the FP equation, the effect of position of elastic-damped barrier is investigated. Figure 8 shows the jpdf, with different positions of elastic-damping barrier with $\Delta_1 = 0, -0.4, -0.8$ and $\Delta_2 = \infty$. It is observed that for $\Delta_1 = 0$, the joint pdf is unimodal indicating that the trajectories are in the vicinity of the attractor at the origin. However, as the barrier distance is increased, limit cycle oscillation (LCO) attractor gains strength, and the attractor changes from unimodal character to bistable character. For $\Delta_1 = -0.8$, the attractor at the origin vanishes completely, and only one stable attractor corresponding to the LCO persists.

Next the system dynamics using various compliant contact force models such as Hunt and Crossley [10] $Kq^n \left[1 + \frac{3(1-e)}{2} \frac{\dot{q}}{\dot{q}^-} \right]$, Lee and Wang [11] $(Kq^n [1 +$

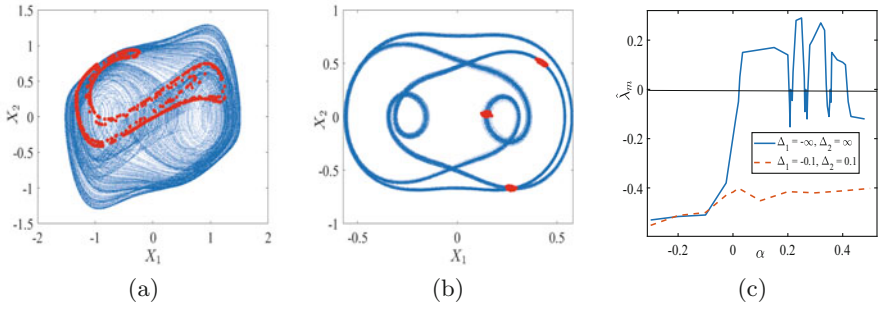


Fig. 5 (a) Phase plane and its Poincare section without barrier, (b) with barrier, and (c) the LLE

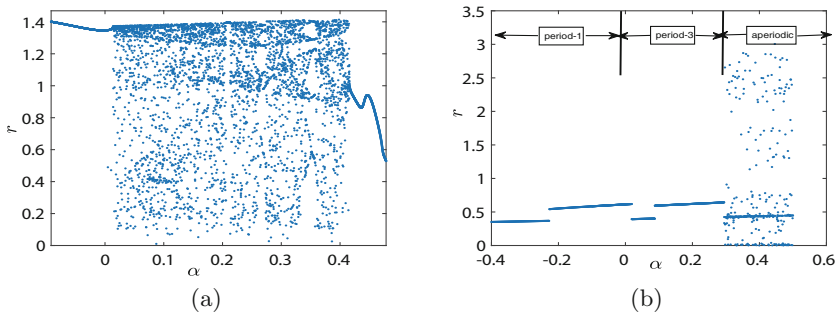


Fig. 6 Bifurcation diagram for (a) smooth and (b) non-smooth oscillators

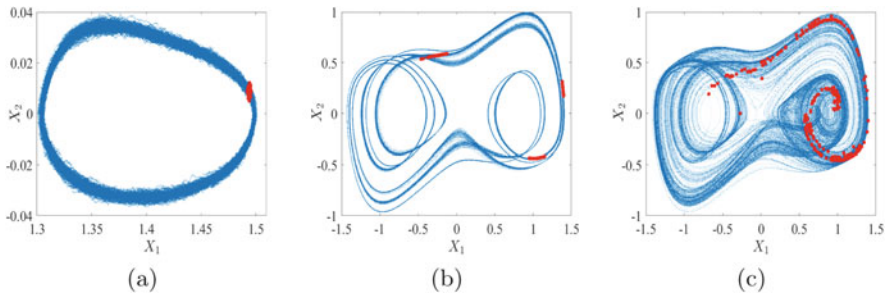


Fig. 7 Phase plane and its Poincare section (a) without impact but with friction, (b) with impact but without friction, (c) with impact and friction, $c = -0.1$, $F = 0.21$, $\omega = 0.3$, $\sigma = 0.0025$

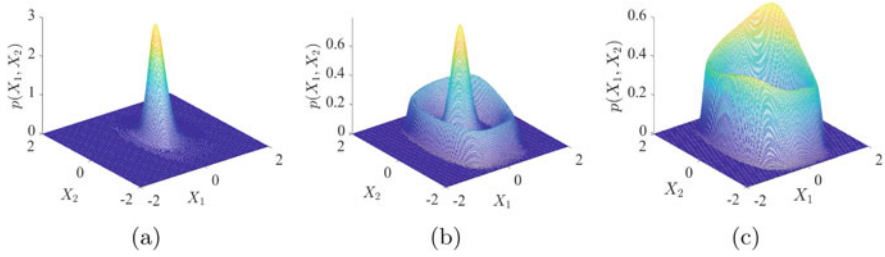


Fig. 8 Stationary joint pdf of $p_{X_1 X_2}(x_1, x_2)$ for (a) $\Delta_1 = 0$, (b) $\Delta_1 = -0.4$, (c) $\Delta_1 = -0.8$ and $\Delta_2 = \infty$, $c = -0.09$, $k_h = 1$, $c_h = 0.075$

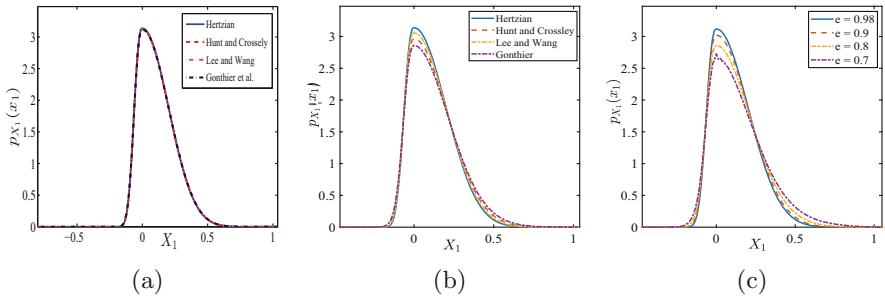


Fig. 9 Marginal pdf of displacement for different contact models (a) $e = 0.98$. (b) $e = 0.8$. (c) Effect of e

$\frac{3(1-e)}{4} \frac{\dot{q}^-}{\dot{q}^-}$], Gonthier et al. [12] ($Kq^n [1 + \frac{(1-e^2)}{e} \frac{\dot{q}^-}{\dot{q}^-}]$) etc. is presented in Fig. 9 with $c = -0.1$, $k_h = 0.95$, $\sigma = 0.1$. For high values of the kinetic coefficient of restitution, such as $e = 0.98$, all the compliant contact force models result in close agreement as in Hertzian elastic contact force model (Fig. 9a). This is expected as for $e \approx 1$ energy dissipation is negligible. However, for a moderately lower value of e , such as $e = 0.8$, significant differences are observed; see Fig. 9b. Furthermore, Lee and Wang’s [11] model is observed to dissipate least amount of energy, while Gonthier et al.’s model [12] dissipates maximum energy during the contact process. The effect of e using Gonthier et al.’s model [12] is presented in Fig. 9c, which indicates damping increases with decrease in e due to energy loss on contact.

The effect of initial indentation impact velocity \dot{q}^- using Gonthier et al.’s model [12] is investigated next. The variation of the contact force with time is shown in Fig. 10a. It is seen that higher initial impact velocity yields a shorter impact duration but higher magnitude of impact force. The marginal pdf of displacement for a different initial indentation impact velocity \dot{q}^- is shown in Fig. 10b, which indicates less energy is dissipated as the initial indentation impact velocity increases.

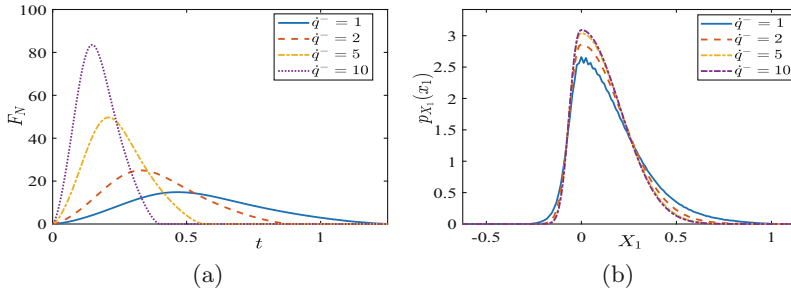


Fig. 10 Effect of initial impact velocity \dot{q}^- . **(a)** Variation of contact force. **(b)** Marginal pdf of displacement

7 Conclusions

The stochastic bifurcation analysis of a stochastic non-smooth system with discontinuous support is numerically investigated. The interaction force of the impact is described by Hertzian as well as by various compliant contact force models that also accommodate energy dissipation in the form of internal damping. An adaptive variable time step numerical integration scheme in combination with the bisection technique is developed to precisely locate the point of discontinuity during numerical simulation advanced by the Milstein scheme. The jpdf of the state variables obtained by the solution of the FP equation and the LLE obtained by the Muller discontinuity mapping is used for the analysis of stochastic bifurcations. The nonlinear dynamical characteristics are studied using the time histories, Poincare section, phase plane plots, joint pdf, and the LLE. The numerical results demonstrate the accuracy and efficiency of the proposed adaptive variable time stepping scheme in investigating the stochastic bifurcations of noisy nonlinear systems with discontinuities.

References

1. R.A. Ibrahim, *Vibro-Impact Dynamics Modeling, Mapping and Applications* (Springer, Berlin, 2009)
2. M. Wiercigroch, Modeling of dynamical systems with motion dependent discontinuities. *Chaos Solitons and Fractals* **11**, 2429–42 (2000)
3. M. Machado, P. Moreira, P. Flores, H.M. Lankarani, Compliant contact force models in multibody dynamics: evolution of the Hertz contact theory. *Mech. Mach. Theory* **53**, 99–121 (2012)
4. P. Kumar, S. Narayanan, S. Gupta, Stochastic bifurcations in a vibro-impact Duffing-van der Pol oscillator. *Nonlinear Dyn.* **85**, 439–52 (2016)
5. P.T. Piiroinen, Y.A. Kuznetsov, An Event driven method to simulate Filippov systems with accurate computing of sliding motions. *ACM Trans. Math. Softw.* **34**, 1–24 (2008)

6. P. Müller, Calculation of Lyapunov exponent for dynamics system with discontinuities. *Chaos Solution Fractals* **5**, 1671–1681 (1995)
7. A. Wolf, J.B. Swift, H.L. Swinney, J.A. Vastano, Determining Lyapunov exponents from a time series. *Phys. D* **16**, 285–317 (1985)
8. P. Kumar, S. Narayanan, S. Gupta, Finite Element solution of Fokker-Planck equation of nonlinear oscillators subjected to colored non-Gaussian noise. *Probab. Eng. Mech.* **38**, 143–155 (2014)
9. P. Levy, *Monographie des Probabilites* (Gauthier-Villars, Paris, 1948)
10. K.H. Hunt, F.R.E. Crossley, Coefficient of restitution interpreted as damping in vibro-impact. *J. Appl. Mech.* **7**, 440–445 (1975)
11. T.W. Lee, A.C. Wang, On the dynamics of intermittent-motion mechanisms, Part 1: dynamic model and response. *J. Mech. Trans. Autom. Design* **105**, 534–540 (1983)
12. Y. Gonthier, J. McPhee, C. Lange, J.-C. Piedboeuf, A regularized contact model with asymmetric damping and dwell-time dependent friction. *Multibody Syst. Dyn* **11**, 209–233 (2004)

Response Analysis of Coupled Non-Smooth Nonlinear Aeroelastic System Subjected to Stochastic Input Fluctuations



Dheeraj Tripathi, Sai Vishal, Chandan Bose, and J. Venkatramani

1 Introduction

Aeroelastic systems exhibit complex dynamical signatures due to the presence of nonlinearities arising from the structure or flow or a combination of both. Beyond a critical airspeed, there is a continuous energy transfer into the system from the oncoming flow, which results in self-sustained oscillations called limit cycle oscillations (LCO) [1, 2]. Classical binary flutter results from the coalescence of pitch and plunge modes where the aerodynamic damping of the critical mode becomes zero. However, in high angle of attack (AoA) applications like wind turbine blades, helicopter blades, turbomachinery blades etc., nonlinearity originates due to flow separation and gives rise to pitch-dominated stall flutter [1]. Such bending and torsional oscillations give rise to multi-axial cyclic stresses that impose serious threat to structural fatigue life. Flutter prediction and fatigue damage analysis are thus very crucial in such aeroelastic systems.

Recent studies suggest that a coupling of aerodynamic and structural nonlinearities can lead to completely different response dynamics that are largely unexplored [3]. Structural nonlinearities can be modelled either as a continuous function or as a non-smooth function. The ageing parts, lose or worn hinges, can be modelled as freeplay nonlinearity. The presence of freeplay nonlinearity in structure alters response dynamics of the system even before the linear flutter boundary. Liu et al. [4] identified period doubling bifurcation and chaos below the classical flutter boundary. Freeplay nonlinearity can be modelled as smooth or non-smooth

D. Tripathi (✉) · S. Vishal · J. Venkatramani
Department of Mechanical Engineering, Shiv Nadar University, Greater Noida, India
e-mail: dt989@snu.edu.in; vishal.gali@snu.edu.in; j.venkatramani@snu.edu.in

C. Bose
Department of Aerospace and Mechanical Engineering, University of Liège, Liège, Belgium
e-mail: chandan.bose@uliege.be

functions. Vasconcellos et al. [5] analysed control surface freeplay nonlinearity through a discontinuous and a continuous representation and concluded that only a non-smooth representation of freeplay can explain the complex dynamics. On the other hand, modelling of aerodynamic nonlinearity is computationally tedious due to the non-smoothness arising from the flow separation. Nevertheless, semi-empirical models based on curve fitting of experimental data from wind tunnel tests like Leishman–Beddoes dynamic stall model [6] give good approximation of aerodynamic nonlinearity. So far, most of the literature investigate the individual effect of nonlinearities either from structural part or from aerodynamics, but the effect of coupling of such nonlinearities is largely unexplored.

Examining the dynamics of coupled non-smooth nonlinear aeroelastic systems is perhaps incomplete if the random nature of input flow fluctuations is ignored. In field conditions, flow is always fluctuating in nature. Recent studies suggest that flutter boundary is preponed and qualitative different dynamical aspects like intermittency [7] are present in pre-flutter regime in the presence of fluctuating inflow. In hitherto literature, the effect of flow fluctuation on system response under non-smooth nonlinearities has rarely been investigated. Devathi and Sarkar [8] studied the effect of random gust on stall flutter of one-dimensional airfoil and reported the dynamics such as stochastic fixed point, stochastic LCO, and intermittency. Recently, Bethi et al. [3] used a canonical sinusoidal gust model and showed the intermittent switching of dynamics between periodic and chaotic states due to wind fluctuation on a pitch–plunge airfoil. The authors showed noise-induced transitions and represented the same using the concept of stochastic phenomenological (P-type) bifurcations.

A concern that arises in the analysis of stochastic nonlinear aeroelastic systems is the susceptibility to large fatigue damage. Fatigue damage is much more prevalent in aeroelastic structures due to periodic and aperiodic oscillations present due to various nonlinearities [9]. Additionally, random fluctuations in wind give rise to NII as well as reduce the flutter margin that may affect the fatigue life of the structure severely [10]. Fatigue calculations in aeroelastic systems are a daunting task as it involves a combination of torsional and bending modes. Additionally, due to the presence of randomness in dynamic responses of bending and torsion modes, the cyclic stresses are also time varying in nature. To extract the fatigue damage-related information from such random stress data, cycle counting is crucial to estimate the number of load cycles. Rain-flow cycle counting (RFC) is one of the most efficient cycle counting method for most of the relevant engineering applications [11]. To the best of the authors' knowledge, damage analysis of coupled non-smooth nonlinear aeroelastic structures under stochastic inflow has not received much attention in the existing literature.

This chapter takes up this analysis under randomly fluctuating inflow. To that end, a pitch–plunge aeroelastic system with freeplay nonlinearity in pitch degree of freedom is subjected to a stochastic flow under dynamic stall condition. Pitch stiffness is modelled as a bilinear function, and aerodynamical states are modelled using Leishman–Beddoes (LB) model. Stochastic bifurcation analysis of the system is carried out with mean flow speed as the bifurcation parameter. Finally, fatigue

damage analysis of the system is carried out using RFC algorithm to quantify the structural safety.

The rest of this chapter is organized as follows. Mathematical modelling of the aeroelastic model is presented in Sect. 2. Methodology for fatigue damage analysis is presented in Sect. 3. Next, we present the salient findings in terms of time response, stochastic bifurcation analysis, and fatigue damage in Sect. 4 along with the related discussions. Finally, the salient conclusions that emerge from the study are summarized in Sect. 5.

2 Mathematical Modelling

For a two-dimensional pitch–plunge aerofoil, the equations of motion are given as [2]

$$\xi'' + x_\alpha \alpha'' + 2\zeta_\xi \frac{\bar{\omega}}{U} \xi' + \left(\frac{\bar{\omega}}{U}\right)^2 \xi = -\frac{1}{\pi\mu} C_L(\tau), \tag{1}$$

$$\frac{x_\alpha}{r_\alpha^2} \xi'' + \alpha'' + 2\zeta_\alpha \frac{1}{U} \alpha' + \left(\frac{1}{U}\right)^2 M(\alpha) = \frac{2}{\pi\mu r_\alpha^2} C_M(\tau). \tag{2}$$

Here, ξ is the non-dimensional plunge displacement, $\bar{\omega}$ is the natural frequency ratio of the uncoupled plunge to pitch mode, U is the non-dimensional flow velocity, τ is the non-dimensional time, and ζ_α and ζ_ξ are the non-dimensional damping coefficients in pitch and plunge, respectively. $C_L(\tau)$ and $C_M(\tau)$ are the coefficients of lift and moment, respectively. The details of the non-dimensionalized parameters and lift and drag coefficients are not mentioned here for the sake of brevity and can be found in Bethi et al. [3].

The pitch stiffness of airfoil ($M(\alpha)$) is modelled as a bilinear function to incorporate freeplay nonlinearity in the pitch degree of freedom

$$M(\alpha) = \begin{cases} \alpha + \delta, & \text{if } \alpha < -\delta, \\ 0, & \text{if } -\delta \leq \alpha \leq \delta, \\ \alpha - \delta, & \text{if } \alpha > \delta, \end{cases} \tag{3}$$

where 2δ represents the freeplay or zero stiffness region.

Aerodynamic loads are formulated using the Leishman–Beddoes dynamic stall model [6], in which, out of the total twelve aerodynamic states, first eight states (x_1 to x_8) capture attached flow and are given in terms of pitch angle and pitch rate. State x_9 represents the vortex shedding and reattachment, x_{10} and x_{12} represent separation point corresponding to trailing edge, and state x_{11} represents vortex-

induced airloads. More details of the twelve states can be found in Bethi et al. [3] and are not repeated here for the sake of brevity.

A canonical model for the input flow fluctuation is considered of the form [3]

$$U(\tau) = U_{mean} + f(\tau). \quad (4)$$

Here, $f(\tau) = \sigma U_{mean} \sin(\tau \omega_r(\tau))$, U_{mean} is the non-dimensional mean wind speed, σ is the intensity of fluctuations, and ω_r is the frequency of sinusoid, randomly varying with time. Moving average filter is used to generate long-time-scale flow fluctuations [3].

3 Fatigue Damage Calculation

For calculating the fatigue damage, three stresses need to be estimated: (i) Shear stresses due to torsion, (ii) Normal stresses due to bending, and (iii) von Mises stresses. Venkatesh et al. [10] showed that normal stresses produced are negligible as compared to torsional stresses and von Mises stresses are numerically almost the same as shear stresses. Due to non-circular section, stresses are defined in terms of Prandtl stress function ϕ .

$$\sigma_{xz} = \frac{\partial \phi}{\partial y}, \sigma_{yz} = -\frac{\partial \phi}{\partial x}. \quad (5)$$

such that

$$\frac{\partial^2 \phi}{\partial y^2} + \frac{\partial^2 \phi}{\partial x^2} = -2G\theta. \quad (6)$$

Here, x and y are the coordinates of airfoil along the chord length and along the thickness, respectively, and z -axis is perpendicular to the cross-section of airfoil. Aluminium alloy AI-6082 T-6 is chosen for analysis. Three different points were taken on NACA0012 airfoil: $P_1(0.244 \text{ m}, 0.0366 \text{ m})$ is the point at maximum thickness, $P_2(0.610 \text{ m}, 0.0007 \text{ m})$ is the point at the trailing edge, and $P_3(0.061 \text{ m}, 0.061 \text{ m})$ is an arbitrary point on airfoil surface. WAFO toolbox [12] was utilized for analysing RFC, and the corresponding fatigue damage is calculated using Palmgren–Miner linear damage accumulation theory [10].

4 Results and Discussions

Two different cases have been taken up in this chapter: one with linear structure and other with structural freeplay nonlinearity. Aerodynamics is governed by LB

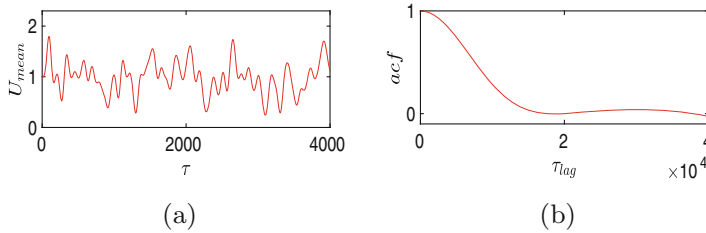


Fig. 1 (a) Variation of flow speed with time about $U_{mean} = 1$, and (b) simulated autocorrelation function (acf) of U_{mean} vs. lag time (τ_{lag})

model in both the cases. Governing state equations are solved using fourth-order explicit Runge–Kutta time integration with adaptive time stepping. However, time integration of current system deals with non-smoothness in both the structural and aerodynamic models, which needs a special attention. Previous studies suggest a very low tolerance value while dealing with discontinuous structural [4] and aerodynamic [3] models. Hence, a tolerance value of $\mathcal{O}(10^{-12})$ is adopted in the present analysis. The structural parameters are adopted from [4]. Initial conditions for pitch mode are taken as 15° , and a freeplay gap of $2\delta = 1^\circ$ is considered throughout the study. The non-dimensional correlation time of the considered fluctuating inflow is computed to be of $\mathcal{O}(10^4)$, which is much higher than the non-dimensional system time scale of $\mathcal{O}(10^1)$. This attributes to long-time-scale fluctuations (Fig. 1a). Figure 1b shows autocorrelation of input noise as a function of delay or lag time (τ_{lag}).

4.1 Validation of the Aerodynamic Model

The present LB model is validated for a pitching airfoil case under dynamic stall with kinematics: $\alpha(\tau) = 12 + 10\sin(\kappa\tau)$, where κ is the reduced frequency. Coefficients of pitching moment (C_m) vs. pitch angle (α) hysteresis curves were plotted for the current LB model with fluctuating inflow and compared with the original LB model [6] in Fig. 2. It can be seen that the pitching moment, captured by the current stochastic model, shows a close agreement with that obtained from the original LB model at low angle of attack but has higher negative pitching moment at higher angles due to random flow fluctuation.

4.2 Pitch Response Dynamics

Pitch responses of linear airfoil structure at different mean speeds are shown in Fig. 3. It can be seen that at lower velocities ($U_{mean} = 3.4$), an interplay between

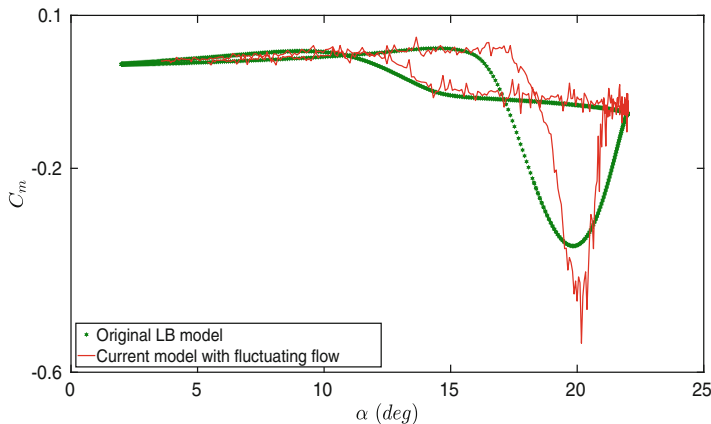


Fig. 2 Variation of coefficient of moment (C_m) vs. pitch angle (α) for kinematics: $\alpha(\tau) = 12 + 10\sin(\kappa\tau)$ at $\kappa = 0.0976$ and Mach number 0.3

aperiodic and periodic oscillations is observed, which is the characteristic of noise-induced intermittency (Fig. 3a, c). Phase portraits of $x_9 - x_{10}$ at $U_{mean} = 3.4$ (Fig. 3e) show that the flow is fully attached and the response dynamics can be attributed to the sole effect of random flow fluctuation. At $U_{mean} = 5.8$, the dynamics changes into large-amplitude random LCO (Fig. 3b, d). The corresponding phase portraits of $x_9 - x_{10}$ at $U_{mean} = 5.8$ (Fig. 3f) show that the flow is fully separated that marks the presence of deep dynamic stall.

Next, the nonlinear structure was taken under consideration, and the corresponding time responses are shown in Fig. 4. At $U_{mean} = 3.4$, intermittent oscillations change into random period-2 signatures when freeplay nonlinearity is taken into account (Fig. 4a, c) with peak-to-peak amplitude approximately 3° . From $x_9 - x_{10}$ phase portrait (Fig. 4e), we can see that the flow is fully attached and thus these responses are due to the coupling of flow fluctuations and structural nonlinearity. At flow velocity $U_{mean} = 5.8$, period-2 signatures transform into high-amplitude random period-1 LCO (Fig. 4b, d). The corresponding $x_9 - x_{10}$ phase portrait (Fig. 4f) shows fully separated flow, representative of large vortex shedding.

4.3 Stochastic Bifurcation Analysis

Next, phenomenological (P-type) stochastic bifurcation analysis of aeroelastic system is carried out to capture the qualitative change in the probabilistic response dynamics. Joint probability density function of pitch and pitch rate is plotted for both linear and nonlinear structure (Fig. 5). For linear aerofoil, various peaks are observed at $U_{mean} = 3.4$ (Fig. 5a), which correspond to intermittent switching between different attractors. At $U_{mean} = 5.8$, peaks disappear and a crater-like

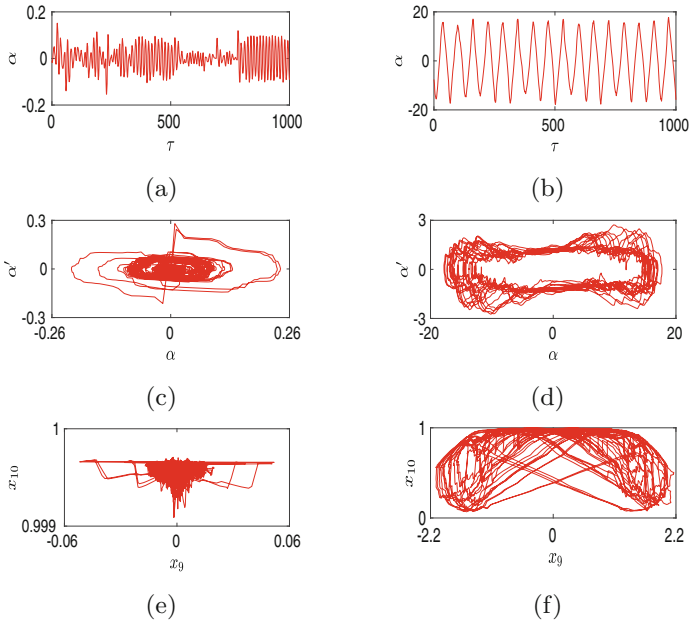


Fig. 3 (a) At $U_{mean} = 3.4$, the pitch time response shows intermittent oscillations, (b) the pitch time response at $U_{mean} = 5.8$ shows large-amplitude LCO, (c) phase portrait of pitch–pitch rate at $U_{mean} = 3.4$, (d) phase portrait of pitch–pitch rate at $U_{mean} = 5.8$ shows random LCO, (e) phase portrait of x_9 - x_{10} at $U_{mean} = 3.4$ shows attached flow condition, and (f) phase portrait of x_9 - x_{10} at $U_{mean} = 5.8$ shows deep dynamic stall conditions with a large amount of vortex shedding

structure appears that implies the presence of LCO with time-varying amplitude (Fig. 5b).

For nonlinear structure, two distinct peaks can be seen at $U_{mean} = 3.4$, which is a characteristic of a random period-2 attractor (Fig. 5c). At $U_{mean} = 5.8$, both peaks merge in a crater-like structure implying the presence of random LCO in pitch response (Fig. 5d). Visual inspection on topological changes in j-pdf of pitch–pitch rate confirms the presence of a P-bifurcation for both linear and nonlinear structure, as the parameter U_{mean} varies.

4.4 Fatigue Damage Estimation

Fatigue damage analysis is shown for pitch motion only as bending stresses due to plunge motion are much smaller as compared to torsional stresses [10]. Torsional stresses σ_{xz} and σ_{yz} are obtained using WAFO toolbox. It was observed that shear stress σ_{yz} is much lesser ($\mathcal{O}(10^2)$ times) as compared to σ_{xz} , and thus maximum shear stress, $S_{max} = \sqrt{\sigma_{xz}^2 + \sigma_{yz}^2}$, is almost the same as σ_{xz} . Time histories for

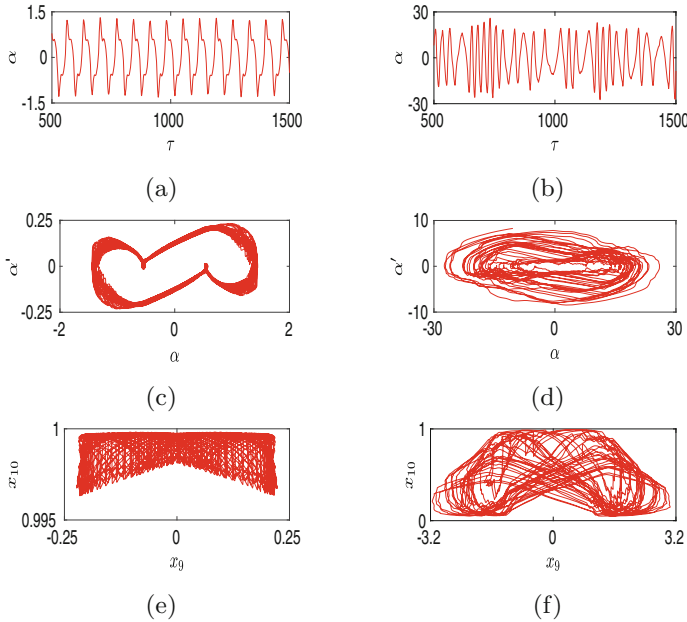


Fig. 4 (a) At $U_{mean} = 3.4$, pitch time response shows random LCO, (b) at $U_{mean} = 5.8$, large-amplitude LCO in pitch time response is observed, (c) phase portrait of pitch–pitch rate at $U_{mean} = 3.4$ shows two additional loops near freeplay limits, (d) phase portrait of pitch–pitch rate at $U_{mean} = 5.8$ shows random LCO, (e) phase portrait of x_9 – x_{10} at $U_{mean} = 3.4$ shows attached flow, and (f) phase portrait of x_9 – x_{10} at $U_{mean} = 5.8$ shows flow is fully separated and large vortex shedding

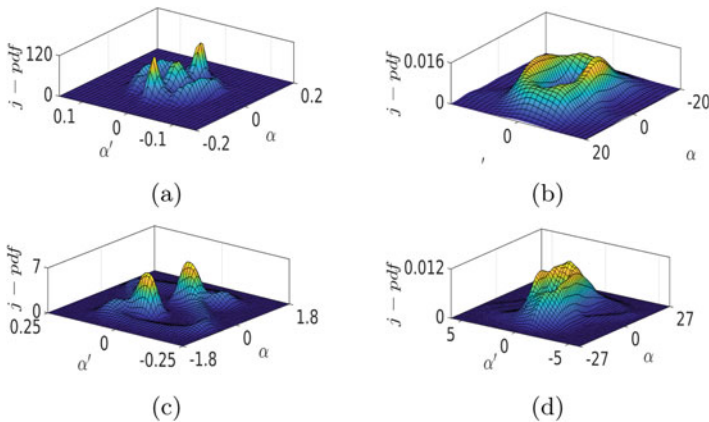


Fig. 5 Joint probability density function of pitch–pitch rate. (a) Linear structure at $U_{mean} = 3.4$ shows the number of intermittent peaks, (b) for linear structure at $U_{mean} = 5.8$, peaks merge in a crater-like structure, (c) for nonlinear structure at $U_{mean} = 3.4$, two different attractors are present, and (d) for nonlinear structure at $U_{mean} = 5.8$, topology changes into a crater-like structure

Table 1 Accumulated damage values

U_{mean}	Damage (steady flow)	Damage (fluctuating flow/linear structure)	Damage (fluctuating flow/freeplay nonlinearity)
3.4	≈ 0	7.67×10^{-12}	5.21×10^{-10}
5.8	7.14×10^{-07}	2.87×10^{-07}	$2.60 \times 10^{+2}$

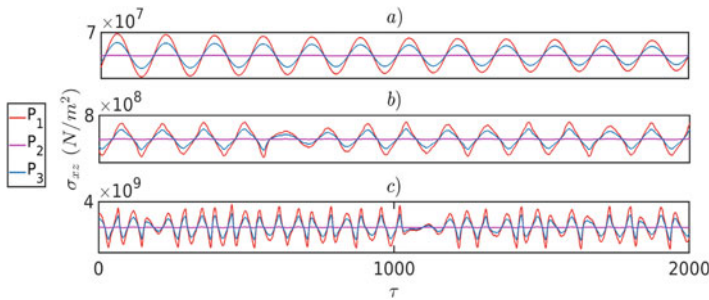


Fig. 6 Stress time histories at $U_{mean} = 5.8$, under (a) deterministic inflow, (b) stochastic inflow for linear airfoil, and (c) stochastic inflow for airfoil with freeplay nonlinearity, show highest cyclic stresses in the presence of freeplay nonlinearity under fluctuating inflow

shear stress σ_{xz} are estimated at different flow speeds for a linear structure with steady inflow, linear structure with stochastic inflow, and the corresponding damage values are summarized in Table 1. Figure 6 shows the comparison of stress cycles for these three cases. Order of stresses in coupled non-smooth nonlinear system is found to be highest as compared to other two cases. It is also observed that magnitude of the shear stresses is highest at maximum thickness (point P_1). Comparing the stresses, it can be concluded that stochastic inflow gives rise to higher amplitude cyclic stresses. Due to coupling of aerodynamic and structural nonlinearities, very high cyclic stresses are produced and their estimated damage values are much higher as compared to other two cases.

5 Conclusions

Response analysis of a coupled non-smooth nonlinear aeroelastic system under stochastic inflow is carried out in this chapter. Recently, another study on the effects of the coupling in aerodynamic and structural nonlinearities was conducted by Bethi et al. [3]. However, the study was largely focused on dynamical changes in pitch and plunge responses due to coupling, but its effect on structural safety was not discussed. Another demarcation from [3] is the non-smooth modelling of structure in the current study.

Dynamic stall-dominated aerodynamics is modelled using LB model, and structural non-smoothness attributing to freeplay nonlinearity is modelled by piece-wise linear stiffness in the pitch degree of freedom. For linear structure under stochastic inflow, it is seen that the onset of stall flutter is presaged by NII. However, NII is not present when the structure is nonlinear. Due to coupling of fluctuating flow and aerodynamic and structural nonlinearities, large-amplitude random LCOs are observed at flutter onset. Pitch–pitching moment hysteresis curve shows that high-negative pitching moment is present at large pitch angles due to flow fluctuation. At higher velocities, almost 90% of flow is separated, and consequently, a large amount of vortex are shed giving rise to very high-negative pitching moments. To analyse the qualitative changes in the response dynamics, stochastic bifurcation analysis has been carried out. Topological changes in j-pdf of pitch–pitch rate are observed as the mean speed is increased marking the presence of P-bifurcations for linear as well as nonlinear structures. Next, we have estimated the cyclic stresses developed in the structure in pre- and post-flutter regime and have calculated the fatigue damage. The fatigue damage analysis shows very high damage values due to the coupling of structural and aerodynamic nonlinearities in the presence of fluctuating inflow that demands a more detailed and in-depth analysis.

Acknowledgments The authors acknowledge the funding received from SERB—start-up research grant (SRG-2019- 000077) from Government of India towards this research.

References

1. G. Dimitriadis, *Introduction to Nonlinear Aeroelasticity* (Wiley, London, 2017)
2. Y.C. Fung, *An Introduction to the Theory of Aeroelasticity* (Courier Dover Publications, Mineola, 2008)
3. R.V. Bethi, S.V. Gali, J. Venkatramani, Response analysis of a pitch–plunge airfoil with structural and aerodynamic nonlinearities subjected to randomly fluctuating flows. *J. Fluids Struct.* **92**, 102820 (2020)
4. L. Liping, Y.S. Wong, and B.H.K. Lee, Non-linear aeroelastic analysis using the point transformation method, part 1: freeplay model. *J. Sound Vib.* **253**, 447–469 (2002)
5. R. Vasconcellos, A. Abdelkefi, F.D. Marques, M.R. Hajj, Representation and analysis of control surface freeplay nonlinearity. *J. Fluids Struct.* **31**, 79–91 (2012)
6. J.G. Leishman, T.S. Beddoes, A Semi-Empirical model for dynamic stall. *J. Am. Helicopter Soc.* **34**, 3–17 (1989)
7. J. Venkatramani, S. Sarkar, S. Gupta, Intermittency in pitch–plunge aeroelastic systems explained through stochastic bifurcations. *Nonlinear Dyn.* **92**, 1225–1241 (2018)
8. H. Devathi, S. Sarkar, Study of a stall induced dynamical system under gust using the probability density evolution technique. *Comput. Struct.* **162**, 38–47 (2016)
9. J. Schijve, Fatigue damage in aircraft structures, not wanted, but tolerated? *Int. J. Fatigue* **31**, 998–1011 (2009)
10. S. Venkatesh, S. Sarkar, I. Rychlik, Uncertainties in blade flutter damage prediction under random gust. *Probab. Eng. Mech.* **36**, 45–55 (2014)
11. N.E. Dowling, *Fatigue Failure Predictions for Complicated Stress-Strain Histories* (Illinois Univ at Urbana Dept of Theoretical and Applied Mechanics, 1971)
12. P.A. Brodtkorb, P. Johannesson, G. Lindgren, I. Rychlik, J. Ryden, E. Sjö, WAFO-a Matlab toolbox for analysis of random waves and loads, in *Proc. 10'th Int. Offshore and Polar Eng. Conf., ISOPE*, Seattle (2000), pp. 343–350

Stability Analysis for a Class of Non-Stationary Impulsive Switched Systems



Alexey Platonov

1 Introduction

The theory of switched and impulsive systems has been actively developed over the past decades. Such systems have many important practical applications (see, for instance, [1–5]). Switching usually involves changing the structure of the considered system while maintaining the continuity of its solutions. Impulsive effects lead to an instantaneous jump of the solutions. Switching and impulsive effects can be caused by external influences. They can also be a part of a control design. One of the most important problems associated with impulsive switched systems is the stability problem. The combination of the direct Lyapunov method with the theory of differential inequalities is the basis for most studies on the stability of hybrid systems. However, most of the studies involved only linear differential inequalities for Lyapunov functions, which were used to establish conditions for exponential stability. Meanwhile, many practical processes can be modeled by systems with essentially nonlinear dynamic behaviors, and exponential stability may not be inherent to such systems. The presence of non-stationary parameters in the considered system can lead to fundamentally new effects in comparison with autonomous systems. Continuous changes of parameters in the impulsive switched system are superimposed on discrete changes of operating modes and impulse actions, and, as a result, many characteristics, for example, the value of dwell time, can get a non-stationary (changeable) character. It is worth noting that systems with discontinuous non-stationary coefficients are quite typical for many practical processes. Such systems can also be considered as switched systems with, generally, infinite numbers of operating modes. Often, the behavior of non-

A. Platonov (✉)
Saint Petersburg State University, St. Petersburg, Russia
e-mail: a.platonov@spbu.ru

stationary parameters changes significantly, and as a result, different estimates for used Lyapunov functions are constructed at different time intervals. In addition, Lyapunov functions also usually depend on the system parameters. Therefore, the discontinuity of these parameters leads to the need to use discontinuous (multiple) Lyapunov functions. As a rule, researchers try to limit non-stationary parameters by some constants in order to deal with autonomous estimates. However, this approach does not work if the coefficients change their sign, are unbounded, or, on the contrary, tend to zero. The problem also arises of evaluating certain non-stationary expressions to obtain the required differential inequalities for Lyapunov functions.

In this chapter, we assume that a multiple Lyapunov function satisfying some non-stationary differential inequality with hybrid degrees is constructed. The change of degrees in the differential inequality can be caused either by a change of operating modes or by a change in the behavior of non-stationary coefficients in the considered system. We use both linear and nonlinear differential inequalities, i.e., we suppose that the system can describe both linear and nonlinear dynamics at different time intervals. The main purpose of this chapter is to find asymptotic stability conditions for solutions of the investigated impulsive switched system. Also, we consider some special classes of systems for which the obtained results are applicable. So, the stability problem for non-stationary complex system is studied. We assume that among the interacting subsystems there are both linear and nonlinear. Also, nonlinear mechanical system under the influence of non-stationary switched dissipative and potential forces is considered.

This chapter is a development of the results obtained in [6–8]. The following notations will be used throughout this chapter: R^n is the Euclidean space of dimension n , and $\|\cdot\|$ is the Euclidean norm of a vector.

2 Statement of the Problem

Consider the switched system

$$\dot{\mathbf{x}} = \mathbf{f}_\sigma(t, \mathbf{x}). \quad (1)$$

Here, $t \geq 0$, $\mathbf{x} \in R^n$ is the state vector; $\sigma = \sigma(t) \in Q$ is a piecewise constant function defining switching law; Q is a finite or countable set of possible values of operating modes of the system.

Let $\tilde{\tau}_l$, $l = 1, 2, \dots$, be the switching times, $0 < \tilde{\tau}_1 < \tilde{\tau}_2 < \dots$, and $\tilde{\tau}_0 = 0$. Assume that the function $\sigma(t)$ is right-continuous ($\sigma(t) = \sigma(\tilde{\tau}_l)$ for $t \in [\tilde{\tau}_l, \tilde{\tau}_{l+1})$, $l = 0, 1, \dots$).

Suppose that the sequence $\hat{\tau}_j$, $j = 1, 2, \dots$, where $0 < \hat{\tau}_1 < \hat{\tau}_2 < \dots$, defines moments of impulse action on the considered system, and

$$\mathbf{x}(\hat{\tau}_j^+) = \mathbf{g}_{\hat{\tau}_j}(\mathbf{x}(\hat{\tau}_j^-)), \quad j = 1, 2, \dots \quad (2)$$

Here, $\mathbf{x}(\hat{\tau}_j^+)$, $\mathbf{x}(\hat{\tau}_j^-)$ are the values of the right-hand and left-hand limits at the point $\hat{\tau}_j$ for a solution of system (1), $j = 1, 2, \dots$. Next, we consider solutions of hybrid system (1), (2) as right-continuous functions ($\mathbf{x}(\hat{\tau}_j) = \mathbf{x}(\hat{\tau}_j^+)$, $j = 1, 2, \dots$).

Without loss of generality, we consider the only case where the interval $(0, +\infty)$ contains the infinite number of switching and impulsive instants. Also, we exclude Zeno behavior for the sequences $\{\tilde{\tau}_l\}_{l=0,1,\dots}$ and $\{\hat{\tau}_j\}_{j=1,2,\dots}$.

Let $\mathbf{f}_{\sigma(t)}(t, \mathbf{0}) = \mathbf{0}$ for $t \geq 0$, and $\mathbf{g}_{\hat{\tau}_j}(\mathbf{0}) = \mathbf{0}$ for $j = 1, 2, \dots$. So, the impulsive switched system (1), (2) has the trivial solution $\mathbf{x} \equiv \mathbf{0}$. We will look for conditions under which this solution is asymptotically stable.

Combine the sequences $\{\tilde{\tau}_l\}_{l=0,1,\dots}$ and $\{\hat{\tau}_j\}_{j=1,2,\dots}$ into one new sequence $\{\tau_i\}_{i=0,1,\dots}$, $0 = \tau_0 < \tau_1 < \tau_2 < \dots$. Thus, for any i , one can choose l or/and j such that $\tau_i = \tilde{\tau}_l$ or/and $\tau_i = \hat{\tau}_j$, i.e., the sequence $\{\tau_i\}_{i=0,1,\dots}$ is the common set of switching and impulsive instants. One can suppose that $\sigma(\tau_p^-) = \sigma(\tau_p^+)$, if $\tau_p \notin \{\tilde{\tau}_l\}_{l=0,1,\dots}$, and $\mathbf{x}(\tau_p^+) = \mathbf{g}_{\tau_p}(\mathbf{x}(\tau_p^-)) = \mathbf{x}(\tau_p^-)$, if $\tau_p \notin \{\hat{\tau}_j\}_{j=1,2,\dots}$; $p = 1, 2, \dots$. Assume that function $\mathbf{f}_{\sigma(t)}(t, \mathbf{x})$ is continuous for $t \in [\tau_i, \tau_{i+1})$, $\mathbf{x} \in R^n$; $i = 0, 1, \dots$.

As it was already noted in Introduction, the main approach to analysis of impulsive switched systems is a combination of direct Lyapunov method with the theory of differential inequalities. One can choose a single or multiple Lyapunov function for the considered system and construct some differential inequality for it. Then under certain assumptions, it is possible to find sufficient stability conditions. However, the problem becomes more complicated if the system's specifics imply the use of nonlinear and non-stationary differential inequalities.

Let some multiple Lyapunov function $V_{\sigma(t)}(t, \mathbf{x})$ be constructed for system (1), (2). In this chapter, we suppose that function $V_{\sigma(t)}(t, \mathbf{x})$ is defined for $t \geq 0$, $\mathbf{x} \in R^n$, continuously differentiable for $t \in (\tau_i, \tau_{i+1})$, $\mathbf{x} \in R^n$ ($i = 0, 1, \dots$), and the following estimates:

$$V_{\sigma(\tau_p)}(\tau_p, \mathbf{x}) \leq \omega_p V_{\sigma(\tau_{p-1})}(\tau_p, \mathbf{x}), \quad p = 1, 2, \dots, \tag{3}$$

$$V_{\sigma(\tau_p)}(\tau_p, \mathbf{g}_{\tau_p}(\mathbf{x})) \leq \beta_p V_{\sigma(\tau_p)}(\tau_p, \mathbf{x}), \quad p = 1, 2, \dots, \tag{4}$$

$$\lambda_1(t) a_1(\|\mathbf{x}\|) \leq V_{\sigma(t)}(t, \mathbf{x}) \leq \lambda_2(t) a_2(\|\mathbf{x}\|) \quad \text{for } t \geq 0, \tag{5}$$

$$\dot{V}_{\sigma(t)}|_{(1)} \leq q(t) V_{\sigma(t)}^{1+\theta_i}(t, \mathbf{x}) \quad \text{for } t \in (\tau_i, \tau_{i+1}), \quad i = 0, 1, \dots, \tag{6}$$

are valid, if $\|\mathbf{x}\| < H$ ($0 < H \leq +\infty$). Here, $\omega_p > 0$, $\beta_p > 0$, $\theta_i \geq 0$, $p = 1, 2, \dots$, $i = 0, 1, \dots$; $\lambda_1(t)$, $\lambda_2(t)$, $q(t)$ are piecewise continuous functions, and $\lambda_1(t)$, $\lambda_2(t)$ are positive for $t \geq 0$; $a_1(z)$ and $a_2(z)$ are continuous, positive, and strictly increasing functions for $z > 0$, $a_1(0) = a_2(0) = 0$. Additionally, we assume that $q(t) \leq 0$ for $t \in (\tau_i, \tau_{i+1})$, if $\theta_i > 0$; $i = 0, 1, \dots$. If $\theta_i = 0$, then we do not impose restrictions on the sign of the function $q(t)$ on the interval (τ_i, τ_{i+1}) , $i = 0, 1, \dots$

It should be noted that one can set $\omega_p = 1$, if $\tau_p \notin \{\tilde{\tau}_l\}_{l=0,1,\dots}$, and $\beta_p = 1$, if $\tau_p \notin \{\hat{\tau}_j\}_{j=1,2,\dots}$; $p = 1, 2, \dots$

3 Stability Conditions

For $t \in [\tau_i, \tau_{i+1})$, let us denote

$$\bar{q}(t) = \begin{cases} q(t), & \text{if } \theta_i = 0, \\ 0, & \text{if } \theta_i > 0, \end{cases} \quad \hat{q}(t) = \begin{cases} 0, & \text{if } \theta_i = 0, \\ q(t), & \text{if } \theta_i > 0, \end{cases}$$

$$\bar{J}(a, b) = \int_a^b \bar{q}(t) dt, \quad \hat{J}(a, b) = \int_a^b \hat{q}(t) dt, \quad i = 0, 1, \dots$$

Here, a, b are positive constants.

Choose some constant $\xi > 0$. Assume

$$\rho_i = \begin{cases} 1, & \text{if } \theta_i = 0, \\ \xi/\theta_i, & \text{if } \theta_i > 0, \end{cases}$$

$$\gamma_i = \min\{1; 2^{\rho_i-1}\}, \quad d_p = (\beta_p \omega_p)^{-\xi}, \quad i = 0, 1, \dots, \quad p = 1, 2, \dots$$

Set t_0 and $t, t > t_0 \geq 0$. Find nonnegative integers m and k such that $t_0 \in [\tau_m, \tau_{m+1})$ and $t \in [\tau_{m+k}, \tau_{m+k+1})$. So, we consider $m = m(t_0)$ and $k = k(t_0, t)$ as piecewise constant functions. In particular, the value of k determines the number of switching or/and impulsive instants on the interval $(t_0, t]$.

Construct auxiliary functions $\psi(t_0, t)$ and $\varphi(t_0, t)$ by the following formulas:

$$\psi(t_0, t) = \gamma_m e^{-\xi \bar{J}(t_0, t)} \left(-\theta_m \hat{J}(t_0, t)\right)^{\rho_m}, \quad \varphi(t_0, t) = \gamma_m,$$

if $k = 0$, and

$$\psi(t_0, t) = (\gamma_m \dots \gamma_{m+k}) (d_{m+1} \dots d_{m+k}) e^{-\xi \bar{J}(t_0, t)} \left(-\theta_m \hat{J}(t_0, \tau_{m+1})\right)^{\rho_m}$$

$$+ \sum_{s=1}^{k-1} (\gamma_{m+s} \dots \gamma_{m+k}) (d_{m+s+1} \dots d_{m+k}) e^{-\xi \bar{J}(\tau_{m+s}, t)} \left(-\theta_{m+s} \hat{J}(\tau_{m+s}, \tau_{m+s+1})\right)^{\rho_{m+s}}$$

$$+ \gamma_{m+k} e^{-\xi \bar{J}(\tau_{m+k}, t)} \left(-\theta_{m+k} \hat{J}(\tau_{m+k}, t)\right)^{\rho_{m+k}},$$

$$\varphi(t_0, t) = (\gamma_m \dots \gamma_{m+k}) (d_{m+1} \dots d_{m+k}),$$

if $k > 0$. Here, we suppose that $\sum_{s=1}^{k-1} (\cdot) = 0$ for $k = 1$.

Choose any $\mathbf{x}_0 \in R^n, \|\mathbf{x}_0\| < H$. Consider the solution $\mathbf{x}(t)$ of system (1), (2) starting at time moment t_0 from the point \mathbf{x}_0 . Integrating differential inequality (6), it is easy to show that if the solution $\mathbf{x}(t)$ remains in the region $\|\mathbf{x}\| < H$ on the interval $[t_0, t]$, then the estimate

$$V_{\sigma(t)}^{-\xi}(t, \mathbf{x}(t)) \geq \varphi(t_0, t)e^{-\xi \bar{J}(t_0, t)} V_{\sigma(t_0)}^{-\xi}(t_0, \mathbf{x}_0) + \psi(t_0, t) \tag{7}$$

holds.

Using estimates (5) and (7), we get the following theorem.

Theorem 1 *Let a multiple Lyapunov function $V_{\sigma(t)}(t, \mathbf{x})$ satisfying estimates (3)–(6) be constructed. Then, the zero solution of system (1), (2) is asymptotically stable, if at least one of the following conditions:*

- (i) $\varphi(t_0, t) e^{-\xi \bar{J}(t_0, t)} \lambda_1^{\xi}(t) \rightarrow +\infty$ as $t \rightarrow +\infty$
- (ii) $\lambda_1^{\xi}(t) \psi(t_0, t) \rightarrow +\infty$ as $t \rightarrow +\infty$

is valid for any value of $t_0 \geq 0$.

Note that if condition (i) or (ii) of Theorem 1 is valid for some value of t_0 , then it is also valid for any $t_0 \geq 0$. Therefore, it is sufficient to check conditions of Theorem 1 for $t_0 = 0$. Also, it should be noted that if $H = +\infty$, then under the fulfillment of conditions of Theorem 1, the zero solution of system (1), (2) is globally asymptotically stable.

Remark 1 Assume that the set of values of $\theta_i, i = 0, 1, \dots$, is bounded at above. For instance, such situation takes place, if the set of possible operating modes for system (1) is finite. In this case, one can choose $\xi = \max_{i=0,1,\dots} \theta_i$. Then, one gets $\gamma_i = 1, i = 0, 1, \dots$, and formulas for functions $\varphi(t_0, t), \psi(t_0, t)$ will take more simple form.

In the following sections, we consider some examples of classes of systems for which estimates of the form (3)–(6) occur naturally.

4 Stability Analysis for Some Non-Stationary Complex System

Let system (1) be of the form

$$\begin{cases} \dot{\mathbf{x}}_1 = \mathbf{P}_{\sigma}(t)\mathbf{x}_1 + \mathbf{G}_{\sigma}(t, \mathbf{x}), \\ \dot{\mathbf{x}}_2 = \mathbf{F}_{\sigma}(t, \mathbf{x}_2) + \mathbf{D}_{\sigma}(t, \mathbf{x}). \end{cases} \tag{8}$$

Here, $\mathbf{x} = (\mathbf{x}_1^T, \mathbf{x}_2^T)^T$, $\mathbf{x}_1 \in R^{n_1}$, $\mathbf{x}_2 \in R^{n_2}$, $n_1 + n_2 = n$; $\sigma = \sigma(t) = [0, +\infty) \rightarrow Q = \{1, \dots, N\}$ (i.e., now we consider the finite number of operating modes for the system). Let matrices $\mathbf{P}_s(t)$ and functions $\mathbf{F}_s(t, \mathbf{x}_2)$, $\mathbf{G}_s(t, \mathbf{x})$, $\mathbf{D}_s(t, \mathbf{x})$ be continuous for $t \geq 0$, $\mathbf{x} \in R^n$; $s = 1, \dots, N$.

System (8) can be considered as a complex system describing the interaction between two subsystems

$$\dot{\mathbf{x}}_1 = \mathbf{P}_\sigma(t)\mathbf{x}_1 \quad (9)$$

and

$$\dot{\mathbf{x}}_2 = \mathbf{F}_\sigma(t, \mathbf{x}_2). \quad (10)$$

Assume that functions $\mathbf{F}_s(t, \mathbf{x}_2)$ are homogeneous of the order $\mu > 1$ with respect to variable \mathbf{x}_2 , $s = 1, \dots, N$.

Functions $\mathbf{G}_\sigma(t, \mathbf{x})$ and $\mathbf{D}_\sigma(t, \mathbf{x})$ set connections between subsystems (9), (10). Let the inequalities

$$\|\mathbf{G}_s(t, \mathbf{x})\| \leq u_s(t)\|\mathbf{x}_1\|^{\eta_1}\|\mathbf{x}_2\|^{\eta_2}, \quad \|\mathbf{D}_s(t, \mathbf{x})\| \leq r_s(t)\|\mathbf{x}_1\|^{v_1}\|\mathbf{x}_2\|^{v_2}$$

hold for $t \geq 0$, $\|\mathbf{x}\| < H$, ($0 < H \leq +\infty$), where $\eta_1 \geq 0$, $\eta_2 > 0$, $v_1 > 0$, and $v_2 \geq 0$ are constants, and $u_s(t)$ and $r_s(t)$ are nonnegative and continuous for $t \geq 0$ functions, $s = 1, \dots, N$.

System (8) has the zero solution. Let us investigate the stability problem for this solution.

We will search for Lyapunov functions for subsystems (9), (10) as a quadratic form $v_1(t, \mathbf{x}_1) = \mathbf{x}_1^T \mathbf{A}(t)\mathbf{x}_1$, where symmetric matrix $\mathbf{A}(t)$ is continuously differentiable for $t \geq 0$ and its eigenvalues are positive for any $t \geq 0$, and a continuously differentiable for $\mathbf{x}_2 \in R^{n_2}$ positive definite homogeneous function $v_2(\mathbf{x}_2)$ of order $\kappa > 1$, correspondingly. Using the properties of homogeneous functions [9], we have for $t \geq 0$, $\mathbf{x} \in R^n$ the estimates

$$g_1(t)\|\mathbf{x}_1\|^2 \leq v_1(t, \mathbf{x}_1) \leq g_2(t)\|\mathbf{x}_1\|^2, \quad b_1\|\mathbf{x}_2\|^\kappa \leq v_2(\mathbf{x}_2) \leq b_2\|\mathbf{x}_2\|^\kappa,$$

$$\left\| \frac{\partial v_1(t, \mathbf{x}_1)}{\partial \mathbf{x}_1} \right\| \leq g_3(t)\|\mathbf{x}_1\|, \quad \left\| \frac{\partial v_2(\mathbf{x}_2)}{\partial \mathbf{x}_2} \right\| \leq b_3\|\mathbf{x}_2\|^{\kappa-1},$$

$$\mathbf{x}_1^T (\dot{\mathbf{A}}(t) + \mathbf{P}_s(t)\mathbf{A}(t) + \mathbf{A}(t)\mathbf{P}_s(t)) \mathbf{x}_1 \leq g_{4s}(t)\|\mathbf{x}_1\|^2, \quad s = 1, \dots, N,$$

$$\left(\frac{\partial v_2(\mathbf{x}_2)}{\partial \mathbf{x}_2} \right)^T \mathbf{F}_s(t, \mathbf{x}_2) \leq b_{4s}(t)\|\mathbf{x}_2\|^{\kappa-1+\mu}, \quad s = 1, \dots, N.$$

Here, b_1, b_2, b_3 are positive constants; functions $g_1(t), g_2(t), g_3(t)$ are positive and continuous for $t \geq 0$; $g_{4s}(t)$ and $b_{4s}(t)$ are some continuous for $t \geq 0$ functions, $s = 1, \dots, N$.

Let us assume that there is at least one value $\bar{s} \in Q$ such that $g_{4\bar{s}}(t) < 0$ and $b_{4\bar{s}}(t) < 0$ for $t \geq 0$. It should be noted that there are no general methods of constructing appropriate Lyapunov functions for non-stationary linear and homogeneous systems. But in a wide class of special cases, this can be done (see, for instance, [9–12]).

We construct a Lyapunov function for complex system (8) in the form

$$V(t, \mathbf{x}) = v_1^\zeta(t, \mathbf{x}_1) + v_2(\mathbf{x}_2),$$

where $\zeta = \text{const} \geq 1$. Then for $t \geq 0, \|\mathbf{x}\| < H$, we have

$$\dot{V}|_{(8), \sigma=s} \leq W_s(t, \mathbf{x}).$$

Here,

$$W_s(t, \mathbf{x}) = c_{1s}(t)\|\mathbf{x}_1\|^{2\zeta} + c_{2s}(t)\|\mathbf{x}_2\|^{\kappa-1+\mu} + c_{3s}(t)\|\mathbf{x}_1\|^{2\zeta-1+\eta_1}\|\mathbf{x}_2\|^{\eta_2} + c_{4s}(t)\|\mathbf{x}_1\|^{v_1}\|\mathbf{x}_2\|^{\kappa-1+v_2},$$

and

$$c_{1s}(t) = \zeta g_2^{\zeta-1}(t)g_{4s}(t), \quad c_{2s}(t) = b_{4s}(t), \\ c_{3s}(t) = \zeta g_2^{\zeta-1}(t)g_3(t)u_s(t), \quad c_{4s}(t) = b_{3r_s}(t).$$

Note that $c_{1\bar{s}}(t) < 0, c_{2\bar{s}}(t) < 0$ for $t \geq 0$.

Lemma 1 *Let the following conditions be fulfilled:*

(i) *The inequalities*

$$\frac{2\zeta - 1 + \eta_1}{2\zeta} + \frac{\eta_2}{\kappa - 1 + \mu} > 1, \quad \frac{v_1}{2\zeta} + \frac{\kappa - 1 + v_2}{\kappa - 1 + \mu} > 1 \tag{11}$$

are valid.

(ii) *There are constants ε_1 and ε_2 satisfying the inequalities*

$$\max\{0; \eta_2 - \kappa + 1 - \mu\} \leq \varepsilon_1 \leq \min\left\{\eta_2; \eta_2 - \frac{(1-\eta_1)(\kappa-1+\mu)}{2\zeta}\right\}, \\ \max\{0; v_1 - 2\zeta\} \leq \varepsilon_2 \leq \min\left\{v_1; v_1 - \frac{2\zeta(\mu-v_2)}{\kappa-1+\mu}\right\}, \tag{12}$$

such that functions

$$\frac{c_{3\bar{s}}(t)}{|c_{1\bar{s}}(t)|} \left(\frac{c_{1\bar{s}}(t)}{c_{2\bar{s}}(t)} \right)^{\frac{\eta_2 - \varepsilon_1}{\kappa - 1 + \mu}}, \quad \frac{c_{4\bar{s}}(t)}{|c_{2\bar{s}}(t)|} \left(\frac{c_{2\bar{s}}(t)}{c_{1\bar{s}}(t)} \right)^{\frac{\nu_1 - \varepsilon_2}{2\zeta}}$$

are bounded for $t \geq 0$.

Then for any $M \in (0, 1)$, one can choose $H_1 \in (0, H]$ so that the estimate

$$W_{\bar{s}}(t, \mathbf{x}) \leq M \left(c_{1\bar{s}}(t) \|\mathbf{x}_1\|^{2\zeta} + c_{2\bar{s}}(t) \|\mathbf{x}_2\|^{\kappa - 1 + \mu} \right)$$

holds for $t \geq 0, \|\mathbf{x}\| < H_1$.

Since parameters ζ and κ can be chosen arbitrarily, then to fulfill inequalities (11) it is sufficient to require that the inequality

$$\max \{0; (1 - \eta_1)/\eta_2\} \max \{0; (\mu - \nu_2)/\nu_1\} < 1 \tag{13}$$

holds. Under (13), inequalities (12) are also consistent.

If function $c_{1\bar{s}}(t)/c_{2\bar{s}}(t)$ is bounded at above for $t \geq 0$, then it is sufficient to check the condition ii) of Lemma 1 for $\varepsilon_1 = \max\{0; \eta_2 - \kappa + 1 - \mu\}$ and $\varepsilon_2 = \min\{\nu_1; \nu_1 - (\mu - \nu_2)(2\zeta)/(\kappa - 1 + \mu)\}$. If $c_{1\bar{s}}(t)/c_{2\bar{s}}(t) \geq m = \text{const} > 0$ for $t \geq 0$, then it is sufficient to check the condition ii) of Lemma 1 for $\varepsilon_1 = \min\{\eta_2; \eta_2 - (1 - \eta_1)(\kappa - 1 + \mu)/(2\zeta)\}$ and $\varepsilon_2 = \max\{0; \nu_1 - 2\zeta\}$.

Next, we assume that conditions of Lemma 1 are fulfilled. Then for $t \geq 0, \|\mathbf{x}\| < H_2$ ($0 < H_2 \leq H_1$), we have the estimates

$$\lambda_1(t) \left(\|\mathbf{x}_1\|^{2\zeta} + \|\mathbf{x}_2\|^\kappa \right) \leq V(t, \mathbf{x}) \leq \lambda_2(t) \left(\|\mathbf{x}_1\|^{2\zeta} + \|\mathbf{x}_2\|^\kappa \right),$$

$$\dot{V}|_{(8), \sigma=\bar{s}} \leq q_1(t) V^{1+\theta}(t, \mathbf{x}), \quad \dot{V}|_{(8), \sigma \neq \bar{s}} \leq q_2(t) V(t, \mathbf{x}).$$

Here, $\theta = (\mu - 1)/\kappa$,

$$\lambda_1(t) = \min\{g_1^\zeta(t); b_1\}, \quad \lambda_2(t) = \max\{g_2^\zeta(t); b_2\},$$

$$q_1(t) = M_1 \max\{c_{1\bar{s}}(t)/g_1^\zeta(t); c_{2\bar{s}}(t)\},$$

$$q_2(t) = M_2 \max\{c_{1s}(t)/g_1^\zeta(t); c_{2s}(t); c_{3s}(t)/g_1^{\zeta+(\eta_1-1)/2}(t); c_{4s}(t)/g_1^{\nu_1/2}(t)\},$$

where M_1 and M_2 are some positive constants.

Since we use a single Lyapunov function $V_{\sigma(t)}(t, \mathbf{x}) = V(t, \mathbf{x})$ for $t \geq 0$, then, in (3), we have $\omega_p = 1, p = 1, 2, \dots$

Let impulse action (2) be of the form

$$\mathbf{x}_1(\hat{\tau}_j^+) = \mathbf{K}_{\hat{\tau}_j}^{(1)} \mathbf{x}_1(\hat{\tau}_j^-), \quad \mathbf{x}_2(\hat{\tau}_j^+) = \mathbf{K}_{\hat{\tau}_j}^{(2)} \mathbf{x}_2(\hat{\tau}_j^-), \quad j = 1, 2, \dots,$$

where $\mathbf{K}_{\hat{\tau}_j}^{(1)}, \mathbf{K}_{\hat{\tau}_j}^{(2)}, j = 1, 2, \dots$, are the constant matrices. Then, in (4) for $\tau_p = \hat{\tau}_j$, we have

$$\beta_p = \frac{\lambda_2(\hat{\tau}_j)}{\lambda_1(\hat{\tau}_j)} \max\{\|\mathbf{K}_{\hat{\tau}_j}^{(1)}\|^{2\zeta}; \|\mathbf{K}_{\hat{\tau}_j}^{(2)}\|^\kappa\}, \quad p, j = 1, 2, \dots$$

Now, one can apply condition ii) of Theorem 1.

5 Stability Analysis for Some Classes of Non-Stationary Mechanical Systems

Let us consider the mechanical system

$$\ddot{\mathbf{q}} + a(t) \frac{\partial F_\sigma(\dot{\mathbf{q}})}{\partial \dot{\mathbf{q}}} + b(t) \frac{\partial \Pi_\sigma(\mathbf{q})}{\partial \mathbf{q}} = \mathbf{0}. \tag{14}$$

Here, $\mathbf{q} \in R^n$ and $\dot{\mathbf{q}} \in R^n$ are the vectors of generalized coordinates and generalized velocities, respectively; $\sigma = \sigma(t) : [0, +\infty) \rightarrow \{1, \dots, N\}$; dissipative functions $F_s(\dot{\mathbf{q}})$ are continuously differentiable for $\dot{\mathbf{q}} \in R^n$, positive definite, and homogeneous of degree $\nu_s + 1, \nu_s > 1$; potential functions $\Pi_s(\mathbf{q})$ are positive definite quadratic forms; $s = 1, \dots, N$; non-stationary coefficients $a(t), b(t)$ are positive and piecewise continuous for $t \geq 0$. Without loss of generality, one can suppose that the break points of functions $a(t)$ and $b(t)$ coincide with the switching instants $\tilde{\tau}_l, l = 0, 1, \dots$. Additionally, we assume that function $b(t)$ is continuously differentiable and monotonously decreasing on intervals $(\tilde{\tau}_l, \tilde{\tau}_{l+1}), l = 0, 1, \dots$

System (14) has the equilibrium position $\mathbf{q} = \dot{\mathbf{q}} = \mathbf{0}$.

Construct a Lyapunov function in the form:

$$V_\sigma(t, \mathbf{q}, \dot{\mathbf{q}}) = b(t)\Pi_\sigma(\mathbf{q}) + \frac{1}{2}\dot{\mathbf{q}}^T \dot{\mathbf{q}} + \gamma c(t)\|\mathbf{q}\|^{\nu_\sigma-1} \mathbf{q}^T \dot{\mathbf{q}}.$$

Here, $\gamma = \text{const} > 0, c(t)$ is a positive and continuously differentiable for $t \in (\tilde{\tau}_l, \tilde{\tau}_{l+1}), l = 0, 1, \dots$, function. Then, we have

$$\begin{aligned} \dot{V}_\sigma|_{(14)} = & -2\gamma c(t)b(t)\|\mathbf{q}\|^{\nu_\sigma-1} \Pi_\sigma(\mathbf{q}) - a(t)(\nu_\sigma + 1)F_\sigma(\dot{\mathbf{q}}) + \dot{b}(t)\Pi_\sigma(\mathbf{q}) \\ & + \gamma c(t)\dot{\mathbf{q}}^T \frac{\partial (\|\mathbf{q}\|^{\nu_\sigma-1} \mathbf{q})}{\partial \mathbf{q}} \dot{\mathbf{q}} - \gamma c(t)a(t)\|\mathbf{q}\|^{\nu_\sigma-1} \mathbf{q}^T \frac{\partial F_\sigma(\dot{\mathbf{q}})}{\partial \dot{\mathbf{q}}} + \gamma \dot{c}(t)\|\mathbf{q}\|^{\nu_\sigma-1} \mathbf{q}^T \dot{\mathbf{q}} \end{aligned}$$

for $t \in (\tilde{\tau}_l, \tilde{\tau}_{l+1}), l = 0, 1, \dots, \mathbf{q}, \dot{\mathbf{q}} \in R^n$.

As in Lemma 1, it is easy to show that if function $c(t)$ can be chosen so that functions

$$\begin{aligned}
 &c(t) \min \{b^{-1/2}(t); b^{-\min\{\nu_\sigma; 2\}/2}(t)\}, \\
 &\quad c(t)b^{-(\nu_\sigma-1)/2}(t)a^{-1}(t), \\
 &c(t) \min \{(a(t)/b(t))^{1/\nu_\sigma}; (a(t)/b(t))^{\nu_\sigma}\}, \\
 &|\dot{c}(t)|c^{-\nu_\sigma/(\nu_\sigma+1)}(t)b^{-\nu_\sigma/(\nu_\sigma+1)}(t)a^{-1/(\nu_\sigma+1)}(t)
 \end{aligned} \tag{15}$$

are bounded for $t \in (\tilde{\tau}_l, \tilde{\tau}_{l+1})$ uniformly with respect to $l = 0, 1, \dots$, then estimates

$$M_1 \left(b(t)\|\mathbf{q}\|^2 + \|\dot{\mathbf{q}}\|^2 \right) \leq V_\sigma(t, \mathbf{q}, \dot{\mathbf{q}}) \leq M_2 \left(b(t)\|\mathbf{q}\|^2 + \|\dot{\mathbf{q}}\|^2 \right), \tag{16}$$

$$\dot{V}_\sigma|_{(14)} \leq -M_3 \left(\gamma c(t)b(t)\|\mathbf{q}\|^{\nu_\sigma+1} + a(t)\|\dot{\mathbf{q}}\|^{\nu_\sigma+1} \right) \tag{17}$$

hold for $t \in (\tilde{\tau}_l, \tilde{\tau}_{l+1})$, $l = 0, 1, \dots$, $\|(\mathbf{q}^T, \dot{\mathbf{q}}^T)^T\| < H$, if constant γ is sufficiently small. Here, M_1, M_2, M_3, H are some positive constants.

To obtain more concrete conditions of stability, one can look for the function $c(t)$, for instance, in the form $c(t) = b^{\kappa_\sigma}(t)$, where $\kappa_1, \dots, \kappa_N$ are constants. Assume that $|\dot{b}(t)| \leq Mb^{r_\sigma}(t)$ for $t \in (\tilde{\tau}_l, \tilde{\tau}_{l+1})$, $l = 0, 1, \dots$, where M, r_1, \dots, r_N are constants, $M \geq 0$.

Let functions $b(t)$ and $b(t)/a(t)$ be bounded at above for $t \geq 0$. Choose some values of $\kappa_1, \dots, \kappa_N$, satisfying the condition

$$\kappa_\sigma \geq (\nu_\sigma + 1) \max\{1/2; 2 - r_\sigma\}.$$

We obtain that, if function $b^{\kappa_\sigma-1/\nu_\sigma}(t)a^{1/\nu_\sigma}(t)$ is bounded for $t \geq 0$, then functions (15) are bounded for $t \in (\tilde{\tau}_l, \tilde{\tau}_{l+1})$ uniformly with respect to $l = 0, 1, \dots$, and estimates (16), (17) hold.

In a similar manner, the cases where functions $1/b(t)$ and $a(t)/b(t)$, or functions $b(t)$ and $a(t)/b(t)$, or functions $1/b(t)$ and $b(t)/a(t)$ are bounded at above for $t \geq 0$, can be considered.

Next, we suppose that estimates (16), (17) hold. Thus, we have

$$\lambda_1(t)\|(\mathbf{q}^T, \dot{\mathbf{q}}^T)^T\|^2 \leq V_\sigma(t, \mathbf{q}, \dot{\mathbf{q}}) \leq \lambda_2(t)\|(\mathbf{q}^T, \dot{\mathbf{q}}^T)^T\|^2, \quad \text{for } t \geq 0$$

$$\dot{V}_\sigma|_{(14)} \leq q(t)V_\sigma^{1+\theta_\sigma}(t, \mathbf{q}, \dot{\mathbf{q}}) \quad \text{for } t \in (\tilde{\tau}_l, \tilde{\tau}_{l+1}), \quad l = 0, 1, \dots,$$

if $\|(\mathbf{q}^T, \dot{\mathbf{q}}^T)^T\| < H$. Here, $\theta_\sigma = (\nu_\sigma - 1)/2$,

$$\lambda_1(t) = M_1 \min\{b(t); 1\}, \quad \lambda_2(t) = M_2 \max\{b(t); 1\},$$

$$q(t) = -M_4 \min\{\gamma c(t)b^{(1-\nu_\sigma)/2}(t); a(t)\},$$

and M_4 is some positive constant.

Constants $\omega_p, \beta_p, p = 1, 2, \dots$, for the corresponding conditions (3) and (4) can be easily evaluated with the aid of estimate (16). So, one can apply condition ii) of Theorem 1.

The proposed approach can be extended to the case where the function $b(t)$ is piecewise monotone on intervals $(\tilde{\tau}_l, \tilde{\tau}_{l+1}), l = 0, 1, \dots$. In this case, points of the change of monotonicity of the function $b(t)$ can be considered as additional switching instants. On intervals of monotonous increasing of the function $b(t)$, one can use a Lyapunov function of the form $V_\sigma(t, \mathbf{q}, \dot{\mathbf{q}})/b(t)$.

6 Conclusions

In this chapter, the influence of the combination of such factors as nonlinearity, non-stationarity, switching, and impulsive actions on the stability of solutions for a class of dynamical systems was studied. Multiple Lyapunov functions satisfying differential inequalities with hybrid degrees were used. It should be noted that the presence of non-stationary coefficients in the system can lead to a significant complication of the dynamics of solutions. To investigate the stability problem in such cases, some non-standard approaches are often used. For instance, the problem of estimating for polynomial expressions with non-stationary coefficients is actual for the constructing appropriate Lyapunov functions. The obtained results were applied to some concrete classes of hybrid systems that often occur under analyzing various real processes.

References

1. D. Liberzon, *Switching in Systems and Control* (Birkhauser, Boston, 2003)
2. V. Lakshmikantham, D. Bainov, P. Simeonov, *Theory of Impulsive Differential Equations* (World Scientific, Singapore, 1989)
3. R. Shorten, F. Wirth, O. Mason, K. Wulf, C. King, Stability criteria for switched and hybrid systems. *SIAM Rev.* **49**(4), 545–592 (2007)
4. G. Zhai, B. Hu, K. Yasuda, A.N. Michel, Disturbance attention properties of time-controlled switched systems. *J. Franklin Inst.* **338**, 765–779 (2001)
5. X. Liu, P. Stechliniski, Switching and impulsive control algorithms for nonlinear hybrid dynamical systems. *Nonlinear Anal. Hybrid Syst.* **27**(2), 307–322 (2018)
6. A.Yu. Aleksandrov, A.A. Kosov, A.V. Platonov, On the asymptotic stability of switched homogeneous systems. *Syst. Control Lett.* **61**(1), 127–133 (2012)
7. A.V. Platonov, On the problem of nonlinear stabilization of switched systems. *Circuits Syst. Signal Process.* **38**(9), 3996–4013 (2019)
8. A.V. Platonov, Stability analysis for nonstationary switched systems. *Russ. Math.* **64**(2), 56–65 (2020)
9. L. Rosier, Homogeneous Lyapunov function for homogeneous continuous vector field. *Syst. Control Lett.* **19**, 467–473 (1992)
10. A.Yu. Aleksandrov, Asymptotic stability of solutions to systems of nonstationary differential equations with homogeneous right-hand sides. *Dokl. Math.* **54**, 534–535 (1996)

11. J. Peuteman, D. Aeyels, Averaging results and the study of uniform asymptotic stability of homogeneous differential equations that are not fast time-varying. *SIAM J. Control Optim.* **37**, 997–1010 (1999)
12. L. Moreau, D. Aeyels, J. Peuteman, R. Sepulchre, A duality principle for homogeneous vector fields with applications. *Syst. Control Lett.* **47**, 37–46 (2002)

State-Dependent Switching Law for Stabilization to a Switched Time-Delay System with Two Unstable Subsystems



Yusheng Zhou and Zaihua Wang

1 Introduction

A switched system is composed of a family of subsystems with a rule governing switching between the subsystems. It has been widely used to model real-world systems, such as networked control system [1], intelligent robot system [2], spacecraft control system [3], and so on. For a practical switched system, the fault of subsystem actuator or sensor is usually inevitable and it might make the whole system unstable. In this case, fault detection and fault-tolerant control design are necessary [4, 5]. For the fault-tolerant flight control system [6], when some subsystems become unstable due to the actuator or sensor faults, the full system can be asymptotically stable by adopting an appropriate switching mechanism, thereby ensuring the safety of the flying aircraft. Roughly speaking, a switched system with fully unstable (or stable) subsystems can be either stabilized or destabilized by a proper switching rule [7]. However, the design and analysis of switching laws remain challenging due to the coupling between nonlinearity and switching mechanism, especially in the study of the switched time-delay systems with fully unstable subsystems.

Lots of methods are available in the literature for design and analysis of switched systems with unstable modes, most of the research works focused on systems with at least one stable subsystem [8]. The main idea used in studying this kind of switched systems is to activate the stable subsystems sufficiently long time to absorb the state divergence caused by unstable subsystems [9]. Meanwhile, the most frequently used

Y. Zhou

School of Mathematics and Statistics, Guizhou University, Guiyang, China

e-mail: yszhou@gzu.edu.cn

Z. Wang (✉)

State Key Lab of Mechanical Structures, Nanjing University of Aeronautics and Astronautics, Nanjing, China

e-mail: zhwang@nuaa.edu.cn

switching laws are time-dependent, based on the average dwell time [10] or the model-dependent average dwell time [11]. When all subsystems are unstable due to uncontrollable or failure controllers, maximum average dwell time switching is a good choice if each unstable subsystem has at least one characteristic root with negative real part [12]. However, if each subsystem is unstable and does not have characteristic roots with negative real parts, the method of average dwell time switching does not work. In this case, state-dependent switching laws are generally adopted to stabilize the switched systems. As done in [13], a state-dependent switching law is designed on the basis of the maximum interval function strategy as well as the technique of linear matrix inequality, but the results depending on inequality estimation might be conservative. In order to reduce the conservativeness of stability conditions, the combination of time-dependent and state-dependent switching laws can be adopted, such as in [14] where the current maximum dwell time of subsystems is calculated by means of the system state of the last switching.

In control engineering applications, time delays are usually inevitable especially when digital controllers or digital filters are used, and in many cases, time delays significantly change the dynamics behavior and control performance of switched systems [15]. The available results mainly focus on the stability and stabilization of switched linear delayed systems with stable and unstable subsystems [16]. Lyapunov–Krasovskii functional and dwell time technique are two major methods for stability of such systems [17]. Besides, a class of switched nonlinear systems with input delays were studied by the combination of Lyapunov–Krasovskii functionals, free-weighting matrices, and average dwell time technique, and input-to-state stability conditions were derived in terms of the linear matrix inequality method [18]. In [19], a family of Lyapunov–Krasovskii functionals were proposed to analyze nonlinear time-varying switched systems with time delays, and less conservative stability conditions were obtained. In addition, the stability of switched systems is in the sense of asymptotic stability, but in some cases, it takes a very long time before the system is stabilized. It is highly demanded to design proper switching laws to have less conservative results and faster decaying ratio of the solution to a steady state of the switched delay system.

In this chapter, a state-dependent switching law is designed for a class of switched delay systems with two unstable subsystems. The design is based on two approximated delay-free subsystems that are all unstable, unlike the available works that require at least one stable subsystem or subsystems having at least one characteristic root with negative real part. With the designed switching law, the original switched delay system is stabilized to the unique equilibrium or periodic solutions. The rest of this chapter is organized as follows. Section 2 is the problem statement. In Sect. 3, a method for designing the switching curves is presented. In Sect. 4, two examples are provided to illustrate how the switched delay systems with two unstable subsystems are stabilized or periodic. This chapter ends in Sect. 5 with some concluding remarks.

2 Problem Description

Let us study a switched nonlinear system with two unstable delayed subsystems

$$\begin{cases} \dot{x}_1 = f_i(x_1, x_2), \\ \dot{x}_2 = g_i(x_1, x_2, x_1(t - \tau_i)), \quad (i = 1, 2), \end{cases} \tag{1}$$

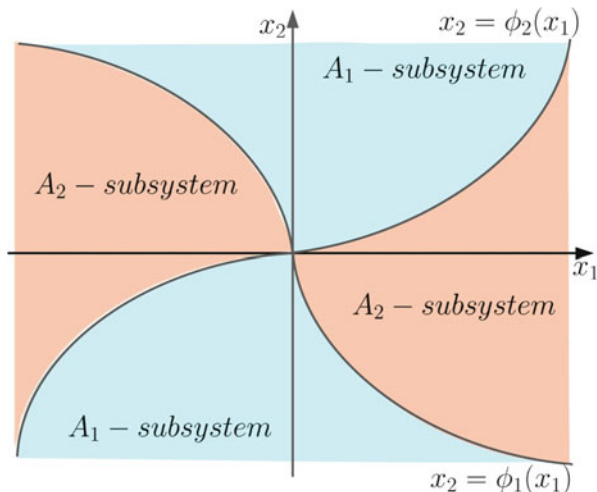
under a pure state-dependent switching law given by

$$\psi(x_1(t), x_2(t)) = \begin{cases} 1, & (x_2 - \phi_1(x_1))(x_2 - \phi_2(x_1)) \geq 0, \\ 2, & (x_2 - \phi_1(x_1))(x_2 - \phi_2(x_1)) < 0, \end{cases} \tag{2}$$

where $\mathbf{x}(t) = [x_1, x_2]^T \in \mathbb{R}^2$ is the state vector, $\tau_i \geq 0$ is the time delay, f_i, g_i are smooth nonlinear functions, and $f_i(x_1, x_2)$ is monotonous with respect to x_2 . In control applications, $x_1(t - \tau_i)$ appears linearly in Eq. (1). In Fig. 1, A_i denotes the i th subsystem and the two subsystems share a common unstable equilibrium point $(0, 0)^T$. System (1) can be formulated as an epidemic model or biological population competition model with switching controllers [20]. In particular, when $f_i(x_1, x_2) = x_2$, system (1) can be represented as a switching model of a second-order mechanical system with two different switching controllers [21].

The objective of this chapter is two aspects. One is to design two switching curves such that the common unstable equilibrium point can be stabilized as fast as possible. The other is to obtain periodic solutions after a stability loss of the common equilibrium point as the delay increases.

Fig. 1 Schematic diagram of the state-dependent switching mechanism



3 Design of Optimal Switched Curves of the Approximated Subsystems

Equation (1) can be converted into an equation similar to one used for describing a vibration system of single degree of freedom, by using an invertible transformation

$$\begin{cases} y_1 = x_1, \\ y_2 = f_i(x_1, x_2). \end{cases} \tag{3}$$

Taking differentiation on both sides of Eq. (3) with respect to t , Eq. (1) becomes

$$\begin{cases} \dot{y}_1 = y_2, \\ \dot{y}_2 = \frac{\partial f_i}{\partial x_1} f_i(x_1, x_2) + \frac{\partial f_i}{\partial x_2} g_i(x_1, x_2, x_1(t - \tau_i)). \end{cases} \tag{4}$$

The time delays are assumed short, and then the delay term $x_1(t - \tau_i) = y_1(t - \tau_i)$ can be approximated by the second-order Taylor expansion as

$$y_1(t - \tau_i) \approx y_1(t) - \tau_i \dot{y}_1(t) + \frac{1}{2} \tau_i^2 \ddot{y}_1(t). \tag{5}$$

Thus, a single delay term $y_1(t - \tau_i)$ changes not only the stability of the subsystems but also their vibration frequencies. When $f_i(x_1, x_2)$ is monotonous and continuous with respect to x_2 as assumed in Sect. 2, the inverse transformation of Eq. (3) is governed and can be expressed by

$$\begin{cases} x_1 = y_1, \\ x_2 = \varphi_i(y_1, y_2), \end{cases} \tag{6}$$

where $x_2 = \varphi_i(y_1, y_2)$ is the inverse function of $y_2 = f_i(x_1, x_2)$ with fixed x_1 .

Substituting Eqs. (5)–(6) into Eq. (4) and separating the stiffness term with respect to y_1 from the right-hand function of the second equation, one has

$$\begin{cases} \dot{y}_1 = y_2, \\ \dot{y}_2 = P_i(\tau_i, y_1) + Q_i(\tau_i, y_1, y_2). \end{cases} \tag{7}$$

Thus, when the delays are short, Eq. (7) in a form of vibration system of single degree of freedom can be regarded as a reasonable approximation of Eq. (1).

As a second-order mechanical system, (7) defines its energy function V_i as the sum of kinetic energy and potential energy, given by

$$V_i = \frac{1}{2} m y_2^2 - m \bar{P}_i(\tau_i, y_1) > 0,$$

where $\bar{P}_i(\tau_i, y_1) = \int_0^{y_1} P_i(\tau_i, s) ds$, m is the mass, and let $m = 1$ without loss of generality. According to Eq. (3), one has

$$V_i = \frac{1}{2} f_i^2(x_1, x_2) - \bar{P}_i(\tau_i, x_1). \tag{8}$$

A switching between subsystems A_1 and A_2 can be regarded as a switching between their energy functions V_1 and V_2 . Thus, it is reasonable to define

$$\mathcal{F}(x_1, x_2) = \frac{V_1}{V_2} > 0$$

and a performance index functional along a switching curve $x_2 = \phi(x_1)$ as follows:

$$I(\phi(\cdot)) = \int_0^{x_{1f}} \mathcal{F}(x_1, \phi(x_1)) dx_1, \tag{9}$$

where $x_{1f} > 0$ is an arbitrary terminal coordinate component. The functional $I(\phi(\cdot))$ represents the accumulation of energy ratio of the two subsystems on the switching curve $x_2 = \phi(x_1)$, $x_1 \in (0, x_{1f})$.

When $I(\phi(\cdot))$ takes the maximum (or minimum) value on $x_2 = \phi_1(x_1)$, the relative energy difference from V_1 to V_2 (or V_2 to V_1) is the largest. Then, when the system switches from A_1 to A_2 or A_2 to A_1 via $x_2 = \phi_1(x_1)$ or $x_2 = \phi_2(x_1)$, as indicated in Fig. 1, the reduced energy is the largest. Thus, in a switching loop $A_1 \rightarrow A_2 \rightarrow A_1 \rightarrow A_2 \rightarrow A_1$, the approximate switched system (7) has a largest energy loss. In this sense, the above two switching curves are approximately optimal when the time delay is small enough. During the switching loops, if the potential energy reduced by switching is greater than the energy increased by the equivalent negative damping, the trajectory of the switched system goes inward to the origin; if the potential energy reduced by switching is less than the energy increased by the equivalent negative damping, the trajectory goes outward away from the origin; if the potential energy reduced by switching is equal to the energy increased by the equivalent negative damping, the trajectory is a closed curve. That is, the equilibrium $(0, 0)^T$ of system (1) is stable, or unstable, or periodic, respectively. As a consequence, in order to guarantee the stability, the equivalent stiffness difference between the two subsystems must be large enough to generate a large enough potential energy difference at switching.

The functional $I(\phi(\cdot))$ takes its extreme value when Euler equation

$$\mathcal{F}_{x_2} - \frac{d}{dt} \mathcal{F}_{x_2'} = 0 \tag{10}$$

is satisfied, where $\mathcal{F}_{x_2} = \frac{\partial \mathcal{F}(x_1, x_2)}{\partial x_2}$ and $\mathcal{F}_{x_2'} = \frac{\partial \mathcal{F}(x_1, x_2)}{\partial x_2'}$ with $x_2' = \frac{dx_2}{dx_1}$. Since $\mathcal{F}(x_1, x_2)$ does not contain x_2' , Eq. (10) is degenerated to $\mathcal{F}_{x_2} = 0$, namely

$$\begin{aligned}
 & f_1(x_1, x_2) \frac{\partial f_1}{\partial x_2} \left[\frac{1}{2} f_2^2(x_1, x_2) - \bar{P}_2(\tau_2, x_1) \right] \\
 & - f_2(x_1, x_2) \frac{\partial f_2}{\partial x_2} \left[\frac{1}{2} f_1^2(x_1, x_2) - \bar{P}_1(\tau_1, x_1) \right] = 0.
 \end{aligned}
 \tag{11}$$

Usually, no closed-form solutions $x_2 = \phi_1(x_1)$ and $x_2 = \phi_2(x_1)$, but approximate solutions in polynomial form, can be obtained from solving Eq. (11).

For example, when $f_1 = x_1 - 10x_2$, $f_2 = x_1 - 100x_2$, $g_1 = x_1^2 + 10x_1 + x_2 + x_1(t - \tau)$, $g_2 = x_1^2 + x_1 + x_2 + x_1(t - \tau)$, and $\tau = 0.1$, Eq. (11) is simplified to

$$x_2^2 - 0.6561x_1^2x_2 - 11.7071x_1x_2 + 0.0021x_1^3 + 0.1036x_1^2 = 0.$$

With $\alpha = 0.3280x_1 + 5.8536$, $\beta = 0.1076x_1^2 + 3.8383x_1 + 34.161$, solving the above equation gives the two switching curves

$$x_2 = \phi_1(x_1) = (\alpha - \sqrt{\beta})x_1, \quad x_2 = \phi_2(x_1) = (\alpha + \sqrt{\beta})x_1.$$

Although the system states of the two subsystems diverge to infinity very quickly, as seen in Fig. 2, but under the designed switching law and as shown in Fig. 3, the equilibrium $(x_1, x_2)^T = (0, 0)^T$ of the switched system is stable at a very fast speed, where the initial conditions are $(x_1(0), x_2(0))^T = (2, 1)^T$ and $x_1(t) = 2$ ($t \in [-0.1, 0]$).

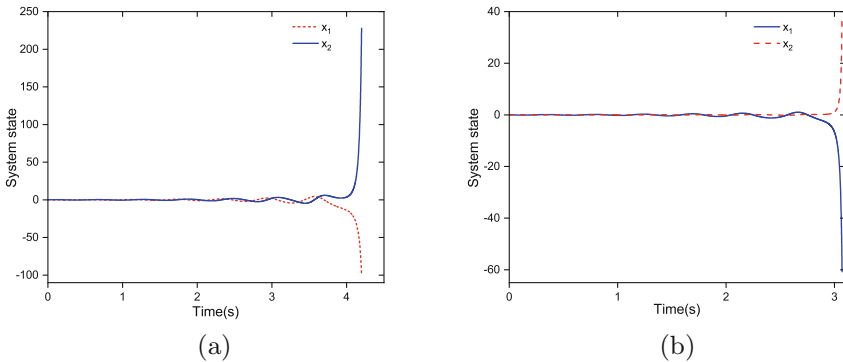


Fig. 2 Time histories of the subsystems with the initial condition $(x_1(0), x_2(0))^T = (0.05, 0.05)^T$ and $x_1(t) = 0.05$, $t \in [-0.1, 0]$. **(a)** Time histories of subsystem A_1 . **(b)** Time histories of subsystem A_2

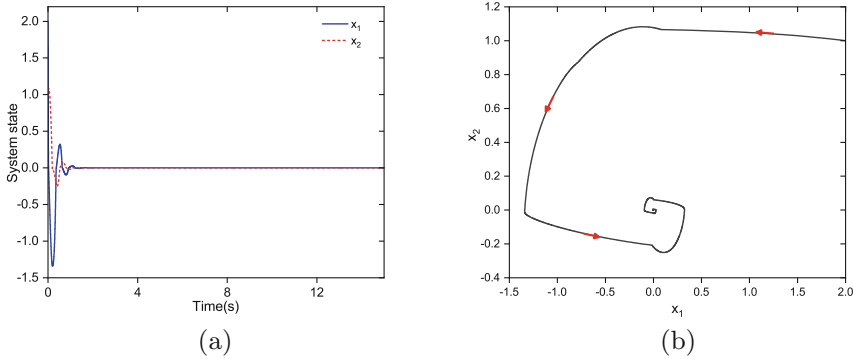


Fig. 3 State of the switched delay system with the designed switching curves. (a) Time histories. (b) Phase trajectory

4 Design of State-Dependent Switching Laws

Stability analysis and stabilization are two major concerns in the study of a switched system. As mentioned before, if there is at least one stable subsystem or each subsystem has at least one characteristic root with negative real part, then some existing methods, say the dwell time method, work well for the stabilization of the switched systems, but the above proposed design method works worse than the dwell time method. On the contrary, for the cases discussed in this chapter, the proposed method works effectively, but the available methods do not work.

4.1 Switching Between Two Different Unstable Delay Subsystems

Let us study system (1), where subsystems A_1 and A_2 are defined as

$$\begin{cases} \dot{x}_1 = x_1 - 4x_2, \\ \dot{x}_2 = 4x_1 + x_2 + x_1(t - \tau), \end{cases} \quad \begin{cases} \dot{x}_1 = x_1 - 16x_2, \\ \dot{x}_2 = x_1 + x_2 + 0.25x_1(t - \tau), \end{cases} \quad (12)$$

respectively. For the subsystem A_1 , the characteristic equation is $p_1(\lambda) = 0$, where the characteristic function $p_1(\lambda)$ is

$$p_1(\lambda) = \det \begin{pmatrix} \lambda - 1 & 4 \\ -4 - e^{-\lambda\tau} & \lambda - 1 \end{pmatrix} = \lambda^2 - 2\lambda + 17 + 4e^{-\lambda\tau}.$$

When $\tau = 0$, $p_1(\lambda) = \lambda^2 - 2\lambda + 21$ has a pair of conjugate complex roots with positive real part. As τ increases from 0, the instability can be changed only if there

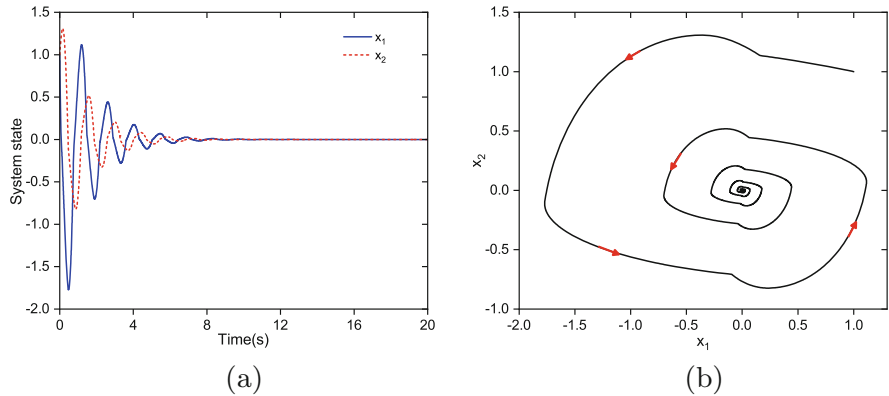


Fig. 4 State of the switched system with $\tau = 0.1$. (a) Time histories. (b) Phase trajectory

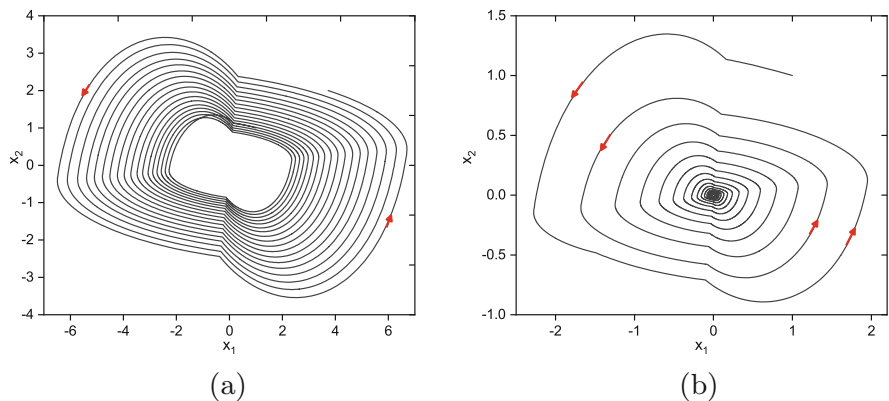


Fig. 5 Phase trajectories of the switched system with different time delays. (a) $\tau = 0.5$. (b) $[\tau = 0.8]$

is a $\tau > 0$ such that $p_1(\lambda)$ has a pair of pure imaginary roots $\lambda = \pm i\omega$. It is necessary to have $|(i\omega)^2 - 2i\omega + 17|^2 - 4^2 = 0$, namely $\omega^4 - 30\omega^2 + 273 = 0$, which has no real roots. This means that the real part of the rightmost characteristic root of subsystem A_1 is kept positive for all $\tau \geq 0$. Thus, subsystem A_1 is unstable for arbitrary $\tau \geq 0$. The same result holds for the subsystem A_2 .

With $\tau = 0.1$, solving Eq. (11) gives the equations of two switching curves

$$x_2 = \phi_1(x_1) = 6.6959x_1, \quad x_2 = \phi_2(x_1) = 0.0504x_1. \tag{13}$$

With the initial conditions $(x_1(0), x_2(0))^T = (1, 1)^T$ and $x_1(t) = 1$ ($t \in [-0.1, 0]$), as shown in Fig. 4, the trajectory approaches to $(0, 0)^T$ in a spiral-like way rapidly by using the switching curves (13).

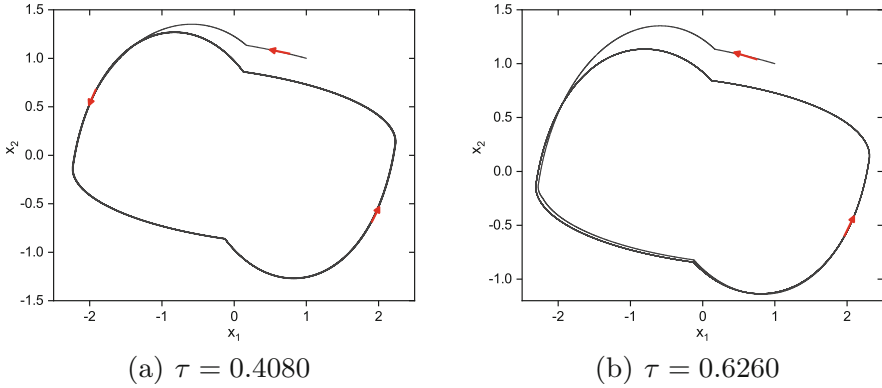


Fig. 6 Periodic solutions of the switched system with different delay values. (a) $\tau = 0.4080$. (b) $\tau = 0.6260$

Now, let τ be a parameter in the region of $\tau \in [0.1, 0.8]$. Although the time delay is no longer small, we can also study the stability of the switched system (1) with unstable subsystems (12) and two fixed switching lines (13). As shown in Fig. 5, when the time delay increases to $\tau = 0.5$, the switched system (12) becomes unstable, and stable again at $\tau = 0.8$. It tells that the switched system (1) should exhibit two times of stability switch from stable to unstable and again to stable. Thus, it is expected to have periodic solutions in $[0.1, 0.5]$ and $[0.5, 0.8]$, respectively, where the potential energy reduced by switching equals to the energy increased by the equivalent negative damping. The delay values that make the solution of the switched system periodic can be found numerically by using the bisection method in $[0.1, 0.5]$ and $[0.5, 0.8]$, respectively. By using the bisection method, both endpoints of the closed intervals at each step admit opposite stability (stable or unstable), resulting in a series of nest closed intervals. At $\tau = 0.4063$ or $\tau = 0.6301$, each as the limit of the nest closed intervals, the switched system (1) is periodic, as shown in Fig. 6.

4.2 Switching of Two Delay Values in an Unstable Delayed System

Consider a time-delay system described by

$$\begin{cases} \dot{x}_1 = 0.1x_1 - 10x_2, \\ \dot{x}_2 = 0.1x_1 + 0.1x_2 + 10x_1(t - \tau). \end{cases} \tag{14}$$

The characteristic equation of Eq. (14) is $p(\lambda) := \lambda^2 - 0.2\lambda + 1.01 + 100e^{-\lambda\tau} = 0$. When $\tau = 0$, $p(\lambda) = 0$ has a pair of conjugate complex roots with positive real part.

When $\tau > 0$, assume that $p(\lambda) = 0$ has a pair of pure imaginary roots $\lambda = \pm i\omega$, then $F(\omega) = (\omega^2 - 1.01)^2 + 0.04\omega^2 - 100^2 = 0$, which has exactly one positive real root $\omega = 10.049$. With $\sin(\omega\tau)$ and $\cos(\omega\tau)$ solved from the real and imaginary parts of $p(\lambda) = 0$, one can find numerically the infinite number of critical delay values $\{\tau_j\}_{j=0,1,2,\dots}$. Moreover, at each critical point $(\lambda, \tau) = (i\omega, \tau_j)$, the crossing direction of the characteristic root is from the left-half complex plan to the right-half one, because $\Re\left(\frac{d\lambda}{d\tau}\right)\Big|_{(\lambda,\tau)=(i\omega,\tau_j)} > 0$. Thus the equilibrium of (14) is unstable for all $\tau \geq 0$. With any $\tau = \tau_1$ or $\tau = \tau_2$, the equilibrium of Eq. (14) alone is unstable, but under a properly chosen switching law between two appropriate delay values, it becomes stable.

Actually, when the delays are short, Eq. (14) is approximated to be

$$\begin{cases} \dot{y}_1 = y_2, \\ \dot{y}_2 = -\frac{101.01}{50\tau_i^2+1}y_1 + \frac{100\tau_i+0.2}{50\tau_i^2+1}y_2, \quad (i = 1, 2). \end{cases}$$

Approximately, the equivalent stiffness coefficient is $\frac{101.01}{50\tau_i^2+1} > 0$, and the equivalent damping coefficient is $-\frac{100\tau_i+0.2}{50\tau_i^2+1} < 0$. In order to stabilize the switched system by the state-dependent switching law only, the difference between the equivalent stiffness coefficient of the two subsystems with different delay values must be large enough. Now, define two unstable subsystems with different delay values τ_1 and τ_2 , respectively, where a large difference between the equivalent stiffness coefficients may be governed. Equation (11) is simplified to $(x_2 - 0.1x_1)x_1^2(\tau_1^2 - \tau_2^2) = 0$. Then, for a pair of arbitrary parameter combinations (τ_1, τ_2) , the two switching curves are found to be $x_2 = 0.1x_1$ and $x_1 = 0$, where $x_1 = 0$ stands for the x_2 -axis. When the switching law is designed as

$$\tau = \begin{cases} \tau_1 = 0.01, & (x_2 - 0.1x_1)x_1 \leq 0, \\ \tau_2 = 1, & (x_2 - 0.1x_1)x_1 > 0, \end{cases} \tag{15}$$

the delay system (14) switched between $\tau = 0.01$ and $\tau = 1$ is stable, where the initial conditions are $(x_1(0), x_2(0))^T = (1, 1)^T$ and $x_1(t) = 1$ ($t < 0$), as depicted in Fig. 7. Figure 8a further shows that the system state occurs in high-frequency switching on the switching line $x_2 = 0.1x_1$, a phenomenon named chatter. Under the same switching law (15), however, when τ_2 is decreased to 0.6, the system energy loss via switching is not large enough due to the insufficient stiffness coefficient difference. In this case, the system (14) switched between $\tau_1 = 0.01$ and $\tau_2 = 0.6$ is not stable, as seen in Fig. 8b.

When $-k x_1(t - \tau)$ is regarded as a delayed feedback, one can prove as done at the beginning of this subsection that the equilibrium $(x_1, x_2) = (0, 0)$ of

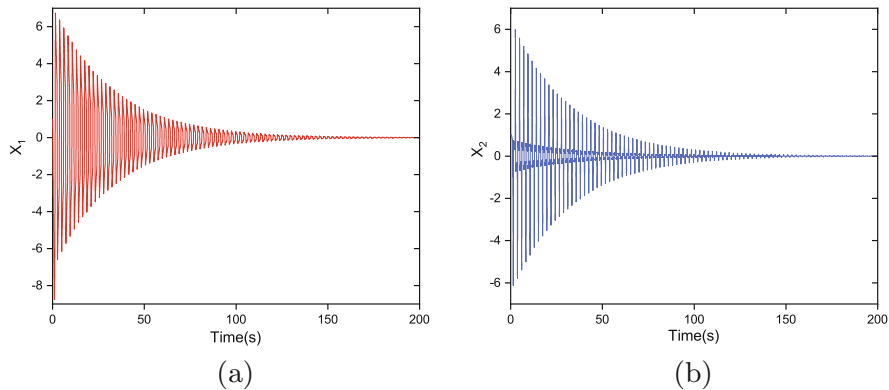


Fig. 7 Stable state under the time-delay switching law (15). (a) The time history of x_1 . (b) The time history of x_2

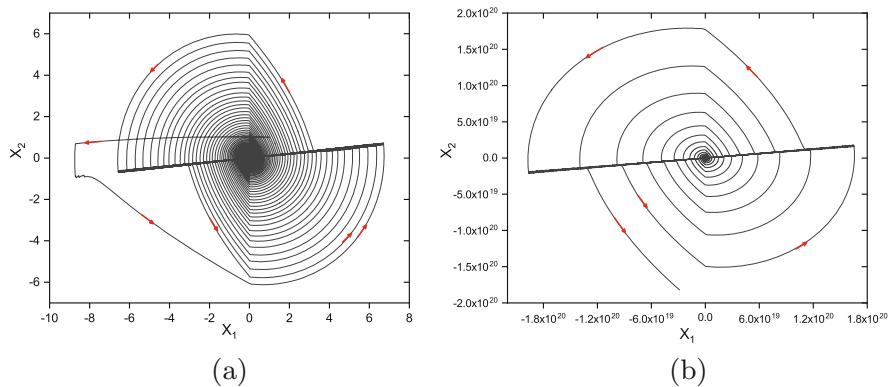


Fig. 8 Phase trajectories under different time-delay switching laws. (a) $\tau_1 = 0.01, \tau_2 = 1$. (b) $\tau_1 = 0.01, \tau_2 = 0.6$

$$\begin{cases} \dot{x}_1 = 0.1x_1 - 10x_2, \\ \dot{x}_2 = 0.1x_1 + 0.2x_2 + kx_1(t - \tau), \end{cases} \tag{16}$$

is unstable for any combination of k and τ . Actually, from the critical stability condition, it is necessary to have $F(\omega) := \omega^4 - 1.95\omega^2 + 1.0404 - 100k^2 = 0$. $F(\omega)$ has no real roots if $|k| < 0.02996$, two pairs of real roots $\pm\omega_1$ and $\pm\omega_2$ if $0.02996 < |k| < 0.1020$, and one pair of real roots $\pm\omega_1$ if $|k| > 0.1020$. Because the delay system (16) is unstable when $\tau = 0$, it is unstable for all $\tau \geq 0$ when $|k| < 0.02996$ or $|k| > 0.1020$. For a delayed negative feedback with $0.02996 < k < 0.1020$, say, $k = 0.08$, $F(\omega)$ has two real roots: $\omega_1 = 1.3103$ and $\omega_2 = 0.4829$, and the corresponding minimal critical delay values are $\tau_{1,0} = 4.4034$ and $\tau_{2,0} = 6.1281$, respectively. Straightforward calculation shows that the crossing

direction at $\tau_{1,0}$ (or $\tau_{2,0}$) is from the left-half (or right-half) complex plane to the right-half (or left-half) complex plan. As τ increases from 0 to $+\infty$, it first passes through $\tau_{1,0}$ (where the characteristic equation increases two unstable roots), then $\tau_{2,0}$ (where the characteristic equation decreases two unstable roots), and so on. As a result, the delayed system (16) is unstable for all $\tau \geq 0$. Similar results can be obtained for other k in $0.02996 < k < 0.1020$. Therefore, a system that cannot be stabilized by using a delayed negative feedback can be stabilized by using a switched law between two chosen delay values.

5 Conclusions

The design of switching law is based on the energy changes of the approximate subsystems in the form of second-order mechanical systems. The approximated subsystems do not have characteristic roots with negative real parts, unlike in the literature where at least one subsystem is assumed stable or each subsystem is assumed to have at least one characteristic root with negative real part. The switching curves are obtained by solving the Euler equation according to the variational principle; thus they are optimal to the approximated subsystems. The simulation analysis shows that even though the two subsystems are unstable for all delay values, stable equilibrium and periodic solutions of the switched systems under a simple switching law designed in this way can be easily achieved. As a result, the stabilization of the unstable equilibrium and the existence of periodic solutions can be understood from the viewpoint of energy changes of the two approximated subsystems. In addition, a delay-independent unstable system can be stabilized by switching between two properly chosen delay values. The proposed method extends the design theory of switched systems, and it is expected to be used to solve other switching problems.

Acknowledgments The first author was supported by NSF of China under Grant 11802065, the Science and Technology Program of Guizhou Province ([2018]1047), the fund project of Key Laboratory of Advanced Manufacturing Technology, Ministry of Education, Guizhou University (KY[2018]478). The second author was supported by NSF of China under Grant 12072370.

References

1. H. Ren G. Zong, H.R. Karimi, Asynchronous finite-time filtering of networked switched systems and its application: an event-driven method. *IEEE Trans. Circuits Syst.* **66**(1), 391–402 (2019)
2. T.C. Lee, Z.P. Jiang, Uniform asymptotic stability of nonlinear switched systems with an application to mobile robots. *IEEE Trans. Autom. Control* **53**(5), 1235–1252 (2008). <https://doi.org/10.1109/TAC.2008.923688>

3. J. Lian C. Li, B. Xia, Sampled-data control of switched linear systems with application to an f-18 aircraft. *IEEE Trans. Ind. Electron.* **64**(2), 1332–1340 (2017). <https://doi.org/10.1109/TIE.2016.2618872>
4. Q.Y. Su, Z.X. Fan, T. Lu, Y. Long, J. Li, Fault detection for switched systems with all modes unstable based on interval observer. *Inf. Sci.* **517**, 167–182 (2020). <https://doi.org/10.1016/j.ins.2019.12.071>
5. H. Shen, M.P. Xing, Z.G. Wu, S.Y. Xu, Multi-objective fault-tolerant control for fuzzy switched systems with persistent dwell-time and its application in electric circuits. *IEEE Trans. Fuzzy Syst.* **99** (2019). <https://doi.org/10.1109/TFUZZ.2019.2935685>
6. S. Yin, B. Xiao, S.X. Ding, D. Zhou, A review on recent development of spacecraft attitude fault tolerant control system. *IEEE Trans. Ind. Electron.* **63**(5), 3311–3320 (2016). <https://doi.org/10.1109/TIE.2016.2530789>
7. X.D. Zhao, Y.G. Kao, B. Niu, T.T. Wu, *Control Synthesis of Switched Systems* (Springer, New York, 2017)
8. H. Yang, B. Jiang, V. Cocquempot, A survey of results and perspectives on stabilization of switched nonlinear systems with unstable modes. *Nonlinear Anal. Hybrid Syst.* **13**, 45–60 (2014). <https://doi.org/10.1016/j.nahs.2013.12.005>
9. Z.M. Wang, A. Wei, X. Zhang, Stability analysis and control design based on average dwell time approaches for switched nonlinear port-controlled Hamiltonian systems. *J. Franklin Inst.* **356**(6), 3368–3397 (2019). <https://doi.org/10.1016/j.jfranklin.2019.02.024>
10. Y.F. Yin, G.D. Zong, X.D. Zhao, Improved stability criteria for switched positive linear systems with average dwell time switching. *J. Franklin Inst.* **354**(8), 3472–3484 (2017). <https://doi.org/10.1016/j.jfranklin.2017.02.005>
11. X.D. Zhao, L.X. Zhang, P. Shi, M. Liu, Stability and stabilization of switched linear systems with mode-dependent average dwell time, *IEEE Trans. Autom. Control.* **57**(7), 1809–1815(2012). <https://doi.org/10.1109/TAC.2011.2178629>
12. X. Mao, H. Zhu, W. Chen, H.B. Zhang, New results on stability of switched continuous-time systems with all subsystems unstable. *ISA Trans.* **87**, 28–33 (2019). <https://doi.org/10.1016/j.isatra.2018.11.042>
13. S. Pettersson, Synthesis of switched linear systems, in *42nd IEEE International Conference on Decision and Control* (2005), pp. 5283–5288. <https://doi.org/10.1109/CDC.2003.1272477>
14. W.M. Xiang, J. Xiao, Stability analysis and control synthesis of switched impulsive systems. *Int. J. Robust Nonlinear Control* **22**(13), 1440–1459 (2012). <https://doi.org/10.1002/rnc.1757>
15. L. Vu, M.A. Kristi, Stability of time-delay feedback switched linear systems. *IEEE Trans. Autom. Control* **55**(10), 2385–2389 (2010). <https://doi.org/10.1109/TAC.2010.2053750>
16. Z. Echreshavi, A. Roosta, The stability analysis of nonlinear switched systems with time delay in input and states with stable and unstable subsystems. *Trans. Inst. Measur. Control* **40**(6), 4298–4308 (2018). <https://doi.org/10.1177/0142331217744618>
17. Y.E. Wang, X.M. Sun, Z. Wang, J. Zhao, Construction of Lyapunov–Krasovskii functionals for switched nonlinear systems with input delay. *Automatica* **50**(4), 1249–1253 (2014). <https://doi.org/10.1016/j.automatica.2014.02.029>
18. S. Pezeshki, M.A. Badamchizadeh, G.A. Rikhtehgar, S. Ghaemi, Stability analysis and robust stabilisation for a class of switched nonlinear systems with input delay. *Int. J. Control* (2019). <https://doi.org/10.1177/0142331218794264>
19. Y.E. Wang, X.M. Sun, F. Mazenc, Stability of switched nonlinear systems with delay and disturbance. *Automatica* **69**, 78–86(2016). <https://doi.org/10.1016/j.automatica.2016.02.015>
20. G. Chowell, H. Nishiura, Transmission dynamics and control of Ebola virus disease (EVD): a review. *BMC Med.* **12**, 196 (2014). <https://doi.org/10.1186/s12916-014-0196-0>
21. T. Erneux, *Applied Delay Differential Equations* (Springer, New York, 2009)

Index

A

- ABAQUS[®] FEM software, 170
- Abdominal aortic aneurysm (AAA), wall shear stress
 - boundary conditions, 29–30
 - geometry, 29–30
 - limitations, 27
 - MRI, 27, 28
 - non-Newtonian blood flow simulation, 30–31
 - pressure distributions, 33–34
 - velocity distribution at late systole, 32–33
 - wall shear stress, 34–35
- Active overload protection system (AOPS), 201, 213
- Adaptive sub-cells interpolation method, 678–679
- Adaptive time stepping procedure (ATSP), 869–870
- Adimensionalization process, 642
- Aerial cable car system
 - cable deflection, 239
 - external force frequency, 245
 - Hamilton principle, 238
 - Kronecker delta, 242
 - line art drawing, 238
 - mass, gyroscopic, and stiffness operator, 242
 - mass–spring system, 238
 - mechanical–mathematical model, 239–243
 - numerical investigation, 243
 - numerical simulation, 245
 - proposed mechanical model, 244
 - Runge–Kutta solver, 244
 - schematic representation, 240
 - stochastic approach, 238
 - total kinetic energy, 240
 - traction cable, 241
 - vertical plane motion, 238
- Aero-elastic flutter oscillations, 49, 50, 54–56, 59, 61, 62
- Aeroelastic system under stochastic inflow
 - canonical sinusoidal gust model, 878
 - fatigue damage, 878–880, 883, 885
 - freeplay nonlinearity, 877–878
 - input flow fluctuation, 880
 - pitch–plunge aerofoil, 879
 - pitch response dynamics, 881–882
 - pitch stiffness of airfoil, 879
 - simulated autocorrelation function, 881
 - stochastic bifurcation analysis, 882–884
 - stress cycles, 885
 - validation of aerodynamic model, 881
 - variation of flow speed with time, 881
- Affine variety, 598
- Aircraft model, 542
- Airy’s stress function, 180
- Algebraic geometry, 598–599
- Alternating Frequency Time method, 610, 613, 735
- AMB-rotor system, 649, 651–653
- Amplitude equation, 800
- Angiography, 40, 41
- Angular frequency, 799
- Angular momentum, 686
- Angular velocity, 633, 779
- Anisotropic bearings, 768
- ANSYS[®] analysis, 41, 42, 225
- Aortic aneurysm, *see* Abdominal aortic aneurysm (AAA), wall shear stress

- Arbitrary Lagrangian–Eulerian (ALE)
 - methods, 267–268
 - Armfield wind tunnel, 23
 - Arrhenius model, 75
 - Artificial neural networks (ANNs), 422, 424
 - Asymptotic numerical method (ANM), 443
 - Atomic force microscope (AFM), 549
 - dynamics of, 561
 - mathematical model, 550
 - problem formulation, 550–552
 - perturbation solution, 552–561
 - self-oscillating regime, 561
 - Autodesk[®] InventorLT[™], 40
 - AUTO software, 149
 - Auxiliary
 - bearings, 654
 - functions, 890–891
 - variables, 602
 - Averaging method, 576, 577, 580, 581, 853
 - dynamical systems, iterative algorithm
 - class for, 457
 - Lyapunov exponents, 577–578, 581–582
 - AVM sensitivity analysis, 282
 - Axial displacement, 819
 - Axial harmonic forcing, 638
- B**
- Backward whirl (BW) frequencies, 761
 - Balancing method
 - conventional techniques of, 749
 - of double-disc rotor system, 750
 - with constant rotational speed, 755–756
 - transient response and modal
 - parameters, 754–755
 - with variable rotational speeds, 757–758
 - FIR filter-based force estimation technique, 750, 752
 - load identification technique, 751–752
 - and TMM, 750–751
 - transient balancing methods, 749
 - unbalance parameters identification
 - procedure, 752–753
- Bayesian Spline regression, 355–356
- Bending acceleration level, 819
- Bernoulli differential equation, 569
- Bernoulli–Euler beam, 550
- Bernoulli–Euler’s cantilever model, 120
- Bifurcation diagrams, 638, 683, 837
- Bilinear amplitude approximation (BAA)
 - method, 497
- Bisection technique, 869
- Bi-variate normal (BVN) distribution, 428–429
- Blood viscosity, 39, 40, 44–46
- Bolotin method, 638
- Boundary conditions, viscoelastic base
 - Airy’s stress function, 180
 - CCSC, 182–184
 - CSCS, 182–184
 - Kelvin–Voigt model, 179–181, 185, 187
 - one-to-one internal resonance, 184
 - plate mode shapes for different B.Cs, 182
 - plate’s lateral deflection, 180
 - Riemann–Liouville derivative, 181, 187
 - SSSS, 182–184
 - T2-dependence of amplitudes of free
 - vibrations, 186
 - T2-dependence of dimensionless
 - displacements of plate, 186
- Bozzak–Newmark method, 854
- Breathing crack model
 - Euler–Bernoulli beam, 763
 - finite element disk-shaft-bearing-rotor
 - system, 763
 - gravity force vector, 768
 - horizontal and vertical vibration whirl
 - amplitudes, 765
 - non-dimensional representation, 763
 - rotordynamic transient whirl response,
 - 768
- Brownian motion, 43
- Brownian tree, 869, 870
- Burton’s method, 155–159, 162–164, 173, 271, 609, 639
- C**
- Canard explosion, 403
 - Cantilevered aspirating pipes
 - aspiration of fluid, 112–113
 - axisymmetric velocity profile, 114
 - constraint enforcement strategy, 111–112
 - hydrodynamic force coefficients, 110
 - Lagrangian of system, 109
 - MMM, 108, 111, 112
 - motion constraints of system, 110
 - non-dimensional arc-length coordinate,
 - 108
 - non-dimensional parameters of model in
 - numerical analyses, 113
 - non-dimensional vortex shedding
 - frequency, 110
 - relaxed model, 111–112
 - root-loci diagram, 114
 - schematic representation, 108
 - stability analysis, 113–114
 - structural damping effects, 109
 - virtual displacements, 109

- VIV response analysis
 - in-line and cross-wise amplitudes of oscillations, 115
 - steady-state trajectories, 115, 116
 - Cardiovascular diseases, 27, 39
 - CARMA(2,1)-process, 98
 - Cauchy principle value, 68
 - C++ Code, to compute Wendland functions, 465–467
 - algorithm, 469–471
 - arrays, 473
 - Use/EXAMPLES, 471–472
 - Wendland functions, generalised interpolation using, 467–468
 - Chain-recurrent set
 - determination of, 460–461
 - values on, 461–462
 - Chebyshev-Ritz method, 225
 - Clamped–clamped beam resonator, 437
 - Cohesive envelope, 412
 - Compass-gait walker, 685
 - Complete Lyapunov function (CLF), 453, 454
 - Computational efficiency, 676–677
 - Computational fluid dynamics (CFD), 28, 39, 267
 - Continuation plots, 619
 - Control-based continuation (CBC), 50–52
 - Bayesian Spline regression, 355–356
 - comparison of, 356–359
 - continuation scheme, 352
 - Gaussian process regression, 355
 - Hodgkin–Huxley neuron, 356, 358
 - signal-to-noise ratio (SNR), 357
 - surrogate regression models, 354–356
 - truncated Fourier series, 354
 - van der Pol signal, 358
 - Convergence-control parameter, 507
 - Coronary artery diseases, 28
 - Craig–Bampton (CB) approach, 374
 - Crank–Nicolson scheme, 82
 - Critical value, 600
 - Cross-flow HE tube conveying fluid
 - dimensionless governing equation of motion, 6
 - dynamic transverse distributed force, 5
 - equation of motion, 4
 - FEI, 3, 4, 9–12
 - flutter amplitude, bifurcations diagram, 7
 - governing equation of motion, 5, 6
 - internal and external fluid, 7
 - internal pulsatile flow on dynamics
 - cross-flow velocity at different pulsatile, 9
 - in-phase and out-of-phase components, 12
 - parametric instability regions, 12
 - pulsatile flow excitation frequency, 10
 - steady-state responses, 11
 - internal steady flow on dynamics, 8
 - oscillation of HE tube steady flow, 8
 - parametric resonant amplitude, 7
 - schematic diagram, 4, 5
 - Cubic nonlinearity case
 - approximation for small damping, 159–162
 - Burton’s method, 157–158
 - Burton’s solution for Duffing oscillator, 159
 - finding approximate solutions, 158–159
 - Cubic-quintic oscillator with viscous damping, 163–164
 - Cubic Takens–Bogdanov bifurcation, 401
 - Cunningham correction factor, 43
 - Cuspidal loop, 401–402
 - Cyclic-fold bifurcation (CFB), 684
 - Cylindrical shells, elastic foundation
 - discontinuous foundation in circumferential direction, 168
 - geometry, 168
 - harmonic lateral pressure, 168
 - linear vibrations, 167
 - membrane and flexural stress, 169
 - modal coupling, 173
 - nonlinear equations of motion, 169
 - nonlinear vibrations, 167
 - phase portraits with Poincaré map, 176
 - quasi-periodic solution and periodic solution, 173
 - reduced-order model
 - accumulated kinetic energy, 170, 171
 - boundary conditions, 172
 - cosine and sine modes of the Fourier series, 170, 171
 - perturbation method, 170–174
 - transversal modal amplitude, 172
 - resonance curves, 173–176
- D**
- Damped backbone curves
 - cubic nonlinearity case
 - approximation for small damping, 159–162
 - Burton’s method, 157–158
 - Burton’s solution for Duffing oscillator, 159
 - finding approximate solutions, 158–159

- Damped backbone curves (*cont.*)
 - definition, 155
 - SDOF with polynomial nonlinearities
 - cubic–quintic oscillator with viscous damping, 163–164
 - general form, 162
 - Damped nonlinear normal mode, 157
 - Damped nonlinear oscillator, 156, 164
 - Data cloud analysis, 825
 - Data quality, 820–821
 - Deep water waves, 96
 - Degree-of-freedom (DOF) mechanical oscillator, 495
 - Different continuation curves, 618
 - Dimensionless pump displacement, 135
 - Direct-acting relief valve
 - dynamic model, 132
 - fluid–structure coupling system, 131
 - Hopf bifurcation, 131
 - 0.4 MPa inlet pressure, 137–139
 - 0.8 MPa inlet pressure, 135–137
 - nondimensionalization of dynamic model, 133–135
 - physical model, 132, 133
 - system parameters, 134
 - vibration conditions, 137, 138
 - Direct differentiation method (DDM), 282–285
 - cubic stiffness coefficient, 288
 - direct sensitivity analysis method, 283–285
 - displacement and phase portraits, 287
 - Duffing oscillator (*see* Duffing oscillator)
 - long time response sensitivity, 288
 - nonlinear dynamic response, 283
 - Direct normal form (DNF), 368–369
 - Direct sensitivity analysis method
 - direct differentiation method (DDM), 283–285
 - Duffing oscillator (*see* Duffing oscillator)
 - nonlinear dynamic response, 283
 - Discontinuous nonlinear oscillators
 - adaptive time stepping procedure, 869–870
 - bifurcation diagram, 872
 - bisection technique, 869
 - Brownian tree, 869, 870
 - equation of motion, 866
 - Fokker–Planck equation, 868–869
 - initial indentation impact velocity, 873, 880
 - marginal pdf of displacement for different contact models, 873
 - phase plane and Poincaré section, 870–872
 - piecewise smooth system dynamics, 866–868
 - stationary joint pdf, 873
 - Dominant dynamical method, 661
 - Donnell shallow theory, 169
 - Double-side impact (DSI) motion, 861
 - Drag coefficient, 90–92, 100
 - Dry friction
 - advantageous effects, 841
 - characteristic of, 842
 - dynamic behavior of, 841
 - experiment set-up, 847–848
 - LuGre model, 842
 - NARX model, 842, 843
 - particle swarm optimization (PSO), 843
 - physical parameters and working conditions, 842
 - representation of Coulomb friction, 842
 - representation of Stribeck curve, 842
 - Stribeck effect, 841
 - swarm intelligence, 843
 - testing data and results, 847–848
 - time-delay recurrent neural network (TDRNN), 842
 - Duffing oscillator, 70, 73, 609, 615–617, 662, 663, 743
 - effect of dynamic behaviors, 286–288
 - effect of secular term, 285–286
 - Duffing–van der Pol (DVIDP) oscillator, 866, 870
 - Dynamical systems, iterative algorithm class
 - for, 453–454
 - algorithm, 456–457
 - average and median, 457
 - chain-recurrent set
 - determination of, 460–461
 - values on, 461–462
 - distribution, 458–459
 - iterations, 459–460
 - Mesh-free collocation methods, 455–456
 - Dynamical viscosity, 76, 83
 - Dynamic axial loads, 638
 - Dynamic response of segmental arch, 309–311
- E**
- Efficient symbolic computation, generic canard
 - explosions via, 537–539
 - classical method, 543
 - reduced Hodgkin–Huxley model, 545–546
 - templator model, 543–544, 547
 - procedure, 539–541
 - symbolic software, implementation in, 541–543
 - Eigenvalues of the Jacobian matrix, 558
 - Electromagnetic force, 650, 652
 - Electromechanical coupling coefficients, 810

- Elliptic–parabolic configuration, 733
 Energy transfer, 807
 Enhanced Vlasov Displacement-based Element (EVDE)
 cross-section warping, 316–318
 displacement-based approach, 319
 element variational formulation, 319–321
 L portal frame, 322–324
 warping representation, 316–318
 Equation of motion, 791
 Equivalent mechanical models (EMMs), 267
 Eringen’s model, 291, 292
 Euclidean distances, 57
 Euclidean space, 820, 821, 888
 Euler–Bernoulli beam, 111, 763
 elastic beam, 108
 elements, 434, 450
 reduced model, 824
 theory, 4, 11, 89
 Euler equations, 96–97, 903
 Euler–Lagrange formulation, 686
 Euler–Lagrange’s equation, 712
 Evolution matrix
 of Lyapunov exponents, 576–577
 averaging scheme, 577–578
 expansion of, 578
 expansion of LEs, 578–579
 Exact augmented perpetual manifolds, 190,
 192–194, 196, 197, 199
 Experimental procedure, 820–821
- F**
- Failure time distribution, 412–417
 Failure time pmf, analytical approximation of,
 411
 analytic pmf with Monte Carlo simulations,
 417–418
 failure time distribution, 412–417
 setup, 412
 Fast Fourier transform (FFT), 740, 741, 813
 Fatigue-crack nucleation, stochastic
 intermittent loading on, 407
 failure time pmf, analytical approximation
 of, 417
 analytic pmf with Monte Carlo
 simulations, 417–418
 failure time distribution, 412–417
 setup, 412
 Serebrinsky–Ortiz (SO) model, 408
 probabilistic decomposition-synthesis
 method, 410–411
 time-discretization of, 408–409
 Fatigue damage, 878–880, 883, 885
- Fatigue failure, 421–422
 Goodman’s correction factor, 423
 learning problem, 424
 learning model, 426
 training set, creating, 424–425
 Miner’s linear cumulative damage rule, 422
 offline prediction, 426
 real-time prediction, 429–430
 uncertainty quantification, 426–427
 bi-variate normal distribution, 428–429
 Gaussian process regression, 429
 FGM shallow shell
 complex planform, 391
 cylindrical panel, 389
 on elastic foundation, 386
 Fiber-reinforced elastomeric enclosure (FREE)
 buckling, 347–348
 co-existing solutions, 348–349
 construction parameters, 343
 design principles, 342–344
 mathematical formulation, 344–346
 under pressurization, 343
 self-contact, 346–347
 single-segment rod, 345
 slender elastic objects, 342
 static force and moment balance, 345
 undeformed state, 343
 Fiber-reinforced polymers (FRP), 637
 Finite difference method (FDM), 282
 Finite element analysis, 247
 Finite Element Model (FEM), 418, 434
 Fitting electromagnetic force, 652
 Flat ribbon vibrations in wind
 advantage, 24
 airflow interaction forces, 19–20
 angle of attack, 16
 average tensile strength, 23, 24
 centre of mass motion in phase plane, 21,
 22
 centre of mass motion in vertical plane, 22
 differential equations of motion, 18
 2DOF, 16
 forces and moments in interaction with air
 flow, 18
 forces in elastic elements, 20–21
 geometrical parameters, 17
 numerical modelling, 18
 rotational motion, 15, 16
 total tensile strength, 22
 wind tunnel, 23
 Flexural-torsional mode, 647
 Floquet exponents, 739
 Floquet multipliers, 724
 Floquet theory, 443, 638, 641, 744

- Flow-induced vibration (FIV), 3, 4
 - FLUENT (ANSYS Academic Research 2020R1), 31
 - Fluid boundary conditions, 41
 - Fluidelastic instability (FEI), 3, 4, 9–12
 - Fluidelastic-stiffness-type mechanism, 3
 - Fluid strain rate, 40, 42
 - Fluid-structure interaction (FSI) techniques, 39–41, 45
 - Fluid viscosity, 75–77, 80–84
 - Flutter oscillations
 - aero-elastic flutter, 54–56
 - CBC, 50–52
 - data-driven models
 - cost function, 57, 58
 - saddle-node bifurcation, 56
 - structure, 53–54
 - transformation between coordinate system, 57
 - hybrid differential equation/machine-learned model, 59
 - normal-form-based model, 58
 - phase portraits of hybrid model, 58, 60
 - PINNs, 49
 - PP-CBC, 50–56
 - time series of two LCOs, 58, 61
 - Fokker–Planck (FP) equation, 866, 868, 869, 871, 880
 - Force-based formulation
 - element mass matrix consistent, 306–308
 - flexibility matrix, 304–306
 - fundamental element equations, 304–306
 - Forced oscillations of nonlinear Helmholtz resonator, 503–504
 - governing equation of, 504–505
 - homotopy analysis method, application of, 506–510
 - simulation, 510–511
 - Forcing frequency, 800
 - Forward whirl (FW), 761
 - Fourier series expansion, 443
 - Fractional calculus standard linear solid model, 179, 185
 - Free-edge shallow spherical shell
 - analytical result, 369, 370
 - analytical von Kármán model, 362–364, 370
 - direct normal form (DNF), 368–369
 - numerical finite element model, 364–365
 - numerical results, 366–368
 - three reduction methods, 365–366
 - type of nonlinearity modes, 370
 - Freeplay nonlinearity, 877
 - Free-surface Biot number, 78
 - Free vibration frequencies, 597
 - Frequency–amplitude dependence, 433
 - Frequency-amplitude relation, 435–437
 - Frequency combs (FCs), 797
 - Frequency-domain
 - approximation method, 831
 - equations of motion, 444–445
 - methods, 421, 609
 - response, 620
 - Frequency-domain stability analysis, IHB
 - method, 443
 - methodology
 - frequency-domain equations of motion, 444–445
 - response analysis, 445–446
 - stability analysis, 446–447
 - time-domain equations of motion, 444
 - numerical implementation
 - stability analysis, 450–451
 - three-dimension tensor, 448–450
 - tensorial implementation, 447–448
 - Frequency–energy dependence, 433
 - Frequency response
 - curves, 790
 - synthesis, 334–337
 - Frequency response functions (FRF), 799–801
 - Fully connected artificial neural network (FC-ANN), 426
 - Functionally graded materials (FGM), 385
 - Fundamental resonance, 664
 - Fuzzy generalized cell mapping (FGCM)
 - method, 673
- ## G
- Galerkin
 - method, 6, 16, 639
 - procedure, 172, 737
 - projection, 124
 - Gamma function, 181
 - Gaussian distribution, 425
 - Gaussian process regression (GPR), 429
 - Gaussian white noise, 866, 868
 - Generalized- α method, 853, 854, 858, 862
 - Generalized cell mapping method (GCM), 673
 - Generalized cell mapping with sampling-adaptive interpolation (GCMSAI), 674
 - Generalized extremal values, 601, 602
 - Generalized rolling pendulums
 - in rotating vertical plane, 627–633
 - in stationary vertical plane, 626–627

- Generic canard explosions, via efficient
 - symbolic computation, 537–539
 - classical method, 543
 - reduced Hodgkin–Huxley model, 545–546
 - templator model, 543–544, 547
 - procedure, 539–541
 - symbolic software, implementation in, 541–543
- Genetic algorithm (GA), 843
- Ginzburg–Landau equation, 81
- Global connections, high-order approximation of, 395–396
 - NTT method, applications of
 - canard explosion, 403
 - perturbing non-Hamiltonian integrable systems, 402–403
 - perturbing Hamiltonian systems, 396–397
 - cubic Takens–Bogdanov bifurcation, 401
 - cuspidal loop, 401–402
 - quadratic Takens–Bogdanov bifurcation, 400–401
 - Rayleigh–Duffing mechanical oscillators, 397–400
 - Takens–Bogdanov, in reversible systems, 402
- Goodman’s correction factor, 423
- Graded Si–Ge alloys, non-rectification of heat, 563–564
 - rectification coefficient and maximization, 564–566
 - thermal conductivity and corresponding rectification coefficient, 571
 - with variable section, 566–570
- Grand-Unified Theory (GUT), 5
- Grassmann variables, 518, 520
- Gravitational unloading
 - damping factor, 261
 - dynamical equations, 261
 - Euler’s angles, 260
 - general inertia moments, 258
 - mathematical model, 258–261
 - modeling parameters, 261
 - spherical damper scheme, 259
 - time-evolution of angular velocities, 262–263
 - time-evolution of spatial angles, 263, 265
- H**
- Hamilton’s principle, 120
- Harmonic balance method (HBM), 443, 490, 609, 658, 736, 802
- Harmonic balance method with alternating-frequency-time scheme (HB-AFT), 833, 838
- Heart attack, 39
- Heat, non-rectification of, 563–564
 - rectification coefficient and maximization, 564–566
 - thermal conductivity and corresponding rectification coefficient, 571
 - with variable section, 566–570
- Hertzian elastic contact force model, 873
- Heteroclinic cycles, 705
- Hilbert transform, 68, 126, 128
- Hill method, 443
- Hill’s equation, T -periodic potential, 723, 724
- Hodgkin–Huxley neuron, 353, 356, 358
- Holomorphic quantum supercharges, 521
- Homotopy analysis method (HAM), 503, 512
 - application of, 506–510
- Hooke’s law, 168
- Hopf bifurcation, 49, 50, 53, 56–58, 131, 398, 402, 403, 700, 706, 711
- Hopf-pitchfork bifurcation, 699
- Horner’s scheme, 470
- Horn-Schunk optical flow method, 41
- Hybrid symbolic numeric computational (HSNC), 490
- Hydrodynamic damping of elastic vibrations
 - computational domain configuration, 89
 - dimensionless local oscillation amplitude, 87
 - dimensionless vibration frequency, 87
 - drag coefficient, 90–92
 - drag force, 90, 92
 - gap-to-width ratio, 88
 - inline force, 90
 - mass coefficient, 90–92
 - mass force, 90, 92
 - motion of beam in fluid, 89
 - Navier-Stokes equations, 87, 88
 - oscillation profile, 89
 - quasi-two-dimensional model, 87, 88, 90, 93
 - two-dimensional modeling, 91
- Hydrodynamic force coefficients, 110
- Hydrodynamic forces
 - irregular sea surface, 102–103
 - random wind influence, 101–102
 - velocity potential
 - on cylindrical pile, 100–101
 - Euler equations, 96–97
 - initial condition choice, 99
 - random wind modeling, 98

Hyperbolic knots, 586
Hysteresis phenomenon, 789

I

Impact-induced motion, 832
Impact oscillator models
 Fourier coefficients, 834
 frequency-domain approximation method, 831
 Newton's second law, 832
 parameters, 833
 time-domain numerical method, 831
 vibro-impact behaviour, 831
Imperial competition algorithm (ICA), 843
Impulse action, 887, 888, 894
Impulsive hybrid nonlinear system, 683, 686
Impulsive systems, 887–890, 897
Incremental harmonic balance (IHB) method, 443
 methodology
 frequency-domain equations of motion, 444–445
 response analysis, 445–446
 stability analysis, 446–447
 time-domain equations of motion, 444
 numerical implementation
 stability analysis, 450–451
 three-dimension tensor, 448–450
 tensorial implementation, 447–448
Independent spike hypothesis, 412
Infimum value, 600
Influence coefficient method (ICM), 749
Interfacial instability, 76
Internal detuning parameters, 791, 811
Internal resonances (IR), 783, 798, 807
 medium forced vibration, 786–787
 strong forced vibration, 791–786
 weak forced vibration, 787–788
Interpolation accuracy, 676–677
Interpolation cell mapping (ICM) method, 673
Intraluminal thrombus (ILT) accumulation, 28, 33, 35
Intrinsic mode function (IMF), 119–120, 126, 128
Invasive angiography, 40, 41
Irrational frequency ratios, 737, 739
Irregular sea surface, 102–103

J
Jacobian matrix, 556, 576, 688, 700, 705, 801, 859
Jensen's inequality, 532

Joint probability density function (jpdf), 866, 868, 871, 880
Jump phenomenon, 650

K

Karman constant, 98
Karush–Kuhn–Tucker multipliers, 602
Kelvin-Voigt model, 132, 179–181, 185, 187
Kirchhoff–Love plates, 179, 180
Kirchhoff plate theory, 228
Kronecker delta, 111

L

Lagrangian
 drift, 102
 equation, 774
 formalism, 518
 variables, 147
Lamé parameters, 144
Laplace transforms, 528
Largest Lyapunov exponent (LLE), 865, 870–872, 880
Lattice-boom offshore cranes
 beam model, 204
 characteristic points, 208
 courses of deflections, 209
 cylinder parameters, 209
 dynamic model, 206
 homogenous transformations, 203
 lattice boom cranes, 202
 longitudinal and torsional deformations, 204
 pseudo-inertial matrix, 206
 rod discretization, 205
 scheme of crane, 207
 simulations, 208–210
 slewing mechanism, 202, 203
 spring-damping elements, 205
 vertical velocity, 209
Learning model, 426
Left circumflex coronary artery, 40, 41, 45
Legendre polynomial, 143, 147
Leishman–Beddoes (LB) model, 878–882, 886
Lemke algorithm, 854, 855, 860, 862
Limit cycle oscillations (LCOs), 57–59, 70
Limit point (LP), 735, 739
Linear complementarity problem (LCP), 854–856, 859–862
Linear damping coefficients, 799
Linear free vibration, 179
Linearized model, 713
Linear stability analysis, 66, 76, 79

- Linear structure oscillator, 69–70
 - Linear superalgebra, 517
 - Linear-Time-Variant (LTV) equations of motions, 763
 - Liouville's formula, 725
 - Load statistics, 412
 - Long-wave expansion method, 75
 - Lorenz
 - braids, 588–589
 - knots, 585–587
 - map, 586
 - system, 680, 681, 708
 - template, 585
 - Lorenz knots, 585–587
 - family of, 589–594
 - Lorenz braids, 588–589
 - symbolic dynamics, 587
 - Low-density-lipoproteins (LDL) transport
 - computational approach
 - discrete phase model approach, 42
 - fluid viscosity, 42
 - Fourier series coefficients for inlet velocity and outlet pressures, 42
 - Horn-Schunk optical flow method, 41
 - particle inlet velocity, 43
 - Rosin-Rammner diameter distribution, 43
 - spherical particles, 42–43
 - transient displacement boundary conditions, 41, 42
 - TAWSS, 44
 - transient wall shear stress and LDL mass concentration, 43, 45
 - in vivo-based model, 40–41
 - von Mises stress, 44, 46
 - WSS and LDL concentration at end systole cycle, 44, 46, 47
 - WSS distribution, 43, 44
 - Low-frequency behaviour
 - centrifugal pendulum absorber, 778–780
 - Eigenfrequency of slow motion, 777–778
 - equilibrium position of slow motion, 777
 - Lyapunov exponents (LEs), 575
 - definition of, 575–576
 - evolution matrix, approximate calculation of, 576–577
 - averaging scheme, 577–578
 - expansion of, 578–579
 - periodic QR factorization, 579–580
 - approximate calculations of $X(k)$, 580–581
 - averaging scheme, 581–582
 - calculations of, 582–583
 - Lyapunov functions, 453, 530, 887, 888, 892, 893, 897
 - Lyapunov–Krasovskii functionals, 900
- M**
- Machine learning (ML) algorithms, 422
 - Magnetoelastic theory, 226
 - MANLAB, 801
 - Maple software, 156
 - Marangoni number, 78
 - Mass coefficient, 90–92
 - Mass density, 76, 110, 146, 228, 229, 250, 320, 450
 - Mathematical model, 713, 738
 - Mathieu–Hill equations, 639
 - MATLAB, 6, 40, 41, 68, 497
 - Meissner's equation, 723
 - Melnikov method, 395, 396
 - Mesh-free collocation methods, 455–456
 - Method of Moving Asymptotes (MMA), 437
 - Method of multiple scale (MMS), 478–479, 784
 - Method of reduction of order, *see* Wentzel, Kramers and Brillouin (WKB) transformation
 - Micro-Electro Mechanical Systems (MEMS), 797
 - Miner's linear cumulative damage rule, 422
 - Miner's rule, 421
 - Modal Balancing Method (MBM), 749
 - Modal coupling, 336–339
 - Modal displacements, 791
 - Modular Modeling Methodology (MMM), 108, 111, 112
 - Monodromy matrix, 724, 726
 - Monomial order, 598, 599
 - Mooney-Rivlin model, 41
 - Morison expansion, 90
 - Moving pulsating ball model (MPBM), 268
 - 0.4 MPa inlet pressure, 137–139
 - 0.8 MPa inlet pressure, 135–137
 - Müller's procedure, 870
 - Multi-degree-of-freedom (MDOF) oscillators, 155, 164, 735, 831, 832, 838, 854, 855, 857, 859, 860
 - Multi-frequency time variational technique (MTVM)
 - differentiation matrices, 614
 - Galerkin's weighted residual method, 613
 - gradient-based iterative methods, 614

- Multi-harmonic balance method (MHBM),
 - 610, 735
 - Fourier shape functions, 612
 - Galerkin's weighted residual approach, 612
 - independent time scales, 611
 - Newton–Raphson method, 612
 - truncated second-order Fourier series, 611
 - Multiple scales (MS) method, 800
 - Multi-stenosis left circumflex coronary artery, 39–47

 - N**
 - Nabla operator, 97
 - NARX model, 843–845
 - Navier–Stokes equations, 31, 87, 88, 95
 - Nayfeh's monograph, 783
 - Neimark–Sacker bifurcation (NSB), 684, 740–742, 798
 - bifurcation diagram of, 691, 692
 - quasi-periodic behavior, 693
 - quasi-periodic motions, 694
 - Neimark–Sacker (NS) boundary curve, 800, 801
 - coefficient of, 805
 - direct time-marching Runge–Kutta 4 (RK4) method, 804
 - Floquet–Hill formulation, 802
 - MANLAB, 804
 - time-marching approach, 804
 - Newmark method, 853
 - Newton iteration, 854, 862
 - Newton–Raphson method, 612, 614, 737, 834
 - Noh–Bathe method, 853
 - No-impact (NI) motion, 861
 - Non-destructive tests (NDT), 421
 - Non-dimensional model, 526
 - construction of, 527–528
 - parametric instability boundaries, 641
 - viscous damping coefficient, 784
 - Nonlinear beams, 808
 - Nonlinear coupling, 799, 825
 - Nonlinear damping, 508, 551
 - Nonlinear differential equations, 735
 - Nonlinear dynamical phenomena, 797
 - Nonlinear dynamic analysis, 658
 - Nonlinear dynamic response, structural
 - optimization of, 433–434
 - methods, 434
 - adjoint method, design sensitivity analysis using, 438–439
 - finite element model and design variables, 434
 - optimization problems and sensitivities, 437–438
 - reduced-order model and frequency–amplitude relation, 435–437
 - optimization, 439, 440
 - original objective function, 441
- Non-linear equilibrium
 - shallow nano-arches, 292–297
 - small-amplitude motion, 297–300
- Nonlinear frequency response curves (NFRCs), 662
- Nonlinear Helmholtz resonator, forced
 - oscillations of, 503–504
 - governing equation of, 504–505
 - homotopy analysis method, application of, 506–510
 - simulation, 510–511
- Nonlinear modal analysis (NMA)
 - benchmark model, 333–334
 - EPMC backbone, 334
 - frequency characteristics, 334
 - frequency responses, 334–336
 - modal coupling, 336–339
 - Rayleigh quotient-based NMA (RQNMA), 329–333
- Nonlinear modal coupling coefficients, 433
- Nonlinear normal modes (NNMs), 661
- Nonlinear supersymmetry, 515–522
 - algebra, 516
 - quantum anomalies and nonlinear supersymmetry, 517–522
- Nonlinear time transformation (NTT) method, 395, 396, 538
 - canard explosion, 403
 - perturbing non-Hamiltonian integrable systems, 402–403
- Non-Newtonian blood flow simulation, 30–31
- Non-smooth systems, PWL, 489–491
 - mechanical oscillator with contacting elements, 495–498
 - methodology, 491–494
 - voltage-dependent resistance, nonlinear analog circuit with, 498–500
- Non-stationary complex system, 891–895
- Non-stationary impulsive switched systems
 - dwelt time, 887
 - stability analysis
 - non-stationary complex, 891–895
 - non-stationary mechanical systems, 895–897
 - stability conditions, 890–891
- Non-stationary mechanical systems, 895–897
- N*-order Fourier series, 833

Normalized stability boundaries, 643
 Novozhilov's nonlinear shell theory, 144–146
 Numerical arc-length continuation method, 834
 Numerical integration, 490, 609, 657, 836
 Numerical simulations
 limit cycle computation, 688–689
 unemployment model, stability analysis of, 533–534

O

ODE system, 149
 Offshore cranes
 AOPS, 213
 boom deflection, 220
 box and lattice booms, 214
 optimization algorithm, 219
 optimization task, 217–219
 Protea, 220
 simulation results, 221
 statics and dynamic models, 213
 substitute crane model, 215–217
 values of reference parameters, 219
 vertical and horizontal courses, 222
 OGY-based state-feedback control, 684, 693
 One-dimensional supersymmetry, nonlinear aspects of, 515–517
 quantum anomalies and nonlinear supersymmetry, 517–522
 OpenFOAM package, 90
 Orr–Sommerfeld equation, 75
 Orthotropic stiffened flexible cantilevered cylinder
 Bernoulli–Euler's cantilever model, 120
 electric energy, 122
 electric power, 127, 129
 empirical mode decomposition, 126
 Hilbert transform, 126, 128
 hydrodynamic forces, 123
 IMF, 119–120, 126, 128
 in-line and cross-wise amplitudes, 119, 120
 kinetic energy, 121
 linear-elastic and piezoelectric behavior, 121
 non-conservative forces, 123
 nonlinear partial differential equations, 123
 potential energy, 121
 reduced-order model, 124
 simulation parameters, 126
 Strouhal number, 125
 system model, 121
 torsional moment of inertia, 122
 transverse amplitudes, 127

twisting–bending coupling, 127
 van der Pol equation, 124
 Oscillatory shear index (OSI), 44
 Overhung rotor systems (OH)
 breathing crack, 761
 finite element program, 762
 2-DOF lumped mass method, 762
 whirl orbit analysis, 761

P

Palmgren–Miner rule, 418
 Parameter transformation, 729
 Parametrically damped van der Pol (PDVDP) equation, 478
 parametric and external excitation, 481–483
 nonresonant case, 483–484
 sub-harmonic resonance of order 1/2, 484–485
 parametric excitation without external excitation, 479–480
 nonresonant case, 480
 sub-harmonic resonance of order 1/2, 481
 perturbation analysis, 478–479
 Parametric damping, 477–478
 Parametric instability, 641, 643, 646, 715
 Parametric reduced-order models (pROMs)
 accuracy performance, 379
 algorithmic process, 377
 Bouc model, 378
 CMS-based approach, 374
 Craig–Bampton (CB) approach, 374
 dominant approach, 374
 evaluation of, 381
 High Fidelity Model, 377, 380
 nonlinear feature inclusion, 375–376
 one-dimensional rod, 377–379
 stress approximation performance, 381
 substructural formulation, 376–377
 3D cantilever beam, 379–381
 Parametric resonance, 638
 Parseval theorem, 170
 Particle swarm optimization (PSO), 843
 Passive-dynamics biped walker
 model description, 684–685
 walking dynamics, model of, 686–687
 Passive dynamic walking, 683
 Pasternak-type model, 179
 P-bifurcation analysis, 866, 883, 886
 Period-doubling bifurcations (PDB), 683
 Periodic interval, 726
 Period- K fixed point, 687
 Peripheral artery diseases, 28

- Perpetual mechanical systems
 - analytical solution, 195–198
 - constant inertia coefficients, 193
 - differential equations, 191
 - equations of motion, 194
 - exact augmented perpetual manifolds, 190, 192–194, 196, 197
 - external force, 194
 - generalized coordinates and velocities, 192
 - inertia matrix, 192
 - internal forces, 195, 197
 - N-dof mechanical systems, 190
 - numerical solution
 - damping coefficient, 198
 - displacements, 198
 - excitation amplitude, 198
 - maximum absolute differences of time series, 199
 - maximum absolute value of internal forces of nonlinear and linear systems, 199
 - velocities, 198
 - reference k-mass external force, 191
 - 2-dof mechanical system, 194
 - zero velocity vectors, 194
- Perpetual points (PPs)
 - definition, 189
 - N-degrees of freedom, 190
 - role in dynamical system, 189
- Perturbation approach, 810–812
- Perturbation method, 170–174, 281, 282, 638, 853
- Perturbing Hamiltonian systems, 396–397
 - cubic Takens–Bogdanov bifurcation, 401
 - cuspidal loop, 401–402
 - quadratic Takens–Bogdanov bifurcation, 400–401
 - Rayleigh–Duffing mechanical oscillators, 397–400
 - Takens–Bogdanov, in reversible systems, 402
- Perturbing non-Hamiltonian integrable systems, 402–403
- Phase-locking value (PLV), 68
- Phase-plane CBC (PP-CBC), 50–56
- Phase resonance nonlinear mode (PRNM), 661, 666–670
- Physical data cloud reduction analysis
 - Euler Bernoulli beam, 824
 - intrinsic characteristic directions (ICDs), 822, 823
 - machine learning classical POD, 821
 - physical data cloud geometry, 824
 - physical geometry and dynamics features, 822
- Physics-informed neural networks (PINNs), 49
- Piecewise linear and nonlinear systems
 - auxiliary variable, 857
 - computational procedure, 858–859
 - convex analysis, 856
 - dynamics equations, 857
 - effective stiffness value, 855
 - elastic restoring force, 855
 - MDOF cases, 860
 - nonlinear time-varying oscillator, 860–861
 - phase diagrams of steady-state responses, 862
 - projection function, 856, 857
 - required CPU time (s) of proposed scheme, 861
 - SDOF system, 856
- Piecewise-linear (PWL) non-smooth systems, 489–491
 - mechanical oscillator with contacting elements, 495–498
 - methodology, 491–494
 - voltage-dependent resistance, nonlinear analog circuit with, 498–500
- Piecewise smooth system dynamics, 866–868
- Pierson–Moskowitz spectrum, 99
- Pitchfork bifurcations, 655, 704
- Pitch response dynamics, 881–882
- Planar slow–fast systems, 537
- Plane boundary, 88, 91–93
- Poincaré-invariant gauge theory, 515–516
- Poincaré map, 683, 687, 688, 691
- Poisson–Dirac brackets, 519
- Poisson’s ratio, 146, 181, 229, 362, 386, 389, 551
- Polynomial, 598
 - equalities, 599
 - inequalities, 599
 - models, 597
 - nonlinearities, 162–164
 - optimization problems, 600–604
- Post-Resonance Backward Whirl (Po-BW), 765–768
- Power law non-Newtonian model, 42
- Prandtl number, 78
- Prandtl stress function, 89
- Pre-resonance Backward Whirl (Pr-BW), 765, 776
- PRNM, duffing oscillator
 - fundamental resonance, 668–669
 - subharmonic resonances, 669
 - superharmonic resonances, 669

Probability density function (PDF), 427
 Prony shear relaxation, 41
 Proper orthogonal decomposition (POD), 374, 819
 PSO-NARX method, 845–846
 Pulsatile blood flow velocity, 30

Q

Quadratic manifold (QM), 361
 Quadratic nonlinear coefficients, 784
 Quadratic Takens–Bogdanov bifurcation, 400–401
 Quantum analog of the supercharges, 521
 Quantum anomalies, 517–522
 Quasi-exactly solvable Hamiltonians, 522
 Quasi-periodic (QP) regime, 798
 Quasi-saturation phenomenon, 791
 Quemada model, 31

R

RADAU5, 150
 Radial Basis Functions (RBFs), 454, 471
 Rain-flow cycle counting (RFC), 878–880
 Random variables, 677
 Random wind, 98, 101–102
 Rayleigh–Duffing oscillators, 396–400
 Rayleigh model damping, 245
 Rayleigh quotient-based NMA (RQNMA), 329–333
 Rayleigh-Ritz method, 147
 Rectification coefficient, 571
 Rectified linear unit (ReLU) activation, 426
 Reduced Hodgkin–Huxley (HH) model, 545–546
 Reduced-order model, 435–437
 Reduced-order modelling (ROM) strategy, *see* Shallow spherical shell
 Reproducing Kernel Hilbert Space (RKHS), 455
 Resonance mechanisms, 783
 Response analysis, IHB method, 445–446
 Reversible systems takens–Bogdanov, 402
 Reynolds number, 7, 66, 78, 80, 81
 R-functions method (RFM)
 FGM shallow shell on elastic foundation, 386
 first-order shear deformation theory (FSDT), 388
 higher order shear deformation shell theory (HSDT), 387
 mathematical formulation, 386–388
 shell stiffness, 387

shells with complex planform, 391–393
 shells with rectangular shape of plan, 389–390
 solution method, 388–389
 values of natural frequency parameter, 392
 Winkler and Pasternak parameters, 387
 Riemann integral, 99
 Riemann–Liouville derivative, 181, 187
 Rigid-liquid-flexible coupling system
 angular velocity response, 277, 344
 dynamic equations, 268–269
 flexible and rigid appendages, 277
 forces and torques of beam, 270–272
 forces and torques of liquid, 269–270
 liquid sloshing and liquid rigidization, 277
 methods of solution, 272–273
 mode superposition method, 271
 orbital driving force, 275–277
 response of, 275–278
 under step excitation, 273–275
 transverse elastic vibration, 270
 viscous damping coefficient, 271
 Ring-type gyroscopes
 actuator configurations, 252
 Coriolis forces, 247
 flexural mode shapes, 249
 Galerkin’s procedure, 247, 250
 magnetic permeability, 251
 mechanical damping ratio, 251
 nonlinear dynamic response, 248
 nonlinear electrometric force, 251, 252
 nonlinear equations of motion, 248–252
 phase diagram, 254
 Poincaré map, 254
 radial displacement, 253
 Rosin-Rammler diameter distribution, 43
 Rotating blade model, 784
 Runge-Kutta Dormand-Prince (RKDP) method, 833, 838
 Runge-Kutta method, 6, 12, 217, 497, 511, 788
 Rydberg atom arrays, 522–523

S

Saddle-node bifurcation (SN), 56, 645
 Satellite knot, 586
 Saturation phenomenon, 790, 791
 Scott–Blair model, 179
 Sea surface, 95, 99, 101–104
 Second-order dynamical systems, 609
 Second-order interpolation, 677–678
 with error estimation, 675–676
 Second-order normal form, 799
 Second-order Taylor expansion, 901

- Self-contact during continuation, 346
- Self-oscillation, 558, 560, 561
- Semi-definite problem, 604
- Serebrinsky–Ortiz (SO) model, 408
 - probabilistic decomposition-synthesis
 - method, simulation of loading time series using, 410–411
 - time-discretization of, 408–409
- Shallow nano-arches
 - Cartesian coordinates, 292
 - displacement-controlled mechanical tests, 295
 - Eringen’s two-phase model, 294
 - Galërkin’s technique, 295, 296
 - orthogonal tensor, 293
 - softening effect, 296
- Shallow spherical shell, 362, 364, 366–367
- Shear center (SC), 640
- Simple cell mapping method (SCM), 673
- Single-degree-of-freedom (SDOF) oscillators, 155, 156, 162–164, 831
- Single-side impact (SSI) motion, 861
- Slow-fast dynamics interactions, 818
- Small-amplitude motion, 297–299
- Soft robotic manipulators, 341–350
- Spherical caps
 - axisymmetric vibration, 143, 144
 - displacement fields expansion
 - clamped boundary conditions, 147
 - dofs of discretized system, 147
 - eigenfunctions, 146
 - generic mode of vibration, 146
 - hydrostatic external pressure, 148
 - Lagrange’s equations, 148
 - Lagrangian variables, 147
 - Rayleigh-Ritz method, 147
 - secular equation, 147, 148
- harmonic pressure
 - amplitude-frequency diagrams, 150
 - dimensions and material properties of structure, 149
 - displacement fields, 150
 - Fourier spectrum, 151, 152
 - period doubling bifurcations, 150, 151
 - Poincaré map, 151, 152
 - time history, 151, 152
- Novozhilov’s nonlinear shell theory, 144–146
- Novozhilov theory, 143
- Stability analysis, 737–738
 - incremental harmonic balance (IHB)
 - method, 446–447, 450–451
- Standard Model, 515–516
- STAR-CCM, 113
- State-dependent switching laws
 - switching between two different unstable delay subsystems, 905–907
 - switching of two delay values in unstable delayed subsystems, 907–910
- State-space model, 500
- Static equilibrium, 655, 657, 658, 819
- Step-load-induced transient response, 180
- Stochastic bifurcation analysis, 882–884
- Stochastic differential equations (SDEs), 866, 869
- Stochastic process, 98, 417, 775
- Stochastic resonance
 - dynamical systems, 771
 - rotating mechanisms
 - equation of fast motions, 774
 - equation of slow motions, 774–776
 - formulation of problem, 772–774
 - vibrational forces, 775
- Stokes-Cunningham drag law, 42
- Stribeck effect, 841
- Strouhal number, 65, 125
- Structural optimization, of nonlinear dynamic response, 433–434
 - adjoint method, design sensitivity analysis using, 438–439
 - finite element model and design variables, 434
 - optimization, 439, 440
 - optimization problems and sensitivities, 437–438
 - original objective function, 441
 - reduced-order model and frequency–amplitude relation, 435–437
- Subdivision algorithm, 675
- Subharmonic components, 616
- Subharmonic resonances, 662
 - even subharmonic resonances, 665–666
 - odd subharmonic resonances, 665
- Supercritical pitchfork bifurcation (PSP), 644
- Superharmonic components, 616
- Superharmonic resonances, 662
 - even superharmonic resonances, 665
 - odd superharmonic resonances, 664–665
- Supersymmetric quantum mechanics, 515, 516
- Surface tension, 75, 76, 83
- Switched delay system with two unstable subsystems
 - optimal switched curves design
 - Euler equation, 903
 - inverse transformation, 902
 - kinetic energy and potential energy, 902
 - performance index, 903
 - second-order Taylor expansion, 902

- state of the switched delay system, 905
- time histories with initial condition, 904
- state-dependent switching laws (*see* State-dependent switching laws)
- state-dependent switching mechanism, 901
- Switched system, 887–890
- Symbolic dynamics, 586, 587

T

- Takens–Bogdanov bifurcation, 398, 700
 - in heteroclinic case, 701
 - in homoclinic case, 701
 - Jacobian matrix, 701
- Takens–Bogdanov, reversible systems, 402
- Taylor expansions, 507
- Taylor series, 80, 184, 397, 539, 542, 632
- Term complexity, 817
- Thermal conductivity, 75, 76, 571, 572
- Thermal gradient, 788
- Thin conductive annular plate
 - ANSYS analysis, 225
 - dynamic stability, 226
 - electromagnetic forces, 226–227
 - induced magnetic field, 226–227
 - for isotropic, 227
 - Lyapunov exponent spectrum, 226
 - magnetoelastic nonlinear free vibration, 227–229
 - variation law
 - electromagnetic forces, 229–231
 - of natural frequency, 231–233
 - non-uniform magnetic field, 229–231
- Thin liquid film flow, 75
- Three-dimensional Lorenz system, 679
- Three-dimensional Vlasov beam FE model
 - enhanced Vlasov displacement-based element (EVDE)
 - cross-section warping, 316–318
 - displacement-based approach, 319
 - element variational formulation, 319–321
 - warping representation, 316–318
 - L portal frame, 322–324
 - numerical validation, 322–324
- 3D reduced-order model
 - aspirating pipes (*see* Cantilevered aspirating pipes)
 - cantilevered piezoelectric harvester (*see* Orthotropic stiffened flexible cantilevered cylinder)
- Three-frequency excitation, 741–743
- Time-averaged wall shear stress (TAWSS), 44
- Time-consuming process, 609

- Time-delay recurrent neural network (TDRNN), 842
- Time-delay system, 899, 907, 909
- Time-domain
 - equations of motion, 444
 - numerical method, 831
 - responses, 658
- Time integration methods, 6, 283, 853, 854
- Time-marching method, 838
- Time to failure (TTF), 422
- Time variational method (TVM), 610, 736
 - three-frequency excitation, 741–743
 - two-frequency excitation, 739–741
- Timoshenko force-based curved beam, 303
- Transient balancing methods, 749
- Trapezoidal rule (TR), 858
- Trivial equilibrium, 656
- Truncated Fourier series, 353
- Truss optimization
 - free vibration frequencies, 606
 - global stability constraints, 605–606
- Two-DOF mathematical model, 131, 133, 138, 194, 199
- Two-frequency excitation, 739–741
- Two-scale curved beam FE
 - dynamic response, 309–311
 - element mass matrix consistent, 306–308
 - flexibility matrix, 304–306
 - fundamental element equations, 304–306
 - masonry arches, 303, 308–309
- Type of nonlinearity, FE models, 368–369

U

- Ueda oscillator, 288
- Unemployment model, stability analysis of, 525–526
 - global stability analysis, 530–533
 - local stability analysis, 528–530
 - mathematical model, 526–527
 - non-dimensional model, construction of, 527–528
 - numerical simulations, 533–534
- Unforced linear oscillator, 667
- Unit Load method, 303

V

- van der Pol equation, with parametric damping, 477–478
 - parametric and external excitation, 481–483
 - nonresonant case, 483–484
 - sub-harmonic resonance of order 1/2, 484–485

- van der Pol equation, with parametric damping, 477–478 (*cont.*)
 - parametric excitation without external excitation, 479–480
 - nonresonant case, 480
 - sub-harmonic resonance of order 1/2, 481
 - perturbation analysis, 478–479
 - van der Pol system, 542
 - Variation law
 - electromagnetic forces, 229–231
 - of natural frequency, 231–233
 - non-uniform magnetic field, 229–231
 - Variation law of natural frequency
 - variation of natural frequency with $\alpha 0$, 231–233
 - variation of natural frequency with I , 231, 232
 - variation of natural frequency with t , 233, 234
 - Velocity coupling, 67, 69
 - Vibrational mechanics, 771, 778
 - Vibro-impact oscillator with discontinuous support, 867
 - Viscoelastic effects, 41
 - Viscoelastic Winkler-type foundation, 180, 183, 185–187
 - Viscosity with variable fluid properties
 - boundary conditions, 78
 - critical Reynolds number, 80
 - flow configuration, 77
 - Ginzburg–Landau equation for filtered waves, 81
 - governing equations, 77–78
 - infinitesimal perturbation, 79
 - long-wave expansion, 78–79
 - maximum amplitude, 82, 84
 - minimum amplitude, 83, 84
 - stability criteria, 81
 - time scale, 77
 - viscous-gravity length scale, 77
 - Viscous-gravity length scale, 77
 - Viscous scales, 76
 - Vlasov’s hypotheses, 637
 - von Karman equation, 180
 - von Mises stress, 44
 - Vortex-induced vibration (VIV), 132
 - applications, 65
 - aspirating pipes (*see* Cantilevered aspirating pipes)
 - orthotropic bending stiffness (*see* Orthotropic stiffened flexible cantilevered cylinder)
 - synchronization and lock-in, 66
 - wake oscillator model (*see* Wake oscillator model, VIV)
 - Vortex-Induced Vibration Aquatic Clean Energy (VIVACE), 119
 - Vortex-shedding frequency, 65
- W**
- WAFO toolbox, 880, 883
 - Wake oscillator model, VIV
 - linear structure oscillator, 69–70
 - non-linear structure oscillator
 - amplitude response to reduced flow velocity, 71
 - bifurcation diagrams of peak, 71
 - overlapped time series, 72
 - peaks of structural oscillations, 73
 - structural displacement and wake parameter, 67
 - structure, 67
 - synchronization measures, 68
 - Weber number, 78
 - Wendland functions, generalised interpolation using, 467–468
 - WendlandXool, 465–467
 - algorithm, 469–471
 - arrays, 473
 - Use/EXAMPLES, 471–472
 - Wendland functions, generalised interpolation using, 467–468
 - Wentzel, Kramers and Brillouin (WKB) transformation, 156
 - Whirl orbit analysis, 761
 - Wind-induced pressure, 96, 97
 - Winkler model, 169, 179
 - Witten’s supersymmetric model, 517–518
 - Wolf’s algorithm, 865, 870
- Y**
- Young’s modulus, 146, 551
- Z**
- Ziegler’s column, nonlinear dynamics of
 - amplitude modulations in, 718
 - piezoelectric effects, 711
 - pulsating follower force, 712, 715
 - van der Pol model, 711
 - Zoelly’s critical buckling pressure, 149